CHEMICAL REVIEWS

pubs.acs.org/CR

Review

A Review of Transition Metal Boride, Carbide, Pnictide, and Chalcogenide Water Oxidation Electrocatalysts

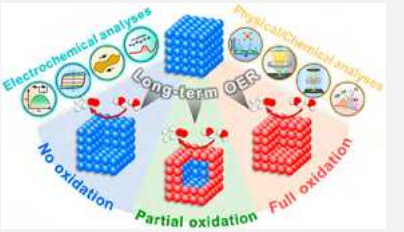
Kenta Kawashima,[†] Raúl A. Márquez,[†] Lettie A. Smith, Rinish Reddy Vaidyula, Omar A. Carrasco-Jaim, Ziqing Wang, Yoon Jun Son, Chi L. Cao, and C. Buddie Mullins*

Cite This: *Chem. Rev.* 2023, 123, 12795−13208

Read Online

ACCESS | Metrics & More | Article Recommendations

ABSTRACT: Transition metal borides, carbides, pnictides, and chalcogenides (*X*-ides) have emerged as a class of materials for the oxygen evolution reaction (OER). Because of their high earth abundance, electrical conductivity, and OER performance, these electrocatalysts have the potential to enable the practical application of green energy conversion and storage. Under OER potentials, *X*-ide electrocatalysts demonstrate various degrees of oxidation resistance due to their differences in chemical composition, crystal structure, and morphology. Depending on their resistance to oxidation, these catalysts will fall into one of three post-OER electrocatalyst categories: fully oxidized oxide/(oxy)hydroxide material, partially oxidized core@shell structure, and unoxidized material. In the past ten years (from 2013 to 2022), over 890 peer-reviewed research papers have focused on *X*-ide OER electrocatalysts. Previous review papers have provided limited conclusions and have omitted the significance of "catalytically active sites/species/phases" in *X*-ide OER electrocatalysts. In this review, a comprehensive summary of (i) experimental parameters (e.g., substrates, electrocatalyst loading amounts, geometric overpotentials, Tafel slopes, etc.) and (ii) electrochemical stability tests and post-analyses in *X*-ide OER electrocatalyst publications from 2013 to 2022 is provided. Both mono and polyanion *X*-ides are discussed and classified with respect to their material transformation during the OER. Special analytical techniques employed to study *X*-ide reconstruction are also evaluated. Additionally, future challenges and questions yet to be answered are provided in each section. This review aims to provide researchers with a toolkit to approach *X*-ide OER electrocatalyst research and to showcase necessary avenues for future investigation.



Downloaded via UNIV OF TEXAS AT AUSTIN on December 13, 2023 at 22:51:16 (UTC).
See https://pubs.acs.org/sharingguidelines for options on how to legitimately share published articles.

CONTENTS

1. Introduction 12796
1.1. Electrocatalytic Overall Water Splitting 12797
1.2. Earth-Abundant Water Oxidation Electrocatalysts 12798
1.3. Materials Electrooxidation Resistance Considerations 12798
1.4. Recommendations on Analytical Technique Selection 12800
Geometric Overpotential/Onset Potential 12800
Specific Overpotential/Onset Potential 12800
Mass Overpotential/Onset Potential 12801
1.5. Scope of This Review 12802
2. Transition Metal Borides 12803
2.1. Electrode Preparation Methods 12803
2.1.1. Solution-Based Methods 12803
2.1.2. Dip-Coating Methods 12815
2.1.3. Electroless Plating Methods 12816
2.1.4. Solid-State Reactions 12818
2.1.5. MOF-Derived Methods 12818
2.1.6. Other Methods 12820
2.2. Final Types of Boride-Based Electrocatalysts 12820
2.3. Structural and Chemical Compositional Effects toward OER Activity 12827
2.3.1. Monometallic Borides 12827
2.3.2. Metal-Doping/Substitution Effects 12829
2.3.3. Composite Materials Effects 12831
2.3.4. pH Effects 12833
2.4. Challenges 12834
3. Transition Metal Carbides 12835
3.1. Electrode Preparation Methods 12836
3.1.1. Hydrothermal Methods 12836
3.1.2. MOF-Derived Methods 12836
3.1.3. Solid-State/Gas-Solid Reactions 12845
3.1.4. Other Methods 12845
3.2. Final Types of Carbide-Based Electrocatalysts 12847
3.2.1. Catalysts 12847

Received: January 6, 2023
Revised: August 10, 2023
Accepted: August 11, 2023
Published: November 15, 2023



ACS Publications

© 2023 American Chemical Society

https://doi.org/10.1021/acs.chemrev.3c00005
Chem. Rev. 2023, 123, 12795−13208

3.2.2. Precatalysts 12848
3.3. Structural and Chemical Compositional Effects toward OER Activity 12850
3.3.1. Monometallic Carbides 12850
3.3.2. Metal-Doping Effects 12851
3.3.3. Multi-cation Effects 12853
3.3.4. Composite Materials Effects 12854
3.4. Challenges 12856
4. Transition Metal Pnictides 12858
4.1. Transition Metal Nitrides 12858
4.1.1. Electrode Preparation Methods 12858
4.1.2. Final Types of Nitride-Based Electrocatalysts 12871
4.1.3. Structural and Chemical Compositional Effects toward OER Activity 12874
4.1.4. Challenges 12887
4.2. Transition Metal Phosphides 12888
4.2.1. Electrode Preparation Methods 12888
4.2.2. Final Types of Phosphide-Based Electrocatalysts 12911
4.2.3. Structural and Chemical Compositional Effects toward OER Activity 12917
4.2.4. Challenges 12931
5. Transition Metal Chalcogenides 12935
5.1. Transition Metal Sulfides 12936
5.1.1. Electrode Preparation Methods 12936
5.1.2. Final Types of Sulfide-Based Electrocatalysts 12984
5.1.3. Structural and Chemical Compositional Effects towards OER Activity 13008
5.1.4. Challenges 13030
5.2. Transition Metal Selenides 13034
5.2.1. Electrode Preparation Methods 13034
5.2.2. Final Types of Selenide-Based Electrocatalysts 13066
5.2.3. Structural and Chemical Compositional Effects toward OER Activity 13079
5.2.4. Challenges 13089
5.3. Transition Metal Tellurides 13093
5.3.1. Electrode Preparation Methods 13093
5.3.2. Final Types of Telluride-Based Electrocatalysts 13103
5.3.3. Structural and Chemical Compositional Effects toward OER Activity 13107
5.3.4. Challenges 13110
6. Transition Metal-Based Polyanion Compounds/Composites 13111
6.1. Compounds 13112
6.1.1. Catalysts 13112
6.1.2. Precatalysts 13121
6.2. Composites 13127
6.2.1. Catalysts 13127
6.2.2. Precatalysts 13128
7. Identifying Active Species/Sites Using Special Characterization Techniques 13134
7.1. Vibrational Spectroscopy 13135
7.2. UV−vis Spectroscopy 13137
7.3. X-ray Absorption Spectroscopy 13138
7.4. Electron Microscopy 13141
7.5. Surface-Sensitive Techniques 13144
7.5.1. X-ray Photoelectron Spectroscopy 13145
7.5.2. Scanning Probe Microscopy 13146
7.6. Multi-elemental Analysis 13149
7.7. Mass Spectrometry 13153
7.8. Other Advanced Characterization Techniques 13154
7.9. Important Remarks and Guidelines for Selecting Special Characterization Techniques 13156
7.10. Lab-Scale Electrochemical Testing toward Practical Application 13160
7.11. Advanced Technologies for Further Developing *X*-ide Electrocatalyst Research 13162
8. Conclusions and General Recommendations 13164
8.1. Overview and Summary of *X*-ide Electrocatalysts 13164
8.2. Best Practices for Studying *X*-ide Precatalysts 13166
8.3. Current Stage of *X*-ide Studies and Developments and Future Directions 13168
Author Information 13168
Corresponding Author 13168
Authors 13168
Author Contributions 13168
Notes 13169
Biographies 13169
Acknowledgments 13169
References 13169
Note Added after ASAP Publication 13208

1. INTRODUCTION

World economic growth relies on the huge consumption of energy, and the amount of energy consumption is still expanding with population growth,[1] mass production of foods and daily necessities,[2] and so forth. Nowadays, 83.1% of global primary energy consumption depends on fossil fuels such as oil (31.2%), natural gas (24.7%), and coal (27.2%).[3] However, it is well-known that fossil fuels are limited resources and will be exhausted in the future (see Figure 1). Even worse,

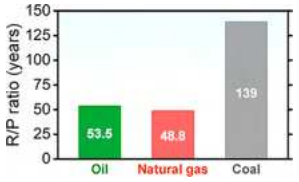


Figure 1. Ratio of reserves to production (R/P ratio: minable years) of fossil fuels (oil, natural gas, and coal) at the end of 2020. (Adapted from ref 3.)

while using/combusting fossil fuels, pollutants (e.g., SO_x, N_xO_y, CO, and CO_2) are generated and cause severe global problems such as the greenhouse effect, acid rain, and other environmental pollution.[4] Accordingly, in order to construct an environmentally sustainable economy before the natural systems are permanently damaged, it is essential to harvest energy from renewable resources (sunlight, wind, rain, tides, waves, geothermal heat, and plants). So far, through the efforts of many scientists, renewable energy (apart from hydroelectricity) currently accounts for 5.7% of global primary energy consumption.[3] Moreover, it is expected that the share of renewable energy in global primary energy will increase to 35% at least by 2050.[5] However, the stability and scope of renewable energy supplies are restricted by geographical and

https://doi.org/10.1021/acs.chemrev.3c00005
Chem. Rev. 2023, 123, 12795−13208

meteorological parameters. To ease these restrictions and further increase the use of renewable energy, environmentally benign energy conversion and storage systems must be built.

1.1. Electrocatalytic Overall Water Splitting

One of the promising energy conversion/storage methods is electrochemical overall water splitting, which converts electrical energy to chemical energy (i.e., hydrogen).[6] As shown in Figure 2, a typical water electrolyzer mainly consists

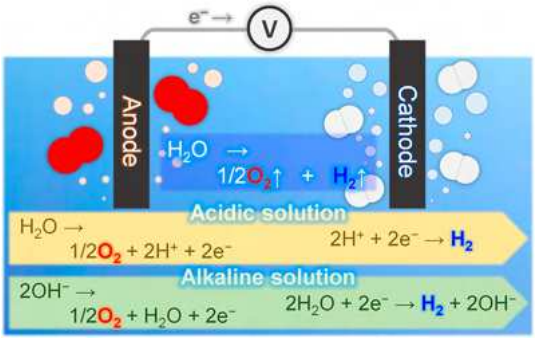


Figure 2. Schematic illustration of a typical water electrolyzer.

of four components: an anode for the oxygen evolution reaction (OER), a cathode for the hydrogen evolution reaction (HER), an aqueous electrolyte, and an external voltage supply. Depending on the pH (potential of hydrogen) value of the aqueous electrolyte, the overall water-splitting reaction mechanism can be described as the following:[7]

In an acidic solution:

$$\text{Anode: } 2H_2O_{(l)} \rightarrow O_{2(g,1\ atm)}\uparrow + 4H^+ + 4e^- \quad E^\circ = 1.23\ V_{SHE} \tag{1}$$

$$\text{Cathode: } 4H^+ + 4e^- \rightarrow 2H_{2(g,1\ atm)}\uparrow \quad E^\circ = 0.00\ V_{SHE} \tag{2}$$

$$\text{Total: } 2H_2O_{(l)} \rightarrow O_{2(g,1\ atm)}\uparrow + 2H_{2(g,1\ atm)}\uparrow \quad E^\circ_{cell} = -1.23\ V \tag{3}$$

In an alkaline solution:

$$\text{Anode: } 4OH^- \rightarrow O_{2(g,1\ atm)}\uparrow + 2H_2O_{(l)} + 4e^- \quad E^\circ = 0.40\ V_{SHE} \tag{4}$$

$$\text{Cathode: } 4H_2O_{(l)} + 4e^- \rightarrow 2H_{2(g,1\ atm)}\uparrow + 4OH^- \quad E^\circ = -0.83\ V_{SHE} \tag{5}$$

$$\text{Total: } 2H_2O_{(l)} \rightarrow O_{2(g,1\ atm)}\uparrow + 2H_{2(g,1\ atm)}\uparrow \quad E^\circ_{cell} = -1.23\ V \tag{6}$$

where E° represents the standard reduction potential (at pH = 0 and 14) versus standard hydrogen electrode (V_{SHE}) in aqueous solutions at 25 °C.[8]

Hydrogen produced via water splitting offers a clean fuel and chemical feedstock crucial to achieving the multi-sector decarbonization to meet the net-zero emission scenario in 2050.[9] Hydrogen has an energy density of 140 MJ/kg H_2, higher than those of numerous existing hydrocarbon fuels.[10] Therefore, hydrogen has the potential to be utilized in place of fossil fuels in a wide variety of applications, including energy-intensive sectors such as steel[11] and cement[12] production or in the transportation industry to store and provide electric power.[13] In fact, transportation is the sector with the majority of the growing policy support in hydrogen technologies worldwide, providing a clear direction for its future with new economic challenges and opportunities.[14] Hydrogen-powered vehicles driven by hydrogen fuel cells offer an overall efficiency of up to 60%.[15] They have attained an average mileage range of 60 miles/kg H_2, higher than that of conventional vehicles, around 25 miles/gallon of gasoline (one kilogram of hydrogen contains the same energy as a gallon of gasoline), with a price of US$ 13/kg H_2.[16]

Using hydrogen as an energy carrier has several advantages. For example, when deriving energy from hydrogen via its combustion ($2H_2 + O_2 \rightarrow H_2O$: a zero deleterious gas emission process), environmentally harmful products are not generated. Moreover, as a chemical feedstock, hydrogen also can be used for the production of useful and valuable chemicals (ammonia and other nitrogenated compounds, methanol, ethanol, dimethyl ether, etc.).[6]

Despite the merits of hydrogen production through electrochemical overall water splitting being well-known for nearly two centuries, its applications are still limited because of the expensive price of electrolysis-derived hydrogen. Only ~4% of global hydrogen production is currently realized by electrochemical overall water splitting.[6,17] Compared to the current hydrogen production technologies such as steam reforming of methane (SRM) and coal gasification with considerable CO_2 emissions [10 kg CO_2e/kg H_2 (CO_2e = carbon dioxide equivalent)],[18] hydrogen produced from water electrolysis exhibits two main advantages: (1) a higher purity (>99.9%),[19] thereby avoiding extra cleaning steps, and (2) a lower carbon footprint, with 0.85 kg CO_2e/kg H_2 when it is powered by a low-carbon electricity source such as wind (also known as green hydrogen).[18]

Water electrolysis has led hydrogen production to be a subject of great interest and potential for achieving decarbonization in the electricity, transport, and industry sectors. According to the U.S. Department of Energy (DOE), the ultimate target for water electrolysis is an energy efficiency of 46 kWh/kg H_2 with a cost of US$ 1/kg H_2 by 2031, utilizing proton exchange membrane (PEM) electrolysis technology and clean electricity with a price of ≤US$ 0.03/kWh.[20]

To expand the production of electrolysis-derived hydrogen and meet the requirements for the global decarbonization transition, further improvement in the overall system efficiency must be achieved by using proper OER and HER electrocatalysts to realize a substantial cost-decrease in the production of hydrogen. Here, in order to understand the general role of electrocatalysts in water splitting, we briefly discuss the operational voltage for electrocatalytic overall water splitting. From a thermodynamic point of view, the necessary voltage for water splitting is 1.23 V (at 1 atm and 25 °C) and does not depend on the reaction media. However, extra voltage must be applied to bring about the water-splitting reaction at a practical rate. Accordingly, the practical operational voltage (V_{OP}) for overall water splitting can be expressed as below:[21]

$$V_{OP} = 1.23\ V + \eta_{OER} + |\eta_{HER}| + \eta_\Omega \tag{7}$$

where η_Ω is the voltage to compensate the internal resistance of the cell (i.e., solution resistance and contact resistance) and

https://doi.org/10.1021/acs.chemrev.3c00005
Chem. Rev. 2023, 123, 12795−13208

η_{OER} and η_{HER} are the anodic and cathodic overpotentials to overcome the kinetic barriers derived from the OER (1,4) and HER (2,5), respectively. The internal resistance can be reduced by optimization of the cell design.[22] Additionally, at the laboratory level, η_{Ω} can be determined with *iR* compensation using an electrochemical workstation or deducted from raw data by multiplying current density and resistance from the Nyquist plot.[23] Note that the electrocatalysts are used for minimizing the reaction-specific kinetic barriers, resulting in lower overpotentials for the OER (η_{OER}) and HER (η_{HER}). Commercially useful electrocatalysts will need to satisfy most or all of these requirements: (i) low intrinsic overpotentials for the target reactions, (ii) highly active surfaces for the efficient molecular transport of gas- or liquid-phase reactants and products, (iii) high electrical conductivity, and (iv) high chemical, electrochemical, and mechanical stabilities.[17]

Generally, electrocatalytic overall water splitting is mainly limited by the sluggish kinetics of the OER.[24] This is because the 4-electron OER involves many intermediates (i.e., O*, HO*, HOO*) and is more complicated than the 2-electron HER.[24−26] Therefore, further research on OER electrocatalysts is of high importance. To date, researchers have reported ruthenium oxide (RuO_2) and iridium oxide (IrO_2) as benchmark OER electrocatalysts having overpotentials at 10 $mA{\cdot}cm_{geo}^{-2}$ (η@10 $mA{\cdot}cm_{geo}^{-2}$) of ∼280 and ∼340 mV in acidic media and ∼290 and ∼390 mV in alkaline medium, respectively.[27] However, since ruthenium and iridium are not abundant elements and both RuO_2 and IrO_2 dissolution occurs during OER operation (regardless of the pH value of an aqueous electrolyte, their dissolution amount increases in the following order: $IrO_2 < RuO_2$),[28] their industrialization is not realistic.

1.2. Earth-Abundant Water Oxidation Electrocatalysts

Thus far, low-cost transition metal oxides and (oxy)hydroxides [as typified by MO_x, $SrMO_3$, and MO_xH_y (*M* = Mn, Fe, Co, and Ni)] have been studied as promising oxygen evolution electrocatalysts with high stability.[29−31] Our group as well as many others has studied the improvement of their OER activity through morphological,[32,33] crystal structural,[34,35] elemental composition,[36,37] synthetic,[38−40] and complex formational approaches.[41−44] However, their low electrical conductivities and poor catalytic kinetics, which lower the activity of OER electrocatalysts, have plagued many researchers.[45,46] Recently, transition metal borides, carbides, pnictides, and chalcogenides [transition metal *X*-ide: MX_y (*M* = transition metal element; *X* = B, C, N, P, S, Se, and Te)] and transition metal-based polyanion compounds/composites (e.g., Se-modified Ni_3S_2,[47] P-substituted $CoSe_2$,[48] nano-polycrystalline Ni−S−P−O,[49] amorphous Fe−Ni−P−B−O,[50] $NiSe_2$/Ni_2P@FeP nanosheets,[51] etc.) have been increasingly (exponential-like) reported as alternative OER electrocatalysts (see Figure 3),[23,52−79] because they can demonstrate high electrical conductivity and excellent catalytic kinetics resulting in superior OER activity while maintaining electrocatalytic performance for tens of hours. For example, according to a state-of-the-art report,[80] the metallic iron and dinickel phosphide hybrid (FeP/Ni_2P) directly fabricated on nickel foam recorded a surprisingly low overpotential of 154 mV at 10 $mA{\cdot}cm_{geo}^{-2}$ in alkaline medium with a quite small Tafel slope of 22.7 $mV{\cdot}dec^{-1}$ in the lower overpotential ranges. To the best of our knowledge, this OER performance is the highest among MX_y-based OER electrocatalysts reported so far. Moreover, this hybrid electrocatalyst successfully delivered 100 $mA{\cdot}cm_{geo}^{-2}$ at 1.47 V_{RHE} for 24 h without any significant decay of its OER performance.[80] However, transition metal borides, carbides, pnictides, and chalcogenides are generally less thermodynamically stable than transition metal oxides under oxidizing potentials and are susceptible to oxidation under OER conditions.[81,82] Their oxidation possibilities make it extremely difficult to clarify the dominant factors for achieving high OER performance and for understanding their chemical and oxidative stress resistance.

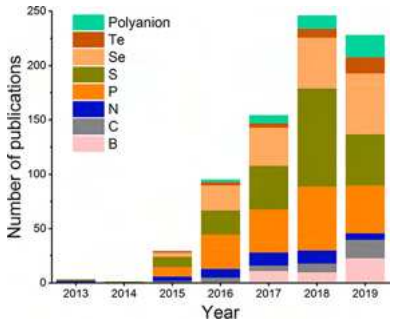


Figure 3. Growth of the number of the MX_y-based OER electrocatalyst publications per year from 2013 to 2019.

1.3. Materials Electrooxidation Resistance Considerations

In this section, we discuss the oxidation resistance of transition/rare-earth metal borides carbides, pnictides, chalcogenides, and oxides in detail on the basis of their reported enthalpies of formation; in particular, we highlight the different electrooxidation behaviors of transition metal-based materials with specific examples. The enthalpies of the formation of certain metal borides, carbides, pnictides, chalcogenides, and oxides with different stoichiometric ratios (*M*/*X* or *M*/O) and crystal structures are shown in Figure 4.[83−85] Here, the more thermodynamically stable the compound becomes, the more negative its enthalpy of formation is. As shown in Figure 4a, metal-based materials containing an element of Group 13, 14, or 15 of the periodic table have lower stabilities compared to their oxide counterparts. The average enthalpy of formation for each Group follows the order: O < P < N < B < C for *MX* and M_2X and O < P < B < C < N for MX_2.[83,84] On the other hand, most of the Group 16 compounds (i.e., chalcogenides) show a decreasing trend in their enthalpies of formation in the following order: O < S < Se < Te for 2H- and 1T-MX_2 (see Figure 4b).[85] These results imply that metal sulfides, selenides, and tellurides are generally less stable than their oxide counterparts. Furthermore, Ciraci *et al.* investigated the stabilities of 88 different MX_2 models [i.e., transition metal dioxides (MO_2) and dichalcogenides (MX_2; *X* = S, Se, Te) with 1T (one-layer unit cell, trigonal) and 2H (two-layer unit cell, hexagonal) crystal structures] via first-principles structure optimization and phonon calculations based on density functional theory (DFT). This study revealed that their stabilities strongly depend on the transition metals and crystal structures, and several of them may be able to be produced experimentally.[86] To examine the thermodynamic stabilities of the metal borides, carbides, pnictides, chalcogenides, and oxides, it is necessary at least to consider anion/cation-, stoichiometric *M*/*X* ratio-, and crystal structure-dependent contributions. It is noteworthy that, from the above-reported results, metal oxides are much more thermodynamically stable

https://doi.org/10.1021/acs.chemrev.3c00005
Chem. Rev. 2023, 123, 12795−13208

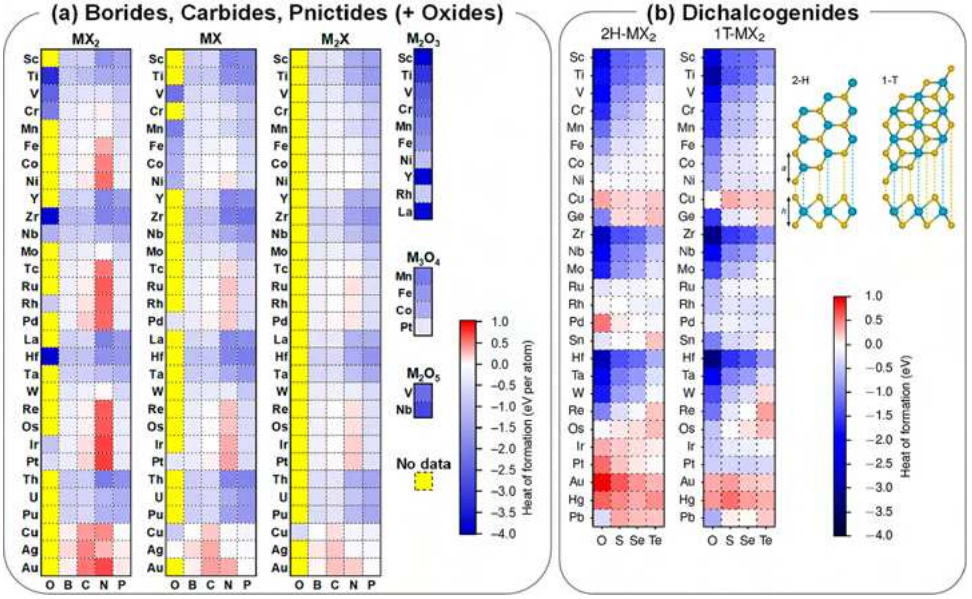


Figure 4. Calculated heat of formation for (a) the metal borides, carbides, pnictides, and oxides with different chemical compositions as well as (b) the metal dichalcogenides and dioxides with different crystal phases. (Adapted from refs 83 and 84.) The inset shows the crystal structures of the monolayer metal dichalcogenides and dioxides with 2H and 1T phases. Figure 4b is reprinted with permission from ref 85. Copyright 2015 American Chemical Society.

than their boride, carbide, pnictide, and chalcogenide counterparts in most cases. Until this point, we have attempted to predict the trend of oxidation resistance of various *X*-ides and oxides using their enthalpies of formation, but enthalpies of formation primarily indicate the material's thermal stability and may not directly correlate with the material's behavior under OER conditions (one may need to consider applied potentials and electrolyte pH values). Note that to check whether a certain material undergoes oxidation under a certain potential and pH, we can still use theoretical calculations. For example, Liu *et al.* recently performed exhaustive phase-diagram calculations on 14 transition metal *X*-ides and oxides (i.e., MoC, ZrN, and various oxides) and found that generally, almost none of them would remain stoichiometrically pristine surfaces (they tend to be either covered by O*/HO* at moderate/high potential or H* or vacancy even at low potential).[82] Additionally, the electrochemical stability maps (Pourbaix diagrams and Gibbs free energy overlays) of various *X*-ides computationally produced in the Materials Project (https://materialsproject.org/) are also useful for predicting their oxidation resistance under the potential and pH of interest.[87−89] The assumptions provided by the Materials Project align with our experimental data in the previous works,[47,90] demonstrating the oxidation of *X*-ides under alkaline OER conditions. Based on the above discussion, one would preliminarily predict that all transition metal boride, carbide, pnictide, and chalcogenide materials are spontaneously/electrochemically and (almost) fully oxidized into their corresponding oxides/(oxy)hydroxides at OER potentials (e.g., operational potentials at 10 mA·cm$_{geo}^{-2}$), an idea partially supported by several studies on $Co_3C \rightarrow CoO_x$,[91] Co_xN_y ($Co_2N_{0.67}$ + $Co_{5.57}N$) → CoO_x,[92] $Ni_3N \rightarrow NiOOH$,[90] $MP \rightarrow MOH$ (M = Fe, Co, Ni),[93] NiS (NiS + Ni_9S_8) → NiO_x,[94] $Ni_3S_2 \rightarrow NiO_x$,[94] $NiSe \rightarrow NiO_xH_y$,[95] $MX_2 \rightarrow MOOH$ (M = Fe, Co, Ni; X = S, Se, Te),[96−99] and $CoSe_{1.26}P_{1.42} \rightarrow CoOOH$.[48]

However, contrary to our expectations, it was reported that some MX_y materials were hardly oxidized into their oxide/(oxy)hydroxide counterparts during long-term OER testing. For instance, Nath *et al.* reported that Ni_3Se_2 and Ni_3Te_2 exhibited relatively low overpotentials at 10 mA·cm$_{geo}^{-2}$ (180 and 290 mV) and 24 and 42 h of continuous OER testing without any significant changes in their chemical composition and crystal structures in alkaline medium, respectively.[100,101] Moreover, according to a number of recent studies,[57] transition metal boride, carbide, pnictide, and chalcogenide electrocatalysts could demonstrate various degrees of oxidation resistance under OER potentials due to their differences in chemical composition, crystal structure, and morphology. Three possible catalyst structures result, as demonstrated in Figure 5: fully oxidized oxide/(oxy)hydroxide (MO_x/MO_xH_y),

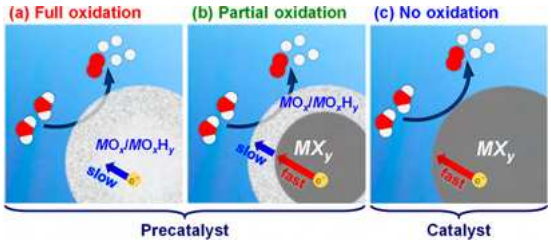


Figure 5. Schematic illustrations of different electrochemical oxidation degrees [(a) > (b) > (c)] on transition metal borides, carbides, pnictides, and chalcogenides after long-term OER testing.

partially oxidized core@shell (MX_y@MO_x/MO_xH_y), and unoxidized (MX_y). Importantly, even partially or fully oxidized MX_y materials [i.e., (amorphous) MO_x/MO_xH_y parts] can work as highly active OER electrocatalysts. The resultant MO_x/MO_xH_y products are electrocatalytically active for the OER and show significantly higher surface areas than the initial materials, increasing the number of OER active sties. The volume expansion results from the replacement of X by O/OH with the increase in the oxidation state of M.[91] Also, the possible electrocatalyst structures after OER testing can be

https://doi.org/10.1021/acs.chemrev.3c00005
Chem. Rev. 2023, 123, 12795−13208

further classified into two major types: "catalyst" (Figures 5a and b) and "precatalyst" (Figure 5c). Here, precatalyst denotes MX_y material which can be partially or fully transformed to active OER species (MO_x/MO_xH_y) under OER potentials. As defined by Wygant *et al.*,[57] MX_y and MO_x/MO_xH_y in catalysts and precatalysts are regarded as the real catalytically-active species for the OER. The investigation of MX_y electrooxidation resistances can clarify whether their real catalytically active species are MX_y or MO_x/MO_xH_y, which is quite useful in explaining electrocatalytic function as well as designing highly efficient electrocatalysts and devices. However, one of the major problems in this research field today is that many researchers have evaluated precatalysts' oxidation resistances under long-term OER testing conditions mainly via cyclic voltammetry (CV) and chronoamperometry (CA)/chronopotentiometry (CP), as is the case with conventional electrocatalysts. These methods give false interpretations, which will be discussed in detail later in the next section.

Among the three possible types, the $MX_y@MO_x/MO_xH_y$ core@shell structure drew special attention due to its high conductivity (metallic core), a large number of active species (oxide/oxyhydroxide shell), and synergistic effects between the core and shell, which all contribute to superior OER performance.[102−107] However, even though the core@shell electrocatalysts show somewhat high stability during long-term OER testing (a few tens of hours) at the laboratory level, the possibility of further oxidation of their cores should be considered for practical use. For practical reasons, commercialized alkaline electrolysis systems are normally forced to deliver high current densities of 250−450 $mA{\cdot}cm_{geo}^{-2}$,[108] which may drive further oxidation of the core in the core@shell. Conversely, the transition metal oxide/(oxy)hydroxide derived from the corresponding MX_y may act as a protective layer toward its further oxidation under OER conditions. Accordingly, further studies that investigate the oxidation resistance of "full oxidation" and "partial oxidation" MX_y types under OER conditions with high potential applied are strongly encouraged in the near future.

1.4. Recommendations on Analytical Technique Selection

In this section, we discuss the electrocatalytic OER activity and stability evaluation metrics for catalyst- and precatalyst-type MX_y materials to form an accurate estimation of their potentials as efficient OER electrocatalysts. We first introduce the typical evaluation metrics and particularly focus on the thorny issues (as discussed briefly in a previous perspective)[57] that prevent us from better understanding the electrocatalytic OER activity and stability of catalysts as well as precatalysts and provide the specific solutions for them.

Experimentally, the summative activity of each OER electrode is firstly examined by checking the overpotential or onset potential through linear sweep voltammetry (LSV) or CV in a three-electrode setup, in which one needs to use an appropriate reference electrode depending on the nature of an electrolyte solution.[109−111] In general, the overpotential and onset potential, which are required to achieve the given current density normalized in three different ways (Figure 6), are the deviation of the potential applied to the electrode from the equilibrium potential [i.e., the potential of the oxygen evolution/reduction reaction (OER/ORR)].[112] Specifically, the overpotential is the extra potential to drive the electrochemical reaction spontaneously at a certain reaction rate, while the onset potential, an ill-defined term,[22,113] can be

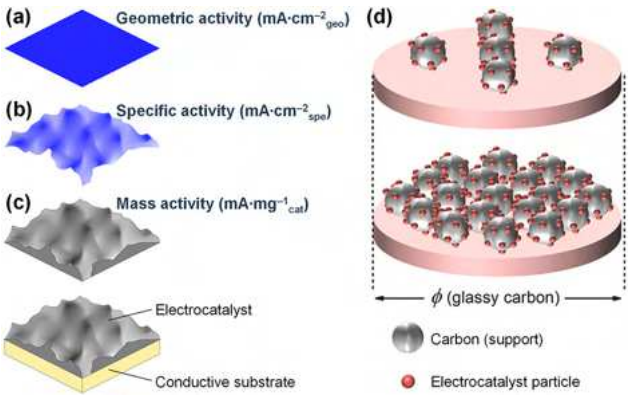


Figure 6. Schematic illustration of a model electrocatalyst surface that visualizes three current densities normalized to (a) projected geometric area, (b) surface area, and (c) mass loading. (Adapted from ref 114.) (d) Schematic illustration of the electrocatalyst-loading mass effect on the geometric overpotential/onset potential of the powder-based (drop-casted) electrode. Reproduced with permission from ref 115. Copyright 2018 Wiley.

defined as the potential at which faradaic current starts to drastically increase in an LSV or CV curve. Additionally, the summative activity of the OER electrode can be determined mainly by these four factors: (i) the intrinsic activity of the electrocatalyst, (ii) the loading mass of the electrocatalyst (i.e., the number of OER active sites), (iii) the surface structural design of the electrocatalyst (i.e., the surface area), and (iv) the synergistic effect of the interaction between electrocatalyst and substrate. Herein, to simplify the following discussion by ignoring factor (iv), we assumed that the same substrate material is used for all the experimental cases in this section. In addition, the overpotential/onset potential has various characteristics depending on the method for normalizing the current,[72,113,114] as described in more detail below:

Geometric Overpotential/Onset Potential. Geometric overpotential (η_{geo}: $\eta@x$ $mA{\cdot}cm_{geo}^{-2}$) and onset potential (E_{geo}: $E_{onset}@x$ $mA{\cdot}cm_{geo}^{-2}$) are defined as the potentials normalized to the current divided by the projected geometric area of the electrode (see Figure 6a), which are good for evaluating the total device performance.[113−115] For the half-cell reactions of water splitting, a current density of 10 $mA{\cdot}cm_{geo}^{-2}$ is utilized to determine the overpotential, which comes from artificial photosynthesis considerations for solar water-splitting. Specifically, 10 $mA{\cdot}cm_{geo}^{-2}$ is the approximate current density expected in a solar water-splitting cell with 10% solar-to-fuel conversion efficiency, which is the target value for practical use, under one sun illumination.[115] Additionally, for determining the onset potential, 0.5−2 $mA{\cdot}cm_{geo}^{-2}$ is a widely accepted value.[22] Note that the geometric overpotential and onset potential are unable to represent the intrinsic activity of the electrocatalyst because these figures of merit cannot neglect both the electrocatalyst-loading and surface structure dependences (Figures 6b and d).[114,115] In order to evaluate the intrinsic activity of the electrocatalyst, the overpotential/onset potential should be normalized to the current per a quantified parameter (e.g., the number of OER active sites on the electrode or the surface area of the electrocatalyst).[115]

Specific Overpotential/Onset Potential. Specific overpotential (η_{spe}: $\eta@x$ $mA{\cdot}cm_{spe}^{-2}$) and onset potential (E_{spe}: $E_{onset}@x$ $mA{\cdot}cm_{spe}^{-2}$) are normalizing the potentials to the current divided by the surface area of the electrocatalyst (see

https://doi.org/10.1021/acs.chemrev.3c00005
Chem. Rev. 2023, 123, 12795−13208

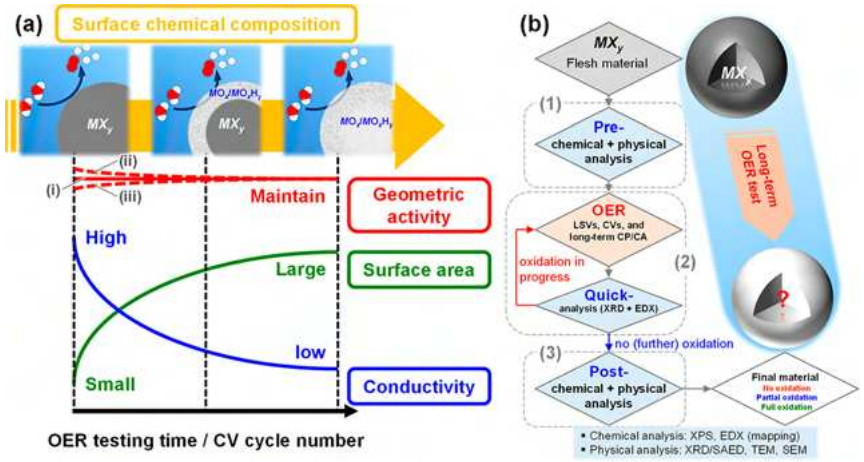


Figure 7. (a) Long-term electrooxidation of transition metal borides, carbides, pnictides, and chalcogenides affecting their geometric stabilities (i.e., $\eta@x$ mA·cm$_{geo}^{-2}$ or $\eta@x$ mA·mg$_{cat}^{-1}$) for the OER. (b) Suggested workflow for judging the final states of transition metal borides, carbides, pnictides, and chalcogenides for use as OER electrocatalysts.

Figure 6b), which can be reasonable activity metrics to reflect the intrinsic activity of the electrocatalyst.[113−115] Generally, the surface area of the electrocatalyst can be determined using the electrochemically active surface area/electrochemical surface area (ECSA) method [reversible surface redox reaction (at metal oxides) or double layer capacitance (C_{dl})], atomic force microscopy (AFM), the Brunauer−Emmett−Teller (BET) method, and electron microscopy.[113] According to a tutorial review,[113] out of the above five techniques, the C_{dl}-based ECSA method is currently the most facile and has high accuracy to some extent. The C_{dl}-based ECSA can be determined by dividing C_{dl} by the specific capacitance (C_s). The typical C_s values reported for metal electrodes are 0.015−0.110 mF·cm^{-2} in H_2SO_4 aqueous solution and 0.022−0.130 mF·cm^{-2} in NaOH/KOH aqueous solution.[116] For more details about the surface area measuring techniques, please see ref 113.

Mass Overpotential/Onset Potential. Mass overpotential (η_{mass}: $\eta@x$ mA·mg$_{cat}^{-1}$) and onset potential (E_{mass}: $E_{onset}@x$ mA·mg$_{cat}^{-1}$) are the potential normalized to the current per unit loading mass of the electrocatalyst (see Figure 6c), which can indicate the cost-effectiveness of a selected electrocatalyst for a target reaction, which may predominantly vary along with its specific surface area but cannot represent the intrinsic activity of the electrocatalyst.[113,114] This is because the electrocatalyst particle size (i.e., the surface area of the electrocatalyst) is the dominant factor for the potential per unit mass, and this factor is closely related to the number of active sites. Accordingly, for example, electrocatalysts with smaller particle sizes are able to demonstrate lower mass overpotential/onset potential. Furthermore, as the definitions of mass overpotential and onset potential assume that all atoms within the loaded electrocatalysts are active sites,[114] these figures of merit are applied to the electrocatalysts with high specific surface areas (e.g., nanoparticle, nanosheet, and so forth) for preference.

So far, from a practical application perspective, many electrochemists have put almost all their energy into finding strategies to significantly lower the geometric/mass overpotential/onset potential of the arbitrary MX_y for the OER through the optimization of the electrode surface morphology to maximize the OER active site number per unit area. However, as previously stated, geometric and mass overpotentials/onset potentials are the figures of merit for evaluating the summative OER performance of the electrode, in which the (i) ∼ (iii) factors are complexly intertwined. Hence, just checking geometric and mass overpotentials/onset potentials is not enough to know how intrinsically active the electrocatalyst is. The "true" ranking of the MX_y for efficient OER can be created when their intrinsic OER activities are quantitatively compared by experimentally confirming their specific overpotentials/onset potentials, which is thus essential to publish articles investigating a series of *X*-ide OER electrocatalysts under the same conditions. Alternatively, turnover frequency (TOF) can also be a method to assess the intrinsic activity of the electrocatalyst, which is however known as a mostly tricky technique. TOF for the OER is defined as the number of produced electrons per active site per unit time. In this technique, since accessible electrocatalytic active sites are just a portion of the total material making up the catalyst and are difficult to be identified, accurately computing TOF is quite hard. After creating the ranking, applying the MX_y with the most outstanding intrinsic OER activity to the optimum electrode design can lead to a high-performance water oxidation electrode that is worthy of practical use. Accordingly, progress in the systematic study regarding the intrinsic OER activities of the MX_y family compounds is eagerly expected in the near future.

Electrochemical and chemical stabilities are also important aspects to consider when determining whether an arbitrary MX_y material has robustness for practical use. Conventionally, both electrochemical and chemical stabilities are investigated via the electrochemical approach, such as time-dependent current density ($J-t$) or potential ($V-t$) measurement [i.e., CA or CP] and CV measurement for long-term OER testing. The tested material can show unnoticeable/no deterioration of the initially examined current density (mA·cm$_{geo}^{-2}$ or mA·mg$_{cat}^{-1}$)/applied potential after long-term CA, CP, and CV measurements, suggesting good stability during the OER. These measurement criteria are still applicable to fair stability assessments of the catalyst-type MX_y materials, but they cannot be applied to stability evaluations of the precatalyst-type MX_y materials due to their full/partial transformation to MO_x/MO_xH_y which is typically accompanied by their surface oxidation/reconstruction. Interestingly, although the MX_y precatalysts actually tend to be spontaneously/electrochemi-

https://doi.org/10.1021/acs.chemrev.3c00005
Chem. Rev. 2023, 123, 12795−13208

cally converted into their MO_x/MO_xH_y counterparts, the variation of OER CA, CP, and CV signals before and after the stability test can be neglected (Figure 7a, i) and sometimes their OER performances are slightly decayed (Figure 7a, ii) or even enhanced (Figure 7a, iii) over the testing time. From these results regarding the precatalyst stability tests, not a few electrochemists come to the conclusion that their MX_y material has excellent electrochemical and chemical stabilities toward long-term OER, which is incorrect since electrochemical and chemical stabilities are not identical, especially for the precatalyst. Also, the stability tests introduced above, which just estimate total electrode stability, cannot distinguish whether the MX_y material is a catalyst or a precatalyst. Furthermore, as shown in Figure 7a, the total electrode activity (geometric activity) of the precatalyst might be somewhat maintained and influenced mainly by (i) a surface area increase, (ii) an electrical conductivity decrease, and (iii) a surface chemical composition change during long-term OER testing, making it more difficult to understand the precatalytic OER stability. Hence, to obtain a deep understanding of the electrochemical stability data for precatalyst-type MX_y materials, one needs to consider the trade-off relations among the above three variable parameters (i−iii).

To elucidate the hidden transformation (oxidation) of the MX_y materials as OER precatalysts, there are additional required techniques: electrochemical approaches and *ex situ* characterizations (chemical and physical approaches) for pre- and post-OER electrodes. Typically, the electrocatalytic reaction happens at the electrode surface/electrolyte interface, which may be strongly influenced by surface states. Thus, it is again important to estimate the intrinsic activity (i.e., specific overpotential/onset potential or TOF) of the precatalyst before and after long-term OER testing. This is because, if the MX_y material is tranformed into the related MO_x/MO_xH_y counterpart during long-term OER testing, the pre- and post-OER precatalysts may exhibit different intrinsic activities. Moreover, a faradaic efficiency (coulometric efficiency) measurement is also helpful for assessing the potentiality of the MX_y being oxidized during long-term OER testing. Here, faradaic efficiency can be defined as the ratio of total oxygen evolution amount to the consumed total charges under the testing time for the OER. A faradaic efficiency of <100% implies that the consumed total charges may be partially utilized for the irreversible oxidation of the MX_y material. Furthermore, a voltammetric study for MX_y oxidation in cationic surfactant-containing NaOH aqueous solution is a critical way to check MX_y's oxidation potentials and its oxidation mechanism (e.g., sulfide → sulfur → sulfite → sulfate).[117−120] The MX_y oxidation voltammetric peak is partially/fully overlapped with the OER voltammetric wave most of the time. In this system, as the cationic surfactant increases the water oxidation potential (by 0.9 V), it is possible to separate the water and MX_y oxidation reactions and directly observe the MX_y oxidation voltammetric peaks, which has already been previously used for examining the oxidation of some chalcogenides such as FeS_2, NiS, MnS, MoS_2, PbS, NiSe, MnSe, $MoSe_2$, NiTe, $MnTe_2$, and $MoTe_2$.[117−120] Revealing the MX_y oxidation potential, of which further extension is expected, may lead to a discussion regarding the possibility that the actually applied potential to drive the OER causes the MX_y oxidation.

In addition to the above electrochemical approaches, *ex situ* characterizations [i.e., X-ray photoelectron spectroscopy (XPS), energy dispersive X-ray spectrometry (EDX), X-ray diffraction (XRD), selected area electron diffraction (SAED), transmission electron microscopy (TEM), scanning electron microscopy (SEM), and so on] are indispensable to confirming the oxidation progress of the MX_y precatalyst as well as ensuring the classification of the MX_y materials into catalyst and precatalyst. Herein, one of the major problems in this research field today is a lack of consistency in performing the full *ex situ* characterizations (physical and chemical analyses) on electrocatalysts before and after long-term OER testing. In particular, it is mandatory to report the physical and chemical characteristics of post-OER electrocatalysts for determining the MX_y's final form. In our previous work,[57] we have already proposed a workflow to accurately characterize the MX_y materials for use as OER electrocatalysts, which checks whether each MX_y material is a catalyst or precatalyst. To the final oxidation degree (partial oxidation or full oxidation), we again offer the newly prototyped workflow to analyze MX_y oxidation behavior using general analytical techniques (XRD, SEM, TEM, EDX, XPS, etc.) in Figure 7b. (1) First, to check the initial state of each MX_y material, *pre-analysis* (XPS, EDX, XRD/SAED, and SEM/TEM) should be conducted. Subsequently, LSVs and CVs of the electrocatalyst are conducted to briefly check initial OER performance and C_{dl}-based ECSA. (2) Then, the ∼1−5 h chronoamperometric/chronopotentiometric testing or ∼50−500 cycles of CV (i.e., a short period of electrooxidation) should be repeated while simultaneously checking whether any oxidation and ECSA change are in progress or not (*quick-analysis* using XRD and EDX at least after each short electrooxidation set) until the MX_y oxidation stops. (3) Finally, the tested material should be further analyzed by XPS, SAED, and SEM/TEM to determine the final structure: fully oxidized, partially oxidized, or unoxidized (*post-analysis*). The workflow outlined above has been partially utilized to unravel the oxidation behavior of a cobalt carbide (Co_3C) electrocatalyst during long-term OER CV testing, which successfully showed a phase transformation: crystalline Co_3C → Co_3C@CoO_x core@shell → amorphous CoO_x (final state).[91]

So far, we have cautioned that the lack of electrochemical, chemical, and physical analyses may cause the misinterpretation of MX_y OER electrocatalytic mechanisms. The activity and stability measurement procedures suggested above are useful as a somewhat simple, rapid, and detailed investigation of intrinsic activities of pre- and post-OER MX_y electrocatalysts and classification of post-OER MX_y electrocatalysts into the three final states (see Figure 5), which enable us to understand the real catalytically active species in the post-OER MX_y electrocatalysts. For the further development of this field, we also hope that these procedures will be widely accepted by electrochemists.

1.5. Scope of This Review

This comprehensive review focuses on the advances in transition metal *X*-ide-based electrocatalysts for the OER, proposes guidelines for analyzing their real OER active species/sites by reviewing the recent experimental developments, and discusses the challenges that electrochemists need to work on in the future. In Sections 2−5, we mainly review the publications from 2013 (the birth of this research area) to 2022 regarding transition metal borides, carbides, pnictides (nitrides and phosphides), and chalcogenides (sulfides, selenides, and tellurides) for electrocatalytic OER. The review

https://doi.org/10.1021/acs.chemrev.3c00005
Chem. Rev. 2023, 123, 12795−13208

for each *X*-ide material group sorted by anionic element (i.e., B, C, N, P, S, Se, and Te) begins with (i) electrode preparation protocols and approaches, (ii) final types of electrocatalysts (i.e., "catalyst" or "precatalyst"), (iii) strategies for enhancing the OER activity of transition metal *X*-ide electrocatalysts, and (iv) specific challenges. Importantly, for subsection (ii), by critically reviewing all the reported electrochemical, chemical, and physical measurement results (except long-term OER tests: CA, CP, CV, etc.) on the post-OER electrodes, we will provide comprehensive classification tables for each *X*-ide material group, from which the real catalytically active species (i.e., MX_y, MO_x/MO_xH_y, and so forth) in the post-OER *X*-ide electrodes can be determined/predicted. Furthermore, in each table, unless otherwise described, we attempt to exhaustively classify almost all the reported *X*-ide electrocatalysts into three groups: "catalyst," "precatalyst," and "unknown" (see Figure 8).

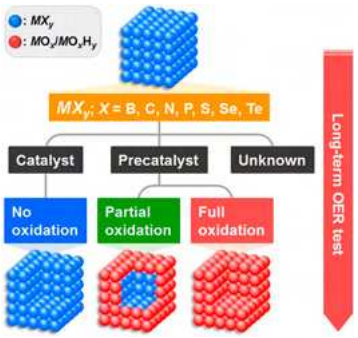


Figure 8. Tree diagram for classification of transition metal boride, carbide, pnictide, and chalcogenide OER electrocatalysts.

Especially for the "precatalyst" group, we will further divide them according to their oxidation degree after the OER: "partial oxidation" and "full oxidation" (see Figure 8). Moreover, we will also include the unique *X*-ides, which demonstrate other types of transformations (e.g., dissolution, decomposition, etc.) during the OER, in the "precatalyst" group. Incidentally, when the passivation layer (e.g., metal oxide/(oxy)hydroxide) is introduced on an *X*-ide electrode prior to OER testing, the *X*-ide acts as a conductive substrate rather than an electrocatalyst. For this case, we will provide a "substrate" indication in the classification table. In the case of a lack of consistency in reporting the full physical and chemical characteristics of *X*-ide samples before and after the electrocatalytic OER, we include them in the "unknown" group. Furthermore, for the samples with "catalyst" or "precatalyst" labels, we provide/propose the post-OER electrocatalyst surface species (= "final types of electrocatalysts") in the classification tables, when we found enough post-OER analytical data and/or the authors' interpretation. Additionally, in Section 6, we also provide a similar classification table and a brief overview of state-of-the-art transition metal-based polyanion compounds/composites reported from 2017 (the birth of this electrocatalyst group) to 2022. In Section 7, we introduce several special characterization approaches (i.e., *in situ* and *ex situ* analyses) to classify the structural, morphological, and electronic changes due to the reconstruction (i.e., oxidation and other phase transformation) of *X*-ides during the OER, develop a table for the proper choice of characterization techniques, and briefly summarize the most critical requirements that *X*-ide OER electrocatalysts need to be considered for successful application in practical water electrolysis technologies. Furthermore, we discuss artificial intelligence prediction/machine learning-based approaches for further advancing *X*-ide OER electrocatalyst researches. Finally, concluding remarks are provided in Section 8, in which we systematically summarize and discuss OER activity and oxidation resistance across all the *X*-ides (borides, carbides, pnictides, and chalcogenides) and polyanion compounds/composites discussed in Sections 2−6. Additionally, we also provide best practices for investigating *X*-ide precatalysts, discuss the limitation of the current stage for *X*-ide OER electrocatalysts, and suggest research and development strategies for future *X*-ide OER electrocatalysts/electrodes.

2. TRANSITION METAL BORIDES

Transition metal borides are promising candidate materials for the electrocatalytic OER and HER processes in alkaline, neutral, and acidic electrolytes.[66,67,73,146] In 1974, Lavrenko *et al.* first reported transition metal borides (ZrB_2, NbB_2, TaB_2, and W_2B_5) as electrocatalysts, specifically for the HER in acidic media (1 N H_2SO_4).[192] In 1981, Osaka *et al.* first reported transition metal boride electrocatalysts (Ni_xB, Co_xB, Fe_xB, and LaB_6) for the OER.[193] And two years later, Osaka *et al.* expanded the class of metal boride electrocatalysts by examining mono- and bimetallic cobalt-based borides (Co−Fe−B, Co−Ni−B, Co−Mn−B, and Co-B) for the OER.[194] In both of Osaka *et al.*'s reports, the boride materials were tested in alkaline media (6 M KOH) as electrocatalysts and the anodic formation of metal oxides was considered to be the OER electroactive species. Despite being published in the early 1980s, metal boride electrocatalysts for the OER have only recently (from 2016) garnered attention from the scientific community with various boride-based electrodes having been studied extensively over the past few years (see Table 1).

2.1. Electrode Preparation Methods

Table 1 shows that the reported transition metal boride electrodes can be classified into two types: (i) powder-coated electrodes (P) and (ii) self-supported electrodes (S). The synthesis of transition metal boride electrocatalysts has been conducted as a one-step (starting materials → final product), two-step (starting materials → precursor → final product), and multistep process and using a variety of different synthetic methods [i.e., solution-based method (refs 105, 137−139, 143, 145, 147, 148, 150, 152, 157, 158, 160−166, 175, 176, 178, 179, 182, 183, and 186−191), dip-coating method,[151,181] electroless plating method,[149,153−155,159] solid-state reaction,[140,141,144,177] MOF-derived method,[185,195] solvothermal method,[142] hydrothermal method,[157] ball-milling method,[156] and pulsed laser deposition[147]] and/or post-treatments [e.g., annealing treatment,[105,163,166] high-temperature pulse treatment,[189] chemical vapor deposition (CVD) treatment,[161] etc.]. Regardless of the synthetic method, almost all the reported synthetic approaches required various "boronizing" processes of the starting materials and precursors with different boron sources (thermal boronization: boron powder; liquid-based boronization: $LiBH_4$, $NaBH_4$, KBH_4, metal bromide, and Et_2NHBH_3). In this Section, we will discuss synthetic approaches for the synthesis of metal borides and provide both typical and unique examples for each synthetic method.

2.1.1. Solution-Based Methods. Among all the reports on transition metal boride OER electrocatalysts, a solution-based method is the most common, as it requires relatively simple equipment (refs 105, 137−139, 143, 145, 147, 148, 150,

https://doi.org/10.1021/acs.chemrev.3c00005
Chem. Rev. 2023, 123, 12795−13208

Table 1. Summary of the Electrocatalytic Properties, Electrochemical Testing Conditions, and Physicochemical Pre- and Post-analyses of Transition Metal Borides Used for Alkaline/Neutral/Acidic OER, and the Final Type of Electrocatalyst after OER Testing[a–e]

Initial Electrocatalyst	Substrate	Shape of Electrocatalyst	Deposition Type	Specific Loading / $mg \cdot cm^{-2}_{geo}$	η@10 $mA \cdot cm^{-2}_{geo}$ / mV	C_{dl} / $mF \cdot cm^{-2}_{geo}$	TOF / s^{-1} (@η or j)	Tafel Slope / $mV \cdot dec^{-1}$	Electrolyte	Pre-analysis	Post-analysis	Long-Term OER Test Conditions	Post-OER Electrocatalyst	Final Type of Electrocatalyst	Ref.
$FeCoB_2$	GC	Nanoparticle covered with nanosheets	P	0.281	~383	-	-	-	1 M KOH	XRD, SEM, TEM, STEM, EDX, EELS, XPS, SXES, XAFS (XANES, EXAFS)	XPS, SXES, XAFS (XANES, EXAFS), TEM	LSV sweeps (activation)	Metal oxyhydroxides, Borates	Precatalyst (partial oxidation)	121
Activated $FeCoB_2$	GC	Nanoparticle	P	0.281	295	0.1145 (mF)	-	84		XPS, SXES, XAFS (XANES, EXAFS), TEM	-	200 h CP (10 $mA \cdot cm^{-2}_{geo}$)	-	-	
FeB	GC	Nanoparticle	P	0.281	~501	0.3135 (mF)	-	101		XRD, SEM	-	-	-	-	
CoB	GC	Nanoparticle	P	0.281	~433	0.0875 (mF)	-	125		XRD, SEM	-	-	-	-	
CoFeNiMnZnB	GC	Porous aggregate of nanoparticles	P	0.13	261	8.98	-	56.8	1 M KOH	XRD, N_2 ISO (BET, PSD), SEM, EDX, TEM, SAED, HAADF, XPS, EPR, ICP–MS	XRD, SEM, EDX, TEM, SAED, HAADF, XPS, EPR, ICP-MS	3000 CV cycles (1.3–1.7 V_{RHE}) 80 h CA (1.49 V_{RHE}) 80 h CP (10 $mA \cdot cm^{-2}_{geo}$)	Metal (oxy)hydroxide species	Precatalyst	122
CoFeNiMnB	GC	Porous aggregate of nanoparticles	P	0.13	265	6.65	-	69.3		XRD, SEM, EDX	-	-	-	-	
CoNiMnZnB	GC	Porous aggregate of nanoparticles	P	0.13	295	5.90	-	72.0		XRD, SEM, EDX	-	-	-	-	
CoNiMnB	GC	Porous aggregate of nanoparticles	P	0.13	336	4.42	-	79.3		XRD, SEM, EDX	-	-	-	-	
CoNiB	GC	Porous aggregate of nanoparticles	P	0.13	395	3.10	-	117.6		XRD, SEM, EDX	-	-	-	-	
CoFeNiZnB	GC	Porous aggregate of nanoparticles	P	0.13	265	-	-	-		XRD, SEM, EDX	-	-	-	-	
NiFeMnZnB	GC	Porous aggregate of nanoparticles	P	0.13	266	-	-	-		XRD, SEM, EDX	-	-	-	-	
CoFeMnZnB	GC	Porous aggregate of nanoparticles	P	0.13	276	-	-	-		XRD, SEM, EDX	-	-	-	-	
$CoFeMoB_4$	CC	Nanoparticle	P	4	251 295 (@50 $mA \cdot cm^{-2}_{geo}$)	4.11	-	27.2	1 M KOH	XRD, SEM, M-H, FC, ZFC, TEM, EELS, XPS, XAFS (XANES, EXAFS), XAS, EDX, TEM, Raman	XRD, SEM, TEM, EELS, XPS, XAFS (XANES, EXAFS), XAS, EDX, TEM, HAADF, Raman (after 30 min CV)	60 h CA (1.54 V_{RHE}) 30 min CV cycles (100 $mV \cdot s^{-1}$, 1.23 V_{RHE} to the potential @50 $mA \cdot cm^{-2}_{geo}$)	$Co(OH)_2$, FeOOH, $Mo_2O_7^{2-}$, BO_2^-	Precatalyst (partial oxidation)	123
Co_2MoB_4	CC	Nanoparticle	P	-	283 322 (@50 $mA \cdot cm^{-2}_{geo}$)	7.5	-	19.9		XRD, SEM, M-H, FC, ZFC, TEM, EELS, XPS, EDX, TEM, XAS, Raman	XRD, SEM, TEM, EELS, XPS, EDX, TEM, EELS, XAS, Raman (after 30 min CV)	30 min CV cycles (100 $mV \cdot s^{-1}$, 1.23 V_{RHE} to the potential @50 $mA \cdot cm^{-2}_{geo}$)	CoOOH, molybdate species (Mo^{6+}), BO_2^-	Precatalyst (partial oxidation)	
Fe_2MoB_4	CC	Nanoparticle	P	-	463 580 (@50 $mA \cdot cm^{-2}_{geo}$)	0.152	-	95.5		XRD, SEM, M-H, FC, ZFC, TEM, EELS, XPS, EDX, XAS, Raman	XRD, SEM, TEM, EELS, XPS, EDX, XAS, Raman (after 30 min CV)	30 min CV cycles (100 $mV \cdot s^{-1}$, 1.23 V_{RHE} to the potential @50 $mA \cdot cm^{-2}_{geo}$)	Fe_2O_3, Molybdate species (Mo^{6+}), BO_2^-	Precatalyst (partial oxidation)	
CoB@300	GC	Nanosheet and nanoplate	P	0.25	290 360 (@50 $mA \cdot cm^{-2}_{geo}$)	33.7	11.25 at 400 mV	62	1 M KOH	XRD, EFSEM, TEM, SAED, EDX, CHN, XPS	XRD, FESEM, XPS	1 CV cycle (activation) 15 h CP (10 $mA \cdot cm^{-2}_{geo}$)	CoOOH, Borate species	Precatalyst (partial oxidation)	124
CoB@450	GC	Nanosheet and nanoplate	P	0.25	295 375 (@50 $mA \cdot cm^{-2}_{geo}$)	31.5	9.78 at 400 mV	76		XRD, EFSEM, TEM, SAED, EDX, CHN	-	-	-	-	
CoB@550	GC	Nanoparticle aggregates	P	0.25	300 392 (@50 $mA \cdot cm^{-2}_{geo}$)	13.8	7.70 at 400 mV	78		XRD, EFSEM, TEM, SAED, EDX, CHN	-	-	-	-	

https://doi.org/10.1021/acs.chemrev.3c00005
Chem. Rev. 2023, 123, 12795−13208

Table 1. continued

Initial Electrocatalyst	Substrate	Shape of Electrocatalyst	Deposition Type	Specific Loading / $mg \cdot cm^{-2}_{geo}$	η@10 $mA \cdot cm^{-2}_{geo}$ / mV	C_{dl} / $mF \cdot cm^{-2}_{geo}$	TOF / s^{-1} (@η or f)	Tafel Slope / $mV \cdot dec^{-1}$	Electrolyte	Pre-analysis	Post-analysis	Long-Term OER Test Conditions	Post-OER Electrocatalyst	Final Type of Electrocatalyst	Ref.
CoB@650	GC	Nanoparticle aggregates	P	0.25	355 441 (@50 $mA \cdot cm^{-2}_{geo}$)	11.6	4.39 at 400 mV	82		XRD, EFSEM, TEM, SAED, EDX, CHN	-	-	-	-	124
NiFeB NPs-300	Ni foam	Nanoparticle	P	~1.45	231 (@20 $mA \cdot cm^{-2}_{geo}$)	0.9	-	85.2	1 M KOH	XRD, SEM, TEM, XPS, EDX	XRD, SEM, XPS	12 h CA (the potential @10 $mA \cdot cm^{-2}_{geo}$)	NiFeOOH, Borate species	Precatalyst (partial oxidation)	125
NiFeB NSs-300	Ni foam	Nanosheet	P	~1.45	~266 (@20 $mA \cdot cm^{-2}_{geo}$)	0.64	-	83.0		XRD, SEM, TEM, XPS, EDX	XRD, SEM, XPS	12 h CA (the potential @10 $mA \cdot cm^{-2}_{geo}$)	NiFeOOH, Borate species	Precatalyst (partial oxidation)	
NiFeB NPs	Ni foam	Nanoparticle	P	~1.45	~257 (@20 $mA \cdot cm^{-2}_{geo}$)	0.53	-	79.8		XRD, SEM, TEM, XPS, EDX	SEM	12 h CA (the potential @10 $mA \cdot cm^{-2}_{geo}$)	-	-	
NiFeB NSs	Ni foam	Nanosheet	P	~1.45	~288 (@20 $mA \cdot cm^{-2}_{geo}$)	0.18	-	91.7		XRD, SEM, TEM, XPS, EDX	SEM	12 h CA (the potential @10 $mA \cdot cm^{-2}_{geo}$)	-	-	
NiB NPs	Ni foam	Nanoparticle	P	~1.45	~334 (@20 $mA \cdot cm^{-2}_{geo}$)	-	-	-		XRD, SEM, XPS	-	-	-	-	
NiB NSs	Ni foam	Nanosheet	P	~1.45	~352 (@20 $mA \cdot cm^{-2}_{geo}$)	-	-	-		XRD, SEM, XPS	-	-	-	-	
WFeNiB (W:Fe:Ni = 2:3:5)	Ni foam	Highly corrugated nanosheet structure	S	7.5	223	4.05	-	38.83	1 M KOH	SEM, EDX, XRD, XPS	SEM, EDX, XPS	12 h CA (the potential @100 $mA \cdot cm^{-2}_{geo}$) 12 h CP (100 $mA \cdot cm^{-2}_{geo}$) 6000 CV cycles	WO_3, NiOOH, FeOOH, Borate species (B_2O_3)	Precatalyst	126
					238	-	-	-	0.1 M KOH		-	-	-	-	
					509	-	-	-	0.1 M KPi (pH = 7)		-	-	-	-	
FeNiB	Ni foam	-	S	-	283	2.445	-	40.12	1 M KOH	-	-	-	-	-	
WFeB	Ni foam	-	S	-	290	2.385	-	43.36		-	-	-	-	-	
WNiB	Ni foam	-	S	-	309	2.195	-	106.16		-	-	-	-	-	
WFeNiB (W:Fe:Ni = 1:2:7)	Ni foam	-	S	-	~243	3.81	-	-		-	-	-	-	-	
WFeNiB (W:Fe:Ni = 3:4:3)	Ni foam	-	S	-	~263	3.48	-	-		-	-	-	-	-	
Mixture of M-B	Ni foam	-	-	-	~288	-	-	-		-	-	-	-	-	
FeB	Ni foam	-	S	-	~334	-	-	-		-	-	-	-	-	
NiB	Ni foam	-	S	-	~313	-	-	-		-	-	-	-	-	
WB	Ni foam	-	S	-	~318	-	-	-		-	-	-	-	-	
Co–Fe–B/NF	Ni foam	Nanochain	S	-	270 (@50 $mA \cdot cm^{-2}_{geo}$) 280 (@100 $mA \cdot cm^{-2}_{geo}$)	21.31	-	36	1 M KOH	XRD, XPS, SEM, TEM, SAED, EDX, N_2 ISO (BET, PSD)	SEM, XPS (after 50 h CP)	5500 s multistep CP (100–200 $mA \cdot cm^{-2}_{geo}$, 10 $mA \cdot cm^{-2}_{geo}$ per 500 s) 4900 s multistep CP [100 (500 s), 110 (700 s), 120 (1000 s), 130 (1200 s), 140 $mA \cdot cm^{-2}_{geo}$ (1500 s)] 50 h CP (10 $mA \cdot cm^{-2}_{geo}$)	Oxidized Co and Fe species, Boron-oxo species	Precatalyst	127
Fe–B/NF	Ni foam	Nanosphere	S	-	296 (@50 $mA \cdot cm^{-2}_{geo}$) 310 (@100 $mA \cdot cm^{-2}_{geo}$)	13.2	-	68		SEM, N_2 ISO (BET, PSD)	-	-	-	-	
Co–B/NF	Ni foam	Nanochain	S	-	343 (@50 $mA \cdot cm^{-2}_{geo}$) 370 (@100 $mA \cdot cm^{-2}_{geo}$)	2.34	-	109		SEM, N_2 ISO (BET, PSD)	-	-	-	-	
CoFe-PBA-B	Ni foam	Nanosheet and nanocage	S	3.6	255	8.62	0.0035 (@ 300 mV)	51	1 M KOH	XRD, SEM, EDX, TEM, XPS, Raman, FTIR, TGA, DSC	SEM, EDX, XPS	40 h CA (1.48 V_{RHE})	CoOOH/FeOOH, Borates	Precatalyst	128
NiFe-Boride	Ni foam	Agglomerated nanoparticles	P	-	167	0.35	-	25	1 M KOH	XRD, SEM, EDX, TEM, XAFS (XANES, EXAFS), XPS, ICP-OES	SEM, EDX, *In-Situ* SRXRD, *In-Situ* XANES, EXAFS, XPS	100 h CP (20 $mA \cdot cm^{-2}_{geo}$) 400 h CP (1 $A \cdot cm^{-2}_{geo}$)	$FeBO_3$, NiB_4O_7	Precatalyst	129
Ni_6Fe-Boride	Ni foam	-	P	-	~206	-	-	-		ICP-OES	-	-	-	-	
Ni_3Fe-Boride	Ni foam	-	P	-	~191	-	-	-		ICP-OES	-	-	-	-	
$NiFe_3$-Boride	Ni foam	-	P	-	~203	-	-	-		ICP-OES	-	-	-	-	
$NiFe_6$-Boride	Ni foam	-	P	-	~198	-	-	-		ICP-OES	-	-	-	-	
$(Co_{1.0}Ni_{0.0})_2B$	GC	Agglomerated particles	P	0.150	~383	2.39	-	67	1 M KOH	SEM	-	-	-	-	130
$(Co_{0.9}Ni_{0.1})_2B$	GC	Network-like structure consisting of small rods	P	0.150	371 355 (after 8 h CP)	2.26	-	77		SEM, XRD, XPS, TEM, SAED, STEM, HAADF, EDX, F-AAS	XPS, F-AAS	CV activation (100 $mV \cdot s^{-1}$, 1–1.5 V_{RHE}) 8 h CP (10 $mA \cdot cm^{-2}_{geo}$)	CoOOH, $Ni(OH)_2$	Precatalyst	
$(Co_{0.8}Ni_{0.2})_2B$	GC	Network-like structure consisting of small rods	P	0.150	383	3.12	-	62		SEM, XRD, XPS	-	CV activation (100 $mV \cdot s^{-1}$, 1–1.5 V_{RHE})	-	-	
$(Co_{0.7}Ni_{0.3})_2B$	GC	Network-like structure consisting of small rods	P	0.150	~433	1.57	-	82		SEM, XRD, XPS	-	CV activation (100 $mV \cdot s^{-1}$, 1–1.5 V_{RHE})	-	-	
$(Co_{0.6}Ni_{0.4})_2B$	GC	Particle- and porous rod-like structures	P	0.150	~454	1.13	-	83		SEM, XRD, XPS	-	CV activation (100 $mV \cdot s^{-1}$, 1–1.5 V_{RHE})	-	-	
$(Co_{0.5}Ni_{0.5})_2B$	GC	Network-like structure consisting of small rods	P	0.150	~402	3.21	-	53		SEM, XRD, XPS	-	CV activation (100 $mV \cdot s^{-1}$, 1–1.5 V_{RHE})	-	-	
F-Ni_2B/$Ni(OH)_x$	GC	Nanoparticle with crater-like surface	P	0.285	340	0.0315	0.043 at 340 mV	23	1 M KOH	XRD, TEM, SAED, EDX, XPS, FTIR, XAFS (XANES, EXAFS)	TEM, SAED, EDX, XPS	> 25 h CA (1.60 V_{RHE})	Ni oxoboride, Ni (oxy)hydroxide	Precatalyst (partial oxidation)	131

https://doi.org/10.1021/acs.chemrev.3c00005
Chem. Rev. 2023, 123, 12795−13208

Table 1. continued

Initial Electrocatalyst	Substrate	Shape of Electrocatalyst	Deposition Type	Specific Loading / $mg \cdot cm^{-2}_{geo}$	η@10 $mA \cdot cm^{-2}_{geo}$ / mV	C_{dl} / $mF \cdot cm^{-2}_{geo}$	TOF / s^{-1} (@η or f)	Tafel Slope / $mV \cdot dec^{-1}$	Electrolyte	Pre-analysis	Post-analysis	Long-Term OER Test Conditions	Post-OER Electrocatalyst	Final Type of Electrocatalyst	Ref.
Ni_2B	GC	Nanoparticle	P	0.285	390	0.0739	0.0003 at 340 mV	42		XRD, TEM, SAED, EDX, XPS, FTIR, XAFS (XANES, EXAFS)	-	10 h CA	-	-	131
Fe_2B NWs/NF	Ni foam	Nanowire	S	0.25	240	1.20	0.298 at 285 mV	30	1 M KOH	XRD, FESEM, EDX, TEM, XPS, ICP-OES	XRD, FESEM, TEM, XPS, FTIR	5 CV cycles (activation: 100 $mV \cdot s^{-1}$, 1.22−1.72 V_{RHE}) 10 h CP (10 $mA \cdot cm^{-2}_{geo}$)	FeOOH, Metaborate	Precatalyst (partial oxidation)	132
Fe_2B NPs/NF	Ni foam	Nanoparticle	S	0.25	258	0.85	-	-		FESEM	-	5 CV cycles (activation: 100 $mV \cdot s^{-1}$, 1.22−1.72 V_{RHE})	-	-	
Gd-CoB	Au sputtered glass slide	Nanosheet	S	-	230	29	1570 at 370 mV	42	Fe-purified 1 M KOH	SEM, AFM, XRD, EDX, TEM, STEM, XPS, UPS	SEM, XRD, XPS, ICP-OES	35 h CP (100 $mA \cdot cm^{-2}_{geo}$) 1000 CV cycles	Oxidized Co and Gd species, Boron oxo species, Meta borate species	Precatalyst	133
CoB	Au sputtered glass slide	Nanoflake array	S	-	370	11	33 at 370 mV	70		SEM, AFM	-	-	-	-	
NiB/SSG	Graphene	Nanoparticle	S	-	369 (@30 $mA \cdot cm^{-2}_{geo}$)	31.9	-	85.2	1 M KOH	SEM, EDX, XPS	-	-	-	-	134
FeB/SS	Graphene	Nanoparticle	S	-	420	12.5	-	70.5		-	-	-	-	-	
$Fe_{0.2}Ni_{0.8}B$/SSG	Graphene	Nanosheet	S	-	263 (@30 $mA \cdot cm^{-2}_{geo}$)	53.2	-	31.4		XRD, SEM, TEM, EDX, XPS, Raman	Raman, XPS	14 h CP @ (10 $mA \cdot cm^{-2}_{geo}$) 70 min CP (25 $mA \cdot cm^{-2}_{geo}$, OWS)	NiFeOOH	Precatalyst	
CoNiB-700	CoNi foam	Nanoflake	S	-	262	10.11	-	58	1 M KOH	XRD, SEM, EDX, TEM, XPS	SEM, EDX, XPS	12 h CP (10 $mA \cdot cm^{-2}_{geo}$) 5000 s multistep CP (10 to 100 $mA \cdot cm^{-2}_{geo}$)	NiOOH/CoOOH, Metaborates	Precatalyst (partial oxidation)	135
NiB-700	Ni foam	-	S	-	398	-	-	93.3		-	-	-	-	-	
CoNiB-600	CoNi foam	Nanodot	S	-	274	2.85	-	-		XRD, SEM, EDX	-	-	-	-	
CoNiB-800	CoNi foam	Agglomerated granules	S	-	312	3.72	-	-		XRD, SEM, EDX	-	-	-	-	
CoNiB-900	CoNi foam		S	-	287	3.08	-	-		XRD, SEM, EDX	-	-	-	-	
CoNiB-1000	CoNi foam		S	-	287	8.14	-	-		XRD, SEM, EDX	-	-	-	-	
NiFeB@$NiFeB_i$	GC	Nanoparticle	P	0.306	237	-	-	58	1 M KOH	XRD, SEM, EDX, TEM, XPS, ICP-AES	SEM, TEM, XPS	2000 CV cycles (1.2–1.7 V_{RHE}) ~ 18 h CP (10 $mA \cdot cm^{-2}_{geo}$)	$NiFeB_i$ (Ni^0 oxidation)	Precatalyst (partial oxidation)	136
NiFeB	GC	Nanoparticle	P	0.306	273	-	-	67		XRD, SEM, EDX, TEM, XPS, ICP-AES	XPS	2000 CV cycles (1.2–1.7 V_{RHE}) ~ 13 h CP (10 $mA \cdot cm^{-2}_{geo}$)	$NiFeB_i$ (Ni^0 oxidation)	Precatalyst	
NiB@NiB_i	GC	Nanoparticle	P	0.306	303	-	-	107		XRD, SEM, TEM	-	2000 CV cycles (1.2–1.7 V_{RHE}); ~ 13 h CP (10 $mA \cdot cm^{-2}_{geo}$)	-	-	
FeB@FeB_i	GC	Nanoparticle	P	0.306	373	-	-	97		XRD, SEM, TEM	-	-	-	-	
Ni_xB/f-MWCNT	GC	Nanosheet	P	~ 0.2	286	12.35	0.058	46.3	1 M KOH	XRD, SEM, EDX, TEM, XPS, Raman, ICP-OES, SAED, AFM, N_2 ISO (BET, PSD)	SEM, EDX, XPS	100 h CP (20 $mA \cdot cm^{-2}_{geo}$)	NiOOH, $Ni(OH)_2$	Precatalyst (partial oxidation)	137
Ni_xB–f-MWCNT	GC	Nanosheet	P	~ 0.2	350	-	-	73		SEM	-	-	-	-	
Ni_xB	GC	Nanosheet	P	~ 0.2	375	3.66	0.0432	107.1		XRD, SEM, XPS, N_2 ISO (BET, PSD)	-	-	-	-	
Ni_2B	GC	-	P	0.21	350	-	0.012 ($mol^{-1} \cdot s^{-1}$)	57.8	1 M KOH	XPS	XPS	100 CV cycles (100 $mV \cdot s^{-1}$, ~1.03–1.63 V_{RHE})	NiOOH	Precatalyst (partial oxidation)	138
Ni_3B	GC	-	P	0.21	~ 360	-	-	117		-	-	100 CV cycles (100 $mV \cdot s^{-1}$, ~1.03–1.63 V_{RHE})	-	-	
Ni-Co-B (Ni_3B+Co_4B, Ni/Co = 1:1)/rGO	GC	Nanosheet	P	-	280	235.7	0.086 at 300 mV	56	1 M KOH	XRD, SEM, TEM, EDX, XPS, Raman	SEM, XPS (after 10 cycles of OER test)	60 h CP (20 $mA \cdot cm^{-2}_{geo}$)	Ni and Co oxyhydroxide/oxy hydrogen	Precatalyst (partial oxidation)	139
Ni-Co-B	GC	Particle	P	-	320	24.3	-	91		SEM	-	-	-	-	
Ni-B (Ni_3B)	GC	Particle	P	-	420	-	-	-		XRD, SEM	-	-	-	-	
Co-B (Co_4B)	GC	Particle	P	-	400	-	-	-		XRD, SEM	-	-	-	-	
boronized Ni (Ni_3B@$Ni(OH)_2$+BO_2^-)	Ni foil	Chunk	S	-	~ 338	0.362	-	-	Fe-purified 1 M KOH	XRD, SEM, TEM, EDX, XPS, Raman	SEM, TEM,	250 LSV sweeps (1 $mV \cdot s^{-1}$, ~1.23–1.62 V_{RHE})	$NiOOH, BO_2^-$	Precatalyst (partial oxidation)	140
activated, boronized Ni (Ni_3B@NiOOH+BO_2^-)	Ni foil	Nanosheet	S	-	300 (after activation)	0.98	-	43		SEM, TEM	SEM, XRD, ICP-OES (after 150 CP)	1500 h CP (after activation, 10 $mA \cdot cm^{-2}_{geo}$)	$NiOOH, BO_2^-$ (after 150 h CP)	Precatalyst (surface oxidized before the OER)	
boronized Fe (Fe_2B)	Fe foil	Chunk	S	-	402	0.42	-	-	Fe-purified 1 M KOH	XRD, SEM, EDX, AFM	SEM, XPS, TEM, AFM	10 h CP (10 $mA \cdot cm^{-2}_{geo}$)	$FeOOH, BO_2^-$	Precatalyst (partial oxidation)	141
boronized Co (Co_2B)	Co foil	Chunk	S	-	371	0.36	-	-		XRD, SEM, EDX, AFM	SEM, XPS, TEM, AFM	10 h CP (10 $mA \cdot cm^{-2}_{geo}$)	$CoOOH, BO_2^-$	Precatalyst (partial oxidation)	
boronized Ni (Ni_2B)	Ni foil	Chunk	S	-	335	0.26	-	40		XRD, SEM, EDX, XPS, AFM	SEM, XPS, AFM, Raman	10 h CP (10 $mA \cdot cm^{-2}_{geo}$)	$NiOOH, BO_2^-$	Precatalyst (partial oxidation)	
boronized 80% NiFe ($Ni_{0.8}Fe_{0.2}B$)	$Ni_{0.8}Fe_{0.2}$ alloy foil	Chunk	S	-	270	0.18	-	-		XRD	SEM, XPS, TEM, AFM, Raman	3000 h CP (10 $mA \cdot cm^{-2}_{geo}$) 25 h CP (500 $mA \cdot cm^{-2}_{geo}$, unpurified 30% KOH)	(Ni,Fe)OOH, BO_2^- (only checked the existence of NiOOH and BO_2^-)	Precatalyst (partial oxidation)	
boronized 50% NiFe ($Ni_{0.5}Fe_{0.5}B$)	$Ni_{0.5}Fe_{0.5}$ alloy foil	Chunk	S	-	~ 291	-	-	-		XRD	SEM, XPS, TEM, AFM, Raman	25 h CP (500 $mA \cdot cm^{-2}_{geo}$, unpurified 30% KOH)	(Ni,Fe)OOH, BO_2^- (only checked the existence of NiOOH and BO_2^-)	Precatalyst (partial oxidation)	
boronized 35% NiFe ($Ni_{0.35}Fe_{0.65}B$)	$Ni_{0.35}Fe_{0.65}$ alloy foil	Chunk	S	-	~ 294	-	-	-		XRD	SEM, XPS, TEM, AFM, Raman, ICP-OES	25 h CP (500 $mA \cdot cm^{-2}_{geo}$, unpurified 30% KOH)	(Ni,Fe)OOH, BO_2^- (only checked the existence of NiOOH and BO_2^-)	Precatalyst (partial oxidation)	

https://doi.org/10.1021/acs.chemrev.3c00005
Chem. Rev. 2023, 123, 12795−13208

Table 1. continued

Initial Electrocatalyst	Substrate	Shape of Electrocatalyst	Deposition Type	Specific Loading / $mg \cdot cm^{-2}_{geo}$	η@10 $mA \cdot cm^{-2}_{geo}$ / mV	C_{dl} / $mF \cdot cm^{-2}_{geo}$	TOF / s^{-1} (@η or j)	Tafel Slope / $mV \cdot dec^{-1}$	Electrolyte	Pre-analysis	Post-analysis	Long-Term OER Test Conditions	Post-OER Electrocatalyst	Final Type of Electrocatalyst	Ref.
Boronized SUS 304	SUS 304 foil	Chunk	S	-	~300 (@50 $mA \cdot cm^{-2}_{geo}$)	-	-	-	Fe-purified 30% KOH	XRD, SEM, EDX, AFM	TEM, ICP-OES	250 h CP (500 $mA \cdot cm^{-2}_{geo}$, unpurified 30% KOH)	oxidized SUS 304	Precatalyst (partial oxidation)	141
CNB	GC	Hollow nanoprism with nanosheet subunits	P	0.285	370	0.068	0.049 at 400 mV	73	1 M KOH	XRD, SEM, TEM, EDX	EDX, TEM (after CA)	0.7 h CA (1.57 V_{RHE})	CoOOH, NiOOH	Precatalyst (partial oxidation)	142
NCB	GC	Hollow nanoprism with nanosheet subunits	P	0.285	~389	0.071	0.009 at 400 mV	-		XRD, SEM, TEM	EDX, TEM (after CA)	0.4 h CA (1.57 V_{RHE})	CoOOH, NiOOH	Precatalyst (partial oxidation)	
V-CNB	GC	Hollow nanoprism with nanosheet subunits	P	0.285	340	1.01	0.09 at 400 mV	58		XRD, SEM, EDX, TEM, XPS	XRD, SEM, EDX, TEM (after CA)	1000 CV cycles (5 $mV \cdot s^{-1}$, ~1.23–1.60 V_{RHE}) 10 h CA (1.57 V_{RHE})	CoOOH, NiOOH	Precatalyst (partial oxidation)	
V-NCB	GC	Hollow nanoprism with nanosheet subunits	P	0.285	~392	-	0.023 at 400 mV	126		SEM, EDX, TEM	-	7.5 h CA (1.57 V_{RHE})	-	-	
CNB-400	GC	Hollow nanoprism with nanosheet subunits	P	0.285	400	0.095	0.026 at 400 mV	81		XRD, SEM	-	-	-	-	
NCB-400	GC	-	P	0.285	~369	-	-	-		-	-	-	-	-	
VCNB without double-layered structure	GC	Hollow nanoprism	P	0.285	410	-	-	-		-	-	10 h CA	-	-	
VCNB	Ni foil	Hollow nanoprism with nanosheet subunits	P	0.285	280 (@30 $mA \cdot cm^{-2}_{geo}$) 370 (@100 $mA \cdot cm^{-2}_{geo}$)	-	-	101		-	-	10 h CA (1.6 V_{RHE})	-	-	
Co_3B*	GC	Nanoparticle	P	-	350 (@20 $mA \cdot cm^{-2}_{geo}$)	-	-	-	1 M KOH	XRD, TEM, EDX, XPS	XRD (after air exposure), XPS (after EC test)	2 month exposure to air 30 CV cycles (100 $mV \cdot s^{-1}$, 1–1.5 V_{RHE})	CoOOH	Precatalyst (partial oxidation)	143
FeNiB-600	FeNi foam (Fe: 1.38 wt.%)	Particulate	S	-	282	6.08	-	170	1 M KOH	XRD, SEM, EDX	-	-	-	-	144
FeNiB-700	FeNi foam (Fe: 1.38 wt.%)	Particulate	S	10	272 (@10 $mA \cdot cm^{-2}_{geo}$) 399 (@100 $mA \cdot cm^{-2}_{geo}$)	8.55	0.06 ($mol_{O2} \cdot s^{-1}$) at 300 mV 0.174 ($mol_{O2} \cdot s^{-1}$) at 350 mV 0.419 ($mol_{O2} \cdot s^{-1}$) at 400 mV	136		XRD, SEM, EDX, TEM, XPS	XRD, SEM, EDX, TEM, XPS (after 12 h CP)	5000 s CP (4–40 $mA \cdot cm^{-2}_{geo}$) 12 h CP (10 $mA \cdot cm^{-2}_{geo}$)	NiOOH, FeNiOOH, BO_x	Precatalyst (partial oxidation)	
FeNiB-800	FeNi foam (Fe: 1.38 wt.%)	Particulate	S	-	294	6.91	-	179.6		XRD, SEM, EDX	-	-	-	-	
FeNiB-900	FeNi foam (Fe: 1.38 wt.%)	Particulate	S	-	309	6.16	-	240.6		XRD, SEM, EDX	-	-	-	-	
FeNi3-B/G (Fe_xNi_y-$B_{(Fe:Ni = 1:3)}$/rGO)	GC	Nanoparticle	P	0.3	230 (@15 $mA \cdot cm^{-2}_{geo}$)	0.25	1.3 at 300 mV	50	1 M KOH	XRD, FESEM, EDX, TEM, XPS, N_2 ISO (BET, PSD)	EDX, TEM, XPS (after CV activation + 1 h CP)	CV activation 1 h CP (20 $mA \cdot cm^{-2}_{geo}$) 1000 CV cycles (100 $mV \cdot s^{-1}$, 0.2–0.6 $V_{Hg/HgO}$) 12 h CP (10 mA cm^{-2}_{geo})	M-B, MOOH (M = Ni, Fe), B-O	Precatalyst (partial oxidation)	145
Fe_xNi_y-$B_{(Fe:Ni = 1:3)}$–rGO	GC	-	P	0.3	270 (@15 $mA \cdot cm^{-2}_{geo}$)	-	-	-		-	-	-	-	-	
FeNi3-B	GC	-	P	0.3	~295 (@15 $mA \cdot cm^{-2}_{geo}$)	0.17	0.16 at 300 mV	-		XRD, N_2 ISO (BET, PSD)	-	-	-	-	
Ni-B/G (Ni-B/rGO)	GC	-	P	0.3	356 (@15 $mA \cdot cm^{-2}_{geo}$)	0.04	0.09 at 300 mV	103		-	-	-	-	-	
Fe-B/G (Fe-B/rGO)	GC	-	P	0.3	448 (@15 $mA \cdot cm^{-2}_{geo}$)	0.017	-	119		-	-	-	-	-	
FeNi-B/G (Fe_xNi_y-$B_{(Fe:Ni = 1:1)}$/rGO)	GC	-	P	0.3	~310 (@15 $mA \cdot cm^{-2}_{geo}$)	0.19	0.27 at 300 mV	77		-	-	-	-	-	
FeNi2-B/G (Fe_xNi_y-$B_{(Fe:Ni = 1:2)}$/rGO)	GC	-	P	0.3	~242 (@15 $mA \cdot cm^{-2}_{geo}$)	0.12	0.61 at 300 mV	55		-	-	-	-	-	
FeNi6-B/G (Fe_xNi_y-$B_{(Fe:Ni = 1:6)}$/rGO)	GC	-	P	0.3	~263 (@15 $mA \cdot cm^{-2}_{geo}$)	0.11	0.48 at 300 mV	50		-	-	-	-	-	
FeNi9-B/G (Fe_xNi_y-$B_{(Fe:Ni = 1:9)}$/rGO)	GC	-	P	0.3	~268 (@15 $mA \cdot cm^{-2}_{geo}$)	0.13	0.55 at 300 mV	52		-	-	-	-	-	
TiB_2	FTO glass	Microparticle	P	2	560 ± 20	-	-	-	1 M $HClO_4$ (pH = 0)	XRD, SEM, ICP-OES, XPS	SEM, XPS (after 0, 1, 5, 30, 60, 120, 240, and 480 min CP), ICP-OES (every 30 min CP up to 10 h)	> 10 h CP (10 $mA \cdot cm^{-2}_{geo}$)	TiO_2, TiB_2, B_2O_3, $TiBO_x$	Precatalyst (partial oxidation + dissolution)	146
TiB_2	FTO glass	Microparticle	P	2	~560	-	-	-	1 M H_2SO_4	XRD, SEM, ICP-OES, XPS	-	> 9 h CP (10 $mA \cdot cm^{-2}_{geo}$)	-	-	

https://doi.org/10.1021/acs.chemrev.3c00005
Chem. Rev. 2023, 123, 12795−13208

Table 1. continued

Initial Electrocatalyst	Substrate	Shape of Electrocatalyst	Deposition Type	Specific Loading / $mg \cdot cm^{-2}_{geo}$	η@10 $mA \cdot cm^{-2}_{geo}$ / mV	C_{dl} / $mF \cdot cm^{-2}_{geo}$	TOF / s^{-1} (@η or j)	Tafel Slope / $mV \cdot dec^{-1}$	Electrolyte	Pre-analysis	Post-analysis	Long-Term OER Test Conditions	Post-OER Electrocatalyst	Final Type of Electrocatalyst	Ref.
Co-B	FTO glass	Spherical particulate	S	-	280	0.0004	-	60	1 M KOH	XRD, SEM, EDX, TEM, XPS	XPS (after CV), SEM (after CA)	25 CV cycles (10 $mV \cdot s^{-1}$, 0–1 $V_{Hg/HgO}$) 45 h CA (1.49 V_{RHE}) 2000 CV cycles (100 $mV \cdot s^{-1}$)	$Co(OH)_2$/CoOOH, BO_x	Precatalyst (dissolution)	147
Co-B	FTO glass	Nanoparticle	P	-	338	0.00196	-	39		XRD, SEM	-	-	-	-	
Co-5Ni-B	GC	-	P	~0.75	~330	-	-	119.8	1 M KOH	ICP-AES	-	-	-	-	148
Co-10Ni-B	GC	Nanoparticle	P	~0.75	330	-	-	73.3		XRD, EDX, TEM, SAED, XPS, N_2 ISO (BET), ICP-AES	XRD, XPS (after CA)	2 h CA (1.56 V_{RHE})	$Co(OH)_2$/CoOOH, $Ni(OH)_2$/NiOOH, BO_x	Precatalyst	
Co-15Ni-B	GC	-	P	~0.75	~340	-	-	101.9		ICP-AES	-	-	-	-	
Co-20Ni-B	GC	-	P	~0.75	~390	-	-	-		ICP-AES	-	-	-	-	
Co-10Ni-B-sp (a smaller particle size)	GC	Nanoparticle	P	~0.75	310	-	-	66		SEM, TEM, N_2 ISO (BET)	-	35 h CA (1.56 V_{RHE})	-	-	
Co-B	GC	-	P	~0.75	360	-	-	112.9		XPS, ICP-AES	-	-	-	-	
Ni-B	GC	-	P	~0.75	402	-	-	161.6		ICP-AES	-	-	-	-	
Fe-Ni-$B_{(Ni:Fe = 1:1)}$	Ni foam	-	S	1	~271	-	-	43	1 M KOH	-	-	CV activation	-	-	149
Fe-2Ni-$B_{(Ni:Fe = 1:2)}$	Ni foam	-	S	1	~252	-	-	43	1 M KOH	ICP-OES	ICP-OES (after CV activation)	CV activation	-	Precatalyst (partial oxidation)	
Fe-3Ni-$B_{(Ni:Fe = 1:3)}$	Ni foam	-	S	1	~242	-	-	39		ICP-OES	ICP-OES (after CV activation)	CV activation	-	Precatalyst (partial oxidation)	
Fe-6Ni-$B_{(Ni:Fe = 1:6)}$	Ni foam	Nanosheet	S	1	237 275 (@100 $mA \cdot cm^{-2}_{geo}$)	-	0.035 at 306 mV	38		XRD, SEM, EDX, TEM, SAED, XPS, ICP-OES	ICP-OES, SEM, XPS (after CV activation)	CV activation, 1000 CV cycles (100 $mV \cdot s^{-1}$, 0.26–0.66 $V_{Hg/HgO}$) 12 h CA (~ 1.48 V_{RHE}) 12 h CP (20 $mA \cdot cm^{-2}_{geo}$)	$Fe(Ni)O_xH_y$, B_2O_3	Precatalyst (partial oxidation)	
Fe-9Ni-$B_{(Ni:Fe = 1:9)}$	Ni foam	-	S	1	~251	-	-	38		-	-	CV activation	-	-	
Ni-B	Ni foam	-	S	1	282 326 (@100 $mA \cdot cm^{-2}_{geo}$)	-	0.006 at 306 mV	41		-	-	CV activation	-	-	
Fe-B	Ni foam	-	S	1	290	-	-	43		-	-	CV activation	-	-	
Fe-6Ni-$B_{(Ni:Fe = 1:6)}$	Ni foam	-	P	1	292 (@100 $mA \cdot cm^{-2}_{geo}$)	-	-	68		-	-	CV activation	-	-	
Fe-Co-2.3Ni-B	GC	Nanoparticle	P	0.3	274 286 (@20 $mA \cdot cm^{-2}_{geo}$)	0.17	-	38	1 M KOH	XRD, SEM, EDX, TEM, SAED	SEM (after CP), EDX	CV activation 1000 CV cycles (100 $mV \cdot s^{-1}$, 0.2–0.6 $V_{Ag/AgCl}$) 10 h CP (10 $mA \cdot cm^{-2}_{geo}$)	-	Precatalyst (partial oxidation)	150
0.1Fe-Co-2.3Ni-B	GC	-	P	0.3	307 325 (@20 $mA \cdot cm^{-2}_{geo}$)	-	-	54		-	-	CV activation	-	-	
Fe-0.1Co-2.3Ni-B	GC	-	P	0.3	306 324 (@20 $mA \cdot cm^{-2}_{geo}$)	-	-	67		-	-	CV activation	-	-	
Fe-Co-Ni-B	GC	-	P	0.3	284 301 (@20 $mA \cdot cm^{-2}_{geo}$)	-	-	49		-	-	CV activation	-	-	
Fe-Co-4.6Ni-B	GC	-	P	0.3	291 312 (@20 $mA \cdot cm^{-2}_{geo}$)	-	-	59		-	-	CV activation	-	-	
Fe-Co-9.0Ni-B	GC	-	P	0.3	292 315 (@20 $mA \cdot cm^{-2}_{geo}$)	-	-	63		-	-	CV activation	-	-	
Fe-2.3Ni-B	GC	-	P	0.3	294 312 (@20 $mA \cdot cm^{-2}_{geo}$)	-	-	53		XRD	-	CV activation 1000 CV cycles (100 $mV \cdot s^{-1}$, 0.2–0.6 $V_{Ag/AgCl}$) 10 h CP (10 mA cm^{-2}_{geo})	-	-	
Co-2.3Ni-B	GC	-	P	0.3	317 331 (@20 $mA \cdot cm^{-2}_{geo}$)	-	-	49		XRD	-	CV activation 1000 CV cycles (100 $mV \cdot s^{-1}$, 0.2–0.6 $V_{Ag/AgCl}$) 10 h CP (10 mA cm^{-2}_{geo})	-	-	
Co-B	GC	-	P	0.3	322 344 (@20 $mA \cdot cm^{-2}_{geo}$)	-	-	72		-	-	CV activation	-	-	
Ni-B	GC	Nanoparticle	P	0.3	314 331 (@20 $mA \cdot cm^{-2}_{geo}$)	0.1	-	52		SEM, TEM	-	CV activation	-	-	
Fe-B	GC	-	P	0.3	365 392 (@20 $mA \cdot cm^{-2}_{geo}$)	-	-	72		-	-	CV activation	-	-	
Mixture of M-B	GC	-	P	0.3	307 328 (@20 $mA \cdot cm^{-2}_{geo}$)	-	-	57		-	-	CV activation	-	-	
Ni-B@$Ni(OH)_2$	Ni foam	Nanoparticle (Ni-B), Nanosheet ($Ni(OH)_2$)	S	7.03	300 (@100 $mA \cdot cm^{-2}_{geo}$)	5.45	-	49	1 M KOH	XRD, SEM, XPS, Raman	SEM (after CP), Raman	CV activation, 10 h CP [50 (5 h) and 100 (5 h) $mA \cdot cm^{-2}_{geo}$]	NiOOH	Precatalyst	151
Ni-B	Ni foam	-	S	1.03	385 (@100 $mA \cdot cm^{-2}_{geo}$)	0.54	-	76		-	-	CV activation	-	-	
$(Co_{0.7}Fe_{0.3})_2B$	GC	Nanorod network	P	-	330	-	-	39	1 M KOH	XRD, SEM, EDX, TEM, XPS	XPS	CV activation ~ 16.4 h CP (10 $mA \cdot cm^{-2}_{geo}$)	$Co(OH)_2$/CoOOH, BO_x	Precatalyst (partial oxidation)	152
$(Co_{0.9}Fe_{0.1})_2B$	GC	-	P	-	~340	-	-	38		XRD, EDX	-	CV activation	-	-	
$(Co_{0.8}Fe_{0.2})_2B$	GC	-	P	-	~350	-	-	45		XRD, EDX	-	CV activation	-	-	
$(Co_{0.6}Fe_{0.4})_2B$	GC	-	P	-	~390	-	-	50		XRD	-	CV activation	-	-	
$(Co_{0.5}Fe_{0.5})_2B$	GC	-	P	-	~395	-	-	50		XRD	-	CV activation	-	-	

https://doi.org/10.1021/acs.chemrev.3c00005
Chem. Rev. 2023, 123, 12795−13208

Table 1. continued

Initial Electrocatalyst	Substrate	Shape of Electrocatalyst	Deposition Type	Specific Loading / $mg \cdot cm^{-2}_{geo}$	η@10 $mA \cdot cm^{-2}_{geo}$ / mV	C_{dl} / $mF \cdot cm^{-2}_{geo}$	TOF / s^{-1} (@η or f)	Tafel Slope / $mV \cdot dec^{-1}$	Electrolyte	Pre-analysis	Post-analysis	Long-Term OER Test Conditions	Post-OER Electrocatalyst	Final Type of Electrocatalyst	Ref.
Co_2B	GC	Nano- rod and sphere agglomeration	P	-	410	-	-	63		XRD, SEM	-	CV activation	-	-	152
Co-B	Ni foil	Porous nodule structure	S	2.4	140	53	0.58 at 300 mV	98	1 M KOH	XRD, FESEM, EDX, ICP-AES, XPS	XRD, FESEM, XPS, EDX (after CP)	CV activation 1000 CV cycles (50 $mV \cdot s^{-1}$, 1.0−1.8 V_{RHE}) 20 h CA (2.12 V_{RHE}: ~ 1000 $mA \cdot cm^{-2}_{geo}$) 20 h CP (10 $mA \cdot cm^{-2}_{geo}$)	$Co(OH)_2$/CoOOH, BO_x	Precatalyst (partial oxidation)	153
Ni-B	Ni foil	-	S	-	272	-	-	76.9		-	-	CV activation	-	-	
Co-Ni-B	Ni foil	-	S	-	270	-	-	98.5		-	-	CV activation	-	-	
Ni-W-B	Ni foil	-	S	-	165	-	-	50.7		-	-	CV activation	-	-	
Co-B	CC	Porous nodule structure	S	-	130	-	-	146.7		FESEM	-	CV activation	-	-	
Ni-B	CC	-	S	-	290	-	-	48		-	-	CV activation	-	-	
Co-Ni-B	CC	-	S	-	281	-	-	108.1		-	-	CV activation	-	-	
Ni-W-B	CC	-	S	-	305	-	-	42		-	-	CV activation	-	-	
Co-B	Ti foil	Porous nodule structure	S	-	300	-	-	108.3		FESEM	-	CV activation	-	-	
Ni-B	Ti foil	-	S	-	291	-	-	99.8		-	-	CV activation	-	-	
Co-Ni-B	Ti foil	-	S	-	300	-	-	94.9		-	-	CV activation	-	-	
Ni-W-B	Ti foil	-	S	-	305	-	-	99.3		-	-	CV activation	-	-	
CoB	Ni foam	Nanosheet	S	~ 12	~ 326	34.38	-	80	1 M KOH	XRD, FESEM, EDX, TEM, SAED	-	CV activation	-	-	154
CoB	Cu foam	-	S	-	~ 328	-	-	-		-	-	CV activation	-	-	
CoB	CC	-	S	-	~ 337	-	-	-		-	-	CV activation	-	-	
CoB	Ti plate	-	S	-	~ 363	-	-	-		-	-	CV activation	-	-	
Ar-annealed CoB	Ni foam	Nanosheet	S	~ 12	315	39.88	0.0004 at 350 mV	83		XPS, FESEM, Raman	FESEM, EDX, TEM, SAED, Raman	CV activation 12 h CA (1.55 V_{RHE})	$Co(OH)_2$/CoOOH	Precatalyst (partial oxidation)	
Co-Ni-B	Ni foam	Nanoparticle	S	-	339 457 (@50 $mA \cdot cm^{-2}_{geo}$)	32	-	131	1 M KOH	XRD, FESEM, TEM, SAED, XPS	-	CV activation	-	-	155
Ar-annealed Co-Ni-B	Ni foam	Nanoparticle agglomeration	S	-	313 402 (@50 $mA \cdot cm^{-2}_{geo}$)	49	-	120		XRD, FESEM, XPS	FESEM, XPS (CV activation)	CV activation 12 h CP (10 and 50 $mA \cdot cm^{-2}_{geo}$)	CoO, CoOOH, NiOOH	Precatalyst	
Co-B	Ni foam	-	S	-	341 534 (@50 $mA \cdot cm^{-2}_{geo}$)	32	-	154		-	-	CV activation	-	-	
Ni_xB	GC	Nanosheet	P	0.21	500	-	-	-	1 M KOH	XRD, SEM, XPS, XAFS (XANES and EXAFS), ICP-OES	-	CV activation	-	-	105
Ni_xB-300	GC	Nanosheet	P	0.21	380	-	0.048 at 370 mV	89		XRD, SEM, TEM, AFM, XPS, XAFS (XANES and EXAFS), ICP-OES, EELS, N_2 ISO (BET)	XPS (CV activation), ICP-OES (50 CV + 2 h CP)	CV activation	$Ni(OH)_2$/NiOOH	Precatalyst (partial oxidation)	
Ni_xB-300	Graphite	Nanosheet	P	0.21	~ 400	-	-	-		XRD, SEM, TEM, AFM, XPS, XAFS (XANES and EXAFS), ICP-OES, EELS, N_2 ISO (BET)	-	60 h CP (10 mA cm^{-2}_{geo})	-	-	
Ni_xB-300	Ni foam	Nanosheet	P	0.180−0.25	280 (@20 $mA \cdot cm^{-2}_{geo}$)	-	-	-		XRD, SEM, TEM, AFM, XPS, XAFS (XANES and EXAFS), ICP-OES, EELS, N_2 ISO (BET)	-	-	-	-	
Ni_xB-300	Graphite paper disk	Nanosheet	P	-	-	-	-	-	0.1 M KOH	XRD, SEM, TEM, AFM, XPS, XAFS (XANES and EXAFS), ICP-OES, EELS, N_2 ISO (BET)	*Operando* XAFS (XANES and EXAFS) (after 10 CV, at 1.0 V_{RHE}, and at 1.7 V_{RHE})	10 CV cycles (1.0−1.6 V_{RHE})	$Ni(OH)_2$/NiOOH	Precatalyst (partial oxidation)	
CoB	CP	particle	P	2.56	340 464 (@100 $mA \cdot cm^{-2}_{geo}$)	1.17	0.5 at 413 mV	63	1 M KOH	XRD, SEM, TEM, EDX, XPS	XRD, SEM, TEM, XPS (after 12 h CP)	12 h CP (50 $mA \cdot cm^{-2}_{geo}$)	CoOOH, Co_3O_4	Precatalyst (partial oxidation)	156
Co_2B	CP	particle	P	2.56	287 389 (@100 $mA \cdot cm^{-2}_{geo}$)	3.7	0.5 at 328 mV	50.7		XRD, SEM, TEM, EDX, XPS	XRD, SEM, TEM, XPS (after 12 h CP)	12 h CP (50 $mA \cdot cm^{-2}_{geo}$) 1000 CV cycles (50 $mV \cdot s^{-1}$)	CoOOH, Co_3O_4	Precatalyst (partial oxidation)	
Co_3B	CP	particle	P	2.56	312 428 (@100 $mA \cdot cm^{-2}_{geo}$)	1.52	0.5 at 370 mV	53		XRD, SEM, TEM, EDX, XPS	XRD, SEM, TEM, XPS (after 12 h CP)	12 h CP (50 $mA \cdot cm^{-2}_{geo}$)	CoOOH, Co_3O_4	Precatalyst (partial oxidation)	
Co_2B	CP	particle	P	2.56	292	-	-	-	0.1 M KOH	XRD, SEM, TEM, EDX, XPS	-	-	-	-	
	GC	particle	P	0.2	371	-	-	-			-	-	-	-	
Co-B/CoO	Ti mesh	Nanoparticle	S	4.87 [2.50 (Co-B) and 2.37 (CoO)]	190 290 (@50 $mA \cdot cm^{-2}_{geo}$) 310 (@100 $mA \cdot cm^{-2}_{geo}$)	29.8	-	78	1 M KOH	XRD, SEM, STEM-EDX, TEM, XPS, N_2 ISO (BET), ICP-AES	XRD, SEM, XPS, ICP-AES	CV activation 20 h CP (50 $mA \cdot cm^{-2}_{geo}$)	CoO/Co(OH)$_2$, BO_x, Co-B	Precatalyst (partial oxidation)	157
Co-B/CoO	Ti mesh	Nanoparticle	S	4.87 [2.50 (Co-B) and 2.37 (CoO)]	250 (@50 $mA \cdot cm^{-2}_{geo}$)	29.8	-	-	30 wt.% KOH	XRD, SEM, STEM-EDX, TEM, XPS, N_2 ISO (BET), ICP-AES	-	CV activation	-	-	
FeB_2	GC	Nanoparticle	P	0.2	296 323 (@20 $mA \cdot cm^{-2}_{geo}$) 408 (@100 $mA \cdot cm^{-2}_{geo}$)	33.68	-	52.4	1 M KOH	XRD, SEM, EDX, TEM, SAED, XPS, ICP-OES, N_2 ISO (BET)	XRD, SEM, TEM, ICP-OES, N_2 ISO (BET) (1 and 12 h CP), XPS (12 h CP), ATR-FTIR (12 h CP)	CV activation 1000 CV cycles (50 $mV \cdot s^{-1}$, 1.20−1.65 V_{RHE}) 48 h CA (1.6 V_{RHE}) 1 and 12 h CP (10 $mA \cdot cm^{-2}_{geo}$)	FeOOH, B-O (borate), Fe-B	Precatalyst (partial oxidation)	158

https://doi.org/10.1021/acs.chemrev.3c00005
Chem. Rev. 2023, 123, 12795−13208

Table 1. continued

Initial Electrocatalyst	Substrate	Shape of Electrocatalyst	Deposition Type	Specific Loading / $mg \cdot cm^{-2}_{geo}$	η@10 $mA \cdot cm^{-2}_{geo}$ / mV	C_{dl} / $mF \cdot cm^{-2}_{geo}$	TOF / s^{-1} (@η or f)	Tafel Slope / $mV \cdot dec^{-1}$	Electrolyte	Pre-analysis	Post-analysis	Long-Term OER Test Conditions	Post-OER Electrocatalyst	Final Type of Electrocatalyst	Ref.
Fe_2B	GC	Nanoparticle	P	0.2	~345	17.76	-	78.7		XRD, SEM, EDX, ICP-OES, N_2 ISO (BET)	-	CV activation	-	-	158
$NiB_{0.45}$-250	Cu foil	Nano-particulate	S	1.4	296 356 (@100 $mA \cdot cm^{-2}_{geo}$)	0.41±0.075	-	58	1 M KOH	XRD, SEM, TEM, SAED, ICP-OES	SEM (after 60 h CP), ICP-OES	CV activation (5 $mV \cdot s^{-1}$, 1.2–1.5 V_{RHE}) 2 h CA (1.536 V_{RHE}) 60 h CA (1.526 V_{RHE})	-	-	159
$NiB_{0.45}$-200	Cu foil	Nano-particulate	S	1.4	311	0.37±0.012	-	-		XRD, SEM	-	CV activation (5 $mV \cdot s^{-1}$, 1.2–1.5 V_{RHE})	-	-	
$NiB_{0.45}$-300	Cu foil	Nano-particulate	S	1.4	350	0.15±0.013	-	-		XRD, SEM	-	CV activation (5 $mV \cdot s^{-1}$, 1.2–1.5 V_{RHE})	-	-	
$NiB_{0.45}$	Cu foil	Nano-particulate	S	1.4	327	0.35±0.005 4	-	81		XRD, SEM, SEM-EDX, TEM-EDX, TEM, SAED, AFT, ICP-OES, XPS	XPS, XAS, Raman, HAADF-STEM, EDX	CV activation (5 $mV \cdot s^{-1}$, 1.2–1.5 V_{RHE})	NiO, (NiOOH surface), BO_x	Precatalyst (partial oxidation)	
$NiB_{0.37}$	Cu foil	-	S	1.478	~336	-	-	-		ICP-OES	-	CV activation	-	-	
$NiB_{0.25}$	Cu foil	-	S	1.575	~393	-	-	-		ICP-OES	-	CV activation	-	-	
Co-3Mo-B	GC	Nanoparticle	P	2.1	320	-	-	155	1 M NaOH	XRD, EDX, TEM, SAED, XPS, N_2 ISO (BET)	XPS (after 50 CV)	1000 and 50 CV cycles 10 h CA (1.58 V_{RHE})	$Co(OH)_2$/CoOOH, MoO_x, BO_x	Precatalyst (partial oxidation)	160
Co-3Mo-B	GC	Nanoparticle	P	2.1	800	0.38	-	-	0.5 M KPi (pH = 7)	XRD, EDX, TEM, SAED, XPS, N_2 ISO (BET)	-	10 h CA (2.08 V_{RHE})	-	-	
CoB	GC	Nanoparticle	P	0.21	390	-	-	-	0.1 M KOH	ADF STEM, TEM, STEM-EELS	-	CV activation	-	-	161
CoB/NCNT-500	GC	Nanoparticle	P	0.21	370	-	-	-		XRD, SEM, EA, TEM, ADF STEM, STEM-EELS, Raman, XPS	ADF STEM, STEM-EELS	CV activation 51 h CP (10.2 $mA \cdot cm^{-2}_{geo}$)	CoO_x	Precatalyst (partial oxidation)	
CoB/NCNT-600	GC	Nanoparticle	P	0.21	430	-	-	-		SEM, EA, XPS	-	CV activation	-	-	
CoB/NCNT-700	GC	Nanoparticle	P	0.21	500	-	-	-		SEM, EA, XPS	-	CV activation	-	-	
Co2-Fe-B	Cu sheet	Nanoparticle	P	1.2	298	-	-	62.6	1 M KOH	XRD, SEM, TEM, EDX, XFS	-	CV activation 12 h CA (η_{10})	-	-	162
Co2-Fe-B	SS	Nanoparticle	P	0.2	-	-	-	-		XRD, SEM, TEM, EDX, XFS	SEM, TEM, EDX, XPS (after CV activation)	CV activation CV cycles (100 $mV \cdot s^{-1}$)	$Co(OH)_2$/CoOOH, FeOOH, B-O species	Precatalyst	
Co2-Fe-B	GC	Nanoparticle	P	0.2	-	-	-	-		XRD, SEM, TEM, EDX, XFS	-	CV activation	-	-	
Co3-Fe-B	Cu sheet	Nanoparticle	P	1.2	~315	-	-	77.9		XRD, SEM, XFS	-	CV activation	-	-	
Co1-Fe-B	Cu sheet	Nanoparticle	P	1.2	~335	-	-	89.2		XRD, SEM, XFS	-	CV activation	-	-	
Co-B	Cu sheet	Nanoparticle	P	1.2	340	-	-	97.3		XRD, SEM, XFS	-	CV activation	-	-	
Co-B	SS	Nanoparticle	P	0.2	-	-	-	-		XRD, SEM, XFS	XPS (after CV activation)	CV activation CV cycles (100 $mV \cdot s^{-1}$)	$Co(OH)_2$/CoOOH, B-O species	Precatalyst	
Co-B	GC	Nanoparticle	P	0.2	-	-	-	-		XRD, SEM, XFS	-	CV activation	-	-	
Fe-B	Cu sheet	Nanoparticle	P	1.2	472	-	-	81.6		XRD, SEM, XFS	-	CV activation 12 h CA (η_{10})	-	-	
Fe-B	SS	Nanoparticle	P	0.2	-	-	-	-		XRD, SEM, XFS	XPS (after CV activation)	CV activation CV cycles (100 $mV \cdot s^{-1}$)	FeOOH, B-O species	Precatalyst	
Fe-B	GC	Nanoparticle	P	0.2	-	-	-	-		XRD, SEM, XFS	-	CV activation	-	-	
$Co_2B_{(Co:B = 1.9:1)}$	GC	Ultrathin particle	P	0.21	~461	-	-	-	0.1 M KOH	XRD, SEM, ICP-AES, N_2 ISO (BET), EDX, XPS, XAFS (XANES and EXAFS)	-	CV activation (1.0–2.0 V_{RHE})	-	-	163
Co_2B-500$_{(Co:B = 2.1:1)}$	GC	Large aggregates	P	0.21	380	-	-	45		XRD, SEM, ICP-AES, N_2 ISO (BET), TEM, XPS, XAFS (XANES and EXAFS)	ICP-AES (after 20 CV and 25 h CP), XPS (after CV activation)	CV activation (1.0–2.0 V_{RHE}) 60 h CP (10 $mA \cdot cm^{-2}_{geo}$) 5000 CV cycles (100 $mV \cdot s^{-1}$, 1.0–1.8 V_{RHE})	$Co(OH)_2$/CoOOH, BO_x	Precatalyst (Partial oxidation)	
Co_2B-500$_{(Co:B = 2.1:1)}$	FTO glass	Large aggregates	P	0.21	450	-	-	-		XRD, SEM, ICP-AES, N_2 ISO (BET), TEM, XPS, XAFS (XANES and EXAFS)	-	CV activation (1.0–2.0 V_{RHE})	-	-	
Co_2B-1000	GC	Fully-agglomerated tubular	P	0.21	360	-	-	-		XRD, SEM, N_2 ISO (BET), TEM	-	CV activation (1.0–2.0 V_{RHE})	-	-	
Co_2B-500/NG	GC	-	P	0.21	~503	-	-	-		-	-	CV activation (1.0–2.0 V_{RHE})	-	-	
Fe-B-O@Fe_2B	Ni foil	Nanoclaster	P	2.8	273	1.07	-	58.7	1 M KOH	XRD, SEM, EDX, ICP-AES	-	-	-	Precatalyst (surface oxidized before the OER)	164
Fe-B-O@FeB_2	Ni foil	Nanoclaster	P	2.8	260	1.58	-	57.9		XRD, SEM, EDX, ICP-AES	-	500 CV cycles (50 $mV \cdot s^{-1}$, 0.8–1.1 V_{SCE})	-	Precatalyst (surface oxidized before the OER)	
Ni-B-O@Ni_3B	Ni foil	Nanoparticle	P	1.6	264	2.3	-	127	1 M KOH	XRD, SEM, EDX, XPS, ICP-OES	-	-	-	Precatalyst (surface oxidized before the OER)	165
Ni-B-O@Ni_2B	Ni foil	Nanoparticle	P	1.6	228	1.7	-	151.2		XRD, SEM, EDX, XPS, ICP-OES	-	-	-	Precatalyst (surface oxidized before the OER)	
Ni-B-O@NiB_2	Ni foil	Nanoparticle	P	1.6	219	1.5	-	126.2		XRD, SEM, EDX, XPS, ICP-OES	-	500 CV cycles 20 h CA (1.45 V_{RHE})	-	Precatalyst (surface oxidized before the OER)	
Co-B@Co-Bi	GC	Nanoparticle	P	0.306	291	91.41	-	120.73	1 M KOH	XRD, SEM, EDX, TEM, XPS, ICP-AES	SEM, XPS, TEM (after 25 h CP)	5000 CV cycles (1.2–1.7 V_{RHE}) 25 h CP (10 $mA \cdot cm^{-2}_{geo}$)	Co-B-O, CoOOH	Precatalyst (surface oxidized before the OER)	166

https://doi.org/10.1021/acs.chemrev.3c00005
Chem. Rev. 2023, 123, 12795−13208

Table 1. continued

Initial Electrocatalyst	Substrate	Shape of Electrocatalyst	Deposition Type	Specific Loading / $mg \cdot cm^{-2}_{geo}$	η@10 $mA \cdot cm^{-2}_{geo}$ / mV	C_{dl} / $mF \cdot cm^{-2}_{geo}$	TOF / s^{-1} (@η or j)	Tafel Slope / $mV \cdot dec^{-1}$	Electrolyte	Pre-analysis	Post-analysis	Long-Term OER Test Conditions	Post-OER Electrocatalyst	Final Type of Electrocatalyst	Ref.
Co-B@Co-Bi-800	GC	-	P	0.306	~444	-	-	-		XRD	-	-	-	-	
Co-B	GC	Nanoparticle	P	0.306	348	48.84	-	111.39		XRD, SEM, TEM, XPS, ICP-AES	-	5000 CV cycles (1.2–1.7 V_{RHE}) ~12.5 h CP (10 $mA \cdot cm^{-2}_{geo}$)	-	-	166
Ni-B@Ni-Bi	GC	Nanoparticle	P	0.306	310	-	-	150.1		SEM, TEM	-	-	-	-	
Ni-B	GC	Nanoparticle	P	0.306	365	-	-	108.49		SEM, TEM	-	-	-	-	
a-Ni-B_i@NB (NB = Ni_3B)	GC	Nanoparticle	P	0.3	364	0.35	0.008 at 300 mV	65	1 M KOH	XRD, TEM, EDX, XPS, N_2 ISO (BET), TGA	-	~4 h CP (10 $mA \cdot cm^{-2}_{geo}$, bad stability)	-	Precatalyst (surface oxidized before the OER)	167
pc-Ni-B_i@NB-0.5	GC	Nanoparticle	P	0.3	341	-	0.019 at 300 mV	-		XRD, TEM, XPS, N_2 ISO (BET)	-	-	-	Precatalyst (surface oxidized before the OER)	
pc-Ni-B_i@NB-1	GC	Nanoparticle	P	0.3	328	-	0.024 at 300 mV	-		XRD, TEM, XPS, N_2 ISO (BET)	-	-	-	Precatalyst (surface oxidized before the OER)	
pc-Ni-B_i@NB-2 (pc-Ni-B_i@NB)	GC	Nanoparticle	P	0.3	302	2.54	0.052 at 300 mV	52		XRD, TEM, EDX, XPS, N_2 ISO (BET)	TEM	8 h CP (10 $mA \cdot cm^{-2}_{geo}$)	-	Precatalyst (surface oxidized before the OER)	
pc-Ni-B_i@NB-2.5	GC	Nanoparticle	P	0.3	302	-	0.026 at 300 mV	-		XRD, TEM, XPS, N_2 ISO (BET)	-	-	-	Precatalyst (surface oxidized before the OER)	
Pure Ni_3B	GC	Nanoparticle	P	0.3	409	-	-	-		XRD, TEM	-	-	-	-	
Co3Ni1B–rGO	GC	Flower-like nanosheet	P	0.36	318	20.1	-	68	1 M KOH	XRD, SEM, EDX, TEM, XPS, N_2 ISO (BET, PSD), Raman	SEM	1000 CV cycles 16 h CP (10 $mA \cdot cm^{-2}_{geo}$)	-	-	168
Co3Ni1B	GC	Flower-like nanosheet	P	0.36	358	7.94	-	79		XRD, SEM, Raman	-	-	-	-	
Co_xB-rGO	GC	-	P	0.36	339	-	-	122		XRD	-	-	-	-	
Ni_xB-rGO	GC	-	P	0.36	459	-	-	197		XRD	-	-	-	-	
CBC (Co–B/BCCNF)	Ni foam	3D nanofiber networks covered with nanosheets	P	4.0	331	2.73	-	220	1 M KOH	XRD, SEM, XPS, Raman	-	-	-	-	169
W-FeB	Ni foam	-	P	-	227 270 (@50 $mA \cdot cm^{-2}_{geo}$) 288 (@100 $mA \cdot cm^{-2}_{geo}$)	7.41	-	55.77	1 M KOH	XRD	-	-	-	-	170
FeB	Ni foam	-	P	-	209 246 (@50 $mA \cdot cm^{-2}_{geo}$) 259 (@100 $mA \cdot cm^{-2}_{geo}$)	7.07	-	47.24		XRD	-	-	-	-	
Ni-Co-B/Cu	Cu sheet	Spherical micro-nodules	S	7	276	10.2	-	88	1 M KOH	XRD, SEM, EDX, ICP-OES, XPS	-	1000 CV cycles (100 $mV \cdot s^{-1}$, 1.0–1.568 V_{RHE}) 10 h CP (100 $mA \cdot cm^{-2}_{geo}$)	-	-	171
Ni-B/Cu	Cu sheet	Micro-crevices	S	7	340	4.3	-	137		XRD, SEM	-	-	-	-	
CoFeB-5-30/NF	Ni foam	Nanosheet	S	2	260 (@20 $mA \cdot cm^{-2}_{geo}$)	11.85	-	38	1 M KOH	XRD, SEM, TEM, EDX, XPS	-	1000 and 3000 CV cycles (100 $mV \cdot s^{-1}$) 70 h CP (20, 50 and 100 $mA \cdot cm^{-2}_{geo}$)	-	-	172
CoB-5-30/NF	Ni foam	Nanosheet	S	2	340 (@20 $mA \cdot cm^{-2}_{geo}$)	3.23	-	81		XRD, SEM	-	-	-	-	
FeB-5-30/NF	Ni foam	Nanosheet	S	2	320 (@20 $mA \cdot cm^{-2}_{geo}$)	6.65	-	65		XRD, SEM	-	-	-	-	
FeMoB (FMB-2)	Ni foam	Nanochain	P	4.0	253	0.61	-	63	1 M KOH	XRD, SEM, TEM, XPS	-	20 h CA (1.49 V_{RHE})	-	-	173
FeB (FB)	Ni foam	Nanosheet	P	4.0	290	0.40	-	82		XRD, SEM, XPS	-	-	-	-	
A-CoB/f-CNF	GC	Nanosheet	P	1.41	350	0.35	0.083 (@ 350 mV)	173	0.1 M KOH	XRD, SEM, EDX, TEM, Raman, XPS	-	1000 CV cycles	-	-	174
A-CoB	GC	Nanosheet	P	1.41	400	-	-	223		-	-	-	-	-	
MoB	GC	Nanosheet	P	1.41	450	-	-	213		-	-	-	-	-	
NCB-1 (Ni-Co-B, Ni/Co = 3:7)	Ni foam	Nanocotton	P	4.0	300 480 (@50 $mA \cdot cm^{-2}_{geo}$)	-	-	113	1 M KOH	XRD, SEM, EDX, TEM, SAED, XPS, ISO (BET)	SEM	55 h CA (1.50 and 1.67 V_{RHE})	-	-	175
NCB-2 (Ni-Co-B, Ni/Co = 5:5)	Ni foam	Nanocotton	P	4.0	~540 (@50 $mA \cdot cm^{-2}_{geo}$)	-	-	119		SEM, ISO (BET)	-	-	-	-	
NCB-3 (Ni-Co-B, Ni/Co = 7:3)	Ni foam	Nanocotton	P	4.0	~570 (@50 $mA \cdot cm^{-2}_{geo}$)	-	-	139		SEM, ISO (BET)	-	-	-	-	
NB (Ni-B)	Ni foam	3D network	P	4.0	~530 (@50 $mA \cdot cm^{-2}_{geo}$)	-	-	179		SEM, XPS, ISO (BET)	-	-	-	-	
CB (Co-B)	Ni foam	Nanosheet	P	4.0	~500 (@50 $mA \cdot cm^{-2}_{geo}$)	-	-	157		SEM, XPS, ISO (BET)	-	-	-	-	
Fe3Co7-B/CNT (Fe_xCo_y-B, Fe/Co = 3:7)	GC	Nanosheet	P	0.3	265	6.0	0.44 at 300 mV	30	1 M KOH	XRD, TEM, SAED, XPS	TEM (after 1000 CV)	12 h CA (1.50 V_{RHE}) 1000 CV cycles (100 $mV \cdot s^{-1}$, 0.208–0.608 $V_{Hg/HgO}$)	-	-	176
Fe2Co8-B/CNT (Fe_xCo_y-B, Fe/Co = 3:7)	GC	-	P	0.3	275	4.3	0.27 at 300 mV	30		-	-	-	-	-	
Fe5Co5-B/CNT (Fe_xCo_y-B, Fe/Co = 3:7)	GC	Nanosheet	P	0.3	270	3.9	0.15 at 300 mV	32		TEM, SAED	-	-	-	-	

https://doi.org/10.1021/acs.chemrev.3c00005
Chem. Rev. 2023, 123, 12795−13208

Table 1. continued

Initial Electrocatalyst	Substrate	Shape of Electrocatalyst	Deposition Type	Specific Loading / $mg \cdot cm^{-2}_{geo}$	η@10 $mA \cdot cm^{-2}_{geo}$ / mV	C_{dl} / $mF \cdot cm^{-2}_{geo}$	TOF / s^{-1} (@η or j)	Tafel Slope / $mV \cdot dec^{-1}$	Electrolyte	Pre-analysis	Post-analysis	Long-Term OER Test Conditions	Post-OER Electrocatalyst	Final Type of Electrocatalyst	Ref.
Fe7Co3-B/CNT (Fe_xCo_y-B, Fe/Co = 3:7)	GC	-	P	0.3	287	0.3	0.26 at 300 mV	31		-	-	-	-	-	
Fe3Co7-B	GC	Nanosheet	P	0.3	282	0.06	0.26 at 300 mV	34		XRD	-	-	-	-	176
Fe-B/CNT	GC	Nanosheet	P	0.3	347	0.1	-	52		XRD, SEM, TEM, SAED, XPS	-	-	-	-	
Co-B/CNT	GC	Nanosheet	P	0.3	338	2.9	0.08 at 300 mV	73		XRD, SEM, TEM, SAED, XPS	-	-	-	-	
NiB	GC	-	P	0.21	350	-	$0.016^{loading}$ ($mol^{-1} \cdot s^{-1}$) $0.175^{Ni\ redox}$ ($mol^{-1} \cdot s^{-1}$)	59.5	1 M KOH	XRD, EDX, XPS	-	100 CV cycles (1.0–1.6 V_{RHE}, activation)	-	-	177
NiCoFeB	GC	Nanochain	P	0.375	284	12.8	-	46.6	1 M KOH	XRD, SEM, TEM, SAED, EDX, XPS, ICP-AES, N_2 ISO (BET)	SEM	10 h CA (1.515 V_{RHE})	-	-	178
NiCoB	GC	Nanochain	P	0.375	375	11.9	-	78.1		TEM, N_2 ISO (BET)	-	-	-	-	
CoB	GC	Nanochain	P	0.375	383	8.5	-	78.9		TEM, N_2 ISO (BET)	-	-	-	-	
Co_1-Fe_1-B + CB	Ni foil	Nanochain	P	0.46	261	5	-	50	1 M KOH	XRD, SEM, TEM	-	-	-	-	179
Co-B + CB	Ni foil	Nanochain	P	0.46	310	2	-	60		SEM	-	-	-	-	
Fe-B + CB	Ni foil	Nanosphere	P	0.46	308	1	-	67		SEM	-	-	-	-	
FeB	Ni foam	-	P	~1	~269	-	-	49	1 M KOH	-	-	-	-	-	180
Co-B (Co:B = 1.88:1)	Ni foam	Nanosheet	S	-	265 (@20 mA/cm^2_{geo})	76.9	-	55.6	1 M KOH	XRD, SEM, EDX, TEM, XPS, ICP-MS	SEM (after CV)	1000 CV cycles (50 mV/s, 1.3–1.7 V_{RHE}) 10 h CP (20 $mA \cdot cm^{-2}_{geo}$)	-	-	181
Co-B	Ni foam	-	P	-	290 (@20 mA/cm^2_{geo})	-	-	67.3		-	-	10 h CP (20 $mA \cdot cm^{-2}_{geo}$)	-	-	
Co-B	GC	Nanoparticle	P	0.3	340	0.065	0.0863 ($atom^{-1} \cdot s^{-1}$) at 500 mV	30	1 M NaOH	XRD, SEM, TEM, XPS, N_2 ISO (BET, PSD), ICP-AES	-	-	-	-	182
Co_xB/NC	GC	Nanoparticle	P	0.5	~374	-	-	80	0.1 M KOH	XRD, SEM, TEM (STEM), EDX, XPS	-	5 h pulse CP [10 (15 min) and −1 (15 min) $mA \cdot cm^{-2}_{geo}$]	-	-	183
Co_xB	GC	-	P	-	~416	-	-	103		-	-	-	-	-	
CoB	Ni disk	-	P	0.21	320 (@1 mA/cm^2_{geo})	-	-	-	1 M KOH	-	-	-	-	-	184
CoB	Ni foam	Nanoparticle	P	1	~350 (@20 mA/cm^2_{geo})	-	-	-		SEM	-	-	-	-	
Co-B/C	GC	Nanoparticle	P	0.16	320	13.5	-	75	1 M KOH	XRD, FESEM, TEM, XPS, N_2 ISO (BET, PSD)	-	20 h CP (10 $mA \cdot cm^{-2}_{geo}$)	-	-	185
Co-B/ZIF-67	GC	-	P	0.16	350	7.9	-	100		XRD, FESEM, XPS	-	-	-	-	
Ni_3B/rGO	CFP	Nanoparticle	P	-	290	-	0.012 at 290 mV	88.4	1 M KOH	XRD, SEM, TEM, SAED, XPS	-	12 h CA (1.52 V_{RHE})	-	-	186
Ni_3B	CFP	Nanoparticle	P	-	340	-	0.001 at 290 mV	81.4		XRD, SEM, TEM, SAED, XPS	-	-	-	-	
Ni-Fe-B/rGO	GC	Nanosheet	P	0.2	265 350 (@50 mA/cm^2_{geo})	-	-	58	1 M KOH	XRD, SEM, TEM, XPS	-	20 h CA (1.495 V_{RHE})	-	-	187
Ni-Fe-B	GC	Nanosheet	P	0.2	340 540 (@50 mA/cm^2_{geo})	-	-	97		SEM	-	-	-	-	
Co_1Fe_2-AMOR	GC	Nanosheet	P	0.36	47.1 ($A \cdot g^{-1}$ at η = 350 mV)	-	-	84	0.1 M KOH	XRD, SEM, ICP-OES	-	10000 s CA (0.7 $V_{Ag/AgCl}$)	-	-	188
Co_3Fe_1-AMOR	GC	Nanoparticle	P	0.36	34.9 ($A \cdot g^{-1}$ at η = 350 mV)	-	-	86		XRD, SEM, EDX, XPS, ICP-OES	-	-	-	-	
Ni_1Fe_2-AMOR	GC	Nanosheet	P	0.36	10.1 ($A \cdot g^{-1}$ at η = 350 mV)	-	-	188		XRD, SEM, ICP-OES	-	-	-	-	
Ni_3Fe_1-AMOR	GC	Nanoparticle	P	0.36	50.9 ($A \cdot g^{-1}$ at η = 350 mV)	-	-	110		XRD, SEM, EDX, XPS, ICP-OES	-	10000 s CA (0.7 $V_{Ag/AgCl}$)	-	-	
$Ba_5Sr_5Co_8Fe_2$-AMOR	GC	Nanoparticle	P	0.36	4.7 ($A \cdot g^{-1}$ at η = 350 mV)	-	-	88		XRD, SEM, EDX, XPS, ICP-OES	-	-	-	-	
$La_6Sr_4Co_2Fe_8$-AMOR	GC	Nanoparticle	P	0.36	3.7 ($A \cdot g^{-1}$ at η = 350 mV)	-	-	88		XRD, SEM, XPS, ICP-OES	-	-	-	-	
Co_2B/rGO	rGO film (rGO: reduced graphene oxide)	Nanoparticle	S	1	~380	-	-	85.4	1 M KOH	XRD, SEM, TEM, EDX, XPS	-	15 h CA (1.61 V_{RHE})	-	-	189

https://doi.org/10.1021/acs.chemrev.3c00005
Chem. Rev. 2023, 123, 12795−13208

Table 1. continued

Initial Electrocatalyst	Substrate	Shape of Electrocatalyst	Deposition Type	Specific Loading / mg·cm$^{-2}_{geo}$	η@10 mA·cm$^{-2}_{geo}$ / mV	C_{dl} / mF·cm$^{-2}_{geo}$	TOF / s^{-1} (@η or j)	Tafel Slope / mV dec^{-1}	Electrolyte	Pre-analysis	Post-analysis	Long-Term OER Test Conditions	Post-OER Electrocatalyst	Final Type of Electrocatalyst	Ref.
Co-W-B	Ni foam	Nanosheet	S	-	~366	-	-	-	1 M KOH	XRD, FESEM, TEM, Raman, XPS, ICP-AES	-	CV activation	-	-	190
Ar-annealed Co-W-B	Ni foam	Nanobranch	S	-	360	-	-	-		XRD, SEM, Raman, XPS	-	CV activation	-	-	
Co-B	Ni foam	-	S	-	~370	-	-	-			-	CV activation	-	-	
Co_2B	GC	-	P	-	370	-	-	-	1 M KOH	-	-	CV activation (1.0–2.0 V_{RHE} in 0.1 M KOH)	-	-	191

[a]Some values (i.e., "specific loading", "η", and "C_{dl}") were calculated or obtained from the descriptions and Figures in the previous papers. "Post-OER Electrocatalyst" and "Final Type of Electrocatalyst" were determined based on the experimental results and descriptions provided in the previous papers. [b]η, Overpotential; j, Current density; C_{dl}, Double layer capacitance; TOF, Turnover frequency; P, Powder-coated electrode; S, Self-supported electrode; CV, Cyclic voltammetry; CA, Chronoamperometry; CP, Chronopotentiometry; OWS, Overall water splitting. [c]Substrate abbreviations: GC (glassy carbon); CC (carbon cloth); CP (carbon paper); CFP (carbon fiber paper); SS (stainless steel); FTO (fluorine-doped tin oxide). [d]Electrolyte abbreviation: KPi (potassium phosphate). [e]Analysis abbreviations (minor terms only): ISO (isotherm); PSD (pore size distribution); SXES (soft X-ray emission spectroscopy); EA (elemental analysis); SRXRD (synchrotron radiation X-ray diffraction); F-AAS (flame atomic absorption spectroscopy); UPS (ultraviolet photoelectron spectroscopy); M-H [M (magnetization)-H (magnetic field) hysteresis loop]; ZFC (zero-field cooled magnetization curve); FC (field cooled magnetisation curve).

152, 157, 158, 160–166, 175, 176, 178, 179, 182, 183, and 186–191). In this method, transition metal salts and alkali borohydrides ($LiBH_4$ and $NaBH_4$) are normally used as transition metal and boron sources, respectively. During the synthesis, transition metal ions from the salts are reduced by borohydrides, forming the transition metal boride. Using the solution-based method, one can typically obtain the amorphous transition metal boride powders with nanostructural morphologies. For instance, Li *et al.* reported the preparation of Co-based Co_xM_yB (M = Ni, Fe) (NiCoFeB) via a one-pot solution-based method.[178] As shown in Figure 9a, $CoCl_2{\cdot}6H_2O$, $NiCl_2{\cdot}6H_2O$, $FeSO_4{\cdot}7H_2O$, and polyvinylpyrrolidone (PVP) were dissolved into deionized water in a three-necked round-bottomed flask while stirring under Ar atmosphere. Herein, PVP acts as a surface stabilizer, growth modifier, nanoparticle dispersant, and reducing agent for nanoparticle synthesis.[196] Subsequently, a $NaBH_4$ solution (a reductant) was added to the mixture-containing flask at room temperature. Then, an exothermic reaction between transition metal cations (Ni^{2+}, Co^{2+}, and Fe^{2+}) and BH_4^- resulted in the formation of the NiCoFeB material with amorphous, nanochain structure (≈20 nm in diameter) (see Figures 9b–e). From the high-resolution B 1s XPS spectrum of the NiCoFeB nanochain (Figure 9f), it is evident that M–B linkages [the interaction of boron with transition metals (Ni, Co, Fe)] were formed and boron-oxo species given the peaks at 187.9 and 192.0 eV. The surface boron-oxo species were likely formed due to the superficial oxidation of transition metal borides and the self-hydrolysis of $NaBH_4$ during synthesis.[150,197] To further investigate the effect of transition metals in the starting materials on the resultant boride morphology, CoB, NiCoB, and NiB were also prepared. As shown in Figures 9g–i, Co-based borides (CoB and NiCoB) successfully showed nanochain-like morphologies. However, NiB possessed a relatively large nanosphere-like shape unlike CoB and NiCoB. Accordingly, the chemical transformation from Co^{2+} and $NaBH_4$ into Co_xB might easily happen and the Co^{2+} cation is essential to obtain the nanochain morphology.

Importantly, post-annealing treatment can change the structural properties of the transition metal borides prepared by a solution-based method.[105,163,166] Recently, Masa *et al.* prepared amorphous cobalt boride (Co_2B) via a similar one-pot solution-based method.[163] Specifically, a $CoCl_2$ aqueous solution was deaerated in a round-bottomed Schlenk flask with a Schlenk vacuum setup, flushed with Ar, and maintained at 0 °C. A deaerated solution containing $NaBH_4$ and NaOH was slowly added to the as-prepared $CoCl_2$ solution, evoking the reaction shown below:

$$2CoCl_2 + 4NaBH_4 + 9H_2O \rightarrow Co_2B + 4NaCl + 12.5H_2 + 3B(OH)_3$$

As a result, the dark precipitate of amorphous Co_2B formed immediately (see Figure 10a). The as-formed Co_2B sample had ultrathin particulate morphology. Furthermore, the portions of the as-formed Co_2B were annealed for 2 h under He at various temperatures (200–1000 °C). At <400 °C, the as-annealed Co_2B samples were amorphous nature. As shown in Figure 10a, the Co_2B samples annealed at 500 and 1000 °C showed a diffraction pattern corresponding to tetragonal Co_2B. In comparing Co_2B prepared at 500 and 1000 °C, an increase in crystallinity with increased annealing temperature becomes apparent. TEM analysis of the Co_2B sample annealed at 500

https://doi.org/10.1021/acs.chemrev.3c00005
Chem. Rev. 2023, 123, 12795–13208

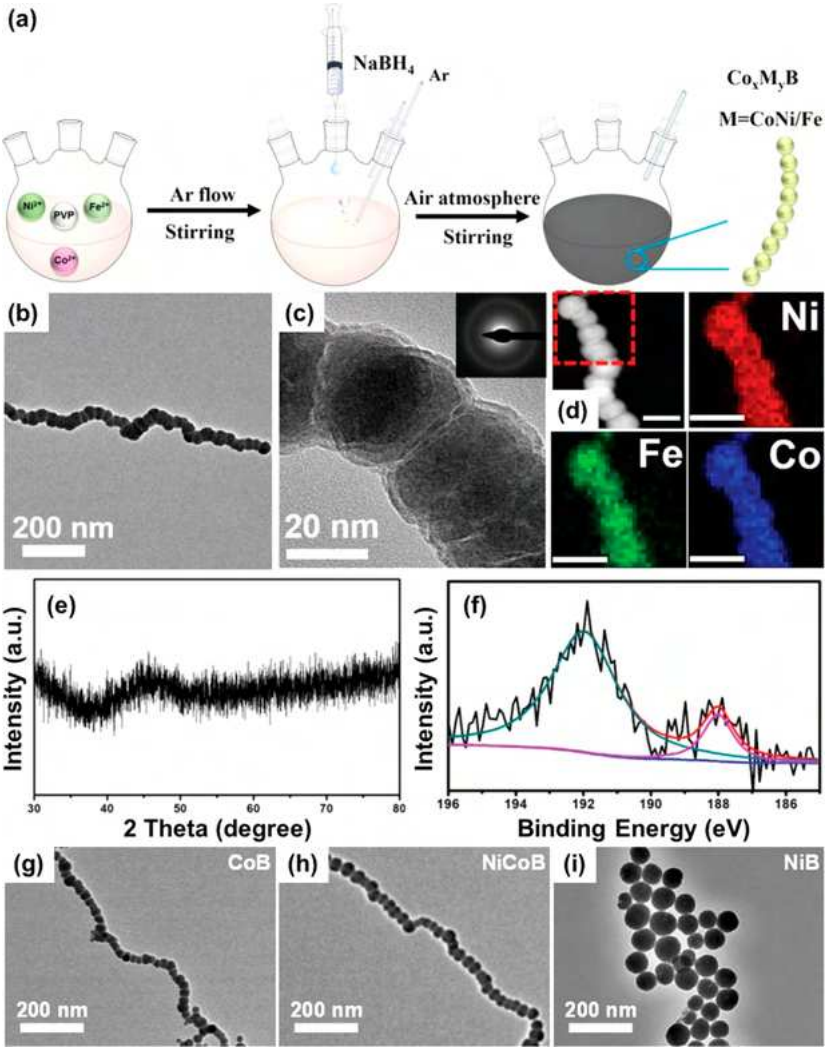


Figure 9. (a) Schematic illustration for the synthesis of Co_xM_yB (M = Fe, Ni) nanochain. (b) TEM and (c) HRTEM images and corresponding SAED pattern of NiCoFeB nanochain. (d) STEM-EDX elemental mapping images, (e) XRD pattern, and (f) B 1s XPS spectrum of NiCoFeB nanochain. (g–i) TEM images of (g) CoB, (h) NiCoB, and (i) NiB. Reproduced with permission from ref 178. Copyright 2018 Wiley.

°C further confirmed that nanocrystalline Co_2B was synthesized (Figures 10b–d). Additionally, SEM and BET specific surface area analyses of the as-prepared and 500 and 1000 °C-annealed Co_2B samples revealed that the particle-agglomeration degree increased and surface area decreased (11.87 $m^2 \cdot g^{-1}$ → 9.26 $m^2 \cdot g^{-1}$ → 1.21 $m^2 \cdot g^{-1}$) with increasing the annealing temperature, respectively. The authors also found that the electrical conductivity of the as-prepared Co_2B sample could be enhanced by annealing. XPS analysis indicated the existence of boron-oxo species on the 500 °C-annealed Co_2B sample surface. Thus, based on the experimental results, the post-annealing treatment using an inert gas atmosphere can both increase and decrease the crystallinity and surface area of the as-prepared transition metal boride.

To further control the morphology of the transition metal boride, the use of various carbon-based materials [multi-walled carbon nanotubes (MWCNTs)[137,176] and reduced graphene oxide (rGO)[139,145,186]] as a template is an effective strategy that has been reported in the literature. Chen *et al.* fabricated ultrathin nickel boride (Ni_xB) nanosheets anchored on surface-functionalized MWCNTs (Ni_xB/f-MWCNT) by using a solution method at room temperature and subsequent Ar-annealing (see Figure 11a).[137] To be specific, f-MWCNTs synthesized by a modified Hummers method[198] were dispersed in an aqueous solution of $Ni(NO_3)_2 \cdot 6H_2O$. In the f-MWCNT dispersion, Ni^{2+} cations were adsorbed on negatively charged surface functional groups on the f-MWCNTs. Subsequently, a $NaBH_4$ solution was added to the as-prepared dispersion. Afterward, the as-collected solid product was annealed at 300 °C under Ar, forming the Ni_xB/f-MWCNT hybrid. As shown in Figure 11b, the XRD peaks of the Ni_xB/f-MWCNT hybrid can be assigned to Ni_3B, and there are no signals for crystalline $Ni_3(BO_3)_2$, indicating that a limited amount of $Ni_3(BO_3)_2$ was generated in this method. However, XPS analysis found that borates or boron oxides existed on the Ni_xB/f-MWCNT hybrid surface owing to the partial oxidation of the Ni_xB surface upon exposure to air. TEM analysis confirmed that the f-MWCNTs were successfully covered with the Ni_xB nanosheets (Figure 11c). As seen in Figure 11d, the as-observed lattice fringe of 0.201 nm corresponds to the (102) plane of hexagonal Ni_3B and the graphitic carbon walls of MWCNTs were also confirmed. Furthermore, the SAED pattern of the Ni_xB/f-MWCNT also indicated the presence of hexagonal Ni_3B. By using a similar solution-based method and subsequent Ar-annealing at 400 °C (see Figure 11e), Sun *et al.* prepared crystalline Ni-Co-B (orthorhombic Ni_3B +

https://doi.org/10.1021/acs.chemrev.3c00005
Chem. Rev. 2023, 123, 12795–13208

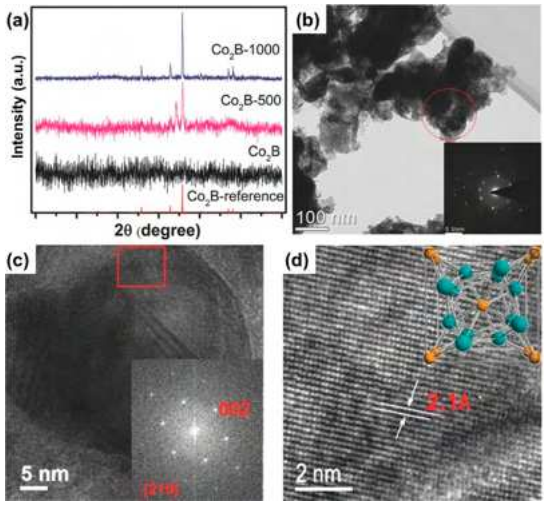


Figure 10. (a) XRD patterns of the Co_2B samples before and after annealing at 500 and 1000 °C for 2 h under He. (b) TEM image and corresponding SAED pattern of the Co_2B sample annealed at 500 °C (c) HRTEM image of the Co_2B sample annealed at 500 °C with the inset showing the SAED pattern of the square marked region along the [210] zone axis. (d) HRTEM image of the Co_2B sample annealed at 500 °C with the inset showing the unit cell crystal structure of Co_2B. Reproduced with permission from ref 163. Copyright 2016 Wiley.

orthorhombic Co_4B) nanosheets vertically aligned on rGO (Ni-Co-B/rGO).[139] To check the effect of rGO on the resultant boride morphology, Ni-Co-B was also prepared without adding rGO. In the absence of rGO (Figure 11f), Ni-Co-B particles in the size range of 100−150 nm were formed. In the presence of rGO (Figure 11g), wrinkled Ni-Co-B nanosheets (lateral size range: 50−100 nm) without obvious agglomeration and stacking were uniformly grown on the surface of rGO. Accordingly, rGO plays an important role in guiding the Ni-Co-B nanosheet formation.

Additionally, by changing the boron source ($LiBH_4$, $NaBH_4$), the transition metal/boron ratio of the resultant transition metal boride can be altered in the solution-based method.[158,164] For example, as reported by Li *et al.*,[158] crystalline Fe_2B particles were synthesized through the chemical reduction of $FeCl_2$ using $LiBH_4$ in tetrahydrofuran solution at reflux condition and the subsequent Ar-annealing at 600 °C, while crystalline Fe_2B particles were prepared via the chemical reduction of $FeCl_2$ using $NaBH_4$ and KOH in aqueous solution and the subsequent Ar-annealing at 600 °C. Similarly, Wang *et al.* prepared surface-activated amorphous Fe_2B and FeB_2 nanoparticles (Fe−B−O@Fe_2B and Fe−B−O@FeB_2) by the reaction of alkali borohydride and iron salt (Fe_2B: $NaBH_4$ + $FeSO_4{\cdot}7H_2O$; FeB_2: $LiBH_4$ + $FeSO_4$) in tetrahydrofuran solution and the subsequent air-oxidation treatment at 60 °C for 90 min.[164]

As discussed above, in the solution-based method, one can obtain the desired structural properties, chemical composition, and morphology of the transition metal boride by changing the starting materials (e.g., transition metal salt and alkali borohydride), applying the post-annealing treatment, and introducing the carbon-based material template.

2.1.2. Dip-Coating Methods. Dip-coating is a simple strategy to directly fabricate transition metal boride films on conductive substrates.[151,181] In general, dip-coating involves (i)

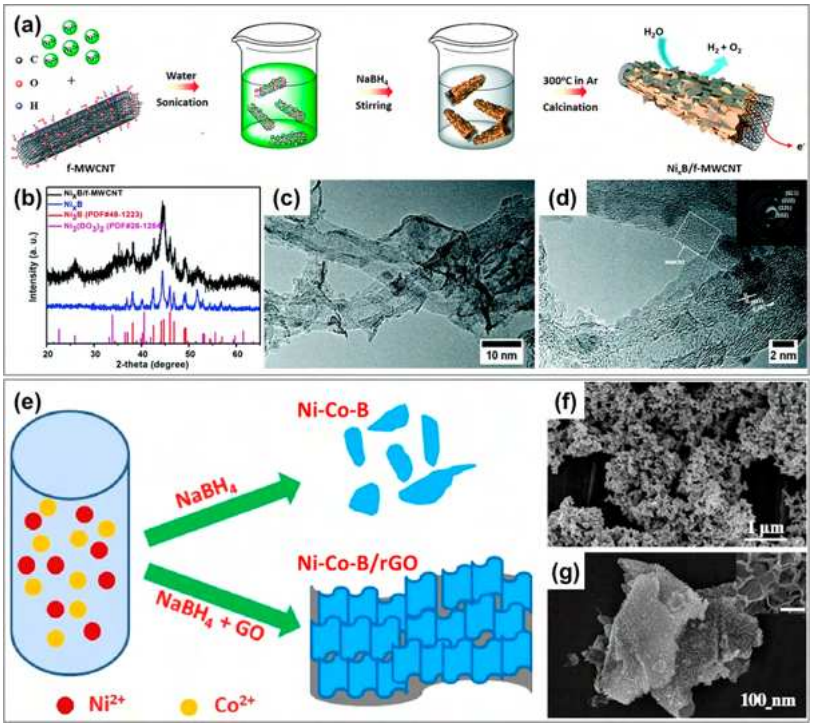


Figure 11. (a) Schematic illustration for the synthesis of ultrathin Ni_xB nanosheets anchored on f-MWCNTs. (b) XRD patterns of Ni_xB with and without f-MWCNT. (c, d) TEM images and [inset of (d)] SAED pattern of the Ni_xB anchored on f-MWCNTs. Reproduced with permission from ref 137. Copyright 2019 Royal Society of Chemistry. (e) Schematic illustration for the preparation of the Ni-Co-B particles and the Ni-Co-B nanosheets coupled with rGO. (f, g) SEM images of (f) the Ni-Co-B particles and (g) the Ni-Co-B nanosheets well dispersed on rGO. The inset of (g) indicates the magnified SEM image (scale bar = 100 nm). Reproduced with permission from ref 139. Copyright 2019 Elsevier.

https://doi.org/10.1021/acs.chemrev.3c00005
Chem. Rev. 2023, 123, 12795−13208

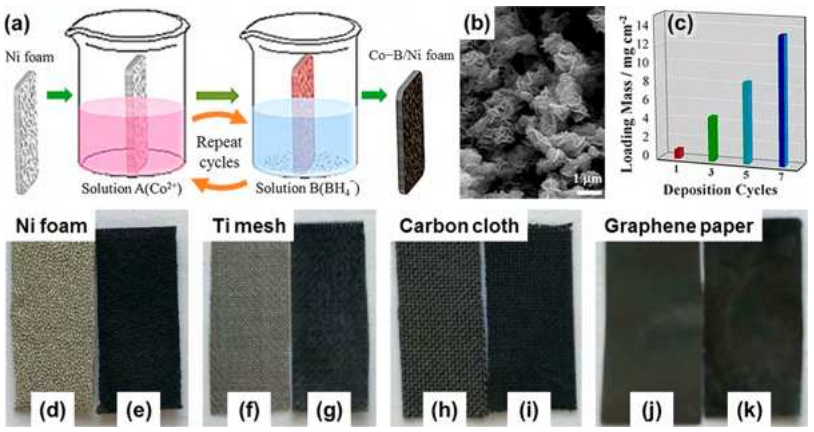


Figure 12. (a) Schematic illustration of the preparation process of hierarchical cobalt boride nanosheets on Ni foam. (b) SEM image of Co-B film on Ni foam. (c) Mass of Co-B loading on NF with 1, 3, 5, and 7 dipping cycles. (d–k) Digital photographs of Ni foam, Ti mesh, carbon cloth, and graphene paper (d, f, h, j) before and (e, g, i, k) after the alternately dipping deposition (for 5 dipping cycles). Reproduced with permission from ref 181. Copyright 2019 Wiley.

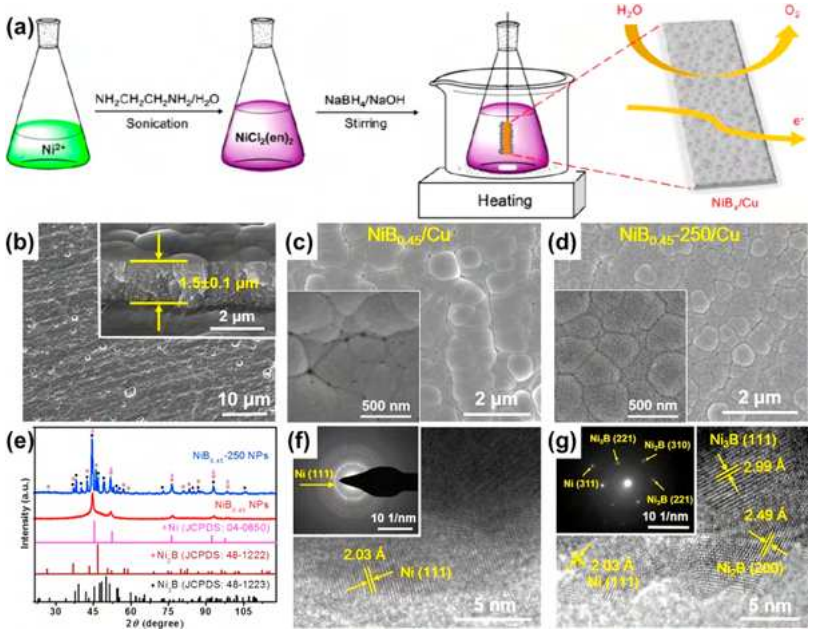


Figure 13. (a) Schematic illustration for the fabrication process of NiB_x film on Cu foil. (b–d) SEM images of the $NiB_{0.45}$ films (b, c) before and (d) after annealing at 250 °C for 3 h under Ar. (e) XRD patterns of the $NiB_{0.45}$ films before and after annealing at 250 °C for 3 h under Ar. (f, g) HRTEM images and corresponding SAED patterns of the (f) as-prepared and (g) Ar-annealed $NiB_{0.45}$ samples. Reproduced with permission from ref 159. Copyright 2017 Elsevier.

the deposition of a wet solution film by immersing a substrate in a precursor solution, keeping it inside the solution for some time, and withdrawing the as-immersed substrate vertically from the solution at constant speed under ambient atmosphere and (ii) the formation of a thin layer by evaporating the solvent from the wet solution film.[199] As for the solution-based method, transition metal boride dip-coating requires a solution of a transition metal salt and alkali borohydride. As shown in Figures 12a and b, Jiang *et al.* prepared amorphous Co-B nanosheets on Ni foam by alternating between dipping Ni foam into an aqueous solution of $Co(NO_3)_2{\cdot}6H_2O$ and an alkaline $NaBH_4$ solution.[181] It is important to note that the mass of the Co-B loading can be controlled by repeating these dipping steps for different numbers of cycles (1, 3, 5, and 7; see Figure 12c). The authors also fabricated Co-B on other conductive substrates such as Ti mesh, carbon cloth, and graphene paper. Figures 12d–k show various substrates before and after the dipping deposition of the Co-B.

2.1.3. Electroless Plating Methods. Electroless plating of the transition metal borides relies on the chemical reduction of transition metal ions via a boron-based reductant [i.e., sodium borohydride ($NaBH_4$) and dimethylammonium borane (Et_2NHBH_3)] in a liquid electrolyte. This synthesis method results in the direct growth of a uniform boride film on a conductive substrate.[149,153−155,159] Thus, the underlying chemical reaction mechanism for electroless plating is quite similar to that for solution-based methods. As seen in Figure 13a, Jiang *et al.* fabricated a NiB_x nanoparticulate film directly on Cu foil by the electroless plating method.[159] An electroless plating solution was prepared by dissolving $NiCl_2$ and ethanediamine (en) in water [$NiCl_2(en)_2$] and then adding an alkaline $NaBH_4$ solution to the as-prepared $NiCl_2(en)_2$

https://doi.org/10.1021/acs.chemrev.3c00005
Chem. Rev. 2023, 123, 12795−13208

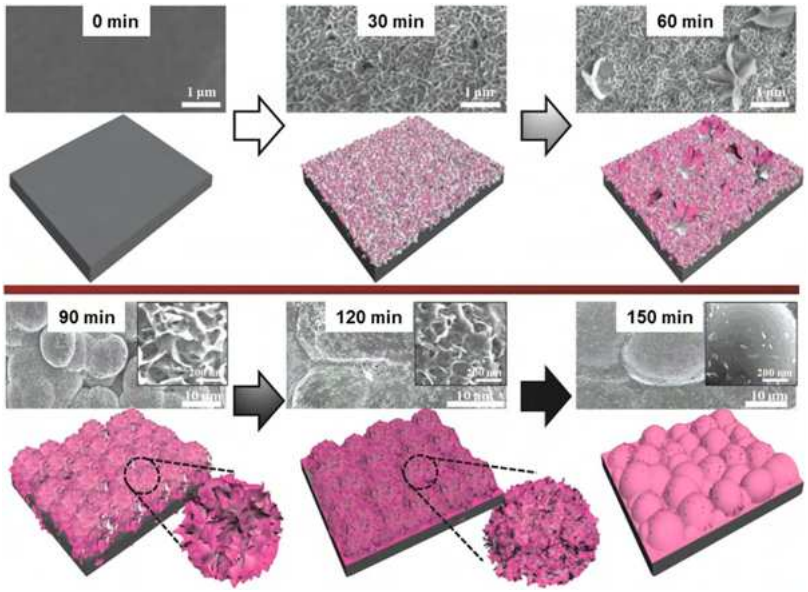


Figure 14. FESEM images and schematic illustrations of the Co-B films prepared with different plating times. Reproduced with permission from ref 153. Copyright 2018 Wiley.

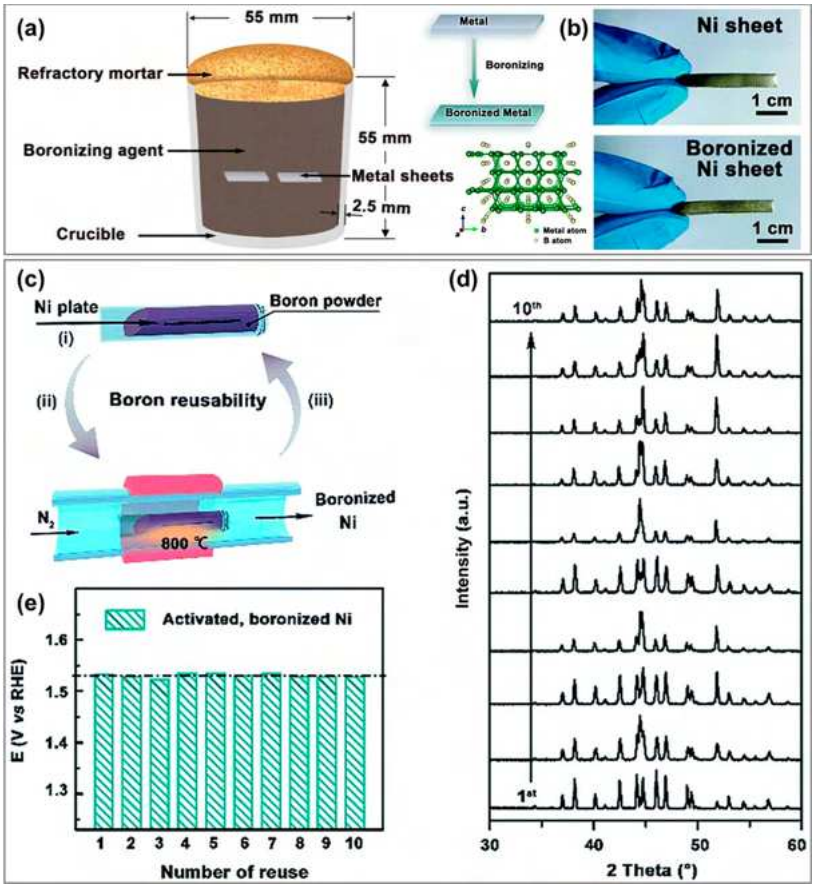


Figure 15. (a) Schematic illustrations for the boronization set-up of metal sheets (Fe, Co, Ni, and SUS 304) and the crystal structure of tetragonal M_2B. (b) Digital photographs of Ni sheets before and after the boronization. Reproduced with permission from ref 141. Copyright 2019 Royal Society of Chemistry. (c) Schematic illustration for the fabrication of boronized Ni plate and the boron reuse process. (d) XRD patterns of the boronized Ni samples prepared through the boron reuse process. (e) OER potential at a current density of 10 mA cm^{-2} for the ten boronized Ni samples. The black dotted line stands for a potential of 1.53 V_{RHE}. Reproduced with permission from ref 140. Copyright 2019 Royal Society of Chemistry.

solution. Subsequently, Cu foil was immersed into the electroless plating bath at 85 °C, forming the NiB_x film on Cu foil. The authors also prepared the NiB_x films with different B/Ni atomic ratios ($x \approx 0.25$, 0.37, and 0.45) by varying the

https://doi.org/10.1021/acs.chemrev.3c00005
Chem. Rev. 2023, 123, 12795−13208

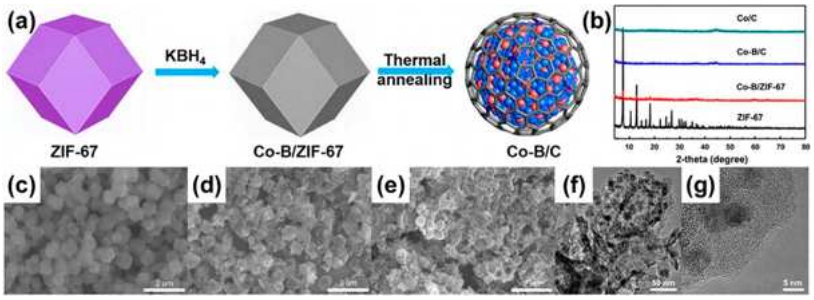


Figure 16. (a) Schematic illustration for the synthesis of Co-B/C. (b) XRD patterns of the samples. (c–e) SEM images of (c) ZIF-67, (d) Co-B/ZIF-67, and (e) Co-B/C. (f) TEM and (g) HRTEM images of Co-B/C. Reproduced with permission from ref 185. Copyright 2018 Elsevier.

$NaBH_4/NiCl_2$ molar ratio in the electroless plating solution. Incidentally, the XPS analysis of the as-prepared $NiB_{0.45}$ sample indicated that boron oxide and borate species were present at the surface. Furthermore, the as-prepared $NiB_{0.45}$ sample was subject to Ar-annealing at 200, 250, and 300 °C for 3 h. The as-prepared $NiB_{0.45}$ film had a thickness of 1.5 ± 0.1 μm (inset in Figure 13b), a rough nanoparticulate surface (Figure 13b), and nanovoids (Figure 13c) formed due to the H_2 evolution during the plating. Figure 13d shows the surface of the $NiB_{0.45}$ annealed at 250 °C ($NiB_{0.45}$-250) as a representative sample. After annealing, the nanovoids disappeared and the $NiB_{0.45}$-250 surface was coarser than the unannealed sample surface. The XRD and TEM analyses revealed that the as-prepared $NiB_{0.45}$ sample consisted of amorphous Ni boride and crystalline Ni metal, whereas the $NiB_{0.45}$-250 sample was composed of crystalline Ni_2B (tetragonal), Ni_3B (orthorhombic), and Ni metal, which indicate that the post-annealing treatment is effective for enhancing the crystallinity of the electroless plated film.

Hao *et al.* prepared an amorphous Co-B film on Ni foil by the electroless plating method using $CoSO_4$ and Et_2NHBH_3 as transition metal and boron sources, respectively.[153] Specifically, in the electroless plating bath, the Co-B layer, which had a porous nodule structure with a lot of internal spaces, is hypothesized to grow via the following reaction: $Co^{2+} + (CH_3)_2HN{\cdot}BH_3 + H_2O \rightarrow Co^0 + Co_2B + H_3BO_3 + (CH_3)_2H_2N^+ + H^+ + H_2\uparrow$. To understand the morphological formation process of the Co-B layer, the Co-B layers were prepared with different plating times (see Figure 14). At 0 min, fresh Ni foam has a relatively smooth surface. After 30 min, a thin layer consisting of nanowires (average diameter ≈ 20 nm) was formed on Ni foam (specific loading: 0.8 mg·cm^{-2}). After 60 and 90 min, a petal-like surface appeared and was continuously growing and agglomerating into spherical porous nodules (specific loading: 1.2 and 2.4 mg·cm^{-2}). This porous structure is possibly formed because of the H_2 evolution during plating. By prolonging the plating time (120 and 150 min), the deposition amount increased (specific loading: 7.5 and 12.8 mg·cm^{-2}). Accordingly, the loading amount of the electrocatalytic material can be controlled by altering the plating time. The authors also show the versatility of the electroless plating method by depositing various boron-based materials (i.e., Co-B, Ni-B, Co-Ni-B, Ni-W-B, Co-P-B, and Ni-P-B) on Ti foil, Ni foil, and carbon cloth.

2.1.4. Solid-State Reactions. Solid-state synthesis is a standard method for obtaining transition metal boride powders and/or films from the reaction between a transition metal powder/substrate and boron powder [+ potassium fluoroborate (and silicon carbide)] at relatively high temperatures (600–900 °C).[140,141,144,177] For instance, Masa *et al.* synthesized crystalline NiB powder through a solid-state reaction.[177] Specifically, homogeneously mixed nickel powder and boron powder were placed in an ampule and annealed at 700 °C for 15 h. By using the solid-state process, the transition metal boride film can be grown directly on a conductive substrate.[140,141,144] As seen in Figure 15a, Guo *et al.* obtained crystalline M_2B layers directly grown on Fe, Co, Ni, and SUS 304 sheets as well as NiFe sheets with different Ni contents (35, 50, and 80 at. % Ni) via the solid-state reaction between metal sheets and boronizing agents at 800 °C for 4 h.[141] Herein, the boronizing agent is amorphous boron [+ potassium fluoroborate (and silicon carbide)]. Incidentally, the XPS analysis of the boronized Ni sheet confirmed the existence of oxidized boron species on its surface.

Through a similar synthetic approach, Li *et al.* fabricated a crystalline Ni_3B chunk-like layer with a smooth surface and distinct grain boundaries on a Ni plate.[140] The Ni plate was boronized using boron powder at 800 °C for 40 min under a N_2 atmosphere. According to the XPS result, the as-prepared Ni_3B contained metaborate (BO_2^-) on its surface due to the partial oxidation of the B surface. The authors also mentioned the ability to reuse excess boron powder obtained after the synthesis. As indicated in Figure 15c, the reusing process consists of three steps: (i) Ni plate is installed in a quartz tube, (ii) high-temperature boronization is performed, and (iii) the boronized Ni plate is taken out, and the excess boron powder is reused for the boronization. By using this reuse process, ten boronized Ni plates could be prepared. Figure 15d shows that the ten samples showed similar XRD patterns, which indicates that boron recycling did not affect the final product's bulk composition. The Raman and XPS analyses of the 1st and 10th samples showed similar results. Hence, the final product surface composition was not influenced by the boron recycling. Moreover, the ten as-prepared Ni_3B electrocatalysts exhibited similar OER overpotentials of ∼300 mV at the current density of 10 mA·cm^{-2} in 1 M KOH (see Figure 15e). These experimental results implied that the recycling of excess boron powder is a reliable strategy for solid-state reaction synthesis of transition metal borides.

2.1.5. MOF-Derived Methods. MOF-derived synthesis is a unique method that can easily form the composite of a transition metal boride and a carbon-based material through liquid-based boronization of the MOF precursor and/or the subsequent post-annealing treatment of an as-boronized MOF.[185,195] For instance, Li *et al.* used a zeolitic imidazolate framework-67 (ZIF-67, 2-methylimidazole cobalt salt) precursor for fabricating Co-B nanoparticles incorporated into porous carbon (Co-B/C).[185] As shown in Figure 16a, the ZIF-

https://doi.org/10.1021/acs.chemrev.3c00005
Chem. Rev. 2023, 123, 12795–13208

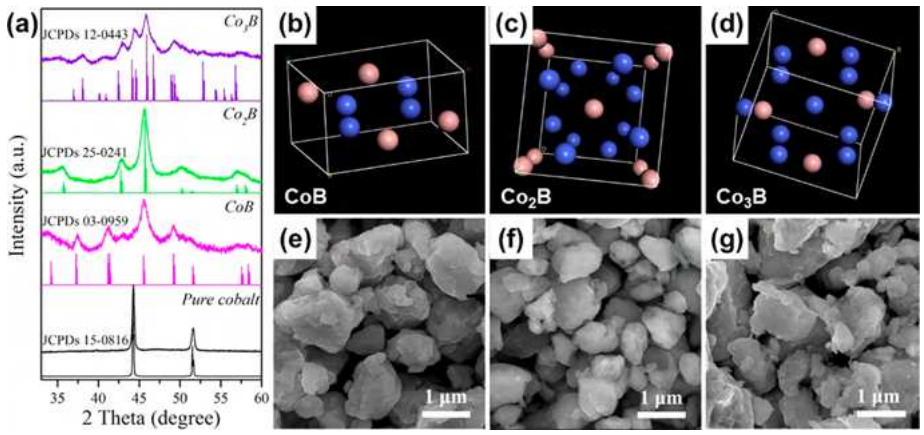


Figure 17. (a) XRD patterns of CoB, Co_2B, and Co_3B samples, fabricated by a ball-milling method, and pure cobalt. (b–d) Schematic illustrations for the crystal structures of (b) CoB, (c) Co_2B, and (d) Co_3B. (e–g) SEM images of (e) CoB, (f) Co_2B, and (g) Co_3B. Reproduced with permission from ref 156. Copyright 2017 American Chemical Society.

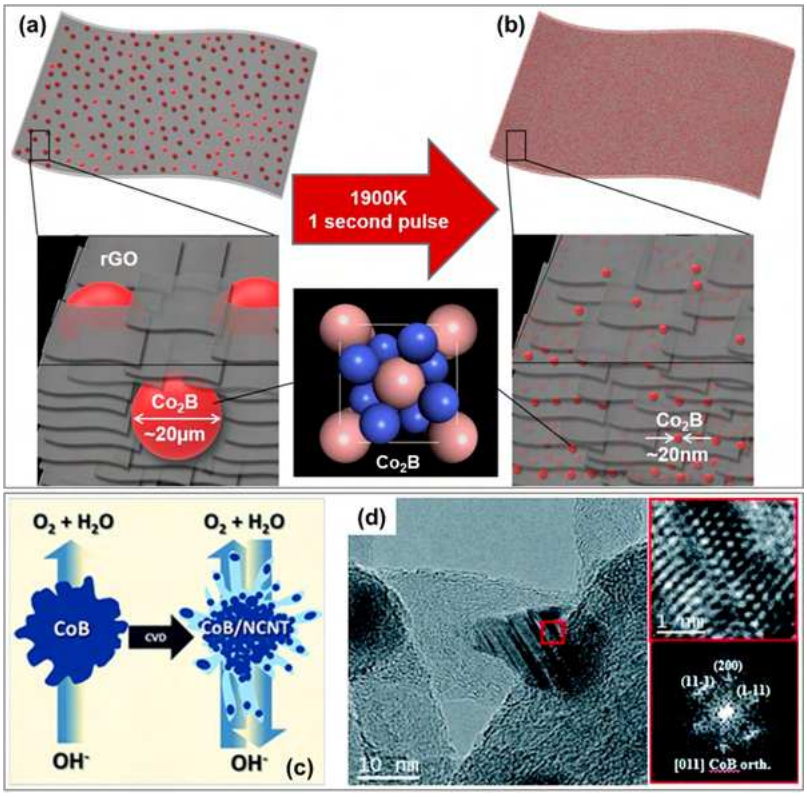


Figure 18. (a, b) Schematic illustration for the synthesis of Co_2B nanoparticles by a novel high-temperature pulse treatment. (a) Co_2B microparticles are incorporated into the rGO sheets through the chemical reaction between $NaBH_4$ and $CoAc_2$. (b) Co_2B microparticles transform into ultrafine Co_2B nanoparticles (diameter: ~20 nm) that are uniformly decorated on the rGO sheets via the high-temperature pulse procedure. The inset shows the Co_2B crystal structure. Reproduced with permission from ref 189. Copyright 2017 American Chemical Society. (c) Schematic illustration for the transformation of CoB into CoB/NCNT through the direct CVD growth of NCNTs on the CoB surface, where the CoB nanoparticles act as both the substrate and the growth catalyst for the NCNTs. (d) HRTEM images of individual CNTs and encapsulated CoB nanoparticles and the red squared region and corresponding FFT pattern. Reproduced with permission from ref 161. Copyright 2017 Royal Society of Chemistry.

67 precursor was boronized in a KBH_4 solution at 60 °C for 10 h:

$$2Co^{2+} + 4BH_4^- + 9H_2O \rightarrow Co_2B + 12.5H_2 + 3B(OH)_3$$

Afterward, the as-boronized ZIF-67 (Co-B/ZIF-67) was transformed into the Co-B/C by annealing in N_2 at 500 °C for 2 h. XRD analysis revealed that after the KBH_4-based boronization, the intensity of the ZIF-67 peaks was drastically weakened due to the reduction of Co^{2+} ions by borohydrides. After the N_2-annealing, the XRD peaks of the ZIF-67 completely disappeared, and the emergence of a weak XRD peak at around 45° appeared, corresponding to the Co-B formation. As seen in Figure 16c, the ZIF-67 precursor had a smooth polyhedral shape. After the KBH_4-based boronization, the surfaces of the polyhedra became rough (see Figure 16d).

https://doi.org/10.1021/acs.chemrev.3c00005
Chem. Rev. 2023, 123, 12795–13208

The subsequent N_2-annealing treatment shrank the polyhedra and made their surface even rougher (Figure 16e). TEM analysis further confirmed that in the as-formed Co-B/C sample, the Co-B nanoparticles were encapsulated by amorphous carbon (see Figures 16f and g). According to the XPS analysis of the as-formed Co-B/C sample, various boron oxide species might exist on its surface, which is owing to the partial oxidation of the Co-B surface upon exposure to air. Incidentally, the authors could also synthesize a Co/C sample by carbonizing the ZIF-67 precursor at 500 °C.

2.1.6. Other Methods. Herein, we briefly introduce less frequently used synthetic approaches (i.e., solvothermal method,[142] hydrothermal method,[157] ball-milling method,[156] and pulsed laser deposition[147]) and unique post-treatments (i.e., high-temperature pulse treatment[189] and CVD treatment[161]). In both hydrothermal and solvothermal approaches, transition metal hydroxide/oxide precursors are converted into transition metal borides via boronization. For example, Han *et al.* prepared hollow V-doped Ni-Co boride nanoprisms through solvothermal boronization (boron source: $NaBH_4$) of Ni-Co hydroxide nanoprisms (precursor) and the subsequent low-temperature atomic layer deposition of a thin vanadium layer on the as-boronized Ni-Co hydroxide nanoprisms.[142] Lu *et al.* hydrothermally grew CoO nanowire arrays (precursor) on Ti mesh.[157] Then, the CoO nanowire array was partially boronized into Co-B nanoparticles on the CoO nanowire surface via room temperature treatment using $NaBH_4$ in alkaline media, resulting in a self-standing Co-B@CoO nanoarray on Ti mesh.

In addition to metal boride preparation using the solvothermal and hydrothermal method, three different Co_xB (x = 1−3) samples have been successfully synthesized from a crystalline cobalt metal precursor (Figure 17a) and boron powder through a ball-milling method by adjusting the ratio of cobalt precursor/boron powder and the rotating speed.[156] The as-synthesized samples were crystalline and possessed orthorhombic CoB, tetragonal Co_2B, and orthorhombic Co_3B phases (see Figure 17a−d). As indicated in Figure 17e−g, the as-prepared CoB, Co_2B, and Co_3B samples had particulate morphologies.

Gupta *et al.* deposited a nanocrystalline Co-B thin film directly on an FTO glass substrate by using a pulsed laser deposition technique.[147] Here, Co-B powder prepared by the solution-based method was cold-pressed to form circular discs as a target material for the deposition. The as-deposited film surface consisted of spherical particulates (size: 0.2−2 μm). Additionally, the as-deposited film possessed a highly metallic core and exhibited minor surface oxidation.

A few unique post-treatments, which can change metal boride material morphologies, have also been reported. Here are some examples. Xu *et al.* prepared crystalline Co_2B nanoparticles with a diameter of 10−20 nm uniformly dispersed on reduced graphene oxide (rGO) nanosheets by using the high-temperature pulse method.[189] At first, Co_2B microparticles were synthesized through the solution-based method using cobalt acetate ($NaBH_4$) and sodium borohydride ($CoAc_2$). The as-synthesized Co_2B microparticles (tens of micrometers in diameter) were mixed with a rGO solution. Then, this mixture was cast onto a glass slide and annealed at 300 °C for 1 h under an Ar atmosphere, forming a Co_2B bulk/rGO composite film (Figure 18a). The Co_2B microparticles were converted into ultrafine nanoparticles (Figure 18b) under the high-temperature pulse at 1900 K for 1 s. The authors also synthesized MoS_2 and Co_3O_4 nanoparticles through the high-temperature pulse method, which implies that this method can be adaptable to the formation of other material nanoparticles. As seen in Figure 18c, Elumeeva *et al.* reported the formation of crystalline CoB nanoparticles with nitrogen-doped carbon nanotubes (NCNTs) through a CVD treatment.[161] To be specific, an initial CoB nanoparticle sample having a flake-like structure was synthesized by the solution-based method with $CoCl_2$ and $NaBH_4$.[163] Subsequently, the NCNTs were grown on the surface of the as-synthesized CoB nanoparticles by CVD under the flow of a mixture gas (C_2H_4, NH_3, and He) at different temperatures (500−700 °C), which formed the composite of the CoB nanoparticles and NCNTs (CoB/NCNT). Figure 18d shows the HRTEM images and fast Fourier transform (FFT) pattern of the CoB/NCNT composite prepared at 500 °C as a representative sample. In this composite, most of the CoB nanoparticles existed on the surfaces of the NCNTs (average diameter: 20−25 nm), and some of them were incorporated inside the NCNT cores (see Figure 18d), which indicates that the CoB nanoparticles apparently act as nuclei for the NCNT growth during the CVD process. The [011] zone-axis FFT pattern of the incorporated CoB nanoparticle (Figure 18d) revealed that the diffraction spots could be indexed to the orthorhombic CoB phase. Additionally, in the B 1s XPS spectrum, the boron oxo-species were confirmed as dominant surface species. These boron oxo-species might be formed due to the air oxidation of boride surfaces under ambient conditions. Note that the amorphous CoB nanoparticles prepared using this solution method showed electrocatalytic OER activity, whereas the CoB/NCNT composite electrocatalyst demonstrated activity for both the OER and ORR.

2.2. Final Types of Boride-Based Electrocatalysts

Boron has lower electronegativity (χ_B = 2.04) than the other anions [e.g., C (χ_C = 2.55), N (χ_N = 3.04), P (χ_P = 2.19), S (χ_S = 2.58), Se (χ_{Se} = 2.55), Te (χ_{Te} = 2.1), and it is somewhat close to the electronegativity of transition metals such as Ti (χ_{Ti} = 1.54), V (χ_V = 1.63), Fe (χ_{Fe} = 1.83), Co (χ_{Co} = 1.88), and Ni (χ_{Ni} = 1.91). Therefore, transition metal borides are expected to have relatively high covalency and great electrical conductivity, which may relax the mobility limitation of holes during the electrochemical OER, leading to suppressed electrooxidation of the metal borides. However, contrary to this hypothesis, all reported metal borides with both crystalline and amorphous structure underwent surface oxidation during the OER (see Table 1). This result means that metal borides are "precatalysts". According to reports with post-OER analyses, two types of OER active species are suggested: (i) metal oxide/(oxy)hydroxide and (ii) metal oxide/(oxy)-hydroxide + oxidized boron species [e.g., metaborate (BO_2^-), borate (BO_3^{3-}), B_2O_3, etc.], as seen in Figure 19. Even if fresh transition metal borides are tested for the OER, it seems inevitable to avoid the oxidation of their surfaces. Thus, a few research groups proposed synthetic approaches to fabricate the transition metal borides with the oxidized layer prior to the OER test.[164−166] As confirmed in Table 1, in almost all the reports, the metal boride electrocatalysts were tested in alkaline media. In only a few reports,[146,160] neutral and acidic electrolytes were used for the electrochemical tests. Especially in an acidic electrolyte, transition metal borides show slightly different precatalytic transformations during the OER, compared with the alkaline electrolyte cases.[146] Herein,

https://doi.org/10.1021/acs.chemrev.3c00005
Chem. Rev. 2023, 123, 12795−13208

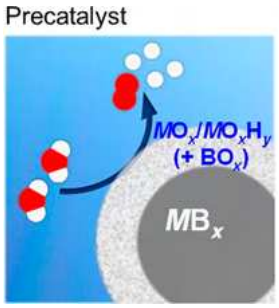


Figure 19. Schematic illustration of suggested final types of transition metal boride-based electrocatalysts after long-term OER testing.

we will discuss the transition metal boride precatalysts and their final OER active species by introducing important and unique examples.

Some researchers suggested that the transition metal borides can be transformed into their oxide/(oxy)hydroxide counterparts along with the continuous dissolution of the oxidized boron species after the OER testing. For example, Masa *et al.* synthesized crystalline nickel boride (NiB) powder via a high-temperature solid-state reaction and drop-cast the NiB powder and Nafion on a glassy carbon electrode.[177] The as-fabricated NiB electrode was subjected to 100 cyclic voltammetry (CV) cycles (potential window: 1.0−1.60 V_{RHE}) with a scan rate of 100 $mV{\cdot}s^{-1}$ in 1 M KOH. During this CV test, the intensity of the Ni^{2+}-to-Ni^{3+} oxidation peak significantly increased, from which the authors confirmed the possible formation of a nickel oxide/(oxy)hydroxide shell over the NiB. According to their previous report about Ni_2B,[138] the post-OER characterizations found surface oxidation of the Ni metals and subsequent formation of a Ni_2B@Ni(O)OH/NiO_xH core@shell structure. Accordingly, in the case of NiB, similar surface oxidation might happen during the OER, and the *in situ*-formed boron oxide (B_2O_3) can possibly react with KOH from the electrolyte to generate soluble tetrahydroxyborate species [$B(OH)_4^-$] as described below:

$$B_2O_3 + 2KOH + 3H_2O \rightarrow 2K[B(OH)_4]$$

For the support of this assumption, Zieschang *et al.* reported the disappearance of boron species from the post-OER boride precatalyst surface.[143] Crystalline Co_3B nanoparticles were synthesized through the reaction between $LiBH_4$ and $CoBr_2$ in tetrahydrofuran (C_4H_8O) and subsequent washing and annealing treatments. The as-synthesized Co_3B sample was drop-cast on the glassy carbon electrode with Nafion to form a Co_3B electrode for the OER. Before and after the electrochemical measurements in 1 M KOH, XPS analysis was conducted for the Co_3B sample/electrode. The pre-OER Co_3B sample already showed strong surface oxidation due to exposure to air (Figures 20a−c) and had hydroxide [$Co(OH)_2$], oxidized boron (BO_x), and oxocarbon (CO_x) species. As shown in Figures 20a, b, and d, the authors observed the formation of CoOOH, the complete disappearance of BO_x, and the presence of Nafion-related species, suggesting that the BO_x species are electrochemically unstable and do not affect the OER process. Thus, in this report, the post-OER Co_3B sample might have a Co_3B@CoOOH core@shell structure, and the CoOOH species acts as an electrocatalytically active phase.

Furthermore, Klemenz *et al.* also found a significant decrease of boron species on the surface of bimetallic boride

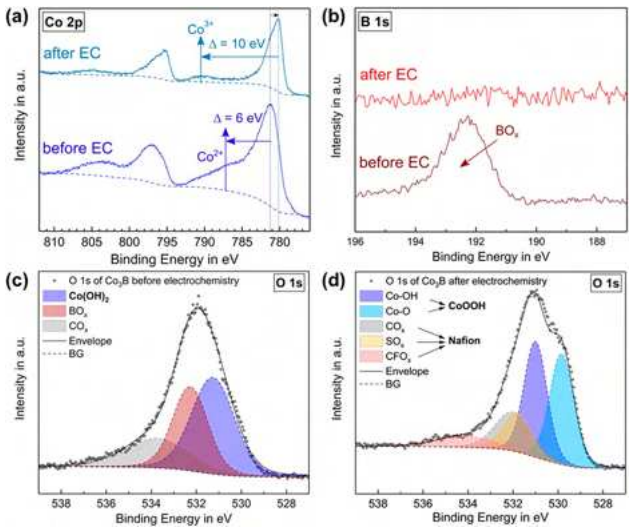


Figure 20. (a) Co 2p, (b) B 1s, and (c, d) O 1s XPS spectra of the Co_3B precatalyst before and after the electrochemical testing. Reproduced with permission from ref 143. Copyright 2019 American Chemical Society.

[$(Co_{0.7}Fe_{0.3})_2B$] after electrochemical measurements.[152] The crystalline $(Co_{0.7}Fe_{0.3})_2B$ powder with a network-like structure was prepared by a solution-based method. The $(Co_{0.7}Fe_{0.3})_2B$ electrode was fabricated by using the drop-casting method with Nafion and glassy carbon electrode. The as-prepared electrode was used for OER testing in 1 M KOH and examined by XPS before and after the electrochemical measurements (Figures 21a−d). In the pre-OER XPS spectrum of Co 2p (Figure 21a), the components located at 778.4 and 793.5 eV correspond to Co^0 in binary cobalt borides. A shoulder peak at ∼781.3 eV indicates the partial oxidation of the boride surface. The pre-OER B 1s XPS spectrum mainly showed two components at 188.7 and 194.0 eV (Figure 21c), which are assignable to the metal boride and B-O_x (i.e., B_2O_3 and other boron-oxo species), respectively. In the pre-OER O 1s XPS spectrum (Figure 21d), three components are observed at 533.5, 532.5, and 530.5 eV, corresponding to boron- and cobalt-oxo species. Two additional components at 534 and 535 eV can be assigned to C-O_x compounds and adsorbed H_2O, respectively. Moreover, based on these XPS results, the percentages of Co, Fe, B, and O were estimated to be 22.1, 10.0, 16.5, and 51.4 wt %, respectively. After the electrochemical tests, the original components related to binary cobalt borides disappeared, and the new signals at 779.9 and 781.2 eV were generated in the Co 2p XPS spectrum (Figure 21b). Additionally, in the O 1s XPS spectrum, the peaks at 529.3 and 530.9 eV appeared. From these results, the authors assumed the formation of a CoOOH (Co^{3+}) and $Co(OH)_2$ (Co^{2+}) mixture at the electrode surface after the electrochemical tests. As shown in Figure 21c, a very weak signal was confirmed in the B 1s XPS spectrum, implying the presence of boron-oxo species. This point is also supported by the presence of the XPS peak at 533 eV in the O 1s spectrum. The quantitative XPS analysis confirmed the decrease of Fe and B after the OER testing (Co: 36.4 wt %; Fe: 8.9 wt %; B: 1.9 wt %; O: 52.9 wt %), indicating the possible dissolution of Fe and B species. Based on these experimental observations, the authors proposed that the oxidation of $(Co_{0.7}Fe_{0.3})_2B$ proceeds during the OER, resulting in the formation of a thick oxide layer (see Figure 21e). Note

https://doi.org/10.1021/acs.chemrev.3c00005
Chem. Rev. 2023, 123, 12795−13208

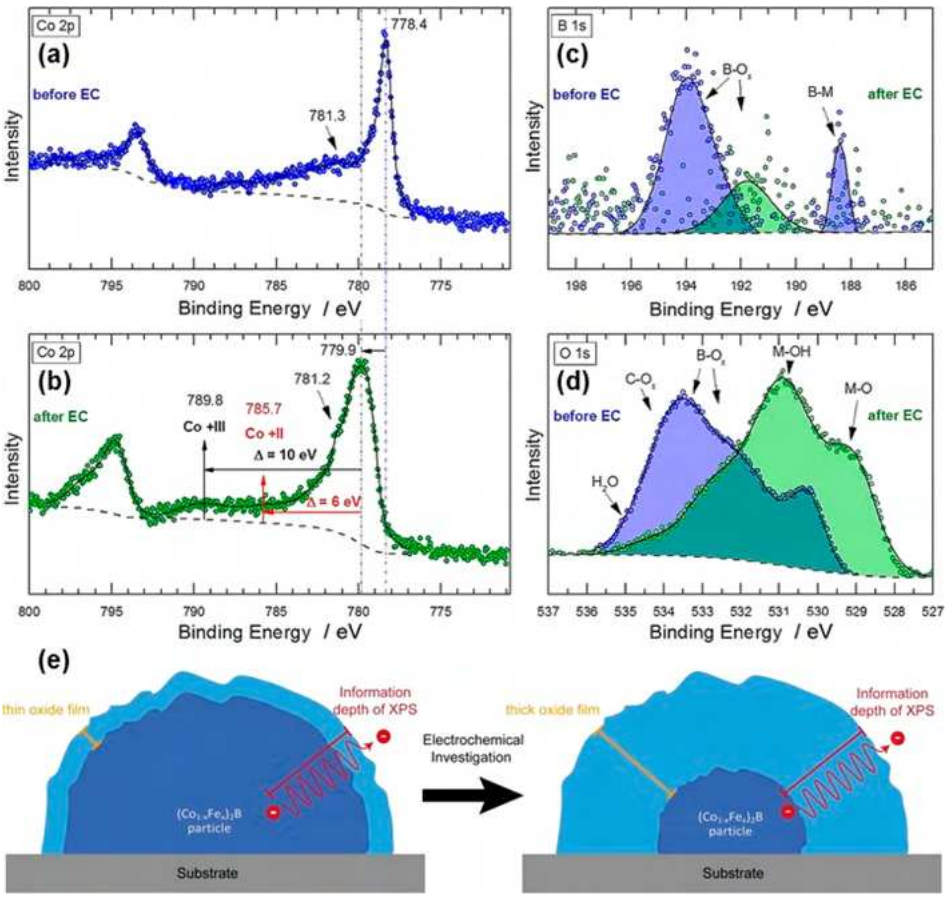


Figure 21. (a, b) Co 2p, (c) B 1s, and (d) O 1s XPS spectra and (e) schematic illustrations of the $(Co_{0.7}Fe_{0.3})_2B$ precatalyst before and after the electrochemical measurements. Reproduced with permission from ref 152. Copyright 2018 Wiley.

that the main surface species is the mixture of Fe-incorporated CoOOH and $Co(OH)_2$ acting as the OER active species. However, the effect of the remaining boron-oxo species after the OER was not taken into account in this study.

Contrary to the above discussions, it is claimed that the BO_x species newly formed on the post-OER metal boride surface may play an important role in the OER. For instance, the Zou group fabricated a crystalline Ni_3B layer with a thickness of ~2 μm on a Ni plate through a solid-state boronization process (see Figure 22).[140] As displayed in Figure 22a, the as-fabricated Ni_3B film has a chunk-like morphology with smooth surfaces and distinct grain boundaries. TEM images show that the surface of the Ni_3B layer was oxidized due to exposure to air or water and that a thin oxide layer (thickness: 3−5 nm) with amorphous nature formed on its surface (Figures 22c and d). According to the XPS and Raman analysis results, this thin layer consisted of nickel hydroxide and metaborate (BO_2^-) species (see Figure 22g). The as-prepared Ni_3B sample was electrochemically tested for the OER in Fe-purified 1 M KOH. To form the Ni_3B sample with a stable surface state (denoted as activated, boronized Ni), 250 LSV scans (i.e., *in situ* electrochemical activation; see inset of Figure 22g) were carried out. During this activation process, the geometric OER activity was continuously increased. Additionally, the Ni^{2+}-to-$Ni^{3+/4+}$ oxidation peak continuously and positively shifted, which indicates the transformation of $Ni(OH)_2$ to NiOOH (and NiO_2).[200] Incidentally, prior to recording the OER activity (i.e., overpotential, Tafel slope, etc.), a similar CV activation was also conducted in many other metal boride reports. After the *in situ* electrochemical activation, the Ni_3B sample was further characterized to understand its precatalytic transformation. Figure 22b shows the SEM of the activated Ni_3B sample. After the activation, the chunk-like shape was maintained, and a large quantity of nanosheets was generated on its surface. The TEM images (Figures 22e and f) further confirmed the appearance of the nanosheets as well as the somewhat thick amorphous layer (thickness: 30−50 nm). Moreover, the activated Ni_3B sample had a higher electrochemical surface area (ECSA) of 4.9 cm^2 than the as-prepared sample (1.8 cm^2). These post-activation characterizations suggest that the as-observed morphological transformation exposes more OER active sites, which improves the geometric OER activity during the activation. The post-activation XPS and Raman analyses found the formation and presence of γ-NiOOH and BO_2^- on the Ni_3B surface, respectively. To further investigate the impact of BO_2^-, the activated Ni plate with NiOOH surfaces was prepared for the purpose of comparison, and the ECSA-based specific OER current densities of the activated Ni_3B and Ni at the OER overpotential at 400 mV were compared in the inset of Figure 22g. Here, the activated Ni_3B showed higher specific OER activity than the activated Ni. Furthermore, the activated Ni_3B showed a slightly different position for the Ni $2p_{3/2}$ XPS peak (855.6 eV) in comparison with the activated Ni (856 eV), suggesting that the BO_2^- species in the NiOOH layer causes electron redistribution and an electron density increase around the Ni atoms.[201,202] Accordingly, the authors speculated that the BO_2^- species positively contributes to the OER activity of

https://doi.org/10.1021/acs.chemrev.3c00005
Chem. Rev. 2023, 123, 12795−13208

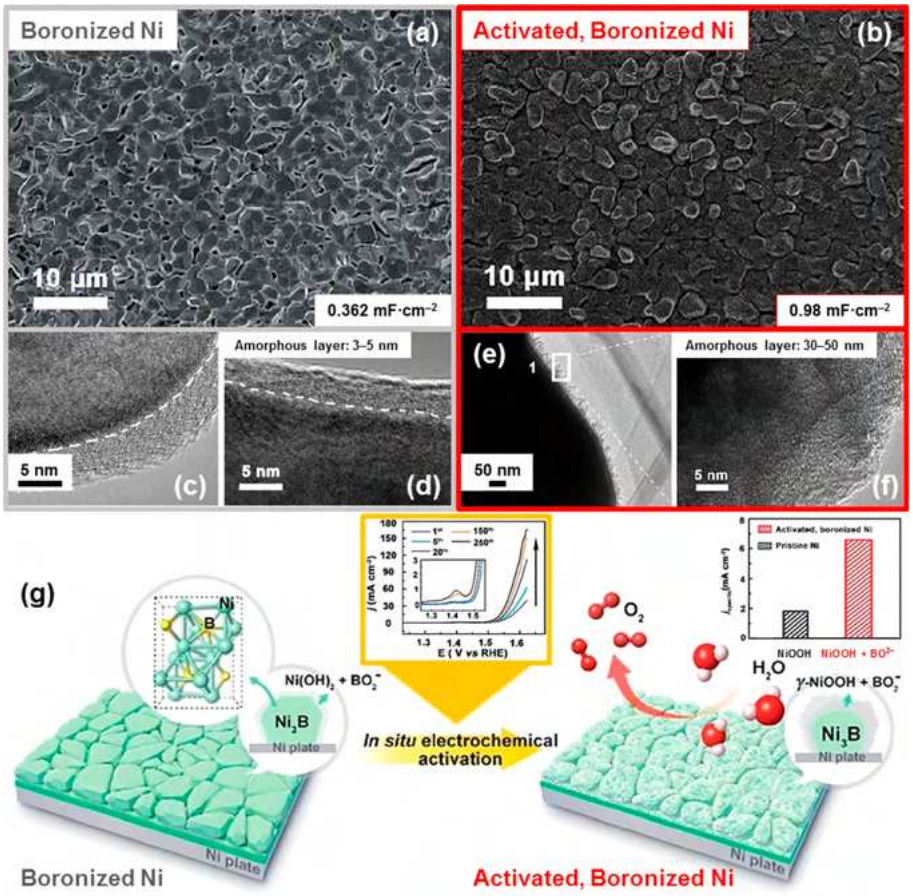


Figure 22. (a, b) SEM and (c–f) TEM images of the boronized Ni plate and the activated, boronized Ni plate after the OER. (g) Schematic illustration of the structural transformation of the boronized Ni sample during the electrochemical activation process. Reproduced with permission from ref 140. Copyright 2019 Royal Society of Chemistry.

the activated Ni_3B sample. Finally, the electrochemical stability of the BO_2^- species was investigated by checking the boron ion concentrations after 15 and 350 h chronopotentiometric tests at 10 mA·cm^{-2} by ICP-OES. The boron ion concentrations for the 15 and 350 h tests were 7.95×10^{-7} and 4.62×10^{-7} M, respectively. This result implies that the boron species exist in the electrocatalytic phase rather than dissolving into the electrolyte after the OER test.

The Zou group further investigated the OER performance of the boronized Ni, Co, Fe, NiFe, and stainless steel (SUS 304) sheets (i.e., crystalline M_2B layers) in alkaline media (1 M KOH for the Ni, Co, Fe, and NiFe samples; 30% KOH for the SUS 304 sample). As shown in Figures 23a–e, all the post-OER, boronized samples exhibited the formation of amorphous, ultrathin layers (thickness: 2–5 nm) due to their surface oxidation. To further investigate the newly formed thin layers on the boronized sheets, further post-OER analyses were conducted. Hereafter, the post-OER, boronized Ni sheet is discussed as a representative example. In the Raman spectrum, the bands at 475 and 556 cm^{-1} corresponding to the $\delta(Ni^{III}-O)$ and $\nu(Ni^{III}-O)$ vibrations were found, which indicates the *in situ* formation of γ-NiOOH. Here, the post-OER, pristine Ni sheet also showed two similar Raman bands. Interestingly, the relative intensity of $\nu(Ni^{III}-O)$ to $\delta(Ni^{III}-O)$ for the post-OER, boronized Ni sheet was higher compared with that for the post-OER Ni sheet. The authors found that similar phenomena were also confirmed in previous reports about heteroatom-doped γ-NiOOH films.[203,204] Therefore, the γ-NiOOH species, which formed on the boronized Ni sheet after the OER, might also contain heteroatom species. To examine this point, XPS analysis of the boronized Ni sheet after the OER was performed. Figure 23f demonstrates the B 1s XPS spectra of the boronized Ni sheet before and after the OER. In the pre-OER B 1s XPS spectrum, two peaks at 192.2 and 187.8 eV are assignable to the oxidized B species [i.e., a mixture of metaborate (BO_2^-) and borate (BO_3^{3-}) species] and B atoms in Ni_2B, respectively. However, in the post-OER B 1s XPS spectrum, only one peak at 191.6 eV can be assigned to the BO_2^- species, suggesting that the boronized Ni sheet surface is oxidized during the OER and the metaborate is stable on the post-OER, boronized Ni sheet surface. Accordingly, after the OER, the BO_2^--containing metal oxyhydroxide species are the real OER active sites in the boronized Ni, Co, Fe, NiFe, and SUS 304 sheets. The authors also claimed that the existence of BO_2^- species in the electrocatalytic active layer affects the electronic structure of the electrocatalytic active layer *in situ*-formed on the boride surface, resulting in superior OER activity. The post-OER XPS results showed a lower chemical bonding energy for Ni in the BO_2^--containing NiOOH layer for the boronized Ni sheet compared with the NiOOH layer for the Ni sheet. This indicates that the BO_2^--containing NiOOH layer has weaker oxophilicity of Ni active sites for the OER. According to previous experimental and theoretical studies,[201,205] the slight decrease of the Ni valence state and the relatively weak oxophilicity of Ni sites are beneficial for the OER.

https://doi.org/10.1021/acs.chemrev.3c00005
Chem. Rev. 2023, 123, 12795–13208

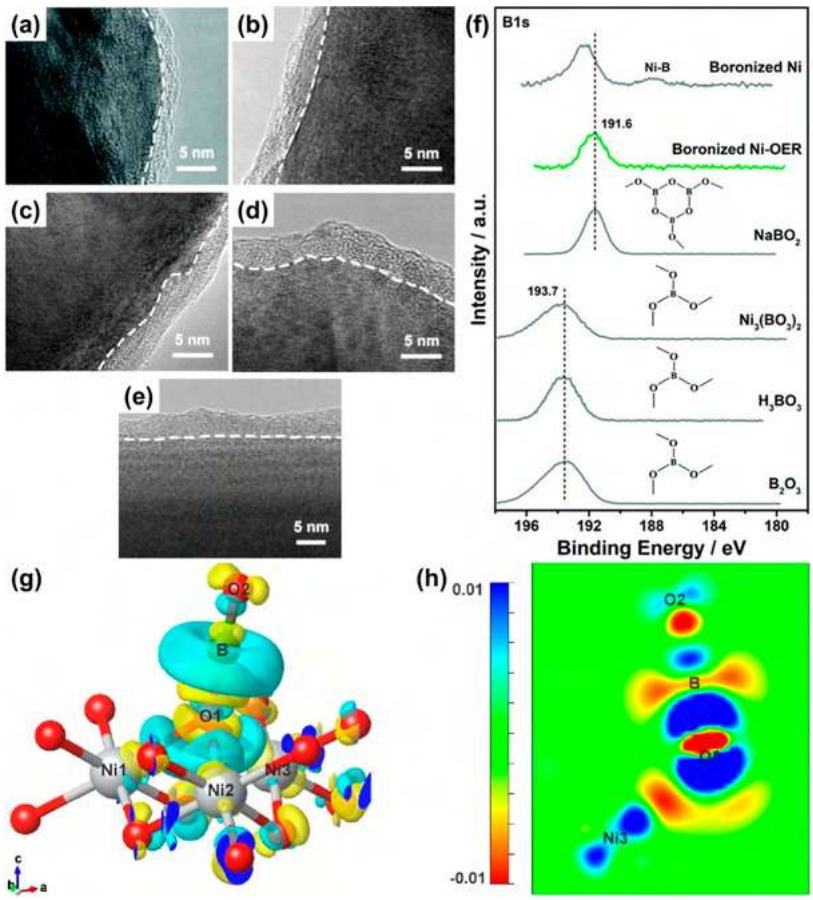


Figure 23. (a–e) HRTEM images of the boronized (a) Ni, (b) Co, (c) Fe, (d) NiFe, and (e) stainless steel (SUS 304) sheets after the OER. (f) B 1s XPS spectra of the boronized Ni sheet before and after the OER. B 1s XPS spectra of four reference compounds are also displayed for comparison. (g) Electron density distribution of the first layer of a BO_2^- reformed γ-NiOOH slab (yellow region: electron accumulation; blue region: electron depletion). (h) 2D plot of electron density distribution for the linear structure of O1–B–O2 and Ni3 (red area: low charge density; blue area: high charge density). Reproduced with permission from ref 141. Copyright 2019 Royal Society of Chemistry.

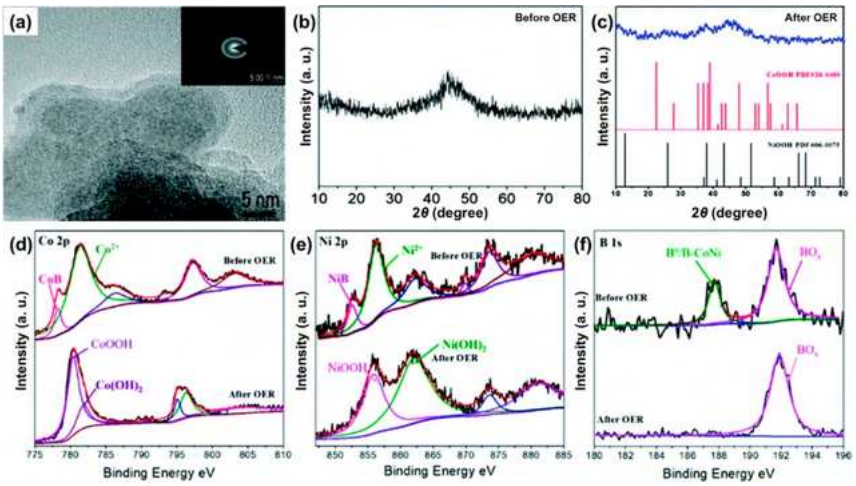


Figure 24. (a) HRTEM image and SAED pattern (inset) of amorphous, bimetallic Co and Ni boride (sample name: Co–10Ni–B). (b, c) XRD patterns of Co–10Ni–B (b) before and (c) after the OER. (d) Co 2p, (e) Ni 2p, and (f) B 1s XPS spectra of Co–10Ni–B before and after the OER. Reproduced with permission from ref 148. Copyright 2018 Royal Society of Chemistry.

Furthermore, their first-principles DFT calculations exhibited that the electron-attracting ability of O atoms and the charge density of Ni atoms in NiOOH are decreased and increased due to the existence of B–O covalent bonding, respectively (see Figures 23g and h). These properties may be effective for stabilizing the key intermediate Ni^{IV}–O during the OER. Based on the above discussion related to the boronized Ni sheet, the electronic effect of the BO_2^- species in the newly formed metal oxyhydroxide layer can boost the OER activity of the metal boride electrode.

https://doi.org/10.1021/acs.chemrev.3c00005
Chem. Rev. 2023, 123, 12795–13208

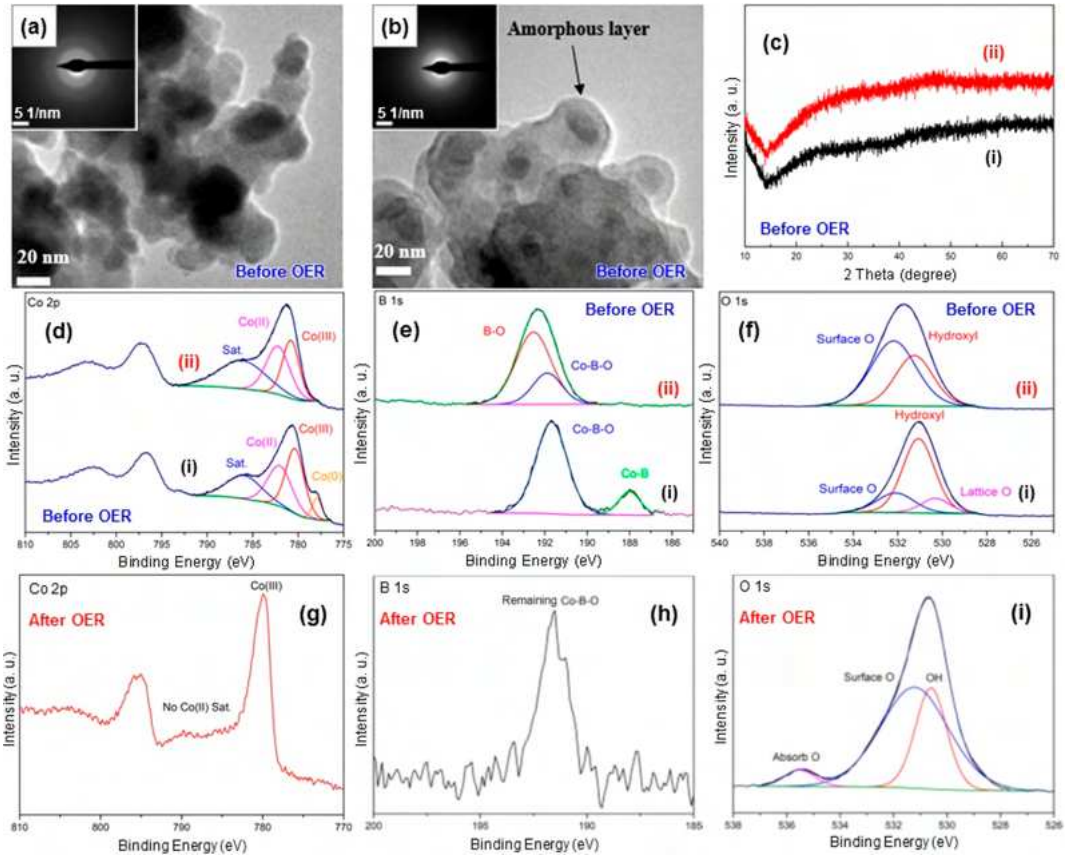


Figure 25. (a, b) TEM images and SAED patterns (insets) of (a) Co−B and (b) Co−B@Co−Bi. (c) XRD patterns and (d) Co 2p, (e) B 1s, and (f) O 1s XPS spectra of (i) Co−B and (ii) Co−B@Co−Bi. (g, h) SEM images of Co−B@Co−Bi (g) before and (h) after the OER. (i) Co 2p, B 1s, and O 1s XPS spectra of Co−B@Co−Bi after the OER. Reproduced with permission from ref 166. Copyright 2019 American Chemical Society.

So far, we have given several examples of transition metal boride precatalysts having a crystalline nature. As seen in Table 1, amorphous transition metal borides also experienced similar transformations (i.e., surface oxidation) during the OER. For example, Zhang *et al.* synthesized a series of amorphous Co−Ni−B samples with different Ni substitution levels for the OER in 1 M KOH.[148] The best-performing sample [denoted as Co−10Ni−B (Co: 73.07 wt %; Ni: 7.04 wt %; B: 6.99 wt %)] was further characterized before and after a 2 h chronoamperometric test at a constant potential of 1.56 V_{RHE} to investigate its precatalytic transformation during the OER. The as-prepared Co−10Ni−B particles showed the particle diameters to be from 15 to 30 nm. As shown in Figure 24a, the HRTEM image confirmed the absence of obvious lattice fringes throughout the observed particles. Also, the inset of Figure 24a shows the presence of diffuse rings in the corresponding SAED pattern. In the XRD pattern of the as-prepared Co−10Ni−B (Figure 24b), there is a single broad diffraction peak centered at 45°. These HRTEM, SAED, and XRD results are evidence for an amorphous state of the Co−10Ni−B sample. In the post-OER XRD pattern (Figure 24c), broad diffraction peaks can be approximately indexed as CoOOH and NiOOH. Figures 24d−f show the Co 2p, Ni 2p, and B 1s XPS spectra of the Co−10Ni−B before and after the OER test. The pre-OER Co 2p XPS spectrum confirmed the existence of the metallic Co^0 species in cobalt borides and the Co^{2+} species in CoO or $Co(OH)_2$ on the Co−10Ni−B surface.[163] Similarly, the pre-OER Ni 2p XPS spectrum revealed that the metallic Ni^0 species in nickel borides and the Ni^{2+} species in NiO or $Ni(OH)_2$ existed on the Co−10Ni−B surface.[105,206] The pre-OER B 1s spectrum was deconvoluted into two components at 187.7 and 191.7 eV corresponding to the *M*−B (i.e., the interaction of metal and boron) and the oxidized B species, respectively. Here, the Co^{2+}, Ni^{2+}, and oxidized B species might be generated due to the partial oxidation of the electrocatalyst surface during preparation and atmospheric exposure. After the OER test, the main binding energy peaks of Co 2p and Ni 2p positively shifted due to the formation of CoOOH and NiOOH, respectively. In the post-OER B 1s XPS spectrum, the peak of the *M*−B species disappeared, and the peak of the oxidized B species was maintained. From the above XRD and XPS results before and after OER testing, the Co−10Ni−B surface was oxidized into CoOOH and NiOOH with the oxidized B species under the OER condition. However, further characterization of the post-OER Co−10Ni−B by TEM may still be necessary to check its oxidation degree.

As we discussed above, it has been proven that both crystalline and amorphous borides tend to transform into their electroactive oxide counterparts (i.e., real OER active species) during the OER tests. Inspired by the reports about the boride OER precatalysts, the Luo group reported the synthesis of metal boride@metal borate nanosheet core@shell-like electrocatalysts (Co−B@Co−Bi and Ni−B@Ni−Bi) through a simple solution-based method (boron source: $NaBH_4$).[166] For comparison, cobalt boride (Co−B) and nickel boride (Ni−B) were also prepared. All the as-prepared samples were tested in 1 M KOH. Here, the electrochemical stability of the Co−B@Co−Bi and Co−B samples was further examined with

https://doi.org/10.1021/acs.chemrev.3c00005
Chem. Rev. 2023, 123, 12795−13208

5000 CV cycles with a range of 1.2−1.7 V_{RHE} and a chronopotentiometric test at the current density of 10 mA·cm^{-2}. In particular, Co−B@Co−Bi exhibited excellent electrochemical durability over 8 h during the chronopotentiometric test. So, we mainly discuss the characterization results of the Co−B@Co−Bi and Co−B samples as representative samples. According to the SEM and TEM images (Figures 25a and b), the Co−B@Co−Bi and Co−B samples were nanoparticulate. Additionally, the core@shell structure was clearly observed in the TEM image of the Co−B@Co−Bi sample (see Figure 25b). The EDX analysis further confirmed the formation of the Co−B@Co−Bi core@shell structure. The SAED and XRD patterns confirmed that the Co−B@Co−Bi and Co−B samples were amorphous (Figures 25a−c). The as-synthesized Co−B@Co−Bi and Co−B samples were analyzed by XPS (see Figures 25d−f). In the Co $2p_{3/2}$ spectrum, the Co−B sample showed three components at 778.0, 782.1, and 780.4 eV, which correspond to Co^0, Co^{2+}, and Co^{3+}, respectively. For the Co−B@Co−Bi sample, there are two Co $2p_{3/2}$ peaks located at 782.3 and 780.8 eV, which can be assigned to Co^{2+} and Co^{3+}, respectively. The Co $2p_{3/2}$ XPS peaks of Co^{2+} and Co^{3+} for Co−B@Co−Bi positively shifted about 0.2 and 0.4 eV above those for Co−B, respectively. The B 1s XPS spectrum of Co−B possessed the two peaks at 188.0 and 191.8 eV corresponding to the boron species in cobalt boride (Co−B) and Co−B−O, respectively. On the other hand, in the B 1s XPS spectrum of the Co−B@Co−Bi, there were two components centered at 191.8 and 192.5 eV, which are assignable to Co−B−O and B−O, respectively. For Co−B, the peaks in the O 1s region can be attributed to the lattice oxygen (at 530.5 eV), substituted hydroxyl species (at 531.5 eV), and surface oxygen (at 532.6 eV). In the O 1s XPS spectrum of Co−B@Co−Bi, there are only two peaks, which are ascribed to the substituted hydroxyl species and surface oxygen. The XPS results further indicate the formation of a cobalt borate shell in the Co−B@Co−Bi sample. The post-OER Co−B@Co−Bi was further characterized by SEM, TEM, and XPS. The authors mentioned that the SEM and TEM analyses revealed that the post-OER Co−B@Co−Bi maintained its initial morphology well. However, the as-provided TEM image does not have a high enough resolution to evaluate the structural stability of the Co−B@Co−Bi sample, which needs to be further investigated by obtaining post-OER TEM images with higher resolution. As shown in Figures 25g−i, the post-OER XPS analysis demonstrated the retention of B species, the formation of Co^{3+} species, and the appearance of absorbed O species. Accordingly, the surface chemical composition was somewhat retained after the OER test.

Similarly, the Guo group intentionally oxidized the surfaces of the as-prepared metal boride powder samples via thermal oxidation in the air to form *M*−B−O shells (*M* = Ni or Fe), possibly acting as real OER active sites.[164,165] To be specific, prior to the OER tests in alkaline media, a series of nickel borides (Ni_xB: Ni_3B, Ni_2B, and NiB_2) and a series of iron borides (Fe_xB: Fe_2B and FeB_2) were heated at 70 and 60 °C for 3 and 1.5 h in air, respectively. From the XRD results, all the samples were amorphous in nature. According to the SEM and TEM analyses, the surface-oxidized Ni_xB and Fe_xB samples had nanoparticle and nanoplate aggregations, respectively. To examine the surface chemical compositions of the surface-oxidized Ni_xB and Fe_xB samples, XPS analysis was carried out (see Figure 26). For all the surface-oxidized Ni_xB samples, Ni^{2+} and boron-oxo species were observed (Figures 26a and b).

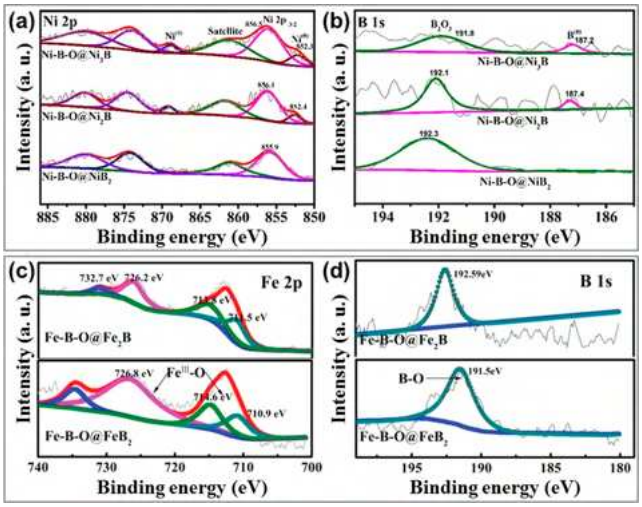


Figure 26. (a) Ni 2p and (b) B 1s XPS spectra of Ni−B−O@Ni_3B, Ni−B−O@Ni_2B, and Ni−B−O@NiB_2. Reproduced with permission from ref 165. Copyright 2019 Wiley. (c) Fe 2p and (d) B 1s XPS spectra of Fe−B−O@Fe_2B and Fe−B−O@FeB_2. Reproduced with permission from ref 164. Copyright 2019 Wiley.

Additionally, the presence of minor Ni_xB species was also confirmed for the surface-oxidized Ni_3B and Ni_2B, which implies that these sample surfaces were partially oxidized. Also, there is a possibility that Ni_3B and Ni_2B have higher oxidation resistance then NiB_2. Here, the authors suggested that boron in Ni_xB facilitates Ni oxidation. As shown in Figures 26c and d, Fe^{3+} and oxidized B species were present on the surfaces of Fe_2B and FeB_2. Moreover, since the peak intensity of Fe_xB species in both the Fe 2p and B 1s XPS spectra is negligible, the surfaces of the Fe_2B and FeB_2 samples might be fully covered with an amorphous oxide/hydroxide layer with oxidized B species. Furthermore, the best OER-performing samples (i.e., Ni−B−O@NiB_2 and Fe−B−O@FeB_2) were employed to evaluate their electrochemical stabilities under OER conditions by 500 CV cycles. The authors mentioned that the Ni−B−O@NiB_2 and Fe−B−O@FeB_2 samples showed satisfactory electrochemical durability after the OER tests. However, little decay of OER activity was observed for the Ni−B−O@NiB_2 sample after the OER test, and the structural and compositional stabilities of the Ni−B−O@NiB_2 and Fe−B−O@FeB_2 samples are still unknown due to a lack of characterization of the post-OER samples. Jiang *et al.* also prepared Ni^{II} borate@Ni_3B core@shell nanoparticles as an alkaline OER electrocatalyst via a simple solution-based method and demonstrated that its OER activity could be tuned by controlling the crystallinity of the Ni^{II} borate shell,[167] which will be discussed in detail later in Section 2.3.3.

Up to here, we have discussed the transition metal boride precatalysts tested in alkaline media. A few groups also studied the metal borides in acidic and neutral media.[146,160] Kirshenbaum *et al.* reported the electrochemical behavior of crystalline titanium diboride (TiB_2) powder (particle size: ∼10 μm) on an FTO substrate (TiB_2/FTO) as an electrode for the OER in 1.0 M $HClO_4$ (pH = 0).[146] The TiB_2/FTO electrode was prepared by drop-casting a TiB_2 powder and Nafion suspension onto an FTO substrate. The electrochemical stability of the TiB_2/FTO electrodes was assessed by conducting three chronopotentiometric tests at the constant current density of 10 mA·cm^{-2}. The TiB_2/FTO electrodes

https://doi.org/10.1021/acs.chemrev.3c00005
Chem. Rev. 2023, 123, 12795−13208

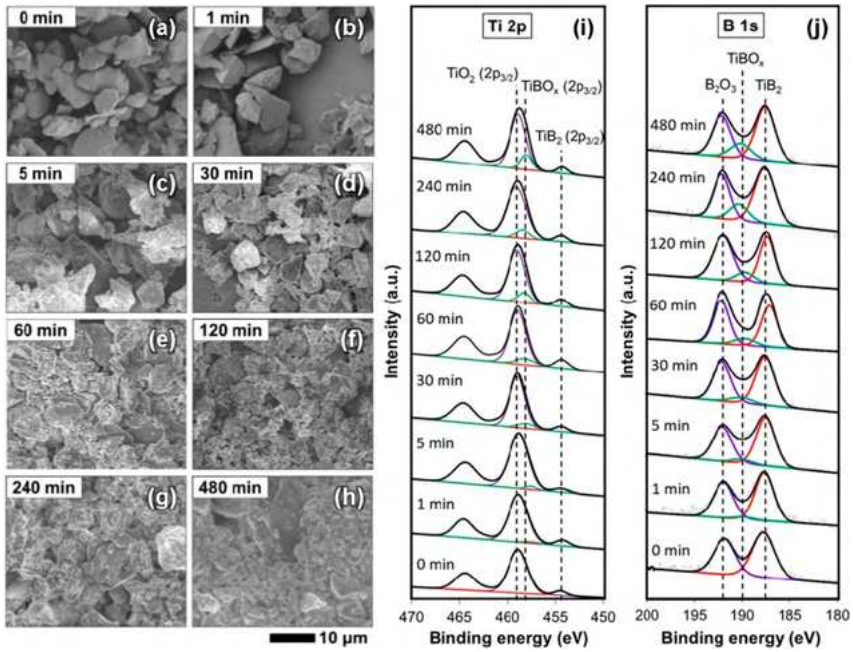


Figure 27. (a–h) SEM images and (i) Ti $2p_{3/2}$ and (j) B 1s fitted XPS spectra of TiB_2/FTO electrodes after various durations of the OER operation at the constant current density of 10 mA·cm^{-2} in 1.0 M $HClO_4$. Reproduced with permission from ref 146. Copyright 2019 Wiley.

maintained OER activity for 10–12 h. After the 10–12 h OER tests, the electrocatalyst films on FTO substrates were delaminated. The authors mentioned that the delamination was probably due to mechanical instability caused by the poor adhesion of the TiB_2 film to the FTO substrate, and bubble accumulation at the TiB_2/FTO interface might further facilitate the delamination. To investigate the morphological and surface compositional transformation of the TiB_2 film during the OER chronopotentiometric test, SEM and XPS analyses were conducted at various time intervals. As shown in Figures 27a–h, smaller particles, formed probably owing to the layered TiB_2 exfoliation during the OER test. Figures 27i and j display the Ti 2p and B 1s XPS results for the TiB_2/FTO electrode. Before the OER test (at 0 min), the electrode surface consisted of TiB_2, TiO_2, and B_2O_3. As the OER test proceeded, $TiBO_x$ was newly formed, and the amounts of $TiBO_x$ and B_2O_3 increased, which may imply the electrode surface oxidation during the OER. After the OER test (at 480 min), the electrode surface is composed of TiB_2, TiO_2, B_2O_3, and $TiBO_x$. Here, during the 1 h chronopotentiometric tests (at 10 mA·cm^{-2}), Nafion/FTO and B_2O_3/FTO electrodes showed the OER overpotentials of ~1.6–2 V, which is much higher than the TiB_2/FTO electrode (560 ± 20 mV). Therefore, Nafion and B_2O_3 may not have electrocatalytic OER activity themselves. However, the contributions of TiO_2 and $TiBO_x$ and the synergistic effects among TiB_2, TiO_2, B_2O_3, and $TiBO_x$ toward the OER are still unknown. Furthermore, to check the electrocatalyst dissolution, the electrolyte was examined by ICP-OES at hourly intervals during the 10 h OER chronopotentiometric test (at 10 mA·cm^{-2}). The rate of the Ti dissolution from the electrode surface was 0.24 μg·cm^{-2}·h^{-1} during the 10 h OER test, indicating that only ~1.2% of the electrocatalyst was dissolved into the electrolyte after 10 h. Based on the SEM, XPS, and ICP-OES results, the authors further claimed that the OER performance loss might be due to poor mechanical adhesion rather than electrochemical instability. However, we herein speculate that the morphological change and dissolution of TiB_2 may also contribute to the performance loss during the OER test. Gupta *et al.* prepared Co–Mo–B nanoparticles on a glassy carbon substrate, and the as-prepared electrode was subjected to a 10 h OER chronoamperometric test at the potential of 2.08 V_{RHE} in 0.5 M potassium phosphate buffer (KPi) (pH = 7). During the 10 h OER test, a steady decrease in current density was observed. The cause of this OER activity decay has not been traced because of the lack of post-OER analyses. As just described, electrochemical instabilities of borides in acidic and neutral media are important issues. Moreover, only a few metal borides have been studied in acidic and neutral electrolytes. Thus, it is necessary to further explore metal boride electrocatalysts for acidic and neutral OER.

2.3. Structural and Chemical Compositional Effects toward OER Activity

In this section, we discuss the compositional and structural properties of transition metal boride electrocatalysts influencing their OER activity. Herein, we also introduce some strategies for enhancing the OER activity of the transition metal borides and briefly mention the impact of experimental conditions (i.e., electrolyte pH) on their OER performance.

2.3.1. Monometallic Borides. As shown in Table 1, transition metal borides tend to be oxidized into the oxides/(oxy)hydroxides with/without oxidized boron species and/or the borates during the OER. Thus, when discussing the OER activity of borides, it is essential to consider these transformations and newly formed species. Herein, we highlight the following important topics: (i) metal (*M* in MB_x) effect; (ii) metal/boron ratio effect; (iii) roles of boron species; and (iv) crystallinities of as-prepared borides and their oxide counterparts for the boride OER activity using examples with relatively simple systems (monometallic borides).

The metal that constitutes a monometallic boride can be one of the key factors in determining its OER activity. The Zou group examined the electrocatalytic OER activities of boronized metal sheet samples (Ni_2B, Co_2B, and Fe_2B) and

https://doi.org/10.1021/acs.chemrev.3c00005
Chem. Rev. 2023, 123, 12795–13208

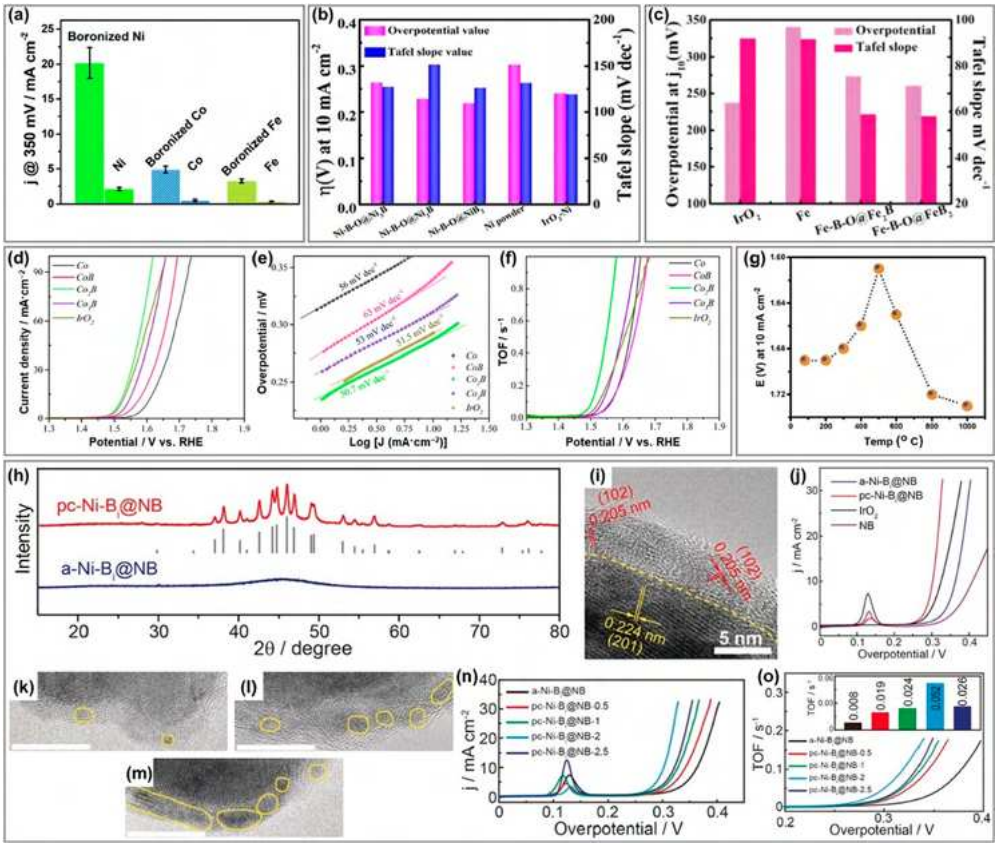


Figure 28. (a) Current densities at the OER overpotential of 350 mV for the boronized metal sheets (Ni_2B, Co_2B, and Fe_2B) and corresponding metal sheets (Ni, Co, and Fe). Reproduced with permission from ref 141. Copyright 2019 Royal Society of Chemistry. (b) OER overpotentials at 10 mA·cm^{-2} (left) and Tafel slopes (right) for Ni-B-O@Ni_xB, IrO_2, and Ni powder. Reproduced with permission from ref 165. Copyright 2019 Wiley. (c) OER overpotentials at 10 mA·cm^{-2} (left) and Tafel slopes (right) for Fe-B-O@Fe_xB, IrO_2, and Fe powder. Reproduced with permission from ref 164. Copyright 2019 Wiley. (d) Polarization curves, (e) Tafel plots, and (f) TOF plots of Co and Co_xB electrodes. Reproduced with permission from ref 156. Copyright 2017 American Chemical Society. (g) OER activity of Co_2B as a function of the annealing temperature under He for 2 h. Reproduced with permission from ref 163. Copyright 2016 Wiley. (h) XRD patterns of a-Ni-B_i@NB and pc-Ni-B_i@NB (pc-Ni-B_i@NB-2). (i) HRTEM image of pc-Ni-B_i@NB (pc-Ni-B_i@NB-2). (j) Polarization curves of a-Ni-B_i@NB, pc-Ni-B_i@NB (pc-Ni-B_i@NB-2), NB, and commercial IrO_2. (k–m)TEM images of (k) pc-Ni-B_i@NB-0.5, (l) pc-Ni-B_i@NB-2, and (m) pc-Ni-B_i@NB-2.5. Scale bars in (k–m) are 10 nm. (n) Polarization curves and (o) TOF per oxidative nickel site (Ni^{2+}) for a-Ni-B_i@NB and pc-Ni-B_i@NB-*x*. Inset in (o) shows the TOF values at the OER overpotential of 300 mV. Reproduced with permission from ref 167. Copyright 2017 Wiley.

the corresponding metal sheet samples (Ni, Co, and Fe) in Fe-purified KOH electrolyte,[141] in order to ignore incidental Fe incorporation from the electrolyte.[200,207] Figure 28a shows the current densities recorded at the OER overpotential of 350 mV. The OER activities of both metal boride and metal sample series were in the following sequence: Ni > Co > Fe. Similarly, Osaka *et al.* also investigated the OER on various transition metal borides (Ni_xB, Co_xB, Fe_xB, and LaB_6) in 6 M KOH.[193] Prior to the OER testing, the boride electrodes were anodically oxidized for 1 h at a potential of 0.80 $V_{Hg/HgO}$. Since the OER kinetics depends on the surface oxidation degree in many cases,[193] this activation step was conducted for stabilizing the electrode surface. Here, pure transition metals such as Co, Ni, and Fe were also tested in the same condition. The as-recorded OER activities were in the following order: $Ni_xB \simeq Co_xB \gg Fe_xB > LaB_6 > Co \simeq Fe > Ni$. All the tested borides showed higher activity than the transition metals. Also, the order of activities for Ni_xB, Co_xB, and Fe_xB is similar to the result provided by the Zou group ($Ni_2B > Co_2B > Fe_2B$). However, the transition metals showed a different OER activity trend ($Co \simeq Fe > Ni$) compared with the Zou group's result (Ni > Co > Fe). We assume that this difference in the OER activity trend might come from the difference in electrolyte concentration and the presence/absence of iron impurities in the KOH electrolytes.

As shown in Figures 28b–d, the metal/boron ratio and surface area (C_{dl}) in the transition metal boride are also key factors that determine its OER activity. For instance, the Guo group synthesized the monometallic nickel and iron boride precatalysts with different metal/boron ratios and oxidized their surfaces through relatively low-temperature annealing in the air (60–70 °C for 1.5–3 h), resulting in Ni–B–O@Ni_xB (Ni_xB: Ni_3B, Ni_2B, and NiB_2) and Fe–B–O@Fe_xB (Fe_xB: Fe_2B and FeB_2) samples.[164,165] For all the as-prepared samples, the existence of oxidized boron species was confirmed by the B 1s XPS peaks at around 192.06 eV. Among all the Ni–B–O@Ni_xB and Fe–B–O@Fe_xB samples, the B-rich Ni–B–O@NiB_2 and Fe–B–O@FeB_2 exhibited the highest OER activities with the overpotentials of 219 and 260 mV at the current density of 10 mA·cm^{-2} in 1 M KOH, respectively. The B-rich nickel and iron borides achieved higher OER activity mainly due to the presence of a larger amount of oxidized boron species in Ni–B–O@NiB_2 and Fe–B–O@FeB_2, which may alter the interaction energies between the electrocatalyst

https://doi.org/10.1021/acs.chemrev.3c00005
Chem. Rev. 2023, 123, 12795–13208

surface and the intermediates for the OER.[73,141,165] Additionally, the Fe−B−O@FeB_2 had a higher C_{dl} value (1.58 mF·cm^{-2}) compared with the Fe−B−O@Fe_2B (1.07 mF·cm^{-2}), which implies the higher ECSA of the Fe−B−O@FeB_2. This higher ECSA may also expand the number of electroactive sites for the OER, which contributes to the higher OER activity of the Fe−B−O@FeB_2. Similarly, Ma *et al.* reported the crystalline Co_xB precatalysts (x = 1, 2, and 3) prepared by ball milling.[156] Importantly, after the long-term OER tests, the formation of Co_3O_4, CoOOH, and boron-oxo species on all the Co_xB surfaces was confirmed by TEM and XPS analyses. Contrary to the above reports by the Guo group, the relatively B-poor Co_2B sample exhibited the lowest and smallest OER overpotential (287 mV) at 10 mA·cm^{-2} and Tafel slope (50.7 mV·dec^{-1}) in 1 M KOH after CV activation. To reveal the reasons for this superior OER activity for the Co_2B sample, the authors measured the TOF and C_{dl} values for all the tested samples. According to the Guo group results, it is expected that the B-rich CoB precatalyst should surpass the B-poor Co_2B and Co_3B in intrinsic OER activity. As shown in Figure 28f, the Co_2B precatalyst, however, demonstrated the largest TOF values over the tested potentials, indicating its high intrinsic OER activity. We assume that the main reason for this phenomenon is the partial dissolution of boron species during the CV activation, which may alter the initial metal/boron surface composition.[163] For the ECSA estimation, the Co_2B samples showed the higher C_{dl} value of 3.7 mF·cm^{-2} compared with the CoB (1.17 mF·cm^{-2}) and Co_3B (1.52 mF·cm^{-2}) samples. Therefore, the highest OER activity of the Co_2B mainly comes from both its high intrinsic OER activity and large ECSA.

Interestingly, the crystallinities of as-prepared borides and their oxide counterparts (i.e., metal borate) can also influence the OER activities. For instance, Masa *et al.* prepared amorphous Co_2B via a solution-based method and annealed it at different temperatures (200−1000 °C) for 2 h under He, which changed the crystallinity of the Co_2B sample.[163] Figure 28g shows the OER potentials of the unannealed and annealed samples at the current density of 10 mA·cm^{-2}. Here, the sample annealed at 500 °C indicated the lowest OER potential (1.61 V) among all the tested samples. To understand the reasons behind this high OER activity, the authors conducted BET specific surface area measurement and XRD analysis. BET specific surface area measurements revealed that the specific surface area of unannealed Co_2B (11.87 m^2·g^{-1}) decreased after annealing treatments (500 °C: 9.70 m^2·g^{-1}; 1000 °C: 1.2 m^2·g^{-1}), indicating that the annealing will facilitate particle agglomeration. Accordingly, the low OER activities of the sample annealed at high temperatures (600−1000 °C) might result from the annealing-derived surface area decrease. Moreover, XRD analysis found that the structural transformation from amorphous to crystalline Co_2B starts at around 500 °C. The authors also mentioned that, in general, amorphous materials have lower electrical conductivity than their crystalline counterparts. Thus, the as-observed superior OER activity of the 500 °C-annealed sample was achieved dominantly due to the electrical conductivity improved by the annealing treatment. Furthermore, Jiang *et al.* prepared an amorphous (a) nickel(II) borate (Ni-B_i) thin layer (∼4 nm thickness) on amorphous nickel boride (NB) nanoparticles with an average size of 44 nm (aNi-B_i@NB), as shown in Figure 28h.[167] To check the crystallinity-dependent OER activity, partially crystalline Ni-B_i@NB (pc-Ni-B_i@NB) was also prepared through the annealing treatment at 350 °C in Ar for 0.5, 1, 2, and 2.5 h (pc-Ni-B_i@NB-0.5, -1, -2, and -2.5). Figures 28h and i show the XRD pattern and HETEM image of pc-Ni-B_i@NB-2 as a representative. After annealing, all the emerged diffraction peaks can be indexed to a Ni_3B phase. However, there is no peak corresponding to the crystallized Ni-B_i due to its low content and crystallinity. In the HRTEM image, the d-spacings of the Ni_3N (201) and $Ni_3(BO_3)_2$ (102) planes were observed. Accordingly, it was found that the annealing treatment can transform amorphous Ni-B_i and Ni_xB into well-crystallized and partially crystalline Ni_3B and Ni-B_i, respectively. Figure 28j shows the polarization curves of a-Ni-B_i@NB, pc-Ni-B_i@NB-2, Ni_3B without a Ni-B_i shell (NB), and commercial IrO_2 in 1 M KOH. a-Ni-B_i@NB and pc-Ni-B_i@NB-2 showed lower OER overpotentials of 364 and 302 mV at 10 mA·cm^{-2} compared with NB (409 mV), respectively, suggesting that Ni-B_i is necessary for achieving decent OER performance. Moreover, pc-Ni-B_i@NB-2 surpassed a-Ni-B_i@NB in OER activity. This is mainly because pc-Ni-B_i@NB-2 had greater ECSA (C_{dl}: 2.54 mF cm^{-2}) than a-Ni-B_i@NB (0.35 mF cm^{-2}). Moreover, as suggested by Masa *et al.*,[163] we assumed that the electrical conductivity of a-Ni-B_i@NB might be improved by the annealing process involving the crystallinity enhancement, which also contributes to the relatively high OER activity of pc-Ni-B_i@NB-2. To further examine the effect of the Ni−B_i crystallinity on OER activity, the samples prepared with different annealing times (0.5−2.5 h) were also characterized and tested for the OER. The as-prepared pc-Ni-B_i@NB-0.5, -1, and -2.5 exhibited almost same XRD patterns as pc-Ni-B_i@NB-2. TEM analysis indicated that the crystallinity of the Ni-B_i layer increased with prolonging the annealing time (see Figures 28k−m). To be specific, the Ni-B_i crystallites of pc-Ni-B_i@NB-0.5, -2, and -2.5 possessed the statistically estimated sizes of 2.48, 5.34, and 12.25 nm^2, respectively. Figures 28n and o indicate the polarization curves and corresponding TOF plots of a-Ni-B_i@NB and pc-Ni-B_i@NB-0.5, -1, -2, and -2.5, which were measured in 1 M KOH. Herein, a-Ni-B_i@NB showed the lowest OER activity among all the tested samples. With increasing the annealing time from 0.5 to 2 h, the OER activity was improved gradually. However, at the longest annealing time of 2.5 h, degradation in OER activity was observed. BET specific surface area analysis showed that the specific surface areas increased with prolonging the annealing time (0.5 h: 14.9 m^2·g^{-1}; 1 h: 15.9 m^2·g^{-1}; 2 h: 26.4 m^2·g^{-1}; 2.5 h: 33.0 m^2·g^{-1}), which does not follow the trend in the as-observed OER activities. Therefore, the authors concluded that the Ni-Bi crystallinity moderation can tune the intrinsic OER activity of electroactive sites.

According to the above discussion, it is worth noting that one needs to consider both intrinsic [e.g., final surface composition: (metal/boron ratio), electrical conductivity, etc.] and extrinsic factors (e.g., ECSA, morphology, etc.) for comparing and discussing the OER activities of various boride precatalysts.

2.3.2. Metal-Doping/Substitution Effects. Incorporation (e.g., doping, substitution, etc.) of foreign metal(s) into monometallic borides is an effective strategy to enhance their electrocatalytic OER activity. So far, various bimetallic borides (Ni−Co−B,[139,148,150,153,175,178] Co−Fe−B,[152,162,179,188] Fe−Ni−B,[144,145,149,150,187,188] Ni−W−B,[153] Co−W−B,[190] Co−Mo−B[160]), trimetallic borides (Ni−Co−Fe−B,[150,178] V−Co−Ni−B[142]), and multimetallic borides (Ba−Sr−Co−Fe−B,[188] La−Sr−Co−Fe−B[188]) have been reported. For instance,

https://doi.org/10.1021/acs.chemrev.3c00005
Chem. Rev. 2023, 123, 12795−13208

Zhang *et al.* prepared a series of bimetallic boride Co−*x*Ni−B particles with different *x* [*x* is the molar content of Ni, *x* = Ni/(Ni + Co)%] via the solution-based method.[148] Ni−B and Co−B samples were also prepared for comparison. Then, the as-prepared particle samples were loaded on glassy carbon electrodes and tested for the OER in 1 M KOH. Figure 29a

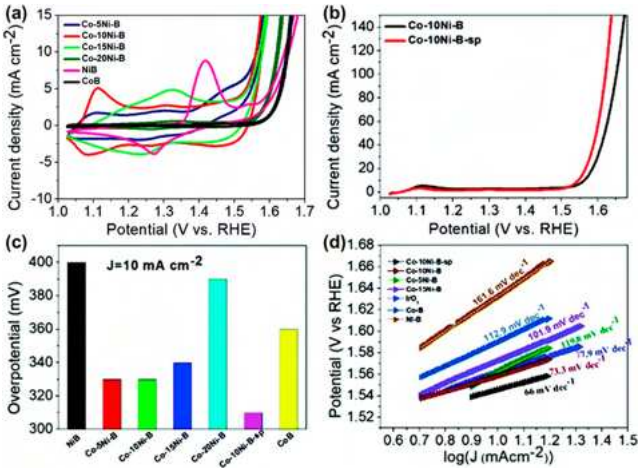


Figure 29. (a) Cyclic voltammetry curves of Co−*x*Ni−B [*x* = Ni/(Ni + Co)%], Co-B, and Ni−B on glassy carbon electrodes at the scan rate of 10 mV·s^{-1} in 1 M KOH. (b) Linear sweep voltammetry curves of Co−10Ni−B and Co−10Ni−B with a smaller particle size (Co−10Ni−B-sp) on glassy carbon electrodes in 1 M KOH. (c) OER overpotentials obtained from OER polarization curves at the current density of 10 mA·cm^{-2}. (d) Tafel plots of borides and IrO_2 electrocatalysts. Reproduced with permission from ref 148. Copyright 2018 Royal Society of Chemistry.

shows the cyclic voltammetry curves of Co−*x*Ni−B, Co−B, and Ni−B samples. The Co−*x*Ni−B sample was the best OER-performing sample, showing an overpotential of 330 mV at a current density of 10 mA·cm^{-2}, which is much smaller than those of the Co−B (360 mV) and Ni−B (330 mV) samples. Below 1.55 V_{RHE}, several oxidation and reduction peaks appeared, which correspond to the electrochemical reactions of the electrocatalyst surfaces. Obviously, the introduction of Ni into cobalt boride increased the oxidation and reduction peak intensities, implying that the Co−Ni−B samples may possess relatively high electroactive surface areas. Furthermore, the post-OER Co−10Ni−B sample was analyzed by XPS and XRD, which revealed the formation of Co and Ni oxyhydroxides on its surface after the OER. Accordingly, the Co−10Ni−B sample might facilitate the formation of oxyhydroxide intermediates, resulting in superior OER activity. To further assess the effect of electroactive surface area, the Co−10Ni−B having a smaller particle size (Co−10Ni−B-sp) was fabricated and tested for the OER in 1 M KOH. Specifically, Co−10Ni−B-sp exhibited a smaller average particle size (~10 ± 3 nm) and higher BET specific surface area (118.85 m^2·g^{-1}) than Co−10Ni−B (20 ± 5 nm; 46.89 m^2·g^{-1}). As indicated in Figure 29b, Co−10Ni−B-sp recorded an OER overpotential of 310 mV at the current density of 10 mA·cm^{-2}, which is 20 mV lower than that of Co−10Ni−B. Here, the improved OER activity of Co−10Ni−B-sp originates from its significantly high surface area. In Figure 29c, the as-recorded OER overpotentials are summarized. Additionally, the as-measured Tafel plots are also displayed in Figure 29d. The Co−10Ni−B-sp sample achieved a Tafel slope of 66 mV·dec^{-1}, which is much lower compared with those of Co−10Ni−B (73.3 mV·dec^{-1}) and IrO_2 (77.9 mV·dec^{-1}), which implies more favorable OER kinetics for the Co−10Ni−B-sp sample.

The incorporation of more metals into monometallic boride can further boost electrocatalytic OER activity. Amorphous trimetallic boride nanoparticle precatalyst (denoted as Fe−Co−2.3Ni−B) was reported by the Wang group.[150] The authors also prepared bimetallic boride samples (Fe−2.3Ni−B and Co−2.3Ni−B). Trimetallic and bimetallic boride samples and commercial Ir/C (20 wt % Ir) were loaded on glassy carbon electrodes, and their OER performance was investigated in O_2-saturated 1.0 M KOH. As seen in Figures 30a and

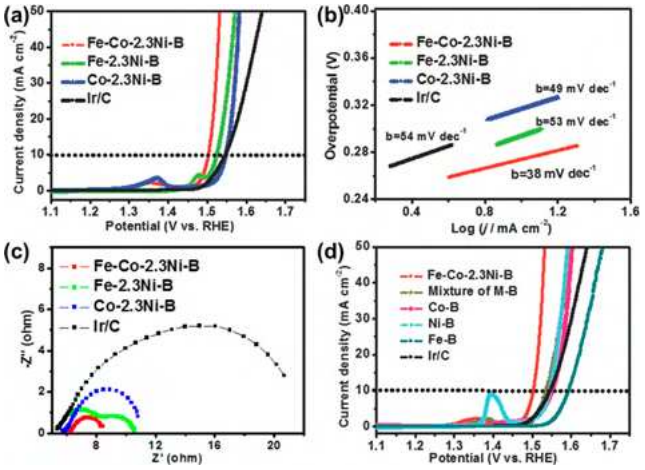


Figure 30. (a) Linear sweep voltammetry curves, (b) corresponding Tafel slopes, and (c) Nyquist plots (at the applied potential of 0.6 $V_{Ag/AgCl}$) for quaternary and ternary borides and commercial Ir/C in 1.0 M KOH. (d) Linear sweep voltammetry curves for quaternary and binary borides, a mixture of *M*−B, and commercial Ir/C in 1.0 M KOH. Reproduced with permission from ref 150. Copyright 2017 Wiley.

b, the Fe−Co−2.3Ni−B sample showed higher OER activity (η@10 mA·cm^{-2}: 274 mV; Tafel slope: 38 mV·dec^{-1}) than the Fe−2.3Ni−B (294 mV, 53 mV·dec^{-1}), Co−2.3Ni−B (317 mV, 49 mV·dec^{-1}), and Ir/C (317 mV, 54 mV·dec^{-1}) samples. Moreover, the OER kinetics were investigated by EIS. As shown in Figure 30c, Fe−Co−2.3Ni−B had a smaller semicircular diameter in comparison with the bimetallic borides and Ir/C, which revealed that incorporating both Co and Fe into nickel boride can reduce charge-transfer resistance. To assess the effect of the incorporation of Co and Fe on the resultant surface area, the C_{dl} values and ECSAs of trimetallic and monometallic borides (Fe−Co−2.3Ni−B and Ni−B) were measured. The C_{dl} value and ECSA of Fe−Co−2.3Ni−B (0.17 mF·cm^{-2}, 4.25 cm^2) were higher than those of Ni−B (0.1 mF·cm^{-2}, 2.5 cm^2), suggesting that Co- and Fe-incorporation can also increase the electrocatalytic active site density. To check the intrinsic OER activity of Fe−Co−2.3Ni−B and Ni−B, the ECSA-based current densities were calculated at the OER overpotential of 314 mV. The as-calculated ECSA-based current densities for Fe−Co−2.3Ni−B and Ni−B were 4.1 and 0.7 mA·cm^{-2}, implying that the intrinsic OER activity of nickel boride can be enhanced by the incorporation of Co and Fe. The authors also suggested that the thermodynamic barrier of a proton-coupled electron transfer pre-equilibrium might be lowered while facilitating the formation of O−O bonding through incorporating a foreign metal into a monometallic

https://doi.org/10.1021/acs.chemrev.3c00005
Chem. Rev. 2023, 123, 12795−13208

compound-based electrocatalyst, enhancing the OER activity. Figure 30d indicates that the Fe−Co−2.3Ni−B sample outperformed its monometallic counterparts (i.e., Co−B, Ni−B, and Fe−B) and their mixture, further confirming that Co- and Fe-incorporation is an effective strategy to improve the OER performance of monometallic boride.

2.3.3. Composite Materials Effects. Fabricating the composite of transition metal borides and other materials [i.e., transition metal oxide/hydroxide materials[151,157] and carbon-based materials (carbon nanotube, reduced graphene oxide, porous carbon, etc.)][137,139,145,161,176,183,185−187,189] is effective for boosting mass activity for the OER by increasing the specific surface area of borides toward electrolytes. For example, Liang *et al.* loaded amorphous nickel boride (Ni−B) nanoparticles loaded on $Ni(OH)_2$ nanosheets (as a support with interconnected conductive networks) hydrothermally grown on Ni foam to fabricate the composite precatalyst electrode Ni−B@$Ni(OH)_2$@Ni foam.[151] Figure 31a shows the

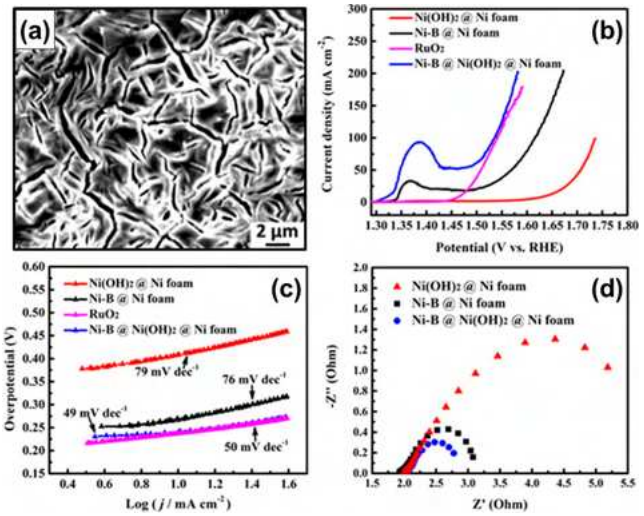


Figure 31. (a) SEM image of Ni−B-loaded $Ni(OH)_2$ nanosheets on Ni foam. (b) *iR*-corrected linear sweep voltammograms and (c) Tafel plots of Ni−B@Ni foam, $Ni(OH)_2$@Ni foam, Ni−B@$Ni(OH)_2$@Ni foam, and RuO_2 on glassy carbon in 1 M KOH. (d) Nyquist plots of Ni−B@Ni foam, $Ni(OH)_2$@Ni foam, and Ni−B@$Ni(OH)_2$@Ni foam electrodes. Reproduced with permission from ref 151. Copyright 2018 Wiley.

top-view SEM image of the as-fabricated Ni−B@$Ni(OH)_2$@Ni foam. The surfaces of the $Ni(OH)_2$ nanosheets are mainly covered with small islands, which were composed of the Ni−B nanoparticle aggregation. For comparison, Ni−B@Ni foam and $Ni(OH)_2$@Ni foam electrodes were also prepared. As shown in Figure 31b, the Ni−B@$Ni(OH)_2$@Ni foam recorded a lower OER overpotential of 300 mV for a current density of 100 mA·cm^{-2} compared with the Ni−B@Ni foam (385 mV) and $Ni(OH)_2$@Ni foam (405 mV) in alkaline media. Even compared with a RuO_2 electrode, the Ni−B@$Ni(OH)_2$@Ni foam exhibited a better OER performance. From the Tafel slopes, the Ni−B@$Ni(OH)_2$@Ni foam possessed the fastest OER reaction kinetics among the measured samples (see Figure 31c). To understand this superior OER activity, C_{dl} values and Nyquist plots were measured for the Ni−B@Ni foam, $Ni(OH)_2$@Ni foam, and Ni−B@$Ni(OH)_2$@Ni foam. The C_{dl} value of the Ni−B@$Ni(OH)_2$@Ni foam (5.45 mF·cm^{-2}) was higher than those of the Ni−B@Ni foam (0.54 mF·cm^{-2}) and $Ni(OH)_2$@Ni foam (0.46 mF·cm^{-2}), indicating that the Ni−B@$Ni(OH)_2$@Ni foam had the largest number of electroactive sites. As displayed in Figure 31d, among the as-measured Ni-based electrodes, the lowest charge transfer resistance was achieved by the Ni−B@$Ni(OH)_2$@Ni foam. Accordingly, the great OER activity of the Ni−B@$Ni(OH)_2$@Ni foam comes from the maximized active sites and the excellent charge transfer ability during the OER. Intentionally, by Raman spectroscopy, the formation of NiOOH intermediates, which are the OER active species, was confirmed after the OER testing.

Similarly, a self-supported Co-B@CoO nanowire array on Ti mesh (Co-B@CoO/Ti) was reported as a high-surface-area composite precatalyst by Lu *et al.*[157] Here, a CoO nanoarray was hydrothermally grown on Ti mesh (CoO/Ti). As seen in Figure 32a, CoO nanowires, which showed 80−100 nm

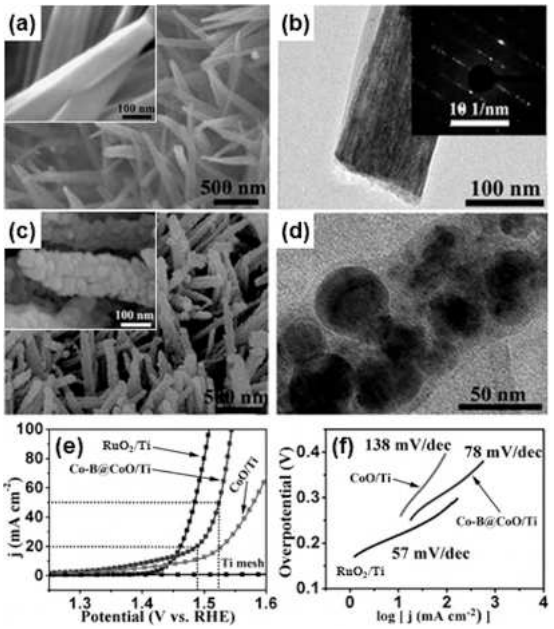


Figure 32. (a−d) SEM and TEM images of (a, b) CoO/Ti and (c, d) Co-B@CoO/Ti. Inset of (b) indicates the corresponding SAED pattern of CoO. (e) Linear sweep voltammograms of Co−B@CoO/Ti mesh, CoO/Ti mesh, RuO_2/Ti mesh, and blank Ti mesh for the OER in 1.0 M KOH (scan rate: 5 mV·s^{-1}). (f) Corresponding Tafel plots of Co−B@CoO/Ti mesh, CoO/Ti mesh, and RuO_2/Ti mesh. Reproduced with permission from ref 157. Copyright 2017 Wiley.

diameters and were several micrometers in length, were uniformly grown on the Ti mesh surface. From the SAED pattern (see Figure 32b), each CoO nanowire was single-crystalline. To form amorphous Co−B nanoparticles on the CoO nanowire surface, the as-prepared CoO/Ti was treated with $NaBH_4$ in alkaline media. The as-treated CoO/Ti maintained its initial 1D structure, and the formation of nanoparticles on its surface was observed (see Figure 32c). From the EDX elemental mapping result, the as-formed Co−B layer had a thickness of approximately 15−40 nm. From the TEM result (Figure 32d), the diameters of the as-formed nanoparticles were in the range of 10−35 nm. Furthermore, CoO/Ti, Co-B@CoO/Ti, RuO_2/Ti, and blank Ti mesh electrodes were tested for the OER in O_2-purged 1 M KOH (Figure 32e). The blank Ti mesh possessed no OER activity, whereas RuO_2/Ti demonstrated excellent OER activity.

https://doi.org/10.1021/acs.chemrev.3c00005
Chem. Rev. 2023, 123, 12795−13208

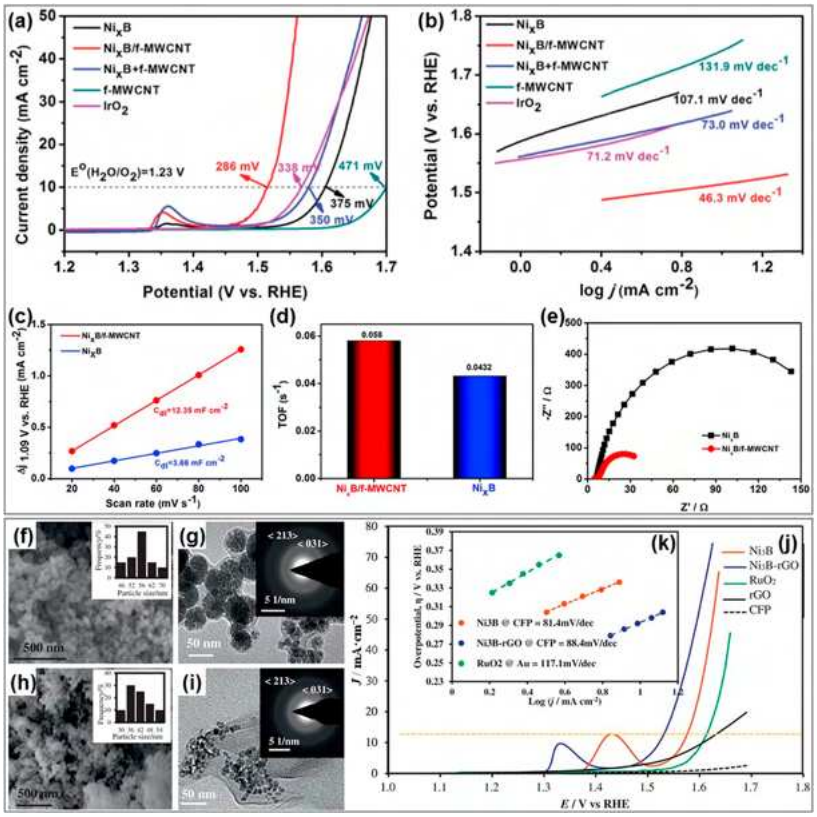


Figure 33. (a) Linear sweep voltammograms and (b) corresponding Tafel plots of Ni_xB/f-MWCNT, Ni_xB, Ni_xB + f-MWCNT, f-MWCNT, and IrO_2 in 1 M KOH. (c) Double-layer capacitances, (d) TOFs (at the OER overpotential of 300 mV), and (e) EIS spectra (at the constant potential of 1.55 V_{RHE}) of Ni_xB/f-MWCNT and Ni_xB. Reproduced with permission from ref 137. Copyright 2019 Royal Society of Chemistry. (f) SEM image, (inset) histogram of particle-size distribution, (g) TEM image, and (inset) SAED pattern of Ni_3B. (h) SEM image, (inset) histogram of particle-size distribution, (i) TEM image, and (inset) SAED pattern of the Ni_3B−rGO nanocomposite. (j) Linear sweep voltammograms (scan rate: 10 $mV{\cdot}s^{-1}$) of Ni_3B@CFP, Ni_3B−rGO@CFP, RuO_2@Au, rGO@CFP, and CFP in 1 M KOH. (k) Corresponding Tafel plots of Ni_3B@CFP, Ni_3B−rGO@CFP, and RuO_2@Au. Reproduced with permission from ref 186. Copyright 2017 Elsevier.

Surprisingly, Co-B@CoO/Ti showed a relatively small OER overpotential (190 mV at 10 $mA{\cdot}cm^{-2}$), which is lower than that for CoO/Ti (285 mV). In Figure 32f, the Tafel slope for RuO_2/Ti was smaller than that for Co-B@CoO/Ti. However, still, Co-B@CoO/Ti showed a much smaller Tafel slope than CoO/Ti. Moreover, according to the EIS results, Co-B@CoO/Ti had a smaller charge transfer resistance for the OER compared with CoO/Ti. Therefore, Co-B@CoO/Ti might achieve faster OER kinetics than CoO/Ti. To further investigate the reason for this improved OER activity, C_{dl} values for Co-B@CoO/Ti, CoO/Ti, and Ti mesh were obtained. Since Co-B@CoO/Ti had a much higher C_{dl} value of 29.8 $mF{\cdot}cm^{-2}$ than Ti mesh (1.86 $mF{\cdot}cm^{-2}$) as well as CoO/Ti (2.9 $mF{\cdot}cm^{-2}$), CoB@CoO/Ti might possess much higher surface roughness and thereby a larger number of active sites electrocatalyzing the OER in comparison with CoO/Ti. Additionally, the pre- and post-OER XPS and ICP-AES analyses found oxide/hydroxide (OER active sites) formation and an almost unchanged Co:B atomic ratio after the OER test, implying that the oxide/hydroxide species might exist on the CoB@CoO surface and that boron species could still stay in the inherent part of the active electrocatalyst.[163]

In addition to the composites of metal boride and metal oxide/hydroxide, the composites of metal boride and carbon-based material were well studied. Herein, we introduce typical examples. The Chen group prepared crystalline nickel boride nanosheets directly grown on surface-functionalized multi-walled carbon nanotubes (Ni_xB/f-MWCNTs) as a composite precatalyst (real OER active sites: *in situ*-formed NiOOH/Ni_xB composite species) for the OER.[137] For the purposes of comparison, Ni_xB, Ni_xB + f-MWCNT (i.e., the physical mixture or Ni_xB and f-MWCNT), f-MWCNT, and commercial IrO_2 were also prepared. All the samples were loaded on glassy carbon electrodes and tested for the OER in O_2-saturated 1 M KOH. As seen in Figures 33a and b, the Ni_xB/f-MWCNT showed the smallest OER overpotential and a Tafel slope smaller than those of Ni_xB, Ni_xB + f-MWCNT, f-MWCNT, and IrO_2. In the Ni_xB-containing samples, anodic peaks at around 1.35 V_{RHE} were observed, which are assignable to Ni^{2+}-to-Ni^{3+} oxidation.[202,208,209] According to TEM analysis results, in the Ni_xB/f-MWCNT sample, the surfaces of f-MWCNTs were covered with a Ni_xB ultrathin layer without large particles and aggregates. On the contrary, the hierarchical aggregates of nanosheet-like Ni_xB particles were present in the Ni_xB and Ni_xB + f-MWCNT samples. Hence, in the Ni_xB/f-MWCNT sample, the relatively high dispersibility of Ni_xB nanosheets might contribute to its superior OER activity. Moreover, Ni_xB + f-MWCNT exhibited excellent electrochemical durability during the long-term OER test (over 100 h of chronopotentiometry at a current density of 20 $mA{\cdot}cm^{-2}$). To further examine the reason why Ni_xB/f-MWCNT showed higher OER activity than Ni_xB the authors checked ECSA, TOF, and electrical conductivity. ECSAs were estimated by measuring CV-based C_{dl} values. As displayed in Figure 33c, the C_{dl} of

https://doi.org/10.1021/acs.chemrev.3c00005
Chem. Rev. 2023, 123, 12795−13208

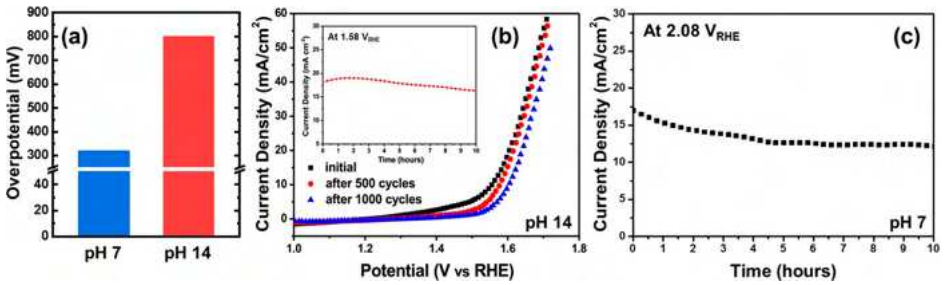


Figure 34. (a) OER overpotentials of Co−Mo−B (sample name: Co-3Mo-B) on glassy carbon substrate at the current density of 10 mA·cm^{-2} in 1 M NaOH (pH = 14) and 0.5 M KPi (pH = 7). (b) Linear sweep voltammetry curves of Co−Mo−B on glassy carbon before and after 500 and 1000 cyclic voltammetry cycles in 1 M NaOH. (c) Potentiostatic curves for Co−Mo−B on classy carbon at 1.58 and 2.08 V_{RHE} in 1 M NaOH (inset) and 0.5 M KPi, respectively. Reproduced with permission from ref 160. Copyright 2017 Elsevier.

Ni_xB/f-MWCNT is much higher than that of Ni_xB, indicating that the ECSA of Ni_xB/f-MWCNT is much larger. TOFs were calculated at the OER overpotential of 300 mV by using the actual number of OER active sites based on the current integration of the Ni^{2+}-to-Ni^{3+} oxidation peaks in the linear sweep voltammograms. The TOF of Ni_xB/f-MWCNT is about 1.34 times as high as that of Ni_xB (see Figure 33d). The electrical conductivities of Ni_xB/f-MWCNT and Ni_xB were measured by EIS. As seen in Figure 33e, Ni_xB/f-MWCNT has a lower charge transfer resistance (24.2 Ω) than Ni_xB (101.7 Ω), suggesting that Ni_xB/f-MWCNT has a faster charge transfer for the OER. Accordingly, the high OER activity and electrochemical stability of Ni_xB/f-MWCNT might be achieved by several synergistic factors: (i) the high intrinsic OER activity from Ni borides and *in situ*-formed Ni oxides/hydroxides, (ii) the ECSA increase by strongly anchoring Ni_xB nanosheets on f-MWCNTs, (iii) the charge transfer (from active OER sites to the glassy carbon electrode surface) improved by MWCNTs, and the strong coupling between Ni_xB nanosheets and f-MWCNTs proven by Raman spectroscopy. The Nath group reported a hybrid nanocomposite of nanocrystalline Ni_3B and reduced graphene oxide (Ni_3B−rGO).[186] Nanocrystalline Ni_3B particles were also prepared for comparison. Figures 33f and h show the SEM images and particle-size distribution histograms of the Ni_3B and Ni_3B−rGO nanocomposite. Both the Ni_3B and Ni_3B−rGO samples mainly consisted of well-dispersed nanoparticles with spherical shapes. The particle size of the Ni_3B−rGO composite [30−55 nm (average: 42 nm)] was smaller than that of Ni_3B [45−70 nm (average: 57 nm)]. TEM images of the Ni_3B and Ni_3B−rGO nanocomposite revealed the existence of randomly distributed nanoparticles (Figures 33g and i). The formation of the nanocrystalline Ni_3B phase in both samples is evidenced by the bright diffraction rings in the SAED patterns. The OER activity of Ni_3B, Ni_3B−rGO, and RuO_2 (a standard sample) was investigated by linear sweep voltammetry in N_2-saturated 1 M KOH. The Ni_3B and Ni_3B−rGO samples exhibited lower OER overpotentials and Tafel slopes compared with the RuO_2 sample (see Figures 33j and k). In particular, the Ni_3B−rGO composite showed a lower OER overpotential (290 mV) than Ni_3B (340 mV). Interestingly, the Ni^{2+}-to-Ni^{3+} oxidation peak appeared at a more cathodic potential in the Ni_3B−rGO composite in comparison with Ni_3B. This phenomenon might be triggered by the synergistic effect produced by the presence of the rGO matrix, lowering the potential required for electrocatalyst activation (Ni^{2+} oxidation) in Ni_3B. Furthermore, the TOF values of the Ni_3B and Ni_3B−rGO samples were determined to be 0.001 and 0.012 s^{-1} at the OER overpotential of 290 mV, respectively, which indicates a better OER performance of the Ni_3B−rGO composite. Based on these experimental results, the excellent OER activity of the Ni_3B−rGO composite might be accomplished because the rGO support can make the particle size of Ni_3B smaller and facilitate charge transfer within the electrocatalyst matrix.[210] The authors also confirmed that the Ni_3B−rGO composite demonstrated great electrochemical durability during a 12 h chronoamperometric test at the constant potential of 1.52 V_{RHE}.

2.3.4. pH Effects. Investigating the pH dependence in OER activity and stability of transition metal boride electrocatalysts is important for expanding their application scope. Gupta *et al.* tested polycrystalline Co−Mo−B nanoparticles (average size: 18 ± 6 nm) on a glassy carbon substrate for the OER in 1 M NaOH (pH = 14) and 0.5 M KPi (pH = 7).[160] As shown in Figure 34a, Co−Mo−B in 1 M NaOH recorded a much lower overpotential of 320 mV at a current density of 10 mA·cm^{-2} than that in 0.5 M KPi (800 mV). In 1 M NaOH, the electrochemical stability of Co−Mo−B was examined by 1000 cyclic voltammetry cycles and a 10 h chronoamperometric test at 1.58 V_{RHE}, from which the authors concluded that the Co−Mo−B sample had favorable stability under the tested conditions (Figure 34b). From the Ni 2p XPS results after 50 cyclic voltammetry cycles, the formation of Co(OH)O and $Co(OH)_2$ species, which are active for the OER, was observed. According to our previous reports,[90,91] we speculate that the initial increase in current density (~0−1.5 h) during the 10 h OER test may originate from the surface area increase due to the formation of Co(OH)O and $Co(OH)_2$ species. On the other hand, Co−Mo−B in 0.5 M KPi did not show a similar increase in current density during the 10 h chronoamperometric test at 2.08 V_{RHE} (see Figure 34c). Moreover, a continuous decrease in current density was observed throughout the 10 h OER test in 0.5 M KPi. After the 10 h OER test, Co−Mo−B in 0.5 M KPi showed a relatively larger current density decrease of ~10 mA·cm^{-2} than that in 1 M NaOH (~4 mA·cm^{-2}). The as-observed differences in between 1 M NaOH and 0.5 M KPi may imply that the electrochemical behavior (i.e., precatalytic transformation, OER reaction route, electrochemical stability, and so forth) of the Co−Mo−B can be altered by changing electrolyte pH, which needs to be further examined by conducting post-OER analyses (e.g., XPS) of the Co−Mo−B in 0.5 M KPi. Furthermore, additional work will probably be necessary for more metal borides to thoroughly understand the pH dependence in electrochemical behavior.

https://doi.org/10.1021/acs.chemrev.3c00005
Chem. Rev. 2023, 123, 12795−13208

2.4. Challenges

In the area of transition metal boride OER electrocatalysts, many studies with sufficient post-OER analyses have been reported thus far, indicating that transition metal borides generally act as precatalysts rather than as catalysts for the OER and that the precatalyst materials are partially oxidized into their oxide/(oxy)hydroxide counterparts during the OER in alkaline media. However, there are still some points that need to be addressed in the future. For example, as discussed in Section 2.2, there are mainly two incompatible interpretations for the surface boron species in the post-OER boride precatalysts. Some proposed that surface boron on the metal boride surface can be oxidized into soluble oxidized boron species (e.g., $B(OH)_4^-$) during the OER, resulting in the oxide/(oxy)hydroxide surface without any boron species. A Pourbaix diagram of boron is shown in Figure 35. Near the

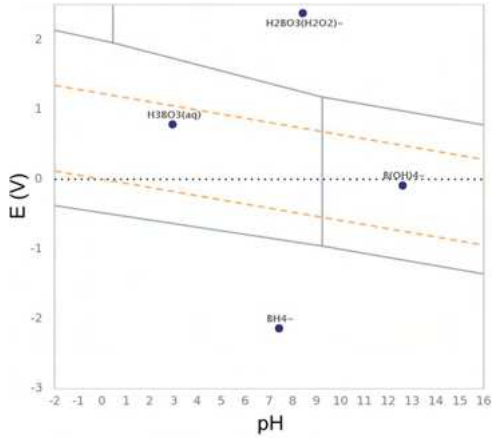


Figure 35. Pourbaix diagram for boron. Orange broken lines represent the thermodynamic potentials for the HER and OER at different pH values. The diagram is produced at the B ion concentration of 10^{-8} M (default) by using the Materials Project.[87−89]

thermodynamic OER potential at pH ∼ 14, the formation of $B(OH)_4^-$ anions can be confirmed, supporting the complete leaching of surface boron species during the OER. On the other hand, others have confirmed that oxidized boron species (e.g., BO_2^-) stay in the newly formed oxide/(oxy)hydroxide even after the OER. According to the findings discussed in Section 2.2, retained boron species may tune the OER active sites (i.e., transition metal center) in the oxide/(oxy)-hydroxide, which facilitates reaction intermediate formation for the OER process, rather than act as a real OER active site. Recently, Gupta *et al.* also made the same interpretation for the role of the retained boron species for the OER.[73] Moreover, as indicated in Table 1, most of the post-OER XPS measurements confirm the existence of oxidized boron species after the OER. However, a few reports experimentally checked the absence of oxidized boron species on the post-OER boride surface. The cause for the difference in these experimental results (e.g., the electrochemical stability of oxidized boron species) is still unclear, and further research is needed.

Incidentally, Ahn *et al.* recently reported boron doping into nickel−iron layered double hydroxide (NiFe LDH) for the electrocatalytic alkaline OER process,[211] which can further support the above observed positive effect of oxidized boron species in the boride precatalysts toward the OER. As shown in Figure 36a, a NiFe LDH precursor hydrothermally grown on Ni foam was subjected to gas−solid boronization (boron source: H_3BO_3) at a relatively low temperature (350 °C) for 3 h. Subsequently, the as-obtained boronized NiFe LDH (B:NiFe LDH) was activated by galvanostatic oxidation (at a constant current density of 0.1 mA·cm^{-2} for 12 h in 1 M KOH), which drastically altered the ratio of Ni:B from 1:0.013 to 1:0.1 × 10^{-3}. Figure 36b shows the FESEM images of NiFe LDH, B:NiFe LDH, and activated B-doped NiFe LDH (Galox-B:NiFe LDH), displaying the formation of nanoplates in all the samples. In the B 1s XPS spectrum of the B:NiFe LDH sample (Figure 36c), the two peaks corresponding to M−B and oxidized B (B−O) species were confirmed at 188 and 193 eV, respectively. After the galvanostatic oxidation, the M−B and B−O peaks were diminished and retained (at ∼192 eV), respectively. Notably, even after a 100 h OER chronoamperometry test (at 1.46 V_{RHE} in 1 M KOH), the B−O XPS peak was observed. As seen in Figures 36d−f, the galox-B:NiFe LDH exhibited the best OER performance (overpotential: 229 mV; Tafel slope: 57 mV·dec^{-1}) and lowest charge transfer resistance (R_{ct}) among the tested samples in 1 M KOH. These results suggest that oxidized boron species in transition metal LDHs can kinetically boost their OER performance, which may also happen in the post-OER/activated boride precatalysts.

So far, most of the reported transition metal borides have demonstrated somewhat high electrochemical stability during long-term OER tests in alkaline media. However, in acidic and neutral electrolytes, the metal borides showed relatively low chemical and electrochemical stability under OER potentials. As introduced earlier in Section 2.2, the TiB_2/FTO electrode was reported for electrocatalyzing the acidic OER.[146] Specifically, the TiB_2/FTO electrodes were tested for long-term OER operations in 1.0 M H_2SO_4 and 1.0 M $HClO_4$ electrolytes (see Figures 37a and b). In 1.0 M H_2SO_4, the TiB_2/FTO electrode showed a continuous increase in overpotential during the OER test and a low Faradaic efficiency of ∼84%, suggesting that TiB_2 may electrochemically leach out. In contrast, although the TiB_2/FTO electrode showed a relatively stable OER overpotential for 10 h and a high Faradaic efficiency of >96%, the TiB_2 film was suddenly delaminated from the FTO substrate. As seen in Figure 37c, the Ti dissolution rate of 0.24 μg·cm^{-2}·h^{-1} was recorded by ICP-OES during the 10 h OER test, suggesting the chemical dissolution of TiB_2 during the OER in 1.0 M $HClO_4$. Therefore, a novel strategy to improve the chemical and electrochemical stability of transition metal borides under OER potentials needs to be developed in the future.

In transition metal oxide/(oxy)hydroxide electrocatalysts [e.g., nickel (oxy)hydroxide and cobalt (oxy)hydroxide], it was revealed that the incidental incorporation of iron impurities from an alkaline electrolyte (i.e., a KOH aqueous solution) could dramatically improve their conductivity as well as resultant OER performance.[200,207,212,213] As shown in Table 1, since most of the reported metal boride precatalysts were tested in Fe-unpurified alkaline media, the incidental iron incorporation might also happen for the metal (oxy)hydroxide species formed after the OER. Note that this phenomenon may also be observed in almost all the transition metal *X*-ide precatalysts tested in Fe-unpurified alkaline media. Actually, the Zuo group reported several transition metal boride precatalysts in Fe-purified 1 M KOH electrolyte in order to negate the iron impurity effect.[140,141] Even without the iron impurities, the metal boride precatalysts could exhibit relatively

https://doi.org/10.1021/acs.chemrev.3c00005
Chem. Rev. 2023, 123, 12795−13208

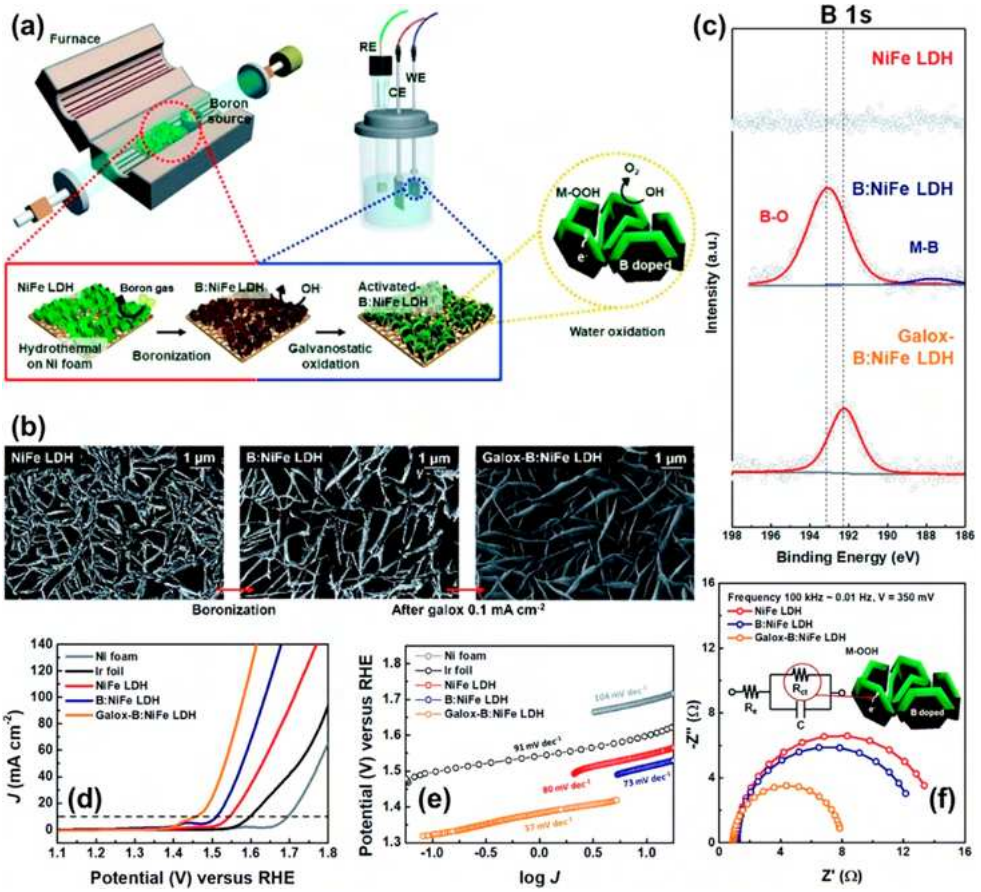


Figure 36. (a) Schematic illustration for the preparation of galvanostatic oxidized B-doped NiFe LDH on Ni foam. (b) FESEM images, (c) B 1s XPS spectra, (d) LSV curves (scan rate: 1.0 mV·s^{-1}), (e) Tafel slopes, and (f) Nyquist plots of NiFe LDH precursor, B-doped NiFe LDH (B:NiFe LDH), and activated B-doped NiFe LDH (Galox-B:NiFe LDH) samples. Reproduced with permission from ref 211. Copyright 2021 Royal Society of Chemistry.

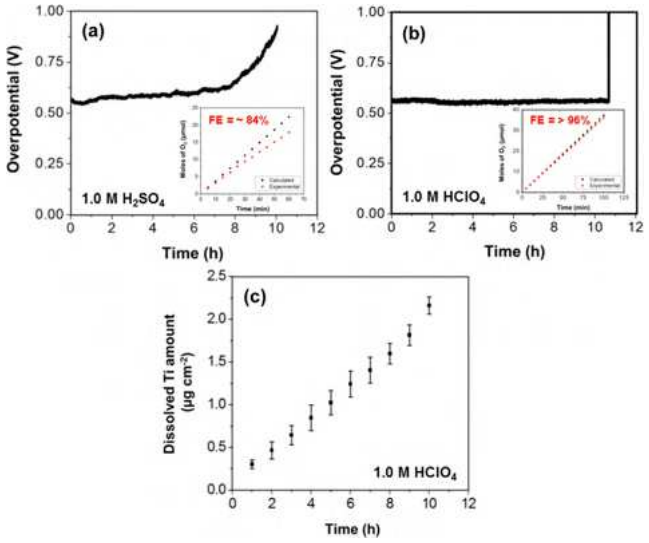


Figure 37. (a, b) Chronopotentiometry and (insets) Faradaic efficiency measurements at a current density of TiB_2/FTO electrodes at the constant current density of 10 mA·cm^{-2} in (a) 1.0 M H_2SO_4 and (b) 1.0 M $HClO_4$. (c) Dissolution rate of TiB_2 in 1.0 M $HClO_4$ electrolyte during the OER operation at the constant current density of 10 mA·cm^{-2}. Reproduced with permission from ref 146. Copyright 2019 Wiley.

high OER activities due to the presence of oxidized boron species (i.e., metaborate), which can modify the electronic structure of the newly formed metal oxyhydroxides. However, the synergistic effect of oxidized boron species and iron impurities is still unclear, which needs to be further examined in the future.

3. TRANSITION METAL CARBIDES

Transition metal carbides have a simple metallic structure with small carbon atoms filling in the interstitial voids of the densely packed metal host lattice.[256] Transition metal carbides have received great attention as electrocatalysts for water splitting due to their high electrical conductivity, unique electronic structure, chemical stability, and low cost.[68,259,284−287] Actually, the studies related to the carbide HER and OER electrocatalysts (i.e., TiC, ZrC, HfC, NbC, Cr_3C_2, Mo_2C, WC, etc.) had already started in the late 1960s.[288,289] Among the carbide materials reported up to now, Ni-, Co-, and Fe-based carbides are good candidates for OER electrocatalysts due to the superb activity of Ni, Co, and Fe metals for alkaline OER electrocatalysis.[91,216,227,238,258,260,264,270,277,283] Additionally, W- and Mo-based carbides, which are good electrocatalysts for the HER, have also been reported as bifunctional electrocatalysts for overall water splitting in the OER field.[225,269,272,282]

https://doi.org/10.1021/acs.chemrev.3c00005
Chem. Rev. 2023, 123, 12795−13208

3.1. Electrode Preparation Methods

As shown in Table 2, transition metal carbides are classified into two types of electrodes: powder-coated electrodes (P) and self-supported electrodes (S). In general, transition metal carbides can be synthesized by annealing the metal and carbon sources together at high temperatures, which is called a thermal carburization process. Depending on the synthesis techniques and types of metal and carbon sources, there are several different strategies for preparing transition metal carbides. For example, transition metal-based precursors obtained from hydrothermal synthesis (refs 216, 224, 228, 229, 235, 257, 259, 262, 269, 276, 280, and 281) and MOF-based precursors (refs 226, 231−233, 238, 260, 261, 263, and 279) are commonly used for two-step synthetic approaches of transition metal carbides (precursor preparation → thermal carburization/pyrolysis). Transition metal carbides can also be prepared through the solid-state/gas-solid reaction between a solid transition metal source and a solid/gaseous carbon source (refs 225, 230, 234, 236, 237, 256, 258, 264, 265, 272, 273, 275, 282, and 283). Notably, in almost all the synthetic approaches, carbon species in the precursors/starting materials not only are utilized as the carbon source for synthesizing transition metal carbide but also are often transformed into carbon supports or carbon shells, resulting in a carbon layer-coated transition metal carbide embedded into a carbon support material. In this Section, we discuss typical strategies to synthesize transition metal carbides and introduce some important and unique examples as well.

3.1.1. Hydrothermal Methods. Hydrothermal methods have been commonly employed to prepare nanostructured oxide-based metal precursors,[229,235,257,259,262,269] which can be transformed into transition metal carbides in the following annealing step (carburization) with additional carbon sources [e.g., melamine, polydopamine, carbon nitride (C_3N_4), and 1,3,5-triamino-2,4,6-trinitrobenzene (TATB)]. For example, Geng *et al.* fabricated 3D NiC/MoC/$NiMoO_4$ heterostructured nanorod arrays on Ni foam via the hydrothermal method and subsequent partial carburization.[262] As seen in Figure 38a, $NiMoO_4$ nanorod arrays were first grown hydrothermally on Ni foam. Afterward, the as-grown $NiMoO_4$ nanorod arrays were soaked in a phosphate-buffered saline solution containing dopamine, forming the $NiMoO_4$ nanorod array coated with polydopamine (carbon source). The polydopamine-coated $NiMoO_4$ nanorod arrays were heated at 450 °C for 2 h and subsequently at 750 °C for 2 h under Ar. During the annealing process, the $NiMoO_4$ nanorods reacted with dopamine and were partly carbonized into NiC/MoC (see Figure 38b), resulting in the NiC/MoC/$NiMoO_4$ heterostructured nanorods.

Using the hydrothermal method, one can also prepare the transition metal-based precursor containing carbon species, which does not require an additional carbon source for the carburization process.[216,224,228,276,280,281] The Lan group prepared N-doped reduced graphene oxide (RGO)-supported metal Co, $Co_6Mo_6C_2$, and Mo_2C composite powders (sample name: Co−Mo−C/NRGO-1) through the hydrothermal method and subsequent calcination.[280] As shown in Figure 39a, the Co-doped polyoxometalate/conductive polymer/graphene (Co-PCG) precursor was first synthesized hydrothermally from graphene oxide (GO), pyrrole monomer (Py), phosphomolybdic acid [polyoxometalate-based open framework (POM): $H_3PMo_{12}O_{40}{\cdot}nH_2O$, PMo_{12}], and cobalt nitrate [$Co(NO_3)_2$]. Then, the as-prepared Co-PCG precursor was calcinated at 800 °C for 3 h under N_2 without adding an additional carbon source (i.e., no carburization process). Figure 39b shows the TEM image of the Co−Mo−C/NRGO-1, indicating that spherical metal/metal carbide nanoparticles (diameter: 2−10 nm) were evenly dispersed on N-doped porous RGO sheets. Furthermore, the HRTEM image (see Figure 39c) of the Co−Mo−C/NRGO-1 revealed the formation of crystalline metal/metal carbide nanoparticles coated by amorphous carbon during the nucleation process. The interplanar distances of 0.26, 0.20, and 0.23 nm were observed, which correspond to the (110), (111), and (422) planes in Mo_2C, metal Co, and $Co_6Mo_6C_2$, respectively. Similarly, the Lan group also synthesized a simpler composite, a pure Co- and Mo-based bimetallic carbide anchored on a conductive carbon-based support, which provided high electrical conductivity and a large surface area for high electrocatalytic activity.[276] As shown in Figure 39d, the Co-PCG precursor was prepared using the hydrothermal method at 180 °C for 12 h by simply mixing $Co(NO_3)_2$, $H_3PMo_{12}O_{40}{\cdot}nH_2O$ (PMo_{12}), pyrrole, and graphene oxide sheets in water. Subsequently, the as-prepared Co-PCG was annealed at 800 °C for 3 h under N_2 (without an additional carbon source), producing the N-doped porous carbon-coated pure bimetallic carbide of $Co_6Mo_6C_2$ without any agglomeration on a N-doped reduced graphene oxide (NCRGO) film, namely a $Co_6Mo_6C_2$/NCRGO composite. The pure bimetallic carbide phase and its uniform distribution on the substrate were confirmed by XRD and EDX elemental mapping analyses (Figures 39e and f).

Transition metal carbide can also be synthesized through a one-step hydrothermal process. Qin *et al.* reported an ionic liquid-assisted hydrothermal method for *in situ* synthesizing of Ni@Ni_3C core@shell hierarchical nanospheres.[268] In brief, $Ni(NO_3)_2$ was added in ionic liquid [1-butyl-3-methylimidazolium acetate ([Bmim]Ac)] and deionized water. The as-prepared solution was transferred in an autoclave and heated at 180 °C for 24 h, producing the Ni@Ni_3C nanospheres (diameter: 400−700 nm). Ni@Ni_3C nanospheres coated with a thin quasigraphitic carbon layer were also prepared by replacing [Bmim]Ac with 1-octyl-3-methylimidazolium acetate ([Omim]Ac).

3.1.2. MOF-Derived Methods. MOF-derived methods have been widely utilized for the syntheses transition metal carbides, which typically require two steps: (i) MOF precursor preparation and (ii) subsequent thermal decomposition. The MOF can become both transition metal and carbon sources and be easily converted to transition metal carbides by subsequent annealing steps.[226,231−233,238,260,261,263,279] Also, the transition metal carbides prepared by the MOF-derived methods are usually *in situ* hybridized with a carbon matrix. For instance, Jia *et al.* synthesized Co-doped Ni_3C/Ni-embedded carbon materials using the two-step MOF-derived method.[260] As depicted in Figure 40a, Co/Ni-BTC MOF, where BTC stands for the organic ligand trimesic acid (i.e., BTC = 1,3,5-benzenetricarboxylate), was synthesized as a precursor via complexing the bimetal chloride with dimethylformamide followed by coordination with trimesic acid. Then, the as-obtained Co/Ni-BTC precursor was heated at 350 °C for 4 h under Ar/H_2 gas to obtain Co-doped Ni_3C/Ni-embedded carbon materials (see Figures 40b−e). Similarly, as shown in Figure 40f, Su *et al.* prepared Co_3ZnC/Co nanojunctions encapsulated in N-doped graphene shell layers from a $Zn_3[Co(CN)_6]_2$ MOF precursor consisting of CN^-

https://doi.org/10.1021/acs.chemrev.3c00005
Chem. Rev. 2023, 123, 12795−13208

Table 2. Summary of the Electrocatalytic Properties, Electrochemical Testing Conditions, and Physicochemical Pre- and Post-analyses of Transition Metal Carbides Used for Alkaline/Acidic/Neutral OER and of the Final Type of Electrocatalyst after OER Testing[a–e]

Initial Electrocatalyst	Substrate	Shape of Electrocatalyst	Deposition Type	Specific Loading / $mg \cdot cm^{-2}_{geo}$	η@10 $mA \cdot cm^{-2}_{geo}$ / mV	C_{dl} / $mF \cdot cm^{-2}_{geo}$	TOF / s^{-1} ($@\eta$ or j)	Tafel Slope / $mV \cdot dec^{-1}$	Electrolyte	Pre-analysis	Post-analysis	Long-Term OER Test Conditions	Post-OER Electrocatalyst	Final Type of Electrocatalyst	Ref.
Fe@NC	GC	Nanoparticles	P	0.306	451	0.75	-	67.25	1 M KOH	XRD, XPS, SEM, TEM, STEM, EDX, Raman, N_2 ISO (BET, PSD)	-	-	-	-	214
Fe_3Mn_1@NC (Fe_3C@N-doped carbon + MnO)	GC	Nanoparticles	P	0.306	357	1.17	-	54.48		XRD, XPS, SEM, TEM, STEM, EDX, HAADF- STEM, Raman, N_2 ISO (BET, PSD)	TEM (after OWS)	30000 s CA (1.65 V_{RHE}) 30 h CA (cell voltage: 1.63 V, OWS)	Fe_3C@N-doped carbon, MnO	Catalyst	
Fe_1Mn_1@NC (Fe_3C@N-doped carbon + MnO)	GC	Nanoparticles	P	0.306	385	1.91	-	63.86		XRD, XPS, SEM, TEM, EDX, Raman, N_2 ISO (BET, PSD)	-	-	-	-	
Fe_1Mn_3@NC (Fe_3C@N-doped carbon + MnO)	GC	Nanoparticles	P	0.306	518	2.34	-	123.37		XRD, XPS, SEM, TEM, EDX, Raman, N_2 ISO (BET, PSD)	-	-	-	-	
α-MoC/NC	GC	Nanoparticles	P	0.333	559	-	-	120.5	1 M KOH	SEM, TEM, HAADF-STEM, EDX, XRD,	-	-	-	-	215
Co_3O_4@α-MoC/NC	GC	Nanoparticles	P	0.333	430	-	-	71.5		SEM, TEM, HAADF-STEM, EDX, XRD, XPS, N_2 ISO (BET)	TEM, HAADF-STEM, EDX, XPS	15 h CA (1.91 V_{RHE})	Co_3O_4, MoC, Oxidized Mo species, N-doped carbon	Catalyst	
Fe_3C/NF	Ni foam	Nanosheets	S	0.84	262	60.17	0.019 at 300 mV	49	0.1 M KOH	XRD, FESEM, EDX. TEM, XPS, ISO (BET), CAM	XRD, FESEM, XPS	100 h CP (10 $mA \cdot cm^{-2}_{geo}$)	Fe_3C	Catalyst	216
Fe_3C/NF-1	Ni foam	Nanosheets	S	0.84	310	43.4	-	51		XRD, FESEM, EDX	-	100 h CP (10 $mA \cdot cm^{-2}_{geo}$)	-	-	
Fe_3C/NF-2	Ni foam	Nanosheets	S	0.84	331	21.99	-	56		XRD, FESEM, EDX	-	100 h CP (10 $mA \cdot cm^{-2}_{geo}$)	-	-	
d-$NiC_{0.2}$NS/Ni/CF	Cu foil	Nanosheets	S	2.74	228	6.22	-	55	1 M KOH	XRD, SEM, EDX, TEM, XPS, ICP-OES	XRD, SEM, TEM, XPS	100 h CA 5000 CV cycles	$NiC_{0.2}$ (NiOOH, $Ni(OH)_2$ from Ni/CF)	Catalyst (conductive substrate partially oxidized during the OER)	217
d-$NiC_{0.2}$NS/CF	Cu foil	Nanosheets	P	2.74	250	-	-	58		-	-	-	-	-	
NiFe-PBA-gel-cal-F (Fe_3O_4 on NiC_x)	GC	Nanoparticles	P	~ 0.02	281 (@100 $mA \cdot cm^{-2}_{geo}$)	87.1	1.33 at 280 mV	63.1	1 M KOH	SEM, TEM, EDX, HAADF-STEM, XRD, FTIR, N_2 ISO (BET, PSD), XPS	TEM, SAED, HAADF-STEM, EDX, XPS, XRD, XPS, *Operando* Raman	60 h CA (1.52 V_{RHE})	Ni (oxy)hydroxides	Precatalyst (full oxidation)	218
NiFe-PBA-gel-cal-S (Fe_3O_4 on NiC_x)	GC	Nanoparticles	P	~ 0.02	329 (@100 $mA \cdot cm^{-2}_{geo}$)	55.2	-	68.7	1 M KOH + 0.5 M NaCl			60 h CA (1.53 V_{RHE})			
Fe_3C	GC	Nanoparticles	P	0.1	576	-	-	165	1 M KOH	XRD, TEM, XPS, Raman	XRD, XPS	100 CV cycles (10 $mV \cdot s^{-1}$, 1.0–1.8 V_{RHE})	FeO_x	Precatalyst (partial oxidation)	219
Co_2C	GC	Nanoparticles	P	0.1	423	-	-	112		XRD, TEM, XPS, Raman	XRD, XPS	100 CV cycles (10 $mV \cdot s^{-1}$, 1.0–1.8 V_{RHE})	CoO_x	Precatalyst (partial oxidation)	
Ni_3C	GC	Nanoparticles	P	0.1	503	-	-	145		XRD, TEM, XPS, Raman	XRD, XPS	100 CV cycles (10 $mV \cdot s^{-1}$, 1.0–1.8 V_{RHE})	NiO_x	Precatalyst (partial oxidation)	
Mo_2C/C	GC	Nanoparticles	P	0.07	~ 351	50.3 μF	-	56.5	1 M KOH	XRD, XPS, TEM	-	-	-	-	220
FeNi-Mo_2C/C	GC	Nanoparticles	P	0.07	288	35.2 μF	-	38.8		XRD, XPS, TEM, STEM, EDX	TEM, XPS	12 h CA (1.774 V_{RHE})	Metal oxide species (Fe^{3+}, Ni^{3+}, and Mo^{6+} species)	Precatalyst (partial oxidation)	
V_8C_7	GC	Microparticles	P	0.49	458	0.299	-	-	1 M KOH	XRD, SEM, EDX, N_2 ISO (BET)	XRD, *Quasi In-Situ* SEM, *Quasi In-Situ* EDX	3000 CV cycles (50 $mV \cdot s^{-1}$, 1.10–1.65 V_{RHE})	VOOH	Precatalyst (V dissolution + partial oxidation)	221
W_2C/CC	CC	Nanosheets	P	-	368	10.385	-	58.54	1 M KOH	XRD, XPS, SEM	-	-	-	-	222
Co_6W_6C/CC	CC	Nanosheets	P	7~10	286	41.425	-	53.96		XRD, XPS, SEM, TEM, SAED, EDX, HAADF-STEM, Raman	XRD, XPS, SEM, TEM, SAED, EDX, HAADF-STEM, Raman	50 h CP (10 $mA \cdot cm^{-2}_{geo}$)	W-doped $Co(OH)_2$, W-doped CoO	Precatalyst (full oxidation)	
Fe_3C@CNOs/GC	GC	Nanoparticles	P	0.255	451	-	0.05 at 400 mV	89	1 M KOH	XRD, XPS, SEM, EDX, N_2 ISO (BET, PSD), Raman	-	-	-	-	223
	Ni foam		P	0.255	345	20.78	-	89.2			-	-	-	-	
FNC@CNOs/GC (Ni-doped Fe_3C@carbon nano-onions)	GC	Nanoparticles	P	0.255	342	-	0.06 at 400 mV	62		XRD, SEM, EDX	-	-	-	-	
FMC@CNOs/GC (Mn-doped Fe_3C@carbon nano-onions)	GC	Nanoparticles	P	0.255	431	-	0.01 at 400 mV	99		XRD, SEM, EDX	-	-	-	-	
FCC@CNOs/GC (Co-doped Fe_3C@carbon nano-onions)	GC	Nanoparticles	P	0.255	320	-	0.21 at 400 mV	57		XRD, XPS, SEM, TEM, EDX, N_2 ISO (BET, PSD), XANES, EXAFS, Raman	XRD, XPS, XANES, EXAFS, Raman	10000 CV cycles (50 $mV \cdot s^{-1}$)	Oxidized metal species ($M^{2+/3+}$ species)	Precatalyst (partial oxidation)	
	Ni foam		P	0.255	271	99.18	-	48.9				> 40 h CA (1.50 and 1.63 V_{RHE})			

https://doi.org/10.1021/acs.chemrev.3c00005
Chem. Rev. 2023, 123, 12795−13208

Table 2. continued

Initial Electrocatalyst	Substrate	Shape of Electrocatalyst	Deposition Type	Specific Loading / $mg \cdot cm^{-2}_{geo}$	η@10 $mA \cdot cm^{-2}_{geo}$ / mV	C_{dl} / $mF \cdot cm^{-2}_{geo}$	TOF / s^{-1} (@η or j)	Tafel Slope / $mV \cdot dec^{-1}$	Electrolyte	Pre-analysis	Post-analysis	Long-Term OER Test Conditions	Post-OER Electrocatalyst	Final Type of Electrocatalyst	Ref.
Mo_6Ni_6C/NF (O-MoNi-C/NF)	Ni foam	Nanoparticles	S	9.8	190	330	-	65.35	1 M KOH	XRD, Raman, FTIR, SEM, EDX, XPS, TEM, HAADF-STEM, EELS, XAFS	XPS, XAFS (*In-Situ* XANES, EXAFS), Raman, FTIR	110 h CP (10 $mA \cdot cm^{-2}_{geo}$)	$NiOOH$, MoO_x (Mo^{6+} species)	Precatalyst (reconstruction + partial oxidation)	224
β-Mo_2C@NC (M-0.01)	Ni foam	Nanospheres	P	1	274 338 (@100 mA/cm^2_{geo})	35.08	-	70.0	1 M KOH	XRD, SEM, EDX, TEM, XPS, Raman, N_2 ISO (BET)	SEM, XPS, TEM	20 h CP (10 $mA \cdot cm^{-2}_{geo}$)	β-Mo_2C@MoO_x core@shell	Precatalyst (partial oxidation)	225
$Co_{0.2}$-β-Mo_2C@NC	GC	Nanoparticles	P	0.28	370	5.9	-	78.6	1 M KOH	-	-	-	-	-	226
$Co_{0.1}$-β-Mo_2C@NC	GC	Nanoparticles	P	0.28	262.2	4.97	-	28.8		XRD, SEM, EDX, TEM, XPS, N_2 ISO (BET), Raman, XANES, EXAFS, ICP-AES	TEM, XPS	60000 s CA (1.49 V_{RHE})	-	Precatalyst	
$Co_{0.05}$-β-Mo_2C@NC	GC	Nanoparticles	P	0.28	400	1.32	-	66.5		Raman, ICP-AES	-	-	-	-	
β-Mo_2C@NC	GC	Nanoparticles	P	0.28	-	-	-	-		Raman, ICP-AES	-	-	-	-	
Co_3C/CNFs	CNFs	Nanoparticles	S	-	320	112.5	-	296	1 M KOH	XRD, SEM, TEM, XPS, ICP	-	-	-	-	227
$V_{0.28}Co_{2.72}C$/CNFs	CNFs	Nanoparticles	S	-	210	176.8	-	147		XRD, SEM, TEM, HAADF-STEM, XPS, ICP	XRD, TEM, XPS, *In-Situ* Raman	10 h CA (1.4 V_{RHE}) 5000 CV cycles	-	Precatalyst	
$V_{0.80}Co_{2.20}C$/CNFs	CNFs	Nanoparticles	S	-	440	113	-	348		XRD, SEM, TEM, XPS, ICP	-	-	-	-	
Mo_2CT_x MFs (Mo_2C)	Ni foam	Microflowers	P	1	240	-	0.0101 at 200 mV	66	1 M KOH	XRD, SEM, EDX, TEM, FTIR, HAADF-STEM, Raman, XPS XANES	-	-	-	-	228
Mo_2CT_x NMs-5 (Mo_2C)	Ni foam	Nanomeshes	P	1	200	-	-	50			-	-	-	-	
Mo_2CT_x NMs-10 (Mo_2C)	Ni foam	Nanomeshes	P	1	185	-	-	40			-	-	-	-	
Mo_2CT_x NMs-15 (Mo_2C)	Ni foam	Nanomeshes	P	1	180	-	0.0315 at 200 mV	36			XRD, TEM, XPS,	2 h CA (1.43 V_{RHE}) 2 h (1.43 V_{RHE}, 3 M KOH)	-	Precatalyst (partial oxidation)	
Ni/Mo_xC@NC (Ni-Mo_xC-100)	GC	Nanobelts	P	~0.86	328	27.2	-	74	1 M KOH	XRD, SEM, EDX, TEM, XPS, Raman, ISO (BET)	XRD, XPS	~14 h CA (1.56 V_{RHE}) 2000 CV cycles (100 $mV \cdot s^{-1}$)	$NiOOH$, MoO_2	Precatalyst (partial oxidation)	229
					~336 (@20 mA/cm^2_{geo})	-	-	-	Fe-purified 1 M KOH		-	-	-	-	
Co-Mo_2C NPs	GC	Nanoparticles	P	0.24	347	-	0.515 at 350 mV (surface Co cations)	38	0.1 M KOH	XRD, SEM, TEM, XPS, ISO (BET), ICP-AES, NH_3-TPD	XPS, PZC, ICP-AES	2000 CV cycles (100 $mV \cdot s^{-1}$, 1.3–1.7 V_{RHE})	CoOOH	Precatalyst (Mo dissolution + partial oxidation)	230
Mo_2C NPs	GC	Nanoparticles	P	0.24	-	-	-	-		XRD, SEM, TEM, XPS, ISO (BET), NH_3-TPD	-	-	-	-	
Mo_xCo_xC@C (PMo/ZIF-67-6-6N)	GC	Nanoparticles (confined in C polyhedrons)	P	0.708	295	47.4	-	35	1 M KOH	XRD, SEM, EDX, TEM, XPS, ICP	XRD, XPS	22 h CA (1.53 V_{RHE}) 1000 CV cycles (100 $mV \cdot s^{-1}$)	$CoO_x/Co(OH)_2$, MoO_x	Precatalyst (partial oxidation)	231
Co_3C	GC	Nanospheres	P	1	455	-	-	-	1 M NaOH	XRD, TEM, XPS	XRD, TEM, XPS	350 CV cycles (1.0–1.9 V_{RHE})	Amorphous CoO_x	Precatalyst (full oxidation)	91
Co-Mo_2C@NC	CC	Nanoparticles	P	1	440	-	-	156	0.2 M PBS (pH = 7)	XRD, SEM, TEM, XPS, Raman	SEM, XPS	> 9 h CA (1.63 V_{RHE})	-	Precatalyst (Mo dissolution)	232
Mo_2C@NC	CC	-	P	1	460	-	-	-		-	-	-	-	-	
Co-Mo_2C@NC	CC	Nanoparticles	P	1	370	-	-	60	0.1 M KOH	XRD, SEM, TEM, XPS, Raman	-	4 h CA (1.6 V_{RHE})	-	-	
$Ni_3ZnC_{0.7}$-550	GC	Nanoparticles	P	0.24	320	26.9	-	52	1 M KOH	XRD, SEM, TEM, Raman, XPS, DSC, TGA	XRD, SEM, TEM, XPS	24 h CA (1.56 V_{RHE})	Metal oxide/hydroxide	Precatalyst (partial oxidation)	233
$Ni_3ZnC_{0.7}$-450	GC	Nanoparticles	P	0.24	380	4.1	-	89			-	-	-	-	
$Ni_3ZnC_{0.7}$-650	GC	Nanoparticles	P	0.24	410	5.5	-	100			-	-	-	-	
Ni_3C	GC	Nanodots	P	~0.15	323	4.8	-	67	1 M KOH	XRD, SEM, TEM, XPS	-	-	-	-	234
Fe-Ni_3C-2%	GC	Nanodots	P	~0.15	275	6.8	-	62		XRD, SEM, TEM, XPS, N_2 ISO (BET, PSD)	XPS, TEM	10 h CA (1.5 V_{RHE}) 1000 CV cycles	Ni oxide	Precatalyst (partial oxidation)	
Fe-Ni_3C-5%	GC	Nanodots	P	~0.15	302	5.1	-	64		XRD, SEM, TEM	-	-	-	-	
Ni/Mo_2C-PC	GC	Nanorods	P	0.50	368	11.2	-	101	1 M KOH	XRD, SEM, EDX, TEM, XPS, N_2 ISO (BET), Raman	XRD, XPS	10 h CA (1.57 V_{RHE}) 20 CV cycles (100 $mV \cdot s^{-1}$)	-	Precatalyst (partial oxidation)	235
Mo_2C-PC	GC	Nanorods	P	0.50	570	6.4	-	140		XRD, SEM, TEM	-	-	-	-	
Co_4Mo_6C@NC	GC	Bamboo-like	P	0.357	420	0.0026	-	54.6	1 M KOH	XRD, SEM, EDX, TEM, XPS	XPS	14 h CP (10 $mA \cdot cm^{-2}_{geo}$)	-	Precatalyst (partial oxidation)	236
Co_6Mo_2C@NC	GC	Irregular aggregates	P	0.357	570	0.0012	-	290.5					-	Precatalyst (partial oxidation)	
Co_4Mo_2C@NC	GC	Porous nanostructure	P	0.357	330	0.007	-	48.7					Co_4Mo_2C@CoOOH	Precatalyst (partial oxidation)	
Mo_2C/C (M2)	GC	Nanoparticles (hexagonal)	P	0.4	320	9.1	-	98	1 M KOH	TGA, XRD, SEM, TEM, Raman, XPS	TEM, XPS	10 h CA (1.61 V_{RHE}) 1000 CV cycles (50 $mV \cdot s^{-1}$, 1.0–1.6 V_{RHE})	-	Precatalyst	237
Fe/Fe_3C@NG	GC	(Encapsulated) nanostructures	P	0.7	506	-	-	-	0.1 M KOH	XRD, SEM, EDX, TEM, XPS, Raman	XPS	1000 CV cycles (100 $mV \cdot s^{-1}$)	-	Precatalyst	238
Ni_3C/C	CFP	Nanoparticles	P	0.285	316	-	0.099 at 400 mV	46	1 M KOH	XRD, TEM, XAS (XANES, EXAFS)	XAS (XANES, EXAFS), TEM, EM	50000 s CA (1.55 and 1.59 V_{RHE}) 1000 CV cycles	NiO_x	Precatalyst (partial oxidation)	239

https://doi.org/10.1021/acs.chemrev.3c00005
Chem. Rev. 2023, 123, 12795−13208

Table 2. continued

Initial Electrocatalyst	Substrate	Shape of Electrocatalyst	Deposition Type	Specific Loading / $mg \cdot cm^{-2}_{geo}$	η@10 $mA \cdot cm^{-2}_{geo}$ / mV	C_{dl} / $mF \cdot cm^{-2}_{geo}$	TOF / s^{-1} (@η or j)	Tafel Slope / $mV \cdot dec^{-1}$	Electrolyte	Pre-analysis	Post-analysis	Long-Term OER Test Conditions	Post-OER Electrocatalyst	Final Type of Electrocatalyst	Ref.
Ni_3C	CFP	Nanoparticles	P	0.285	354	-	0.014 at 400 mV	55		XRD, TEM, TDR, EFM, N_2 ISO (BET, PSD)	-	-	-	-	239
TiC NP/rGO	CP	Nanoparticles	P	1	-	16.5	-	140	1 M $HClO_4$	XRD, XPS, EPR, XANES, EXAFS, TEM, HAADF-STEM	-	-	-	-	240
TaC NP/rGO	CP	Nanoparticles	P	1	-	18.2	-	169		XRD, XPS, EPR, XANES, EXAFS, TEM, HAADF-STEM	-	-	-	-	
$TiTaC_2$ NP/rGO	CP	Nanoparticles	P	1	420	62.0	-	106		XRD, XPS, EPR, XANES, EXAFS, TEM, HAADF-STEM	-	-	-	-	
$TiTaF_xC_2$ NP/rGO	CP	Nanoparticles	P	1	280	295.8	-	36		XRD, XPS, EPR, XANES, EXAFS, TEM, HAADF-STEM, SEM	XRD, Raman	40 h CA (1.6 V_{RHE})	-	-	
Fe-NC (Fe_3C/N-doped carbon)	GC	Nanoparticles	P	0.127	545	2.6	-	82	1 M KOH	SEM, TEM, EDX, XRD, XPS, N_2 ISO (BET), Raman	-	-	-	-	241
NiFe-PBA/Ni_3C	GC	Nanosheets, Nanoparticles	P	1	246	1.8	-	38.0	1 M KOH	XRD, SEM, FTIR, TGA	-	-	-	-	242
NiFe-PBA/Ni_3C(B)	GC	Nanosheets, Nanoparticles	P	1	196	2.2	-	30.1		XRD, XPS, SEM, TEM, SAED, FTIR, TGA, N_2 ISO (BET)	-	22 h CA 2000 CV cycles	-	-	
FeNi@WC-NCL-1	GC	Nanoparticles	P	0.25	349	2.85	-	86	1 M KOH	XRD, XPS, TEM, N_2 ISO (BET, PSD)	-	-	-	-	243
FeNi@WC-NCL	GC	Nanoparticles	P	0.25	279	5.85	-	76		XRD, XPS, TEM, SEM, EDX, N_2 ISO (BET, PSD)	SEM, EDX	24 h CP (10 $mA \cdot cm^{-2}_{geo}$)	-	-	
FeNi@WC-NCL-2	GC	Nanoparticles	P	0.25	470	0.47	-	103		XRD, XPS, TEM, N_2 ISO (BET, PSD)	-	-	-	-	
WC_x-CNFs	GC	Nanoparticles	P	0.197	477	-	-	194	1 M KOH	SEM, XRD	-	-	-	-	244
Ni/WC_x-CNFs-1	GC	Nanoparticles	P	0.197	425	-	-	99		SEM, TEM, EDX, XRD, XPS	-	-	-	-	
Ni/WC_x-CNFs-2	GC	Nanoparticles	P	0.197	404	-	-	101		SEM, TEM, EDX, XRD, XPS	-	-	-	-	
Ni/WC_x-CNFs-3	GC	Nanoparticles	P	0.197	378	0.2457	-	93		SEM, TEM, EDX, XRD, XPS, Raman	SEM, TEM	2000 CV cycles	-	-	
Ni/WC_x-CNFs-4	GC	Nanoparticles	P	0.197	392	-	-	110		SEM, TEM, EDX, XRD	-	-	-	-	
CoC_2/$Co_{0.55}Fe_{1.945}$@C	GC	-	P	~0.3	420	-	-	84	1 M KOH	XRD, XPS, Raman, N_2 ISO (BET), UV-Vis	-	-	-	-	245
Fe_3C@C	GC	-	P	~0.3	~544 (@2 $mA \cdot cm^{-2}_{geo}$)	-	-	-		XRD, Raman, N_2 ISO (BET)	-	-	-	-	
Mo_2C MXene	GC	Stacked layers	P	1.428	~486	0.57	~0.3 at 300 mV	340	1 M KOH	XRD, SEM, N_2 ISO (BET, PSD)	-	-	-	-	246
CoMo-MI-400 (Co-Mo-C/N–C)	GC	Flower-like powder	P	~0.70	371	15.4	-	113.3	1 M KOH	XRD, SEM, N_2 ISO (BET, PSD), Raman	-	-	-	-	247
CoMo-MI-500 (Co-Mo-C/N–C)	GC	Flower-like powder	P	~0.70	335	17.1	-	96.3		XRD, SEM, N_2 ISO (BET, PSD), Raman	-	-	-	-	
CoMo-MI-600 (Co_3Mo_3C/N–C)	GC	Flower-like powder	P	~0.70	316	100.0	-	89.9		XRD, SEM, TEM, SAED, HAADF-STEM, EDX, N_2 ISO (BET, PSD), Raman, XPS	SEM, XRD	40000 s CA (1.55 V_{RHE})	-	-	
CoMo-MI-700 (Co_3Mo_3C/N–C)	GC	Flower-like powder	P	~0.70	342	39.5	-	104.5		XRD, SEM, N_2 ISO (BET, PSD), Raman	-	-	-	-	
Co-MI-600 (Co-C/N–C)	GC	-	P	~0.70	419.7	-	-	80.5		XPS	-	-	-	-	
Pure Mo_2C	Ni foam	Nanoparticles	P	50	340	-	-	441	1 M alkaline solution	XRD	-	-	-	-	248
MCZ-1 (Co-NC@Mo_2C)	Ni foam	Nanoparticles	P	50	380	-	-	390		XRD	-	-	-	-	
MCZ-2 (Co-NC@Mo_2C)	Ni foam	Nanoparticles	P	50	169	154.8	-	127		XRD, XPS, SEM	-	24 h CP (100 μA) 1000 CV cycles	-	-	
MCZ-3 (Co-NC@Mo_2C)	Ni foam	Nanoparticles	P	50	375	-	-	784		XRD	-	-	-	-	
Fe_3C NPs	GC	Nanoparticles	P	0.228	~590	-	-	132	0.1 M KOH	SEM, STEM-HAADF, TEM, SAED, EDX, XRD	-	~1.5 h CA (1.70 V_{RHE})	-	-	249
Fe_3C@C	GC	Nanoparticles	P	0.228	~500	-	-	97		STEM-HAADF, TEM, SAED, EDX, XRD, N_2 ISO (BET, PSD)	-	13.8 h CA (1.70 V_{RHE})	-	-	
Fe_3C@C-N	GC	Nanoparticles	P	0.228	~474	-	0.74 at 570 mV	89		STEM-HAADF, TEM, SAED, EDX, XRD, XPS, XANES, N_2 ISO (BET, PSD), TGA, ICP-MS	XRD, TEM	13.8 h CA (1.70 V_{RHE}) 1000 CV cycles	-	-	
					~355	-	-	59.5	3 M KOH		-	3 h CA (1.54 V_{RHE})	-	-	

https://doi.org/10.1021/acs.chemrev.3c00005
Chem. Rev. 2023, 123, 12795−13208

Table 2. continued

Initial Electrocatalyst	Substrate	Shape of Electrocatalyst	Deposition Type	Specific Loading / $mg \cdot cm^{-2}_{geo}$	η@10 $mA \cdot cm^{-2}_{geo}$ / mV	C_{dl} / $mF \cdot cm^{-2}_{geo}$	TOF / s^{-1} (@η or j)	Tafel Slope / $mV \cdot dec^{-1}$	Electrolyte	Pre-analysis	Post-analysis	Long-Term OER Test Conditions	Post-OER Electrocatalyst	Final Type of Electrocatalyst	Ref.
600 MoC-BN/C	Ni foam	Nanoparticles	P	8	273	46.22	-	53.6	1 M KOH	SEM, XRD, N_2 ISO (BET, PSD)	-	-	-	-	250
700 MoC-BN/C	Ni foam	Nanoparticles	P	8	271	38.84	-	53.3		SEM, XRD, N_2 ISO (BET, PSD)	-	-	-	-	
800 MoC-BN/C	Ni foam	Nanoparticles	P	8	268	36.89	-	50.7		SEM, TEM, XRD, XPS, N_2 ISO (BET, PSD)	SEM, XRD	5.6 h CP (10 $mA \cdot cm^{-2}_{geo}$)	-	-	
CoNi-C/rGO-450	CP	Nanoparticles	P	0.2	364	21.1	-	101.6	1 M KOH	SEM, TEM, HAADF-STEM, EDX, XRD, N_2 ISO (BET, PSD)	-	-	-	-	251
NS-GR/Fe_3C (S1)	GC	Nanoparticles (Fe_3C) encapsulated in CNT	P	-	397	-	-	-	1 M KOH	SEM, XRD, XPS Raman, N_2 ISO (BET, PSD)	-	500 CV cycles (10 $mV \cdot s^{-1}$)	-	-	252
NS-GR/Fe_3C (S2)	GC	Nanoparticles (Fe_3C) encapsulated in CNT	P	-	475	-	-	-		SEM, XRD, Raman	-	-	-	-	
NS-GR/Fe_3C (S3)	GC	Nanoparticles (Fe_3C) encapsulated in CNT	P	-	463	-	-	-		SEM, XRD	-	-	-	-	
NS-GR/Fe_3C (S4)	GC	Nanoparticles (Fe_3C) encapsulated in CNT	P	-	672	-	-	-		SEM, Raman	-	-	-	-	
NS-GR/Fe_3C (S5)	GC	Nanoparticles (Fe_3C) encapsulated in CNT	P	-	643	-	-	-		SEM	-	-	-	-	
NS-GR/Fe_3C (S6)	GC	Nanoparticles (Fe_3C) encapsulated in CNT	P	-	442	-	-	-		SEM, XRD, Raman	-	-	-	-	
NS-GR/Fe_3C (S7)	GC	Nanoparticles (Fe_3C) encapsulated in CNT	P	-	436	-	-	-		SEM, XRD	-	-	-	-	
$Co_6Mo_6C_2$	GC	Nanoparticles ($Co_6Mo_6C_2$)	P	0.306	480	-	-	97.71	1 M KOH	XRD	-	-	-	-	253
$Co_6Mo_6C_2$-NCNT	GC	Nanoparticles ($Co_6Mo_6C_2$) encapsulated in nanotubes (NCNT)	P	0.306	~ 436	-	-	63.48		-	-	-	-	-	
$Co_6Mo_6C_2$@NCNT -700	GC	Nanoparticles ($Co_6Mo_6C_2$) encapsulated in nanotubes (NCNT)	P	0.306	~ 426	-	-	60.03		XRD, XPS, SEM, Raman	-	-	-	-	
$Co_6Mo_6C_2$@NCNT -800	GC	Nanoparticles ($Co_6Mo_6C_2$) encapsulated in nanotubes (NCNT)	P	0.306	360	-	-	48.37		XRD, XPS, SEM, Raman, N_2 ISO (BET, PSD)	-	24 h CA 3000 CV cycles	-	-	
$Co_6Mo_6C_2$@NCNT -900	GC	Nanoparticles ($Co_6Mo_6C_2$) encapsulated in nanotubes (NCNT)	P	0.306	~ 398	-	-	58.01		XRD, XPS, SEM, Raman	-	-	-	-	
Ni/Ni_3C-NCNT 650-2	GC	Nanoparticles (Ni/Ni_3C) encapsulated in nanotubes (NCNT)	P	~ 0.28	277 317 (@20 $mA \cdot cm^{-2}_{geo}$) 382 (@50 $mA \cdot cm^{-2}_{geo}$)	51.6	0.025 at 300 mV	109.3	1 M KOH	SEM, TEM, EM, EDX, XRD, Raman, N_2 ISO (BET), XPS	-	1000 CV cycles 8 h CA (1.5 V_{RHE})	-	-	254
Ni/Ni_3C-NCNT 650-4	GC	Nanoparticles (Ni/Ni_3C) encapsulated in nanotubes (NCNT)	P	~ 0.28	~ 317	15.7	0.021 at 300 mV	136.5		SEM, TEM, XRD, N_2 ISO (BET)	-	-	-	-	
NiO/Ni/Ni_3C-NCNT 600-2	GC	Nanoparticles (NiO/Ni/Ni_3C) encapsulated in nanotubes (NCNT)	P	~ 0.28	~ 338	9.4	0.012 at 300 mV	138.8		SEM, XRD, N_2 ISO (BET)	-	-	-	-	
Mo_2C	GC	-	P	~ 0.18	~ 480 (@2.5 $mA \cdot cm^{-2}_{geo}$)	-	-	-	0.1 M KOH	XRD, Raman, XPS	-	-	-	-	255
Mo_2C (h-TMC)	Ni foam	Nanosheets	P	1	280	155	0.019 at 300 mV	126.9	1 M KOH	XRD, TEM	-	-	-	-	256

https://doi.org/10.1021/acs.chemrev.3c00005
Chem. Rev. 2023, 123, 12795−13208

Table 2. continued

Initial Electrocatalyst	Substrate	Shape of Electrocatalyst	Deposition Type	Specific Loading / $mg \cdot cm^{-2}_{geo}$	η@10 $mA \cdot cm^{-2}_{geo}$ / mV	C_{dl} / $mF \cdot cm^{-2}_{geo}$	TOF / s^{-1} (@η or j)	Tafel Slope / $mV \cdot dec^{-1}$	Electrolyte	Pre-analysis	Post-analysis	Long-Term OER Test Conditions	Post-OER Electrocatalyst	Final Type of Electrocatalyst	Ref.
Mo_2Co_0@N-CNS/CNT	Ni foam	Nanowires	S	0.4	400	-	-	122.4	1 M KOH	XRD, SEM, TEM, ICP, Raman, XPS	-	-	-	-	257
$Mo_2Co_{0.25}$@N-CNS/CNT	Ni foam	Nanosheets/Nanowires	S	0.4	340	-	-	115.7			-	-	-	-	
$Mo_2Co_{0.5}$@N-CNS/CNT	Ni foam	Nanosheets/Nanowires	S	0.4	340	-	-	97.4			-	-	-	-	
Mo_2Co_1@N-CNS/CNT	Ni foam	Nanosheets/Nanowires	S	0.4	300	59.68	-	74.4			SEM	20 h CP (20 $mA \cdot cm^{-2}_{geo}$)	-	-	
Mo_2Co_2@N-CNS/CNT	Ni foam	Nanosheets/Nanowires	S	0.4	310	-	-	90			-	-	-	-	
Mo_0Co_2@N-CNS/CNT	Ni foam	Nanosheets/Nanowires	S	0.4	470	-	-	92.7			-	-	-	-	
Fe_3C@Fe,N,S-GCM	GC	Nanoparticles	P	0.32	327	-	-	253.8	0.1 M KOH	XRD, SEM, TEM, Raman, N_2 ISO (BET), XPS	-	1000 CV cycles	-	-	258
$Ni_3ZnC_{0.7}$/NCNT-550	Ni foam	Nanodots	S	0.8	440	5	-	94	1 M KOH	XRD, SEM, EDX, TEM, XPS, Raman	-	-	-	-	259
$Ni_3ZnC_{0.7}$/NCNT-600	Ni foam	Nanodots	S	0.8	400	12.4	-	91			-	-	-	-	
$Ni_3ZnC_{0.7}$/NCNT-700	Ni foam	Nanodots	S	0.8	380	15	-	89			SEM	24 h CA (1.66 V_{RHE}) 1000 CV cycles	-	-	
$Ni_3ZnC_{0.7}$/NCNT-800	Ni foam	Nanodots	S	0.8	420	8.8	-	117			-	-	-	-	
Co-Ni_3C/Ni@C	GC	Nanoparticles	P	0.2	325	0.134	-	67.76	1 M KOH	XRD, SEM, EDX, TEM, XPS, ICP-AES	-	100000 s CP (10 $mA \cdot cm^{-2}_{geo}$) 1000 CV cycles	-	-	260
Ni_3C/Ni@C	GC	Nanoparticles	P	0.2	350	0.068	-	112.45		XRD, SEM, EDX, TEM, XPS	-	-	-	-	
CoC_x/FeCo@C/rGO	GC	Nanoparticles	P	-	390	-	-	77.1	0.1 M KOH	XRD, SEM, EDX, TEM, XPS, Raman, N_2 ISO (BET)	-	10 h CP (1.6 V_{RHE})	-	-	261
CoC_x@NC	GC	Nanoparticles	P	-	450	-	-	128.3		XRD, SEM, TEM, XPS, Raman	-	10 h CP (1.6 V_{RHE})	-	-	
NiC/MoC/$NiMoO_4$ (30)	Ni foam	Nanorods	S	7.4	280	100.5	-	144	1 M KOH	XRD, SEM, EDX, TEM, HAADF, XPS	-	24 h CA (1.51 V_{RHE}) 1000 CV cycles	-	-	262
Co/WC@NCNSs (800)	GC	Nanosheets	P	0.35	323	9.83	-	75.5	0.1 M KOH	XRD, TGA, N_2 ISO (BET), SEM, TEM, XPS	XRD, SEM	10 h CA (1.54 V_{RHE}) 1000 CV cycles 2000 CV cycles (500 $mV \cdot s^{-1}$, activation)	-	-	263
Co/WC@NCNSs (600)	GC	Nanosheets	P	0.35	495	1.68	-	96.2			-	2000 CV cycles (500 $mV \cdot s^{-1}$, activation)	-	-	
Fe_3C/NCNTs	GC	Nanoparticles	P	0.255	590	-	-	-	0.1 M KOH	XRD, Raman, SEM, TEM, XPS, TGA	-	-	-	-	264
Mn_7C_3/V_8C_7/MnO @MWCNTs (1-900)	GC	Nanoparticles	P	0.3	370	205.8	-	70	0.1 M KOH	XRD, TEM, XPS, ICP-MS	-	12 h CA (1.6 V_{RHE})	-	-	265
					410		-	300	0.5 M H_2SO_4		-	12 h CA (1.64 V_{RHE})	-	-	
GC/Mo_2C	GC	-	P	0.2	~ 1047	-	-	-	0.5 M H_2SO_4	-	-	-	-	-	266
					~ 1070 (@7.5 mA/cm^2_{geo})	-	-	-	1 M KOH	-	-	-	-	-	
Fe_3C/PG	Ni foam	Pomegranate structure	P	0.2	299	-	-	59.5	1 M KOH	XRD, SEM, TEM, SAED, XPS, TGA, N_2 ISO	-	-	-	-	267
					530	1.1	-	-	0.1 M KOH	XRD, SEM, TEM, SAED, XPS, TGA, N_2 ISO	XRD, SEM, TEM	10000 CV cycles 60 h CA	-	-	
Fe_3C/C	Ni foam	Microsized plates	P	-	382	-	-	110.5	1 M KOH	XRD, SEM, N_2 ISO	-	-	-	-	
					591	0.9	-	-	0.1 M KOH	XRD, SEM, N_2 ISO	-	10 h CA	-	-	
Ni/Ni_3C	GC	Nanospheres	P	~ 0.197	350	-	-	57.6	0.1 M KOH	XRD, SEM, TEM, EM, EDX, XPS	XRD, SEM	24 h CA (1.58 V_{RHE}) 2000 CV cycles (100 $mV \cdot s^{-1}$)	-	-	268
Ni/Ni_3C-C	GC	Nanospheres	P	~ 0.197	~ 350	-	-	58.2		XRD, SEM, TEM, EM, EDX, XPS	-	-	-	-	
WC@CFP	CFP	Nanoarray	P	10	-	70.3	-	-	0.5 M H_2SO_4	XRD, SEM	-	-	-	-	269
Co_3C	GC, CC	Nanoparticles	P	0.353	459	-	0.05 at 487 mV	95	0.1 M KOH	XRD, SEM, EDX, TEM, SAED, XPS, N_2 ISO (BET)	-	24 h CP (50 $mA \cdot cm^{-2}_{geo}$)	-	-	270
Co-Mo_2C@NCNT	GC	Nanotubes	P	0.025	377	28.6	-	-	1 M KOH	XRD, SEM, TEM, HAADF-STEM, XPS	-	10 h CP (10 $mA \cdot cm^{-2}_{geo}$)	-	-	271
Mo_2C@NC	GC	Nanotubes	P	0.025	520	1.15	-	-			-		-	-	
Mo_2C@C	GC	Nanoparticles	P	1	365	-	-	84	1 M KOH	XRD, SEM, XPS	-	-	-	-	272
Mo_2C-NSC	GC	-	P	0.425	590	8.39	-	186.2	1 M KOH	XRD, XPS, Raman, N_2 ISO (BET)	-	-	-	-	273
$Ti_3C_2T_x$	GC	Nanosheets	P	~ 0.21	-	0.21	-	227.3	1 M KOH	Raman, N_2 ISO (BET), XRD	-	-	-	-	274
$Ni_{2.6}Mo_{0.39}$@NC (β-Mo_2C, γ-MoC/Ni)	GC	Nanoparticles/Nanosheets	P	~ 0.28	328	-	0.0086 at 400 mV	83.2	1 M KOH	XRD, SEM, TEM, N_2 ISO (BET, PSD), XPS, ICP-AES	-	-	-	-	275
$Ni_{2.6}Mo_{0.26}$@NC (γ-MoC/Ni)	GC	Nanoparticles	P	~ 0.28	310	24.9	0.012 at 400 mV	62.7		XRD, SEM, EDX, TEM, N_2 ISO (BET, PSD), XPS, ICP-AES	-	10 h CA (1.55 V_{RHE}) 1000 CV cycles (100 $mV \cdot s^{-1}$)	-	-	

https://doi.org/10.1021/acs.chemrev.3c00005
Chem. Rev. 2023, 123, 12795−13208

Table 2. continued

Initial Electrocatalyst	Substrate	Shape of Electrocatalyst	Deposition Type	Specific Loading / $mg \cdot cm^{-2}_{geo}$	η@10 $mA \cdot cm^{-2}_{geo}$ / mV	C_{dl} / $mF \cdot cm^{-2}_{geo}$	TOF / s^{-1} (@η or j)	Tafel Slope / $mV \cdot dec^{-1}$	Electrolyte	Pre-analysis	Post-analysis	Long-Term OER Test Conditions	Post-OER Electrocatalyst	Final Type of Electrocatalyst	Ref.
$Ni_{2.8}Mo_{0.13}$@NC (γ-MoC/Ni)	GC	Nanoparticles	P	~ 0.28	332	-	0.0054 at 400 mV	78.8		XRD, SEM, TEM, N_2 ISO (BET, PSD), XPS, ICP-AES	-	-	-	-	275
$Ni_0Mo_{0.26}$@NC (β-Mo_2C)	GC	Nanosheets	P	~ 0.28	-	-	-	-		XRD, SEM, TEM, XPS, ICP-AES	-	-	-	-	
Mo_2C/NCRGO	GC	Microspheres	P	0.143	-	1.4	-	77	1 M KOH	XRD, SEM, TEM, EDX, XPS, Raman, N_2 ISO (BET, PSD)	-	-	-	-	276
Co/Mo_2C/$Co_6Mo_6C_2$/NCRGO (1:1)	GC	Nanoparticles	P	0.143	430	6.7	-	45			-	-	-	-	
$Co_6Mo_6C_2$/NCRGO (2:1)	GC	Nanoparticles	P	0.143	260	42	-	50			-	2000 CV cycles (100 $mV \cdot s^{-1}$, 1.331–1.531 V_{RHE})	-	-	
$Co_6Mo_6C_2$/Co_6Mo_6 C/NCRGO (3:1)	GC	Nanoparticles	P	0.143	400	20	-	58			-	-	-	-	
F-1 : 2.5[620] (θ-Fe_3C)	GC	Microparticles	P	0.57	483	-	-	71	1 M KOH	XRD, TEM, XPS, VSM	-	-	-	-	277
F-1 : 2.5[580] (χ-Fe_5C_2)	GC	Microparticles	P	0.57	494	-	-	59			-	-	-	-	
W-WC_x/C	GC	-	P	~ 0.789	480	-	-	216	0.1 M KOH	XRD	-	-	-	-	278
WC	GC	Nanoparticles	P	~ 0.789	-	-	-	621		-	-	-	-	-	
Co_3ZnC/Co@CN/NG (S-600)	GC	(Encapsulated) Nanoparticles	P	0.344	380	-	-	-	1 M KOH	XRD, SEM, XPS	-	-	-	-	279
Co_3ZnC/Co@CN/NG (S-650)	GC	(Encapsulated) Nanoparticles	P	0.344	366	-	-	81		XRD, SEM, TEM, EDX, XPS, N_2 ISO (BET, PSD), Raman	-	5000 CV cycles (100 $mV \cdot s^{-1}$)	-	-	
Co_3ZnC/Co@CN/NG (S-700)	GC	(Encapsulated) Nanoparticles	P	0.344	410	-	-	-		XRD, SEM, XPS	-	-	-	-	
Co_3ZnC/Co@CN/NG (S-800)	GC	(Encapsulated) Nanoparticles	P	0.344	419	-	-	-		XRD, SEM, XPS	-	-	-	-	
Co-Mo-C/NRGO-1	GC	Nanoparticles	P	0.14	330	16.3	-	42	1 M KOH	XRD, SEM, TEM, EDX, XPS, Raman, N_2 ISO (BET, PSD)	-	2000 CV cycles (1.4–1.6 V_{RHE})	-	-	280
Mo_2C/$Co_6Mo_6C_2$/NRGO	GC	Nanoparticles	P	0.14	360	6.2	-	50		XRD, SEM, TEM, EDX, XPS, BET	-	-	-	-	
Mo_2C/NRGO	GC	Nanoparticles	P	0.14	570	0.4	-	78			-	-	-	-	
Mo_2C-C microspheres (C-5)	GC	Nanoparticles	P	0.4	570	-	-	-	0.1 M KOH	XRD, SEM, EDX, TEM, XPS, TGA, N_2 ISO (BET, PSD), Raman	-	10 h CA (1.775 V_{RHE})	-	-	281
Mo_2C	GC	Nanoparticles	P	0.4	-	-	-	-			-	10 h CA (1.775 V_{RHE})	-	-	
β-Mo_2C (MW)@ MWCNTs	GC	Nanopowder	P	0.24	367	-	-	-	0.1 M KOH	XRD, TGA, N_2 ISO (BET), SEM, TEM, Raman	-	1000 CV cycles (100 $mV \cdot s^{-1}$)	-	-	282
β-Mo_2C (AM)	GC	Nanopowder	P	0.24	437	-	-	-			-		-	-	
β-Mo_2C (SF)	GC	Nanopowder	P	0.24	496	-	-	-			-		-	-	
β-Mo_2C (DC)	GC	Nanopowder	P	0.24	634	-	-	-			-		-	-	
Fe_3C@NG	GC	Nanoparticles	P	0.204	361	-	-	62	0.1 M KOH	XRD, SEM, EDX, TEM, TGA, Raman, N_2 ISO (BET, PSD), XPS	-	20 h CA (1.59 V_{RHE})	-	-	283

[a]Some values (i.e., "specific loading", "η", and "C_{dl}") were calculated or obtained from the descriptions and figures in the previous papers. "Post-OER Electrocatalyst" and "Final Type of Electrocatalyst" were determined based on the experimental results and descriptions provided in the previous papers. [b]η, overpotential; j, current density; C_{dl}, double layer capacitance; TOF, turnover frequency; P, powder-coated electrode; S, self-supported electrode; CV, cyclic voltammetry; CAc chronoamperometry; CP, chronopotentiometry; OWS, Overall water splitting. [c]Substrate abbreviations: GC (glassy carbon); CC (carbon cloth); PAN (polyacrylonitrile); CNF (carbon nanofiber). [d]Electrolyte abbreviation: PBS (phosphate buffer solution). [e]Analysis abbreviations (minor terms only): ISO (isotherm); PSD (pore size distribution); CAM (contact angle measurement); VSM (vibrating sample magnetometry); TPD (temperature programmed desorption analysis); PZC (point of zero charge measurement); DSC (differential scanning calorimetry); TDR (temperature-dependent resistance measurement); EFM (electrical behaviors measurement).

https://doi.org/10.1021/acs.chemrev.3c00005
Chem. Rev. 2023, 123, 12795−13208

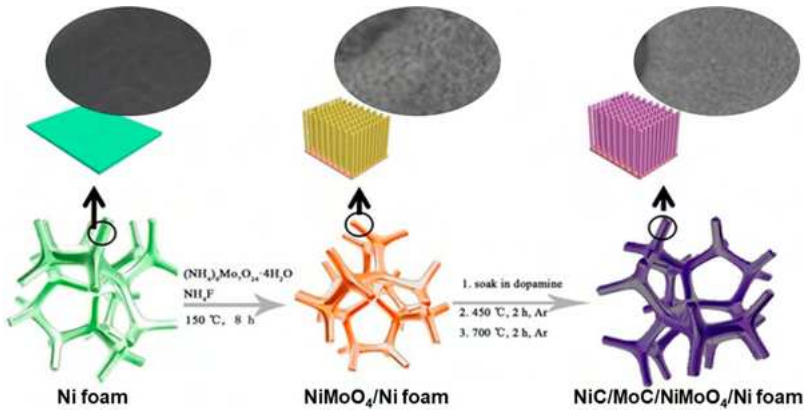


Figure 38. Schematic illustration for the fabrication of NiC/MoC/$NiMoO_4$ heterostructured nanorod arrays on Ni foam through (a, left) hydrothermal and (b, right) annealing processes. Reprinted with permission from ref 262. Copyright 2019 Wiley.

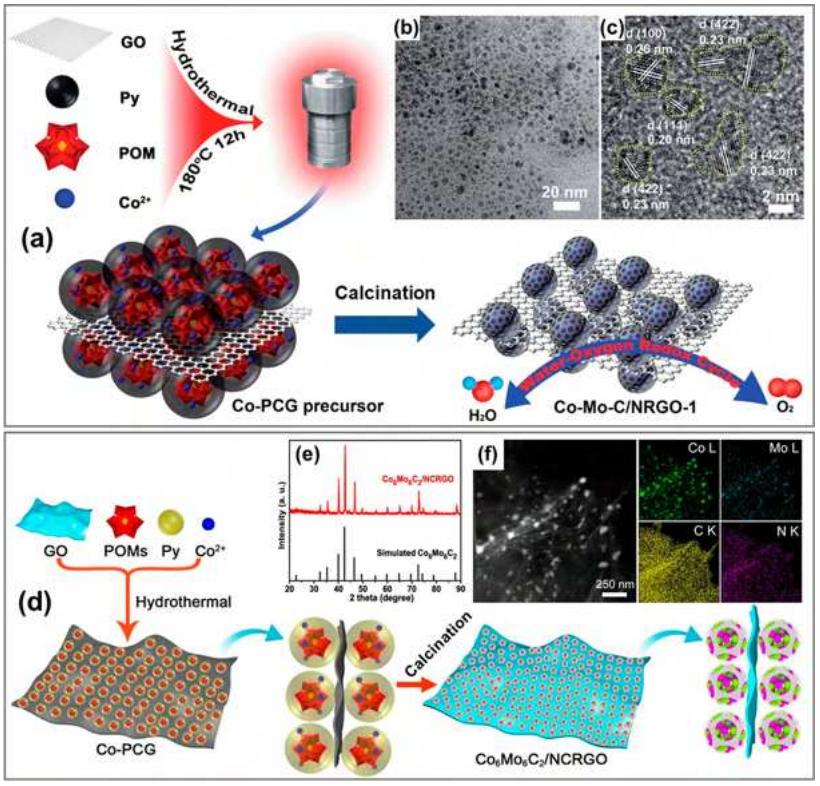


Figure 39. Hydrothermal synthesis and subsequent calcination procedures to form transition metal carbides. (a) Schematic illustration for the preparation of the composite of metal Co, $Co_6Mo_6C_2$, and Mo_2C anchored within N-doped porous carbon on N-doped RGO sheets (Co−Mo−C/NRGO-1). (b) TEM and (c) HRTEM images of Co−Mo−C/NRGO-1 composite. Reprinted with permission from ref 280. Copyright 2016 Royal Society of Chemistry. (d) Schematic illustration for the synthesis process of the composite of $Co_6Mo_6C_2$ coated by N-doped porous carbon on N-doped RGO film ($Co_6Mo_6C_2$/NCRGO). (e) XRD pattern and (f) EDX mapping analysis of $Co_6Mo_6C_2$/NCRGO composite. Reprinted with permission from ref 276. Copyright 2017 American Chemical Society.

groups as linkers and transition metals (Zn, Co) as metallic nodes.[279] Figure 40g shows the SEM image of the $Zn_3[Co(CN)_6]_2$ MOF, which possessed a sphere-like shape with a relatively rough surface (mean diameter: ∼900 nm). The Co_3ZnC/Co nano-heterojunctions in N-doped graphene layers were obtained through the thermal decomposition of the MOF precursor at 650 °C for 4 h under N_2. As seen in Figure 40h, the as-annealed sample inherited the spherical shape of the MOF precursor. TEM analysis revealed that each large sphere was composed of small Co_3ZnC and Co composite particles (diameter: ∼10−30 nm) coated with graphene layers with a thickness of about 3−5 layers (see Figures 40i and j).

Interestingly, Zhu *et al.* reported the synthesis of Co-doped *β*-molybdenum carbide encapsulated by an N-doped carbon framework with different Co doping levels (sample names: Co_n-*β*-Mo_2C@NC, n = 0.05, 0.1, and 0.2) by using a zeolitic imidazolate framework (ZIF-8) with various Co/Zn molar ratios (Co/Zn = 0.05, 0.1, and 0.2). The ZIF precursors were synthesized by mixing $Zn(NO_3)_2$, $Co(NO_3)_2$, and 2-methylimidazole in methanol for 24 h. Then the *N*,*N*-dimethylformamide (DMF) solution of $MoO_2(acac)_2$ (molybdenum

https://doi.org/10.1021/acs.chemrev.3c00005
Chem. Rev. 2023, 123, 12795−13208

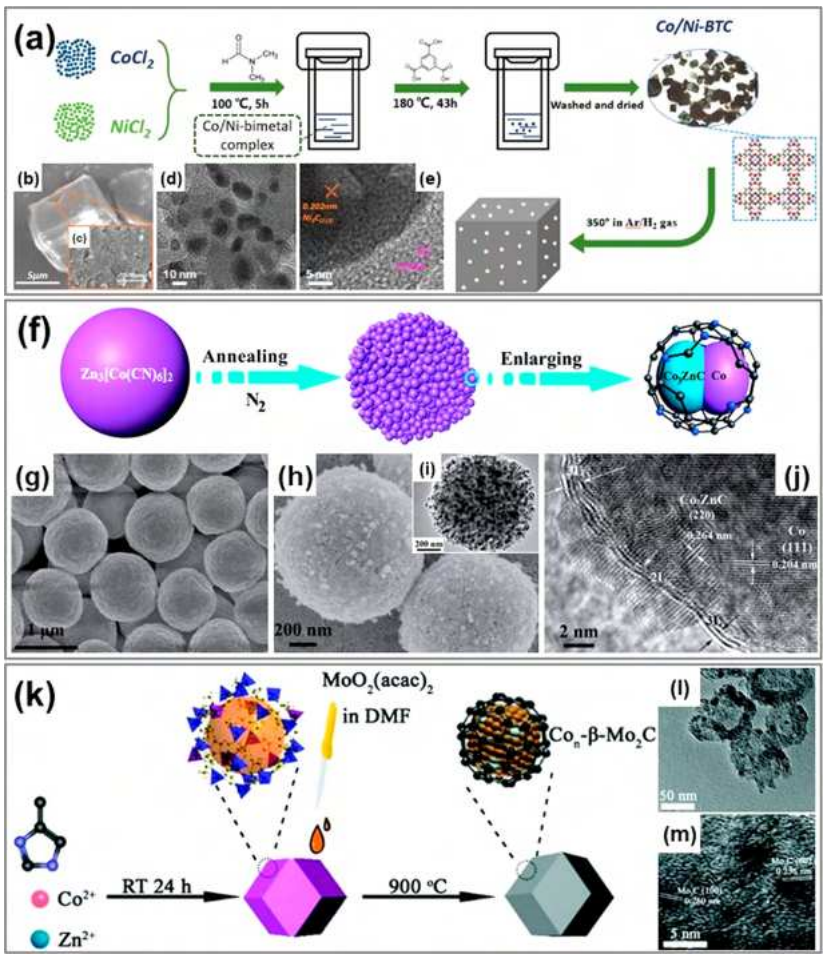


Figure 40. Solvothermal synthesis and subsequent carburization procedures to form transition metal carbides. (a) Schematic illustration for the synthesis of cobalt-doped Ni_3C/Ni dispersed in a graphitic carbon matrix (sample name: Co/Ni-350). (b, c) SEM and (d, e) TEM images of the Co/Ni-350 sample. Reprinted with permission from ref 260. Copyright 2019 Elsevier. (f) Schematic illustration for the preparation process of Co_3ZnC/Co nanoparticles encapsulated in N-doped graphene layers (sample name: S-650). (g) SEM image of the spherical $Zn_3[Co(CN)_6]_2$ MOF precursor. (h) SEM, (i) TEM, and (j) HRTEM images of the S-650 sample. Reprinted with permission from ref 279. Copyright 2016 Royal Society of Chemistry. (k) Schematic illustration of Co-doped β-Mo_2C encapsulated by an N-doped carbon framework ($Co_{0.1}$-β-Mo_2C@NC). (l) TEM and (m) HRTEM images of the $Co_{0.1}$-β-Mo_2C@NC. Reprinted with permission from ref 226. Copyright 2019 Royal Society of Chemistry.

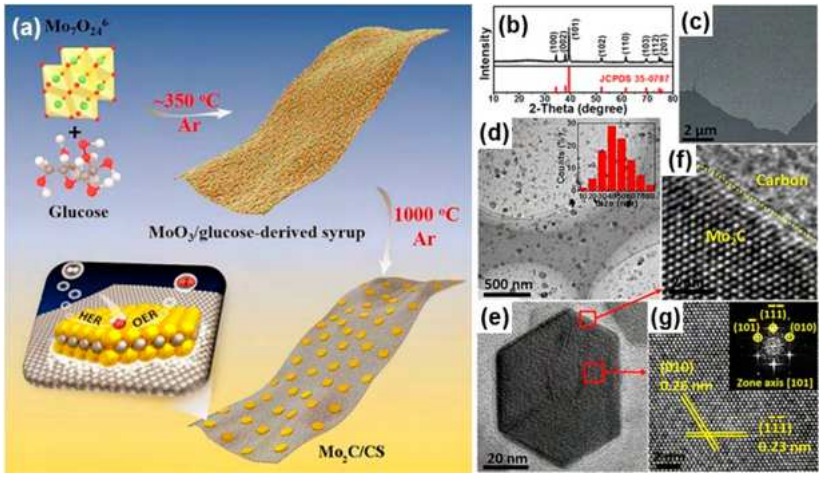


Figure 41. (a) Schematic illustration for the preparation process of Mo_2C nanoparticles coupled on carbon sheets (Mo_2C/CS). (b) XRD pattern and (c) SEM, (d, e) TEM, and (f) HRTEM images of the Mo_2C/CS. Inset of (d) indicates the size distribution of the Mo_2C nanoparticles on carbon sheets. (g) HRTEM image of the Mo_2C nanoparticle and inset showing the corresponding Fourier transform pattern. Reprinted with permission from ref 237. Copyright 2017 Wiley.

https://doi.org/10.1021/acs.chemrev.3c00005
Chem. Rev. 2023, 123, 12795−13208

source) was inhaled thoroughly into the as-prepared ZIFs. The as-prepared precursors were calcinated at 900 °C for 3 h under N_2, resulting in the Co_n-β-Mo_2C@NC samples (see Figure 40k). Figure 40l shows the TEM image of the $Co_{0.1}$-β-Mo_2C@NC as a representative sample. In the as-obtained sample, Co-doped β-Mo_2C nanoparticles were embedded in a carbonized polyhedron. In the HRTEM image (Figure 40m), the lattice fringes can be observed, and their spacings of 0.236 and 0.260 nm are assigned to the (002) and (100) planes of β-Mo_2C.

3.1.3. Solid-State/Gas-Solid Reactions. The solid-state reaction generally consists of a two-step process: (i) preparation of the solid mixture/precursor material from starting materials (i.e., transition metal and carbon sources) via the dry-/wet-mixing method and (ii) an annealing process at relatively high temperature for the carburization of the as-prepared solid mixture/precursor (refs 225, 230, 234, 236, 237, 256, 258, 264, 265, 272, 273, 275,282, and 283). The solid-state reaction is differentiated from the hydrothermal method in that the solid mixture/precursor for the following solid-state reaction is prepared by simply mixing the solid starting materials[230,236,237,282] or drying the mixture of transition metal and carbon sources in the solvent (refs 225, 234, 256, 258, 264, 265, 272, 273, 275, 282, and 283), while the hydrothermal method requires a relatively long-term annealing process to prepare the precursor materials. Wang *et al.* prepared crystalline Mo_2C nanoparticles coupled on carbon sheets (Mo_2C/CS) through the dry mixing of ammonium molybdate (molybdenum source) and glucose (carbon source) and the subsequent heat treatment of the as-prepared solid mixture at 1000 °C for 3 h under Ar.[237] As shown in Figure 41a, the authors provided the synthetic reaction progress based on the results of a TGA analysis. The dehydration and decomposition of glucose happen from 200 to 300 °C, and its further carbonization results in the formation of carbon sheets. Meanwhile, the decomposition of ammonium molybdate into MoO_3 proceeds over the temperature range of 100−350 °C, and its sublimation occurs at over 750 °C. In the heated mixture of ammonium molybdate and glucose, the thermally formed MoO_3 is dispersed in a glucose-polymerized lamellar syrup. At higher temperatures, both the carbonization of the syrup into carbon sheets and the carbon species-driven carburization of the MoO_3 into Mo_2C proceed at the same time. Note that glucose acts as the precursor for carbon sheets and the carbon source for the formation of Mo_2C. Figure 41b shows the XRD pattern of the Mo_2C/CS, which confirms the formation of hexagonal Mo_2C. As seen in Figures 41c and d, numerous Mo_2C nanoparticles (main size: 30−60 nm) were anchored evenly on carbon sheets. Additionally, each Mo_2C nanoparticle possessed a hexagonal shape (see Figure 41e). The HRTEM images of Mo_2C/CS further revealed that the Mo_2C nanoparticle is strongly coupled with the carbon sheet (Figure 41f) and has a single-crystalline nature (Figure 41g).

Jiang *et al.* prepared a homogeneous mixture of urea, glucose, and metal salts (i.e., $Fe(NO_3)_3{\cdot}6H_2O$), which was prepared by stirring in ultrapure water and simultaneously drying at 80 °C, and simply annealed the as-prepared solid mixture at relatively high temperatures (700, 800, and 900 °C) in an Ar atmosphere to synthesize the porous Fe-N-doped graphene-like carbon hybrids with Fe_3C nanoparticles encapsulated in graphitic layers (Fe_3C@NG) (see Figure 42a).[283] The TEM image in Figure 42b shows that Fe_3C nanoparticles are uniformly loaded on thin carbon sheets and have an average size of 11.1 nm with a narrow distribution.

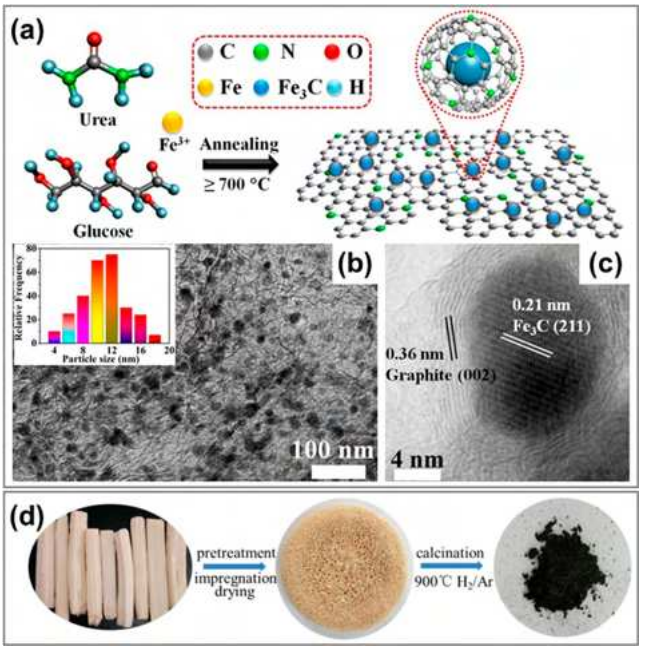


Figure 42. Solid-state synthesis of transition metal carbides. (a) Schematic illustration for the fabrication of porous Fe-N-doped graphene-like carbon hybrids with Fe_3C nanoparticles encapsulated in graphitic layers (Fe_3C@NG). (b) TEM and (c) HRTEM images of Fe_3C@NG800-0.2. The inset of (b) is the corresponding particle size distribution histogram. Reprinted with permission from ref 283. Copyright 2015 American Chemical Society. (d) Schematic illustration for the preparation of Mo_2C in carbon nanosheets using cornstalks as the carbon source. Reprinted with permission from ref 225. Copyright 2019 Elsevier.

The HRTEM image in Figure 42c displays the well-defined crystalline lattice spacing of 0.21 and 0.36 nm, which matches well with the (211) planes of a cubic Fe_3C phase and the (002) planes of a graphite phase, respectively. This HRTEM result indicates that these Fe_3C nanoparticles are surrounded by a few graphitic carbon layers. Xing *et al.* prepared the solid precursor for the solid-state reaction by drying the mixture of carbon and metal sources in solvent and synthesized Mo_2C nanoparticles uniformly embedded into the carbon matrix via solid-state reaction.[225] As shown in Figure 42d, pristine cornstalk, which is the carbon source, was pretreated with acid, freeze-dried, soaked into ammonium molybdate solution, and freeze-dried again. Subsequently, the as-obtained solid precursor mixture was carbonized at 900 °C for 3 h under H_2/Ar (5/95 vol %).

Additionally, transition metal carbides can be simply synthesized via gas-solid reaction at high temperature by using as-purchased chemicals or prepared solid metal oxide precursors as the metal source and carbonaceous gases (e.g., CH_4, C_2H_6, and CO) as the carbon source. For example, Kim *et al.* synthesized Mo_2C nanoparticles from the heat treatment of $(NH_4)_2MoO_4$ at 800 °C for 1 h under H_2/CH_4 (80/20 vol %) gas.[230] However, it is to be noted that there is a security risk of using flammable and explosive carbonaceous gases at high temperatures. Also, the resultant transition metal carbides from the gas-solid reaction could be contaminated by chars that could block the pores and even cover the active sites of the transition metal carbide electrocatalysts.[225]

3.1.4. Other Methods. Transition metal carbides can also be prepared with other synthetic techniques such as electro-

https://doi.org/10.1021/acs.chemrev.3c00005
Chem. Rev. 2023, 123, 12795−13208

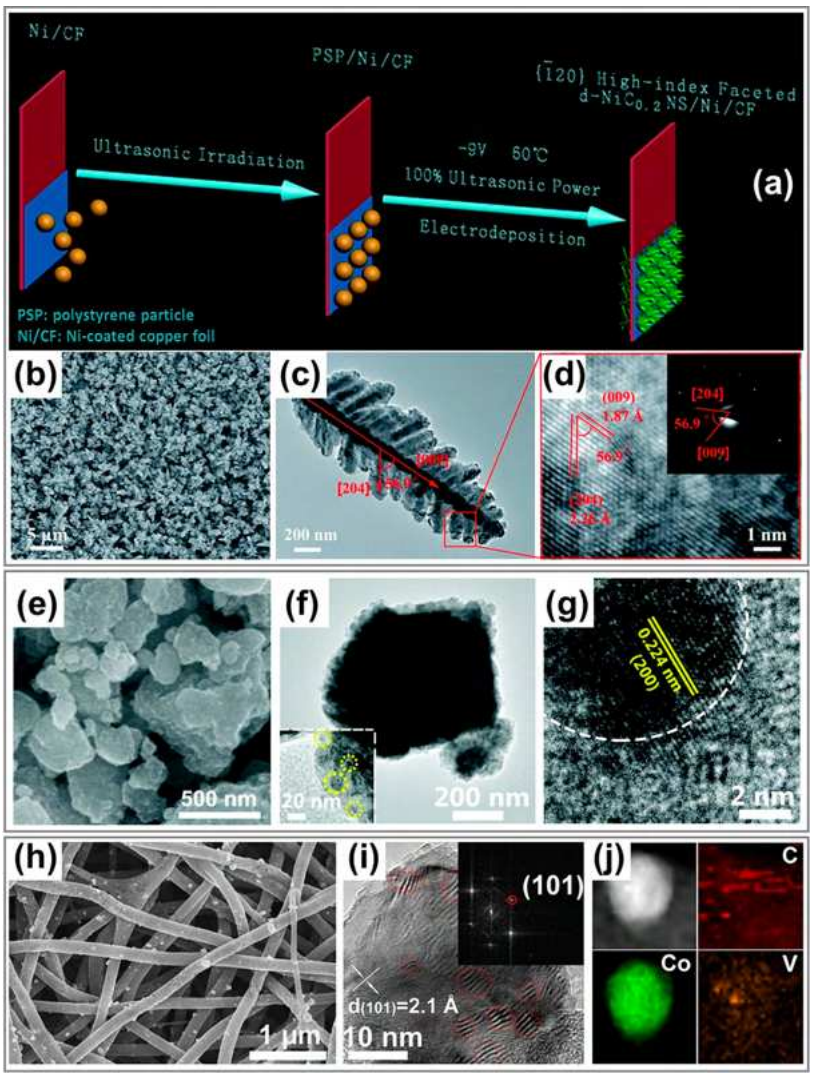


Figure 43. (a) Schematic illustration for the electrodeposition of {$\bar{1}$20} high-index faceted dendritic hexagonal NiC_x nanosheets on Ni-coated Cu foil (d-$NiC_{0.2}$NS/Ni/CF). (b) Top-view SEM image of the d-$NiC_{0.2}$NS/Ni/CF. (c) TEM and (d) HRTEM images of the d-$NiC_{0.2}$NS. The inset of (d) shows the corresponding SAED pattern. Reprinted with permission from ref 217. Copyright 2016 Royal Society of Chemistry. (e) SEM, (f) TEM, and (g) HRTEM images of Co_3C particles prepared by the ball-milling method. The inset of (f) is a partially enlarged image. Reprinted with permission from ref 270. Copyright 2019 Royal Society of Chemistry. (h) FESEM, (i) HRTEM, and (j) STEM-EDX elemental mapping images of $V_{0.28}Co_{2.72}C$ nanocrystals anchored on electrospun carbon nanofibers ($V_{0.28}Co_{2.72}C$/CNFs). The inset of (i) indicates the corresponding FFT pattern. Reprinted with permission from ref 227. Copyright 2019 American Chemical Society.

deposition,[217] ball milling,[270] electrospinning,[227] the solvothermal method,[254] the salt-template method,[267] the solution-based method (wet-chemistry),[91,239] the flux method (molten salt method),[282] and so forth. Herein, we introduce some unique synthetic approaches using them. Yang *et al.* fabricated {$\bar{1}$20} high-index faceted dendritic hexagonal NiC_x nanosheets on Ni-coated Cu foil (d-$NiC_{0.2}$NS/Ni/CF) via electrodeposition under ultrasound assistance (see Figure 43a).[217] The electrodeposition was performed using a three-electrode electrochemical cell [working electrode (cathode), Ni-coated Cu foil; counter electrode (anode), Pt plate; reference electrode, Ag/AgCl (sat. KCl)] in an aqueous electrolyte under ultrasonic irradiation at 60 °C. In the electrolyte, $NiSO_4 \cdot 6H_2O$ (nickel source), H_3BO_3, and NaCl were dissolved, and polystyrene particles (carbon source) were dispersed. To proceed with the deposition, the authors applied a potential of −9 $V_{Ag/AgCl}$. During the electrodeposition, ultrasound induced intimate contact between the polystyrene particles and the Ni-coated Cu foil. Importantly, ultrasound also caused high-energy transient cavitation and localized hot spots (transient temperatures: ∼5000 K; pressures: ∼1800 atm; cooling rates: $>10^{10}$ $K \cdot s^{-1}$)[290] on the cathode surface. The ohmic heating of the cathode surface was simultaneously generated by elevated cathodic current density. This applied heating and pressurizing converted the carbonized polystyrene particles into carbon-ion species. The as-generated carbon ions reacted with Ni^{2+} cations in the electrolyte, forming d-$NiC_{0.2}$NS. As shown in Figure 43b, the d-$NiC_{0.2}$NS was grown vertically and evenly over the Ni/CF substrate surface. TEM analysis revealed that the d-$NiC_{0.2}$NS had a dendritic nanosheet shape and the dendritic nanosheet exhibited two distinct growth directions (i.e., [204] and [009]) with an angle of 56.9° between each other (Figure 43c). HRTEM images further confirmed that the interplanar spacings of 2.26 and 1.87 Å correspond to the hexagonal NiC_x (204) and (009) planes, respectively (Figure 43d). The corresponding SAED pattern indicates the single-

https://doi.org/10.1021/acs.chemrev.3c00005
Chem. Rev. 2023, 123, 12795−13208

crystalline nature of the d-$NiC_{0.2}$NS. Accordingly, these results found that the exposed facets of the d-$NiC_{0.2}$NS are hexagonal NiC_x {$\bar{1}$20}. Ma *et al.* prepared Co_3C particles through a simple ball-milling method.[270] To be specific, cobalt powder and active carbon (Co/C molar ratio = 1:1) were mixed and then ball-milled at a rotation speed of 900 rpm·min^{-1} for 10 h under a bowl pressure of 95 kPa. According to the XRD results, the as-prepared sample can be assignable to orthorhombic Co_3C. SEM observations revealed that the Co_3C samples were irregular particles (diameter: 20−600 nm) having rough surfaces (Figure 43e). Figure 43f shows the TEM image of the Co_3C particle. The enlarged TEM image (inset of Figure 43f) shows that the Co_3C particle is composed of numerous smaller particles (diameter: <20 nm). In the HRTEM image (Figure 43g), an interplanar spacing of 0.224 nm was observed, which corresponds to the (200) planes of the orthorhombic Co_3C phase. The SAED pattern also confirmed the diffraction ring derived from Co_3C (210), which implies the polycrystalline nature of the product. Zhang *et al.* reported the combination of electrospinning and high-temperature annealing to synthesize V-substituted cobalt carbide ($V_xCo_{3-x}C$, $0 \leq x \leq 0.80$) anchored on carbon nanofibers (CNFs).[227] First, cobalt chloride and vanadium acetylacetonate were dissolved into a polyacrylonitrile/dimethylformamide (PAN/DMF) solution. The as-prepared mixture solution was electrospun into a CoV salt/PAN nanofiber membrane (precursor). Subsequently, the precursor membrane was pre-oxidized at 230 °C for 3 h under air and annealed at 800 °C for 3 h under Ar, in which the $V_xCo_{3-x}C$ nanocrystals were *in situ* formed in the electrospun CNFs. As shown in Figure 43h, $V_{0.80}Co_{2.20}C$ nanocrystals (representative sample) were homogeneously formed on the CNFs with a nanofiber diameter of ∼200 nm. The HRTEM image in Figure 43i indicates the crystalline nature of the $V_{0.80}Co_{2.20}C$ nanoparticles. Furthermore, STEM-EDX elemental mapping analysis confirmed vanadium signals throughout the nanoparticle (see Figure 43j), indicating homogeneous vanadium substitution.

3.2. Final Types of Carbide-Based Electrocatalysts

As shown in Figure 44, there are two types of transition metal carbide electrocatalysts: a "catalyst" (Figure 44a) and a

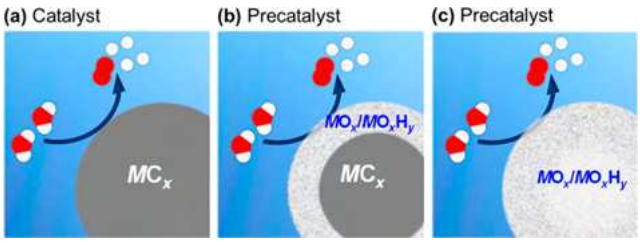


Figure 44. Schematic illustrations of suggested final types of transition metal carbide-based electrocatalysts after long-term OER testing.

"precatalyst" (Figures 44b and c). According to Table 2, however, most of the reports have concluded that transition metal carbides act as a "precatalyst" that undergoes partial/full oxidation and, thereby, significant transformation of their material properties (e.g., transition metal carbide → its oxide counterpart such as MO_x/MO_xH_y) during the OER. It is to be noted that there is no report that oxidized carbon species (e.g., CO_3^{2-}) decomposed from transition metal carbide are present in the *in situ* formed MO_x/MO_xH_y layer. Herein, we review several case studies of transition metal carbide "catalysts" and "precatalysts" with an emphasis on post-OER material characterization, which will help to better understand the electrochemical behavior of the transition metal carbides.

3.2.1. Catalysts. Based on the post-OER characterization results, a few studies (i.e., $NiC_{0.2}$,[217] Fe_3C,[216] MnO functionalized Fe_3C@N-doped carbon,[214] and CoO_x@α-MoC/N-doped carbon[215]) have concluded that a transition metal carbide is a "catalyst" that is stable during the OER without any noticeable oxidation. For example, Yang *et al.* reported dendritic hexagonal NiC_x nanosheets, that have {$\bar{1}$20} as exposed facets, electrodeposited on Ni-coated Cu foil (d-$NiC_{0.2}$NS/Ni/CF) (see Figures 45a–d). To examine the

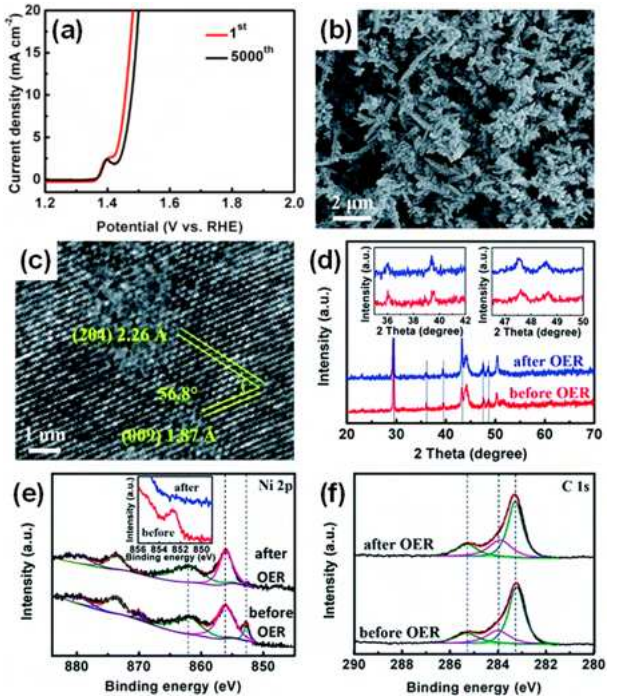


Figure 45. (a) LSV curves of {$\bar{1}$20} high-index faceted dendritic hexagonal NiC_x nanosheets on Ni-coated Cu foil (d-$NiC_{0.2}$NS/Ni/CF) before and after 5000 CV cycles for the OER. (b) SEM and (c) HRTEM images of d-$NiC_{0.2}$NS/Ni/CF after the OER test. (d) XRD patterns and (e) Ni 2p and (f) C 1s XPS spectra of d-$NiC_{0.2}$NS/Ni/CF before and after the OER test. In the XRD patterns, the diffraction peaks at 29.4, 36.2, 39.9, 43.2, 47.7, and 48.6° can be indexed to hexagonal NiC_x. The diffraction peaks at 44.5, 51.8, and 76.4° are assignable to metallic Ni (from the Ni/CF substrate). Reprinted with permission from ref 217. Copyright 2016 Royal Society of Chemistry.

electrochemical stability of d-$NiC_{0.2}$NS/Ni/CF, it was tested by 100 h CP and 5000 CV cycles in 1 M KOH. During the 100 h CP test, the d-$NiC_{0.2}$NS/Ni/CF exhibited stable activity for the OER. As shown in Figure 45a, the post-OER d-$NiC_{0.2}$NS/Ni/CF electrode also showed an LSV curve which is similar to the pre-OER electrode. After a 100 h CP test, SEM, TEM, XRD, and XPS analyses of the d-$NiC_{0.2}$NS/Ni/CF electrode were conducted to further investigate its physical and chemical stability (Figure 45b), from which the authors concluded that the morphology, crystal structure, and chemical composition of the post-OER d-$NiC_{0.2}$NS/Ni/CF were almost identical to the pre-OER ones. However, in the XRD patterns and XPS spectra, increases in the relative peak intensities of NiC_x versus metallic Ni were observed after the OER test. The authors

https://doi.org/10.1021/acs.chemrev.3c00005
Chem. Rev. 2023, 123, 12795−13208

mentioned that these phenomena result from the conversion of metallic Ni (from the Ni/CF substrate surface) into $Ni(OH)_2$ or NiOOH during the OER test. More specifically, the Ni 2p XPS peak (at 852.8 eV) corresponding to metallic Ni diminished after the OER test, which is due to the above conversion. Accordingly, the authors claimed that the d-$NiC_{0.2}$NS/Ni/CF could present superior stability for the OER.

Another example was discussed by Zhu *et al.*[216] The authors grew a nanosheet-like structure of Fe_3C on Ni foam (Fe_3C/NF) and performed its material characterizations before and after the OER in 1 M KOH to confirm whether Fe_3C/Ni was stable or not. The SEM images before and after the OER showed that the morphology of Fe_3C/Ni was well preserved during the OER (Figures 46a and b). The pre- and post-OER

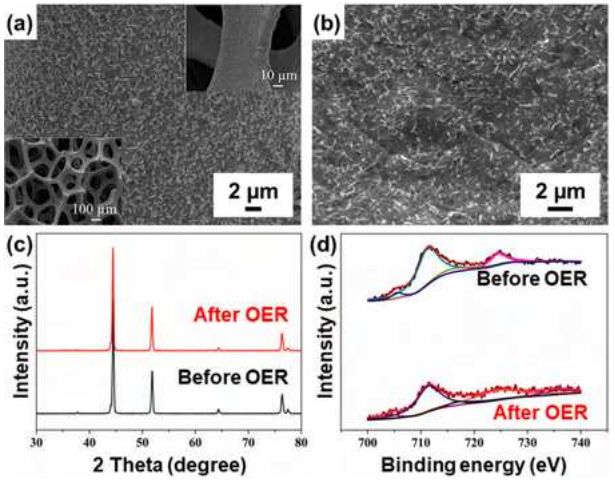


Figure 46. (a, b) FESEM images of Fe_3C/NF (a) before and (b) after OER testing. (c) XRD patterns and (d) Fe 2p XPS spectra of Fe_3C/NF before and after OER testing. Reproduced with permission from ref 216. Copyright 2019 Elsevier.

XRD patterns in Figure 46c indicate that the bulk crystal structure of Fe_3C was well maintained after the OER. Moreover, it was argued that the Fe 2p XPS spectra for Fe_3C before and after the OER exhibited no discernible changes, implying that the active substance for the OER is still Fe_3C after the OER (Figure 46d). Similarly, Zhang *et al.* also studied Fe_3C nanoparticles encapsulated in 3D porous graphite frameworks (Fe_3C/PG) for long-term OER testing (10000 CV cycles in 0.1 M KOH).[267] Based on the post-OER XRD, SEM, and TEM results, the authors concluded that the Fe_3C/PG electrode possessed excellent stability for the OER.[267] However, because of the lack of the post-OER surface analysis, we classify the Fe_3C/PG as "unknown" in Table 2.

3.2.2. Precatalysts. Investigations into the pre- and post-OER material properties of transition metal carbide precatalysts have been conducted using various material characterization techniques (e.g., XRD, SEM, EDX, HRTEM, XPS, EXAFS, XANES, etc.). According to previous studies, transition metal carbide precatalysts undergo different degrees of *in situ* oxidation (i.e., partial oxidation and full oxidation) depending on their compositions and morphologies (e.g., grain size, pore size, porosity, etc.). To be specific, partial oxidation brings about a core@shell structure (transition metal carbide core@oxide shell) or the composite of transition metal carbide and oxide, while full oxidation results in the complete transformation of a transition metal carbide to its oxide counterpart.

As indicated in Table 2, several monometallic carbides such as Ni_3C,[239] Co_3C,[91] Fe_3C,[238] and MoC_2[225,237] exhibited the transformation (i.e., oxidation) during the OER process. Xu *et al.* synthesized the composite of crystalline Ni_3C nanoparticles (size: 20−50 nm) and conductive carbon (Ni_3C/C, see Figure 47a) and performed a long-term OER test in alkaline media (1 M KOH).[239] To examine its transformation during the OER, the Ni_3C/C was characterized after the OER (Figures 47b−d). Figure 47b shows the Ni K-edge Fourier transform-EXAFS spectra of the Ni_3C/C before and after the OER test. In the pre-OER EXAFS spectrum, the first and second peaks at around 1.7 and 2.54 Å correspond to the Ni−C and Ni−Ni bonds, respectively. For the post-OER EXAFS spectrum, the phase shift to higher R in the first peak position and the decrease in the second peak intensity (Ni−Ni) with its slight position change were confirmed, which implies that the surface Ni atoms of the Ni_3C/C might be oxidized during the OER. In the XANES spectra, a strong pre-edge peak, which is a typical nickel alloy feature, was found before the OER, whereas this

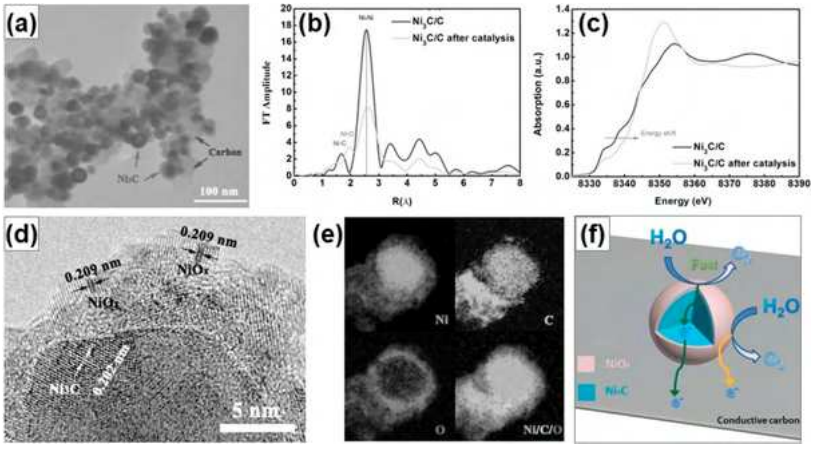


Figure 47. (a) TEM image of the composite of metallic Ni_3C nanoparticles and conductive carbon (Ni_3C/C). (b) Ni K-edge Fourier transform-EXAFS and (c) XANES spectra of the Ni_3C/C composite before and after 1000 cycles of OER electrocatalysis. (d) HRTEM and (e) corresponding EELS elemental mapping images of the Ni_3C/C composite after 1000 cycles of OER electrocatalysis. (f) Schematic illustration for the electron transportation in the Ni_3C/C composite during the OER. Reproduced with permission from ref 239. Copyright 2016 Wiley.

https://doi.org/10.1021/acs.chemrev.3c00005
Chem. Rev. 2023, 123, 12795−13208

peak was weakened, and the rising edge shifted toward higher energy after the OER. These phenomena also suggested the surface oxidation of the Ni_3C/C after the OER test. The post-OER HRTEM image also showed the *in situ* formation of a nickel oxide/hydroxide layer over the Ni_3C surface while the core of the Ni_3C nanoparticle was preserved from oxidation (Figure 47d). Furthermore, as indicated in Figure 47e, the post-OER EELS elemental mapping images clearly demonstrated the $Ni_3C@NiO_x$ core@shell structure. According to these characterization results, the authors provided the conclusion that real OER active $NiO_x/Ni_3C/C$ heterostructures are eventually OER effective species (see Figure 47f). Additionally, note that the *in situ*-formed NiO_x layer can become an electroactive species as well as protect the Ni_3C core from further oxidation during the OER.

Kim *et al.* prepared crystalline Co_3C nanoparticles and studied their complete oxidation into amorphous Co oxide nanoparticles during the OER in 1 M NaOH.[91] Figure 48a illustrates the gradual transformation of Co_3C into a $Co_3C@CoO_x$ core@shell structure and completely amorphous CoO_x nanoparticles with the proceeding electrochemical sweep. This gradual transformation process of a Co_3C precatalyst during the OER was demonstrated by post-OER characterizations using XPS and TEM analyses. As shown in Figures 48b and c,

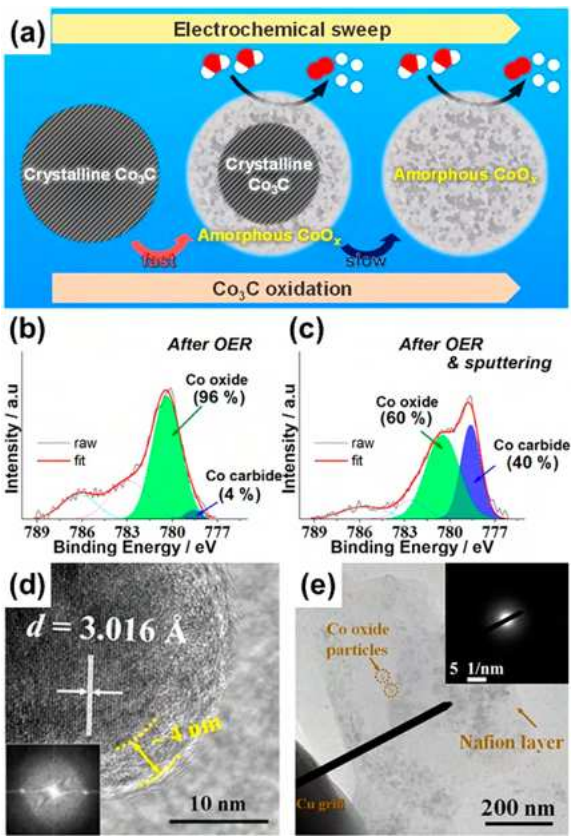


Figure 48. (a) Schematic illustration of Co_3C oxidation during OER testing. (b, c) Co $2p_{3/2}$ XPS spectra of Co_3C after OER testing (after two LSV sweeps) (b) on the surface and (c) with Ar^+ sputtering for 10 s at a rate of 0.5 nm·s^{-1}. (d) HRTEM image of Co_3C after two sweeps of the OER. The inset of (d) shows its corresponding FFT pattern. (e) Bright-field TEM image of Co_3C after 350 sweeps of the OER. The inset of (e) shows its corresponding SAED pattern. Reprinted with permission from ref 91. Copyright 2018 American Chemical Society.

the XPS spectra of the Co $2p_{1/2}$ region for Co_3C was analyzed with and without Ar^+ sputtering after two sweeps of LSV in the OER potential region. The area of the peak for Co_3C significantly increased from 4% on the surface (without Ar^+ sputtering) to 40% in the bulk (with Ar^+ sputtering), while that of the CoO_x peak decreased from 96% on the surface (without Ar^+ sputtering) to 60% in the bulk (with Ar^+ sputtering). Moreover, the HRTEM image of Co_3C after two LSV sweeps in Figure 48d exhibits the lattice fringe of 3.016 Å corresponding to the (111) plane for Co_3C in the core part of the particle and the amorphous structure with a thickness of ~4 nm on the outer surface, supporting the core@shell structure of $Co_3C@CoO_x$ after two LSV sweeps. Furthermore, the TEM image and SAED pattern in Figure 48e show the full oxidation of a Co_3C particle into an amorphous CoO_x particle after 350 LSV sweeps for the OER. These results indicate that cobalt carbide is a precatalyst that is intrinsically unstable in the water oxidizing condition during OER testing.

Bimetallic carbides also experience similar oxidation during the OER process (see Table 2). For instance, Wang *et al.* studied the partial oxidation of bimetallic carbide $Ni_3Zn_{0.7}C$ during the OER in 1 M KOH by conducting post-OER material characterization.[233] As shown in Figure 49a, the XRD results of $Ni_3ZnC_{0.7}$-550 before and after OER testing were identical, indicating that the crystal structure of $Ni_3ZnC_{0.7}$-550 was well maintained without significant composition and structure changes during the OER test. XPS results for $Ni_3ZnC_{0.7}$-550 before and after the OER display that the peak intensity for the Ni^{2+} state increased after the OER test (Figures 49b and c). This implies that metal oxide or hydroxide, which is hard to be detected by XRD analysis, is formed on the surface. These post-OER characterizations indicate that the crystalline $Ni_3ZnC_{0.7}$ remains in the core even after the OER test and that the partial oxidation of $Ni_3ZnC_{0.7}$ occurs only on its surface during the OER.

Precatalytic transformation of a transition metal carbide during OER testing may not only undergo simple oxidation but could also undergo complicated, chemical and structural alterations. Zu *et al.* prepared Mo_6Ni_6C on a Ni foam substrate (Mo_6Ni_6C/NF) and reported its unique reconstruction involving the phase transformation (Mo_6Ni_6C → $MoNi_3$, $MoNi_4$, and amorphous carbon) and performed subsequent partial oxidation during the OER in alkaline media (1 M KOH) as shown in Figure 49d.[224] Interestingly, the XRD patterns for Mo_6Ni_6C/NF before and after the OER indicate that the large unit cell of Mo_6Ni_6C collapses into $MoNi_3$ and $MoNi_4$ alloys during the OER (see Figure 49e). It is noted that no oxide counterparts of these MoNi alloys (i.e., MoO_x and NiOOH) were observed in the XRD pattern after the OER, mainly due to their poor crystallinity. Additionally, XPS spectra of Mo_6Ni_6C/NF before and after the OER were obtained to analyze the change of surface valence states. As shown in Figure 49f, the Ni 2p XPS spectra display that the peaks for metallic Ni disappear and that the oxidized Ni peak shifts to a more positive valence state after the OER. Also, in Figure 49g, the Mo 3d XPS spectra exhibit the highest oxidation state of Mo^{6+} after the OER. Furthermore, XAFS analyses were performed to further probe the bulk structures of the Mo_6Ni_6C precatalyst. XANES results display that before the OER process, the Ni element in Mo_6Ni_6C exhibits similar valence states as the Ni foil, indicating its intrinsic metallic properties. However, after the OER process, the valence of Ni is close to that of NiO formed by oxidation during the OER

https://doi.org/10.1021/acs.chemrev.3c00005
Chem. Rev. 2023, 123, 12795−13208

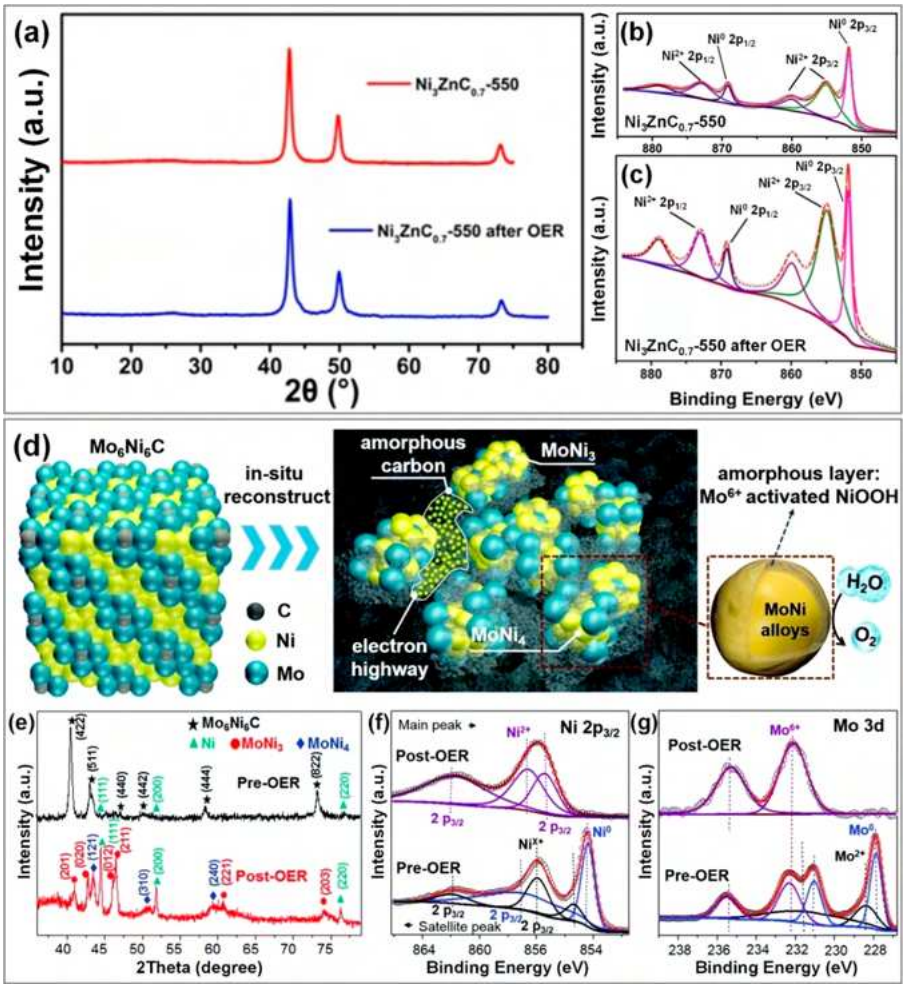


Figure 49. (a) XRD patterns of $Ni_3ZnC_{0.7}$-550 before and after long-term OER measurement. (b, c) Ni 2p XPS spectra of $Ni_3ZnC_{0.7}$-550 (b) before and (c) after long-term OER measurement. Reprinted with permission from ref 233. Copyright 2017 Royal Society of Chemistry. (d) Schematic illustration for the *in situ* reconstruction of Mo_6Ni_6C during the OER. (e) XRD patterns and (f) Ni $2p_{3/2}$ and (g) Mo 3d XPS spectra of Mo_6Ni_6C before and after the OER test. Reproduced with permission from ref 224. Copyright 2019 Royal Society of Chemistry.

process. These XANES results are also consistent with Ni K-edge EXAFS results in which Ni−Ni bonds disappear and Ni−O bonds appear. Moreover, *in situ* XAFS analyses for the Mo element demonstrate that the Mo valence state increases and Mo−O bonds appear as the applied potential increases. All these XRD, XPS, and XAFS results indicate that the Mo_6Ni_6C precatalyst is oxidized during the OER process and transformed into MoNi alloy particles with Mo^{6+} incorporated NiOOH surface species.

In addition to the above-mentioned transition metal carbide precatalysts in alkaline media, there is a report regarding the carbide precatalyst studied in neutral media. Wang *et al.* reported the transformation of the composite of cobalt metal and molybdenum carbide coated with N-doped graphene (Co-Mo_2C@NC) during the OER test (see Figure 50a) in a neutral electrolyte of pH = 7 (0.2 M phosphate buffer solution).[232] The pre- and post-OER SEM images (Figures 50b and c) show that the Co-Mo_2C@NC drop-cast on carbon cloth turned from densely attached nanoclusters with some irregular particles into a dense and smooth shell-like structure with cracks after the OER. As seen in Figures 50d and e, the XPS analysis shows that the Mo 3d signals for the Co-Mo_2C@NC became very weak after the OER test. These results indicate that the Co-Mo_2C@NC might undergo structural transformation and decomposition during the OER test and that the dissolution of Mo into the electrolyte happens simultaneously.

3.3. Structural and Chemical Compositional Effects toward OER Activity

There have been approaches to develop highly active and stable transition metal carbide-based electrocatalysts for the OER by controlling the composition and structure. Herein, we first look into the advantages of transition metal carbides as OER electrocatalysts over pure transition metal oxides. Then, several design strategies for controlling composition (e.g., heteroatom doping and multimetallic carbides) and structure (e.g., heterostructural design by making composites) of transition metal carbides are introduced, and their effects on the OER performance are discussed. Since most of the reported transition metal carbides belong to the group "precatalyst", the role of the reconstruction processes of precatalysts on OER activity is also considered here.

3.3.1. Monometallic Carbides. There have been reports on monometallic transition metal carbides as OER electrocatalysts, such as Ni_3C (refs 234, 239, 254, 260, and 268), Co_3C,[270,91,227] Fe_3C (refs 216, 238, 258, 264, 267, 277, and 283), γ-MoC,[275] β-Mo_2C (refs 225, 226, 232, 235, 237, 256,

https://doi.org/10.1021/acs.chemrev.3c00005
Chem. Rev. 2023, 123, 12795−13208

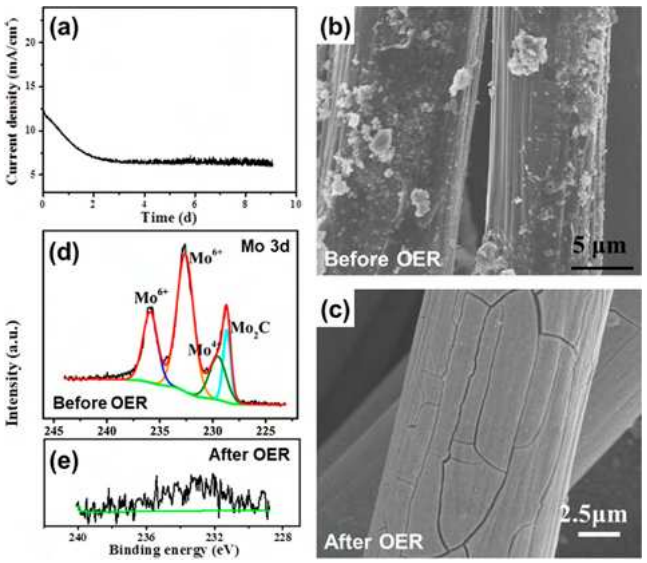


Figure 50. (a) J–t curve of Co-Mo_2C@NC film on carbon cloth (Co-Mo_2C@NC/CC) at the constant potential of 1.63 V_{RHE}. (b, c) SEM images and (d, e) Mo 3d XPS spectra of Co-Mo_2C@NC/CC on carbon cloth (b, d) before and (c, e) after the OER test. Reproduced with permission from ref 232. Copyright 2018 Elsevier.

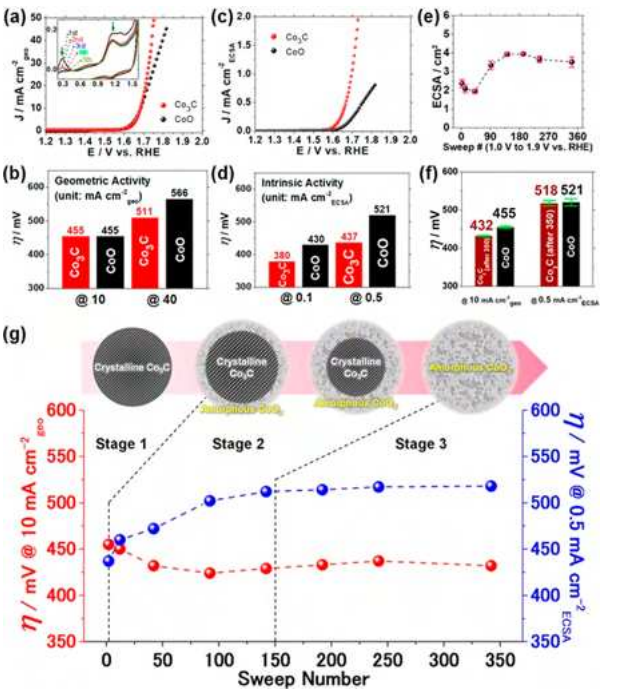


Figure 51. (a–d) OER polarization curves and overpotential (η) from the second sweep LSV curve of Co_3C and commercial CoO, based on (a, b) geometric surface area and (c, d) ECSA. (e) Trend of ECSA vs sweep number for Co_3C. (f) OER activity comparison after 350 LSV OER sweeps. (g) Trend of η based on geometric electrode surface area (red) and ECSA (blue) vs sweep number (1.0–1.9 V_{RHE}) for the Co_3C sample. Reprinted with permission from ref 91. Copyright 2018 American Chemical Society.

271, 272, and 282), and WC.[269] Unfortunately, however, it is difficult to compare the OER activity of monometallic transition metal carbides with different transition metals, because the reported transition metal carbides not only have distinct morphologies but also were prepared using different synthesis methods, supported on different materials, and electrochemically analyzed in nonidentical experimental conditions. Thus, in this Section, instead of comparing the OER activity of different monometallic transition metal carbides, the characteristics of monometallic transition metal carbides as OER electrocatalysts and the effects of their reconstruction processes on OER activity are discussed.

Kim *et al.* reported Co_3C as an OER precatalyst and compared its electrochemical and material properties with commercial CoO.[91] The geometric surface area-normalized polarization curves and overpotentials (at 10 and 40 mA·cm^{-2}_{geo}) from the second sweep LSV curve for the Co_3C precatalyst and commercial CoO sample are provided in Figures 51a and b. Co_3C had an OER performance similar to that of commercial CoO at a low current density of 10 mA·cm^{-2}_{geo} but showed higher performance (higher current density and lower overpotential) at a high current density (40 mA·cm^{-2}_{geo}). To decouple the surface area effects from the intrinsic activity, electrochemically active surface area (ECSA)-normalized polarization curves and overpotential (at 0.1 and 0.5 mA·cm^{-2}_{ECSA}) were compared (Figures 51c and d). At the early stage of electrochemical sweeps (2nd sweep LSV), Co_3C exhibited a higher intrinsic activity than CoO at both low and high current densities. Additionally, the trend of ECSA of the Co_3C nanoparticles during various numbers of OER LSV sweeps was obtained, as shown in Figure 51e. The ECSA continuously increased until ∼150 sweeps, possibly due to the gradual oxidation of Co_3C, and became stable after ∼150 sweeps. Combining these electrochemical data with material characterization (TEM, SAED, XRD, etc.), it was concluded that the oxidation of a Co_3C nanoparticle into an amorphous Co oxide nanoparticle was completed at ∼150 sweeps. The OER overpotentials for Co_3C and CoO after 350 LSV sweeps in Figure 51f demonstrate that although the fully oxidized Co_3C showed a lower geometric area-normalized overpotential (432 mV) compared to commercial CoO (455 mV), its ECSA-normalized intrinsic overpotential (518 mV) was very similar to that of the commercial Co oxide (521 mV), which is different from those of Co_3C and CoO after two LSV sweeps in Figure 51d. Figure 51g summarizes the entire oxidation process of Co_3C during OER testing, the trends of OER overpotentials based on the geometric surface area, and ECSA against sweep number. As Co_3C gradually transformed into amorphous CoO_x from the surface to the core with increasing sweep number, and the enlargement of the active surface area via continuous formation of nanostructured amorphous Co oxide gradually decreased the overpotential at 10 mA·cm^{-2}_{geo} but increased the overpotential at 0.5 mA·cm^{-2}_{ECSA} due to the low electron conductivity of amorphous Co oxide. All these results led to the following conclusions: (i) amorphous Co oxide is the true electrocatalytic site for the OER, while Co_3C is just a superior electron conductor that does not appear to be catalytically active itself, and (ii) the primary origin of the improved OER activity of the Co_3C precatalyst over the CoO sample is the increase in active surface area by its reconstruction process during the OER, not any electronic and/or synergistic effect of Co_3C.

3.3.2. Metal-Doping Effects. Doping of small amounts of heteroatoms into transition metal carbides can improve the OER activity by tuning the electronic structure or creating more active sites.[227] In this Section, the candidate materials for metal doping and the effects of metal doping into transition

https://doi.org/10.1021/acs.chemrev.3c00005
Chem. Rev. 2023, 123, 12795–13208

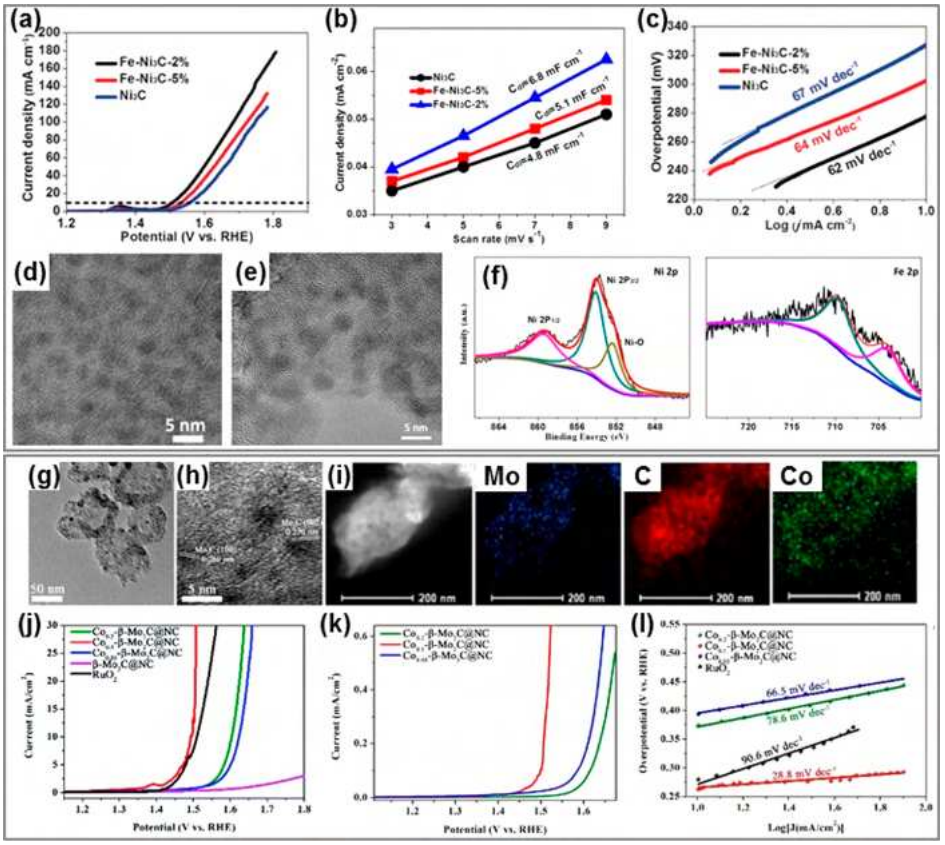


Figure 52. (a–c) Electrochemical analyses of Ni_3C, Fe-Ni_3C-5%, and Fe-Ni_3C-2%. (a) OER LSV curves, (b) C_{dl} measurements, and (c) Tafel plots. (d–f) Material characterization results of Fe-Ni_3C-2%: (d, e) TEM images (d) before and (e) after the OER; (f) Ni 2p and Fe 2p XPS spectra. Reprinted with permission from ref 234. Copyright 2017 Wiley. (g) TEM, (h) HRTEM, and (i) STEM images of $Co_{0.1}$-β-Mo_2C@NC. (j) OER LSV curves, (k) specific OER LSV curves normalized by ECSA, and (l) Tafel plots of Co_n-β-Mo_2C@NC. Reprinted with permission from ref 226. Copyright 2019 Royal Society of Chemistry.

metal carbides are discussed. As for metal doping, one effective strategy is to dope the highly OER active transition metals (e.g., Ni and Co) into relatively less OER active carbide materials (e.g., Mo- and W-based carbides). Additionally, given that Fe doping into Ni- or Co-based oxides can lead to significant OER activity enhancement,[213,291] doping Fe into Ni- and Co-based carbides can also be effective.

Fan *et al.* prepared Ni_3C and Fe-doped Ni_3C nanodots on N-doped carbon nanosheets and evaluated their OER performance.[234] In Figure 52a, the Fe-doped Ni_3C samples showed higher OER activity than the pure Ni_3C sample, and Fe-Ni_3C-2% exhibited the highest OER activity. To understand the OER activity enhancement of Fe-doped Ni_3C compared to pure Ni_3C, the C_{dl} value of each sample, which reflects ECSA, was obtained. Figure 52b displays that Fe-Ni_3C-2% has the largest C_{dl} value of 6.8 mF·cm^{-2} followed by 5.1 mF·cm^{-2} for Fe-Ni_3C-5% and 4.8 mF·cm^{-2} for Ni_3C, which almost aligns with the OER activity trend in Figure 52a. The Tafel slope results, which can represent the intrinsic catalytic activity, show that Fe-Ni_3C-2% has the lowest Tafel slope of 62 mV·dec^{-1} followed by 64 mV·dec^{-1} of Fe-Ni_3C-5% and 67 mV·dec^{-1} of Ni_3C, implying that the intrinsic activity of Fe-doped Ni_3C is higher than that of pure Ni_3C, possibly due to the Fe-doping effect (Figure 52c). Additionally, to ensure that the distinct OER activity mainly results from the Fe-doping effects, it is crucial to check after the OER test whether the material properties have changed and whether the doped Fe atoms in Ni_3C remain by conducting post-OER material characterization. The TEM images of Fe-Ni_3C-2% before and after the OER test in Figures 52d and e show that as-prepared Ni_3C nanodots with the size of 3–5 nm are embedded in the nanosheet structure and are well maintained even after the long-term OER stability test. Figure 52f demonstrates that Fe atoms doped into the Ni_3C exist in Ni_3C even after OER testing without significant dissolution into the electrolyte. The authors concluded that a suitable Fe-doping level could optimize the electronic properties and improve the OER performance. However, considering that the difference in Tafel slope between the prepared samples is very small and geometric area-based OER activity almost follows the trend of C_{dl}, it is unlikely that Fe-doping improved the intrinsic OER activity of Fe-doped Ni_3C. Rather, the OER activity trend can be simply explained by the formation of more active sites during the Fe-doping process. This interpretation sounds contrary to the previous reports that Fe-doping can effectively tune the electronic structure of Ni- and Co-based OER electrocatalysts and enhance the intrinsic OER activity.[291] There is a possibility that the negligible enhancement of the intrinsic activity of Fe-doped Ni_3C samples in this study is due to the low amounts of actual Fe-doping for Fe-Ni_3C-2% and Fe-Ni_3C-5%, which were 1.1 and 2.8%, respectively.

Zhu *et al.* prepared cobalt doped β-molybdenum carbide nanoparticles encapsulated within N-doped carbon ($Co_{0.05}$-β-Mo_2C@NC, $Co_{0.1}$-β-Mo_2C@NC, and $Co_{0.2}$-β-Mo_2C@NC) and investigated their OER performance.[226] The TEM image in Figure 52g reveals the nanostructure of $Co_{0.1}$-β-Mo_2C@NC

https://doi.org/10.1021/acs.chemrev.3c00005
Chem. Rev. 2023, 123, 12795–13208

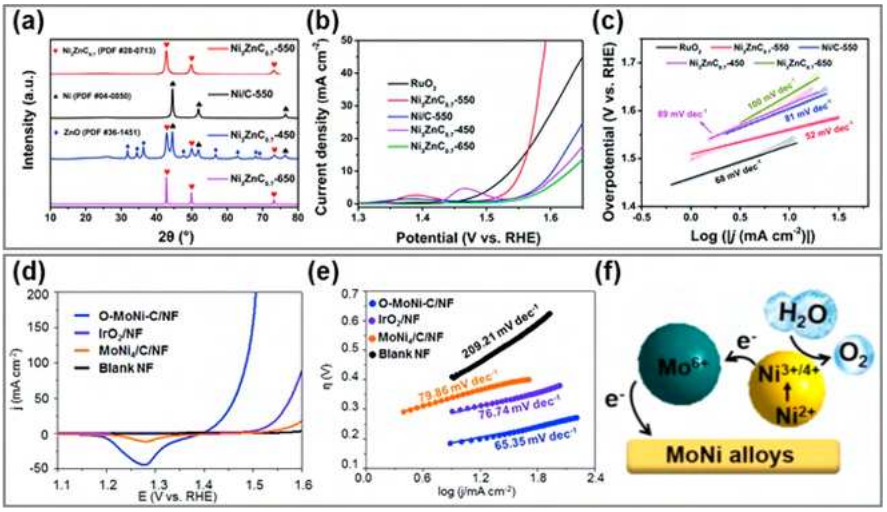


Figure 53. Influence of multi-cation compositions on the performance of transition metal carbides. (a) XRD patterns of fresh $Ni_3ZnC_{0.7}$ samples prepared at different pyrolysis temperatures. (b) OER LSV curves of $Ni_3ZnC_{0.7}$ samples. (c) Tafel plots of $Ni_3ZnC_{0.7}$ samples. Reprinted with permission from ref 233. Copyright 2017 Royal Society of Chemistry. (d, e) Electrochemical analyses of O-MoNi-C in 1 M KOH. (d) OER LSV curves and (e) Tafel plots. (f) Schematic illustration of the effect of high-valence Mo^{6+} to activate 3d metal Ni active sites for the OER. Reprinted with permission from ref 224. Copyright 2019 Royal Society of Chemistry.

consists of nanoparticles embedded in a carbonized polyhedron. The HRTEM image of $Co_{0.1}$-β-Mo_2C@NC in Figure 52h shows that the nanoparticles have lattice distances of 0.236 and 0.260 nm, corresponding to the (002) and (100) facets of β-Mo_2C, respectively. The elemental mapping of STEM indicates that Mo, C, and Co are distributed uniformly (Figure 52i). The OER performance of β-Mo_2C@NC and Co-doped β-Mo_2C@NC was compared in Figure 52j. The Co-doped β-Mo_2C@NC samples had superior OER performance compared to pure β-Mo_2C@NC, possibly due to the synergistic effect between β-Mo_2C and Co atoms, and $Co_{0.1}$-β-Mo_2C@NC exhibited the highest OER performance among Co-doped β-Mo_2C@NC. The C_{dl} values of $Co_{0.2}$-β-Mo_2C@NC, $Co_{0.1}$-β-Mo_2C@NC, and $Co_{0.05}$-β-Mo_2C@NC were 5.90, 4.97, and 1.32 mF·cm^{-2}, respectively. To understand the intrinsic OER activity, geometric area-based OER LSV curves were normalized by the corresponding ECSA values, and the specific OER activity of the samples was calculated (Figure 52k). Though the specific OER performance of $Co_{0.05}$-β-Mo_2C@NC and $Co_{0.2}$-β-Mo_2C@NC was reversed compared to their geometric area-based OER performance, $Co_{0.1}$-β-Mo_2C@NC still performed with the highest specific OER activity. The Tafel slope results in Figure 52l show that $Co_{0.1}$-β-Mo_2C@NC has the lowest Tafel slope of 28.8 mV·dec^{-1} followed by 66.5 mV·dec^{-1} of $Co_{0.05}$-β-Mo_2C@NC and 78.6 mV·dec^{-1} of $Co_{0.2}$-β-Mo_2C@NC. This trend of the Tafel slope is consistent with the specific OER activity, suggesting that $Co_{0.1}$-β-Mo_2C@NC has the optimal doping amount and thereby exhibits the highest intrinsic OER activity. The effect of cobalt doping into Mo_2C was explained by the increased electron density around the Fermi level, which contributes to the synergistic effect between cobalt and Mo_2C and the promotion of OER activity. However, it is not identified in this study why the doping amount of $Co_{0.1}$-β-Mo_2C@NC is optimal for the highest OER activity. Given that Co metal is well-known as a highly OER active site while the Mo metal site is not, it seems counterintuitive that $Co_{0.1}$-β-Mo_2C@NC shows higher OER performance than $Co_{0.2}$-β-Mo_2C@NC in terms of the number of Co metal active sites. For an in-depth understanding of the Co doping effect, a thorough investigation into how the synergistic effect between Co and Mo_2C changes with Co doping amount and how this synergistic effect affects the intrinsic activity of Co and Mo sites would be necessary.

3.3.3. Multi-cation Effects. Multi-cation carbides, especially bimetallic transition metal carbides, have been reported as high-performance OER electrocatalysts.[224,227,233,276,279] Although the preparation of pure-phase bimetallic carbides is difficult due to the synthesis condition using high-temperature calcination that can bring about the segregation and formation of mixed phases, the incorporation of a secondary metal into transition metal carbides can improve the OER performance by tuning the electronic structure and exposing abundant active sites.[276]

Wang *et al.* successfully synthesized a single-phase bimetallic $Ni_3Zn_{0.7}C$ from the bimetallic NiZn-MOFs and evaluated its OER performance.[233] Here, although the metal Zn site cannot drive the electrocatalysis due to its fully occupied 3d orbitals, Zn was incorporated to modulate the electronic property of the $Ni_3Zn_{0.7}C$ electrocatalyst through the hybridization with active Ni metal sites. The XRD patterns in Figure 53a exhibit that a single-phase bimetallic $Ni_3ZnC_{0.7}$ is successfully formed from bimetallic MOFs after calcination at a temperature above 550 °C, while the sample prepared at 450 °C ($Ni_3ZnC_{0.7}$-450) consists of ZnO, Ni metal, and $Ni_3ZnC_{0.7}$. Also, the diffraction peaks of $Ni_3ZnC_{0.7}$ show a shift toward lower angle compared with those of Ni/C-550 that is obtained by pyrolyzing Ni-MOFs at 550 °C, which suggests that Zn atoms, with a larger atomic size than that of Ni atoms, are well incorporated into the crystal lattice of $Ni_3ZnC_{0.7}$. The Ni 2p XPS spectra of Ni/C-550 and $Ni_3ZnC_{0.7}$-550 showed that the peaks for the Ni^{2+} state of $Ni_3ZnC_{0.7}$ have higher intensities and are positively shifted compared to Ni/C, manifesting the modulation of Ni valence by Zn. As depicted in Figure 53b, $Ni_3ZnC_{0.7}$-550 exhibited a higher OER activity than Ni/C-550 and other $Ni_3ZnC_{0.7}$ samples ($Ni_3ZnC_{0.7}$-450 and $Ni_3ZnC_{0.7}$-650). It is worth noting though that the redox charge of $Ni_3ZnC_{0.7}$-550 for the Ni^{2+} to Ni^{3+} transition, which is correlated to the

https://doi.org/10.1021/acs.chemrev.3c00005
Chem. Rev. 2023, 123, 12795−13208

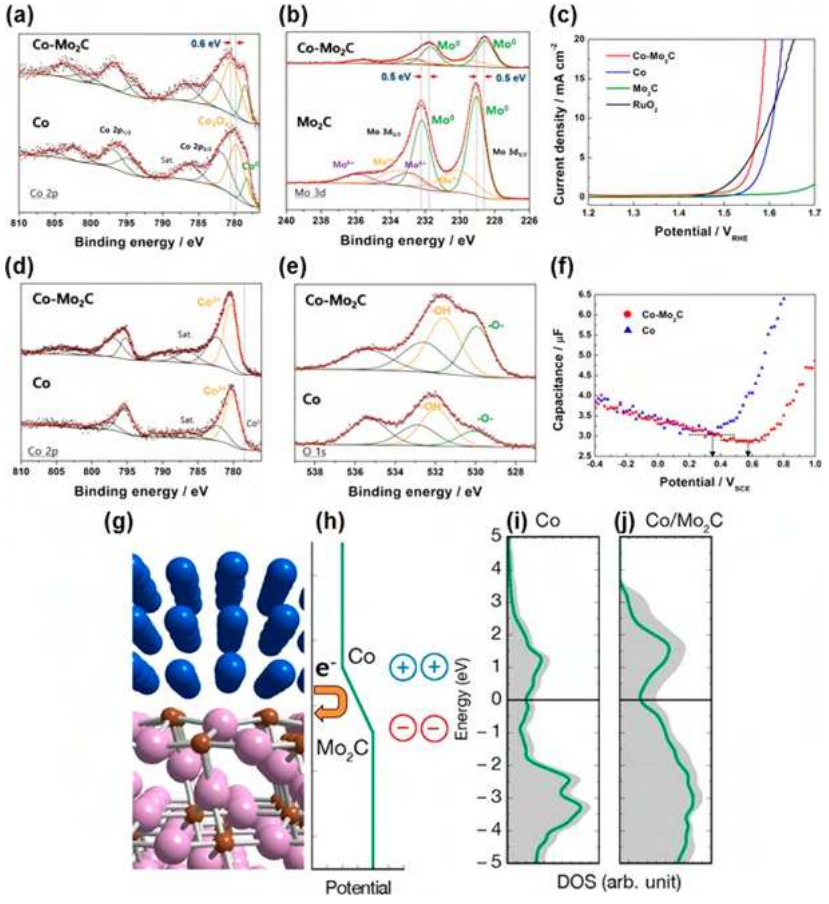


Figure 54. (a) Co 2p XPS spectra of Co-Mo_2C and Co nanoparticles, and (b) Mo 3d XPS spectra of Co-Mo_2C and Mo_2C nanoparticles before the OER. (c) OER LSV curves of Co-Mo_2C, Co, and Mo_2C nanoparticles and commercial RuO_2 in 0.1 M KOH. (d) Co 2p and (e) O 1s XPS spectra of Co-Mo_2C and Co nanoparticles after three OER cycles. (f) PZC for Co-Mo_2C and Co samples. (g) Atomic structure of Co/Mo_2C. Blue, pink, and brown balls represent Co, Mo, and C atoms, respectively. (h) Schematic diagram of the potential shift due to electron transfer across the interface. (i, j) Total densities of states (gray shade) and the projected DOS of the d-orbitals of Co (green line) for (i) Co slab and (j) Co/Mo_2C. Reprinted with permission from ref 230. Copyright 2018 Elsevier.

number of electrochemically active Ni sites,[113] was smaller than that of $Ni_3ZnC_{0.7}$-450, with $Ni_3ZnC_{0.7}$-550 showing the higher OER activity. This implies that bimetallic NiZn carbides have a significant electronic effect for superb intrinsic OER activity compared with $Ni_3ZnC_{0.7}$-450, which is a composite of ZnO, Ni, and $Ni_3ZnC_{0.7}$. This interpretation is also consistent with the Tafel slope results in Figure 53c showing that $Ni_3ZnC_{0.7}$-550 has a lower Tafel slope of 52 mV·dec^{-1} than Ni/C-550 and other $Ni_3ZnC_{0.7}$ samples.

Also, Zu *et al.* prepared the bimetallic carbide Mo_6Ni_6C on a Ni foam substrate as a new type of precatalyst for the OER. As depicted in Figure 53d, Mo_6Ni_6C was oxidized to form a carbon-interconnected MoNi alloy with Mo^{6+} incorporated NiOOH species on the surface and was denoted as O-MoNi-C/NF.[224] O-MoNi-C/NF exhibited a higher OER activity and a lower Tafel slope compared to IrO_2/NF and $MoNi_4$/NF (Figures 53d and e). The high intrinsic activity of O-MoNi-C/NF is due to its superb electrical conductivity and the electronic effect between Mo and Ni. Specifically, the MoNi alloy core of O-MoNi-C/NF has excellent intrinsic metallic properties for superb electrical conductivity, and each fragment of O-MoNi-C/NF is interconnected at an atomic level by amorphous carbon that is transformed from elemental carbon in Mo_6Ni_6C, relieving the poor charge transport caused by the interstitial spaces. Furthermore, as shown in Figure 53f, the high-valence Mo^{6+} draws electrons from the Ni in NiOOH, which is the OER active site, resulting in a more active high-valence state ($Ni^{3+/4+}$) of Ni, and thereby superior intrinsic activity.

3.3.4. Composite Materials Effects. Compared with single transition metal carbides, composite materials have advantages such as enhanced electron and mass transport properties, better stability, or more exposed active sites, depending on the material properties of paired composite material. Additionally, by creating a heterojunction interface between composite materials, the electronic structure of active sites can be tuned properly to have higher intrinsic activity. There are largely three types of transition metal carbide-based composite materials: (i) transition metal carbide/transition metal (refs 217, 226, 229, 230, 232, 235, 236, 238, 260, 261, 263, 271, and 275), (ii) transition metal carbide/transition metal oxide,[262,265] and (iii) transition metal carbide/carbon-based materials.[258,281,283]

As to the transition metal carbide/transition metal composite, Kim *et al.* synthesized a composite of Co and Mo_2C nanoparticles (Co-Mo_2C) and investigated the interaction between Co and Mo_2C for enhanced OER activity.[230] The electronic interaction between Co and Mo_2C was analyzed by XPS spectra of as-prepared Co-Mo_2C, Co, and Mo_2C nanoparticles. The binding energies of the Co 2p

https://doi.org/10.1021/acs.chemrev.3c00005
Chem. Rev. 2023, 123, 12795−13208

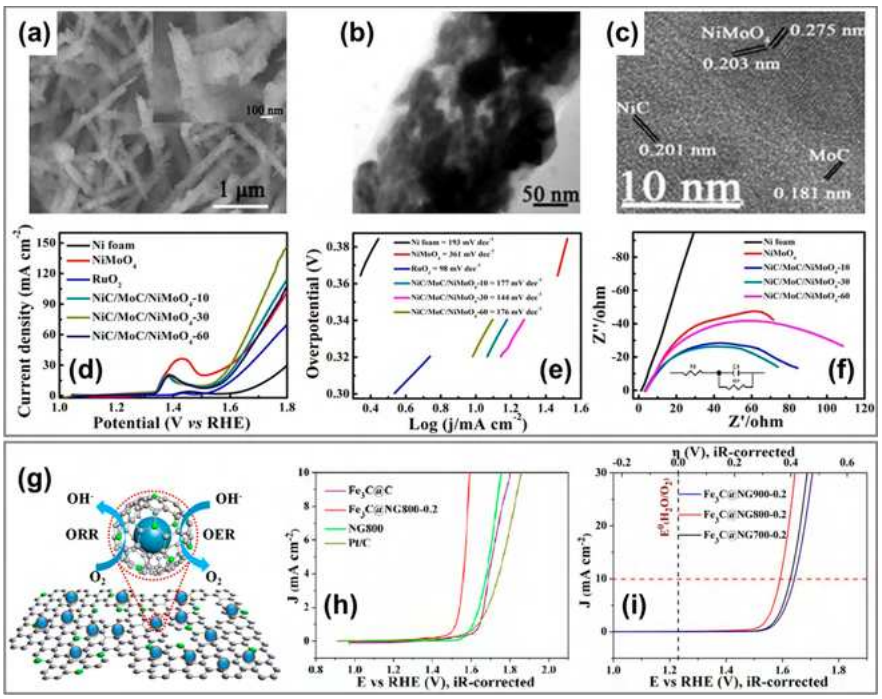


Figure 55. (a) SEM, (b) TEM, and (c) HRTEM images of 3D heterostructured NiC/MoC/$NiMoO_4$ nanorod arrays on Ni foam (NiC/MoC/$NiMoO_4$-30). (d) LSV curves, (e) corresponding Tafel slopes, and (f) Nyquist plots of Ni foam, $NiMoO_4$, NiC/MoC/$NiMoO_4$-10, -30, and -60 on Ni foam, and commercial RuO_2 on a glassy carbon electrode for the OER in 1.0 M KOH. Reproduced with permission from ref 262. Copyright 2019 Wiley. (g) Schematic illustration of Fe_3C@NG for the OER. (h, i) OER LSV curves of (h) Fe_3C@C, Fe_3C@NG800-0.2, NG800, and Pt/C and of (i) Fe_3C@NGT-0.2 at different temperatures. Reproduced with permission from ref 283. Copyright 2015 American Chemical Society.

spectra for Co-Mo_2C were positively shifted by 0.8 eV compared to those of Co, implying that Co atoms in Co-Mo_2C lost electrons (Figure 54a). This was consistent with the Mo 3d spectra of Co-Mo_2C and Mo_2C (Figure 54b) in that the binding energies of the Mo 3d spectra for Co-Mo_2C were negatively shifted by 0.5 eV, implying that the Mo atoms in Co-Mo_2C obtained electrons. These results suggest that Mo_2C withdraws electrons from Co in the Co-Mo_2C composite and makes Co have a higher valence state, which is beneficial for the OER. Figure 54c demonstrates that the OER activity of Co-Mo_2C was higher than those of Mo_2C and Co despite a lower Co loading for Co-Mo_2C compared to that for Co nanoparticles. Considering that Mo_2C is nearly inactive to the OER, the superb OER activity of the Co-Mo_2C can be attributed to the enhanced intrinsic activity of the Co atoms in Co-Mo_2C. This interpretation is also supported by the fact that the TOF values of Co-Mo_2C calculated based on the Co loading amount and the redox charge for $Co^{2+/3+}$ were five times higher than those of Co nanoparticles. Additionally, the ratio of Co to Mo content was controlled from 1:4 to 4:1, and the Co-Mo_2C sample with 1:1 ratio exhibited the highest OER activity, implying the existence of the optimal ratio that can balance the degree of chemical coupling of Co to Mo_2C and the number of OER active sites. To ensure that the electronic interaction between Co and Mo_2C in Co-Mo_2C was well maintained during the OER, post-OER XPS analyses were conducted. Although the Co-Mo_2C and Co samples had more oxidized Co 2p peaks after the OER corresponding to Co^{3+} than those before the OER test, both samples looked very similar in the Co 2p region (Figure 54d). On the other hand, the O 1s spectra after the OER test showed a clear difference that Co-Mo_2C had a higher proportion of oxo (−O−) species than the Co sample (Figure 54e). The oxo coordinated Co cations can be found in the *in situ*-formed Co hydrous oxide layer, and the higher portion of oxo coordinated Co sites for Co-Mo_2C can be formed due to the more electrophilic Co sites of the Co-Mo_2C sample and thereby their strong attraction of OH^-. Also, the higher proportion of oxo-coordinated-Co cations resembles the structure of OER-active CoOOH, which consists of [CoO_6] subunits. This suggests that the *in situ*-formed hydrous oxide layers of the Co-Mo_2C sample would have suitable Co-oxo or -hydroxo configurations similar to those of CoOOH, and it thereby exhibited superior OER performance compared with the Co sample with a lower proportion of oxo coordinated Co sites. To better understand the nature of the hydrous oxide on the Co-Mo_2C and Co samples, the point of zero charge (PZC), which is linearly correlated to the electrochemical work function of the electrode in contact with the electrolyte, was measured for Co-Mo_2C and Co samples in 2 mM sodium fluoride solution after the OER test. Here, a higher PZC value means a higher electrochemical work function and more favorability for the oxidation reaction. As depicted in Figure 54f, the Co-Mo_2C sample showed a higher PZC value than the Co sample by 0.23 V, indicating that the Co-Mo_2C sample has a more favorable work function for the OER than the Co sample. The electronic effect between Co and Mo_2C for the Co-Mo_2C composite is also supported by DFT calculations. As shown in Figures 54g and h, electrons are transferred from Co to Mo_2C across the interface. Due to this electron transfer, the d-band center, which is correlated to the adsorption strength of OH^- on the surface, of Co-Mo_2C is upshifted, making Co more electrophilic to increase OH^- affinity and favorable for the OER (Figures 54i and j). All these experimental and DFT calculation results indicate that the excellent OER activity of

https://doi.org/10.1021/acs.chemrev.3c00005
Chem. Rev. 2023, 123, 12795−13208

the Co-Mo_2C sample is attributed to the modulation of the electronic structure of Co sites in junction with Mo_2C.

As for the composite of transition metal carbide/transition metal compound, Geng *et al.* prepared 3D NiC/MoC/$NiMoO_4$ heterostructured nanorod arrays on Ni foam through the annealing of the polydopamine-coated $NiMoO_4$ nanorod precursor on Ni foam (details of its preparation are available in Figure 38).[262] Specifically, the authors prepared samples (NiC/MoC/$NiMoO_4$-T, where T stands for the dopamine coating time) with the different dopamine coating times (10, 30, and 60 min) and obtained the optimal NiC/MoC/$NiMoO_4$ sample toward the electrocatalytic OER. Figure 55a shows the SEM images of NiC/MoC/$NiMoO_4$-30 as a representative sample. The growth of composite nanorods uniformly on Ni foam can be confirmed. From the TEM image in Figure 55b, the as-fabricated nanorod was found to be polycrystalline in nature and consisted of numerous interconnected nanoparticles. Moreover, the HRTEM image showed the lattice fringes with the spacings of 0.203, 0.275, 0.201, and 0.181 nm corresponding to the $NiMoO_4$ (330) and (022), NiC (111), and MoC (101) planes, respectively (see Figure 55c), which suggests the successful formation of a heterogeneous carbide/oxide nanocomposite. The electrocatalytic OER activities of the NiC/MoC/$NiMoO_4$ sample series, $NiMoO_4$, and commercial RuO_2 (control sample) were investigated by LSV at a scan rate of 10 $mV{\cdot}s^{-1}$ in alkaline media (Figure 55d). The NiC/MoC/$NiMoO_4$-30 sample recorded the highest OER activity (the overpotential of 340 mV at 20 $mA{\cdot}cm^{-2}$) among the tested samples. NiC/MoC/$NiMoO_4$-30 also exhibited a relatively low Tafel slope of 144 $mV{\cdot}dec^{-1}$ and the lowest charge transfer resistance (see Figures 55e and f), suggesting faster OER kinetics. Additionally, these experimental results indicate that the OER activity of the resultant carbide-based electrocatalyst can be optimized by altering the carbon source amount for the carburization.

In the composite of transition metal carbide and carbon-based material, transition metal carbides are usually dispersed and anchored on the carbon materials as supports. Generally, carbon materials as supports have several advantages, as follows. Carbon materials can commonly provide good electrical conductivity and restrain large aggregations of transition metal carbide nanoparticles for efficient exposure of active sites. Also, carbon materials with a 2D/3D porous structure are beneficial for exposing more active surface area and facilitating the mass transport of OH^- reactants and O_2 products.[225] Furthermore, some heteroatom-doped carbon materials can have electronic interactions with transition metal carbide at the heterojunction, thereby tuning the adsorption energy of reaction intermediates and the OER activity on transition metal carbide.[258,283] Jiang *et al.* synthesized uniform Fe_3C nanoparticles on Fe-N-doped graphene-like carbon supports using several different carburization temperatures (Fe_3C@NG*T*, where *T* denotes the carburization temperature of 700, 800, or 900 °C) as depicted in Figure 55g, and evaluated their OER performance.[283] Figure 55h demonstrates that Fe_3C/NG800-0.2 exhibited superior performance compared with Fe_3C@C and N-doped graphene-like carbon (NG800), implying the Fe-related components (Fe_3C or Fe-N_x) of the Fe_3C/N-doped carbon composite enhance the OER activity. Furthermore, the effect of carburization temperature on the OER activity of Fe_3C@NGT was investigated. Figure 55i shows that Fe_3C@NG800-0.2 had the highest OER activity followed by Fe_3C@NG700-0.2 and Fe_3C@NG900-0.2. This is because the Fe_3C@NG700-0.2 sample prepared at low temperature has low electrical conductivity, which impedes the charge transfer, while the Fe_3C@NG900-0.2 sample prepared at high temperature lacks catalytically active sites. These results suggest that the carburization temperature affects the material properties of transition metal carbide/carbon composites, such as porosity, electrical conductivity, and the type and density of active sites, thereby determining the OER performance.

3.4. Challenges

The synthesis methods of transition metal carbides require high-temperature annealing steps for the carburization of precursors, which can cause agglomeration of the synthesized transition metal carbide materials. This agglomeration can bring about low active surface area and poor mass transfer of reactants and products that lower the overall OER performance.[228] Thus, the agglomeration issue should be avoided by designing the transition metal carbides with good morphology. One possible solution is to directly carburize the precursors that already have uniform and stable structures. The transition metal carbides obtained from these precursors can maintain good morphologies of the precursors without severe agglomeration.[280]

Additionally, due to the high-temperature carburization process (700−900 °C), carbon sources for transition metal carbides can be unintentionally transformed into a carbon matrix[258,281,283] and/or carbon shell (refs 226, 229, 232, 233, 258, 260, 261, 276, 277, and 292). For example, Figure 56a illustrates that when Co-Mo_2C nanoparticles were synthesized through a high-temperature calcination process, a N-doped graphite carbon shell was *in situ* generated.[232] Similarly, during

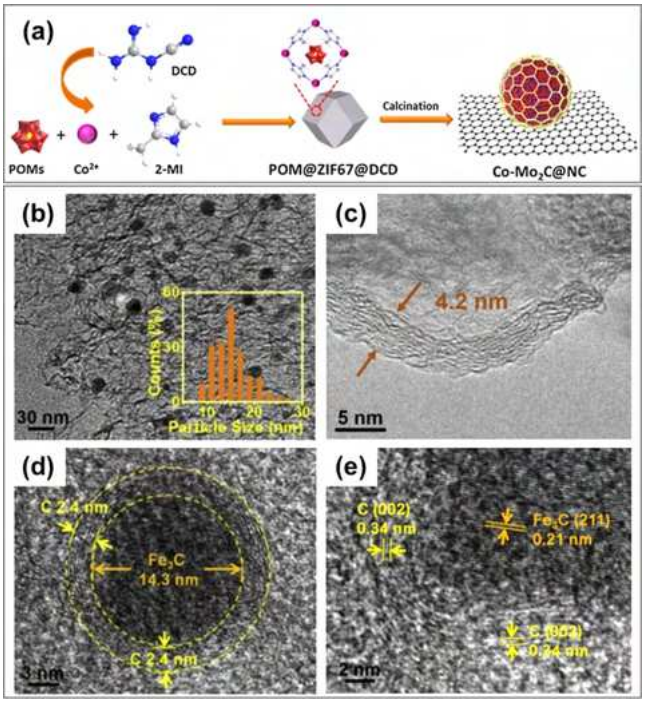


Figure 56. (a) Schematic illustration of the fabrication of Co-Mo_2C coated with a nitrogen-doped graphite shell using dicyandiamide. Reprinted with permission from ref 232. Copyright 2018 Elsevier. (b, c) TEM and (d, e) HRTEM images of Fe_3C nanoparticles with a carbon shell. Reprinted with permission from ref 258. Copyright 2019 Elsevier.

https://doi.org/10.1021/acs.chemrev.3c00005
Chem. Rev. 2023, 123, 12795−13208

the synthesis of Fe_3C via pyrolysis of ferric nitrate, melamine, and methionine, carbon-coated Fe_3C nanoparticles dispersed on the surface of the graphene-like matrix were obtained (Figure 56b).[258] The HRTEM images in Figures 56c and d demonstrate that a carbon shell with a thickness of 2−4 nm covers the Fe_3C nanoparticle core. The d-spacings of 0.34 and 0.21 nm are identified as the (002) lattice planes of a graphitic carbon shell and the (211) lattice planes of the Fe_3C nanoparticle core, respectively (Figure 56e). These *in situ*-formed carbon supports and carbon shells have both advantages and disadvantages for developing and investigating OER electrocatalysts.

The *in situ*-formed carbon support during the transition metal carbide synthesis has advantages for electrocatalysis, such as superb electron and mass transport, more exposure of active surface area, and synergistic effects at the interface between transition metal carbide and *in situ*-formed carbon materials, which can play a positive role in enhancing the OER activity of transition metal carbide electrocatalysts. However, the electronic interaction of an *in situ*-formed carbon support with transition metal carbide and the above-mentioned other advantages can rather complicate the interpretation of the intrinsic OER activity of the prepared transition metal carbide electrocatalysts and hinder a fair comparison of OER activity among different electrocatalysts.

The carbon shell *in situ* formed during the transition metal carbide synthesis has the advantages of enhancing the electrical conductivity, preventing the agglomeration of transition metal carbide particles, and increasing the dispersion of active sites, which contribute to the improved OER performance. Moreover, the carbon shell can act as a protective layer that prevents transition metal carbide particles from coalescing and etching, thereby enhancing stability during the OER. However, these advantages can also make rather it difficult to evaluate the intrinsic activity and stability of the transition metal carbide in the following ways: (i) the interaction between the transition metal carbide electrocatalyst and carbon shell affects the OER activity of the electrocatalyst or carbon shell by electronic effects, (ii) the carbon shell can bring about mass transport issues of reactants and/or block the surface active sites of the transition metal carbide, and (iii) the intrinsic stability of transition metal carbides, such as resistance to *in situ* oxidation and electrochemical stability to long-term OER, can be complicated due to the enhanced stability by the protective carbon shell.

Moreover, there are additional challenges that can result from the instability of *in situ*-formed carbon supports and carbon shells. When transition metal carbides undergo the reconstruction process (i.e., *in situ* oxidation) during the OER and generate oxidized species, it is expected that C species decomposed from transition metal carbides are dissolved into the electrolyte, although there is an exception where oxidation and the consequent dissolution of elemental carbon from a transition metal carbide can be prevented if the surface of the transition metal carbide is already functionalized with an oxygen group.[228] Also, according to the Pourbaix diagram of carbon in Figure 57, carbon materials including carbon supports and carbon shells can be dissolved into the electrolyte together with transition metal carbides under the thermodynamic OER potentials in the form of CO_3^{2-} for high pH, HCO_3^- for neutral pH, and $CO_{2(aq)}$ for low pH electrolytes, which can trigger several issues as follows. First, the dissolution of the carbon support/carbon shell could lead to the loss of a

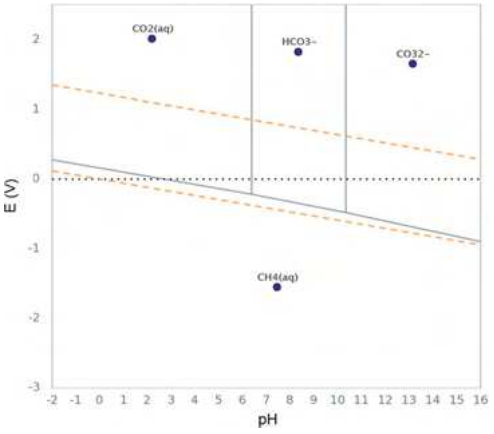


Figure 57. Pourbaix diagram for carbon. Orange broken lines represent the thermodynamic potentials for the HER and OER at different pH values. The diagram is produced at the C ion concentration of 10^{-8} M (default) by using the Materials Project.[87−89]

synergistic effect between the carbon shell/carbon support and transition metal carbide during the OER and a decrease in OER activity. Second, as the carbon support is dissolved into the electrolyte during the OER, the transition metal carbide electrocatalyst supported on carbon support can be physically removed together from the current collector, resulting in severe instability issues. Third, the dissolution of carbon materials can make the study of the stability of transition metal carbide electrocatalysts more difficult. The electrochemical stability of electrocatalysts is commonly measured by constant current/potential signals from electrochemical techniques including CV, CA, and CP.[213] However, the constant current/potential signals during the OER do not always guarantee the real stability of electrocatalysts. This is because, despite the loss of electrocatalytic materials on the surface during the OER, there is a possibility that current and potential signals remain constant as the underlying electrocatalytic materials are newly exposed to the electrolyte. In this regard, to gain a correct understanding of the real physical/chemical stability of electrocatalysts, it has become crucial to analyze the chemical species of electrocatalysts dissolved into the electrolyte using characterization techniques, such as ICP-MS and TXRF.[293,294] To analyze the C-species in the electrolyte dissolved from transition metal carbides, characterization tools including GC-MS[295] and ion chromatography[296] can be employed. However, the dissolved C-species (CO_3^{2-}, HCO_3^-, $CO_{2(aq)}$) from carbon supports and carbon shells are the same as those from transition metal carbides, which could hinder the interpretation of the dissolved C species in the electrolyte to investigate the degree of reconstruction (i.e., *in situ* oxidation) and long-term stability of transition metal carbides during the OER. Additionally, there is another challenge that CO_2 gas in the air easily dissolves into the aqueous electrolyte in the form of CO_3^{2-}, HCO_3^-, and $CO_{2(aq)}$, making it more complex to analyze the dissolved C-species for a stability study.

Regarding the structure of transition metal carbide precatalysts after the OER, it is generally described that an MO_x/MO_xH_y layer is formed on the surface of the transition metal carbide, as illustrated in Figure 44b. However, considering the case for transition metal phosphide precatalysts where phosphate decomposed from transition metal phosphide during the OER remains in the *in situ*-formed oxide layer,[297]

https://doi.org/10.1021/acs.chemrev.3c00005
Chem. Rev. 2023, 123, 12795−13208

there is a possibility that some of the carbonate species decomposed from the transition metal carbide precatalysts are incorporated into the *in situ*-formed oxide layer, instead of all the C species being dissolved into the electrolyte. So far, this has not been reported, nor has it been identified. It is speculated that this may be due to the technical difficulty associated with the material characterization. To be specific, the presence of carbonate species on the surface oxide layer can be detected by XPS analysis. However, the C 1s XPS spectra of the carbonate, which occurs at a binding energy of around 288−290 eV, can overlap with the O—C═O bond of adventitious carbon, carbon supports, or a carbon shell layer of a transition metal carbide, making it difficult to tell the presence of carbonate species on the surface. Moreover, there is no clear difference in the XPS spectra for a carbonate (or O—C═O) peak between before and after the OER. For example, if a carbonate (or O—C═O) peak exists for the as-prepared transition metal carbide samples, that peak tends to remain after the OER,[255,272] and *vice versa*.[91] Consequently, despite the presence of a carbonate (or O—C═O) peak in post-OER C 1s XPS spectra, it is hard to conclude that the carbonate species dissolved from transition metal carbide is incorporated into the *in situ*-formed surface oxide layer.

Depending on the pH of the electrolytes and the types of transition metal, transition metal carbide electrocatalysts can exhibit severe instability during the OER ranging from degradation of electrochemical performance to dissolution of the transition metal into the electrolyte together with C species. In particular, transition metal carbides tend to be less stable to the OER in acidic and neutral electrolytes compared to those in an alkaline electrolyte. For example, the N-doped WC nanoarray showed decent OER activity in an acidic electrolyte (0.5 M H_2SO_4).[269] However, when the OER stability of the N-WC nanoarray was measured employing CP at 10 mA·cm^{-2}, the applied potential dramatically increased from 1.35 to 1.54 V_{RHE} only after 1 h of the OER, indicating poor stability of N-WC in acidic OER conditions. Also, Wang *et al*. compared the OER stability of Co-Mo_2C@NC in alkaline (0.1 M KOH, pH = 13) and neutral (0.2 M PBS, pH = 7) electrolytes by employing CA at 1.6 and 1.63 V_{RHE}, respectively.[232] As opposed to the constant $J-t$ curve of Co-Mo_2C@NC in 0.1 M KOH for 4 h, its OER current density in 0.2 M PBS significantly decreased within 2 h (Figure 50a). Furthermore, the significant dissolution of Mo from Co-Mo_2C@NC after the OER testing into a neutral electrolyte was confirmed by post-OER Mo 3d XPS analysis, indicating a poorer stability of Co-Mo_2C@NC in the neutral electrolyte compared to the alkaline electrolyte. In addition to the OER in acidic and neutral electrolytes, dissolution of transition metal carbides can also occur during the OER in alkaline electrolytes. Kawashima *et al*. reported the selective dissolution of the V_8C_7 particulate precatalyst from its (110) and (111) facets as VO_4^{3-} species into the basic electrolyte (1 M KOH).[221] Moreover, Kim *et al*. also studied the dissolution of chemically coupled Co and Mo_2C nanoparticles (Co-Mo_2C) in 0.1 M KOH aqueous electrolyte during the OER CV cycles by using ICP-AES.[230] During the first OER cycle, most of the Mo_2C nanoparticles were primarily dissolved into the electrolyte (Mo concentration: 0.35 μM) by forming molybdate anions (MoO_4^{2-}). After 1000 CV cycles, a small amount of Co from the Co-Mo_2C was also dissolved into the electrolyte (Co concentration: 9.66×10^{-4} μM; Mo concentration: 0.47 μM). In this regard, it is necessary to understand the intrinsic stability of various transition metal carbide electrocatalysts in the electrolytes with different pH values and to develop highly active and stable transition metal carbide OER electrocatalysts based on this understanding.

4. TRANSITION METAL PNICTIDES

Transition metal pnictides such as nitrides and phosphides are a class of cost-effective and active materials for electrocatalytic water splitting.[106,286,298−302] The use of pnictides as electrocatalysts for the HER and OER was proposed and studied during the 1980s and 1990s.[303−310] Especially for the OER, in 1982, Matsuda *et al*. firstly presented the anodic behavior of transition metal nitrides (TiN and VN) in acidic and alkaline electrolytes (0.5 M H_2SO_4 and 1 M NaOH),[303] in which their anodic transformations were carefully examined. During cyclic voltammetry tests, the TiN surface was partially oxidized, generating a TiO_2 (or Ti hydroxide) passivation layer, and simultaneously dissolved into the electrolytes by forming TiO_2^{2+} under anodic polarization. In the case of VN, only its anodic dissolution into the electrolytes was observed. On the other hand, the first transition metal phosphide OER electrocatalysts were reported by Kupka and Budniok in 1989 and 1990,[307,308] where both amorphous and crystalline Ni−Co−P alloys were tested in alkaline media (5 M KOH). In these reports, the authors claimed that the partial transformation of amorphous and crystalline Ni−Co−P into their metal-oxygen counterparts [$Ni(OH)_2$/NiO(OH) and Co-$(OH)_2$/CoO(OH)] might happen after 18 h of cyclic polarization, which for the first time demonstrated the precatalytic behavior of the transition metal phosphide during the OER. The interest in evaluating transition metal nitrides and phosphides as OER electrocatalysts significantly increased since 2013 and 2015, respectively, and extensive research has so far been conducted in diverse aspects including synthesis methods, chemical compositions, use of different conductive substrates and operating conditions, and so forth. In the following Sections, we divide the transition metal pnictides into two groups [nitrides (Section 4.1) and phosphides (Section 4.2)] and describe recent progress for each group toward the electrocatalytic OER process.

4.1. Transition Metal Nitrides

4.1.1. Electrode Preparation Methods. As seen in Table 3, transition metal nitride-based electrodes can be classified into two types of electrodes: powder-coated electrodes and self-supported electrodes. Generally, transition metal nitrides can be prepared by chemical and physical methods. According to reports, the chemical method is the most common approach. Here, chemical synthesis involves forming the $M-N$ bond when the precursor directly reacts with the nitrogen source at a high temperature. In contrast, physical synthesis involves using different techniques such as laser ablation, evaporation, arc discharge, radio-frequency plasma, or pulsed-laser deposition to generate the transition metal nitrides.[53,286,300,302,393] Among different categories of chemical synthesis, transition metal nitrides are usually prepared by thermal nitridation of transition metal oxide precursors with nitrogen sources such as N_2, NH_3, and N-rich organic compounds such as urea and hydrazine (i.e., gas-solid reaction and solid-state reaction).[53,286,302,348] While nitridation with N_2 requires temperatures above 1000 °C to produce transition metal nitrides, thermal ammonia reduction, also known as nitridation and thermal ammonolysis, allows for lower

https://doi.org/10.1021/acs.chemrev.3c00005
Chem. Rev. 2023, 123, 12795−13208

Table 3. Summary of the Electrocatalytic Properties, Electrochemical Testing Conditions, and Physicochemical Pre- and Post-analyses of Transition Metal Nitrides Used for Alkaline/Neutral/Acidic OER and of the Final Type of Electrocatalyst after OER Testing[a–e]

Initial Electrocatalyst	Substrate	Shape of Electrocatalyst	Deposition Type	Specific Loading / $mg \cdot cm^{-2}_{geo}$	η@10 $mA \cdot cm^{-2}_{geo}$ / mV	C_{dl} / $mF \cdot cm^{-2}_{geo}$	TOF / s^{-1} (@η or j)	Tafel Slope / $mV \cdot dec^{-1}$	Electrolyte	Pre-analysis	Post-analysis	Long-Term OER Test Conditions	Post-OER Electrocatalyst	Final Type of Electrocatalyst	Ref.
Co_3FeN_x-5	CC	Nanoleaf arrays + Nanoparticles	S	-	305	26.8	-	54.2	1 M KOH	SEM	-	-	-	-	311
Co_3FeN_x-10	CC	Nanoleaf arrays + Nanoparticles	S	-	270	31.2	48.04 at 270 mV	52.5		SEM, XRD, TEM, HAADF-STEM, EDX, XPS	SEM, TEM, XRD, XPS	40 h CA (1.5 V_{RHE}) 5000 CV cycles	FeN, Co_4N	Catalyst	
Co_3FeN_x-20	CC	Nanoleaf arrays + Nanoparticles	S	-	316	22.3	-	68.8		SEM	-	-	-	-	
Co_4N	CC	Nanoleaf arrays	S	-	337	9.8	2.24 at 270 mV	93.7		SEM, TEM, XRD, XPS	-	-	-	-	
NC-Cu-CuN	Ni foam	Nanowire	S	1.5	334	13	-	90	1 M KOH	XRD, SEM, TEM, XPS	-	-	-	-	312
NC-Ni-NiN	Ni foam	Nanowire	S	1.5	282	24	-	77		XRD, SEM, TEM, XPS	-	-	-	-	
NC-NiCu-NiCuN	Ni foam	Nanowire	S	1.5	232	39.5	-	41		XRD, SEM, EDX, TEM, XPS, Raman, N_2 ISO (BET, PSD)	XRD, SEM, TEM, XPS (after OWS)	50 h CA (1.52 V_{RHE}) 1000 CV cycles 50 h CA (cell volatege: 1.56 V, OWS)	-	Catalyst	
CoFe-NA2/NF	Ni foam	Nanosheets + Nanoparticles	S	-	250 311 (@50 $mA \cdot cm^{-2}_{geo}$) 363 (@100 $mA \cdot cm^{-2}_{geo}$)	-	-	69.9	1 M KOH	SEM, XRD, EDX, TEM, SAAED, HAADF-STEM, XPS, N_2 ISO (BET, PSD)	SEM, XRD, Raman, XPS (after OWS)	3000 CV cycles (1.2–1.8 V_{RHE}) 14 h multistep CP (10, 50, 100, 200 $mA \cdot cm^{-2}_{geo}$) 50 h CP (10 $mA \cdot cm^{-2}_{geo}$, OWS)	CoOOH, FeOOH	Precatalyst (partial oxidation)	313
CoFe-NA1/NF	Ni foam	Nanosheets + Nanoparticles	S	-	296 384 (@50 $mA \cdot cm^{-2}_{geo}$) 456 (@100 $mA \cdot cm^{-2}_{geo}$)	-	-	146.6		SEM, TEM, SAED, XPS	-	-	-	-	
CoFe-NA3/NF	Ni foam	Nanosheets + Nanoparticles	S	-	273 343 (@50 $mA \cdot cm^{-2}_{geo}$) 406 (@100 $mA \cdot cm^{-2}_{geo}$)	-	-	96.5		SEM, XPS	-	-	-	-	
CoFe-NA4/NF	Ni foam	Nanosheets + Nanoparticles	S	-	275 343 (@50 $mA \cdot cm^{-2}_{geo}$) 410 (@100 $mA \cdot cm^{-2}_{geo}$)	-	-	113.2		SEM, XPS	-	-	-	-	
CoFe-NA5/NF	Ni foam	Nanosheets + Nanoparticles	S	-	271 354 (@50 $mA \cdot cm^{-2}_{geo}$) 430 (@100 $mA \cdot cm^{-2}_{geo}$)	-	-	156.6		SEM, XRD, XPS	-	-	-	-	
Co_4N_{1-x} (N-3%)	Au glass	Thin film	S	-	560 (@3 $mA \cdot cm^{-2}_{geo}$)	-	-	82	0.1 M KOH	XRD, XRR, AFM, XPS	XPS, XRD	10 CV cycles (50 $mV \cdot s^{-1}$)	CoO_x	Precatalyst (partial oxidation)	314
Co_4N_{1-x} (N-3%-A)	Au glass	Thin film	S	-	552 (@3 $mA \cdot cm^{-2}_{geo}$)	-	-	79		XRD, XRR, AFM, XPS	XPS, XRD	10 CV cycles (50 $mV \cdot s^{-1}$)	CoO_x	Precatalyst (partial oxidation)	
Co_4N_{1-x} (N-5%)	Au glass	Thin film	S	-	578 (@3 $mA \cdot cm^{-2}_{geo}$)	-	-	87		XRD, XRR, AFM, XPS	XPS, XRD	10 CV cycles (50 $mV \cdot s^{-1}$)	CoO_x	Precatalyst (partial oxidation)	
Co_4N_{1-x} (N-7%)	Au glass	Thin film	S	-	596 (@3 $mA \cdot cm^{-2}_{geo}$)	-	-	90		XRD, XRR, AFM, XPS	XPS, XRD	10 CV cycles (50 $mV \cdot s^{-1}$)	CoO_x	Precatalyst (partial oxidation)	
NiFeLDH/V-Co_4N	Ni foam	Nanowires + Nanosheets	S	-	203 (@10 $mA \cdot cm^{-2}_{geo}$) 240 (@100 $mA \cdot cm^{-2}_{geo}$)	26.4	0.28 at 270 mV	26.0	1 M KOH	SEM, TEM, EDX, XPS	SEM, XRD, XPS, ICP-OES	24 h multistep CA	NiFe LDH, V-doped Co_3O_4	Precatalyst (partial oxidation)	315
NiFeLDH/Co_4N	Ni foam	Nanowires + Nanosheets	S	-	230 340 (@100 $mA \cdot cm^{-2}_{geo}$)	-	-	-		XPS	-	-	-	-	
V-Co_4N	Ni foam	Nanowires	S	-	256 363 (@100 $mA \cdot cm^{-2}_{geo}$)	17.9	0.03 at 270 mV	64.2		SEM, XPS	-	-	-	-	
Co_4N	Ni foam	Nanowires	S	-	296	-	-	91.5		SEM	-	-	-	-	
NiFeLDH/V-Co_4N	CC	Nanowires + Nanosheets	S	-	207	-	-	-		-	-	-	-	-	
Co/VN-500	GC	Hexagon sheets + nanoparticles	P	0.28	350	1.39	-	52.2	1 M KOH	SEM, XRD, Raman	-	-	-	-	316
Co/VN-600	GC	Hexagon sheets + nanoparticles	P	0.28	320	3.87	-	50.4		SEM, XRD, XPS, TEM, EDX	*In-Situ* Raman, SEM,	40 h CP (10 $mA \cdot cm^{-2}_{geo}$)	Co_3O_4, $Co_2V_2O_7$	Precatalyst (oxidation + $Co_2V_2O_7$ dissolution)	
Co/VN-700	GC	Hexagon sheets + nanoparticles	P	0.28	340	2.34	-	66		SEM, XRD, Raman	-	-	-	-	
Co/VN-900	GC	Hexagon sheets + nanoparticles	P	0.28	370	2.26	-	82		SEM, XRD, Raman	-	-	-	-	
Co_4N	GC	Nanorods	P	0.125	333	-	-	75	1 M KOH	XRD, SEM	-	-	-	-	317
Mo_3N_2	GC	Nanorods	P	0.125	430	-	-	93		XRD, SEM	-	-	-	-	

https://doi.org/10.1021/acs.chemrev.3c00005
Chem. Rev. 2023, 123, 12795−13208

Table 3. continued

Initial Electrocatalyst	Substrate	Shape of Electrocatalyst	Deposition Type	Specific Loading / $mg \cdot cm^{-2}_{geo}$	η@10 $mA \cdot cm^{-2}_{geo}$ / mV	C_{dl} / $mF \cdot cm^{-2}_{geo}$	TOF / s^{-1} (@η or j)	Tafel Slope / $mV \cdot dec^{-1}$	Electrolyte	Pre-analysis	Post-analysis	Long-Term OER Test Conditions	Post-OER Electrocatalyst	Final Type of Electrocatalyst	Ref.
Co_3Mo_3N	GC	1 D porous rods	P	0.125	290	-	-	60		XRD, SEM, TEM, HAADF-STEM, EELS, EDX	XRD, SEM, XPS, TEM, EELS	24 h CA (cell voltage: 1.63 V, OWS)	Co oxide, Oxidized Mo species	Precatalyst (partial oxidation)	317
$CoMoN_x$-300	Ni foam	Nanosheet arrays	S	1.35	290 370 (@100 $mA \cdot cm^{-2}_{geo}$)	14.65	0.27 at 270 mV	77.1	1 M KOH	SEM, ICP-MS	-	-	-	-	318
$CoMoN_x$-400	Ni foam	Nanosheet arrays	S	1.35	280 360 (@100 $mA \cdot cm^{-2}_{geo}$)	26.96	0.42 at 270 mV	81.2		SEM, ICP-MS	-	-	-	-	
$CoMoN_x$-500	Ni foam	Nanosheet arrays	S	1.35	231 300 (@100 $mA \cdot cm^{-2}_{geo}$)	33.64	1.57 at 270 mV	50.6		SEM, TEM, EDX, XPS, ISO (BET), ICP-MS	SEM, XPS	5000 CV cycles 100 h CP (10 $mA \cdot cm^{-2}_{geo}$)	CoOOH, MoOOH	Precatalyst (partial oxidation)	
$CoMoN_x$-600	Ni foam	Nanosheet arrays	S	1.35	291 365 (@100 $mA \cdot cm^{-2}_{geo}$)	13.93	0.28 at 270 mV	80.2		SEM, ICP-MS	-	-	-	-	
Co_2N	Ni foam	Microparticles	P	1.35	338	-	-	112.1		SEM	-	-	-	-	
Mo_2N	Ni foam	Microparticles	P	1.35	387	-	-	117.0		SEM	-	-	-	-	
Co_2N-Mo_2N	Ni foam	Microparticles	P	1.35	312	-	-	102.2		-	-	-	-	-	
Ni_3N@OOH	CC	Aggregated nanoparticles	S	-	348 (@50 $mA \cdot cm^{-2}_{geo}$)	11.2	0.005 at 1330 mV	62	1 M KOH	SEM, TEM, XRD, XPS, EIS	-	20 h multistep CP (10, 20, 50, and 100 $mA \cdot cm^{-2}_{geo}$)	-	-	319
NiVN@OOH	CC	Nanosheet arrays + Nanoparticles	S	-	233 (@50 $mA \cdot cm^{-2}_{geo}$)	13.7	0.005 at 230 mV	33		SEM, TEM, EDX, XRD, XPS, Raman	SEM, STEM, XRD, XPS, ICP-MS, EDX	20 h multistep CP (10, 20, 50, and 100 $mA \cdot cm^{-2}_{geo}$)	NiVOOH	Precatalyst (partial oxidation + Ni & V dissolution)	
Ni_3N@Ni_3VN	CC	Nanosheet arrays + Nanoparticles	S	-	-	-	-	-		SEM, XRD, TEM, STEM EDX, XPS, ICP-MS	SEM, TEM, EDX, XRD, XPS, Raman	20 LSV scans (0.2–0.9 $V_{Hg/HgO}$)	NiVOOH	Precatalyst (partial oxidation)	
Ni_3N	CC	Aggregated nanoparticles	S	-	-	-	-	-		SEM, TEM, HAADF, EDX, XPS, ICP-MS	SEM, TEM, XRD, XPS	20 LSV scans (0.2–0.9 $V_{Hg/HgO}$)	NiOOH	Precatalyst (partial oxidation)	
Ni_2Fe_2N@N-CS	CP	Nanoparticles	P	-	264	22.7	-	47.8	1 M KOH	TEM, EDX, XPS, N_2 ISO (BET, PSD)	TEM, EDX, XRD, XPS	24 h CP (10 $mA \cdot cm^{-2}_{geo}$)	NiFe (oxy)hydroxide	Precatalyst (partial oxidation)	320
H-Ni_2Fe_2N/Ni_3Fe@N-CS	CP	Nanoparticles	P	-	251	23.5	-	35.0		TEM, EDX, XPS, N_2 ISO (BET, PSD)	TEM, EDX, XRD, XPS	24 h CP (10 $mA \cdot cm^{-2}_{geo}$)	NiFe (oxy)hydroxide	Precatalyst (partial oxidation)	
H-Ni_3Fe/Ni_2Fe_2N ANPs	CP	Nanoparticles	P	-	264	20.3	-	47.4		TEM, EDX, XPS, N_2 ISO (BET, PSD)	TEM, EDX, XRD, XPS	24 h CP (10 $mA \cdot cm^{-2}_{geo}$)	NiFe (oxy)hydroxide	Precatalyst (partial oxidation)	
$Cu_{0.5}NFe_{3.5}$	CP	Microparticles	P	2	359	3.73	-	91	1 M KOH	XRD, XPS, SEM	XPS, Raman	-	FeOOH	Precatalyst (partial oxidation)	321
$Cu_{0.5}NFe_3Ni_{0.5}$	CP	Microparticles	P	2	244 310 (@100 $mA \cdot cm^{-2}_{geo}$)	4.53	-	59		XRD, XPS, SEM. TEM, HAADF, EDX	Raman, XPS, TEM	30 h multistep CA	FeNiOOH	Precatalyst (partial oxidation)	
Fe_3N	Ni foam	Nano-spindle	P	1	282	1.23	-	40.7	1 M KOH	SEM, XRD, N_2 ISO (BET, PSD)	-	-	-	-	322
Fe_3N@Ni_2Co-LDHs	Ni foam	Nano-spindle + nanosheets	P	1	240	6.14	-	37.5		SEM, XRD, TEM, HR-TEM, STEM, EDX, XPS, TGA, N_2 ISO (BET, PSD)	TEM, XPS	2000 CV cycles	Oxidized metal species (Ni^{3+}, Co^{3+}), Fe_3N	Precatalyst (partial oxidation)	
Ni-N	CP	Nanosheet	S	-	280 410 (@100 $mA \cdot cm^{-2}_{geo}$)	0.386	-	107	1 M KOH	SEM, TEM, HAADF-STEM, EDX, XRD, XPS	-	-	-	-	323
$NiFe_{0.01}$-N	CP	Nanosheet	S	-	360 (@100 $mA \cdot cm^{-2}_{geo}$)	0.437	-	84		SEM	-	-	-	-	
$NiFe_{0.05}$-N	CP	Nanosheet	S	-	238 320 (@100 $mA \cdot cm^{-2}_{geo}$)	0.476	-	76		SEM, AFM, EDX, TEM, SAED, XRD, XPS	SEM, XPS, EDX	4200 s multistep CA (0.55 to 0.7 $V_{Ag/AgCl}$, an increment of 0.25 V) 24 h CA	Ni–Fe (oxy)hydroxide	Precatalyst (partial oxidation)	
$NiFe_{0.1}$-N	CP	Nanosheet	S	-	340 (@100 $mA \cdot cm^{-2}_{geo}$)	0.435	-	80		SEM	-	-	-	-	
$NiFe_{0.2}$-N	CP	Nanosheet	S	-	350 (@100 $mA \cdot cm^{-2}_{geo}$)	-	-	83		SEM	-	-	-	-	
Fe-N	CP	Nanosheet	S	-	430	0.358	-	206		-	-	-	-	-	
Ni_3N	Ni foam	Rough particulate surface	S	-	442.5 (@15 $mA \cdot cm^{-2}_{geo}$)	3.44	-	-	Fe-purified 1 M KOH	XRD, SEM, EDX, XPS	XRD, SEM, EDX, XPS	1000 CV cycles (50 $mV \cdot s^{-1}$, 0.25–0.75 $V_{Hg/HgO}$)	NiOOH	Precatalyst (partial oxidation)	90, 324
					335.8 (@15 $mA \cdot cm^{-2}_{geo}$)	7.9	-	-	1 M KOH		XRD, XPS	300 CV cycles (50 $mV \cdot s^{-1}$, 0.25–0.70 $V_{Hg/HgO}$)	$Ni_{1-x}Fe_xOOH$	Precatalyst (partial oxidation)	
Ni_3N	Ni foam	Rough particulate surface	S	-	315.7 (@15 $mA \cdot cm^{-2}_{geo}$)	0.59	-	-	1 M KOH (flow cell)	XRD, XPS, SEM	XRD, XPS, SEM	~ 20 h CP (10 $mA \cdot cm^{-2}_{geo}$)	$Ni_{1-x}Fe_xOOH$	Precatalyst (partial oxidation)	
Ni_3N-CV (after 1000 cycles)	Ni foam	Porous particulate surface	S	-	463.2 (@15 $mA \cdot cm^{-2}_{geo}$)	9.87	-	-	Fe-purified 1 M KOH	XRD, SEM, EDX, XPS	-	-	-	-	
Ni_3N-CV (after 300 cycles)	Ni foam	-	S		314.3 (@15 $mA \cdot cm^{-2}_{geo}$)	13.9	-	-	1 M KOH	XRD, XPS	-	-	-	-	
Ni_3N-CP (after 20 h)	Ni foam	Porous particulate surface	S	-	293.3 (@15 $mA \cdot cm^{-2}_{geo}$)	2.12	-	-	1 M KOH (flow cell)	XRD, SEM, EDX, XPS	-	-	-	-	
BGO/Ni_3N (1:1)	CP	Nanoparticles + nanosheets	P	0.8	320	-	-	-	1 M KOH	EDX	-	-	-	-	325
BGO/Ni_3N (3:1)	CP	Nanoparticles + nanosheets	P	0.8	280	0.4	-	77.9		SEM, TEM, TEM, XRD, Raman, XPS, EDX	XRD	24 h CP (10 $mA \cdot cm^{-2}_{geo}$) 48 h CP (20 $mA \cdot cm^{-2}_{geo}$) 10 h CP (100 $mA \cdot cm^{-2}_{geo}$)	NiOOH	Precatalyst (partial oxidation)	

https://doi.org/10.1021/acs.chemrev.3c00005
Chem. Rev. 2023, 123, 12795−13208

Table 3. continued

Initial Electrocatalyst	Substrate	Shape of Electrocatalyst	Deposition Type	Specific Loading / $mg \cdot cm^{-2}_{geo}$	η@10 $mA \cdot cm^{-2}_{geo}$ / mV	C_{dl} / $mF \cdot cm^{-2}_{geo}$	TOF / s^{-1} (@η or f)	Tafel Slope / $mV \cdot dec^{-1}$	Electrolyte	Pre-analysis	Post-analysis	Long-Term OER Test Conditions	Post-OER Electrocatalyst	Final Type of Electrocatalyst	Ref.
BGO/Ni_3N (5:1)	CP	Nanoparticles + nanosheets	P	0.8	350	-	-	-		EDX	-	-	-	-	
Ni_3N	CP	Nanoparticles	P	0.8	380	0.03	-	-		XPS	-	-	-	-	325
GO/Ni_3N	CP	Nanoparticles + nanosheets	P	0.8	390	-	-	170.8		-	-	-	-	-	
Ni_3FeN	GC	Nanoflowers	P	-	230	-	-	29	1 M KOH	XPS, SEM, XRD	-	-	-	-	
Ni_3FeN/Ni	GC	Nanoflowers	P	-	200	-	-	36		XRD, XPS, SEM, TEM, STEM, EDX, XRD	TEM, HRTEM, XPS, EDX	5.5 h CA (1.43 V_{RHE}) 1000 CV cycles	NiFeOOH/Ni_3FeN /Ni heterostructures	Precatalyst (partial oxidation)	326
Ni_2Mo_3N	GC	Micro particles	P	-	~292	-	-	-	1 M KOH	XRD, TEM, SAED, HAADF-STEM, EELS, XPS, EDX, SEM	-	10 h CP (100 $mA \cdot cm^{-2}_{geo}$)	-	-	327
					270	3.27	-	59	0.1 M KOH		TEM, SAED, HR-TEM, HAADF-STEM, EELS, XPS	10 h CA > 5 h CP	Oxide rich layer [Ni^{2+}, Ni^{2+}, Mo-N, Oxidized Mo (Mo^{4+}, Mo^{6+}) species]	Precatalyst (partial oxidation)	
Ni_3N	GC	-	P	-	360	0.87	-	91		XRD	-	-	-	-	
Mo_2N	GC	-	P	-	450	2.34	-	107		XRD	-	-	-	-	
Co-NiMoN-400	Ni foam	Nanowire	P	3.5	294	14.86	-	73.0	1 M KOH	XRD, SEM, EDX, TEM, XPS, ICP-OES	SEM, EDX, TEM, XPS	10 h CA (1.547 V_{RHE}) 1000 CV cycles (50 $mV \cdot s^{-1}$)	NiO_x, $Ni(OH)_2$	Precatalyst (partial oxidation)	328
NiMoN-400	Ni foam	Nanowire	P	3.5	326	10.46	-	85.6		XRD, SEM, EDX, TEM, XPS, ICP-OES	-	-	-	-	
Co_xN-$VN_{1-y}O_z$ (CVN/CC)	CC	Nanoflake	S	2.03	263	16.7	-	64.1	1 M KOH	XRD, SEM, TEM, XPS, EDX, ICP-OES	SEM, TEM, XPS, ICP-OES	20 h CA (1.56 V_{RHE})	CoO_x [$Co(OH)_2$, CoOOH, Co_3O_4]	Precatalyst (partial oxidation)	329
Co_xN (CN/CC)	CC	Nanoflake	S	2.45	327	13.7	-	99.2		XRD, SEM, TEM, XPS, EDX, ICP-OES	-	-	-	-	
$NiMo_4N_5$@Ni-1	Ni foam	Nanorod	S	2.5	280	30.1	-	33.6	1 M KOH	XRD, SEM, EDX, TEM, XPS, FTIR, ICP-AES	XRD, SEM, TEM, EDX, FTIR	24 h CA (1.47 V_{RHE})	MoO_x, NiOOH	Precatalyst (partial oxidation)	330
$NiMo_4N_5$@Ni-2	Ni foam	Nanorod	S	2.5	300	17.9	-	44.1			-	-	-	-	
$NiMo_4N_5$@Ni-3	Ni foam	Nanorod	S	2.5	320	14.3	-	59.9			-	-	-	-	
Co_3N@amorphous N-C	CP	Nanoparticle	P	2.6	280	39	0.0023 at 300 mV	69.6	1 M KOH	XRD, SEM, EDX, TEM, XPS, FTIR, ICP-OES, N_2 ISO (BET, PSD), NH_3-TPD	XRD, TEM, XPS	24 h CP (20 $mA \cdot cm^{-2}_{geo}$)	CoOOH, CoO_x	Precatalyst (partial oxidation)	331
Co-N@N-C	CP	Nanoparticle	P	2.6	318	9	0.00035 at 300 mV	86.4			-	-	-	-	
NiMoN@NiFeN	Ni foam	Nanoparticle + Nanorod	S	1270	~170 (@100 $mA \cdot cm^{-2}_{geo}$) 337 (@500 $mA \cdot cm^{-2}_{geo}$)	238.7	0.09 at 300 mV	58.6	1 M KOH	XRD, SEM, EDX, TEM, XPS	SEM, TEM, EDX, XPS, *In-Situ* Raman	48 h CA [1.507 (24 h), 1.567 V_{RHE} (24 h)]	$(Ni,Fe)O_x$, $(Ni,Fe)(OH)_2$, (Ni,Fe)OOH	Precatalyst (partial oxidation)	332
NiFeN	Ni foam	Nanoparticle	S	-	~290	65.4	-	68.9		SEM, XRD, XPS	-	-	-	-	
NiMoN	Ni foam	Nanorod	S	-	-	188.3	-	82.1		SEM, XRD, XPS	-	-	-	-	
NiMoN@NiFeN	Ni foam	Nanoparticle + Nanorod	S	1270	286 (@100 $mA \cdot cm^{-2}_{geo}$) 347 (@500 $mA \cdot cm^{-2}_{geo}$) 377 (@1000 $mA \cdot cm^{-2}_{geo}$)	-	-	-	1 M KOH + 0.5 M NaCl	XRD, SEM, EDX, TEM, XPS	-	-	-	-	
		Nanoparticle + Nanorod	S	1270	307 (@100 $mA \cdot cm^{-2}_{geo}$) 369 (@500 $mA \cdot cm^{-2}_{geo}$) 398 (@1000 $mA \cdot cm^{-2}_{geo}$)	-	-	-	1 M KOH + Seawater		-	-	-	-	
Fe_2Ni_2N/rGO NHSs	CP	Nanosheet	P	2.6	290	18.2	-	49.1	0.1 M KOH	XRD, SEM, EDX, TEM, FTIR, Raman, XPS	SEM, EDX, TEM, XPS	24 h CP (10 $mA \cdot cm^{-2}_{geo}$)	$(Ni,Fe)O_x$, $(Ni,Fe)(OH)_2$, (Ni,Fe)OOH	Precatalyst (partial oxidation)	333
Fe_2Ni_2N NPs	CP	Nanoparticle	P	2.6	335	7.4	-	72.9			-	-	-	-	
CoN-400/CC	CC	Nanowire	S	-	251	9.94	0.5 at 343 mV	75.4	1 M KOH	XRD, SEM, EDX, TEM, XPS	XRD, XPS [after 2 h CP (10 $mA \cdot cm^{-2}_{geo}$)]	35 h CA (1.498 V_{RHE})	CoOOH	Precatalyst (partial oxidation)	334
CoN-300/CC	CC	Nanowire	S	-	265	7.09	0.5 at 365 mV	109.8		XRD, SEM, EDX, TEM, XPS	-	-	-	-	
CoN-500/CC	CC	Nanowire	S	-	326	6.67	0.5 at 421 mV	112.6		XRD, SEM, EDX, TEM, XPS	-	-	-	-	
NiMoN/NF700	Ni foam	Nanowire	S	1.2	~260 290 (@50 $mA \cdot cm^{-2}_{geo}$)	82.68	-	54	1 M KOH	XRD, SEM, EDX, XPS, TEM	XRD, SEM, EDX, XPS, TEM	48 h CP (10 $mA \cdot cm^{-2}_{geo}$) 5 h CP (10–50 $mA \cdot cm^{-2}_{geo}$) 2000 CV cycles (2 $mV \cdot s^{-1}$)	-	Precatalyst (partial oxidation)	335
NiMoN/NF	Ni foam	Coraline nanostructure	S	1.2	~270	24.56	-	76		XRD, SEM, EDX	-	-	-	-	
NiMoN/NF	Ni foam	Nanorod (~200 nm)	S	1.2	~310	47.19	-	81		XRD, SEM, EDX	-	-	-	-	
NiMoN/NF	Ni foam	Nanoparticle	S	1.2	~350	5.09	-	128		XRD, SEM, EDX	-	-	-	-	
CoN/CC	CC	Nanoflower	S	2.3	280	20.48	-	84	1 M KOH	XRD, SEM	-	-	-	-	
Ni_3N/CC (NiN/CC)	CC	Nanoparticle	S	2.5	390	11.1	-	120		XRD, SEM	-	-	-	-	336
Ni_3N-CoN/CC (NCN/CC)	CC	Nanograss	S	2.1	247	29.07	-	63		XRD, SEM, EDX, XPS, TEM, ICP-OES	SEM, TEM, XPS, ICP-OES	24 h CP (10 $mA \cdot cm^{-2}_{geo}$) 1000 CV cycles	$(Ni,Co)(OH)_2$, (Ni,Co)OOH	Precatalyst (partial oxidation)	
NC@CoN/Cu_3N/CF	Cu foam	Nanotube array	S	0.8 (Co)	257 303 (@50 $mA \cdot cm^{-2}_{geo}$)	103.3	-	75.7	1 M KOH	XRD, SEM, EDX, TEM, XPS, ICP-MS, Raman	XRD, SEM, EDX, XPS	20 h CP (20 $mA \cdot cm^{-2}_{geo}$)	CuO, $Cu(OH)_2$, CoO_x	Precatalyst (partial oxidation)	337

https://doi.org/10.1021/acs.chemrev.3c00005
Chem. Rev. 2023, 123, 12795−13208

Table 3. continued

Initial Electrocatalyst	Substrate	Shape of Electrocatalyst	Deposition Type	Specific Loading / $mg \cdot cm^{-2}_{geo}$	η@10 $mA \cdot cm^{-2}_{geo}$ / mV	C_{dl} / $mF \cdot cm^{-2}_{geo}$	TOF / s^{-1} (@η or j)	Tafel Slope / $mV \cdot dec^{-1}$	Electrolyte	Pre-analysis	Post-analysis	Long-Term OER Test Conditions	Post-OER Electrocatalyst	Final Type of Electrocatalyst	Ref.
CoN/Cu_3N/CF	Cu foam	Nanotube array	S	-	260	94.4	-	114.6		XRD, SEM, EDX, TEM, XPS, ICP-MS, Raman	-	-	-	-	337
CoN/CF	Cu foam	Nanorod	S	-	320	30.2	-	123.9		XRD, SEM, EDX, TEM, XPS, ICP-MS	-	-	-	-	
Cu_3N/CF	Cu foam	Nanotube	S	-	320	77.8	-	235.7		XRD, SEM, EDX, TEM, XPS, ICP-MS	-	-	-	-	
Ni_3N-NiMoN-4	CC	Nanosheet	S	1.63	300	204	-	121		XRD, SEM, EDX, TEM, XPS, ICP-OES	-	-	-	-	
Ni_3N-NiMoN-5	CC	Nanosheet	S	1.63	277	241	-	118	1 M KOH	XRD, SEM, EDX, TEM, XPS, ICP-OES	XRD, XPS	20 h CA 20, 200, 1000, 5000 CV cycles	NiOOH, MoO_x (Mo^{6+} species)	Precatalyst (partial oxidation)	338
Ni_3N-NiMoN-6	CC	Nanosheet	S	1.63	343	121	-	136		XRD, SEM, EDX, TEM, XPS, ICP-OES	-	-	-	-	
Ni_3N	CC	Nanosheet	S	1.63	~350	-	-	112		XRD, SEM	-	-	-	-	
Co_3N/NCNT	GC	Nanoparticle	P	0.286	400	-	-	62.5		TEM	-	-	-	-	
$Ni_{0.5}Co_{2.5}N$/NCNT (SS/NCNT)	GC	Nanoparticle	P	0.286	324	-	-	48.9		XRD, SEM, EDX, TEM, N_2 ISO (BET, PSD), Raman	XRD, SEM, XPS	60000 s CA (~ 1.55 V_{RHE})	$Ni(OH)_2$/NiOOH, $Co(OH)_2$/CoOOH, $-NO_3$/$-NO_2$ species	Precatalyst (partial oxidation)	
$NiCo_2N$/NCNT	GC	Nanoparticle	P	0.286	330	-	-	83.25	1 M KOH	TEM	-	-	-	-	339
$Ni_{1.5}Co_{1.5}N$/NCNT	GC	Nanoparticle	P	0.286	390	-	-	88.1		TEM	-	-	-	-	
$Ni_{2.5}Co_{0.5}N$/NCNT	GC	Nanoparticle	P	0.286	390	-	-	100.3		TEM	-	-	-	-	
Ni_2CoN/NCNT	GC	Nanoparticle	P	0.286	360	-	-	102.1		TEM	-	-	-	-	
Ni_3N/NCNT	GC	Nanoparticle	P	0.286	360	-	-	105.6		TEM	-	-	-	-	
DR-Ni_3FeN/N-G	GC	Nanosheet	P	0.1	250	3.13	0.46 at 350 mV	38		XRD, SEM, EDX, TEM, XPS, HAADF-STEM, Raman	XRD, TEM, XPS, HAADF-STEM	2000 CV cycles	NiOOH, FeOOH	Precatalyst (partial oxidation)	
Ni_3FeN/N-G	GC	Nanosheet	P	0.1	320	1.46	0.08 at 350 mV	45	1 M KOH		-	-	-	-	340
Ni_3N/N-G	GC	-	P	0.1	420	-	-	78		XRD, Raman	-	-	-	-	
Fe_2N/N-G	GC	-	P	0.1	440	-	-	66		XRD, Raman	-	-	-	-	
$Co_{3.47}N$@N-PC	GC	Nanoparticle	P	0.453	248	24.8	0.054 at 280 mV	72	1 M KOH	XRD, SEM, TEM, EDX, XPS, N_2 ISO (BET, PSD), Raman	TEM, EDX, XPS	10 h CA (1.478 V_{RHE})	CoO_x, $Co(OH)_2$	Precatalyst (partial oxidation)	341
CoFe(3:1)-N	GC	Nanosheet	P	0.4586	200	93.59	-	42.44		XRD, SEM, TEM, N_2 ISO (BET, PSD), EDX, XPS	SEM, TEM, XPS	3000 s CP (10 $mA \cdot cm^{-2}_{geo}$) 3000 CV cycles (1.30−1.48 V_{RHE}) 10 h CA (1.43 V_{RHE})	$(Co,Fe)O_x$, $(Co,Fe)(OH)_2$,	Precatalyst (partial oxidation)	
CoFe(1:1)-N	GC	Nanosheet	P	0.4586	250	23.48	-	51.85		XRD	-	-	-	-	
CoFe(1:3)-N	GC	Nanosheet	P	0.4586	340	20.82	-	68.65		XRD	-	-	-	-	
CoNi(3:1)-N	GC	Nanosheet	P	0.4586	320	21.67	-	70.45		XRD, SEM, N_2 ISO (BET, PSD), XPS	-	-	-	-	
CoNi(1:1)-N	GC	-	P	0.4586	350	-	-	75.35		-	-	-	-	-	
CoNi(1:3)-N	GC	-	P	0.4586	410	-	-	82.58		-	-	-	-	-	
CoMn(3:1)-N	GC	Nanosheet	P	0.4586	330	21.19	-	73.53		XRD, SEM, N_2 ISO (BET, PSD), XPS	-	-	-	-	
CoMn(1:1)-N	GC	-	P	0.4586	370	-	-	75.47	1 M KOH	-	-	-	-	-	342
CoMn(1:3)-N	GC	-	P	0.4586	400	-	-	79.7		-	-	-	-	-	
CoZn(3:1)-N	GC	Nanosheet	P	0.4586	350	20.31	-	75.06		XRD, SEM, N_2 ISO (BET, PSD), XPS	-	-	-	-	
CoZn(1:1)-N	GC	-	P	0.4586	360	-	-	77.67		-	-	-	-	-	
CoZn(1:3)-N	GC	-	P	0.4586	390	-	-	82.72		-	-	-	-	-	
CoFe(4:1)-N	GC	-	P	0.4586	233	-	-	-		-	-	-	-	-	
CoFe(5:1)-N	GC	-	P	0.4586	262	-	-	-		-	-	-	-	-	
CoFe(2:1)-N	GC	-	P	0.4586	290	-	-	-		-	-	-	-	-	
$Co_{5.47}N$	GC	-	P	0.4586	344	20.8	-	73.23		XRD, XPS	-	-	-	-	
Fe_3N	GC	-	P	0.4586	-	-	-	130.69		-	-	-	-	-	
Ni_3FeN	GC	Nanosheet	P	0.3	-	11.22	-	51		XRD, SEM, EDX, TEM, AFM, N_2 ISO (BET, PSD)	XRD, TEM, XPS	25 h CP (100 $A \cdot g^{-1}$) 1000 CV cycles	$(Ni,Fe)(OH)_2$, $(Ni,Fe)O_x$	Precatalyst (partial oxidation)	343
Ni_3CoN	GC	Nanosheet	P	0.3	-	10.76	-	55	1 M KOH		-	~17 h CP (100 $A \cdot g^{-1}$)	-	-	
Ni_3MnN	GC	Nanosheet	P	0.3	-	8.71	-	64			-	~24 h CP (100 $A \cdot g^{-1}$)	-	-	
NC@$CuCo_2N_y$/CF	CFC	Nanosheet	S	2	230	150.9	-	84		XRD, SEM, EDX, TEM, XPS	XRD, SEM, EDX, XPS	2000 CV cycles	$(Cu,Co)O_x$	Precatalyst (partial oxidation)	
NC@CoN_x/CF	CFC	Nanosheet	S	2	310	101.5	-	101	1 M KOH	XRD, SEM, EDX, TEM, XPS	-	-	-	-	344
NC@CuN_x/CF	CFC	Nanosheet	S	2	380	-	-	97		XRD, SEM, EDX, TEM, XPS	-	-	-	-	
FeNi-N/CFC	CFC	Nanosheet	S	0.25	232	1.79	0.2 at 300 mV	115	1 M KOH	XRD, SEM, EDX, TEM, XPS, ICP-OES	SEM, XPS, ICP-OES	32 h CA (1.485 V)	NiOOH, FeOOH	Precatalyst (partial oxidation)	345
Ni-N/CFC	CFC	Nanosheet	S	0.25	308	1.41	0.2 at 300 mV	116		XRD, SEM, EDX, TEM, XPS, ICP-OES	-	-	-	-	
Co-Fe-N@MWCNT	GC	Nanoparticle	P	0.24	290	14.1	-	32		XRD, SEM, TEM, XPS, ICP-MS, EA, N_2 ISO (BET, PSD)	XRD, TEM, XPS	20000 s CA	FeOOH, CoOOH	Precatalyst (partial oxidation)	
Co-Fe-N	GC	Nanoparticle	P	0.24	-	0.722	-	60	1 M KOH	XRD	-	-	-	-	
Co-N@MWCNT	GC	Nanoparticle	P	0.24	350	8.86	-	66		XRD	-	-	-	-	
Fe-N@MWCNT	GC	Nanoparticle	P	0.24	-	2.44	-	75		XRD	-	-	-	-	346
Co-Fe-N@MWCNT	GC	Nanoparticle	P	0.24	320	-	-	51		XRD	-	-	-	-	
Co-Fe-N	GC	Nanoparticle	P	0.24	-	-	-	86	0.1 M KOH	XRD	-	-	-	-	
Co-N@MWCNT	GC	Nanoparticle	P	0.24	420	-	-	103		XRD	-	-	-	-	

https://doi.org/10.1021/acs.chemrev.3c00005
Chem. Rev. 2023, 123, 12795−13208

Table 3. continued

Initial Electrocatalyst	Substrate	Shape of Electrocatalyst	Deposition Type	Specific Loading / $mg \cdot cm^{-2}_{geo}$	η@10 $mA \cdot cm^{-2}_{geo}$ / mV	C_{dl} / $mF \cdot cm^{-2}_{geo}$	TOF / s^{-1} (@η or j)	Tafel Slope / $mV \cdot dec^{-1}$	Electrolyte	Pre-analysis	Post-analysis	Long-Term OER Test Conditions	Post-OER Electrocatalyst	Final Type of Electrocatalyst	Ref.
Fe-N@MWCNT	GC	Nanoparticle	P	0.24	470	-	-	109		XRD	-	-	-	-	346
hNi$_3$N	Ni foam	Nanocoral	S	1.51	325	5.79	-	50	1 M KOH	XRD, SEM, TEM, Raman, XPS	SEM, TEM, XPS	30 h CA [1.555 (10 h), 1.565 (10 h), 1.575 V_{RHE} (10 h)]	NiOOH	Precatalyst (partial oxidation)	347
Ni$_3$N/NC	GC	Nanoparticle	P	0.28	310	0.053	-	-	1 M KOH	XRD, SEM, EDX, TEM, N_2 ISO (BET, PSD), XPS, ICP-AES, Raman	XPS, Raman	10 h CP (10 $mA \cdot cm^{-2}_{geo}$)	NiOOH, NiO$_x$	Precatalyst (partial oxidation)	348
NiMoN-550	CP	Nanotube	P	3.5	295	-	1 at 300 mV	94	1 M KOH	XRD, SEM, TEM, EDX, XPS, ICP-OES	SEM, TEM, EDX, XPS	20 h CP (50−200 $mA \cdot cm^{-2}_{geo}$) 1000 CV cycles 20 h CA (1.525 V_{RHE})	NiOOH	Precatalyst (partial oxidation)	349
NiMoN-350	CP	Nanotube	P	3.5	260	-	0.42 at 300 mV	107		SEM	-	-	-	-	
NiMoN-450	CP	Nanotube	P	3.5	303	-	0.75 at 300 mV	98		SEM	-	-	-	-	
NiMoN-650	CP	Nanotube	P	3.5	355	-	0.31 at 300 mV	100		SEM	-	-	-	-	
NiMoN-750	CP	Nanotube	P	3.5	441	-	0.065 at 300 mV	157		SEM	-	-	-	-	
Ni-N	CP	-	P	3.5	330	-	-	-		XRD	-	-	-	-	
Mo-N	CP	-	P	3.5	570	-	-	-		XRD	-	-	-	-	
Ni$_3$N@Ni-Ci NA/CC	CC	Nanoarray	S	1.8	400	5.58	0.1 at 480 mV	143	1 M $KHCO_3$ (pH = 8.3)	XRD, SEM, EDX, TEM, XPS	TEM	12 h CA (1.71, 1.83 V_{RHE}) 6000 s CP (1−50.5 $mA \cdot cm^{-2}_{geo}$)	Ni bicarbonate (Ni-Ci)	Precatalyst (partial oxidation)	350
Ni$_3$N NA/CC	CC	Nanoarray	S	1.8	540	4.16	0.028 at 480 mV	162		XRD, SEM, EDX, TEM, XPS	XPS	Oxidative polarization (5 $mV \cdot s^{-1}$)	Ni bicarbonate (Ni-Ci)	Precatalyst (partial oxidation)	
Ni$_3$FeN	GC	Nano/microstructure	P	0.13	355	-	-	70	0.1 M KOH	XRD, SEM, EDX, TEM, N_2 ISO (BET, PSD), XPS	XPS	12000 s CA (1.60 V_{RHE})	-	Precatalyst (partial oxidation)	351
Co$_4$N	GC	-	P	0.285	370	-	-	80	0.1 M KOH	XRD, STEM, EDX, XPS, TEM, EELS	XRD, XPS	13000 s CA (1.667 V_{RHE}) 1000 CV cycles	Co$_4$N/CoOOH/CoO_2	Precatalyst (partial oxidation)	352
Co$_3$N	GC	-	P	0.285	470	-	-	130		XRD, STEM, EDX, XPS, TEM, EELS	XRD, XPS	13000 s CA (1.667 V_{RHE}) 1000 CV cycles	Co$_3$N/CoOOH/CoO_2	Precatalyst (partial oxidation)	
Co$_2$N	GC	-	P	0.285	510	-	-	145		XRD, STEM, EDX, XPS, TEM, EELS	XRD, XPS	13000 s CA (1.667 V_{RHE}) 1000 CV cycles	Co$_2$N/CoOOH/CoO_2	Precatalyst (partial oxidation)	
Co$_4$N	GC	-	P	0.285	330	-	-	58	1 M KOH	XRD, STEM, EDX, XPS, TEM, EELS	-	-	-	-	
Co$_3$N	GC	-	P	0.285	380	-	-	72		XRD, STEM, EDX, XPS, TEM, EELS	-	-	-	-	
Co$_2$N	GC	-	P	0.285	390	-	-	80		XRD, STEM, EDX, XPS, TEM, EELS	-	-	-	-	
CoN (30 s)	Ni foam	Nanowire	S	1.5	304	92	-	72	1 M KOH	XRD, XPS, SEM, TEM	-	-	-	-	353
CoN (1 min)	Ni foam	Nanowire	S	1.5	290	92	-	70		XRD, XPS, SEM, TEM	SEM, XPS, TEM, Raman	30 h CP [10 (10 h), 30 (10 h), 50 $mA \cdot cm^{-2}_{geo}$ (10 h)]	CoOOH, CoO_x (Co_3O_4)	Precatalyst (partial oxidation)	
CoN (3 min)	Ni foam	Nanowire	S	1.5	306	92	-	70		XRD, XPS, SEM, TEM	-	-	-	-	
Co_3FeN_x	Ni foam	Nanowire	S	0.8	222 (@20 $mA \cdot cm^{-2}_{geo}$) 241 (@50 $mA \cdot cm^{-2}_{geo}$) 254 (@100 $mA \cdot cm^{-2}_{geo}$)	-	-	46	1 M KOH	XRD, SEM, TEM, ICP, XPS, N_2 ISO (BET)	XPS (after 2000 CV)	30000 s CA (1.452 V_{RHE}) 2000 CV cycles	CoOOH, FeOOH	Precatalyst (partial oxidation)	354
TiN@Ni$_3$N	Ti foil	Nanowire	S	0.6	350	-	-	93.7	1 M KOH	XRD, SEM, EDX, TEM, XPS, ICP	XPS	16 h CA	NiOOH	Precatalyst (partial oxidation)	355
TiN@NiO	Ti foil	Nanowire	S	1	~420	-	-	136.8		XRD, SEM	-	-	-	-	
Ni$_3$N	Ti foil	Nanosheet	S	1	~410	-	-	103.2		XRD, SEM	-	-	-	-	
Modified Ni/Ni$_3$N	Ni foam	Nanoparticle	S	-	~403 (@20 $mA \cdot cm^{-2}_{geo}$)	~7.3	-	65	1 M KOH	XRD, SEM, EDX, TEM, XPS	XRD, SEM, EDX, XPS, ICP-OES	1, 2 h CP (100 $mA \cdot cm^{-2}_{geo}$) 12 h CP (250 $mA \cdot cm^{-2}_{geo}$) 500 CV cycles (25 $mV \cdot s^{-1}$)	NiOOH, Ni(OH)$_2$	Precatalyst (partial oxidation)	356
					~403 (@20 $mA \cdot cm^{-2}_{geo}$)	-	-	-	Fe-purified 1 M KOH		-	-	-	-	
Ni$_3$N nanosheets	GC	Nanosheet	P	0.285	350	-	-	45	1 M KOH	XRD, SEM, EDX, TEM, XPS, AFM, XAS, EXAFS, HAADF-STEM, N_2 ISO (BET), TDR	XRD, XPS	10000 CA (1.68 V_{RHE}) 1000 CV cycles	NiOOH	Precatalyst (partial oxidation)	357
Bulk Ni$_3$N	GC	Bulk powder	P	0.285	470	-	-	85			-	10000 CA (1.68 V_{RHE})	-	-	
Ni$_3$N nanosheets	CC	Nanosheet	S	-	256	-	-	41			-	18 h CA (1.63 V_{RHE})	-	-	
Fe_xN NPs-I	Graphite sheet	Nanoparticles	P	~2	370	-	-	69	1 M KOH	TEM, EDX	-	-	-	-	358
Fe_xN NPs-II	Graphite sheet	Nanoparticles	P	~2	340	-	-	73		TEM, EDX	-	-	-	-	
ε-Fe$_3$N NPs	Graphite sheet	Nanoparticles	P	~2	280	-	-	57		TEM, EDX, XPS	-	6 h CP (10 $mA \cdot cm^{-2}_{geo}$)	-	-	
Fe$_4$N-F-1.5mL(400)	GC	Nanoparticles	P	-	-	-	-	-	1 M KOH	XRD	-	-	-	-	359
Fe$_4$N-F-1.5mL(500)	GC	Nanoparticles	P	-	-	-	-	-		XRD	-	-	-	-	
Fe$_4$N-F-1.5mL(540)	GC	Nanoparticles	P	-	381	-	-	64		XRD	-	-	-	-	
Fe$_4$N-F-1.5mL(580)	GC	Nanoparticles	P	-	362	-	-	57		XRD	-	-	-	-	

https://doi.org/10.1021/acs.chemrev.3c00005
Chem. Rev. 2023, 123, 12795−13208

Table 3. continued

Initial Electrocatalyst	Substrate	Shape of Electrocatalyst	Deposition Type	Specific Loading / $mg \cdot cm_{geo}^{-2}$	η@10 $mA \cdot cm_{geo}^{-2}$ / mV	C_{dl} / $mF \cdot cm_{geo}^{-2}$	TOF / s^{-1} (@η or j)	Tafel Slope / $mV \cdot dec^{-1}$	Electrolyte	Pre-analysis	Post-analysis	Long-Term OER Test Conditions	Post-OER Electrocatalyst	Final Type of Electrocatalyst	Ref.
Fe_4N-F-1.5mL(620)	GC	Nanoparticles	P	-	337	-	-	40		XRD, SEM, TEM, EDX, XPS	-	-	-	-	359
Fe_4N-F-1.5mL(640)	GC	Nanoparticles	P	-	333	-	-	57		XRD	-	-	-	-	
Fe_4N-F-1.5mL(660)	GC	Nanoparticles	P	-	-	-	-	-		XRD	-	-	-	-	
Fe_4N-F-1.0mL(620)	GC	Nanoparticles	P	-	-	-	-	-		XRD, EDX	-	-	-	-	
Fe_4N-F-2.0mL(620)	GC	Nanoparticles	P	-	-	-	-	-		XRD	-	-	-	-	
Fe_4N-F-3.0mL(620)	GC	Nanoparticles	P	-	-	-	-	-		XRD	-	-	-	-	
VN/CNT/IF	Fe foam	Nanotube arrays	S	-	270 400 (@100 $mA \cdot cm_{geo}^{-2}$)	45	-	60	1 M KOH	HAADF-STEM, EDX, TEM, XPS	SEM, TEM	50 h CP (10 $mA \cdot cm_{geo}^{-2}$) 50 h CP (500 $mA \cdot cm_{geo}^{-2}$) 50 h CP (1000 $mA \cdot cm_{geo}^{-2}$)	-	-	360
VN/CNT/IF	Fe foam	Nanotube arrays	S	-	158 276 (@100 $mA \cdot cm_{geo}^{-2}$)	-	-	-	30 wt.% KOH	-	-	100 h CP (1000 $mA \cdot cm_{geo}^{-2}$)	-	-	
$FeNi_3$	Ni foam	Nanospheres	P	0.26	360	-	-	63.24	1 M KOH	SEM, TEM, N_2 ISO (BET, PSD)	-	-	-	-	361
$FeNi_3$-N-350-4	Ni foam	Nanospheres	P	0.26	296 366 (@100 $mA \cdot cm_{geo}^{-2}$)	2.85	0.028 at 300 mV	61.73		XRD, XPS	-	-	-	-	
$FeNi_3$-N-350-8	Ni foam	Nanospheres	P	0.26	222 307 (@100 $mA \cdot cm_{geo}^{-2}$)	8.22	0.195 at 300 mV	41.53		SEM, TEM, XRD, N_2 ISO (BET, PSD), HAADF-STEM, EDX, XPS	-	30 h multistep CP (20, 50, 100, 200 $mA \cdot cm_{geo}^{-2}$) 36 h CA (1.60 V_{RHE})	-	-	
$FeNi_3$-N-350-12	Ni foam	Nanospheres	P	0.26	279 345 (@100 $mA \cdot cm_{geo}^{-2}$)	3.72	0.057 at 300 mV	62.54		XRD, XPS	-	-	-	-	
$FeNi_3$-N-550-4	Ni foam	Nanospheres	P	0.26	296	1.32	-	58.79		XRD, N_2 ISO (BET, PSD), SEM	-	-	-	-	
$FeNi_3$-N-450-8	Ni foam	Nanospheres	P	0.26	310	1.34	-	53.94		XRD	-	-	-	-	
Ni_3N-4	GC	Aggregated particles	P	-	400	0.62	-	92.12	1 M KOH	SEM, XRD, XPS, EDX	-	-	-	-	362
Ni_3N-4.5	GC	Aggregated particles	P	-	380	0.21	-	77.71		XRD, SEM, XPS, EDX	-	6 h CP (10 $mA \cdot cm_{geo}^{-2}$)	-	-	
Ni_3N-12	GC	Regular planar (densely packed nanoparticles)	P	-	380	-	-	102.53		SEM, XRD	-	-	-	-	
Ni_3N/GCNs-4	GC	Particle dispersion + nanosheets	P	-	360	-	-	95.15		SEM, XRD, XPS, EDX	-	-	-	-	
NR-Ni_3N/GCNs-4.5	GC	Stacked nano flat morphology + nanosheets	P	-	290	4.38	-	70.66		XRD, TEM, SAED, EDX, SEM, Raman, XPS, N_2 ISO (BET)	-	36 h CP (10 $mA \cdot cm_{geo}^{-2}$)	-	-	
Ni_3N/GCNs-12	GC	Frizzy cluster + nanosheets	P	-	330	1.94	-	103.56		SEM, XRD, XPS, EDX	-	-	-	-	
NiFeN	Ni foam	Nanosheet	S	-	259	29.3	0.082 at 300 mV	51.8	1 M KOH	XRD, SEM, EDX, XPS, CAM	-	-	-	-	363
					~ 270	-	-	-	1 M KOH + Seawater		-	-	-	-	
CoN-F	CC	Flower like spheres	S	-	276	94.87	-	52.3	1 M KOH	SEM, TEM, XRD, EDX, HAADF-STEM, N_2 ISO (BET, PSD), XPS	TEM	20000 s CA (1.6 V_{RHE})	-	-	364
CoN-S	CC	Irregular spheres	S	-	304	57.58	-	57.58		SEM, TEM, XRD, N_2 ISO (BET, PSD)	-	-	-	-	
CoN-P	CC	Stacked nanoparticles	S	-	338	44.05	-	44.05		SEM, TEM, XRD, N_2 ISO (BET, PSD), XPS	-	-	-	-	
Co-Mo-N	CP	Nanosheet	S	-	281 324 (@50 $mA \cdot cm_{geo}^{-2}$) 346 (@100 $mA \cdot cm_{geo}^{-2}$)	72.24	0.118 at 300 mV	63	1 M KOH	SEM, TEM, XRD, XPS	-	-	-	-	365
Co-Mo-N@Ag-0	CP	Nanosheet	S	-	280	-	-	63		SEM, EDX, XRD	-	-	-	-	
Co-Mo-N@Ag-80	CP	Nanosheet	S	-	250	-	-	59		SEM, EDX, XRD	-	-	-	-	
Co-Mo-N@Ag-160	CP	Nanosheet	S	-	234 275 (@50 $mA \cdot cm_{geo}^{-2}$) 296 (@100 $mA \cdot cm_{geo}^{-2}$)	97.54	0.358 at 300 mV	54		SEM, EDX, TEM, SAED, XRD, XPS	XRD	2000 CV cycles 30 h multistep CP (10, 50, 100 $mA \cdot cm_{geo}^{-2}$)	-	-	
Co-Mo-N@Ag-320	CP	Nanosheet	S	-	252	-	-	61		SEM, EDX, XRD	-	-	-	-	
Co-Mo-N@Ag-640	CP	Nanosheet	S	-	270	-	-	62		SEM, EDX, XRD	-	-	-	-	
Co_2N@Ag-160	CP	Nanosheet	S	-	277 325 (@50 $mA \cdot cm_{geo}^{-2}$)	57.84	-	68		SEM, XRD	-	-	-	-	

https://doi.org/10.1021/acs.chemrev.3c00005
Chem. Rev. 2023, 123, 12795−13208

Table 3. continued

Initial Electrocatalyst	Substrate	Shape of Electrocatalyst	Deposition Type	Specific Loading / $mg \cdot cm^{-2}_{geo}$	η@10 $mA \cdot cm^{-2}_{geo}$ / mV	C_{dl} / $mF \cdot cm^{-2}_{geo}$	TOF / s^{-1} (@η or j)	Tafel Slope / $mV \cdot dec^{-1}$	Electrolyte	Pre-analysis	Post-analysis	Long-Term OER Test Conditions	Post-OER Electrocatalyst	Final Type of Electrocatalyst	Ref.
					350 (@100 $mA \cdot cm^{-2}_{geo}$)										365
MoN@Ag-160	CP	Nanosheet	S	-	424	27.87	-	63		SEM, XRD	-	-	-	-	
$NiFeN_x$	Ni foam	Nanoparticles	S	-	286	3.28	-	44.6	1 M KOH	XRD, SEM, TEM, XPS	-	20 h CP (10 $mA \cdot cm^{-2}_{geo}$)	-	-	366
Ni_3N	GC	Nanoparticle aggregation (mesoporous)	P	0.203	315	0.43	-	63	1 M KOH	XRD, TEM, XPS, N_2 ISO (BET, PSD), SEM,	-	-	-	-	367
Ni_3FeN	GC	Nanoparticle aggregation (mesoporous)	P	0.203	259	3.85	-	54		XRD, TEM, XPS, N_2 ISO (BET, PSD), SEM, EDX	-	10 h CA (1.6 V_{RHE})	-	-	
$Co_{5.47}N$@N-rGO-650	GC	Nanosheets + nanoparticles	P	0.24	410	1.8	-	97	1 M KOH	SEM, TEM, XRD, Raman, N_2 ISO (BET, PSD)	-	-	-	-	368
$Co_{5.47}N$@N-rGO-700	GC	Nanosheets + nanoparticles	P	0.24	390	4.9	-	82		SEM, TEM, XRD, Raman, N_2 ISO (BET, PSD)	-	-	-	-	
$Co_{5.47}N$@N-rGO-750	GC	Nanosheets + nanoparticles	P	0.24	350	13.5	-	79		SEM, TEM, HAADF-STEM, EDX, XRD, Raman, XPS, N_2 ISO (BET, PSD)	-	-	-	-	
$Co_{5.47}N$@N-rGO-800	GC	Nanosheets + nanoparticles	P	0.24	380	2.3	-	104		SEM, TEM, XRD, Raman, N_2 ISO (BET, PSD)	-	-	-	-	
$Co_{5.47}N$@N-rGO-750-2h	GC	Nanosheets + nanoparticles	P	0.24	-	-	-	-		SEM, XRD	-	-	-	-	
$Co_{5.47}N$@N-rGO-750-3h	GC	Nanosheets + nanoparticles	P	0.24	-	-	-	-		SEM, XRD	-	-	-	-	
Co@N-rGO-750	GC	Nanosheets + nanoparticles	P	0.24	-	-	-	-		TEM. XRD	-	-	-	-	
$FeNi_3N$	GC	Semihexagonal-shaped particle	P	0.425	270	-	~ 0.11 at 270 mV	39	1 M KOH	XRD, SEM, TEM, XPS	-	40000 s CP (10 $mA \cdot cm^{-2}_{geo}$)	-	-	369
Ni_3FeN:Mo(5 %)	Ni foam	Nanosheet	S	-	250 (@20 $mA \cdot cm^{-2}_{geo}$) 288 (@100 $mA \cdot cm^{-2}_{geo}$)	38.06	-	52.39	1 M KOH	XRD, SEM, EDX, TEM, XPS	SEM (after 3000 CV)	50 CV cycles (100 $mV \cdot s^{-1}$, 1.1−1.65 V_{RHE}) 3000 CV cycles (1−1.65 V_{RHE}) 12 h CA (1.5 V_{RHE})	-	-	370
Ni_3FeN	Ni foam	Nanosheet	S	-	255 (@20 $mA \cdot cm^{-2}_{geo}$) 293 (@100 $mA \cdot cm^{-2}_{geo}$)	25.84	-	53.49		XRD, SEM, EDX, TEM, XPS	-	50 CV cycles (100 $mV \cdot s^{-1}$, 1.1−1.65 V_{RHE})	-	-	
Ni_3N	Ni foam	Nanosheet	S	-	358 (@20 $mA \cdot cm^{-2}_{geo}$) 431 (@100 $mA \cdot cm^{-2}_{geo}$)	-	-	93.66		XRD	-	50 CV cycles (100 $mV \cdot s^{-1}$, 1.1−1.65 V_{RHE})	-	-	
W_2N/WC	GC	Nanorod	P	0.31	320	13.12	0.15 at 370 mV	122.8	1 M KOH	XRD, SEM, TEM, HAADF-STEM, XPS, XAFS, Raman, N_2 ISO (BET, PSD)	-	12 h CA 1000 CV cycles	-	-	371
WO_3/W_2N	GC	Nanorod	P	0.31	410	5.14	0.1 at 370 mV	187.5			-	-	-	-	
W_2N	GC	-	P	0.31	520	2.35	0.03 at 370 mV	200.5			-	-	-	-	
$Co_{5.47}N$@N-rGO	GC	Nanoparticle	P	0.5	350	13.5	-	80	1 M KOH	XRD, SEM, EDX, XPS, TEM, Raman, N_2 ISO (BET, PSD)	-	-	-	-	368
VN	GC	Nanowire	P	-	458	-	-	-	1 M KOH	XRD, SEM, EDX, XPS	-	-	-	-	372
VN-Co	GC	Nanowire	P	-	395	-	-	-		XRD, SEM	-	-	-	-	
$NiCo_2N$	GC	Nanoparticle	P	0.203	289	37	-	56	1 M KOH	XRD, SEM, TEM, EDX, XPS, N_2 ISO (BET, PSD)	SEM	10 h CA (1.6 V_{RHE}) 2000 CV cycles	-	-	373
CoN	GC	Nanoparticle	P	0.203	323	20.5	-	55		XRD, SEM, TEM, EDX	-	-	-	-	
Ni_3N	GC	Nanoparticle	P	0.203	332	0.43	-	63		XRD, SEM, TEM, EDX	-	-	-	-	
NiCo-N/$NiCo_2O_4$/GF	Graphite fiber	Nanosphere	S	0.3	183	114	-	56	1 M KOH	XRD, SEM, EDX, TEM, Raman, XPS, XAFS, XANES	-	40 h CA (1.41, 1.60 V_{RHE})	-	-	374
NiCo-N/$NiCo_2O_4$/GF	Graphite fiber	Nanosphere	S	0.3	460	-	-	73	0.5 M H_2SO_4		-	-	-	-	
NiCo-N/$NiCo_2O_4$/GF	Graphite fiber	Nanosphere	S	0.3	673	-	-	183	1 M PBS (pH = 7.0)		-	-	-	-	
Ni_3N	GC	Nanoflower	P	0.124	320	1.3	-	74	0.1 M KOH	XRD, SEM, TEM	-	-	-	-	375
Au/Ni_3N (2 % Au)	GC	Nanoflower	P	0.124	280	2.35	-	52		XRD, SEM, EDX, TEM, XPS, TXRF	XRD	10 h CA (1.50 V_{RHE})	-	-	
Ni_3N/BP-AG 1	GC	Nanosheet	P	0.255	233	6.28	-	42	1 M KOH	XRD, SEM, EDX, TEM, XPS, Raman, AFM	-	10000 s CA (1.463 V_{RHE}) 2000 CV cycles (50 $mV \cdot s^{-1}$)	-	-	376
Ni_3N/BP-AG 0.5	GC	Nanosheet	P	0.255	245	4.25	-	126		XPS, TEM	-	-	-	-	
Ni_3N/BP-AG 2	GC	Nanosheet	P	0.255	308	2.4	-	161		XPS, TEM	-	-	-	-	
Ni_3N/BP	GC	Nanosheet	P	0.255	292	2.17	-	168		-	-	-	-	-	
Ni_3N/AG	GC	Nanosheet	P	0.255	317	1.86	-	177		XPS	-	-	-	-	

https://doi.org/10.1021/acs.chemrev.3c00005
Chem. Rev. 2023, 123, 12795−13208

Table 3. continued

Initial Electrocatalyst	Substrate	Shape of Electrocatalyst	Deposition Type	Specific Loading / $mg \cdot cm_{geo}^{-2}$	η@10 $mA \cdot cm_{geo}^{-2}$ / mV	C_{dl} / $mF \cdot cm_{geo}^{-2}$	TOF / s^{-1} (@η or j)	Tafel Slope / $mV \cdot dec^{-1}$	Electrolyte	Pre-analysis	Post-analysis	Long-Term OER Test Conditions	Post-OER Electrocatalyst	Final Type of Electrocatalyst	Ref.
CoO/Co_4N	Ni foam	Nanowhisker	S	3.8	389	2.92	-	83	1 M PBS (pH = 7.0)	XRD, SEM, EDX, TEM, XPS, N_2 ISO (BET, PSD)	-	20 h CA 2000 CV cycles	-	-	377
Fe_2Ni_2N/CNTs	GC	Nanoparticle	P	0.408	282	-	-	38	1 M KOH	XRD, SEM, EDX, TEM, XPS, TGA, XPS, ICP	-	40 h CP (10 $mA \cdot cm_{geo}^{-2}$)	-	-	378
Fe_2Ni_2N	GC	Nanoparticle	P	0.408	340	-	-	97		-	-	40 h CP (10 $mA \cdot cm_{geo}^{-2}$)	-	-	
Co_2N	GC	Sheet	P	-	480	-	-	89	0.1 M KOH	XRD, SEM, TEM, XPS, N_2 ISO (BET)	-	-	-	-	379
CoN	GC	Sheet	P	-	460	-	-	93		XRD, SEM, TEM, XPS, N_2 ISO (BET)	-	-	-	-	
$Co_2N_{0.67}$	GC	Sheet	P	-	465	-	-	83		XRD, SEM, TEM, XPS, N_2 ISO (BET)	-	-	-	-	
Co-Ni_3N	CC	Nanowire	S	2.91	307	-	0.0134 at 350 mV	57.0	1 M KOH	XRD, SEM, TEM, EDX, N_2 ISO (BET, PSD), XPS, Raman	-	24 h multistep CP (10–50 $mA \cdot cm_{geo}^{-2}$)	-	-	380
Ni_3N	CC	Nanowire	S	3.35	397	-	0.00086 at 350 mV	101.9		XRD, SEM, TEM, EDX, N_2 ISO (BET, PSD), XPS, Raman	-	-	-	-	
$NiCo_2N$/NF	Ni foam	Nanosheet	S	-	290	75	-	65	1 M KOH	XRD, SEM, EDX, XPS, TEM	-	40 h CP (10 $mA \cdot cm_{geo}^{-2}$) 40 h CP (50 $mA \cdot cm_{geo}^{-2}$)	-	-	381
CoN/NF	Ni foam	Nanosheet	S	-	300	45	-	69		XRD, SEM, EDX, XPS, TEM	-	-	-	-	
CoN NMs/CFC	CFC	Nanowire	S	-	320	8.53	-	68	1 M KOH	XRD, SEM, EDX, TEM, XPS, ICP-AES	-	-	-	-	382
Mn-CoN NMs/CFC	CFC	Nanowire	S	-	270	5.64	-	46			SEM	3000 CV cycles 30 h CP (1.51 V_{RHE})	-	-	
CoN NMs/CFC	CFC	Nanowire	S	-	315	-	-	82	1 M PBS (pH = 7.0)	XRD, SEM, EDX, TEM, XPS, ICP-AES	-	-	-	-	
Mn-CoN NMs/CFC	CFC	Nanowire	S	-	280	-	-	64			XRD, SEM	3000 CV cycles 30 h CP (1.51 V_{RHE})	-	-	
$Ni_{1.5}Co_{1.5}N$/PF	GC	Nanorod	P	0.269	280	14	0.0014 at 350 mV	66.1	1 M KOH	XRD, SEM, EDX, TEM, HAADF-STEM, XPS	-	1000 CV cycles) 20 h CA (1.51 V_{RHE})	-	-	383
Ni_3N/PF	GC	-	P	0.269	300	-	-	81		-	-	-	-	-	
Co_3N/PF	GC	-	P	0.269	310	-	-	86.2		-	-	-	-	-	
$Ni_{0.75}Co_{2.25}N$/PF	GC	Nanorod	P	0.269	290	-	-	77.5		-	-	-	-	-	
$Ni_{2.25}Co_{0.75}N$/PF	GC	Nanorod	P	0.269	330	-	-	109.2		-	-	-	-	-	
Ni_3FeN	CC	Nanoparticle	S	-	241	-	-	66.1	1 M KOH	XRD, SEM, EDX, TEM, Raman, N_2 ISO (BET), XPS, ICP	-	-	-	-	384
NiCoN-1H/CC	CC	Nanowire	S	-	360	14.3	-	46.9	1 M NaOH	XRD, SEM, EDX, XPS	-	20 h CA (1.61 V_{RHE})	-	-	385
NiCoN-5H/CC	CC	Nanowire	S	-	370	20.4	-	64.3		XRD, SEM, EDX, XPS	-	-	-	-	
Ni_3FeN/NrGO	GC	Nanoplate	P	0.1	400	2.15	-	-	0.1 M KOH	XRD, TEM, AFM, HAADF-STEM, EELS	-	2 h CP (10 $mA \cdot cm_{geo}^{-2}$)	-	-	386
Ni_3FeN	GC	-	P	0.1	500	0.27	-	-		XRD	-	-	-	-	
Ni_3N	GC	-	P	0.1	460	0.74	-	-		XRD	-	-	-	-	
Ni_3N/NrGO	GC	-	P	0.1	430	-	-	-		XRD	-	2 h CP (10 $mA \cdot cm_{geo}^{-2}$)	-	-	
$FeNi_3N$/NF	Ni foam	Nanorod	S	-	202	8.6	-	40	1 M KOH	XRD, SEM, EDX, TEM, XPS, EELS, ICP	XRD	30 h CP (50 $mV \cdot s^{-1}$, 100 $mA \cdot cm_{geo}^{-2}$) 1000 CV cycles (50 $mV \cdot s^{-1}$, 1–1.45 V_{RHE})	-	-	387
Ni_3N	GC	Bulk powder	P	0.35	430	-	-	64	1 M KOH	XRD, SEM, EDX, TEM, XPS, AFM, XANES	-	-	-	-	388
Ni_3FeN-Bulk	GC	Bulk powder	P	0.35	320	-	-	67			-	-	-	-	
Ni_3FeN-NPs	GC	Nanoplate	P	0.35	280	-	-	46			-	9 h CA (1.514 V_{RHE})	-	-	
IISERP-COF3_Ni_3N	GC	Nanofiber	P	0.0708	230	0.036	0.52 at 300 mV	79	1 M KOH	XRD, SEM, EDX, TEM, XPS, TGA, FTIR	-	20 h CA 500 CV cycles	-	-	389
IISERP-COF3_$Ni_3N(N_2)$	GC	Nanofiber	P	0.0708	275	-	-	-		XRD, SEM, EDX, TEM, XPS	-	-	-	-	
IISERP-COF1_Ni_3N	GC	Nanofiber	P	0.0708	208	-	-	-			-	-	-	-	
Ni_3N (air)	GC	Nanofiber	P	0.0708	302	-	-	-			-	-	-	-	
Ni_3N (N_2)	GC	Nanofiber	P	0.0708	350	-	-	-			-	-	-	-	
Fe_2Ni_2N	Ni foam	Nanoplate	S	-	230	-	-	34	1 M KOH	XRD, SEM, TEM, EDX, N_2 ISO (BET), XPS	XRD	10 h CA (1.5 V_{RHE})	-	-	390
Ni_3N	Ni foam	Nanoplate	S	-	320	-	-	56		SEM, XRD	-	-	-	-	

https://doi.org/10.1021/acs.chemrev.3c00005
Chem. Rev. 2023, 123, 12795−13208

Table 3. continued

Initial Electrocatalyst	Substrate	Shape of Electrocatalyst	Deposition Type	Specific Loading / mg cm$^{-2}_{geo}$	η@10 mA cm$^{-2}_{geo}$ / mV	C_{dl} / mF cm$^{-2}_{geo}$	TOF / s^{-1} (@η or j)	Tafel Slope / mV dec^{-1}	Electrolyte	Pre-analysis	Post-analysis	Long-Term OER Test Conditions	Post-OER Electrocatalyst	Final Type of Electrocatalyst	Ref.
Ni_3FeN/NF	Ni foam	Nanosheet	S	1.6	223	-	-	40	1 M KOH	XRD, SEM, EDX, TEM, XPS, N_2 ISO (BET)	-	2000 CV cycles	-	-	391
Ni foam-NH_3	Ni foam	-	S	-	330	-	-	93		-	-	-	-	-	
Co_3Mo_3N	GC	Mesoporous	P	0.3536	470	-	-	-	0.1 M KOH	XRD, SEM, TEM, XPS, N_2 ISO (BET, PSD)	-	-	-	-	392

"Some values (i.e., "specific loading", "η", and "C_{dl}") were calculated or obtained from the descriptions and figures in the previous papers. "Post-OER Electrocatalyst" and "Final Type of Electrocatalyst" were determined based on the experimental results and descriptions provided in the previous papers. $^b\eta$, overpotential; j, current density; C_{dl}, double layer capacitance; TOF, turnover frequency; P, powder-coated electrode; S, self-supported electrode; CV, cyclic voltammetry; CA, chronoamperometry; CP, chronopotentiometry; OWS, overall water splitting. ^{c}Substrate abbreviations: GC (glassy carbon); CC (carbon cloth); CP (carbon paper); CFC (carbon fiber cloth). ^{d}Electrolyte abbreviation: PBS (phosphate buffer solution). ^{e}Analysis abbreviations (minor terms only): ISO (isotherm); PSD (pore size distribution); TPD (temperature programmed desorption); TDR (temperature-dependent resistivity measurement); XRR (X-ray reflectometry).

temperatures in the range of 300−800 °C.[302] So far, almost all the reported transition metal nitrides prepared from gas-solid nitridation are crystalline, proving the effectiveness of this method. Additionally, gas-solid nitridation is preferred because of its simplicity and the quality of the final product, as the nitrides somewhat maintain the morphologies of the precursors.[53,286] In addition to the gas-solid and solid-state reactions, other methods involving hydrothermal and solvothermal synthesis (refs 329, 331, 334, 337, 344, 353, 355, 357, and 370), nitrogen-plasma treatment,[347,353] and microwave synthesis[394,395] have also been introduced. In the following, we will classify the preparation reports according to the synthetic method (the shape-determining step) and introduce some specific examples.

4.1.1.1. Hydrothermal Methods. Some synthetic approaches have relied on preparing high-quality and highly crystalline precursors using hydrothermal methods, followed by conventional nitridation in an NH_3 atmosphere.[312,329,338,340,344,355] In general, hydrothermal synthesis involves crystallizing materials in a sealed container at moderate temperatures (130−250 °C) and pressures (0.3−4 MPa).[396] Specifically in the transition metal nitride field, certain studies have used the hydrothermal method to produce nanostructured transition metal nitrides since one can easily control the nano-morphologies and compositions of the precursors for transition metal nitrides by using the hydrothermal method, and the subsequent nitridation process can somewhat maintain the nano-morphologies of the precursors. For example, Zhang *et al.* employed the gas-solid nitridation to directly grow TiN, TiN@NiO, and TiN@Ni_3N nanowire arrays on Ti foil.[355] As depicted in Figure 58a, by combining nitridation in an NH_3 atmosphere at different temperatures and annealing in air, Ti and Ni nitride species were prepared *in situ*. Specifically, hydrothermally grown TiO_2 precursors were converted into TiN using NH_3 gas at 800 °C, while NiO precursors were prepared, via a solution-based method followed by thermal treatment in air at 350 °C, and then converted into Ni_3N by the gas-solid reaction of NH_3 at 450 °C. This demonstrates that nitridation temperature is essential and will vary depending on the desired material and precursor. As shown in Figure 58b, the resulting TiN@Ni_3N composites exhibited Myriophyllum-like morphology, where the nanowire morphology of the precursors was retained. Moreover, HRTEM analysis (Figure 58c) revealed a polycrystalline structure with d-spacings characteristic of TiN and Ni_3N planes, confirming that nitride species decorated the surface of the nanowires.

Wu *et al.* utilized hydrothermal methods to obtain Ni-Mo-O nanosheets and consequently transform them into Ni_3N-NiMoN heterostructures upon gas-solid nitridation (Figure 59a, (i).[338] According to the authors, preparation of the precursor was crucial because a uniform and dense layer of Ni-Mo-O over carbon cloth (CC) is necessary to obtain sufficient Ni_3N and NiMoN species covering the surface. After nitridation, nanosheets composed of several nanoparticles (NPs) covered the material's surface, contrary to the smooth surface of the Ni-Mo-O precursor (Figure 59a, ii). TEM images confirmed the presence of heterointerfaces, where Ni_3N particles were surrounded by $Ni_{0.2}Mo_{0.8}N$ (Figure 59a, iii). Defect-rich Ni_3FeN nanocrystals anchored to N-doped graphene (N-G) were synthesized through combined hydrothermal and conventional nitridation/annealing procedures by Zhao *et al.*[340] As shown in Figure 59b, NiFe layered double

https://doi.org/10.1021/acs.chemrev.3c00005
Chem. Rev. 2023, 123, 12795−13208

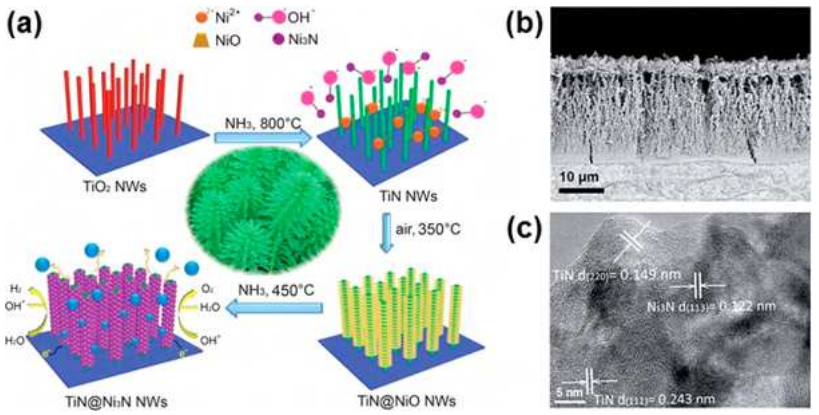


Figure 58. Synthesis of TiN@Ni_3N nanowire arrays on Ti foil via gas-solid nitridation. (a) Schematic illustration of the synthesis method. (b) Cross-sectional SEM and (c) HRTEM images of the TiN@Ni_3N nanowire. Reprinted with permission from ref 355. Copyright 2016 Royal Society of Chemistry.

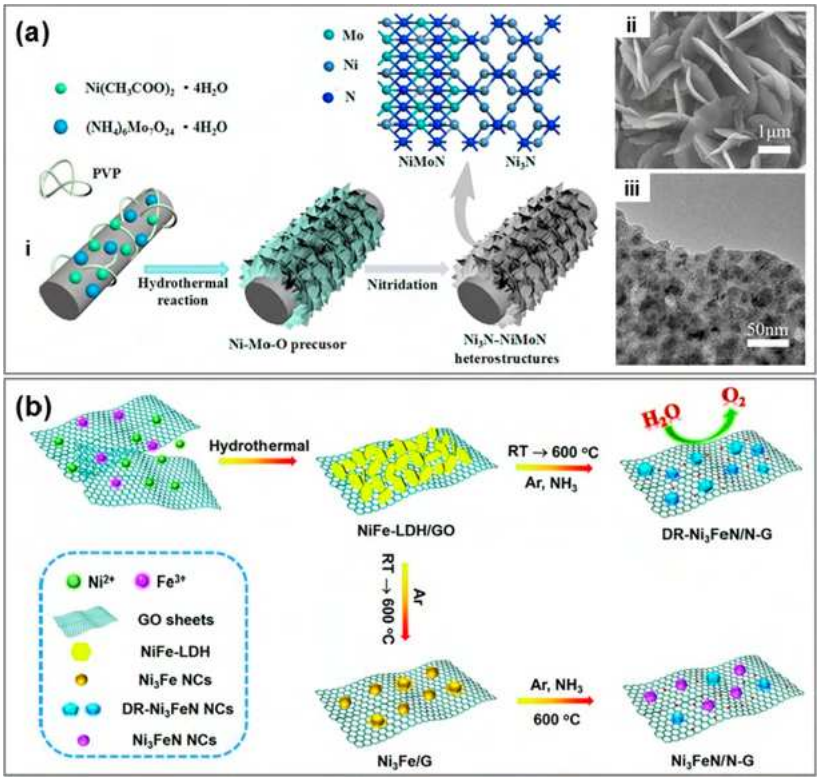


Figure 59. Two-step hydrothermal + nitridation procedures to synthesize transition metal nitrides. (a) Fabrication of Ni_3N-NiMoN heterostructures: schematic illustration of the synthesis approach (i), SEM image of the sheet-like structures (ii), and TEM image. Reprinted with permission from ref 338. Copyright 2018 Elsevier. (b) Schematic illustration of the synthesis of defect-rich (DR) and defect-free Ni_3FeN/N-G nanohybrids. Reprinted with permission from ref 340. Copyright 2018 Wiley.

hydroxides (LDHs) were first grown on graphene oxide (GO) using a hydrothermal step. Followed by nitridation using NH_3 at 600 °C, the defect-rich Ni_3FeN/N-G was obtained. On the other hand, the nearly defect-free control sample was obtained by increasing the temperature to 600 °C in an Ar atmosphere and introducing the NH_3 flow at this temperature. Notably, the hydrothermal step produced positively charged LDH frameworks that interacted strongly with the negatively charged GO layer, facilitating the composite's assembly. After the nitridation step, the Ni-Fe nitride was directly grown over this assembly. Moreover, the Ni/Fe ratio can be effectively tuned during the hydrothermal step, allowing for more versatile material optimization.

4.1.1.2. Solvothermal Methods. Unlike hydrothermal methods, solvothermal methods rely on nonaqueous solvents to perform the crystallization process at moderate temperatures (i.e., above the boiling point) and high pressure.[396−398] Notably, solvothermal synthesis is widely utilized to synthesize high-quality organic-inorganic hybrid materials with high crystallinity and metastable phases. Moreover, certain starting materials can only be dissolved in nonaqueous solvents, which expands the applicability of the resulting materials.[396,399] In the transition metal nitride field, certain studies have also used solvothermal synthesis to prepare the precursors for transition metal nitrides. For example, Chang *et al.* anchored $NiMoO_4 \cdot xH_2O$ nanowires to Ni foam using a solvothermal reaction with

https://doi.org/10.1021/acs.chemrev.3c00005
Chem. Rev. 2023, 123, 12795−13208

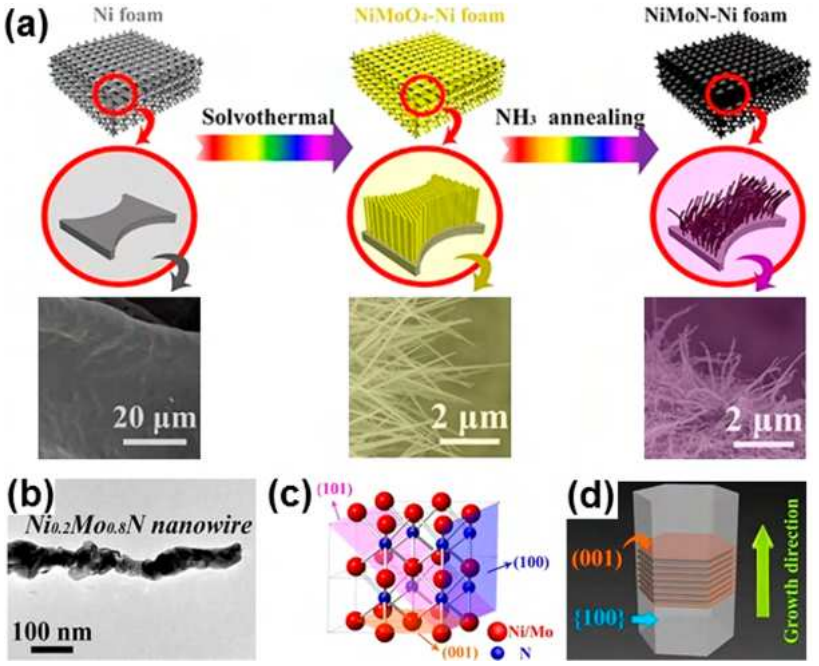


Figure 60. Two-step (solvothermal + nitridation) preparation of NiMoN nanowires on Ni foam: (a) Schematic illustration of the synthesis method. (b) TEM image of the $Ni_{0.2}Mo_{0.8}N$ nanowire. (c) Crystal structure of $Ni_{0.2}Mo_{0.8}N$. (d) Schematic illustration of the growth process depicting exposed facets of $Ni_{0.2}Mo_{0.8}N$. Reprinted with permission from ref 335. Copyright 2018 Wiley.

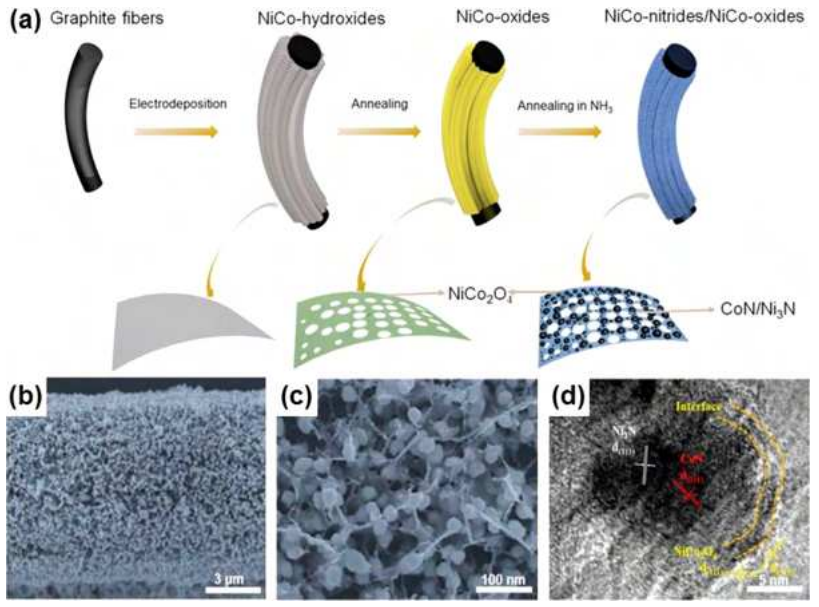


Figure 61. Multistep growth of NiCo-nitride/$NiCo_2O_4$ on graphite fibers: (a) Schematic illustration of the electrodeposition + nitridation synthesis method. (b) SEM image of the as-deposited material on a graphite fiber. (c) Close-up of the NiCo-nitride/$NiCo_2O_4$ NPs. (d) HRTEM image showing a NiCo-nitride NP surrounded by $NiCo_2O_4$. Reprinted with permission from ref 374. Copyright 2019 Wiley.

dodecyl trimethylammonium bromide (DTAB) surfactant, followed by conventional nitridation with ammonia (Figure 60a).[335] This strategy produced $Ni_{0.2}Mo_{0.8}N$ nanowires (Figure 60b) with a hexagonal crystal structure (Figure 60c). Interestingly, the nanowires grew along the ⟨001⟩ direction, selectively exposing the (100) facet to the surface, as depicted in Figure 60d. Furthermore, by precisely varying the dosage of DTAB and the proportion of the mixed solvents, NiMoN with different sizes and shapes can be prepared, demonstrating the versatility of solvothermal methods for precursor preparation. Thanks to this selective exposure of certain crystal facets, solvothermal methods may also be able to pave the way to examine the intrinsic surface oxidation and OER activity.

4.1.1.3. Electrodeposition. Electrodeposition, also known as electrochemical deposition and electroplating, includes such approaches in which crystallites or condensed matter are deposited on a conductive substrate utilizing an applied external electric current. This robust, simple, and cheap approach enables the formation of nano- and microstructures directly on various conductive substrates, precisely controlling the growth rate by tuning the applied current.[397,400] Only a few electrodeposition approaches have been reported to prepare

https://doi.org/10.1021/acs.chemrev.3c00005
Chem. Rev. 2023, 123, 12795−13208

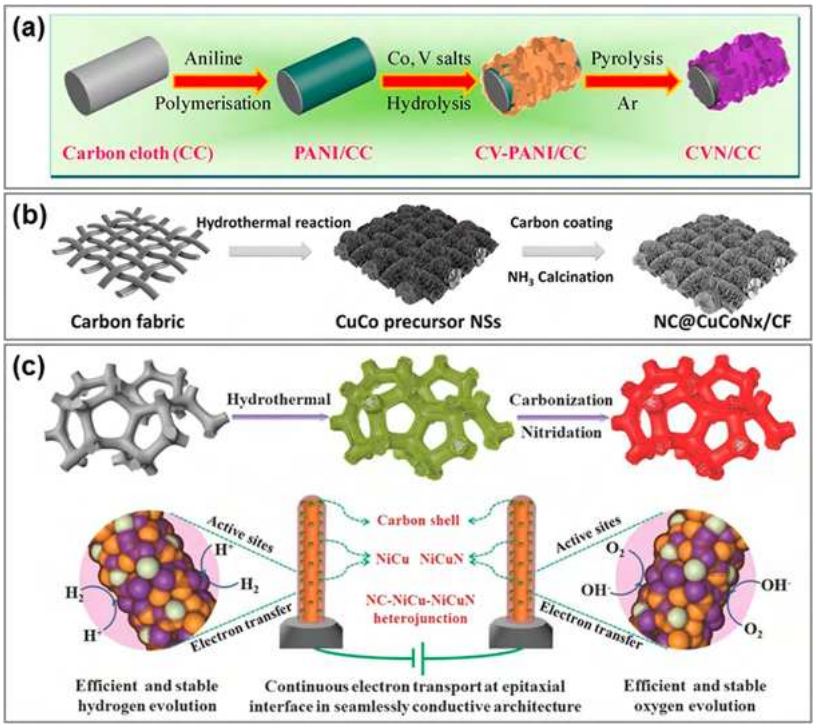


Figure 62. Two-step hydrothermal + nitridation/carbonization methods to synthesize transition metal nitrides: (a) Schematic illustration of the synthesis of CVN/CC electrocatalysts. Reprinted with permission from ref 329. Copyright 2019 Elsevier. (b) Schematic illustration of the synthesis of a NC@$CuCo_2N_x$/CF porous electrode. Reprinted with permission from ref 344. Copyright 2017 Wiley. (c) Schematic illustration of the fabrication of an encapsulated NiCu nanoalloys/NiCuN nanowire electrocatalyst. Reprinted with permission from ref 312. Copyright 2018 Wiley.

the precursors for transition metal nitrides.[374,381] Liu *et al.* synthesized NiCo-nitride/NiCo-oxide assembles on graphite fibers by combining simple electrodeposition and annealing steps.[374] As displayed in Figure 61a, co-electrodeposition of Ni and Co was used to cover the graphite fibers with NiCo-hydroxides. Then, the hydroxides were transformed into NiCo-oxides during annealing and subsequent nitridation with an NH_3 atmosphere, partially converting the oxides into NiCo-nitrides (CoN and Ni_3N). The nitridation step produced several nanospheres on the surface of interconnected nanoflakes, as shown in Figures 61b and c. The nitride-oxide interface can be seen from the HRTEM image (Figure 61d), where $NiCo_2O_4$ surrounded polycrystalline nanospheres composed of CoN and Ni_3N over the nanoflakes. This interface improved the electron transport due to the metallic behavior of $NiCo_2O_4$, CoN, and Ni_3N, demonstrating that electrodeposition can produce oxides that can be readily converted into polycrystalline nitrides.

4.1.1.4. Carbon-Contained Precursor-Derived Methods. Several studies have utilized carbon-based precursors to prepare transition metal nitrides to increase the electrical conductivity, improve the diffusion of reactants, and increase the surface area and dispersion of the electrocatalysts, generally producing core@shell structures and carbon composites.[312,329] Different approaches have relied on nitrogen- and carbon-rich precursors where pyrolysis/calcination steps were necessary (refs 312, 329, 333, 336, 339−341, 344, 368, 376, 386, and 389). Dutta *et al.* synthesized cobalt nitride−vanadium oxynitride (CVN) nanohybrids supported on CC using polyaniline (PANI) as the nitrogen source.[329] As shown in Figure 62a, polymerization of aniline was used to cover the CC substrate, and then metal hydroxides were deposited from Co and V salts. Finally, pyrolysis under an Ar atmosphere at 700 °C produced nitride and oxynitride species directly on the material. Moreover, this protocol allowed for the generation of N-doped carbon over the CC, which increased the conductivity of the support. Notably, this method effectively avoided toxic ammonia gas through a facile and low-cost synthetic strategy. Using Co/Cu salts and urea, Zheng *et al.* prepared CuCo nanosheet precursors on conductive carbon fibers (CFs) through hydrothermal synthesis.[344] However, before performing the nitridation step with ammonia gas, the CuCo precursors were immersed into an aqueous glucose solution, resulting in an N-doped carbon shell covering the CuCo nitrides (Figure 62b). Although NH_3 was still necessary, the N-doped carbon provided a conductive, porous shell that improved the mass transfer, electron transfer, and mechanical stability. In a similar approach, Hou *et al.* encapsulated NiCuN nanowires and NiCu nanoalloys inside N-doped carbon.[312] As shown in Figure 62c, a Ni foam substrate, glucose, urea, and Ni and Cu salts were employed to prepare the NiCu precursor with carbon through a hydrothermal step. By subsequent annealing in N_2 and nitridation in an NH_3/H_2 atmosphere at 400 °C, the NiCu-NiCuN nanowire array encapsulated in an N-doped carbon framework was obtained. This synthesis protocol produced integrated, synergetic heterojunctions that enhanced the electron transfer, accessibility to the active sites, and material durability. These examples demonstrate that carbon-based precursors can be effectively used in conventional thermal steps to yield enhanced carbon frameworks with superior properties.

4.1.1.5. Other Methods. Recent studies have also proposed unique strategies to improve certain features of the precursors for the transition metal nitrides, such as the surface area and porosity. For example, Saad *et al.* prepared mesoporous NiCo nitrides by using a sophisticated nano-casting approach.[373] As

https://doi.org/10.1021/acs.chemrev.3c00005
Chem. Rev. 2023, 123, 12795−13208

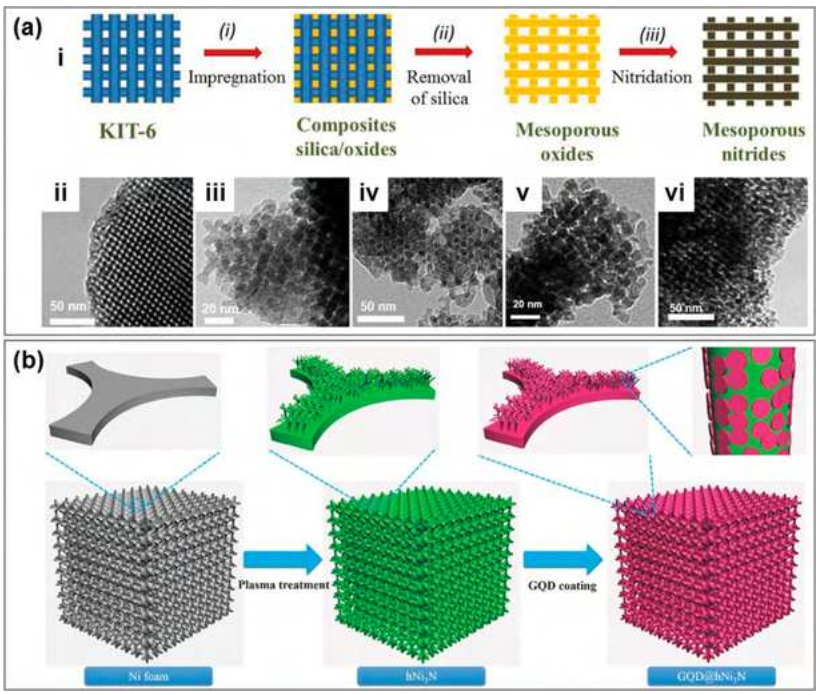


Figure 63. Unique approaches to synthesize transition metal nitrides. (a) Fabrication of 3D-ordered mesoporous $NiCo_2N$ electrocatalysts: schematic illustration of the nano casting procedure (i), TEM images depicting the ordered morphologies of the KIT-6 precursor (ii), Co_3O_4 (iii), Ni_3N (iv), CoN (v), and $NiCo_2N$ (vi). Reprinted with permission from ref 373. Copyright 2019 Wiley. (b) Schematic illustration of the coating process of homogeneous graphene quantum dots on hNi_3N through the plasma strategy. Reprinted with permission from ref 347. Copyright 2017 Wiley.

depicted in Figure 63a, i, a KIT-6 (a high-quality mesoporous silica molecular sieve) template was impregnated with a mixture of the metal salts in ethanol. After evaporating the solvent, calcination at 550 °C, and removal of silica with NaOH, ordered mesoporous Co_3O_4 and spinel-type $NiCo_2O_4$ were obtained. Finally, conventional nitridation with ammonia produced the corresponding mesoporous nitrides. Notably, a highly ordered structure similar to the template (Figure 63a, ii) was preserved when Co_3O_4 (Figure 63a, iii), $NiCo_2O_4$ (Figure 63a, iv), Ni_3N (Figure 63a, v), and CoN (Figure 63a, vi) were obtained. Furthermore, this efficient strategy demonstrated that hard templates such as silica could increase the porosity and, therefore, the surface area of the final nitride material, which ultimately demonstrated superior activity for the OER. In addition to chemical approaches, physical methods such as N_2 plasma treatment have received particular attention recently due to their simplicity. For example, Ouyang *et al.* synthesized 3D hierarchical nickel nitride electrocatalysts on Ni foam using a novel one-step plasma treatment.[347] As depicted in Figure 63b, Ni_3N is generated *in situ* after applying N_2 plasma. Notably, the plasma treatment step produces nitride species in less than 15 min without requiring the previous generation of oxides or toxic nitrogen sources at moderate temperatures (< 450 °C). Furthermore, plasma activation also produced porous nanoarchitecture, increasing the surface area of the final hNi_3N. This makes nitrogen plasma activation a facile and environmentally benign nitridation step with the potential for large-scale application.

4.1.2. Final Types of Nitride-Based Electrocatalysts. Although some researchers considered transition metal nitrides as electrocatalysts with excellent chemical and physical stability,[312,370,373] numerous studies have provided extensive evidence of the reconstruction (e.g., oxidation) of transition metal nitrides during the OER. As shown in Table 3, a substantial amount of reports classify the transition metal nitride as a "precatalyst" rather than a stable "catalyst" according to different post-OER characterization results (see Figure 64). This suggests that although the transition metal

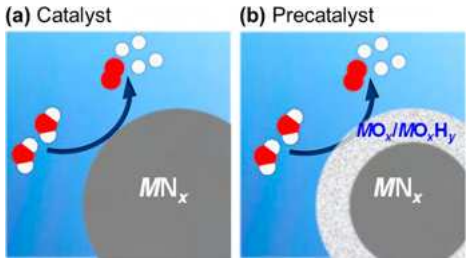


Figure 64. Schematic illustrations of suggested final types of transition metal nitride-based electrocatalysts after long-term OER testing.

nitrides generally have relatively high covalency, their covalent *M*−N bonds can be broken during the OER, producing metal oxides/oxyhydroxides (without any remaining N species in most of the reports) that could be regarded as the true electrocatalytic species for the OER in the transition metal nitride precatalyst (see Figure 64b). Herein, particular case studies in which the identity of transition metal nitrides is regarded as either catalyst or precatalyst are debated. Post-OER characterization evidence is summarized and utilized to provide strong arguments for the precatalytic effect.

4.1.2.1. Catalysts. Based on the post-OER characterization results, only several studies have concluded that the transition metal nitride electrocatalysts (e.g., NiCuN, $NiCo_2N$, Ni_3FeN, Co_3FeN_x, etc.) were stable during the OER.[311,312,370,373] One particular example was discussed by Hou *et al.*[312] As shown in

https://doi.org/10.1021/acs.chemrev.3c00005
Chem. Rev. 2023, 123, 12795−13208

Figure 65b, the authors used a nitrogen-doped carbon (NC)−NiCu−NiCuN electrocatalyst (see the inset of Figure 65b) on Ni foam for both cathode and anode in an electrolyzer to drive ~10 mA·cm^{-2} water splitting in 1 M KOH. After long-term electrochemical overall water splitting (Figure 65b) at a cell voltage of 1.56 V, XRD, SEM, TEM, and XPS characterizations were performed to confirm whether the NC−NiCu−NiCuN was stable or not. XRD patterns before and after the overall water splitting were almost identical (Figure 65c), and the morphology was retained (Figures 65d and e). The authors only showed XPS results of the C 1s peak (Figure 65f), which exhibited no remarkable changes. Interestingly, due to a lack of XPS results for surface Ni and Cu species, the absence of metal oxide/oxyhydroxide species cannot be ruled out. Although specific articles have mentioned that carbon coatings can effectively protect the electrocatalyst in the core while improving the accessibility to the active sites,[401−403] it is still necessary to provide post-OER characterizations based on not only the morphological and structural stability of the CN shell but also the chemical stability of the inner transition metal nitride (NiCuN).

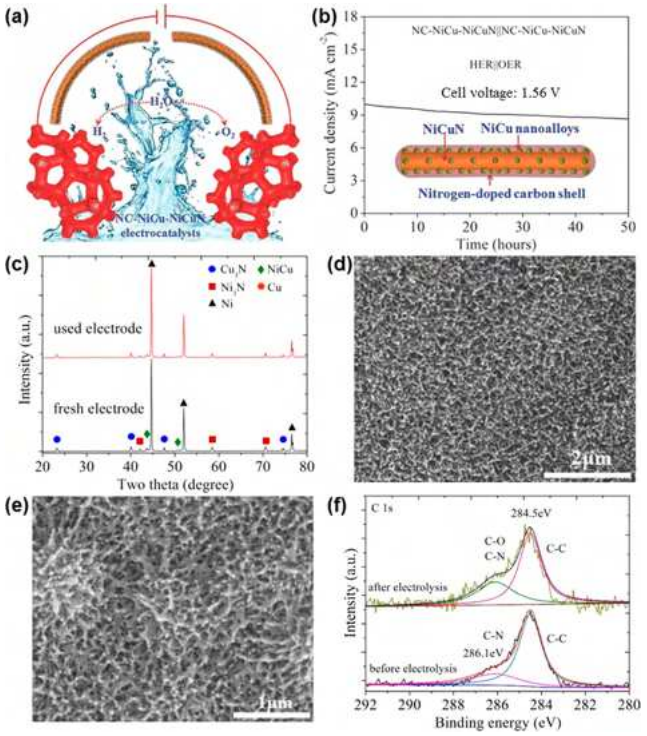


Figure 65. Characterization of an NC−NiCu−NiCuN catalyst after an OER stability test: (a) Schematic illustration of an NC−NiCu−NiCuN||NC−NiCu−NiCuN cell. (b) Long-term electrochemical stability test at the cell voltage of 1.56 V for overall water splitting (inset: schematic illustration of the NC−NiCu−NiCuN catalyst). (c) Comparison of XRD patterns. (d, e) SEM images of the sample (d) before and (e) after 50 h of electrolysis. (f) C 1s XPS spectra of the sample before and after the stability test. Reprinted with permission from ref 312. Copyright 2018 Wiley.

Saad *et al.* evaluated the stability of a 3D mesoporous $NiCo_2N$ electrocatalyst prepared on a mesoporous silica hard template for the OER.[373] After a 10 h chronoamperometric test at a constant OER overpotential of 370 mV in 1 M KOH, nearly 90% of the initial current density was maintained. The authors carried out post-OER SEM analysis of the electrocatalyst in which the well-defined structure and morphology of the template and $NiCo_2N$ NPs were retained. Despite the relevance of structural integrity, no chemical information was provided about the post-OER electrocatalyst. Therefore, it is challenging to define evidence regarding the identity of the real OER active species. Hence, this electrocatalyst is regarded as "unknown" in Table 3. Similarly, even though the authors provided specific post-OER characterization results, which cannot be authoritative evidence to check the oxidation degree of the transition metal nitride and identify the real OER active species, we classify their reported nitrides as "unknown" in Table 3.[370,375,382,390,404,405]

4.1.2.2. Precatalysts. Some reports have provided extensive characterization results to support the transformation of transition metal nitride electrocatalysts during the OER. However, the precise estimation of the oxidation degree and the specific role of oxidized nitrogen species (e.g., -NO_2 and -NO_3 groups)[339] for the OER remain elusive in the literature. Nevertheless, significant findings of how the electrooxidation

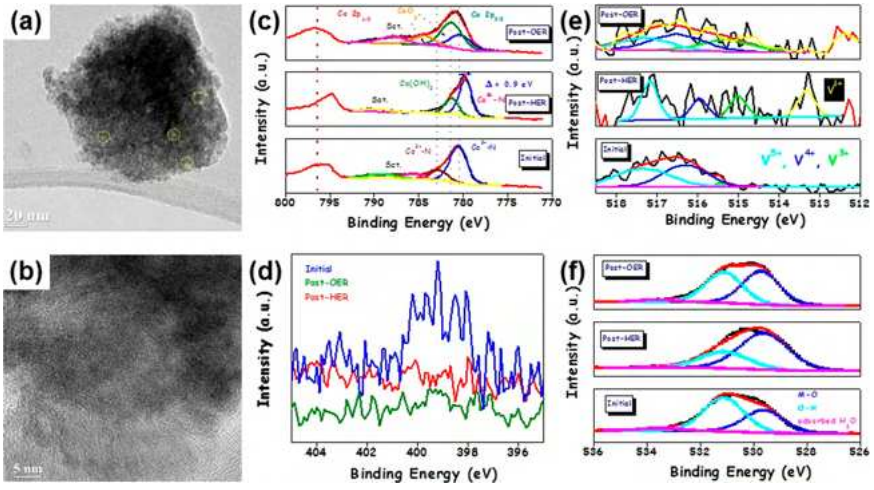


Figure 66. Characterization of a cobalt nitride-vanadium oxynitride nanohybrid precatalyst on carbon cloth (CVN/CC) before and after OER and HER tests. (a) TEM and (b) HRTEM images of the CVN/CC after the OER. (c) Co $2p_{3/2}$, (d) N 1s, (e) V $2p_{3/2}$, and (f) O 1s XPS spectra of the CVN/CC before and after OER and HER tests. Reprinted with permission from ref 329. Copyright 2019 Elsevier.

https://doi.org/10.1021/acs.chemrev.3c00005
Chem. Rev. 2023, 123, 12795−13208

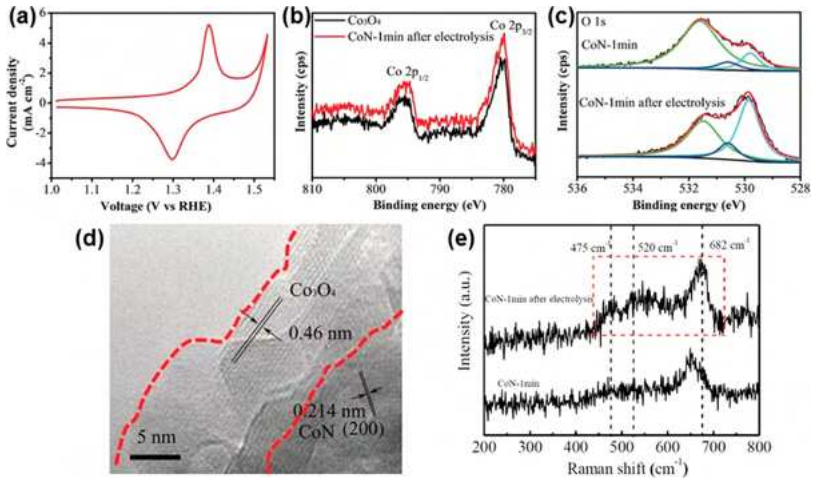


Figure 67. Characterization of a cobalt nitride precatalyst before and after OER tests. (a) CV scan of the CoN-1 min sample (at 1 mV·s^{-1}). (b, c) XPS (b) Co $2p_{3/2}$ and (c) O 1s spectra of the CoN-1 min sample before and after electrolysis. (d) HRTEM image of the CoN-1 min sample after 30 h of electrolysis. (e) Raman spectra of the CoN-1 min sample before and after 30 h of electrolysis. Reprinted with permission from ref 353. Copyright 2016 Wiley.

of the transition metal nitride is promoted during the OER have been given by some reports. The following case studies summarize the evidence regarding the role of transition metal nitrides as precatalysts for the OER. Dutta *et al.* provided extensive post-OER characterization of a cobalt nitride-vanadium oxynitride nanohybrid (Co_4N-$VN_{1-x}O_x$) precatalyst on carbon cloth.[329] After the long-term CA testing in 1 M KOH, SEM analysis suggested that the material was structurally stable. However, ICP-OES results indicated that vanadium was leaching out during the OER. Moreover, as depicted in Figures 66a and b, TEM and HRTEM images revealed that the sample underwent complete amorphization and that vanadium leaching led to vacancies in the structure. Incidentally, crystalline $Co(OH)_2$-$Co\delta^+$-N ($0 < \delta < 2$) layers were generated during the HER. Post-OER and HER XPS characterization results are shown in Figures 66c–f. Focusing on the post-OER XPS results, the Co peak shifted toward higher binding energies, which suggests oxidation of Co^{2+} into Co^{3+}, and the intensity decrease also confirmed the formation of oxidized species. Furthermore, while the N 1s peak completely vanished after the OER, the O 1s spectra exhibited an increase of peak contribution for metal-oxygen species. Furthermore, the V $2p_{3/2}$ XPS spectra suggested the decrease in vanadium content, which also agrees with ICP-OES results about leaching during the OER. These results suggest that the Co_4N-$VN_{1-x}O_x$ can undergo chemical and structural transformations into amorphous cobalt oxo-hydroxide species (i.e., CoO_x: $Co(OH)_2$, CoOOH, Co_3O_4) during the OER.

Zhang *et al.* evaluated the stability of CoN nanowires on Ni foam during the OER in 1 M KOH using CV, XPS, TEM, and Raman spectroscopy techniques.[353] As shown in Figure 67a, the redox peaks in the 1.3–1.4 V_{RHE} range in the CV scan can be associated with the $Co^{3+/4+}$ couple, suggesting the oxidation of the CoN sample. From Figure 67b, it can be seen that the Co $2p_{3/2}$ spectrum of the CoN sample after the OER testing resembles that of Co_3O_4, suggesting that the binding energies are very similar. Moreover, the O 1s peak (Figure 67c) showed increased contributions after the OER. Furthermore, HRTEM analysis (Figure 67d) found that a cobalt oxide shell covered the cobalt nitride nanowire, suggesting that the oxide formation occurred only at the surface and that the cobalt nitride was preserved below this oxide layer. Finally, Raman spectroscopy measurements confirmed the presence of new oxidized species since new peaks at 475, 520, and 682 cm^{-1} were observed (Figure 67e), which also imply the formation of cobalt oxide. Overall, these results suggest that at least the surface of CoN nanowires can be partially oxidized during the OER, producing a cobalt oxide layer that can protect the inner metallic nitride core. The authors also suggested that the real OER active site may be the CoOOH formed on the CoN surface before the OER. This report could explain the reason why post-OER XRD and SEM measurements may wrongly suggest that the nitrides have not changed during the OER, as this newly formed oxide/(oxy)hydroxide layer could be extremely thin and might not affect the morphologies of the nitrides and would not be detected by XRD.

Ouyang *et al.* studied the morphological, structural, and chemical changes of a hierarchical Ni_3N precatalyst on Ni foam during the OER using SEM, TEM, and XPS.[347] By comparing the SEM images before and after the 48 h OER test in 1 M KOH aqueous electrolyte, the Ni_3N sample seemingly retained its morphology (Figures 68a and b). However, according to post-OER TEM and HRTEM images (Figures 68c and d), the formation of a thin layer of NiOOH on the Ni_3N surface was confirmed. As seen in Figure 68c, the layer exhibited a thickness of approximately 8 nm. Moreover, the Ni $2p_{3/2}$ XPS spectra showed a remarkable Ni–N peak decrease, while in the N 1s XPS spectra, the Ni–N peak was almost absent after the OER (Figure 68e). Finally, the O 1s peak exhibited an increased Ni–O signal, confirming the formation of oxidized Ni species. Accordingly, in the hierarchical Ni_3N precatalyst, the newly formed NiOOH species act as the active species for the OER.

Shalom *et al.* also evaluated the electrochemical behavior of a Ni_3N precatalyst directly grown on Ni foam during the OER in an alkaline electrolyte.[356] At first, the pristine Ni_3N and Ni foam samples were modified through 500 CV cycles (i.e., CV activation) in 0.1 M KOH. As depicted in Figure 69a, the areas of the oxidation (at ~1.5 V_{RHE}) and reduction peaks (at ~1.35 V_{RHE}) continuously increased during the CV activation, which is attributed to the formation of $Ni(OH)_2$ that is further electrooxidized into NiOOH. Interestingly, the redox peak

https://doi.org/10.1021/acs.chemrev.3c00005
Chem. Rev. 2023, 123, 12795–13208

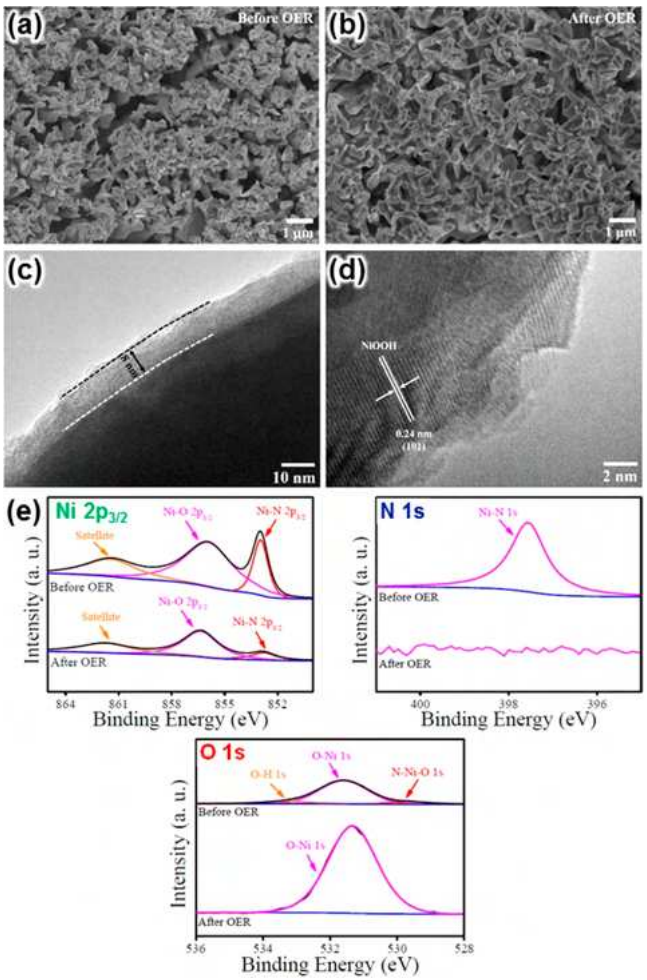


Figure 68. Pre- and post-OER characterization of a 3D hierarchical nickel nitride precatalyst: (a, b) SEM images of the hNi_3N sample (a) before and (b) after 48 h of OER testing. (c) TEM and (d) HRTEM images. (e) XPS spectra of the material before and after stability tests. Reprinted with permission from ref 347. Copyright 2017 Wiley.

areas were stabilized after 500 CV cycles, while the redox peak areas did not drastically increase for the pristine Ni foam. This result suggests that Ni_3N may be favorable for the formation of $Ni(OH)_2$ and NiOOH compared to metallic Ni.[90] From XPS measurements (Figure 69e), the disappearance of the N 1s peak was confirmed after CV activation, confirming the oxidation of the Ni_3N surface during the CV activation. Furthermore, the XRD patterns of the sample before and after OER activation were almost identical (Figure 69f), which confirms that bulk Ni_3N is preserved under the surface oxide layer. Moreover, the electrochemically active surface area (ECSA) measurements of the modified foam samples (Figure 69b) confirmed the larger surface area of the modified Ni_3N sample, which is attributed to the surface reconstruction during the CV activation. From the OER CA tests in 1 M KOH (Figure 69c), the modified Ni_3N foam maintained an initial OER overpotential for 60 h, lower than that of the Ni foam. The superior stability was also demonstrated by 500 CV cycling with a scan rate of 25 $mV \cdot s^{-1}$ in 1 M KOH (Figure 69d), where the CV profiles before and after the 500 CV cycles were indistinguishable. Finally, the ICP-OES measurement of the KOH electrolyte before and after the 500 CV cycles confirmed that the content of Ni was below 1 ppm in both samples, implying negligible Ni dissolution during the CV test. Their experimental results indicate that in the Ni_3N precatalyst, the newly formed $Ni(OH)_2$/NiOOH species become the real electroactive species for the OER and protect the inner bulk Ni_3N from electrooxidation.

Overall, these case studies demonstrate four critical points that must be carefully addressed when evaluating the precatalytic effect of transition metal nitrides: (i) XRD and SEM analysis must be supported by additional techniques, as the reconstruction of transition metal nitrides can occur on the surface, where extremely thin metal oxide layers could form without modifying the morphology and keeping metallic nitride in bulk; (ii) XPS analysis should show the comparison before and after the OER of the significant components, for transition metal nitrides being the metal, nitrogen, and oxygen at least; (iii) the continuous reconstruction of the surface may induce amorphization or even leaching of other cations in the structure, eventually leading to the formation of vacancies and increasing porosity/ECSA; and (iv) metallic nitrides seem to enhance the oxidation compared to metallic counterparts (e.g., bare Ni). However, it is not entirely understood whether transition metal nitrides offer characteristic features that facilitate the formation of oxidized species. This point will be discussed more in Section 4.2.4.

4.1.3. Structural and Chemical Compositional Effects toward OER Activity. In addition to the reconstruction processes during the OER, some reports have studied specific structural, compositional, and morphological activity trends of different transition metal nitride-based electrocatalysts. Herein, the relevance of these effects in the electrocatalytic OER performance of transition metal nitrides is discussed. Furthermore, since most of the reported transition metal nitrides belong to the group "precatalyst", we also emphasize the roles of transition metal nitrides in the reconstruction processes of several precatalysts.

4.1.3.1. Synthetic Parameter Effects. Some reports have studied different synthesis variables to understand their effect on the electrocatalytic properties of the final transition metal nitrides. Due to the relevance of conventional ammonia nitridation, Xue *et al.* evaluated the temperature effect on the electrochemical performance of cobalt nitrides supported on CC.[334] As shown in Figure 70a, the CoN synthesized at 400 °C exhibited the lowest overpotential (i.e., 251 mV at 10 $mA \cdot cm^{-2}$), being close to that of IrO_2. Among the prepared cobalt nitrides, the sample prepared at 400 °C exhibited the smallest Tafel slope (Figure 70b), the largest surface area (Figure 70c), and the lowest charge transfer resistance, R_{ct} (Figure 70d), as denoted by the smallest semicircle in the EIS analysis. Overall, the authors found that increasing the temperature during nitridation improved the crystallinity of the sample, according to the X-ray diffraction (XRD) results. However, further increases above 400 °C led to larger particle sizes, decreasing the electrochemically active surface area (ECSA). Although the authors did not exhaustively discuss it, the R_{ct} trends from EIS analysis suggest that temperature might also have a substantial effect on the conductivity of the nitrides. Therefore, these findings suggest that optimal nitridation temperatures must be found to improve the material's crystallinity without affecting the surface area and conductivity of the material.

The effect of N_2 plasma treatment has also been studied in detail. Zhang *et al.* prepared cobalt nitride nanowires at different times and evaluated the effects on the morphological and electrochemical properties.[353] As shown in Figure 71a,

https://doi.org/10.1021/acs.chemrev.3c00005
Chem. Rev. 2023, 123, 12795−13208

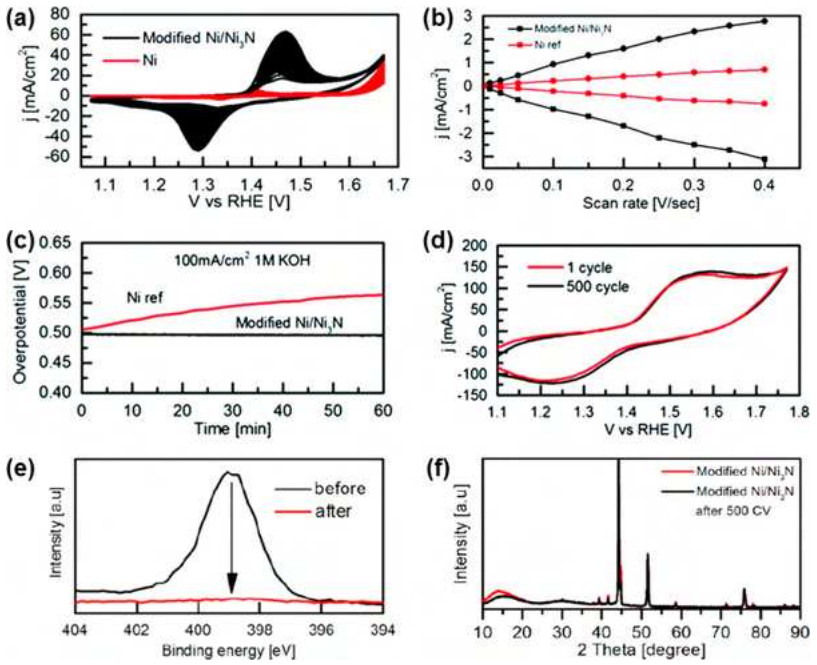


Figure 69. Evaluation of a nickel nitride OER precatalyst on Ni foam substrate: (a) CV scans at 25 mV·s^{-1}. (b) C_{dl} measurements depicting both the cathodic and anodic charging currents at 0.86 V_{RHE}. (c) OER stability tests at 100 mA·cm^{-2}. (d) CV scans before and after OER stability tests for the Ni_3N sample. (e) XPS N 1s spectra and (f) XRD patterns of the Ni_3N sample before and after 500 CV oxidation cycles. Reprinted with permission from ref 356. Copyright 2015 Royal Society of Chemistry.

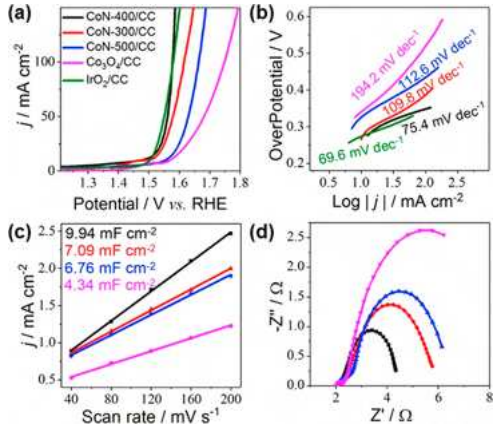


Figure 70. Effect of the nitridation temperature on the electrocatalytic performance of CoN porous nanowire arrays: (a) OER polarization curves. (b) Tafel plots. (c) C_{dl} measurements for ECSA comparison. (d) Nyquist plots. Reprinted with permission from ref 334. Copyright 2018 Elsevier.

SEM images of the nanowires revealed that by increasing the plasma treatment time, the nanowires' curvature, entanglement, and roughness are increased. However, extended activation via a 3 min exposure led to severe etching by the nitrogen ions, destroying the nanowire array. This explains why the plasma time should be optimized, as the nanostructures can be severely damaged after prolonged exposure. Electrochemical characterization of the CoN nanowires led to a similar trend. As shown in Figure 71b, the sample prepared after 1 min (CoN-1 min) exhibited the lowest overpotential of 290 mV at 10 mA·cm^{-2}. Additionally, the CoN-1 min sample exhibited the smallest Tafel slope (Figures 71c and d). Interestingly, the plasma treatment time did not affect the ECSA (Figure 71e), with the 30 s, 1 min, and 3 min samples exhibiting similar double-layer capacitance (C_{dl}) of nearly 92 mF·cm^{-2}. This suggests that the morphology might have more significant effects on the activity rather than the roughness (i.e., ECSA) of the nanowires since the vertical alignment of the nanowire array could favor the transport of reactants and products. Nevertheless, more studies are necessary to evaluate the effect of the morphology on the activity of transition metal nitrides, especially when the surface can be precisely modified through efficient synthesis approaches such as plasma treatment.

Similarly, Ouyang *et al.* evaluated the effect of plasma treatment on the morphology of hierarchical nickel nitrides.[347] As displayed in Figure 72a, SEM images revealed that the surface changed during the nitrogen plasma treatment. Overall, the nanocoral structure grew continuously during the plasma activation. Furthermore, by increasing the activation time, the Ni_3N layer became thicker, as depicted in Figure 72b, demonstrating that treatment time can be effectively used to control the thickness of the nitride layer. Interestingly, the Ni_3N layer obtained via plasma activation (denoted as hNi_3N) exhibited an earlier onset for the OER than nickel foam, resulting in an overpotential of 325 mV at 10 mA·cm^{-2} [about 250 mV lower than that for Ni foam (NF)]. The hNi_3N electrocatalyst exhibited similar overpotentials to those of the same composition in the literature, prepared by thermal nitridation with ammonia: Ni_3N nanosheets (350 mV)[357] and Ni_3N nanoparticles (302 mV).[389] Furthermore, surface area measurements through the double-layer capacitance method showed that the ECSA of the hNi_3N electrocatalyst increased almost three times compared to that of the NF. These results confirmed that synthesizing nickel nitrides by plasma activation improves the morphology and the activity and increases the ECSA of the resulting material. The authors proposed a growth mechanism to account for the characteristic nanocoral architecture (Figure 72c). Plasma treatment produces N_2,

https://doi.org/10.1021/acs.chemrev.3c00005
Chem. Rev. 2023, 123, 12795−13208

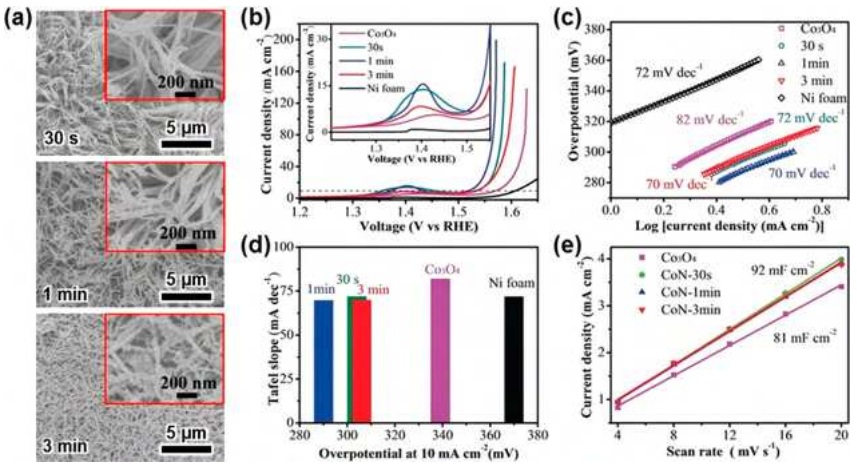


Figure 71. Effect of N_2 plasma treatment for different times on the catalytic performance of cobalt nitride nanowires: (a) Morphologies from SEM images at different times. (b) OER polarization curves. (c) Tafel plots. (d) Overpotentials at 10 mA·cm^{-2} and corresponding Tafel slopes. (e) C_{dl} measurements. Reprinted with permission from ref 353. Copyright 2016 Wiley.

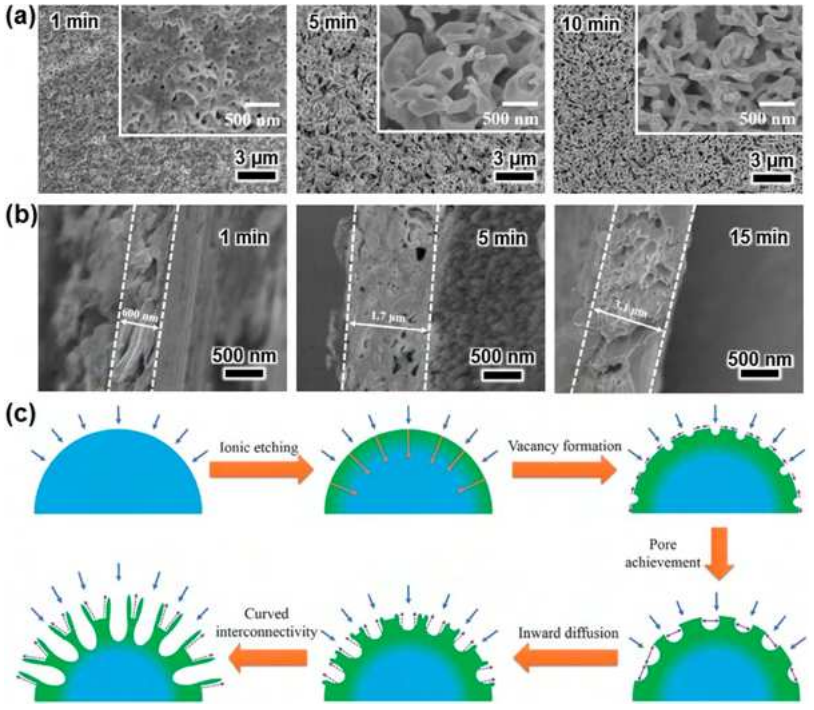


Figure 72. Preparation of hierarchical 3D nickel nitride nanocorals using the N_2 plasma treatment: (a) Top-view SEM images depicting the morphologies of the hNi_3N sample at different treatment times. (b) Cross-sectional views showing the thickness of the Ni_3N layer. (c) Schematic illustration of the hNi_3N growth mechanism during N_2 plasma treatment. Reprinted with permission from ref 347. Copyright 2017 Wiley.

N^+, and N_2^+ species that react with nickel atoms to produce Ni_3N. Moreover, the plasma increases the temperature of the substrate surface to around 450 °C, which results in higher diffusion of N species and, therefore, increased production of Ni_3N. The formation of nitride species produces vacancies in the crystal structure, which accumulate progressively until pores are formed. These structures become rough, and a network of interconnected cavities is obtained. This growth rate is also driven by the inward diffusion of vacancies, which could explain the formation of curved shapes. Eventually, more significant stresses due to prolonged treatment times cause the collapse of the interconnected cavities and channels, increasing the number of smaller structures with nanocoral morphology. Although this mechanism explains the observed morphology, further evidence from surface area measurements of nickel nitrides synthesized by other methods is absent, which impedes the morphology and ECSA comparison. However, this case study demonstrates that morphologies can be precisely tuned with nitrogen plasma methods and that highly active transition metal nitrides can be prepared through this facile and straightforward approach.

4.1.3.2. Metal/Nitrogen Composition Effects. The metal-to-nitrogen ratio is a vital variable closely related to the performance of transition metal nitrides because of the changes in the electronic and structural properties. An interesting evaluation of this parameter was reported by Chen *et al.*, who synthesized serial cobalt nitrides with well-defined crystal structures.[352] As depicted in Figure 73a, three cobalt nitrides

https://doi.org/10.1021/acs.chemrev.3c00005
Chem. Rev. 2023, 123, 12795−13208

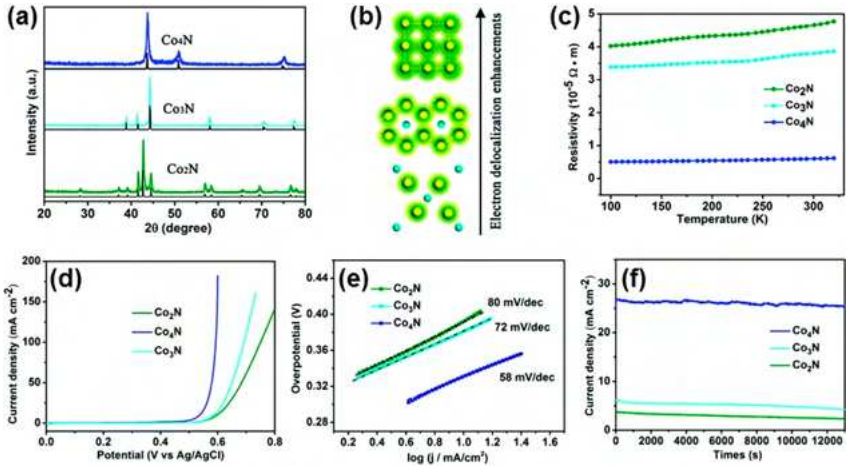


Figure 73. Effect of the *M*/N composition on the electrocatalytic performance of cobalt nitrides: (a) XRD patterns of three serial Co-based nitrides. (b) Schematic illustration of the electron delocalization for corresponding Co_xN compositions (viewed from the c-orientation). (c) Temperature-dependent electrical resistivity of each Co_xN. (d) OER polarization curves and (e) Tafel plots in 1 M KOH. (f) OER stability tests at a constant overpotential of 437 mV in 0.1 M KOH. Reprinted with permission from ref 352. Copyright 2016 Royal Society of Chemistry.

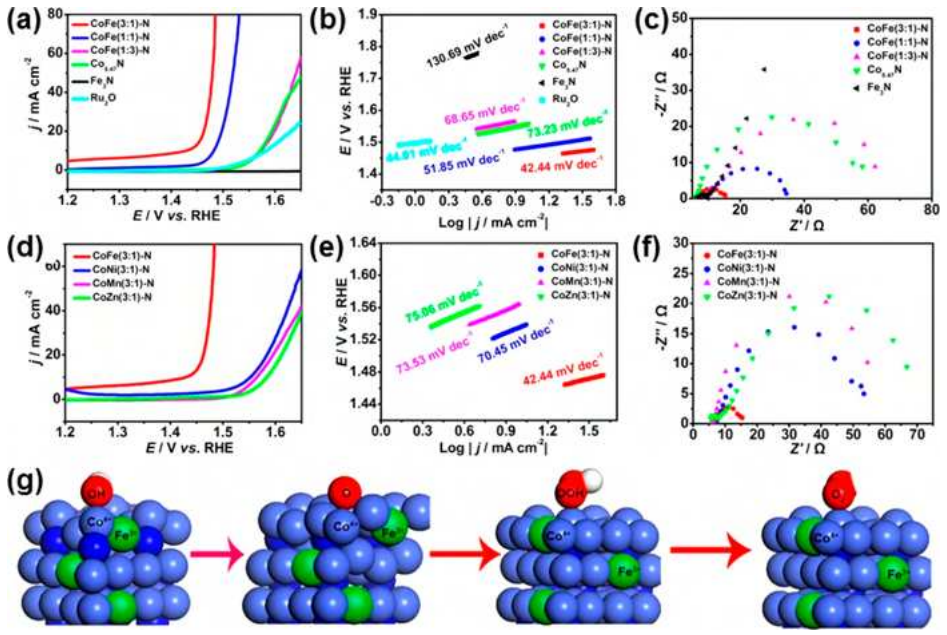


Figure 74. Influence of metal doping on $Co_{5.47}N$ OER precatalysts: (a) LSV curves of different Co/Fe compositions in 1 M KOH. (b) Corresponding Tafel plots. (c) Nyquist plots for EIS analysis at 1.58 V_{RHE}. (d) LSV curves for different Co*M*(3:1)-N (*M* = Fe, Ni, Mn, Zn) precatalysts. (e) Corresponding Tafel plots. (f) Nyquist plots at 1.58 V_{RHE}. (g) Schematic illustration of the OER mechanism on Co atoms located at the edges of CoFe(3:1)-N precatalysts. Reprinted with permission from ref 342. Copyright 2018 American Chemical Society.

were synthesized, and their crystal structures were found through XRD measurements. The Co_2N, Co_3N, and Co_4N samples exhibited crystal structures of orthorhombic, hexagonal, and face-centered cubic (fcc), respectively. Notably, this nitrogen depletion from Co_2N to Co_4N leads to electron cloud overlapping (Figure 73b), suggesting that electron delocalization might lead to better conductivity. Temperature-dependent resistivity measurements (Figure 73c) confirmed that Co_4N exhibited the lowest resistivity (i.e., the highest electrical conductivity), and it was almost stable in the range of 100−320 K. As shown in Figures 73d and e, the Co_4N sample exhibited the lowest OER overpotential (370 mV at 10 mA·cm^{-2}) and the smallest Tafel slope among the three compositions, suggesting that the higher conductivity might improve the charge transfer at the electrode. CA tests to evaluate the stability (Figure 73f) confirmed the superior performance of metallic Co_4N, which exhibited the highest current density and subtle degradation (4.5%) after nearly 4 h of OER testing. Based on previous reconstruction evidence,[406,407] the authors proposed that the cobalt nitrides were transformed into CoOOH and subsequently into CoO_2, acting as the OER active species. Although it was not evaluated in this study, it is essential to note that the metallic Co_4N sample also has a higher amount of Co, which might yield more active sites than Co_2N and Co_3N. Overall, this study demonstrates that the *M*/N composition modifies the crystal structure of the material, and therefore the electronic properties can be significantly improved when the metallic character of Co-based nitrides is favored.

https://doi.org/10.1021/acs.chemrev.3c00005
Chem. Rev. 2023, 123, 12795−13208

4.1.3.3. Metal-Doping Effects. Analogous to the *M*/N composition, the addition of cations into the metal nitride crystal is also of great interest because of its effects on the electronic and structural properties. Certain studies have incorporated low content of metals into the crystal lattice to evaluate the activity and stability performance. Liu *et al.* evaluated the performance of metal-doped $Co_{5.47}N$ nanosheets [Co*M*(3:1)-N] in an alkaline environment, emphasizing Fe doping.[342] First, the authors evaluated the effect of the Co/Fe ratio on the OER activity (Figure 74a). Notably, the Fe_3N sample was not active toward the OER in the examined potential window, suggesting that Fe is not the active site. On the other hand, $Co_{5.47}N$ exhibited a moderate overpotential of 334 mV at 10 mA·cm^{-2}. Only when Fe was incorporated into the material was the overpotential reduced significantly, and the sample with a higher Co content, CoFe(3:1)-N, exhibited the lowest overpotential among all the samples (200 mV at 10 mA·cm^{-2}). A similar trend was observed for the Tafel slopes (Figure 74b), where the CoFe(3:1)-N sample exhibited the smallest Tafel slope. Additional electrochemical impedance spectroscopy (EIS) analysis (Figure 74c) further demonstrated the superior features of the Fe-doped sample at a 3:1 ratio, exhibiting the lowest charge transfer resistance (R_{ct}) value according to the shortest diameter of the semicircle in Nyquist plots. This sample also displayed the largest ECSA and superior stability according to ECSA measurements and galvanostatic tests, respectively. Furthermore, the authors evaluated the effect of doping the cobalt nitride sample with different metals (*M* = Fe, Ni, Mn, Zn) at a fixed 3:1 Co/*M* composition. As displayed in Figure 74d, the Fe-doped cobalt nitride showed the best activity among all the samples. Additional Tafel (Figure 74e) and EIS analysis (Figure 74f) also demonstrated the effectiveness of Fe-doping in improving the OER kinetics and reducing the R_{ct}. Further morphological, structural, and chemical characterization of the samples was performed to unveil the explanations behind these trends. It was found that while Ni, Fe, and Mn were successfully incorporated into the crystal structure, Zn formed the ZnO phase. Interestingly, although adsorption isotherms suggested that the Fe-doped sample displayed the smallest surface area, normalized LSV curves still confirmed the superior activity of this sample among all the doped cobalt nitrides, suggesting that the improvement came from intrinsic OER catalysis. XPS analysis provided a more reasonable explanation, as it was found that Fe doping led to the largest positive shift (~1.2 eV) of the binding energies of Co $2p_{3/2}$. On the other hand, Ni and Mn led to smaller positive shifts (~0.4 and ~0.2 eV, respectively). These findings suggest that metal doping induces different electronic interactions, with the Fe-Co interaction being the strongest. The authors concluded that the Lewis acid effect of Fe^{3+} increased the population of Co^{4+} sites in the cobalt nitride precatalyst, improving the binding energy with surface oxygen intermediates (Figure 74g). Post-OER analysis measurements confirmed the formation of a thin oxide/hydroxide layer after the OER, which provided the active sites for the reaction while the rose-like 3D porous architecture was retained.

Yin *et al.* studied the Co-doping of bimetallic MoNi nitrides for water electrolysis.[328] In the Co-doped $Ni_{0.2}Mo_{0.8}N$ sample, the coexistence of Co-doped $Ni_{0.2}Mo_{0.8}N$ and CoNi alloys with abundant defects and amorphous/crystalline interfaces was confirmed by HRTEM analysis (Figure 75a). Furthermore, from electrochemical performance tests in alkaline media

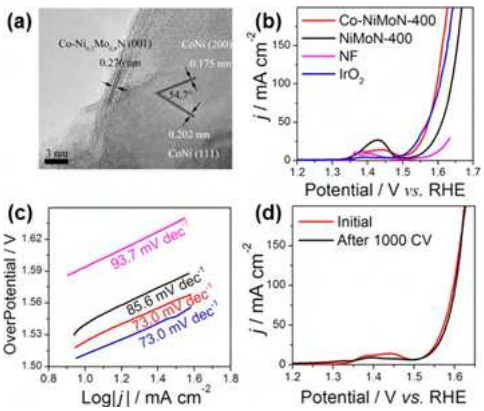


Figure 75. Influence of Co incorporation into MoNi nitride precatalysts: (a) HRTEM image of Co-doped $Ni_{0.2}Mo_{0.8}N$ (NiMoN-400) nanowire. (b) OER polarization curves in 1 M KOH. (c) Corresponding Tafel plots. (d) Polarization curves before and after 1000 CV cycles at a scan rate of 50 mV·s^{-1}. Reprinted with permission from ref 328. Copyright 2019 American Chemical Society.

(Figure 75b), the Co-doped sample exhibited the lowest overpotential (294 mV at 10 mA·cm^{-2}), similar to that of IrO_2. As displayed in Figure 75c, the Co-doped sample also exhibited the smallest Tafel slope (73 mV·dec^{-1}). Finally, the material exhibited almost the same LSV profile after 1000 CV cycles, denoting good stability (Figure 75d). In order to explain this trend, ECSA and EIS measurements were performed. The Co-doped sample showed the largest double-layer capacitance (C_{dl}) and the smallest R_{ct}. Furthermore, post-OER characterizations confirmed an amorphous layer composed of $NiO_x/Ni(OH)_2$ species on the material. Based on these findings, the authors concluded that properties originating from Co-doping, such as the numerous defects, increased surface area, and improved conductivity from the low charge transfer resistance, promoted the transformation of the original precatalyst into active oxidized Ni species. As a result, the OER performance was improved compared to that of the NiMoN sample without Co.

These case studies reveal significant impacts of metal doping on transition metal nitrides, particularly the following: (i) modulation of the electronic and structural properties of the materials, leading to electron transfer at the interfaces as well as stabilization of cations and OER intermediates due to electronic interactions; (ii) conductivity enhancement and better charge transfer at the electrode; and (iii) increase of the number of defects and surface area, which might lead to a faster reconstruction of the surface. However, a more fundamental understanding of these processes is needed, especially with other metallic nitrides in the literature. Furthermore, the effect of non-metal doping is scarce in the literature, and it is necessary to comprehend the role of electronic interactions on the OER mechanism in much more detail.

4.1.3.4. Metal Nitride Coupling Effects. Instead of incorporating cations into the crystal structure of metallic nitrides, some reports have evaluated the benefits of coupling two different metallic nitrides or creating a metal-nitride interface (i.e., heterojunctions) in the same material. By creating these heterojunctions, different studies have reported transition metal nitride electrocatalysts with enhanced conductivity, electron transfer, and stimulated oxidation due to changes in the oxidation states.[336,338,344,380] Zhu *et al.*

https://doi.org/10.1021/acs.chemrev.3c00005
Chem. Rev. 2023, 123, 12795−13208

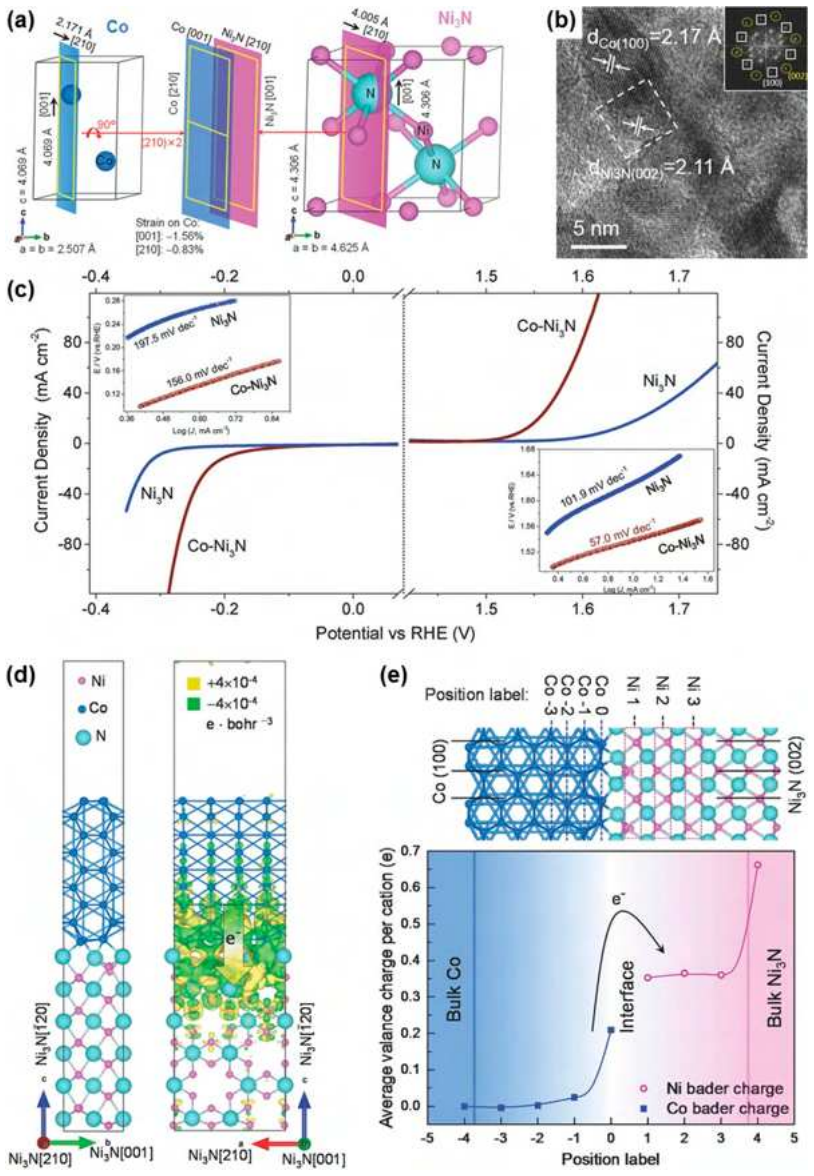


Figure 76. Effect of the Co-Ni_3N heterojunction on the electrocatalytic performance and electronic structure: (a) Schematic illustration of the lattice matching between metallic Co and Ni_3N. (b) HRTEM image of a Co-Ni_3N nanorod (inset: FFT image of the selected area). (c) OER and HER polarization curves (insets: Tafel plots). (d) Schematic illustration of the crystal structures (left) and charge density difference (right) between hcp Co and Ni_3N linked by the N-Co interface. (e) Bader charge profiles of Ni and Co cations near the N-Co interface. Reprinted with permission from ref 380. Copyright 2018 Wiley.

evaluated the performance of a Co-Ni_3N heterojunction with facilitated electron transfer at an epitaxial interface.[380] As displayed in Figure 76a, the material exhibits an epitaxial relationship between hexagonal metallic Co and nickel nitride, where the Co [001] and Ni_3N [210] planes are aligned, and a stable N-Co interface is developed at the edge. By using hydrothermal + nitridation synthesis using $NiCo_2O_4$ nanorods as a precursor, Co-Ni_3N nanoarrays were obtained. HRTEM images (Figure 76b) confirmed the presence of lattice planes of both the nickel nitride and metallic Co, as well as the presence of a clear interface. Notably, the first-principle calculation results showed that the confinement with the epitaxial interface between Co and Ni_3N prevents the detachment of these two materials. Regarding OER activity (Figure 76c), the Co-Ni_3N heterojunction exhibited the best electrocatalytic activity and kinetics, with an OER overpotential of 307 mV at 10 $mA{\cdot}cm^{-2}$ and a slight Tafel slope of only 57 $mV{\cdot}dec^{-1}$. In the case of the HER, the activity was also significantly improved compared to that of Ni_3N. EIS analysis also revealed enhanced electrical conductivity, suggesting better electron transfer when Co and Ni_3N are conjugated. Further CP tests confirmed the excellent stability of the material, and surface oxidation was assumed based on previous findings. Finally, first-principle calculations were performed to reveal the electronic effects of the heterojunction. As displayed in Figure 76d, the interface allowed electron transfer from Co to Ni_3N due to the charge density difference. Furthermore, Bader charge analysis (Figure 76e) revealed that while the average valence charge of Co increased closer to the interface, the valence charge of Ni decreased, confirming the electron transfer. This transfer can occur through Co 3d−N 2p−Ni 3d hybridizations that allow electrons to move from one side to another. Although it was not discussed for the OER, these charge differences might likely assist in stabilizing oxygen intermediates by increasing

https://doi.org/10.1021/acs.chemrev.3c00005
Chem. Rev. 2023, 123, 12795−13208

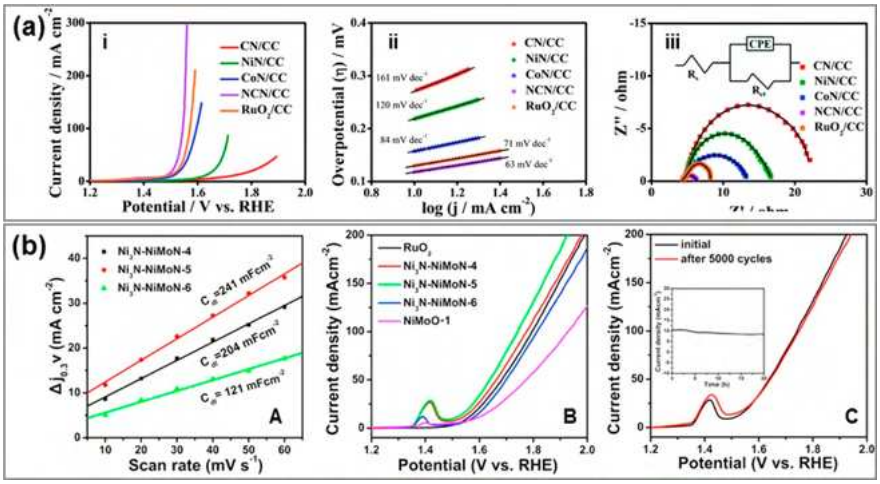


Figure 77. Transition metal nitride coupling effects. (a) Electrochemical performance of coupled CoN/Ni_3N precatalysts: OER polarization curves in 1 M KOH (i), corresponding Tafel plots (ii), and Nyquist plots at 1.6 V_{RHE} (iii). Reprinted with permission from ref 336 Copyright 2018 Royal Society of Chemistry. (b) Integrated Ni_3N-NiMoN heterostructures for overall water splitting: C_{dl} measurements (A), OER polarization curves in 1 M KOH (B), and LSV curves before and after 5000 CV cycles at a scan rate of 100 mV·s^{-1}. Reprinted with permission from ref 338. Copyright 2018 Elsevier.

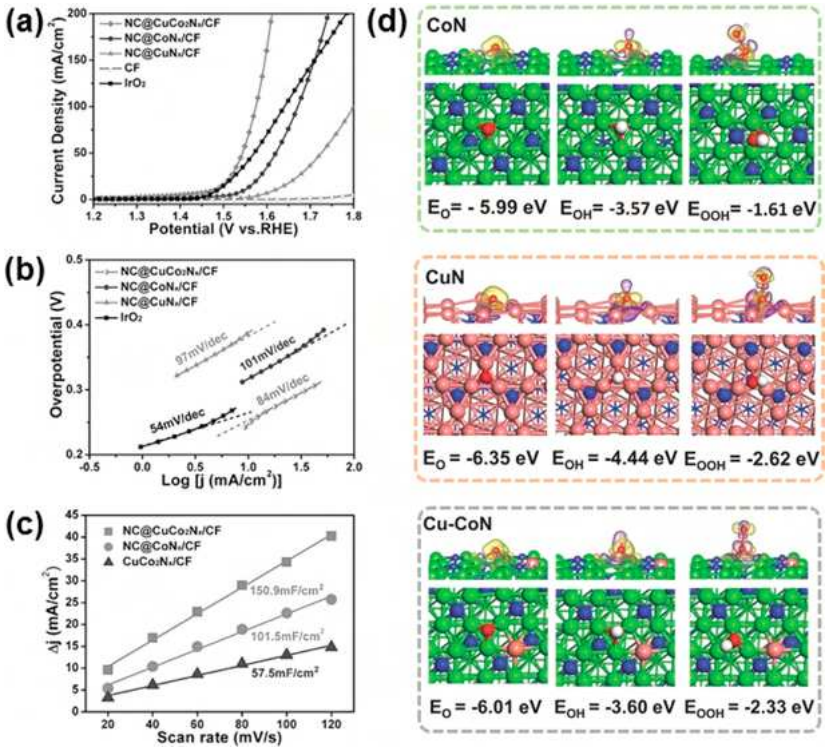


Figure 78. Performance of an integrated CuCo-based nitride precatalyst on carbon fiber substrate: (a) OER polarization curves in 1 M KOH, (b) Corresponding Tafel plots. (c) C_{dl} measurements. (d) Structures and adsorption energies of O, OH, and OOH intermediates at CoN, CuN, and Cu-CoN surfaces from DFT calculations. The Co, Cu, N, O, and H atoms are marked in green, brown, blue, red, and white, respectively. Reprinted with permission from ref 344. Copyright 2017 Wiley.

the oxidation state of Co. However, more details on the Co-Ni role as active sites are needed, as the authors only explained the stabilization of H adatoms and the decrease of the HER free energy due to the additional electrons on the Ni side.

Ray *et al.* coupled CoN and Ni_3N heterostructures on commercial CC (NCN/CC) and assessed the electrochemical performance for the OER.[336] As depicted in Figure 77a, the coupled nitride electrode exhibited the lowest overpotential (247 mV at 10 mA·cm^{-2}), the smallest Tafel slope, and the smallest R_{ct} compared to the monometallic nitride counterparts. Additionally, the C_{dl} of the NCN/CC electrode was 1.4 and 2.6 times larger than those of the monometallic Co and Ni nitrides, respectively. Moreover, post-OER analysis confirmed the formation of amorphous Ni-Co oxide/hydroxide species on the NCN/CC electrode surface. The authors attributed these features to the incorporation of Ni_3N, which created more defect sites for the OER and promoted the amorphization of the material. Moreover, the generation of

https://doi.org/10.1021/acs.chemrev.3c00005
Chem. Rev. 2023, 123, 12795−13208

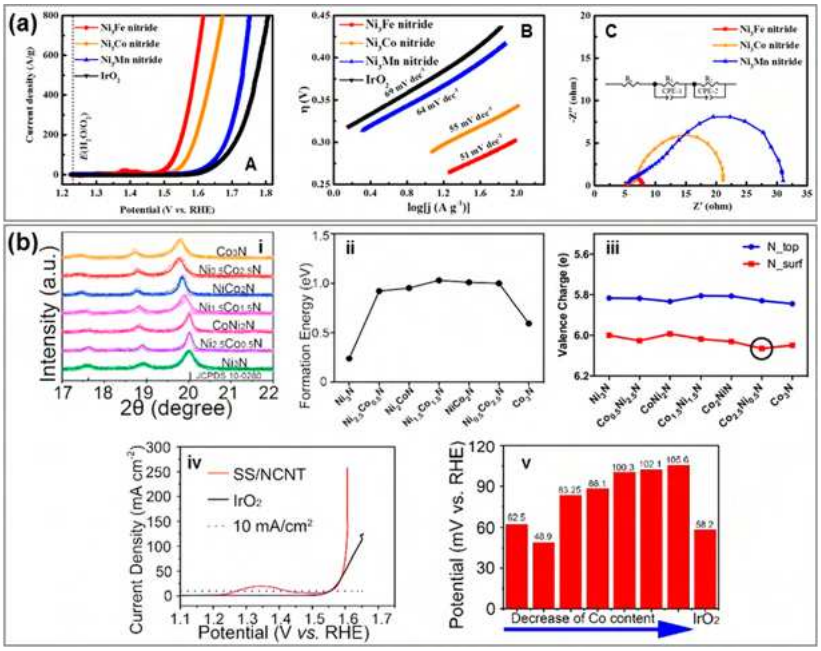


Figure 79. Influence of multi-cation compositions on the performance of transition metal nitrides. (a) Evaluation of 2D Ni_3M (M = Fe, Co, Mn) nanosheets: OER polarization curves in 1 M KOH (A), Tafel plots (B), and Nyquist plots at 0.607 V_{RHE} (C). Reprinted with permission from ref 343. Copyright 2018 American Chemical Society. (b) Evaluation of $Ni_xCo_{3-x}N$/NCNT precatalysts: XRD patterns (i) and theoretical formation energies at different compositions (ii), Bader charge of N at the surface and top positions in $Ni_xCo_{3-x}N$ (111) surfaces (iii), OER polarization curves (iv) and Tafel slopes for different compositions (v). Reprinted with permission from ref 339. Copyright 2018 Elsevier.

higher oxidation states was also attributed to the synergistic effect between both nitrides, as the heterojunctions could induce charge transfer between both species. Similarly, Wu *et al.* coupled NiMoN and Ni_3N components to form a bifunctional heterostructure for overall water splitting.[338] By varying the nitridation temperature (i.e., 400, 500, and 600 °C), the Ni_3N-NiMoN heterostructures (Ni_3N-NiMoN-4, -5, and -6) were synthesized. The coupled nitride prepared at 500 °C exhibited the largest ECSA (Figure 77b, A). Electrochemical tests for the OER revealed that this sample also offered the lowest overpotential of 277 mV at 10 mA·cm^{-2}, with a remarkable oxidation peak increase at ∼1.4 V_{RHE} (Figure 77b, B). According to this LSV result, the Ni_3N-NiMoN heterostructure can provide more active metal species (e.g., $Ni^{2+} \rightarrow Ni^{3+}$) at the surface. Stability tests confirmed the stability of the material (Figure 77b, C), and remarkably, the oxidation peak slightly increased after 5000 CV cycles. Based on additional XPS measurements, it was confirmed that the coupled nitride was oxidized during the OER and that NiOOH and high-valence Mo species were produced. The authors attributed the good activity of the Ni_3N-NiMoN heterojunction to the formation of NiOOH, which could be explained by the increase of the Mo oxidation state during the OER. Therefore, the presence of highly-oxidized Mo^{6+} could induce charge transfer to Ni_3N to stimulate its oxidation into NiOOH.[202,357,406]

In a more detailed study, Zheng *et al.* evaluated the integration of Cu- and Co-based nitrides (Co_3N and $Cu_{5.47}N$ species) in self-supported, N-doped carbon and carbon fiber (CF) substrates.[344] Specifically, the coupled nitride sample (NC@$CuCo_2N_x$/CF) consisted of $CuCo_2N_x$ nanosheets composed of small interconnected $CuCoN_x$ NPs coated by a carbon layer. Samples including only one monometallic nitride (i.e., NC@CoN_x/CF and NC@CuN_x/CF) were also synthesized as a comparison. Analogous to the above-mentioned case studies, electrochemical characterization of the materials revealed the superior performance of the coupled nitride electrode. From OER polarization curves (Figure 78a), the NC@$CuCo_2N_x$/CF displayed the lowest overpotential (230 mV at 10 mA·cm^{-2}), followed by NC@CoN_x/CF (310 mV) and NC@CuN_x/CF (380 mV). As depicted in Figure 78b, the coupled nitride exhibited a slight Tafel slope of 84 mV·dec^{-1}, only surpassed by IrO_2. ECSA measurements also confirmed the large surface area of the NC@$CuCo_2N_x$/CF electrode (Figure 78c). In order to define the reasons behind these trends, the authors performed DFT calculations. As depicted in Figure 78d, the adsorption of O, OH, and OOH intermediates was studied on CoN(111), CuN(111), and Cu-CoN(111) surfaces. Interestingly, the adsorption energies were higher in CuN than CoN, and the mixed Cu-CoN model exhibited intermediate values. Additional Bader charge analysis revealed that the charge of O adsorbed on CuN is approximately 0.1 higher than that of CoN, explaining the higher adsorption energies on CuN. Overall, the authors concluded that the superior OER activity was explained by the conjugation of CuN and CoN, as the electronic coupling induced charge transfer from CuN to CoN. This reduced the intermediate adsorption energy on CuN and increased the adsorption energy on CoN up to an optimal level. These results demonstrate that nitride conjugation modifies the electronic structure of the materials and improves the OER mechanism when the correct compounds are brought together. In general, the following charge transfer across the interface in these heterojunctions promotes (i) the stabilization of OER intermediates by tuning the adsorption energies of the conjugated species, (ii) the conductivity due to the faster electron transfer, and (iii) the oxidation of metal centers and, therefore, the formation of metal oxyhydroxides as active

https://doi.org/10.1021/acs.chemrev.3c00005
Chem. Rev. 2023, 123, 12795−13208

species for the OER. Undoubtedly, these features enhance the OER activity by creating more active sites, improving the electron transfer across the material and reducing the energetic barriers of the OER mechanism.[336,380]

4.1.3.5. Multi-cation Effects. Similar to the doping and nitride coupling effects, some authors have synthesized multi-cation nitrides, especially bimetallic nitrides, to improve the electronic and structural properties of the final materials. Guo *et al.* synthesized a series of Ni-based bimetallic nitride nanosheets (Ni_3M-N, where M = Fe, Co, Mn) and evaluated their OER performance in alkaline electrolytes.[343] From OER polarization curves (Figure 79a, A), the 2D holey Ni_3Fe nitride exhibited the lowest overpotential of 300 mV at 100 $A{\cdot}g^{-1}$, followed by Ni_3Co nitride (340 mV) and Ni_3Mn nitride (429 mV). The bimetallic nitrides exhibited the same trend when comparing the Tafel slope (Figure 79a, B) and R_{ct} values from EIS (Figure 79a, C), suggesting that the Ni, Fe-based bimetallic nitride possesses superior activity, kinetics, and charge transfer at the electrode surface. The superior conductivities of the synthesized nitrides were also confirmed by the four-point probe method, where the Fe-, Co-, and Mn-based bimetallic nitrides exhibited electrical conductivities of 270, 200, and 70 $S{\cdot}m^{-1}$. Additionally, HRTEM and XPS characterizations after 1000 CV stability cycles confirmed the formation of a thin oxide layer composed of NiFe oxides/oxyhydroxides. Finally, oxygen adsorption energies using the (111) plane followed the trend Ni_3Fe nitride (−3.47 eV) < Ni_3Mn nitride (−3.29 eV) < Ni_3Co nitride (−2.80 eV), with the Fe-based bimetallic nitride being the most favorable for the OER. The authors concluded that Ni-Fe electronic interactions and larger lattice spacing were responsible for the favorable oxygen adsorption energy. He *et al.* evaluated the OER performance of different compositions of Ni, Co-based bimetallic nitrides ($Ni_xCo_{3-x}N$) to find the optimized composition.[339] DFT calculations were performed to unveil the electronic properties of these seven nitrides. Resultant formation energies are shown in Figure 79b, ii. The trend suggests that the mixed Ni and Co compositions demand more energy when prepared, but they vary similarly (i.e., the bimetallic nitrides could be obtained with any composition). Further, density of states (DOS) calculations confirmed the metallic nature of these nitrides. In addition, valence charge analysis (Figure 79b, iii) demonstrated that the valence charge of surface N atoms (i.e., N atoms bonded with four transition metals) does not change significantly with the bimetallic nitride composition. Moreover, the surface N atoms possessed more electrons than the N atoms at the top (coordinated by only three TMs). This suggests that transition metals bonded with N atoms at the surface (higher M/N ratio) are more charge-deficient (i.e., experience higher oxidation states). Notably, the $Ni_{0.5}Co_{2.5}N$ composition (denoted as SS/NCNT) exhibited the more charge-deficient state, that is, the weakest metal−nitride bonds (in the bulk), and highest charge-deficient states (at the surface), which are expected to improve the electrocatalytic performance of the material, as more transition metals can be easily oxidized. From OER polarization curves (Figure 79b, iv), the $Ni_{0.5}Co_{2.5}N$ sample exhibited the best performance (overpotential: 324 mV at 10 $mA{\cdot}cm^{-2}$), being comparable to that of IrO_2. The $Ni_{0.5}Co_{2.5}N$ nitride also exhibited the smallest Tafel slope (48.9 $mV{\cdot}dec^{-1}$), while the rest of the slopes increased with the Ni content (Figure 79b, v). Finally, post-OER XPS characterization confirmed the oxidation of the material, suggesting that the abundance of charge-deficient transition metal sites produced during oxidation is responsible for the enhanced OER performance, as more metal oxide/oxyhydroxide species are generated.

Due to the relevance of Fe in bimetallic transition metal nitrides, Jia *et al.* studied bimetallic NiFe nitride NPs in an alkaline environment.[388] As depicted in Figure 80a, the

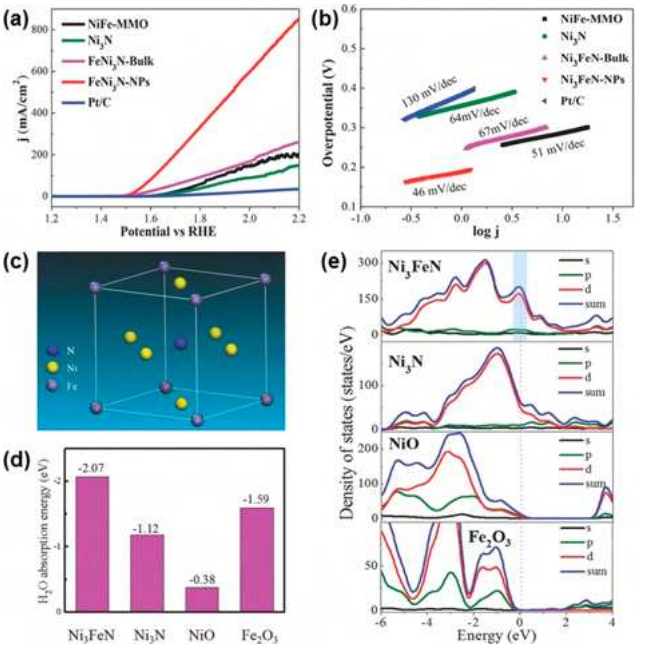


Figure 80. Electrocatalytic evaluation of Ni_3FeN nanoparticles: (a) OER polarization curves in 1 M KOH. (b) Corresponding Tafel plots. (c) Atomic model of the Ni_3FeN crystal utilized for DFT calculations. (d) Theoretical adsorption energies of H_2O on different surfaces. (e) Total and partial electronic density of states calculated for different materials. Reprinted with permission from ref 388. Copyright 2016 Wiley.

Ni_3FeN-NPs sample exhibited the best performance (overpotential: 280 mV at 10 $mA{\cdot}cm^{-2}$) among different samples, including monometallic Ni_3N and Ni_3FeN bulk samples. The bimetallic nitride NPs also exhibited the smallest Tafel slope (Figure 80b), suggesting improved OER kinetics. In order to unveil the reasons for this enhanced OER performance, DFT calculations were performed using the fcc structure of Ni_3FeN (Figure 80c). As shown in Figure 80d, the bimetallic nitride exhibited the highest H_2O adsorption energy, which is attributed to the extended electronic DOS close to the Fermi level of Fe, possibly acting as the active sites. Additionally, the DOS and band structure were also studied (Figure 80e). Notably, Ni_3FeN exhibited a continuous DOS, suggesting metallic behavior and explaining the superior conductivity of Fe addition. Moreover, the more covalent interaction of N in the nitride samples also explains the facile electron transport. Additional EIS analysis confirmed these findings, demonstrating the superior conductivity and charge transfer of the bimetallic nitride. Overall, these case studies also show that incorporating additional cations into the nitride compound favors the electronic properties, charge carrier concentrations, and electrical conductivity of transition metal nitride precatalysts. These properties have important implications for the OER activity, as enhanced electron transfer across the nitride phase (even if the surface is oxidized) offers high

https://doi.org/10.1021/acs.chemrev.3c00005
Chem. Rev. 2023, 123, 12795−13208

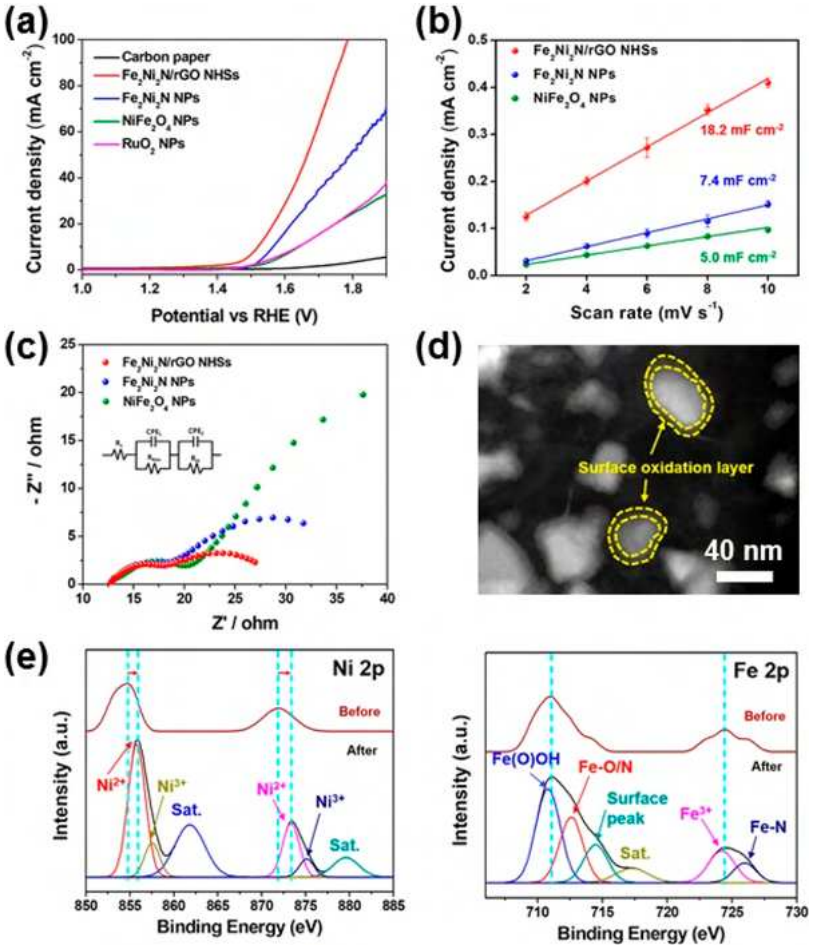


Figure 81. Evaluation of a 2D-NC Fe_2Ni_2N/rGO hybrid nanocomposite OER precatalyst: (a) OER polarization curves in 0.1 M KOH. (b) C_{dl} measurements. (c) Nyquist plots at 1.65 V_{RHE} for NiFe oxide, NiFe nitride, and the hybrid composite. (d) HAADF-STEM image. (e) High-resolution XPS Ni 2p and Fe 2p spectra of the hybrid composite after OER stability tests at 10 mA·cm^{-2} for 24 h. Reprinted with permission from ref 333. Copyright 2019 American Chemical Society.

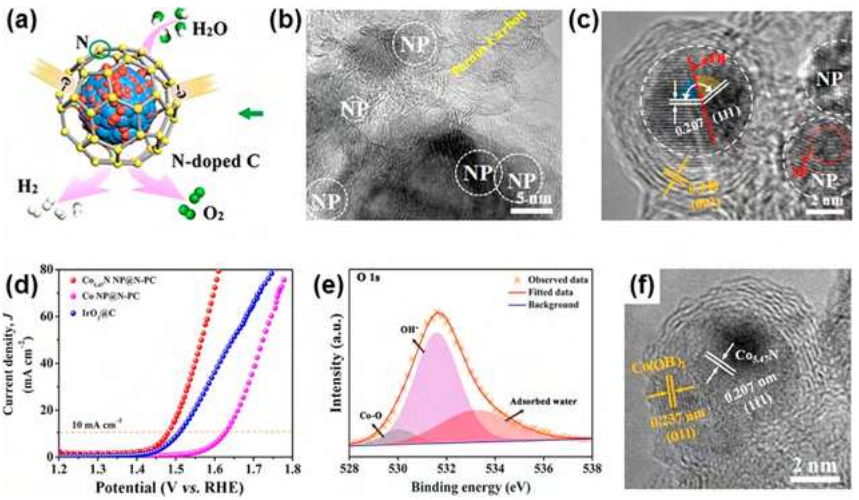


Figure 82. Performance of $Co_{5.47}N$ NPs encapsulated within a 3D N-doped porous carbon matrix: (a) Schematic illustration of the $Co_{5.47}N$ NP@N-PC precatalyst. (b, c) HRTEM images of the as-prepared sample. (d) OER polarization curves comparing the cobalt nitride composite and the metallic Co composite in 1 M KOH. (e) High-resolution XPS O 1s spectra. (f) HRTEM image of the $Co_{5.47}N$ NP@N-PC precatalyst after OER tests. Reprinted with permission from ref 341. Copyright 2018 American Chemical Society.

conductivity.[343] Moreover, charge differences between metals might stabilize OER intermediates and enhance the formation of oxidized transition metal species.[339] DFT calculations have played a notorious role in describing these properties, facilitating the understanding behind the improved features of transition metal nitrides. It should be emphasized that these

https://doi.org/10.1021/acs.chemrev.3c00005
Chem. Rev. 2023, 123, 12795−13208

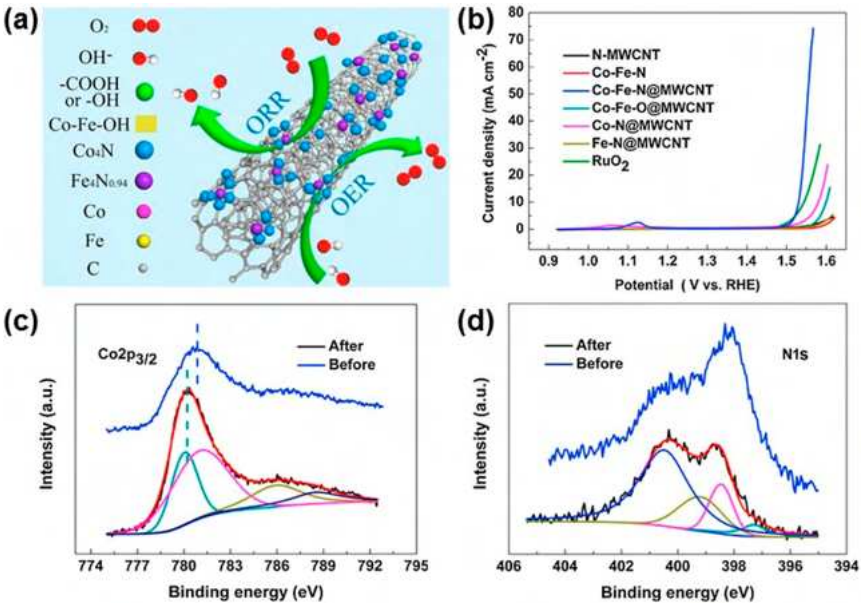


Figure 83. Evaluation of bimetallic Co-Fe nitride precatalyst on N-doped MWCNTs: (a) Schematic illustration of the Co-Fe-N@MWCNT precatalyst. (b) OER polarization curves for different samples in 1 M KOH. (c, d) XPS (c) Co $2p_{3/2}$ and (d) N 1s spectra of the Co-Fe-N@MWCNT precatalyst after OER tests. Reprinted with permission from ref 346. Copyright 2017 Elsevier.

theoretical calculations do not provide direct evidence of the transition metal nitrides acting as active sites. However, a better description of the structural and electronic properties of these transition metal nitrides provides valuable information regarding the reconstruction process. One example is the production of highly oxidized transition metal centers due to inductive and electronic effects. Nevertheless, more studies focused on the comparison of pristine and oxidized transition metal nitrides are necessary.

4.1.3.6. Composite Materials Effects. In order to improve the stability, conductivity, and mass transfer of the transition metal nitride precatalysts, several studies have synthesized composite electrocatalysts (transition metal nitride + carbon-based material). Kwag *et al.* prepared 2D, nanocrystalline (NC) Fe_2Ni_2N with reduced graphene oxide (rGO) nanohybrid sheets (NHSs) using conventional nitridation.[333] As displayed in Figure 81a, the 2D-NC Fe_2Ni_2N/rGO NHS precatalyst exhibited the lowest overpotential (290 mV at 10 mA·cm^{-2}) when compared with the Fe_2Ni_2N NP and $NiFe_2O_4$ NP counterparts. The nanohybrid sheets also exhibited the largest surface area (Figure 81b) and the lowest R_{ct} from EIS analysis (Figure 81c), which is attributed to better nitride dispersion, faster charge transfer, and good electrical conductivity contact with rGO. After CP stability tests for 24 h, post-OER TEM and XPS characterizations were performed. As shown in Figure 81d, the high-angle annular dark-field scanning transmission electron microscopy (HAADF-STEM) image revealed a thin, amorphous surface oxide layer, although the material retained its morphology. XPS analysis (Figure 81e) confirmed the formation of highly oxidized Ni species and Fe^{2+} and Fe^{3+}, suggesting the formation of NiFe oxide/oxyhydroxide species during the OER. Since the material retained its superior OER activity after 24 h of testing, these results suggest that the rGO was still responsible for the higher conductivity and distribution of the bimetallic nitride. Notably, using carbon nanotubes (CNTs) instead of rGO with Fe_2Ni_2N also improved the electrocatalytic performance, demonstrating that there is a synergetic effect between metallic NiFe nitrides and conductive carbon-based materials.[378]

Chen *et al.* prepared 3D cobalt nitride−N-doped porous graphitic carbon composites ($Co_{5.47}N$ NP@N-PC).[341] As depicted in Figure 82a, the N-doped carbon encapsulated the ultrafine $Co_{5.47}N$ nanoparticles. Interestingly, the $Co_{5.47}N$ structure exhibits some N vacancies in the octahedral sites, giving the cobalt nitride a more metallic nature. From HRTEM images (Figures 82b and c), cobalt nitride NPs are scattered along with the porous graphitic carbon matrix, and closer inspection confirms that each NP is encapsulated by 3 to 5 graphitic carbon layers. According to OER polarization curves in an alkaline electrolyte (Figure 82d), the cobalt nitride composite exhibited a low overpotential of 248 mV at 10 mA·cm^{-2}, surpassing those of IrO_2 and the metallic cobalt−carbon composite. TEM and XPS characterizations were performed after OER cycling durability tests to check the composites' stability. As shown in Figure 25e, the O 1s XPS spectrum included contributions from Co−O bonds and low-coordinated oxygen ions, suggesting the formation of oxidized species during the OER. The Co 2p spectra also suggested the presence of Co with a higher oxidation state. The HRTEM image (Figure 82f) revealed a $Co_{5.47}N$@$Co(OH)_2$ core@shell structure. The authors concluded that although the material was oxidized, it reached a steady state preventing further oxidation of the core, thus giving a more stable oxide interface which was thermodynamically favorable for the OER. Nevertheless, the superior activity of the composite was attributed to the higher conductivity, hierarchically porous structure, and electronic modulation of N-doped carbon.

Finally, Gao *et al.* coupled cobalt-iron bimetallic nitrides with N-doped multi-walled carbon nanotubes (MWCNTs) as OER and ORR precatalysts.[346] As depicted in Figure 83a, the Co-Fe-N@MWCNT composite included $Fe_4N_{0.94}$ and Co_4N nitrides distributed along with the MWCNT structure, providing superior electronic transport and enlarging the surface area of the final composite. Electrochemical performance tests confirmed this improvement, as the bimetallic

https://doi.org/10.1021/acs.chemrev.3c00005
Chem. Rev. 2023, 123, 12795−13208

nitride composite exhibited the lowest OER overpotential (290 mV at 10 mA·cm^{-2}), surpassing all the monometallic and carbon-free counterparts (Figure 83b). Moreover, this composite exhibited the smallest Tafel slope and the lowest R_{ct} value and retained 97% of its OER activity during stability tests. Notably, post-OER XPS analysis confirmed the presence of oxidized species, as the negative shift of the Co $2p_{3/2}$ peak suggested the formation of Co^{3+} (Figure 83c), and the intensity of the N 1s peaks decreased considerably (Figure 83d). Additional XRD analysis confirmed the presence of oxides, and TEM images revealed the formation of a thin amorphous oxide layer around the nitride NPs. These case studies depict the relevance of making nitride-based composites with superior OER activity and stability. Based on the previous case studies, the following points can be established: (i) carbon-based composites can provide superior conductivity and electron transport; (ii) the use of porous materials increases the surface area and effectively distributes metallic nitride nanoparticles in conductive carbon-based support; and (iii) these examples demonstrate that carbon-based composites do not necessarily protect the transition metal nitride from oxidation, which is commonly stated by some studies without demonstrating the absence of oxide species after the OER.[401−403] In fact, morphologies and porous matrices could retain their structure without noticeable aggregation or degradation, but additional chemical and structural characterization techniques are needed to confirm the presence of oxides.[331] It is important to note that oxidation is not an undesirable transformation and that the composite will still exhibit improved performance due to other properties such as conductivity and surface area rather than "protection" or "shielding" abilities.

4.1.3.7. pH Effects. The pH is an important parameter closely related to the activity and stability of water-splitting electrocatalysts. Transition metal nitrides are usually regarded as materials with excellent stability in both alkaline and acidic electrolytes.[301,408] However, in most reports, the authors have only tested the OER performance of transition metal nitride precatalysts in alkaline media (see Table 3). There are only a few case studies in which transition metal nitrides have been studied in other environments.[336,350] Ray *et al.* tested the OER performance of coupled CoN-Ni_3N nitrides in both 1 M KOH and 0.5 M H_2SO_4.[336] As previously discussed in the Metal Nitride Coupling Effects section, the NCN/CC sample exhibited precatalyst behavior in alkaline media during the OER. Under acidic conditions, the authors reported an overpotential of 300 mV at 10 mA·cm^{-2} and 90% potential retention during 24 h stability tests. When assembled in an electrolyzer, the cell operated without any visible changes for 100 h. Although the material exhibited a higher overpotential in acidic media, the performance was comparable in both electrolytes and better than that of RuO_2. However, no post-OER analysis measurements were performed in acidic media, and the precatalytic behavior was not directly confirmed. This has significant implications, as OER active species such as Ni oxide/hydroxide species are not stable in neutral and acidic conditions, according to the Pourbaix diagrams.[409] Therefore, it is essential to determine why the activity and stability were improved in alkaline and acidic media. More implications related to this aspect are discussed in Section 4.2.4.

Regarding other electrolytes, Xie *et al.* evaluated the OER performance of a Ni_3N nanoarray precatalyst in a near-neutral bicarbonate electrolyte [1.0 M $KHCO_3$ (bulk pH: 8.3)].[350] Before the OER testing, the Ni_3N precatalyst was activated by the oxidative polarization treatment in 1.0 M $KHCO_3$, forming an amorphous nickel-carbonate (Ni-Ci) layer and giving a Ni_3N@Ni-Ci core@shell structure as a result. As depicted in Figure 84a, the Ni_3N@Ni-Ci/CC electrode exhibited better

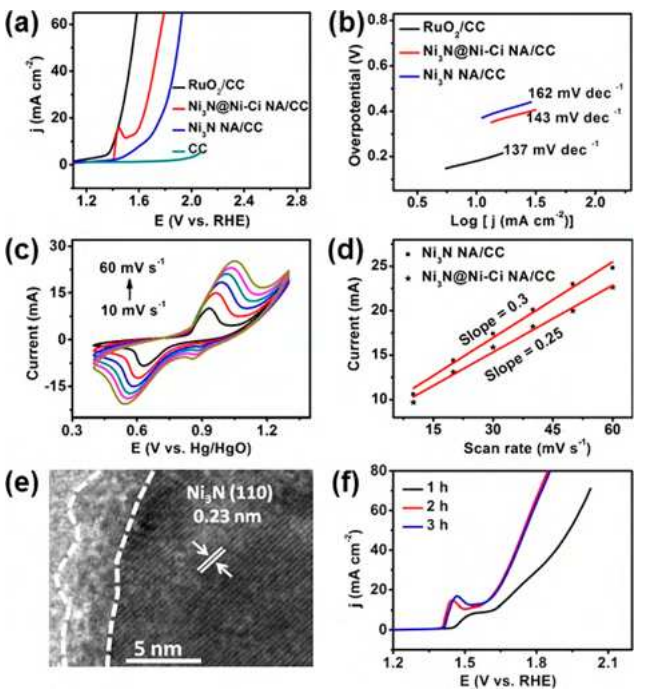


Figure 84. Electrocatalytic performance of a Ni_3N@Ni-Ci precatalyst in 1 M K-Ci electrolyte (pH 8.3): (a) OER polarization curves at a scan rate of 5 mV·s^{-1}. (b) Corresponding Tafel plots. (c) CV scans at increasing scan rates. (d) C_{dl} measurements. (e) HRTEM image of the sample after 1 h of continuous oxidative polarization. (f) OER polarization curves at different times during oxidative polarization. Reprinted with permission from ref 350. Copyright 2017 Elsevier.

OER activity (overpotential: 400 mV at 20 mA·cm^{-2}) than the inactivated Ni_3N counterpart. Moreover, the Tafel slope of the core@shell sample was lower than that of the inactivated Ni_3N sample (Figure 84b). Notably, the core@shell sample exhibited an intense Ni oxidation peak around 1.5 V_{RHE} (Figure 84a), suggesting the oxidation of surface Ni species ($Ni^{2+} \rightarrow Ni^{3+}$). This Ni oxidation peak intensity estimated the number of active sites (Figures 84c and d). The turnover frequency was estimated from the as-estimated active sites, being 0.10 mol_{O_2} s^{-1} at an OER overpotential of 480 mV. This value did not change after 12 h of stability tests, and it was higher than that of Ni_3N (0.028 mol_{O_2} s^{-1}). Furthermore, the authors evaluated the effect of oxidation time on the formation of the Ni-Ci layer. As depicted in Figure 84e, a thin layer of Ni-Ci was formed after only 1 h of the oxidative polarization treatment. The layer thickness stabilized at around 2 h, and oxidation for extended periods did not significantly change the Ni redox peak (Figure 84f).

Notably, the Ni_3N@Ni-Ci core@shell sample was electrochemically stable for 12 h at constant overpotentials of 480 and 600 mV in 1.0 M $KHCO_3$ electrolyte. Post-OER TEM characterization revealed that the thickness of the Ni-Ci shell was retained, and XPS measurements confirmed the presence of oxidized $Ni^{2+/3+}$ species and C(O)O- and C−O groups, which were initially present after the oxidation polarization

https://doi.org/10.1021/acs.chemrev.3c00005
Chem. Rev. 2023, 123, 12795−13208

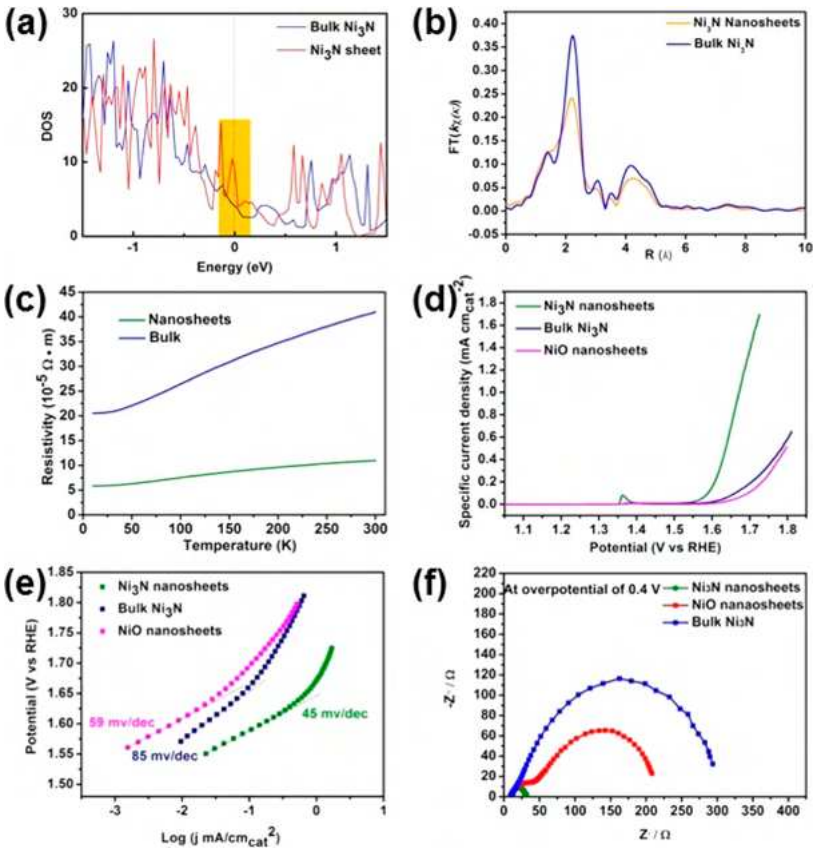


Figure 85. Performance comparison between bulk and 2D Ni_3N nanosheets as OER precatalysts: (a) Calculated DOS for bulk and sheet-type Ni_3N. (b) Fourier transforms of the Ni K-edge extended EXAFS oscillations. (c) Temperature-dependent electrical resistivity of Ni_3N. (d) OER polarization curves in 1 M KOH. (e) Corresponding Tafel plots. (f) Nyquist plots at 1.63 V_{RHE}. Reprinted with permission from ref 357. Copyright 2015 American Chemical Society.

treatment. Although the precatalytic effect was confirmed in 1.0 M $KHCO_3$ electrolyte, a detailed discussion of how the Ni-Ci layer enhanced the OER activity and stability was not determined. However, the authors emphasize that the OER activity was associated with the shell thickness. More studies are necessary to reveal if oxidized carbon groups have any synergetic effects or act as the OER active sites instead of the oxidized Ni sites (both sites found by XPS).

4.1.3.8. Morphological and Structural Effects. Certain reports have also studied the effect of specific morphologies and structural properties of transition metal nitride precatalysts on the OER performance. Xu *et al.* compared the properties and performance of bulk Ni_3N and 2D Ni_3N nanosheets using experimental and theoretical methods.[357] From DOS calculations (Figure 85a), although both Ni_3N can be considered metallic, the DOS of the 2D Ni_3N nanosheets is more intense, suggesting that dimensional confinement improves the electronic conduction. Moreover, as seen in Ni K-edge extended X-ray absorption fine structure spectroscopy (EXAFS) oscillations of bulk Ni_3N and 2D Ni_3N nanosheets (Figure 85b), it was found that the 2D nanosheets exhibited more vacancies and disordered structure due to the dimensional decrease, which could induce more electrocatalytically active sites and a larger surface area. Additionally, temperature-dependent resistivity measurements (Figure 85c) confirmed the superior electrical conductivity of 2D Ni_3N nanosheets, suggesting that morphology and structural properties have important effects on the conductivity even for the same material. To confirm the effect of these properties on electrocatalytic performance, electrochemical measurements were performed. As depicted in Figure 85d, the Ni_3N nanosheets exhibited an evident intrinsic activity increase compared to bulk Ni_3N, and the Ni oxidation peaks indicate the oxidation of Ni_3N into Ni oxide/(oxy)hydroxide species. The 2D Ni_3N also exhibited the smallest Tafel slope (Figure 85e), suggesting improved OER kinetics. Finally, EIS analysis revealed low R_{ct} for the Ni_3N nanosheet sample, confirming its improved electronic properties and fast charge transfer compared to its bulk counterpart. Overall, the authors attributed the superior performance of 2D Ni_3N to the presence of more defects (i.e., more active sites produced during oxidation) and superior electrical conductivity due to the ultrathin 2D nanosheets with metallic nature increasing the electron transfer. Finally, the superior performance was retained even after growing the nanosheets on CC, demonstrating the excellent properties and versatility of the 2D transition metal nitride precatalyst.

The presence of defect-rich structures is considered an important property to increase the number of active sites. Zhao *et al.* characterized defect-rich and near defect-free bimetallic Ni_3FeN nanocrystals and their OER performance in alkaline media.[340] By following a sequence of different gas-solid nitridation steps, sheet-like nanostructures with abundant defects (wrinkles, edges, etc.) were obtained. As depicted in Figure 86a, the TEM images display several bimetallic nitride nanocrystals dispersed on N-doped graphene sheets (N-G). Upon closer inspection, two general types of defects were seen: five-fold twinned crystals (Figure 86b) and micro-twinned

https://doi.org/10.1021/acs.chemrev.3c00005
Chem. Rev. 2023, 123, 12795−13208

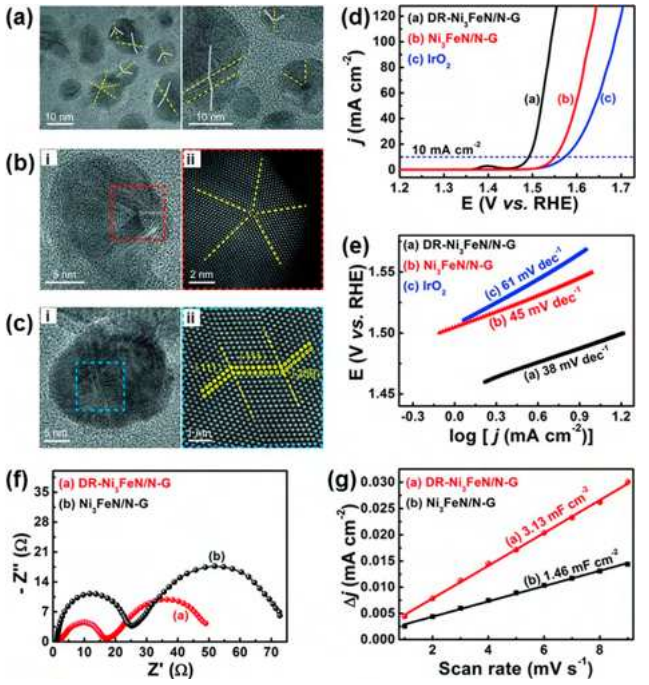


Figure 86. Influence of the structural defects in Ni_3FeN nanocrystals: (a) TEM images of the DR-Ni_3FeN/N-G nanohybrids. (b, c) Representative images of (b) the five-fold twinned and (c) the micro-twinned crystal structures (i and ii depict the HTREM and HAADF-STEM images, respectively). (d) OER polarization curves comparing the defect-rich sample with the defect-free nitride and IrO_2 in 1 M KOH. (e) Corresponding Tafel plots. (f) Nyquist plots at 1.53 V_{RHE}. (g) C_{dl} measurements. Reprinted with permission from ref 340. Copyright 2018 Wiley.

structures (Figure 86c). The patterns of these defects can be seen from the aberration-corrected HAADF-STEM images and reveal that certain planes were preferentially formed (i.e., the (111) and (200) planes of the cubic phase of Ni_3FeN). Then, the electrochemical characterization of both defect-rich (DR-Ni_3FeN/N-G) and near defect-free (Ni_3FeN/N-G) samples was performed. From OER polarization curves (Figure 86d), the defect-rich sample exhibited the lowest overpotential (250 mV at 10 mA·cm^{-2}), being 70 mV lower than that of the near defect-free sample. The DR-Ni_3FeN/N-G sample also exhibited the smallest Tafel slope (Figure 86e), confirming the superior kinetics of the sample. EIS analysis (Figure 86f) and C_{dl} measurements (Figure 86g) revealed that the defect-rich sample also possessed the lowest R_{ct} and the largest ECSA, respectively. Interestingly, the post-OER microstructural analysis revealed that the defects were preserved after CV stability tests, although XPS analysis confirmed the partial oxidation into amorphous Ni-Fe oxides/(oxy)hydroxides. Overall, the authors concluded that abundant defects increased the number of active sites, improved the interaction with the N-G support, and enhanced the charge transfer/OER kinetics of the bimetallic nitride. These case studies confirm that the morphological and structural features of the material can have significant effects on the OER activity and stability of transition metal nitride precatalysts.

4.1.4. Challenges. From the cases mentioned above, it is evident that most of the reported transition metal nitrides can be considered as precatalysts due to the extensive evidence about their reconstruction (oxidation) during the OER. According to the Pourbaix diagram of N species (Figure 87),

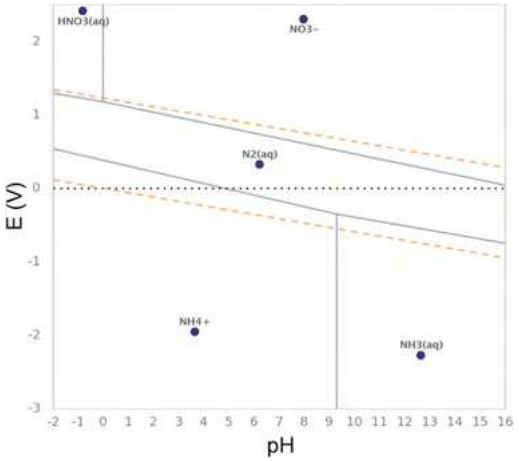


Figure 87. Pourbaix diagram for nitrogen. Orange broken lines represent the thermodynamic potentials for the HER and OER at different pH values. The diagram is produced at the N ion concentration of 10^{-8} M (default) by using the Materials Project.[87−89]

the N species in the oxidized transition metal nitride surface may be released as soluble NO_3^- anions into the electrolyte (pH ≈ 0−16) under the thermodynamic OER potential. However, one report found a residual N species (e.g., -NO_3/-NO_2 species) existing on the surface of the partially electrooxidized transition metal nitride,[339] which possibly affects the resultant OER activity. Some studies reporting the presence of transition metal nitrides in the core of core@shell structures should also confirm if N atoms are entirely removed from the surface.[332,353] Moreover, other studies showed from post-OER XPS analysis that some *M*−N species remain at the oxidized transition metal surface,[332,336] which may also provide the nitride/oxide heterointerfaces influencing the OER process positively/negatively. These points need to be examined in the near future. Additionally, there are still more considerations that remain elusive in the literature. Here, we highlight special case studies describing relevant challenges that must be understood to comprehend the reconstruction of transition metal nitrides during the OER.

Although a considerable number of studies have focused on studying the effect of different electronic, structural, morphological, and synthetic trends, there is a lack of fundamental understanding of how these features affect the OER and the reconstruction of the transition metal nitride precatalyst. For example, it is not clear if nitride coupling is benefited only because of the differences in conductivity or also due to charge densities between different nitrides that increase the oxidation state of the active sites,[336,338] analogous to the metal-nitride doping effects discussed by Zhu *et al.*[380] Studies with different nitride species with emphasis on the reconstruction behavior and charge localization are necessary. Furthermore, future studies need to focus on the structural properties of the materials, mainly when severe reconstruction occurs. This is important because structural defects and specific morphologies might lead to more active sites, implying that the oxidation extent might increase.[332,340,357] We recommend disclosing the following properties about reported transition metal nitrides: (i) confirmation of the presence of amorphous oxide/hydroxides after/during the OER, (ii) estimation of the thickness of this surface layer or confirmation if complete oxidation occurred, and (iii) evaluation of the ECSA and TOF values before and after stability tests. This information might

https://doi.org/10.1021/acs.chemrev.3c00005
Chem. Rev. 2023, 123, 12795−13208

provide more evidence about the effect of the structural properties of the precatalysts in the reconstruction process. Furthermore, the synthesis of well-faceted transition metal nitride precatalysts would be advantageous to describe any effects caused by preferential crystal planes, which have not been thoroughly studied for transition metal nitrides.

Another interesting topic is the effect of the electrolyte properties on stability, especially the presence of specific ions (e.g., Fe^{2+}) that can readily incorporate into the formed oxide surface layer, as well as the dissolution of species (i.e., N species, transition metal cations) from the electrodes.[90,329,349,356,410] Certain studies have shown that the shell consists of mainly an amorphous oxide/hydroxide layer.[332,353] Although transition metal nitrides are usually regarded as stable materials in all pH environments,[301,408] the surface reconstruction during the OER is a clear example that transition metal nitrides might undergo severe changes during catalysis, and care must be taken when evaluating their properties. There is solid evidence in the literature that some materials such as Ni_3N do not dissolve in alkaline environments.[356] However, although the main transition metal nitride may not dissolve, other cations such as Mo in multi-cation materials could be dissolved during operation.[349,410] This suggests that although an initial material could contain specific amounts of dopants, the composition of the precatalyst might vary during performance tests. Similarly, there is a possibility that bimetallic nitrides can change their composition and become monometallic near the surface, at least, which needs to be checked in the future. Therefore, precise analyses of the electrolyte environment, pH effects, and compositional stability must be performed. Furthermore, Fe incorporation must be considered, especially in the transition metal nitride precatalysts, and future studies should demonstrate that Fe is not improving the OER activity during performance tests. Recently, Kawashima *et al.* found that exposure of Ni_3N to Fe-unpurified KOH electrolyte resulted in increased OER activity during the formation of NiOOH sites, suggesting that Fe incorporation into bulk NiO_xH_y and edge/defect sites induces important effects on the NiOOH, explaining the superior OER performance.[90] Dealing with these concerns will improve the understanding of transition metal nitride precatalysts and will also enable more thorough comparison of the proposed materials in this field.

4.2. Transition Metal Phosphides

4.2.1. Electrode Preparation Methods. As shown in Table 4, we can also find two types of transition metal phosphide electrodes: (i) powder-coated electrodes (P) and (ii) self-supported electrodes (S). Generally, transition metal phosphides can be formed through different approaches using a broad range of precursors. In this Section, a particular emphasis is made on the synthesis strategy due to its strong connection with the physicochemical properties of the transition metal phosphide products. Among different methods, gas-solid thermal approaches, which are favorable to yielding crystalline phosphides, have been extensively used to synthesize transition metal phosphides due to their simplicity and capacity to retain the morphology of precursors. This gas-solid strategy is also known as phosphidation (also known as phosphorylation),[23] which relies on the use of chemicals (phosphorous sources) such as red phosphorus,[518] hypophosphites (e.g., NaH_2PO_2),[597] phosphine (PH_3) gas,[598] and so forth. Especially, the solid phosphorous sources can generate reactive intermediates [e.g., phosphine (PH_3) gas, phosphorus vapor, etc.] *in situ* during the gas-solid synthesis. For example, the synthesis using red phosphorus may produce toxic PH_3 gas at relatively low-to-moderate temperatures when elemental P reacts with moisture or hydrogen due to its poor thermostability.[599,600] On the other hand, *in situ* generation of PH_3 gas from hypophosphites ($2NaH_2PO_2 \rightarrow PH_3\uparrow + Na_2HPO_4$), demands lower temperatures (over 250 °C), favoring retention of the morphology of the metal oxide,[298] hydroxide, and metal-organic framework (MOF) precursors. In addition to the above phosphidation, there are other thermal approaches such as the solid-state phosphidation using red phosphorus/phosphate ($NH_4H_2PO_4$),[495,595,601,602] the reduction of metal orthophosphates using H_2 above 650 °C (which is commonly applied to synthesize Mo- and W-based transition metal phosphides),[298,603] as well as the direct solvothermal synthesis using trioctylphosphine ($C_{24}H_{51}P$) as the phosphorous source in organic solvent (220−385 °C).[23,604,605] Additionally, the researchers also used electrodeposition, radio-frequency plasma treatment, and the synthesis of precursors using hydrothermal methods, which we will introduce later in this Section. In the following, we will introduce each synthetic method used as the shape-determining step in the electrocatalyst preparation process by demonstrating some specific and unique examples.

4.2.1.1. Gas-Solid/Solid-State Reactions. The gas-solid reaction is the most straightforward approach to obtain transition metal phosphide samples because as-purchased chemicals or substrates can be used as their precursors. Wang *et al.* exposed Ni foam (NF) to red phosphorus at 500 °C, producing Ni_2P skeletons covered by vertically aligned Ni_5P_4−NiP_2 nanosheets (NSs) (Figure 88a).[518] Notably, P-rich phases were obtained in only 15 min by increasing the amount of red phosphorus, and SEM and EDX elemental mapping images revealed a uniform distribution of the NSs with Ni-P. This example demonstrates that high-quality transition metal phosphides can be synthesized quickly through high-temperature phosphidation (gas-solid reaction). Therefore, this strategy is highly recommended when highly crystalline transition metal phosphide samples are needed. In addition, carbon-based precursors have also been employed in solid-state reactions to produce transition metal phosphides encapsulated in carbonaceous materials. Pu *et al.* employed the solid-state reaction to synthesize a series of Fe-, Co-, and Ni-based transition metal phosphides with different metal phases in a N-doped carbon (NC) matrix.[495] As displayed in Figure 88b, metal salt precursors [i.e., $M(NO_3)_x{\cdot}6H_2O$ (M = Co, Ni, Fe)], $NH_4H_2PO_4$, and melamine were mixed and heated at high temperature (700 or 800 °C) for 2 h under Ar gas to yield Co_2P@NC, CoP@NC, Ni_2P@NC, $Ni_{12}P_5$@NC, Fe_2P@NC, and FeP@NC nanoparticles (NPs) depending on the molar ratios and temperatures. The TEM and HRTEM images in Figure 88b confirm the presence of several Ni_2P NPs distributed along with the NC matrix with well-defined crystal structures. Furthermore, the use of NC improved the stability of the transition metal phosphides through the encapsulation of the NPs.

4.2.1.2. Hydrothermal Methods. Hydrothermal methods have been used to uniformly create oxide and hydroxide species on the precursors in a simple way.[299,399,482] Furthermore, hydrothermal methods allow precise tuning of the properties of the precursor (e.g., morphology) by varying the composition of the bath and the synthesis time.[543] Han *et*

https://doi.org/10.1021/acs.chemrev.3c00005
Chem. Rev. 2023, 123, 12795−13208

Table 4. Summary of the Electrocatalytic Properties, Electrochemical Testing Conditions, and Physicochemical Pre- and Post-analyses of Transition Metal Phosphides Used for Alkaline/Neutral/Acidic OER and of the Final Type of Electrocatalyst after OER Testing[a−e]

Initial Electrocatalyst	Substrate	Shape of Electrocatalyst	Deposition Type	Specific Loading / $mg \cdot cm^{-2}_{geo}$	η@10 $mA \cdot cm^{-2}_{geo}$ / mV	C_{dl} / $mF \cdot cm^{-2}_{geo}$	TOF / s^{-1} (@η or j)	Tafel Slope / $mV \cdot dec^{-1}$	Electrolyte	Pre-analysis	Post-analysis	Long-Term OER Test Conditions	Post-OER Electrocatalyst	Final Type of Electrocatalyst	Ref.
P-NiFe-600 NPs	GC	Nanoparticle	P	0.2	283.6	1.13	-	50	1 M KOH	XRD, SEM	-	-	-	-	411
P-NiFe-700 NPs	GC	Nanoparticle	P	0.2	279.6	1.76	-	40		XRD, SEM	-	-	-	-	
P-NiFe-800 NPs	GC	Nanoparticle	P	0.2	270.1	2.13	-	39		XRD, SEM, EDX, TEM, XPS, N_2 ISO (BET, PSD)	XPS	12 h CA (0.42 V_{SCE}) 2000 CV cycles (100 $mV \cdot s^{-1}$, 0.43−0.53 V_{SCE})	NiP_2, FeP, P–O species	Catalyst	
P-NiFe-900 NPs	GC	Nanoparticle	P	0.2	286.3	1.62	-	42		XRD, SEM	-	-	-	-	
P-NiFe NCs	GC	Nanocube	P	0.2	418.3	0.192	-	190		XRD, SEM, TEM	-	-	-	-	
Mo_1Ni_1P	GC	Nanoflower	P	-	275	-	-	56.3	1 M KOH	XRD, SEM, EDX, TEM, XPS, AFM, N_2 ISO (BET, PSD)	TEM, EDX	36 h CP (10 $mA \cdot cm^{-2}_{geo}$) 3000 CV cycles	Mo-Ni-P	Catalyst	412
$Mo_1Ni_{1.2}P$	GC	Nanoflower	P	-	306	-	-	85.2		TEM, EDX	-	-	-	-	
$Mo_1Ni_{0.8}P$	GC	Nanoflower	P	-	331	-	-	90.6		TEM, EDX	-	-	-	-	
NiP	GC	Nanoparticle	P	-	347	-	-	112.4		TEM	-	-	-	-	
CoNiP	Ni foam	Nanosheet	S	-	~310	-	-	~92	1 M KOH	XRD, SEM, TEM, XPS	-	-	-	-	413
CoNiP@LDH-20	Ni foam	Nanoflake (core@shell)	S	-	~250	-	-	~64		XRD, SEM	-	-	-	-	
CoNiP@LDH-50	Ni foam	Nanoflake (core@shell)	S	-	~230	-	-	~60		XRD, SEM	-	-	-	-	
CoNiP@LDH-100	Ni foam	Nanoflake (core@shell)	S	-	216	-	-	45		XRD, SEM, EDX, TEM, XPS	SEM, EDX	500 h CP (50 $mA \cdot cm^{-2}_{geo}$)	CoNiP@NiFe-LDH (core@shell)	Catalyst (substrate)	
CoNiP@LDH-200	Ni foam	Nanoflake (core@shell)	S	-	~225	-	-	~50		XRD, SEM	-	-	-	-	
NiCoP/NC PHCs	GC	Polyhedral structure	P	0.28	297	50.7	-	51	1 M KOH	XRD, SEM, EDX, TEM, XPS, FTIR, N_2 ISO (BET, PSD), Raman	XRD, SEM, XPS	10 h CA (1.55 V_{RHE}) 1000 CV cycles (100 $mV \cdot s^{-1}$)	MP (M = Ni and Co), PO_4^{3-}	Catalyst	414
NiCoP/NC PH	GC	Polyhedral structure	P	0.28	334	34.5	-	58			-	-	-	-	
CoP/NC PH	GC	Polyhedral structure	P	0.28	356	18.9	-	75			-	-	-	-	
FeP@Au	Au glass	Nanoparticles	P	0.71	320	-	0.004 at 330 mV	56.8	1 M KOH	XRD, SEM, TEM, EDX, XPS, Raman	SEM, EDX, XPS	4 h CP (1.55 V_{RHE})	FeP, PO_x (oxidized P species)	Catalyst	415
FeP-rGO (50:50) @Au	Au glass	Nanoparticle	P	0.71	290	-	0.019 at 330 mV	85.2			-	-	-	-	
FeP-rGO (50:50) @CFP	CFP	Nanoparticle	P	0.71	260	-	0.032 at 330 mV	174.9			-	-	-	-	
FeP-rGO (70:30) @Au	Au glass	Nanoparticle	P	0.71	280	-	0.026 at 330 mV	49.6			-	8 h CP (1.52 V_{RHE})	-	-	
NiFeP	GC	Nanocubes	P	0.2	350	-	-	87.9	1 M KOH	SEM, TEM, XRD, N_2 ISO (BET, PSD), XPS	-	-	-	-	416
NiFeP-DBD	GC	Nanocubes	P	0.2	265	-	-	40.9		SEM, TEM, XRD, N_2 ISO (BET, PSD), XPS, Raman	Raman (after 1 h CA)	20 h CA (1.50 V_{RHE}) 1 h CA (1.2 V_{RHE}, surface reconstruction)	NiOOH	Precatalyst	
FeCo-P	Ni foam	-	S	-	316 (@50 $mA \cdot cm^{-2}_{geo}$)	6.5	-	73.3	1 M KOH	XRD, XPS	-	55 h CP (100 $mA \cdot cm^{-2}_{geo}$)	-	-	417
5M-P (CrMnFeNiCo-P)	Ni foam	-	S	-	282 (@50 $mA \cdot cm^{-2}_{geo}$)	3.2	-	68.7		XRD, XPS	-	-	-	-	
5MT-P (CrMnFeNiCo-P)-Ti	Ni foam	Microspheres/nanosheets	S	-	226 (@50 $mA \cdot cm^{-2}_{geo}$)	3.5	-	35.3		XRD, FTIR, SEM, TEM, SAED, HAADF-STEM, EDX, XPS	XRD, FTIR, Raman, XPS, SEM, TEM, SAED, EDX, ICP	60 h CP (10 $mA \cdot cm^{-2}_{geo}$) 60 h CP (100 $mA \cdot cm^{-2}_{geo}$)	Metal (oxy)hydroxides, Phosphates	Precatalyst (partial oxidation)	
5MV-P(CrMnFeNiCo-P)-V	Ni foam	-	S	-	267 (@50 $mA \cdot cm^{-2}_{geo}$)	4.5	-	54.8		XRD, XPS	-	-	-	-	
5MZ-P (CrMnFeNiCo-P)-Zn	Ni foam	-	S	-	270 (@50 $mA \cdot cm^{-2}_{geo}$)	6.7	-	60.1		XRD, XPS	-	-	-	-	
Ni_2P-Fe_2P/NF	Ni foam	Walnut shell-like structure	P	-	222 (@100 $mA \cdot cm^{-2}_{geo}$)	4.52	-	40.9	1 M KOH	XRD, FESEM, FTIR, TEM, HAADF-STEM, EDX, XPS	XRD, XPS, SEM	100 h CP (100 $mA \cdot cm^{-2}_{geo}$) 1000 CV cycles	Metal hydroxides, Metal hydroxyl oxides, P-O species	Precatalyst (partial oxidation)	418
CNF@CoP-5-CNTs	CP	Nanoparticles/nanofibers	P	4	376 (@50 $mA \cdot cm^{-2}_{geo}$)	131.56	-	111.6	1 M KOH	XRD, SAED, SEM	-	-	-	-	419
CNF@CoP-10-CNTs	CP	Nanoparticles/nanofibers	P	4	398 (@50 $mA \cdot cm^{-2}_{geo}$)	37.02	-	107.2		XRD, SAED, SEM	-	-	-	-	
CNF@CoP-12-CNTs	CP	Nanoparticles/nanofibers	P	4	411 (@50 $mA \cdot cm^{-2}_{geo}$)	81.5	-	179.6		XRD, SAED, SEM	-	-	-	-	
CNF@CoP-15-CNTs	CP	Nanoparticles/nanofibers	P	4	367 (@50 $mA \cdot cm^{-2}_{geo}$)	265.72	-	126.1		XRD, SAED, SEM, TEM, EDX, XPS	SEM, XRD, XPS	1000 CV cycles 48 h CP (10 $mA \cdot cm^{-2}_{geo}$)	$Co(OH)_2$, Phosphates	Precatalyst (full oxidation)	
CNF@CoP-18-CNTs	CP	Nanoparticles/nanofibers	P	4	380 (@50 $mA \cdot cm^{-2}_{geo}$)	73.48	-	129.9		XRD, SAED, SEM	-	-	-	-	

https://doi.org/10.1021/acs.chemrev.3c00005
Chem. Rev. 2023, 123, 12795−13208

Table 4. continued

Initial Electrocatalyst	Substrate	Shape of Electrocatalyst	Deposition Type	Specific Loading / $mg \cdot cm^{-2}_{geo}$	η@10 $mA \cdot cm^{-2}_{geo}$ / mV	C_{dl} / $mF \cdot cm^{-2}_{geo}$	TOF / s^{-1} (@η or j)	Tafel Slope / $mV \cdot dec^{-1}$	Electrolyte	Pre-analysis	Post-analysis	Long-Term OER Test Conditions	Post-OER Electrocatalyst	Final Type of Electrocatalyst	Ref.
CNF@CoP-20-CNTs	CP	Nanoparticles/nanofibers	P	4	512 (@50 $mA \cdot cm^{-2}_{geo}$)	97.63	-	145.0		XRD, SAED, SEM	-	-	-	-	419
$Fe_{0.5}Co$-P	CP	Rhomboid dodecahedron	P	0.45	260	5.59	0.03797 at 300 mV	65.53	1 M KOH	SEM, TEM, SAED, XRD, Raman, N_2 ISO (BET, PSD), XPS, ICP-MS	XPS, SEM, Raman	24 h CA (the potential at 10 $mA \cdot cm^{-2}_{geo}$) 1000 CV cycles	CoOOH, FeOOH, P-C species	Precatalyst	420
Co-P	CP	-	P	0.45	304	4.37	0.0299 at 300 mV	104.8		XRD, Raman, XPS	XPS, Raman	24 h CA (the potential at 10 $mA \cdot cm^{-2}_{geo}$) 1000 CV cycles	CoOOH	Precatalyst	
NiFeCo-P@CAP/NF Fast cooling down	Ni foam	Nanosheets (flower-like nanostructure)	S	-	202	4.6	-	28.5	1 M KOH	FESEM, TEM, SAED, HAADF, EDX, XRD, XPS	SEM, XPS, *In-Situ* Raman	30 h CA (the potential at 10 $mA \cdot cm^{-2}_{geo}$) 30 h CA (the potential at 50 $mA \cdot cm^{-2}_{geo}$) 30 h CA (the potential at 100 $mA \cdot cm^{-2}_{geo}$)	FeCo/NiOOH, Phosphates	Precatalyst	421
NiFeCo-P@CP/NF Slow cooling down	Ni foam	-	S	-	223	3.5	-	35.9		TEM, XRD	-	-	-	-	
Ni_2P /NF	Ni foam	-	S	-	332	0.1	-	72.7		XPS	-	-	-	-	
d-NiFeP/CC (d = defects)	CC	Nanosheets	S	5.46	185	5.95	-	24.56	1 M KOH	SEM, ICP-AES, HAADF-STEM, EDX, TEM, N_2 ISO (BET), XPS	XPS, XRD, TEM, *In-Situ* Raman, Raman	100 h CP (10 $mA \cdot cm^{-2}_{geo}$) 6000 CV cycles	NiOOH, Phosphates	Precatalyst (partial oxidation)	422
NiFeP/CC	CC	-	S	-	209	4.46	-	50.35		TEM, N_2 ISO (BET)	-	-	-	-	
Zn-NiFeP/CC	CC	Nanosheets	S	-	216	3.95	-	55.20		ICP-AES, TEM, XPS	-	-	-	-	
CFP (Co-Fe-P/C)	GC	Nanosheets	P	0.255	277	103.9	0.953 at 362 mV	69.2	1 M KOH	FESEM, EFTEM, EDX, TEM, AFM, XRD, Raman, TGA, ZPA, XPS, ICP-AES, N_2 ISO (BET, PSD)	XPS, EFTEM, TEM, EDX	2000 CV cycles 100 h CP (switching 10 and 200 $mA \cdot cm^{-2}_{geo}$)	Co-Fe oxyhydroxides, Oxidized P species	Precatalyst (partial oxidation)	423
Co_xP/NC	GC	Agglomerated particles	P	0.78	345	33.2	-	57.8	1 M KOH	XRD, TEM, N_2 ISO (BET, PSD)	-	-	-	-	424
Co_xP/NC-Mel	GC	Nanoparticles /rod-like supporting material	P	0.78	312	43.1	-	52.2		XRD, SEM, TEM, N_2 ISO (BET, PSD), XPS	XRD, XPS	4 h CP (10 $mA \cdot cm^{-2}_{geo}$)	CoO, CoOOH, P-O species	Precatalyst (partial oxidation)	
Co_xP/NC-Hex	GC	Nanoparticles /rod-like supporting material	P	0.78	324	31.5	-	57.1		SEM	-	-	-	-	
Co_xP/NC-Phe	GC	Nanoparticles /rod-like supporting material	P	0.78	322	40.3	-	61.8		SEM	-	-	-	-	
CoCuMo-P	GC	Microparticles (porous structure)	P	~0.45	309	79	-	76	1 M KOH	XRD, SEM, TEM, SAED, N_2 ISO (BET, PSD), FTIR, XPS	XPS, AAS	25 h CP (10 $mA \cdot cm^{-2}_{geo}$)	Metal (oxy)hydroxides, Metal oxides, Phosphorous oxide	Precatalyst	425
Ni_2P	CC	Nanoparticles	S	-	350 (@100 $mA \cdot cm^{-2}_{geo}$)	5.2	-	68	1 M KOH	XRD, SEM, XPS	-	-	-	-	426
$(Fe_{0.33}Ni_{0.67})_2P$/CC	CC	Nanoparticles	S	-	290 (@100 $mA \cdot cm^{-2}_{geo}$)	-	-			XRD, SEM, XPS	-	-	-	-	
$(Fe_{0.5}Ni_{0.5})_2P$/CC	CC	Nanoparticles	S	4.011	260 (@100 $mA \cdot cm^{-2}_{geo}$)	17.8	-	45		XRD, TEM, ICP-OES, SEM, XPS	XRD, TEM, SAED, SEM, XPS	24 h CA (1.50 V_{RHE}) 10 h CA (1.55 V_{RHE}) 200 CV cycles	FeNiOOH, PO_x	Precatalyst (full oxidation)	
$(Fe_{0.67}Ni_{0.33})_2P$/CC	CC	Nanoparticles	S	-	310 (@100 $mA \cdot cm^{-2}_{geo}$)	-	-			XRD, SEM, XPS	-	-	-	-	
Fe_2P/CC	CC	Nanoparticles	S	-	470 (@100 $mA \cdot cm^{-2}_{geo}$)	8.7	-	86		XRD, SEM	-	-	-	-	
CoP-B0	GC	Nanorods	P	~0.35	333	0.045	-	78.9	1 M KOH	XRD, EPR, TEM, SAED, SEM, EDX, XPS	-	11 h CA	-	-	427
CoP-B1	GC	Nanorods	P	~0.35	297	0.051	-	58.1		XRD, EPR, TEM, SAED, SEM, EDX, XPS, Raman	XPS	1000 CV cycles 11 h CA	$CoO_x(OH)_y$, P-O species	Precatalyst	
CoP-B2	GC	Nanorods	P	~0.35	348	-	-	-		SEM, EDX, XPS	-	11 h CA	-	-	
CoP-B3	GC	Nanorods	P	~0.35	356	-	-	-		SEM, TEM, EDX, XPS	-	11 h CA	-	-	
CoP-O	GC	-	P	~0.35	346	0.031	-	106.6		XRD	-	11 h CA	-	-	
Ni_2P/CNT/GC	GC	Nanoflower-like structure	P	0.15	360	~0.65	-	49	1 M KOH	XRD, SEM, EDX, TEM, XPS, XPS	-	22 h CA (1.62 V_{RHE})	-	-	428
Ni_2P/CNT/CP	CP	Nanoflower-like structure	P	0.15	370	~0.0055	-	105		XRD, SEM, EDX, TEM, XPS, XPS	XPS	22 h CA (1.65 V_{RHE})	-	Precatalyst	
Ni_2P/GC	GC	Nanoflower-like structure	P	0.15	390	~0.11	-	55		XRD, SEM, EDX, TEM, XPS, XPS	XPS	22 h CA (1.60 V_{RHE})	-	Precatalyst	
Mn-Co-P YS	GC	Yolk-shell particles	P	0.283	330	47.7	-	59	1 M KOH	XRD, ICP, SEM, N_2 ISO (BET, PSD), TEM, EDX, HAADF, XPS	SEM, XPS	8 h CA (1.56 V_{RHE}) 100 CV cycles	Metal oxyhydroxides, Phosphate species	Precatalyst	429
Co-P HS	GC	Sphere particles	P	0.283	410	4.7	-	61.3		XRD, SEM, N_2 ISO (BET, PSD)	-	-	-	-	
NiP/NF	Ni foam	Numerous grains covered with nanosheets	S	~2.5	325 501 (@50 $mA \cdot cm^{-2}_{geo}$)	0.69	-	108	Fe-purified 1 M KOH	XRD, SEM, EDX, TEM, XPS, TXRF	XRD, SEM, EDX, XPS, TXRF	20 h CP (20 $mA \cdot cm^{-2}_{geo}$)	NiO_xH_y, Phosphate (PO_x^{3-})	Precatalyst	49

https://doi.org/10.1021/acs.chemrev.3c00005
Chem. Rev. 2023, 123, 12795−13208

Table 4. continued

Initial Electrocatalyst	Substrate	Shape of Electrocatalyst	Deposition Type	Specific Loading / $mg \cdot cm^{-2}_{geo}$	η@10 $mA \cdot cm^{-2}_{geo}$ / mV	C_{dl} / $mF \cdot cm^{-2}_{geo}$	TOF / s^{-1} (@η or j)	Tafel Slope / $mV \cdot dec^{-1}$	Electrolyte	Pre-analysis	Post-analysis	Long-Term OER Test Conditions	Post-OER Electrocatalyst	Final Type of Electrocatalyst	Ref.
					695 ($@_{mA \cdot cm^{-2}_{geo}}^{100}$)										429
CoP	GC	Nanosheets	P	0.56	324	0.244	0.029 at 400 mV	82	1 M KOH	SEM, N_2 ISO (BET, PSD), XRD, EDX, ICP-MS, XPS	-	-	-	-	430
Mn-CoP-1 Co/Mn 5.4/0.6	GC	Nanosheets	P	0.56	308	0.288	0.054 at 400 mV	79.3		SEM, N_2 ISO (BET, PSD), XRD, EDX, ICP-MS, XPS	-	-	-	-	
Mn-CoP-2 Co/Mn 5/1	GC	Nanosheets	P	0.56	288	0.337	0.063 at 400 mV	77.2		SEM, N_2 ISO (BET, PSD), XRD, TEM, SAED, EDX, ICP-MS, XPS	XRD, SEM, XPS	24 h CP (10 $mA \cdot cm^{-2}_{geo}$) 2000 CV cycles	Mn-CoOOH, Phosphates	Precatalyst (full oxidation)	
Mn-CoP-3 Co/Mn 4/2	GC	Nanosheets	P	0.56	306	0.266	0.044 at 400 mV	86.5		SEM, N_2 ISO (BET, PSD), XRD, EDX, ICP-MS, XPS	-	-	-	-	
Mn-CoP-4 Co/Mn 3/3	GC	Nanosheets	P	0.56	323	0.244	0.022 at 400 mV	93		SEM, N_2 ISO (BET, PSD), XRD, EDX, ICP-MS, XPS	-	-	-	-	
CoP	GC	-	P	0.255	366	10.2	-	63	1 M KOH	XRD	-	-	-	-	431
$Co_{0.83}Fe_{0.17}P$	GC	1D nanocuboid-like	P	0.255	298	49.7	-	42		XRD, FESEM	-	-	-	-	
$Co_{0.8}Fe_{0.2}P$	GC	1D nanocuboid-like	P	0.255	285	60.4	-	40		XRD, FESEM, TEM, SAED, HAADF, EDX, N_2 ISO (BET, PSD), XPS	XPS, FESEM	~ 10 h CP (10 $mA \cdot cm^{-2}_{geo}$)	CoOOH, FeOOH, PO_x	Precatalyst	
$Co_{0.75}Fe_{0.25}P$	GC	1D nanocuboid-like	P	0.255	302	33.2	-	46		XRD, FESEM	-	-	-	-	
$Co_{0.6}Fe_{0.4}P$	GC	1D nanocuboid-like	P	0.255	310	13.1	-	48		XRD, FESEM	-	-	-	-	
Co-P@PC-650	CP	Nanoparticles	P	1.0	333	-	-	71	1 M KOH	XRD, Raman, SEM, TEM, N_2 ISO (BET), XPS	-	-	-	-	432
Co-P@PC-750	CP	Nanoparticles	P	1.0	280	-	-	53		XRD, Raman, SEM, TEM, N_2 ISO (BET), XPS	XPS, TEM, XRD	100 CV cycles 20 h CA (1.51 V_{RHE})	Co oxides/hydroxides, Phosphates	Precatalyst (full oxidation)	
Co-P@PC-850	CP	Nanoparticles	P	1.0	341	-	-	91		XRD, Raman, SEM, TEM, N_2 ISO (BET), XPS	-	-	-	-	
CoP	GC	-	P	0.25	~ 360	-	-	93	1 M KOH	XRD	-	-	-	-	433
$CoNi_{0.8}P$	GC	Hollow nanocages	P	0.25	~ 290	33	-	86		SEM, XRD	XPS	10 h CA (~ 1.52 V_{RHE})	NiOOH, CoOOH	Precatalyst	
$CoNi_{1.5}P$	GC	Hollow nanocages	P	0.25	278	39	-	76		SEM, XRD, TEM, EDX, XPS	XPS	1000 CV cycles 10 h CA (1.508 V_{RHE})	NiOOH, CoOOH, Oxidized P species	Precatalyst	
$CoNi_{2.2}P$	GC	Hollow nanocages	P	0.25	~ 300	43	-	93		SEM, XRD	-	-	-	-	
$CoNi_{3.5}P$	GC	Hollow nanocages	P	0.25	~ 330	49	-	112		SEM, XRD	XPS	10 h CA (~ 1.56 V_{RHE})	NiOOH, CoOOH	Precatalyst	
Fe_2P	CFP	Rod-like nanoparticles	P	0.5	430	8.5	-	150	0.1 M KOH	SEM, TEM, XRD	-	-	-	-	434
Fe_2CoP	CFP	Rod-like nanoparticles	P	0.5	410	16.5	-	70		SEM, TEM, XRD, N_2 ISO (BET, PSD)	-	-	-	-	
FeCoP	CFP	Spindle-like nanoparticles	P	0.5	390	25.8	-	60		SEM, TEM, XRD, N_2 ISO (BET, PSD)	-	-	-	-	
$FeCo_2P$	CFP	Hollow-structured polyhedron	P	0.5	320	30.5	-	55		SEM, TEM, XRD, STEM, EDX, XPS, N_2 ISO (BET, PSD)	XPS, XRD	1000 CV cycles 12 h CA	Fe-Co (oxy)hydroxide	Precatalyst (partial oxidation)	
NiCoP	GC	Urchin-like hierarchical nanoneedles	P	0.25	327	2.31	-	61	1 M KOH	SEM, XRD, XPS, N_2 ISO (BET, PSD)	-	-	-	-	435
5FeNiCoP	GC	Urchin-like hierarchical nanoneedles	P	0.25	288	3.25	-	54		SEM, XRD, ICP-MS	-	-	-	-	
10FeNiCoP	GC	Urchin-like hierarchical nanoneedles	P	0.25	259	8.09	-	40		SEM, TEM, SAED, XRD, ICP-MS, XPS, N_2 ISO (BET, PSD)	SEM, TEM, XRD, XPS	1000 CV cycles 10 h CA (1.49 V_{RHE})	FeNiCoOOH, $FeNiCoPO_x$	Precatalyst (partial oxidation)	
15FeNiCoP	GC	Urchin-like hierarchical nanoneedles	P	0.25	269	5.58	-	44		SEM, XRD, ICP-MS	-	-	-	-	
20FeNiCoP	GC	Urchin-like hierarchical nanoneedles	P	0.25	276	3.74	-	46		SEM, XRD, ICP-MS	-	-	-	-	
FeCoP-400	GC	Cubic framework	P	0.4	261	18.5	-	50	1 M KOH	XRD, SEM, EDX, TEM, SAED, XPS, N_2 ISO (BET, PSD), ICP-OES, TGA, Raman, FTIR	TEM, XPS	24 h CP (10 $mA \cdot cm^{-2}_{geo}$)	*M*OOH (*M* = Fe, Co), PO_x	Precatalyst (partial oxidation)	436
FeNiP-400	GC	Cubic framework	P	0.4	264	13.6	-	72					*M*OOH (*M* = Fe, Ni), PO_x	Precatalyst (partial oxidation)	
FeMnP-400	GC	Cubic framework	P	0.4	-	1.2	-	106					FeOOH, PO_x	Precatalyst (partial oxidation)	
$FeNi_2P$@HDC	GC	Nanoparticle	P	0.54	280	1.04	-	56	1 M KOH	XRD, SEM, STEM-EDX, N_2 ISO (BET, PSD), XPS, Raman	XRD, XPS, STEM-EDX	12 h CA (1.51 V_{RHE}) 5000 CV cycles (100 $mV \cdot s^{-1}$)	MO_x, *M*OOH (*M* = Fe, Ni)	Precatalyst (partial oxidation)	437

https://doi.org/10.1021/acs.chemrev.3c00005
Chem. Rev. 2023, 123, 12795−13208

Table 4. continued

Initial Electrocatalyst	Substrate	Shape of Electrocatalyst	Deposition Type	Specific Loading / $mg \cdot cm^{-2}_{geo}$	η@10 $mA \cdot cm^{-2}_{geo}$ / mV	C_{dl} / $mF \cdot cm^{-2}_{geo}$	TOF / s^{-1} (@η or j)	Tafel Slope / $mV \cdot dec^{-1}$	Electrolyte	Pre-analysis	Post-analysis	Long-Term OER Test Conditions	Post-OER Electrocatalyst	Final Type of Electrocatalyst	Ref.
Ni_2P@HDC	GC	Nanoparticle	P	0.54	360	0.32	-	80		XRD, SEM, N_2 ISO (BET, PSD), XPS, Raman	-	-	-	-	437
Fe_2P@HDC	GC	Nanoparticle	P	0.54	387	9.49	-	187		XRD, SEM, N_2 ISO (BET, PSD), XPS, Raman	-	-	-	-	
NF-P	Ni foil	Nanotube array	S	-	350 (@50 $mA \cdot cm^{-2}_{geo}$)	0.065	-	109.4	1 M KOH	XRD, SEM	-	1000 CV cycles	-	-	438
Ni_3P/NF	Ni foil	Nanoparticle	S	-	330 (@50 $mA \cdot cm^{-2}_{geo}$)	1.45	-	109.4		XRD, SEM, XPS	-		-	-	
FeP/NF	Ni foil	Nanoparticle	S	-	270	15.68	-	68.1		XRD, SEM, XPS	-		-	-	
FeP@Ni_2P/NF	Ni foil	Nanotube array	S	-	290 (@50 $mA \cdot cm^{-2}_{geo}$)	17.06	-	55.9		XRD, SEM, TEM, EDX, XPS	XRD, SEM, TEM, XPS	20 h CA (1.49 V_{RHE}) 1000 CV cycles	MO_x, $MOOH$ (M = Ni, Fe), PO_x	Precatalyst (partial oxidation)	
FeP@Ni_2P/NF-350	Ni foil	Nanotube array	S	-	345 (@50 $mA \cdot cm^{-2}_{geo}$)	-	-	78.2		XRD, SEM	-	1000 CV cycles	-	-	
FeP@Ni_2P/NF-450	Ni foil	Nanotube array	S	-	300 (@50 $mA \cdot cm^{-2}_{geo}$)	-	-	59.4		XRD, SEM	-		-	-	
NF-P	Ni foam	-	S	-	350 (@50 $mA \cdot cm^{-2}_{geo}$)	1.8	-	203.0	1 M KOH	XRD, Raman	-	-	-	-	439
Ni-Fe-P@NC/NF	Ni foam	Nanotube with nanoparticle	S	-	140 220 (@50 $mA \cdot cm^{-2}_{geo}$) 260 (@100 $mA \cdot cm^{-2}_{geo}$)	5.6	-	84.6		XRD, SEM, TEM, SAED, HAADF-STEM, EDX, XPS, Raman, N_2 ISO (BET, PSD)	XPS, Raman, HAADF-STEM, EDX	24 h CP (100 $mA \cdot cm^{-2}_{geo}$)	Ni-Fe oxide/hydroxide	Precatalyst (partial oxidation)	
Ni_3P_4/NF	Ni foam	-	S	-	~ 272 (@50 $mA \cdot cm^{-2}_{geo}$)	-	-	-		-	-	-	-	-	
FeP/NF	Ni foam	-	S	-	~ 281 (@50 $mA \cdot cm^{-2}_{geo}$)	-	-	-		-	-	-	-	-	
FeP/NC	GC	Nanoparticle	P	0.28	411	-	-	-	1 M KOH	XRD, SEM, N_2 ISO (BET, PSD)	-	-	-	-	440
$Co_{0.06}Fe_{0.92}P$/NC	GC	Nanoparticle	P	0.28	347	-	-	-		XRD, SEM, N_2 ISO (BET, PSD)	-	-	-	-	
$Co_{0.11}Fe_{0.83}P$/NC	GC	Nanoparticle	P	0.28	321	-	-	-		XRD, SEM, N_2 ISO (BET, PSD)	-	-	-	-	
$Co_{0.17}Fe_{0.79}P$/NC	GC	Nanoparticle	P	0.28	299	6.1	-	44		XRD, SEM, EDX, TEM, SAED, HAADF-STEM, XPS, ICP-OES, N_2 ISO (BET, PSD), Raman	XRD, SEM, TEM (after OWS)	24 h CA (1.53 V_{RHE}) 35 h (cell voltage: 1.7 V, OWS)	$MOOH$ (M = Fe, Co)	Precatalyst (partial oxidation)	
$Co_{0.17}Fe_{0.79}P$	GC	Nanoparticle	P	0.28	355	-	-	-		XRD, SEM, N_2 ISO (BET, PSD)	-	-	-	-	
W,Fe@CoP/CNTs	GC	Nanosheet	P	0.25	290	87.7	-	33	1 M KOH	XRD, SEM, EDX, TEM, XPS, ICP-OES	TEM, EDX, XPS, ICP-OES, XPS	20 h CP (10 $mA \cdot cm^{-2}_{geo}$) 2000 CV cycles	W- and Fe-incorporated CoOOH, CoO_x	Precatalyst (partial oxidation)	441
CoP/CNTs	GC	Nanosheet	P	0.25	340	171.8	-	54		XRD, XPS	-	-	-	-	
Fe@CoP/CNTs	GC	Nanosheet	P	0.25	300	143.5	-	49		XPS	-	-	-	-	
W@CoP/CNTs	GC	Nanosheet	P	0.25	320	150	-	52		XPS	-	-	-	-	
$NiFeO_x$@NiFeP (20 % Fe)	NiFeP strips	Nanoporous/amorphous matrix	S	-	~ 260	-	-	-	1 M NaOH	XRD, SEM, EDX, TEM, XPS, N_2 ISO (BET)	-	-	-	-	442
$NiFeO_x$@NiFeP (30 % Fe)	NiFeP strips		S	-	~ 250	-	-	-			-	-	-	-	
$NiFeO_x$@NiFeP (40 % Fe)	NiFeP strips		S	-	~ 210	-	-	37			SEM, EDX, XPS	28 h CP [10 (14 h), 100 $mA \cdot cm^{-2}_{geo}$ (14 h)]	$NiFeO_x$, PO_4^{3-}	Precatalyst (partial oxidation)	
$NiFeO_x$@NiFeP (50 % Fe)	NiFeP strips		S	-	220	-	-	-			-	-	-	-	
$NiFeO_x$@NiFeP (20 % Fe)	NiFeP strips		S	-	~ 750	-	-	-	0.5 M H_2SO_4		-	-	-	-	
$NiFeO_x$@NiFeP (30 % Fe)	NiFeP strips		S	-	~ 700	-	-	-			-	-	-	-	
$NiFeO_x$@NiFeP (40 % Fe)	NiFeP strips		S	-	680	-	-	94			-	-	-	-	
$NiFeO_x$@NiFeP (50 % Fe)	NiFeP strips		S	-	~ 700	-	-	-			-	-	-	-	
S-1 (Co_xP NPs@NC)	GC	Nanoparticle	P	0.14	380	4.81	-	68.1	1 M KOH	XRD, SEM, TEM, XPS, N_2 ISO (BET, PSD)	XRD, TEM (after OWS), XPS	1000 CV cycles 10 h CA (cell voltage: ~ 1.71 V, OWS) 10 h CA (cell voltage: ~ 1.95 V, OWS)	CoO_x, P–O species	Precatalyst (partial oxidation)	443
S-2 (Co_xP NPs@NC)	GC	Aggregated particle	P	0.14	450	0.47	-	79.3			-	-	-	-	
rGO/CoFe-P	GC	Nanosheet	P	0.1	270	19.2	0.1385 at 300 mV	38.3	1 M KOH	XRD, SEM, EDX, TEM, XPS	TEM, EDX, XPS	18 h CP (10 $mA \cdot cm^{-2}_{geo}$)	MO_x, $MOOH$ (M = Co, Fe), P–O species	Precatalyst (partial oxidation)	444
rGO/Fe-P	GC	Nanosheet	P	0.1	> 520	0.9	-	128.3			-	-	-	-	
rGO/Co-P	GC	Nanosheet	P	0.1	333	10.25	0.0105 at 300 mV	55			-	-	-	-	
CoFe-P	GC	Flower-like particle/nanosheet	P	0.1	338	14.45	-	69			-	-	-	-	
rGO/NiFe-P	GC	Nanosheet	P	0.1	255	-	-	42.4			TEM, EDX	18 h CP (10 $mA \cdot cm^{-2}_{geo}$)	MO_x, $MOOH$ (M = Ni, Fe)	Precatalyst (partial oxidation)	
rGO/Ni-P	GC	Nanosheet	P	0.1	317	-	-	60			-	-	-	-	

https://doi.org/10.1021/acs.chemrev.3c00005
Chem. Rev. 2023, 123, 12795−13208

Table 4. continued

Initial Electrocatalyst	Substrate	Shape of Electrocatalyst	Deposition Type	Specific Loading / $mg \cdot cm^{-2}_{geo}$	η@10 $mA \cdot cm^{-2}_{geo}$ / mV	C_{dl} / $mF \cdot cm^{-2}_{geo}$	TOF / s^{-1} (@η or j)	Tafel Slope / $mV \cdot dec^{-1}$	Electrolyte	Pre-analysis	Post-analysis	Long-Term OER Test Conditions	Post-OER Electrocatalyst	Final Type of Electrocatalyst	Ref.
NiFe-P	GC	Flower-like particle/nanosheet	P	0.1	337	-	-	88.8			-	-	-	-	444
rGO/CoNi-P	GC	Nanosheet	P	1.1	314	-	-	60			TEM, EDX	18 h CP (10 $mA \cdot cm^{-2}_{geo}$)	MO_x, $MOOH$ (M = Co, Ni)	Precatalyst (partial oxidation)	
CoNi-P	GC	Flower-like particle/nanosheet	P	2.1	327	-	-	75.4			-	-	-	-	
rGO/CoNiFe-P	GC	Nanosheet	P	0.1	261	-	-	48			-	-	-	-	
CoNiFe-P	GC	Flower-like particle/nanosheet	P	0.1	323	-	-	68.1			-	-		-	
Ni_2P	Ni foam	-	S	-	246	62.3	-	226.4	1 M KOH	XRD	-	-	-	-	445
Fe_2P	Ni foam	-	S	-	215	58.4	-	119.8		XRD	-	-	-	-	
$(Ni_{0.5}Fe_{0.5})_2P$	Ni foam	-	S	-	209	66.9	-	72.6		XRD, EDX	-	-	-	-	
$(Ni_{0.66}Fe_{0.33})_2P$	Ni foam	Nanoplate	S	-	182	70.5	-	53.6		XRD, SEM, EDX, TEM, XPS	XRD, SEM, XPS	24 h CP (10 $mA \cdot cm^{-2}_{geo}$)	MO_x, $MOOH$ (M = Ni, Fe)	Precatalyst (partial oxidation)	
$(Ni_{0.75}Fe_{0.25})_2P$	Ni foam	-	S	-	206	65.3	-	128.3		XRD, EDX	-	-	-	-	
$Co_{0.6}Fe_{0.4}P$-0	GC	Nanoframe	P	0.27	308	9.36	-	53	1 M KOH	N_2 ISO (BET, PSD), ICP-AES	-	-	-	-	446
$Co_{0.6}Fe_{0.4}P$-0.75	GC	-	P	0.27	301	20.02	-	54		-	-	-	-	-	
$Co_{0.6}Fe_{0.4}P$-1.125	GC	Nanoframe	P	0.27	298	22.05	0.046 at ~ 300 mV	48		XRD, SEM, EDX, TEM, XPS, TGA, Raman, N_2 ISO (BET, PSD), ICP-AES, HADDF, FTIR	XRD, SEM, EDX, TEM, XPS	5000 CV cycles (100 $mV \cdot s^{-1}$, 1.20–1.65 V_{RHE})	MO_x, $MOOH$ (M = Co, Fe)	Precatalyst (partial oxidation)	
$Co_{0.6}Fe_{0.4}P$-1.5	GC	-	P	0.27	304	18.33	-	55		-	-	-	-	-	
CoP/NF	Ni foam	-	S	6.43	560 (@100 $mA \cdot cm^{-2}_{geo}$)	21.7	-	92	1 M KOH	-	-	-	-	-	447
Al-CoP/NF (Co:Al = 10:1)	Ni foam	Nanosheet	S	6.51	330 480 (@100 $mA \cdot cm^{-2}_{geo}$)	36.8	-	69		XRD, SEM, EDX, TEM, XPS	XPS	24 h CP (21 $mA \cdot cm^{-2}_{geo}$) 1000 CV cycles (100 $mV \cdot s^{-1}$)	CoO_x, PO_4^{3-}	Precatalyst (partial oxidation)	
Al-CoP/NF (Co:Al = 10:0.5)	Ni foam	Nanosheet	S	6.51	~ 533 (@100 $mA \cdot cm^{-2}_{geo}$)	-	-	-			-	-	-	-	
Al-CoP/NF (Co:Al = 10:2)	Ni foam	Nanosheet	S	6.51	~ 547 (@100 $mA \cdot cm^{-2}_{geo}$)	-	-	-			-	-	-	-	
Ni_2P	GC	-	P	0.210	360	-	0.012 at 370 mV	57	1 M KOH	XRD, TEM, XPS,	TEM, XPS, HAADF-STEM, EELS	CV cycles (100 $mV \cdot s^{-1}$, 1.0–1.8 V_{RHE})	NiOOH	Precatalyst (partial oxidation)	138
NiP_x (1st cycle)	GC	Particulate	S	-	450	-	-	-	1 M NaOH	XRD, SEM, XPS	XRD, SEM, XPS	10 CV cycles	NiOOH	Precatalyst (partial oxidation)	448
NiP_x (10th cycle)	GC	Particulate	S	-	430	-	-	-			-	-	NiOOH	Precatalyst (partial oxidation)	
CoP/MoP@NC	CC	Nanoparticle	S	0.8	270	223	-	81	1 M KOH	XRD, SEM, EDX, TEM, XPS, N_2 ISO (BET, PSD)	XRD, SEM, XPS	20 h CA (1.53 V_{RHE}) 5000 CV cycles	MoO_x, CoOOH, P–O species	Precatalyst (partial oxidation)	449
CoP@NC	CC	Aggregated particle	S	0.8	270	158	-	82		XRD, SEM, TEM, N_2 ISO (BET, PSD)	-	-	-	-	
MoP@NC	CC	Aggregated particle	S	0.8	420	22	-	97		XRD, SEM, TEM, N_2 ISO (BET, PSD)	-	-	-	-	
$Ni_{0.8}Fe_{0.2}$-P/CC	CC	Nanosheet	S	2.2	204	7.1	-	41.2	1 M KOH	XRD, SEM, EDX, TEM, XPS, ICP-OES	SEM, EDX, TEM, XPS, ICP-OES	24 h CA (1.47 V_{RHE}) 3000 CV cycles	NiFe-hydroxide	Precatalyst (partial oxidation)	450
$Ni_{0.7}Fe_{0.3}$-P/CC	CC	-	S	2.2	~ 215	6.2	-	56.4		XRD, EDX, ICP-OES	-	-	-	-	
$Ni_{0.9}Fe_{0.1}$-P/CC	CC	-	S	2.2	~ 225	6.5	-	53.6		XRD, EDX, ICP-OES	-	-	-	-	
$Ni_{0.6}Fe_{0.4}$-P/CC	CC	-	S	2.2	241	5.6	-	71.6		XRD, EDX, ICP-OES	-	-	-	-	
FeP_x@Fe	Fe foam	Branch with coral-like structure	S	-	274	19	-	75	1 M KOH	XRD, SEM, EDX, TEM, STEM, XPS, N_2 ISO (BET, PSD)	XRD, SEM, EDX, TEM, STEM, XPS	24 h CP (10 $mA \cdot cm^{-2}_{geo}$) 3000 CV cycles (100 $mV \cdot s^{-1}$)	Fe_2O_3, FeOOH	Precatalyst (partial oxidation)	451
FeP_x-4	Fe foam	Branch with smoother surface	S	-	283	17.8	-	79		XRD, SEM, N_2 ISO (BET, PSD)	-	-	-	-	
FeP_x-16	Fe foam	Branch with coral-like structure	S	-	286	14.8	-	79		XRD, SEM, N_2 ISO (BET, PSD)	-	-	-	-	
NiFeP	Ni foam	Micro-flower with nanoplate	S	~ 1.2	201	6.95	-	86.3	1 M KOH	XRD, SEM, EDX, TEM, XPS, HAADF-STEM	-	-	-	-	452
$NiFeO_x$/NiFeP-3min	Ni foam	Nanosheet	S	-	165	5.01	-	57.9		XRD, SEM, EDX, TEM, XPS	XRD, SEM, XPS	15 h CP (40 $mA \cdot cm^{-2}_{geo}$)	$NiFeO_x$, metal phosphate species	Precatalyst (partial oxidation)	
Ni_2P	GC	Nanoparticle	P	0.71	~ 330 390 (@20 $mA \cdot cm^{-2}_{geo}$)	-	-	58	1 M KOH	XRD, TEM, EDX, EXAFS	-	-	-	-	453
NiFeP	GC	Nanoparticle	P	0.71	~ 260 330 (@20 $mA \cdot cm^{-2}_{geo}$)	-	-	39		XRD, TEM, EDX, EXAFS, XPS	XRD, TEM, EDX	10 h CP (20 $mA \cdot cm^{-2}_{geo}$)	MO_x (M = Ni, Fe)	Precatalyst	
NiCoP	GC	Nanoparticle	P	0.71	~ 360 410 (@20 $mA \cdot cm^{-2}_{geo}$)	-	-	52		XRD, TEM, EDX	-	-	-	-	
NiMnP	GC	Nanoparticle	P	0.71	~ 450 550 (@20 $mA \cdot cm^{-2}_{geo}$)	-	-	63		XRD, TEM, EDX	-	-	-	-	

https://doi.org/10.1021/acs.chemrev.3c00005
Chem. Rev. 2023, 123, 12795−13208

Table 4. continued

Initial Electrocatalyst	Substrate	Shape of Electrocatalyst	Deposition Type	Specific Loading / $mg \cdot cm^{-2}_{geo}$	η@10 $mA \cdot cm^{-2}_{geo}$ / mV	C_{dl} / $mF \cdot cm^{-2}_{geo}$	TOF / s^{-1} (@η or j)	Tafel Slope / $mV \cdot dec^{-1}$	Electrolyte	Pre-analysis	Post-analysis	Long-Term OER Test Conditions	Post-OER Electrocatalyst	Final Type of Electrocatalyst	Ref.
NiMoP	GC	Nanoparticle	P	0.71	~380 430 (@30 $mA \cdot cm^{-2}_{geo}$)	-	-	86		XRD, TEM, EDX	-	-	-	-	453
FeP_x	GC	Nanoparticle	P	~0.15	320	-	-	42	1 M KOH	XRD, HAADF-STEM, EDX, XPS, TGA	-	-	-	-	454
NiP_x	GC	Nanoparticle	P	~0.15	377	-	-	47			-	-	-	-	
CoP_x	GC	Nanoparticle	P	~0.15	427	-	-	63			-	-	-	-	
FeP_x	GC	Nanoparticle	P	~0.15	310	-	-	42	Fe-purified 1 M KOH		HAADF-STEM, EDX	1 h CA (1.58 V_{RHE})	FeO_x, FeOOH	Precatalyst (partial oxidation)	
NiP_x	GC	Nanoparticle	P	~0.15	460	-	-	79					NiO_x, NiOOH	Precatalyst (partial oxidation)	
CoP_x	GC	Nanoparticle	P	~0.15	460	-	-	63					CoO_x CoOOH	Precatalyst (partial oxidation)	
Ambient oxidized FeP_x (FeP_x-ox)	GC	-	P	~0.15	>~510	-	-	-	1 M KOH	-	-	-	-	-	
CoP/C	GC	Nanoparticle on nanosheet	P	0.4	357	27.18	0.013 at 300 mV	62	1 M KOH	XRD, EDX, TEM, XPS	-	-	-	-	455
$Co_{0.8}Fe_{0.2}P$/C	GC	Nanoparticle on nanosheet	P	0.4	291	67.41	0.15 at 300 mV	41		XRD, EDX, XPS	-	-	-	-	
$Co_{0.7}Fe_{0.3}P$/C	GC	Nanoparticle on nanosheet	P	0.4	270	63.57	0.92 at 300 mV	27		XRD, SEM, EDX, TEM, XPS, AFM	XPS	1000 CV cycles (1.0–1.6 V_{RHE})	MO_x (M = Co, Fe)	Precatalyst	
$Co_{0.6}Fe_{0.4}P$/C	GC	Nanoparticle on nanosheet	P	0.4	283	18.18	0.16 at 300 mV	54		XRD, EDX, XPS	-	-	-	-	
Ni_2P	CC	Hollow microsphere consisting of nanosheet	P	0.20	280	0.041	-	115	1 M KOH	XRD, SEM, EDX, TEM, XPS, ISO (BET)	XRD, XPS	10 h CP (5, 10, 20 $mA \cdot cm^{-2}_{geo}$) 500 CV cycles	NiO_x, Oxidized P species	Precatalyst (partial oxidation)	456
PdP_2@CB	GC	Nanoparticle on carbon black	P	0.283	270 338 (@30 $mA \cdot cm^{-2}_{geo}$)	26.5	-	78.6	1 M KOH	XRD, XPS, TEM, HAADF-STEM, EDX, TGA	XPS, TEM, HAADF-STEM, EDX	5000 CV cycles	Pd oxide, Pd hydroxides	Precatalyst (almost full oxidation)	457
					277 342 (@30 $mA \cdot cm^{-2}_{geo}$)	14.7	-	96	1 M PBS (pH ≈ 7)						
NiFe(3:1)-P	GC	Flower-like microstructure with inner-stacked nanoparticle	P	0.1	233	-	-	42.5	1 M KOH	XRD, SEM, EDX, TEM, XPS, ICP-OES	TEM, EDX, XPS	30 h CP (10 $mA \cdot cm^{-2}_{geo}$)	Ni-Fe oxo/hydroxide, P–O species	Precatalyst (partial oxidation)	458
NiP_x	GC		P	0.1	305	-	-	62		XRD, TEM, XPS	-	-	-	-	
FeP_x	GC		P	0.1	420	-	-	120.1		XRD, SEM, TEM, XPS	-	-	-	-	
NiP3	ZrO_2 mesh	Particulate	S	-	375	-	-	162.5	Fe-purified 1 M KOH	EDX	SEM, EDX, XPS	20 CV cycles (5 $mV \cdot s^{-1}$, activation)	NiOOH, PO_4^{3-}	Precatalyst (partial oxidation)	459
NiP15	ZrO_2 mesh	Particulate	S	-	343	1.24	-	90.9		EDX	SEM, EDX		-	Precatalyst (partial oxidation)	
NiP60	ZrO_2 mesh	Particulate	S	-	326	12.98	-	88.8		SEM, EDX, TEM, XPS, Raman	SEM, EDX, XPS, Raman		NiOOH, PO_4^{3-}	Precatalyst (partial oxidation)	
HT-NiP60	ZrO_2 mesh	Particulate	S	-	352	4.07	-	89.1		TEM, EDX, XPS	SEM, EDX, XPS		NiOOH, PO_4^{3-}	Precatalyst (partial oxidation)	
NiP60-P	ZrO_2 mesh	Particulate	S	-	371	-	-	121.9		-	SEM, EDX		-	Precatalyst (partial oxidation)	
NiP120	ZrO_2 mesh	Particulate	S	-	330	-	-	75.1		XRD, SEM, EDX	XRD, SEM, EDX, XPS	10 h CP (15 $mA \cdot cm^{-2}_{geo}$) 20 CV cycles (5 $mV \cdot s^{-1}$, activation)	NiOOH, PO_4^{3-}	Precatalyst (partial oxidation)	
FeP/Ni_2P/NF	Ni foam	Nanoparticle	S	8	154	19.3	-	22.7	1 M KOH	XRD, SEM, EDX, TEM, SAED, XPS	XRD, XPS	24 h CP (100 $mA \cdot cm^{-2}_{geo}$) 5000 CV cycles	(Ni,Fe)O_x, (Ni,Fe)OOH	Precatalyst (partial oxidation)	80
Ni_2P/NF	Ni foam	Nanoparticle	S	8	-	14.5	-	102.3		-	-	-	-	-	
$Co_{0.4}Fe_{0.2}P$	GC	Nanocube	P	0.2	270	23.9	-	25.6	1 M KOH	XRD, SEM, EDX, TEM, XPS, N_2 ISO (BET, PSD)	EDX, TEM, XPS, ICP-OES	30 CV cycles (0.9–1.5 V_{RHE}) 3 h CA (1.53 V_{RHE})	$MOOH$ (M = Co, Fe), PO_x	Precatalyst (partial oxidation)	460
CoP	GC	Porous nanocube	P	0.2	~320	-	-	-		XRD, SEM	-	-	-	-	
O3-V10-Ni_2P	GC	Nanosheet	P	~0.255	257	10.02	-	43.5	1 M KOH	XRD, SEM, EDX, TEM, XPS, N_2 ISO (BET, PSD), CAM	XRD, SEM, XPS	1 and 20 h CP (30 $mA \cdot cm^{-2}_{geo}$) 1 h CP (10 mA)	MO_x, MO_xH_y (M = Ni, V), PO_4^{3-}	Precatalyst (partial oxidation)	461
V15-Ni_2P	GC	Nanosheet	P	~0.255	325	-	-	70.6		SEM, ICP-OES	-	-	-	-	
V10-Ni_2P	GC	Nanosheet	P	~0.255	308	6.77	-	75.1		XRD, SEM, EDX, TEM, XPS, ICP-OES, CAM	-	-	-	-	
V5-Ni_2P	GC	Nanosheet	P	~0.255	326	-	-	98.9		SEM, ICP-OES	-	-	-	-	
Ni_2P	GC	Nanosheet	P	~0.255	333	5.31	-	131		XRD, SEM, N_2 ISO (BET, PSD), ICP-OES	-	-	-	-	
Fe_3O_4/Ni_2P	GC	Nanoparticle	P	0.2	260	4.1	-	43	1 M KOH	XRD, EDX, TEM, XPS	XRD, TEM, XPS	25 h CP (10 $mA \cdot cm^{-2}_{geo}$)	NiO, $Ni(OH)_2$, NiOOH, FeOOH, Higher-valent P species (e.g., PO_4^{3-})	Precatalyst (partial oxidation)	462
$Ni_{12}P_5$	GC	Nanoparticle	P	0.2	320	5.6	-	128		XRD, TEM, ICP-OES	ICP-AES	-	-	-	
NiCoFeP	GC	Nanocube	P	0.283	273	69	-	35	1 M KOH	XRD, SEM, EDX, TEM, XPS, FTIR, ICP, N_2 ISO (BET, PSD)	SEM, EDX, XPS	10 h CA (1.503 V_{RHE}) 2000 CV cycles	(Ni,Co,Fe) oxo/hydroxides, P–O species	Precatalyst (partial oxidation)	463

https://doi.org/10.1021/acs.chemrev.3c00005
Chem. Rev. 2023, 123, 12795−13208

Table 4. continued

Initial Electrocatalyst	Substrate	Shape of Electrocatalyst	Deposition Type	Specific Loading / $mg \cdot cm^{-2}_{geo}$	η@10 $mA \cdot cm^{-2}_{geo}$ / mV	C_{dl} / $mF \cdot cm^{-2}_{geo}$	TOF / s^{-1} (@η or j)	Tafel Slope / $mV \cdot dec^{-1}$	Electrolyte	Pre-analysis	Post-analysis	Long-Term OER Test Conditions	Post-OER Electrocatalyst	Final Type of Electrocatalyst	Ref.
$Ni_{high}CoFeP$	GC	Nanoparticle	P	0.283	348	24	-	39	1 M KOH	SEM, TEM, ICP, N_2 ISO (BET)	-	-	-	-	463
CoFeP	GC	Nanocube	P	0.283	295	43	-	35		SEM, TEM, ICP, N_2 ISO (BET)	-	-	-	-	
NiFeP	GC	Nanocube	P	0.283	308	36	-	45		SEM, TEM, ICP, N_2 ISO (BET)	-	-	-	-	
Co_2P	GC	Nanoparticle	P	0.2	360	0.37	-	54	1 M KOH	XRD, SEM, TEM, XPS	-	-	-	-	464
Fe_2P	GC	Nanosheet	P	0.2	497	0.22	-	110		XRD, SEM, TEM, XPS	-	-	-	-	
Fe-Co_2P	GC	Nanoparticle	P	0.2	289	0.51	-	40		XRD, SEM, EDX, TEM, XPS	-	-	-	-	
Fe-Co_2P/NF	Ni foam	Nanoparticle	P	1.0	250	-	-	36			XRD, SEM, TEM, XPS	28 h CA (1.53 V_{RHE})	CoO_x, CoOOH, PO_4^{3-}	Precatalyst (partial oxidation)	
NiP_2	CF	-	S	-	180	-	-	53	1 M KOH	XRD, EDX	-	-	-	-	465
O-$Ni_{0.75}Fe_{0.25}P_2$	CF	Nanosheet	S	-	155	-	-	55		XRD, SEM, EDX TEM, XPS	XRD, SEM, EDX, TEM, XPS	24 h CA (1.43 V_{RHE})	MO_x (M = Ni, Fe), Oxidized metal phosphate species	Precatalyst (partial oxidation)	
O-$Ni_1Fe_{0.0}P_2$	CF	-	S	-	~ 190	-	-	~ 75		-	-	-	-	-	
O-$Ni_{0.85}Fe_{0.15}P_2$	CF	-	S	-	~ 185	-	-	~ 72		XRD, EDX	-	-	-	-	
O-$Ni_{0.65}Fe_{0.35}P_2$	CF	-	S	-	~ 175	-	-	~ 70		XRD, EDX	-	-	-	-	
$(NiFe)_2P$	GC	Cubic framework	P	0.194	308	-	-	55.5	1 M KOH	XRD, SEM, XPS, FTIR	TEM, XPS	-	(NiFe)OOH, P–O species	Precatalyst (partial oxidation)	466
$Ni_{0.6}Co_{1.4}P$	GC	Nanocage	P	0.35	300	58.57	-	80	1 M KOH	XRD, SEM, EDX, TEM, XPS, HAADF-STEM, N_2 ISO (BET, PSD), ICP-MS, UPS	SEM, EDX, TEM, XPS	10 h CA (1.53 V_{RHE})	Ni-Co oxide/hydroxide species	Precatalyst (partial oxidation)	467
$Ni_{0.2}Co_{1.8}P$	GC	Nanocage	P	0.35	~ 350	-	-	93		XRD, SEM, TEM, ICP-MS	-	-	-	-	
$Ni_{0.8}Co_{1.2}P$	GC	Nanocage	P	0.35	~ 310	-	-	91		XRD, SEM, TEM, ICP-MS	-	-	-	-	
NiCoP	GC	Nanocage	P	0.35	~ 320	-	-	90		XRD, SEM, TEM, UPS, ICP-MS	-	-	-	-	
CoP	GC	Nanocage	P	0.35	370	12.49	-	100		XRD, SEM, TEM, ICP-MS	-	10 h CA (1.53 V_{RHE})	-	-	
Ni_2P	GC	Nanocage	P	0.35	420	4.39	-	128		XRD, SEM, TEM, ICP-MS	-		-	-	
Ru-RuP_x-Co_xP	GC	Polyhedral structure with nanoparticle	P	-	291	80.9	-	85.4	0.1 M KOH	XRD, STEM, EDX, TEM, XPS, N_2 ISO (BET, PSD), HAADF-STEM, EELS, ICP-AES	HAADF-STEM, EELS	6 h CA 6 h CP (10 $mA \cdot cm^{-2}_{geo}$) 10000 CV cycles	RuO_2, CoOOH	Precatalyst (partial oxidation)	468
Co_2P	GC	Nanorod	P	-	322	70.1	-	108.9		XRD, STEM, EDX, TEM, XPS, N_2 ISO (BET, PSD)		10000 CV cycles	-	-	
$CoNi_{0.2}$-Z-H-P	GC	Hollow sphere	P	0.14	~ 360	0.0128	-	67.3	1 M NaOH	XRD, SEM, TEM, HAADF, EDX, XPS, XANES, EXAFS	-	-	-	-	469
$CoFe_{0.05}$-Z-H-P	GC	Hollow sphere	P	0.14	~ 355	0.0146	-	62.8		XRD, SEM, XPS, XANES, EXAFS	-		-	-	
$CoNi_{0.2}Fe_{0.05}$-Z-H-P	GC	Hollow sphere	P	0.14	329	0.017	-	48.2		XRD, SEM, EDX, HAADF, TEM, XPS, Raman, XRF, XANES, EXAFS	TEM, XPS	10 h CA	MO_x, $MOOH$ (M = Co, Ni, Fe), PO_x	Precatalyst (partial oxidation)	
CoP/CNTs	CFP	Nanoparticles	P	0.8	238	-	-	-	1 M KOH	XRD, SEM, EDX, XPS	XPS	10 min CA (1.67 V_{RHE})	CoO_x, CoOOH, PO_4^{3-}	Precatalyst (partial oxidation)	470
Ni_2P/$(NiFe)_2P$(O) NAs	Ni foam	Ordered nanocube array	S	-	150	37	-	60	1 M KOH	XRD, SEM, EDX, TEM, XPS	XRD, SEM, TEM, XPS	100 h CA (1.60, 1.79, 1.92 V_{RHE})	$M(OH)_2$, $MOOH$ (M = Ni, Fe), P–O species	Precatalyst (partial oxidation)	471
$(NiFe)_2P$	Ni foam	Nanocube	S	-	240	23	-	67		SEM	-	-	-	-	
Ni_2P	Ni foam	-	S	-	300	17	-	105		XRD	-	-	-	-	
Ni_2P/$(NiFe)_2P$(O) NAs	Ni foam	Ordered nanocube array	S	-	170 (@100 $mA \cdot cm^{-2}_{geo}$)	-	-	-	30 wt.% KOH	XRD, SEM, EDX, TEM, XPS	-	50 h CA (2.0 V_{RHE})	-	-	
$(NiFe)_2P$	Ni foam	Nanocube	S	-	270 (@100 $mA \cdot cm^{-2}_{geo}$)	-	-	-		SEM	-	-	-	-	
Ni_2P	Ni foam	-	S	-	320 (@100 $mA \cdot cm^{-2}_{geo}$)	-	-	-		XRD	-	-	-	-	
np-$(Ni_{0.75}Fe_{0.25})_4P_3$	NiFe alloy	Nanoporous structure	S	-	280	0.148	-	33.7	1 M KOH	XRDXRD, SEM EDX, XPS	-	-	-	-	472
np-$(Ni_{0.67}Fe_{0.33})_4P_3$	NiFe alloy	Nanoporous structure	S	-	245	0.396	-	32.9		XRD, SEM, TEM XPS	XRD, SEM, TEM, XPS	20 h CP (10 $mA \cdot cm^{-2}_{geo}$) 80 CV cycles (5 $mV \cdot s^{-1}$)	$Ni_xFe_{1-x}OOH$, PO_4^{3-}	Precatalyst (partial oxidation)	
np-$(Ni_{0.5}Fe_{0.5})_4P_3$	NiFe alloy	Nanoporous structure	S	-	310	0.229	-	37.5		XRD, SEM, EDX, XPS	-	-	-	-	
np-Ni_4P_3	Ni alloy	Nanoporous structure	S	-	362	0.115	-	40.9		XRD, SEM, EDX, XPS	-	-	-	-	
NiP	Ni foam	-	S	-	~ 230	-	0.08 at 300 mV	54	1 M KOH	XRD, STEM, EDX, XPS, N_2 ISO (BET), ICP-OES	-	180 h CP (10 $mA \cdot cm^{-2}_{geo}$)	-	-	473

https://doi.org/10.1021/acs.chemrev.3c00005
Chem. Rev. 2023, 123, 12795−13208

Table 4. continued

Initial Electrocatalyst	Substrate	Shape of Electrocatalyst	Deposition Type	Specific Loading / $mg \cdot cm^{-2}_{geo}$	η@10 $mA \cdot cm^{-2}_{geo}$ / mV	C_{dl} / $mF \cdot cm^{-2}_{geo}$	TOF / s^{-1} (@η or j)	Tafel Slope / $mV \cdot dec^{-1}$	Electrolyte	Pre-analysis	Post-analysis	Long-Term OER Test Conditions	Post-OER Electrocatalyst	Final Type of Electrocatalyst	Ref.
AlNiP	Ni foam	Bulk	S	-	180	-	-	27		XRD, STEM, EDX, XPS, N_2 ISO (BET), ICP-OES	XRD, HAADF-STEM, TEM, EDX, XPS ICP-OES, N_2 ISO (BET)	200 h CP (10 $mA \cdot cm^{-2}_{geo}$) 40 CV cycles (5 $mV \cdot s^{-1}$)	$Ni(OH)_2$, NiO	Precatalyst (partial oxidation)	473
Ni_1Mo_1P NSs@MCNTs	GC	Nanosheet	P	-	255	6.8	-	45.1	1 M KOH	XRD, EDX, TEM, XPS, N_2 ISO (BET, PSD)	TEM, EDX, XPS (after OWS)	36 h CP (10 $mA \cdot cm^{-2}_{geo}$) 3000 CV cycles 36 h CP (10 $mA \cdot cm^{-2}_{geo}$, OWS) 40 h CP (60 $mA \cdot cm^{-2}_{geo}$, OWS)	NiO_x, NiOOH, PO_4^{3-}	Precatalyst (partial oxidation)	474
$Ni_1Mo_{1.2}P$ NSs@MCNTs	GC	Nanosheet	P	-	283	5.3	-	75.5		TEM, EDX	-	-	-	-	
$Ni_1Mo_{0.5}P$ NSs@MCNTs	GC	Nanosheet	P	-	289	3.3	-	77.6		TEM, EDX	-	-	-	-	
NiP NPs@MCNTs	GC	Nanoparticle	P	-	325	2	-	107.3		TEM	-	-	-	-	
FeP	GC	Nanoparticle	P	0.3 (TM loading: 0.06)	325	~ 7	-	132	1 M KOH	XRD, TEM, XPS, ICP-MS, STEM-HAADF	-	24 h CP (10 $mA \cdot cm^{-2}_{geo}$)	-	-	93
NiP	GC	Nanoparticle	P	0.3 (TM loading: 0.06)	~ 310	~ 11	-	~ 108			-		-	-	
CoP	GC	Nanoparticle	P	0.3 (TM loading: 0.06)	~ 295	~ 14	-	~ 96			-		-	-	
FeNiP	GC	Nanoparticle	P	0.3 (TM loading: 0.06)	~ 280	~ 13	~ 0.05 at 300 mV	~ 92			-		-	-	
FeCoP	GC	Nanoparticle	P	0.3 (TM loading: 0.06)	~ 260	~ 27	~ 0.13 at 300 mV	~ 83			-		-	-	
CoNiP	GC	Nanoparticle	P	0.3 (TM loading: 0.06)	~ 230	~ 27	~ 0.17 at 300 mV	~ 78			-		-	-	
FeCoNiP (support less)	GC	Nanoparticle	P	0.3 (TM loading: 0.06)	268	17	-	-			-	-	-	-	
FeCoNiP	GC	Nanoparticle	P	0.06	200	30	0.47 at 300 mV	70			TEM, STEM-HAADF, XPS	24 h CP (10 $mA \cdot cm^{-2}_{geo}$) 30 CV cycles (5 $mV \cdot s^{-1}$, 1.0–1.6 V_{RHE})	$M(OH)_2$, $MOOH$ (M = Ni, Fe, Co), PO_x/P–O species	Precatalyst (partial oxidation)	
Hollow CoP OCHs	CP	Octahedral Nanoparticle	P	0.5	240	2.7	0.072 at 300 mV	38	1 M KOH	XRD, SEM, EDX, TEM, XPS	SEM, EDX, XPS	60 h CP (10 $mA \cdot cm^{-2}_{geo}$)	CoOOH, P–O species	Precatalyst (partial oxidation)	475
Porous CoP NSs	CP	Nanosphere	P	0.5	280	1.6	~ 0.04 at 300 mV	45			SEM, EDX, XPS	60 h CP (10 $mA \cdot cm^{-2}_{geo}$)	CoOOH, P–O species	Precatalyst (partial oxidation)	
R-CoP_x/rGO	GC	Self-supported nanoflower	P	0.28	268 [R-CoP_x/rGO(O)]	0.85	-	103	1 M KOH	XRD, SEM, STEM-EDX, TEM, XPS, N_2 ISO (BET, PSD), Raman, EPR	XRD, SEM, EDX, TEM, XPS, EPR	10 h CP (10 $mA \cdot cm^{-2}_{geo}$) 5 h CA (1.498 V_{RHE}) 1 h CP (10 $mA \cdot cm^{-2}_{geo}$) 2000 CV cycles (0–0.7 $V_{Ag/AgCl}$)	β-CoOOH, PO_x^{n-}	Precatalyst (full oxidation)	476
CoP_x/rGO	GC	Nanorod	P	0.28	389 [CoP_x/rGO(O)]	0.04	-	105		XRD, SEM, XPS, N_2 ISO (BET, PSD), Raman, EPR	EIS	5 h CA (1.619 V_{RHE})	-	-	
CoP_x	GC	Nanorod	P	0.28	373 [CoP_x(O)]	0.04	-	104		XRD, SEM, XPS, Raman	-	5 h CA (1.603 V_{RHE})	-	-	
R-CoP_x@C	GC	3D network structure with carbon shell	P	0.28	339 [R-CoP_x@C(O)]	-	-	-		XRD, SEM, EDX, TEM, XPS, Raman	XPS	10 h CA (1.569 V_{RHE}) 1 h CP (10 $mA \cdot cm^{-2}_{geo}$)	CoOOH, PO_x^{n-}	Precatalyst (partial oxidation)	
CoP_x@C	GC	Nanorod	P	0.28	387 [CoP_x@C(O)]	-	-	-		XRD, SEM, XPS, Raman	-	10 h CA (1.617 V_{RHE})	-	-	
CNTs@NiCoP/C	GC	Nanosheet@nanocage	P	0.35	297	13.38	0.088 at 350 mV	57.35	1 M KOH	XRD, SEM, EDX, TEM, HAADF-STEM, XPS, N_2 ISO (BET), ICP-AES, Raman	XRD, SEM, TEM, EDX, XPS	8 h CP (10 $mA \cdot cm^{-2}_{geo}$) 1000 CV cycles (50 $mV \cdot s^{-1}$)	oxidized Ni and Co species (e.g., CoOOH), PO_4^{3-}	Precatalyst (partial oxidation)	477
NiCoP/C	GC	Nanocage	P	0.35	~ 356	1.33	0.013 at 350 mV	113.84		SEM, XPS, N_2 ISO (BET)	-	-	-	-	
CNTs@CoP/C	GC	Nanosheet@nanocage	P	0.35	~ 330	5.59	0.028 at 350 mV	67.76		SEM, XPS, N_2 ISO (BET), Raman	-	-	-	-	
CNTs+NiCoP/C	GC	Nanocage	P	0.35	~ 350	-	-	64.8		XPS	-	-	-	-	
Fe_2P@APC	GC	Nanoparticles on amorphous carbon	P	0.35	385	5.4	-	95	1 M KOH	XRD, SEM, TEM, EDX, XPS, Raman, ICP	-	20 h CA (1.615 V_{RHE}) 3000 CV cycles	-	-	403
Fe_2P/FeP@GPC	GC	Graphitic shell encapsulated nanostructure	P	0.35	333	6.35	-	90		XRD, SEM, TEM, EDX, XPS, Raman, ICP	-	-	-	-	
FeP@GPC	GC		P	0.35	278	9.65	-	87		XRD, SEM, TEM, EDX, XPS, Raman, ICP, PSD	XRD, TEM, EDX, XPS	20 h CA (1.508 V_{RHE}) 3000 CV cycles	$Fe_3(PO_4)_2$	Precatalyst (partial oxidation)	
CMP@PNC	GC	Nanoparticle@nanosheet	P	0.3	330	25.36	-	74	0.1 M KOH	XRD, SEM, EDX, TEM, XPS, XANES, EXAFS, TGA	XPS	~ 30 h CA (1.55 V_{RHE}) 7000 CV cycles	$MOOH$ (M = Mn, Co), P–O species (from carbon P,N co-doped carbon support)	Precatalyst (partial oxidation)	478

https://doi.org/10.1021/acs.chemrev.3c00005
Chem. Rev. 2023, 123, 12795−13208

Table 4. continued

Initial Electrocatalyst	Substrate	Shape of Electrocatalyst	Deposition Type	Specific Loading / $mg \cdot cm^{-2}_{geo}$	η@10 $mA \cdot cm^{-2}_{geo}$ / mV	C_{dl} / $mF \cdot cm^{-2}_{geo}$	TOF / s^{-1} (@η or j)	Tafel Slope / $mV \cdot dec^{-1}$	Electrolyte	Pre-analysis	Post-analysis	Long-Term OER Test Conditions	Post-OER Electrocatalyst	Final Type of Electrocatalyst	Ref.
CP@PNC	GC	Aggregated nanoparticle	P	0.3	401	12.32	-	100		XRD, SEM, EDX, TEM, XPS, XANES, EXAFS	-	-	-	-	478
MP@PNC	GC	Aggregated nanoparticle	P	0.3	409	9.36	-	127		XRD, SEM, EDX, TEM, XPS, XANES, EXAFS	-	-	-	-	
CMP@PC	GC	Aggregated nanoparticle	P	0.3	391	21.59	-	88		XRD, SEM, EDX, TEM	-	-	-	-	
Ni-Fe_xP/NF	Ni foam	Interconnected porous structure	S	~ 8	267 (@100 $mA \cdot cm^{-2}_{geo}$)	3.62	-	37	1 M KOH	XRD, SEM, EDX, TEM, XPS	XPS	30 h CP (10 $mA \cdot cm^{-2}_{geo}$) 1000 CV cycles (100 $mV \cdot s^{-1}$)	MO_x, $M(OH)_2$ (M = Ni, Fe), PO_4^{3-}	Precatalyst (partial oxidation)	479
Fe_xP/IF	Fe foam	-	S	~ 8	~ 390 (@100 $mA \cdot cm^{-2}_{geo}$)	-	-	85		-	-	-	-	-	
FeP/NF	Ni foam	Nanoparticle	P	-	227	1.01	-	54	1 M KOH	XRD, SEM, EDX, TEM, XPS, ICP-AES, FTIR, Mössbauer, EPR, ^{1}H NMR, MSM, XAS	TEM, EDX, ICP-AES, XPS, FTIR	15 h CA (1.46 V_{RHE})	$Fe(OH)_2$, FeOOH, PO_4^{3-}	Precatalyst (partial oxidation)	480
NiFePi/P	NiFe foam	Irregular biscuit-shaped morphology	S	-	230	2.6	-	57	1 M KOH	XRD, SEM, EDX, XPS, CAM	SEM, EDX, *Operando* XAS	24 h CP (10 $mA \cdot cm^{-2}_{geo}$)	Metal phosphate (Ni^{3+} and Fe^{3+} species)	Precatalyst (partial oxidation)	481
NiFePi	NiFe foam	Nano-latticed nanoparticle	S	-	256	1.6	-	63		XRD, SEM, XPS, CAM	-	-	-	-	
NiFeP	NiFe foam	Nano-latticed nanoparticle	S	-	290	1.2	-	66		XRD, SEM, XPS, CAM	-	-	-	-	
NiCoP/NF	Ni foam	Nanosheet	S	3	336 (@100 $mA \cdot cm^{-2}_{geo}$) 381 (@200 $mA \cdot cm^{-2}_{geo}$)	7.7	-	150	1 M KOH	XRD, SEM, TEM, XPS	-	-	-	-	482
NiCoFeP/NF	Ni foam	Nanosheet	S	3	271 (@200 $mA \cdot cm^{-2}_{geo}$)	5.2	-	45		XRD, SEM, EDX, TEM, XPS	XRD, SEM, TEM XPS	10 h CA (1.485 V_{RHE}) 2000 CV cycles (100 $mV \cdot s^{-1}$)	Ni-Co-Fe oxide/hydroxide, Oxidized P species	Precatalyst (partial oxidation)	
AG (Mg-modified Ni_2P)	CP	Nanoparticle	S	1.33	280	-	0.03 at 350 mV	48	1 M KOH	XRD, HAADF-STEM, EDX, XPS, ICP-OES, ISO (BET)	XRD, SEM, HAADF-STEM, XPS	200 h CP (10 $mA \cdot cm^{-2}_{geo}$)	Ni hydroxide/phosphate on MgO	Precatalyst (partial oxidation)	483
Ni_2P	CP	-	S	1.16	310	-	-	71		XRD	-	-	-	-	
h-CoNiP/rGO	GC	Nanoparticle on rGO nanosheet	P	0.21	280	-	-	65.2	1 M KOH	XRD, SEM, EDX, TEM, XPS, Raman	XPS	8 h CA (1.51 V_{RHE})	Ni-Co oxo/hydroxide, Oxidized P species	Precatalyst (partial oxidation)	484
Co_1Ni_3P/rGO	GC	Nanoparticle on rGO nanosheet	P	0.21	340	-	-	94.4		-	-	-	-	-	
Co_3Ni_1P/rGO	GC	Nanoparticle on rGO nanosheet	P	0.21	330	-	-	87.3		-	-	-	-	-	
CoNiP	GC	Nanoparticle	P	0.21	370	-	-	99.1		-	-	-	-	-	
NiP_x/rGO	GC	Nanoparticle on rGO nanosheet	P	0.21	390	-	-	124		-	-	-	-	-	
CoP_x/rGO	GC	Nanoparticle on rGO nanosheet	P	0.21	380	-	-	113		-	-	-	-	-	
Ni_2P	Ni foam	Nanosheet	S	-	~ 320 (@100 $mA \cdot cm^{-2}_{geo}$)	8.6	-	99.9	1 M KOH	XRD, SEM, Raman	Raman	10000 CV cycles	NiO_x	Precatalyst	485
$Fe(PO_3)_3/Ni_2P$	Ni foam	Aggregated particle	S	8	177 221 (@100 $mA \cdot cm^{-2}_{geo}$)	12.0	0.12 at 300 mV	51.9		XRD, SEM, TEM, XPS, Raman	SEM, TEM, XPS, Raman	~ 22 h CA (1.503 and 1.451 V_{RHE}) 10000 CV cycles	MO_x (M = Ni, Fe), FeOOH, $Ni(OH)_2$	Precatalyst (partial oxidation)	
Ni_2P	Ni foam	Nanosheets	S	-	330	-	-	-	0.1 M KOH	XRD, SEM, Raman	-	-	-	-	
$Fe(PO_3)_3/Ni_2P$	Ni foam	Aggregated particles	S	8	218	-	-	-		XRD, SEM, TEM, XPS, Raman	-	~ 22 h CA (1.455 V_{RHE})	-	-	
Co-P	GC	-	P	0.19	~ 300	28.5	0.014 at 300 mV	125	1 M KOH	XRD, N_2 ISO (BET)	-	-	-	-	486
Ni-P	GC	-	P	0.19	~ 360	21.3	0.0082 at 300 mV	96		XRD, N_2 ISO (BET)	-	-	-	-	
Co9Ni1-P	GC	Rough nanorod	P	0.19	~ 280	44.8	0.019 at 300 mV	87		XRD, N_2 ISO (BET)	-	-	-	-	
Co4Ni1-P	GC	-	P	0.19	245	59.9	0.032 at 300 mV	61		XRD, SEM, EDX, TEM, XPS N_2 ISO (BET, PSD)	XRD, SEM, EDX, TEM, XPS (after OWS)	20 h CA (1.48 V_{RHE}) 20 h CA (1.53 V_{RHE}) 3000 CV cycles (100 $mV \cdot s^{-1}$) 50 h CA (cell voltage: 1.59 V, OWS)	Oxidized Ni and Co species	Precatalyst (partial oxidation)	
Co1Ni1-P	GC	-	P	0.19	~ 360	26.9	0.0075 at 300 mV	105		XRD, N_2 ISO (BET)	-	-	-	-	
Co1Ni4-P	GC	-	P	0.19	~ 400	13.6	0.0021 at 300 mV	94		XRD, N_2 ISO (BET)	-	-	-	-	
Co1Ni9-P	GC	-	P	0.19	~ 380	17	0.0057 at 300 mV	99		XRD, N_2 ISO (BET)	-	-	-	-	
Co4Ni1-P	GC	Rough nanorod	P	0.19	261	-	-	64	0.5 M H_2SO_4	XRD, SEM, EDX, TEM, XPS, N_2 ISO (BET, PSD)	-		-	-	
Co4Ni1-P	GC	Rough nanorod	P	0.19	268	-	-	67	1 M PBS (pH = 7)		-		-	-	
CoP@NSP-C	GC	Nanoparticle	P	0.50	500	-	-	202	0.1 M KOH	XRD, SEM, TEM, STEM, EDX, XPS	-	-	-	-	487
CoP@mNSP-C	GC	Nanoparticle	P	0.50	410	-	-	126		XRD, SEM, TEM, STEM, EDX, XPS,	XRD, SEM, TEM (after 100 cycles of ZAB)	24 h CP (10 $mA \cdot cm^{-2}_{geo}$) 1000 CV cycles (250 $mV \cdot s^{-1}$, 0.2–1.9 V_{RHE})	CoO_x, Oxidized P species	Precatalyst (partial oxidation)	

https://doi.org/10.1021/acs.chemrev.3c00005
Chem. Rev. 2023, 123, 12795−13208

Table 4. continued

Initial Electrocatalyst	Substrate	Shape of Electrocatalyst	Deposition Type	Specific Loading / $mg \cdot cm_{geo}^{-2}$	η@10 $mA \cdot cm_{geo}^{-2}$ / mV	C_{dl} / $mF \cdot cm_{geo}^{-2}$	TOF / s^{-1} (@η or j)	Tafel Slope / $mV \cdot dec^{-1}$	Electrolyte	Pre-analysis	Post-analysis	Long-Term OER Test Conditions	Post-OER Electrocatalyst	Final Type of Electrocatalyst	Ref.
										ICP, N_2 ISO (BET, PSD)					487
Co-Pi/CoP/Ti	Ti plate	Nanorod	S	~2	310	-	-	58	1 M KOH	XRD, SEM, TEM, EDX, XPS, HAADF-STEM, Raman, FTIR, H_2-TPR	XRD, SEM, EDX, XPS, Raman, H_2-TPR	24 h CP (50 $mA \cdot cm_{geo}^{-2}$) 120 min multistep CP (100–350 $mA \cdot cm_{geo}^{-2}$)	Phosphate-intercalated Co (oxy)hydroxide	Precatalyst (full oxidation)	488
Core-oxidized Co_xP_y	GC	Nanoparticle	P	0.205	287	-	-	70	1 M KOH	XRD, SEM, TEM, EDX, XPS	TEM, EDX, XPS	12 h CA (1.532 V_{RHE}) 250 CV cycles (200 $mV \cdot s^{-1}$)	$Co(OH)_2$, PO_4^{3-}	Precatalyst (partial oxidation)	489
Cu_3P@NF	Ni foam	Nanosheet	S	1.2	320	-	-	54	1 M KOH	XRD, SEM, EDX, TEM, XPS, ICP-OES	SEM, TEM, EDX, XPS	50 CV cycles (50 $mV \cdot s^{-1}$, 1.2–1.7 V_{RHE}, activation) 100 h CP (10 $mA \cdot cm_{geo}^{-2}$) 100 h CA (1.6 V_{RHE})	CuO, Cu phosphate	Precatalyst (partial oxidation)	490
$Ni_{1.5}Fe_{0.5}P$/CF	CF	Nanosheet	S	1.38	293 (@100 $mA \cdot cm_{geo}^{-2}$)	-	-	114	1 M KOH	XRD, SEM, EDX, TEM, XPS	SEM, EDX, XPS (after OWS)	50 h CP (100 $mA \cdot cm_{geo}^{-2}$) 5000 s multistep CP (50–500 $mA \cdot cm_{geo}^{-2}$) 20 h CP (20 $mA \cdot cm_{geo}^{-2}$, OWS)	Ni phosphide/oxide/hydroxide heterojunctions, PO_4^{3-}	Precatalyst (partial oxidation)	491
$Ni_{1.5}Fe_{0.5}P$	GC	Nanosheet	P	0.2	264	-	-	55		XRD, SEM, XPS, TEM, EDX, ICP-MS	-	12 h CP (10 $mA \cdot cm_{geo}^{-2}$) 1000 CV cycles (100 $mV \cdot s^{-1}$, 1.2–1.7 V_{RHE})	-	-	
$Ni_{1.6}Fe_{0.4}P$	GC	Nanosheet	P	0.2	~330	-	-	79		XRD, SEM, XPS, ICP-MS	-	-	-	-	
$Ni_{1.33}Fe_{0.67}P$	GC	-	P	0.2	~325	-	-	89		XRD, XPS, ICP-MS	-	-	-	-	
$Ni_{1.67}Fe_{0.33}P$	GC	Nanosheet	P	0.2	~335	-	-	94		XRD, SEM, XPS, ICP-MS	-	-	-	-	
$Ni_{1.0}Fe_{1.0}P$	GC	Nanosheet	P	0.2	~360	-	-	83		XRD, SEM, EDX, XPS, ICP-MS	-	-	-	-	
Ni_2P	GC	Microsheet	P	0.2	~375	-	-	105		XRD, SEM, XPS	-	-	-	-	
Fe_2P	GC	Microsphere	P	0.2	>570	-	-	-		XRD, SEM, XPS	-	-	-	-	
$Fe_{2-x}Mn_xP$ (Mn=0)	GC	Nanorod	P	~0.284	590	-	-	135	1 M KOH	XRD, TEM	-	-	-	-	492
$Fe_{2-x}Mn_xP$ (Mn=0.2)	GC	Nanorod	P	~0.284	620	-	-	100		XRD, TEM	-	-	-	-	
$Fe_{2-x}Mn_xP$ (Mn=0.3)	GC	Nanorod	P	~0.284	550	-	-	~75		XRD, TEM	-	-	-	-	
$Fe_{2-x}Mn_xP$ (Mn=0.5)	GC	Nanorod	P	~0.284	520	-	-	81		XRD, TEM, HAADF, STEM-EDX	-	-	-	-	
$Fe_{2-x}Mn_xP$ (Mn=0.7)	GC	Nanorod	P	~0.284	480	-	-	53		XRD, TEM	-	-	-	-	
$Fe_{2-x}Mn_xP$ (Mn=0.9)	GC	Nanorod	P	~0.284	440	-	-	39		XRD, TEM, HAADF, EDX-EDX, FTIR	-	-	-	-	
$Fe_{2-x}Mn_xP$ (Mn=0.5) after annealing	GC	-	P	~0.284	430	-	-	-		-	-	-	-	-	
$Fe_{2-x}Mn_xP$ (Mn=0.9) after annealing	GC	Nanorod	P	~0.284	350	-	-	-		XRD, TEM, EDX, XPS, FTIR, ICP-MS	TEM, EDX, XPS, ICP-MS	20 h CA (1.58 V_{RHE})	M_2O_3, M(O)OH, MPO_4 (M = Fe, Mn)	Precatalyst (partial oxidation)	
Ni_2P NPs	GC	-	P	0.1	~420	-	-	88.9	0.1 M KOH	-	-	-	-	-	493
Ni_2P/NC QDs (10 %)	GC	Nanoparticle	P	0.1	~350	-	-	49.7		XRD, TEM, EDX, XPS	TEM, XPS	30000 s CP (10 $mA \cdot g^{-1}$) 200 CV cycles (100 $mV \cdot s^{-1}$)	NiO_x, $Ni(OH)_2$, Oxidized P species	Precatalyst (partial oxidation)	
Ni_2P/NC QDs (5 %)	GC	-	P	0.1	~380	-	-	-		-	-	-	-	-	
Ni_2P/NC QDs (15 %)	GC	-	P	0.1	~380	-	-	-		-	-	-	-	-	
Ni_2P/NC QDs (20 %)	GC	-	P	0.1	~390	-	-	-		-	-	-	-	-	
$Ni_{12}P_5$	FTO	Net-like structure	P	~1	295	-	-	106	1 M KOH	XRD, SEM, EDX, TEM, XPS, N_2 ISO (BET), XAS	TEM, EDX, XPS, XAS	16 h CA (1.52 V_{RHE})	$Ni(OH)_2$, NiOOH, $(NiHPO_4)_2 \cdot 3H_2O$	Precatalyst (partial oxidation)	494
Ni_2P	FTO	Net-like structure	P	~1	330	-	-	112				16 h CA (1.56 V_{RHE})	$Ni(OH)_2$, NiOOH, $(NiHPO_4)_2 \cdot 3H_2O$	Precatalyst (partial oxidation)	
$Ni_{12}P_5$	Ni foam	Net-like structure	P	~3	240	-	-	-			-	-	-	-	
Ni_2P	Ni foam	Net-like structure	P	~3	260	-	-	-			-	-	-	-	
Ni_2P@NC	GC	Nanoparticle	P	1	320	16.5	-	50	1 M KOH	XRD, SEM, EDX, TEM, XPS, ISO (BET), Raman	XRD, TEM, XPS	10 h CA (1.56 V_{RHE}) 1000 CV cycles (100 $mV \cdot s^{-1}$, 1.07–1.87 V_{RHE})	NiOOH, Oxidized P species	Precatalyst (partial oxidation)	495
Ni_2P	GC	Aggregated particle	P	1	~420	-	-	178		XRD, SEM	-	-	-	-	
Co_2P@NC	GC	Nanoparticle	P	1	383	0.89	-	99		XRD, TEM, XPS, ISO (BET), Raman	-	-	-	-	
CoP@NC	GC	Nanoparticle	P	1	348	0.94	-	64		XRD, TEM, XPS, ISO (BET), Raman	-	-	-	-	
Fe_2P@NC	GC	Nanoparticle	P	1	415	0.74	-	117		XRD, TEM, XPS, ISO (BET), Raman	-	-	-	-	
FeP@NC	GC	Nanoparticle	P	1	409	9.65	-	104		XRD, TEM, XPS, ISO (BET), Raman	-	-	-	-	
$Ni_{12}P_5$@NC	GC	Nanoparticle	P	1	330	1.36	-	55		XRD, TEM, XPS, ISO (BET), Raman	-	-	-	-	

https://doi.org/10.1021/acs.chemrev.3c00005
Chem. Rev. 2023, 123, 12795−13208

Table 4. continued

Initial Electrocatalyst	Substrate	Shape of Electrocatalyst	Deposition Type	Specific Loading / $mg \cdot cm^{-2}_{geo}$	η@10 $mA \cdot cm^{-2}_{geo}$ / mV	C_{dl} / $mF \cdot cm^{-2}_{geo}$	TOF / s^{-1} (@η or j)	Tafel Slope / $mV \cdot dec^{-1}$	Electrolyte	Pre-analysis	Post-analysis	Long-Term OER Test Conditions	Post-OER Electrocatalyst	Final Type of Electrocatalyst	Ref.
$Ni_{12}P_5$	CP	Nanoparticle	P	1	296 (@20 $mA \cdot cm^{-2}_{geo}$)	-	0.025 at 300 mV	126	1 M KOH	XRD, HAADF-SEM, TEM, EDX, XPS, N_2 ISO (BET)	XPS	40 h CP (10 $mA \cdot cm^{-2}_{geo}$)	NiOOH	Precatalyst (partial oxidation)	496
$(Ni_{0.51}Fe_{0.49})_{12}P_5$	CP	Nanoparticle	P	1	216 (@20 $mA \cdot cm^{-2}_{geo}$)	-	0.076 at 300 mV	39		XRD, TEM, XPS, N_2 ISO (BET), ICP-OES	XPS		*M*OOH (*M* = Ni, Fe), FeO, $Ni(PO_4)_4$, $FePO_4$	Precatalyst (partial oxidation)	
$(Ni_{0.49}Fe_{0.51})_{12}P_5$	CP	Nanoparticle	P	1	~ 238 (@20 $mA \cdot cm^{-2}_{geo}$)	-	0.052 at 300 mV	57		XRD, HAADF-SEM, EDX, TEM, STEM, STEM-EDX, XPS, N_2 ISO (BET), ICP-OES	TEM, XPS		*M*OOH (*M* = Ni, Fe), FeO, $Ni(PO_4)_4$, $FePO_4$	Precatalyst (partial oxidation)	
$(Ni_{0.46}Fe_{0.54})_{12}P_5$	CP	Nanoparticle	P	1	~ 258 (@20 $mA \cdot cm^{-2}_{geo}$)	-	0.042 at 300 mV	50		XRD, TEM, XPS, N_2 ISO (BET), ICP-OES	XPS		*M*OOH (*M* = Ni, Fe), FeO, $Ni(PO_4)_4$, $FePO_4$	Precatalyst (partial oxidation)	
Fe_2P	CP	Nanoparticle	P	1	~ 324 (@20 $mA \cdot cm^{-2}_{geo}$)	-	0.018 at 300 mV	66		XRD, HAADF-SEM, EDX, TEM, XPS, N_2 ISO (BET)	XPS		FeOOH, FeO	Precatalyst (partial oxidation)	
$Ni_{1.85}Fe_{0.15}P$ NSAs/NF	Ni foam	Nanosheet	S	5	270 (@20 $mA \cdot cm^{-2}_{geo}$)	8.48	-	96	1 M KOH	XRD, SEM, EDX, TEM, XPS, ICP-MS	XRD, SEM, XPS	10 h CA (1.568 V_{RHE})	$Ni(OH)_2 \cdot 0.75$ H_2O, NiOOH, Oxidized P species	Precatalyst (partial oxidation)	497
$Ni_{1.79}Fe_{0.21}P$ NSAs/NF	Ni foam	Nanosheet	S	5	278 (@20 $mA \cdot cm^{-2}_{geo}$)	6.04	-	-		XRD, SEM, ICP-MS	-	-	-	-	
$Ni_{1.92}Fe_{0.08}P$ NSAs/NF	Ni foam	Nanosheet	S	5	278 (@20 $mA \cdot cm^{-2}_{geo}$)	5.77	-	-		XRD, SEM, ICP-MS	-	-	-	-	
Ni_2P NSAs/NF	Ni foam	Nanosheet	S	5	323 (@20 $mA \cdot cm^{-2}_{geo}$)	4.01	-	110		XRD, SEM, ICP-MS	-	-	-	-	
$Ni_{2-x}Ru_xP$ (x = 0.00)	GC	Nanosphere	P	~ 0.284	440	-	-	-	1 M KOH	XRD, TEM, ICP-MS	-	-	-	-	498
$Ni_{2-x}Ru_xP$ (x = 0.25)	GC	Nanosphere	P	~ 0.284	410	-	-	-		XRD, TEM, ICP-MS	-	-	-	-	
$Ni_{2-x}Ru_xP$ (x = 0.50)	GC	Nanosphere	P	~ 0.284	370	-	-	-		XRD, TEM, ICP-MS	-	-	-	-	
$Ni_{2-x}Ru_xP$ (x = 0.75)	GC	Nanosphere	P	~ 0.284	340	-	-	-		XRD, STEM, EDX, TEM, XPS, ICP-MS	XPS, TEM, EDX, ICP-MS	20 h CA (1.57 V_{RHE}) 300 CV cycles	$Ni(OH)_2$, NiOOH, RuO_2, RuOH, Oxidized P species	Precatalyst (partial oxidation)	
$Ni_{2-x}Ru_xP$ (x = 1.00)	GC	Nanosphere	P	~ 0.284	365	-	-	-		XRD, TEM, ICP-MS	-	-	-	-	
$Ni_{2-x}Ru_xP$ (x = 2.00)	GC	Worm-like structure	P	~ 0.284	560	-	-	-		XRD, TEM, ICP-MS	-	-	-	-	
$Co_{0.63}Fe_{0.21}P_{0.16}$	CP	Nanosphere	P	0.2	217	-	-	40	1 M KOH	XRD, SEM, EDX, TEM, XPS, ICP-MS	XPS	16 h CP (10, 50 $mA \cdot cm^{-2}_{geo}$)	Co oxide, Co phosphate, Fe phosphate	Precatalyst (partial oxidation)	499
$Co_{0.84}P_{0.16}$	CP	-	P	0.2	~ 240	-	-	77		XRD	-	-	-	-	
$Fe_{0.84}P_{0.16}$	CP	-	P	0.2	> 470	-	-	113		XRD	-	-	-	-	
$Co_{0.42}Fe_{0.42}P_{0.16}$	CP	-	P	0.2	200	-	-	52		-	-	-	-	-	
NiCuP	SS foil	Honeycomb with dendritic structure	S	6.70	292	9.9	-	49	1 M KOH	XRD, SEM, EDX, XPS, ICP-AES, N_2 ISO (BET, PSD)	SEM, XPS	120 h CP (50 $mA \cdot cm^{-2}_{geo}$) 5000 s CP (50−500 $mA \cdot cm^{-2}_{geo}$)	$Ni(OH)_2$, NiOOH, $Cu(OH)_2$, PO_4^{3-}	Precatalyst (partial oxidation)	500
FeNi-P/NF-A (activated sample)	Ni foam	Nanoparticle-stack array	S	2.86 ± 0.42	186 (@100 $mA \cdot cm^{-2}_{geo}$)	1.95	31.86 at 230 mV	57	1 M KOH	HAADF-STEM, XPS, UV-Vis	SEM	12 h CP (100 $mA \cdot cm^{-2}_{geo}$) 2000 CV cycles (100 $mV \cdot s^{-1}$)	Fe-Ni hydroxide	Precatalyst (partial oxidation)	501
Ni-P/NF-A (activated sample)	Ni foam	-	S	3.74 ± 0.42	~ 290 (@100 $mA \cdot cm^{-2}_{geo}$)	0.8	-	136		-	-	-	-	-	
FeNi-P/NF-A (activated sample)	Ni foam	Nanoparticle-stack array	S	2.86 ± 0.42	429	5.1	-	136	0.1 M KPi (pH = 7)	HAADF-STEM, XPS, UV-Vis	-	23 h CP (10 $mA \cdot cm^{-2}_{geo}$) 10 h CP (10 $mA \cdot cm^{-2}_{geo}$, 1.1 $mg \cdot cm^{-2}$)	-	-	
FeNi-P/NF	Ni foam	Nanoparticle-stack array	S	-	590	3.8	-	167		XRD, SEM, HAADF-STEM, EDX, XPS	-	-	-	-	
Co_2P@Co/N-C-5	GC	Porous nanostructure	P	~ 0.2	320	10.2	-	48.8	1 M KOH	XRD, HAADF-STEM, EDX, TEM, XPS	XRD, TEM, XPS	60000 s CA (~ 1.55 V_{RHE})	CoO_x, Oxidized Co phosphate	Precatalyst (partial oxidation)	502
Co_2P@Co/N-C-10	GC	Porous nanostructure	P	~ 0.2	340	-	-	48.8		XRD, TEM	-	-	-	-	
Co_2P@Co/N-C-20	GC	Porous nanostructure	P	~ 0.2	350	-	-	50.6		XRD, TEM	-	-	-	-	
FeMnP/GNF (GNF: graphene-protected NF)	Ni foam	Nanoplatelet	S	2.4	230	71	0.28 at 280 mV	35	0.1 M KOH	SEM, EDX, TEM, XPS, WDS	-	75 h CA (1.6 V_{RHE}) 1000 CV cycles (100 $mV \cdot s^{-1}$)	-	Precatalyst (partial oxidation)	503
FeMnP/NF	Ni foam	Nanoplatelet	S	2.6	280	57	-	56		XRD, SEM, EDX, TEM, XPS, WDS	XRD, WDS, XPS	75 h CA (1.6 V_{RHE}) over 20 h CA (1.53 V_{RHE}) 1000 CV cycles (100 $mV \cdot s^{-1}$)	MO_x (*M* = Fe, Mn), Oxidized P species	Precatalyst (partial oxidation)	
SiO_2-coated N-C/Ni_5P_4/Fe_3P	Graphite electrode	Hollow nanocube	P	0.5	374	0.078	-	50.6	1 M KOH	XRD, SEM, EDX, TEM, Raman, N_2 ISO (BET, PSD)	-	-	-	-	504
N-C/Ni_5P_4/Fe_3P	Graphite electrode	Hollow nanocube	P	0.5	252	0.25	-	24		XRD, SEM, TEM, EDX, XPS, N_2 ISO (BET, PSD)	SEM, EDX, XPS	24 h CP (10, 250 $mA \cdot cm^{-2}_{geo}$) 24 h CA (~ 1.482, ~ 1.615 V_{RHE})	Ni-Fe hydro(oxy)oxide	Precatalyst (partial oxidation)	
N-C/Ni_5P_4/Fe_3P	Graphite electrode	Nanoparticle	P	0.5	300	0.11	-	57.2		XRD, SEM, TEM, EDX, Raman, N_2 ISO (BET, PSD)	-	-	-	-	

https://doi.org/10.1021/acs.chemrev.3c00005
Chem. Rev. 2023, 123, 12795−13208

Table 4. continued

Initial Electrocatalyst	Substrate	Shape of Electrocatalyst	Deposition Type	Specific Loading / $mg \cdot cm^{-2}_{geo}$	η@10 $mA \cdot cm^{-2}_{geo}$ / mV	C_{dl} / $mF \cdot cm^{-2}_{geo}$	TOF / s^{-1} (@η or j)	Tafel Slope / $mV \cdot dec^{-1}$	Electrolyte	Pre-analysis	Post-analysis	Long-Term OER Test Conditions	Post-OER Electrocatalyst	Final Type of Electrocatalyst	Ref.
$(Fe_{0.5}Ni_{0.5})_2P$/NF	Ni foam	Nanosheet	S	3.34 ± 0.37	156 ± 6.5 ~ 241 (@300 $mA \cdot cm^{-2}_{geo}$)	4.2	-	66	1 M KOH	XRD, SEM, HAADF-STEM, EDX, XPS, ICP-MS	SEM, EDX, HAADF-STEM, XPS	24 h CP (50 $mA \cdot cm^{-2}_{geo}$)	Fe-Ni hydroxide, Fe-Ni phosphate	Precatalyst (partial oxidation)	505
$(Fe_{0.3}Ni_{0.7})_2P$/NF	Ni foam	Nanosheet	S	3.86 ± 0.43	~ 263 (@300 $mA \cdot cm^{-2}_{geo}$)	3.6	-	120		XRD, SEM, XPS, ICP-MS	-	-	-	-	
$(Fe_{0.1}Ni_{0.9})_2P$/NF	Ni foam	Nanosheet	S	4.49 ± 0.5	~ 296 (@300 $mA \cdot cm^{-2}_{geo}$)	1.8	-	185		XRD, SEM, XPS, ICP-MS	-	-	-	-	
Ni_2P/NF	Ni foam	-	S	-	~ 505 (@300 $mA \cdot cm^{-2}_{geo}$)	1.7	-	227		XRD, SEM, XPS, ICP-MS	-	-	-	-	
$(Fe_{0.5}Ni_{0.5})_2P$/NF	Ni foam	Nanosheet	S	3.34 ± 0.37	396 ± 8 ~ 419 (@80 $mA \cdot cm^{-2}_{geo}$)	-	-	182	0.1 M KPi (pH = 7)	XRD, SEM, HAADF-STEM, EDX, XPS, ICP-MS	XPS	1000 CV cycles (100 $mV \cdot s^{-1}$)	Fe-Ni hydroxide, Fe-Ni phosphate	Precatalyst (partial oxidation)	
$(Fe_{0.3}Ni_{0.7})_2P$/NF	Ni foam	Nanosheet	S	3.86 ± 0.43	~ 490 (@80 $mA \cdot cm^{-2}_{geo}$)	-	-	220		XRD, SEM, XPS, ICP-MS	-	-	-	-	
$(Fe_{0.1}Ni_{0.9})_2P$/NF	Ni foam	Nanosheet	S	4.49 ± 0.5	~ 525 (@80 $mA \cdot cm^{-2}_{geo}$)	-	-	375		XRD, SEM, XPS, ICP-MS	-	-	-	-	
Ni_2P/NF	Ni foam	-	S	-	~ 570 (@80 $mA \cdot cm^{-2}_{geo}$)	-	-	512		XRD, SEM, XPS, ICP-MS	-	-	-	-	
FeP@CNT	GC	Nanorod	P	~ 0.204	300	-	-	53	1 M KOH	XRD, SEM, EDX, TEM, XPS, N_2 ISO (BET)	XPS	14 h CP (10 $mA \cdot cm^{-2}_{geo}$)	Fe-O species, P-O species	Precatalyst (partial oxidation)	506
CoP NS/C	GC	Nanosheet	P	0.71	277	-	-	85.6	1 M KOH	-	-	-	-	-	507
CoP NS	GC	Nanosheet	P	0.71	361	-	-	69.5		XRD, SEM, EDX, TEM, STEM, XPS, ICP-OES, XPS, N_2 ISO (BET, PSD), AFM	XRD, SEM, EDX, TEM, XPS, EDX (after OWS)	24 h CP (10 $mA \cdot cm^{-2}_{geo}$) 1000 CV cycles (100 $mV \cdot s^{-1}$, 1.25–1.75 V_{RHE}) 24 h CP (10 $mA \cdot cm^{-2}_{geo}$, OWS) 24 h CP (300 $mA \cdot cm^{-2}_{geo}$, OWS)	Co_3O_4, orthophosphate	Precatalyst (partial oxidation)	
CoP power	Ni foam	Nanowire	P	6	~ 401 (@100 $mA \cdot cm^{-2}_{geo}$)	-	-	192.6	1 M KOH	XRD, SEM, EDX, TEM, HAADF-STEM	-	-	-	-	508
Ni@Co-Ni-P	Ni foam	Nanowire	S	6	~ 368 (@100 $mA \cdot cm^{-2}_{geo}$)	-	-	65.3		XRD, SEM, EDX, TEM, HAADF-STEM, XPS	XRD, SEM, EDX, HAADF-STEM, TEM (after OER and OWS)	100 h CP (10 $mA \cdot cm^{-2}_{geo}$) 1000 CV cycles (50 $mV \cdot s^{-1}$, 1.06–1.56 V_{RHE}) ~ 24 h multistep CP (10–240 $mA \cdot cm^{-2}_{geo}$, OWS) 3000 h CP (100 $mA \cdot cm^{-2}_{geo}$, OWS)	$(Co_xNi_y)(OH)_2$	Precatalyst (partial oxidation)	
Co_2P/C	GC	Nanoneedle	P	0.2	310	3.71	-	50	1 M KOH	XRD, TEM, EDX, HAADF-STEM	XRD, TEM, EDX, HAADF-STEM, XPS, ICP-OES	10 h CP (10 $mA \cdot cm^{-2}_{geo}$)	CoO_x, PO_4^{3-}	Precatalyst (partial oxidation)	509
					~ 310	-	-	53	Fe-purified KOH		-	-	-	-	
Co_3Ni_1P	GC	Mesoporous nanostructure	P	~ 0.1	280	15	-	66.5	1 M KOH	XRD, TEM, XPS	TEM, XPS	12 h CA (1.51 V_{RHE})	Co-Ni oxide/hydroxide, Oxidized P species	Precatalyst	510
Co_1Ni_1P	GC	Mesoporous nanostructure	P	~ 0.1	290	-	-	77.5		XRD, TEM, XPS	-	-	-	-	
Co_1Ni_3P	GC	Mesoporous nanostructure	P	~ 0.1	300	-	-	8.3		XRD, TEM, XPS	-	-	-	-	
CoP	GC	Mesoporous nanostructure	P	~ 0.1	300	24	-	59.6		XRD, TEM, XPS	XPS	12 h CA (1.53 V_{RHE})	Co oxide/hydroxide, Oxidized P species	Precatalyst	
NiP	GC	Mesoporous nanostructure	P	~ 0.1	330	0.3	-	92.8		XRD, TEM, XPS	XPS	12 h CA (1.56 V_{RHE})	Ni oxide/hydroxide, Oxidized P species	Precatalyst	
Ni_xP_y-325	CFP	Porous network of nanoparticle	P	~ 0.15	320	-	-	72.2	1 M KOH	XRD, TEM, XPS	XRD, XPS	18 h CA (1.66 V_{RHE})	NiOOH, Oxidized P species	Precatalyst (partial oxidation)	511
Bulk Co-P film	Co foil	Bulk	S	0.17	370	-	-	-	1 M KOH	XRD, SEM, EDX, XPS	-	-	-	-	512
CoP NWs	GC	Nanowire	P	0.17	320	-	-	64		XRD, SEM, EDX, TEM, XPS, XRF	-	-	-	-	
Co_2P NWs	GC	Nanowire	P	0.17	260	-	-	52		XRD, SEM, EDX, TEM, XPS, XRF	XRD, TEM, *In-Situ* XPS	-	Co oxo/hydroxide (CoO_x), PO_4^{3-}	Precatalyst (partial oxidation)	
Co/Co_2P@GCE	GC	Aggregated particle	P	0.21	390	-	0.11 at 420 mV	59.8	1 M KOH	XRD, SEM, EDX, STEM, TEM, XPS	STEM, TEM, EDX, XPS	50 CV cycles (100 $mV \cdot s^{-1}$, 1.0–1.65 V_{RHE}) 300 s/30 h CP (10 $mA \cdot cm^{-2}_{geo}$)	CoO_x, phosphate, Pyrophosphate	Precatalyst (partial oxidation)	107
Co/Co_2P@Ni	GC	Aggregated particle	P	0.21	360	-	-	-		XRD, SEM, EDX, STEM, TEM, XPS	-	-	-	-	
Co/Co_2P@NF	Ni foam	Aggregated particles	P	0.18–0.25	190 (@50 $mA \cdot cm^{-2}_{geo}$)	-	-	-		XRD, SEM, EDX, STEM, TEM, XPS	-	-	-	-	
C-$(Co_{0.54}Fe_{0.46})_2P$	GC	Sea-urchin nanostructure	P	0.2	370	-	-	-	0.1 M KOH	TEM, ICP-AES	ICP-AES, STEM-EELS	1000 CV cycles (50 $mV \cdot s^{-1}$, 1.4–1.8 V_{RHE})	Co–Fe–O species	Precatalyst (partial oxidation)	513
C-Fe_2P	GC	Nanowire	P	0.2	560	-	-	-		-	-	-	-	-	
C-Co_2P	GC	Hollow nanostructure	P	0.2	430	-	-	-		-	-	-	-	-	
NiFeP	NiFe foil	Porous coating with microplatelets	S	-	277	-	-	-	1 M KOH	XRD, SEM	SEM, EDX	15 h CP (10 $mA \cdot cm^{-2}_{geo}$)	*M*OOH (*M* = Ni, Fe)	Precatalyst (partial oxidation)	514
Co_2P	Co foil	Porous coating	S	-	367	-	-	-		XRD, SEM, TEM	-	-	-	-	
Ni_2P	Ni foil	Porous coating	S	-	339	-	-	-		XRD, SEM, EDX	-	-	-	-	
Fe_2P	Fe foil	Porous coating	S	-	390	-	-	-		XRD, SEM	-	-	-	-	

https://doi.org/10.1021/acs.chemrev.3c00005
Chem. Rev. 2023, 123, 12795−13208

Table 4. continued

Initial Electrocatalyst	Substrate	Shape of Electrocatalyst	Deposition Type	Specific Loading / $mg \cdot cm^{-2}_{geo}$	η@10 $mA \cdot cm^{-2}_{geo}$ / mV	C_{dl} / $mF \cdot cm^{-2}_{geo}$	TOF / s^{-1} (@η or j)	Tafel Slope / $mV \cdot dec^{-1}$	Electrolyte	Pre-analysis	Post-analysis	Long-Term OER Test Conditions	Post-OER Electrocatalyst	Final Type of Electrocatalyst	Ref.
CoP (after preconditioning)	CC	Nanoneedle	S	3.30	281	-	-	62	1 M KOH	XRD, SEM, TEM, HAADF, EDX	TEM, HAADF, EDX	12 h CA (1.53 V_{RHE}, precond.) 72 h CP (10 $mA \cdot cm^{-2}_{geo}$, OWS)	Co_3O_4, $Co(OH)_2$	Precatalyst (partial oxidation)	515
CoP (after preconditioning)	CC	Nanoneedle	P	0.284	322	-	-	62		XRD, SEM, TEM, HAADF, EDX	-	45 CV cycles (10 $mV \cdot s^{-1}$, 0.4–0.6 $V_{Ag/AgCl}$, precond.) 17 h CP (10 $mA \cdot cm^{-2}_{geo}$)	-	-	
CoP (after preconditioning)	CC	Nanoneedle	S	1.65	~305	-	-	-		XRD, SEM, TEM, HAADF, EDX	-	12 h CA (1.53 V_{RHE}, precond.)	-	-	
CoP (after preconditioning)	CC	Nanoneedle	S	4.95	271	-	-	-		XRD, SEM, TEM, HAADF, EDX	-	12 h CA (1.53 V_{RHE}, precond.)	-	-	
CoP after 72 h's electrolysis	CC	Nanoneedle	S	3.30	293	-	-	62		XRD, SEM, TEM, HAADF, EDX	-	-	-	-	
CP@Ni-P	CFP	Nanosheet	S	25.8	190 230 (@20 $mA \cdot cm^{-2}_{geo}$)	-	-	73	1 M KOH	XRD, SEM, EDX, TEM, XPS, HAADF-STEM	XRD, SEM, TEM, EDX, XPS, HAADF-STEM	180 h CP (10 $mA \cdot cm^{-2}_{geo}$) 700 CV cycles (50 $mV \cdot s^{-1}$, 1.1–1.5 V_{RHE})	$Ni(OH)_x$	Precatalyst (partial oxidation)	516
Cu_3P/Cu	Cu mesh	Nanobush	S	-	380 390 (@20 $mA \cdot cm^{-2}_{geo}$)	-	-	-	1 M KOH	XRD, SEM, EDX, TEM, XPS	SEM, TEM, EDX, XPS	10 h CA (1.65 V_{RHE}) 1000 CV cycles (100 $mV \cdot s^{-1}$, 1.2–1.8 V_{RHE})	Cu-O species	Precatalyst (partial oxidation)	517
Porous Ni-P foam	Ni foam	Nanosheet array	S	-	350 (@191 $mA \cdot cm^{-2}_{geo}$)	-	-	179.9	1 M KOH	XRD, SEM, EDX, TEM, HAADF-STEM	XRD, SEM, EDX, TEM, HADDF-STEM	26 h CP (10 $mA \cdot cm^{-2}_{geo}$) 700 CV cycles (50 $mV \cdot s^{-1}$, 1.0–1.5 V_{RHE})	NiO_x, $Ni(OH)_2$	Precatalyst (partial oxidation)	518
CP@FeP	CFP	Nanorod	P	0.7	350	-	-	63.6	1 M KOH	XRD, SEM, EDX, TEM, XPS, HAADF-STEM	SEM, EDX, TEM, HAADF-STEM	48 h CP (15 $mA \cdot cm^{-2}_{geo}$) 1000 CV cycles (50 $mV \cdot s^{-1}$, 1.0–1.6 V_{RHE}, pre-activation)	FeO_x	Precatalyst (partial oxidation)	519
Ni-P	GC	Porous nanoplate	P	0.2	300	-	-	64	1 M KOH	XRD, SEM, EDX, TEM, XPS, N_2 ISO (BET)	TEM, EDX, XPS	1000 LSV scans (20 $mV \cdot s^{-1}$) 10 h CA (1.53 V_{RHE})	Ni oxide/hydroxide, Oxidized P species	Precatalyst (partial oxidation)	520
Ni_8P_3	Ni foam	Nanosheet array	S	1.7	283	4.0	-	78	1 M KOH	XRD, SEM, STEM, TEM, XPS, Raman	XPS	1 h CA (1.5 V_{RHE}) 90000 s CP (10 $mA \cdot cm^{-2}_{geo}$, OWS) 90000 s CA (cell voltage: 1.65 V, OWS)	Ni oxide/hydroxide, Oxidized P species	Precatalyst (partial oxidation)	402
C@Ni_8P_3	Ni foam	Nanosheet array	S	1.9	267	6.9	-	51		XRD, SEM, EDX, TEM, STEM, XPS, Raman	SEM (after OWS), STEM, TEM, EDX, XPS	90000 s CP (20 $mA \cdot cm^{-2}_{geo}$) 1000 CV cycles (50 $mV \cdot s^{-1}$) 1 h CA (1.5 V_{RHE}) 90000 s CP (10 $mA \cdot cm^{-2}_{geo}$, OWS) 90000 s CA (cell voltage: 1.65 V, OWS)	Ni oxide/hydroxide, Oxidized P species	Precatalyst (partial oxidation)	
C@Ni_8P_3-2	Ni foam	Nanosheet array	S	2.3	~ 330 (@50 $mA \cdot cm^{-2}_{geo}$)	-	-	64		SEM	-	-	-	-	
NiP	Ni foam	Spherical particle congeries with smooth surface	S	-	362	1.2	-	112	1 M KOH	XRD, SEM, XPS	-	-	-	-	521
$Ni_{0.71}Co_{0.29}P$	Ni foam	Spherical particle congeries with nanosheet cover	S	-	341	21.3	-	89		XRD, SEM, EDX, XPS	-	-	-	-	
$Ni_{0.62}Co_{0.38}P$	Ni foam		S	-	285	37.8	-	72		XRD, SEM, EDX, XPS	-	-	-	-	
$Ni_{0.51}Co_{0.49}P$	Ni foam		S	-	239	70.7	-	45		XRD, SEM, EDX, STEM, TEM, HAADF-STEM, XPS	SEM, TEM, STEM, EDX	100 h CP (10 $mA \cdot cm^{-2}_{geo}$) 1000 CV cycles 1 h CA (1.5 V_{RHE})	Ni/Co oxide/hydroxides	Precatalyst (partial oxidation)	
$Ni_{0.23}Co_{0.77}P$	Ni foam		S	-	265	56.4	-	63		XRD, SEM, EDX, XPS	-	-	-	-	
CoP	Ni foam		S	-	329	31.5	-	77		XRD, SEM, XPS	-	-	-	-	
CF@NiP_x	CF	Fibrous surface with nanoflake	S	-	200	6.1	-	54.7	1 M KOH	XRD, SEM, EDX, TEM, XPS, Raman	SEM, XPS, Raman	12 h CP (30 $mA \cdot cm^{-2}_{geo}$) 5000 s CP (50–500 $mA \cdot cm^{-2}_{geo}$)	NiO_x, NiOOH	Precatalyst	522
CoP@RGO/GC	GC	Nanoparticle	P	~ 0.28	280	7.18	0.015 at 350 mV 0.12 at 500 mV	75	1 M KOH	XRD, SEM, EDX, TEM, XPS, XAFS, XANES, EXAFS	XPS, ICP-MS	5000 CV cycles (20 $mV \ s^{-1}$) 240 min CA (1.60 V_{RHE})	CoOOH	Precatalyst (partial oxidation)	523
CoP/GC (Inorg. P source)	GC	Aggregated particle	P	~ 0.28	400	3.93	0.005 at 350 mV 0.055 at 500 mV	110		SEM, XAFS, XANES, EXAFS	ICP-MS	-	-	-	
Ni_2P nanowires	GC	Nanowire	P	0.14	330	-	-	47	1 M KOH	XRD, TEM	-	-	-	-	103
Ni_2P nanoparticles	GC	Nanoparticle	P	0.14	290	176.9	-	59		XRD, TEM, EDX, XPS, HAADF-STEM	TEM, EDX, XPS	10 h CP (10 $mA \cdot cm^{-2}_{geo}$) 210 min CP (14 $mA \cdot cm^{-2}_{geo}$) 1 h CA (1.5 V_{RHE})	NiO_x, P species	Precatalyst (partial oxidation)	
CoP NR/C	GC	Nanorod	P	0.71	320	-	-	71	1 M KOH	-	-	12 h CP (10 $mA \cdot cm^{-2}_{geo}$) 3000 CV cycles (100 $mV \cdot s^{-1}$, 1.4–1.8 V_{RHE})	CoO_x, PO_x/P–O species	Precatalyst (partial oxidation)	524
CoP NP/C	GC	Nanoparticle	P	0.71	340	-	-	99		-	-		CoO_x, PO_x/P–O species	Precatalyst (partial oxidation)	
CoP NR	GC	Nanorod	P	0.71	490	-	-	84		XRD, SEM, STEM, EDX, TEM, XPS, ICP-OES, N_2 ISO (BET, PSD)	-	-	CoO_x, PO_x/P–O species	Precatalyst (partial oxidation)	
CoP NP	GC	Nanoparticle	P	0.71	520	-	-	96			-	-	CoO_x, PO_x/P–O species	Precatalyst (partial oxidation)	
Ni_5P_4	Ni foil	Disk-like microstructure	S	-	290	-	-	40	1 M KOH	XRD, SEM, EDX, TEM, XPS, FTIR, Raman, ICP-OES	XRD, SEM, EDX, XPS, ICP-OES, FTIR, Raman	20 h CP (10 $mA \cdot cm^{-2}_{geo}$) 500 CV cycles (40 $mV \cdot s^{-1}$, −0.43–1.75 V_{RHE})	NiOOH	Precatalyst (partial oxidation)	525
Iron phosphide nanotubes (IPNTs)	CC	Hollow tube nanostructure	S	1.6	288	-	-	43	1 M KOH	XRD, SEM, EDX, TEM, XPS	XPS	14 h CP (10 $mA \cdot cm^{-2}_{geo}$)	Fe_2O_3, $FePO_4$	Precatalyst	526
CoP-MNA	Ni foam	Nanorod	S	6.2	290	-	-	65	1 M KOH	XRD, SEM, EDX, TEM, XPS, N_2 ISO (BET, PSD)	TEM, XPS	32 h CA (1.52 V_{RHE}) 30 min CP (10 $mA \cdot cm^{-2}_{geo}$)	Co oxo/hydroxyl species, PO_4^{3-}	Precatalyst (partial oxidation)	297

https://doi.org/10.1021/acs.chemrev.3c00005
Chem. Rev. 2023, 123, 12795−13208

Table 4. continued

Initial Electrocatalyst	Substrate	Shape of Electrocatalyst	Deposition Type	Specific Loading / $mg \cdot cm^{-2}_{geo}$	η@10 $mA \cdot cm^{-2}_{geo}$ / mV	C_{dl} / $mF \cdot cm^{-2}_{geo}$	TOF / s^{-1} (@η or j)	Tafel Slope / $mV \cdot dec^{-1}$	Electrolyte	Pre-analysis	Post-analysis	Long-Term OER Test Conditions	Post-OER Electrocatalyst	Final Type of Electrocatalyst	Ref.
Ni_2P nanowires	FTO	Nanowire	P	~0.1	~400 (after 500 CV cycles)	-	-	60	1 M KOH	XRD, TEM, EDX, XPS	SEM, XPS	500 CV cycles (50 $mV \cdot s^{-1}$, activation) 5 h CA (1.60 V_{RHE}) 10 h CA (1.59 V_{RHE})	NiO_x, PO_4^{3-}	Precatalyst (partial oxidation)	527
Ni_2P nanoparticles	FTO	Nanoparticle	P	~0.1	~500 (after 500 CV cycles)	-	-	70		XRD, TEM, EDX, XPS	SEM	500 CV cycles (50 $mV \cdot s^{-1}$, activation) 5 h CA (1.60 V_{RHE})	-	-	
Ni_2P	Ni foam	Lamellar-like structure	S	-	474 (@50 $mA \cdot cm^{-2}_{geo}$)	-	-	164	3 M KOH	XRD, SEM	-	-	-	-	528
CoNiP-0.10M	Ni foam	-	S	-	457 (@50 $mA \cdot cm^{-2}_{geo}$)	-	-	-		-	-	-	-	-	
CoNiP-0.15M	Ni foam	Nanosheets (Lamellar layered structure)	S	-	400 (@50 $mA \cdot cm^{-2}_{geo}$)	-	-	122		SEM, TEM, EDX, XPS	-	48 h CP (100 $mA \cdot cm^{-2}_{geo}$) 48 h CP (100 $mA \cdot cm^{-2}_{geo}$ at 80 °C)	-	-	
CoNiP-0.2M	Ni foam	-	S	-	420 (@50 $mA \cdot cm^{-2}_{geo}$)	-	-	-		-	-	-	-	-	
Fe-Ni_2P	Ni foam	-	S	-	270	4	-	147	1 M KOH	-	-	-	-	-	529
Co-P	GC	-	S	-	380	-	-	-	1 M KOH	-	-	-	-	-	530
Co-Mo-P (1) Mo/Co 0.1:0.2	GC	-	S	-	378	-	-	-		-	-	-	-	-	
Co-Mo-P (2) Mo/Co 0.2:0.2	GC	-	S	-	357	-	-	-		-	-	-	-	-	
Co-Mo-P (3) Mo/Co 0.3:0.2	GC	-	S	0.17	348	1.9	0.017 at 340 mV	58		-	-	-	-	-	
Co-Mo-P (4) Mo/Co 0.4:0.2	GC	-	S	-	367	-	-	-		-	-	-	-	-	
CoP@FeNiP/NF	Ni foam	Hierarchical nanospheres/nanosheets	S	-	265 (@50 $mA \cdot cm^{-2}_{geo}$)	16.5	-	31.8	1 M KOH	SEM, EDX, TEM, XRD, XPS	SEM, XRD	110 h CP (10 $mA \cdot cm^{-2}_{geo}$) 2000 CV cycles	-	-	531
FeNiP/NF	Ni foam	Hierarchical nanospheres/nanosheets	S	-	283 (@50 $mA \cdot cm^{-2}_{geo}$)	15.5	-	38.3		SEM, XRD	-	-	-	-	
CoP	CP	Nanoparticle	P	2	360	-	~0.0014 at 350 mV	~50	1 M NaOH	XRD, SEM, XPS, TEM, EDX, HAADF-STEM	-	~14 h CP (10 $mA \cdot cm^{-2}_{geo}$)	-	-	532
CoP	GC	Nanoarray	P	1.428	290	5.38	~15 at 300 mV	121	1 M KOH	SEM, N_2 ISO (BET)	-	-	-	-	246
NiCoPO/NC nanosheets	GC	Nanosheets	P	0.2	300	0.56	-	94	1 M KOH	XRD, ICP, SEM, TEM, HAADF-STEM, EDX, AFM, N_2 ISO (BET, PSD), XPS	TEM	10 h CP (10 $mA \cdot cm^{-2}_{geo}$)	-	-	533
NiCoPO/NC nanocages	GC	Nanocages	P	0.2	400	0.27	-	176		XRD, SEM, N_2 ISO (BET, PSD), XPS	-	10 h CP (10 $mA \cdot cm^{-2}_{geo}$)	-	-	
Ni1Co1-P	GC	Agglomerated nanoparticles	P	~0.35	343	4.2	0.00069 at 300 mV	77	1 M KOH	XRD, SEM, TEM, SAED, EDX, ICP-AES, N_2 ISO (BET, PSD), XPS	SEM	30 h CP (10 $mA \cdot cm^{-2}_{geo}$) 30 h CP (50 $mA \cdot cm^{-2}_{geo}$) 2000 CV cycles	-	-	534
Ni-P + Co-P	GC	-	P	~0.35	~390	1.9	0.00047 at 300 mV	102		-	-	-	-	-	
Ni-P	GC	Agglomerated nanoparticles	P	~0.35	415	1.6	0.00039 at 300 mV	110		SEM, XRD, N_2 ISO (BET, PSD)	-	-	-	-	
Co-P	GC	Agglomerated nanoparticles	P	~0.35	431	1.7	0.00035 at 300 mV	113		SEM, XRD, N_2 ISO (BET, PSD)	-	-	-	-	
CoNiP-1:1	GC	Nanowires	P	0.3	301	4.65	0.022 at 350 mV	54	1 M KOH	ICP-OES, TEM, SEM, EDX, HAADF-STEM, XRD, XPS, N_2 ISO (BET)	-	24 h CP (10 $mA \cdot cm^{-2}_{geo}$)	-	-	535
CoNiP-2:1	GC	Nanowires	P	0.3	-	3.92	-	~60		ICP-OES, SEM, XRD, N_2 ISO (BET)	-	24 h CP (10 $mA \cdot cm^{-2}_{geo}$)	-	-	
CoNiP-10:1	GC	Nanowires	P	0.3	-	3.52	-	~65		ICP-OES, SEM, XRD, N_2 ISO (BET)	-	17 h CP (10 $mA \cdot cm^{-2}_{geo}$)	-	-	
CoP	GC	Nanowires	P	0.3	-	0.82	-	~68		ICP-OES, SEM, XRD, N_2 ISO (BET)	-	20 h CP (10 $mA \cdot cm^{-2}_{geo}$)	-	-	
Ni_5P_4	GC	Nanosheets	P	0.3	373	0.79	-	~78		ICP-OES, SEM, XRD, N_2 ISO (BET)	-	24 h CP (10 $mA \cdot cm^{-2}_{geo}$)	-	-	
Ni-P	Ni foam	Nanosphere	S	-	294 (@20 $mA \cdot cm^{-2}_{geo}$) 386 (@100 $mA \cdot cm^{-2}_{geo}$)	17.4	-	88	1 M KOH	XRD, SEM, TEM, EDX	-	-	-	-	536
NiCoP	CC	Nanoparticle	S	-	275	4.6	-	87	1 M KOH	XRD, SEM, TEM, EDX, XPS, Raman, ICP-AES	-	80 h CA (1.56 V_{RHE})	-	-	537
NiP-1	Ni foam	Nanoparticle	P	-	~310	-	-	-	3 M KOH	XRD, SEM, TEM, EDX	-	1000 CV cycles (100 $mV \cdot s^{-1}$)	-	-	538
NiP-2	Ni foam	Nanoparticle	P	-	300	-	-	-			-		-	-	
CoP/CNTs	CFP	Nanoparticle	P	0.8	305	27.15	-	103	1 M KOH	XRD, SEM, EDX, TEM, XPS, Raman	-	-	-	-	539
Ni_2P	Ni foam	Nanosheet	S	-	370 (@20 $mA \cdot cm^{-2}_{geo}$)	8.7	-	245	1 M KOH	XRD, SEM, EDX, TEM, XPS, N_2 ISO (BET, PSD)	-	-	-	-	540
Ni_2Mn_1P	Ni foam	Nanosheet	S	-	~310 340 (@20 $mA \cdot cm^{-2}_{geo}$)	27	-	220			-	-	-	-	

https://doi.org/10.1021/acs.chemrev.3c00005
Chem. Rev. 2023, 123, 12795−13208

Table 4. continued

Initial Electrocatalyst	Substrate	Shape of Electrocatalyst	Deposition Type	Specific Loading / $mg \cdot cm^{-2}_{geo}$	η@10 $mA \cdot cm^{-2}_{geo}$ / mV	C_{dl} / $mF \cdot cm^{-2}_{geo}$	TOF / s^{-1} (@η or j)	Tafel Slope / $mV \cdot dec^{-1}$	Electrolyte	Pre-analysis	Post-analysis	Long-Term OER Test Conditions	Post-OER Electrocatalyst	Final Type of Electrocatalyst	Ref.
Ni_3Mn_1P	Ni foam	Nanosheet	S	-	~280 330 (@20 $mA \cdot cm^{-2}_{geo}$)	22.8	-	190			-	-	-	-	540
Ni_1Mn_1P	Ni foam	Nanosheet	S	-	250 (@20 $mA \cdot cm^{-2}_{geo}$)	19.9	-	119			-	20 h CA (1.48 V_{RHE})	-	-	
$NC_{0.9}Fe_{0.1}P$ HHAs	Ni foam	Nanosheet with Nanowire	S	-	269	-	-	72.01	1 M KOH	XRD, SEM, EDX, TEM, XPS, N_2 ISO (BET)	SEM	24 h CA (1.5 V_{RHE})	-	-	541
NCP HHAs	Ni foam	-	S	-	326	-	-	104.52		XRD	-	-	-	-	
Co_2P	GC	2D flake	P	0.25	335	38.1	-	71	1 M KOH	XRD, SEM, EDX, TEM, XPS, AFM	-	-	-	-	542
$Ni_{12}P_5$	GC	2D flake	P	0.25	375	-	-	76			-	-	-	-	
Fe_2P	GC	2D flake	P	0.25	~510	-	-	-			-	-	-	-	
$Co_{1.5}Fe_{0.5}P$	GC	2D flake	P	0.25	278	76.8	-	57			-	10 h CP (10 $mA \cdot cm^{-2}_{geo}$) 5000 CV cycles (50 $mV \cdot s^{-1}$)	-	-	
Co_xP/NC	GC	Nanoparticle	P	0.5	400	-	-	80	0.1 M KOH	XRD, SEM, TEM, EDX, XPS	-	-	-	-	183
Co_xP	GC	Nanoparticle	P	0.5	440	-	-	80			-	-	-	-	
Co-P	GC	Nanoflake	P	0.3	340	0.071	0.0231 at 500 mV	48	1 M NaOH	XRD, SEM, TEM, XPS, ICP-OES, N_2 ISO (BET, PSD)	-	-	-	-	182
$MnCo_2O_4$@NiP_2	Ni foam	(Collapsed) Nanosheet	S	-	390	33.83	-	141.79	1 M KOH	XRD, SEM, XPS	-	-	-	-	543
CoP@NG	GC	Sheet-like, stacked structure	P	-	354	26.62	-	63.8	1 M KOH	XRD, SEM, EDX, TEM, XPS, Raman	XRD, SEM	15 h CA (1.60 V_{RHE}) 1000 CV cycles	-	-	544
CoP@NG-0.5	GC	Sheet-like, stacked structure	P	-	~370	19.2	-	66.36			-	-	-	-	
CoP@NG-1.5	GC	Sheet-like, stacked structure	P	-	~380	18.9	-	74.28			-	-	-	-	
CoP@NG-2.0	GC	Sheet-like, stacked structure	P	-	~385	14.1	-	76.95			-	-	-	-	
Bare CoP	GC	Sheet-like, stacked structure	P	-	395	13.43	-	67.56			-	-	-	-	
Co-P/NF (2 min)	Ni foam	Hairball-like structure / aggregated nanoflake	S	-	314	-	-	76.7	1 M KOH	XRD, SEM, EDX, TEM, XPS	-	-	-	-	545
Co-P/NF (6 min)	Ni foam		S	-	313	-	-	70.9			-	-	-	-	
Co-P/NF (10 min)	Ni foam		S	-	306	126.1	-	51.1			XRD, SEM, XPS	25 h CA (1.9 V_{RHE})	-	-	
Co-P/NF (14 min)	Ni foam		S	-	330	-	-	61.7			-	-	-	-	
HfP-rGO NS	GC	Nanosheet	P	-	730	-	-	479	0.1 M KOH	XRD, SEM, EDX, TEM, XPS, Raman	-	10000 s CA	-	-	546
NiP/NF	Ni foam	Nanosheet	S	-	330 (@50 $mA \cdot cm^{-2}_{geo}$)	27	-	109	1 M KOH	XRD, SEM, TEM, XPS	-	1000 CV cycles	-	-	547
Cu-P	Ni foam	Bumpy morphology	S	-	370	6.6	-	111	1 M KOH	XRD, SEM, EDX, XPS	-	-	-	-	548
CuP-300	Ni foam	Smooth surface with some void	S	-	310	9.4	-	88			SEM	20 h CP (10 $mA \cdot cm^{-2}_{geo}$)	-	-	
CP	GC	Nanoparticle	P	0.42	370	0.00023	-	96	1 M KOH	XRD, SEM, EDX, TEM, XPS	-	5 h CA (1.63 V_{RHE})	-	-	549
NP	GC	Nanoparticle	P	0.42	380	0.0003	-	106.7			-		-	-	
FP	GC	Aggregated nanoparticle	P	0.42	550	0.0002	-	196.2			-		-	-	
Co_2P/EWC	GC	Honeycomb with embedded nanoparticle	P	0.51	380	-	-	-	0.1 M KOH	XRD, SEM, EDX, TEM, XPS, Raman, N_2 ISO (BET, PSD)	-	-	-	-	550
Fe_2P/EWC	GC		P	0.51	430	-	-	-			-	-	-	-	
CoFeP/EWC	GC		P	0.51	300	-	-	-			-	-	-	-	
CNT-NC-CoP	GC	Nanoparticle	P	-	251	39.2	-	82.1	1 M KOH	XRD, SEM, EDX, TEM, XPS, N_2 ISO (BET, PSD)	-	10 h CP (10 $mA \cdot cm^{-2}_{geo}$)	-	-	551
CNT-CoP	GC	Nanoparticle	P	-	279	6.5	-	118.2			-	-	-	-	
NC-CoP	GC	Nanoparticle	P	-	366	1	-	130.2			-	-	-	-	
CNT+NC-CoP	GC	Nanoparticle	P	-	336	18.8	-	116.8			-	-	-	-	
CoP_2@3D-NPC-1.2	GC	Nanoparticle	P	0.255	~360	4	-	75	1 M KOH	XRD, SEM, EDX, TEM, XPS	-	-	-	-	552
CoP_2@3D-NPC-1.5	GC	Nanoparticle	P	0.255	~340	5	-	67			-	8 h CA (~1.57 V_{RHE})	-	-	
CoP_2@3D-NPC-1.8	GC	Nanoparticle	P	0.255	~390	3.5	-	76			-	-	-	-	
CoP_2	GC	Bulk	P	0.255	~420	0.16	-	90			-	-	-	-	
Ni/Co-P-1/2	GC	Nanoparticle	P	0.157	369	9.4	-	79	1 M KOH	XRD, SEM, EDX, TEM, XPS, N_2 ISO (BET, PSD)	-	-	-	-	553
Ni/Co-P-1/1	GC	Nanoparticle	P	0.157	360	13	-	60			-	30000 s CA	-	-	
Ni/Co-P-2/1	GC	Nanoparticle	P	0.157	388	8.06	-	109			-	-	-	-	
Ni/Co-P-1/0	GC	Nanoparticle	P	0.157	423	9.59	-	113			-	-	-	-	
CoP NPs@NF	Ni foam	Nanoparticle	S	~1.2	320	2.78	0.19 at 350 mV	102	1 M KOH	XRD, SEM	-	20 h CA (1.58 V_{RHE})	-	-	554
Ni_5P_4/NiP_2 foam	Ni foam	Vertically aligned microsheet	S	-	~330 (@100 $mA \cdot cm^{-2}_{geo}$)	30.8	-	169.5	1 M KOH	XRD, SEM, XPS	-	-	-	-	555
Ni_5P_4/NiP_2/NiFe LDH	Ni foam	Microsheet with nanosheet	S	2.4	197 243 (@100 $mA \cdot cm^{-2}_{geo}$)	63.6	-	46.6		XRD, SEM, EDX, TEM, XPS	SEM, TEM	72 h CP [10 (24 h), 100 (24 h), 200 $mA \cdot cm^{-2}_{geo}$ (24 h)]	-	-	

https://doi.org/10.1021/acs.chemrev.3c00005
Chem. Rev. 2023, 123, 12795−13208

Table 4. continued

Initial Electrocatalyst	Substrate	Shape of Electrocatalyst	Deposition Type	Specific Loading / $mg \cdot cm^{-2}_{geo}$	η@10 $mA \cdot cm^{-2}_{geo}$ / mV	C_{dl} / $mF \cdot cm^{-2}_{geo}$	TOF / s^{-1} (@η or j)	Tafel Slope / $mV \cdot dec^{-1}$	Electrolyte	Pre-analysis	Post-analysis	Long-Term OER Test Conditions	Post-OER Electrocatalyst	Final Type of Electrocatalyst	Ref.
CoP	CFP	Nanosheet	S	2.68	339	9.8	-	77.7	Fe-purified 1 M KOH	XRD, SEM, TEM, EDX, XPS, Raman	-	25 h CA (1.60 V_{RHE})	-	-	556
$Ni_{0.5}Co_{0.5}P$/CP	CP	Nanowire	S	-	240	-	-	58.3	1 M KOH	XRD, SEM, EDX, TEM, XPS, ICP-OES	SEM (after OWS)	24 h CA (1.53 V_{RHE}) 28 h CA (cell voltage: 1.65 V, OWS)	-	-	557
CoP/CP	CP	Nanowire	S	-	320	-	-	82.8			-	-	-	-	
NiP/CP	CP	Rough, porous nanoplate	S	-	270	-	-	75.4			-	-	-	-	
Ni-P (2h)	Ni foam	Nanorod	S	2.37–2.74	270 ($@30\ mA \cdot cm^{-2}_{geo}$)	16.2	-	122	1 M KOH	XRD, SEM, EDX, TEM, XPS	SEM	24 h CA (1.5 V_{RHE}) 3000 CV cycles (10 $mV \cdot s^{-1}$)	-	-	558
$Ni_2P/Ni_{12}P_5$	CC	Sponge-like structure with nanoparticle	P	-	278	-	-	112	1 M KOH	XRD, SEM, EDX, TEM, XPS	SEM	25 h CA (1.56 V_{RHE})	-	-	559
$Ni_{12}P_5$	CC	Aggregated particle	P	-	311	-	-	116			-	-	-	-	
Ni_2P	CC	Sponge-like structure with nanoparticle	P	-	336	-	-	119			-	-	-	-	
BP/Co_2P	GC	Nanosheet	P	0.14	390	-	-	78	1 M KOH	XRD, SEM, EDX, TEM, XPS, AFM, UV-Vis, Raman	-	-	-	-	560
FeNi-P/GA	GC	Porous network	P	0.31	280	-	-	43	1 M KOH	XRD, SEM, TEM	-	8 h CA (1.51 V_{RHE}) 1000 CV cycles (100 $mV \cdot s^{-1}$)	-	-	561
CoP@NPC/CP	CP	Nanofibers with nanoparticle	S	1.2	300	93.1	-	-	1 M KOH	XRD, SEM, EDX, TEM, XPS, N_2 ISO (BET, PSD), Raman	-	10 h CP (10 $mA \cdot cm^{-2}_{geo}$)	-	-	562
Ni/Ni_2P	GC	Nanosheet	P	0.28	316	3.62	-	120	1 M KOH	XRD, SEM, XPS	-	10 h CA (1.53 V_{RHE}) 1000 CV cycles (100 $mV \cdot s^{-1}$)	-	-	563
$Ni/(Ni_{0.87}Fe_{0.13})_2P$	GC	Nanosheet	P	0.28	257	7.9	-	96		XRD, SEM, EDX, TEM, HAADF-STEM, XPS	-		-	-	
Ni_2P	Ni foam	-	S	3.5	340	6.51	-	112.7	1 M KOH	XRD, XANES, EXAFS	-	-	-	-	564
P-NiFe	GC	Nanocube	P	-	~ 420	0.201	-	169	1 M KOH	XRD, SEM, EDX, XPS	-	-	-	-	565
S-P-NiFe	GC	Nanocube	P	-	~ 400	0.217	-	68			-	-	-	-	
CoFe-P	GC	Accumulated nanostructure	P	-	240	5.765	-	122	0.1 M KOH	XRD, SEM, TEM, XPS	-	-	-	-	566
CoP (0 % Fe)	ITO glass	Microsphere	P	0.4	390	-	-	-	1 M KOH	XRD, SEM, EDX, TEM, XPS, HAADF-STEM, N_2 ISO (BET, PSD)	-	-	-	-	567
CoP (10 % Fe)	ITO glass	Microsphere	P	0.4	~ 410	-	-	-			-	10 h CP (10 $mA \cdot cm^{-2}_{geo}$)	-	-	
CoP (20 % Fe)	ITO glass	Microsphere	P	0.4	~ 325	-	-	-			-		-	-	
CoP (30 % Fe)	ITO glass	Microsphere	P	0.4	302	-	-	-			SEM (after OWS)	10 h CP (10 $mA \cdot cm^{-2}_{geo}$) 1000 CV cycles (50 $mV \cdot s^{-1}$) 10 h OWS test	-	-	
CoP (40 % Fe)	ITO glass	Microsphere	P	0.4	~ 310	-	-	-			-	10 h CP (10 $mA \cdot cm^{-2}_{geo}$)	-	-	
CoP (50 % Fe)	ITO glass	Microsphere	P	0.4	~ 320	-	-	-			-		-	-	
CoP (100 % Fe)	ITO glass	Microsphere	P	0.4	~ 520	-	-	-			-		-	-	
CoP-NS/C	GC	Nanosheet	P	0.14	292	-	-	64	1 M KOH	XRD, SEM, EDX, TEM, XPS, AFM, N_2 ISO (BET, PSD)	-	24 h CA (1.522 V_{RHE}) 3000 CV cycles (100 $mV \cdot s^{-1}$)	-	-	568
CoP	GC	Nanosheet	P	0.14	408	-	-	97			-	-	-	-	
CoP/C	GC	Nanosheet	P	0.14	382	-	-	78			-	-	-	-	
CoP/CoP_2@NPCNTs	CP	Nanoparticle	P	0.2	300	1.749	-	50	1 M KOH	XRD, SEM, EDX, TEM, XPS, Raman, CAM	-	100 h CA (1.56 V_{RHE})	-	-	569
CoP/CoP_2	CP	Nanoparticle	P	0.2	330	0.978	-	67			-	-	-	-	
Co_2P@NPC-1	GC	Nanoparticle/Nanorod	P	0.71	327	-	-	118	1 M KOH	XRD, SEM, TEM, XPS, N_2 ISO (BET, PSD)	-	500 CV cycles (100 $mV \cdot s^{-1}$)	-	-	570
Co_2P@NPC-2	GC	Nanoparticle/Nanorod	P	0.71	337	-	-	135			-	-	-	-	
$Co_{0.7}Fe_{0.3}P$@C	GC	Nanorod	P	-	300	130	-	52	1 M KOH	XRD, SEM, EDX, TEM, XPS, ICP-AES, TGA, Raman, FTIR	-	3000 CV cycles (100 $mV \cdot s^{-1}$)	-	-	571
$Co_{0.7}Fe_{0.3}P$	GC	Nanorod	P	-	320	-	-	~ 55			-	-	-	-	
CoP	GC	Urchin-like microsphere	P	0.4013	~ 450	-	-	-	0.1 M KOH	XRD, SEM, XPS	-	-	-	-	572
pre-CoP (CoP trace)	GC	Urchin-like microsphere	P	0.4013	~ 530	-	-	-			-	-	-	-	
CoP/CDs (28.79 wt.%)	GC	Nanorod	P	1.41	400	-	-	93	1 M KOH	XRD, SEM, EDX, TEM, XPS, HAADF-STEM, FTIR, UV-Vis, Raman	TEM, EDX, XPS	10 h CA (in 0.1 M KOH)	-	-	573
CoP	GC	-	P	1.41	~ 440	-	-	195			-	-	-	-	
CoNi(20:1)-P-NS@GCE	GC	Nanosheet	P	0.153	273	-	-	45	1 M KOH	XRD, SEM, EDX, TEM, XPS, AFM, ICP-AES, N_2 ISO (BET, PSD)	-	11 h CA (1.51 V_{RHE}) 3000 CV cycles (50 $mV \cdot s^{-1}$)	-	-	574
CoZn(20:1)-P-NS@GCE	GC	Sheet-like structure	P	0.153	276	-	-	-			-	-	-	-	
CoCu(20:1)-P-NS@GCE	GC	Sheet-like structure	P	0.153	281	-	-	-			-	-	-	-	
CoMn(20:1)-P-NS@GCE	GC	Sheet-like structure	P	0.153	298	-	-	-			-	-	-	-	
CoP-NS@GCE	GC	Sheet-like structure	P	0.153	315	-	-	88			-	-	-	-	
CoNi(20:1)-P-NS@NF	Ni foam	Nanosheet	P	0.153	209	-	-	52			-	-	-	-	

https://doi.org/10.1021/acs.chemrev.3c00005
Chem. Rev. 2023, 123, 12795−13208

Table 4. continued

Initial Electrocatalyst	Substrate	Shape of Electrocatalyst	Deposition Type	Specific Loading / $mg \cdot cm^{-2}_{geo}$	η@10 $mA \cdot cm^{-2}_{geo}$ / mV	C_{dl} / $mF \cdot cm^{-2}_{geo}$	TOF / s^{-1} (@η or j)	Tafel Slope / $mV \cdot dec^{-1}$	Electrolyte	Pre-analysis	Post-analysis	Long-Term OER Test Conditions	Post-OER Electrocatalyst	Final Type of Electrocatalyst	Ref.
CoNi(20:1)-ZIF-P@GCE	GC	Irregularly-shaped nanoparticle	P	0.153	348	-	-	85			-	-	-	-	574
$Cu_{0.3}Co_{2.7}P$/NC	GC	Polyhedral structures with nanoparticle	P	0.41	190	~ 12	0.00582 at 190 mV	44	1 M KOH	XRD, SEM, EDX, TEM, XPS, N_2 ISO (BET), ICP-MS	-	1000 CV cycles	-	-	575
$Cu_{0.6}Co_{2.4}P$/NC	GC	Polyhedral structures with nanoparticle	P	0.41	~ 280	~ 7	0.00272 at 190 mV	50			-	-	-	-	
$Cu_{1.6}Co_{2.0}P$/NC	GC	Polyhedral structures with nanoparticle	P	0.41	~ 300	~ 4	0.00196 at 190 mV	65			-	-	-	-	
$Zn_{0.3}Co_{2.7}P$/NC	GC	-	P	0.41	330	-	-	-			-	-	-	-	
$Ni_{0.3}Co_{2.7}P$/NC	GC	-	P	0.41	280	-	-	-			-	-	-	-	
CoP/NC	GC	-	P	0.41	~ 290	~ 8	0.00287 at 190 mV	57			-	-	-	-	
Au/$Ni_{12}P_5$ core-shell NPs	GC	Nanoparticle	P	0.13	340	11	-	49	1 M KOH	XRD, SEM, EDX, TEM, XPS	-	10000 s CA (1.57 V_{RHE})	-	-	576
Au/$Ni_{12}P_5$ oligomer-like NPs	GC	Nanoparticle	P	0.13	360	1.1	-	42			-	-	-	-	
$Ni_{12}P_5$ core-shell NPs	GC	Nanoparticle	P	0.13	380	0.97	-	43			-	-	-	-	
$(Ni_{0.62}Fe_{0.38})_2P$	GC	Hollow nanocube	P	0.3	290	-	-	44	1 M KOH	XRD, SEM, EDX, TEM, XPS, N_2 ISO (BET, PSD), ICP-OES, Raman	-	10 h CA (1.53 V_{RHE})	-	-	577
$(Ni_{0.72}Fe_{0.28})_2P$	GC	Hollow nanocube	P	0.3	340	-	-	-			-	-	-	-	
$(Ni_{0.35}Fe_{0.65})_2P$	GC	Hollow nanocube	P	0.3	350	-	-	-			-	-	-	-	
Fe-P	GC	Nanofiber	P	0.3	390	-	-	72			-	-	-	-	
Ni-P	GC	Nanofiber	P	0.3	460	-	-	112			-	-	-	-	
Co_2P/Co-foil	Co foil	Porous and rough surface	S	-	319	-	-	79	1 M KOH	XRD, SEM, EDX, TEM, XPS	XPS	12 h CA (1.55 V_{RHE}) 1000 CV cycles (5 $mV \cdot s^{-1}$)	-	-	578
Co_2P	GC	-	P	-	394	-	-	-				-	-	-	
FeP	GC	-	P	1.0	-	-	-	127	1 M KOH	XRD, SEM, TEM, XPS	-	-	-	-	579
CoP	GC	-	P	1.0	399	-	-	66			-	-	-	-	
$Co_{0.68}Fe_{0.32}P$	GC	Porous polyhedron / nanosheet	P	1.0	289	-	-	66			-	1 h CA (~ 1.519 V_{RHE})	-	-	
$Co_{0.44}Fe_{0.56}P$	GC	Porous polyhedron / nanosheet	P	1.0	408	-	-	92			-	-	-	-	
NiP	Cu woven gauze	Nanoparticle	S	-	~ 305	47.7	-	90	1 M KOH	XRD, SEM, EDX, TEM, XPS, Raman, FTIR, N_2 ISO (BET)	-	-	-	-	580
$Co_{0.2}Ni_{0.8}P$	Cu woven gauze	Nanosheet	S	-	~ 300	-	-	-			-	-	-	-	
$Co_{0.4}Ni_{0.6}P$	Cu woven gauze	Nanosheet	S	-	~ 295	-	-	-			-	-	-	-	
$Co_{0.6}Ni_{0.4}P$	Cu woven gauze	Nanosheet	S	-	~ 285	-	-	-			-	-	-	-	
$Co_{0.8}Ni_{0.2}P$	Cu woven gauze	Nanosheet	S	-	~ 280	143.8	-	60			-	-	-	-	
GDs/$Co_{0.8}Ni_{0.2}P$	Cu woven gauze	Nanosheet	S	-	~ 275 287 (@15 $mA \cdot cm^{-2}_{geo}$)	179.4	-	50			SEM, XPS	50 h CA (1.55 V_{RHE}) 5000 CV cycles (100 $mV \cdot s^{-1}$)	-	-	
CoP	Cu woven gauze	Nanosheet	S	-	~ 290	102.8	-	75			-	-	-	-	
NiCoP	GC	Nanobox	P	0.255	370	28.93	-	115	1 M KOH	XRD, SEM, EDX, TEM, XPS, Raman	-	10 h CA (1.58 V_{RHE})	-	-	581
NiCoP/C	GC	Nanobox	P	0.255	330	146	-	96			-		-	-	
NiP/NF	Ni foam	Nanosheet	S	2.7	300 (@20 $mA \cdot cm^{-2}_{geo}$)	20.3	-	78	1 M KOH	XRD, SEM, EDX, XPS	-	24 h CP (25 $mA \cdot cm^{-2}_{geo}$) 1000 CV cycles (5 $mV \cdot s^{-1}$)	-	-	582
BNiP/NF	Ni foam	Cracked surface	S	2.7	331 (@20 $mA \cdot cm^{-2}_{geo}$)	10.6	-	-			-	-	-	-	
Co/Co_2P (0 % Ni)	GC	Nanoparticle	P	0.21	410	-	-	105	1 M KOH	XRD	-	-	-	-	583
Co/Co_2P (5 % Ni)	GC	Nanoparticle	P	0.21	390	-	-	77			-	-	-	-	
Co/Co_2P (10 % Ni)	GC	Nanoparticle	P	0.21	388	-	-	76			-	-	-	-	
Co/Co_2P (50 % Ni)	GCE	Nanoparticle	P	0.21	385	-	-	60			-	-	-	-	
Co/Co_2P (90 % Ni)	GC	Nanoparticle	P	0.21	370	-	-	60			-	-	-	-	
NiP (100 % Ni)	GC	Nanoparticle	P	0.21	360	-	-	59			-	-	-	-	
$NiFeP_x$@NPS-C	GC	Nanoparticle/N anospindle	P	0.2	265	-	-	43	1 M KOH	XRD, SEM, EDX, TEM, XPS, N_2 ISO (BET, PSD)	TEM, EDX	20 h CP (10 $mA \cdot cm^{-2}_{geo}$)	-	-	584
FeP_x	GC	Nanospindle	P	0.2	410	-	-	~ 96			-	-	-	-	
$NiFeP_x$	GC	Nanospindle	P	0.2	370	-	-	~ 70			-	-	-	-	
$NiFeP_x$@NPS-C (2^{nd} etched)	GC	Nanoparticle (low content)	P	0.2	~ 390	-	-	-			-	-	-	-	
Ni_2P	GC	Nanoparticle	P	0.255	367	-	-	72	0.1 M KOH	XRD, SEM, EDX, TEM, XPS, FTIR, HAADF-STEM	-	-	-	-	585
CoP	GC	Nanoparticle	P	0.255	348	-	-	63			-	-	-	-	
Ni_2P+CoP	GC	(Aggregated) Nanoparticle	P	0.255	360	-	-	71			-	-	-	-	
Ni_2P-CoP	GC	Nanoparticle	P	0.255	320	-	-	69			-	-	-	-	

https://doi.org/10.1021/acs.chemrev.3c00005
Chem. Rev. 2023, 123, 12795−13208

Table 4. continued

Initial Electrocatalyst	Substrate	Shape of Electrocatalyst	Deposition Type	Specific Loading / $mg \cdot cm^{-2}_{geo}$	η@10 $mA \cdot cm^{-2}_{geo}$ / mV	C_{dl} / $mF \cdot cm^{-2}_{geo}$	TOF / s^{-1} (@η or j)	Tafel Slope / $mV \cdot dec^{-1}$	Electrolyte	Pre-analysis	Post-analysis	Long-Term OER Test Conditions	Post-OER Electrocatalyst	Final Type of Electrocatalyst	Ref.
Ni-doped CoP	GC	Nanoparticle	P	0.255	358	-	-	105			-	-	-	-	585
Co-Fe-P-1.7	GC	Nanowire @spindle-like structure	P	0.424	260	23	Co: 0.036 at 280 mV Fe: 0.057 at 280 mV	58	1 M KOH	XRD, SEM, EDX, TEM, XPS, ICP-MS	-	10 h CA (1.49 V_{RHE})	-	-	586
Co-Fe-P-1.7/NF	Ni foam	Nanowire @spindle-like structure	P	1.0	244	-	-	-			-	30 h CA (1.475 V_{RHE})	-	-	
Co-P	GC	-	P	0.424	~330	-	-	72			-	-	-	-	
Fe-P	GC	-	P	0.424	~280	-	-	53			-	-	-	-	
Co-Fe-P-0.67	GC	Nanowire @spindle-like structure	P	0.424	~350	-	-	57			-	-	-	-	
Co-Fe-P-1.1	GC	Nanowire @spindle-like structure	P	0.424	~310	-	-	56			-	-	-	-	
Co-Fe-P-1.3	GC	Nanowire @spindle-like structures	P	0.424	~270	-	-	61			-	-	-	-	
Co-Fe-P-2.0	GC	Nanowire @spindle-like structure	P	0.424	~270	-	-	61			-	-	-	-	
Co-P@NC-800	GC	Nanosheet decorated with nanoparticle	P	0.283	370	-	-	79	1 M KOH	XRD, SEM, EDX, TEM, XPS, N_2 ISO (BET, PSD), Raman	SEM	6000 s CP (10 $mA \cdot cm^{-2}_{geo}$)	-	-	587
Cu_3P-350°C	Ni foam	Microsheet	S	-	320	0.235	-	83	1 M KOH	XRD, SEM, EDX, TEM, XPS, CAM	-	-	-	-	588
Cu_3P-450°C	Ni foam	Microsheet	S	-	290	0.75	-	84			-	24 h CA (1.55 V_{RHE}) 1000 CV cycles (100 $mV \cdot s^{-1}$, 1.2–1.6 V_{RHE})	-	-	
Cu_3P-550°C	Ni foam	Microsheet	S	-	360	0.165	-	77			-	-	-	-	
CoP/G	GC	Nanoparticle	P	0.41	292	-	-	80	1 M KOH	XRD, SEM, EDX, TEM, XPS, Raman	-	10 h CA (1.55 V_{RHE})	-	-	589
CoP	GC	Nanoparticle	P	0.41	342	-	-	90			-	-	-	-	
Ni_2P	GC	Nanosheet	P	0.285	-	0.92	-	105	0.1 M KOH	XRD, SEM, TEM, XPS, TDR	-	-	-	-	590
O-incorporated Ni_2P	GC	Nanosheet	P	0.285	347	5.61	-	63			-	1000 CV cycles (50 $mV \cdot s^{-1}$)	-	-	
CoP particles	GC	Aggregated particle	P	0.102	427	-	-	59	1 M KOH	XRD, SEM, EDX, TEM, STEM, XPS, N_2 ISO (BET, PSD)	SEM	20 h CA (1.63 V_{RHE}) 3000 CV cycles (2 $mV \cdot s^{-1}$, 1.3–1.8 V_{RHE})	-	-	591
CoP hollow polyhedrons	GC	Hollow polyhedron	P	0.102	400	-	-	57					-	-	
CoP@GC	GC	Polyhedral structure with nanoparticle	P	0.25	345	-	-	56	1 M KOH	XRD, SEM, EDX, TEM, HAADF-STEM, XPS, N_2 ISO (BET, PSD)	-	10 h CA (1.575 V_{RHE}) 1000 CV cycles (100 $mV \cdot s^{-1}$)	-	-	592
CoP	GC	-	P	0.25	410	-	-	61			-	-	-	-	
Ni-P NA/NF	Ni foam	Nanowire array	S	31.5	357 (@20 $mA \cdot cm^{-2}_{geo}$)	86.4	-	76	1 M KOH	XRD, SEM, EDX, TEM, XPS	SEM	20 h CA (1.63 V_{RHE}) 4000 s CP (20–160 $mA \cdot cm^{-2}_{geo}$)	-	-	593
CoP/TM	Ti mesh	Nanowire	S	2.1	310	-	-	87	1 M KOH	XRD, SEM, EDX, TEM, XPS	-	20 h CA (1.56 V_{RHE}) 500 CV cycles (100 $mV \cdot s^{-1}$)	-	-	594
					270 (@14 $mA \cdot cm^{-2}_{geo}$)	-	-	85	30 wt.% KOH		-	24 h CA (1.5 V_{RHE})	-	-	
CoP_3 NAs/CFP	CFP	Porous nanoneedle array	S	1.09	334 407 (@50 $mA \cdot cm^{-2}_{geo}$)	93.4		62	1 M KOH	XRD, SEM, EDX, TEM, Raman, N_2 ISO (BET, PSD), XPS	XRD, SEM	5000 CV cycles 20 h CA (1.6 V_{RHE}) 90 min CA (1.564 V_{RHE})	-	-	595
CoP_3 NPs	CFP	Nanoparticle	P	1	452	44.6		81		XRD, SEM, Raman, N_2 ISO (BET)	-	5000 CV cycles 20 h CA (1.6 V_{RHE})	-	-	
C-$(Co_{0.54}Fe_{0.46})_2P$	GC	Nanourchin	P	0.2	280	-	-	-	2 M KOH	XRD, TEM, EDX, ICP-AES, VSM	-	-	-	-	596
					370	-	-	-	0.1 M KOH		-	-	-	-	
C-Fe_2P	GC	Nanowire	P	0.2	~560	-	-	-		XRD, TEM	-	-	-	-	
C-Co_2P	GC	Hollow nanostructure	P	0.2	~430	-	-	-		XRD, TEM	-	-	-	-	

[a]Some values (i.e., "specific loading", "η", and "C_{dl}") were calculated or obtained from the descriptions and figures in the previous papers. "Post-OER Electrocatalyst" and "Final Type of Electrocatalyst" were determined based on the experimental results and descriptions provided in the previous papers. [b]η, overpotential; j, current density; C_{dl}, double layer capacitance; TOF, turnover frequency; P, powder-coated electrode; S, self-supported electrode; CV, cyclic voltammetry; CA, chronoamperometry; CP, chronopotentiometry; OWS, overall water splitting. [c]Substrate abbreviations: GC (glassy carbon); CC (carbon cloth); CP (carbon paper); CFP (carbon fiber paper); CF (carbon fiber); SS (stainless steel); FTO (fluorine-doped tin oxide); ITO (indium tin oxide). [d]Electrolyte abbreviations: PBS (phosphate buffer solution); KPi (potassium phosphate). [e]Analysis abbreviations (minor terms only): ISO (isotherm); PSD (pore size distribution); UPS (ultraviolet photoelectron spectroscopy); MSM (magnetic susceptibility measurement); EPR (electron paramagnetic resonance measurement); WDS (wavelength-dispersive X-ray spectroscopy); H_2-TPR (hydrogen temperature-programmed reduction); CAM (contact angle measurement); TDR (temperature-dependent resistivity measurement); VSM (vibrating sample magnetometry); EFTEM (energy-filtered transmission electron microscopy); ZPA (zeta potential analysis); AAS (atomic absorption spectrometry).

https://doi.org/10.1021/acs.chemrev.3c00005
Chem. Rev. 2023, 123, 12795−13208

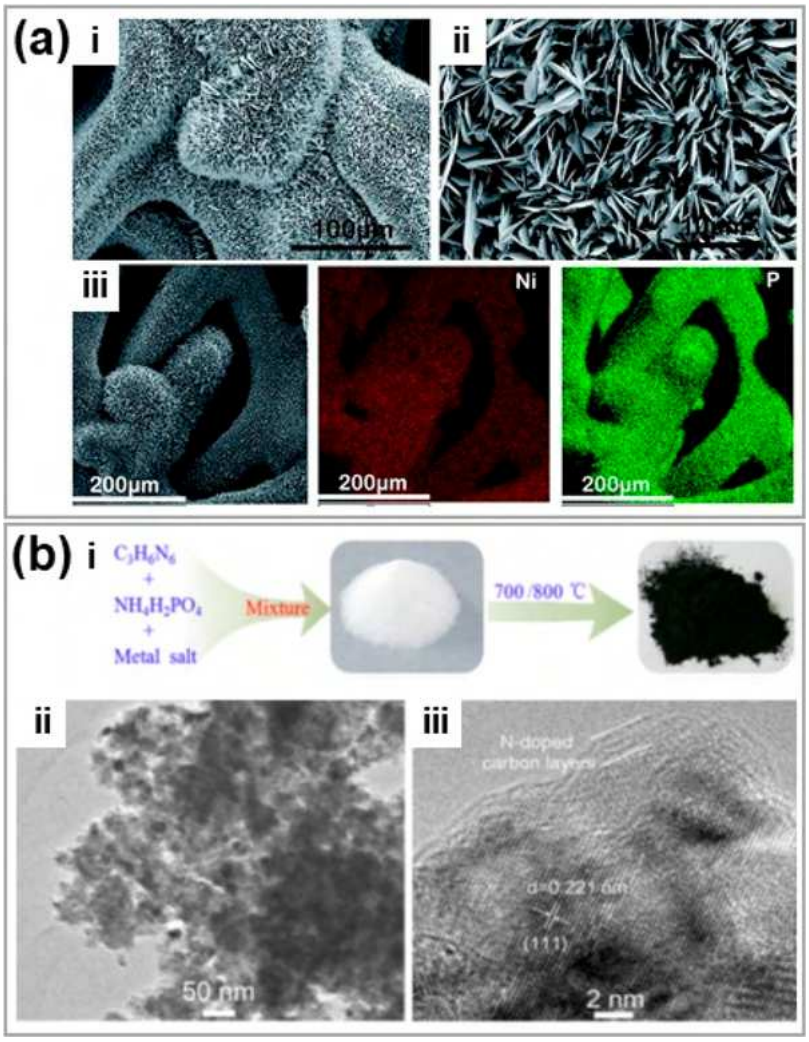


Figure 88. (a) Direct synthesis of self-supported porous Ni-P electrocatalysts on Ni foam: (i) low- and (ii) high-magnification SEM and (iii) SEM/EDX elemental mapping images of the as-prepared electrodes. Reprinted with permission from ref 518. Copyright 2016 Royal Society of Chemistry. One-step calcination methods to synthesize transition metal phosphides: (b) Synthesis of Fe-, Ni-, and Co-based phosphides encapsulated in NC. (i) Schematic illustration of the gas-solid thermal approach. (ii) TEM and (iii) HRTEM images of the Ni_2P@NC electrocatalyst. Reprinted with permission from ref 495. Copyright 2017 American Chemical Society.

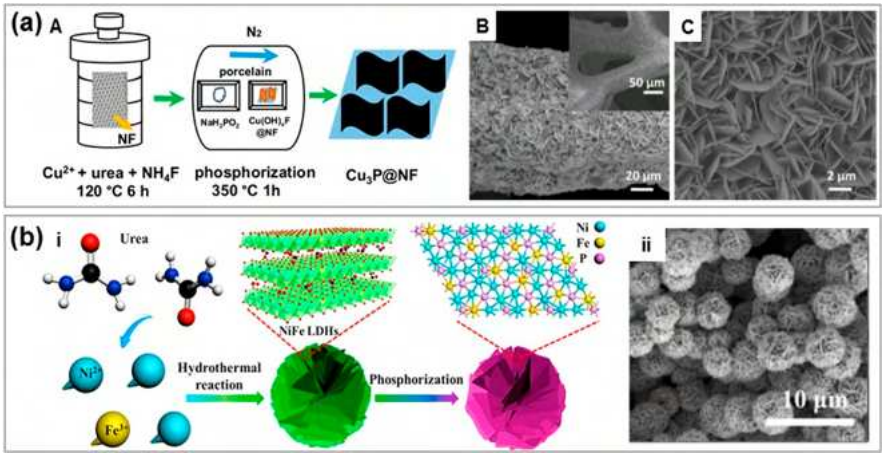


Figure 89. Two-step hydrothermal methods to synthesize transition metal phosphides. (a) Growth of Cu_3P phosphide nanosheets on Ni foam: (A) schematic illustration of the hydrothermal + phosphidation synthesis; (B−C) SEM images at different magnifications of the as-prepared Cu_3P@NF electrode. Reprinted with permission from ref 490. Copyright 2017 American Chemical Society. (b) Synthesis of Fe-tuned Ni_2P electrocatalysts: (i) schematic illustration of the hydrothermal + phosphidation approach; (ii) FESEM image of the $Ni_{1.5}Fe_{0.5}P$ electrocatalyst. Reprinted with permission from ref 491. Copyright 2017 Elsevier.

https://doi.org/10.1021/acs.chemrev.3c00005
Chem. Rev. 2023, 123, 12795−13208

al. synthesized Cu_3P nanosheets (NSs) directly onto Ni foam following an initial hydrothermal step and a subsequent phosphidation step (Figure 89a).[490] In the initial hydrothermal step, the Cu^{2+} salt, urea, and NH_4F were placed into a Teflon-lined autoclave along with a clean piece of Ni foam (NF), producing the $Cu(OH)_xF$@NF precursor. The subsequent gas-solid reaction step produced Cu_3P nanosheets that uniformly covered the Ni foam backbone (Figures 89a, B–C). Remarkably, a hydrothermal step was used instead of direct phosphidation of the metal because the copper oxide/hydroxide precursor required lower temperatures to produce the same phosphide. In a similar approach, Huang *et al.* employed a scalable method to synthesize $Ni_xFe_{2-x}P$ ($0 < x < 2$) phosphides, by producing NiFe layered double hydroxide (LDH) precursors in the initial hydrothermal step.[491] The hydrolysis of urea in the presence of Ni and Fe cations produced NiFe LDHs that were subsequently transformed into NiFe phosphides by the phosphidation step (Figure 89b, i). Notably, the initial hydrothermal step was optimized by tuning the Ni/Fe molar ratio, yielding bimetallic phosphides with different compositions. This strategy produced sphere-like microstructures composed of several nanosheets radially grown outward from their centers (Figure 89b, ii).

4.2.1.3. Solvothermal Methods. Instead of using water as the reaction medium, organic solvents in solvothermal methods enable the formation of solvent-reactant complexes that modify the reaction rate. Even some compounds can be used as P sources, including triphenylphosphine, tributylphosphine, and trioctylphosphine reagents.[23,399,604,605] Moreover, solvothermal methods can be used to selectively form specific precursors (e.g., layered double hydroxides) on substrates at moderate temperatures.[402,444] Yan *et al.* employed a solvothermal step before phosphidation to grow FeO(OH) nanospindles onto carbon nanotubes (CNTs).[506] As depicted in Figure 90a, ferric ions were first dissolved in a glycerol/water mixed solvent with CNTs to favor the selective nucleation of FeO(OH). The subsequent low-temperature phosphidation produced FeP nanorods on the CNT backbones (Figures 90b–d) and increased the material's porosity. Solvothermal steps have also been used to introduce heteroatoms to transition metal phosphides on different substrates. For example, Anjum *et al.* produced a cobalt-urea-phosphate precursor through an ion-assisted solvothermal step, and S-doped CoP NPs were subsequently generated by reducing the precursor under H_2 gas at 600 °C onto carbon cloth, N-doped graphene, and Ni foam substrates.[554] These examples demonstrate that precursors with superior features can be made through hydro-/solvothermal steps and that high-quality phosphides can be produced with subsequent gas-solid reactions. In the following, we discuss typical and unique synthetic methods. Herein, the reported synthetic approaches were arranged in terms of the shape-determining step. At the end of this Section, the importance of the phosphidation temperature is also discussed.

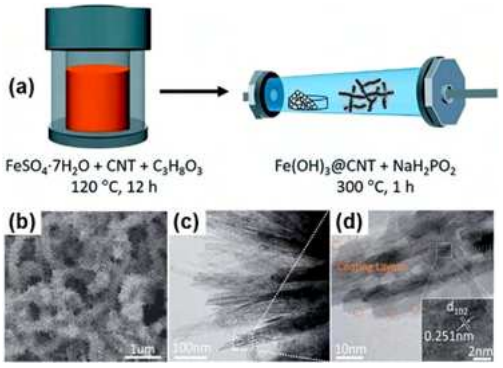


Figure 90. Solvothermal-based synthesis of hierarchical FeP@CNT OER electrocatalysts: (a) Schematic illustration of the solvothermal + phosphidation approach. (b) FESEM, (c) TEM, and (d) HRTEM images of the as-prepared electrodes. Reprinted with permission from ref 506. Copyright 2016 Royal Society of Chemistry.

4.2.1.4. Electrodeposition. Electrodeposition is a low-temperature and facile strategy that can be used to selectively grow transition metal phosphides on conductive substrates by reducing metal- and hypophosphite-based species in the deposition bath.[23,299] Notably, electrodeposition is a highly tunable method that can be used to control the composition and morphology of the materials finely.[49,537] However, although this method reduces the required temperature, electrodeposition of transition metal phosphides is usually accompanied by the presence of phosphates.[23,606] Zhu *et al.* synthesized CoP nanorods on NF via cathodic electrodeposition in the solution containing Co^{2+} and $H_2PO_2^-$ ions, as seen in Figure 91a.[297] Since CoP is conductive, initial deposits served as nucleation sites that allowed the growth of nanorods with numerous mesopores. According to SEM and EDX elemental mapping images, these vertically aligned CoP nanorods uniformly covered the Ni foam branches (Figures 91a, ii–v), demonstrating the effectiveness of the electrodeposition approach to roughen the surface and increase the surface area.

Furthermore, the electrodeposition approach has been used to generate transition metal phosphide films with different morphologies. Yu *et al.* synthesized amorphous NiCoP films with a triple-layered, hierarchical morphology on Ni foam.[521] As displayed in Figure 91b, three components were grown by increasing the deposition times: the innermost layer consisted of nanosheets, the second layer was covered by nanospheres, and the top layer contained spherical particles. Moreover, the spherical particles formed a uniform film at the top covered with vertically aligned nanosheets, increasing the surface area (Figure 91b, ii). Additionally, the activity of the films was controlled by varying the chemical composition of the ternary phosphides using different Ni/Co ratios in the electrolyte, and it is discussed in more depth in Section 4.2.3. These examples demonstrate that one-step electrodeposition methods can effectively deposit films with high surface area and tunable morphologies without requiring energy-intensive synthetic strategies or toxic gases.

In addition, electrodeposition steps have been used to grow high-quality precursors (such as LDHs) or create metallic deposits on various conductive substrates before performing conventional phosphidation steps. Ternary $(Ni_xFe_y)_2P$ nanoplates were grown on Ni foam by Li *et al.* using a co-electrodeposition followed by low-temperature phosphidation (Figure 92a).[445] The electrodeposited Ni_xFe_y-LDHs were converted into $(Ni_xFe_y)_2P$ nanoplates through the subsequent gas-solid phosphorylation with NaH_2PO_2. Moreover, the facile co-electrodeposition approach finely tuned the Ni/Fe ratio in the final transition metal phosphides.

Wei *et al.* deposited NiCu alloy precursors onto stainless-steel foils using H_2 bubble-templated electrodeposition, followed by the subsequent phosphidation of the as-electro-

https://doi.org/10.1021/acs.chemrev.3c00005
Chem. Rev. 2023, 123, 12795–13208

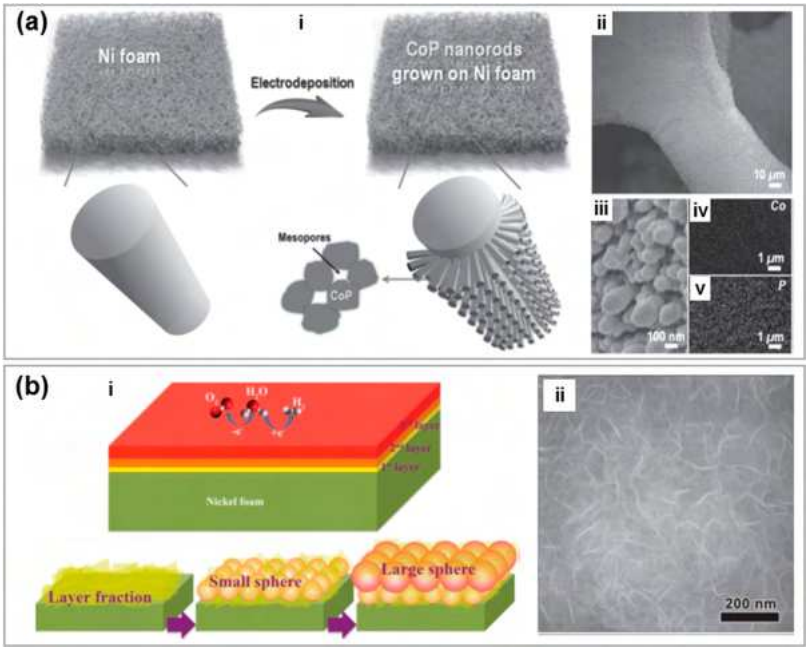


Figure 91. One-step electrodeposition methods to synthesize transition metal phosphides. (a) Electrodeposition of CoP mesoporous nanorod arrays on Ni foam: (i) schematic illustration of the fabrication of CoP electrocatalysts; (ii–iii) SEM images at low (ii) and high (iii) magnifications of the as-prepared electrodes; (iv–v) EDX elemental mapping. Reprinted with permission from ref 297. Copyright 2015 Wiley. (b) Electrodeposition of ternary NiCoP films on Ni foam: (i) schematic illustration of the formation of a NiCoP film with triple-layered structures; (ii) SEM image of the as-deposited amorphous $Ni_{0.51}Co_{0.49}P$ film. Reprinted with permission from ref 521. Copyright 2016 Wiley.

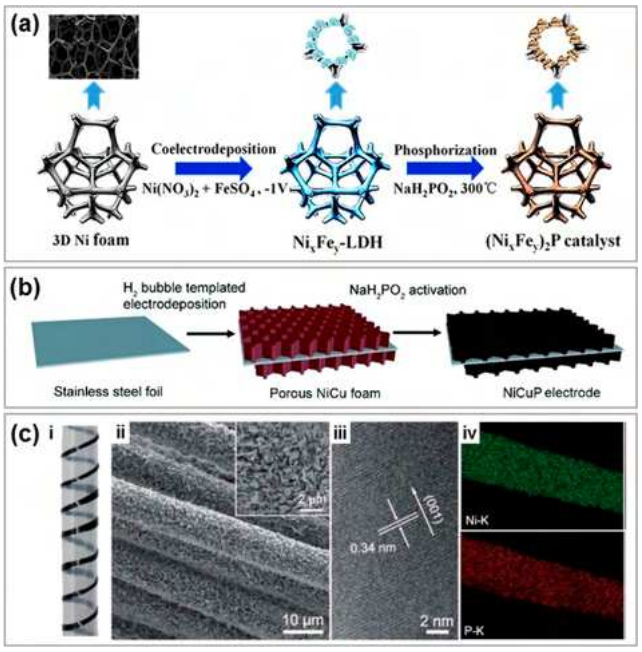


Figure 92. Electrodeposition + phosphidation methods to synthesize transition metal phosphides: (a) Schematic illustration for synthesizing $(Ni_xFe_y)_2P$ electrocatalysts on Ni foam. Reprinted with permission from ref 445. Copyright 2019 Elsevier. (b) Schematic illustration for the synthesis of NiCuP electrocatalysts on stainless steel foil. Reprinted with permission from ref 500. Copyright 2017 Royal Society of Chemistry. (c) Facile electrodeposition of NiP_x NPs on carbon fiber followed by low-temperature phosphidation: (i) as-prepared flexible CF@NiP_x electrode wrapped on a plastic rod; (ii) SEM and (iii) HRTEM images; (iv) EDX elemental mappings. Reprinted with permission from ref 522. Copyright 2016 Royal Society of Chemistry.

deposited precursors to yield NiCuP samples (Figure 92b).[500] Interestingly, this precursor-deposition step created a porous, hierarchical nano-foam with a honeycomb structure, resulting from the H_2 bubble evolution during the electrodeposition. The precursor morphology was maintained after the phosphidation, and further evaluation of the electrochemically active surface area (ECSA) revealed high surface roughness of the resultant NiCuP, about two orders of magnitude greater than that of commercial NF substrates. By using 3D carbon fiber as a flexible substrate, Zhang *et al.* deposited vertical NiP_x nanoflakes through the electrodeposition of Ni NPs and subsequent phosphidation with NaH_2PO_2.[522] This strategy produced a flexible carbon fiber electrode (Figure 92c, i) in which the fibers were covered by vertically aligned NiP_x nanoflakes (Figure 92c, ii). TEM analysis confirmed the presence of Ni_2P (Figure 92c, iii), and SEM-EDX elemental mappings demonstrated the uniform dispersion of Ni and P elements on the surface of the deposited film (Figure 92c, iv). Overall, electrodeposition-based synthesis can control the morphologies and chemical compositions of the transition metal phosphides. Furthermore, these strategies are facile, highly reproducible, and potentially scalable.[49,521,537]

4.2.1.5. MOF-Derived Methods. Several studies have utilized MOF-based precursors due to their controllable pore structure, good thermal stability, tunable morphology, and large surface area.[436,439,440] Moreover, MOFs can be easily prepared by different methods, particularly solvothermal approaches that can be precisely tuned to change the composition of the final material.[299,402,568] Yu *et al.* synthesized carbon-coated nickel phosphide nanoplates from a Ni-Ni Prussian blue analogue (PBA) MOF.[520] As depicted in Figure 93a, simple co-precipitation was used to produce Ni-Ni PBA precursors through three different processes: ion exchange to yield $Ni(OH)_2$ porous nanoplates, calcination in air to give

https://doi.org/10.1021/acs.chemrev.3c00005
Chem. Rev. 2023, 123, 12795−13208

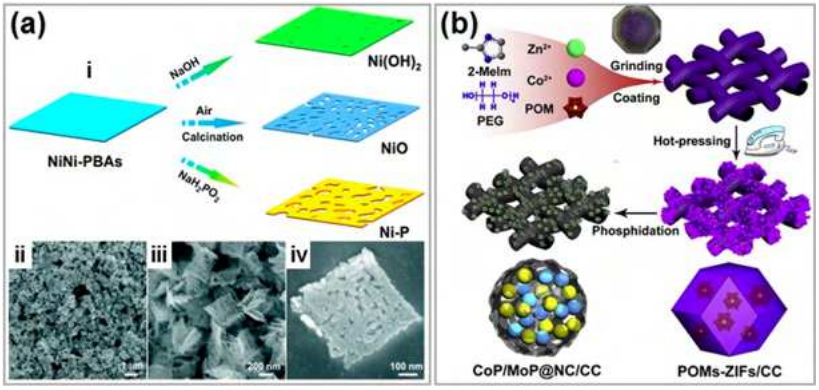


Figure 93. MOF-derived methods to synthesize transition metal phosphides. (a) Synthesis of porous carbon-coated nickel phosphides nanoplates from Ni-Ni Prussian blue analogues: (i) schematic illustration of the synthetic strategy; (ii–iv) FESEM images of the Ni-P nanoplates at different magnifications. Reprinted with permission from ref 520. Copyright 2016 Royal Society of Chemistry. (b) Synthesis of MOF-derived CoP/MoP@NC/CC electrodes through a hot-pressing approach. Reprinted with permission from ref 449. Copyright 2019 Elsevier.

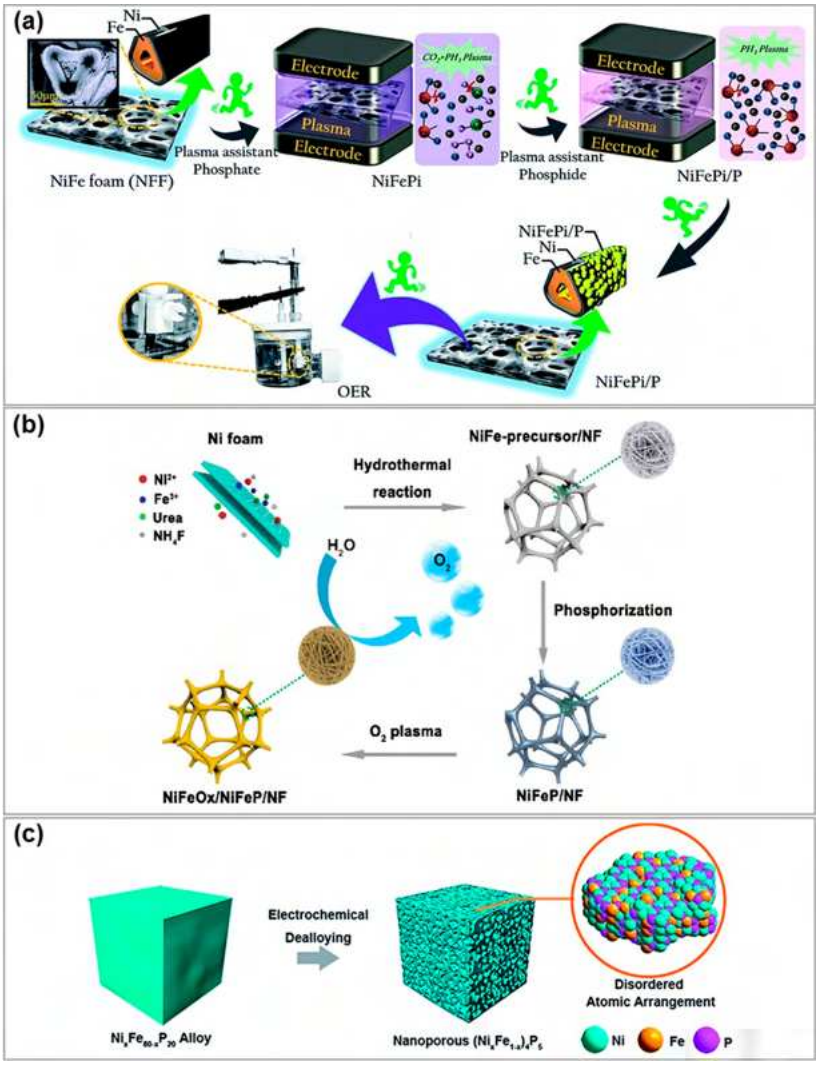


Figure 94. Unique approaches to synthesize transition metal phosphides: (a) Plasma-assisted synthesis of a NiFe-phosphate/phosphide electrocatalyst. Reprinted with permission from ref 481. Copyright 2018 Royal Society of Chemistry. (b) Preparation of a hierarchical $NiFeO_x$/NiFeP/NF electrocatalyst by O_2 plasma treatment. Reprinted with permission from ref 452. Copyright 2019 Elsevier. (c) Preparation of amorphous np-$(Ni_yFe_{1-y})_4P_5$ electrocatalysts through an electrochemical dealloying method. Reprinted with permission from ref 472. Copyright 2018 Royal Society of Chemistry.

NiO nanoplates, and low-temperature phosphidation using NaH_2PO_2 in Ar to give Ni-P nanoplates. The porous nanoplate morphology of the precursor was maintained after the phosphidation step (Figures 93a, ii–iv), and the material was

https://doi.org/10.1021/acs.chemrev.3c00005
Chem. Rev. 2023, 123, 12795–13208

composed mainly of Ni_2P and Ni_5P_4. This created a carbon-coated Ni-P electrocatalyst with a large surface area. Recently, Tang *et al.* reported the synthesis of MOF-derived, Co- and Mo-based phosphides on carbon cloth (CC) using this strategy.[449] As shown in Figure 93b, the CC substrates were coated with metal salts, polyoxometalate (POM) pastes, and a hot-pressing step at ∼150 °C formed the MOF precursor *in situ*. Subsequently, a phosphidation step generated N-doped graphitic carbon layers covered with well-dispersed CoP and MoP particles (CoP/MoP@NC/CC). Interestingly, this method allows the *in situ* growth of MOF precursors on conductive substrates without requiring solvents, operating at mild conditions and high yields.

4.2.1.6. Other Methods. In addition to conventional methods, novel synthetic approaches have been reported in recent years. Notably, special attention has been paid to plasma-assisted methods. This is a fast and straightforward approach used to increase the roughness of the surface, increase the porosity, and oxidize the surface (when O_2 is employed).[452,461] Zhang *et al.* employed a plasma-enhanced chemical vapor deposition (PECVD) method in which a mixture of PH_3, CO_2, and H_2 reacted on NiFe foam (NFF) to generate metal phosphate (Pi) and phosphide species (see Figure 94a).[481] In the first step, the NFF is exposed to $PH_3/CO_2/H_2$ plasma, generating NiFe phosphate (NiFePi). Then, the material was treated only with PH_3/H_2 plasma, further converting partially NiFePi species into metal phosphide species (NiFeP). As a result, the PECVD method increased the surface area of the NFF by creating irregular biscuit-shaped NiFePi/P composite structures. Moreover, this method enabled the use of relatively low temperatures (280 °C) and short reaction time (20 min) and significantly increased the wettability of the material by producing oxidized phosphorus species (P_2O_5, PO_4^{3-}). A plasma-assisted approach was used as a post-treatment to activate the transition metal phosphide intentionally. NiFe phosphides prepared with conventional methods have been treated with an O_2 plasma to generate an amorphous layer of $NiFeO_x$ on the surface.[452] As displayed in Figure 94b, NiFeP nanosheet arrays on Ni foam were prepared for the phosphidation of a hydrothermally grown NiFe precursor. The resultant NiFeP/NF electrode was exposed to radio frequency (RF) plasma treatment (where O^{2-} ions were deposited onto the crystalline NiFeP), creating a disordered $NiFeO_x$ layer. Notably, this method allowed control of the oxygen content by changing the treatment time.

Recently, electrochemical dealloying has been proposed as a simple and efficient strategy to increase the surface area of the final transition metal phosphide, avoiding the use of toxic chemicals and performing simple melt-spinning syntheses of amorphous metal-phosphorous alloys and subsequent acid etching at low temperature. Xu *et al.* reported a unique strategy in which $Ni_yFe_{80-y}P_{20}$ (y = 70, 65, and 60) alloy precursors, obtained from an initial melt-spinning method, were electrochemically dealloyed into amorphous np-$(Ni_xFe_{1-x})_4P_5$ electrocatalysts with bicontinuous structure (Figure 94c).[472] Briefly, the precursor alloys were selectively etched with 1 M HCl, creating vacancies and aggregation into interconnected nanopore channels inside the material. Then, the generated clusters were self-assembled into a uniform nanoporous electrocatalyst. This method produced an amorphous atomic arrangement, with abundant defects that acted as catalytically active sites.

4.2.2. Final Types of Phosphide-Based Electrocatalysts. According to Table 4, most of the reports have concluded that pristine transition metal phosphides acted as precatalysts and that the noticeable reconstruction of the surface occurred during/after the OER process. Compared to other materials such as transition metal tellurides, the number of studies concluding that the transition metal phosphide is a "catalyst" is considerably small. Interestingly, P has relatively low electronegativity (χ_P = 2.19), which should provide a relatively higher covalency of M−P bonds in transition metal phosphides, resulting in their better stability than that of transition metal nitrides (χ_N = 3.04). However, evidence suggests that this is not the case and that most of the transition metal phosphides are prone to oxidize and even dissolve under OER potentials. Therefore, it is necessary to unveil the reasons behind this transformation (transition metal phosphide → its oxide counterpart). Additionally, in most of the reports with the pre- and post-OER XPS results, regardless of "catalyst" or "precatalyst," oxidized P species (e.g., PO_4^{3-}) existed on the as-prepared phosphide surfaces and remained and/or were generated at the phosphide surfaces after the OER testing (see Table 4 and Figure 95). The role of the oxidized P species

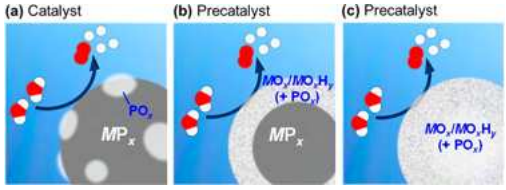


Figure 95. Schematic illustrations of suggested final types of transition metal phosphide-based electrocatalysts after long-term OER testing.

in the OER is not yet understood. There is even a possibility that the oxidized P species positively contribute to the OER process over the transition metal phosphide electrocatalysts, which needs to be examined thoroughly in future studies. Herein, we review several case studies, emphasizing post-OER analysis results to understand better the electrochemical behaviors of the transition metal phosphide "catalyst" and "precatalyst."

4.2.2.1. Catalysts. Among many studies that have reported the characterization results of post-OER transition metal phosphides, only a few of them (i.e., FeP,[415] Ni-Co-P,[414] Ni-Fe-P,[411] and Mo-Ni-P[412]) were concluded to be stable materials during the OER testing. The most remarkable example was discussed by Gao *et al.* in 2019.[411] In this study, bimetallic NiFe phosphide nanoparticles were prepared by conventional gas-solid phosphidation and deposited on glassy carbon. As shown in Figure 96a, the NiFe phosphide sample possessed an irregular spherical-like morphology with rough surfaces. The as-prepared sample consisted mainly of NiP_2, FeP, NiFe, and C species (Figures 96b and c). Moreover, the XPS results of the as-prepared sample (Figure 96d) confirmed the presence of Ni−P and Fe−P bonds and P−O bonds, suggesting the partial oxidation of surface P species by ambient air exposure. After the OER stability test (12 h chronoamperometry at 0.42 V_{SCE}) in 1 M KOH, XPS analysis was performed (Figure 96e). According to the authors, the XPS peaks before and after the OER test were very similar, ruling out any material change. Slight changes were attributed to long-term charge transfer of Fe, Ni, and P. However, when comparing Figures 96d and e more carefully, it is evident that

https://doi.org/10.1021/acs.chemrev.3c00005
Chem. Rev. 2023, 123, 12795−13208

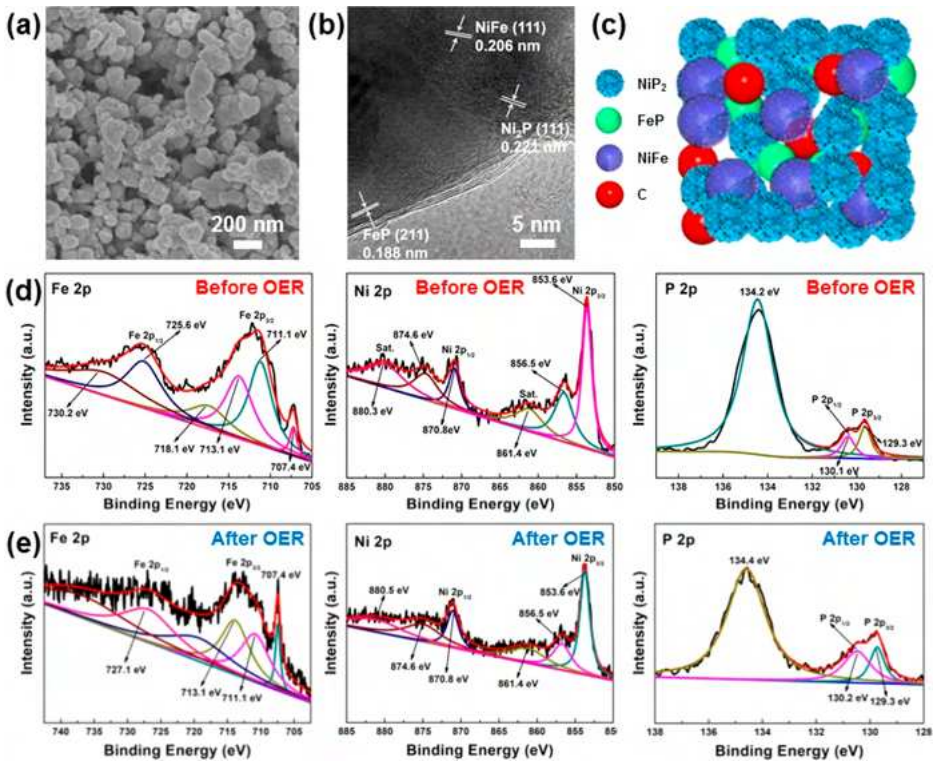


Figure 96. Evaluation of bimetallic nickel−iron phosphide catalysts: (a) SEM image; (b) HRTEM image with corresponding lattice spacings; (c) schematic illustration; (d, e) XPS spectra of Fe 2p, Ni 2p, and P 2p regions (d) before and (e) after OER tests. Reprinted with permission from ref 411. Copyright 2019 Elsevier.

the intensity of some peaks decreased, such as the P−O bond peak at 134.2 eV and the Fe $2p_{3/2}$ peak at 711.1 eV. This difference might indicate a depletion of FeP and oxidized P species during the OER, although more evidence is needed to corroborate that transformation of the sample occurred. Nevertheless, as Ni−P and Fe−P bonds were present after 12 h of OER testing, the authors concluded that the NiFe phosphide acted as a "catalyst".

The morphological and compositional stability of the transition metal phosphides has also been proved through the combination of X-ray- and electron-beam-based characterization techniques before and after OER testing. Zhang *et al.* claimed that a nickel-cobalt phosphide/nitrogen-doped carbon (NiCoP/NC) electrocatalyst was structurally stable after 10 h chronoamperometry tests at the constant potential of 1.55 V_{RHE} in 1 M KOH.[414] According to pre- and post-OER SEM images (Figures 97a and b), the polyhedral nanocage morphology was retained. Additionally, the author claimed that pre- and post-OER XRD and XPS results confirmed that the NiCoP/NC maintained the initial composition even after long-term OER testing. However, slight intensity changes in the pre- and post-OER XPS peaks were also observed. For example, the intensity increase in the P 2p peak (at ∼134 eV) after the OER test, which could be attributed to the surface oxidation of P species, was not discussed. In another instance, Chen *et al.* prepared ultrathin nickel-molybdenum phosphide electrocatalysts with a 3D hollow nanoflower morphology, subject to long-term OER testing and subsequent characterization.[412] Figures 97c−f show TEM and EDX results before and after 36 h chronopotentiometry tests at 10 $mA{\cdot}cm^{-2}$ in 1 M KOH. Notably, the hollow nanoflower structure was retained, and EDX quantitative analysis revealed that the composition did not change even after long-term OER testing. Accordingly, compositional and morphological characterization results are more effective for convincing proof of the stability of the transition metal phosphide electrocatalyst.

Similarly, Masud *et al.* reported the performance of ultrasmall FeP nanoparticles on Au-coated glass and carbon fiber paper (CFP) as an OER electrocatalyst in 1 M KOH.[415] To check the conductive additive effect on the OER activity of the FeP sample, a mixture of FeP and reduced graphene oxide (FeP−rGO) was also prepared. Here, the FeP on Au-coated glass (FeP@Au) showed the OER overpotential to be 320 mV at a current density of 10 $mA{\cdot}cm^{-2}$. The FeP−rGO hybrid on CFP exhibited the lowest OER overpotential (260 mV at 10 $mA{\cdot}cm^{-2}$). Furthermore, the electrochemical stability of the FeP@Au was tested through 4 h chronoamperometry testing at the constant potential of 1.55 V_{RHE} (see Figure 98). Interestingly, as seen in the inset of Figure 98, the overpotential at the current density of 10 $mA{\cdot}cm^{-2}$ decreased after aging (320 → 290 mV), which was attributed to a likely increase in the porosity and wettability of the material. However, post-OER SEM images suggested that the surface was unchanged, while post-OER EDX and XPS analyses revealed that the material retained its chemical and compositional features. These results disagree with the observed OER performance improvement during aging, as the authors did not uncover a clear explanation for this change. Therefore, although the post-OER characterization suggests that the electrocatalyst was stable (and therefore, the FeP acted as the active site), the reason behind the overpotential decrease after the OER remains elusive, and further studies are necessary to validate the role of FeP as a "catalyst".

https://doi.org/10.1021/acs.chemrev.3c00005
Chem. Rev. 2023, 123, 12795−13208

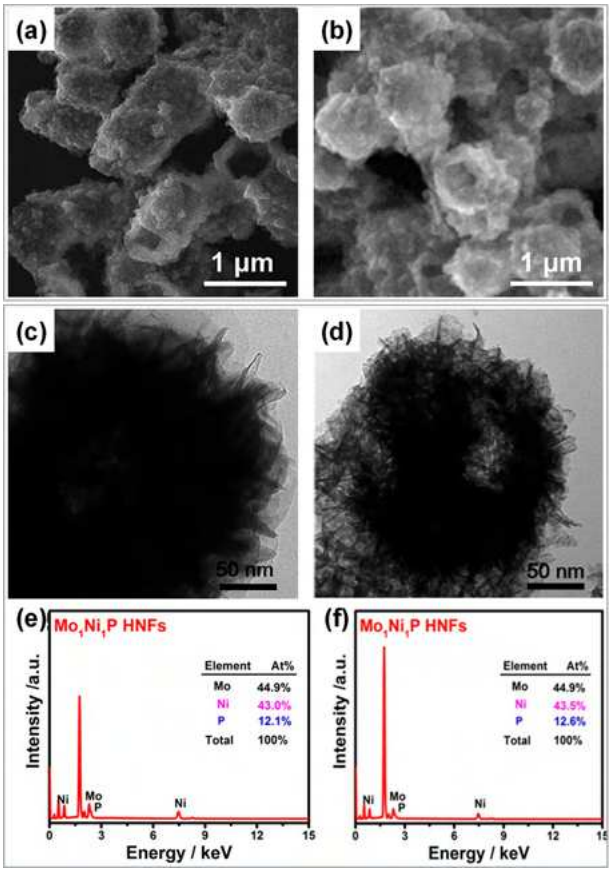


Figure 97. (a, b) SEM images of nickel-cobalt phosphide/nitrogen-doped carbon polyhedral nanocages (NiCoP/NC PHCs) (a) before and (b) after the OER test. Reproduced with permission from ref 414. Copyright 2017 Royal Society of Chemistry. (c–f) TEM images and EDX spectra of Mo_1Ni_1P HNFs (c, e) before and (d, f) after the OER testing. Reproduced with permission from ref 412. Copyright 2019 Elsevier.

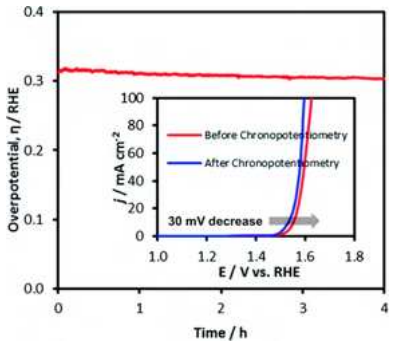


Figure 98. Time-dependent current density curve of FeP@Au at the constant potential of 1.55 V_{RHE} for 4 h in N_2-saturated 1 M KOH. Inset: linear-sweep voltammograms of pre- and post-OER FeP@Au. Reproduced with permission from ref 415. Copyright 2016 Royal Society of Chemistry.

Since the transition metal phosphide is a highly covalent compound with high electrical conductivity, electrochemists can also use the phosphide as a conductive substrate rather than an actual electroactive site for the OER. Zhou *et al.* fabricated CoNiP@NiFe-layered double hydroxide core@shell nanosheet arrays (CoNiP@LDH NSAs) on Ni foam (see Figure 99a).[413] TEM analysis revealed that NiFe-LDH

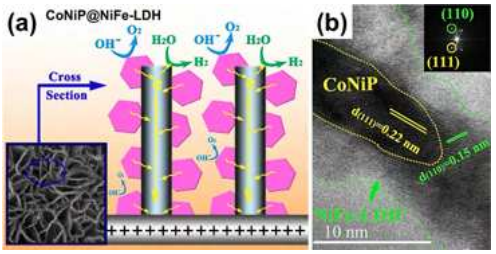


Figure 99. (a) Schematic illustration and (b) side-view TEM image of CoNiP@NiFe-LDH NSAs directly grown on Ni foam. Reproduced with permission from ref 413. Copyright 2018 American Chemical Society.

nanosheets were vertically grown on the CoNiP nanosheets. Figure 99b shows the side-view TEM image of the core@shell nanostructure, which confirms that the thicknesses of the CoNiP core and LDH shell are ∼5.5 and ∼10 nm, respectively. The as-fabricated CoNiP@LDH electrode was used for the long-term OER testing (500 h chronopotentiometric measurement at the current density of 50 mA·cm^{-2}) in 1 M KOH. The CoNiP@LDH electrode exhibited a nearly unchanged OER overpotential during the 500 h OER test. According to the pre- and post-OER SEM analysis, the CoNiP@LDH electrode retained the initial morphology after the 500 h OER test. The authors also mentioned that the post-EDX analysis found marginal leaching of P species owing to the strong core@shell interaction, and accordingly, the CoNiP@LDH electrode has excellent stability for the alkaline OER process. However, this marginal P leaching possibly suggests the partial exposure of the CoNiP core toward the electrolyte and its partial oxidation. In that case, the CoNiP might act as a conductive substrate and an OER precatalyst. To confirm these points, further structural studies (e.g., TEM) may need to be conducted.

As displayed in Table 4, a considerable number of materials can only be categorized as "unknown" because they lacked post-OER characterization results. Therefore, it is difficult to illustrate case studies in which the material can be classified as a "catalyst" without evidence of its stability after the OER. We emphasize providing such results to validate that the material is genuinely stable and that a reconstruction process does not occur.

4.2.2.2. Precatalysts. On the other hand, a significant fraction of the studies in Table 4 has provided sufficient evidence to support the reconstruction of the original transition metal phosphides, acting as a "precatalyst" and transforming into the active material during the OER. The following case studies represent a select group of transition metal phosphides that exhibit remarkable changes during the OER and for which the authors provided sufficient post-characterization evidence. For checking further references and details, the reader may refer to Table 4.

Yu *et al.* reported a carbon-coated Ni_8P_3 electrocatalyst with a nanosheet morphology on glassy carbon.[520] This sample showed an OER overpotential of 267 mV at 10 mA·cm^{-2} and was able to withstand 25 h of continuous operation at the constant current density of 20 mA·cm^{-2}. Interestingly, oxidation peaks at 1.32–1.34 V_{RHE} observed in LSV scans indicated the apparent oxidation of the Ni_8P_3 into nickel oxides/hydroxides during the OER. Furthermore, as depicted in Figure 100a, the post-OER TEM image confirmed the presence of numerous NiO_x NPs surrounding the Ni_8P_3 nanosheets. Although the outermost layer consisted of a

https://doi.org/10.1021/acs.chemrev.3c00005
Chem. Rev. 2023, 123, 12795–13208

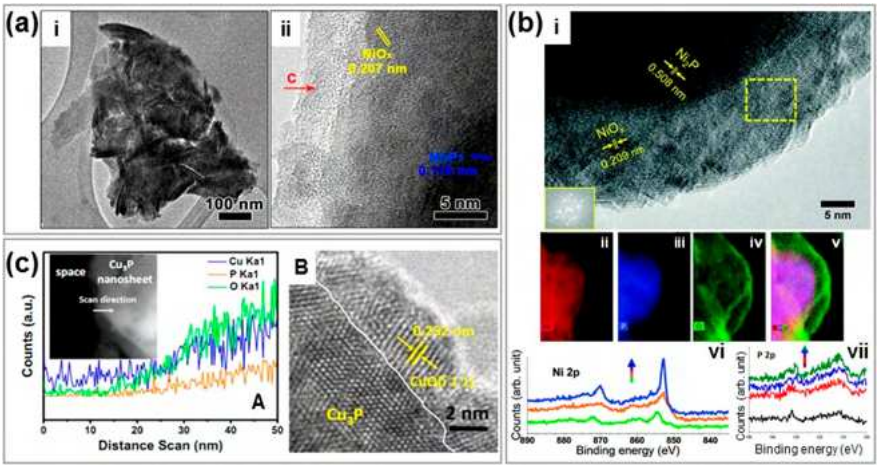


Figure 100. Characterization of transition metal phosphide precatalysts after OER tests. (a) Ni_8P_3@C core@shell precatalyst after the OER test at 1.5 V_{RHE} for 1 h: (i) TEM and (ii) HRTEM images. Reprinted with permission from ref 402. Copyright 2016 American Chemical Society. (b) Ni_2P NPs after electrochemical pretreatment at 1.5 V_{RHE}: (i) HRTEM image; (ii–iv) elemental mapping images for (ii) Ni, (iii) O, (iv) P, and (v) combined; (vi, vii) depth-profiling XPS spectra of the (vi) Ni 2p and (vii) P 2p regions. Reprinted with permission from ref 103. Copyright 2015 Royal Society of Chemistry. (c) Cu_3P precatalyst after OER activation: (A) EDX elemental line scan with STEM image as inset; (B) HRTEM image. Reprinted with permission from ref 490. Copyright 2017 American Chemical Society.

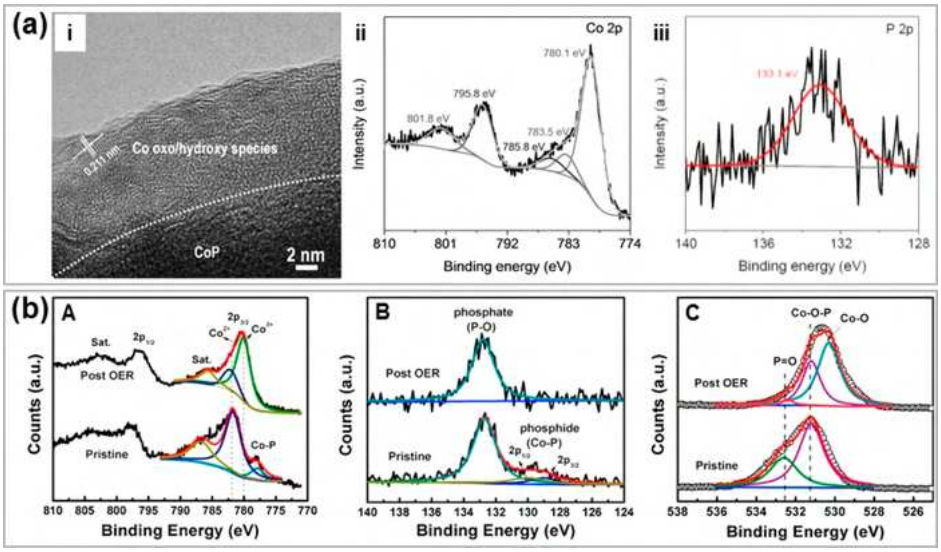


Figure 101. (a) (i) HRTEM image and (ii) Ni 2p and (iii) P 2p XPS spectra of the CoP-MNA precatalyst after the OER. Reprinted with permission from ref 297. Copyright 2015 Wiley. (b) (A) Co 2p, (B) P 2p, and (C) O 1s XPS spectra of the Co-Pi/CoP precatalyst after the OER test. Reprinted with permission from ref 488. Copyright 2017 Elsevier.

carbon layer that protected the Ni_8P_3 core, surface oxidation was confirmed by post-OER XPS and EDX analysis, concluding that a nickel oxide/hydroxide shell formed around the Ni_8P_3 framework. Therefore, the nickel oxide/hydroxide likely acted as the OER active site, the Ni_8P_3 core might become a conducting support, and the carbon layer reduced the dissolution of P species. Interestingly, post-OER XPS revealed the formation of oxidized P species and reduced the P 2p peak. Thus, the oxidized P species might still exist in the newly formed nickel oxide/hydroxide shell and positively affect OER activity, which is still a question. Similarly, Stern *et al.* studied the OER activity of Ni_2P NPs on glassy carbon.[103] Post-OER characterizations revealed that the Ni_2P underwent surface oxidation and that a Ni_2P@NiO_x core@shell structure was produced (Figure 100b, i). Notably, this significant transformation occurred after 1 h of OER operation at the constant potential of 1.5 V_{RHE}, suggesting that the core-shell formation is relatively fast. Moreover, EDX elemental mappings (Figures 100b, ii–v) also confirmed the higher concentration of oxidized species in the shell, whereas P was located mainly in the core. Finally, depth-profiling XPS spectra (Figure 100b, vi) demonstrated that the metallic Ni content increased as the profiling depth was increased (denoted by the arrow direction). Additionally, XPS intensity increase and decrease of phosphorus (see Figure 100b, vii) and oxygen were confirmed along a 50 nm sputtering depth, respectively. These results confirmed that the initial Ni_2P electrocatalyst acted as a "precatalyst" and that the NiO_x shell and metallic phosphide core might mainly act as an OER active site and a conductive support, respectively.

An analogous activation process was also reported by Han *et al.* using Cu_3P nanosheets supported on Ni foam.[490] The characteristic Ni oxidation peak was seen in LSV curves at ~1.38 V_{RHE}, and the activity was significantly increased after

https://doi.org/10.1021/acs.chemrev.3c00005
Chem. Rev. 2023, 123, 12795–13208

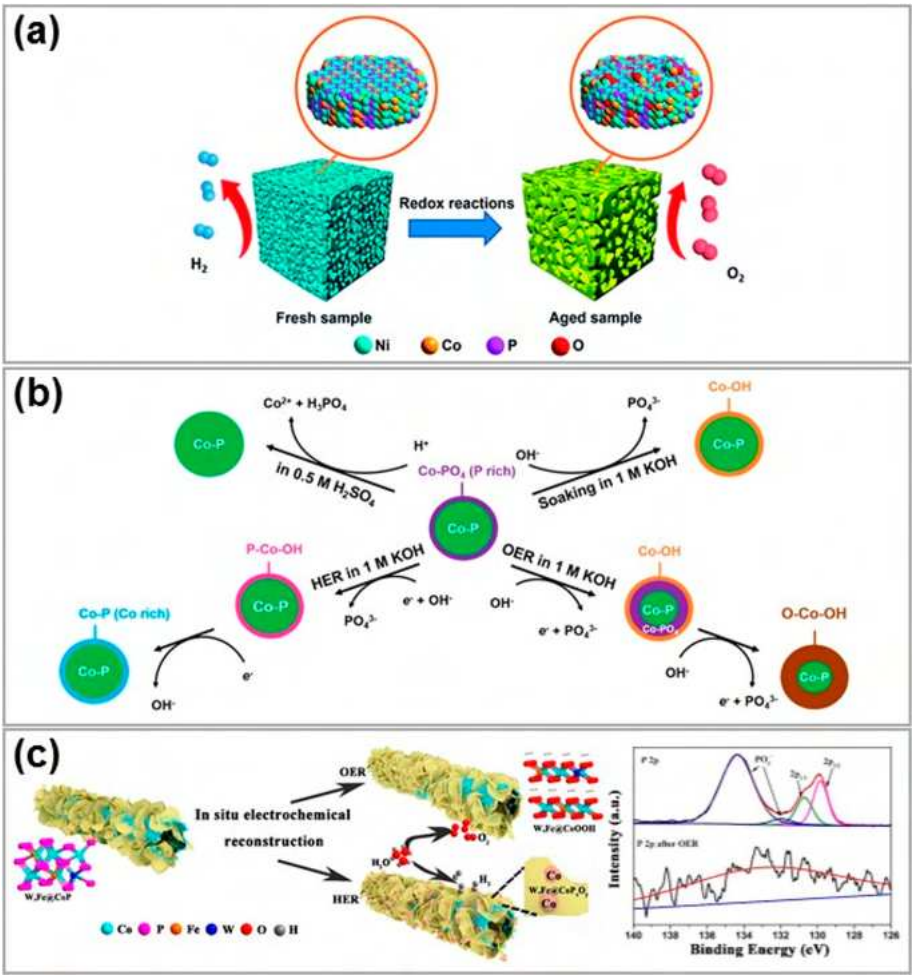


Figure 102. Schematic illustration of proposed electrocatalytic reconstruction models: (a) Aging process of np-$(Ni_{0.67}Fe_{0.33})_4P_5$ precatalysts to generate *M*OOH species on the surface. Reprinted with permission from ref 472. Copyright 2018 Royal Society of Chemistry. (b) Surface reconstruction of CoP NPs under different electrochemical conditions. Reprinted with permission from ref 470. Copyright 2018 American Chemical Society. (c) Electroderived self-reconstruction of W,Fe@CoP/CNTs during the OER and HER and their P 2p XPS spectra before and after the OER test. Reprinted with permission from ref 441. Copyright 2019 American Chemical Society.

50 CV cycles between 1.2 and 1.7 V_{RHE} (i.e., OER activation) in 1 M KOH. Furthermore, EIS measurements revealed that the charge transfer resistance decreased after 50 CV cycles, suggesting an activation process that enhanced the electron transfer. To understand these electrochemical trends, characterization of the sample after the activation was performed. Pre- and post-OER SEM images revealed that the nanosheet structure was maintained. According to a close inspection of the Cu_3P nanosheets using EDX line scans (Figure 100c, A), the P content drastically decreased close to the nanosheet edge, while Cu, O, and P elements mainly resided far from the edge. HRTEM images (Figure 100c, B) confirmed the Cu_3P@CuO core@shell structure. Interestingly, curved lattice fringes were seen in the crystalline core, suggesting that the reconstruction process promoted defects in the material. EDX elemental mappings of the entire nanosheet revealed that P was mainly present in the core, while oxygen was seen in the shell. XPS results also suggest that copper oxide (CuO) formed *in situ* during the OER test, indicating the "precatalytic" nature of the Cu_3P@NF electrode. Interestingly, in the P 2p XPS spectrum after the OER test, the presence of copper phosphate was also confirmed.

Zhu *et al.* also reported the precatalytic transformation of CoP mesoporous nanorod arrays (CoP-MNA) on Ni foam.[297] The 32 h chronoamperometric test of the CoP-MNA was performed at the constant potential of 1.52 V_{RHE} in 1 M KOH. After the OER, the HRTEM image (Figure 101a, i) showed several cobalt oxo/hydroxo nanoparticles, creating a shell over a crystalline CoP core. Pre- and post-OER XPS results (Figures 101a, ii and iii) confirmed the disappearance of the phosphide and the generation of phosphate, validating the role of initial CoP as a "precatalyst" rather than the OER active site. However, the authors proposed that the presence of a CoP core facilitated the electron transfer to the outermost oxide layer. Ai *et al.* synthesized phosphate-modified CoP nanorod bundles on Ti foil and tested its performance for the OER in 1 M KOH.[488] Characterization of the as-prepared material showed the presence of both Co-P and Co-Pi species at the surface. However, XPS analysis after the 24 h chronopotentiometric test at 50 $mA{\cdot}cm^{-2}$ (Figure 101b) indicated that CoP species were removed entirely from the surface, whereas only phosphate ions remained. Moreover, the concentration of oxygen species increased. Furthermore, the XPS peaks associated with Co-O and P-O species were evident after the OER, implying phosphate-intercalated Co (oxy)hydroxides.

https://doi.org/10.1021/acs.chemrev.3c00005
Chem. Rev. 2023, 123, 12795−13208

Post-OER Raman spectroscopy measurements also suggest the formation of (oxy)hydroxide species after the OER. In the XRD pattern of the post-OER sample, the diffraction peaks of CoP disappeared. According to the EDX results, significant phosphorous leaching was observed after the OER (the atomic ratio of Co:P:O = 1:0.65:0.68 → 1:0.12:1.77). However, post-OER EDX elemental mapping results found a uniform distribution of Co, O, and P throughout the as-observed sample surface. Moreover, the post-SEM measurements revealed a significant change in morphology (nanorod bundles → intertwined nanoplates). From these pre- and post-OER characterization results, the Co-Pi/CoP seems to be converted into phosphate-intercalated cobalt (oxy)hydroxides. Note that only a few studies reported the almost full oxidation of the transition metal phosphides into their oxide counterparts and oxidized P species so far.[476,488]

Recently, Yao *et al.* prepared ultrasmall FeP nanoparticles derived from a diiron triphosphide complex ($Fe^{II}P_3Fe^{III}$ core + cyclo-$P_{(2+1)}$ ligand) precursor on a glassy carbon electrode.[480] Interestingly, this precursor turned into the FeP phase due to favorable thermodynamics (cohesive energy and formation enthalpy). The FeP electrocatalyst exhibited an OER overpotential of 227 mV at 10 mA·cm^{-2} in 1 M KOH and decent stability during the 15 h chronoamperometric test at 1.46 V_{RHE}. Furthermore, post-*operando* HRTEM analysis revealed that the FeP particles were transformed into an amorphous material. ICP-AES and EDX revealed the considerable loss of P (∼ 45%), and XPS analysis confirmed the oxidation of Fe into $Fe(OH)_2$/FeOOH phases, as well as the presence of P^{5+} species (i.e., phosphates) at the surface. Importantly, it was found that the particle's core was still crystalline FeP, suggesting that this oxidation process was confined to the surface, creating a Fe-rich amorphous shell that ultimately acted as the OER active sites.

Interestingly, recent studies have also deliberately exploited this reconstruction process to enhance transition metal phosphide electrocatalytic activity, providing specific pathways to promote the *in situ* transformation during the OER in 1 M KOH. Using their attractive electrochemical dealloying method, Xu *et al.* generated $Ni_xFe_{1-x}OOH$ species on NiFe phosphide on NiFe alloy ingots using a CV-assisted aging procedure (see Figure 102a).[472] After 50 CV cycles, the total charge associated with the Ni redox peaks significantly increased, suggesting that more OER-active Ni centers were created, which implies the formation of $Ni_xFe_{1-x}OOH$. Interestingly, the authors found that while the aged $Ni_xFe_{1-x}P$ catalysts were more active toward the OER, their HER activity was decreased, suggesting that the oxidized transition metal phosphide serves as the real active site only for the OER and not for the HER. Incidentally, the fresh bimetallic phosphide could act as the "catalyst" for the HER. Moreover, the presence of phosphate was confirmed by XPS, and it was assumed to act as an essential proton transport mediator during the OER.

Wu *et al.* tested CoP nanoparticles (NPs) on carbon fiber paper in different environments to characterize their reconstruction processes using *quasi in situ* XPS.[470] Interestingly, four different transformation pathways were found depending on the electrolyte and catalytic reaction (see Figure 102b). First, the CoP NPs were naturally oxidized when exposed to air. Then, soaking the CoP NPs in KOH electrolyte immediately (∼2 min) created a Co-OH surface, as the polyphosphate ions were replaced by hydroxide ions (almost all the polyphosphate ions were dissolved in the electrolyte). Under OER conditions in alkaline media, more CoP was electrochemically oxidized, and phosphate ions were continuously leached into the electrolyte. However, a modest amount of phosphate ions might remain, creating Co-OH/Co-PO_4/CoP layers. If the OER occurs at a sufficient time, the oxide/hydroxide layer will get thicker. On the other hand, oxidized P and Co species were reduced during the HER in alkaline conditions, creating a Co-rich phosphide surface that acts as the active site. Finally, surface oxides were dissolved under HER conditions in acidic media, thus exposing fresh Co-P. The XPS analysis demonstrated that different Co and P species would be generated depending mainly on (i) the environment (i.e., the electrolyte) and (ii) the electrochemical conditions (i.e., the HER/OER). Therefore, the abundance of certain species could be used to determine the real active sites for each catalytic reaction. Furthermore, it was confirmed that oxidation of CoP could occur at around 1.07 V_{RHE}, which is below the equilibrium potential for the OER, and that some phosphate-like species might remain during the OER, suggesting that these ions might have a particular role in the OER.

So far, we have discussed the transition metal phosphide precatalyst having the oxidized P species after OER testing. Here, we also provide precatalyst examples without the oxidized P species after the OER. Ding *et al.* confirmed that W- and Fe-incorporated CoP nanosheets decorated on the entangled carbon nanotubes (W,Fe@CoP/CNTs) on glassy carbon acted differently for the HER and OER in 1 M KOH.[441] As depicted in Figure 102c, cobalt oxyhydroxide species were generated *in situ* during OER stability testing (∼20 h chronopotentiometric measurement at 10 mA·cm^{-2}). In contrast, metallic Co species were seen after the HER. Especially, post-OER XPS, EDX, and ICP-OES results confirmed the disappearance and significant decrease of P species from the material surface (see Figure 102c) and bulk, respectively, suggesting that the CoP samples acted as "precatalysts" until the real active species (i.e., W- and Fe-incorporated CoOOH and CoO_x) were formed. As shown in Table 4, almost complete P leaching from the phosphide surface was also reported by several investigators. Furthermore, it was theorized that incorporating W and Fe species increased the number of defects in the CoP, enhancing the reconstruction process. Remarkably, this study demonstrated that the transition metal phosphide precatalyst could generate different active species depending on the electrochemical and environmental conditions.

Theoretical studies were also performed to explain the activity enhancement of transition metal phosphide precatalysts and assess the importance of surface reconstruction. Xiao *et al.* reported Co-based phosphide nanosheets on glassy carbon with high OER activity in alkaline media (1 M KOH).[574] Since XPS results confirmed that the as-obtained samples were partially oxidized, they performed the DFT calculations comparing pristine Co-P with oxidized Co-P-O and Co-Ni-P-O models (see Figure 103). Interestingly, while *OOH formation was the rate-limiting step in the OER mechanism for Co-P (ΔG = 1.69 eV), Co-P-O was limited by *O formation (ΔG = 1.62 eV), as indicated in Figures 103a and b. Furthermore, Ni-doping decreased the binding energies even further (Figure 103c), which is attributed to Co's oxophilicity reduction by Ni. These trends confirm that transition metal phosphide "precatalysts" exhibit different activation barriers after being oxidized but that the overall

https://doi.org/10.1021/acs.chemrev.3c00005
Chem. Rev. 2023, 123, 12795−13208

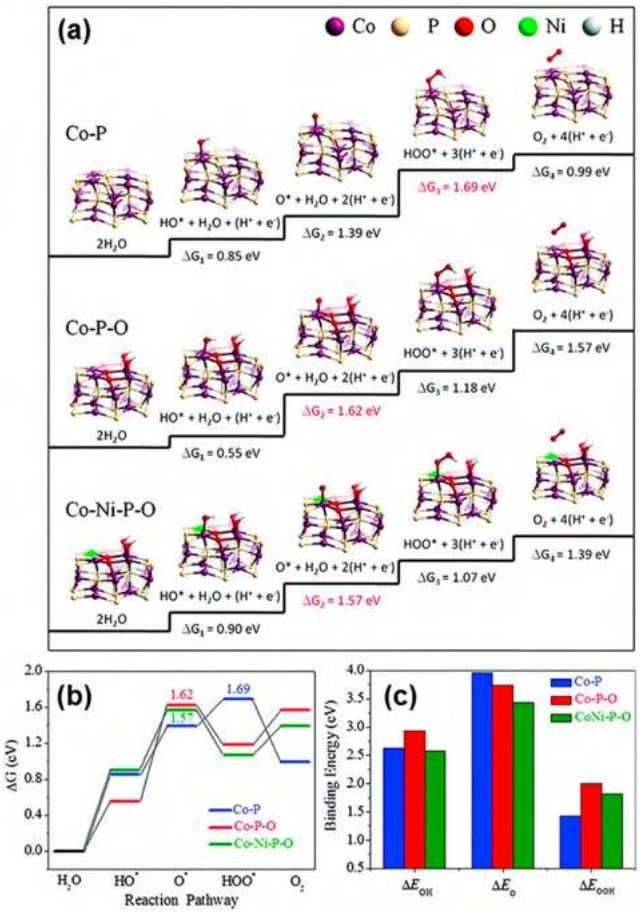


Figure 103. DFT calculations of Co-based bimetallic phosphides: (a) Primitive steps and (b) standard free energy diagram of the OER mechanism; (c) calculated binding energies of the OER intermediates from different electrocatalytic active sites. Reprinted with permission from ref 574. Copyright 2017 Royal Society of Chemistry.

energy requirement is lower, which might explain the enhanced activity.

Similarly, Liu *et al.* performed DFT calculations to unveil the role of oxyhydroxide species on O-$Ni_{(1-x)}Fe_xP_2$.[465] Free energy changes during the OER mechanism for NiP_2, $Ni_{0.75}Fe_{0.25}P_2$, and O-$Ni_{0.75}Fe_{0.25}P_2$(111) surfaces were calculated, considering the adsorption of *OH, *O, and *OOH intermediates (Figure 104a). For NiP_2, the third (*OH → *OOH) and fourth (*OOH → O_2) steps were rate-limiting in the mechanism (Figure 104b). When Fe atoms were introduced, the third step became downhill at high potentials, suggesting that the fourth step was the only rate-limiting step for the OER (Figure 104c). This was attributed to the capacity of Fe sites to decompose *OOH back into *O and *OH. However, when O atoms were introduced on the Fe−Fe bridge site, the fourth step proceeded without *OOH decomposition. At high potentials, all steps became downhill except for the third one (Figure 104d). When comparing the free energy diagrams for all of the materials (Figure 104e), it is evident that the oxidized bimetallic phosphide reduced the number of limiting steps and decreased the energy barriers for the OER. Therefore, activity enhancement of transition metal phosphides can be explained by the inherent surface transformation and the generation of local O-rich environments that facilitate the OER.

These case studies are formidable examples of the importance of surface reconstruction processes of transition metal phosphides during the OER. Oxidized species are generated *in situ*, meaning that the initial phosphides should be considered "precatalysts". However, rather than just classifying the materials as "precatalysts" or "catalysts", we seek to provide more details on the factors that regulate these transformations. Undoubtedly, this will provide a more precise understanding of how to enhance the activity of OER electrocatalysts. Nevertheless, we believe that further studies are still necessary to identify the transformation-regulating factors.

4.2.3. Structural and Chemical Compositional Effects toward OER Activity. To explain the classification mentioned above of several transition metal phosphides as "precatalysts", recent studies have systematically modified different parameters and features to unveil the driving forces behind the electrocatalytic OER activity enhancement and the oxidation of transition metal phosphides during the OER. Next, the effects of these parameters are summarized, emphasizing their relationship with the surface reconstruction processes during the OER.

4.2.3.1. Phosphidation Temperature Effects. The phosphidation temperature has a significant impact on the phosphidation degree of the precursor. Ding *et al.* prepared Fe-based phosphides from bimetallic PBA precursors using a typical phosphidation method using NaH_2PO_2 at different temperatures.[436] From X-ray diffraction (XRD) patterns of the resulting transition metal phosphides (Figure 105a), the diffraction peaks of the PBA precursors disappear at around 300 °C, whereas new peaks emerge at 400 °C. According to the authors, these peaks were attributed to CoP, FeP, FeP_2, NiP_2, and MnP species. Additionally, XPS analysis confirmed the disappearance of precursors at 400 °C. Furthermore, SEM and BET characterizations demonstrated that this temperature produced cubic morphologies with superior roughness and the broadest pore size distribution, explaining the enhanced electrocatalytic performance. The crystal phases in the resultant transition metal phosphide samples can be controlled by varying the phosphidation temperature. Li *et al.* synthesized Ni_xP_y electrocatalysts with different phases via the phosphidation (P source: $NaH_2PO_2{\cdot}H_2O$) of a hydrothermally grown β-$Ni(OH)_2$ nanoplate precursor by tuning the phosphidation temperature.[511] Interestingly, it was found that low temperatures (~300 °C) produced mainly the hexagonal Ni_2P phase (Figure 105b). Within the 325−375 °C range, the dominant phases were hexagonal Ni_5P_4 and cubic NiP_2, while further increases up to 475 °C produced Ni_2P again as the primary phase. This trend was verified with additional XPS and TEM analysis, revealing that temperature modulation was responsible for generating preferential Ni_xP_y compositions. Furthermore, the superior OER activities for the Ni_xP_y samples prepared at 325 °C were attributed to the increased number of Ni sites (i.e., high content of Ni_5P_4), creating more OER-active NiOOH species. The resultant transition metal phosphide morphology can be tuned by changing the phosphidation temperature. Similarly, NiFe-based transition metal phosphides prepared from solvothermal growth of NiFe-LDH precursors and conventional phosphidation with NaH_2PO_2 were studied in a broader range of phosphidation temperatures (200, 300, 400, 500, and 600 °C), as shown in Figure 105c.[458] In Figure 105c, the sample prepared at 300 °C showed the highest OER activity, and further increase of the phosphidation temperature deactivated the samples as an OER electrocatalyst. This

https://doi.org/10.1021/acs.chemrev.3c00005
Chem. Rev. 2023, 123, 12795−13208

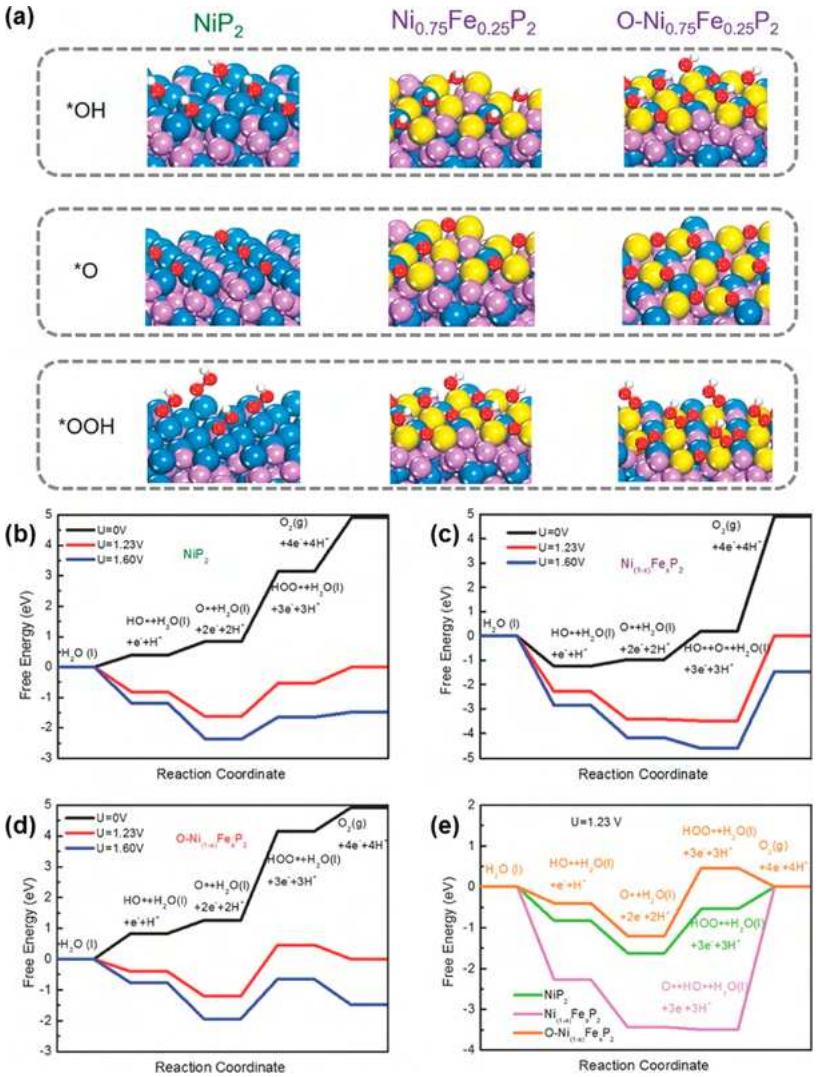


Figure 104. DFT calculations for NiP_2, $Ni_{0.75}Fe_{0.25}P_2$, and O-$Ni_{0.75}Fe_{0.25}P_2$ catalysts: (a) Atomic configurations of the (111) surfaces; (b–d) free energy diagrams at different OER potentials for (b) NiP_2, (c) $Ni_{0.75}Fe_{0.25}P_2$, and (d) O-$Ni_{0.75}Fe_{0.25}P_2$; (e) free energy diagram at the equilibrium potential (U = 1.23 V) for all of the catalytic surfaces. Reprinted with permission from ref 465. Copyright 2018 Wiley.

deactivation trend can be derived from sintering-induced structural deterioration at elevated temperatures, decreasing active sites, and mass diffusion/transfer efficiency. Hao *et al.* synthesized Cu_3P microsheets through the phosphidation of CuCl microsheets on Ni foam, which is fabricated by the solution-based method [a simple redox reaction: $Ni(s) + CuCl_2(aq) \rightarrow NiCl_2(aq) + CuCl(s)$] at different temperatures (see Figure 105d).[588] The Cu_3P sample prepared at 450 °C exhibited a superhydrophilic and superaerophobic surface, as confirmed by contact angle measurements (Figures 105d, iii–v). Moreover, this sample produced the smallest oxygen bubbles in additional bubble generation tests in 10% H_2O_2 (Figure 105d, vi). These trends were attributed to changes in the hierarchical microsheet morphology, as the samples prepared at 350 and 550 °C exhibited smother surfaces and smaller ECSA values. Notably, the sample prepared at 450 °C exhibited the best OER activity and the lowest charge transfer resistance. Overall, it is evident that the phosphidation temperature has an important effect on the structural and morphological properties of the transition metal phosphide products regardless of the synthetic approaches.

4.2.3.2. Metal Effects. Only a few reports have compared the OER activity of monometallic transition metal phosphides with different transition metals. Leonard *et al.* prepared a series of CoP_x, NiP_x, and FeP_x precatalysts through typical phosphidation and evaluated their performance in alkaline media.[454] As depicted in Figure 106a, among all of the transition metal phosphides, FeP_x exhibited the best performance in 1 M KOH electrolyte (Figure 106a, i), requiring an overpotential of 320 mV at 10 $mA \cdot cm^{-2}$ and a Tafel slope of 42 $mV \cdot dec^{-1}$. The NiP_x sample exhibited larger metal redox (Ni^{3+}/Ni^{2+}) peaks before the OER onset potential (Figure 106a, ii), while the CoP_x and FeP_x samples exhibited smaller redox peaks. The authors also evaluated the performance of these transition metal phosphides in Fe-purified 1 M KOH. Interestingly, the overpotential of NiP_x significantly increased from 377 to 460 mV by removing Fe impurities, and the Tafel slope almost doubled its initial value (Figure 106a, iii). Looking closely at the redox peaks (Figure 106a, iv), both the NiP_x and CoP_x samples exhibited clear oxidation peaks. The FeP_x sample was unaffected by the KOH electrolyte change, and the activity was the same. EDX measurements revealed an increase in the oxygen-to-metal ratio, confirming the partial

https://doi.org/10.1021/acs.chemrev.3c00005
Chem. Rev. 2023, 123, 12795–13208

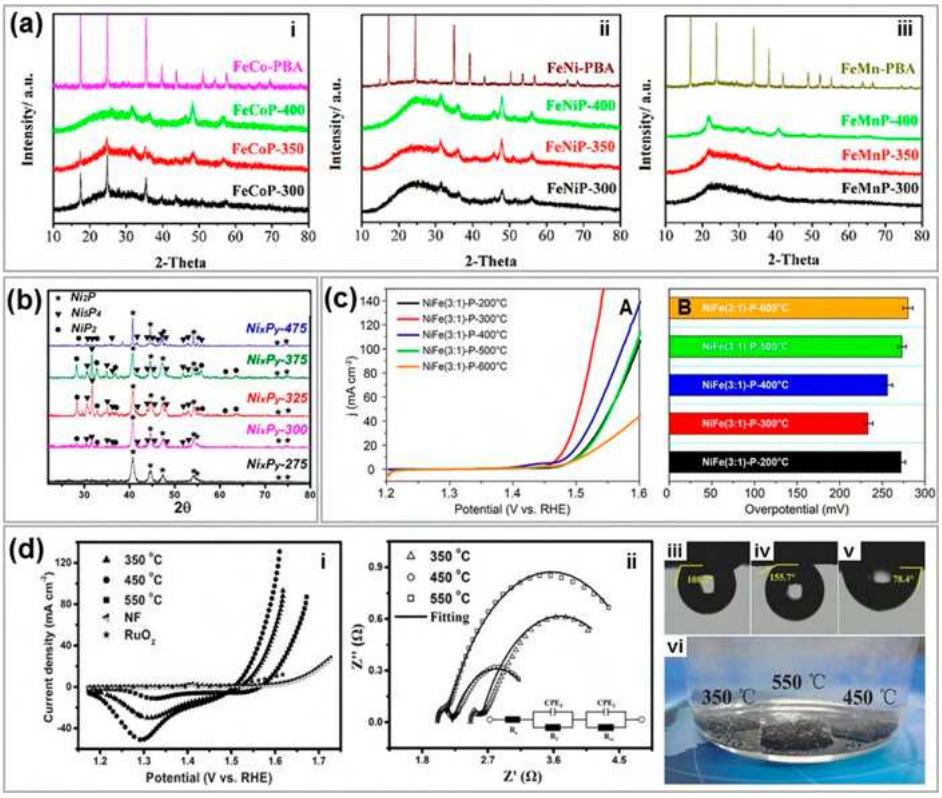


Figure 105. Effects of the phosphidation temperature on the catalytic performance of transition metal phosphides. (a) XRD patterns of Fe-based Prussian blue analogs and corresponding phosphides at different temperatures: (i) FeCoP, (ii) FeNiP, and (iii) FeMnP. Reprinted with permission from ref 436. Copyright 2020 Elsevier. (b) XRD patterns of Ni_xP_y-T electrocatalysts at different phosphidation temperatures. Reprinted with permission from ref 511. Copyright 2016 American Chemical Society. (c) (A) OER activity of NiFe phosphide nanocomposites synthesized at different phosphidation temperatures; (B) overpotentials at 10 mA·cm^{-2}. Reprinted with permission from ref 458. Copyright 2018 Royal Society of Chemistry. (d) Effects of the phosphidation temperature on Cu_3P/NF electrocatalysts: contact angle measurements of (iii) Cu_3P-350, (iv) Cu_3P-450, and (v) Cu_3P-550 electrodes and (vi) bubble generation in 10% H_2O_2. Reprinted with permission from ref 588. Copyright 2016 Wiley.

oxidation of the material. Furthermore, the authors also found an activity decrease of FeP_x after leaving the catalyst 24 h under ambient conditions. This activity decrease was attributed to the oxidation of Fe^{2+} into Fe^{3+}, suggesting that the oxidation via contact with O_2 or cycling in the KOH electrolyte would render different active sites, being an inactive oxide in the former and active oxides/hydroxides in the latter. Similarly, Tang *et al.* prepared CoP and MoP with N-doped graphitic carbon layers on carbon cloth.[449] As displayed in Figure 106b, the authors compared the activity and kinetics of the composite (CoP/MoP@NC/CC) and the monometallic transition metal phosphides (CoP@NC/CC and MoP@NC/CC). Notably, both the composite and the Co-based transition metal phosphide exhibited comparable activities (overpotential: 270 mV at 10 mA·cm^{-2}), while the MoP sample exhibited a high overpotential of 420 mV at 10 mA·cm^{-2} (Figure 106b, ii). A similar trend was observed for the Tafel analysis, where the MoP sample exhibited the largest Tafel slope (Figure 106b, iii). These results suggest that the superior performance of the composite mainly arises from CoP, although the role of MoP was not discussed in detail by the authors. Further SEM, XRD, and XPS analysis after 20 h CA tests at an overpotential of 300 mV revealed that the CoP/MoP@NC/CC precatalyst was partially transformed into $Co(OH)_2$, CoOOH, and MoO_x species being considered as the real active sites.

Although these two case studies demonstrate that the metal has an essential role in the OER activity of transition metal phosphides, the reason why different metals produce distinct behaviors is still elusive. Therefore, it is necessary to conduct systematic studies to understand the activity and stability trends of transition metal phosphides with different metals (e.g., Fe, Co, Ni, Mo, Mn, Cu, etc.) and to unveil the driving forces behind the transformations using theoretical and experimental approaches.

4.2.3.3. Metal/Phosphorus Composition Effects. Recent reports have studied the activity trends of monometallic transition metal phosphides using different *M*/P compositions. Menezes *et al.* compared the OER performance of two nickel phosphides, Ni_2P and $Ni_{12}P_5$, in alkaline media.[494] As seen in Figure 107a, i, the $Ni_{12}P_5$ catalyst exhibited a higher OER activity than Ni_2P. Post-OER TEM analysis revealed the formation of a thick amorphous layer (10−15 nm) for the crystalline $Ni_{12}P_5$ core (Figure 107a, ii), while a thinner amorphous shell (8−10 nm) formed over the crystalline Ni_2P core (Figure 107a, iii). HRTEM, XAS, and XPS analyses confirmed NiOOH/$Ni(OH)_2$ and phosphate species formation. The superior OER activity of $Ni_{12}P_5$ was attributed to a higher quantity of Ni sites, providing more NiOOH/$Ni(OH)_2$ species after the reconstruction process in the amorphous shell. Notably, this trend followed an opposite direction for the HER, as larger concentrations of P and Pi groups were linked to the superior HER activity of Ni_2P. According to this study, the difference in OER activity of transition metal phosphides can be explained by the number of active sites generated via the reconstruction process. Similarly, Jin *et al.* performed an extensive comparison of the performance between Co_2P and

https://doi.org/10.1021/acs.chemrev.3c00005
Chem. Rev. 2023, 123, 12795−13208

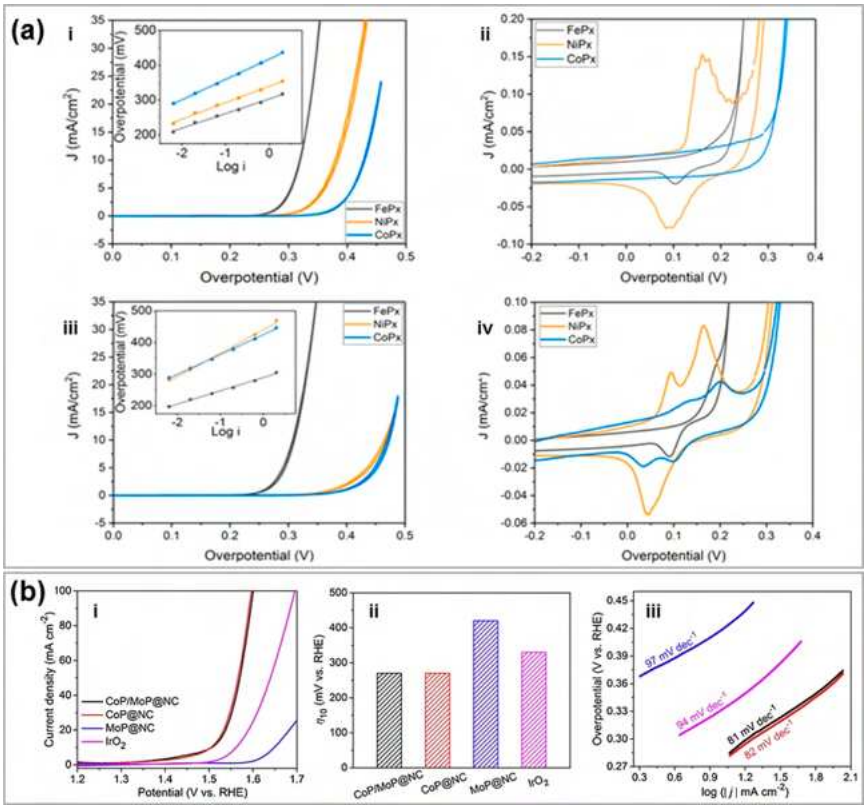


Figure 106. Evaluation of the metal effect in transition metal phosphides. (a) Comparison of iron triad (Ni, Co, Fe) phosphides: (i) CV polarization curves after Tafel analysis in 1 M KOH electrolyte (inset: Tafel plots); (ii) enlarged view of the reversible redox peaks; (iii) CV scans after Tafel analysis in Fe-purified 1 M KOH (inset: Tafel plots); (iv) enlarged view of the redox peaks. Reprinted with permission from ref 454. Copyright 2018 American Chemical Society. (b) Co- and Mo-based phosphides coated with N-doped graphitic carbon layers: (i) OER polarization curves; (ii) overpotentials at 10 mA·cm^{-2} in 1 M KOH electrolyte; (iii) Tafel slopes. Reprinted with permission from ref 449. Copyright 2019 Elsevier.

CoP electrocatalysts.[512] From XPS results (Figure 107b, A), there was a difference in binding energies of the Co $2p_{3/2}$ peaks, where CoP was shifted toward higher binding energy. This suggests that in CoP, the oxidation state of Co was increased, while the lower P content in Co_2P can be associated with its lower valence of Co. EIS measurements (Figure 107b, B) revealed that Co_2P is more conductive than CoP. Figure 107b, C shows that Co_2P exhibited a higher OER activity and a larger oxidation ($Co^{2+} \rightarrow Co^{3+}$) peak at ~1.2 V_{RHE}. The as-formed Co^{3+} species become the OER active sites. The Co_2P precatalyst also exhibited the lowest Tafel slope (Figure 107b, D). Furthermore, DFT calculations were performed. A higher density of states (DOS) near the Fermi level for Co_2P suggests that this composition exhibits a higher electrical conductivity (Figure 107b, E). The increased electron density for the $Co_2P(020)$ plane also supports this finding (Figure 107b, E inset). As shown in Figure 107b, F, Co_2P allows for a better structure with excellent electron transport and abundant Co sites. Finally, the authors performed potential-controlled XPS measurements to monitor the *in situ* transformation of Co_2P during the OER (Figure 107b, G). Notably, activation CV scans below the OER onset (from −0.2 to 0.4 V_{RHE}) produced $Co(OH)_2$ species, as denoted by the positive shift of the Co 2p peak. Under OER potentials (0.4 to 1.5 V_{RHE}), Co exhibited a higher valence state, while the negative binding energy shift for the P 2p suggests the formation of phosphate. HRTEM images confirmed the generation of an amorphous layer after the OER. Undoubtedly, these results confirm the reconstruction of Co_2P into cobalt oxyhydroxide species, and the superior OER activity of Co_2P is mainly derived from a higher quantity of Co sites and higher electrical conductivity.

The reported trends suggest that compositions with higher metal content tend to exhibit better OER performance, which is strongly related to the oxidation and generation of high-valent metal sites. Interestingly, parallel HER validations have also supported that higher P content is not favorable for the OER but improves the HER instead.

4.2.3.4. Metal-Doping Effects. Several studies of heteroatom-doped transition metal phosphide precatalysts to improve specific properties such as conductivity and stability have been conducted. This section discusses the effect of metal doping (e.g., Mo, Mn, Fe, etc.). Liu *et al.* prepared Fe-doped Co_2P NPs and evaluated their OER performance.[464] The Fe-doped Co_2P precatalyst consisted of several nanoparticles in a granular morphology (Figures 108a, i–ii). EDX elemental mappings revealed a uniform distribution of Fe, Co, and P (Figure 108a, iii). However, only the $Co_2P(121)$ plane was indexed in the HRTEM image (Figure 108a, iv), suggesting that Fe was successfully incorporated into the material. The Fe-doped Co_2P precatalyst exhibited the highest OER activity (Figure 108a, v) and lowest Tafel slope (Figure 108a, vi) compared to the Fe-free Co_2P and Fe_2P. The Fe-doped precatalyst also exhibited the largest ECSA (Figure 108a, vii) and lowest charge transfer resistance from EIS plots (Figure 108a, viii). After 28 h CA tests at 1.53 V_{RHE}, XRD, SEM, TEM, and XPS analyses revealed the *in situ* formation of CoOOH

https://doi.org/10.1021/acs.chemrev.3c00005
Chem. Rev. 2023, 123, 12795−13208

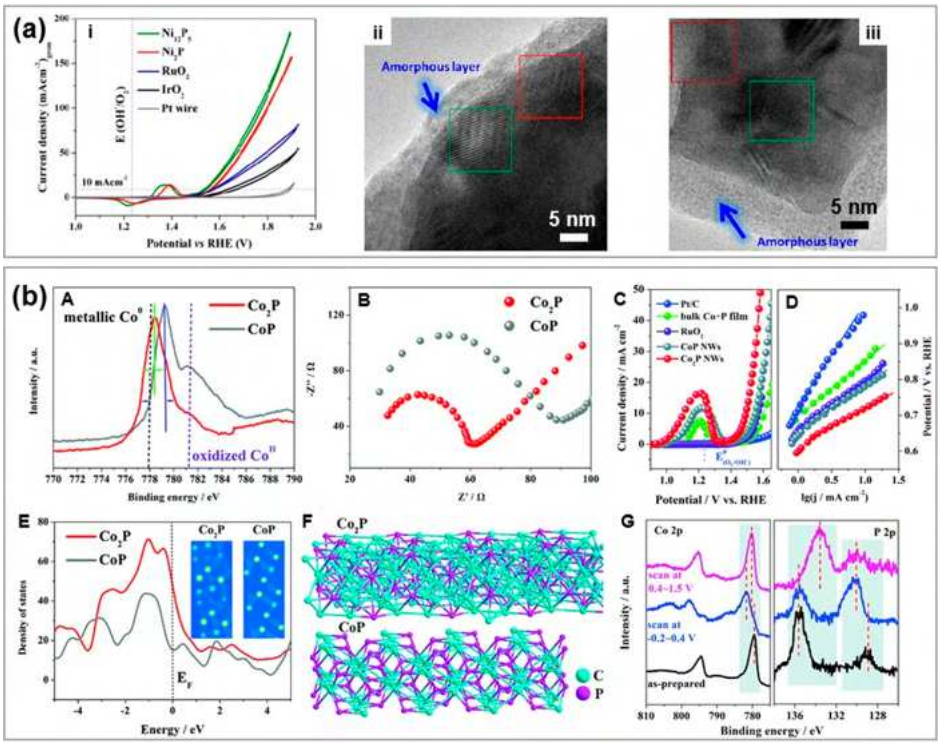


Figure 107. Evaluation of metal/phosphorus compositional effects on the performance of transition metal phosphides. (a) Activity comparison of $Ni_{12}P_5$ and Ni_2P catalysts: (i) CV scans of the materials deposited on FTO substrates in 1 M KOH; (ii, iii) HRTEM images of (ii) $Ni_{12}P_5$ and (iii) Ni_2P after CA stability tests for 16 h. Reprinted with permission from ref 494. Copyright 2017 American Chemical Society. (b) Comparison of metallic Co_2P and CoP catalysts: (A) XPS spectra; (B) EIS plots; (C) OER polarization curves in 1 M KOH; (D) Tafel plots; (E) calculated DOS and electron density distribution of the (020) plane; (F) supercell models; (G) controlled-potential XPS spectra. Reprinted with permission from ref 512. Copyright 2016 Royal Society of Chemistry.

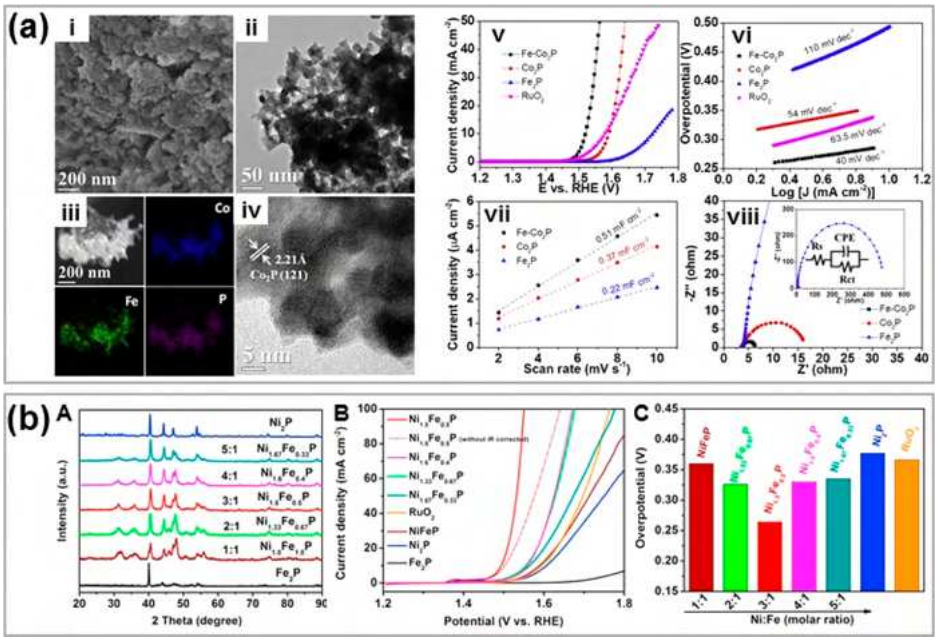


Figure 108. Metal doping effects on the performance of transition metal phosphides. (a) Fe-doped Co_2P nanoparticles: (i) SEM, (ii) TEM, (iii) elemental mapping, and (iv) HRTEM images of the as-prepared material; (v) LSV curves; (vi) Tafel slopes; (vii) the relationship of the current density at 1.10 V_{RHE} at different scan rates; (viii) EIS plots. Reprinted with permission from ref 464. Copyright 2018 Elsevier. (b) Fe-doped Ni_2P nanosheets: (A) XRD patterns at different chemical compositions; (B) OER polarization curves in 1 M KOH; (C) overpotentials at 10 mA·cm^{-2}. Reprinted with permission from ref 491. Copyright 2017 Elsevier.

species, and the granular structures were transformed into NPs covered by numerous nanosheets. Although this evidence suggests that Fe doping was responsible for increasing the activity, the precise role of Fe was not described. However,

https://doi.org/10.1021/acs.chemrev.3c00005
Chem. Rev. 2023, 123, 12795−13208

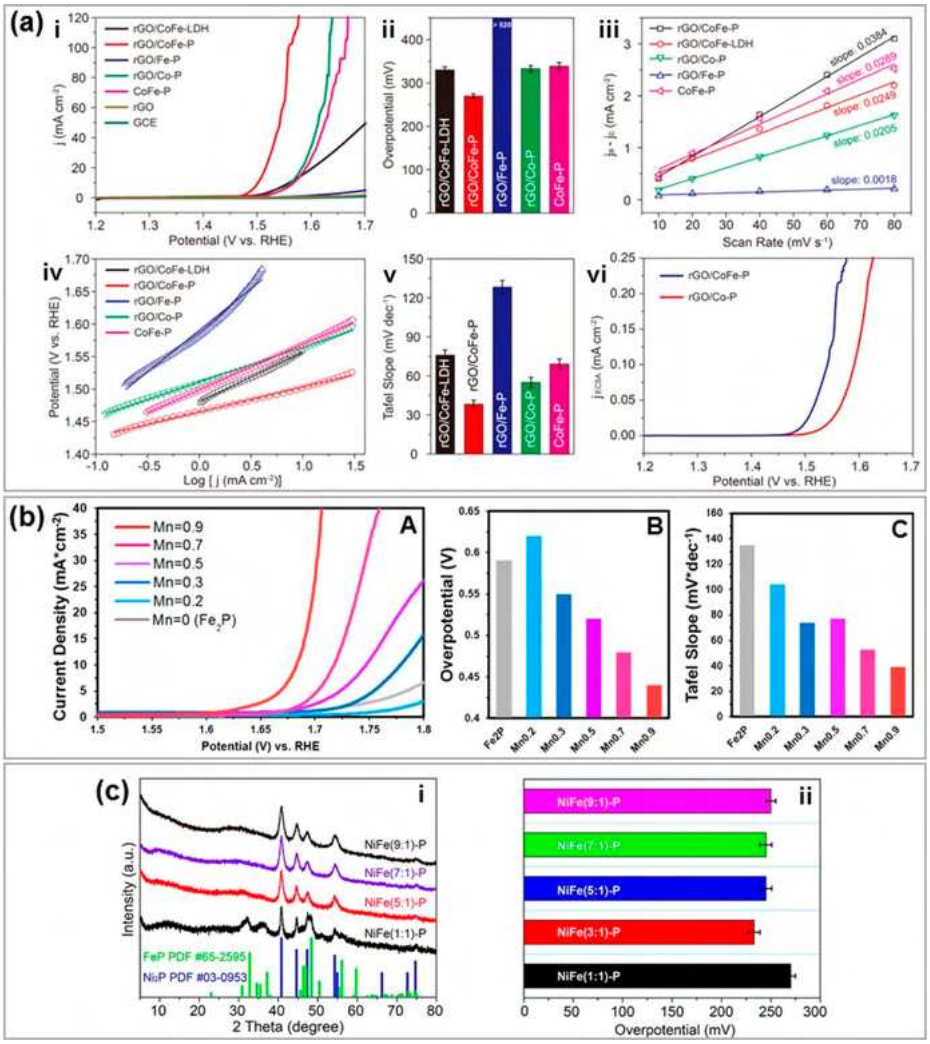


Figure 109. Performance trends of multi-cation transition metal phosphides. (a) Electrochemical characterization of Co- and Fe-based phosphides on rGO: (i) OER polarization curves; (ii) overpotentials at 10 mA·cm^{-2}; (iii) C_{dl} measurements; (iv) Tafel plots; (v) Tafel slopes; (vi) ECSA-normalized polarization curves. Reprinted with permission from ref 444. Copyright 2019 American Chemical Society. (b) OER performance of $Fe_{2-x}Mn_xP$ nanorods with controlled Mn incorporation ($0 \leq x \leq 0.9$): (A) polarization curves; (B) overpotentials at 10 mA·cm^{-2}; (C) Tafel slopes. Reprinted with permission from ref 492. Copyright 2017 American Chemical Society. (c) Study of bimetallic Ni-Fe phosphide nanocomposites: (i) XRD patterns of NiFe(n:1)-P samples; (ii) overpotentials at 10 mA·cm^{-2}. Reprinted with permission from ref 458. Copyright 2018 Royal Society of Chemistry.

different studies have suggested that defects generated by doping promote the generation of metal oxides/oxyhydroxides as active sites, explaining the enhanced activity and stability.[340,411] Furthermore, FeOOH species were not seen, suggesting that Fe did not participate directly during the OER. Similarly, Huang *et al.* prepared the Fe-doped Ni_2P sample with different Fe doping levels.[491] XRD measurements revealed that the samples mainly consist of Ni_2P, suggesting that Fe was successfully incorporated (Figure 108b, A). As seen in Figures 108b, B and C, the $Ni_{1.5}Fe_{0.5}P$ (Ni:Fe = 3:1) precatalyst exhibited the lowest overpotential (264 mV at 10 mA·cm^{-2}). The incorporation of Fe decreased the size of the nanosheets, providing more active sites and improved mass transport. Finally, post-OER SEM, EDX, and XPS analysis revealed that the samples partially oxidized during the OER and that the concentration of P decreased considerably. However, the constant potential observed for 5 h CP tests at 10 mA·cm^{-2} denotes that the oxidized materials were stable and became the OER active species.

These case studies confirm the OER enhancement due to the doping of heteroatoms into the transition metal phosphide. In the case of Huang *et al.*, the incorporation of Fe was related to the change in morphology, tuning the number of active sites. Future studies should carefully observe any changes in conductivity, stability, or morphology when dopants are introduced into the precatalyst in order to detect any noticeable trends.

4.2.3.5. Multi-cation Effects. Contrary to other factors, the effect of adding a secondary metal to the transition metal phosphide on OER activity has been extensively reported (refs 444, 458, 460, 467, 469, 471, 474, 492, 505, 508, 510, 513, 537, and 574). This means that bimetallic transition metal phosphides are very common, and most of the reports have varied the metal ratio to find the composition with the best performance. Li and Zeng demonstrated that the bimetallic CoFe phosphides exhibit superior performance compared to their monometallic counterparts.[444] Notably, various Co- and Fe-based transition metal phosphides (Co-P, CoFe-P, Fe-P)

https://doi.org/10.1021/acs.chemrev.3c00005
Chem. Rev. 2023, 123, 12795−13208

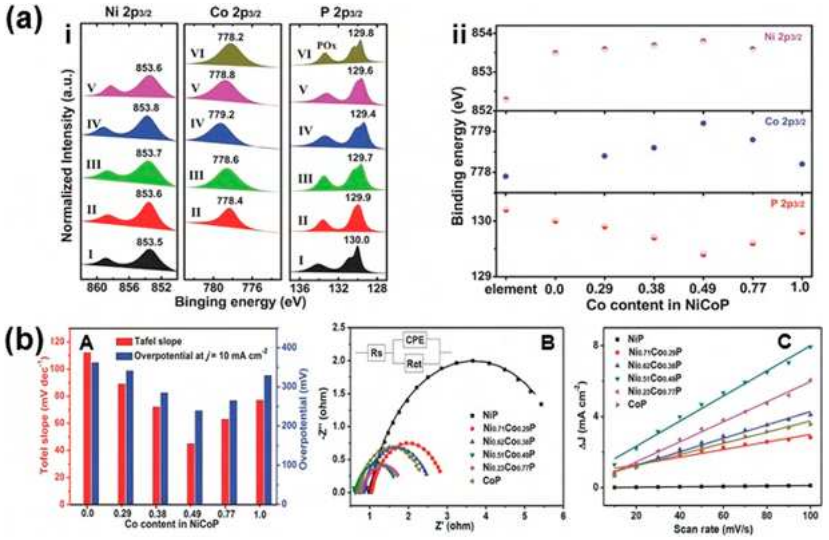


Figure 110. Performance trends of multi-cation transition metal phosphides. (a) Evaluation of electrodeposited NiCo phosphides with triple-layered structure: (i) XPS spectra at different compositions; (ii) binding energy shifts. (b) Electrochemical characterization: (A) overpotentials at 10 mA·cm^{-2} and Tafel slopes; (B) EIS plots; (C) C_{dl} measurements. Reprinted with permission from ref 521. Copyright 2016 Wiley.

were synthesized on reduced graphene oxide (rGO) from their metal LDH precursors. As shown in Figure 109a, i, the bimetallic phosphide (rGO/CoFe-P) exhibited the lowest overpotential (270 mV at 10 mA·cm^{-2}). Moreover, note that the activities of the LDH precursor and the rGO/Co-P were comparable (Figure 109a, ii), although the precursor exhibited high overpotentials at large current densities (Figure 109a, i). The overpotential of CoFe-P without rGO was also comparable to that of monometallic rGO/Co-P, suggesting that the substrate affects the activity. The rGO/CoFe-P precatalyst also exhibited the highest ECSA (Figure 109a, iii) and the lowest Tafel slope (Figures 109a, iv–v). Furthermore, by normalizing the polarization curves using ECSA (Figure 109a, vi), it is evident that the activity difference between the bimetallic and the monometallic phosphide comes from the incorporation of Fe and not from the substrate. Notably, XPS analysis of the as-prepared samples showed that Fe incorporation shifted the Co 2p peak positively and the P 2p peak negatively, suggesting that intentional Fe incorporation enhances the electron interaction between Co and P. The sample with a Co/Fe ratio of 3:1 exhibited the best performance, suggesting that an increased number of Co sites is advantageous. After the stability tests, TEM and XPS analyses confirmed oxidized Co, Fe, and P species. Overall, the authors concluded that the presence of Fe modified the Co–O* bond strength in the OER mechanism, thus lowering the activation energy compared to the monometallic counterpart (i.e., Co-P). Trimetallic phosphides (rGO/CoNiFe-P) produced similar trends, demonstrating that additional metals can modulate the electronic structure and, therefore, improve the OER activity. Li *et al.* synthesized bimetallic $Fe_{2-x}Mn_xP$ nanorods and varied the Mn content ($0 < x < 0.9$).[492] Interestingly, by increasing the content of Mn, the OER activity was enhanced (Figure 109b, A). Although adding small amounts of Mn ($x = 0.2$) increased the overpotential (Figure 109b, B), further addition significantly improved the OER activity. A similar trend was observed for the Tafel slope (Figure 109b, C), suggesting that the Mn incorporation into Fe_2P directly affects the OER mechanism. The authors suggested that this trend could be explained by morphological changes (i.e., shorter nanorods) and synergism between Mn and Fe sites (i.e., faster kinetics) at higher Mn content. In particular, the presence of Mn might decrease the energy barrier associated with the O–O bond formation.[607,608] Moreover, post-OER XPS, EDX, and FTIR analyses confirmed the oxidation of Fe and Mn sites and the generation of phosphates during the OER. Similarly, Li and Zeng prepared bimetallic NiFe phosphide precatalysts with different Ni/Fe ratios.[458] As the Ni content was increased in NiFe-P, the phosphide phase varied, as observed in the XRD patterns (Figure 109c, i). While the samples with the Ni/Fe ratios of 1:1 and 3:1 were composed of Ni_2P and FeP phases, higher Ni contents of NiFe(n:1)-P (n = 5, 7, and 9) produced only Fe-doped Ni_2P. Notably, the NiFe(3:1)-P sample exhibited the highest activity, while too low or high Ni content produced higher overpotentials. Moreover, post-OER XPS and EDX results confirmed the oxidation of the samples. This trend suggests that there is an optimal NiFe composition that enables adequate electron transfer. Furthermore, the as-oxidized Ni and Fe species were identified as OER active sites. This trend is likely related to the ideal compositions of NiFe oxyhydroxides, which are still under debate.[609−611]

The synergy between Ni and Co in bimetallic phosphides has also been studied. Yu *et al.* compared the effect of Co content in bimetallic NiCoP precatalysts.[521] Analogous to previous studies, it was found that the activity was strongly related to the Ni/Co ratio. First, XPS was used to compare the binding energies of the precatalysts at different Ni/Co ratios (Figure 110a, i). Notably, metal 2p peaks shifted toward more positive binding energies, while the P 2p peak shifted toward negative values, suggesting partial electron transfer (i.e., electron donation for P, electron transfer for Ni/Co). The $Ni_{0.51}Co_{0.49}P$ sample exhibits the highest partial positive and negative charges (Figure 110a, ii). This means that the largest electric dipole is formed at that composition and that the energy barrier for the OER is reduced. Interestingly, overpotential and Tafel slope trends coincide with this description (Figure 110b, A). Furthermore, the $Ni_{0.51}Co_{0.49}P$ sample exhibited the lowest charge transfer resistance from EIS plots (Figure 110b, B) and the largest ECSA from C_{dl} measurements

https://doi.org/10.1021/acs.chemrev.3c00005
Chem. Rev. 2023, 123, 12795−13208

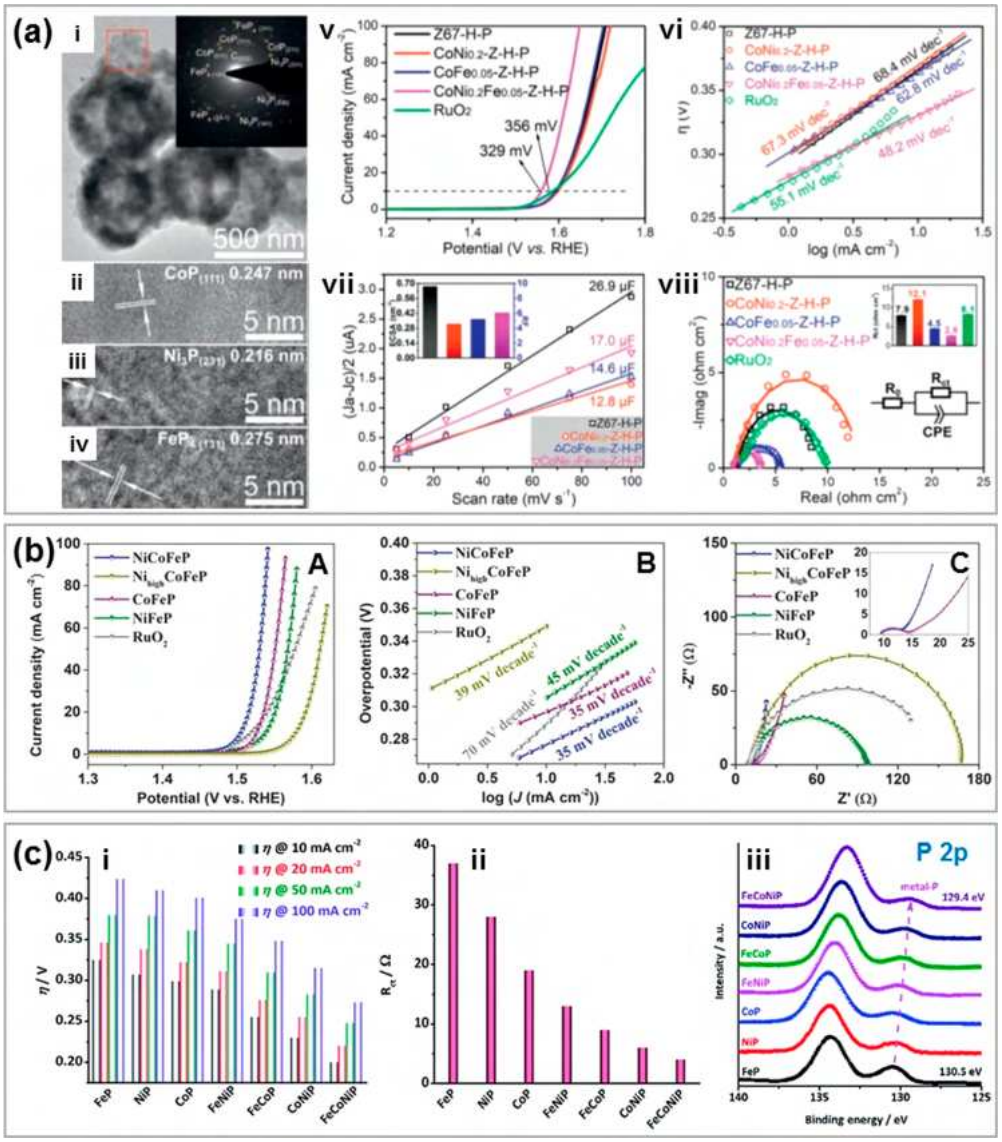


Figure 111. Performance trends of multi-cation transition metal phosphides. (a) Evaluation of MOF-derived tricomponent metal (Fe, Co, Ni) phosphides: (i) TEM image with SAED pattern as inset; (ii–iv) crystal planes for (i) CoP, (ii) Ni_3P, and (iv) FeP_4. (v–viii) Electrochemical characterization: (v) LSV curves; (vi) Tafel slopes; (vii) C_{dl} measurements; (viii) and EIS plots. Reprinted with permission from ref 469. Copyright 2018 Wiley. (b) Electrochemical characterization of NiCoFe phosphide nanocubes: (A) OER polarization curves; (B) Tafel slopes; (C) EIS plots. Reprinted with permission from ref 463. Copyright 2018 Wiley. (c) Evaluation of mono-, bi-, and trimetallic phosphide OER precatalysts: (i) overpotentials at 10 $mA{\cdot}cm^{-2}$ trends; (ii) charge transfer resistance trends from EIS analysis; (iii) high-resolution core-level XPS spectra of the P 2p signal. Reprinted with permission from ref 93. Copyright 2018 Royal Society of Chemistry.

(Figure 110b, C). Therefore, it was concluded that the incorporation of Co induced these conductivity, kinetics, and surface area changes. Furthermore, the use of XPS revealed how the binding energies shifted at different compositions, providing a more reasonable explanation of the multi-cation effect. Finally, partial oxidation was also confirmed after the OER by post-OER analysis characterizations.

Trimetallic phosphides have also been studied. Wang *et al.* synthesized Fe-, Co-, and Ni-based phosphides using MOF precursors and evaluated their OER performance in 1 M NaOH.[469] After phosphidation, the as-synthesized precatalysts exhibited a hollow sphere morphology with small particles along the surface. According to HRTEM analysis, the tricomponent sample (sample name: $CoNi_{0.2}Fe_{0.05}$-Z-H-P) consisted of CoP, Ni_3P, and FeP_4 phases (Figures 111a, i–iv). The trimetallic transition metal phosphide exhibited the highest activity from electrochemical tests, surpassing the bimetallic counterparts (Figure 111a, v). The material also showed the lowest Tafel slope (Figure 111a, vi), suggesting improved OER kinetics. Although ZIF-67 showed a large ECSA, the trimetallic transition metal phosphide had the largest ECSA among the synthesized transition metal phosphides (Figure 111a, vii). EIS plots also revealed superior conductivity for the tricomponent phosphide (Figure 111a, viii). By considering XAS measurements of the as-prepared sample, the tricomponent phosphide exhibited increased P sites and more Co 4p unoccupied states, improving the charge transfer. Together with the observed reconstruction and partial oxidation during the OER, the authors concluded that the material exhibited a reduced activation energy thanks to the incorporation of three metals. In a similar approach, Guo *et al.* synthesized tricomponent phosphide nanocubes through the

https://doi.org/10.1021/acs.chemrev.3c00005
Chem. Rev. 2023, 123, 12795–13208

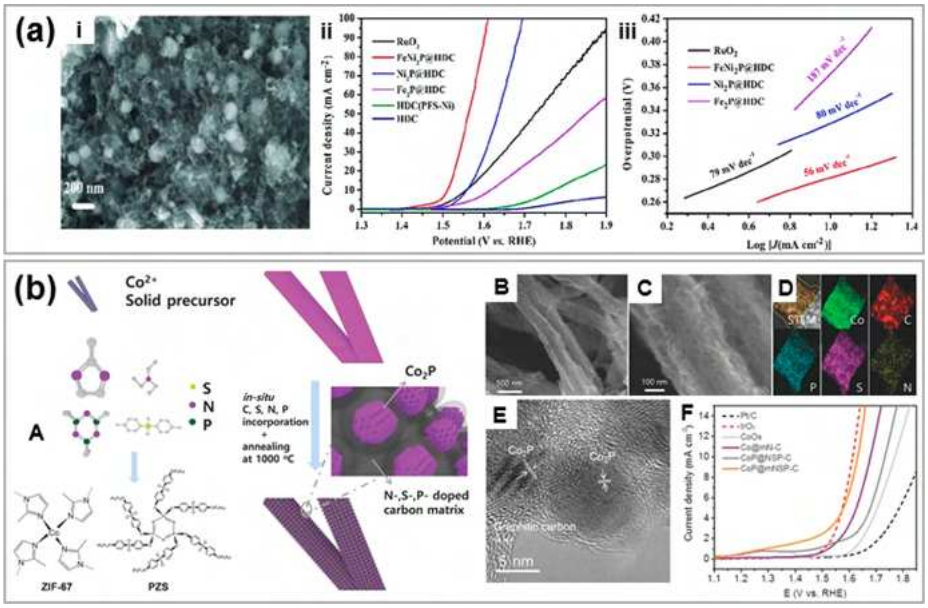


Figure 112. Heteroatom doping effects on the performance of transition metal phosphides. (a) Mesoporous heteroatom-doped carbon-supported (HDC) NiFe phosphide from Ni-coagulated iron sludge: (i) SEM image of the $FeNi_2P$@HDC electrode; (ii) LSV curves of different electrocatalysts supported on HDC in 1 M KOH electrolyte; (iii) Tafel slopes. Reprinted with permission from ref 437. Copyright 2020 Wiley. (b) Heteroatom-doped nanocarbon hybrid cobalt phosphide catalyst: (A) schematic illustration of the material synthesis; (B–E) SEM images (B, C), elemental mapping (D), and HRTEM image (E) of the as-prepared CoP@mNSP-C electrode; (F) OER polarization curves. Reprinted with permission from ref 487. Copyright 2017 Wiley.

phosphidation of NiCoFe Prussian-blue analogues.[463] As expected, the incorporation of a third metal (i.e., NiCoFeP) increased the OER activity (Figure 111b, A) and decreased the Tafel slopes (Figure 111b, B) under an alkaline medium (1 M KOH). The tricomponent phosphide also exhibited the lowest charge transfer resistance (Figure 111b, C), denoting excellent electrical conductivity. Although the multi-cation effect was not discussed in detail, the authors concluded that introducing a third metal accelerated the water electrolysis process by reducing the charge transfer at the electrode-electrolyte interface and providing numerous active sites. Notably, post-analysis also revealed the formation of oxide/oxyhydroxide species. Finally, Xu *et al.* performed an extensive comparison of several Fe-, Co-, and Ni-based mono-, bi-, and trimetallic phosphide precatalysts with equimolar metal components in 1 M KOH.[93] As depicted in Figure 111c, i, an evident decrease in overpotential was observed as the number of metals was increased in the transition metal phosphide. Furthermore, notice that mono- and bimetallic transition metal phosphides can be readily compared with their counterparts. For instance, FeP exhibited the highest overpotentials, whereas CoP exhibited the lowest among monometallic samples. Furthermore, the CoNi pair exhibited the lowest overpotentials among bimetallic transition metal phosphides. Notice that the charge transfer resistance (R_{ct}) followed the same trend, which agrees with previous studies. Notably, the authors also found through XPS measurements that the metal 2p peaks shifted toward higher binding energies with more components, while the P 2p peak shifted toward more negative binding energies. This suggests that as more cations are introduced into the precatalyst, the electron transfer from the metal to P is enhanced, thus favoring the formation of high-valent species. This means that bi- and trimetallic transition metal phosphides facilitate the formation of *M*OH species where *M* possesses a high oxidation state. Furthermore, the Tafel analysis suggests that the adsorption of OH^- groups was favored. CP stability tests for 24 h caused the partial oxidation of the materials, and oxyhydroxide species were formed.

Thanks to several case studies that provided extensive XPS and electrochemical characterization of different multi-cation compositions, specific trends can be interpreted: (i) incorporation of additional cations (e.g., Ni, Co, Fe) into the transition metal phosphide tends to increase the electron transfer toward P atoms, increasing the oxidation state of the transition metal; (ii) the synergy between these metal sites decreases the activation barriers for the OER, in particular, the OH^- adsorption step; and (iii) incorporation of additional cation(s) might modify the morphology and structural properties of the film, creating rougher surfaces, as well as thinner/smaller structures. These factors explain the OER activity trends of the reported transition metal phosphide precatalysts. Although XPS and Tafel analyses seem to give reasonable explanations for these trends, we consider that more studies regarding morphological changes are needed to give a more comprehensive view of the multi-cation effect. Also, more studies focused on other transition metals, such as Cu, Mo, or Mn, could give additional insights into these trends.

4.2.3.6. Substrate Effects. Typically, powder-based electrocatalysts are dispersed in a binder and deposited on conductive, flat substrates, such as the glassy carbon electrode (GCE). However, there is an increasing interest in growing transition metal *X*-ides on cheap supports with high electrical conductivity and large geometric surface area. In the field of transition metal phosphides, these supports include carbon paper/cloth/fibers,[470,475,522,537,554] Cu foil,[495] Co foil,[578] Ni foil,[438,525,582] Ti foil,[488] conductive glass [indium tin oxide (ITO), F-doped tin oxide (FTO)],[448,494,567] and metallic 3D electrodes such as Cu mesh,[517] Fe foam,[451] NiFe foam,[481] and Ni foam.[107,471,479,485,518,582] Therefore, it is necessary to unveil the effect of these substrates on the OER activity and stability.

https://doi.org/10.1021/acs.chemrev.3c00005
Chem. Rev. 2023, 123, 12795–13208

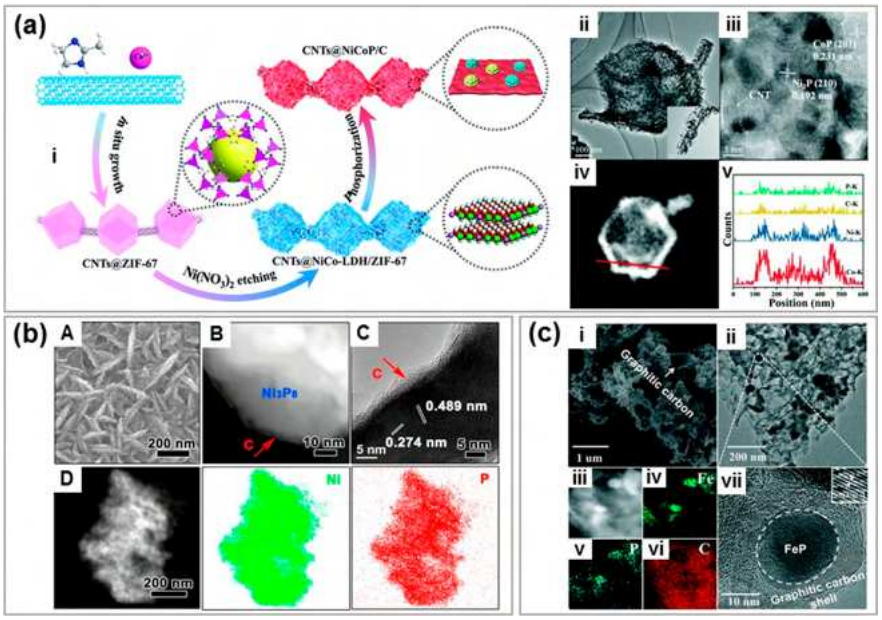


Figure 113. (a) Hierarchical CNTs@NiCoP/C catalysts: (i) schematic illustration of the synthesis method; (ii–iv) TEM (ii), HRTEM (iii), and HAADF-STEM (iv) images of the as-prepared materials; (v) EDX line scan spectra. Reprinted with permission from ref 477. Copyright 2018 Royal Society of Chemistry. (b) Characterization of the Ni_8P_3@C core@shell nanosheets array: (A–C) SEM (A), HAADF (B), and HRTEM (C) images; (D) STEM images with elemental mapping. Reprinted with permission from ref 402. Copyright 2016 American Chemical Society. (c) FeP@GPC electrocatalyst: SEM (i), TEM (ii), dark-field TEM (iii) with elemental mapping (iv–vi), and HRTEM (vii) images. Reprinted with permission from ref 403. Copyright 2018 Royal Society of Chemistry.

In the transition metal phosphide field, only a few studies have studied the effect of different substrates on the OER activity and stability. P-block heteroatom-doped carbon substrates are a prevalent strategy used to improve the performance of transition metal phosphides. Carbon-based precursors with high content of heteroatoms are usually employed, and the doped material is obtained after typical hydrothermal or gas-solid thermal reactions. In a novel approach, Li *et al.* employed sludge waste from wastewater treatment plants to produce mesoporous heteroatom (N)-doped carbon (HDC) supports for NiFe phosphides.[437] As displayed in Figure 112a, i, the as-prepared $FeNi_2P$@HDC sample consisted of a porous matrix with uniformly dispersed NPs, conferring a large surface area. Regarding the OER activity (Figure 112a, ii), the $FeNi_2P$@HDC precatalyst exhibited a low overpotential of 280 mV at 10 $mA{\cdot}cm^{-2}$ that is significantly lower than that of the monometallic counterparts and RuO_2. A similar trend was found for the Tafel slopes (Figure 112a, iii), suggesting that the bimetallic phosphide supported on HDC expedites the charge transfer. Moreover, subsequent stability tests and post-OER XRD, XPS, and TEM-EDX analyses confirmed the oxidation of $FeNi_2P$ into $Ni(OH)_2$ and FeOOH active species. Notably, the authors attributed the superior performance of the $FeNi_2P$@HDC precatalyst to the superior conductivity and wettability of the HDC and the increased surface area that provided more active sites after the reconstruction.

Similarly, Ahn and Manthiram supported CoP NPs on a N, S, P-doped carbon matrix from a MOF precursor.[487] Specifically, ultrasmall CoP NPs dispersed on a heteroatom-doped carbon matrix (CoP@mNSP-C). SEM images revealed the 1D structure (Figures 112b, B and C), and STEM-EDX elemental mappings confirmed the uniform distribution of all of the elements (Figure 112b D). From HRTEM images, the presence of Co_2P and graphitic carbon was confirmed (Figure 112b, E). The CoP@mNSP-C sample exhibited the highest OER activity among all samples (Figure 112b, F), including metallic Co, CoO_x, and CoP@NSP-C (without 2-methylimidazole during the synthesis). Importantly, OER, ORR, and zinc–air battery (ZAB) stability tests transformed the precatalyst into Cobalt oxide, as confirmed by post-OER XRD, XPS, and HRTEM analysis. However, the 1D structure was preserved, and the material exhibited a stable performance even after 80 h of continuous operation using potential cycling at 20 $mA{\cdot}cm^{-2}$. Overall, the CoP@mNSP-C precatalyst exhibited notable features, such as minimized corrosion of the carbon substrate, higher OER activity due to the *in situ* transformation of Co_2P, and the carbon structure giving a large surface area. However, even though it was evident that the material exhibited superior performance and stability, the precise role of the heteroatoms was not studied in detail. Nevertheless, this precatalyst demonstrated outstanding performance for two reactions (OER and ORR) in energy conversion/strorage systems [e.g., water electrolyzer and zinc–air battery (ZAB)], and stability was significantly increased by using a robust, heteroatom-doped carbon substrate. Other studies have confirmed that heteroatom-doped graphitic carbon improves the performance of the final transition metal phosphide. For instance, Yao *et al.* compared Fe_2P on P-doped amorphous carbon (Fe_2P@APC) with FeP encapsulated in P-doped graphitic carbon (FeP@GPC).[403] The authors found that the latter exhibited the best performance, and this was attributed to the superior conductivity, decreased corrosion, and large surface area by preventing agglomeration. However, the exact role of P was not discussed in detail, and more studies focused on the particular role of dopants are needed to determine their specific effect on the enhanced activity/stability.

4.2.3.7. Composite Materials Effects. Composite materials (e.g., transition metal phosphide + carbon-based matrix,

https://doi.org/10.1021/acs.chemrev.3c00005
Chem. Rev. 2023, 123, 12795–13208

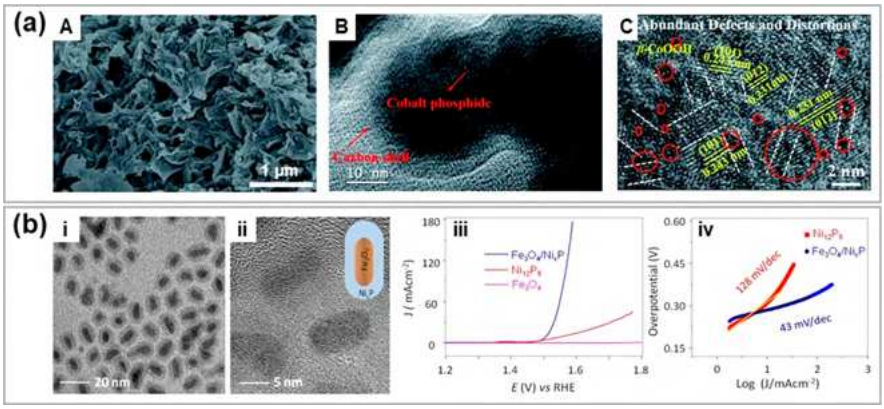


Figure 114. (a) 3D hierarchical R-CoP$_x$@C precatalyst: (A, B) SEM (A) and HRTEM (B) images; (C) HRTEM image with lattice distortion regions. Reprinted with permission from ref 476. Copyright 2018 Royal Society of Chemistry. (b) Core-shell Fe_3O_4/Ni_xP electrocatalyst: (i, ii) TEM images of the core-shell nanostructures; (iii) polarization curves; (iv) Tafel plots. Reprinted with permission from ref 462. Copyright 2018 American Chemical Society.

transition metal phosphide + transition metal oxide, etc.) have been synthesized to enhance the electrocatalytic properties of transition metal phosphides and conductivity, stability, or hydrophilicity. Particularly, carbon-based composites have received particular attention due to their superior features and resistance against corrosion. Zhao *et al.* synthesized NiCoP/C nanocages anchored to carbon nanotubes (CNTs).[477] The material was prepared through a three-step process using Co-based ZIF-67 MOFs as precursors (Figure 113a, i). Hollow nanocages with a shell thickness of ∼50 nm and abundant nanosheets on the surface were obtained (Figure 113a, ii). As shown in Figure 113a, iii, the precatalyst consists of Ni_2P and CoP species. EDX line-scan spectra (Figures 113a, iv−v) confirmed the hollow structure, where Co and Ni mainly resided at the shell. From electrochemical measurements, the CNTs@NiCoP/C precatalyst exhibited a low overpotential of 297 mV at 10 mA·cm^{-2} and low Tafel slope (∼ 57 mV), and the material was able to operate at 10 mA·cm^{-2} for over 8 h. Although the post-OER analysis revealed the oxidation of the sample, the morphology was preserved. Notably, the CNTs might aid in stabilizing the superstructure and generating a composite material with abundant channels and active sites. Yu *et al.* also demonstrated the effectiveness of protective carbon layers on Ni_8P_3 precatalysts.[402] Using a simple solvothermal method, Ni_8P_3@C core@shell nanosheets were grown on conductive NF, uniformly covering the Ni foam branches (Figure 113b, A). HRTEM images further confirmed the presence of a thin, amorphous carbon layer (Figure 113b, B), and lattice fringes corresponding to Ni_8P_3 were found (Figure 113b, C). Moreover, the Ni and P atoms were homogeneously distributed along the Ni_8P_3 nanosheets (Figure 113b, D). Notably, the Ni_8P_3@C precatalyst exhibited a low overpotential of 267 mV at 10 mA·cm^{-2}, being 16 mV lower than that of the Ni_8P_3 material without the C layer. OER kinetics (i.e., Tafel slopes) were also improved, suggesting that the C layer also improved the OER mechanism. This could be attributed to the decrease in the R_{ct} of the C-coated nickel phosphide, suggesting that the carbon layer boosted the conductivity and charge transfer capabilities. Although the sample was partially oxidized during stability tests, the almost superimposed CV curve after 100 CV cycles, the broadened Ni redox peak, and the high intensity of the phosphate bands suggest that the C shell prevented the dissolution of Ni sites and stabilized the material during the OER. However, more evidence is necessary to support the dissolution control claim. Similarly, Yao *et al.* protected FeP NPs with P-doped graphitic carbon (GPC).[403] After pyrolysis and phosphidation of a MOF precursor, well-dispersed FeP NPs were covered by a graphitic shell (Figure 113c, i−ii). EDX elemental mappings confirmed the uniform distribution of Fe and P around the NPs, and C along with the layers (Figure 113c, iii). HRTEM images differentiated FeP cores surrounded by graphitic carbon shells (Figure 113c, iv). Interestingly, the effect of using amorphous carbon layers (Fe_2P@APC) instead of graphitic carbon was also studied. The FeP@GPC electrode required 278 mV at 10 mA·cm^{-2}, which is lower than the overpotential for amorphous carbon (385 mV). The former also exhibited the largest ECSA and the lowest R_{ct}. After 3000 CV cycles, post-OER analysis confirmed the partial oxidation of the material and the formation of iron phosphate. Note that the graphitic carbon layer might provide a faster electron transport network. However, a clear discussion about the OER enhancement was not provided. It is speculated that encapsulating the precatalyst in P-doped carbon also possibly stabilized the material during the reconstruction.

Zhou *et al.* integrated reduced cobalt phosphide nanoflowers with graphene oxide (R-CoP$_x$/rGO) through a simple reduction with $NaBH_4$.[476] Additionally, N-doped, carbon-coated R-CoP$_x$/rGO (denoted as R-CoP$_x$@C) was also synthesized. The R-CoP$_x$@C precatalyst consisted of a 3D network (Figure 114a, A). HRTEM images confirmed that the CoP was protected by a carbon shell (Figure 114a, B). On the other hand, the R-CoP$_x$/rGO sample exhibited numerous nanoflowers and abundant P vacancies. Notably, this sample exhibited the best activity (268 mV at 10 mA·cm^{-2}). During the OER, the R-CoP$_x$/rGO nanosheets were oxidized and became thicker. HRTEM confirmed the presence of CoOOH species and abundant defects (Figure 114a, C), which were attributed to the abundant P vacancies in the material. This increased the OER activity during electrochemical measurements. On the other hand, Co species were not completely oxidized to CoOOH species in the R-CoP$_x$@C material, which was attributed to the protection of the carbon layer. According to XPS analysis, the carbon layer also reduced the number of O vacancies compared to the unprotected sample, meaning fewer defects and lattice distortions were generated during the OER. Unlike other reports, this study suggests that by covering the transition metal phosphide with carbon layers, the oxidation of

https://doi.org/10.1021/acs.chemrev.3c00005
Chem. Rev. 2023, 123, 12795−13208

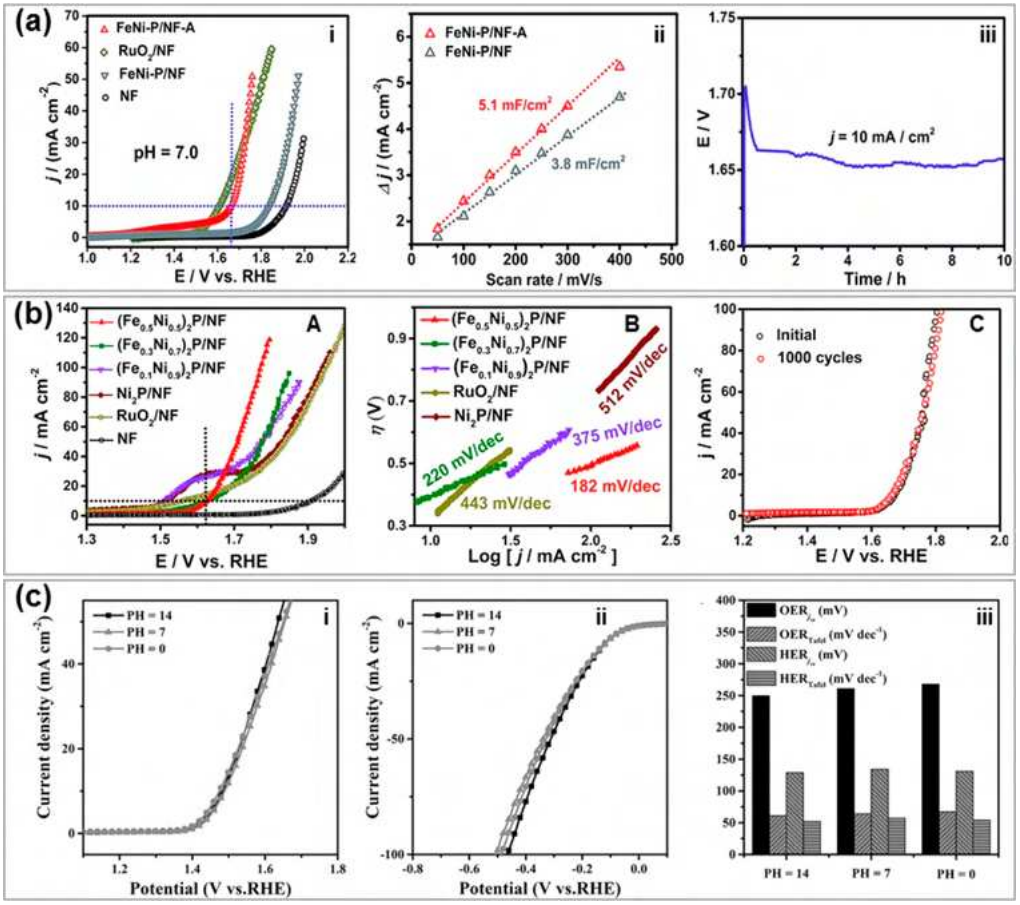


Figure 115. Effect of the pH on the performance of transition metal phosphides. (a) FeNi-P/NF catalyst in 0.1 M KPi (pH = 7): (i) OER polarization curves; (ii) C_{dl} measurements; (iii) stability tests of FeNi−P/NF-A. Reprinted with permission from ref 501. Copyright 2017 Royal Society of Chemistry. (b) $(Fe_xNi_{1-x})_2P$/NF catalyst in 0.1 M KPi: (A) polarization curves; (B) Tafel plots; (C) polarization curves before and after 1000 cycles. Reprinted with permission from ref 505. Copyright 2017 Elsevier. (c) Co_4Ni_1P catalyst in 1 M KOH (pH = 14), 1 M PBS (pH = 7), and 0.5 M H_2SO_4 (pH = 0): (i, ii) OER (i) and HER (ii) polarization curves; (iii) summary of Tafel slopes and overpotentials at 10 mA·cm^{-2}. Reprinted with permission from ref 486. Copyright 2017 Wiley.

active sites can be reduced, decreasing the OER activity. Finally, as a non-carbonaceous composite case study, Dutta *et al.* synthesized a core@shell precatalyst, where OER-inactive, crystalline Fe_3O_4 and amorphous Ni_xP acted as the core and the shell, respectively (Figure 114b, i).[462] HRTEM images revealed the core's crystalline nature, while the shell seemed amorphous (Figure 114b, ii). Interestingly, without the iron precursor, the nickel phosphide crystallized differently and had a crystalline $Ni_{12}P_5$ phase. In contrast, with the iron precursor, an amorphous Ni_xP was formed. As seen in Figure 114b, iii, the Fe_3O_4@Ni_xP exhibited the highest OER activity. Moreover, the Tafel slope of the Fe_3O_4@Ni_xP was significantly lower than that of the crystalline nickel phosphide (Figure 114b, iv). Post-OER XPS analysis confirmed the generation of high-valent Ni and Fe species on the precatalyst. Importantly, it was found that both the core and the shell were transformed into oxyhydroxide species. The authors concluded that iron atoms in the vicinity of nickel allowed partial charge transfer between them (i.e., activation), boosting the OER activity as a result. Finally, studies regarding the incorporation of Fe from the electrolyte suggested that the core-shell structure indeed caused the activity enhancement, not by the adventitious incorporation of Fe. Undoubtedly, this study confirmed the close relationship between Ni_xP and Fe_3O_4 with different roles for catalyzing the OER.

Overall, these case studies demonstrate the intimate relationship between materials with different properties in the OER performance. It is still unclear from carbon-based materials if carbon layers protect the catalyst and decrease the dissolution without decreasing the number of active sites. Nevertheless, such combinations improve critical features such as conductivity, surface area, and metal center activation. Therefore, it is necessary to find the optimal conditions and materials in which these composites must be prepared to boost the OER effectively.

4.2.3.8. pH Effects. The electrolyte pH is another parameter that has been modified for the study of transition metal phosphide precatalysts. According to Table 4, most reports have been carried out under alkaline conditions (1 M KOH, pH = 14). Working under the same pH conditions allows for a fair comparison of the electrocatalytic activity. However, a few studies have explored the activity and stability of transition metal phosphides in neutral and acidic conditions, expanding the applicability of these precatalysts in the field. Zhang *et al.* evaluated the OER performance of FeNi-P nanoparticle-stacked arrays on Ni foam in both alkaline and neutral environments.[501] After being electroactivated in 1 M KOH, the material was partially oxidized (FeNi-P/NF-A). The electrode exhibited extremely low overpotentials (186 and 235 mV at 100 and 500 mA·cm^{-2}, respectively), low Tafel slope (57 mV·

https://doi.org/10.1021/acs.chemrev.3c00005
Chem. Rev. 2023, 123, 12795−13208

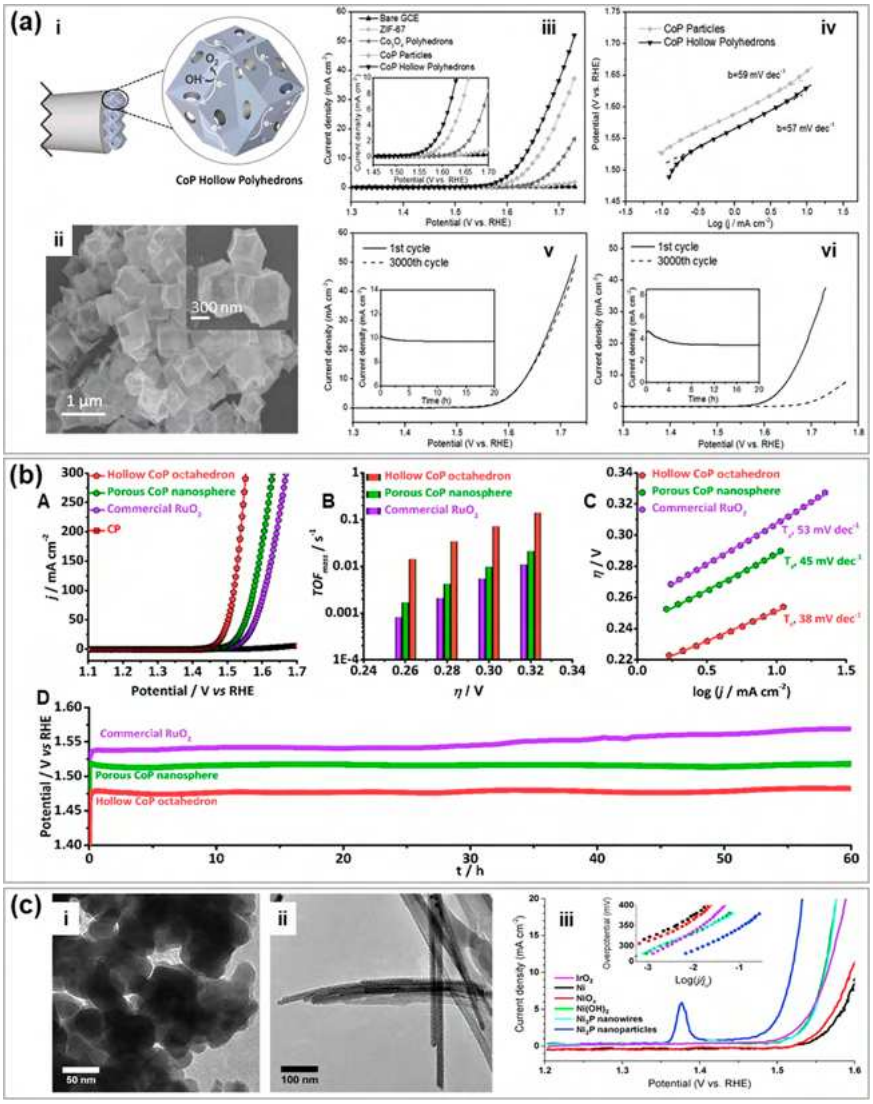


Figure 116. Morphology effects on transition metal phosphides. (a) CoP hollow catalyst: (i) illustration of the polyhedral morphology; (ii) SEM image; (iii) polarization curves; (iv) Tafel plots; (v, vi) polarization curves before and after 3000 CV scans for CoP hollow polyhedron (v) and CoP particles (vi). Insets: CA tests. Reprinted with permission from ref 591. Copyright 2016 American Chemical Society. (b) CoP octahedral precatalysts: (A–D) polarization curves (A), mass-based TOF values (B), Tafel plots (C), and stability tests (D) at 10 mA·cm^{-2}. Reprinted with permission from ref 475. Copyright 2018 Royal Society of Chemistry. (c) Ni_2P Janus catalyst: (i, ii) TEM images of polydispersed Ni_2P NPs (i) and Ni_2P NWs; (iii) polarization curves in 1 M KOH. Inset: Tafel plots. Reprinted with permission from ref 103. Copyright 2015 Royal Society of Chemistry.

dec^{-1}), and high electrical conductivity. Furthermore, the same precatalyst was tested in neutral electrolyte (0.1 M KPi). Notably, the electroactivated precatalyst also exhibited the lowest overpotential (Figure 115a, i), and ECSA measurements revealed a larger surface area than that of the sample without electroactivation (Figure 115a, ii). The authors concluded that more active sites were generated during the activation step and the that presence of OH^- species on the activated sample increased the hydrophilicity of the electrode, reducing the electrode–electrolyte contact resistance and enhancing the charge transfer. Interestingly, while the material was stable in an alkaline environment, long-term tests (i.e., >10 h) in neutral conditions showed activity decay. This was attributed to the dissolution of Ni and Fe species, as the electrolyte exhibited a light-yellow green color. The authors did not provide a detailed post-OER characterization of the material after stability tests, and therefore, it is difficult to assess the driving force behind the transformation in neutral electrolytes. The same group studied $(Fe_xNi_{1-x})_2P$ precatalysts in the same environments (1 M KOH and 0.1 M KPi, pH = 7).[505] Similarly, the samples tested in an alkaline environment exhibited a reasonable activity, stability, and partial oxidation after stability tests. Regarding neutral conditions, the $(Fe_{0.5}Ni_{0.5})_2P$/NF sample exhibited the lowest overpotential (396 mV at 10 mA·cm^{-2}, Figure 115b, A) and the lowest Tafel slope (182 mV·dec^{-1}, Figure 115b, B) among all of the studied compositions. The authors reported that the material was stable after 1000 CV cycles in 0.1 M KPi (Figure 115b, C), and the XPS results showed the disappearance of Ni^{3+} and the formation of phosphate species on the surface. Interestingly, the stability trend of the FeNi-P precatalysts seems to be contradictory in this case, as no decay in the current density was recorded. Moreover, no color change was seen, nor was a dissolution assessment. According to the evidence, there is one

https://doi.org/10.1021/acs.chemrev.3c00005
Chem. Rev. 2023, 123, 12795–13208

difference between both studies: when the $(Fe_{0.5}Ni_{0.5})_2P$/NF sample was not "preactivated" in alkaline environment,[505] the material exhibited NiFe phosphates after neutral media tests and was considered as "stable". This suggests that the generation of oxidized species might not be favorable for the electrocatalyst in neutral media when activated in KOH electrolyte. However, sufficient post-OER characterization results were not obtained and this claim must be further investigated.

Yan *et al.* evaluated the OER and HER performance of Co_xNi_yP precatalysts in alkaline (1 M KOH), neutral (phosphate buffer saline, PBS, 1 M), and acidic (0.5 M H_2SO_4) environments.[486] As depicted in Figure 115c, the Co_4Ni_1P sample exhibited similar behaviors in all three conditions for the OER (Figure 115c, i) and HER (Figure 115c, ii). Interestingly, the Co_xNi_yP exhibited similar HER and OER overpotentials in all the conditions (Figure 115c, iii), which does not agree with previous studies in which activity was different in neutral conditions.[501,505] Moreover, the stability tests and post-OER analysis were only reported for the alkaline electrolyte, in which partial oxidation was confirmed. Unfortunately, this activity similarity among the three conditions lacks necessary corroboration with additional measurements, and the stability in acidic and neutral electrolytes is still questionable.

Although evaluation of different transition metal phosphide precatalysts has been performed in a few studies, clear activity trends remain elusive, and some results seem contradictory. Overall, evidence suggests that working outside alkaline environments favors the dissolution of species into the electrolyte. This aspect is discussed later in Section 4.2.4. Therefore, we recommend employing other electrolytes to perform exhaustive electrochemical and physicochemical characterization of the transition metal phosphides.

4.2.3.9. Morphological Effects. The morphology of the precatalyst is another property that is commonly highlighted by several studies in the transition metal phosphide field. In addition to seeking large surface areas, a few studies have studied the role of different transition metal phosphide morphologies on the OER activity. Liu and Li compared the performance of CoP samples with two different morphologies: hollow polyhedrons and NPs.[591] The hollow polyhedron morphology (Figure 116a, i) was obtained using a MOF-based phosphidation approach. After phosphidation, the sample retained the polyhedron morphology of the precursor, although the number of cracks and defects was increased (Figure 116a, ii). The CoP hollow polyhedron exhibited the best activity (overpotential: 400 mV at 10 $mA{\cdot}cm^{-2}$), while the CoP NPs demanded a higher overpotential of 427 mV at 10 $mA{\cdot}cm^{-2}$ (Figure 116a, iii). However, the Tafel slopes were similar (Figure 116a, iv), suggesting that the kinetics of both morphologies are comparable. The hollow polyhedron sample also exhibited the lowest charge transfer resistance as determined from EIS analysis. However, the most exciting result was the stability comparison. While the hollow polyhedrons showed remarkable stability after 3000 CV cycles (Figure 116a, v), the CoP NPs showed a noticeable activity loss (Figure 116a, vi). Although only post-overall water electrolysis (OWE) SEM analysis was carried out for the CoP hollow polyhedron, XPS characterization of the as-prepared materials revealed that the samples were oxidized by exposure to air. Therefore, it is likely that the active sites during the OER were oxidized species rather than CoP sites. The authors concluded that the superior activity and stability of the hollow polyhedron morphology were related to the large surface area and high porosity. The CoP NPs exhibited a poor performance due to the greater oxidation extent of the initial material. Nevertheless, it is difficult to make this claim without post-OER analysis, and the reason these morphologies exhibited different performances is still unclear. In a similar approach, Xu *et al.* examined hollow CoP NPs with well-defined octahedral morphology and porous CoP nanospheres (NSs).[475] The hollow CoP octahedral NPs mainly belong to the orthorhombic CoP phase, while the porous CoP NSs consist of randomly oriented fine crystallites, mainly composed of orthorhombic CoP phase as well. Notably, the octahedral CoP NPs exhibited the best OER activity (240 mV at 10 $mA{\cdot}cm^{-2}$), while the porous CoP NSs required an extra 40 mV (Figure 116b, A). The same trend remained when the activity was normalized by the mass and ECSA. TOF comparisons (Figure 116b, B) confirmed the enhanced OER activity of the octahedral CoP NPs, and Tafel slopes (Figure 116b, C) indicate that hollow CoP NPs (38 $mV{\cdot}dec^{-1}$) exhibited a higher OER rate than the CoP NSs (45 $mV{\cdot}dec^{-1}$). Therefore, this suggests that the activity disparity could be attributed to the morphology and microstructure difference since both samples exhibited the same crystal phase, electrical conductivity, and surface chemistry. Moreover, both precatalysts operated at a constant current of 10 $mA{\cdot}cm^{-2}$ during long-term stability tests (60 h). Post-OER XPS analysis confirmed the formation of CoOOH and oxidized P species, while the SEM-EDX evidenced the transformation of both octahedral NPs and porous NSs into granular particles without defined geometries, although the CoP NSs suffered from agglomeration compared to the octahedral CoP NPs. Evidently, these results suggest that although the sample reconstructed during the OER, the morphology of the precatalysts provided notable capabilities that improved the activity and kinetics. However, it is unclear if this improvement was caused only by the increased number of defects, and large surface area, or mass transport and if these factors accelerated the reconstruction process at some degree.

Finally, Stern *et al.* studied Ni_2P OER precatalysts with nanowire and nanoparticle morphologies.[103] The Ni_2P NPs were coated with an amorphous layer of surfactant and exhibited an average particle size of 50 nm (Figure 116c, i), while the Ni_2P nanowires had an average width of 11 nm (Figure 116c, ii). Notably, the Ni_2P NPs exhibited the best OER activity (overpotential: 290 mV at 10 $mA{\cdot}cm^{-2}$) (Figure 116c, iii), while the Ni_2P nanowire, IrO_2, and $Ni(OH)_2$ samples exhibited similar behavior. However, the OER activity increased (291 mV) after annealing at 450 °C in 5% H_2/Ar atmosphere, for the Ni_2P nanowires, which was attributed to removing a surfactant layer on the nanowire surface. This suggests that rather than a morphology effect, the Ni_2P nanowires and nanoparticles exhibited a different activity due to this amorphous surfactant layer, and upon removal, both samples exhibited similar activity. Furthermore, the Ni_2P nanoparticles exhibited the largest ECSA compared to those of Ni, NiO_x, and $Ni(OH)_2$ samples. After galvanostatic stability tests at 10 $mA{\cdot}cm^{-2}$, HRTEM, EDX, and XPS analysis confirmed the formation of a $Ni_2P@NiO_x$ core@shell structure, which was considered the real active site. Overall, the authors concluded that the Ni_2P NPs were the best precatalyst since the fabrication was more straightforward and the ECSA was larger and delivered almost identical activity

https://doi.org/10.1021/acs.chemrev.3c00005
Chem. Rev. 2023, 123, 12795−13208

after 10 h galvanostatic electrolysis tests (~10 mV increase in the overpotential). This demonstrates that care must be taken when comparing different morphologies, as initial trends might be caused by a surfactant that covered the Ni_2P nanowires rather than the different morphologies.

4.2.4. Challenges. Although many studies have demonstrated that transition metal phosphides act as precatalysts and undergo significant reconstruction processes during the OER, the role of specific mechanisms and species is still under debate. In this Section, we highlight special case studies related to two main topics that are not fully understood and remain elusive in the literature: the role of phosphate ions and dissolution processes. We consider these to be critical challenges that future studies must address to gain a comprehensive understanding of the enhanced OER activity and stability of transition metal phosphides.

According to the vast majority of case studies discussed in this Section, transition metal phosphides undergo the reconstruction processes (i.e., oxidation) during the OER, and oxidized species are obtained as a result. In this regard, several studies have confirmed the formation of phosphate anions (PO_4^{3-}) and other related oxidized P species, primarily based on XPS post-analysis (see Table 4).[447,491,499,505,507,556] Incidentally, Figure 117 shows a Pourbaix diagram of

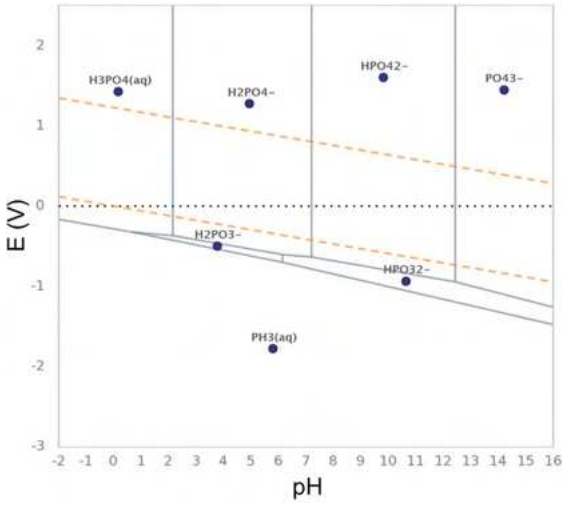


Figure 117. Pourbaix diagram for phosphorous. Orange broken lines represent the thermodynamic potentials for the HER and OER at different pH values. The diagram is produced at the P ion concentration of 10^{-8} M (default) by using the Materials Project.[87−89]

phosphorous. In the relatively high pH (~ 14), PO_4^{3-} anions are generated around the thermodynamic OER potential, which agrees with the experimental observations.[446,455,470,488] Indeed, many studies have reported the presence of such species (e.g., PO_4^{3-}, oxidized P species, etc.) even before electrochemical tests in the as-prepared materials.[446,447,455,464,490,497,507,556] According to these findings, it is challenging to avoid generating oxidized P species since these are prone to react with ambient air.[491,499] This suggests that phosphate anions will likely be produced either before or during the OER tests. However, their role in the surface reconstruction process and OER activity enhancement and their stability are still uncertain, and more research is necessary. Herein, we summarize a few case studies in which phosphate ions were present during the OER, either intentionally as a "catalyst" or generated on a "precatalyst".

Wang *et al.* prepared CoP nanoarrays on carbon cloth.[515] According to the HRTEM image of the as-prepared sample (Figure 118a), the CoP nanoneedle exhibited three distinctive

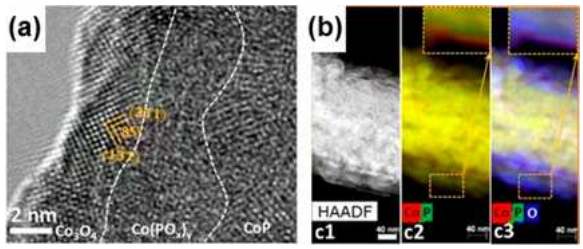


Figure 118. Partially oxidized CoP interlayer, denoted as $Co(PO_x)_y$, in the as-prepared CoP nanoneedle: (a) HRTEM image; (b) HAADF image and corresponding elemental mapping images. Reprinted with permission from ref 515. Copyright 2016 Wiley.

layers: the outermost layer was composed of Co_3O_4, the innermost layer consisted of CoP, and there was a transitional region between both layers that comprised oxidized P species, denoted as $Co(PO_x)_y$. As shown in Figure 118b, HAADF images confirmed that O atoms were concentrated at the surface, while Co and P were uniformly distributed across the nanoneedle, particularly at the core, suggesting the surface oxidation of the as-prepared sample by ambient air. Moreover, the phosphate-rich transitional region increased its thickness after preconditioning the sample at 1.53 V_{RHE}, and $Co(OH)_2$ particles were seen at the surface. Notably, the preconditioned electrode exhibited the relatively low OER overpotential of 281 mV, surpassing the activity of pure Co_3O_4 nanoarrays. The authors attributed this superior performance to the synergetic effect between the outer oxide layer, which was active toward the OER, and the conductive CoP core. However, there is still a possibility that the transitional layer probably protected the core from further oxidation or stabilized the $Co^{2+/3+}$ sites. Furthermore, phosphate ions were directly employed by Zhou *et al.* to prepare a $Fe(PO_3)_2/Ni_2P$ precatalyst on Ni foam for water oxidation.[485] As depicted in Figure 119a, i, the phosphate-based precatalyst showed a high OER activity (overpotential: 265 mV at 500 $mA{\cdot}cm^{-2}$). The precatalyst also exhibited a low Tafel slope of ~52 $mV{\cdot}dec^{-1}$ (Figure 119a, ii) and the largest ECSA (Figure 119a, iii). Moreover, the sample was reconstructed during the OER. Specifically, while the as-prepared material exhibited only interplanar spaces for crystalline $Fe(PO_3)_2$ (Figure 119b, A), the sample was utterly amorphous after 10000 CV cycles (Figure 119b, B). Raman spectroscopy was used to get more insights into the chemical transformation. While no vibrational modes for $Fe(PO_3)_2$ were detected, characteristic signals of iron oxides were seen after the OER (Figure 119b, C). XPS analysis revealed the disappearance of P signals, the intensity increase of the Fe^{3+} satellite peak, and evidence for Ni−O and Fe−O bonds, as shown in Figure 119c. These results suggest that NiFe oxide, hydroxide, and oxyhydroxide species were generated *in situ* during the OER, acting as the active sites. Without further evidence for the role of phosphate ions in this study, these results suggest that phosphate species were not the active sites.

Furthermore, Zhang *et al.* prepared a NiFe-based phosphate/phosphide hybrid precatalyst on NiFe foam through plasma-enhanced chemical vapor deposition (PECVD).[481]

https://doi.org/10.1021/acs.chemrev.3c00005
Chem. Rev. 2023, 123, 12795−13208

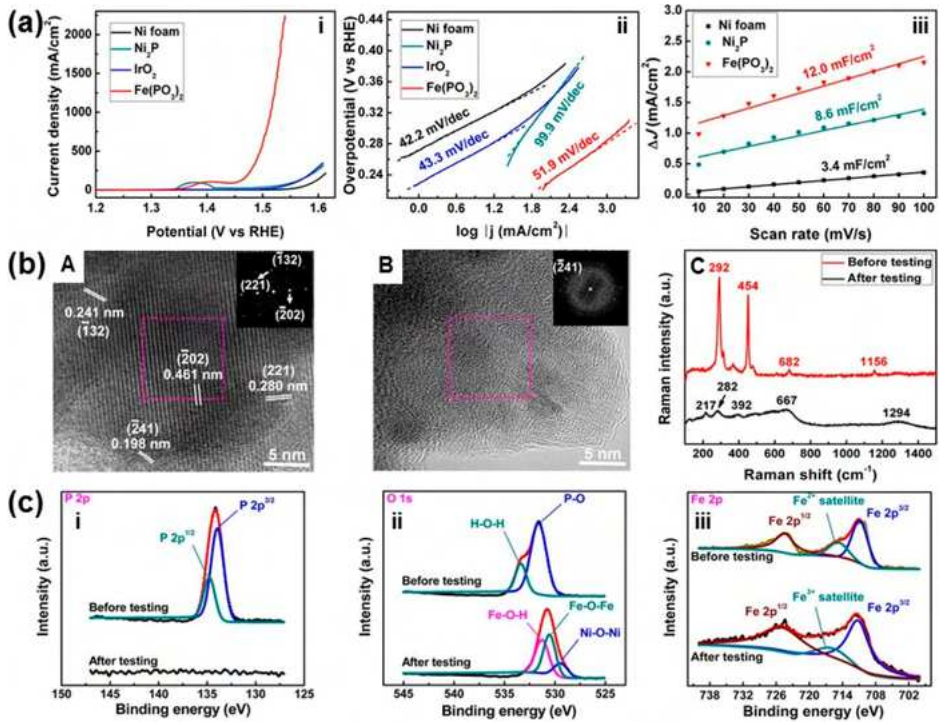


Figure 119. Evaluation of the $Fe(PO_3)_2/Ni_2P$ catalyst supported on Ni foam. (a) Electrochemical characterization: (i) OER polarization curves in 1 M KOH; (ii) Tafel plots; (iii) C_{dl} measurements. (b) Structural characterization: (A, B) HRTEM images and FFT patterns (A) of the as-prepared catalyst and (B) after OER stability tests; (C) Raman spectra before and after the OER; (c) XPS spectra before and after OER tests at different peaks: (i) P 2p; (ii) O 1s; (iii) Fe 2p. Reprinted with permission from ref 485. Copyright 2017 National Academy of Sciences.

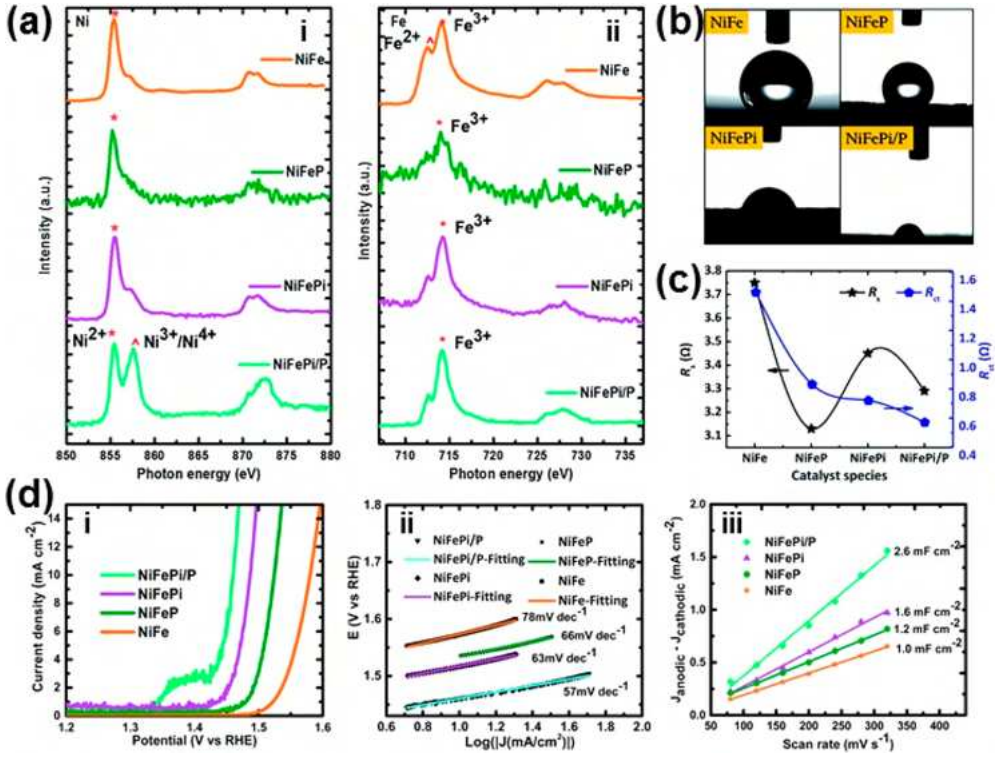


Figure 120. Characterization of NiFe-based phosphate/phosphide catalysts: (a) *Operando* XAS measurements at 1.6 V_{RHE}: (i, ii) Ni (i) and Fe (i) L-edge X-ray absorption spectra; (b) Contact angle measurements; (c) series and charge transfer resistance trends. (d) Electrochemical characterization: (i) OER polarization curves in 1 M KOH electrolyte; (ii) Tafel plots; (iii) C_{dl} measurements. Reprinted with permission from ref 481. Copyright 2018 Royal Society of Chemistry.

Through this approach, both phosphide and phosphate groups (denoted as NiFePi/P) were directly grown on the foam, creating biscuit-shaped morphologies with large surface areas. The creation of both P species was confirmed by XPS analysis.

https://doi.org/10.1021/acs.chemrev.3c00005
Chem. Rev. 2023, 123, 12795−13208

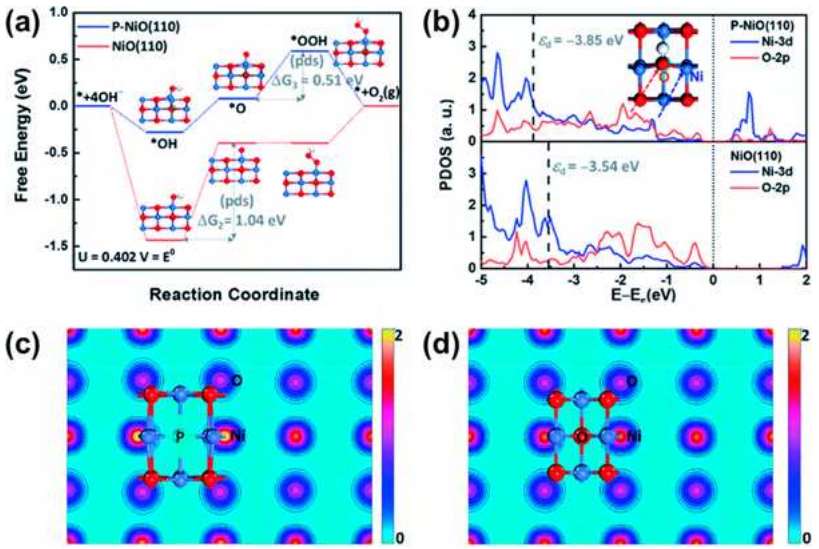


Figure 121. Study of the P incorporation into NiO crystals using DFT calculations: (a) Gibbs free energy diagrams of the OER on perfect NiO(110) and single P atom-doped NiO(110) in an alkaline medium; (b) projected density of states for the Ni 3d and O 2p orbitals in OH adsorbed on NiO(110) and P-NiO(110); (c, d) calculated charge density diagrams for (c) P-NiO(110) and (d) perfect Ni(110). Reprinted with permission from ref 612. Copyright 2021 Royal Society of Chemistry.

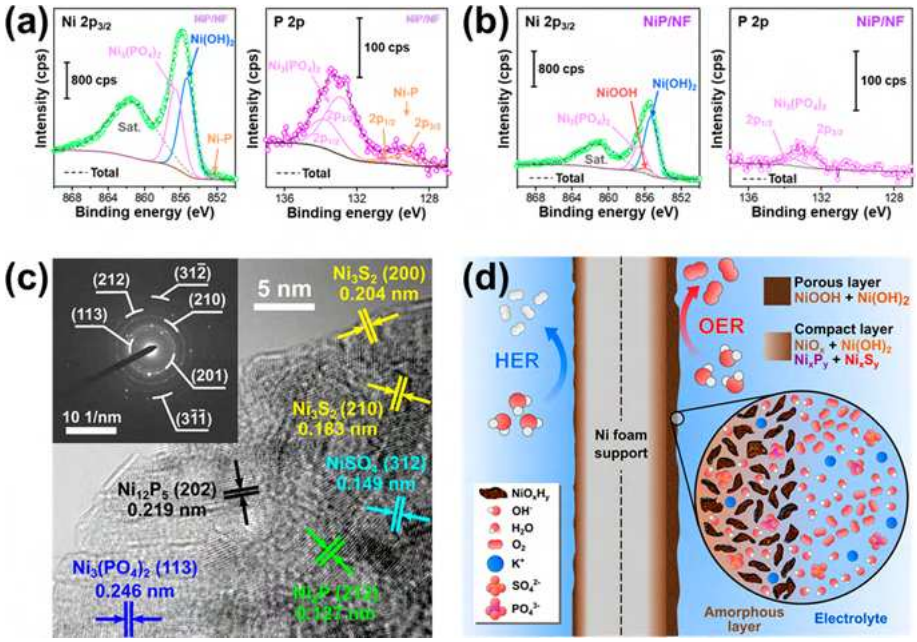


Figure 122. Evaluation of Ni-S-P-O and Ni-P-O electrocatalytic films deposited on Ni foam substrates through flow cell-assisted electrodeposition: (a, b) XPS characterization of the NiP film (a) before and (b) after OER stability tests; (c) HRTEM image of the as-prepared Ni-S-P-O film (inset: SAED pattern); (d) schematic illustration of the *in situ* reconstruction process occurring during the HER and the OER on Ni-S-P-O electrocatalytic films. Reprinted with permission from ref 49. Copyright 2021 Royal Society of Chemistry.

Moreover, real-time XAS was used to acquire the spectra of the NiFePi/P precatalyst and its counterparts (i.e., NiFe, NiFeP, NiFePi) at 1.6 V_{RHE} (Figure 120a). Notably, XAS measurements revealed that the oxidation state of Ni increased with the following order: NiFe (metallic) < NiFeP < NiFePi < NiFePi/P, the latter exhibiting the largest content of $Ni^{3+/4+}$ sites (Figure 120a, i). Moreover, the L-edge spectra of Fe (Figure 120a, ii) showed that Fe remained as Fe^{3+} in all the samples and that the largest amount of Fe^{3+} was also seen in the NiFePi/P hybrid. To test the wettability of the samples, water contact angles were measured. As shown in Figure 120b, the phosphate-based samples exhibited the lowest contact angles, meaning that these groups favor the electrode−electrolyte contact, improving the charge transfer at the surface. To support this claim, EIS measurements were also performed. As depicted in Figure 120c, the hybrid sample exhibited the lowest charge transfer resistance, while the phosphide-based sample exhibited the lowest series resistance (i.e., electrical conductivity). Since NiFeP exhibited a relatively high R_{ct} and NiFePi showed a high R_s, the NiFePi/P precatalyst exhibits the best trade-off by combining the high conductivity and wettability of the phosphide phosphate. The hybrid sample exhibited the highest OER activity (Figure 120d, i), the lowest Tafel slope (Figure 120d, ii), and the largest ECSA (Figure

https://doi.org/10.1021/acs.chemrev.3c00005
Chem. Rev. 2023, 123, 12795−13208

120d, iii). The authors attributed these trends to the synergetic relationship between phosphate and phosphide species, as the high conductivity and low R_{ct} improved the OER kinetics. Moreover, the large ECSA suggests abundant active sites, likely caused by the sequential plasma treatment steps. Finally, the hybrid sample was stable during the CP tests at 10 mA·cm^{-2} for 24 h, and post-OER EDX analysis confirmed the presence of oxygen. Overall, this study demonstrated the synergism between Pi and P species and how the presence of phosphate ions improved the wettability of the precatalyst and stimulated the formation of high-valent Ni sites. We speculate that phosphate ions might explain the enhanced activity and kinetics in most studies that reported their presence before or after the OER. However, more research should be done in this regard, and future studies should compare the activity of phosphate-rich precatalysts to support this claim.

Recent studies have discussed the relevance of *in situ* phosphorus and phosphate substitution during the OER surface reconstruction process. Dai *et al.* studied the formation of defect-rich NiO nanosheets on the surface of Ni_5P_4 electrocatalysts during the OER, resulting in the formation of P-doped NiO nanosheets.[612] Using DFT calculations, they examined the effect of the heteroatom P substitution into the crystal defects of NiO by replacing a subsurface oxygen atom with a single P atom. As depicted in Figure 121a, doping P atoms into the crystal structure of NiO(110) caused a reduction in the adsorption strength of the OER intermediates and changed the potential-determining step to the formation of the *OOH intermediate, which could explain the decrease in overpotential. Moreover, the projected density of states (PDOS) for the *OH adsorption revealed a lower hybridization degree between the Ni 3d and O 2p orbitals for the P-doped NiO electrocatalyst (Figure 121b), confirming a weaker binding strength. Finally, charge density mappings in Figure 121c showed a higher density of electrons in adjacent Ni sites when single P atoms were incorporated into the crystal structure, suggesting a reduced transfer ability of the Ni active sites compared to O atoms (Figure 121d). Interestingly, XPS characterization results revealed the presence of P-O species after the reconstruction process, which was not explained further by the authors. Since no binding peak for the Ni−P bond was found after the reconstruction process, and only a small amount of P was incorporated into the NiO crystal, what happened to the rest of the P remains unclear. Recently, our group synthesized and tested Ni-P-O, Ni-S-O, and Ni-S-P-O electrocatalytic films on NF through flow cell-assisted electrodeposition.[49] According to the XPS spectra in Figure 122a, the as-prepared Ni-P-O films exhibited both Ni−P and P−O bonds, while post-XPS analysis (Figure 122b) confirmed the complete disappearance of Ni-P and only P-O species remained. Similarly, HRTEM and SAED results revealed that as-prepared Ni-S-P-O films contained Ni-S, Ni-P, Ni-SO_4^{2-}, and Ni-PO_4^{3-} species (Figure 122c). However, post-OER characterization results confirmed that only small quantities of oxidized P and S species remained. By examining the $Ni^{2+/3+}$ redox peaks for Ni-P-O, Ni-S-O, and Ni-S-P-O films, we found that the nano-polycrystalline sample with the most pronounced heteroatom substitution (i.e., Ni-S-P-O) exhibited the most significant number of active sites, and it was oxidized faster than the Ni-P-O and Ni-S-O films. Based on previous findings of the surface reconstruction during the OER, we hypothesized that the electrocatalytic films underwent a dynamic reconstruction process where S and P heteroatoms induced significant structural and electronic effects (Figure 122d). First, incorporation of S and P atoms into the Ni lattice favored the fragmentation and reconstruction due to the abundance of vacancies and defects. Second, since S and P atoms were oxidized by the penetrating electrolyte and diffusing oxygen, oxidized species (i.e., SO_4^{2-}, PO_4^{3-}) produced *in situ* remained during the OER, as confirmed by XPS post-analysis. Third, these anions could have improved the conductivity of the porous layer and stabilized intermediates and high-valent Ni sites, as mentioned by other works.[48,459,613] Still, further studies are necessary to unveil the true structural and electronic effects of these oxidized species during the *in situ* OER reconstruction process.

Material integrity is essential to provide robust and durable electrocatalysts capable of withstanding the intermittent nature of renewable energy sources and the reverse current flow in electrolyzer during operating cycles.[448] One crucial issue that must be considered is the loss of electrocatalyst during long-term operation, caused by the dissolution of the transition metal phosphide and mechanical degradation of the transition metal phosphide/support. Several studies have reported the leaching of P and metallic species during the OER, although exhaustive research on this aspect is scarce. Typically, indirect observations are used to infer the occurrence of dissolution of the transition metal phosphide after the OER testing, such as the lack of M-P signals in post-OER XPS analysis. However, other reports have confirmed the dissolution directly through specialized analytical techniques. For example, Ledendecker *et al.* found small amounts of Ni in the electrolyte after HER stability measurements (20 h) of a Ni_5P_4 precatalyst using inductively coupled plasma optical emission spectroscopy (ICP-OES), which can be used for the other transition metal phosphide OER electrocatalysts.[525] ICP-MS has been used to confirm the leaching of P, likely as soluble phosphate ions, when evaluating $Fe_{2-x}Mn_xP$ precatalysts.[492] Lastly, high-angle annular dark-field (HAADF) imaging and elemental mappings revealed increased nanoporosity of Ni-P nanosheets after OER tests in 1 M KOH, which was attributed to leaching of P.[516] Considering that most of the studies in Table 4 did not report the use of such techniques to verify the dissolution of the sample, it is necessary to establish detailed guidelines to evaluate the stability of the materials. Further aspects are detailed in Section 7.

Evidence of the metallic and phosphate dissolution process can be tracked several years back to work done by Lutterman *et al.*[614] Due to the instability of Co during the OER, the behavior of $Co^{2+/3+}$ and P species in 0.1 M Pi (pH = 7.0) electrolyte was evaluated. By taking aliquots from the electrolyte at regular times, ^{57}Co and ^{32}P radioactive isotopes were used to monitor the dynamic dissolution processes of a Co-Pi OER electrocatalyst on ITO substrates, and the effects of the applied potential and the Pi electrolyte were assessed (Figure 123a). As shown in Figure 123b, Co continuously leached when the electrode was held at the open-circuit potential (OCP) or after removing the potential, while it was reabsorbed when a constant potential of 1.3 V_{NHE} was applied. P species (i.e., phosphates) continuously leached into the electrolyte under both the applied potential of 1.3 V_{NHE} and the OCP, although the dissolution rate was higher without the applied potential (Figure 123c). The same trend was observed when several fresh catalyst samples were redissolved from the ITO substrates using HCl after being tested for different periods (Figure 123d). Finally, the effect of removing 0.1 M Pi

https://doi.org/10.1021/acs.chemrev.3c00005
Chem. Rev. 2023, 123, 12795−13208

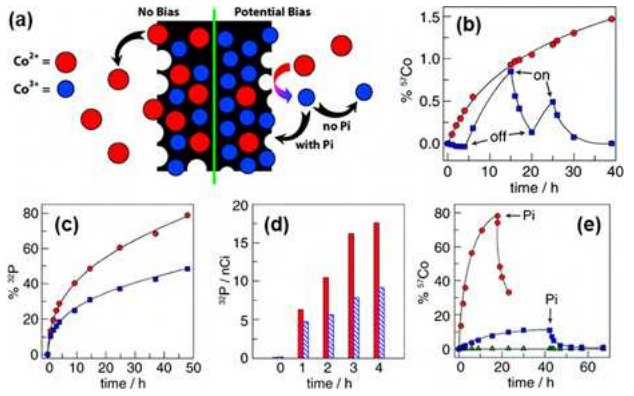


Figure 123. Dynamic dissolution processes on cobalt-phosphate (Co-Pi) OER electrocatalyst: (a) schematic illustration of the self-healing process; (b) ^{57}Co leaching profiles of the Co-Pi film with a potential of 1.3 V_{NHE} (blue squares) and turned on and off at times designated and held at OCP (red circles); (c) ^{32}P leaching and (d) ^{32}P uptake profiles of the Co-Pi film at an applied potential of 1.3 V_{NHE} (blue squares and bars) and held at OCP (red circles and bars); (e) ^{57}Co leaching profiles of Co-*X* films at the applied potentials of 1.3 V_{NHE} (red circles) and 1.5 V_{NHE} (blue squares) and held at OCP (green triangles). The arrows indicate the addition of Pi. Reprinted with permission from ref 614. Copyright 2009 American Chemical Society.

and making Co-*X* films (where *X* = SO_4^{2-}, NO_3^-, and ClO_4^-) instead was evaluated. Unlike the results in Figure 123b, the Co leaching profiles in Figure 123e show that in the absence of Pi, the Co-*X* film suffered from increased corrosion at 1.3 V_{NHE} and it was more intense at 1.5 V_{NHE}. However, adding Pi (i.e., proton-accepting electrolyte) to the system stopped the dissolution and regenerated the film. Overall, these results indicate that the electrodeposited Co-*X* films act as proton acceptors in the absence of proton-accepting electrolytes (Pi), leading to corrosion and higher potentials (i.e., more protons), accelerating the dissolution of Co-*X* films. These findings are of particular interest for the transition metal phosphide field, as they confirm that (i) Co-Pi films will dissolve even under OCP conditions (e.g., when the bias is removed after the OER), (ii) the films can be regenerated only if proton-accepting electrolytes are present and a bias is applied, and (iii) in the absence of such electrolytes, electrocatalyst dissolution is likely to occur and can be accelerated at higher potentials. Overall, these case studies demonstrate the importance of carefully selecting electrolytes (e.g., when transition metal phosphides are evaluated in neutral conditions) and evaluating the dissolution processes on transition metal phosphides. Additionally, the regenerating abilities of phosphate species open new questions about the role of phosphates in the OER process. We encourage future studies to evaluate such trends and confirm the stability of transition metal phosphides under thorough characterization approaches.

Although most of the studies discussed in this Section provide sufficient evidence that an oxidation process occurs during the OER in transition metal phosphide electrocatalysts, specific conflicting results demand further analysis. One remarkable example is the case of FeP, which has been regarded as a "catalyst" by one study,[415] while others have proven that oxidized species were produced during the OER.[506] In the case of Masud *et al.*, post-OER SEM images showed no modification to the surface morphology, EDX elemental mappings confirmed the uniform distribution of Fe and P, and XPS spectra before and after the OER were virtually identical. Remarkably, the stability test (CP, 10 mA·cm^{-2}) was relatively short (4 h), which might explain the absence of oxidized species. However, other studies suggest that soaking the electrocatalyst in KOH is enough to create a surface *M*-OH layer, meaning that even short stability tests should produce a detectable layer of oxides/hydroxides.[470] Furthermore, no TEM or XRD analysis was provided to confirm that FeP was unaffected. On the other hand, Yan *et al.* demonstrated that Fe increases its oxidation state after stability tests through XPS analysis.[506] Moreover, Li *et al.* confirmed the formation of amorphous MO_x|*M*OOH species (*M* = Ni, Fe) in FeP-coated Ni_2P electrocatalysts through SEM, XRD, and XPS post-OER analysis.[438] Finally, Yao *et al.* also confirmed the presence of oxidized Fe and P^{5+} (phosphate) species through XPS analysis, and even the loss of P during the OER (~45%) was confirmed through ICP-AES, suggesting that FeP is not entirely stable in strongly alkaline conditions. Notably, this study confirmed that this behavior does not occur in the HER, where the P loss is significantly lower (~3%) and the oxidation extent is much lower.[480]

Another interesting case is the role of Fe incorporation into transition metal phosphides. Valizadeh *et al.* confirmed through various analytical techniques (i.e., SEM, TEM, EDX, XRD, Raman spectroscopy, XPS, spectroelectrochemistry, etc.) and electrochemical tests that the Ni_2P@NiO_x core@shell material can readily absorb Fe ions from solution, increasing the OER activity as a result.[615] Notably, it was found that it might be challenging to detect nickel oxide/hydroxide species (especially using Raman spectroscopy and XRD) since a thin amorphous layer of Ni oxide/hydroxide is formed, which mainly consists of small (0.5−5 nm) nanoparticles covering the Ni_2P core. By adding Fe salt to the electrolyte, the authors confirmed a significant increase (~20 times) of the OER activity of the Ni_2P electrocatalyst as well as a higher O/Ni ratio, suggesting that Fe incorporation promotes the oxidation of the material. This case study demonstrates that detecting oxidized species might be difficult for specific techniques and that various complementary methods must be employed. Furthermore, it reveals the importance of evaluating the performance of transition metal phosphides in purified electrolytes to precisely measure the activity of the material without the interference of other species in the solution.

5. TRANSITION METAL CHALCOGENIDES

Since the mid-1970s, a group of materials called transition metal chalcogenides (sulfides, selenides, and tellurides) has started to receive interest as an electrocatalyst.[616−618] Specifically, in 1974, Baresel *et al.*, for the first time, studied various transition metal (Ti, Co, Ni, Mo, Ta, W) sulfides, selenides, and tellurides for the oxygen reduction reaction (ORR) in acidic media (4 N H_2SO_4).[616] Ten years later, nickel sulfide was reported as the first electrocatalyst for the HER in alkaline media (1 N NaOH) by Vandenborre *et al.*,[619] which was the trigger for studying transition metal chalcogenides for the HER.[620−623] After Gao *et al.* reported a Mn_3O_4/$CoSe_2$ nanocomposite as an alkaline OER electrocatalyst in 2012,[624] researchers began exploring many types of transition metal chalcogenides for the electrocatalytic OER process, which brought the rapid growth of the chalcogenide OER electrocatalyst field. In this context, transition metal chalcogenides have also become recognized by scientists today as one of the most active material groups for electrocatalytic water splitting,[72,625−631] thanks to the persistent research efforts.

https://doi.org/10.1021/acs.chemrev.3c00005
Chem. Rev. 2023, 123, 12795−13208

Regarding the compositional transformations of chalcogenides during the OER, in 2015, Tang *et al.* tested NiSe nanowire film on Ni foam in alkaline media (1 M KOH) and first revealed that NiOOH species formed on the NiSe surface during the OER act as real electrocatalytic sites.[208] Right after this report, Cui and co-workers reported *in situ* electrooxidation of transition metal (Co, Ni, Fe) dichalcogenides (disulfides, diselenides, ditellurides) into their oxide counterparts in 1 M KOH electrolyte. They revealed that the chalcogenide-derived oxides could act as excellent OER electrocatalysts.[96,97] Their findings extended our understanding of the electrochemical behaviors of chalcogenides under OER potentials in general. In the same line, in 2016, our group also studied NiS film in an alkaline electrolyte (1 M KOH), observed a similar transformation (NiS → NiO_x) under an anodic potential, and explained this kind of transformable OER electrocatalysts with a new technical term: precatalyst,[94] which is nowadays becoming a widely accepted term in the electrocatalyst field.[57,70,81,106,229,628,632,633] At present, chalcogenide OER electrocatalysts have increasingly been reported to achieve efficient water oxidation and/or understand their behaviors during the OER. In the following Sections, reported transition metal chalcogenides are divided into three groups: sulfides (Section 5.1), selenides (Section 5.2), and tellurides (Section 5.3). Each section is devoted to recent progress in the development of OER electrocatalysts.

5.1. Transition Metal Sulfides

5.1.1. Electrode Preparation Methods. As seen in Table 5, transition metal sulfide electrocatalysts are typically tested for the OER by fabricating (i) powder-coated electrodes (P), where electrocatalytic materials are synthesized in powder form and coated on conductive substrates, or (ii) self-supported electrodes (S), in which the electrocatalysts are directly grown on the substrates. For either the powder-coated or self-supported electrode, the synthesis can mainly be divided into either a one-step process (starting material → final product) or a two-step process (starting material → precursor → final product). It is important to note that the starting material-to-precursor step and the precursor-to-final product step can have multiple reactions/steps (refs 274, 543, 547, 671, 676, 683, 700, 701, 764, 766, and 770). Here, for the synthesis of metal sulfide-based electrocatalysts, the most commonly used starting materials are Ni foam,[669,690,702] Cu foam,[681] and metal complexes/salts (i.e., central atoms/ions bonded to one/more ligands) (refs 448, 636, 685, 688, 697, 699, 703, and 781), among which the metal complexes/salts are the most popular option. In the case of precursors, the most commonly used/prepared precursors reported in the literature were MOFs (refs 274, 686, 701, 703, and 778), metal complexes/salts,[676,771,794] and metal oxides/hydroxides (refs 274, 547, 673, 683, 689, 700, 701, 764, and 772). Among the above precursors, the metal oxides/hydroxides are the most popular precursors for transition metal sulfide synthesis.

As mentioned above, the precursor-to-final product step can involve a single process [i.e., sulfidation (also known as sulfurization)] or multiple processes; these multiple processes mainly contain sulfidation and post-calcination,[689] post-sintering,[791] or post-annealing.[689,766,788] Sulfidation is a process where a sulfur source is used to sulfidize (= sulfurize) the precursor into the metal sulfide electrocatalysts (final product). There are different types of sulfidation processes, such as hydrothermal, solvothermal, gas-solid, and solid-state approaches. Here, hydrothermal sulfidation is one of the most utilized conversion techniques (refs 673, 683, 687, 688, 690, 766, 772, and 773). Regarding sulfur sources used in the sulfidation process for both one-step and two-step processes, the most frequently used are sodium sulfide (Na_2S) (refs 543, 672, 673, 700, 763, and 772), thioacetamide (C_2H_5NS) (refs 686, 701, 703, and 778), sulfur powder (refs 547, 676, and 685), thiourea (CH_4N_2S) (refs 448, 688, 697, and 790), CS_2 gas,[274] and [PDA][2HSO_4] (PDA: *p*-phenylenediamine).[794] There are, however, some unique synthetic cases for metal sulfide preparation that do not involve the sulfidation process: the precursor itself contains sulfur and can be transformed into the metal sulfide electrocatalyst upon annealing.[792]

Regardless of whether the one-step or two-step process is used for the preparation of the metal sulfides, all the above-mentioned synthetic steps involve some standard synthetic methods [i.e., hydrothermal method, solvothermal method, electrodeposition, MOF-derived method, and other less frequently used methods (e.g., chemical vapor deposition, anion exchange method, solid-state reaction, fast annealing method, and so on)]. These methods are discussed in detail below. For the following subsections, we divide the metal sulfide synthesis reports according to the synthetic method, explain their concepts briefly, and describe the resultant sulfide properties (e.g., chemical compositions, morphologies, etc.).

5.1.1.1. Hydrothermal Methods. In the literature, the majority of reports have used the hydrothermal method to synthesize electrocatalytic sulfide materials owing to its ability to produce well-defined morphologies, crystalline structures, and large surface area materials.[862] Additionally, the hydrothermal method uses water as a solvent, making it cost-effective, simple to handle, and less energy-intensive (synthetic temperatures: <200 °C). Most of the reported sulfide preparations involving the hydrothermal method can be divided into two types: the one-step process (refs 636, 675, 688, 690, 697, 699, 702, 724, and 781) and the two-step process (refs 543, 547, 637, 674, 707, 764, 766, 770, 772, 773, 787, 791, 793, and 799). We have seen more reports on the two-step process than on the one-step process. In this section, for the two-step approach (precursor preparation + sulfidation), we have taken the reports that used the hydrothermal method as the precursor preparation and selected the hydrothermal method[637,766,770,772]/other synthetic methods (e.g., the solvothermal method, etc.) for the subsequent sulfidation. In addition, we have also included reports wherein the first precursor synthesis step in a two-step process is not through the hydrothermal method.[448,641,673,687] For both the one- and two-step approaches, one of the most common starting materials is metal complexes/salts (refs 636, 675, 688, 697, 699, 702, 715, 723, and 781). For the two-step process especially, the most common precursors for the metal sulfides are MOFs,[674] boron nitride-carbon nanotubes (BN-CNTs),[791] and metal oxides/hydroxides (refs 543, 547, 637, 707, 764, 766, 770, 772, 773, 787, 793, and 799). Among them, metal oxides/hydroxides are the most frequently used precursors.

As mentioned above, the sulfurization using sulfur source(s) is an essential step for the preparation of metal sulfides for the electrocatalytic OER. There are many reports which used the hydrothermal method for sulfurization. Here, the most common sulfur sources used are salts such as sodium sulfide (Na_2S), sodium sulfite (Na_2SO_3), thiourea (CH_4N_2S), thioacetamide (C_2H_5NS), carbon disulfide (CS_2), sodium thiosulfate ($Na_2S_2O_3$), and elemental sulfur powder (S) (refs

https://doi.org/10.1021/acs.chemrev.3c00005
Chem. Rev. 2023, 123, 12795−13208

Table 5. Summary of the Electrocatalytic Properties, Electrochemical Testing Conditions, and Physicochemical Pre- and Post-analyses of Transition Metal Sulfides Used for Alkaline/Neutral/Acidic OER and of the Final Type of Electrocatalyst after OER Testing[a−e]

Initial Electrocatalyst	Substrate	Shape of Electrocatalyst	Deposition Type	Specific Loading / $mg \cdot cm^{-2}_{geo}$	η@10 $mA \cdot cm^{-2}_{geo}$ / mV	C_{dl} / $mF \cdot cm^{-2}_{geo}$	TOF / s^{-1} (@η or j)	Tafel Slope / $mV \cdot dec^{-1}$	Electrolyte	Pre-analysis	Post-analysis	Long-Term OER Test Conditions	Post-OER Electrocatalyst	Final Type of Electrocatalyst	Ref.
CuNiS-C2	Ni foam	Nanoplatelet	S	-	363	4	0.090 at 500 mV	53	1 M KOH	XRD, SEM, XPS	-	-	-	--	634
CuNiS-C3	Ni foam	Nanoplatelet Nanosphere	S	-	337	17.5	0.092 at 500 mV	43		XRD, SEM, XPS	XRD, XPS (after OWS)	~ 9200 s multistep CP [10, 20, 50, 100 $mA \cdot cm^{-2}_{geo}$] 50 h CP (200 $mA \cdot cm^{-2}_{geo}$, OWS)	Ni_3S_4, Cu_7S_4, SO_3^{2-}	Catalyst	
CuNiS-C4	Ni foam	Nanoplatelet Nanosphere	S	-	354	8.5	0.091 at 500 mV	45		XRD, SEM, XPS	-	~ 9200 s multistep CP [10, 20, 50, 100 $mA \cdot cm^{-2}_{geo}$]	-	-	
CuNiS-C5	Ni foam	Nanosphere	S	-	347	22	0.069 at 500 mV	55		XRD, SEM, XPS	-	~ 9200 s multistep CP [10, 20, 50, 100 $mA \cdot cm^{-2}_{geo}$]	-	-	
$MnCo_2O_4$@Ni_3S_2	Ni foam	Nanosheets	S	-	200 (@40 $mA \cdot cm^{-2}_{geo}$)	34.45	-	43.90	1 M KOH	XRD, SEM, XPS	XRD, SEM, XPS (after OWS)	15 h CA (cell voltage: 1.60 V, OWS)	$MnCo_2O_4$@Ni_3S_2, SO_4^{2-}	Catalyst	543
Fe-Co_9S_8 NM/NF	Ni foam	Nano/microspheres	S	3.32	270	22.34	-	70	1 M KOH	XRD, XPS, SEM, TEM, EDX	XRD, SEM, XPS	10 h CA (0.46 V_{SCE}) 10000 CV cycles (100 $mV \cdot s^{-1}$, 0.42–0.52 V_{SCE})	Fe-Co_9S_8, SO_4^{2-}	Catalyst	635
Ni-Co_9S_8 NM/NF	Ni foam	Hill-shaped bulges	S	3.84	340.1	9.27	-	150		XRD, SEM	-	-	-	-	
Co_9S_8 NM/NF	Ni foam	Nano/microspheres	S	2.83	283.5	18	-	150		XRD, SEM, TEM	-	-	-	-	
NiS_x/NF	Ni foam	Irregular surface	S	1.06	371.2	2.98	-	80		XRD, SEM	-	-	-	-	
CoCuFe-S-8	GC	3D hierarchical structure	P	0.23	300	1.51	0.270 at 300 mV	79	1 M KOH	XRD, TEM, SAED, SEM, HAADF-STEM, EDX, XPS, N_2 ISO (BET)	SEM, ICP-MS, XPS	> 45000 s CP (10 $mA \cdot cm^{-2}_{geo}$)	Co_9S_8, CuS, FeS, SO_x, Cu-O species	Catalyst	636
FeS	GC	-	P	0.23	520	-	-	145		XRD, XPS	-	-	-	-	
CuS	GC	-	P	0.23	570	-	-	431		XRD, XPS	-	-	-	-	
Co_9S_8	GC	Aggregated nanoparticles	P	0.23	380	0.18	0.013 at 300 mV	84		XRD, TEM, SAED, SEM, XPS	-	-	-	-	
Co_9S_8	Ni foam	Nanowires	S	-	299	8.4	-	67	1 M NaOH	SEM, XRD, XPS	SEM, XPS	2000 CV cycles > 15 h CA > 15 h CP (100 $mA \cdot cm^{-2}_{geo}$)	Co_9S_8	Catalyst	637
Co_9S_9	GC	Nanowires	P	-	385	-	-	-		-	-	-	-	-	
$Co_{1-x}S$/N-S-G	GC	Nanoparticle	P	0.5	371	-	-	~ 63	0.1 M KOH	XRD, SEM, TEM, N_2 ISO (BET, PSD), Raman	XRD, Raman, XPS	200 CV cycles	$Co_{1-x}S$, $Co-N_x$ (trace), N, S co-doped graphene	Catalyst	638
Fe–Ni_3S_2/FeNi	FeNi alloy foil	Nanosheet	S	-	282	-	-	54	1 M KOH	SEM, TEM, XRD, EDX, XPS, N_2 ISO (BET), ICP-MS	XPS	1000 CV cycles 9 h CA (1.56 V_{RHE}) 2800 s multistep CP (25−175 $mA \cdot cm^{-2}_{geo}$, 25 $mA \cdot cm^{-2}_{geo}$ per 400 s)	Fe^{3+}-doped Ni_3S_2, Sulfate	Catalyst	639
Ni_3S_2/Ni	Ni foil	Nanosheet	S	-	341	-	-	87		SEM, XRD, N_2 ISO (BET)	-	5 h CA (1.56 V_{RHE})	-	-	
FeS/Fe	Fe foil	Nanosheet	S	-	477	-	-	143		SEM, XRD	-	-	-	-	
Ni-Fe-OH@Ni_3S_2/NF	Ni foam	Nanosheets covered in bimetallic-oxide thin film	S	-	165 300 (@100 $mA \cdot cm^{-2}_{geo}$) 530 (@500 $mA \cdot cm^{-2}_{geo}$)	1.3	-	93	1 M KOH	XRD, Raman, SEM, STEM, TEM, EDX, XPS, ICP-OES	TEM, SEM	50 h CP (100 and 500 $mA \cdot cm^{-2}_{geo}$)	Ni-Fe-OH	Catalyst (substrate)	640
					283 (@100 $mA \cdot cm^{-2}_{geo}$) 479 (@1000 $mA \cdot cm^{-2}_{geo}$)	-	-	-	30 wt.% KOH	XRD, Raman, SEM, STEM, TEM, EDX, XPS, ICP-OES		50 h CP (1000 $mA \cdot cm^{-2}_{geo}$)	Ni-Fe-OH	Catalyst (substrate)	
Ni_3S_2/NF	Ni foam	Nanosheet array	S	-	~ 458 (@100 $mA \cdot cm^{-2}_{geo}$)	46	-	124	1 M KOH	XRD, Raman, SEM, TEM	-	-	-	-	
					~ 447 (@100 $mA \cdot cm^{-2}_{geo}$)	-	-	-	30 wt.% KOH	XRD, Raman, SEM, TEM	-	-	-	-	
NiCoS/NF	Ni foam	Nanorods	S	-	370 (@100 $mA \cdot cm^{-2}_{geo}$)	154	-	145	1 M KOH	XRD, XPS, SEM, EDX, FTIR	SEM, XRD, XPS	500 CV cycles (100 $mV \cdot s^{-1}$, 1.49–1.59 V_{RHE}) 10 h CA (1.53 V_{RHE})	Ni_3S_2, CoS, Co_9S_8, NiO	Catalyst	641
CoS_x/NF	Ni foam	Nanorods	S	-	390 (@100 $mA \cdot cm^{-2}_{geo}$)	69	-	157		XRD, XPS, SEM, EDX	-	-	-	-	
NiS_x/NF	Ni foam	-	S	-	490 (@100 $mA \cdot cm^{-2}_{geo}$)	-	-	221		-	-	-	-	-	
High-entropy metal sulfide $(CrMnFeCoNi)S_x$	Carbonized wood	Nanoparticles	S	~ 11.2 wt.%	295 (@100 $mA \cdot cm^{-2}_{geo}$)	84	-	66	1 M KOH	TEM, HAADF-STEM, EDX, SEM, XRD, XPS	XRD, EDX, XPS	10 h CP (100 $mA \cdot cm^{-2}_{geo}$) 5 h multistep CP (20, 50, 100, 150, 200 $mA \cdot cm^{-2}_{geo}$)	$(CrMnFeCoNi)S_x$	Catalyst	642
$(CrMnFeCoNi)S_x$	CP	Nanoparticles	S	0.35	116	-	-	-		-	-	100 h CP (100 $mA \cdot cm^{-2}_{geo}$)	-	-	
$(MnFeCoNi)_9S_8$	Carbonized wood	Nanoparticles	S	~ 11.2 wt.%	315 (@100 $mA \cdot cm^{-2}_{geo}$)	-	-	76		XRD, XPS	-	-	-	-	
$(FeCoNi)_9S_8$	Carbonized wood	Nanoparticles	S	~ 11.2 wt.%	330 (@100 $mA \cdot cm^{-2}_{geo}$)	-	-	87		XRD, XPS	-	-	-	-	

https://doi.org/10.1021/acs.chemrev.3c00005
Chem. Rev. 2023, 123, 12795−13208

Table 5. continued

Initial Electrocatalyst	Substrate	Shape of Electrocatalyst	Deposition Type	Specific Loading / $mg \cdot cm^{-2}_{geo}$	η@10 $mA \cdot cm^{-2}_{geo}$ / mV	C_{dl} / $mF \cdot cm^{-2}_{geo}$	TOF / s^{-1} (@η or f)	Tafel Slope / $mV \cdot dec^{-1}$	Electrolyte	Pre-analysis	Post-analysis	Long-Term OER Test Conditions	Post-OER Electrocatalyst	Final Type of Electrocatalyst	Ref.
$(NiFe)_9S_8$	Carbonized wood	Nanoparticles	S	~ 11.2 wt.%	345 (@100 $mA \cdot cm^{-2}_{geo}$)	-	-	81	1 M KOH	XRD	XRD	~ 8 h CP (100 $mA \cdot cm^{-2}_{geo}$)	-	Precatalyst	642
Mn-$NiCo_2S_4$ /Ni_3S_2	Ni foam	Nanoflowers	S	-	256 (@50 $mA \cdot cm^{-2}_{geo}$)	6.1	-	118.12		XRD, SEM	-	-	-	-	643
Fe-$NiCo_2S_4$ /Ni_3S_2	Ni foam	Nanorods	S	-	159 (@50 $mA \cdot cm^{-2}_{geo}$)	17.3	-	69.38		XRD, XPS, SEM, TEM, EDX	SEM, XRD, Raman, XPS	20 h CA (1.45 V_{RHE})	Metal oxides/hydroxides, SO_4^{2-}	Precatalyst (partial oxidation)	
Cu-$NiCo_2S_4$ /Ni_3S_2	Ni foam	Nanosheets Nanorods	S	-	224 (@50 $mA \cdot cm^{-2}_{geo}$)	12.7	-	92.35		XRD, SEM	-	-	-	-	
Zn-$NiCo_2S_4$ /Ni_3S_2	Ni foam	Nanosheets	S	-	208 (@50 $mA \cdot cm^{-2}_{geo}$)	4.2	-	104.45		XRD, SEM	-	-	-	-	
$NiCo_2S_4$ /Ni_3S_2	Ni foam	-	S	-	326 (@50 $mA \cdot cm^{-2}_{geo}$)	3.3	-	137.71		XRD, XPS	-	-	-	-	
Co(Zn)S_2/CC (Co:Zn = 4:1)	CC	Nanoarray	S	0.238	~ 309 (@100 $mA \cdot cm^{-2}_{geo}$)	-	-	-	30% KOH	SEM, TEM STEM, EDX, XRD, XPS, Raman	-	24 h CA	-	-	644
					248	5.75	-	72.9	1 M KOH		*In-Situ* Raman, XRD, TEM, SEM, EDX, XPS	1000 CV cycles (1.3−1.9 V_{RHE}) 24 h CA 3000 s multistep CP (10, 20, 30, 40, 50 $mA \cdot cm^{-2}_{geo}$)	Co(Zn)OOH, SO_4^{2-}	Precatalyst (almost full oxidation)	
CoS_2/CC	CC	Nanoarray	S	0.238	324	4.3	-	86.8		SEM, XRD, XPS, Raman	Raman, XPS	1000 CV cycles (1.3−1.9 V_{RHE})	CoOOH, SO_4^{2-}	Precatalyst	
ZnS/CC	CC	Nanoarray	S	0.238	584	1.91	-	332.3		SEM, XRD, XPS	-	-	-	-	
Co(Ni)S_2/CC	CC	Nanoarray	S	0.238	~ 292	-	-	-		SEM, XRD	-	-	-	-	
Co(Cu)S_2/CC	CC	Nanoarray	S	0.238	~ 305	-	-	-		SEM, XRD	-	-	-	-	
Co(Zn)S_2/CC (Co:Zn = 2:1)	CC	Nanoarray	S	0.238	~ 365	-	-	-		SEM, XRD	-	-	-	-	
Co(Zn)S_2/CC (Co:Zn = 8:1)	CC	Nanoarray	S	0.238	~ 316	-	-	-		SEM, XRD	-	-	-	-	
Co_9S_8@Fe_3O_4	Ni foam	Nanosheets (nanoflowers)	S	-	350 (@500 $mA \cdot cm^{-2}_{geo}$) 416 (@1000 $mA \cdot cm^{-2}_{geo}$)	23.7	-	54	1 M KOH	XRD, Raman, SEM, TEM, EDX, XAS, XAFS	*Operando* Raman, XAFS, XAS, XPS, SEM, TEM, CAM, *Operando* XAFS, XANES, SR-FTIR (SR: synchrotron radiation)	120 h CP (500 $mA \cdot cm^{-2}_{geo}$) 1 h CP (100 $mA \cdot cm^{-2}_{geo}$)	CoOOH@Fe_3O_4	Precatalyst	645
Co_9S_8	Ni foam	Nanosheets	S	-	410 (@500 $mA \cdot cm^{-2}_{geo}$)	17.5	-	92		XRD, Raman, SEM	*Operando* Raman, SEM	60 h CP (500 $mA \cdot cm^{-2}_{geo}$) 1 h CP (100 $mA \cdot cm^{-2}_{geo}$)	CoOOH	Precatalyst	
NiS_2	CFP	Nanosheets & nanoparticles	S	-	~ 315	2.60	-	94	1 M KOH	FESEM, UV-Vis, UPS, CAM, XANES, EXAFS	-	10 h CP (10 $mA \cdot cm^{-2}_{geo}$)	-	-	646
NiO/NiS_2	CFP	Nanosheets & nanoparticles	S	-	~ 367	0.895	-	98		XRD, FESEM, UPS, UV-Vis, TEM, EDX, CAM, XPS, UPS, XAS, XANES, EXAFS, XAFS, FTIR, Raman	*In-Situ* Raman, *In-Situ* ATR-IR, XPS	10 h CP (10 $mA \cdot cm^{-2}_{geo}$)	NiOOH, NiO, Adsorbed Fe species, SO_4^{2-}	Precatalyst (almost full oxidation)	
Fe-NiO/NiS_2 (8.7% Fe)	CFP	Nanosheets & nanoparticles	S	-	270	1.41	-	40		ICP-OES, XRD, FESEM, UV-Vis, TEM, EDX, CAM, XPS, UPS, XAS, XANES, EXAFS, XAFS, FTIR, Raman	*In-Situ* Raman, *In-Situ* ATR-IR, XRD, SEM, EDX, STEM, TEM, XPS	10 h CP (10 $mA \cdot cm^{-2}_{geo}$) ~ 105 h CP (10 $mA \cdot cm^{-2}_{geo}$) ~ 35 multistep CP (1, 10, 20, 30, 40, 50, 60 $mA \cdot cm^{-2}_{geo}$)	NiOOH, NiO, Fe dopant, SO_4^{2-}	Precatalyst (almost full oxidation)	
Ti-CoSx HSS	GC	Hollow superstructure	P	0.26	249	28.8	-	45.5	1 M KOH	SEM, TEM, XRD, HAADF-STEM, EDX, N_2 ISO (BET, PSD), XPS, FTIR	TEM, XPS, SEM	24 h CA 500 CV cycles (10 $mV \cdot s^{-1}$, 1.1−1.6 V_{RHE})	Metal hydroxides, S-O species	Precatalyst (partial oxidation)	647
Ti-CoSx SHSS	GC	Single layer Hollow superstructure	P	0.26	252	26.2	-	48.3		SEM, TEM	-	-	-	-	
CoSx HSS	GC	Hollow superstructure	P	0.26	272	22.1	-	56.6		TEM, XPS, N_2 ISO (BET, PSD)	-	-	-	-	
CoSx HP	CNF	Hollow particles	S	0.26	301	10.2	-	85.2		SEM, TEM, XRD, N_2 ISO, XPS	-	-	-	-	
Fe/FeS	CNF	Nanoparticles	S	-	270	-	-	-	1 M KOH	XRD, SEM, TEM, HAADF, EDX	-	-	-		648
Ni/Ni_3S_2	CNF	Nanoparticles	S	-	-	-	-	-		XRD, SEM, TEM, HAADF, EDX	-	-	-	-	
Co/Co_9S_8	CNF	Nanoparticles	S	-	274	-	-	68.7		SEM, TEM, HAADF-STEM, EDX, XRD, XPS	-	~ 11 h CP (10 $mA \cdot cm^{-2}_{geo}$)	-	-	
$(FeNi/FeNi)_9S_8$	CNF	Nanoparticles	S	-	-	-	-	-		XRD, SEM, HAADF, EDX	-	-	-	-	
FeCo/(FeCo)S	CNF	Nanoparticles	S	-	270	-	-	53.4		XRD, SEM, TEM, HAADF, EDX	XRD, TEM, HAADF-STEM, EDX	~ 10 h CP (10 $mA \cdot cm^{-2}_{geo}$)	FeCo hydroxides	Precatalyst (partial oxidation)	
CoNi$(CoNi)_9S_8$	CNF	Nanoparticles	S	-	-	-	-	-		XRD, SEM, TEM, HAADF, EDX	-	-	-	-	
(FeCoNi/(FeCoNi) $)_9S_8$	CNF	Nanoparticles	S	-	238	-	-	70.4		XRD, SEM, TEM, HAADF, EDX	-	~ 7.5 h CP (10 $mA \cdot cm^{-2}_{geo}$)	-	-	
(FeCoNiCu/(FeCo NiCu)$_9S_8$	CNF	Nanoparticles	S	-	-	-	-	-		XRD, SEM, TEM, HAADF, EDX	-	-	-	-	
CoOOH/Co_9S_8 (CV activated)	CC	Roughened nanorods	S	-	240 ± 6	6.67	~ 0.33 at 400 mV	86.4	1 M KOH	UV-Vis, XRD, SEM, TEM, HAADF-	TEM, AFM, XRD, ICP-OES, XRF,	2000 CV cycles (1.2−1.7 V_{RHE}) 150 h CP (100 $mA \cdot cm^{-2}_{geo}$) 24 h CP (100 $mA \cdot cm^{-2}_{geo}$)	CoOOH (at low potential), CoO_2 (at high potential)	Precatalyst (partial oxidation)	649

https://doi.org/10.1021/acs.chemrev.3c00005
Chem. Rev. 2023, 123, 12795−13208

Table 5. continued

Initial Electrocatalyst	Substrate	Shape of Electrocatalyst	Deposition Type	Specific Loading / $mg \cdot cm^{-2}_{geo}$	η@10 $mA \cdot cm^{-2}_{geo}$ / mV	C_{dl} / $mF \cdot cm^{-2}_{geo}$	TOF / s^{-1} (@η or f)	Tafel Slope / $mV \cdot dec^{-1}$	Electrolyte	Pre-analysis	Post-analysis	Long-Term OER Test Conditions	Post-OER Electrocatalyst	Final Type of Electrocatalyst	Ref.
										STEM, XPS, ICP-OES, XRF	*Operando* EPR, *In-Situ* Raman				
$CoOOH/CoS_2$ (CV activated)	CC	Roughened nanorods	S	-	326 ± 5	5.04	~ 0.17 at 400 mV	117.1		UV-Vis, XRD, SEM, TEM, XPS, ICP-OES, XRF	TEM, AFM, ICP-OES, XRF, *Operando* EPR, *In-Situ* Raman	24 h CP (100 $mA \cdot cm^{-2}_{geo}$)	CoOOH (at low potential), CoO_2 (at high potential)	Precatalyst (partial oxidation)	
$CoOOH/Co_3S_4$ (CV activated)	CC	Roughened nanorods	S	-	288 ± 5	5.09	~ 0.19 at 400 mV	110.2		UV-Vis, XRD, SEM, TEM, XPS, ICP-OES, XRF	TEM, AFM, ICP-OES, XRF, *Operando* EPR, *In-Situ* Raman	24 h CP (100 $mA \cdot cm^{-2}_{geo}$)	CoOOH (at low potential), CoO_2 (at high potential)	Precatalyst (partial oxidation)	649
CoOOH/CoS (CV activated)	CC	Roughened nanorods	S	-	273 ± 8	5.64	~ 0.25 at 400 mV	95.5		UV-Vis, XRD, SEM, TEM, XPS, ICP-OES, XRF	TEM, AFM, ICP-OES, XRF, *Operando* EPR, *In-Situ* Raman	24 h CP (100 $mA \cdot cm^{-2}_{geo}$)	CoOOH (at low potential), CoO_2 (at high potential)	Precatalyst (partial oxidation)	
$CoOOH/Co_9S_8$ (CV activated)	CC	Roughened nanorods	S	-	296 ± 5	5.15	~ 0.17 at 400 mV	114.2		UV-Vis, XRD, SEM, TEM, XPS, ICP-OES, XRF	TEM, AFM, ICP-OES, XRF, *Operando* EPR, *In-Situ* Raman	24 h CP (100 $mA \cdot cm^{-2}_{geo}$)	CoOOH (at low potential), CoO_2 (at high potential)	Precatalyst (partial oxidation)	
Ni(OH)S	-	Amorphous nanosheets	P	-	250	-	-	51	1 M KOH	TEM, EDX, XRD, XPS, Raman, FT-IR	-	-	-	-	650
Ni(OH)S/NF	Ni foam	Amorphous nanosheets	S	5	250	6.92	-	52.38		SEM, TEM, FTIR, Raman, XPS	*In-Situ* Raman, FTIR, XPS	40 h CP [20 (for 20 h), 50 $mA \cdot cm^{-2}_{geo}$ (for 20 h)]	NiOOH, SO_4^{2-}	Precatalyst (almost full oxidation)	
FeS_2-MoS_2@CoS_2-MOF	Ni foam	Mesoporous CoS_2 nanoarrays covered by FeS_2@MoS_2	S	-	211 (@20 $mA \cdot cm^{-2}_{geo}$)	30.5	-	64.5	1 M KOH	SEM, EDX, XRD, TEM, N_2 ISO, XPS	SEM, EDX, XPS (after OWS)	30 h CP (50 mA cm^{-2}) 30 h CP (10 $mA \cdot cm^{-2}_{geo}$, OWS) 30 h CP (50 $mA \cdot cm^{-2}_{geo}$, OWS) 30 h CP (100 $mA \cdot cm^{-2}_{geo}$, OWS)	Metal oxide, Metal oxy-hydroxide, SO_4^{2-}	Precatalyst (partial oxidation)	
MoS_2@CoS_2-MOF	Ni foam	Nodules on MOF	S	-	241 (@20 $mA \cdot cm^{-2}_{geo}$)	19.6	-	89.7		SEM, EDX, XRD	-	-	-	-	651
FeS_2-MoS_2	Ni foam	Nanoarray	S	-	238 (@20 $mA \cdot cm^{-2}_{geo}$)	8.7	-	84.6		SEM, EDX, XRD	-	-	-	-	
CoS_2-MOF	Ni foam	@2D vertical MOF, mesoporous	S	-	380 (@20 $mA \cdot cm^{-2}_{geo}$)	7.1	-	114.2		SEM, EDX, XRD, N_2 ISO	-	-	-	-	
MoS_2	Ni foam	Nanoarray	S	-	411 (@20 $mA \cdot cm^{-2}_{geo}$)	3.9	-	118.1		SEM, EDX, XRD, TEM	-	-	-	-	
Au-$NiCoFe_2S_8$	GC	Nanoplatelets	P	~ 0.255	243	-	-	43	1 M KOH	STEM, TEM, XRD, SAED, HAADF-STEM, XPS, Raman	STEM, TEM, XPS, Raman	10 CV cycles (10 $mV \cdot s^{-1}$) 24 h CP (10 $mA \cdot cm^{-2}_{geo}$), 12 h CP (10 $mA \cdot cm^{-2}_{geo}$, CP substrate)	Au-$NiCoFe_2S_8$, SO_4^{2-}	Precatalyst (sulfide dissolution)	
Au-$CoFe_2S_8$	GC	Nanoplatelets	P	~ 0.255	275	-	-	44		STEM, TEM, XRD, SAED, HAAFD-STEM, XPS, Raman	-	-	-	-	652
Au-$NiFe_2S_8$	GC	Nanoplatelets	P	~ 0.255	259	-	-	41		STEM, TEM, XRD, SAED, HAADF-STEM, XPS, Raman	-	-	-	-	
$CoS_{1.97}$	CFP	Nanoplate clusters	S	-	310	5.03	-	69	1 M KOH	XRD, SEM, TEM, CAM, ESR, XPS, XANES, EXAFS	XPS, SEM, XRD, Raman, TEM, *In-Situ* Raman, *Quasi-Operando* XPS	24 h CP (10 $mA \cdot cm^{-2}_{geo}$) ~ 75 h CP (1000 $mA \cdot cm^{-2}_{geo}$)	CoOOH, SO_4^{2-}	Precatalyst (partial oxidation)	
CeO_2-$CoS_{1.97}$ (CeO_2 acts as substrate)	CFP	Nanoplate clusters	S	-	264	8.96	-	64	1 M KOH	XRD, ICP-AES, SEM, EDX, TEM, CAM, ESR, HADDF-STEM, XPS, XANES, EXAFS	XPS, SEM, XRD, Raman, TEM, *In-Situ* Raman, *Quasi-Operando* XPS	50 h CP (10 $mA \cdot cm^{-2}_{geo}$) 150 h CP (1000 $mA \cdot cm^{-2}_{geo}$)	CoOOH, SO_4^{2-}	Precatalyst (partial oxidation)	653
$CoS_{1.97}$-CeO_2 (CeO_2 as surface decoration)	CFP	Nanoplate clusters	S	-	270 323 (@100 $mA \cdot cm^{-2}_{geo}$)	7.61	-	49		XRD, ICP-AES, SEM, EDX, TEM, CAM, ESR, HADDF-STEM, XPS, XANES, EXAFS	XPS, SEM, XRD, Raman, TEM, *In-Situ* Raman, *Quasi-Operando* XPS	50 h CP (10 $mA \cdot cm^{-2}_{geo}$) 150 h CP (1000 $mA \cdot cm^{-2}_{geo}$)	CoOOH, CoO_2, SO_4^{2-}	Precatalyst (partial oxidation)	
Ni_3S_2/FeS	Ni foam	Nanosheets	S	~ 2.0	295 (@30 $mA \cdot cm^{-2}_{geo}$)	16.5	-	79.8	1 M KOH	XRD, SEM, TEM, XPS	SEM, TEM, XPS (after OWS)	3000 CV cycles (1.2–1.6 V_{RHE}) 100 h CA [1.52 (for 50 h), 1.6 V_{RHE} (for 50 h)] 100 h CA (cell voltage: 1.71 V, OWS)	-	Precatalyst (partial oxidation)	654
Ni_3S_2	Ni foam	Nanoparticulate	S	-	~ 390 (@30 $mA \cdot cm^{-2}_{geo}$)	7.9	-	82.5		SEM	-	-	-	-	
FeS	Ni foam	Roughened surface	S	-	~ 330 (@30 $mA \cdot cm^{-2}_{geo}$)	7.5	-	244.6		SEM	-	-	-	-	
NiCoS (Ni_3S_2/Co_3S_4)	Ni foam	Nanosheet array	S	14.3	210 270 (@100 $mA \cdot cm^{-2}_{geo}$) 360 (@500 $mA \cdot cm^{-2}_{geo}$) 430 (@1000 $mA \cdot cm^{-2}_{geo}$)	-	-	-	1 M KOH + 0.5 M NaCl	SEM, TEM, EDX, XRD, XPS	-	100 h CA (1.5 V_{RHE})	-	-	655
					280 360 (@100 $mA \cdot cm^{-2}_{geo}$) 440 (@500 $mA \cdot cm^{-2}_{geo}$) 470 (@1000 $mA \cdot cm^{-2}_{geo}$)	-	-	-	1 M KOH + seawater		SEM, TEM, XRD, XPS, EDX	100 h CP (100 $mA \cdot cm^{-2}_{geo}$)	NiCoOOH	Precatalyst (partial oxidation)	
					220 270 (@100 $mA \cdot cm^{-2}_{geo}$) 330 (@500 $mA \cdot cm^{-2}_{geo}$)	148.6	-	42	1 M KOH		-	-	-	-	

https://doi.org/10.1021/acs.chemrev.3c00005
Chem. Rev. 2023, 123, 12795−13208

Table 5. continued

Initial Electrocatalyst	Substrate	Shape of Electrocatalyst	Deposition Type	Specific Loading / $mg \cdot cm^{-2}_{geo}$	η@10 $mA \cdot cm^{-2}_{geo}$ / mV	C_{dl} / $mF \cdot cm^{-2}_{geo}$	TOF / s^{-1} (@η or f)	Tafel Slope / $mV \cdot dec^{-1}$	Electrolyte	Pre-analysis	Post-analysis	Long-Term OER Test Conditions	Post-OER Electrocatalyst	Final Type of Electrocatalyst	Ref.
					390 (@1000 $mA \cdot cm^{-2}_{geo}$)										655
Ni_3S_2	Ni foam	-	S	-	340	70.0	-	116		XPS	-	-	-	-	
$FeNiCoCrMnS_2$	Ni foam	Nodulated nanoparticles	S	2	199 246 (@100 $mA \cdot cm^{-2}_{geo}$) 285 (@500 $mA \cdot cm^{-2}_{geo}$) 308 (@1000 $mA \cdot cm^{-2}_{geo}$)	0.59	-	39.1	1 M KOH	XRD, SEM, TEM, SAED, HAADF, EDX, ICP-MS, XPS, *In-Situ* Raman, CAM	TEM, SAED, HAADF, EDX, *In-Situ* Raman, XPS, ICP-MS, CAM	55 h CP (10 $mA \cdot cm^{-2}_{geo}$) 55 h CP (100 $mA \cdot cm^{-2}_{geo}$) ~ 53 h CP (500 $mA \cdot cm^{-2}_{geo}$) 12000 CV cycles (100 $mV \cdot s^{-1}$)	Metal (oxy)hydroxide, SO_4^{2-}	Precatalyst (full oxidation)	656
$FeNiCoCrCuS_2$	Ni foam	Nodulated nanoparticles	S	2	257 (@100 $mA \cdot cm^{-2}_{geo}$) 303 (@500 $mA \cdot cm^{-2}_{geo}$)	0.46	-	42.7		XRD, SEM, ICP-MS, XPS	-	-	-	-	
$FeNiCoCrZnS_2$	Ni foam	Nodulated nanoparticles	S	2	258 (@100 $mA \cdot cm^{-2}_{geo}$) 309 (@500 $mA \cdot cm^{-2}_{geo}$)	0.495	-	41.5		XRD, SEM, ICP-MS, XPS	-	-	-	-	
$FeNiCoCrAlS_2$	Ni foam	Nodulated nanoparticles	S	2	252 (@100 $mA \cdot cm^{-2}_{geo}$) 293 (@500 $mA \cdot cm^{-2}_{geo}$)	0.685	-	39.5		XRD, SEM, ICP-MS, XPS	-	-	-	-	
$FeNiCoCrS_2$	Ni foam	Nodulated nanoparticles	S	2	259 (@100 $mA \cdot cm^{-2}_{geo}$) 312 (@500 $mA \cdot cm^{-2}_{geo}$)	0.484	-	42.5		XRD, SEM, ICP-MS, XPS, *In-Situ* Raman	*In-Situ* Raman	-	Metal (oxy)hydroxide, Likely SO_4^{2-}	Precatalyst	
$FeNiCoS_x$	Ni foam	Nodulated nanoparticles	S	2	270 (@100 $mA \cdot cm^{-2}_{geo}$) 335 (@500 $mA \cdot cm^{-2}_{geo}$)	0.343	-	43.9		XRD, SEM, ICP-MS, XPS, *In-Situ* Raman	*In-Situ* Raman, ICP-MS	-	Metal (oxy)hydroxide, Likely SO_4^{2-}	Precatalyst (full oxidation)	
$FeNiS_x$	Ni foam	Nodulated nanoparticles	S	2	272 (@100 $mA \cdot cm^{-2}_{geo}$) 354 (@500 $mA \cdot cm^{-2}_{geo}$)	0.267	-	52		XRD, SEM, ICP-MS, XPS, *In-Situ* Raman	*In-Situ* Raman	-	Metal (oxy)hydroxide, Likely SO_4^{2-}	Precatalyst	
FeS_x	Ni foam	Nodulated nanoparticles	S	2	297 (@100 $mA \cdot cm^{-2}_{geo}$) 429 (@500 $mA \cdot cm^{-2}_{geo}$)	-	-	57.7		XRD, SEM, ICP-MS, XPS	-	-	-	-	
NiS_x	Ni foam	Nodulated nanoparticles	S	2	360 (@100 $mA \cdot cm^{-2}_{geo}$) 483 (@500 $mA \cdot cm^{-2}_{geo}$)	-	-	91		XRD, SEM, ICP-MS, XPS	-	-	-	-	
CoS_2	Ni foam	Nodulated nanoparticles	S	2	342 (@100 $mA \cdot cm^{-2}_{geo}$) 437 (@500 $mA \cdot cm^{-2}_{geo}$)	-	-	67.5		XRD, SEM, ICP-MS, XPS	-	-	-	-	
CrS_x	Ni foam	Nodulated nanoparticles	S	2	391 (@100 $mA \cdot cm^{-2}_{geo}$) 503 (@500 $mA \cdot cm^{-2}_{geo}$)	-	-	75		XRD, SEM, ICP-MS, XPS	-	-	-	-	
MnS	Ni foam	Nodulated nanoparticles	S	2	459 (@100 $mA \cdot cm^{-2}_{geo}$)	-	-	98		XRD, SEM, ICP-MS	-	-	-	-	
Ni_3S_2@$FeNi_2S_4$@NF	Ni foam	Nanosheet	S	-	235	4.34	-	92	1 M KOH	XRD, SEM, TEM, EDX, XPS	SEM, XPS	1000 CV cycles 24 h CA	Metal oxyhydroxide	Precatalyst	657
$FeNi_2S_4$@NF	Ni foam	-	S	-	225	10.79	-	52		-	-	-		-	
Ni_3S_2@NF	Ni foam	-	S	-	300	3.61	-	143		XRD	-	-	-	-	
Ni_3S_2@Fe_9S_{10}@CC	CC	Nanosheet	S	-	274	0.42	-	175		-	-	-	-	-	
Fe_xCo_{1-x}-AO1 (AO: activated amorphous oxide)	CC	-	P	-	351	-	-	66	1 M KOH	-	-	10 CV cycles (5 $mV \cdot s^{-1}$, activation applied before OER testing)	-	-	658
Fe_xCo_{1-x}-AO2 (AO: activated amorphous oxide)	CC	-	P	-	325	-	-	70		-	-	10 CV cycles (5 $mV \cdot s^{-1}$, activation applied before OER testing)	-	-	
Fe_xCo_{1-x}-AO3 (AO: activated amorphous oxide)	CC	-	P	-	315	-	-	64		-	-	10 CV cycles (5 $mV \cdot s^{-1}$, activation applied before OER testing)	-	-	
Fe_xCo_{1-x}-AO4 (AO: activated amorphous oxide)	CC	-	P	-	295	-	-	62		-	-	10 CV cycles (5 $mV \cdot s^{-1}$, activation applied before OER testing)	-	-	
Co_xFe_{1-x}-AO1 (AO: activated amorphous oxide)	CC	-	P	-	280	-	-	48		-	-	10 CV cycles (5 $mV \cdot s^{-1}$, activation applied before OER testing)	-	-	
Co_xFe_{1-x}-AO2 (AO: activated amorphous oxide)	CC	-	P	-	275	-	-	79		-	-	10 CV cycles (5 $mV \cdot s^{-1}$, activation applied before OER testing)	-	-	
Co_xFe_{1-x}-AO3 (AO: activated amorphous oxide)	CC	Nanowires	P	-	267	-	-	34		EDX, SEM, TEM, XRD, HAADF-STEM, XPS	-	10 CV cycles (5 $mV \cdot s^{-1}$, activation applied before OER testing) 40 h CP (10 $mA \cdot cm^{-2}_{geo}$)	Metal oxide species, Sulfate	Precatalyst (surface oxidized before the OER)	
Co_xFe_{1-x}-AO4 (AO: activated amorphous oxide)	CC	-	P	-	277	-	-	37		-	-	10 CV cycles (5 $mV \cdot s^{-1}$, activation applied before OER testing)	-	-	
NiS/NF	Ni foam	Numerous grains	S	~ 3.1	294 453 (@50 $mA \cdot cm^{-2}_{geo}$) 575 (@100 $mA \cdot cm^{-2}_{geo}$)	1.50	-	168	Fe-purified 1 M KOH	XRD, SEM, EDX, TEM, XPS, TXRF	XRD, SEM, EDX, XPS, TXRF	20 h CP (20 $mA \cdot cm^{-2}_{geo}$)	NiO_xH_y, Sulfate (SO_4^{2-})	Precatalyst	49
$Fe_{0.8}Ni_{0.15}S_{1.05}$	GC	Stacked nanosheets	P	~ 0.2 mg (catalyst and carbon powder)	228	83.8	-	53	1 M KOH	XRD, SEM, TEM, EDX, N_2 ISO, XPS, ICP	XPS, TEM	1000 CV cycles (50 $mV \cdot s^{-1}$, 1–1.7 V_{RHE}) 10 h CP (10 $mA \cdot cm^{-2}_{geo}$)	Ni-Fe oxy-sulfide, Ni-Fe oxide, Ni-Fe hydroxide	Precatalyst (partial oxidation)	659
$Fe_{0.75}Ni_{0.2}S_{1.05}$	GC	Smoothed platelets	P	~ 0.2 mg (catalyst	240	75	-	54		SEM, XRD, ICP	-	-	-	-	

https://doi.org/10.1021/acs.chemrev.3c00005
Chem. Rev. 2023, 123, 12795−13208

Table 5. continued

Initial Electrocatalyst	Substrate	Shape of Electrocatalyst	Deposition Type	Specific Loading / $mg \cdot cm^{-2}_{geo}$	η@10 $mA \cdot cm^{-2}_{geo}$ / mV	C_{dl} / $mF \cdot cm^{-2}_{geo}$	TOF / s^{-1} (@η or f)	Tafel Slope / $mV \cdot dec^{-1}$	Electrolyte	Pre-analysis	Post-analysis	Long-Term OER Test Conditions	Post-OER Electrocatalyst	Final Type of Electrocatalyst	Ref.
				and carbon powder)											
$Fe_{0.85}Ni_{0.1}S_{1.05}$	GC	Stacked platelets	P	~ 0.2 mg (catalyst and carbon powder)	247	56.5	-	63		SEM, ICP, ICP	-	-	-	-	659
$Fe_{0.9}Ni_{0.05}S_{1.05}$	GC	Stacked platelets	P	~ 0.2 mg (catalyst and carbon powder)	264	42.1	-	59		SEM	-	-	-	-	
$Fe_{0.95}S_{1.05}$	GC	Agglomerates	P	~ 0.2 mg (catalyst and carbon powder)	381	15.5	-	96		SEM, N_2 ISO, XPS, ICP	-	-	-	-	
NiS_{100}	GC	Spherical particles	P	0.24	354	-	-	-	1 M KOH	XRD, SEM, TEM, EDX, XPS, Kr ISO (BET)	TEM, EDX, HAADF, ICP-MS	6 and ~ 11 h CP (10 $mA \cdot cm^{-2}_{geo}$) FE test	NiO_xH_y, NiO	Precatalyst (partial oxidation)	47
MoCoNiS/NF	Ni foam	Nanoparticulates	S	-	151	4.12	-	44.7	1 M KOH	SEM, XRD, XPS, EDX, TEM, SAED	TEM, EDX, XPS (after 1000 CV)	12 h CA (1.3895 V_{RHE}) 1000 CV cycles	Metal oxide/hydroxide	Precatalyst (partial oxidation)	660
CoNiS/NF	Ni foam	Islands	S	-	175	3.1	-	220.7		SEM, XRD	-	-	-	-	
NiS/NF	Ni foam	Nanoparticulates	S	-	259	4.2	-	158.9		SEM, XRD, TEM, SAED	-	-	-	-	
NiFe-MS/MOF@NF (M = metal) (Fe:Ni = 1:4)	Ni foam	Nanosheet array (MS clusters embedded in NiFe-MOF)	S	-	230 (@ 50 $mA \cdot cm^{-2}_{geo}$)	20.2	-	32	1 M KOH	XRD, SEM, EDX, TEM, SAED, XPS	XRD, Raman, SEM, XPS (after 20 CV)	20 CV cycles (50 $mV \cdot s^{-1}$, 1−1.8 V_{RHE}, activation) 17 h CP (50 $mA \cdot cm^{-2}_{geo}$) 2000 CV cycles (1.05−2.05 V_{RHE})	Ni/Fe oxyhydroxide	Precatalyst (partial oxidation)	661
NiFe-MS/MOF@NF (M = metal) (Fe:Ni = 1:2)	Ni foam	Nanorod	S	-	~ 235 (@ 50 $mA \cdot cm^{-2}_{geo}$)	-	-	-		XRD, SEM	-	-	-	-	
NiFe-MS/MOF@NF (M = metal) (Fe:Ni = 1:6)	Ni foam	Nanostructure	S	-	~ 240 (@ 50 $mA \cdot cm^{-2}_{geo}$)	-	-	-		XRD, SEM	-	-	-	-	
(Fe)-Ni_3S_2@NF	Ni foam	Nanosheet	S	-	270 (@ 50 $mA \cdot cm^{-2}_{geo}$)	11	-	45		XRD, SEM, XPS	-	-	-	-	
H–Fe–CoMoS	CP	Hollow spherical particles	P	0.4	282	79	-	58.0	1 M KOH	XRD, SEM, TEM, XPS, Raman, N_2 ISO (BET)	TEM, XPS	20 h CA	Metal oxide/(oxy)hydroxide	Precatalyst	662
H–CoMoS	CP	Hollow spherical particles	P	0.4	315	54	-	74.0		XRD, SEM, TEM, EDX, XPS	-	-	-	-	
CoMoS	CP	Spherical particles	P	0.4	358	32	-	76.0		XRD, SEM, TEM, N_2 ISO (BET), XPS	-	-	-	-	
$NiCo_2S_4$	CC	Cactus-like structure	S	-	290	8.8	0.0026 at 300 mV	97	1 M KOH	HAADF, STEM, SEM	-	-	-	-	663
$NiCo_2S_4$/Fe-1	CC	Nanowire	S	-	250	15.2	0.0064 at 300 mV	80		N_2 ISO (BET, PSD), XPS, XAS, XANES, EDX, SEM	-	20 h CP (10 $mA \cdot cm^{-2}_{geo}$)	-	-	
$NiCo_2S_4$/Fe-2	CC	Nanowire	S	-	200	30.3	0.017 at 300 mV	71		XRD, SEM, TEM, SAED, N_2 ISO (BET, PSD), HAADF, STEM-EDX, XPS, XAS, XANES	SEM, XANES	20 h CP (10 $mA \cdot cm^{-2}_{geo}$)	Metal hydroxides/oxyhydroxides	Precatalyst	
$NiCo_2S_4$/Fe-3	CC	Flake aggregation	S	-	230	19.0	0.011 at 300 mV	73		SEM, EDX	-	20 h CP (10 $mA \cdot cm^{-2}_{geo}$)	-	-	
Ferrocene-incorporated Co_xS_y/CNTs	GC	Nanostructures	P	~ 0.4	304	0.718	1.9×10^{-3} at ~ 350 mV	54.2	1 M KOH	XRD, Raman, SEM, TEM, ICP-MS, XPS	-	1000 CV cycles (50 $mV \cdot s^{-1}$)	-	-	664
Ferrocene-incorporated Co_xS_y	GC	Spherical nanoparticles, aggregated	P	~ 0.4	336	0.254	0.7×10^{-3} at ~ 350 mV	65.3		XRD, Raman, SEM, TEM, ICP-MS, CHNS, XPS	-	-	-	-	
Co_xS_y	GC	Spherical nanoparticles, aggregated	P	~ 0.4	369	0.223	0.3×10^{-3} at ~ 350 mV	81.0		XRD, Raman, SEM, TEM, ICP-MS, CHNS, XPS	-	-	-	-	
Fe_xS_y	GC	Nanoparticles, microparticles	P	~ 0.4	-	-	-	-		XRD, Raman, SEM, ICP-MS, CHNS, XPS	-	-	-	-	
Ferrocene-incorporated Co_xS_y/ACF (ACF: acid pretreated carbon fiber)	Acid pre-treated CF (ACF)	Nanostructures (nanoparticles and nanosheets)	S	~ 0.3	315	-	-	82.1		XRD, SEM, EDX, Raman	XRD, Raman, EDX	25 & 50 CV cycles > 60000 s CA (1.55 V_{RHE})	Co/Fe oxides/(oxy)hydroxides	Precatalyst	
$CoFe_{0.2}S_z$	GC	Hollow, small vesicles	P	0.14	320 [304 (1 M KOH)]	15.3 μF	-	48.7	1 M NaOH	SEM, TEM, XRD, STEM EDX, XPS	TEM, XPS, *Operando* Raman, *Operando* XAS	~ 11 h CA (NF, 0.67 $mg \cdot cm^{-2}$)	CoOOH	Precatalyst (partial oxidation)	665
CoS_z	GC	Hollow, small vesicles	P	0.14	390	7.7 μF	-	71.5		SEM, TEM, XRD, STEM EDX, XPS	TEM, XPS, *Operando* Raman, *Operando* XAS	~ 1 h CA (NF, 0.67 $mg \cdot cm^{-2}$)	CoOOH	Precatalyst (partial oxidation)	
FeS_z	GC	-	P	0.14	-	7.7 μF	-	89.7		XPS	-	~ 11 h CA (NF, 0.67 $mg \cdot cm^{-2}$)	-	-	

https://doi.org/10.1021/acs.chemrev.3c00005
Chem. Rev. 2023, 123, 12795−13208

Table 5. continued

Initial Electrocatalyst	Substrate	Shape of Electrocatalyst	Deposition Type	Specific Loading / $mg \cdot cm^{-2}_{geo}$	η@10 $mA \cdot cm^{-2}_{geo}$ / mV	C_{dl} / $mF \cdot cm^{-2}_{geo}$	TOF / s^{-1} (@η or f)	Tafel Slope / $mV \cdot dec^{-1}$	Electrolyte	Pre-analysis	Post-analysis	Long-Term OER Test Conditions	Post-OER Electrocatalyst	Final Type of Electrocatalyst	Ref.
Co-Fe-S@PB NBs (PB: Prussian blue) (NB: nanoboxes)	GC	Nanoboxes	P	~0.2	286	26.51	1.03 at 300 mV	37.84	1 M KOH	XRD, STEM, EDX, TEM, SAED, FTIR, XANES, EXAFS, XPS, ICP-AES, ICP-MS	SEM, TEM, Raman, XANES, EXAFS, HAADF-STEM, EDX, STEM, XPS, ICP-MS	~24000 s CP (5 & 10 $mA \cdot cm^{-2}_{geo}$) 33 h CA (1.52 V_{RHE}, NF)	$(Co,Fe)O_x$, $(Co,Fe)OH_y$, SO_4^{2-}	Precatalyst (partial oxidation)	666
Co-Fe-S@PB particles (PB: Prussian blue)	GC	Particles	P	~0.2	~300	17.36	0.44 at 300 mV	42.08		XPS, XANES, EXAFs	-	~24000 s CP (5 & 10 $mA \cdot cm^{-2}_{geo}$)	-	-	
Co-S@PB NBs	GC	Nanoboxes	P	~0.2	~350	-	-	-		-	TEM, HAADF-STEM, EDX	-	CoO_x, CoOOH	Precatalyst (partial oxidation)	
Co-Fe-Mo-S NBs [$(Co,Fe)_9S_8$@MoS_2]	GC	Double-layered nanoboxes	P	~0.2	303	45.10	-	42.06		XRD, EDX, SEM, TEM, STEM-EDX, ICP-AES	-	10000 s CA (1.535 & 1.445 V_{RHE})	-	-	
Ni-Fe-S@PB NBs	GC	Nanoboxes	P	~0.2	~330	-	-	125.53		XRD, SEM, EDX, TEM	TEM, HAADF-STEM, EDX	5 h CP (10 $mA \cdot cm^{-2}_{geo}$)	$(Ni,Fe)O_x$, (Ni,Fe)OOH	Precatalyst (partial oxidation)	
3D $NiMoO_x$/NiMoS	Ni foam	Heterostructure array	P	-	186	21.5	-	34	1 M KOH	XRD, SEM, EDX, TEM, HAADF-STEM, XPS	XPS, SEM, TEM (after OWS)	25 h CA (1.455 V_{RHE}) 25 h CA (1.508 V_{RHE}) 500 h CA (1.75 V_{RHE}, OWS)	Metal hydroxide, Metal (oxy)hydroxide	Precatalyst (partial oxidation)	667
NiO_x/Ni_3S_2	Ni foam	-	P	-	214	11.1	-	56		XRD, XPS	-	-	-	-	
MoO_x/MoS_2	Ni foam	-	P	-	266	9.6	-	62		XRD, XPS	-	-	-	-	
NiMoS	Ni foam	Nanosheets on microrods	P	-	370	7.9	-	74		XRD, SEM, XPS	-	-	-	-	
$Fe_{1.2}Ni_{1.8}S_2$@NF	Ni foam	Nano-aggregates	S	-	268 (@100 mA/cm^2_{geo})	49	-	68	1 M KOH	SEM, TEM, XRD, XPS	-	-	-	-	668
$Fe_{0.9}Ni_{2.1}S_2$@NF	Ni foam	Nanosheets	S	-	252 (@100 mA/cm^2_{geo})	67	-	64		SEM, AFM, TEM, SAED, XRD, XPS, EDX	SEM, XRD, XPS	24 h CP (1.48 V_{RHE})	Ni-Fe (oxy)hydroxide, Oxidized S species	Precatalyst (partial oxidation)	
$Fe_{0.6}Ni_{2.4}S_2$@NF	Ni foam	Nanosheets	S	-	261 (@100 mA/cm^2_{geo})	20	-	147		SEM, TEM, XRD, XPS	-	-	-	-	
$Fe_{0.3}Ni_{2.7}S_2$@NF	Ni foam	Nanoparticles/ sheets	S	-	300 (@100 mA/cm^2_{geo})	14	-	88		SEM, TEM, XRD, XPS	-	-	-	-	
Ni_3S_2@NF	Ni foam	Nanoparticles	S	-	331 (@100 mA/cm^2_{geo})	10	-	74		SEM, TEM, XRD, XPS	-	-	-	-	
FeS@IF	Fe foam	Nanoflowers/ sheets	S	-		-	-	-		FESEM, XPS	-	-	-	-	
Cu_2S@CF	Cu foam	Nanoplatelets	S	-	280	-	-	-		FESEM, XRD, TEM, XPS	-	-	-	-	
$Fe_xCu_{2-x}S$@CF	Cu foam	Thick nanosheets	S	-	262	-	-	-		FESEM, XRD, TEM, XPS	-	-	-	-	
TiS@TF	Ti foam	Nanoporous array	S	-	370	-	-	-		FESEM, XRD	-	-	-	-	
Fe_xTi_yS@TF	Ti foam	Nanosheets	S	-	329	-	-	-		FESEM, XRD	-	-	-	-	
AlS@AF	Al foam	Nano-particulates	S	-	-	-	-	-		FESEM, XRD	-	-	-	-	
Fe_xAl_yS@AF	Al foam	Dispersed nanosheets	S	-	-	-	-	-		FESEM, XRD	-	-	-	-	
NiS	Ni foam	Nanogranular	S	-	266 (@30 mA/cm^2_{geo})	3.1 mF	-	296.0	1 M KOH	XRD, SEM, TEM, Raman	FESEM, Raman	50 h CP (100 $mA \cdot cm^{-2}_{geo}$)	Ni_3S_2	Precatalyst (unique transformation)	669
Cu_2S@Cu	Cu foam	Densely packed cube-like	S	6.2	345 (@20 mA/cm^2_{geo})	41.8	0.64 at 370 mV	83	1 M KOH	SEM, XRD, TEM, STEM, EDX, XPS	SEM, EDX	10 h CP (20 $mA \cdot cm^{-2}_{geo}$)	-	Precatalyst	670
Cu_2S-100	Cu foam	Particulate	S	7.5	384 (@20 mA/cm^2_{geo})	-	-	136		SEM	-	-	-	-	
Cu_2S-10	Cu foam	Particulate	S	3.2	360 (@20 mA/cm^2_{geo})	-	-	116		SEM	-	-	-	-	
CeO_x/$NiCo_2S_4$/CC	CC	Nanotube	S	~4	270	5.4	-	126	1 M KOH	XRD, TEM, SEM, XPS, ICP-AES, Raman	SEM, TEM, XPS	20 h CP (10 $mA \cdot cm^{-2}_{geo}$)	-	Precatalyst	671
$NiCo_2S_4$/CC	CC	Nanotube	S	-	300	3.4	-	133		XRD, TEM, SEM, XPS, Raman	-	20 h CP (10 $mA \cdot cm^{-2}_{geo}$)	-	-	
Cu_2S/CF	CF	Nanowires	S	-	328 (after CV activation)	-	-	87	1 M KOH	XRD, SEM	XRD	500 CV cycles (100 $mV \cdot s^{-1}$, 0–0.8 $V_{Hg/HgO}$, activation) 16 CP (10 $mA \cdot cm^{-2}_{geo}$)	-	-	672
Cu_2S/CM_200CVs	Cu mesh	Nanowires	S	-	380	93	-	96		XRD, SEM, Raman	-	10000 s CP (10 $mA \cdot cm^{-2}_{geo}$)	-	-	
Cu_2S/CM	Cu mesh	Nanowires	S	-	-	-	-	-		SEM, TEM, XRD, XPS, HAADF-STEM, EELS	XRD, SEM, Raman, EELS (HAADF-STEM), TEM	200 CV cycles (100 $mV \cdot s^{-1}$, 0–0.8 $V_{Hg/HgO}$) 10000 s CP (10 $mA \cdot cm^{-2}_{geo}$)	CuO	Precatalyst (full oxidation)	
$MnCo_2S_4$/SS	SS mesh	Nanosheets	S	-	290 350 (@50 mA/cm^2_{geo})	52	-	67	1 M KOH	SEM, XRD, XPS, TEM, EDX	SEM, XPS, EDX	100 h CA (1.54 V_{RHE})	MnOOH, $Co(OH)_2$	Precatalyst (partial oxidation)	673

https://doi.org/10.1021/acs.chemrev.3c00005
Chem. Rev. 2023, 123, 12795−13208

Table 5. continued

Initial Electrocatalyst	Substrate	Shape of Electrocatalyst	Deposition Type	Specific Loading / $mg \cdot cm^{-2}_{geo}$	η@10 $mA \cdot cm^{-2}_{geo}$ / mV	C_{dl} / $mF \cdot cm^{-2}_{geo}$	TOF / s^{-1} (@η or f)	Tafel Slope / $mV \cdot dec^{-1}$	Electrolyte	Pre-analysis	Post-analysis	Long-Term OER Test Conditions	Post-OER Electrocatalyst	Final Type of Electrocatalyst	Ref.
NiS_x	ITO, GC	Nanoparticles	S	-	480 (1st ED cycle) 670 (10th ED cycle)	-	-	-	1 M NaOH	SEM, XRD, XPS	SEM, XRD, XPS	10 CV cycles (5 $mV \cdot s^{-1}$, 1.0–1.8 V_{RHE})	NiOOH, SO_4^{2-}	Precatalyst (partial oxidation)	448
NiS-GN-1 (Ni_9S_8-GN)	GC	Nanosheets and nanoparticles	P	0.459	278	15.3	0.216 at 313 mV	87	1 M KOH	TEM, XRD, EDX, N_2 ISO (BET, PSD), XPS, Raman, SEM	XPS	20 h CP (10 $mA \cdot cm^{-2}_{geo}$)	Ni oxides/hydroxides	Precatalyst (partial oxidation)	674
NiS-GN-3 (NiS_2-GN)	GC	Nanosheets and nanoparticles	P	0.459	374	2	0.053 at 313 mV	124		TEM, XRD, EDX, N_2 ISO (BET, PSD), XPS, Raman, SEM	-	-	-	-	
NiS-GN-2 (NiS-GN)	GC	Nanosheets and nanoparticles	P	0.459	339	7	0.029 at 313 mV	92		TEM, XRD, EDX, N_2 ISO (BET, PSD), XPS, Raman, SEM	-	-	-	-	
CoS_2@N-GN	CFP	Nanosheets and nanoparticles	P	~1.5	243	76.7	-	51.8	1 M KOH	TEM, SEM, XPS, EDX, XRD, N_2 ISO (BET), TGA	TEM, SEM, XPS	1000 CV cycles 12 h CP (10 $mA \cdot cm^{-2}_{geo}$)	Oxidized Co species, S-O species	Precatalyst (partial oxidation)	675
Pure CoS_2	CFP	-	P	~1.5	327	13.6	-	81.4		-	-	-	-	-	
CoS_2/N-GN	CFP	-	P	~1.5	307	20.1	-	71.6		-	-	-	-	-	
Co_3S_4/AC 20%	GC	Hollow nanoparticle	P	0.57	270	-	0.07 at 270 mV	93	1 M KOH	SEM, TEM, XPS, XRD, EPR, EDX, Raman, N_2 ISO (BET, PSD)	XPS, FTIR, TEM	48 h CP (10 $mA \cdot cm^{-2}_{geo}$)	$Co(OH)_2$, CoOOH	Precatalyst (partial oxidation)	676
Co_3S_4/AC 30%	GC	Hollow nanoparticle	P	0.57	290	-	-	-		-	-	-	-	-	
Co_3S_4/AC 10%	GC	Hollow nanoparticle	P	0.57	290	-	-	115		-	-	-	-	-	
Co_3S_4	GC	Hollow nanoparticle	P	0.57	320	-	-	187		N_2 ISO (BET, PSD)	-	-	-	-	
Co_3S_4/AC 20% after activation	GC	Hollow nanoparticle	P	0.57	320	-	-	105	1 M PBS (pH = 7.0)	SEM, TEM, XPS, XRD, EPR, EDX, Raman, N_2 ISO (BET, PSD)	XRD	12 h CP (10 $mA \cdot cm^{-2}_{geo}$)	-	-	
Co_3S_4/AC 20%	GC	Hollow nanoparticle	P	0.57	340	-	-	170		SEM, TEM, XPS, XRD, EPR, EDX, Raman, N_2 ISO (BET, PSD)	XRD	12 h CP (10 $mA \cdot cm^{-2}_{geo}$)	-	-	
Co_3S_4/AC 20% after activation	GC	Hollow nanoparticle	P	0.57	330	-	-	81	0.5 M H_2SO_4	SEM, TEM, XPS, XRD, EPR, EDX, Raman, N_2 ISO (BET, PSD)	XRD	18 h CP (10 $mA \cdot cm^{-2}_{geo}$)	-	-	
Co_3S_4/AC 20%	GC	Hollow nanoparticle	P	0.57	470	-	-	103		SEM, TEM, XPS, XRD, EPR, EDX, Raman, N_2 ISO (BET, PSD)	XRD	18 h CP (10 $mA \cdot cm^{-2}_{geo}$)	-	-	
Cu_2S NRs@CoS	Cu foam	Nanorods	S	~5	275 (@50 $mA \cdot cm^{-2}_{geo}$)	298	-	54	1 M KOH	SEM, XRD, TEM, SAED, STEM-EELS, EDX, XPS	SEM, XRD, XPS	36 h CA (1.53 V_{RHE}) 24 h CP (50 $mA \cdot cm^{-2}_{geo}$) 24 h CA (1.6 V_{RHE})	Metal oxides, Metal hydroxides	Precatalyst (partial oxidation)	677
CoS	Cu foam	-	S	-	324 (@50 $mA \cdot cm^{-2}_{geo}$)	142	-	93		-	-	-	-	-	
Cu_2S NRs	Cu foam	-	S	-	366 (@50 $mA \cdot cm^{-2}_{geo}$)	36	-	200		-	-	-	-	-	
3DG-Au-Ni_3S_2 (15c)	Ni foam	Nanosheets	S	-	91.15 $mA \cdot cm^{-2}_{geo}$ at 1.6 V_{RHE}	37.98	-	106	1 M KOH	SEM, TEM, XPS, EDX	XPS	19 h CA (1.6 V_{RHE})	$Ni(OH)_2$, NiOOH	Precatalyst (partial oxidation)	678
3DG-Ni_3S_2 (15c)	Ni foam	Nanosheets	S	-	3.6 $mA \cdot cm^{-2}_{geo}$ at 1.6 V_{RHE}	-	-	-		XRD,	-	-	-	-	
3DG-Au-Ni_3S_2 (20c)	Ni foam	Nanosheets	S	-	36.27 $mA \cdot cm^{-2}_{geo}$ at 1.6 V_{RHE}	27.81	-	240		SEM	-	-	-	-	
3DG-Au-Ni_3S_2 (10c)	Ni foam	Nanosheets	S	-	22.23 $mA \cdot cm^{-2}_{geo}$ at 1.6 V_{RHE}	24.30	-	243		SEM	-	-	-	-	
3DG-Au-Ni_3S_2 (5c)	Ni foam	Nanosheets	S	-	8.36 $mA \cdot cm^{-2}_{geo}$ at 1.6 V_{RHE}	10.39	-	475		SEM	-	-	-	-	
MoS_2/Ni	Ni foam	Flower like flakes	S	-	230 340 (@20 $mA \cdot cm^{-2}_{geo}$)	-	-	~115	1 M NaOH	XRD, N_2 ISO (BET, PSD), XPS, SEM, TEM, EDX, Raman	SEM, XRD, Raman	> 6 h CA (1.63 V_{RHE})	MoO_3	Precatalyst (partial oxidation)	679
MoS_2	GC	Nanoparticles	P	~0.20	-	-	-	-		XRD, N_2 ISO (BET, PSD), TEM, SAED, XPS, EDX, Raman	-	-	-	-	
V-Ni_3S_2	Ni foam	Nanorods	S	~1.2	148	32.8	-	42	1 M KOH	TEM, SEM, XRD, XPS, EDX	SEM, TEM, XPS	60 h CP (1.42 V_{RHE})	Metal hydroxides	Precatalyst (partial oxidation)	680
Ni_3S_2	Ni foam	Nanorods	S	~1.2	182	19.9	-	59		SEM, XPS	-	-	-	-	
$CuS_{0.55}$ HNP	Cu foam	Hollow nanoparticles	S	5.5	329 386 (@100 $mA \cdot cm^{-2}_{geo}$) 398 (@200 $mA \cdot cm^{-2}_{geo}$)	1.35 mF	0.018 at 345 mV	33	1 M KOH	SEM, EDX, TEM, SAED, XPS	XPS, EDX	20 h CP (10, 20, 50, 100 $mA \cdot cm^{-2}_{geo}$, 5 h for each j)12 h CP (10 $mA \cdot cm^{-2}_{geo}$)	Cu-OH species	Precatalyst (partial oxidation)	681
$CuS_{0.57}$ NS	Cu foam	Nanosheets	S	-	406 (@100 $mA \cdot cm^{-2}_{geo}$)	0.98 mF	0.0024 at 345 mV	42		SEM, EDX	-	-	-	-	
Co_9S_8@NC	Ni foam	Nanoparticles	P	0.5	288	0.35 μF	-	65	1 M KOH	XRD, TEM, XPS, EDX	XPS	11 h CP (100 $mA \cdot cm^{-2}_{geo}$) 15 h CP (10 $mA \cdot cm^{-2}_{geo}$)	CoOOH, $Co(OH)_2$, S-O species	Precatalyst (partial oxidation)	682
NiCuCo-sulfides ($NiCo_2S_4$, $CuCo_2S_4$)	GC	Nanosphere (continues inner sphere)	P	0.0998	340	4.19	-	96	1 M KOH	XRD, SEM, TEM, EDX, XPS, N_2 ISO (BET)	SEM, XRD, XPS	2000 CV cycles (1.0–2.0 V_{RHE}) 60000 s CA (1.45 V_{RHE})	M-OOH (M = metal cations)	Precatalyst (partial oxidation)	683

https://doi.org/10.1021/acs.chemrev.3c00005
Chem. Rev. 2023, 123, 12795−13208

Table 5. continued

Initial Electrocatalyst	Substrate	Shape of Electrocatalyst	Deposition Type	Specific Loading / $mg \cdot cm^{-2}_{geo}$	η@10 $mA \cdot cm^{-2}_{geo}$ / mV	C_{dl} / $mF \cdot cm^{-2}_{geo}$	TOF / s^{-1} (@η or f)	Tafel Slope / $mV \cdot dec^{-1}$	Electrolyte	Pre-analysis	Post-analysis	Long-Term OER Test Conditions	Post-OER Electrocatalyst	Final Type of Electrocatalyst	Ref.
NF-Ni_3S_2/MnO_2	Ni foam	Nanoflowers (nanosheets)	S	-	260	-	-	61	1 M KOH	TEM, SEM, AFM, XRD, XPS, EDX, N_2 ISO (BET)	SEM, TEM (after OWS)	36 h CA 5000 CV cycles 48 h CA (cell voltage: 1.6 V, OWS)	NiO, Ni_3S_2, MoO_2	Precatalyst (partial oxidation)	684
NF-Ni_3S_2	Ni foam	Nanosheets	S	-	342	-	-	81		XRD, XPS	-	-	-	-	
Co-S-130	GC	Nanosheets	P	0.17	338	36	-	69	1 M KOH	XRD, XPS, SEM TEM, ICP-OES, EDX, FTIR	SEM, TEM, XPS, ICP-OES, XRD	2000 CV cycles (100 $mV \cdot s^{-1}$, 1.05–1.75 V_{RHE}) 36 h CA (1.538 V_{RHE})	CoOOH, Oxidized S species	Precatalyst (partial oxidation)	685
				0.37–0.45	312	-	-	-			-	-	-	-	
Co-S-190	GC	Nanosheets	P	0.17	400	9	-	-		XRD, XPS, TEM, ICP-OES, FTIR	-	-	-	-	
Co-S-150	GC	Nanosheets	P	0.17	390	10.7	-	82		XRD, XPS, TEM, ICP-OES, FTIR	-	-	-	-	
Co-S-60	GC	Nanosheets	P	0.17	380	6.2	-	80		XRD, XPS, TEM, ICP-OES, FTIR	-	-	-	-	
Co-S-16	GC	Nanosheets	P	0.17	390	2.5	-	-		XRD, XPS, TEM, ICP-OES, FTIR	-	-	-	-	
holey NiCoS-NS	GC	Nanosheets	P	0.14	280 ~ 345 (@50 $mA \cdot cm^{-2}_{geo}$)	2.51	0.18 at 350 mV	85	1 M KOH	XRD, EDX, SEM, TEM, HAADF-STEM, XPS, ICP-OES, SAED, AFM, N_2 ISO	TEM, XPS, EDX	15 h CA (1.51 V_{RHE}) 8000 CV cycles	NiOOH, Co(OOH), S-O species	Precatalyst (partial oxidation)	686
nonporous NiCoS-NS	GC	Nanosheets	P	0.14	290	2.33	0.087 at 350 mV	111		XRD, TEM, ICP-OES, N_2 ISO	-	-	-	-	
NiFeS	GC	Nanosheets	P	0.14	~ 316 (@50 $mA \cdot cm^{-2}_{geo}$)	-	-	64		TEM	-	-	-	-	
NiMnS	GC	Nanosheets	P	0.14	~ 390 (@50 $mA \cdot cm^{-2}_{geo}$)	-	-	149		TEM	-	-	-	-	
NiS	GC	Nanosheets	P	0.14	~ 385 (@50 $mA \cdot cm^{-2}_{geo}$)	-	-	-		TEM	-	-	-	-	
CoS	GC	Microhollow	P	0.14	~ 395 (@50 $mA \cdot cm^{-2}_{geo}$)	-	-	-		TEM	-	-	-	-	
1.5-CuS-CC	CC	Nanosheets and Nanorods	S	3.5	358	13.2	-	76.1	1 M KOH	SEM, XRD, XPS, EDX, TEM	SEM, TEM, XPS	10 h CA (1.6 V_{RHE}) 1000 CV cycles (50 $mV \cdot s^{-1}$, 1.2–1.9 V_{RHE})	$Cu(OH)_2$	Precatalyst (partial oxidation)	687
CuS powder	GC	-	P	-	630	3.2	-	107.0		-	-	-	-	-	
2.0-CuS-CC	CC	Nanorods	S	4.6	453	10.3	-	86.8		XRD, SEM	-	-	-	-	
1.0-CuS-CC	CC	Nanosheets	S	2.8	541	5.7	-	99.3		XRD, SEM	-	-	-	-	
0.5-CuS-CC	CC	Nanosheets	S	1.5	590	6.8	-	101.1		XRD, SEM	-	-	-	-	
CoMoNiS-NF-31	Ni foam	Nanosheets and nanorods	S	1.86	166	-	-	58	1 M KOH	SEM, ICP-AES, TEM, AFM, XPS, XRD	SEM, XPS (after OWS)	24 h CA (cell voltage: 1.70 V, OWS)	Metal (oxy)hydroxides, SO_4^{2-}	Precatalyst (partial oxidation)	688
Ni_3S_2/NF	Ni foam	Nanorods	S	1.12	395	-	-	74		SEM, XRD	-	-	-	-	
MoS_2/Ni_3S_2/NF	Ni foam	Nanosheets and nanorods	S	1.84	239	-	-	71		SEM, XRD	-	-	-	-	
Co_9S_8/Ni_3S_2/NF	Ni foam	Nanosheets and nanorods	S	1.79	192	-	-	70		SEM, XRD	-	-	-	-	
CoMoNiS-NF-13	Ni foam	Nanosheets and nanorods	S	1.87	228	-	-	-		SEM, ICP-AES	-	-	-	-	
CoMoNiS-NF-12	Ni foam	Nanosheets and nanorods	S	1.84	218	-	-	-		SEM, ICP-AES	-	-	-	-	
CoMoNiS-NF-11	Ni foam	Nanosheets and nanorods	S	1.79	217	-	-	-		SEM, ICP-AES	-	-	-	-	
CoMoNiS-NF-21	Ni foam	Nanosheets and nanorods	S	1.82	212	-	-	-		SEM, ICP-AES	-	-	-	-	
CoMoNiS-NF-41	Ni foam	Nanosheets and nanorods	S	1.87	179	-	-	-		SEM, ICP-AES	-	-	-	-	
CoMoNiS-NF-51	Ni foam	Nanosheets and nanorods	S	1.90	188	-	-	-		SEM, ICP-AES	-	-	-	-	
Ni_3S_2/NF	Ni foam	Nanorods	S	1.12	575	-	-	269	1 M PBS (pH = 7.0)	SEM, XRD	-	-	-	-	
MoS_2/Ni_3S_2/NF	Ni foam	Nanosheets and nanorods	S	1.84	525	10	-	243		SEM, XRD	-	-	-	-	
Co_9S_8/Ni_3S_2/NF	Ni foam	Nanosheets and nanorods	S	1.79	495	15.0	-	226		SEM, XRD	-	-	-	-	
CoMoNiS-NF-13	Ni foam	Nanosheets and nanorods	S	1.87	462	14.9	-	-		SEM, ICP-AES	-	-	-	-	
CoMoNiS-NF-12	Ni foam	Nanosheets and nanorods	S	1.84	455	26.6	-	-		SEM, ICP-AES	-	-	-	-	
CoMoNiS-NF-11	Ni foam	Nanosheets and nanorods	S	1.79	451	29.2	-	-		SEM, ICP-AES	-	-	-	-	
CoMoNiS-NF-21	Ni foam	Nanosheets and nanorods	S	1.82	408	57.2	-	-		SEM, ICP-AES	-	-	-	-	
CoMoNiS-NF-31	Ni foam	Nanosheets and nanorods	S	1.86	405	60.9	-	71		SEM, ICP-AES, TEM, AFM, XPS, XRD	-	20 h CA (cell voltage: 1.80 V, OWS)	-	-	
CoMoNiS-NF-41	Ni foam	Nanosheets and nanorods	S	1.87	419	30.9	-	-		SEM, ICP-AES	-	-	-	-	
CoMoNiS-NF-51	Ni foam	Nanosheets and nanorods	S	1.90	433	23.8	-	-		SEM, ICP-AES	-	-	-	-	
Ni_3S_2/NF	Ni foam	Nanorods	S	1.12	569	-	-	268	0.5 M H_2SO_4	SEM, XRD	-	-	-	-	
MoS_2/Ni_3S_2/NF	Ni foam	Nanosheets and nanorods	S	1.84	525	-	-	271		SEM, XRD	-	-	-	-	

https://doi.org/10.1021/acs.chemrev.3c00005
Chem. Rev. 2023, 123, 12795−13208

Table 5. continued

Initial Electrocatalyst	Substrate	Shape of Electrocatalyst	Deposition Type	Specific Loading / $mg \cdot cm^{-2}_{geo}$	η@10 $mA \cdot cm^{-2}_{geo}$ / mV	C_{dl} / $mF \cdot cm^{-2}_{geo}$	TOF / s^{-1} (@η or j)	Tafel Slope / $mV \cdot dec^{-1}$	Electrolyte	Pre-analysis	Post-analysis	Long-Term OER Test Conditions	Post-OER Electrocatalyst	Final Type of Electrocatalyst	Ref.
Co_9S_8/Ni_3S_2/NF	Ni foam	Nanosheets and nanorods	S	1.79	395	-	-	175		SEM, XRD	-	-	-	-	688
CoMoNiS-NF-13	Ni foam	Nanosheets and nanorods	S	1.87	350	-	-	-		SEM, ICP-AES	-	-	-	-	
CoMoNiS-NF-12	Ni foam	Nanosheets and nanorods	S	1.84	307	-	-	-		SEM, ICP-AES	-	-	-	-	
CoMoNiS-NF-11	Ni foam	Nanosheets and nanorods	S	1.79	280	-	-	-		SEM, ICP-AES	-	-	-	-	
CoMoNiS-NF-21	Ni foam	Nanosheets and nanorods	S	1.82	255	-	-	-		SEM, ICP-AES	-	-	-	-	
CoMoNiS-NF-31	Ni foam	Nanosheets and nanorods	S	1.86	255	-	-	78		SEM, ICP-AES, TEM, AFM, XPS, XRD	-	80 min CA (cell voltage: 1.53 V, OWS)	-	-	
CoMoNiS-NF-41	Ni foam	Nanosheets and nanorods	S	1.87	275	-	-	-		SEM, ICP-AES	-	-	-	-	
CoMoNiS-NF-51	Ni foam	Nanosheets and nanorods	S	1.90	295	-	-	-		SEM, ICP-AES	-	-	-	-	
NiSO-BDC (Ni-BCD-modified Ni_3S_2/NiS)	GC	Nanoparticles	P	0.2	298	126	-	58.6	1 M KOH	TEM, SEM, XRD, XPS, FTIR, TGA, N_2 ISO (BET, PSD), CAM	TEM, XPS, XRD	15 h CP (10 $mA \cdot cm^{-2}_{geo}$)	$Ni(SO_4)_{0.3}(OH)_{1.4}$	Precatalyst	689
NiSO (Ni_3S_2/NiS)	GC	Nanoparticles	P	0.2	327	70	-	72.4		TEM, SEM, XRD, XPS, FTIR, TGA, N_2 ISO (BET, PSD), CAM	-	15 h CP (10 $mA \cdot cm^{-2}_{geo}$)	-	-	
Ni_xS_y-STS	Ni foam	Nanorods	S	-	200	-	-	138	1 M KOH	FESEM, EDX, Raman, XPS, XRD, N_2 ISO (BET), TEM	FESEM, XRD, XPS	1000 CV cycles 50 h CA	-	Precatalyst (partial oxidation)	690
Ni_xS_y-SS	Ni foam	Nanopetals	S	-	230	-	-	152		FESEM, EDX, Raman, XPS, XRD, N_2 ISO (BET)	-	-	-	-	
Ni_xS_y-TU	Ni foam	Budlike structure	S	-	220	-	-	145		FESEM, EDX, Raman, XPS, XRD, N_2 ISO (BET)	-	-	-	-	
Ni_xS_y-TAA	Ni foam	Nanoflakes	S	-	210	-	-	142		FESEM, EDX, Raman, XPS, XRD, N_2 ISO (BET)	-	-	-	-	
Ni_7S_6-F	Ni foam	Nanostructure	S	-	140	52.2	0.70 at 140 mV	119	0.1 M KOH	XRD, TEM, SEM, XPS, Raman, EDX	XRD, SEM, XPS	24 h CA (1.35 V_{RHE}) 1000 CV cycles	-	Precatalyst (partial oxidation)	
Ni_3S_2-F	Ni foam	Nanostructure	S	-	240	3.0	0.06 at 140 mV	159		XRD, TEM, SEM, XPS, Raman, EDX	-	-	-	-	
βNiS-F	Ni foam	Nanostructure	S	-	200	3.2	0.10 at 140 mV	151		XRD, TEM, SEM, XPS, Raman, EDX	-	-	-	-	
αNiS-F	Ni foam	Nanostructure	S	-	190	12.3	0.30 at 140 mV	125		XRD, TEM, SEM, XPS, Raman, EDX	-	-	-	-	
S-incorporated $Ni_{6/7}Fe_{1/7}$-OH-6/CNT	GC	Wrapped nanoflakes and connected nanosheets	P	0.2	190	-	-	24	1 M KOH	EDX, ICP-AES, SEM, TEM	XPS	20 h CP (10 $mA \cdot cm^{-2}_{geo}$)	S-incorporated NiFe (oxy)hydroxides	Precatalyst (bulk oxidized before the OER)	691, 692
S-incorporated $Ni_{6/7}Fe_{1/7}$-OH-2	GC	Nanoflakes	P	0.2	~290	-	-	-		EDX, ICP-AES, SEM, XAS, XPS, XANES, EXAFS, XRD	-	-	-	-	
S-incorporated $Ni_{6/7}Fe_{1/7}$-OH-6	GC	Flower-like nanoflakes	P	0.2	270	5.2	-	40		EDX, ICP-AES, SEM, TEM, HAADF-STEM, XPS, XANES, EXAFS, XRD	-	-	-	-	
S-incorporated $Ni_{6/7}Fe_{1/7}$-OH-24	GC	Nanosheets	P	0.2	~340	-	-	-		EDX, ICP-AES, SEM, XPS, XRD	-	-	-	-	
$Ni_{6/7}Fe_{1/7}S_2$	GC	Nanorods	P	0.2	350	1.3	-	69		EDX, ICP-AES, SEM, XAS, XANES, EXAFS, XPS, XRD	-	-	-	-	
$FeNiS_2$ NS/rGO	GC	Nanosheets	P	~0.10	200	-	4.9 at 270 mV	40	1 M KOH	XRD, SEM, STEM, EDX, Raman, TEM, HAADF, XPS, N_2 ISO (BET, PSD), TGA	TEM, XPS	1 and 50 h CA (0.7 $V_{Ag/AgCl}$) 5000 CV cycles (100 $mV \cdot s^{-1}$, 1.2−1.6 V_{RHE})	-	Precatalyst	693
$FeNiS_2$ NS	GC	Nanosheets	P	~0.10	410	-	-	135		TEM, XRD, N_2 ISO (BET), Raman	TEM, EDX	1 h CA (0.7 $V_{Ag/AgCl}$) 5000 CV cycles (100 $mV \cdot s^{-1}$, 1.2−1.6 V_{RHE})	-	Precatalyst	
$FeNiS_2$ NS + rGO	GC	Nanosheets	P	~0.10	260	-	0.88 at 270 mV	68		-	-	1 h CA (0.7 $V_{Ag/AgCl}$) 5000 CV cycles (100 $mV \cdot s^{-1}$, 1.2−1.6 V_{RHE})	-	-	
$FeNiS_2$ NS/rGO	GC	Nanosheets	P	~0.10	270	-	3.1 at 310 mV	38	0.1 M KOH	XRD, SEM, STEM, EDX, Raman, TEM, HAADF, XPS, N_2 ISO (BET, PSD), TGA	-	-	-	-	
$FeNiS_2$ NS	GC	Nanosheets	P	~0.10	430	-	-	93		TEM, XRD, N_2 ISO (BET), Raman	-	-	-	-	
$FeNiS_2$ NS + rGO	GC	Nanosheets	P	~0.10	310	-	0.88 at 310 mV	54		-	-	-	-	-	

https://doi.org/10.1021/acs.chemrev.3c00005
Chem. Rev. 2023, 123, 12795−13208

Table 5. continued

Initial Electrocatalyst	Substrate	Shape of Electrocatalyst	Deposition Type	Specific Loading / $mg \cdot cm^{-2}_{geo}$	η@10 $mA \cdot cm^{-2}_{geo}$ / mV	C_{dl} / $mF \cdot cm^{-2}_{geo}$	TOF / s^{-1} (@η or j)	Tafel Slope / $mV \cdot dec^{-1}$	Electrolyte	Pre-analysis	Post-analysis	Long-Term OER Test Conditions	Post-OER Electrocatalyst	Final Type of Electrocatalyst	Ref.
FeCoNi-HNTAs [(Co,Fe,Ni)$_3$S$_8$, MoS_2]	Ni foam	Nanotubes	S	-	184	186.1	-	49.9	1 M KOH	SEM, STEM, EDX, TEM, XRD, BRB, EXAFS, XANES, XPS, sXAS, AF, CAM	XRD, SEM, TEM, EDX, XPS, *In-Situ* EXAFS *In-Situ* XANES, XAFs	80 h CA (1.796 V_{RHE}) 30 h galvanic pulses (100−200 $mA \cdot cm^{-2}_{geo}$, iteration period: 2000 s) 1000 CV cycles 12 h CP (20 $mA \cdot cm^{-2}_{geo}$, *In-Situ* EXAFS)	Oxidized (Co,Fe,Ni)$_3$S$_8$, Oxidized MoS_2	Precatalyst (partial oxidation)	694
MoS_2/NF	Ni foam	Particulate film with roughened surface	S	-	~279	37.4	-	92.1		SEM, XPS, BRB, AF, CAM	-	-	-	-	
FeCoNiS-NTAs	Ni foam	Nanotubes	S	-	~250	129.2	-	73.5		SEM, BRB, AF, CAM	-	-	-	-	
CoS	SS	Thin film	S	0.40	300	-	-	55	1 M KOH	XRD, EDX, FESEM, TEM, SAED, XPS	XRD, FESEM	14 h CP (10 $mA \cdot cm^{-2}_{geo}$)	-	Precatalyst	695
Fe^0-Ni_xS_y/NF	Ni foam	Nanosheets	S	8	186 (@100 $mA \cdot cm^{-2}_{geo}$) ~279 (@300 $mA \cdot cm^{-2}_{geo}$) 306 (@500 $mA \cdot cm^{-2}_{geo}$) 345 (@1000 $mA \cdot cm^{-2}_{geo}$)	33.6	-	92	1 M KOH	FESEM, EDX, TEM, SAED, XRD, Raman, XPS	XPS	2800 s multistep CP (40−280 $mA \cdot cm^{-2}_{geo}$, 40 $mA \cdot cm^{-2}_{geo}$ per 200 s)10 h CA (1.47 V_{RHE})	-	Precatalyst	696
Ni_xS_y/NF	Ni foam	Particulate	S	-	~396 (@100 $mA \cdot cm^{-2}_{geo}$) ~456 (@300 $mA \cdot cm^{-2}_{geo}$)	9.1	-	158		FESEM, EDX, XRD, Raman, XPS	-	-	-	-	
Ni-Ni_xS_y/NF	Ni foam	-	S	-	~391 (@300 $mA \cdot cm^{-2}_{geo}$)	-	-	-		-	-	-	-	-	
Co-Ni_xS_y/NF	Ni foam	-	S	-	~460 (@300 $mA \cdot cm^{-2}_{geo}$)	-	-	-		-	-	-	-	-	
Mn-Ni_xS_y/NF	Ni foam	-	S	-	~451 (@100 $mA \cdot cm^{-2}_{geo}$)	-	-	-		-	-	-	-	-	
Cu-Ni_xS_y/NF	Ni foam	-	S	-	~507 (@300 $mA \cdot cm^{-2}_{geo}$)	-	-	-		-	-	-	-	-	
Ni_3S_2/VS_2	Ni foam	Nanosheets	S	~17.06	227	36.0	-	59.9	1 M KOH	FESEM, EDX, TEM, XRD, XPS, N_2 ISO (BET), Raman	XRD, SEM, TEM, Raman, XPS	100 CV cycles	NiO, SO_4^{2-}	Precatalyst (partial oxidation and V dissolution)	697
Ni_3S_2	Ni foam	Nanoparticles	S	~15.19	312	19.8	-	76.2		SEM, TEM, XPS, N_2 ISO (BET)	-	-	-	-	
$FeS_{1.4}$(Dmim)$_{0.5}$	GC	Nanosheets	P	~0.2	348	1.29	0.024 at 350 mV	57	1 M KOH	TEM, SEM, AFM, XRD, SAED, ICP-OES, FTIR, TGA, XPS, N_2 ISO (BET), EA	XPS, XRD, SEM	12 h CP (50 $mA \cdot cm^{-2}_{geo}$) 1000 CV cycles (50 $mV \cdot s^{-1}$)	$Fe(OH)_2$, FeOOH	Precatalyst (partial oxidation)	698
Fe_7S_8	GC	Nanosheets	P	~0.2	465	0.28	0.0019 at 350 mV	135		TEM, SEM, XRD, SAED, N_2 ISO (BET)	-	-	-	-	
FeS_2	GC	Nanosheets	P	~0.2	395	0.76	0.0045 at 350 mV	79.5		TEM, SEM, XRD, SAED, N_2 ISO (BET)	-	-	-	-	
Co_9S_8.60	GC	Nanosheets	P	0.55	206	45	-	87	1 M KOH	XRD, SEM, TEM, SAED, EDX, Raman, N_2 ISO (BET, PSD)	XPS	28800 s CA (1.56 V_{RHE}) 2000 CV cycles (50 $mV \cdot s^{-1}$)	Co oxides/hydroxides, SO_4^{2-}	Precatalyst (partial oxidation)	699
Co_9S_8.80	GC	Nanosheets	P	0.55	346	2.9	-	143		XRD, SEM, TEM, N_2 ISO (BET, PSD)	-	-	-	-	
Co_9S_8.70	GC	Nanosheets	P	0.55	299	23	-	140		XRD, SEM, TEM, N_2 ISO (BET, PSD)	-	-	-	-	
Co_9S_8.50	GC	Nanosheets	P	0.55	236	33	-	95		XRD, SEM, TEM, N_2 ISO (BET, PSD)	-	-	-	-	
$Fe_{11.1\%}$-Ni_3S_2	Ni foam	Nanosheets	S	-	234 (@100 $mA \cdot cm^{-2}_{geo}$) 252 (@100 $mA \cdot cm^{-2}_{geo}$) 297 (@500 $mA \cdot cm^{-2}_{geo}$)	-	-	61.7	1 M KOH	SEM, TEM, EDX, XPS, XRD	SEM, XRD, XPS	5 h CP (10 $mA \cdot cm^{-2}_{geo}$) 5500 s multistep CP (10−110 $mA \cdot cm^{-2}_{geo}$, 10 $mA \cdot cm^{-2}_{geo}$ per 500 s)	Fe-NiOOH/ Fe-Ni_3S_2	Precatalyst (partial oxidation)	700
Co5Ni5Fe2-S MNs	CFP	Mesoporous nanospheres	P	~0.7	199	210	-	50.1	1 M KOH	TEM, EDX, XPS, XRD, N_2 ISO (BET, PSD), SEM, sXAS	TEM, EDX, XPS	50 h CA (1.54 V_{RHE}) 24 h galvanic pulses (40−80 $mA \cdot cm^{-2}_{geo}$, iteration period: 1 h)	Oxides, Hydroxides, Sulfate species	Precatalyst (partial oxidation)	701
Co1Ni1Fe2-S	CFP	Nanospheres	P	~0.7	268	-	-	64.5		TEM, XRD	-	-	-	-	
Co1Ni2Fe1-S	CFP	Nanospheres	P	~0.7	274	-	-	60.0		TEM, XRD	-	-	-	-	
Co2Ni1Fe1-S	CFP	Nanospheres	P	~0.7	243	-	-	87.1		TEM, XRD	-	-	-	-	
Co1Ni1Fe1-S	CFP	Nanospheres	P	~0.7	257	-	-	71.3		TEM, XRD	-	-	-	-	
Co1Ni2Fe2-S	CFP	Nanospheres	P	~0.7	251	-	-	71.6		TEM, XRD	-	-	-	-	
Co2Ni1Fe2-S	CFP	Nanospheres	P	~0.7	256	-	-	54.5		TEM, XRD	-	-	-	-	
CoNiFe-S SNs	CFP	Solid nanospheres	P	~0.7	199	176	-	49.5		TEM, EDX, XRD, sXAS	-	-	-	-	
Ni-S	CFP	Nanoparticles	P	~0.7	280	32	-	90.9		SEM, XRD, EDX, XPS, sXAS	-	-	-	-	
Co-S	CFP	Nanoparticles	P	~0.7	272.	152	-	59.6		TEM, SEM, XRD, EDX, XPS, sXAS	-	-	-	-	
Fe-S	CFP	Nanoparticles	P	~0.7	294	40	-	70.0		TEM, SEM, XRD, EDX, XPS, sXAS	-	-	-	-	
NiS-Ni_3S_2	Ni foam	Tree-like structure	S	1.70	269	16.5	-	119	1 M KOH	XRD, SEM, EDX, TEM, XPS	SEM, XRD, XPS, TEM	12 h CP (50 $mA \cdot cm^{-2}_{geo}$)	NiOOH	Precatalyst (partial oxidation)	702
Ni_3S_2	Ni foam	Nanorods	S	1.70	338	5.5	-	149		XRD, SEM, EDX	-	-	-	-	
CoFeS-1	GC	Nanoplates	P	~0.55	342	2.35	-	105.1	1 M KOH	SEM, XRD	-	-	-	-	703
CoFeS-2	GC	Nanoplates	P	~0.55	290	1.63	-	52.6		SEM, TEM, XRD, XPS, EDX	EDX, TEM, XPS	10 h CP (10 $mA \cdot cm^{-2}_{geo}$)	Co(Fe) oxides/hydroxides	Precatalyst (partial oxidation)	
CoFeS-3	GC	Nanoplates	P	~0.55	313	3.18	-	78.4		SEM, XRD	-	-	-	-	

https://doi.org/10.1021/acs.chemrev.3c00005
Chem. Rev. 2023, 123, 12795−13208

Table 5. continued

Initial Electrocatalyst	Substrate	Shape of Electrocatalyst	Deposition Type	Specific Loading / $mg \cdot cm^{-2}_{geo}$	η@10 $mA \cdot cm^{-2}_{geo}$ / mV	C_{dl} / $mF \cdot cm^{-2}_{geo}$	TOF / s^{-1} (@η or f)	Tafel Slope / $mV \cdot dec^{-1}$	Electrolyte	Pre-analysis	Post-analysis	Long-Term OER Test Conditions	Post-OER Electrocatalyst	Final Type of Electrocatalyst	Ref.
CoFeS-CP (CoFeS-2)	CFP	Nanoplates	S	-	260	-	-	24.7		SEM, XRD, TEM	-	10 h CP (10 $mA \cdot cm^{-2}_{geo}$)	-	-	703
CoS	GC	Nanoplates	P	~0.55	404	3.86	-	162.7		XRD, SEM, XPS	-	-	-	-	
FeS	GC	-	-	~0.55	393	-	-	-		-	-	-	-	-	
$NiFeS_2$/S-GO	GC	Nanosheets	P	~1.3	240	0.67	-	46.7	1 M KOH	SEM, TEM, XRD, XPS, SAED, Raman, N_2 ISO (BET), EPR	SEM, XPS	24 h CP (50 $mA \cdot cm^{-2}_{geo}$)	$NiFeO_x$, $NiFe(OOH)_x$	Precatalyst (partial oxidation)	704
$NiFeS_2$+S-GO	GC	-	P	~1.3	~287	0.45	-	-		N_2 ISO (BET), EPR	-	-	-	-	
CoS_x	GC	Rhombic dodecahedral particles	P	0.21	396	10.6	-	69	1 M KOH	SEM, TEM, SAED, EDX, EELS, CP, XRD, XPS, FTIR	SEM, TEM, *In-Situ* TEM, SAED, EDX, EELS, XPS, NEXAS, CP, FTIR	3 h CP (10 $mA \cdot cm^{-2}_{geo}$)	CoOOH	Precatalyst (partial oxidation)	705
CoS_x/NGF (NGF: N-doped graphene foam)	GC	Rhombic dodecahedral particles	P	0.21	330	45.5	0.10 at 300 mV	62		SEM, TEM, EDX, XPS, ICP-AES, XRD	SEM, TEM, EDX, XPS	40000 s CP (10 $mA \cdot cm^{-2}_{geo}$)	CoOOH	Precatalyst (almost full oxidation)	
$(NiFe)S_2$	GC	Nanocubes	P	-	338	-	-	60.8	1 M KOH	SEM, XRD, XPS, FTIR	XPS, TEM	-	(NiFe)OOH, $(NiFe)(OH)_2$, Oxidized S species	Precatalyst (partial oxidation)	466
$(Co_9S_8/N,S\text{-}DLCTs)_{HF}$ (DLCTs: N,S-co-doped double-layered carbon tubes)	GC	Nanocrystals embedded in DLCTs	P	~0.40	367	93.7	-	95	0.1 M KOH	TEM, SEM, STEM, EELS, XRD, N_2 ISO (BET), XPS, Raman, EA	TEM, XPS	10 h CA (1.60 V_{RHE})	Co_3O_4, CoOOH, SO_x (x = 3, 4)	Precatalyst (partial oxidation)	706
$(Co_9S_8/N,S\text{-}DLCTs)_{NaOH}$	GC	Nanocrystals embedded in DLCTs	P	~0.40	422	35.1	-	107		XRD, SEM, TEM, N_2 ISO (BET), Raman, EA	-	-	-	-	
Co_9S_8/N,S-SLCTs (N,S-SLCTs: N,S-co-doped single-layered carbon tubes)	GC	Nanocrystals embedded in SLCTs	P	~0.40	392	59.7	-	124		XRD, SEM, TEM, EA	-	-	-	-	
NCS-0.5-NF (NCS: Ni_3S_2/Co_9S_8)	Ni foam	3D branched nanoarray	S	-	340 (@100 $mA \cdot cm^{-2}_{geo}$)	155.0	-	66	1 M KOH	XRD, XPS, SEM, TEM, SAED EDX	SEM, XRD, XPS	12 h CP (100 $mA \cdot cm^{-2}_{geo}$)	Metal sulfides/oxides heterostructures	Precatalyst (partial oxidation)	707
NCS-0.5-CC	CC	-	S	-	496 (@100 $mA \cdot cm^{-2}_{geo}$)	107.2	-	78		-	-	-	-	-	
NS-0.5-NF (NS: Ni_3S_2)	Ni foam	-	S	-	396 (@100 $mA \cdot cm^{-2}_{geo}$)	29.5	-	70		XRD	-	-	-	-	
Ni_3S_2/NF (annealed 300°C for 50 s)	Ni foam	Rough, porous film	S	~1.4	370	-	-	-	0.1 M KOH	XRD, SEM, EDX, TEM, XPS	-	-	-	-	708
					190	-	-	-	30 wt.% KOH		-	-	-	-	
					312	9.7	-	111	1 M KOH		XRD, EDX, XPS	14 h CA (1.68 V_{RHE}) 3000 CV cycles (100 $mV \cdot s^{-1}$, 1.2–1.6 V_{RHE})	Ni oxides/hydroxides ($Ni(OH)_x$)	Precatalyst (partial oxidation)	
Ni_3S_2/NF (annealed 250°C for 50 s)	Ni foam	Smooth, porous film	S	~1.4	~410	-	-	152	1 M KOH	XRD, SEM	-	-	-	-	
Ni_3S_2/NF (annealed 350°C for 50 s)	Ni foam	Dense film	S	~1.4	~400	-	-	139		XRD, SEM	-	-	-	-	
Ni_3S_2/NF (annealed 300°C for 70 s)	Ni foam	Dense film	S	~1.4	~330	-	-	119		XRD, SEM	-	-	-	-	
Ni_3S_2/NF (annealed 300°C for 30 s)	Ni foam	Smooth, porous film	S	~1.4	~420	-	-	160		XRD, SEM	-	-	-	-	
Ni_3S_2	Ni foam	Nanorods	S	~3.0	370	8.45 mF	-	151,2	1 M KOH	SEM, XRD, XPS, XANES, EXAFS	XANES, EXAFS	-	-	Precatalyst	564
Ni_3S_2	Ni foam	Nanorods	S	~3.0	~437	83.4 μF	-	589.3	0.5 M $KHCO_3$ (pH = 8.54)	SEM, XRD, XPS, XANES, EXAFS	-	-	Green precipitation (maybe $NiCO_3$) observed on electrode surface after the long-term OER test	Precatalyst	
$(Fe_{0.2}Ni_{0.8})_{0.96}S$ TSs/Ni	Ni foam	Tubular spheres	S	2.5	233 310 (@100 $mA \cdot cm^{-2}_{geo}$)	100.1	-	46.2	1 M KOH	XRD, ICP-OES, EDX, N_2 ISO (BET), TEM, XPS	SEM, TEM, N_2 ISO (BET), XPS	12 h CA (1.46, 1.50, and 1.52 V_{RHE}) 2000 CV cycles (100 $mV \cdot s^{-1}$)	Ni-Fe oxo/hydroxyl species	Precatalyst (partial oxidation)	709
Ni_3S_2/Ni	Ni foam	-	S	-	549 (@100 $mA \cdot cm^{-2}_{geo}$)	-	-	-		XRD	-	-	-	-	
FeS/Ni	Ni foam	-	P	-	471 (@100 $mA \cdot cm^{-2}_{geo}$)	-	-	-		XRD	-	-	-	-	
$Mo_{5.9}Ni_{94.1}S$/NF	Ni foam	Nanowires	S	~2	213	11.4	-	35.1	1 M KOH	ICP-AES, TEM. SEM, EDX, XRD, XPS, N_2 SM	XRD, SEM, XPS	> 55 h CP (10 $mA \cdot cm^{-2}_{geo}$)	Metal oxides/hydroxides, Sulfur oxides (SO_x^{2-}, x = 3, 4)	Precatalyst (partial oxidation)	710
$Mo_{1.8}Ni_{98.2}S$/NF	Ni foam	Aggregated network	S	~2	220	-	-	44.4		ICP-AES, XRD, SEM	-	-	-	-	
$Mo_{2.6}Ni_{97.4}S$/NF	Ni foam	Nanoparticles and coarse nanowires	S	~2	223	-	-	47.6		ICP-AES, XRD, SEM	-	-	-	-	
Ni_3S_2/NF	Ni foam	-	-	-	293	5	-	69.5		XRD, XPS	-	-	-	-	
$NiCo_2O_4/Ni_3S_2$	Ni foam	Nanosheets (Ni_3S_2) on nanoneedle arrays ($NiCo_2O_4$)	S	3.2	360 (@40 $mA \cdot cm^{-2}_{geo}$)	79	-	20.7, 180.7	1 M KOH	XRD, SEM, STEM, XPS, N_2 SM	XRD, SEM, XPS (after OWS)	8 h CA (1.4 V_{RHE}) 500 CV cycles 1 h CA (~1.43 V_{RHE}, O_2 production) 8 h CA (cell voltage: 1.6 V, OWS)	Oxides/(oxy)hydroxides ($Co(OH)_2$, NiOOH), SO_4^{2-}	Precatalyst	711
Ni_3S_2	Ni foam	-	-	-	420 (@40 $mA \cdot cm^{-2}_{geo}$)	35	-	156.6, 199.8		XRD	-	-	-	-	

https://doi.org/10.1021/acs.chemrev.3c00005
Chem. Rev. 2023, 123, 12795−13208

Table 5. continued

Initial Electrocatalyst	Substrate	Shape of Electrocatalyst	Deposition Type	Specific Loading / $mg \cdot cm^{-2}_{geo}$	η@10 $mA \cdot cm^{-2}_{geo}$ / mV	C_{dl} / $mF \cdot cm^{-2}_{geo}$	TOF / s^{-1} (@η or j)	Tafel Slope / $mV \cdot dec^{-1}$	Electrolyte	Pre-analysis	Post-analysis	Long-Term OER Test Conditions	Post-OER Electrocatalyst	Final Type of Electrocatalyst	Ref.
c-Ti-Fe-S boxes	GC	Nanoparticles on nanoboxes	P	0.1	350	0.0665	-	55	1 M KOH	XRD, SEM, TEM, EDX, N_2 ISO (BET), XPS	TEM, XPS	12 h CP (5 and 10 $mA \cdot cm^{-2}_{geo}$)	Oxidized metal species (Fe-O, Ti-O, $FeSO_x$, $TiSO_x$)	Precatalyst	712
a-Ti-S/c-Fe-S boxes	GC	Nanoparticles on nanoboxes	P	0.1	420	0.0605	-	66		XRD, SEM, TEM, EDX	-	-	-	-	
c-Ti-Fe-S cubes	GC	Nanoparticles on cubes	P	0.1	360	0.0525	-	58		XRD, SEM, TEM, EDX	-	-	-	-	
FeS_2	GC	Aggregated nanoparticles	P	0.1	420	-	-	-		XRD, SEM	-	-	-	-	
HCSN 11 EW (HCSN: hierarchical cobalt sulfide nanocomposite)	GC	Nanoplates with nanosheet rich edges	P	0.19	275	-	1.0497 at 330 mV	30	1 M KOH	XRD, SEM, TEM, EDX, XPS, N_2 ISO (BET, PSD)	SEM, XPS	10 h CP (10 $mA \cdot cm^{-2}_{geo}$)	Co oxides/hydroxides	Precatalyst (partial oxidation)	713
HCSN 03 EW	GC	Nanoplates and nanorods	P	0.19	324	-	0.1388 at 330 mV	~55		XRD, SEM, XPS, N_2 ISO (BET)	-	10 h CP (10 $mA \cdot cm^{-2}_{geo}$)	-	-	
HCSN 12 EW	GC	Flower-like nanoplates with protruding nanosheets	P	0.19	307	-	0.2817 at 330 mV	45		XRD, SEM, XPS, N_2 ISO (BET)	-	10 h CP (10 $mA \cdot cm^{-2}_{geo}$)	-	-	
HCSN 21 EW	GC	Nanoplates with nanosheet passivated edges	P	0.19	318	-	0.1677 at 330 mV	55		XRD, SEM, XPS, N_2 ISO (BET)	-	10 h CP (10 $mA \cdot cm^{-2}_{geo}$)	-	-	
HCSN 30 EW	GC	Irregular nanoparticles	P	0.19	318	-	0.1755 at 330 mV	~55		XRD, SEM, XPS, N_2 ISO (BET)	-	10 h CP (10 $mA \cdot cm^{-2}_{geo}$)	-	-	
Co_9S_8	CFP	Ultrathin freestanding nanosheets	P	-	288	146	-	79	1 M KOH	XRD, SEM, EDX, TEM, SAED, TGA, N_2 ISO (BET, PSD), XPS, EELS	XPS	36 h CA (1.58 V_{RHE}) CV cycles (10 $mV \cdot s^{-1}$, activation)	CoOOH, SO_4^{2-}	Precatalyst (partial oxidation)	714
CoS_x (unannealed)	CFP	Ultrathin freestanding nanosheets	P	-	326	81	-	91		XRD, SEM, EDX, TEM, SAED, AFM, TGA, N_2 ISO (BET, PSD), XPS, EELS, MB UV-Vis	-	-	-	-	
CNS-NGA ($Co_{1.2}Ni_3S_2$-N-doped reduced graphene oxide aerogel)	GC	Nanoparticles (CNS) on porous network (NGA)	P	~0.285	330	10.25 21.28 (after long-term OER testing)	-	47	1 M KOH	SEM, TEM, SAED, EDX, XRD, Raman, XPS, N_2 ISO (BET), XANES, EXAFS, UPS	TEM, EDX, XRD	7 h CA (1.6 V_{RHE}) 1000 CV cycles (5 $mV \cdot s^{-1}$, 1.23–1.60 V_{RHE})	Ni-Co (hydr)oxide	Precatalyst (partial oxidation)	715
CNS	GC	Aggregated microparticles	P	~0.285	440	-	-	117		SEM, EDX, XRD, TEM, SAED, XANES, EXAFS	-	-	-	-	
CS-NGA (CS: CoS_2)	GC	-	P	~0.285	400	-	-	72		XRD, Raman	-	-	-	-	
NS-NGA (NS: NiS_2)	GC	-	P	~0.285	370	-	-	98		XRD, Raman	-	-	-	-	
LCT-deposited FeNiS-3/NF (3/1 Fe/Ni)	Ni foam	Porous film of nanospheres covered with interwoven nanosheets	S	0.50	290 ($@100\ mA \cdot cm^{-2}_{geo}$)	-	-	68	1 M KOH	XRD, SEM, XPS, EDX	SEM, EDX, XPS	500 CV cycles (100 $mV \cdot s^{-1}$, 0.40–0.70 V_{SCE}) 10000 s CA	NiOOH, FeOOH, SO_4^{2-}	Precatalyst	716
LCT-deposited FeNiS-1/NF (1/3 Fe/Ni)	Ni foam	Porous film of nanospheres covered with interwoven nanosheets	S	0.10	~380 ($@100\ mA \cdot cm^{-2}_{geo}$)	-	-	129		XRD, SEM, EDX	-	-	-	-	
LCT-deposited FeNiS-2/NF (1/1 Fe/Ni)	Ni foam	Porous film of nanospheres covered with interwoven nanosheets	S	0.10	~300 ($@100\ mA \cdot cm^{-2}_{geo}$)	-	-	86		XRD, SEM, EDX	-	-	-	-	
LCT-deposited FeNiS-4/NF (6/1 Fe/Ni)	Ni foam	Porous film of nanospheres covered with interwoven nanosheets	S	0.90	~310 ($@100\ mA \cdot cm^{-2}_{geo}$)	-	-	117		XRD, SEM, EDX	-	-	-	-	
LCT-deposited FeNiS-5/NF (9/1 Fe/Ni)	Ni foam	Porous film of nanospheres covered with interwoven nanosheets	S	2.20	~330 ($@100\ mA \cdot cm^{-2}_{geo}$)	-	-	87		XRD, SEM, EDX	-	-	-	-	
LCT-deposited Ni-S/NF	Ni foam	-	S	0.40	~460 ($@100\ mA \cdot cm^{-2}_{geo}$)	-	-	138		XRD	-	-	-	-	
LCT-deposited Fe-S/NF	Ni foam	-	S	0.50	~350 ($@100\ mA \cdot cm^{-2}_{geo}$)	-	-	103		XRD	-	-	-	-	
WS-deposited FeNiS-3/NF (3/1 Fe/Ni)	Ni foam	Planar film of small particles	S	4.40	293 ($@100\ mA \cdot cm^{-2}_{geo}$)	-	-	63		XRD, SEM, EDX	-	-	-	-	
WS-deposited FeNiS-1/NF (1/3 Fe/Ni)	Ni foam	Planar film of small particles	S	1.00	~321 ($@100\ mA \cdot cm^{-2}_{geo}$)	-	-	67		XRD, SEM, EDX	-	-	-	-	

https://doi.org/10.1021/acs.chemrev.3c00005
Chem. Rev. 2023, 123, 12795−13208

Table 5. continued

Initial Electrocatalyst	Substrate	Shape of Electrocatalyst	Deposition Type	Specific Loading / $mg \cdot cm^{-2}_{geo}$	η@10 $mA \cdot cm^{-2}_{geo}$ / mV	C_{dl} / $mF \cdot cm^{-2}_{geo}$	TOF / s^{-1} (@η or j)	Tafel Slope / $mV \cdot dec^{-1}$	Electrolyte	Pre-analysis	Post-analysis	Long-Term OER Test Conditions	Post-OER Electrocatalyst	Final Type of Electrocatalyst	Ref.
WS-deposited FeNiS-2/NF (1/1 Fe/Ni)	Ni foam	Planar film of small particles	S	1.30	~311 (@100 $mA \cdot cm^{-2}_{geo}$)	-	-	72		XRD, SEM, EDX	-	-	-	-	716
WS-deposited FeNiS-4/NF (6/1 Fe/Ni)	Ni foam	Planar film of small particles	S	4.50	~300 (@100 $mA \cdot cm^{-2}_{geo}$)	-	-	71		XRD, SEM, EDX	-	-	-	-	
WS-deposited FeNiS-5/NF (9/1 Fe/Ni)	Ni foam	Planar film of small particles	S	5.80	~305 (@100 $mA \cdot cm^{-2}_{geo}$)	-	-	139		XRD, SEM, EDX	-	-	-	-	
WS-deposited Ni-S/NF	Ni foam	-	S	3.20	~381 (@100 $mA \cdot cm^{-2}_{geo}$)	-	-	150		XRD	-	-	-	-	
WS-deposited Fe-S/NF	Ni foam	-	S	3.50	~321 (@100 $mA \cdot cm^{-2}_{geo}$)	-	-	69		XRD	-	-	-	-	
Ni_3S_2 (3000 ALD cycles)	Au/Si wafer	Thin film	S	-	473	-	-	79	1 M KOH	SEM, XRD, XPS, AFM	-	100 h CP (10 $mA \cdot cm^{-2}_{geo}$)	-	-	717
Ni_3S_2 (2000 ALD cycles)	Au/Si wafer	Thin film	S	-	434	-	-	66		SEM, TEM, SAED, XRD, Raman, AFM	-	100 h CP (10 $mA \cdot cm^{-2}_{geo}$)	-	-	
Ni_3S_2 (1000 ALD cycles)	Au/Si wafer	Thin film	S	-	410	-	-	52		SEM, XRD, AFM	SEM	100 h CP (10 $mA \cdot cm^{-2}_{geo}$)	-	-	
Ni_3S_2 (500 ALD cycles)	Au/Si wafer	Thin film	S	-	400	-	-	51		SEM, XRD, AFM, XPS	XPS	< 100 h CP (10 $mA \cdot cm^{-2}_{geo}$)	Ni oxides/hydroxides ($Ni(OH)_2$, NiOOH)	Precatalyst (partial oxidation)	
H_2S_NF (Ni_3S_2) (Elox_H_2S_NF)	Ni foam	Wrinkled surface with irregular crack	S	-	256	-	-	41	1 M KOH	SEM, XRD, Raman, XPS	SEM, TEM, SAED, HAADF-STEM, EDX, XRD, Raman, XPS, TOF-SIMS	10 CV cycles (30 $mV \cdot s^{-1}$, 0.9–1.6 V_{RHE}, activation) 10 h multistep CP (10–200 $mA \cdot cm^{-2}_{geo}$) 5 h CP (20 $mA \cdot cm^{-2}_{geo}$, H_2/O_2 ratio)	Fe-incorporated γ-NiOOH	Precatalyst (partial oxidation)	718
Co_9S_8@NC-500	GC	Hollow nanocubes	P	~0.57	~410	5.2	0.013 at 320 mV	113	0.1 M KOH	SEM, TEM, XRD, Raman, XPS, XANES, EXAFS	-	-	-	-	719
Co_9S_8@NC-600	GC	Hollow nanocubes	P	~0.57	~340	~5.8	~0.032 at 320 mV	96		SEM, TEM, XRD, Raman, XPS, XANES, EXAFS	-	-	-	-	
Co_9S_8@NC-700	GC	CNTs on nanocubes	P	~0.57	~315	~7.1	~0.048 at 320 mV	87		SEM, TEM, XRD, HAADF-STEM, EM, Raman, XPS, XANES, EXAFS	-	-	-	-	
Co_9S_8@NC-800	GC	Longer CNTs on nanocubes	P	~0.57	~302	15.4	0.063 at 320 mV	67		SEM, TEM, XRD, Raman, XPS, XANES, EXAFS	XPS, TEM	500 CV cycles	$Co(OH)_2$	Precatalyst (partial oxidation)	
HPMS Co_3O_4/CoS_2	GC	Hierarchical porous nanosheet-assembled microspheres	P	0.34	280	113	-	63	1 M KOH	XRD, TEM, SEM, EDX, N_2 ISO (BET, PSD), XPS	SEM, EDX	160 s multistep CP (10–80 $mA \cdot cm^{-2}_{geo}$, 10 $mA \cdot cm^{-2}_{geo}$ per 20 s) 15000 s CP (20 $mA \cdot cm^{-2}_{geo}$) > 2 h CP (40 $mA \cdot cm^{-2}_{geo}$) 1000 CV cycles	Co^{IV}(-O) species	Precatalyst (almost full oxidation)	720
MS CoS_2	GC	Microspheres	P	0.34	~320	70	-	92		SEM, XRD	-	-	-	-	
1T-$Co_{1-x}S$	GC	Porous hexagonal microplates	P	0.202	494 (@1 $mA \cdot cm^{-2}_{geo}$) 651 (@5 $mA \cdot cm^{-2}_{geo}$)	-	-	117	1 M PBS (pH = 7)	XRD, SEM, TEM, EDX, XPS, N_2 ISO	-	-	-	-	721
					311	38.54	-	55	1 M KOH	XRD, SEM, TEM, EDX, XPS, N_2 ISO	TEM, EDX, XPS	12 h CP (10 $mA \cdot cm^{-2}_{geo}$)	Co (oxy)hydroxides, Sulfate groups	Precatalyst	
0.5T-Co_9S_8	GC	Porous barely formed microplates	P	0.202	330	-	-	69		XRD, SEM, N_2 ISO	-	-	-	-	
1.5T-$Co_{1-x}S$	GC	More compact porous microplates	P	0.202	316	-	-	59		XRD, SEM, N_2 ISO	-	-	-	-	
2T-$Co_{1-x}S$	GC	Agglomerated microplates	P	0.202	321	-	-	63		XRD, SEM, N_2 ISO	-	-	-	-	
$Co_{0.37}Fe_{0.26}S$	GC	Nanocubes	P	0.2	270	23.5	-	37.2	1 M KOH	EDX, XRD, XPS, SEM, TEM, N_2 ISO	XPS, TEM, SAED, EDX, ICP-OES	30 CV cycles (50 $mV \cdot s^{-1}$, 0.9–1.5 V_{RHE}, activation) 3 h CA (1.53 V_{RHE})	CoOOH, FeOOH, S–O species	Precatalyst	460
CoS_2	GC	Nanocubes	P	-	~324	-	-	-		XRD, SEM	-	30 CV cycles (50 $mV \cdot s^{-1}$, 0.9–1.5 V_{RHE}, activation)	-	-	
NiS_2 (PC-1)	GC	Sea urchins consisting of rod-like building blocks	P	0.102 (total metal loading)	373	1.78	0.0046 at 300 mV	75.6	1 M KOH	ICP-OES, XRD, XPS, TEM, SAED, EDX, STEM, sXAS	TEM, XPS, sXAS	1 h CP (10 $mA \cdot cm^{-2}_{geo}$) 2 h CA (1.53 V_{RHE})	S-doped Ni-Fe (oxy)hydroxides	Precatalyst	722
$(Ni_{0.86}Fe_{0.14})S_2$ (PC-2)	GC	Porous cubes	P	0.109 (total metal loading)	264	1.75	0.035 at 300 mV	56.2		ICP-OES, XRD, XPS, TEM, sXAS	TEM, STEM, EDX, XPS, sXAS	1 h CP (10 $mA \cdot cm^{-2}_{geo}$) 2 h CA (1.53 V_{RHE})	S-doped Ni-Fe (oxy)hydroxides	Precatalyst	
$(Ni_{0.74}Fe_{0.26})S_2$ (PC-3)	GC	Porous cubes	P	0.101 (total metal loading)	269	1.76	0.034 at 300 mV	52.4		ICP-OES, XRD, XPS, TEM, sXAS	XPS, sXAS	1 h CP (10 $mA \cdot cm^{-2}_{geo}$) 2 h CA (1.53 V_{RHE})	S-doped Ni-Fe (oxy)hydroxides	Precatalyst	
$(Ni_{0.63}Fe_{0.37})S_2$ (PC-4)	GC	Porous cubes	P	0.0996 (total metal loading)	262	1.70	0.034 at 300 mV	56.4		ICP-OES, XRD, XPS, TEM, sXAS	TEM, STEM, EDX, XPS, sXAS	1 h CP (10 $mA \cdot cm^{-2}_{geo}$) 10 h CA (1.53 V_{RHE})	S-doped Ni-Fe (oxy)hydroxides	Precatalyst	
CoS_2	CP	Hollow nanospheres	P	1.5	290	20.05	-	57	1 M KOH	XRD, SEM, TEM, EDX, N_2 ISO, XPS	XRD, TEM, Raman, XPS	12 h CP (10 $mA \cdot cm^{-2}_{geo}$) 1000 CV cycles (400 $mV \cdot s^{-1}$)	Co_3O_4, CoOOH	Precatalyst (partial oxidation)	723

https://doi.org/10.1021/acs.chemrev.3c00005
Chem. Rev. 2023, 123, 12795−13208

Table 5. continued

Initial Electrocatalyst	Substrate	Shape of Electrocatalyst	Deposition Type	Specific Loading / $mg \cdot cm^{-2}_{geo}$	η@10 $mA \cdot cm^{-2}_{geo}$ / mV	C_{dl} / $mF \cdot cm^{-2}_{geo}$	TOF / s^{-1} (@η or j)	Tafel Slope / $mV \cdot dec^{-1}$	Electrolyte	Pre-analysis	Post-analysis	Long-Term OER Test Conditions	Post-OER Electrocatalyst	Final Type of Electrocatalyst	Ref.
Co_9S_8	CP	Hollow nanospheres	P	1.5	342	7.39	-	104		XRD, SEM, TEM, EDX, N_2 ISO, XPS	-	12 h CP (10 $mA \cdot cm^{-2}_{geo}$)	-	-	723
Co_3S_4	CP	Hollow nanospheres	P	1.5	307	15.32	-	108		XRD, SEM, TEM, EDX, N_2 ISO, XPS	-	12 h CP (10 $mA \cdot cm^{-2}_{geo}$)	-	-	
nc-NiS	CFP	Nanocrystalline particles	P	-	354	-	-	116	1 M KOH	SEM, TEM, SAED, XRD, XPS, EDX, EDX	TEM, EDX, XPS	1000 CV cycles (100 $mV \cdot s^{-1}$, –0.2–0.2 V_{RHE}) 10 h CA (1.61 V_{RHE})	Ni oxide	Precatalyst (partial oxidation)	724
CST-1 (CoS_2-TiO_2, 0.2 g Co thiourea)	GC	Nanoparticles	P	-	-	-	-	-	1 M KOH	XRD, TGA, SEM, XPS, DRS	-	-	-	-	725
CST-2 (CoS_2-TiO_2, 0.3 g Co thiourea)	GC	Nanoparticles	P	-	461	-	-	-		XRD, TGA, SEM, XPS, DRS	-	-	-	-	
CST-3 (CoS_2-TiO_2, 0.4 g Co thiourea)	GC	Nanoparticles	P	-	231	-	0.0052 at 270 mV	92		XRD, TGA, SEM, TEM, EDX, EA, XPS, DRS	XPS	1000 CV cycles	CoOOH, $Co(OH)_2$, Sulfoxides	Precatalyst	
CST-4 (CoS_2-TiO_2, 0.5 g Co thiourea)	GC	Nanoparticles	P	-	351	-	-	-		XRD, TGA, SEM, XPS, DRS	-	-	-	-	
CST-5 (CoS_2-TiO_2, 0.6 g Co thiourea)	GC	Nanoparticles	P	-	411	-	0.0033 at 270 mV	114		XRD, TGA, SEM, TEM, EDX, EA, XPS, DRS	-	1000 CV cycles	-	-	
CST-6 (CoS_2-TiO_2, 0.8 g Co thiourea)	GC	Nanoparticles	P	-	311	-	-	-		XRD, TGA, SEM, XPS, DRS	-	-	-	-	
CoS_2	GC	Nanoparticles	P	-	491	-	0.0001 at 270 mV	-		TGA, XPS, DRS	-	-	-	-	
eFe/NiVS/NF	Ni foam	Nanowire	S	-	225 (@100 $mA \cdot cm^{-2}_{geo}$)	18.2	-	75	1 M KOH	XRD, SEM, TEM, XPS	XRD, XPS (after 1000 CV)	1000 CV cycles (0.2–0.6 V_{SCE}) 100 h CP (100 $mA \cdot cm^{-2}_{geo}$)	-	Precatalyst (partial oxidation)	726
uFe/NiVS/NF	Ni foam	Nanowires covered with thin nanosheets	S	-	240 (@100 $mA \cdot cm^{-2}_{geo}$)	12.4	-	176		XRD, SEM, TEM, XPS	-	-	-	-	
NiVS/NF	Ni foam	Nanowires covered with thin nanosheets	S	-	180 (@100 $mA \cdot cm^{-2}_{geo}$)	10.1	-	158		XRD, SEM, TEM, XPS	-	-	-	-	
eFe/Ni_3S_2/NF	Ni foam	Dendritic nanowires	S	-	340 (@100 $mA \cdot cm^{-2}_{geo}$)	3.4	-	77		XRD, SEM	-	-	-	-	
uFe/Ni_3S_2/NF	Ni foam	Triangle-like particles with nanoparticles	S	-	350 (@100 $mA \cdot cm^{-2}_{geo}$)	3.1	-	115		XRD, SEM, XPS	-	-	-	-	
Ni_3S_2/NF	Ni foam	Triangle-like particles	S	-	470 (@100 $mA \cdot cm^{-2}_{geo}$)	2.4	-	115		XRD, SEM, XPS	-	-	-	-	
CoS_x	Au-plated Ni foam	Nanosheets	P	~ 0.24	271	-	0.055 at 300 mV	48.8	1 M KOH	UV-Vis, XRD, SEM, TEM, EDX, ICP-OES, TGA, N_2 SM, XPS, Raman, N_2 ISO (BET)	XPS	300 h CP (30 $mA \cdot cm^{-2}_{geo}$)	CoOOH, $Co(OH)_2$, Oxidized S species (S^{6+})	Precatalyst (partial oxidation)	727
	Au (111) electrode		P	~ 0.28	386	-	-	84.2			-	-	-	-	
	GC		P	~ 0.21	302	18.55 ± 0.92	-	64.8			-	1000 CV cycles (0–0.65 V_{SCE})	-	-	
					335			-	0.5 H_2SO_4						
CoS_x-400	GC	-	P	~ 0.21	~ 355	-	-	-	1 M KOH	XRD, N_2 ISO (BET)	-	-	-	-	
CoS_x-800	GC	-	P	~ 0.21	~ 443	-	-	-		XRD, N_2 ISO (BET)	-	-	-	-	
FeS_x	GC	-	P	~ 0.21	~ 361	-	-	-		-	-	-	-	-	
NiS_x	GC	-	P	~ 0.21	~ 336	-	-	-		-	-	-	-	-	
Ni(Fe)S_2	GC	Microspheres consisting of nanosheets	P	0.18	-	-	-	-	1 M KOH	XRD, XPS, SEM, EDX, TEM	XRD, TEM, EDX	100 CV cycles (10 $mV \cdot s^{-1}$, 0–0.65 $V_{Ag/AgCl}$, activation)	γ-Ni(Fe)OOH	Precatalyst (partial oxidation)	728
Ni(Fe)S_2@Ni(Fe)OOH	GC	Microspheres consisting of nanosheets	P	0.18	230	0.228	-	42.6		XRD, TEM, EDX	TEM, XRD, XPS	50 h CP (10 $mA \cdot cm^{-2}_{geo}$) 24 h CA (1.6 V_{RHE})	γ-Ni(Fe)OOH	Precatalyst (partial oxidation)	
$Ni_{0.3}Fe_{0.3}S_2$	Ni foam	Microflower	S	~ 3	198	3.0	-	56	1 M KOH	XRD, SEM, ICP-AES, TEM, STEM, EDX, N_2 ISO (BET), XPS	XRD, SEM, XPS	50000 s CP (10 $mA \cdot cm^{-2}_{geo}$) 500 CV cycles (100 $mV \cdot s^{-1}$)	Ni-Fe oxo/hydroxide	Precatalyst (partial oxidation)	99
$Ni_{0.86}Fe_{0.14}S_2$	Ni foam	Microflower	S	-	220	-	-	65		SEM, ICP-AES	-	-	-	-	
$Ni_{0.58}Fe_{0.42}S_2$	Ni foam	Microflower	S	-	212	-	-	64		SEM, ICP-AES	-	-	-	-	
NiS_2	Ni foam	Nanoplate	S	-	255	2.6	-	136		SEM, XPS	-	-	-	-	
NiS	GC	Hollow microsphere	P	0.7 ± 0.2	320 390 (@20 $mA \cdot cm^{-2}_{geo}$)	1.49	-	59	1 M KOH	XRD, Raman, FESEM, TEM, EDX, XPS, N_2 ISO (BET)	XPS, XRD, SEM	2000 CV cycles 10 h CP (10 $mA \cdot cm^{-2}_{geo}$)	NiS, NiO	Precatalyst (partial oxidation)	729
Co_9S_8	GC	Hierarchical hollow microplates	P	0.37	278	125	-	53	1 M KOH	SEM, EDX, TEM, SAED, XRD	SEM, SAED, EDX, XPS, XRD	20 h CA (1.58 V_{RHE})	Co oxides/hydroxides ($Co(OH)_2$, CoOOH, CoO_2)	Precatalyst (full oxidation)	730
$Co_{1-x}S$	GC	Hierarchical hollow microplates	P	0.37	300	42.5	-	53.7		SEM, EDX, TEM, SAED, XRD	-	20 h CA (1.58 V_{RHE})	-	-	
Co@Co_9S_8-180	Co foam	Agglomerated particle	S	1.09	350	67.2	-	55	1 M KOH	SEM, EDX, N_2 ISO (BET, PSD), XRD, XPS, TEM, HAADF-STEM	SEM, XRD, EDX	100 h CP (20 $mA \cdot cm^{-2}_{geo}$ for 50 h, 100 $mA \cdot cm^{-2}_{geo}$ for 50 h) 55 h CA (1.58 V_{RHE}) 1000 CV cycles (50 $mV \cdot s^{-1}$, 1.2–1.7 V_{RHE})	Co (oxy)hydroxide (β-CoOOH)	Precatalyst (partial oxidation)	731
Co@Co_9S_8-220	Co foam	Agglomerated particle	S	9.73	360	43.2	-	52		SEM, EDX, N_2 ISO (BET, PSD), XRD,	SEM, XRD, EDX	100 h CP (20 $mA \cdot cm^{-2}_{geo}$ for 50 h, 100 $mA \cdot cm^{-2}_{geo}$ for 50 h) 55 h CA (1.58 V_{RHE})	Co (oxy)hydroxide (β-CoOOH)	Precatalyst (partial oxidation)	

https://doi.org/10.1021/acs.chemrev.3c00005
Chem. Rev. 2023, 123, 12795−13208

Table 5. continued

Initial Electrocatalyst	Substrate	Shape of Electrocatalyst	Deposition Type	Specific Loading / $mg \cdot cm^{-2}_{geo}$	η@10 $mA \cdot cm^{-2}_{geo}$ / mV	C_{dl} / $mF \cdot cm^{-2}_{geo}$	TOF / s^{-1} (@η or f)	Tafel Slope / $mV \cdot dec^{-1}$	Electrolyte	Pre-analysis	Post-analysis	Long-Term OER Test Conditions	Post-OER Electrocatalyst	Final Type of Electrocatalyst	Ref.
										XPS, TEM, HAADF-STEM		1000 CV cycles (50 $mV \cdot s^{-1}$, 1.2–1.7 V_{RHE})			751
Ni_3S_2/MoS_x/NF	Ni foam	Nanosheet	S	-	215 (@50 $mA \cdot cm^{-2}_{geo}$) 265 (@100 $mA \cdot cm^{-2}_{geo}$) 305 (@150 $mA \cdot cm^{-2}_{geo}$)	-	-	67.5	1 M KOH	XRD, SEM, TEM, EDX, XPS, CHNS, ICP-AES	SEM, XPS	1000 LSV sweeps (1.1–1.9 V_{RHE}) 4500 s multistep CP (50–450 $mA \cdot cm^{-2}_{geo}$, 50 $mA \cdot cm^{-2}_{geo}$ per 500 s) 14 h CP (100 $mA \cdot cm^{-2}_{geo}$)	NiOOH, MoS_x (MoS_2, MoS_3), SO_4^{2-}	Precatalyst (partial oxidation)	732
Ni_3S_2/NF	Ni foam	Nanosheet	S	-	420 (@100 $mA \cdot cm^{-2}_{geo}$)	-	-	83		XRD, SEM, TEM, XPS, CHNS	-	-	-	-	
MoS_x/NF	Ni foam	Nanosheet	-	-	430 (@100 $mA \cdot cm^{-2}_{geo}$)	-	-	105		XRD, SEM, TEM, XPS, CHNS	-	-	-	-	
NiS/NF (Ni_3S_4)	Ni foam	Nanosheet	S	~1.2	320 (@20 $mA \cdot cm^{-2}_{geo}$)	-	0.013 at 350 mV	71	1 M KOH	XRD, SEM, TEM, EDX, XPS	SEM, EDX, XRD, TEM, XPS	20 h CA (1.57 V_{RHE}) 20 h CP (20 $mA \cdot cm^{-2}_{geo}$)	Ni oxides/hydroxides, Oxidized S species	Precatalyst (partial oxidation)	733
NiS-10/NF (Ni_3S_4)	Ni foam	Nanosheet	S	-	344 (@20 $mA \cdot cm^{-2}_{geo}$)	-	0.011 at 350 mV	-		XRD, SEM	-	-	-	-	
NiS_x	GC	Dot-like	S	-	408	0.145 mF	-	56	1 M KOH	TEM, SAED, XRD, AFM, SEM, XPS	SEM, EDX, XPS	10 h CA (1.602 V_{RHE}) 20 h CP (10 $mA \cdot cm^{-2}_{geo}$)	Ni (oxy)hydrate ($Ni(OH)_n$, NiO_x) with Fe incorporation	Precatalyst (partial oxidation)	734
NiFeS/NF	Ni foam	Bulge-like	S	-	65 189 (@100 $mA \cdot cm^{-2}_{geo}$)	8.20	-	119.4	1 M KOH	XRD, SAED, SEM, EDX, XPS	SEM	1000 CV cycles (100 $mV \cdot s^{-1}$, 0.2–0.6 V_{SCE})	NiOOH	Precatalyst	735
NiFeS-Fe/NF	Ni foam	Nanosheet	S	-	221 (@100 $mA \cdot cm^{-2}_{geo}$)	6.95	-	117.3		XRD, SAED, XPS	SEM	1000 CV cycles (100 $mV \cdot s^{-1}$, 0.2–0.6 V_{SCE})	NiOOH	Precatalyst	
Ni_xS_y/NF	Ni foam	-	S	-	240 (@100 $mA \cdot cm^{-2}_{geo}$)	9.37	-	45.4		-	-	-	-	-	
NiS	FTO glass	Nanoparticle	S	0.05	320	-	-	-	1 M KOH	EDX, ICP-MS, XRD, XPS, SEM	XRD, XPS, SEM	6 h CP (1.55 V_{RHE})	NiO_x	Precatalyst (full oxidation)	94
Ni_3S_2	Ni foil	-	S	-	-	-	-	-		XRD	XRD	-	-	Precatalyst (full oxidation)	
$FeNiS_2$ NS	GC	Nanoflower	P	~0.10	310	-	-	46	0.1 M KOH	XRD, Raman, SEM, TEM, HAADF-STEM, EDX, XPS, N_2 ISO (BET)	TEM, XRD	10 h CA (1.7 V_{RHE})	NiOOH	Precatalyst (partial oxidation)	736
Ni_9S_8 NR	GC	Nanorod	P	~0.10	410	-	-	58		XRD, Raman, TEM, XPS, N_2 ISO (BET)	-	10 h CA (1.7 V_{RHE})	-	-	
FeS NS	GC	Nanosheet	P	~0.10	530	-	-	51		XRD, Raman, SEM, XPS, N_2 ISO (BET)	-	10 h CA (1.7 V_{RHE})	-	-	
NiS/NF	Ni foam	Microsphere	S	~43	335 (@50 $mA \cdot cm^{-2}_{geo}$)	-	-	89	1 M KOH	XRD, SEM, EDX, TEM, XPS, Raman	SEM, XRD, Raman	20 h CA (1.52 V_{RHE}) 1000 CV cycles (100 $mV \cdot s^{-1}$, 1.0–2.0 V_{RHE})	NiOOH	Precatalyst (partial oxidation)	737
MoS_2/Ni_3S_2	Ni foam	Nanoparticle	S	~9.7	218	15.6 μF	-	88	1 M KOH	XRD, Raman, SEM, TEM, FESEM, EDX, ICP-MS, XPS	SEM, TEM, EDX, XPS	10 h CP (10 $mA \cdot cm^{-2}_{geo}$)	NiO, MoS_2	Precatalyst (partial oxidation)	738
MoS_2	CC	Nanosheet	S	-	~445	8.2 μF	-	166		SEM, EDX, Raman, XPS	-	-	-	-	
Ni_3S_2	Ni foam	Nanoparticle	S	-	~340	2.1 μF	-	98		SEM, EDX, Raman, XPS	-	-	-	-	
CP/CTs/Co-S	CP	Nanosheet	S	~0.32	306	103.7	1.6×10^{-2} at 300 mV	72	1 M KOH	SEM, TEM, XRD, SAED, EDX, ICP-AES, XPS	SEM, EDX, XPS	1000 CV cycles (50 $mV \cdot s^{-1}$) > 10000 s CA	$Co(OH)_2$	Precatalyst (partial oxidation)	739
CP/Co-S	CP	Nanosheet	S	~0.32	363	29.8	-	101		SEM	-	-	-	-	
h-NiS_x	Ni foam	Microsphere	S	-	180	54	-	96	1 M KOH	XRD, ICP, SEM, EDX, N_2 ISO (BET), XPS	XRD, SEM, EDX, XPS	10 h CP (10 $mA \cdot cm^{-2}_{geo}$)	Ni oxides, Oxidized S species	Precatalyst (partial oxidation)	740
NiS_x	Ni foam	Agglomerated particle	S	-	~210	11	-	176		SEM	-	-	-	-	
$NiCo_2S_4$ NW/NF	Ni foam	Nanowires	S	-	260	40	-	40.1	1 M KOH	XRD, FESEM, TEM, SAED, XPS, CAM	XRD, SEM, XPS	50 h CA (1.527 V_{RHE})	$Co(OH)_2$, NiOOH	Precatalyst (partial oxidation)	741
$NiCo_2S_4$	GC	Aggregated clusters	P	-	350	-	-	75.5		XRD, FESEM	-	10 h CA (1.527 V_{RHE})	-	-	
Ni_3S_2/NF	Ni foam	Nanowires	S	-	300	6.9	-	51		XRD, FESEM	-	10 h CA (1.527 V_{RHE})	-	-	
MoS_2/NF	Ni foam	Hollow microsphere	S	25	310	-	-	105	1 M NaOH	SEM, FESEM, EDX, TEM, N_2 ISO (BET, PSD), XRD, XPS, Raman	SEM, XRD, Raman	1200 CV cycles	MoS_2, MoO_3 ($Ni(OH)_2$, NiOOH from Ni foam)	Precatalyst (partial oxidation)	742
NiCoFeS/NF	Ni foam	Needle-like	S	-	40 160 (@100 $mA \cdot cm^{-2}_{geo}$)	6.28	-	128	1 M KOH	XRD, XPS, SEM, EDX	SEM, XRD, XPS	500 CV cycles (100 $mV \cdot s^{-1}$, 0.1–0.5 V_{SCE}) 10000 s CA	NiOOH, CoOOH, FeOOH	Precatalyst (partial oxidation)	743
NiCoFeS-Fe/NF	Ni foam	Nanosheet	S	-	210 (@100 $mA \cdot cm^{-2}_{geo}$)	4.70	-	94		XRD, XPS, SEM, EDX	SEM, XRD, XPS	500 CV cycles (100 $mV \cdot s^{-1}$, 0.1–0.5 V_{SCE}) 10000 s CA	NiOOH, CoOOH, FeOOH	Precatalyst (partial oxidation)	
$CuCo_2S_4$	GC	Nanosheet	P	0.7	310	-	0.1431 at 310 mV	86	1 M KOH	XRD, TEM, FESEM, HAADF–STEM, EDX, AFM, XPS, EPR, N_2 ISO (BET), Raman, FTIR	XRD, XPS, SEM, TEM, FTIR	10000 CV cycles (10 $mV \cdot s^{-1}$, 0.2–0.8 $V_{Ag/AgCl}$) 12 h CA (1.54 V_{RHE})	$CuCo_2S_4$, Co_9S_8, CoS, SO_4^{2-}/SO_3^{2-}, Cu-O, Co-O	Precatalyst (partial decomposition)	744
$Cu_{0.5}Co_{2.5}S_4$	GC	Nanosheet	P	0.7	~383	-	-	98		XRD, SEM, TEM, FESEM, XPS	-	-	-	-	
Co_3S_4	GC	Nanosheet	P	0.7	~471 (@5 $mA \cdot cm^{-2}_{geo}$)	-	-	144		XRD, SEM, TEM, FESEM, XPS, FTIR	FTIR	500 CV cycles (10 $mV \cdot s^{-1}$, 0.2–0.8 $V_{Ag/AgCl}$)	-	-	

https://doi.org/10.1021/acs.chemrev.3c00005
Chem. Rev. 2023, 123, 12795−13208

Table 5. continued

Initial Electrocatalyst	Substrate	Shape of Electrocatalyst	Deposition Type	Specific Loading / $mg \cdot cm^{-2}_{geo}$	η@10 $mA \cdot cm^{-2}_{geo}$ / mV	C_{dl} / $mF \cdot cm^{-2}_{geo}$	TOF / s^{-1} (@η or f)	Tafel Slope / $mV \cdot dec^{-1}$	Electrolyte	Pre-analysis	Post-analysis	Long-Term OER Test Conditions	Post-OER Electrocatalyst	Final Type of Electrocatalyst	Ref.
Co_9S_8/CNT/CC	CC	Nanotube	P	0.5	321	-	-	58	0.1 M KOH	TEM, SEM, XRD, Raman, XPS	-	20 h CA (1.551 V_{RHE})	-	-	745
Co_9S_8/CNT	GC		P	0.2	369	6.22	-	58			XPS	2000 CV cycles (100 $mV \cdot s^{-1}$, 0.97–1.77 V_{RHE}) 10 h CA (1.599 V_{RHE})	Co oxyhydrate (CoO_x, $Co(OH)_x$)	Precatalyst	
thin-film Co_9S_8	Glass	-	S	-	511	0.205	-	63		XRD, Raman, XPS	-	-	-	-	
Co@MoS_2-500	Co foam	Nanoparticle	S	0.06	270 297 (@20 $mA \cdot cm^{-2}_{geo}$)	36.4	-	74	1 M KOH	XRD, SEM, TEM, EDX, XPS	SEM, EDX, XRD	100 h CP (20 $mA \cdot cm^{-2}_{geo}$ for 50 h,100 $mA \cdot cm^{-2}_{geo}$ for 50 h)	-	Precatalyst (partial oxidation)	746
Co@MoS_2-1000	Co foam	Nanoparticle	S	0.09	296 314 (@20 $mA \cdot cm^{-2}_{geo}$)	28.2	-	61		XRD, SEM, TEM, EDX, Raman	SEM, EDX, XRD, Raman	100 h CP (20 $mA \cdot cm^{-2}_{geo}$ for 50 h,100 $mA \cdot cm^{-2}_{geo}$ for 50 h)	MoO_3, CoOOH, Co_3O_4	Precatalyst (partial oxidation)	
CoS_x (TU 0.5 M)	GC	Nanoflake	S	-	~ 370	-	-	67	1 M NaOH	HIM, XRD, XPS	XPS	24 h CP (10 $mA \cdot cm^{-2}_{geo}$)	CoO, $Co(OH)_2$	Precatalyst	747
CoS_x (TU 0.005 M)	GC	Nanoflake	S	-	~ 370	-	-	-		HIM, XRD, XPS	SEM, XPS	24 h CP (10 $mA \cdot cm^{-2}_{geo}$)	CoO, $Co(OH)_2$	Precatalyst	
$Ni_{1.2\%}$-CoS_2/CC	CC	-	S	-	~ 425 (@100 $mA \cdot cm^{-2}_{geo}$)	-	-	-	1 M KOH	-	-	-	-	-	748
$Ni_{2.3\%}$-CoS_2/CC	CC	Nanowire array	S	0.97	370 (@100 $mA \cdot cm^{-2}_{geo}$)	-	-	119		XRD, EDX, ICP-OES, SEM, TEM, XPS	XPS	12 h CA	NiOOH, $Co(OH)_2$, CoO, SO_x	Precatalyst	
$Ni_{3.5\%}$-CoS_2/CC	CC	-	S	-	~ 385 (@100 $mA \cdot cm^{-2}_{geo}$)	-	-	-		-	-	-	-	-	
$Ni_{4.5\%}$-CoS_2/CC	CC	-	S	-	~ 404 (@100 $mA \cdot cm^{-2}_{geo}$)	-	-	-		-	-	-	-	-	
CoS_2/CC	CC	Nanowire array	S	-	510 (@100 $mA \cdot cm^{-2}_{geo}$)	-	-	127		XRD, SEM	-	12 h CA	-	-	
CoS_2 (ECT-S-CoO)	CFC	Nanosheet	S	-	284	270.8	-	62.1	1 M KOH	SEM, XRD	SEM, XRD, XPS (after CV oxidation)	38 h CP (20 $mA \cdot cm^{-2}_{geo}$)	CoOOH	Precatalyst (full oxidation)	97
$Co_{0.5}Fe_{0.5}S_2$ (ECT-S-$Co_{0.5}Fe_{0.5}O$)	CFC	Nanosheet	S	-	258	-	-	38.9		SEM	SEM (after CV oxidation)	25 h CP (20 $mA \cdot cm^{-2}_{geo}$)	-	-	
$Co_{0.37}Ni_{0.26}Fe_{0.37}S_2$ (ECT-S-$Co_{0.37}Ni_{0.26}Fe_{0.37}O$)	CFC	Nanosheet	S	-	232	-	-	37.6		-	SEM (after CV oxidation)	200 h CP (20 $mA \cdot cm^{-2}_{geo}$)	-	-	
NiS@SLS	SS mesh	Nanosheet	S	~ 1	294	0.6 mF	-	47	0.1 M KOH	EDX, SEM, TEM, XRD, XPS, Raman, N_2 ISO (BET)	EDX, SEM, TEM, XRD, XPS	10 h CA (1.542 V_{RHE})	Ni(II) species	Precatalyst (partial dissolution)	749
Ni_3S_2@Ni	Ni foam	Nanosheet	S	-	347	10.65 mF	-	70		SEM, XRD	-	-	-	-	
NiS on SLS	SS mesh	Nanosheet	P	-	324	0.9 mF	-	75		SEM	-	10 h CA (1.542 V_{RHE})	-	-	
Ni_xS_y/$NF_{(a)}$	Ni foam	Conical aggregation	S	13.6	~ 210 (@100 $mA \cdot cm^{-2}_{geo}$)	-	-	106	1 M KOH	XRD, Rietveld, XPS, SEM	XRD, XPS, SEM	1000 CV cycles (100 $mV \cdot s^{-1}$, 0.2–0.4 V_{SCE})	-	Precatalyst	750
Ni_xS_y/$NF_{(o)}$	Ni foam	Vertical nanosheets with partial accumulation	S	10.1	~ 230 (@100 $mA \cdot cm^{-2}_{geo}$)	-	-	134		XRD, Rietveld, XPS, SEM	-	-	-	-	
Ni_3S_2/NF	Ni foam	Nanosheets with holes	S	-	~ 210 (@100 $mA \cdot cm^{-2}_{geo}$)	-	-	178		XRD, SEM	-	-	-	-	
$NiCo_2S_4$ NA/CC	CC	Nanowire array	S	4.0	280 (@20 $mA \cdot cm^{-2}_{geo}$) 310 (@50 $mA \cdot cm^{-2}_{geo}$) 340 (@100 $mA \cdot cm^{-2}_{geo}$)	31.5	-	89	1 M KOH	XRD, SEM, TEM, EDX, XPS	XRD (after CV), SEM, XPS (after OWS)	12 h CA (1.51 V_{RHE}) 500 CV cycles (2 $mV \cdot s^{-1}$, 1.1–1.6 V_{RHE}) 10 h CP (14 $mA \cdot cm^{-2}_{geo}$, OWS)	$Co(OH)_2$, NiOOH	Precatalyst (partial oxidation)	751
					296 (@20 $mA \cdot cm^{-2}_{geo}$)	-	-	-	0.1 M KOH	XRD, SEM, TEM, EDX, XPS	-	-	-	-	
Co-S/Ti mesh	Ti mesh	Nanosheet	S	-	361	-	-	64	1 M KOH	XRD, XPS, SEM, TEM, SAED, ICP-MS	SEM, XPS, ICP-MS	20 h CA (1.67 V_{RHE}) 20 LSV sweeps (5 $mV \cdot s^{-1}$)	Co oxide/hydroxide	Precatalyst (partial oxidation)	752
Ni_3S_2/NF	Ni foam	Particulate	S	-	431 (@100 $mA \cdot cm^{-2}_{geo}$)	6.5	-	107.1	1 M KOH	XRD, SEM	-	-	-	-	753
$Fe_{11.8\%}$-Ni_3S_2/NF	Ni foam	Particulate	S	-	253 (@100 $mA \cdot cm^{-2}_{geo}$)	14.6	-	65.6		XRD, EDX, SEM, TEM, XPS, Raman	XPS, Raman	5500 s multistep CP (100–600 $mA \cdot cm^{-2}_{geo}$, 50 $mA \cdot cm^{-2}_{geo}$ per 500 s) 14 h CP (200 $mA \cdot cm^{-2}_{geo}$)	NiOOH, FeOOH, Ni–O–S species	Precatalyst	
					222 (@300 $mA \cdot cm^{-2}_{geo}$) 269 (@1000 $mA \cdot cm^{-2}_{geo}$)	31.3	-	64.3	30 wt.% KOH		-	14 h CP (500 $mA \cdot cm^{-2}_{geo}$)	-	-	
$Fe_{6.5\%}$-Ni_3S_2/NF	Ni foam	Particulate	S	-	261 (@300 $mA \cdot cm^{-2}_{geo}$)	15.6	-	77.1		XRD, SEM	-	-	-	-	
$Fe_{14.9\%}$-Ni_3S_2/NF	Ni foam	Particulate	S	-	280 (@300 $mA \cdot cm^{-2}_{geo}$)	12.4	-	108.7		XRD, SEM	-	-	-	-	
Ni_3S_2/NF	Ni foam	Particulate	S	-	322 (@300 $mA \cdot cm^{-2}_{geo}$)	-	-	105.4		XRD, SEM	-	-	-	-	
NiS/NF	Ni foam	-	S	-	390	5.59	0.1233	113.73	1 M KOH	-	-	-	-	-	754
1 wt% CdS/ZIF-67	Ni foam	-	P	-	316	0.236	-	105	1 M KOH	XRD, N_2 ISO (BET, PSD)	-	-	-	-	755
2.5 wt% CdS/ ZIF-67	Ni foam	-	P	-	299	0.226	-	103.9		XRD, N_2 ISO (BET, PSD)	-	-	-	-	
5 wt% CdS/ZIF-67	Ni foam	-	P	-	294	0.68	-	100		XRD, XPS, Raman, FTIR, EPR, TEM, SAED, EDX, SEM, N_2 ISO (BET, PSD)	-	10 h CP (10 $mA \cdot cm^{-2}_{geo}$)	-	-	
10 wt% CdS/ ZIF-67	Ni foam	-	P	-	314	0.284	-	104		XRD, N_2 ISO (BET, PSD)	-	-	-	-	
$CuCo_2S_4$	Nafion-115 membrane	Microsphere	P	2	290	-	5.25 at 290 mV	121	0.5 M H_2SO_4	XRD, Raman, TEM, SEM, EDX	-	3000 CV cycles 72 h CA	-	-	756

https://doi.org/10.1021/acs.chemrev.3c00005
Chem. Rev. 2023, 123, 12795−13208

Table 5. continued

Initial Electrocatalyst	Substrate	Shape of Electrocatalyst	Deposition Type	Specific Loading / $mg \cdot cm^{-2}_{geo}$	η@10 $mA \cdot cm^{-2}_{geo}$ / mV	C_{dl} / $mF \cdot cm^{-2}_{geo}$	TOF / s^{-1} (@η or f)	Tafel Slope / $mV \cdot dec^{-1}$	Electrolyte	Pre-analysis	Post-analysis	Long-Term OER Test Conditions	Post-OER Electrocatalyst	Final Type of Electrocatalyst	Ref.
$CuNi_2S_4$	Nafion-115 membrane	Microsphere	P	2	340	-	-	115		XRD, Raman, TEM, SEM, EDX	-	72 h CA	-	-	756
$CuMn_2S_4$	Nafion-115 membrane	Microsphere	P	2	370	-	-	102		XRD, Raman, TEM, SEM, EDX	-	72 h CA	-	-	
$CuZn_2S_4$	Nafion-115 membrane	Microsphere	P	2	400	-	-	41		XRD, Raman, TEM, SEM, EDX	-	72 h CA	-	-	
Amorphous Co-S-O BBHS	GC	Sea urchin like hollow nanostructure	P	-	285	13.02	-	44.87	1 M KOH	XRD, XPS, SEM, TEM, EDX	-	12 h CA	-	-	757
$NiCuCoS_3$	Au-electrode	Rock like nanostructure	P	-	690	13.5	-	130.3	1 M KOH	SEM, EDX, XRD, FTIR	-	12 h CP (10 $mA \cdot cm^{-2}_{geo}$) 12 h CA (1.92 V)	-	-	758
CoS	Au-electrode	-	P	-	690	4.25	-	188		-	-	-	-	-	
Ni-Co-S/NF	Ni foam	Nanosheet	S	-	362 (@50 $mA \cdot cm^{-2}_{geo}$) 401 (@100 $mA \cdot cm^{-2}_{geo}$)	1.137	-	148	1 M KOH	XRD, SEM, Raman	-	-	-	-	759
$FeCo_2S_4$–$NiCo_2S_4$/Ti	Ti mesh	Nanosheet arrays	S	0.48	230 300 (@20 $mA \cdot cm^{-2}_{geo}$)	12.7	-	65	1 M KOH	XRD, SEM, EDX, TEM, SAED, XPS, FTIR	SEM (after OWS)	10 h CP (20 mA cm^{-2}_{geo}) 10 h CP (10 mA cm^{-2}_{geo}, OWS)	-	-	760
NiFe–S/Ti	Ti mesh	-	S	-	260 330 (@20 $mA \cdot cm^{-2}_{geo}$)	-	-	78		-	-	-	-	-	
CoFe–S/Ti	Ti mesh	-	S	-	275 340 (@20 $mA \cdot cm^{-2}_{geo}$)	-	-	104		XRD	-	-	-	-	
NiCo–S/Ti	Ti mesh	-	S	-	272 335 (@20 $mA \cdot cm^{-2}_{geo}$)	-	-	107		XRD	-	-	-	-	
MoS_2	Ni foam	Nanorods	P	-	~416 (@50 $mA \cdot cm^{-2}_{geo}$)	-	-	44	1 M KOH	XRD, SEM, TEM, Raman, UV-Vis, FTIR, PL	-	12 h CA (0.32 $V_{Ag/AgCl}$) 1 h CA (0.32 $V_{Ag/AgCl}$)	-	-	
CoS	Ni foam	Nanofeathers	P	-	~486 (@50 $mA \cdot cm^{-2}_{geo}$)	-	-	73		XRD, SEM, Raman, UV-Vis, FTIR, PL	-	1 h CA (0.37 $V_{Ag/AgCl}$)	-	-	
CuS	Ni foam	Nanoparticles	P	-	~596 (@50 $mA \cdot cm^{-2}_{geo}$)	-	-	98		XRD, SEM, Raman, UV-Vis, FTIR, PL	-	1 h CA (0.39 $V_{Ag/AgCl}$)	-	-	
CoNi-S/NS-rGO-450	CP	Nanoparticles	P	0.2	300	32.1	-	88.2	1 M KOH	SEM, XRD, HAADF-STEM, TEM, N_2 ISO (BET, PSD)	-	-	-	-	251
CoNi-S/NS-rGO-550	CP	Nanoparticles	P	0.2	274	30.6	-	70.5		SEM, XRD, HAADF-STEM, TEM, N_2 ISO (BET, PSD), XPS	SEM	40 h CA (0.55 V_{SCE})	-	-	
CoNi-S/NS-rGO-550 (no iR comp)	CP	Nanoparticles	P	0.2	290	30.6	-	79.5							
Ni_3S_2/NiF	Ni foam	Nanodendrite	S	-	~286	-	-	87	1 M KOH	XRD, SEM, TEM, N_2 ISO (BET)	-	-	-	-	761
NiS/NiS_2	GC	-	P	~0.136	365 (@20 $mA \cdot cm^{-2}_{geo}$) 436 (@50 $mA \cdot cm^{-2}_{geo}$)	2.24	0.0414 at 300 mV	163	1 M KOH	XRD, Raman, XPS	-	-	-	-	762
Zn-Co-S	GC	Porous symmetric star-like microstructures	S	321	321	2.8	0.016 at 340 mV	49	1 M KOH	FESEM, EDX, XRD, FTIR	-	-	-	-	530
MoS_2	GC	-	P	~0.18	~480 (@2.5 $mA \cdot cm^{-2}_{geo}$)	-	-	-	0.1 M KOH	XPS	-	-	-	-	255
NiS	Ni foam	Nanoparticles	S	-	362 (@100 $mA \cdot cm^{-2}_{geo}$)	7.2	0.007 at 300 mV	146	1 M KOH	SEM, XPS	-	-	-	-	763
Ni_3S_2/NF	Ni foam	Nanosheets	S	-	355 (@50 $mA \cdot cm^{-2}_{geo}$)	38.0	-	39	1 M KOH	XRD, SEM, TEM, SAED	-	-	-	-	764
Ni1Fe10-LDH@Ni_3S_2/NF	Ni foam	Nanosheets	S	-	230 (@50 $mA \cdot cm^{-2}_{geo}$)	21.2	-	29		XRD, SEM, TEM, EDX, XPS	SEM	12 h CP (20 $mA \cdot cm^{-2}_{geo}$)	-	-	
NiS-3 [NiS (hex)]	Ni foam	Nanoparticles	P	-	389 (@50 $mA \cdot cm^{-2}_{geo}$)	-	-	-	3 M KOH	XRD	-	-	-	-	538
NiS-2 [NiS (rhom)]	Ni foam	Nanoparticles	P	-	389 (@50 $mA \cdot cm^{-2}_{geo}$)	-	-	-		XRD, SEM	-	-	-	-	
NiS-1 [NiS (hex)]	Ni foam	Nanoparticles	P	-	371 (@50 $mA \cdot cm^{-2}_{geo}$)	-	-	-		XRD, SEM	-	1000 CV cycles (100 $mV \cdot s^{-1}$)	-	-	
HfS_2-rGO NS	GC	Nanosheets	P	-	~742 (@5 $mA \cdot cm^{-2}_{geo}$)	-	-	572	0.1 M KOH	SEM, TEM, XRD, XPS, Raman, EDX	-	10000 s CA	-	-	546
Co_8FeS_8/N-doped carbon	GC	Cubic nanoparticles-covered nanotubes	P	~0.5	316	352	-	197	1 M KOH	STEM-EDX, XRD, TEM, XPS, ICP-MS	-	6000 CV cycles	-	-	765
$(Ni,Fe)_9S_8$/N-doped carbon	GC	Cubic nanoparticles-covered nanotubes	P	~0.5	185	188	-	157		STEM-EDX, XRD, TEM, XPS, ICP-MS	-	6000 CV cycles	-	-	
$(Ni,Co,Fe)_9S_8$/N-doped carbon	GC	Cubic nanoparticles-covered nanotubes	P	~0.5	116	324	-	184		STEM-EDX, XRD, TEM, XPS, ICP-MS	-	6000 CV cycles	-	-	

https://doi.org/10.1021/acs.chemrev.3c00005
Chem. Rev. 2023, 123, 12795−13208

Table 5. continued

Initial Electrocatalyst	Substrate	Shape of Electrocatalyst	Deposition Type	Specific Loading / $mg \cdot cm^{-2}_{geo}$	η@10 $mA \cdot cm^{-2}_{geo}$ / mV	C_{dl} / $mF \cdot cm^{-2}_{geo}$	TOF / s^{-1} (@η or f)	Tafel Slope / $mV \cdot dec^{-1}$	Electrolyte	Pre-analysis	Post-analysis	Long-Term OER Test Conditions	Post-OER Electrocatalyst	Final Type of Electrocatalyst	Ref.
$Ni:Co_3S_4$	Ni foam	Hollow nanowires (nanotubes)	S	-	293	-	-	65	1 M KOH	XRD, XPS, ICP-OES, SEM, TEM, EDX	-	10 h (10 $mA \cdot cm^{-2}_{geo}$)	-	-	766
Co_3S_4	Ni foam	Nanowires	S	-	283	-	-	66		XRD, XPS, SEM, TEM	XRD, SEM (after OWS)	10 h (10 $mA \cdot cm^{-2}_{geo}$) 40 h CP (10 $mA \cdot cm^{-2}_{geo}$, OWS)	-	-	
amorphous CoS_x@C	CFP	Dodecahedron (nanoparticles)	P	~0.9	297	61.2	-	99	1 M KOH	XRD, SEM	-	-	-	-	767
$Co_{1-x}S$@C	CFP	Porous dodecahedron (nanoparticles)	P	~0.9	260	74.2	-	85		XRD, SEM, TEM, EDX, XPS, N_2 ISO (PSD)	-	80 h CP (10 $mA \cdot cm^{-2}_{geo}$)	-	-	
Co_9S_8	GC	Nanospheres	P	0.37	297	55	-	117	1 M KOH	SEM, XRD, Raman	-	-	-	-	768
Co_9S_8 nps/N,S-rGO	GC	Nanosheets + Nanoparticles	P	0.37	292	10.9	-	90		SEM, XRD, Raman	-	-	-	-	
Co_9S_8/N,S-rGO	GC	Nanosheets + Nanoparticles	P	0.37	266	90	-	75.5		XRD, Raman, TEM, XPS, N_2 ISO (BET), EDX, SEM	-	1000 CV cycles (1.0–1.5 V_{RHE}) 20 h CP (10 $mA \cdot cm^{-2}_{geo}$) 20 h CP (30 $mA \cdot cm^{-2}_{geo}$)	-	-	
CoS/CNT	GC	Nanosheets	P	~0.11	330	~2.43	-	142	1 M KOH	SEM, XRD, XPS, EDX	-	500 CV cycles (1.4–1.7 V_{RHE}) 600 s CA	-	-	769
CoS/C	GC	Nanosheets	P	~0.11	380	~2.36	-	176		-	-	500 CV cycles (1.4–1.7 V_{RHE}) 600 s CA	-	-	
CoS	GC	Nanosheets	P	~0.11	440	~1.74	-	270		SEM, XRD	-	500 CV cycles (1.4–1.7 V_{RHE}) 600 s CA	-	-	
MoS_2/NiS-Ni_3S_2	Ni foam	Core@shell nanoparticles	S	-	433 (@100 $mA \cdot cm^{-2}_{geo}$)	43.3	-	30.3	1 M KOH	SEM, XRD, TEM, XPS, EDX	SEM	12 h CA (1.69 V_{RHE})	-	-	770
NiS-Ni_3S_2	Ni foam	Micro-hexagons	S	-	457 (@100 $mA \cdot cm^{-2}_{geo}$)	25.2	-	56.8		SEM, XRD	-	-	-	-	
Co_9S_8/N,S-CNs-3	GC	Nanosheets	P	0.37	341	-	-	142	1 M KOH	XRD, SEM	-	-	-	-	771
Co_9S_8/N,S-CNs-2	GC	Nanosheets	P	0.37	325	-	-	86.3		XRD, SEM	-	-	-	-	
Co_9S_8/N,S-CNs-1	GC	Nanosheets	P	0.37	335	-	-	121		XRD, SEM	-	-	-	-	
Co_9S_8/N,S-CNs-0.6	GC	Nanosheets	P	0.37	357	-	-	80		SEM, TEM, SAED, EDX, XPS, XRD	-	10 h CP (10 $mA \cdot cm^{-2}_{geo}$)	-	-	
NiO-Ni_3S_2-5	Ni foam	Nanosheets	S	-	365 (@20 $mA \cdot cm^{-2}_{geo}$)	4	-	109.8	1 M KOH	-	-	-	-	-	772
NiO-Ni_3S_2-4	Ni foam	Nanosheets	S	-	343 (@20 $mA \cdot cm^{-2}_{geo}$)	5	-	77.4		-	-	-	-	-	
NiO-Ni_3S_2-3	Ni foam	Nanosheets	S	-	289 (@20 $mA \cdot cm^{-2}_{geo}$)	16	-	114.8		-	-	-	-	-	
NiO-Ni_3S_2-2	Ni foam	Nanosheets	S	1.05	290 (@20 $mA \cdot cm^{-2}_{geo}$)	15.14/22	-	75/74.6		SEM, TEM, SAED, EDX, XRD, XPS	SEM (after OWS)	50 h CP (100 $mA \cdot cm^{-2}_{geo}$, OWS)	-	-	
NiO-Ni_3S_2-1	Ni foam	Nanosheets	S	-	312 (@20 $mA \cdot cm^{-2}_{geo}$)	14.10	-	83.1		-	-	-	-	-	
Ni_3S_2	Ni foam	Nanosheets	S	-	327 (@20 $mA \cdot cm^{-2}_{geo}$)	13.99	-	93		SEM, XRD, XPS	-	-	-	-	
NiO/NiS	Ni foam	Nanoparticles	P	-	279 (@40 $mA \cdot cm^{-2}_{geo}$)	-	-	60	1 M KOH	XRD, FTIR, SEM, N_2 ISO (BET)	-	14 h CP (1.65 V_{RHE})	-	-	773
NiS	Ni foam	Nanoparticles	P	-	294 (@40 $mA \cdot cm^{-2}_{geo}$)	-	-	65		XRD, FTIR, SEM, N_2 ISO (BET)	-	-	-	-	
NiCoDH/NiCoS-0.2	GC	Nanosheets	P	~0.136	303 (@20 $mA \cdot cm^{-2}_{geo}$)	3.93	0.069 at 300 mV	77.6	1 M KOH	SEM, TEM, XRD, AFM, EDX, XPS, N_2 ISO (BET), ICP-MS	-	5000 CV cycles (100 $mV \cdot s^{-1}$, 0–0.6 $V_{Hg/HgO}$) 50 h CP (10 $mA \cdot cm^{-2}_{geo}$)	-	-	774
NiDH/NiS	GC	Nanosheets	P	~0.136	319 (@20 $mA \cdot cm^{-2}_{geo}$)	2.63	0.0295 at 300 mV	144.6		SEM, TEM, XRD, XPS, ICP-MS	-	-	-	-	
CoDH/CoS	GC	Nanosheets	P	~0.136	353 (@20 $mA \cdot cm^{-2}_{geo}$)	-	0.0212 at 300 mV	98.8		SEM, TEM, XRD, XPS, ICP-MS	-	-	-	-	
NiCoS-0.2	GC	Nanosheets	P	~0.136	336 (@20 $mA \cdot cm^{-2}_{geo}$)	2.77	0.012 at 300 mV	111.5		SEM, TEM, XRD, XPS, N_2 ISO (BET), ICP-MS	-	-	-	-	
Co_9S_8/C	GC	Nanosheets	P	-	434	-	-	119	1 M KOH	Raman, XRD, SEM, XPS, TEM, EDX	-	1000 CV cycles	-	-	775
NiS/NF	Ni foam	Nanosheets	S	-	350 (@50 $mA \cdot cm^{-2}_{geo}$)	24	-	125	1 M KOH	XRD, SEM, TEM, XPS	-	1000 CV cycles	-	-	547
NiS/NC	GC	3D Carbon matrix with nanoparticles	P	0.204	371	-	-	75	1 M KOH	SEM, XRD, TEM, N_2 ISO (BET), XPS	-	-	-	-	776
Ni/NiS/NC	GC	3D Carbon matrix with nanoparticles	P	0.204	337	-	-	52		SEM, XRD, TEM, N_2 ISO (BET), XPS	SEM	3000 CV cycles	-	-	
CISC-Ag-5%	GC	-	P	~0.28	380	1.15	-	53.6	1 M KOH	-	-	-	-	-	777
CISC-Ag-3%	GC	Nanosheets + Nanoparticles	P	~0.28	329	5.16	-	53.2		XRD, XPS, SEM, TEM, EDX	-	7 h CA (1.57 V_{RHE})	-	-	
CISC-Ag-0.1%	GC	-	P	~0.28	340	2.98	-	50.9		XRD	-	-	-	-	
CISC-Ag-0.02%	GC	-	P	~0.28	350	2.74	-	51.4		XRD	-	-	-	-	
CISC (Fe-Co-S)	GC	Nanosheets + Nanoparticles	P	~0.28	366	3.26	-	51.3		XRD, XPS, TEM, SEM	-	-	-	-	
CoS_2 NBs-30	GC	Nanocube	P	-	340	6.7	-	88.3	1 M KOH	TEM, EDX	-	-	-	-	778
CoS_2 NBs-12	GC	Nanocube	P	-	290	7.7	-	72.2		TEM, XRD, XPS, EDX, HAADF-STEM, STEM	TEM	10000 s CA (1.5 V_{RHE}) 24 h CP (10 $mA \cdot cm^{-2}_{geo}$)	-	-	
CoS_2 NBs-6	GC	Nanocube	P	-	317	2.6	-	78.4		TEM, EDX	-	-	-	-	
C_3M_1S (CoS_x@MoS_2)	Ni foam	Nanostructure	P	~0.5	295	25.10	-	36.02	1 M KOH	FESEM, XRD	-	-	-	-	779

https://doi.org/10.1021/acs.chemrev.3c00005
Chem. Rev. 2023, 123, 12795−13208

Table 5. continued

Initial Electrocatalyst	Substrate	Shape of Electrocatalyst	Deposition Type	Specific Loading / $mg \cdot cm^{-2}_{geo}$	η@10 $mA \cdot cm^{-2}_{geo}$ / mV	C_{dl} / $mF \cdot cm^{-2}_{geo}$	TOF / s^{-1} (@η or f)	Tafel Slope / $mV \cdot dec^{-1}$	Electrolyte	Pre-analysis	Post-analysis	Long-Term OER Test Conditions	Post-OER Electrocatalyst	Final Type of Electrocatalyst	Ref.
C_2M_1S (CoS_x@MoS_2)	Ni foam	Nanostructure	P	~0.5	276	68.20	-	26.08		FESEM, XRD, XPS, TEM	XRD	1000 CV cycles (100 $mV \cdot s^{-1}$, 1.23–1.58 V_{RHE}) 18 h CA (1.529 V_{RHE})	-	-	779
C_1M_1S (CoS_x@MoS_2)	Ni foam	Nanostructure	P	~0.5	324	10.92	-	71.07		FESEM, XRD	-	-	-	-	
MoS_2	Ni foam	Nanosheets	P	~0.5	-	12.02	-	90.51		SEM, XRD, XPS	-	-	-	-	
CoS_x	Ni foam	Nanocube	P	~0.5	~433	31.25	-	45.37		SEM, XRD, XPS	-	-	-	-	
Mo-Ni_3S_2/NF-100	Ni foam	Nanorod array	S	-	350 (@100 $mA \cdot cm^{-2}_{geo}$)	33.34	-	408.74	1 M KOH	XRD, SEM, XPS	-	-	-	-	780
Mo-Ni_3S_2/NF-80	Ni foam	Nanorod array	S	-	390 (@100 $mA \cdot cm^{-2}_{geo}$)	13.35	-	562.75		XRD, SEM	-	-	-	-	
Mo-Ni_3S_2/NF-20	Ni foam	Bulge-like structures	S	-	470 (@100 $mA \cdot cm^{-2}_{geo}$)	11.79	-	242.96		XRD, SEM	-	-	-	-	
Ni_3S_2/NF	Ni foam	Ripple-like morphology	S	-	520 (@50 $mA \cdot cm^{-2}_{geo}$)	11.05	-	343.05		XRD, SEM	-	-	-	-	
Ni_3S_2	Ni foam	Nanosheet arrays	S	-	~524 (@50 $mA \cdot cm^{-2}_{geo}$)	-	-	286	1 M KOH	SEM, XRD, Raman, XPS	-	-	-	-	781
NiCoS	GC	Nanosheets	P	~0.21	~420	1.2	-	73.7	1 M KOH	Raman, N_2 ISO (BET), SEM, TEM, XRD	-	20000 s CP (10 $mA \cdot cm^{-2}_{geo}$)	-	-	274
$CoNi_2S_4$@CoS_2	Ni foam	Nanosheets	S	-	365 (@30 $mA \cdot cm^{-2}_{geo}$)	66.1	-	237.6	1 M KOH	XRD, SEM	-	-	-	-	782
Co_9S_8 NPs imbedded in GMT with CNTs (GMT: N,S-co-doped graphite microtube)	Ni foam	Microtubes (GMT) with encapsulated nanoparticles (Co_9S_8)	P	0.1	-	-	-	145	1 M KOH	XRD, TEM, SEM, EDX, EDX, XPS, ICP-AES, N_2 ISO (BET, PSD), Raman, IR, MM, TGA	XRD, SEM, TEM	120 h CA (1.53 V_{RHE})	-	-	783
Co-Mo-O/Ni_3S_2/NF	Ni foam	Nanosheet array	S	~1.9	290 (@50 $mA \cdot cm^{-2}_{geo}$)	1.05	-	46	1 M KOH	XRD, SEM, EDX, TEM, XPS, N_2 ISO (BET, PSD)	SEM, EDX	12 h CA (1.51 V_{RHE})	-	-	784
Ni_3S_2/NF	Ni foam	Irregular particles	S	~2.4	310 (@50 $mA \cdot cm^{-2}_{geo}$)	0.9	-	48		XRD, SEM	-	-	-	-	
p-MoS_2/Ni_3S_2/NF	Ni foam	Distinctive porous structure	S	~58.74	185	55.1	-	46	1 M KOH	XRD, SEM, ICP-AES, EDX, XPS, CAM	SEM	35 h CP (10 $mA \cdot cm^{-2}_{geo}$) 4500 s multistep CA (1.3–1.7 V_{RHE}, 50 mV per 500 s)	-	-	785
MoS_2/Ni_3S_2/NF	Ni foam	Rough surface (nonporous)	S	~58.74	230	32.3	-	101		XRD, SEM, TEM, CAM	-	-	-	-	
MoS_2/NF	Ni foam	-	S	~58.74	321	3.46	-	161		CAM	-	-	-	-	
Ni_3S_2/NF	Ni foam	-	S	-	285	12.1	-	143		CAM	-	-	-	-	
CoS_x/Ni_3S_2@NF	Ni foam	Porous network (Ni_3S_2) covered with cuboids (CoS_x)	S	~2.83	280 (@20 $mA \cdot cm^{-2}_{geo}$) 373 (@100 $mA \cdot cm^{-2}_{geo}$) 414 (@200 $mA \cdot cm^{-2}_{geo}$)	8.68	-	105.4	1 M KOH	FESEM, TEM, EDX, XRD, XPS	SEM, EDX	20 h CA (1.58 V_{RHE} for 10 h, 1.60 V_{RHE} for 10 h) 500 CV cycles (100 $mV \cdot s^{-1}$, 1.23–1.58 V_{RHE})	-	-	786
Ni_3S_2@NF	Ni foam	Crumpled sheet-like structures with a porous network	S	-	347 (@20 $mA \cdot cm^{-2}_{geo}$) 448 (@100 $mA \cdot cm^{-2}_{geo}$)	3.69	-	133.0		FESEM, XRD, XPS	-	-	-	-	
CoS_x@NF	Ni foam	-	P	-	353 (@20 $mA \cdot cm^{-2}_{geo}$) 440 (@100 $mA \cdot cm^{-2}_{geo}$) 509 (@200 $mA \cdot cm^{-2}_{geo}$)	6.12	-	113.4		XRD	-	-	-	-	
U-CoNi-S-NSA/MnO_2	Ni foam	Nanoparticles (MnO_2) on nanosheet array (CoNi-S)	S	-	170	21.7	-	73.8	1 M KOH	XRD, SEM, TEM, STEM, EDX, N_2 ISO, XPS, AFM	SEM, TEM	10 h CA 10000 CV cycles (100 $mV \cdot s^{-1}$, 1.2–1.8 V_{RHE})	-	-	787
CoNi-S-NSA	Ni foam	Nanosheet array	S	-	210	5.40	-	91.5		XPS, SEM, XRD	-	-	-	-	
bulk NiCoS	GC	Nanoparticles	P	~0.21	410	-	-	112.5	1 M KOH	SEM	-	-	-	-	788
Co_3S_4	GC	Hollow Nanoparticles	P	~0.21	391	20.2	-	95.0		XRD, FESEM	-	40000 s CA (1.55 V_{RHE})	-	-	
NiCoS-10	GC	Hollow Nanoparticles	P	~0.21	430	-	-	109.9		XRD, FESEM	-	-	-	-	
NiCoS-7	GC	Hollow Nanoparticles	P	~0.21	405	-	-	99.9		XRD, FESEM	-	-	-	-	
NiCoS-5	GC	Hollow Nanoparticles	P	~0.21	380	-	-	92.5		XRD, FESEM	-	-	-	-	
NiCoS-3	GC	Hollow Nanoparticles	P	~0.21	320	89.5	-	58.8		XRD, TEM, SAED, XPS, EDX, FESEM, N_2 ISO (BET)	-	1000 CV cycles 40000 s CA (1.55 V_{RHE})	-	-	
NiCoS-1	GC	Hollow Nanoparticles	P	~0.21	340	-	-	80.9		XRD, FESEM	-	-	-	-	
$CoS_{1.097}$ nanoclusters	GC	Nanocluster	P	0.128	354	-	-	61.60	1 M KOH	SEM, XRD	-	-	-	-	789
$CoS_{1.097}$ nanotubes	GC	Nanotube	P	0.128	331	14.17	-	55.54		SEM, TEM, XRD, XPS, Raman, N_2 ISO (BET), EDX	XRD, SEM, EDX	2 h CP (10 $mA \cdot cm^{-2}_{geo}$, substrate: ITO)	-	-	
$Ni_{1.03}Co_{0.97}S_{1.097}$ nanotubes	GC	Nanotube	P	0.128	316	26.42	-	54.72		SEM, XRD, XPS, Raman, BET, EDX	-	2 h CP (10 $mA \cdot cm^{-2}_{geo}$, substrate: ITO)	-	-	

https://doi.org/10.1021/acs.chemrev.3c00005
Chem. Rev. 2023, 123, 12795−13208

Table 5. continued

Initial Electrocatalyst	Substrate	Shape of Electrocatalyst	Deposition Type	Specific Loading / $mg \cdot cm^{-2}_{geo}$	η@10 $mA \cdot cm^{-2}_{geo}$ / mV	C_{dl} / $mF \cdot cm^{-2}_{geo}$	TOF / s^{-1} (@η or f)	Tafel Slope / $mV \cdot dec^{-1}$	Electrolyte	Pre-analysis	Post-analysis	Long-Term OER Test Conditions	Post-OER Electrocatalyst	Final Type of Electrocatalyst	Ref.
MoS_2/NiS NCs	Ni foam	Nanocuboids	S	-	271 (@15 $mA \cdot cm^{-2}_{geo}$)	64.7	-	53	1 M KOH	XRD, SEM, TEM, XPS, N_2 ISO (BET), EDX	-	1000 CV cycles (50 $mV \cdot s^{-1}$, 1.2−1.65 V_{RHE}) 80 h CP (15 $mA \cdot cm^{-2}_{geo}$)	-	-	790
MoS_2/NiS NWs	Ni foam	Nanowires	S	-	330 (@15 $mA \cdot cm^{-2}_{geo}$)	14.1	-	60		XRD, SEM, N_2 ISO (BET), EDX	-	-	-	-	
MoS_2/NiS Ags	Ni foam	Aggregations	S	-	364 (@15 $mA \cdot cm^{-2}_{geo}$)	13.5	-	107		XRD, SEM, N_2 ISO (BET), EDX	-	-	-	-	
NiS foam	Ni foam	Rough particulate	S	-	~ 390 (@15 $mA \cdot cm^{-2}_{geo}$)	7.4	-	119		SEM	-	-	-	-	
MoS_2/NiS NCs	Ni foam	Nanocuboids	S	-	202	-	-	-	0.5 M H_2SO_4	XRD, SEM, TEM, XPS, N_2 ISO (BET), EDX	-	24 h CP (10 $mA \cdot cm^{-2}_{geo}$)	-	-	
$CoMoS_{3.13}$	GC	Nanosheets	P	~ 0.22	520	1.05	-	187	1 M KOH	TEM	-	-	-	-	791
BN-CNT@$CoMoS_{3.13}$	GC	Nanotube	P	~ 0.22	400	7.68	-	68		SEM, TEM, XRD, XPS, Raman, EDX	-	1000 CV cycles 10 h CA (1.63 V_{RHE})	-	-	
$NiS_{1.03}$-NSC	CC	Hollow nanospherical structure	P	0.25	270	9.0	-	68.9	1 M KOH	XRD, SEM, TEM, HAADF-STEM, EDX, N_2 ISO (BET, PSD), XPS, Raman, ICP-MS	SEM, TEM	10 h CA (1.54 V_{RHE})	-	-	792
Ni_9S_8-$NiS_{1.03}$-NSC	CC	Hollow nanospherical structure	P	0.25	290	6.8	-	63.8		XRD, SEM, TEM, HAADF-STEM, EDX, N_2 ISO (BET, PSD), XPS, Raman, ICP-MS	-	30000 s CA (1.6 V_{RHE})	-	-	
Ni_9S_8-NSC	CC	Hollow nanospherical structure	P	0.25	310	5.4	-	69.6		XRD, SEM, TEM, HAADF-STEM, EDX, N_2 ISO (BET, PSD), XPS, Raman, ICP-MS	-	30000 s CA (1.6 V_{RHE})	-	-	
$NiCo_2S_4$	Ni foam	Nanostructured needle-grass array	S	-	293	17.4	-	95	1 M KOH	XRD, SEM, EDX, XPS	-	2000 CV cycles > 17 h CA	-	-	793
Ni-MoS_2/NC	-	Nanosheets	P	~ 0.25	261	-	-	53	1 M KOH	XRD, SEM, EDX, TEM, XPS, TGA, N_2 ISO (BET), Raman	-	1000 CV cycles (100 $mV \cdot s^{-1}$, 1.2−1.7 V_{RHE}) 12000 s CA	-	-	794
$CoMo_2S_4$/NC	-	Nanosheets	P	~ 0.25	290	-	-	69		XRD, TGA, N_2 ISO (BET), Raman	-	12000 s CA	-	-	
Mo_3S_4/NC	-	Nanosheets	P	~ 0.25	531	-	-	105		XRD	-	12000 s CA	-	-	
ZnCoS-NSCNP	GC	Nanotube/nano polyhedra	P	~ 0.21	430	6.1	-	96	1 M KOH	XRD, SEM, TEM, N_2 ISO (BET, PSD)	-	-	-	-	795
CoS_2-NSCNT/NP	GC	Nanotube/nano polyhedra	P	~ 0.21	380	9.7	-	92		XRD, SEM, TEM, N_2 ISO (BET, PSD)	-	-	-	-	
ZnCoS-NSCNT/NP	GC	Nanotube/nano polyhedra	P	~ 0.21	270	16.5	-	73		XRD, EDX, XPS, SEM, TEM, N_2 ISO (BET, PSD)	TEM, XPS (after OWS)	1000 CV cycles 10 h CP (1.53 V_{RHE}) 40 h CA (OWS)	-	-	
CoS-8 cycles	CC	Nanosheets	S	-	~ 563	-	-	-	1 M KOH	XRD, SEM	-	-	-	-	796
CoS-4 cycles	CC	Nanosheets	S	-	430	-	-	-		XRD, SEM	-	-	-	-	
CoS-2 cycles	CC	Nanosheets	S	-	~ 656	-	-	-		XRD, SEM	-	-	-	-	
CoS-1 cycles	CC	Nanosheets	S	-	-	-	-	-		XRD, SEM	-	-	-	-	
Co_3S_4--B (hydrophobic)	GC stick	Nanosheets	P	~ 0.42	~ 510	-	-	108.6	1 M KOH	XRD, IRAS, CAM	-	5 h CA 10 h CA (OWS)	-	-	797
Co_3S_4--L (hydrophilic)	GC stick	Nanosheets	P	~ 0.42	360	-	-	84.7		XRD, XPS, TEM, SAED, SEM, EDX, IRAS, CAM	TEM (after OWS)	5 h CA 10 h CA (cell voltage: 1.63 V, OWS)	-	-	
CoS-1-C50	CFP	Nanosheets	S	-	328	-	-	48.5	1 M KOH	SEM, BET, XRD	-	1000 CV cycles (100 $mV \cdot s^{-1}$, 0−1.6 V_{RHE})	-	-	798
CoS-1-C30	CFP	Nanosheets	S	-	335	-	-	49.1		SEM, BET, XRD	-	-	-	-	
CoS-1-C10	CFP	Nanosheets	S	-	370	-	-	57.5		SEM, BET, XRD, XPS, TEM	-	-	-	-	
CoS-10-C10	CFP	Nanosheets	S	-	410	-	-	57.5		SEM, BET, XRD, XPS, TEM	-	-	-	-	
CoS-50-C10	CFP	Nanosheets	S	-	420	-	-	59.2		SEM, BET, XRD, XPS, TEM	-	-	-	-	
CoS-1-C10	GC	-	-	-	440	-	-	73.7		-	-	-	-	-	
CoMnS/Ni (Co_9S_8 + MnS)	Ni foam	3D hexagram-like nanosheet	S	4.1	298 (@100 $mA \cdot cm^{-2}_{geo}$)	56.3	-	43.9	1 M KOH	XRD, EDX, SEM, TEM, XPS	SEM	10 h CA (1.46 V_{RHE}) 1000 CV cycles	-	-	799
Co_9S_8/Ni	Ni foam	Nanosheet	S	-	439 (@100 $mA \cdot cm^{-2}_{geo}$)	24.0	-	71.5		XRD, EDX, SEM	-	-	-	-	
MnS/Ni	Ni foam	Nanosheet	S	-	492 (@100 $mA \cdot cm^{-2}_{geo}$)	13.0	-	100.3		XRD, EDX, SEM	-	-	-	-	
Co_9S_8/N,S-CNTs	GC	Nanoparticles on CNTs	P	0.429	379	67	-	106	0.1 M KOH	XRD, TEM, STEM, XPS, N_2 ISO (BET), Raman, UPS, TGA	-	8 h CA (1.60 V_{RHE}) 3000 CV cycles (50 $mV \cdot s^{-1}$, 0.964−1.664 V_{RHE})	-	-	800
Cu_xS-1	GC	Aggregated particles	P	-	-	-	-	-	0.1 M KOH	XRD, SEM, EDX	-	-	-	-	801
Cu_xS-2	GC	Aggregated particles	P	-	530 (@1 $mA \cdot cm^{-2}_{geo}$)	-	-	-		XRD, SEM, EDX	-	-	-	-	
Cu_xS-3	GC	Aggregated particles	P	-	430 (@1 $mA \cdot cm^{-2}_{geo}$)	-	-	-		XRD, SEM, EDX	-	-	-	-	

https://doi.org/10.1021/acs.chemrev.3c00005
Chem. Rev. 2023, 123, 12795−13208

Table 5. continued

Initial Electrocatalyst	Substrate	Shape of Electrocatalyst	Deposition Type	Specific Loading / $mg \cdot cm^{-2}_{geo}$	η@10 $mA \cdot cm^{-2}_{geo}$ / mV	C_{dl} / $mF \cdot cm^{-2}_{geo}$	TOF / s^{-1} (@η or f)	Tafel Slope / $mV \cdot dec^{-1}$	Electrolyte	Pre-analysis	Post-analysis	Long-Term OER Test Conditions	Post-OER Electrocatalyst	Final Type of Electrocatalyst	Ref.
TMS-rGO (NCO-200) (Ni-Co sulfide)	GC	Nanoparticles	P	0.285	322	21.47	0.08 at 360 mV	52	1 M KOH	FESEM, XRD, XPS, N_2 ISO (BET), Raman	-	10 h CA (1.6 V_{RHE})	-	-	802
TMS-rGO (NCS-200) (Ni-Co sulfide)	GC	No visible nanoparticles	P	0.285	335	18.55	0.04 at 360 mV	60		FESEM, XRD, N_2 ISO (BET), Raman	-	-	-	-	
TMS-rGO (NCS-A200) (Ni-Co sulfide)	GC	Agglomerated nanoparticles	P	0.285	338	12.98	0.05 at 360 mV	49		FESEM, XRD, N_2 ISO (BET), Raman	-	-	-	-	
TMS-rGO (NCO-120) (Ni-Co sulfide)	GC	Nanoparticles	P	0.285	348	10.12	0.03 at 360 mV	59		FESEM, XRD, N_2 ISO (BET), Raman	-	-	-	-	
TMS-rGO (NCS-120) (Ni-Co sulfide)	GC	No visible nanoparticles	P	0.285	350	0.985	0.01 at 360 mV	95		FESEM, XRD, N_2 ISO (BET), Raman	-	-	-	-	
TMS-rGO (NCS-A120) (Ni-Co sulfide)	GC	Agglomerated nanoparticles	P	0.285	361	9.12	0.02 at 360 mV	77		FESEM, XRD, N_2 ISO (BET), Raman	-	-	-	-	
Co_9S_8@NS-3DrGO-650	GC	Nanoparticles embedded in graphene	P	0.2	470	-	-	108	1 M KOH	SEM, TEM, STEM, EDX, XRD, Raman, XPS, ICP-AES, N_2 SM	-	-	-	-	803
Co_9S_8@NS-3DrGO-750	GC	Nanoparticles embedded in graphene	P	0.2	361	-	-	105		SEM, TEM, XRD, XPS, ICP-AES, Raman, N_2 ISO (BET)	-	-	-	-	
Co_9S_8@NS-3DrGO-850	GC	Nanoparticles embedded in graphene	P	0.2	317	-	-	102		SEM, TEM, XRD, XPS, ICP-AES, Raman, N_2 ISO (BET)	-	1000 CV cycles (50 $mV \cdot s^{-1}$, 0.2–0.7 $V_{Ag/AgCl}$)	-	-	
Co_9S_8@NS-3DrGO-950	GC	Nanoparticles embedded in graphene	P	0.2	371	-	-	140		SEM, TEM, XRD, XPS, ICP-AES, Raman, N_2 ISO (BET)	-	-	-	-	
$NiCo_2S_4$	Ni foam	Nanorods	S	-	220 (@30 $mA \cdot cm^{-2}_{geo}$)	-	-	88.6	1 M KOH	SEM, TEM, EDX, XRD, XPS	-	18 h CA (1.55 V_{RHE})	-	-	804
Ni_3S_2	Ni foam	Nanorods	S	-	370 (@30 $mA \cdot cm^{-2}_{geo}$)	-	-	183.8		SEM, XRD, XPS	-	18 h CA (1.55 V_{RHE})	-	-	
8 h FNSH/GA ($FeNi_2S_4$ hollow balloons/graphene aerogel)	Ni foam	Hollow microspheres (hollow balloons)	P	0.75	273	2.95	-	66	1 M KOH	SEM, TEM, XRD, Raman, N_2 ISO	-	50000 s CA (1.668 V_{RHE}) 40000 s CP (10 $mA \cdot cm^{-2}_{geo}$)	-	-	805
FNSH ($FeNi_2S_4$ hollow balloons)	Ni foam	Hollow microspheres (hollow balloons)	P	0.75	~360	-	-	109		XRD, XPS, SEM, TEM, EDX, ICP-OES, DLS	-	-	-	-	
$Ni_{0.96}S$/GA	Ni foam	Hollow microspheres	P	0.75	440	-	-	-		XRD, SEM	-	-	-	-	
Fe_3S_4/GA	Ni foam	Hollow microspheres	P	0.75	360	-	-	-		XRD, SEM	-	-	-	-	
Ni_3S_2/NF	Ni foam	Nanosheets	S	-	467 (@100 $mA \cdot cm^{-2}_{geo}$)	-	-	143	1 M KOH	FESEM, N_2 ISO	-	-	-	-	806
CoS-A (annealing treatment)	CC	Nanosheets	S	-	390	-	-	-	1 M KOH	XRD, SEM, EDX, TEM, XPS	-	12 h CA (1.76 V_{RHE})	-	-	807
CoS	CC	Nanosheets	S	-	420	-	-	-		XRD, SEM	-	-	-	-	
S-NiFe NCs	GC	Aggregated particles	P	-	~348	0.22923	-	65	1 M KOH	XRD, SEM	-	-	-	-	565
ED-CoS (1200 s)	Ti foil	3D flower-like nanostructure	S	0.83	310	1.050 mF	-	55	1 M KOH	XRD, SEM, TEM, XPS, FTIR	-	20 h CA (1.55 V_{RHE})	-	-	808
ED-CoS (2400 s)	Ti foil	Dense spheres (aggregation)	S	4.72	340	0.375 mF	-	67		SEM	-	-	-	-	
ED-CoS (1800 s)	Ti foil	Dense spheres (aggregation)	S	2.01	330	0.437 mF	-	62		SEM	-	-	-	-	
ED-CoS (600 s)	Ti foil	Nanoflower-like clusters	S	0.44	320	0.794 mF	-	62		SEM	-	-	-	-	
ED-CoS (150 s)	Ti foil	Nanoflower-like clusters	S	0.16	350	0.340 mF	-	77		SEM	-	-	-	-	
ED-CoS (30 s)	Ti foil	Nanosheets	S	0.04	400	0.308 mF	-	90		SEM	-	-	-	-	
ED-CoS (15 s)	Ti foil	Nanosheets	S	0.03	440	0.180 mF	-	95		SEM	-	-	-	-	
ED-CoS (5 s)	Ti foil	Nanosheets	S	0.01	580	0.156 mF	-	153		SEM	-	-	-	-	
MNCC4 ($Fe_3Ni_4S_8$)	GC	Spherical nanoparticles on meshy carbon base	P	0.1212	240	43.47 $\mu F \cdot mg^{-1} \cdot cm^{-2}$	-	43.52	1 M KOH	XRD, Raman, XPS, SEM, TEM, EDX	-	50 h CP (20 $mA \cdot cm^{-2}_{geo}$)	-	-	809
MNCC5 ($Fe_3Ni_4S_8$ + Ni_3S_2)	GC	-	P	0.1212	~348	-	-	69.71		XRD, Raman	-	-	-	-	
MNCC3 ($Fe_3Ni_4S_8$ + FeS)	GC	-	P	0.1212	~304	-	-	84.04		XRD, Raman	-	-	-	-	
MNCC2 (Ni_3S_2)	GC	-	P	0.1212	~376	-	-	98.37		XRD, Raman, XPS	-	-	-	-	
MNCC1 (FeS)	GC	-	P	0.1212	~390	-	-	94.32		XRD, Raman, XPS	-	-	-	-	
CoS after treatment	SS	Thin film	S	-	270	-	-	102	1 M KOH	XRD, FTIR	-	~8.4 h CP (10 $mA \cdot cm^{-2}_{geo}$)	-	-	810
CoS before treatment	SS	Thin film	S	-	300	-	-	81		XRD, FTIR	-	-	-	-	

https://doi.org/10.1021/acs.chemrev.3c00005
Chem. Rev. 2023, 123, 12795−13208

Table 5. continued

Initial Electrocatalyst	Substrate	Shape of Electrocatalyst	Deposition Type	Specific Loading / $mg \cdot cm^{-2}_{geo}$	η@10 $mA \cdot cm^{-2}_{geo}$ / mV	C_{dl} / $mF \cdot cm^{-2}_{geo}$	TOF / s^{-1} (@η or j)	Tafel Slope / $mV \cdot dec^{-1}$	Electrolyte	Pre-analysis	Post-analysis	Long-Term OER Test Conditions	Post-OER Electrocatalyst	Final Type of Electrocatalyst	Ref.
Co_9S_8-NSC	GC	Polyhedral nanoparticles	P	0.425	336	9.11	-	87.7	1 M KOH	SEM, XRD, XPS, Raman, N_2 ISO	-	-	-	-	273
Co_4S_3/NSG-NaCl	GC	Nanoparticles on graphene nanosheets	P	0.28	340	-	-	81	1 M KOH	SEM, TEM, SAED, EDX, XRD, XPS, Raman, N_2 ISO (BET, PSD)	-	5000 CV cycles (1.1−1.8 V_{RHE})	-	-	811
$Ni_{4.3}Co_{4.7}S_8$	Ni foam	Granular nanospheres with nanosheets on surface	P	~4.0	133.8 (@20 $mA \cdot cm^{-2}_{geo}$)	-	-	194.2	1 M KOH	AAS, XRD, TEM, SEM, EDX, XPS, Raman, N_2 ISO (PSD)	-	8 h CA (1.33 V_{RHE})	-	-	812
$Ni_{1.4}Co_{7.6}S_8$	Ni foam	Granular microspheres	P	~4.0	189.4 (@20 $mA \cdot cm^{-2}_{geo}$)	-	-	303.1		AAS, XRD, SEM, XPS, Raman, N_2 ISO (PSD)	-	-	-	-	
$Ni_{0.1}Co_{0.9}S$	Ni foam	Sheet-assembled hollow spheres	P	~4.0	243.2 (@20 $mA \cdot cm^{-2}_{geo}$)	-	-	153.5		AAS, XRD, SEM, XPS, Raman, N_2 ISO (PSD)	-	-	-	-	
CoS	Ni foam	Sheet-assembled hollow spheres	P	~4.0	200.1 (@20 $mA \cdot cm^{-2}_{geo}$)	-	-	139.9		XRD, SEM, XPS, Raman, N_2 ISO (PSD)	-	-	-	-	
Ni_3S_2	Ni foam	-	P	~4.0	388.3 (@20 $mA \cdot cm^{-2}_{geo}$)	-	-	148.3		XRD, Raman	-	-	-	-	
NCS-2h ($NiCo_2S_4$ + Co_9S_8)	CFP	Nano-bud	S	1.6	331 (@30 $mA \cdot cm^{-2}_{geo}$)	-	-	-	1 M KOH	XRD, SEM, EDX, TEM, N_2 ISO (BET, PSD)	-	-	-	-	813
NCS-8h ($NiCo_2S_4$ + Co_9S_8)	CFP	Nano-mesh	S	2.0	299 (@30 $mA \cdot cm^{-2}_{geo}$)	-	-	-		XRD, SEM, EDX, TEM, N_2 ISO (BET, PSD)	-	-	-	-	
Co_9S_8/NSCNFs-850	GC	Nanoparticles on carbon fiber nanowire	P	~0.212	302	26.8	0.056 at 320 mV	54	1 M KOH	FESEM, TEM, XRD, Raman, XPS, HAADF-STEM, EM, N_2 ISO (BET, PSD)	-	10 h CA (1.55 V_{RHE}) 1000 CV cycles	-	-	814
Co_9S_8/NSCNFs-750	GC	Nanoparticles on carbon fiber nanowire	P	~0.212	333	9.4	0.017 at 320 mV	104		FESEM, TEM, XRD, Raman, XPS, N_2 ISO (BET, PSD)	-	-	-	-	
Co_9S_8/NSCNFs-950	GC	Aggregated nanoparticles on carbon fiber nanowire	P	~0.212	314	19.5	0.030 at 320 mV	60		FESEM, TEM, XRD, Raman, XPS, N_2 ISO (BET, PSD)	-	-	-	-	
Co_9S_8	GC	-	P	~0.212	~340	-	-	-		-	-	-	-	-	
H-3DRG@$NiCo_2S_4$ (H-3DRG: heteroatom-doped edge-enriched 3D rivet graphene)	Nanoporous Cu	Hierarchical nanostructures consisting of nanosheets	S	-	264	-	-	80.3	1 M KOH	SEM, TEM, STEM, EM, XRD, Raman, GCD curves, XPS	SEM, TEM, EM	20 h CP (10 $mA \cdot cm^{-2}_{geo}$)	-	-	815
$NiCo_2S_4$	GC	Sphere-like aggregated structures consisting of nanosheets	P	~0.283	314	-	-	146.4		SEM, N_2 ISO (BET, PSD)	-	5 h CP (10 $mA \cdot cm^{-2}_{geo}$)	-	-	
Co_9S_8/$Zn_{0.8}Co_{0.2}S$@C	GC	Co_9S_8 nanoparticles and co-doped ZnS nanorods rooted in N-doped carbon polyhedra	P	~0.566	292	88	0.011 at 320 mV	52	0.1 M KOH	XRD, SEM, TEM, EDX, STEM, Raman, XPS, N_2 ISO (PSD)	-	20000 s h CA (1.58 V_{RHE})	-	-	816
ZnS@C	GC	-	P	~0.566	-	-	-	-		XRD, XPS	-	-	-	-	
$Zn_{0.8}Co_{0.2}S$@C	GC	Nanorods	P	~0.566	348	4	0.0033 at 320 mV	136		SEM, XRD, Raman, XPS	-	-	-	-	
Co_9S_8@C	GC	Nanoparticles	P	~0.566	316	67	0.0045 at 320 mV	96		SEM, XRD, Raman, XPS	-	-	-	-	
Co_9S_8@C + $Zn_{0.8}Co_{0.2}S$@C	GC	Nanoparticles, nanorods, carbon polyhedra	P	~0.566	337	-	0.0048 at 320 mV	124		-	-	-	-	-	
Co_9S_8 aerogel	Ni foil	Porous network assembled by nanoparticles	P	2	220	165	-	89	1 M KOH	FTIR, XRD, Raman, XPS, N_2 ISO, SEM, TEM, SAED	-	24 h CP (100 $mA \cdot cm^{-2}_{geo}$)	-	-	817
Co_3S_4@MoS_2	GC	Hollow cubic heterostructure	P	0.283	280	62	-	43	1 M KOH	SEM, XRD, TEM, EDX, XPS	SEM	10 h CA (1.51 V_{RHE}) 2000 CV cycles (100 $mV \cdot s^{-1}$, 1.0−1.6 V_{RHE})	-	-	818
Co_3S_4	GC	Nanoboxes	P	0.283	300	57	-	61		SEM, XPS	-	-	-	-	
MoS_2	GC	Nanosheets	P	0.283	460	12	-	-		SEM, XPS	-	-	-	-	
α-NiFeS/NIF	NiFe alloy foam (Fe 15%)	Particulate	S	-	210	~7	-	59	1 M KOH	SEM, XRD, TEM	-	20 h CP (10 $mA \cdot cm^{-2}_{geo}$)	-	-	819
NiCoS/NF	Ni foam	Urchin-like nanorod array	S	-	360 (@100 $mA \cdot cm^{-2}_{geo}$)	263	-	145	1 M KOH	XRD, XPS, SEM, EDX	-	30000 s CA (1.5 V_{RHE}) 500 CV cycles	-	-	820
Co_9S_8/CS-800	GC	Nanoparticles on/imbedded in carbon spheres	P	0.15	370	-	-	98	0.1 M KOH	XRD, Raman, SEM, TEM, HAADF-STEM, EDX, TGA, N_2 ISO (BET), EPMA, XPS	-	30000 s CA (1.62 V_{RHE})	-	-	821

https://doi.org/10.1021/acs.chemrev.3c00005
Chem. Rev. 2023, 123, 12795−13208

Table 5. continued

Initial Electrocatalyst	Substrate	Shape of Electrocatalyst	Deposition Type	Specific Loading / $mg \cdot cm^{-2}_{geo}$	η@10 $mA \cdot cm^{-2}_{geo}$ / mV	C_{dl} / $mF \cdot cm^{-2}_{geo}$	TOF / s^{-1} (@η or f)	Tafel Slope / $mV \cdot dec^{-1}$	Electrolyte	Pre-analysis	Post-analysis	Long-Term OER Test Conditions	Post-OER Electrocatalyst	Final Type of Electrocatalyst	Ref.
Co_9S_8/CS-700	GC	Nanoparticles on/imbedded in carbon spheres	P	0.15	440	-	-	111		XRD, Raman, SEM, TGA, N_2 ISO (BET), XPS	-	-	-	-	
Co_9S_8/CS-900	GC	Nanoparticles on/imbedded in carbon spheres	P	0.15	380	-	-	136		XRD, Raman, SEM, TGA, N_2 ISO (BET), XPS	-	-	-	-	821
Co_9S_8/CS-1000	GC	Nanoparticles on/imbedded in carbon spheres	P	0.15	400	-	-	104		XRD, Raman, SEM, TGA, N_2 ISO (BET), XPS	-	-	-	-	
FCNMS (MoS_2/TS_2/MoO_3; T = Fe, Co, and Ni)	GC	Nanosheets and nanocubes on nanorods	P	0.20	300	3.43	-	48		XRD, SEM, EDX, TEM, STEM, N_2 ISO (BET, PSD), XANES	-	10 h CA (1.53 V_{RHE}) 3000 CV cycles (50 $mV \cdot s^{-1}$, 1.25−1.7 V_{RHE})	-	-	
CoS_2	GC	-	P	0.20	-	1.40	-	97		-	-	-	-	-	
NiS_2	GC	-	P	0.20	-	0.21	-	106	1 M KOH	-	-	-	-	-	822
50% CoS_2+50% FCNMO	GC	-	P	0.20	~350	-	-	-		-	-	-	-	-	
50% NiS_2+50% FCNMO	GC	-	P	0.20	~350	-	-	-		-	-	-	-	-	
$(CoS_x/N, S\text{-}CNT)_{700}$	GC	-	P	~0.4	390	26.2	-	88.1		XRD, Raman, XPS, N_2 ISO (BET)	-	-	-	-	
	CFP		P	~1	~389	-	-	-	0.1 M KOH		-	19 h CA (1.62 V_{RHE})	-	-	823
CoS_x/N, S-C	GC	Urchin-like architecture	P	~0.4	433	13.7	-	92.4		XRD, SEM, TEM, STEM, EELS, Raman, XPS, N_2 ISO (BET)	-	-	-	-	
N0–NiS_2-500 (pure NiS_2)	CP	-	S	-	~415 (@50 mA/cm^2_{geo})	-	~0.13 at 370 mV ~0.36 at 470 mV	-	1 M KOH	-	-	-	-	-	824
CoMoS/CC	CC	Nanoflake	S	2.23	347	20.5	-	81.3	1 M KOH	XRD, XPS, FESEM, TEM, ICP-OES, N_2 ISO (BET)	-	-	-	-	
CoMoS/CC	CC	Nanoflake	S	2.23	385	-	-	-	1 M PBS (pH = 6.8)	XRD, XPS, FESEM, TEM, ICP-OES, N_2 ISO (BET)	-	24 h CA	-	-	825
CoMoS/CC	CC	Nanoflake	S	2.23	367	-	-	-	0.5 M H_2SO_4	XRD, XPS, FESEM, TEM, ICP-OES, N_2 ISO (BET)	-	24 h CA	-	-	
EG/Co_9S_8	Graphite foil	Nanosheet	S	~1.3	~373 (@25 mA/cm^2_{geo}) ~473 (@50 mA/cm^2_{geo})	-	-	244	1 M KOH	AFM, TEM, XPS, N_2 ISO (BET), XRD	-	-	-	-	826
sNiFeCo/NF	Ni foam	Ripple-like nanosheets	S	-	180 (@100 mA/cm^2_{geo})	11.14	-	50.4	1 M KOH	XRD, SEM, XPS, EDX, TEM, N_2 ISO	-	500 CV cycles (100 $mV \cdot s^{-1}$, 0.1−0.5 V_{SCE})	-	-	827
sNiFeCo-Fe/NF	Ni foam	Porous nanosheets	S	-	230 (@100 mA/cm^2_{geo})	9.18	-	112.8		XRD, SEM, XPS, EDX, TEM, N_2 ISO	-	500 CV cycles (100 $mV \cdot s^{-1}$, 0.1−0.5 V_{SCE})	-	-	
Co_9S_8/N_xS-CNS	GC	Nanosheet	P	0.28	350	-	-	112	1 M KOH	XRD, SEM, TEM, SAED, EDX, TGA, XPS, N_2 ISO (BET, PSD)	-	12000 s CA (1.58 V_{RHE})	-	-	828
Cobalt sulfide	GC	Nanoparticle	P	-	450	-	-	142		XRD, SEM	-	12000 s CA (1.58 V_{RHE})	-	-	
Bulk Co_9S_8/C	GC	Micrometer-sized particle	P	-	450	-	-	114		XRD, SEM, EDX	-	-	-	-	
$CoMoS_3$ nanotubes	GC	Nanotube	P	~0.5	320	-	-	-		XRD, SEM, TEM, EDX, XPS, N_2 ISO (BET, PSD), Raman	EDX	10 h CA (1.55 V_{RHE})	-	-	
$CoMoS_3$ particles	GC	Agglomerated particle	P	-	~400	-	-	-	1 M KOH	SEM	-	-	-	-	829
MoS_2	GC	Agglomerated particle	P	-	~530	-	-	-		SEM	-	-	-	-	
CoS_2	GC	Agglomerated particle	P	-	~480	-	-	-		SEM	-	-	-	-	
A-$CoS_{4.6}O_{0.6}$ PNCs	GC	Porous microcube	P	~0.8	152	89	-	67	1 M KOH	TEM, XRD, XPS, XANES, EXAFS, N_2 ISO	-	10 h CA (1.555 V_{RHE})	-	-	
Bulk CoS_2	GC	-	P	~0.8	171	2.4	-	160		XPS, XANES	-	-	-	-	
A-$CoS_{4.6}O_{0.6}$ PNCs	GC	Porous microcube	P	~0.8	4.59 $mA \cdot cm^{-2}_{geo}$ at 1.8 V_{RHE}	-	-	164	0.1 M PBS (pH = 7.0)	TEM, XRD, XPS, XANES, EXAFS, N_2 ISO	-	-	-	-	830
Bulk CoS_2	GC	-	P	~0.8	1.75 $mA \cdot cm^{-2}_{geo}$ at 1.8 V_{RHE}	-	-	175		XPS, XANES	-	-	-	-	
NiS_2/CoS_2-O NWs	CFP	Nanowire	S	Co: 0.143 Ni: 0.075	235	-	0.088 at 300 mV	31		XRD, SEM, TEM, EM, N_2 ISO (PSD), XPS, ESR, ICP-AES	-	70 h CP (10 $mA \cdot cm^{-2}_{geo}$) 10000 CV cycles (100 $mV \cdot s^{-1}$, 1.0−1.4 V_{RHE})	-	-	
NiS_2/CoS_2 NWs	CFP	Nanowire	S	Co: 0.153 Ni: 0.081	320	-	-	54	1 M KOH	XRD, SEM, TEM, EM, N_2 ISO (PSD), XPS, ESR, ICP-AES	-	-	-	-	831
NiS_2	-	-	-	-	~339	-	-	-		-	-	-	-	-	
CoS_2	-	-	-	-	~350	-	-	-		-	-	-	-	-	
Zn-Co-S NS/CFP	CFP	Nanosheet	S	~0.56	390	9.99	-	136	1 M KOH	XRD, SEM, EDX, TEM, AFM	-	-	-	-	832

https://doi.org/10.1021/acs.chemrev.3c00005
Chem. Rev. 2023, 123, 12795−13208

Table 5. continued

Initial Electrocatalyst	Substrate	Shape of Electrocatalyst	Deposition Type	Specific Loading / $mg \cdot cm^{-2}_{geo}$	η@10 $mA \cdot cm^{-2}_{geo}$ / mV	C_{dl} / $mF \cdot cm^{-2}_{geo}$	TOF / s^{-1} (@η or j)	Tafel Slope / $mV \cdot dec^{-1}$	Electrolyte	Pre-analysis	Post-analysis	Long-Term OER Test Conditions	Post-OER Electrocatalyst	Final Type of Electrocatalyst	Ref.
Zn-Co-S NP/CFP	CFP	Nanoplate	S	~0.60	330	32.23	-	97		XRD, SEM, EDX, TEM, AFM	-	-	-	-	832
Zn-Co-S NN/CFP	CFP	Nanoneedle	S	~0.60	320 350 (@20 mA/cm^{-2}_{geo})	35.47	-	55		XRD, SEM, EDX, TEM, XPS, N_2 ISO (BET, PSD)	SEM	1000 CV cycles sweeps (1.20−1.72 V_{RHE})	-	-	
SW Ni−Ni_3S_2/NF	Ni foam	Spider web-like	S	3.3	310	3.0	-	63	1 M KOH	XRD, SEM, FESEM, TEM, EDX, XPS	-	24 h CA (1.7 V_{RHE})	-	-	833
HC−Ni_3S_2/NF	Ni foam	Honeycomb-like	S	16	310	1.1	-	100		XRD, FESEM, TEM, EDX	-	24 h CA (1.7 V_{RHE})	-	-	
$Ni_{3.5}Co_{5.5}S_8$ NAHNs	GC	Nanosheet-assembled hollow nanocage	P	0.21	333	35	-	48.8	1 M KOH	XRD, SEM, TEM, SAED, EDX, STEM-EDX, XPS, N_2 ISO (BET, PSD)	SEM	2000 LSV sweeps (20 $mV \cdot s^{-1}$, 1.563–1.577 V_{RHE}) 5 h CA (1.6 V_{RHE})	-	-	834
Co_9S_8 HNs	GC	Hollow nanocage	P	0.21	400	21	-	71.9		XRD, SEM	-	5 h CA (1.6 V_{RHE})	-	-	
Bulk Co_9S_8	GC	-	P	0.21	440	-	-	77.3		-	-	-	-	-	
Co_9S_8-140	Glass	Hollow microsphere	P	0.8	420	-	-	113	0.1 M KOH	TEM, SAED, FESEM, EDX, XRD, XPS, N_2 ISO (BET, PSD)	TEM	400 CV cycles (50 $mV \cdot s^{-1}$, 1−1.85 V_{RHE})	-	-	835
Co_9S_8-80	Glass	Core@shell microsphere	P	0.8	460	-	-	142		TEM, FESEM, XRD, N_2 ISO (BET, PSD)	-	-	-	-	
Co_9S_8-60	Glass	Microsphere	P	0.8	490	-	-	168		TEM, FESEM, XRD, N_2 ISO (BET, PSD)	-	-	-	-	
NS/rGO-Co4	GC	Crumpled sheets with nanoparticles	P	0.404	265	-	-	72	1 M KOH	SEM, TEM, EDX, XRD, XPS, N_2 ISO (BET, PSD), Raman, DTA	-	30000 s CA 10 h CA	-	-	836
NS/rGO-Co2	GC	Crumpled sheets with nanoparticles	P	0.404	330	-	-	72		TEM, N_2 ISO (BET, PSD), Raman, DTA	-	-	-	-	
NS/rGO-Co1	GC	Crumpled sheets with nanoparticles	P	0.404	380	-	-	85		TEM, N_2 ISO (BET, PSD), Raman, DTA	-	-	-	-	
Co_9S_8/WS_2	Ti foil	Nanobelt	S	2.2	~223	65.2	-	-	1 M KOH	XRD, EDX, XPS, ICP, FESEM, TEM, N_2 ISO (BET, PSD)	SEM (after OWS)	24 h CA (cell voltage: 1.65 V, OWS)	-	-	837
Co_9S_8/WS_2	Ti foil	Nanoneedle	S	6.2	~278	46.1	-	-		XRD, EDX, ICP, SEM, N_2 ISO (BET, PSD), TEM	-	-	-	-	
Co_9S_8/WS_2	Ti foil	Nanorhombus	S	4.5	~343	33.5	-	-		XRD, EDX, ICP, SEM, N_2 ISO (BET, PSD), TEM	-	-	-	-	
CoS@NF	Ni foam	Nanosheet	S	-	297	388	-	106	1 M KOH	SEM, TEM, HAADF-STEM, EM, XRD, XPS	SEM	40 h CP (10 $mA \cdot cm^{-2}_{geo}$)	-	-	838
$Co_9S_8@Co_3O_4$	Ni foam	Core@shell nanowire	S	-	260 (@20 mA/cm^{-2}_{geo})	38	-	56	1 M KOH	SEM, TEM, EDX, XRD	-	30 h CP (20, 30, 50 $mA \cdot cm^{-2}_{geo}$, 10 h for each j)	-	-	839
NiFeS-0	GC	Pomegranate-like	P	0.25	329	2.12	-	82.3	0.1 M KOH	SEM, TEM, XRD, XPS, EDX	-	-	-	-	840
NiFeS-0.5	GC	Nanoparticle	P	0.25	308	3.30	-	79.7		SEM, TEM, XRD, XPS, EDX	-	-	-	-	
NiFeS-2	GC	Nanoparticle	P	0.25	286	3.99	-	56.3		SEM, TEM, XRD, XPS, EDX	SEM, TEM	20000 s CP (10 $mA \cdot cm^{-2}_{geo}$)	-	-	
NiFeS-8	GC	Nanoparticle	P	0.25	364	0.31	-	54.7		SEM, TEM, XRD, XPS, EDX	-	-	-	-	
Zn-Ni_3S_2/NF	Ni foam	Nanosheet	S	2.3	330 (@100 mA/cm^{-2}_{geo})	6.28	0.47 $mol_{O2} \cdot s^{-1}$ at 400 mV	87	1 M KOH	XRD, ICP-AES, SEM, TEM, EDX, XPS	-	500 CV cycles (100 $mV \cdot s^{-1}$, 0.4−0.8 $V_{Hg/HgO}$) 20 h CA (1.53 V_{RHE}) 6000 s multistep CP (40−260 $mA \cdot cm^{-2}_{geo}$, 20 $mA \cdot cm^{-2}_{geo}$ per 500 s)	-	-	841
Ni_3S_2/NF	Ni foam	Nanosheet	S	-	420 (@100 mA/cm^{-2}_{geo})	2.76	0.04 $mol_{O2} \cdot s^{-1}$ at 400 mV	162		XRD, SEM	-	-	-	-	
Zn-Ni_3S_2/NF	Ni foam	Nanosheet	S	2.3	200 (@100 mA/cm^{-2}_{geo})	-	-	-	30 % KOH	XRD, ICP-AES, SEM, TEM, EDX, XPS	-	-	-	-	
					500 (@50 mA/cm^{-2}_{geo})	-	-	-	1 M KCi (pH = 8.3)		-	-	-	-	
					~740 (@50 mA/cm^{-2}_{geo})	-	-	-	1 M PBS (pH = 7)		-	-	-	-	
$NiCo_2S_4$	GC	Sea urchin-like	P	0.07	337	9.950×10^{-3}	-	64.0	1 M KOH	XRD, XPS, SEM, TEM, N_2 ISO (BET, PSD)	SEM (after 30 h CP)	30 h CP (10 $mA \cdot cm^{-2}_{geo}$) 5 h CA (1.6 V_{RHE}) 2000 CV cycles (100 $mV \cdot s^{-1}$, 1.00−1.65 V_{RHE})	-	-	842
NiS_2	GC	Nanoparticle	P	0.07	413	9.637×10^{-3}	-	94.0		XRD, SEM, TEM, N_2 ISO (BET, PSD)	-	~12.5 h CP (10 $mA \cdot cm^{-2}_{geo}$) 5 h CA (1.6 V_{RHE})	-	-	
CoS_2	GC	Nanoparticle	P	0.07	428	9.090×10^{-3}	-	103		XRD, SEM, TEM, N_2 ISO (BET, PSD)	-	~14 h CP (10 $mA \cdot cm^{-2}_{geo}$) 5 h CA (1.6 V_{RHE})	-	-	
Ni_2CoS_4	GC	Nanorod	P	0.07	386	9.008×10^{-3}	-	91.0		XRD, SEM, TEM, N_2 ISO (BET, PSD)	-	~13.2 h CP (10 $mA \cdot cm^{-2}_{geo}$) 5 h CA (1.6 V_{RHE})	-	-	

https://doi.org/10.1021/acs.chemrev.3c00005
Chem. Rev. 2023, 123, 12795−13208

Table 5. continued

Initial Electrocatalyst	Substrate	Shape of Electrocatalyst	Deposition Type	Specific Loading / $mg \cdot cm^{-2}_{geo}$	η@10 $mA \cdot cm^{-2}_{geo}$ / mV	C_{dl} / $mF \cdot cm^{-2}_{geo}$	TOF / s^{-1} (@η or f)	Tafel Slope / $mV \cdot dec^{-1}$	Electrolyte	Pre-analysis	Post-analysis	Long-Term OER Test Conditions	Post-OER Electrocatalyst	Final Type of Electrocatalyst	Ref.
$Ni_2CoS_4 + CoS_2$	GC	Nanorod and nanoparticle	P	0.07	399	9.264×10^{-3}	-	94.0		SEM, TEM, N_2 ISO (BET, PSD)	-	-	-	-	842
Ni_3S_2/NF	Ni foam	Nanosheet	S	-	-	8.1	-	108	1 M KOH	SEM, XRD	-	-	-	-	843
Ni_3S_2/NF	Ni foam	Nanowire	S	~ 19.3	222 306 (@100 $mA \cdot cm^{-2}_{geo}$)	80.8	-	60	1 M KOH	XRD, SEM, TEM, EDX, XPS	SEM	20 h CA (~ 1.38 V_{RHE})	-	-	844
NiS/NF	Ni foam	-	S	4.0	~ 330 (@25 $mA \cdot cm^{-2}_{geo}$)	-	-	89.6	1 M KOH	XPS, N_2 ISO (BET)	-	-	-	-	845
NiFeS/NF	Ni foam	Graphene-like nanosheet	S	3.7	260 (@50 $mA \cdot cm^{-2}_{geo}$)	-	-	86.7		EDX, XRD, SEM, TEM, XPS, N_2 ISO (BET)	-	-	-	-	
Ni_1Co_4S@C-600	GC	Nanoparticle	P	0.1415	510	-	-	107	0.1 M KOH	TEM, SAED, XPS, XRD, Raman, N_2 ISO (BET), TGA	-	-	-	-	846
Ni_1Co_4S@C-800	GC	Nanoparticle	P	0.1415	420	-	-	98		TEM, SAED, XPS, XRD, Raman, N_2 ISO (BET), TGA	-	-	-	-	
Ni_1Co_4S@C-1000	GC	Nanoparticle	P	0.1415	280	-	-	64		TEM, SAED, STEM, EDX, XPS, XRD, Raman, N_2 ISO (BET), TGA	-	7000 s CA (1.6 and 1.8 V_{RHE}) 1000 CV cycles	-	-	
Ni_1Co_2S@C-600	GC	Nanoparticle	P	0.1415	~ 630 (@5 $mA \cdot cm^{-2}_{geo}$)	-	-	123		XRD, Raman, TEM	-	-	-	-	
Ni_1Co_2S@C-800	GC	Nanoparticle	P	0.1415	430	-	-	112		XRD, Raman, TEM	-	-	-	-	
Ni_1Co_2S@C-1000	GC	Nanoparticle	P	0.1415	430	-	-	101		XRD, Raman, TEM	-	-	-	-	
Ni_1Co_4S@C-1000	GC	Nanoparticle	P	0.1415	~ 660 (@2 $mA \cdot cm^{-2}_{geo}$)	-	-	-	PBS (pH = 7)	TEM, SAED, STEM, EDX, XPS, XRD, Raman, N_2 ISO (BET), TGA	-	-	-	-	
	GC		P	0.1415	~ 180 (@2 $mA \cdot cm^{-2}_{geo}$)	-	-	-	0.5 M H_2SO_4		-	-	-	-	
NN@NF-1 (Ni_3S_2)	Ni foam	Nanoneedle	S	-	370	-	-	170	1 M KOH	XRD, SEM, EDX, TEM, XPS	-	12 h CA (1.68 V_{RHE})	-	-	847
NL@NF-1 (Ni_3S_2)	Ni foam	Leaf-like	S	-	340	-	-	150		XRD, SEM, EDX, TEM, XPS	-	12 h CA (1.68 V_{RHE})	-	-	
Fe_3O_4@Co_9S_8/rGO-1	GC	-	P	~ 0.25	360	-	0.0036 at 350 mV	82.8	1 M KOH	XRD, Raman, N_2 ISO (BET), XPS, ICP-OES	-	-	-	-	848
Fe_3O_4@Co_9S_8/rGO-2	GC	Agglomerated particle	P	~ 0.25	320	-	0.009 at 350 mV	54.5		XRD, Raman, TEM, STEM, N_2 ISO (BET), XPS, ICP-OES	-	1000 CV cycles (50 $mV \cdot s^{-1}$, 0.2–0.7 $V_{Ag/AgCl}$) 6 h CA (0.550 $V_{Ag/AgCl}$)	-	-	
Fe_3O_4@Co_9S_8/rGO-3	GC	-	P	~ 0.25	338	-	0.006 at 350 mV	92.9		XRD, Raman, N_2 ISO (BET), XPS, ICP-OES	-	-	-	-	
CoS_x/rGO-600	GC	Agglomerated particle	P	~ 0.25	~ 375	-	-	95		XRD, SEM, TEM, Raman, XPD	-	-	-	-	
Fe_3O_4@Co_9S_8/rGO-2	GC	Agglomerated particle	P	~ 0.25	340	-	-	65.5	0.1 M KOH	XRD, Raman, TEM, STEM, N_2 ISO (BET), XPS, ICP-OES	-	-	-	-	
Co_9S_8/G	GC	Nanoparticle	P	0.2	441	-	-	93.9	0.1 M KOH	TEM, Raman, XRD, TGA	-	-	-	-	849
Co_9S_8	GC	-	P	0.2	602	-	-	307.2		-	-	-	-	-	
S-1 (Ni_xS_y)	Ni foam	Nanosheet	S	5.0–6.6	-	0.0016 mF	-	158	1 M KOH	XRD, Rietveld, SEM	-	-	-	-	850
S-1.5 (Ni_xS_y)	Ni foam	Nanosheet	S	7.8	-	0.0027 mF	-	174		XRD, Rietveld, SEM	-	-	-	-	
S-2 (Ni_xS_y)	Ni foam	Aggregated flake-like	S	5.6	-	0.0018 mF	-	116		XRD, Rietveld, XPS, SEM	XPS	500 CV cycles (100 $mV \cdot s^{-1}$, 0.2–0.4 V_{SCE}) 10000 s CA (0.26 V_{SCE})	-	-	
S-2.5 (Ni_xS_y)	Ni foam	Aggregated flake-like	S	5.5	-	0.0031 mF	-	178		XRD, Rietveld, SEM	-	-	-	-	
S-3 (Ni_xS_y)	Ni foam	Flower-like	S	10.1–13.6	-	0.0028 mF	-	153		XRD, Rietveld, SEM	-	-	-	-	
Co_9S_8/N-C	GC	Nanoparticle	P	0.8	0.57 $V_{Ag/AgCl}$ (@5 $mA \cdot cm^{-2}_{geo}$)	-	-	75	0.1 M KOH	XRD, TGA, N_2 ISO (BET, PSD), SEM, TEM, XPS	-	55000 s CA	-	-	851
Co_9S_8+N-C	GC	Nanoparticle	P	0.8	~ 0.61 $V_{Ag/AgCl}$ (@5 $mA \cdot cm^{-2}_{geo}$)	-	-	105		-	-	-	-	-	
Co_9S_8+AB	GC	Nanoparticle	P	0.8	0.69 $V_{Ag/AgCl}$ (@5 $mA \cdot cm^{-2}_{geo}$)	-	-	110		-	-	-	-	-	
NGC@Co_4S_2/Ni_xS_6 ($7 \geq x \geq 6$)/NiOOH	GC	Nanoparticle	P	0.28	362	-	-	37	1 M KOH	XRD, Raman, N_2 ISO (BET, PSD), SEM, TEM, EDX, XPS	-	200 LSV sweeps (1.0–2.07 V_{RHE})	-	-	852
NGC@NiS	GC	Nanoparticle	P	0.28	510	-	-	40		XRD, N_2 ISO (BET), SEM, TEM, XPS	-	200 LSV sweeps (1.0–2.07 V_{RHE})	-	-	
GeS	GC	Layered bulk	P	-	~ 1110 (@1 $mA \cdot cm^{-2}_{geo}$)	-	-	-	0.1 M KOH	SEM, EDX, Raman, XRD, XPS, PL	-	-	-	-	853
Co_9S_8@MoS_2/CNF	GC	Core@shell hexagon	P	0.212	430	-	-	61	1 M KOH	TEM, FESEM, EDX, XPS, XRD	FESEM, TEM	1000 CV cycles (100 $mV \cdot s^{-1}$, 0–1.2 V_{RHE})	-	-	854
Co_9S_8/CNF	GC	Nanocrystal	P	0.212	512	-	-	78		FESEM	-	1000 CV cycles (100 $mV \cdot s^{-1}$, 0–1.2 V_{RHE})	-	-	
MoS_2/CNF	GC	Nanoplate	P	0.212	-	-	-	80		FESEM	-	-	-	-	
Ni_3S_2/Ni foam	Ni foam	Nanosheet	S	-	~ 410	-	-	331	0.1 M KOH	XRD, Raman, SEM, TEM	-	-	-	-	855
Ni_3S_2/AT-Ni foam	Ni foam	Nanosheet	S	-	217	-	-	163		XRD, Raman, SEM, TEM	-	1000 CV cycles (50 $mV \cdot s^{-1}$, 1.0–1.9 V_{RHE})	-	-	
$Co_{0.5}Fe_{0.5}S$@N-MC	GC	Nanoparticle	P	0.8	410	-	-	159	1 M KOH	SEM, TEM, EDX, N_2 ISO (BET, PSD),	-	20000 s CP (10 $mA \cdot cm^{-2}_{geo}$)	-	-	856

https://doi.org/10.1021/acs.chemrev.3c00005
Chem. Rev. 2023, 123, 12795−13208

Table 5. continued

Initial Electrocatalyst	Substrate	Shape of Electrocatalyst	Deposition Type	Specific Loading / $mg \cdot cm^{-2}_{geo}$	η@10 $mA \cdot cm^{-2}_{geo}$ / mV	C_{dl} / $mF \cdot cm^{-2}_{geo}$	TOF / s^{-1} ($@\eta$ or j)	Tafel Slope / $mV \cdot dec^{-1}$	Electrolyte	Pre-analysis	Post-analysis	Long-Term OER Test Conditions	Post-OER Electrocatalyst	Final Type of Electrocatalyst	Ref.
										TGA, XRD, Rietveld, XPS					856
CoS_2(400)/N,S-GO	GC	Nanoparticle	P	0.25	37.1 $mA \cdot mg^{-1}$ (@1.62 V_{RHE})	-	-	75	0.1 M KOH	XRD, SEM, UV-Vis, XPS, STEM, FTIR, Raman, CHNS, N_2 ISO (BET, PSD)	-	100 LSV sweeps (0.9–1.8 V_{RHE})	-	-	857
CoS_2(500)/N,S-GO	GC	Nanoparticle	P	0.25	36.9 $mA \cdot mg^{-1}$ (@1.62 V_{RHE})	-	-	80		XRD, SEM, CHNS, N_2 ISO (BET, PSD)	-	-	-	-	
CoS_2(600)/N,S-GO	GC	Nanoparticle	P	0.25	26.2 $mA \cdot mg^{-1}$ (@1.62 V_{RHE})	-	-	96		XRD, SEM, CHNS, N_2 ISO (BET, PSD)	-	-	-	-	
Co_xS_y@C-600	GC	Nanoparticle	P	0.1415	-	-	-	-	0.1 M KOH	SEM, TEM, SAED, XRD, Raman, XPS, N_2 ISO (BET), TGA	-	-	-	-	858
Co_xS_y@C-800	GC	Nanoparticle	P	0.1415	630	-	-	-		SEM, TEM, SAED, XRD, Raman, XPS, N_2 ISO (BET), TGA	-	-	-	-	
Co_xS_y@C-1000	GC	Core@shell	P	0.1415	470	-	-	-		SEM, TEM, SAED, EDX, XRD, Raman, XPS, N_2 ISO (BET), TGA	-	10000 s CA (0.8 $V_{Ag/AgCl}$)	-	-	
Co_3S_4/NCNTs-TAA	GC	Nanoparticle	P	~0.2	430	-	-	70	0.1 M KOH	XRD, XPS, EDX, TEM	-	150 LSV sweeps (0–0.8 V_{SCE})	-	-	859
Co_3S_4/NCNTs-Na_2S	GC	-	P	~0.2	-	-	-	-		XRD	-	-	-	-	
Co_3S_4/NCNTs-Thiourea	GC	-	P	~0.2	-	-	-	-		XRD	-	-	-	-	
Co_3S_4	GC	-	P	~0.2	480	-	-	-		XRD	-	-	-	-	
$NiCo_2S_4$	GC	Urchin-like sub-micron spheres	P	0.70	~22 $mA \cdot cm^{-2}_{geo}$ ($@\eta$ = 400 mV)	-	-	-	0.1 M KOH	XRD, SEM, TEM, SAED, EDX	-	-	-	-	860
$NiCo_2S_4$@N/S-rGO	GC	Nanoparticle	P	~0.283	~467	-	-	-	0.1 M KOH	TEM, SAED, XRD, XPS	-	-	-	-	861
Ni_3S_4@N/S-rGO	GC	-	P	~0.283	~643	-	-	-		XRD, XPS	-	-	-	-	
Co_3S_4@N/S-rGO	GC	-	P	~0.283	~507	-	-	-		XRD, XPS	-	-	-	-	
$NiCo_2S_4$@N/S-rGO	GC	Nanoparticle	P	~0.283	~300 ($@5\ mA \cdot cm^{-2}_{geo}$)	-	-	-	0.1 M PBS (pH = 7.0)	TEM, SAED, XRD, XPS	-	-	-	-	
Ni_3S_4@N/S-rGO	GC	-	P	~0.283	~445 ($@5\ mA \cdot cm^{-2}_{geo}$)	-	-	-		XRD, XPS	-	-	-	-	
Co_3S_4@N/S-rGO	GC	-	P	~0.283	~382 ($@5\ mA \cdot cm^{-2}_{geo}$)	-	-	-		XRD, XPS	-	-	-	-	

[a]Some values (i.e., "specific loading", "η", and "C_{dl}") were calculated or obtained from the descriptions and figures in the previous papers. "Post-OER Electrocatalyst" and "Final Type of Electrocatalyst" were determined based on the experimental results and descriptions provided in the previous papers. [b]η, overpotential; j, current density; C_{dl}, double layer capacitance; TOF, turnover frequency; P, powder-coated electrode; S, self-supported electrode; CV, cyclic voltammetry; CA, chronoamperometry; CP, chronopotentiometry; OWS, overall water splitting. [c]Substrate abbreviations: GC (glassy carbon); CC (carbon cloth); CP (carbon paper); CFP (carbon fiber paper); SS (stainless steel); FTO (fluorine-doped tin oxide); ITO (indium tin oxide); CNF (carbon nanofiber). [d]Electrolyte abbreviations: PBS (phosphate buffer solution); KCi (potassium carbonate). [e]Analysis abbreviations (minor terms only): ISO (isotherm); PSD (pore size distribution); CAM (contact angle measurement); PL (photoluminescence); AAS (atomic absorption spectrophotometer); CHNS (C, H, N, S analyzer); IR (infrared spectroscopy); HIM (helium ion microscope); DLS (dynamic light scattering measurement); EM (elemental mapping); MM (magnetometer measurement); ESR (electron spin resonance); BAF (bubble adhesive force measurement); BRB (bubble releasing behavior); EA (elemental analysis); UPS (ultraviolet photoelectron spectroscopy).

https://doi.org/10.1021/acs.chemrev.3c00005
Chem. Rev. 2023, 123, 12795−13208

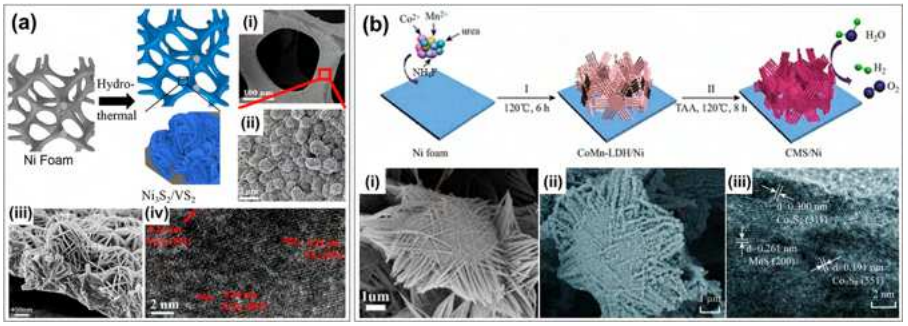


Figure 124. Sulfide nanosheets prepared via (a) one-step and (b) two-step hydrothermal synthesis. (a) Schematic illustration for the synthesis of Ni_3S_2/VS_2 nanosheets on Ni foam. (a, i and ii) Top and (a, iii) side view SEM and (a, iv) HRTEM images of the Ni_3S_2/VS_2. Reprinted with permission from ref 697. Copyright 2018 Elsevier. (b) Schematic illustration for the preparation of bimetallic cobalt-manganese sulfide (CMS) composite supported on Ni foam. (b, i) SEM image of the CoMn-LDH on Ni foam. (b, ii) SEM and (b, iii) HRTEM images of the CMN on Ni foam. Reprinted with permission from ref 799. Copyright 2017 Springer Nature.

636, 637, 641, 673, 683, 687, 688, 690, 702, 766, 770, 772, 773, and 791). And while there are many sulfur sources, it is important to notice that the sulfur source has a high impact on the final product (sulfide). For instance, Shinde *et al.* have studied the effect of sulfur sources and found that different sulfur sources led to different morphologies: the Ni_xS_y samples synthesized using sodium thiosulfate, thioacetamide, thiourea, and sodium sulfide showed volcano-type nanorods, volcano-type nanoflakes, budlike structures, and nanopetals, respectively.[690] This report indicates that the morphology of metal sulfides can be tuned simply by using different sulfur sources.[690]

While the starting materials, precursors, and sulfur sources are crucial for sulfide synthetic processes, the final types of electrodes produced have a significant effect on OER activity. As mentioned above, there are mainly two types of electrodes: self-supported electrodes and powder-coated electrodes. In general, the powder-coated electrodes require extra materials such as polymer binder (e.g., Nafion) and coating procedures (e.g., drop-coating), which enable simple and rapid electrochemical testing. However, the powder-coated electrodes possess a potential problem regarding short-term electrochemical stability due to their relatively weak mechanical adhesion between the electrocatalytic film and conductive substrate, resulting in its peeling off.[547] Additionally, polymeric binders could block active catalyst sites, leading to lower electrocatalytic activity.[547] In contrast, self-supported electrodes tend to show better long-term electrocatalytic OER activity and electrochemical stability compared to the powder-based ones, which is likely due to improved electrical connectivity and high mechanical adhesion.[547] Importantly, we can fabricate both self-supported[688,690,697,702,781] and powder-coated electrodes[636,675,699,715,723] through the hydrothermal method. Thus, depending on one's purpose, one can select either electrode type and use the hydrothermal method.

According to previous reports, using the hydrothermal method, one can synthesize sulfide-based electrocatalysts with various nanostructured morphologies such as nanosheet (refs 640, 674, 675, 699, 700, 764, 772, and 781), nanoflower,[543,547,697,699] nanoparticle,[636,773] nanosphere,[720,723,729,793] nanowire,[637,707,766] nanorod,[688,690,702] nanotube,[671,766,791] core@shell,[770] and 3D structures (3D carbon matrix[715] and 3D hierarchical nanosheets[636]). Combinations of different morphologies (e.g., nanosheets + nanoparticles[675,787] and nanorods/nanowires + nanosheets[675,688,702,707]) have also been reported. In the following paragraphs, we introduce and discuss the typical and unique examples of the hydrothermal method-involved synthetic approaches resulting in nanostructured sulfide-based electrocatalysts.

Nanosheets are one of the most well-studied morphologies because of their inherent advantages for electrocatalysis, such as large surface area, high exposure of surface atoms, and reduced diffusion lengths for mass/charge transfer.[686] When we consider various transition metal sulfides, Ni_3S_2 nanostructures have been regarded as promising electrocatalysts for both the HER and OER under alkaline conditions due to their high electrical conductivity and unique 3D architectures. However, low active surface area, low stability, and sluggish reaction kinetics have limited their practical use.[863] These limitations can be overcome when Ni_3S_2 is prepared with nanosheet morphology, as it enables high surface area and reduced charge diffusion lengths. For example, Zhong *et al.* have used a simple one-step hydrothermal method to synthesize the heterostructure of nickel and vanadium sulfides (Ni_3S_2 and VS_2) with a nanosheet morphology to achieve high surface area and benefit from synergetic effects via exposing heterointerfacial sites.[697] First, vanadium complex ($Na_3VO_4{\cdot}12H_2O$), block copolymer (Pluronic F127), and thiourea (sulfur source) were dissolved in deionized water. Then, Ni foam and the as-prepared solution were put together into a Teflon-lined stainless-steel autoclave for hydrothermal synthesis (160 °C, 24 h), resulting in the Ni_3S_2/VS_2 heterostructure as the final product. The schematics for the synthesis process are shown in Figure 124a. The synthesis of 3D structured nanosheets can be confirmed from the SEM images in Figures 124a, i–iii. These images show that the nanosheets were vertically grown on the Ni foam surface and interconnected spatially, which led to many void spaces and, as a result, high surface area. The HRTEM image (Figure 124a, iv) and XRD pattern of the as-prepared sample confirmed that VS_2 was embedded in Ni_3S_2, indicating the successful formation of the sulfide heterostructure. Notably, the as-synthesized Ni_3S_2 and VS_2 heterointerfacial nanosheets exhibited a much higher BET specific area of 18.29 $m^2{\cdot}g^{-1}$ compared to bulk Ni_3S_2 nanoparticles grown on Ni foam (4.8 $m^2{\cdot}g^{-1}$). From XPS analysis, it was confirmed that the electronic interaction between nickel and vanadium led to a shift of the Ni $2p_{3/2}$ peak toward higher binding energy, further suggesting the V-

https://doi.org/10.1021/acs.chemrev.3c00005
Chem. Rev. 2023, 123, 12795−13208

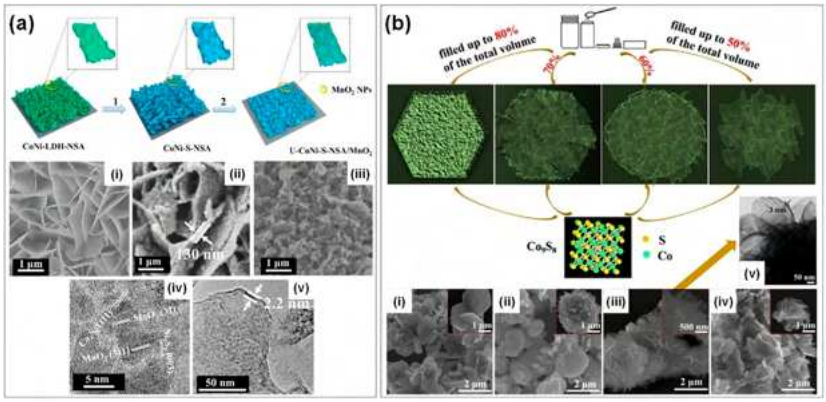


Figure 125. (a) Schematic illustration for *in situ* synthesis of MnO_2 nanoparticle-anchored ultrathin CoNi-sulfide nanosheet arrays on Ni foam via the hydrothermal process and post-vulcanization treatment. (a, i–iii) SEM images of (i) CoNi-LDH-NSA, (ii) CoNi-S-NSA, and (iii) U-CoNi-S-NSA/MnO_2. (a, iv–v) TEM images of U-CoNi-S-NSA with scale bar (iv) 5 nm and (v) 50 nm. Reprinted with permission from ref 787. Copyright 2018 Elsevier. (b) Schematic illustration for the controllable synthesis of Co_9S_8 nanosheets. (b, i–iv) SEM images of the Co_9S_8 nanosheet samples prepared at (i) 80, (ii) 70, (iii) 60, and (iv) 50% fill factor. (b, v) TEM image of the Co_9S_8 nanosheet sample prepared at 60% fill factor. Reprinted with permission from ref 699. Copyright 2018 Elsevier.

incorporation into Ni_3S_2 and the presence of Ni_3S_2/VS_2 coupling interfaces.

For a two-step hydrothermal process, the majority of reports used metal complexes to prepare metal sulfides with nanosheet morphology. Interestingly, using two different metal complexes instead of one metal complex led to an entirely different morphology. For example, Li *et al.* have used manganese and cobalt complexes to synthesize a CoMnS (CMS) composite with a nanosheet morphology consisting of nanorods on Ni foam.[799] As shown in Figure 124b, the authors used the two-step hydrothermal approach to synthesize the CMS composite sample. In the first step, $MnCl_2{\cdot}4H_2O$, $Co(NO_3)_2{\cdot}6H_2O$, urea, and NH_4F were dissolved in distilled water, and the as-prepared aqueous solution was poured into a Teflon-lined stainless-steel autoclave with a clean piece of Ni foam (120 °C, 6 h). This step led to the formation of a 3D hexagram-like CoMn-LDH precursor on Ni foam (CoMn-LDH/Ni) through the release of CO_3^{2-} and OH^- ions due to the hydrolysis of urea and their co-precipitation with Co^{2+} and Mn^{2+} ions (see Figure 124b, i). Subsequently, for the second step, the sulfurization of the CoMn-LDH/Ni was carried out with thioacetamide through a hydrothermal process (120 °C, 6 h). Figure 124b, ii shows that 3D hexagram-like sulfide nanosheets made up of solid nanorods were generated on Ni foam. The distinct lattice fringes of Co_9S_8 and MnS in the TEM image (Figure 124b, iii) confirm the formation of the sulfide composite material on Ni foam (CMS/Ni). From a comparison of SEM images of the precursor (Figure 124b, i) and the sulfide composite product (Figure 124b, ii), we can see that the hydrothermal sulfurization can increase surface roughness, resulting in high surface area. The authors also prepared Co_9S_8/Ni and MnS/Ni samples, possessing nanosheet shapes, as comparisons. Here, the CMS/Ni sample possessed a higher electrochemically active surface area (ECSA) estimated from its double-layer capacitance (C_{dl}) of 56.3 $mF{\cdot}cm^{-2}$ than those of Co_9S_8/Ni (24.0 $mF{\cdot}cm^{-2}$) and MnS/Ni (13.0 $mF{\cdot}cm^{-2}$). This result implies that the use of different metal complexes can enhance the number of electrocatalytically active sites.

For further exposing electrocatalytically active sites for efficient OER electrocatalysis, one strategy is the synthesis of electrocatalytic materials with ultrathin nanosheet morphologies of only a few nanometers in thickness to achieve super high specific surface areas (i.e., large number of active sites per unit projected area).[699,787] Hu *et al.* have demonstrated this by first preparing CoNi-sulfide (Co_4S_3 + Ni_3S_2) nanosheet arrays (CoNi-S-NSA) on Ni foam via a two-step hydrothermal process.[787] Then, they reduced the sulfide nanosheet thickness from 130 to 2.2 nm while simultaneously decorating the surface with numerous MoO_2 nanoparticles via MnO_4^- anion-derived oxidative etching. The final product formed was MnO_2 nanoparticles anchored on ultrathin CoNi-sulfide nanosheet arrays (U-CoNi-S-NSA/MnO_2) on Ni foam. The schematic illustration of the entire synthetic process is shown in Figure 125a. In the first step, $Co(NO_3)_2{\cdot}6H_2O$, $Ni(NO_3)_2{\cdot}6H_2O$, NH_4F, and hexamethylenetetramine were dissolved in water. This mixture was placed in an autoclave with a clean piece of Ni foam. The hydrothermal process was then carried out at 110 °C for 12 h to produce a CoNi-LDH precursor (nanosheet arrays, see Figure 125a, i). In the second step, the precursor was sulfurized through another hydrothermal process (140 °C, 6 h) with thioacetamide as a sulfur source, forming CoNi-S-NSA on the Ni foam (Figure 125a, ii). Finally, oxidative etching using $KMnO_4$ was performed to complete the synthesis of the ultrathin U-CoNi-S-NSA nanosheets. The SEM and TEM images of the U-CoNi-S-NSA sample (Figures 125a, iii–v) confirm the successful formation of the ultrathin nanosheets. Notably, as shown in Figures 125a, ii and iv, the oxidative etching process led to the decrease in nanosheet thickness from ~130 to ~2.2 nm. Figure 125a, v further reveals the presence of MnO_2 nanoparticles (~3.2 nm in diameter) on the sulfide nanosheet surface. Furthermore, U-CoNi-S-NSA recorded a higher C_{dl} value of 21.7 $mF{\cdot}cm^{-2}$ compared with that of CoNi-S-NSA (5.4 $mF{\cdot}cm^{-2}$), indicating that the thickness reduction in the nanosheet structure is effective at enlarging the ECSA of the electrocatalytic material. In another instance, Yang *et al.* used a simple one-step hydrothermal method to synthesize Co_9S_8 powder samples with different morphologies (i.e., nanoplates, nanoflowers, ultrathin nanosheets, and thick nanosheets), which was achieved by adjusting the filled volume fraction of the autoclave (i.e., filling factor).[699] Figure 125b shows a schematic illustration of the synthesis process. The aqueous solution mixtures containing the starting materials [$CoSO_4{\cdot}7H_2O$ (metal source), sulfur

https://doi.org/10.1021/acs.chemrev.3c00005
Chem. Rev. 2023, 123, 12795–13208

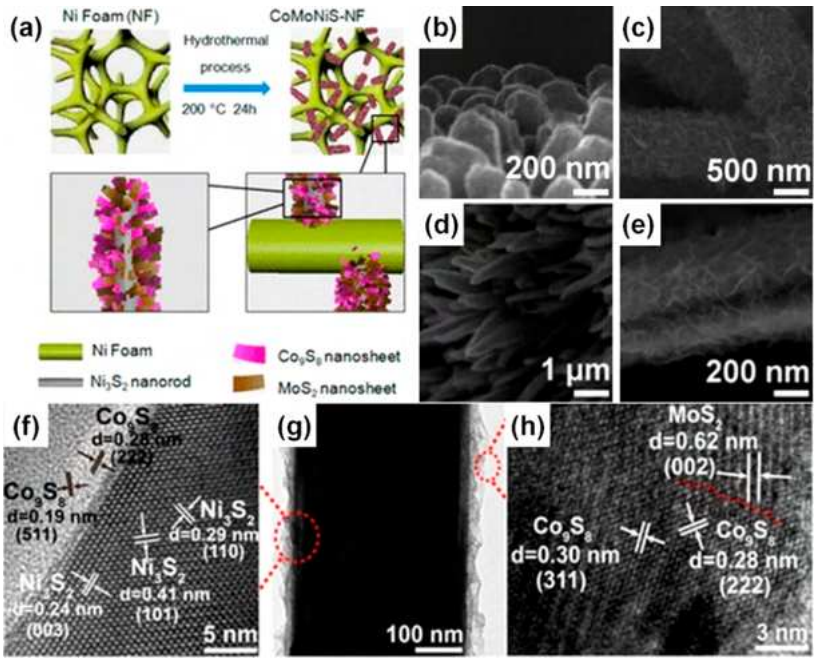


Figure 126. (a) Schematic illustration for the synthesis of hierarchical CoMoNiS-NF composite through the one-step hydrothermal process. (b–e) SEM images of the Co_9S_8/Ni_3S_2/NF (b), MoS_2/Ni_3S_2/NF (c), and CoMoNiS-NF-31 samples (d, e). (f–h) HRTEM images of the CoMoNiS-NF-31 sample. Reprinted with permission from ref 688. Copyright 2019 American Chemical Society.

source Na_2SO_3 (sulfur source), and $N_2H_4{\cdot}H_2O$ (mineralizer)[864]] were placed in autoclaves filled up to 50, 60, 70, and 80%. The hydrothermal process was carried out at 180 °C for 72 h. Since the applied temperature of 180 °C is higher than the boiling points of water (100 °C) and $N_2H_4{\cdot}H_2O$ (118.5 °C), high vapor pressure was achieved inside the autoclave. By decreasing the filling factor for the synthesis of Co_9S_8, the speed of mass transfer slowed down owing to the vapor pressure drop, at which point the growth of Co_9S_8 grains was facilitated. Additionally, because of this pressure decrease in the autoclave's atmosphere, extra space was present and allowed for the transformation from compact hexagonal structures to open and porous nanostructures (i.e., ultrathin nanosheets). Hence, in this work, the filling factor is the key parameter that controls the resultant shapes of the sulfide samples. Figures 125b, i–iv show that the resultant sulfide products had various morphologies that resulted from different filling factors (50%: 3D network microstructures; 60%: nanosheets; 70%: nanoflowers; 80%: nanoplates). In particular, at the filling factor of 60%, the sample exhibited an ultrathin nanosheet shape with ∼3 nm thickness (Figure 125b, v). According to the XRD results, all the as-prepared samples were identified as cubic Co_9S_8. The BET specific surface area analysis verified that the sample prepared at 60% filling factor had the highest specific surface area (84.3 $m^2{\cdot}g^{-1}$) among the as-prepared samples (50%: 39.4 $m^2{\cdot}g^{-1}$; 70%: 36.5 $m^2{\cdot}g^{-1}$; 80%: 24.4 $m^2{\cdot}g^{-1}$) and showed a pore diameter of 4.41 nm, implying the existence of hierarchical mesoporous structures. These results also indicate that the formation of ultrathin nanosheet-shaped electrocatalyst can provide more catalytically active sites. Additionally, this filling factor strategy for product morphological control is possibly applicable for other types of transition metal sulfides, which warrants further investigate in the future.

In addition to the above-introduced various nanosheet-based shapes, the combination of nanosheets with different nanostructures (e.g., nanorods, nanotubes, etc.) can also lead to the development of improved transition metal sulfide electrocatalysts for the OER.[688,707] For example, to utilize the unique properties of both nanorods and nanosheets, Yang *et al.* used a one-step hydrothermal process to synthesize an electrocatalytic hierarchical nanoassembly, consisting of Ni_3S_2 nanorods decorated by ultrathin MoS_2 and Co_9S_8 nanosheets, on Ni foam.[688] For the hydrothermal process, they placed a mixture of $CoSO_4{\cdot}7H_2O$, $Na_2MoO_4{\cdot}2H_2O$, thiourea (CH_4N_2S), hydrazine hydrate, and deionized water into a Teflon-lined autoclave containing a clean piece of Ni foam. The hydrothermal reaction was performed at 200 °C for 24 h. The schematic for this synthetic process is shown in Figure 126a. By preparing the samples with different Co:Mo ratios (i.e., 1:0, 5:1, 4:1, 3:1, 2:1, 1:1, 1:2, 1:3, and 0:1), the effect of the Co:Mo ratio was also investigated. When only a Co source was introduced (see Figure 126b), Ni_3S_2 nanorods (diameter: 300–600 nm) with a uniform coating of Co_9S_8 nanosheets (Co_9S_8/Ni_3S_2/NF) were obtained, while only Mo introduction (see Figure 126c) led to slightly thicker Ni_3S_2 nanorods (diameter: 0.6–1 μm) covered with more MoS_2 nanosheets (MoS_2/Ni_3S_2/NF). When both Co and Mo were introduced, the increase of Co content led to an increased number of nanosheets and, ultimately, their aggregation. On the other hand, by decreasing the Mo content, nanorods gradually transformed into nanobelts. These observations clearly indicate that the Co:Mo ratio adjustment can control the number of nanosheets and the size of nanorods. Here, the Co:Mo ratio of 3:1, $Co_9S_8/MoS_2/Ni_3S_2$/NF (CoMoNiS-NF-31), was determined to be the best condition for obtaining the optimal nanorod shape while minimizing nanosheets. As shown in Figures 126d and e, the SEM images of CoMoNiS-NF-31 confirm the formation of the nanorod and nanosheet combination. The HRTEM images of CoMoNiS-NF-31 (Figures 126f–h) revealed that the as-formed nanorods and nanosheets are Ni_3S_2 and Co_9S_8 + MoS_2, respectively.

https://doi.org/10.1021/acs.chemrev.3c00005
Chem. Rev. 2023, 123, 12795–13208

Furthermore, the CoMoNiS-NF-31 sample exhibited the largest C_{dl} value of 60.9 mF·cm^{-2} among all the prepared samples (Co_9S_8/Ni_3S_2/NF: 15.0 mF·cm^{-2}; CoMoNiS-NF-51: 23.8 mF·cm^{-2}; CoMoNiS-NF-41: 30.9 mF·cm^{-2}; CoMoNiS-NF-21: 57.2 mF·cm^{-2}; CoMoNiS-NF-11: 29.2 mF·cm^{-2}; CoMoNiS-NF-12: 26.6 mF·cm^{-2}; CoMoNiS-NF-13: 14.9 mF·cm^{-2}; MoS_2/Ni_3S_2/NF: 10.0 mF·cm^{-2}). Thus, by combining nanorods and nanosheets the ECSA can be increased, leading to improved electrocatalytic performance.

For another example regarding a nanostructure combination, Lin *et al.* have used a two-step hydrothermal approach to grow a core@branch structure (the combination of nanotubes and nanosheets) of Ni_3S_2/Co_9S_8 on Ni foam (NCS/NF) (see Figure 127a).[707] In the first step, the NiCo-nanowire precursor

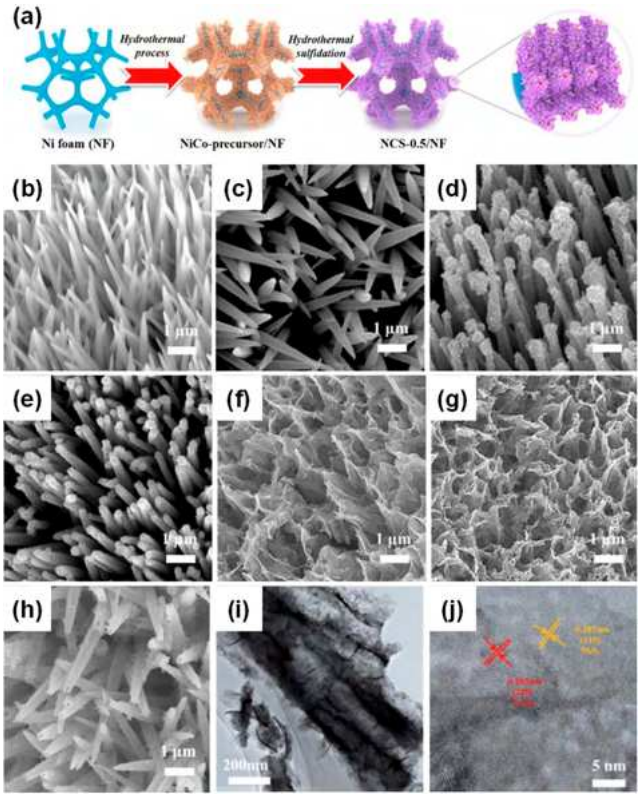


Figure 127. (a) Schematic illustration for the fabrication of a core@branch Ni_3S_2/Co_9S_8 (NCS) nanostructure on Ni foam prepared via a two-step hydrothermal process. (b–h) SEM images of (b) NiCo-precursor/NF, (c) NCS-0.05/NF, (d) NCS-0.1/NF, (e) NCS-0.2/NF, (f) NCS-0.5/NF, (g) NCS-0.8/NF, and (h) NCS-0.5/CC. (i) TEM and (j) HRTEM images of the NCS/NF. Reprinted with permission from ref 707. Copyright 2018 Elsevier.

(Figure 127b) was prepared using nickel and cobalt complexes ($NiCl_2·6H_2O$ and $CoCl_2·6H_2O$) and urea via a hydrothermal process (120 °C, 8 h). In the second step, the sulfurization of the as-prepared precursor was performed using disodium sulfide nonahydrate ($Na_2S·9H_2O$) as the sulfur source via a hydrothermal ion exchange process (120 °C, 6 h). For the hydrothermal sulfidation step, the sulfur source concentration was altered (0.05, 0.1, 0.2, 0.5, and 0.8 M) to investigate its effect on the resultant product morphology (Figures 127c–g). All the products, that were prepared with different sulfur source concentrations [NCS-*x*/NF: *x* represents the used concentration value (M)], could be identified as Ni_3S_2 and Co_9S_8 phases by XRD. At the concentration of 0.05 M, the sample had a nanowire shape with a rough surface (Figure 127c). When increasing the concentration from 0.1 to 0.5 M, different-sized nanosheets were generated on the nanowire surfaces, resulting in core@branch structures (Figures 127d–f). When the concentration of the sulfur source reached 0.8 M, thick and porous nanosheets were formed over the Ni foam surface (Figure 127g). Thus, the concentration of the sulfur source during hydrothermal sulfidation affects the resulting morphology. The authors also provide a possible formation mechanism for the Ni_3S_2/Co_9S_8 core@branch structure. During the sulfurization process, the Na_2S species release S^{2-} ions, which react with the NiCo precursor to generate thin Ni_3S_2/Co_9S_8 layers. As the sulfurization process proceeds, hollow Ni_3S_2/Co_9S_8 nanotubes are formed due to the Kirkendall effect.[865] Simultaneously, Ni foam also reacts with S^{2-} ions to grow extra Ni_3S_2 species. As a result, at high concentration(s) of the sulfur source, rich Ni_3S_2 nuclei can be generated. Furthermore, simultaneously formed hollow Ni_3S_2/Co_9S_8 nanotubes also promote the growth of Ni_3S_2 nanosheets. These Ni_3S_2 nanosheets likely aggregate over the Ni_3S_2/Co_9S_8 nanotubes to decrease the surface free energy, resulting in an intertwined nanosheet network around the nanotube arrays. Hence, the "branched" growth may be a result of the "oriented attachment" and "self-assembly" processes.[866,867] To gauge the role of Ni foam in the synthesis of the final product, the authors prepared the Ni_3S_2/Co_9S_8 sample on carbon cloth (CC) using the same hydrothermal process with a sulfur source concentration of 0.5 M. As shown in Figures 127f and h, more nanosheets were observed for NCS-0.5/NF than NCS-0.5/CC (nanowires + tiny nanosheets), indicating that the presence of Ni foam is essential for the formation of excess Ni_3S_2 nanosheets. Importantly, the authors found that NCS-0.5/NF had the best OER performance among all the as-synthesized samples and exhibited a C_{dl} value of 155.0 mF·cm^{-2}), which was even larger than that of NCS-0.5/CC (107.2 mF·cm^{-2}). Moreover, the TEM and HRTEM images (Figures 127i and j) of the best-performing NCS-0.5/NF also show that the as-formed surface structure mainly consisted of nanotubes (core) and thin nanosheets (branch). According to the TEM, XRD, and XPS results, the bulk and surface structures of the as-formed core@branch structure seemed to be the mixture of the two different sulfide phases (Ni_3S_2 and Co_9S_8). This work successfully presented an example of the direct growth of bimetallic sulfide nanosheet/nanotube arrays on a conductive substrate, providing large ECSA, open channels, and intimate contact with the substrate, which are beneficial for OER electrolysis.

So far, we have discussed only the examples of one- and two-step hydrothermal approaches for preparing nanostructured sulfide electrocatalysts. Here, we specifically discuss the preparation of three unique nanostructured composites: (i) sulfide-oxide-,[543] (ii) sulfide-hydroxide-,[640] and (iii) sulfide-carbon-based materials[715] synthesized via incorporation of the hydrothermal method in the synthetic process. Du *et al.* synthesized a nano-mesh $MnCo_2O_4$@Ni_3S_2 network structure through a three-step hydrothermal synthesis method.[543] In the first step, $MnCl_2$, $CoCl_2.6H_2O$, urea, and NH_4F were dissolved in water. The as-prepared solution was placed in a Teflon-lined stainless-steel autoclave with a clean piece of Ni foam. Then, the hydrothermal reaction was conducted at 140 °C for 8 h, forming $MnCo_2(OH)_6$ on the Ni foam. The $MnCo_2(OH)_6$ was further calcinated at 350 °C for 3 h to obtain $MnCo_2O_4$ on Ni foam. In the second step, the as-prepared $MnCo_2O_4$ on Ni

https://doi.org/10.1021/acs.chemrev.3c00005
Chem. Rev. 2023, 123, 12795–13208

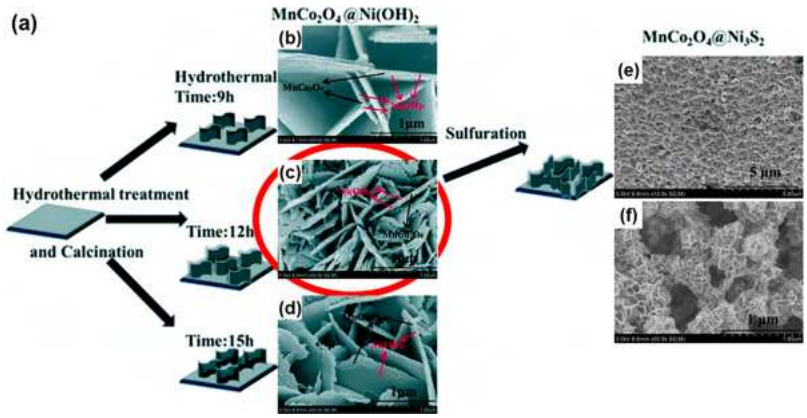


Figure 128. (a) Schematic illustration for the fabrication process of nano-mesh $MnCo_2O_4$@Ni_3S_2 networks on Ni foam through a three-step hydrothermal process. (b–d) SEM images of $MnCo_2O_4$@$Ni(OH)_2$ precursors prepared via (b) 9, (c) 12, and (d) 15 h hydrothermal processes. (e, f) SEM images of $MnCo_2O_4$@Ni_3S_2 on Ni foam. Reproduced with permission from ref 543. Copyright 2019 Royal Society of Chemistry.

foam and an aqueous mixture of $NiCl_2.6H_2O$, urea, and NH_4F were poured into the autoclave and kept at 150 °C for different holding times (9, 12, and 15 h), producing nanoflower-like $MnCo_2O_4$@$Ni(OH)_2$ precursors on Ni foam ($MnCo_2O_4$@$Ni(OH)_2$-9h, -12h, and -15h). In the last step, the sulfurization of the as-prepared $MnCo_2O_4$@$Ni(OH)_2$ precursor was performed with Na_2S as the sulfur source in a polytetrafluoroethylene-lined autoclave at 160 °C for 6 h, resulting in $MnCo_2O_4$@Ni_3S_2 on Ni foam. Figure 128a shows a schematic illustration of the entire synthetic process. From XRD patterns, all the precursors prepared at different holding times in the second step showed similar diffraction peak positions attributed to $MnCo_2O_4$ and $Ni(OH)_2$ phases. However, the holding time in the second step affected the resultant precursor morphology (see Figures 128b–d). The SEM image of the $MnCo_2O_4$@$Ni(OH)_2$-9h (Figure 128b) shows a hollow network structure was formed consisting of sheet-like structures cross-linked with each other, in which thin $Ni(OH)_2$ films partially covered $MnCo_2O_4$. The $MnCo_2O_4$@$Ni(OH)_2$-12h possessed thicker film-like $Ni(OH)_2$ wherein $MnCo_2O_4$ were still exposed at the surface (Figure 128c). However, in $MnCo_2O_4$@$Ni(OH)_2$-15h, the loose porous structure, which was observed in the 12 h sample, gradually disappeared owing to increased growth of $Ni(OH)_2$ species leading to build-up at the surface (Figure 128d). The increased thickness of the film-like $Ni(OH)_2$ also contributed to the coverage of $MnCo_2O_4$ surfaces. To determine the best $MnCo_2O_4$@$Ni(OH)_2$ precursor for electrocatalyst synthesis, the authors performed electrochemical tests for the HER and OER in 1.0 M KOH. For both the HER and OER, $MnCo_2O_4$@$Ni(OH)_2$-12h showed the best electrocatalytic activity because the increased thickness of the $Ni(OH)_2$ thin film and the vertical and horizontal extensions of $MnCo_2O_4$ led to more surface-active sites and synergistic effects. To further enhance the electrocatalytic performance of the $MnCo_2O_4$@$Ni(OH)_2$-12h, the authors hydrothermally sulfurized it. The sulfurized $MnCo_2O_4$@$Ni(OH)_2$-12h product contained both Ni_3S_2 and $MnCo_2O_4$ phases. Figures 128e and f show the SEM images of the $MnCo_2O_4$@Ni_3S_2 sample, indicating the formation of a nano-mesh network structure. Notably, the sulfidation increased the crystal grain diameters, narrowing the distance between the nanosheets. The authors assumed that these morphological changes could shorten the electron transfer path, accelerating electrolysis. Furthermore, $MnCo_2O_4$@Ni_3S_2 also showed a larger C_{dl} value of 34.45 mF·cm^{-2} compared to that of the $MnCo_2O_4$@$Ni(OH)_2$-12h precursor (16.79 mF·cm^{-2}), implying that the sulfidation led to enlarged surface area. This work shows the importance of precursor optimization in the multistep hydrothermal synthesis of a sulfide-oxide composite for use as an electrocatalyst for the OER.

In another instance, Zou *et al.* prepared amorphous Ni-Fe hydroxide film-coated Ni_3S_2 nanosheet arrays, sulfide-hydroxide composite nanostructures, on Ni foam (Ni-Fe-OH@Ni_3S_2/NF) via a hydrothermal process and subsequent ultrafast solution-based immersion treatment (see Figure 129a).[640] First, the authors synthesized a Ni_3S_2 nanoarray precursor by direct hydrothermal sulfurization of Ni foam (NF) using thiourea (CH_4N_2S) as the sulfur source. This hydrothermal process was performed at 150 °C for 5 h. Then the as-prepared Ni_3S_2/NF precursor was immersed in a pre-heated aqueous solution containing Fe^{3+} ions at 100 °C for 5 s, forming the Ni-Fe-OH@Ni_3S_2/NF. The SEM images in Figures 129b and c show the formation of many soft ultrathin Ni-Fe-OH nanoflakes on Ni_3S_2/NF nanosheets (thickness: 20–30 nm) after the immersion treatment. From the STEM images, the average thickness of the Ni-Fe-OH nanoflakes was 2.5–3 nm. At the same time, elemental mapping showed that iron was only present on the nanosheet surface and sulfur was present in the inner regions of the nanosheet, indicating that the Ni-Fe-OH thin films covered the Ni_3S_2 nanosheets and confirming the formation of Ni-Fe-OH@Ni_3S_2/NF core@shell nanostructures. Note that, in the resultant composite, the Ni_3S_2/NF can function as a 3D conductive nanostructure due to the high electrical conductivity of Ni_3S_2 originating from its Ni–Ni metal bonds, which can support less conductive electrocatalytically active sites (i.e., Ni-Fe-OH). To check the versatility of their synthetic approach, the authors also prepared the composite samples by using the pre-heated solution containing different transition metal ions (i.e., Ni^{2+}, Co^{2+}, Mn^{2+}, Cr^{3+}). Replacing Fe^{3+} ions with other cations like Ni^{2+}, Co^{2+}, Mn^{2+}, or Cr^{3+} ions resulted in different composites [i.e., Ni-*M*-OH@Ni_3S_2/NF (*M* = Ni, Co, Mn, Cr)] (see Figures 129d–g). This work showed the potential for a hydrothermal method-involved synthetic approach to the fabrication of 3D hierarchical sulfide@hydroxide core@shell nanoarchitectures. The authors demonstrated that rational design of the structure of electrocatalytic materials can result in surface structures and

https://doi.org/10.1021/acs.chemrev.3c00005
Chem. Rev. 2023, 123, 12795–13208

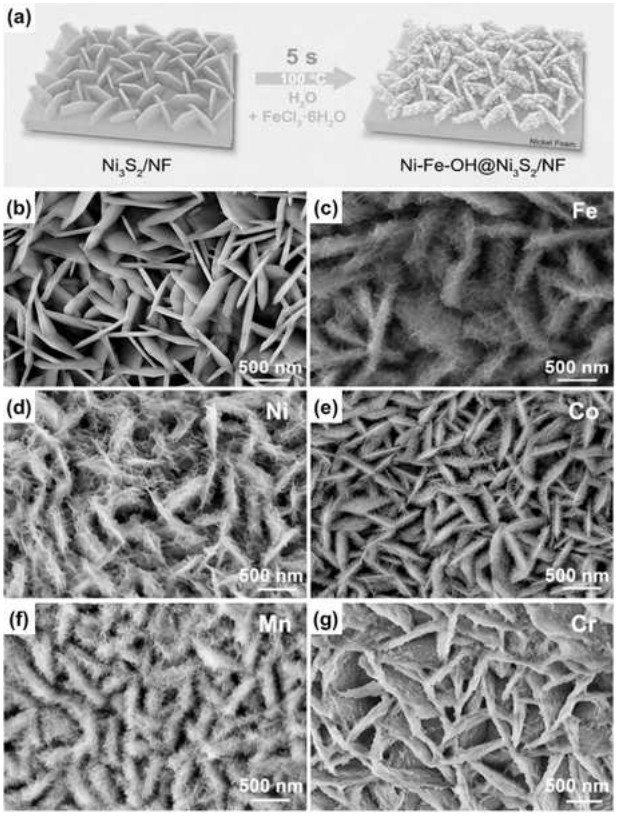


Figure 129. (a) Schematic illustration for the fabrication of Ni-Fe-OH@Ni_3S_2/NF through a typical hydrothermal process and following ultrafast immersion treatment. (b–g) SEM images of (b) Ni_3S_2/NF precursor and (c–g) Ni-*M*-OH@Ni_3S_2/NF (*M* = Fe, Ni, Co, Mn, Cr). Reprinted with permission from ref 640. Copyright 2017 Wiley.

optimized electron transfer in the electrocatalyst bulk, and thereby high electrocatalytic activity.

Finally, we provide one more example regarding hydrothermal preparation of a nanocomposite of a sulfide and carbon-based material. Han *et al.* used a one-step hydrothermal process to synthesize a 3D porous nanocomposite of Ni-doped CoS_2 and a N-doped reduced graphene oxide aerogel (CNS-NGA).[715] First, graphene oxide (GO) was prepared via chemical exfoliation of graphite powder following a modified Hummer method. The as-prepared GO aqueous suspension was combined with cobalt chloride hexahydrate ($CoCl_2·6H_2O$), nickel chloride hexahydrate ($NiCl_2·6H_2O$), and thiourea (CH_4N_2S), stirred vigorously, and then ultrasonicated for 20 min. Then the suspension was transferred to a Teflon-lined stainless-steel autoclave. Following the hydrothermal reaction at 200 °C for 24 h, the as-obtained sample (i.e., CNS-NG hydrogel) was washed with deionized water and freeze-dried at −50 °C for 3 days, resulting in a porous CNS-NG aerogel composite. A schematic illustration for this synthesis is shown in Figure 130a. Figure 130b shows a digital photograph of the CNS-NGA composite. The SEM and TEM images (Figures 130c–f) of the 3D porous CNS-NGA hybrid show that a porous structure was successfully synthesized, where diamond-like CNS nanoparticles (300–500 nm) were anchored onto the NGA support. Furthermore, BET specific surface area analysis revealed that the 3D porous CNS-NGA hybrid had a specific surface area of 99.1 $m^2·g^{-1}$, which is comparable to the reported specific surface areas of other GA-based nanocomposites.[868−870] The CNS-NGA electrocatalyst also showed a moderate ECSA (C_{dl}: 10.25 $mF·cm^{-2}$). Thus, this report suggests that the composite of the sulfide and 3D porous carbon-based support with a high surface area can effectively increase the electrochemically active sites and achieve enhanced OER performance.

5.1.1.2. Solvothermal Methods. Similar to the hydrothermal method, the resulting morphologies and compositions of prepared metal sulfides can be controlled by changing the starting materials or precursors in the solvothermal method. However, especially for the solvothermal method, it is essential to remember that the selection of different nonaqueous solvents [e.g., dimethylformamide (DMF), acetone, methanol, ethanol, toluene, ethyl glycol] as reaction media can also become an important factor for tuning final product structures and composition.[702] This can further expand flexibility in

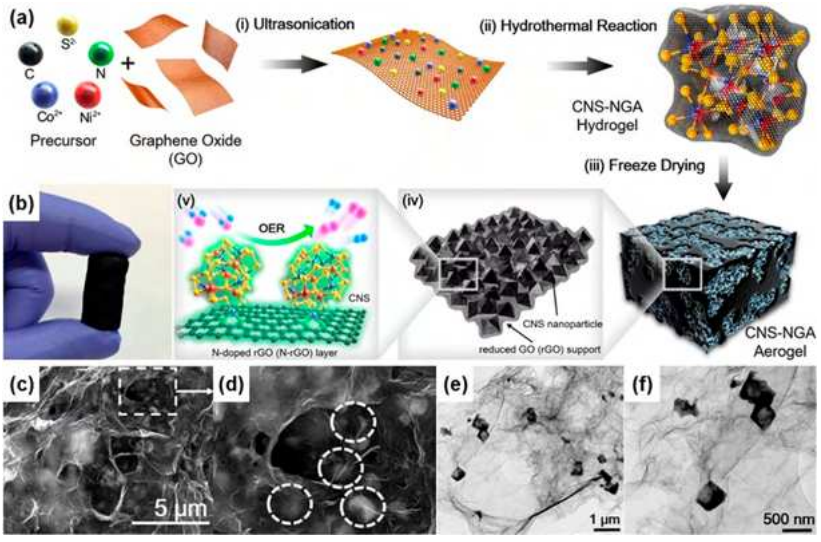


Figure 130. (a) Schematic illustration for the one-step hydrothermal synthesis of a 3D porous nanocomposite of Ni-doped CoS_2 nanoparticles and N-doped reduced graphene oxide aerogel (CNS-NGA). (b) Digital photograph of the 3D porous CNS-NGA hybrid. (c, d) SEM and (e, f) TEM images of the 3D porous CNS-NGA hybrid. Reprinted with permission from ref 715. Copyright 2018 American Chemical Society.

https://doi.org/10.1021/acs.chemrev.3c00005
Chem. Rev. 2023, 123, 12795−13208

sulfide synthesis. In general, for solvothermal synthesis, the reaction media tends to be prepared by mixing two different organic solvents (refs 683, 686, 691, 701, 703, 732, 774, 776, 789, and 790), in which researchers frequently use DMF (refs 669, 683, 689, 694, 701, and 789). This predominant use of DMF may be due to the formation of uniform mesoporous structures with DMF as a solvent, generally resulting in better electrocatalytic activity.[871] In some reports, water has also been used as a cosolvent for the solvothermal process (refs 691, 694, 765, 774, 776, and 789). As for hydrothermal synthesis, solvothermal synthesis can also be divided into two categories: one-step (refs 669, 685, 691, 703, 732, 774, and 789) and two-step approaches (refs 546, 679, 683, 686, 689, 694, 701, 765, 776, 788−790, and 818). Because multistep processes enable more control over morphology and composition, the majority of reports on solvothermal synthesis of metal sulfides use a two-step approach as opposed to one-step. In this section for the two-step approaches, we have discussed examples where precursor synthesis is through the solvothermal method, while the sulfurization step can be through the solvothermal method,[686,701,776,789] or other synthetic methods like the solution-based method (reaction in a flask),[789] and the thermal treatment (with a sulfur source),[790] and so forth.

Each solvothermal approach can use different precursor/starting material(s) and sulfur source(s), which is somewhat analogous to the hydrothermal method. For example, the most common starting materials were metal complexes/salts in both the one-step and two-step approaches.[669,685,691,703,732,774,789] Similar to the hydrothermal method, various sulfur sources (e.g., Na_2S,[689] thiourea,[774,790] $(NH_4)_2MoS_4$,[694,732] etc.) have been used for both one-step and two-step approaches, and the most commonly used are thioacetamide[686,701,703,788,789,818] and sulfur powder.[669,679,685,691,776] In two-step approaches involving solvothermal precursor preparation, a nonaqueous solvent causes oxygen deficiency in the reaction media, making it difficult to form crystalline metal oxide precursors. Thus, unlike in the case of the hydrothermal precursor preparation, solvothermal synthesis of crystalline metal oxide precursors has gone unreported to our knowledge (e.g., $MnCo_2O_4$@Ni-$(OH)_2$,[543] NiO,[773] NiFe-LDH,[764] etc.). Instead of the crystalline oxide precursors, MOFs[686,689,701,788] and amorphous metal oxide precursors[683,774] can be solvothermally synthesized as precursors for metal sulfide preparation using the solvothermal method (the importance of the use of the MOF precursors for sulfide synthesis will also be discussed in detail in Section 5.1.1.4). Additionally, solvothermal sulfurization is one of the most frequently used conversion techniques for converting precursors into sulfide products in two-step synthetic approaches (refs 546, 669, 685, 686, 689, 691, 694, 701, 703, 732, 765, 774, 776, 788, 789, and 818). Solvothermal sulfidation has been carried out on precursors prepared via the solvothermal method[686,689,701,776,788] and other synthetic methods (e.g., the solution-based method,[788] the hydrothermal method,[683] etc.).

As for the hydrothermal method, two types of electrodes can be prepared using the solvothermal method: powder-based (refs 679, 683, 685, 686, 689, 691, 701, 703, 765, 774, 776, 788, 789, and 818) and self-supported.[669,694,732,790] The majority of reports, however, used the solvothermal synthesis method to prepare powder-based electrodes instead of self-supported electrodes, which is likely due to the successful formation of hollow particles (a hollow shape can realize a large surface area as well as expose more active sites) using the solvothermal method,[788] or the use of structure-directing components that might not work in self-supporting electrode synthesis.[774] Finally, from previous reports, irrespective of electrode type, via the solvothermal synthesis method, researchers have synthesized transition metal sulfides with various morphologies such as nanosheet,[546,685,732] nanoflower,[679,686,691,774,774] nanoparticle,[790] nanosphere,[683,683,701] nanowire,[790] nanotube,[694,765] hollow nanoparticles,[676,689,788] core@shell,[818] and 3D structures (3D carbon matrix).[776] Additionally, there are some reports with combinations of different morphologies such as nanosheets + nanoparticles,[774] nanosheets + nanocubes,[779] and so forth. In the following paragraphs, reports on the solvothermal method-involved preparation of sulfide-based electrocatalysts with unique morphologies are introduced and discussed in detail.

As mentioned in the previous section (Section 5.1.1.1), nanosheet morphologies have many good properties for OER electrocatalysis (large surface area, reduced diffusion lengths for mass transfer, etc.). However, 2D nanosheets in powder form tend to be re-stacked easily, which reduces the surface area available for the OER. To solve this problem, Qin *et al.* synthesized an amorphous, holey Ni-Co sulfide nanosheet (NiCoS-NS) assembly through a two-step solvothermal process (see Figure 131a).[686] In the first step, transition metal complexes (i.e., $Ni(NO_3)_2{\cdot}6H_2O$ and $Co(NO_3)_2{\cdot}6H_2O$) were dissolved in methanol. Subsequently, a mixture of methanol and 2-methyl imidazole was added to the as-prepared solution. The resulting solution was placed in a Teflon-lined autoclave for solvothermal synthesis (140 °C, 12 h) to obtain a NiCo-MOF precursor. In the second step, the as-obtained precursor was mixed with ethanol and thioacetamide (sulfur source) and solvothermally sulfidized into the holey NiCoS-NS at 90 °C for 6 h. The reactions possibly involved in the sulfidation are shown below:[872]

$$CH_3CSNH_2 + C_2H_5OH \rightarrow CH_3(NH_2)C(OC_2H_5)\text{-}SH$$

$$CH_3(NH_2)C(OC_2H_5)\text{-}SH + C_2H_5OH \rightarrow CH_3(NH_2)C(OC_2H_5)_2 + H_2S$$

$$H_2S + \text{NiCo-MOF} \rightarrow \text{holey NiCoS-NS} + H_2O$$

Figures 131b−e show that, after the sulfidation, the nanosheet shape of the precursor was inherited and that numerous pores (average pore size: ∼18 nm) were introduced on the nanosheet structures. The SAED pattern (the inset of Figure 131e) of the holey NiCoS-NS sample indicates its amorphous nature. Moreover, AFM analysis revealed that the holey NiCoS-NS exhibited a higher surface roughness (Rq: 0.428 nm) compared with the NiCo-MOF precursor (Rq: 0.149 nm). The thickness of the holey NiCoS-NS was in the range of 1.53 to 3.90 nm. According to a previous report,[873] the authors also prepared a nonporous NiCoS-NS as a comparison. BET specific surface area analysis confirmed that the holey NiCoS-NS possessed a larger specific surface area of 49 $m^2{\cdot}g^{-1}$ than the nonporous NiCoS-NS (39 $cm^2{\cdot}g^{-1}$). Furthermore, the holey NiCoS-NS has a larger ECSA of 62.75 cm^2 compared to that of the nonporous NiCoS-NS (58.25 cm^2). These results imply that the incorporation of pores into the nanosheets can effectively increase their surface area. Notably, the authors also mentioned that this synthetic process can also be applied to other Ni-based bimetallic sulfides (such as NiFeS and NiMnS) (see Figures 131g and h).

https://doi.org/10.1021/acs.chemrev.3c00005
Chem. Rev. 2023, 123, 12795−13208

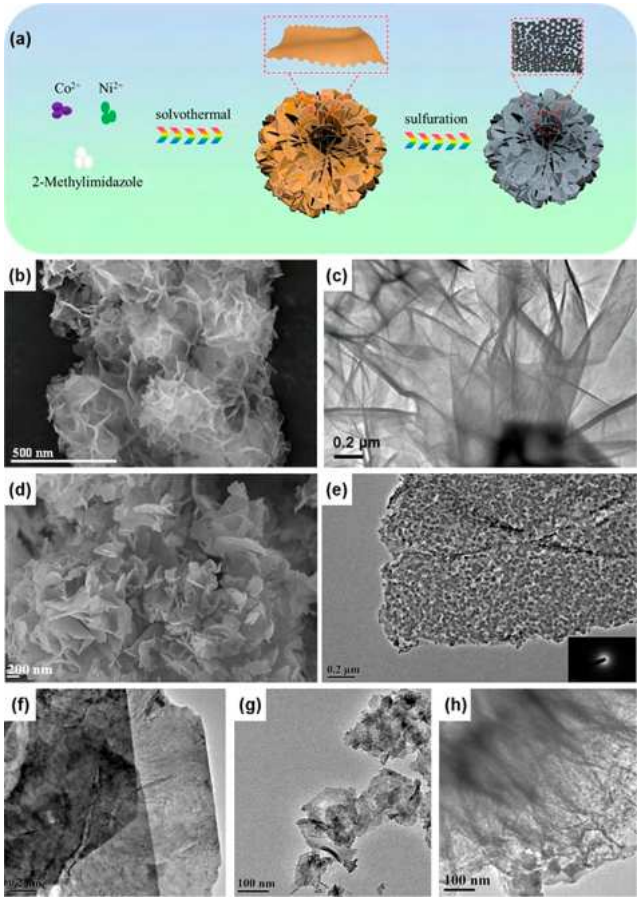


Figure 131. (a) Schematic illustration of the synthesis of holey Ni-Co sulfide nanosheets (NiCoS-NS) through a two-step solvothermal process. (b) SEM and (c) TEM images of the NiCo-MOF precursor. (d) SEM and (e) TEM images of holey NiCoS-NS. Inset of (e) indicates a corresponding SAED pattern. (f–h) TEM images of (f) nonporous NiCoS-NS, (g) holey NiFeS-NS, and (h) holey NiMnS-NS. Reprinted with permission from ref 686. Copyright 2019 Elsevier.

The formation of 3D nanoflowers, an organized aggregation of nanosheets, is another strategy to overcome the surface area decrease due to nanosheet stacking. Zhao *et al.* prepared a flowerlike 3D NiCo-sulfide (NiCoS) nanostructure decorated with NiCo double layered hydroxide (NiCoDH) nanodots (NiCoDH/NiCoS) through a one-step solvothermal process.[774] This NiCoDH/NiCoS sample has the advantage of the high surface area of ultrathin nanosheets and the open structure of flower-like structures for improved OER electrocatalysis. To prepare the material, the authors first mixed transition metal complexes [$Ni(Ac)_2{\cdot}4H_2O$ and $Co(Ac)_2{\cdot}H_2O$], hexamethylenetetramine (HMTA), triblock copolymer (Pluronic P123), thiourea (CH_4N_2S), ethanol, water, and ethylene glycol. The as-prepared mixture was then aged statically for 24 h, resulting in lamellar structures, as shown in Figure 132a. Note that, during this process, P123 and ethylene glycol acted as the cosurfactants to form inverse lamellar micelles. For the solvothermal process, the resultant solution was placed in a Teflon-lined stainless-steel autoclave and maintained at 170 °C for 2 h to produce the flower-like 3D NiCoDH/NiCoS structure. For comparison, the authors also prepared the NiCoDH and NiCoS samples by only using HMTA or thiourea as an anion source, respectively. It was observed that the thiourea content could affect the resulting morphology. When increasing the thiourea content, the 3D flower-like structure became more regular. However, at high thiourea content, a lot of nanoparticles were generated and became dominant, implying that S^{2-} ions generated from thiourea decomposition are essential to growing the well-ordered flower-like 3D architecture consisting of interconnected nanosheets (see Figure 132b). Importantly, during the synthesis, HMTA released OH^- ions through its hydrolysis. The as-generated OH^- ions reacted with Ni^{2+} and Co^{2+} ions, inducing the formation of NiCoDH nanodots. Simultaneously, S^{2-} ions from thiourea are absorbed onto the nanodots to prevent their further growth. The TEM image (Figure 132c) shows the thin nanosheets with crumbled edges (which will increase the active surface area). Finally, the HRTEM image (Figure 132d) shows that NiCoDH nanodots (average diameter: 2–3 nm) are spread out on the ultrathin NiCoS nanosheets (thickness: ~1.5 nm). The combination of both the nanodot and nanosheet morphologies led to a relatively high ECSA (NiCoDH/NiCoS: 3.93 $mF{\cdot}cm^{-2}$), which is

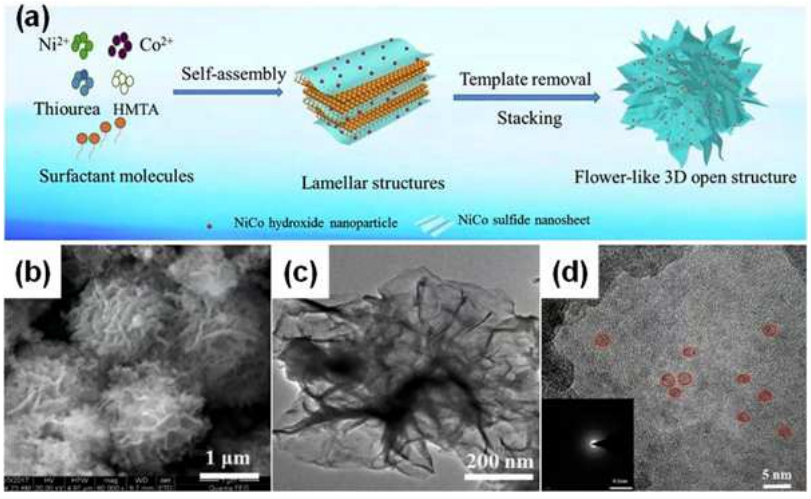


Figure 132. (a) Schematic illustration for the synthesis of a flower-like 3D NiCoDH/NiCoS nanostructure through a one-step solvothermal process. (b) SEM, (c) TEM, and (d) HRTEM images and [inset of (d)] SAED pattern of the NiCoDH/NiCoS. Reprinted with permission from ref 774. Copyright 2019 Elsevier.

https://doi.org/10.1021/acs.chemrev.3c00005
Chem. Rev. 2023, 123, 12795–13208

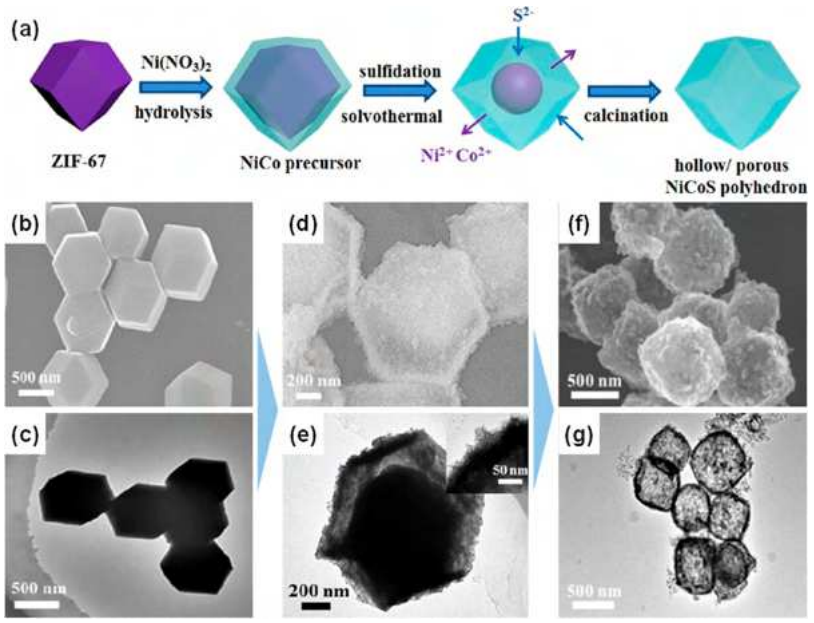


Figure 133. (a) Schematic illustration of the formation of a porous single-shelled hollow NiCoS polyhedron through a two-step solvothermal method. (b) FESEM and (c) TEM images of the ZIF-67 template. (d) FESEM and (e) TEM images of the NiCo precursor. (f) FESEM and (g) TEM images of the porous hollow NiCoS. Reproduced with permission from ref 788. Copyright 2018 Elsevier.

greater than those of NiCoDH (2.64 $mF \cdot cm^{-2}$) and NiCoS (2.77 $mF \cdot cm^{-2}$). Furthermore, the authors also examined the porous structures and specific surface areas of all the as-prepared samples via N_2 adsorption−desorption isotherms. The NiCoDH sample showed a type II isotherm with a small pore size of 2.69 nm, while the NiCoDH/NiCoS and NiCoS samples exhibited type IV isotherms with H_3 type hysteresis. Notably, the NiCoDH/NiCoS exhibited a relatively broad mesoporous distribution and a much higher specific surface area of 61.6 $m^2 \cdot g^{-1}$ than NiCoDH (21.8 $m^2 \cdot g^{-1}$) and NiCoS (44.9 $m^2 \cdot g^{-1}$). This report demonstrated the use of surfactants to control a resultant product morphology and obtain an organized 3D assembly of nanosheets for effective mass transport and decent structural stability during the OER.

The solvothermal method can also produce transition metal OER electrocatalysts with hollow structures composed of well-defined shell layer(s) and inner cavities. The hollow structures generally possess large surface areas, providing an abundance of accessible electroactive sites that can also lead to optimized mass transfer for electrolysis.[874] For example, Yu *et al.* synthesized porous single-shelled hollow nickel-cobalt sulfide (NiCoS) through the solvolysis, solvothermal sulfidation, and calcination of zeolitic imidazolate framework-67 (ZIF-67) acting as a sacrificial template (see Figure 133a).[788] In the first step, the solvolysis of ZIF-67 powder (size: ∼600 nm) (see Figures 133b and c) with $Ni(NO_3)_2 \cdot 6H_2O$ in ethanol was carried out to synthesize a NiCo precursor. In this process, Co^{2+} ions released from ZIF-67 precipitated with Ni^{2+} ions by forming their layered double hydroxide sheet on ZIF-67 (see Figures 133d and e). In the next step, the authors put the as-prepared NiCo precursor in a Teflon-lined stainless-steel autoclave with thioacetamide and ethanol for solvothermal sulfurization (120 °C, 6 h). During the solvothermal sulfidation, S^{2-} ions generated from thioacetamide reacted with Co^{2+} and Ni^{2+} ions on the NiCo precursor surface and formed a thin NiCoS layer. As the sulfidation proceeded, the organic framework cores were gradually consumed, and the generated metal ions diffused to the outer shell and further reacted with S^{2-} ions. Finally, the as-sulfidized NiCo precursor was calcinated under N_2 atmosphere at 350 °C for 2 h, resulting in the porous hollow NiCoS (Figures 133f and g). The rough surfaces of the as-obtained porous hollow NiCoS polyhedrons were composed of closely packed nanoparticles (see Figure 133f). XRD analysis of the porous hollow NiCoS confirmed the formation of cubic $NiCo_2S_4$ without any impurities. The specific surface area and pore-size distribution of the porous hollow NiCoS were examined by N_2 adsorption−desorption analysis. The porous hollow NiCoS showed a type IV isotherm with obvious hysteresis, indicating that the sample possessed mesoporous structure. The porous hollow NiCoS exhibited a relatively large specific surface area of ∼123 $m^2 \cdot g^{-1}$ and pore sizes of ∼18.2 nm. This large surface area and mesoporous structure are preferable for promoting active site exposure and mass transport to achieve efficient OER electrocatalysis.

In addition, Wu and co-workers prepared a thiospinel-type transition metal sulfide nanocomposite (NiCuCo-sulfide: $NiCu_2S_4$ + $CuCo_2S_4$) having unique multishelled hollow structures with mesopores via solvothermal coordination, calcination, and sulfidation (Figure 134a).[683] First, the authors prepared a mixture of nickel(II), copper(II), cobalt(II) nitrates, isophthalic acid, DMF, and acetone, which was subjected to a solvothermal reaction at 160 °C for 4 h, resulting in a Ni, Cu, Co-coordinated polymer (NiCuCo-polymer) precursor with spherical morphology. Then, the as-obtained NiCuCo-polymer precursor was calcinated at 500 °C for 10 min to obtain a hollow yolk−shell structured Ni, Cu, Co-based mixed oxide (NiCuCo-oxides: $NiCo_2O_4$ + $CuCo_2O_4$) as shown in the SEM and TEM images in Figures 134b and c. The authors hypothesized that this precursor structure formed because of heterogeneous contraction.[875] Finally, the as-obtained NiCuCo-oxide precursor was immersed in a Na_2S aqueous solution and sulfurized at 160 °C for 8 h, resulting in mesoporous hollow nested NiCuCo-sulfide

https://doi.org/10.1021/acs.chemrev.3c00005
Chem. Rev. 2023, 123, 12795−13208

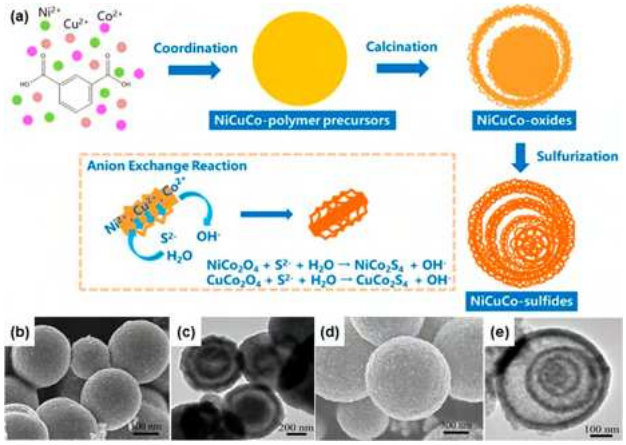


Figure 134. (a) Schematic illustration for the fabrication of mesoporous multishelled hollow NiCuCo-sulfide nanospheres through solvothermal coordination, calcination, and sulfidation. (b) SEM and (c) TEM images of NiCuCo-oxides. (d) SEM and (e) TEM images of NiCuCo-sulfides. Reprinted with permission from ref 683. Copyright 2019 American Chemical Society.

nanospheres consisting of nanoparticles (size: ∼10 nm) (see Figures 134d and e). The reactions during the sulfidation (i.e., anion exchange) are indicated in Figure 134a. The complex morphology of the NiCuCo-sulfide was most likely the result of the pseudo-Kirkendall effect during the anion exchange reaction,[876,877] wherein the anion exchange and cation diffusion occur at different rates, leading to the hollowing-out of a material. Based on N_2 adsorption−desorption results, the authors also estimated the specific surface area and the pore size distribution. The NiCuCo-sulfide sample had a larger specific surface area of 43.32 $m^2 \cdot g^{-1}$ compared with the NiCuCo-oxide sample (18.63 $m^2 \cdot g^{-1}$). These results agreed with the TEM observation (see Figures 134c and e): the NiCuCo-sulfide had a looser microstructure (i.e., a multishell nested hollow nanosphere) than the NiCuCo-oxide. Moreover, in the pore size distribution plot of the NiCuCo-sulfide, the sharp and broad peaks located in the ranges of 2−5 and 10−50 nm correspond to the mesoporous spaces between the nanoparticles in the shells and the hollow cavities between the nested nanospheres. Notably, the authors emphasized that both the mesoporous structure and large surface area are preferable for OER electrocatalysts and can give additional, low-resistance mass transport pathways, realize faster interfacial charge transfer and efficient ion diffusion, and promote electrolyte permeation and O_2 gas release.[878,879] This example also demonstrated that the use of polymers as sacrificial templates (NiCuCo-polymer precursors) is effective for synthesizing the hollow sulfide electrocatalysts.

So far, transition metal sulfides with various 1D structures (e.g., nanowire, nanocuboid, nanotube, etc.) have also been synthesized through solvothermal method-involved synthetic approaches and reported as efficient OER electrocatalysts.[694,765,790] One such example was provided by Zhai *et al.*,[790] in which three types of MoS_2/NiS composites with different morphologies [i.e., MoS_2 nanosheet-coupled NiS nanocuboids (MoS_2/NiS NCs), MoS_2 nanoparticle-coupled NiS nanowires (MoS_2/NiS NWs), and MoS_2/NiS aggregations (MoS_2/NiS AGs)] were synthesized by the solvothermal method and subsequent thermal sulfidation (see Figure 135a). For the solvothermal step, the solvent was prepared by mixing *n*-hexane, *n*-pentanol, and ultrapure water. For preparing the MoS_2/NiS NCs, molybdic acid, trimethylammonium bromide (CTAB), and dioctyl sodium sulfosuccinate (AOT) were also added to the as-prepared solvent. In this step, for the MoS_2/NiS AGs and MoS_2/NiS NWs, only AOT or CTAB was added to the solvent solution, respectively. In a Teflon-lined autoclave, the as-prepared solution mixture and Ni foam were placed in a Teflon-lined autoclave, and the solvothermal process was carried out at 150 °C for 2 h. Afterward, the as-prepared precursors with different morphologies were subject to sulfidation at 450 °C under N_2 with thiourea (sulfur source). During the solvothermal process, AOT and CTAB acted as surfactants, leading to altered final precursor morphologies. More specifically, the bromide counterions in CTAB were thought to chemisorb on the Mo-Ni surfaces, leading to controlled crystal growth on favorable crystal faces, forming one-dimensional morphologies (i.e., nanowire and nanocuboid). On the other hand, the addition of AOT could lead to enlarged micelle size (surfactant) of CTAB and thereby induce the transformation of nanowires into nanocuboids. Accordingly, CTAB is the main player in the growth of 1D morphologies. The SEM images in Figures 135b−d show the formation of the sulfide composite samples with different morphologies (i.e., nanocuboid, nanowire, and aggregation). Here, the authors examined the C_{dl} values for the resultant samples. The MoS_2/NiS NCs exhibited a higher C_{dl} value of 65.6 $mF \cdot cm^{-2}$ compared with those of the MoS_2/NiS NWs (14.1 $mF \cdot cm^{-2}$) and MoS_2/NiS AGs (13.5 $mF \cdot cm^{-2}$). Moreover, the MoS_2/NiS NCs, MoS_2/NiS NWs, and MoS_2/NiS AGs showed BET specific surface areas of 5.22, 2.90, and 0.93 $m^2 \cdot g^{-1}$, respectively, which roughly followed the as-observed C_{dl} trend. In this study, the MoS_2/NiS NCs with the largest surface area of the prepared samples showed the best alkaline OER performance. Note that this work pointed out the advantage of precursor morphology control using the solvothermal method for the preparation of metal sulfides of a desired morphology (e.g., 1D structures).

Wang and co-workers were able to prepare complex 1D nanostructures using a multistep synthetic approach involving the solvothermal method, solution-based reactions, and calcination. Specifically, they prepared 1D (Ni, Co, Fe)$_9S_8$/N-doped carbon, (Ni, Fe)$_9S_8$/N-doped carbon, and Co_8FeS_8/N-doped carbon nanocomposites (see Figure 135e).[765] In the first step, CdS nanowires (NWs) were prepared with cadmium diethyldithiocarbamate [$Cd(S_2CNEt_2)_2$] and ethylenediamine (solvent) through the solvothermal process at 180 °C for 24 h. Then, the authors used the as-prepared CdS NWs as templates for the solution-based synthesis of hybrids of CdS and Prussian blue analog (PBA): CdS@(Ni, Co, Fe)-PBA, CdS@(Ni, Fe)-PBA, and CdS@(Co, Fe)-PBA. Subsequently, for the as-prepared samples, polydopamine (PDA) was incorporated in order to reduce CdS and also as a nitrogen source. All the PDA-incorporated samples were calcinated at 800 °C under an Ar atmosphere, producing the 1D sulfide/N-doped carbon nanocomposites. During the calcination, it was hypothesized that the evaporation of Cd vapors promoted the release of free S atoms, resulting in the sulfidation of Ni, Co, and Fe species. Simultaneously, the complete removal of Cd occurred, which was confirmed by XRD and ICP-MS. Figures 135f−h show the TEM images of the resultant sulfide/N-doped carbon composite samples. Here, different combinations of Ni, Co, and Fe gave rise to different morphologies. The (Ni, Fe)$_9S_8$/N-doped carbon had monodisperse cubes (size: ∼200 nm) on

https://doi.org/10.1021/acs.chemrev.3c00005
Chem. Rev. 2023, 123, 12795−13208

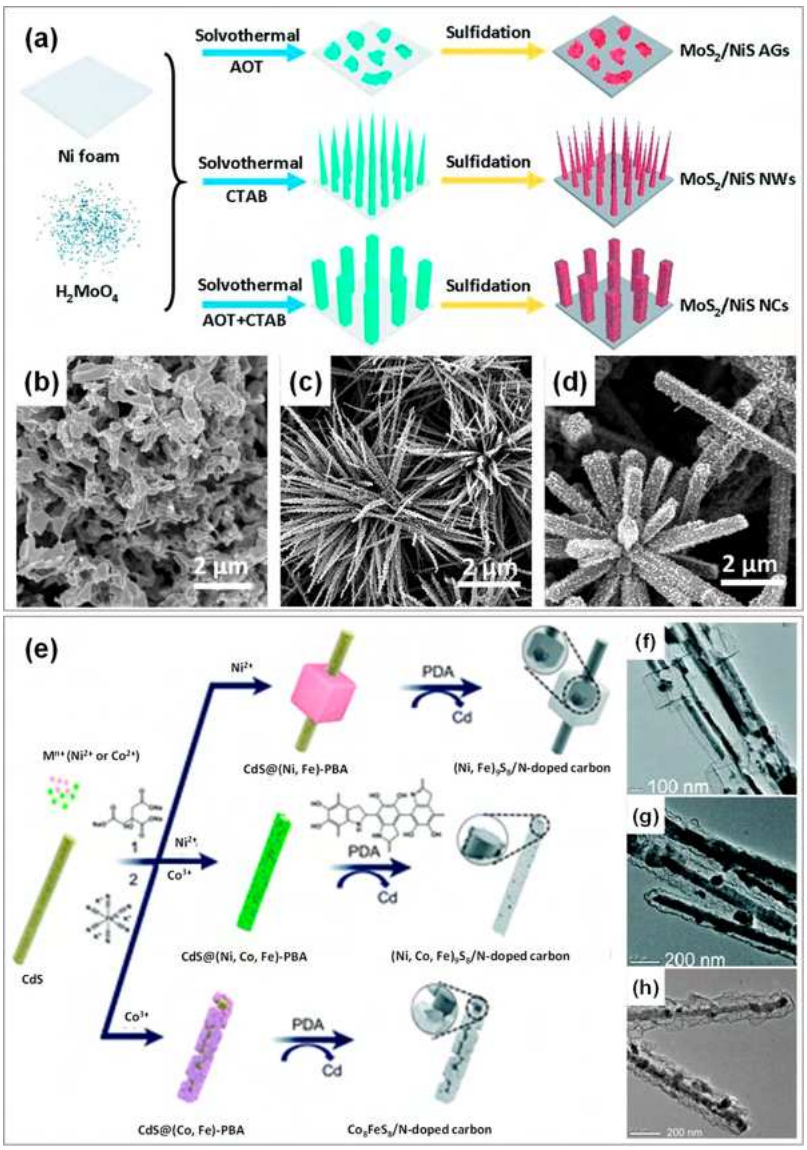


Figure 135. (a) Schematic illustration for the fabrication of MoS_2/NiS heterostructures with different morphologies through the two-step approach (solvothermal reaction + thermal sulfidation). (b–d) SEM images of (b) MoS_2/NiS AGs, (c) MoS_2/NiS NWs, and (d) MoS_2/NiS NCs. Reprinted with permission from ref 790. Copyright 2018 Royal Society of Chemistry. (e) Schematic illustration for the synthesis of 1D sulfide/N-doped carbon nanocomposites through the multistep approach. (f–h) TEM images of (f) (Ni, Fe)$_9S_8$/N-doped carbon, (g) (Ni, Co, Fe)$_9S_8$/N-doped carbon, and (h) Co_8FeS_8/N-doped carbon nanocomposites. Reprinted with permission from ref 765. Copyright 2019 Royal Society of Chemistry.

the nanowires (i.e., candied haws-like structures). For the (Ni, Co, Fe)$_9S_8$/N-doped carbon, void spaces and some cubic nanoparticles (size: ∼50 nm) wrapped in the nanowires were observed. The Co_8FeS_8/N-doped carbon had a morphology similar to that of the (Ni, Co, Fe)$_9S_8$/N-doped carbon but had larger cubic nanoparticles (size: ∼100 nm). Furthermore, all the as-prepared sulfide samples indicated relatively high C_{dl} values: Co_8FeS_8/N-doped carbon, 352 mF·cm^{-2}; (Ni, Co, Fe)$_9S_8$/N-doped carbon, 324 mF·cm^{-2}; and (Ni, Fe)$_9S_8$/N-doped carbon, 188 mF·cm^{-2}. Of the as-prepared composites, (Ni, Co, Fe)$_9S_8$/N-doped carbon demonstrated the highest electrocatalytic OER activity in alkaline media. Its superior performance is likely the result of synergic effects between Ni, Co, and Fe. This report demonstrates how the solvothermal method can be used to prepare precursor templates with tuned morphologies such that the structure of the final product can be controlled, enabling engineering of metal sulfide materials for superior OER performance.

Nanotubes are another type of 1D morphology that has been reported for transition metal sulfides.[789,800] They have recently been in the spotlight because nanotube-based architectures have high porosity, high surface area, and uneven surface characteristics (i.e., superaerophobicity), etc.[694,880,881] Li *et al.* fabricated sulfide [Mo_2S + (Co, Fe, Ni)$_9S_8$] hybrid nanotube arrays (FeCoNi-HNTAs) on Ni foam through a two-step approach: hydrothermal precursor-preparation and solvothermal sulfidation (see Figure 136a).[694] In the hydrothermal process (120 °C, 10 h), ternary Fe, Co, Ni-based layered double hydroxide nanowire arrays (FeCoNi-LDH-NWAs) were formed on Ni foam. In the solvothermal sulfidation step, the as-prepared FeCoNi-LDH-NWAs (self-sacrificing templates), $(NH_4)_2MoS_4$ (sulfur source), and hydrazine hydrate (HZH) were mixed in *N*,*N*-dimethylforma-

https://doi.org/10.1021/acs.chemrev.3c00005
Chem. Rev. 2023, 123, 12795−13208

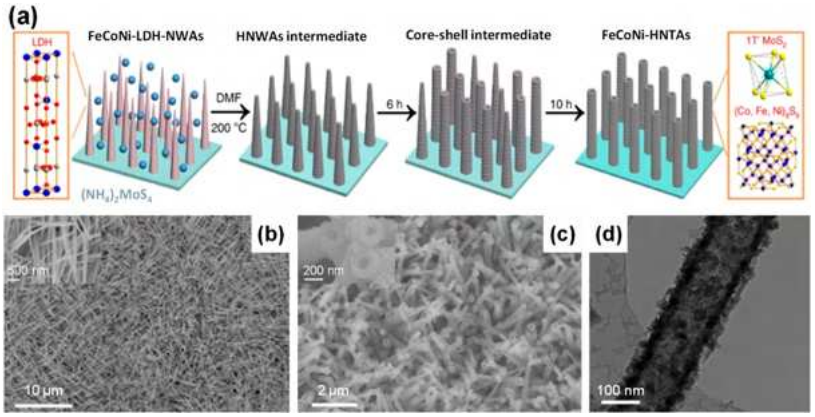


Figure 136. (a) Schematic illustration for the fabrication of sulfide hybrid nanotube arrays (FeCoNi-HNTAs) through the hydrothermal process and subsequent solvothermal sulfidation. (b, c) SEM images of (b) FeCoNi-LDH-NWAs and (c) FeCoNi-HNTAs. (d) TEM image of FeCoNi-HNTAs. Reproduced with permission from ref 694. Copyright 2018 Springer Nature.

mide (DMF) solvent, placed in an autoclave, and then heated at 200 °C for 10 h. Here, HZH can limit crystallization and assist in forming porous structures.[882] As the sulfidation started, MoS_2 nanosheets grew on the walls of the precursor. At the sulfidation time of 2 h, the as-obtained hybrid nanowires still had solid structures and uneven surfaces. However, at the reaction time of 6 h, the formation of core@shell nanostructures was observed, which likely resulted from the different diffusion rates between the outward process of the Fe, Co, Ni-based part and the inward process of the MoS_2 part. At the end of the sulfidation, Kirkendall voids were generated, and well-defined nanotube structures emerged. Figures 136b–d show the SEM and TEM images of the FeCoNi-LDH-NWAs and FeCoNi-HNTAs, indicating the morphological transformation from nanowire to nanotube during the solvothermal sulfidation. Each of the FeCoNi-HNTAs had a diameter of ∼150 nm and a tube wall thickness of 30−80 nm. Moreover, the FeCoNi-HNTAs were irregularly aligned on Ni foam, resulting in the high porosity of the electrode. To verify the versatility of this synthetic approach, the authors even applied this approach to different LDH precursors such as CoNi-LDH-nanowire arrays and NiFe-LDH-nanosheet arrays and successfully obtained sulfide hybrid nanotube and nanosheet arrays (CoNi-HNTAs and NiFe-HNSAs), respectively. Here, when $(NH_4)_2MoS_4$ was replaced with thioacetamide, the final product was FeCoNi nanotube arrays (FeCoNiS-NTAs), but it was not hybrid material (no MoS_2) because of the absence of the Mo source. The author also estimated the ECSA for the OER from the C_{dl} value. Surprisingly, the FeCoNi-HNTAs showed a high ECSA of 4652.5 cm^2 (geometric area: 0.9 cm^2), which is even higher than that of the FeCoNi-LDH-NWAs. This study found that solvothermal sulfidation can further modify the precursor morphology and expand the resultant electrode surface area and porosity.

5.1.1.3. Electrodeposition. Electrodeposition is another prominent method for the synthesis of transition metal sulfide electrocatalysts for the OER because of its simplicity and ease of control. The electrochemical techniques used for electrodeposition can be divided into current- and voltage-controlled deposition methods. For current-controlled deposition, a galvanostatic technique (i.e., chronopotentiometry)[681,687] has been utilized. For voltage-controlled deposition, a potentiostatic technique (i.e., chronoamperometry),[641,673,726,820] cyclic voltammetry (CV),[448,678,716,798] and square wave voltammetry[678] have been used. Of all the techniques mentioned above, CV has been most commonly reported for sulfide electrodeposition, likely due to the amorphous nature of the product deposited via CV, which could increase the number of active sites for the OER.[95,448,678,716,796] Similar to the hydrothermal and solvothermal methods, the electrodeposition of transition metal sulfides can be divided into two categories: one-step[448,681,798] and two-step approaches.[641,673,678,687,716,820] Electrodeposition has also been used for post-synthetic treatment of sulfide films to introduce heterogeneity, specifically to prepare metal sulfide/metal hydroxide composite materials, as will be discussed in this section.[726]

As for hydrothermal and solvothermal methods, the most commonly used starting materials for electrodeposition are metal complexes/salts for both one-step and two-step processes. In two-step approaches, the sulfurization step is performed either by electrodeposition[678] or by another synthesis method such as the hydrothermal method.[641,673,687,820] For electrodeposition-involved synthetic approaches, thiourea (CH_4N_2S) is most often used as the sulfur source for sulfurization;[448,678,716,798] however, other sources such as Na_2S[673] and $(NH_4)_2MoS_4$[820] have also been used. Unlike for the hydrothermal and solvothermal methods, the electrodeposition method is only used to prepare self-supported electrodes, specifically electrocatalyst films on conducted substrates. The ability to prepare self-supported electrodes with ease positions electrodeposition as an advantageous synthetic approach, as it eliminates the need for conducting and adhesive agents that lead to higher loading of active materials compared to the powder-coated electrodes.[671]

So far, using the electrodeposition method, electrochemists have synthesized transition metal sulfides with various morphologies such as nanosheets,[678,687,716,798] nanoflakes,[673] nanowires,[726] nanorods,[641,820] nanoparticles,[448] and hollow nanoparticles.[681] Among these reported morphologies, the nanosheet-based structure has been the most heavily studied in the literature. In this section, we introduce typical and novel examples of the synthesis of nanostructural transition metal sulfide films via electrodeposition and discuss their resulting properties (i.e., chemical composition, morphology, surface area, etc.).

As aforementioned, nanosheet-based structures, which are generally cited as having high surface area for enhanced

https://doi.org/10.1021/acs.chemrev.3c00005
Chem. Rev. 2023, 123, 12795−13208

electrocatalysis, are one of the most common morphologies synthesized via electrodeposition. For example, Shang *et al.* prepared binary Fe-Ni sulfides supported on Ni foam (FeNi-S/NF) using a liquid crystal template (LCT) electrodeposition method and investigated the effect of using an LCT on the final synthetic products.[716] Notably, this work achieved the formation of the FeNi-S nanospheres covered by numerous interwoven nanosheets. For the LCT-assisted electrodeposition, an aqueous solution containing $Ni(NO_3)_2{\cdot}6H_2O$, $Fe(NO_3)_3{\cdot}9H_2O$, and thiourea was prepared, mixed with the surfactant Triton X-100 (LCT), and then heated at 50 °C overnight. As a control experiment, the electrodeposition without adding the LCT (i.e., water solution-assisted electrodeposition) was also prepared. The electrodeposition was performed by using a standard three-electrode system with Ni foam [working electrode (WE)], carbide [counter electrode (CE)], and Ag/AgCl [reference electrode (RE)]. The sulfide films were electrodeposited on Ni foam via cyclic voltammetry (potential window: −1.2 to 0.2 $V_{Ag/AgCl}$; scan rate: 20 $mV{\cdot}s^{-1}$; cycle number: 20). A schematic illustration for the LCT- and water solution-assisted electrodeposition processes is shown in Figure 137a. During the LCT-assisted electrodeposition, Fe, Ni, and S species were encapsulated by the surfactant (Triton X-100), leading to phase separation in the electrolyte in the form of surfactant spheres. These surfactant spheres led to the more uniform dispersion of Fe, Ni, and S on the Ni foam surface as opposed to the water solution-assisted method, which resulted in a planar material consisting of randomly stacked nanoparticles on the Ni foam substrate. For both the LCT- and water solution-assisted electrodepositions, amorphous films were obtained on Ni foam, as confirmed by XRD. EDX analysis confirmed that both the LCT- and water solution-electrodeposited samples contained Fe, Ni, and S elements (see Figures 137b and c), indicating the successful synthesis of the binary Fe-Ni sulfide films. The SEM images in Figures 137d and e show the morphological difference in the FeNi-S films electrodeposited with and without the LCT. As aforementioned, the use of the LCT resulted in the formation of a uniform porous FeNi-S film consisting of nanospheres covered with interwoven nanosheets, whereas, in the absence of LCT, the FeNi-S planar film with closely stacked nanoparticles was formed. Here, the nanosheet-based structure on the LCT-electrodeposited sample may be more favorable for exposing abundant electroactive sites for the OER. From this report, it was found that surfactant incorporation in the electrolyte can modify the resultant morphology of the electrodeposited sulfide film.

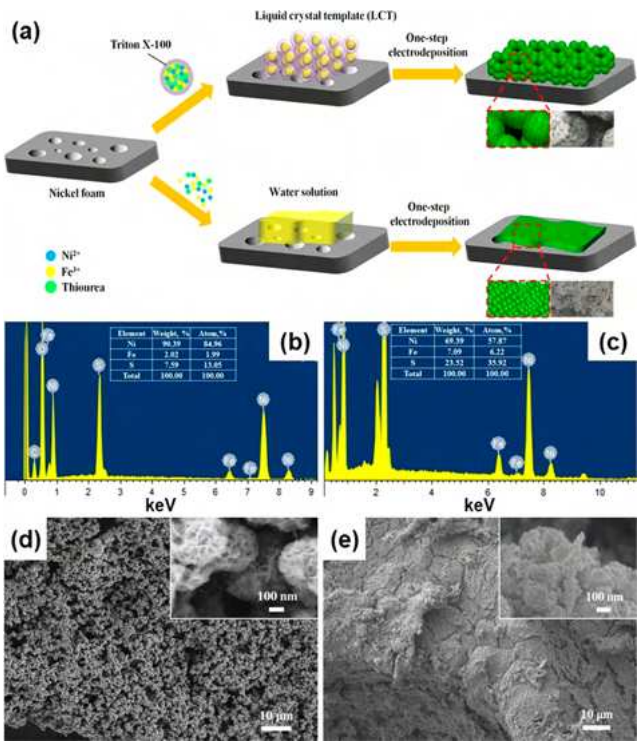


Figure 137. (a) Schematic illustration for the fabrication of binary Fe-Ni sulfide films on Ni foam (FeNi-S/NF) through liquid crystal template (LCT)- and water solution-assisted electrodeposition approaches. (b, c) EDX spectra of the FeNi-S/NF samples prepared by (b) LCT- and (c) water solution-assisted electrodeposition. (d, e) SEM images of the FeNi-S/NF samples prepared by (d) LCT- and (e) water solution-assisted electrodeposition. Reprinted with permission from ref 716. Copyright 2018 Elsevier.

Transition metal sulfide films with hollow nanostructures can also be prepared via electrodeposition. Zhang *et al.* synthesized a hollow $CuS_{0.55}$ nanoparticulate film on Cu foam using an anodic oxidation electrodeposition process.[681] The electrodeposition was performed in a standard three-electrode system (WE: Cu foam; CE: graphite bar; RE: graphite bar) in an aqueous electrolyte consisting of KOH (5 M) and CH_4N_2S (0.064 M). During the deposition, a constant current of 5 mA was applied for 500 s. After rinsing the as-deposited film with deionized water, ethanol, and carbon disulfide, the $CuS_{0.55}$ sample was obtained. The authors then repeated the same synthesis without CH_4N_2S and then at a higher CH_4N_2S concentration (0.128 M). As a result, CuO nanorods and $CuS_{0.57}$ nanosheets were obtained, respectively. Figures 138a–d show the as-obtained Cu-based samples with different morphologies. As shown in Figure 138b, the average size of the hollow $CuS_{0.55}$ nanoparticle was about 70 nm. Furthermore, in the TEM image of the $CuS_{0.55}$ sample (Figure 138e), it was observed that hollow nanoparticles with a mean wall thickness of 30 nm were tightly connected with each other. The corresponding SAED pattern further revealed that the $CuS_{0.55}$ sample was polycrystalline, where grain boundaries of polycrystalline materials can act as active sites for electrocatalytic reactions.[883] The $CuS_{0.55}$ sample also exhibited a larger ECSA (10.4 cm^2) as compared to those of $CuS_{0.57}$ (7.5 cm^2) and CuO (4.0 cm^2). This result indicates that the hollow nanostructure of $CuS_{0.55}$ leads to increased exposure of electroactive sites for the OER. Note that, in this one-step metal sulfide electrodeposition, the sulfur source concentration in the electrolyte had an effect on both final product composition and morphology, meaning that prepared metal sulfides can be easily tuned via changes in the components of the deposition solution.

In the previous examples, the sulfide films produced by one-step electrodeposition were introduced. Here, we discuss the cases in which sulfide films were prepared through two-step approaches, in which the electrodeposition was used in conjunction with another synthetic method (i.e., the hydrothermal method).[641,687,820] For example, Dong and co-workers prepared crystalline urchin-like NiCoS nanorod arrays on Ni foam via an electrodeposition-hydrothermal sulfidation process (see Figure 139a).[820] The authors first synthesized an amorphous NiCo hydroxide precursor on Ni foam through electrodeposition using a standard three-electrode setup [WE:

https://doi.org/10.1021/acs.chemrev.3c00005
Chem. Rev. 2023, 123, 12795−13208

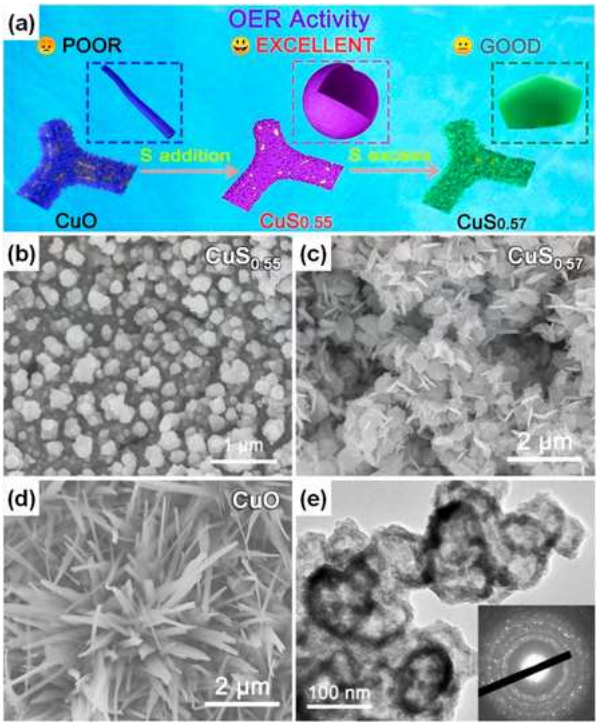


Figure 138. (a) Schematic illustration of the Cu-based samples (i.e., $CuS_{0.55}$, $CuS_{0.57}$, and CuO) prepared through the electrodeposition with different sulfur source contents. (b–d) SEM images of (b) $CuS_{0.55}$, (c) $CuS_{0.57}$, and (d) CuO. (e) TEM image of $CuS_{0.55}$. The inset of (e) shows the corresponding SAED pattern. Reprinted with permission from ref 681. Copyright 2019 Elsevier.

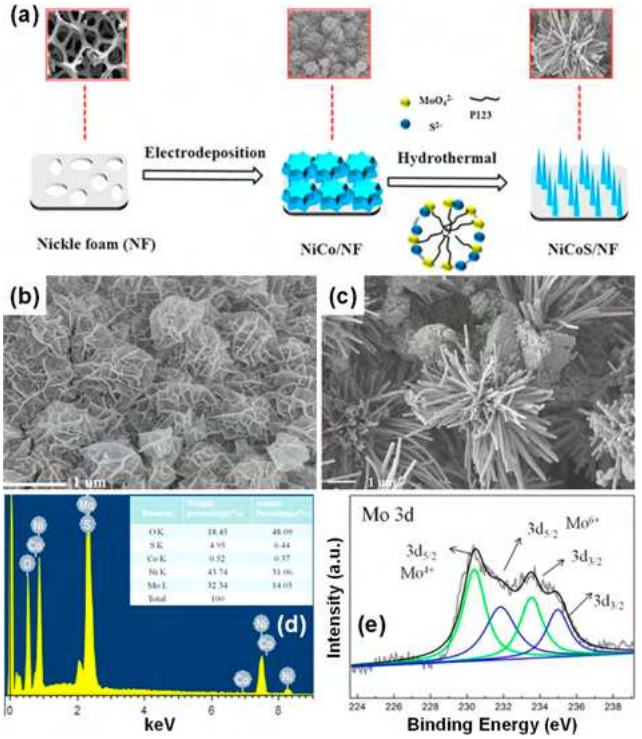


Figure 139. (a) Schematic illustration for the fabrication of NiCoS urchin-like nanorods on Ni foam (NiCoS/NF) via electrodeposition and subsequent hydrothermal sulfidation. (b, c) SEM images of (b) a NiCo hydroxide film on Ni foam and (c) the NiCoS/NF. (d) EDX and (e) Mo 3d XPS spectra of the NiCoS/NF. Reprinted with permission from ref 820. Copyright 2018 The Electrochemical Society.

Ni foam; CE: Pt plate; RE: Ag/AgCl (3 M KCl)]. The precursor deposition was performed at a constant applied potential of $-1.0\ V_{Ag/AgCl}$ for 600 s in an aqueous electrolyte containing $Co(NO_3)_2{\cdot}6H_2O$ and $Ni(NO_3)_2{\cdot}6H_2O$. Afterward, the hydrothermal method was used for sulfurization of the as-prepared NiCo hydroxide precursor on Ni foam: the NiCo hydroxide sample was put in an autoclave with an aqueous solution of ammonium molybdate $[(NH_4)_2MoS_4]$, Pluronic P123, and thiourea and heated at 200 °C for 24 h. During the hydrothermal sulfurization, P123 and ammonium molybdate acted as structure-directing agents and thiourea as the sulfur source. As shown in the SEM image of the NiCo hydroxide precursor (Figure 139b), rippled nanosheet structures were produced via electrodeposition. After the hydrothermal sulfurization, the rippled nanosheet structures were converted into urchin-like nanorods (see Figure 139c). From the XRD results, the as-sulfidized sample was identified as mixed transition metal sulfides (Ni_3S_2 + Co_9S_8 + CoS). As shown in Figures 139d and e, a relatively large amount of Mo species was also present in the as-sulfidized sample. Moreover, the authors also found that there were no obvious peaks in the Co 2p XPS spectrum of the as-sulfidized sample. Accordingly, it is worth mentioning that the dominant transition metal species in the final product are Ni and Mo. Additionally, the hydrothermal sulfurization dramatically increased the electrochemical C_{dl} value of the product (63 → 263 $mF{\cdot}cm^{-2}$ before and after sulfurization, respectively). A similar result was also found by Yan and co-workers, who used an electrodeposition-hydrothermal sulfurization approach to synthesize NiCoS and CoS_x nanorod-array films on Ni foam.[641] Relatively high C_{dl} values were observed for both the NiCoS and CoS_x films at 154 and 69 $mF{\cdot}cm^{-2}$, respectively, just as was observed for the NiCoS nanorod arrays on Ni foam prepared by Dong *et al.* These reports demonstrate that electrodeposition can be used to prepare precursor films for subsequent sulfurization to produce high surface area, self-supported metal sulfide electrodes for OER electrocatalysis.

So far, we have discussed the use of electrodeposition in one- and two-step sulfide film fabrication. Here, we introduce one example in which the electrodeposition can also act as a postsynthetic treatment for modification of the metal sulfide electrocatalyst surface for efficient OER electrolysis. Shang *et al.* modified the surface of V-doped nickel sulfide (Ni_3S_2 and NiS) nanowires hydrothermally grown on Ni foam (NiVS/NF) by electrodeposition.[726] Specifically, the authors electrodeposited an ultrathin Fe hydroxide film on the NiVS/NF surface (eFe/NiVS/NF) (see Figure 140a). This ultrathin Fe hydroxide film acts as a passivation layer that protects the NiVS from oxidation during the OER and, with it, as a highly active species for the OER. In addition, this ultrathin layer leads to an increase in the electrode surface area. For the electrodeposition of the ultrathin Fe film, a standard three-electrode system [WE: NiVS/NF; CE: Pt foil; RE: Ag/AgCl (saturated KCl)] and an aqueous electrolyte containing $Fe(NO_3)_3{\cdot}9H_2O$ were used. The electrodeposition of Fe hydroxides on the NiVS/NF was performed at a constant applied potential of $-1.0\ V_{Ag/AgCl}$ for 30 s. For comparison, Fe hydroxides were also deposited on the NiVS/NF surface through ultrafast chemical deposition (uFe/NiVS/NF), in which the NiVS/NF was soaked in a preheated aqueous solution (at 100 °C) containing $Fe(NO_3)_3{\cdot}9H_2O$ and NaCl for

https://doi.org/10.1021/acs.chemrev.3c00005
Chem. Rev. 2023, 123, 12795−13208

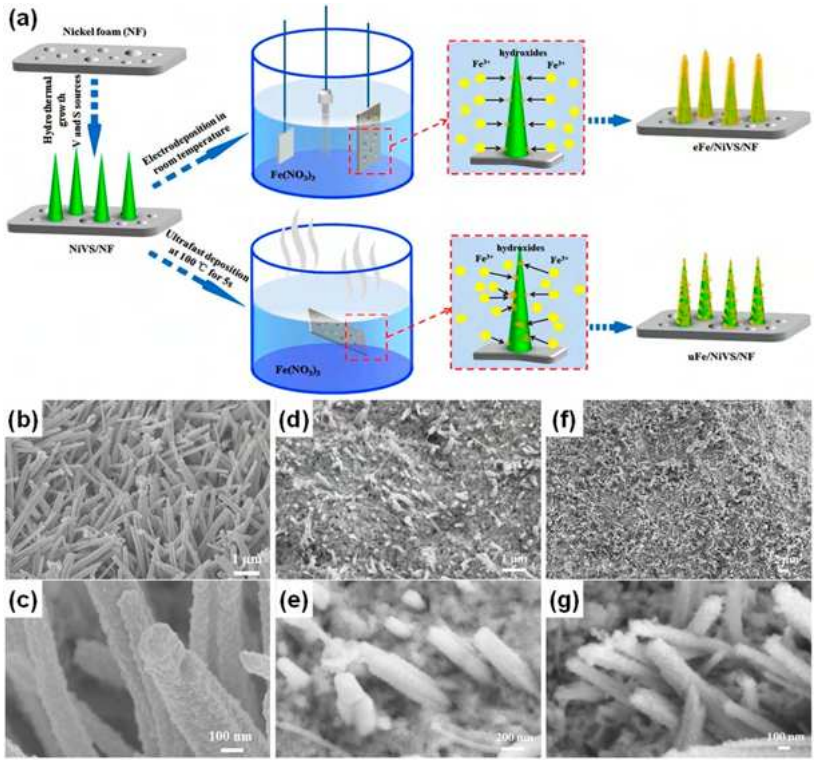


Figure 140. (a) Schematic illustration for the fabrication of Fe hydroxide-decollated NiVS/NF samples through electrodeposition (eFe/NiVS/NF) and ultrafast chemical deposition (uFe/NiVS/NF). (b–g) SEM images of the (b, c) NiVS/NF, (d, e) eFe/NiVS/NF, and (f, g) uFe/NiVS/NF. Reprinted with permission from ref 726. Copyright 2017 Elsevier.

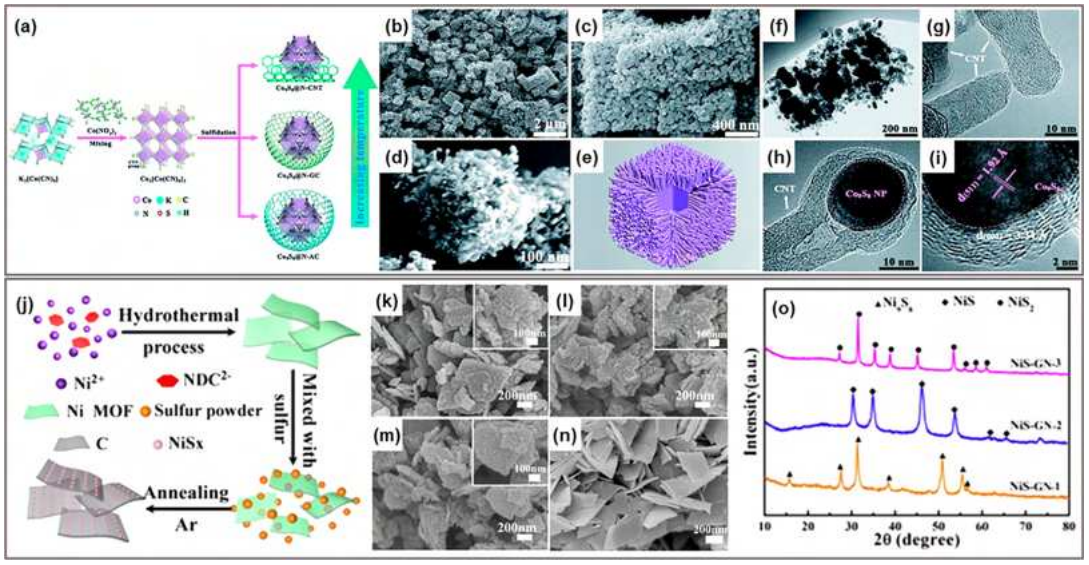


Figure 141. Preparation and characterization of MOF-derived metal sulfides embedded in a carbon matrix. (a) Schematic of the preparation of Co_9S_8@NC. (b–d) SEM images, (e) visual representation, and (f) TEM and (g–i) HRTEM images of Co_9S_8@NC-700. Reprinted with permission from ref 719. Copyright 2018 Royal Society of Chemistry. (j) Schematic of the preparation method for NiS-GN. (k–n) SEM images of (k) NiS-GN-1, (l) NiS-GN-2, (m) NiS-GN-3, and (n) Ni-MOF precursor. (o) XRD patterns of NiS-GN-1, -2, and -3. Reprinted with permission from ref 674. Copyright 2019 Elsevier.

5 s (see Figure 140a). Figures 140b–g show the SEM images of the as-prepared NiVS/NF, eFe/NiVS/NF, and uFe/NiVS/NF. As seen in Figures 140b and c, the NiVS/NF was composed of nanowire arrays with average diameters of 100–300 nm on its surface. For both the eFe/NiVS/NF and uFe/NiVS/NF samples, the initial surface morphology was somewhat maintained even after Fe hydroxide-deposition, and only a slight decrease in the number of the nanowire arrays was observed (see Figures 140d and f). The nanowire surfaces were covered with nanosheets containing pores and voids as a result of the deposition of Fe hydroxides (Figures 140e and g). In comparing the electrodeposition and chemical deposition methods for the Fe-hydroxide step, it is evident that incomplete coverage of Fe hydroxides occurred for uFe/

https://doi.org/10.1021/acs.chemrev.3c00005
Chem. Rev. 2023, 123, 12795–13208

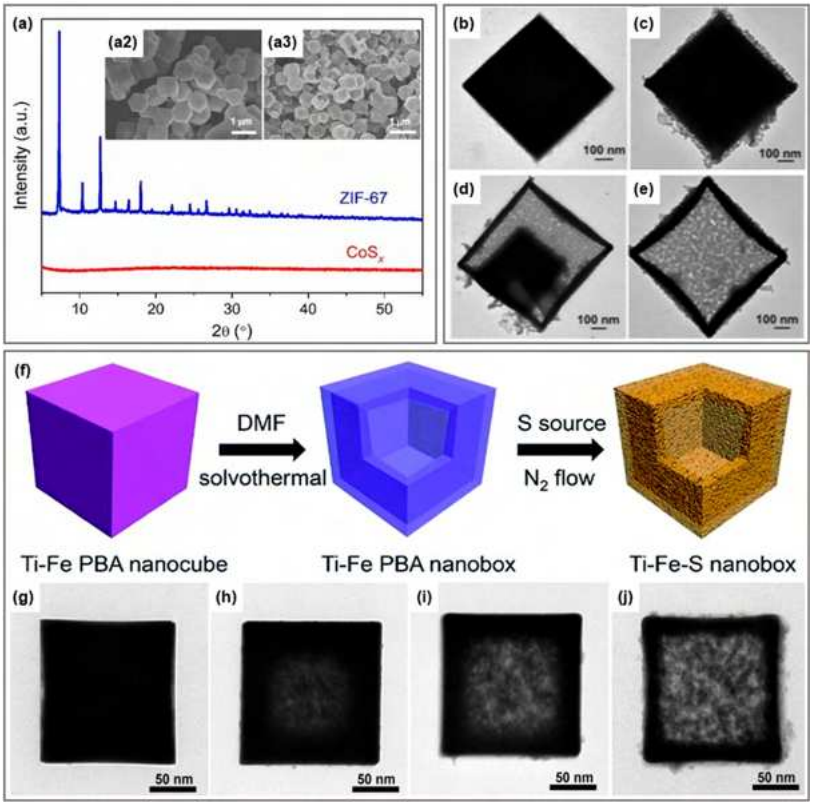


Figure 142. MOF-derived metal sulfides-hollow structures. (a) XRD pattern of ZIF-67 precursor and prepared amorphous CoS_x. SEM images of the ZIF-67 precursor (a2) before and (a3) after the hydrothermal process. Reprinted with permission from ref 705. Copyright 2018 American Chemical Society. (b–e) CoS hollow structure generation after (b) 0, (c) 5, (d) 20, and (e) 120 min of the reaction of a ZIF-67 nanocube precursor with thioacetamide. Reprinted with permission from ref 886. Copyright 2016 Elsevier. (f) Schematic of the synthesis of Ti-Fe-S nanoboxes. (g–j) Conversion of Ti-Fe PBA nanocubes to Ti-Fe PBA nanoboxes after (g) 0, (h) 6, (i) 15, and (j) 21 h of the solvothermal process. Reprinted with permission from ref 712. Copyright 2018 Royal Society of Chemistry.

NiVS/NF while complete coverage was observed for eFe/NiVS/NF. Due to the more uniformly distributed Fe hydroxides on the eFe/NiVS/NF surface, it is unsurprising that this sample had a higher C_{dl} value of 18.2 mF·cm^{-2} than those of NiVS/NF (10.1 mF·cm^{-2}) and uFe/NiVS/NF (12.4 mF·cm^{-2}). Thus, this report highlights that the electrodeposition method can be a more efficient means to generate a uniform Fe hydroxide film on an electrode surface, which may be useful for application to other types of metal sulfides and metal chalcogenide electrocatalysts as well.

5.1.1.4. MOF-Derived Methods. Metal-organic frameworks (MOFs) can act as sacrificial templates for the preparation of porous metal sulfides for the OER.[884] A typical MOF-derived synthesis of a metal sulfide involves the preparation of the MOF, sulfurization of the MOF, and thermal treatment. The sulfurization step is performed either before or during the thermal treatment step (Figures 141a and j). Following thermal treatment, a material consisting of metal nanoparticles and/or dopants embedded within a carbon matrix is produced (Figures 141d, f–i, and k–m). The MOFs used to prepare these materials are most often zeolitic imidazolate frameworks (ZIFs) or Prussian blue analogs (PBAs). ZIFs and PBAs are popular MOF precursor templates because of their high thermal stability, chemical stability, surface area, and intrinsic porous structure.[885] The resulting material prepared from such MOF precursors and a sulfur source is often reminiscent of the MOF precursor itself, as shown in Figure 141n, in which an SEM image of a Ni-MOF precursor is compared to its sulfurized and annealed counterparts (Figure 141k–m). For this reason, MOF-based metal sulfide preparation is advantageous, as greater control over catalyst morphology/structure and improved material reproducibility can be attained via MOF templates.

Metal sulfide/carbon composites are the most common materials that result from MOF-derived metal sulfide syntheses. These composites result because, upon heating, the carbon component of the MOF will thermally decompose.[719,814,834] The extent of thermal decomposition can vary with temperature, as Chen and co-workers have demonstrated using their MOF-derived cobalt sulfide electrocatalysts. Following the preparation of their MOF, cobalt-PBA, the MOF was combined with sulfur powder (1:0.5 weight ratio) and heated to 300 °C at a ramping rate of 1 °C·min^{-1} for 30 min. The temperature was then ramped to either 500, 600, 700, 800, or 900 °C at a ramping rate of 3 °C·min^{-1} and held at that temperature for 2 h under a 5% H_2 and 95% Ar atmosphere. As the pyrolysis temperature was increased from 500 to 800 °C, the initial morphology of the Co-PBA precursor became less and less recognizable. At 900 °C, the original morphology of the Co-PBA precursor completely decomposed to form agglomerates.[719] Thus, the degree of decomposition can be easily tuned via pyrolysis temperature. When taking their sample prepped at 700 °C, Co_9S_8@NC-700, as an example case, they determined that a hollow, cubic structure was obtained and that Co_9S_8 nanoparticles were encapsulated in the carbon nanotubes (CNTs) characteristic of

https://doi.org/10.1021/acs.chemrev.3c00005
Chem. Rev. 2023, 123, 12795–13208

the surface of the material as determined from SEM, TEM, and HRTEM images (Figures 141b–d and f–i). HRTEM results confirmed that Co_9S_8 nanoparticles were encapsulated within the CNTs given the presence of lattice fringes corresponding to the (511) lattice plane of Co_9S_8 and the (002) lattice plane of graphite (Figure 141i). Elemental mapping results also showed a homogeneous distribution of Co, S, C, and N within Co_9S_8@NC-700, likely due to the use of the MOF precursor for the preparation of the material. Thus, by using a MOF-precursor and a certain pyrolysis temperature, the structure of the electrocatalyst can be controlled. When preparing their nickel sulfide@graphite nanosheet (NiS-GN) composites using a similar preparation method, Ma and co-workers achieved similar results and also showed how the ratio of precursor MOF to sulfur source could tune the final electrocatalyst composition (Figure 141j).[674] They mixed their prepared Ni-based MOF precursor with sulfur powder and annealed the mixture at 600 °C for 1 h under Ar at different mass ratios of 1:0.5, 1:1, and 1:2. As a result, they produced Ni_9S_8 NPs (NiS-GN-1), NiS NPs (NiS-GN-2), and NiS_2 NPs (NiS-GN-3) embedded in carbon, respectively, as confirmed by XRD (Figure 141o). Additionally, SEM images revealed that each catalyst retained the flake-like morphology of the original MOF (Figure 141n) with the addition of nanoparticles on the surface of the flakes (Figures 141k–m). TEM confirmed the presence of NPs within the carbon matrix, and Raman results indicated that graphitic carbon was present in excess given the G-band was higher in intensity than the D-band. Thus, in addition to attaining more reproducible material morphologies and porous structures, another advantage of MOF-based synthesis is the ability to tune the final electrocatalyst composition from precursor ratios.

MOF-derived synthesis has been extensively used to prepare metal sulfide nanoboxes, nanocubes, nanocages, hollow structures such as polyhedral, and amorphous materials, to name a few.[460,705,712,778,834] For the preparation of these materials, the initial pristine MOF structure is sacrificed to prepare a metal sulfide that preserves some of the MOF structure as aforementioned. Fan and co-workers were able to prepare amorphous CoS_x on nitrogen-doped graphene foam (NGF) by first preparing ZIF-67 on NGF, mixing the composite with 30 mg of thioacetamide (sulfur source) in 30 mL of ethanol for 6 h, and then carrying out a hydrothermal process to convert ZIF-67/NGF to CoS_x/NGF. The final material retained the rhombic dodecahedral shape of the ZIF-67 precursor while also becoming completely hollow and void of any crystal structure (Figure 142a).[705] Guo *et al.* were also able to convert ZIF-67 to amorphous Co sulfide, specifically ZIF-67 nanocubes to CoS_2 nanoboxes, using thioacetamide as the sulfur source via a simple heat reflux method. As for the previous example, the resulting hollow Co sulfide nanoboxes retained the initial MOF-precursor frame/skeleton.[778] A hollow metal sulfide results in these cases because of the reaction of S^{2-} ions from the sulfur source, thioacetamide, with the metal centers of ZIF-67. As the reaction occurs, the interior of the ZIF-67 breaks down such that metal ions diffuse to the outer edge of the ZIF-67 to react with S^{2-} ions present in the solution.[778,788,886] This hollowing out of the ZIF-67 precursor occurs from the outer edge to the center of the precursor (see Figures 142b–e).[886] In addition to metal sulfides synthesized using ZIF-67 and a sulfur source, metal sulfides prepared using a PBA precursor and a sulfur source also experience this hollowing out effect. For instance, Ti-Fe sulfide nanoboxes have been prepared via a two-step process using a MOF precursor (Figure 142f).[712] In the first step, Ti-Fe PBA nanocubes were converted to Ti-Fe PBA nanoboxes via a solvothermal process in DMF. The conversion of the Ti-Fe PBA nanocubes to hollow Ti-Fe PBA nanoboxes occurred from the inside-out, as shown in the TEM images taken at different times during the solvothermal process (Figures 142g–j). This hollowing process was surmised to be the result of a weak PBA center and etching from ammonia species generated from DMF decomposition that occurred during the solvothermal process. In the second step, the Ti-Fe PBA nanoboxes and thiourea powder, the sulfur source, were annealed in a tube furnace at 350 °C for 2 h at a heating rate of 2 °C·min^{-1} under nitrogen to produce Ti-Fe sulfide nanoboxes. Thus, MOF-derived synthesis of metal sulfides opens up a multitude of possibilities for controlled synthesis of metal sulfides with specific morphologies and structures.

As made notable by the previous example, MOF-derived synthesis has been used to prepare bimetallic sulfides in addition to nonmetallic sulfides. MOF-derived synthesis of bimetal sulfides is favorable, as it offers a means by which to prepare electrocatalysts with dispersed bimetal centers. The MOFs used for the synthesis of bimetallic sulfides either contain more than one metal center initially or began as a monometallic MOF that undergoes postsynthetic metal exchange.[460,712,788,816,834,846,887] For example, Ganesan and co-workers prepared $Ni_{3.5}Co_{5.5}S_8$ hollow nanocrystals from a Co-ZIF MOF. First, a Co-ZIF (60 mg) was mixed with $Ni(NO_3)_2{\cdot}6H_2O$ (0.4 mmol) in ethanol and heated at 90 °C for 1 h in a Teflon-lined stainless-steel autoclave to obtain Co_ZIF@Ni-LDH crystals. Following centrifugation, cooling, washing, and drying steps, the Co_ZIF@Ni-LDH crystals were sonicated in ethanol with thioacetamide and, once again, a Teflon-lined stainless-steel autoclave was used. The mixture was heated at 100 °C for 2 h in the autoclave to complete the sulfurization process. Then, the resulting sample was annealed at 500 °C under a N_2 atmosphere for 2 h to produce $Ni_{3.5}Co_{5.5}S_8$ nanosheet assembled hollow nanocages (NAHNs) (Figure 143a).[834] The XRD pattern of the MOF-derived synthesized Co_9S_8 hollow nanocages (HNs) was nearly

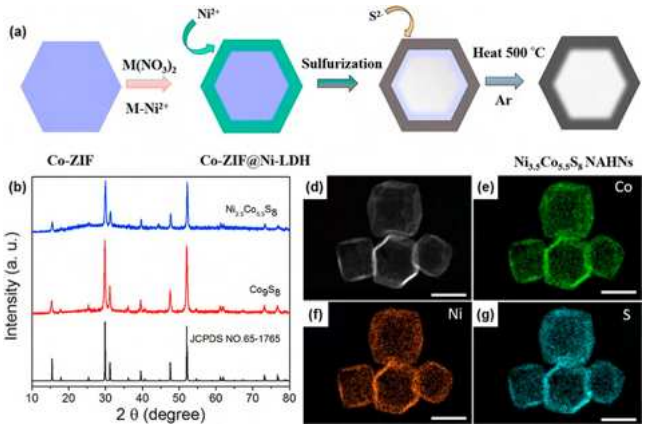


Figure 143. Preparation and characterization of $Ni_{3.5}Co_{5.5}S_8$ NAHNs from a ZIF. (a) Schematic of the material preparation procedure. (b) XRD patterns of Co_9S_8 HNs and $Ni_{3.5}Co_{5.5}S_8$ NAHNs. (d–g) STEM-EDX elemental mapping images of $Ni_{3.5}Co_{5.5}S_8$ NAHNs. All scale bars are 500 nm. Reprinted with permission from ref 834. Copyright 2017 Elsevier.

https://doi.org/10.1021/acs.chemrev.3c00005
Chem. Rev. 2023, 123, 12795–13208

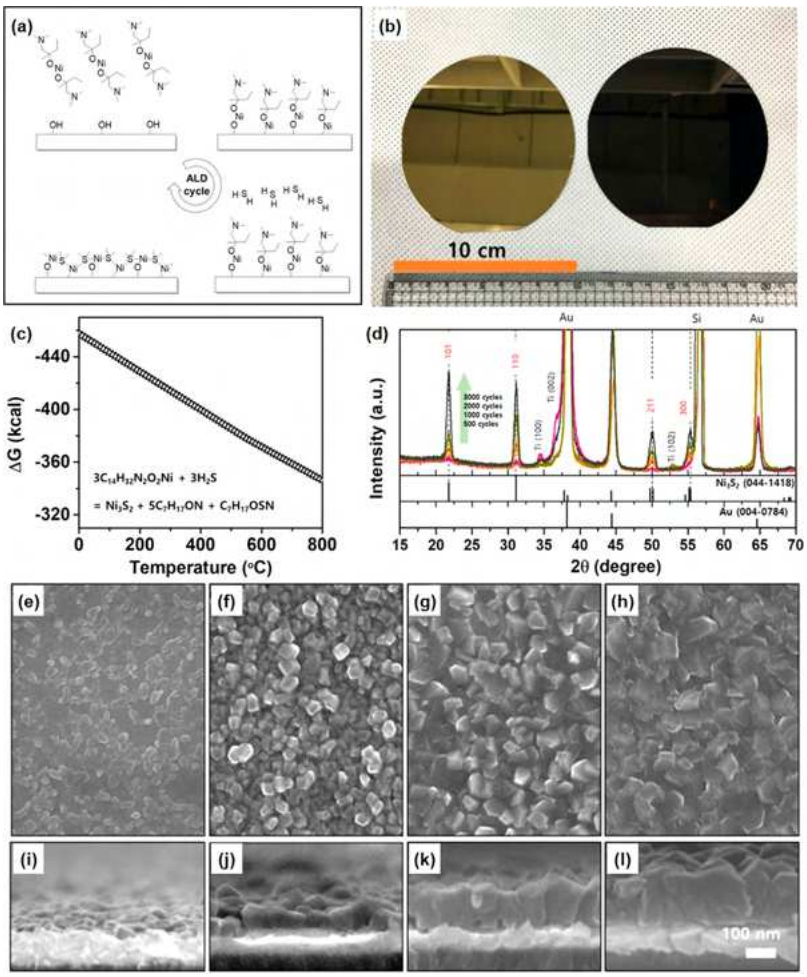


Figure 144. Atomic layer deposition (ALD) of Ni sulfide film. (a) ALD cycling steps. (b) Au/Si wafer before (left) and after 2000 ALD cycles (right). (c) Gibbs free energy of reaction with respect to temperature. (d) XRD patterns of the materials deposited with 500, 1000, 2000, and 3000 ALD cycles. (e–l) SEM planar and cross-sectional images of the samples after (e, i) 500, (f, j) 1000, (g, k) 2000, and (h, l) 3000 ALD cycles. Reprinted with permission from ref 717. Copyright 2018 American Chemical Society.

identical to that of Co_9S_8, indicating that Ni^{2+} was evenly dispersed throughout the material, as confirmed by elemental mapping (Figures 143b–f). The MOF-based synthesis of the $Ni_{3.5}Co_{5.5}S_8$ NAHNs enabled the even distribution of an additional metal within the original MOF, while also maintaining the initial crystal structure and morphology.

Multiple metals have also been incorporated using MOF-derived methods to prepare composite sulfide materials.[273,274,816,818] Using this method for composite synthesis of metal sulfides has been shown to provide an improved degree of synergism via the incorporation of multiple metals. A $Zn_{0.8}Co_{0.2}S/Co_9S_8$ electrocatalyst on C, prepared from a Zn-Co-ZIF precursor and S powder (1:2) heated to 300 °C in a tube furnace at 2 °C·min^{-1} and held for 1 h, demonstrated superior OER performance to a physical mixture of Co_9S_8 and $Zn_{0.8}Co_{0.2}S$ prepared via hand-milling. The MOF-derived $Zn_{0.8}Co_{0.2}S/Co_9S_8$ on C achieved an overpotential of 292 mV, whereas its physically mixed counterpart only achieved 337 mV at 10 mA·cm^{-2}.[816] It has also been shown that when incorporating MOF-derived synthesis with 2D materials, issues that plague MOF-derived metal sulfides such as material aggregation and a reduction in conductivity following electrocatalysis can be overcome.[888] This integration of a 2D material and a MOF-derived metal sulfide was used by Zou and co-workers to prepare their NiCoS/$Ti_3C_2T_x$ nanosheets. First, they prepared their few-layer MXene $Ti_3C_2T_x$ nanosheets by etching Ti_3AlC_2 with HF and then delaminating under nitrogen using dimethyl sulfoxide. Second, they integrated ZIF-67 onto the $Ti_3C_2T_x$ nanosheets by dispersing 0.1 g of the nanosheets into a 0.1 M $Co(NO_3)_2{\cdot}6H_2O$ solution, incorporating 2-methylimidazole, and then stirring for 30 min at room temperature followed by washing steps. The resulting ZIF-67/$Ti_3C_2T_x$ was then converted to NiCo-LDH/$Ti_3C_2T_x$ via stirring in 20 mL of ethanol and then stirring in a solution of $Ni(NO_3)_2$ in ethanol followed by washing steps. Sulfurization to obtain NiCoS/$Ti_3C_2T_x$ was then carried out by heating the material to 400 °C for 2 h (ramping rate of 3 °C·min^{-1}) under CS_2 gas in a tube furnace. As in previous cases, they observed that the overall porous structure was maintained and that all elements were evenly dispersed via SEM, TEM, HRTEM, and elemental mapping results.[274] Thus, MOF-derived synthesis can be used to prepare all sorts of materials, from NPs embedded in a carbon matrix to hybrid structures, while retaining precursor morphology and achieving hollow and/or porous structures with high surface area.

5.1.1.5. Other Methods. In addition to the aforementioned methods for the preparation of transition metal sulfides, there

https://doi.org/10.1021/acs.chemrev.3c00005
Chem. Rev. 2023, 123, 12795–13208

also exist less frequently used and more unique methods that will be described herein.

5.1.1.5.1. Chemical Vapor Deposition. Chemical vapor deposition is a synthetic method used for the preparation of thin films via the reaction of gases on the surface of a substrate. This method has many advantages, as it results in more uniform films than physical vapor deposition, high-vacuum levels are not required, and contamination is rare, as reactants can be flowed into the deposition chamber. Despite the promise of uniformity and high-quality material synthesis, however, CVD and a subclass of CVD, atomic layer deposition (ALD), have rarely been employed to make metal sulfides for OER electrocatalysis.[717,783]

The use of CVD and ALD is uncommon for metal sulfide synthesis, as they often entail the use of dangerous reactants and high temperatures.[889] Nevertheless, there are reports of the successful preparation of metal sulfides using these methods. For example, Ho and co-workers have prepared Ni_3S_2 thin films via ALD using bis(1-dimethylamino-2-methyl-2-butoxy) nickel(II) [$Ni(dmamb)_2$] and H_2S as precursors and N_2 as the carrier gas. This technique works by introducing reactive precursors, which are $Ni(dmamb)_2$ and H_2S in this case, to a substrate sequentially to create a layer on its surface. Multiple layers can be formed via ALD cycling, resulting in a thin film with nanometers in thickness. Ho *et al.* performed this process by exposing their substrate to the aforementioned precursors in pulses, with $Ni(dmamb)_2$ being introduced to the substrate's surface first, followed by H_2S (Figure 144a). Between each precursor exposure, N_2 gas was used to remove any unreactive vapors at the substrate's surface. The pulsing time of each gas was controlled by high-temperature pneumatic valves (3 and 0.2 s pulses followed by 10 s of purging N_2 gas at a flow rate of 200 sccm). The Ni source, $Ni(dmamb)_2$, was stored in a canister at 60 °C before use, and all depositions were carried out at 250 °C. Various substrates were also used, including Au on SiO_2/Si wafer, SiO_2/Si wafer, Ni foam, carbon paper, and carbon cloth.[717] Gibbs free energy calculations (Figure 144c) confirmed that the precursors would react to produce Ni_3S_2, as it was determined to be a spontaneous process with a Gibbs free energy of −421.78 kcal at 250 °C. Inspection of the Au/Si wafer substrate after 2000 ALD cycles indicated that a thin film had formed at the surface (Figure 144b). Initial characterization of the material also confirmed that a Ni_3S_2 thin film was formed. Figure 144d shows the XRD patterns after 500, 1000, 2000, and 3000 ALD cycles. From these diffraction patterns, it is clear that, with increasing ALD cycling number, the crystalline Ni_3S_2 phase is present. The additional gold peaks in each diffraction pattern are expected given the Au/Si wafer used as the ALD substrate. From SEM images, the formation of the Ni_3S_2 film is also apparent. As the ALD cycling number increased from 500 to 3000, the film became denser, as depicted in the planar SEM images, and wider, as shown in the cross-sectional SEM images (Figure 144e–l). Given that ALD offers high control over both electrocatalyst uniformity and chemical makeup, it comes as no surprise that uniform Ni_3S_2 thin films were prepared. ALD is a favorable synthesis method for metal sulfide preparation, as it entails a higher degree of reproducibility in comparison to other methods.

5.1.1.5.2. Anion Exchange Reactions. Another unique synthesis method that has been used to prepare metal sulfides is the anion exchange method. In this method, an oxygen-containing precursor and a sulfur source are mixed at low temperature and, just as the method implies, the oxygen anion in the oxygen-containing precursor is exchanged with the sulfur anion from the sulfur source to produce a metal sulfide. This method has many advantages, including low-temperature synthesis (below 200 °C) and retention of the initial oxygen-containing precursor's morphology. Gao and co-workers used this method to prepare a Co sulfide aerogel for water oxidation. For the anion-exchange process, they used cobalt nitrate hexahydrate and thioacetamide as their precursors.[817] First, a cobalt nitrate hexahydrate solution and a citric acid solution in ethanol were prepared. The solutions were then mixed in a 1:2 ratio of Co solution to citric acid solution and formamide was added at 5% volume. Citric acid was used as the accelerator for gel formation. The resulting gel was then submerged in a thioacetamide/ethanol/H_2O solution for 3 days, with the solution being replaced every 12 h for anion exchange to occur. Additionally, supercritical drying was performed in an autoclave to complete the metal sulfide aerogel synthesis. This supercritical drying step was completed to avoid loss of aerogel porous structure. One of the main advantages for the use of anion exchange to develop a metal sulfide aerogel is that a highly porous material with large surface area could be produced at relatively low temperature, making it a less intensive strategy to prepare a metal sulfide for OER electrocatalysis.

Another advantage of the anion exchange method is that it can be used with a completely aqueous system for the preparation of metal sulfides for the OER. Zuo and co-workers demonstrated this advantage by growing CuS_2 nanowires on copper mesh (CM). First, $Cu(OH)_2$ nanowires were grown on the CM by taking a cleaned CM piece and immersing it into an aqueous NaOH (40 mmol) and ammonium persulfate (APS) (2 mmol) solution. The CM was immersed for 30 min and then transformed into CuS_2 nanowires on CM via anion exchange by immersing the $Co(OH)_2$/CM material into an aqueous Na_2S solution (0.1 M) for 1 h at 60 °C. The conversion of the material was clear upon visual inspection, as the greenish-blue $Co(OH)_2$/CM became black following the anion exchange/sulfurization step. XRD, EDX, TEM, and EELS also confirmed this transformation.[672] Thus, metal sulfides can be prepared facilely using aqueous-based solutions via anion exchange in a short amount of time.

5.1.1.5.3. Solid-State Reactions. Solid-state reactions provide a means by which to prepare metal sulfides with high crystallinity without the use of solvent. For example, Sivanantham and co-workers used this method, specifically solvent- and catalyst-free auto-pressurized (Swagelok) solid-state thermolysis to prepare core@shell Co_9S_8@nanocarbon (NC). To synthesize the Co sulfide, a Co-PBA precursor and sulfur powder were physically mixed in a 2:1 ratio and then placed into a Swagelok cell for solid-state thermolysis. The cell was heated to 500 °C at 2 °C·min^{-1} and held at 500 °C for 3 h. Their solvent-free solid-state method involved only one step while also being more facile than other methods. It also avoids the use of toxic solvents and high temperatures that are often required for ion-exchange synthesis methods.[682] Solid-state methods should be explored further given Sivanantham *et al.*'s work as the solid state reaction method could make metal sulfide synthesis more practical for large-scale industrial applications given the reduction in steps, simple procedure, and less extreme safety hazards as compared to other synthetic routes.

https://doi.org/10.1021/acs.chemrev.3c00005
Chem. Rev. 2023, 123, 12795−13208

In addition, solid-state reactions have been employed for the preparation of the less common transition metal sulfides, gallium sulfide and germanium sulfide. To synthesize gallium sulfide via this method, glass ampules were prepared via hydrofluoric acid, DI water, and acetone washing steps. These ampules were also further purified using an oxygen-hydrogen torch under pressure before being filled with a mixture of gallium and selenium. Once the tube was filled, it was evacuated to less than 5 mPa. An oxygen-hydrogen torch was then used and the ampule was heated to 970 °C for 1 h and then cooled. The germanium sulfide was prepared similarly, with gallium being replaced by germanium and a different heating process. The mixture of germanium and sulfur in the ampule was only heated to 700 °C and held there for 5 h.[853] This temperature was used, as germanium sulfide should theoretically melt at 667 °C. All heating and cooling steps were carried out at a ramping rate of 1 °C·min^{-1}. The resulting gallium and germanium sulfides were highly crystalline and had to be ground down before testing for the OER.

5.1.1.5.4. Fast Annealing Methods. Solid-state-like reactions, incorporating a solid and a liquid, have also been used to prepare metal sulfides, specifically Ni_3S_2/NF films. To prepare these Ni_3S_2/NF films, Ni foam (NF) was first soaked in HCl (3 M) to remove surface oxides and washed with DI water and ethanol. The as-cleaned Ni foam was then dried under vacuum and, once dry, the Ni foam was covered in a 2-mercaptoethanol solution and annealed at 300 °C using a hot plate for 50 s under a nitrogen atmosphere. The entire synthesis was carried out in a glovebox. The steps of this synthesis process are outlined in Figure 145a.[708] Unlike other

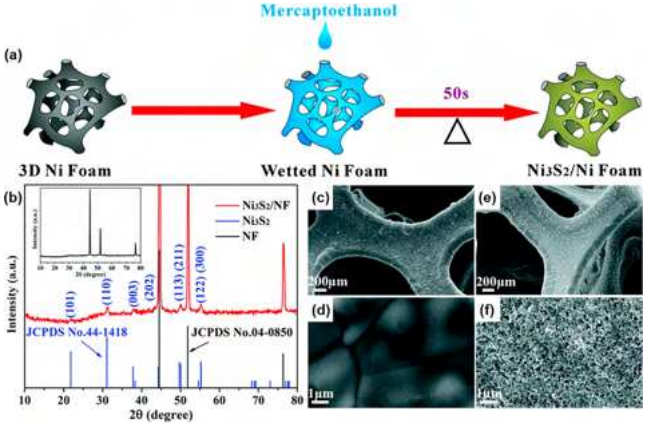


Figure 145. Preparation and characterization of Ni_3S_2 film. (a) Schematic of the fast annealing method for the synthesis of Ni_3S_2 film. (b) XRD pattern of prepared Ni_3S_2 film at high magnification (low magnification in inset). (c–f) SEM images of (c, d) bare Ni foam (NF) and (e, f) as-prepared Ni_3S_2 film. Reprinted with permission from ref 708. Copyright 2018 Royal Society of Chemistry.

methods where precursor materials are held at high temperatures for several hours, this method has the benefit of ultrafast annealing, cutting down on material processing time. It also avoids the use of hazardous gases such as H_2S, which is often employed in CVD to prepare metal sulfide films (see Section 5.1.1.5.1). Additionally, a highly uniform Ni_3S_2 was produced, as indicated by XRD and SEM images before and after synthesis, which indicates the presence of heazlewoodite Ni_3S_2 and even dispersion of the deposited film across the Ni foam surface (Figures 145b–f). From Figure 145f, it is also clear that some porosity is present, which could aid in the exposure of active sites and help combat mass transport limitations. TEM images not shown here revealed that this film was made up of Ni_3S_2 nanoparticles dozens of nanometers in size. Thus, using this method, uniform metal sulfide films could be prepared *in situ* in little time with less expertise on behalf of the researcher and with less potential exposure to highly toxic vapors.

5.1.1.5.5. Gas-Solid Reactions. Gas-solid reactions have been employed for the preparation of metal sulfides on Ni foam (NF) for water oxidation. For example, Lee and co-workers exposed Ni foam to H_2S gas (1% H_2S with nitrogen carrier gas) in a tube furnace at 300 °C for 1 h to prepare a H_2S_NF electrode.[718] The Ni foam was cleaned via sonication in ethanol and water and dried before the preparation of the electrode. Cheng *et al.* used a similar method to prepare their Fe^0-Ni_xS_y/NF electrocatalyst by dipping acid-treated Ni foam into an iron nitrate solution and drying at room temperature to produce a Fe/Ni foam. The Fe/Ni foam was then sulfurized using sulfur powder in a quartz tube heated to 300 °C for 1 h to produce Fe^0-Ni_xS_y/NF, which consisted of 33 nm thick and 400 nm long Fe^0-Ni_xS_y nanosheets across the Ni foam surface, as determined from SEM images (not shown here).[696] In both of these cases, sulfurization was completed in one step using a gas-solid reaction, with Lee *et al.* preparing their H_2S_NF in one step altogether. Gas-solid reactions enable the preparation of electrocatalysts using minimal steps, making it a less laborious method for the synthesis of metal sulfides.

5.1.1.5.6. Ball Milling Methods. Ball milling methods have been used for the preparation of metal sulfides via mechanical alloying and via the combination of the method with pyrolysis. In mechanical alloying, ball milling is used to enable the solid-state synthesis of electrocatalysts. For example, Dai and co-workers used mechanical alloying to prepare nanocrystalline NiS for the OER.[724] They combined elemental nickel sulfide powders in a 1:1 ratio to ball milling tanks (powder:ball ratio at 1:20). Argon was flown through the tanks to prevent oxidation, and rotation was set to 250 rpm for 60 h. Dai *et al.* were inspired to use mechanical alloying, as it is known to result in a high level of defects in a material, which could positively affect OER electrocatalysis, as it would likely lead to greater surface area and extensive active site exposure.

The combination of ball milling and pyrolysis, two techniques that have been used extensively in material synthesis, has been employed to prepare a bimetal sulfide using protic salt precursors. By combining metal salts, $MoCl_5$ and $NiCl_2$, with the protic salt *p*-phenylenediamine bisulfate ([PDA][2HSO$_4$]), a precursor rich in S and N, via ball-milling and pyrolysis at 800 °C under nitrogen atmosphere, a N-doped carbon-coated Ni-Mo sulfide (Ni-MoS_2/NC) was produced. Ni-MoS_2/NC resulted because, at 800 °C, the protic salt transformed into a N-doped carbon shell, releasing S from its structure, which reacted with Mo to form MoS_2, as confirmed by XPS results.[794] Thus, the resulting material, Ni-MoS_2/NC, consisted of a Ni-MoS_2 core covered by a N-doped carbon shell, which could serve as a protective layer against oxidation for the transition metal sulfide core under alkaline conditions at oxidizing potentials. Figure 146 shows the schematic for this synthesis process and an SEM image showcasing the nanosheet material's core@shell structure.

5.1.1.5.7. Microwave-Assisted Methods. Microwave-assisted synthesis has been used extensively for the preparation of metal oxides and hydroxides for energy storage applications, as it allows for fast and selective heating, is easy to use, and is

https://doi.org/10.1021/acs.chemrev.3c00005
Chem. Rev. 2023, 123, 12795–13208

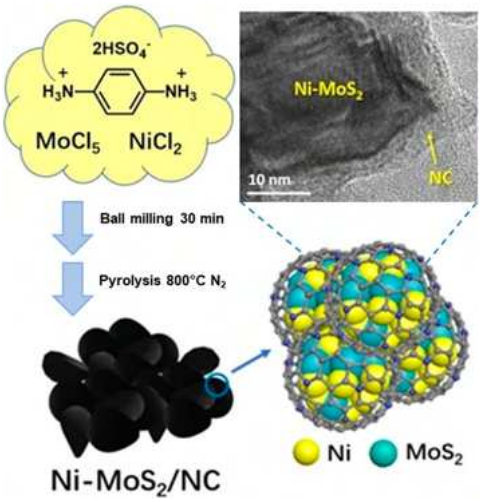


Figure 146. Schematic of Ni-MoS_2/NC preparation and inset SEM image of the prepared electrocatalyst. Reproduced with permission from ref 794. Copyright 2019 Wiley.

cost-effective.[890] It has been used to assist both hydrothermal and solvothermal processes, among other methods, as it provides more even heating, leading to greater crystal uniformity while also enabling a faster heating rate than either process alone. As an example, Souleymen and co-workers enlisted microwave-assisted synthesis for the preparation of Co_9S_8 by using it specifically to prepare a $Co(OH)_2$ precursor.[714] The $Co(OH)_2$ precursor was first prepared by dissolving $Co(NO_3)_2{\cdot}6H_2O$ and CH_4N_2O in DI water/ethylene glycol (1/7) for 1 h to obtain a pink and homogeneous solution. The solution was then transferred to a three-neck round-bottom flask and treated with microwave radiation at 700 W for 15 min while stirring. The result was a puffy, purple colloid precipitate that was cooled to room temperature naturally and obtained via centrifugation and washing with DI water. This puffy, purple substance was the $Co(OH)_2$ precursor with an ultrathin freestanding nanosheet morphology. To prepare the Co_9S_8 electrocatalyst from this precursor, it was first dispersed in ethylene glycol while $Na_2S{\cdot}9H_2O$ was also dissolved in DI water. The $Na_2S{\cdot}9H_2O$ solution (sulfur source) was then added to the $Co(OH)_2$ solution at room temperature. The precipitate was then obtained via centrifugation and washing with DI water, frozen in DI water at 0 °C, and dried by sublimation in a vacuum freeze-drying machine at −60 °C for 24 h. CoS_x was then annealed at 400 °C for 90 min under Ar gas to obtain Co_9S_8.[714] The entire process to obtain the CoS_x sheets prior to annealing is depicted visually in the schematic in Figure 147. By using microwave-assisted synthesis, Souleymen *et al.* were able to prepare a uniform material at low cost, solidifying microwave-assisted synthesis as a well-suited method for the preparation of metal hydroxide precursors for metal sulfide synthesis.

5.1.1.5.8. CO_2-Assisted Methods. Extensive research efforts have been focused on the development of metal sulfides and metal chalcogenides as electrocatalysts more generally, as these materials could make water oxidation and, in turn, overall water splitting a viable form of sustainable energy storage. In addition to keeping this end-goal of more environmentally friendly energy storage in mind, the carbon footprint that results from the preparation of these materials must also be considered, as the energy required for synthesis could detract

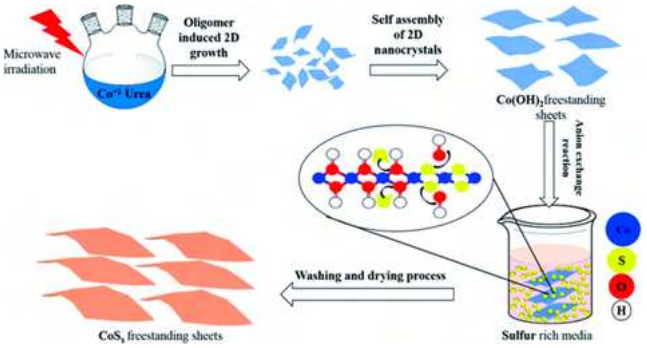


Figure 147. Schematic illustration for the microwave-assisted synthesis of CoS_x freestanding sheets. Reprinted with permission from ref 714. Copyright 2018 Royal Society of Chemistry.

from their use as catalysts for alternative energy storage, especially those requiring high temperatures. Zhao and co-workers were able to develop a synthesis method that could be used in the future as a clean and sustainable route for transition metal sulfide synthesis using compressed CO_2. Specifically, they prepared amorphous Co sulfide using a thiol/amine-based quasi-ionic liquid and CO_2. To generate the quasi-ionic liquid, elemental cobalt and sulfur, in a 1:1 ratio, were dissolved in a 1,2-ethanedithiol/*n*-butylamine (EDT-BA) solution. Compressed CO_2 was then used to produce amorphous CoS_x nanosheets via charging a stainless steel autoclave with CO_2 at 6 MPa using a DB-80 high-pressure syringe pump, reacting for 3 h using magnetic stirring (1100 rpm), and slowly releasing CO_2.[727] The compressed CO_2 enabled cobalt sulfide precipitation from the EDTA-BA solution and control over the catalyst's morphology. Additionally, all procedural steps were carried out under ambient conditions, making this a favorable method for future metal sulfide syntheses and industrial scale-up. This method could become especially viable upon optimization of CO_2 capture, as such CO_2 could be directly funneled into this application and lead to additional green energy processes.

5.1.1.5.9. Salt Template-Assisted Methods. Salt templates offer a facile means by which to generate pores within electrocatalytic materials by combining salt with precursor materials and carrying out pyrolysis at high temperatures. The porous structure is generated because, after cooling the pyrolyzed material, all the salts can be easily flushed away using a simple washing procedure. Given the advantages of highly porous metal sulfides for water oxidation, salt templates have often been used to prepare such materials, especially NaCl.[771,776,828] This salt, NaCl, was used as a template by Wu and co-workers to prepare nitrogen and sulfur-doped carbon nanosheets with Co_9S_8 NPs (Co_9S_8/N,S-CNS).[828] The precursors used were $CoCl_2$ as the Co-source, citric acid as the carbon source, and thiourea as the sulfur source. First, a saturated NaCl solution was prepared using NaCl powder and recrystallization was performed to obtain a reproducible NaCl crystal size via the addition of ethanol to the saturated solution. After filtration and drying of the obtained NaCl crystals, the NaCl crystals (2 g), $CoCl_2{\cdot}6H_2O$ (0.075 g), thiourea (0.1 g), and citric acid (0.05 g) were dissolved in 1 mL of DI water, sonicated for 10 min, and then dried at 80 °C until only powder remained. These powders were then pyrolyzed at 750 °C for 2 h (ramping rate of 5 °C·min^{-1}) under argon. The resulting material was then washed with DI water using sonication and centrifugation to remove the NaCl crystals and

https://doi.org/10.1021/acs.chemrev.3c00005
Chem. Rev. 2023, 123, 12795−13208

dried overnight. The steps for this NaCl-templated pyrolysis method are outlined in the schematic in Figure 148a. From

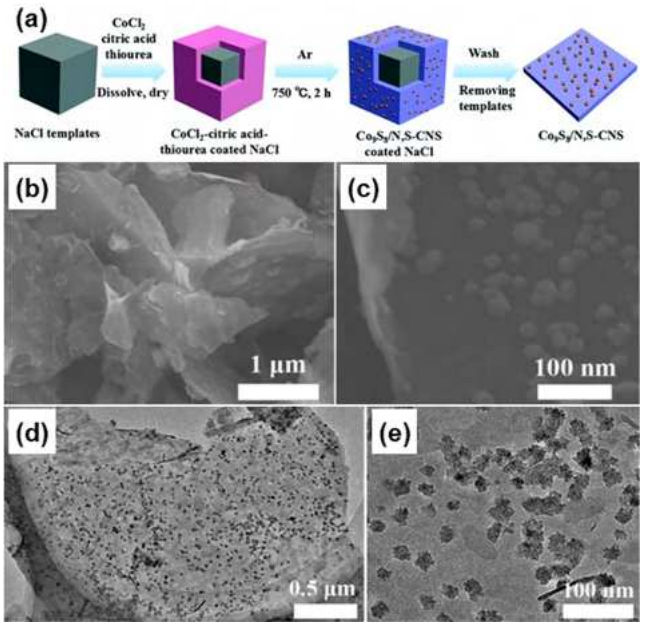


Figure 148. (a) Schematic illustration for NaCl-template-assisted preparation of Co_9S_8/N,S-CNS. (b) Low- and (c) high-magnification SEM and (d) low- and (e) high-magnification TEM images of Co_9S_8/N,S-CNS. Reprinted with permission from ref 828. Copyright 2017 Royal Society of Chemistry.

low- and high-magnification SEM results, it is clear that a nanosheet morphology was obtained with ~25 nm size NPs at the surface of these nanosheets (Figures 148b and c). TEM images also confirmed that Co_9S_8 NPs were present throughout the nanosheets, as shown in Figures 148d and e. HRTEM of a single NP and XRD results indicated that the Co_9S_8 cubic phase was characteristic of the formed NPs. From N_2 adsorption−desorption measurements, the BET surface area was determined to be ~22 $m^2 \cdot g^{-1}$, and from the pore size distribution curve, most of the NPs were around 10 nm in diameter. The hysteresis of the N_2 adsorption−desorption isotherms also indicated the presence of mesopores that were likely generated due to the evolution of gases during pyrolysis.[828] By using salt templates, metal sulfide composites consisting of a porous carbon support and metal sulfide NPs can be prepared given a metal and sulfur precursor are also introduced during pyrolysis. The salt template can then be facilely washed away to produce an electrocatalytic material for the OER. Salts, such as NaCl used here, that are environmentally benign can be used for this synthesis method, making it both simple and more environmentally friendly than other synthesis routes.

5.1.2. Final Types of Sulfide-Based Electrocatalysts. Transition metal sulfides, easily the most studied transition metal chalcogenides for the OER, often fall into one of two categories: catalyst or precatalyst (see Figure 149). Those defined as a catalyst do not undergo any alterations to their morphology or composition during the OER. Precatalysts, on the other hand, undergo either partial or full oxidation during the OER process, resulting in a transition metal sulfide/transition metal oxide/(oxy)hydroxide hetero-interface where the transition metal oxide/(oxy)hydroxide surface can

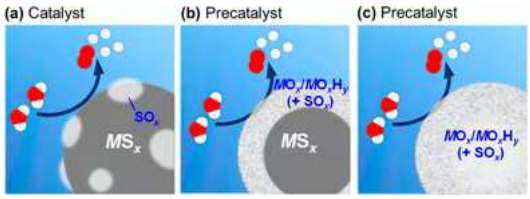


Figure 149. Schematic illustrations of suggested final types of transition metal sulfide-based electrocatalysts after long-term OER testing.

potentially act as the real active site(s) for the OER. Oftentimes, the transition metal sulfides that act as catalysts are those prepared from a transition metal sulfide that has undergone partial oxidation at the surface as a pre-OER testing step. Thus, these catalysts are formed via the oxidation of a transition metal sulfide precursor to produce a transition metal sulfide/transition metal oxide/(oxy)hydroxide interfaced material with the transition metal oxide/(oxy)hydroxide at the surface. There do exist, however, reports of as-prepared transition metal sulfides as catalysts themselves. Nevertheless, the partial/full oxidation of transition metal precatalysts and transition metal sulfide precursors for prepared catalysts almost always results in the formation of an amorphous transition metal (oxy)hydroxide layer and the formation of SO_4^{2-} ions at the surface of the material. While the metal (oxy)hydroxide layer has been explored as the possible real active site of the transition metal sulfides for the OER, the effect of the SO_4^{2-} ions has gone essentially uninvestigated. The role of the SO_4^{2-} ions in both transition metal precatalysts and catalysts remains unknown. The transition metal sulfides prepared for OER electrocatalysis are often crystalline materials, with some instances of amorphous materials being reported. In both of these cases, oxidation of the crystalline and amorphous as-prepared sulfide material has been reported; however, potential differences between the degree of oxidation based on the starting degree of crystallinity have not been thoroughly discussed in a single work. Thus, as in the case of the SO_4^{2-} ions, this area of study for metal sulfides for the OER remains unexplored. In this section, the findings regarding the status of metal sulfides as catalysts or precatalysts are discussed.

5.1.2.1. Catalysts. While the majority of metal sulfide electrocatalysts for the OER are considered to be precatalysts, there are some reports in the literature that indicate metal sulfides may act as catalysts. For instance, three reports on Co sulfide have reported little to no surface modification after long-term OER testing.[635,637,638] For example, Gao *et al.* determined that a Co-based catalyst, Fe-doped Co_9S_8 nanomicrospheres (NM) prepared on Ni foam (NF), was a catalyst after extensive testing and post-OER characterization.[635] Following a 10 h CA test and a 10000 CV cycling test, the nano-microsphere morphology of their material was maintained. XPS results after both stability tests also showed little change to the surface composition of the material. The Co 2p and Fe 2p XPS spectra showed retention of initial metal valence states following long-term OER, as shown in Figures 150a and b. The Ni $2p_{1/2}$ and Ni $2p_{3/2}$ peaks were also retained; however, the intensity of the Ni^0 peak decreased after stability testing, indicating some oxidation of the surface (Figure 150c). The S 2p XPS spectra may also indicate slight oxidation, as there is a decrease in S 2p intensity after both the 10 h CA test and 10000 CV cycling test and a clear increase in SO_4^{2-} peak intensity at least for the 10 h CA test spectrum

https://doi.org/10.1021/acs.chemrev.3c00005
Chem. Rev. 2023, 123, 12795−13208

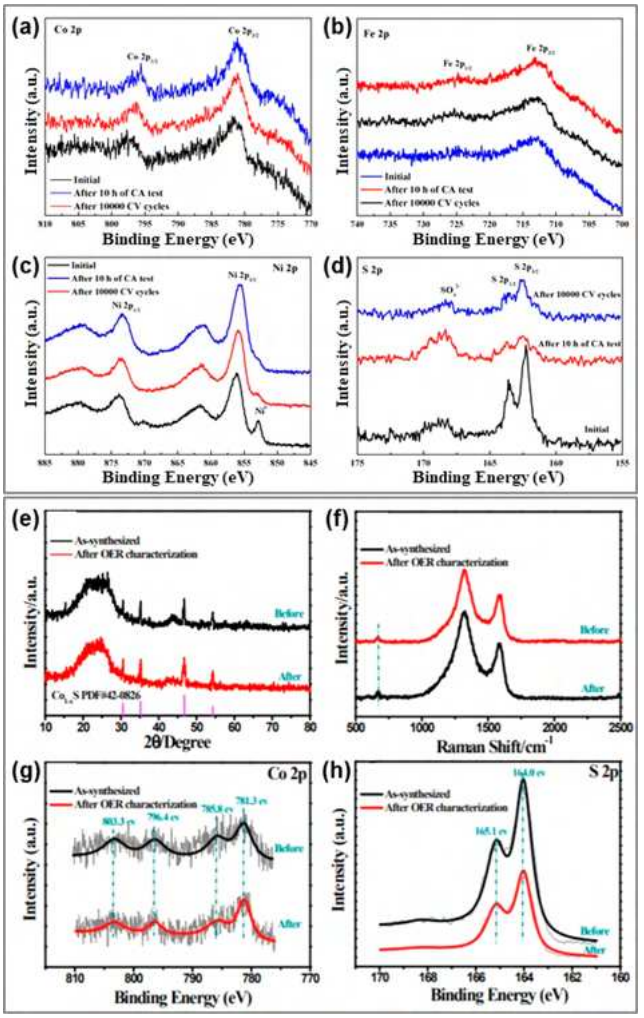


Figure 150. Pre- and post-OER characterization of Co sulfide catalysts. High-resolution (a) Co 2p, (b) Fe 2p, (c) Ni 2p, and (d) S 2p XPS spectra of Fe-doped Co_9S_8 NM before and after the OER. Reprinted with permission from ref 635. Copyright 2018 Elsevier. (e) XRD patterns, (f) Raman spectra, and (g) Co 2p and (h) S 2p XPS spectra of Co sulfide hollow nanospheres in N and S co-doped graphene nanoholes ($Co_{1-x}S$/N-S-G) before and after the OER. Reprinted with permission from ref 638. Copyright 2017 Royal Society of Chemistry.

compared to the initial spectrum (Figure 150d). Compared to other metal sulfides for the OER (see below), their Fe-doped Co_9S_8 NM/NF catalyst appears to experience less surface oxidation and loss of sulfur from the initial material following OER testing. Thus, their material is approaching classification as a catalyst over a precatalyst and their work warrants further investigation with respect to understanding how surface oxidation can be minimized for metal sulfide electrocatalysts.

Qiao and co-workers have reported that their cobalt sulfide hollow nanospheres embedded in nitrogen and sulfur co-doped graphene nanohole ($Co_{1-x}S$/N-S-G) electrocatalyst are completely stable during the OER in an alkaline electrolyte (0.1 M KOH).[638] XPS results from before and after stability testing indicated that there was no loss of the thiophene−S and Co−S bonds at the surface or oxidization of Co (Figures 150g and h). There were also no observable changes in the XRD pattern for the material or Raman spectra before and after the OER (Figures 150e and f). The authors credit the activity and stability of their material to the use of nanohole edges as binding sites for metal nanoparticles. This stability, however, is unexpected given the tendency of Co sulfides and carbon to undergo oxidation at high oxidizing potentials in alkaline media.[613,891,892] Given this unusual finding, further investigation is recommended to verify the stability enhancement of Co sulfide using co-doped carbon-containing nanoholes as a support.

In addition to Co sulfides, there are also reports of Ni-based sulfides as a catalyst for the OER.[639,640] Yuan and co-workers have reported the high stability of a Fe-doped Ni_3S_2 (Fe-Ni_3S_2) catalyst for the OER (see Figure 151a).[639] The Fe-Ni_3S_2 nanosheet arrays were grown on FeNi alloy foil via a one-step solvothermal method. As shown in Figures 151b and c, no binding energy shifts and relative intensity changes were detected in the Ni 2p and Fe 2p XPS spectra following OER testing, which implies the excellent chemical stability of the Fe-Ni_3S_2 catalyst. We assume that this enhanced stability of the as-prepared catalyst could result from (i) its good conductivity, leading to fast electron transport in the material, (ii) the strong catalyst/substrate interaction generated from the *in situ* solvothermal process, facilitating electron transfer during the OER, and (iii) Fe incorporation into Ni_3S_2, increasing the number of active sites and providing more conductive paths to allow much faster electron transport for the OER. The improved electron transport may prevent the accumulation of holes at the Fe-Ni_3S_2 surface and the subsequent surface oxidation during the OER, making the Fe-Ni_3S_2 nanosheet arrays a catalyst instead of the anticipated precatalyst.

Another way in which Ni sulfides have been engineered to enable high stability under harsh OER conditions is via the formation of a protective hydroxide layer. Zou *et al.* demonstrated this case with their Ni-Fe-OH@Ni_3S_2/NF electrocatalysts prepared via the ultrafast growth of Ni-Fe-OH films onto Ni_3S_2 nanosheet arrays on Ni foam (NF).[640] SEM and TEM images of the material before and after the OER indicated little to no change in morphology and microstructure (Figures 152a−d). As shown in Figures 152b and d, the crystal structure of the material went unaltered.

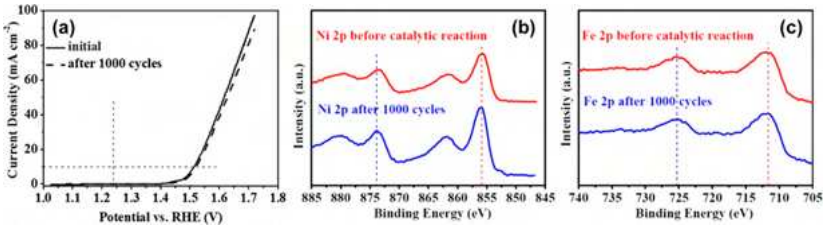


Figure 151. (a) LSV curves of the Fe-Ni_3S_2/FeNi electrode before and after 1000 potential cycles. (b) Ni 2p and (c) Fe 2p XPS spectra of the Fe-Ni_3S_2/FeNi electrode before and after 1000 potential cycles. Reprinted with permission from ref 639. Copyright 2017 Wiley.

https://doi.org/10.1021/acs.chemrev.3c00005
Chem. Rev. 2023, 123, 12795−13208

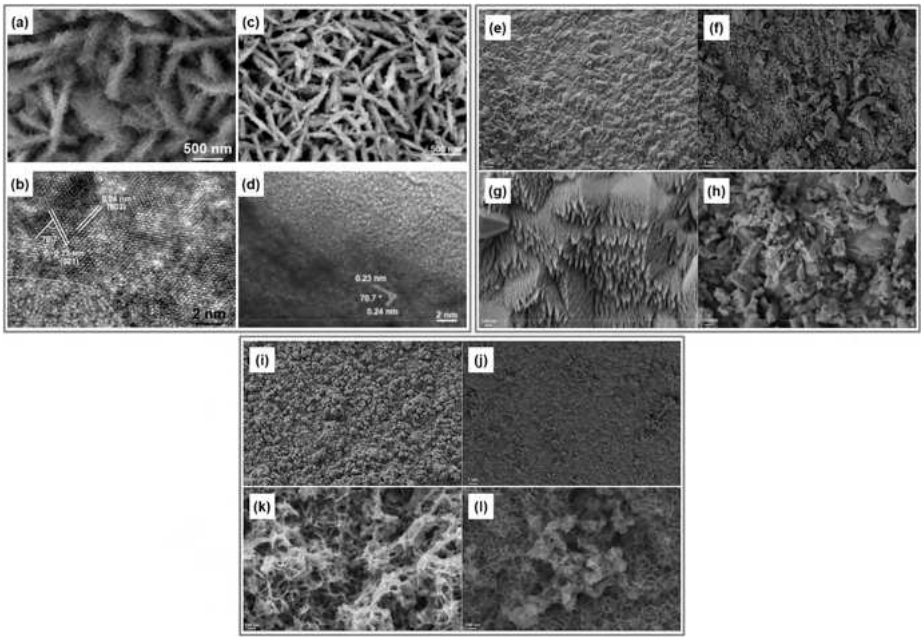


Figure 152. (a, c) SEM images of Ni-Fe-OH@Ni_3S_2/NF (a) before and (c) after OER testing. (b, d) TEM images of Ni-Fe-OH@Ni_3S_2/NF (b) before and (d) after OER testing. Reprinted with permission from ref 640. Copyright 2017 Wiley. (e–h) SEM images of NiFeS/NF (e, g) before and (f, h) after the OER test. (i–l) SEM images of NiFeS-Fe/NF (i, k) before and (j, l) after the OER test. Reprinted with permission from ref 735. Copyright 2016 Royal Society of Chemistry.

From the SEM images in Figures 152a and c, there only appears to be a slight reduction in nanosheet thickness following the OER. Considering that, during the OER, most metal sulfide materials undergo partial oxidation to metal sulfide/metal oxide/(oxy)hydroxide interfaced materials, it stands to reason that metal sulfides oxidized *ex situ* would act as stable catalysts under oxidizing and alkaline conditions, as Zou and co-workers indicate. This concept, however, is called into question by the reduction in nanosheet size, as aforementioned. In another report of a similar material, slight morphological changes were also observed. Specifically, Dong *et al.* found that when Fe hydroxides were incorporated at the surface of their NiFeS/NF precatalyst, denoted as NiFeS-Fe/NF, less dramatic changes in morphology were observed following the OER (Figures 152e–l).[735] While the incorporation of Fe hydroxides did make the as-prepared material less precatalytic, it did not completely stabilize the material. The formation of a metal hydroxide layer for the protection of metal sulfide electrocatalysts, therefore, warrants further study and necessitates optimization. When preparing materials with a protective hydroxide layer, it is recommended that, in addition to electron microscopy techniques, XPS also be used to confirm that no additional surface oxidation has occurred. The slight morphological changes depicted by the SEM and TEM images before and after the OER in Figure 152 could, after all, be the result of the oxidation of the metal hydroxides at the material surface. In addition, XPS results could also ensure that *ex situ*-formed protective layers are, in fact, not subject to oxidation and that materials prepared via this method are true catalysts.

In addition to metal hydroxide/metal sulfide structured materials, a transition metal spinel/metal sulfide heterostructure material ($MnCo_2O_4$@Ni_3S_2) prepared by Du and co-workers has also shown promise as a catalyst for the OER.[543] They observed no changes in the overall morphology and structure of the as-prepared $MnCo_2O_4$@Ni_3S_2 from post-OER material characterization. SEM images and XRD results following OER testing showed that the flake-like morphology and bulk crystal structure were maintained. XPS results also indicated that the surface composition was left unchanged following testing of the OER. Figures 153a–f, the survey, Mn 2p, Co 2p, Ni 2p, S 2p, and O 1s XPS spectra before and after the OER, are nearly the same—there are no obvious shifts in peak position and little change to the overall peak shape and intensity, thus establishing their material as a catalyst and not a precatalyst.

In the literature, multimetal sulfides without hydroxide or oxide incorporation have also been reported as stable catalysts for the OER.[641,636,634,642] For example, Yan and co-workers have reported a NiCoS/NF catalyst prepared using an electrodeposition-hydrothermal process wherein molybdate ions were used as directing agents for the construction of a nanorod morphology.[641] Their catalyst demonstrated similar catalytic activity before and after 500 CV cycles and maintained a steady current over 10 h at 1.33 V_{RHE} in 1 M KOH (Figures 154a and b). And it was confirmed that this consistent activity was due to the intrinsic activity of the prepared NiCoS/NF and not changes to the material during the OER via post-OER characterization. XRD results from before and after 10 h of OER testing indicated that the bulk crystal structure of the as-prepared catalyst was retained, as the crystal phases Ni_3S_2, CoS, and Co_9S_8 were each detected during pre- and post-OER characterization (Figure 154c). It was also confirmed via XPS that the surface composition of the catalyst was maintained following long-term OER testing, given only slight differences in peak intensities in the high-resolution spectra for Co 2p, Ni 2p, Mo 3d, S 2p, and O 1s were observed (Figures 154d–f). These results affirm their as-prepared NiCoS/NF material as a catalyst, unchanged throughout the OER process. It should be noted here, however, that there is a clear decrease in the S 2p signal before and after OER testing, indicating that either some

https://doi.org/10.1021/acs.chemrev.3c00005
Chem. Rev. 2023, 123, 12795–13208

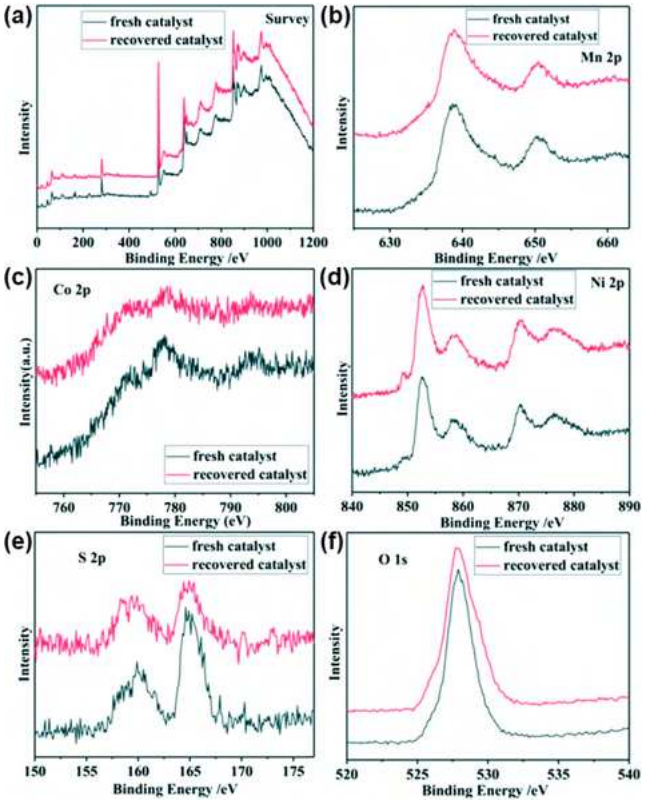


Figure 153. (a) Survey, (b) Mn 2p, (c) Co 2p, (d) Ni 2p, (e) S 2p, and (f) O 1s XPS spectra of $MnCo_2O_4$@Ni_3S_2 before and after the OER. Reprinted with permission from ref 543. Copyright 2019 Royal Society of Chemistry.

surface oxidation occurred or sulfur may have been lost from the material during the OER.

The results from these works raise questions in regard to the effects of structure, oxide/hydroxide incorporation, multimetal incorporation, and the as-prepared crystal structure on the stability of metal sulfides for the OER. For the Co sulfides discussed, it appears as though a spherical morphology and a highly porous support could possibly contribute to stability. From reports on Ni sulfides, it also seems that the inclusion of oxide/hydroxides may lead to enhanced stability of metal sulfides as catalysts for the OER. More work needs to be done to determine the oxide incorporation effect on the metal sulfide for the OER and why certain material compositions/structures may enhance rather than have a deleterious effect on electrocatalyst stability.

5.1.2.2. Precatalysts. The majority of prepared metal sulfides for the electrocatalysis of the OER are precatalysts, meaning they undergo some modification during the electrocatalytic process, giving rise to the true active sites for electrocatalysis (refs 94, 97, 99, 448, 466, 564, 669−753, and 887). When taking a look at the Pourbaix diagrams for CoS and Ni_3S_2 (Figure 155), two common compositions for metal sulfides, the precatalyst status of metal sulfide materials comes as no surprise given the high oxidizing potentials required for OER electrocatalysis and the alkaline conditions under which these electrocatalysts are usually studied. It is clear from these Pourbaix diagrams that at the oxidizing potentials necessary for the OER (above 1.23 V_{RHE}) and alkaline pH (13−14), Co sulfides and Ni sulfides are unstable materials—metal oxyhydroxide and sulfate ion formation is expected. During post-analysis of metal sulfides used for the OER, these chemical species are often detected using techniques such as XRD, SEM, TEM, and XPS. Improved OER performance is also often observed after the transformation of the material's surface to

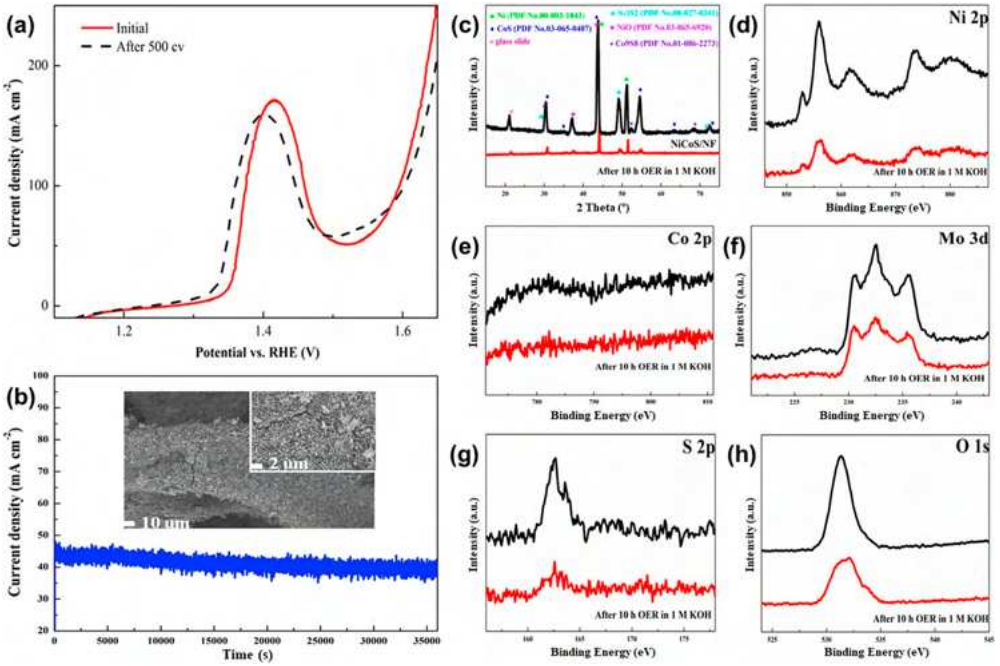


Figure 154. (a) LSV curves of NiCoS/NF before and after 500 CV scans. (b) Chronoamperogram of NiCoS/NF at an overpotential of 300 mV for 10 h (inset: SEM image of NiCoS/NF after a 10 h CA test). (c) XRD patterns and (d−h) XPS spectra of NiCoS/NF before (black) and after (red) 10 h OER testing in 1 M KOH. Mo 3d XPS spectra are displayed because of the use of molybdate ions during synthesis to produce nanorod morphology. Reprinted with permission from ref 641. Copyright 2017 Elsevier.

https://doi.org/10.1021/acs.chemrev.3c00005
Chem. Rev. 2023, 123, 12795−13208

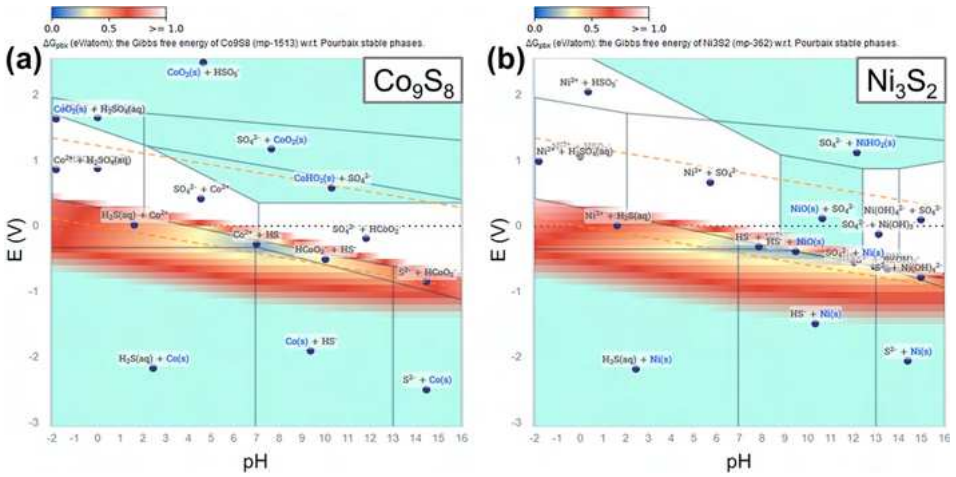


Figure 155. Electrochemical stability maps (Pourbaix diagram and Gibbs free energy overlay) of common metal sulfide compositions: (a) CoS and (b) Ni_3S_2. The Gibbs free energy overlay indicates areas of aqueous stability for the compound, with blue regions being the most stable and red/uncolored regions being the least stable. Orange broken lines represent the thermodynamic potentials for the HER and OER at different pH. The diagrams were produced by using the Materials Project.[87−89]

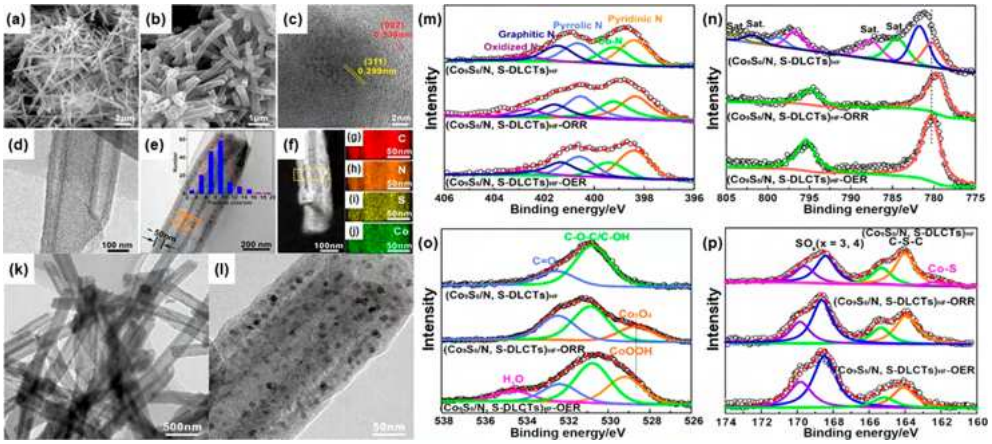


Figure 156. (a, b) SEM images of double-layer silica tube templates. (c) HRTEM and (d) TEM images of silica tube template. (e) TEM, (f) STEM, and (g−j) EELS elemental mapping images of $(Co_9S_8/N,S\text{-DLCTs})_{HF}$ before the OER. (k, l) TEM and HRTEM images of $(Co_9S_8/N,S\text{-DLCTs})_{HF}$ after the OER. (m) N 1s, (n) Co 2p, (o) O 1s, and (p) S 2p XPS spectra of $(Co_9S_8/N,S\text{-DLCTs})_{HF}$ before and after the OER and ORR. Reprinted with permission from ref 706. Copyright 2018 American Chemical Society.

metal oxides/(oxy)hydroxides, indicating that such species act as the real active sites for the OER for transition metal sulfide materials. Herein, Co-based, Ni-based, other single-metal-based, and multimetal-based transition metal sulfide precatalysts will be discussed.

In the literature, cobalt sulfides have been extensively reported on as OER precatalysts. Of those reported, the Co_9S_8, CoS, and CoS_2 compositions are most common and have been prepared with various morphologies and on a variety of substrates. These Co sulfide compositions are known to undergo oxidation during the OER process, resulting in the formation of the real active sites for the OER-Co metal oxides/(oxy)hydroxides.

Of the reported Co_9S_8 precatalysts for the OER, as aforementioned, the real active site reported for these materials has most commonly been Co oxides/(oxy)hydroxides (refs 682, 706, 713, 714, 719, 731, 745, and 893). For example, Hu and co-workers determined that their best performing electrocatalyst consisting of Co_9S_8 nanocrystals on nitrogen and sulfur co-doped double-layered carbon tubes etched using hydrogen fluoride, $(Co_9S_8/N,S\text{-DLCTs})_{HF}$, was a precatalyst, giving rise to the true active site, CoOOH, during the OER process.[706] This active site(s) was confined to the surface of the prepared material given post-OER characterization results. The initial double-layered tubular morphology of the as-prepared $(Co_9S_8/N,S\text{-DLCTs})_{HF}$, as seen from the SEM, TEM, STEM, and EELS elemental mapping images provided in Figures 156a−j, was maintained following the OER as shown in Figure 156k. Figure 156l, the HRTEM image of the material post-OER, also showcases how there has been no bulk change to the structure—Co NPs are still embedded within the carbon matrix just as they were prior to the OER (Figures 156d and e). Thus, full oxidation of the as-prepared $(Co_9S_8/N,S\text{-DLCTs})_{HF}$ did not occur. XPS results indicated that only the surface was oxidized following the OER process. Figure 156n reveals that, while the as-prepared $(Co_9S_8/N,S\text{-DLCTs})_{HF}$ had peaks at binding energies corresponding to Co^{3+} (Co $2p_{3/2}$ and Co $2p_{1/2}$ peaks at the binding energies of 780.2 and 796.6 eV, respectively) and Co^{2+} (Co $2p_{3/2}$ and Co $2p_{1/2}$ peaks at the binding energies of 781.7 and 798.8 eV, respectively) for Co 2p, the post-OER material has peaks at the binding energies of 780.3 and 795.4 eV indicative of CoOOH

https://doi.org/10.1021/acs.chemrev.3c00005
Chem. Rev. 2023, 123, 12795−13208

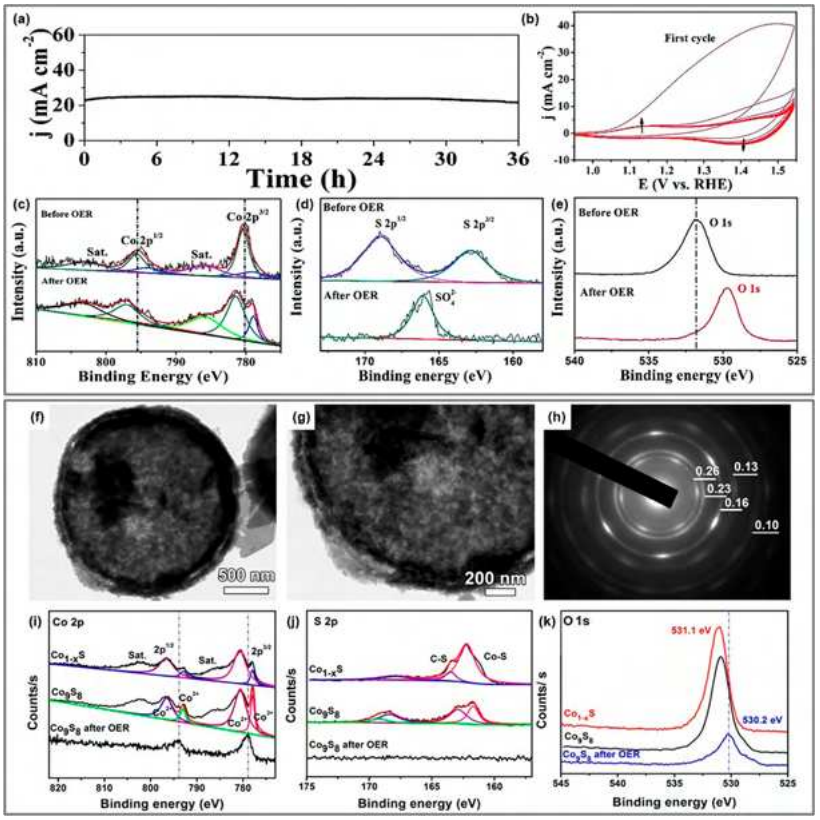


Figure 157. (a) Chronopotentiostatic curve of Co_9S_8 at 1.58 V_{RHE} in 1 M KOH. (b) CV activation of Co_9S_8 at a scan rate of 10 mV·s^{-1}. (c) Co 2p, (d) S 2p, and (e) O 1s XPS spectra of Co_9S_8 before and after the OER process. Reprinted with permission from ref 714. Copyright 2018 Royal Society of Chemistry. (f, g) TEM images and (h) SAED pattern of Co_9S_8 after the OER. (i) Co 2p, (j) S 2p, and (k) O 1s XPS spectra of Co_9S_8 before and after the OER. Reprinted with permission from ref 730. Copyright 2017 American Chemical Society.

formation at the surface. The high-resolution O 1s spectrum (Figure 156o) also indicated the formation of CoOOH given the peak at 529.2 eV, which was not present prior to the OER. In the high-resolution S 2p spectra (Figure 156p), it is clear that, following the OER, the Co−S peak disappeared, implying that Co−S sites evolved into CoOOH, the active sites for the OER. It is interesting to note that the Co−S peak also disappeared in the S 2p spectrum and Co_3O_4 was generated following testing for the oxygen reduction reaction (ORR).

In addition to determining the actual active site for $(Co_9S_8/N,S\text{-DLCTs})_{HF}$, Hu *et al.* also investigated the effect of etching agent by preparing $(Co_9S_8/N,S\text{-DLCTs})_{NaOH}$ in addition to $(Co_9S_8/N,S\text{-DLCTs})_{HF}$.[706] They found that $(Co_9S_8/N,S\text{-DLCTs})_{HF}$ outperformed $(Co_9S_8/N,S\text{-DLCTs})_{NaOH}$ and attributed this difference to a larger ECSA and partial dissolution of cobalt species upon etching with HF (see Table 5). From this result, it could be implied that etching with HF rather than NaOH leads to a greater extent of surface oxidation and, therefore, a material more predisposed to the electrocatalysis of the OER.

Similar findings have been made regarding the active site for OER electrocatalysis for metal sulfides (Co_9S_8) to those of Hu and co-workers. For instance, Souleymen *et al.* found that their Co_9S_8 ultrathin freestanding nanosheets on carbon fiber paper (CFP) also experienced surface oxidation during the OER, resulting in the formation of a CoOOH active site at the surface, as confirmed by XPS.[714] Figure 157c displays the high-resolution Co 2p spectra before and after a long-term OER stability test (see Table 5 and Figure 157a). It is clear from Figure 157c that the Co $2p_{1/2}$ and Co $2p_{3/2}$ peaks have shifted in binding energy. The post-OER Co $2p_{3/2}$ peak was deconvoluted into two peaks with binding energies of 778.4 and 781.2 eV, corresponding to CoOOH, which corresponds to Co with a 3+ oxidation state, and $Co(OH)_2$, which corresponds to Co with a 2+ oxidation state. The peak area ratio of the CoOOH and $Co(OH)_2$ peaks indicated larger Co^{3+} content on the surface in comparison to Co^{2+} after the OER. As a result, the authors proposed that Co_9S_8 would first be oxidized to $Co(OH)_2$, which would undergo further oxidation to CoOOH (see below chemical equations). This finding also matched well with changes to the high-resolution O 1s and S 2p spectra. Following long-term OER testing, the O 1s peak shifted from 532.1 to 529.9 eV, a binding energy that corresponds to lattice oxygen incorporation. Peaks corresponding to Co−S bonds completely disappeared, leaving behind only SO_4^{2-} ions at the surface. The mechanism of CoOOH formation was then further supported by cyclic voltammetry data.

$$Co_9S_8 + OH^- \rightarrow Co(OH)_2 + e^-$$

$$Co(OH)_2 + OH^- \leftrightarrow CoOOH + H_2O + e^-$$

In Figure 157b, CV activation of the initial Co_9S_8 material is shown. The first CV cycle shows a large oxidation peak from 1.00 to 1.55 V_{RHE} whose intensity drops drastically after the initial cycle, indicating an irreversible process has occurred. This irreversible process is the oxidation of Co^{2+} to Co^{3+}, which supports the proposed mechanism for $Co(OH)_2$ being further oxidized to CoOOH. Another oxidation peak then

https://doi.org/10.1021/acs.chemrev.3c00005
Chem. Rev. 2023, 123, 12795−13208

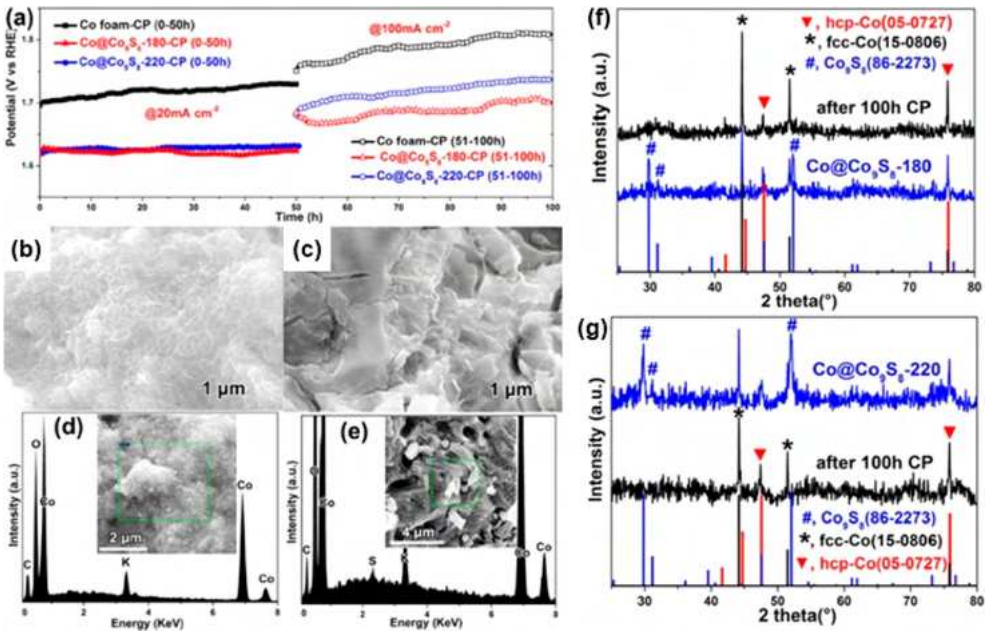


Figure 158. (a) Chronopotentiometry of Co@Co_9S_8-180, Co@Co_9S_8-220, and bare Co foam at 20 and 100 mA·cm^{-2}. (b, c) SEM images and (d, e) EDX spectra of bare Co foam and Co@Co_9S_8-180, respectively. SEM images and EDX spectra were obtained following chronopotentiometry stability tests at 20 and 100 mA·cm^{-2}. (f, g) XRD patterns of Co@Co_9S_8-180 and Co@Co_9S_8-220 before and after the OER testing. Reprinted with permission from ref 731. Copyright 2017 Wiley.

appears after the initial cycles at ∼1.1 V_{RHE}. This additional peak was also attributed to *in situ* oxidation.

Liu and co-workers also studied the initial CV scans at oxidizing potentials for their prepared Co_9S_8 hollow microplates using cyclic voltammetry.[730] Instead of one large oxidation peak from 1.1−1.5 V_{RHE}, they observed two oxidation peaks upon the first CV scan—the first peak at 1.1 V_{RHE} and the second at 1.3 V_{RHE}, likely due to a slower scan rate of 2 mV·s^{-1} instead of 10 mV·s^{-1} as used in the previously discussed paper. The first peak was attributed to the oxidation of Co^{1+} to Co^{2+}, and the second, to Co^{2+} to Co^{3+}. Upon the second CV scan, no peaks were observed, indicating that irreversible oxidation reactions had occurred. XPS results further indicated that the surface had been oxidized to CoOOH during the OER process. Prior to OER testing, peaks for Co^{2+} and Co^{3+} were found, and after 20 h of OER stability testing at 1.58 V_{RHE}, Co^{2+} peaks were no longer present. Only the Co $2p_{3/2}$ and $2p_{1/2}$ peaks for Co^{3+} remained with a shift in peak position to higher binding energies (Figure 157i). The shift in the binding energy of the Co^{3+} peaks and the complete absence of Co^{2+} peaks supported the conclusion that the surface was oxidized to $Co(OH)_2$ and then to CoOOH, as indicated by CV data. Surface oxidation was then further confirmed by the loss of the Co-S and C-S peaks in the high-resolution S 2p spectrum (Figure 157j) and the shift in the binding energy of the single peak in the high-resolution O 1s spectrum to 530.2 eV, which is representative of cobalt oxide/hydroxides (Figure 157k). Figures 157f and g show how the bulk morphology of the material was maintained but thin nanosheets at the surface were no longer present as they were before the OER, indicating surface oxidation had occurred, which was further supported by the SEAD pattern (Figure 157h). The SEAD pattern confirmed the presence of Co oxides/hydroxides on the surface. Thus, through the application of several different techniques, the initial CV scan analysis conclusions could be confirmed, and there is further evidence of CoOOH as the real active site for Co_9S_8 electrocatalysts for the OER.

Other reports have also determined CoOOH to be the real active site for Co_9S_8 electrocatalysts for the OER using material characterization techniques; however, not all reports have found that oxidation was confined to the surface during the OER.[731,745] For instance, Xiong and co-workers determined that CoOOH was likely the active site for their electrocatalyst, Co_9S_8 particles on Co foam prepared via a hydrothermal process at 180 and 220 °C (Co@Co_9S_8-180 and Co@Co_9S_8-220, respectively), given observed surface smoothing from the SEM images taken (shown for bare Co foam and Co@Co_9S_8-180 in Figures 158b and c, respectively) after 50 h of chronopotentiometry at 20 mA·cm^{-2} and 50 h of chronopotentiometry at 100 mA·cm^{-2}, EDX results, and XRD analysis.[731] Along with surface smoothing, from the SEM image of Co@Co_9S_8-180, it is also clear that the overall morphology of the material changed from its initial particulate morphology, indicating nearly complete oxidation of the material. EDX results, following long-term OER, then showed a large oxygen peak that was not present prior to OER testing and a drastic drop in the intensity of the sulfur peak for Co@Co_9S_8-180, further confirming the oxidation of the material (Figure 158e). When comparing the XRD patterns for Co@Co_9S_8-180 and Co@Co_9S_8-220 from before and after long-term testing (Figures 158f and g), diffraction peaks for the Co_9S_8 phase had also disappeared following OER testing, indicating full oxidation of Co_9S_8 to CoOOH. Xiong *et al.* also evaluated bare Co foam using XRD before and after OER measurements and found diffraction peaks corresponding to the *β*-CoOOH phase in the pattern that were not there prior to the OER process. The choice of substrate, Co foam, likely impacted the extent of oxidation of the as-prepared material, as Co is known to be oxidized during the OER process. It is, however, difficult to confirm the complete oxidation of the material, given a sulfur peak is still present on the post-OER

https://doi.org/10.1021/acs.chemrev.3c00005
Chem. Rev. 2023, 123, 12795−13208

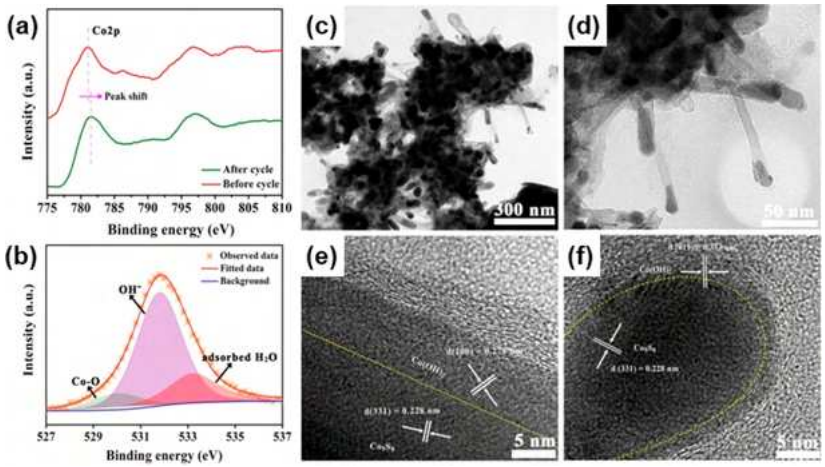


Figure 159. Characterization of MOF-derived Co_9S_8 NPs in nitrogen-doped carbon. (a) Co 2p and (b) O 1s XPS spectra after the OER. (c, d) TEM images and (e, f) HRTEM images of Co_9S_8@NC-800. Reprinted with permission from ref 719. Copyright 2018 Royal Society of Chemistry.

EDX spectrum. Further post-characterization should, therefore, be explored, such as XPS, which could confirm the complete loss of sulfur on the surface of the material and serve to further substantiate post-OER XRD results.

While *in situ* oxidation of Co_9S_8 electrocatalysts for the OER is confirmed by multiple papers, further investigation is still warranted because some reports, such as those discussed above, indicate CoOOH as the active site for as-prepared Co_9S_8-based OER electrocatalysts, while others indicate that it is $Co(OH)_2$ or both CoOOH and $Co(OH)_2$.[682,719] Chen *et al.*'s MOF-derived Co_9S_8 NPs embedded in porous nitrogen-doped carbon prepared at 800 °C (Co_9S_8@NC-800) experienced surface oxidation to $Co(OH)_2$ following 500 LSV sweeps from 1.1 to ~1.65 V_{RHE}.[719] In the high-resolution Co 2p XPS spectrum, the Co 2p peak was shifted toward higher binding energy, indicating surface oxidation (Figure 159a). This surface oxidation was also indicated by the O 1s high-resolution XPS spectrum, with peaks ascribed to Co-O, OH^- ions, and absorbed water (Figure 159b). From TEM images (Figures 159c and d), it was evident that the overall morphology was maintained, while HRTEM images (Figures 159e and f) indicate the presence of $Co(OH)_2$ at the surface and Co_9S_8 at the core of the post-OER material, given the detected lattice fringes of 0.275 and 0.228 nm, which correspond to the (100) and (331) planes of $Co(OH)_2$ and Co_9S_8, respectively. The contrasting conclusions regarding the active sites for Co_9S_8-based materials, especially those with similar carbon-based supports, evoke a need for further investigation into the true mechanism of surface oxidation and the variables that may affect said mechanism or lead to alternate pathways such as different types and lengths of stability tests and/or contrasting preparation methods. It should also be noted that many papers provide contrasting reports regarding the oxidation of S in metal sulfides during the OER, with some indicating the complete dissolution of S and others reporting the presence of SO_4^{2-} ions on the surface of their as-prepared electrocatalysts.[682,706,714,719,730,731,893] These and other challenges will be discussed in the Challenges portion of this section of the review.

Another cobalt sulfide precatalyst composition that has been studied extensively for the OER is CoS_x, where the Co:S ratios of 1:1 and 1:2 are most common. As for the Co_9S_8 OER electrocatalysts, the CoS_x materials have also been reported to undergo compositional and morphological changes during the OER that lead to the formation of the real active sites for the OER during long-term stability testing. As for the Co_9S_8 metal sulfides, the determined active sites vary—$Co(OH)_2$, CoOOH, and Co_3O_4 have all been discussed.[727,747,752] In 2016, Wang *et al.* found that their integrated three-dimensional (3D) electrode of carbon paper/carbon tubes/cobalt-sulfide sheets (CP/CTs/Co-S) underwent partial oxidation prior to long-term OER testing (see Table 5).[739] The as-prepared material consisted of Co-S nanosheets protruding from the CT (some Co-S nanosheets were also deposited on the CP, which served as the tube backbone). From initial XPS and ICP-AES results, it was also determined that some $CoO/Co(OH)_2$ species were also present. When comparing SEM images before and after the OER, it was clear that plates had formed at the surface, whereas nanosheets were only present at the surface initially. This change is attributed to the formation of $Co(OH)_2$ at the surface and loss of sulfur from the surface (Figures 160a and b). High-resolution Co 2p and S 2p XPS spectra taken after the OER showed an increase in the $Co(OH)_2$ peak intensity and a decrease in the Co-S_x peak in the Co 2p spectrum while all sulfur peaks in the S 2p spectrum had essentially disappeared (Figure 160c). From EDX taken after the OER (Figure 160d), it was determined that the Co/S ratio was ~5, which is much higher compared to the initial Co/S ratio of 1.33 as determined by ICP-AES, confirming sulfur loss from the surface of the material.

Porous hexagonally-shaped $Co_{1-x}S$ microplates prepared using $Co(OH)_2$ microplates as a template also experienced a change in surface morphology after stability testing like the aforementioned Co−S nanosheets.[721] This surface-roughening can be seen from the comparison of TEM images from before and after the OER (Figures 160f and h). This roughening was attributed to the formation of cobalt (oxy)hydroxides and loss of sulfur as indicated by the change in the EDX spectra from before and after the OER (Figures 160e and g) and by XPS results not shown here. Similar conclusions were drawn by Ju and co-workers for their hydrothermally prepared Co sulfide nanosheets (Co−S) using different sulfur powder amounts for synthesis. Their Co-S-130 sample, synthesized using 0.13 g of sulfur powder, was most extensively studied following the OER (see Table 5).[685] As shown in Figure 161, there was a clear change to the surface of the material after 36 h of the OER.

https://doi.org/10.1021/acs.chemrev.3c00005
Chem. Rev. 2023, 123, 12795−13208

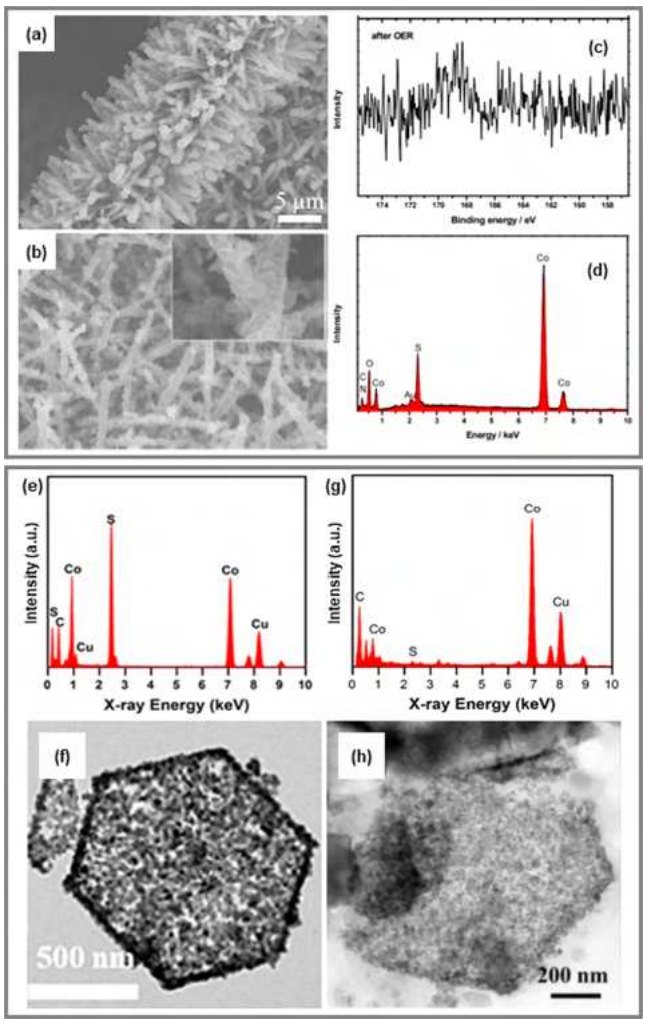


Figure 160. Pre- and post-OER characterization of Co sulfides. (a, b) SEM images of CP/CTs/Co-S before and after the OER, respectively. (c) S 2p XPS and (d) EDX spectra of CP/CTs/Co-S after the OER. Reprinted with permission from ref 739. Copyright 2016 American Chemical Society. (e, g) EDX spectra and (f, h) TEM images of $Co_{1-x}S$ microplates before and after the OER, respectively. Reprinted with permission from ref 721. Copyright 2018 Wiley.

The nanosheet morphology at the surface of the as-prepared Co-S-130 (Figures 161a–h) transformed to smaller nanosheet units based on the post-OER SEM image (Figure 161i) and appeared to break down into rodlike units given the post-OER TEM images (Figures 161j and k). Phase transformation at the surface was also apparent given the detected 0.23 nm lattice fringe, which corresponds to the (012) plane of CoOOH (Figure 161l). This crystal plane is in direct contrast to that detected for the as-prepared material prior to the OER, the (200) plane of cubic CoS_2 (Figure 161d). The presence of CoOOH at the surface of the material following the OER was also confirmed by XPS. From the high-resolution Co 2p spectra from before and after OER testing (Figure 161m), it is apparent that the Co^{2+} peaks have disappeared and that the peaks present at 779.5 and 781.1 eV correspond to the Co^{3+} valence state, indicative of CoOOH. This is further supported by the O 1s high-resolution spectra, which only showed peaks corresponding to lattice oxygen and OH groups after OER testing (Figure 161n). The high-resolution S 2p spectrum after OER testing also indicated that surface oxidation had taken place given the reduction in intensity of the Co–S peak and the increase in intensity of the S–O peak (Figure 161o). As a result, the authors postulate that the retained S–O species could contribute to enhanced electrocatalytic activity as has been reported in the literature.[873] From ICP and XPS analysis, it was also confirmed that oxidation was confined to the surface as the cobalt content decreased to 36.4 wt % from 55.9 wt %, indicating retention of Co-sites at the core, and only Co^{3+} was detected at the surface via XPS (recall XPS is only sensitive to 7–10 nm). Thus, oxidation of the surface of Co-S-130 was thoroughly confirmed.

Several reports, such as those discussed above, have concluded that *in situ*-formed Co oxides/(oxy)hydroxides at the surface of as-prepared metal sulfides act as the real active sites for the OER; however, there exist few in-depth studies of the mechanism of this process that explain why cobalt oxide, cobalt hydroxide, or cobalt oxyhydroxide predominate at the surface. One outstanding work by Fan and co-workers has provided this much needed information for hydrothermally prepared amorphous CoS_x using both *ex situ* and *in situ* characterization techniques. They found that the prepared amorphous CoS_x was transformed into a crystalline material following OER stability testing at 10 mA·cm^{-2}.[705] As can be seen from SEM images taken before and after OER testing, the initial CoS_x material had retained the ZIF-67 rhombic dodecahedron structure only for it to decompose into nanoplates following OER testing (Figures 162a and b). This change in morphology was further confirmed by EDX and TEM images taken before and after OER testing (Figures 162e and g). From EDX measurements, it is clear that S and Co have been lost from the material while O appears to be more abundant. The HRTEM results then indicate that a polycrystalline phase is present that was not detected prior to OER testing (Figures 162f and h). XPS results then showed a complete loss of sulfur from the surface of the material (Figure 162j). From the high-resolution pre- and post-OER Co 2p spectra, there is also an observable shift in the peak positions to higher binding energies indicative of the Co^{3+} valence state. In the post-OER high-resolution O 1s spectrum, peaks associated with Co–O and OH^-, which were not present in the pre-OER O 1s spectrum, were detected (Figure 162k). Thus, XPS results indicated the formation of Co oxide/(oxy)hydroxides at the surface of the post-OER CoS_x material and this finding was supported by the changes in morphology and surface composition uncovered by electron microscopy imaging and near edge X-ray absorption spectroscopy (NEXAS) results that showed an abundance of the Co^{3+} valence state. From these results, however, they could not determine whether or not Co(III) oxide or CoOOH was the real active site generated during OER testing. To determine the actual active site and to unravel the mechanism behind its formation, Fan and co-workers resorted to *in situ* characterization. From *in situ* TEM, they found that after 2.5 min of anodization using 10 nA of current, lattice fringes corresponding to $Co(OH)_2$ were present and that after 12.5 min, lattice fringes corresponding to CoOOH predominated. These results provided direct evidence of the transformation of cobalt sulfides to $Co(OH)_2$ and then, finally, to CoOOH during OER testing. These results were supported by an additional chronopotentiometry stability test at 0.5 mA·cm^{-2} (Figure 162m). Instead of observing a line indicative of constant potential with time as for the previous stability test at 10 mA·cm^{-2}, several plateaus were observed corresponding to the

https://doi.org/10.1021/acs.chemrev.3c00005
Chem. Rev. 2023, 123, 12795–13208

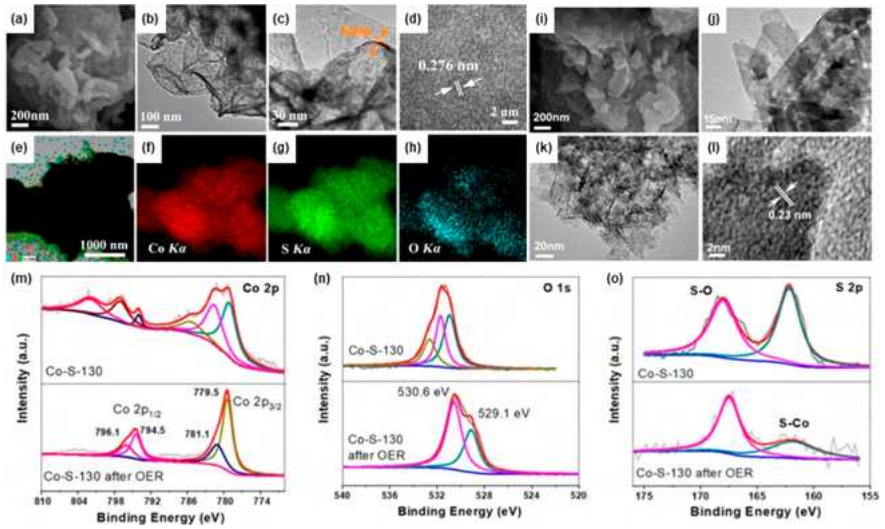


Figure 161. Pre- and post-OER characterization of Co-S-130. (a) SEM, (b–d) TEM, and (e–h) elemental mapping images of Co-S-130. (i) SEM image and (j–l) TEM images of post-OER Co-S-130. (m) Co 2p, (n) O 1s, and (o) S 2p XPS spectra of Co-S-130 before and after the OER. Reprinted with permission from ref 685. Copyright 2019 American Chemical Society.

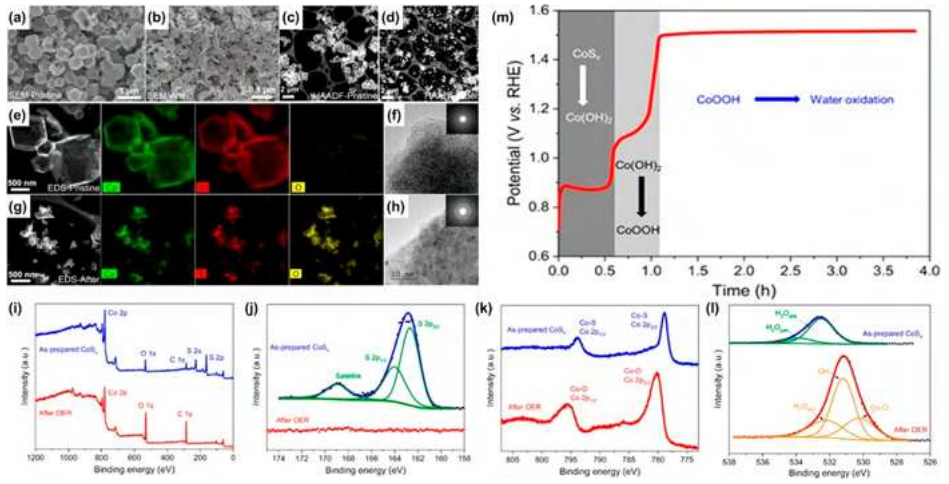


Figure 162. Transformation of surface amorphous CoS_x to $Co(OH)_2$/CoOOH. (a, b) SEM and (c, d) HAADF images of CoS_x before and after the OER. (e, g) EDX elemental mapping and (f, h) HRTEM images of CoS_x before and after the OER, respectively. (i) Survey, (j) S 2p, (k) Co 2p, and (l) O 1s XPS spectra before and after the OER. (m) Additional CP stability test of CoS_x at 0.5 mA·cm^{-2}. Reprinted with permission from ref 705. Copyright 2018 American Chemical Society.

transformation of the material. The first plateau corresponded to the transformation of CoS_x to $Co(OH)_2$, the second to the $Co(OH)_2$ conversion to CoOOH, and the third to only CoOOH present at the surface. This stability test contrasts the initial test likely due to 10 mA·cm^{-2} being too high of a current to see the steps corresponding to material conversion with time on the given time scale or because pre-electrochemical tests were done on the material prior to the 10 mA·cm^{-2} test and not the 0.5 mA·cm^{-2} test. *In situ* FTIR measurements were also performed, and the findings confirmed the aforementioned conclusions. For more information on *in situ* TEM and *in situ* FTIR studies, please see the special techniques section (Section 7).

In addition to CoS composition, the CoS_2 composition has also been explored for the catalysis of the OER and has been found to undergo surface oxidation during the process. Guo *et al.* prepared composite Co_3O_4/CoS_2 hierarchical porous microspheres (HPMs) and studied changes to the material after 0, 200, 1800, and 1500 s of OER testing at a current density of 20 mA·cm^{-2} using SEM and EDX.[720] They observed swelling of the material, aggregation at its surface, loss of CoS_2 HPMs after OER testing, loss of detectable sulfur, and an increase in oxygen content after 1800 s (Figure 163a, iii). They determined that CoS_2 improved electron transfer throughout the material, speeding up Co–O bond breakage in the Co_3O_4 component of the composite, and that it gave rise to more catalytically active oxide species. Additional *ex situ* analysis could be helpful in determining the identity of these active species. Another report of spherical CoS_2, specifically CoS_2 hollow nanospheres (HNSs), found that surface oxidation also occurred, resulting in the formation of a Co_3O_4 and CoOOH layer at the surface of the material after long-term testing (see Table 5).[723] The presence of the Co_3O_4 and CoOOH surface layer was confirmed using TEM, Raman, and XPS (Figures 163b–d). From the XPS results, it was determined that the Co^{3+}:Co^{2+} ratio increased compared to that of the as-synthesized CoS_2 material, and this higher valence state was further confirmed using Raman spectroscopy. Given the Co

https://doi.org/10.1021/acs.chemrev.3c00005
Chem. Rev. 2023, 123, 12795–13208

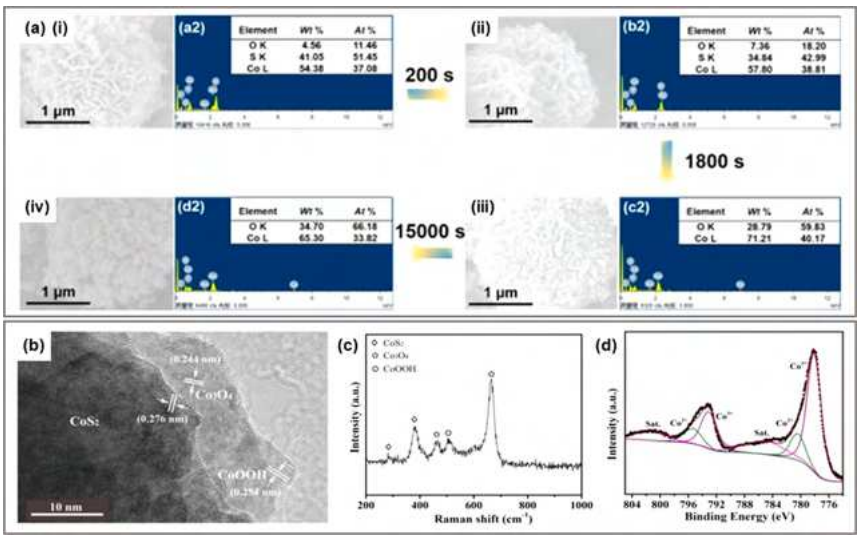


Figure 163. Transformation of CoS_2 HPMs after long-term OER testing. (a, i–iv) SEM images and EDX spectra of Co_3O_4/CoS_2 after 0, 200, 1800, and 1500 s of the OER at a current density of 20 $mA{\cdot}cm^{-2}$. Reprinted with permission from ref 720. Copyright 2018 Elsevier. (b) HRTEM image and (c) Raman and (d) Co 2p XPS spectra of post-OER CoS_2 HNSs. Reprinted with permission from ref 723. Copyright 2018 Royal Society of Chemistry.

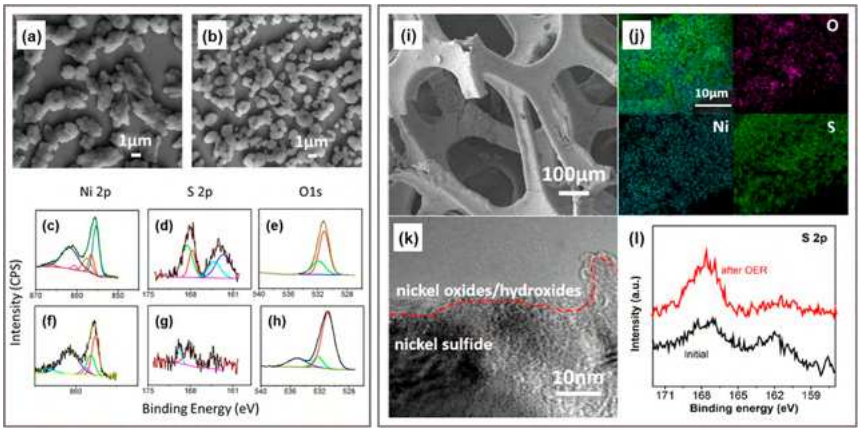


Figure 164. Pre- and post-OER characterization of Ni sulfides. (a, b) SEM images of NiS_x films (a) before and (b) after the OER. (c, f) Ni 2p, (d, g) S 2p, and (e, h) O ls XPS spectra of NiS_x films before and after the OER, respectively. Reprinted with permission from ref 448. Copyright 2019 Wiley. (i) SEM, (j) elemental mapping, and (k) HRTEM images and (l) S 2p XPS spectra of NiS/NF before and after the OER. Reprinted with permission from ref 733. Copyright 2017 American Chemical Society.

oxide/(oxy)hydroxide phases found at the surface of the material following OER testing, the authors stated that the Co sites at the surface of the as-prepared material would be transformed from Co → $Co(OH)_2$ → Co_3O_4 → CoOOH under alkaline conditions. The final active site is expected given the results of other reports, but the presence of the Co_3O_4 phase, which was not detected in the previously discussed mechanistic study, evokes further need for *in situ* analysis of materials during OER testing to deconvolute the effect of starting material composition on the mechanism of formation of the actual active sites toward the OER. Thus, just as with Co_9S_8 electrocatalysts for the OER, CoS_x electrocatalysts require further study to unravel the mechanism of real active site formation.

Another transition metal commonly used for transition metal sulfides is Ni, and like Co sulfides, there exist multiple reports of Ni sulfide electrocatalysts that undergo surface oxidation to Ni oxide/(oxy)hydroxides during the OER (refs 448, 691, 708, 717, 718, 724, 734, 737, and 740). For example, Sultana and O'Mullane found that electrochemically synthesized NiS_x films underwent surface oxidation after 10 CV cycles from 1.0 to 1.8 V_{RHE}.[448] Surface oxidation of the Ni sulfide film was made evident by morphological, crystallographic, and compositional changes to the material. Figure 164b shows the SEM image of the NiS_x film after OER testing, which presents less aggregated clusters than the as-prepared material (Figure 164a). XPS results further indicated that surface oxidation had occurred, as the sulfur peaks in the S 2p high-resolution spectrum before the OER suffered a drastic drop in intensity after OER testing, indicating loss of sulfur from the surface (Figures 164d and g). The post-OER Ni 2p high-resolution spectrum indicated Ni in the +3 state, indicative of NiOOH, in addition to the Ni^{2+} state, indicative of NiO and $Ni(OH)_2$—the oxidation state indicated by the pre-OER Ni 2p spectrum (Figures 164c and f). Changes to the O 1s spectrum following OER testing also indicated that surface oxidation had occurred along with signifying the presence of absorbed water given the introduction of a high-

https://doi.org/10.1021/acs.chemrev.3c00005
Chem. Rev. 2023, 123, 12795–13208

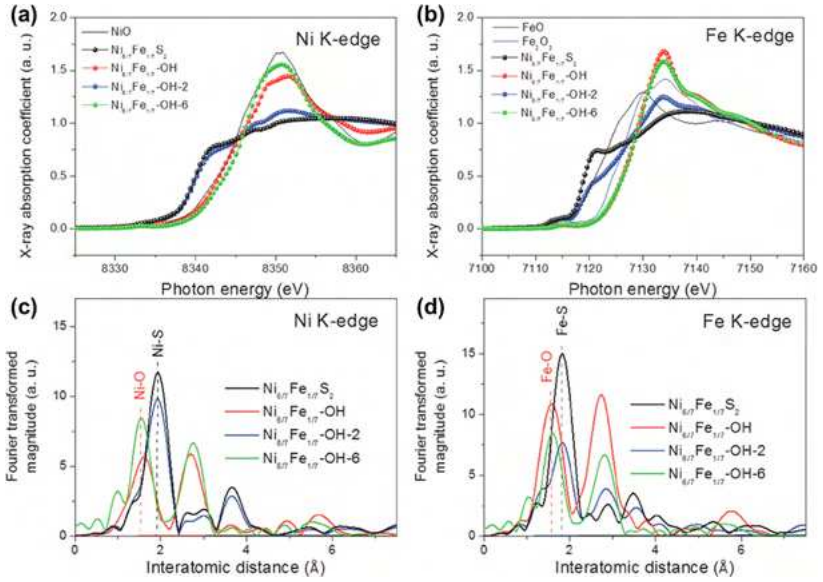


Figure 165. (a, b) Normalized Ni and Fe K-edge XANES spectra of $Ni_{6/7}Fe_{1/7}S_2$ and as-prepared $Ni_{6/7}Fe_{1/7}$-OH, $Ni_{6/7}Fe_{1/7}$-OH-2, and $Ni_{6/7}Fe_{1/7}$-OH-6, respectively. (c, d) Radial distribution functions of Ni and Fe K-edge k^3-weighted EXAFS spectra of $Ni_{6/7}Fe_{1/7}S_2$ and as-prepared $Ni_{6/7}Fe_{1/7}$-OH, $Ni_{6/7}Fe_{1/7}$-OH-2, and $Ni_{6/7}Fe_{1/7}$-OH-6, respectively. Reprinted with permission from ref 691. Copyright 2018 Wiley.

energy peak not present in the pre-OER spectrum (Figures 164e and h). XRD results confirmed that surface oxidation had occurred, as two peaks indicative of the NiS and NiO phases were observed following OER testing. Given the initial diffraction pattern, which signified that NiS was an amorphous material, it is evident that oxidation imparted crystalline structure to the NiS_x material without fully oxidizing it.

In another report, hydrothermally prepared Ni_3S_4 nanosheets on Ni foam (NiS/NF) also experience surface oxidation after long-term OER testing; however, there was no notable change in morphology following OER testing, with the hierarchical structure being completely maintained (Figure 164i).[733] From elemental mapping, sulfur loss was also found to be limited, but there was still a noticeable increase in oxygen content (Figure 164j). This matched well with XRD and XPS results, which indicated that oxidation was confined to the material's surface, as the XRD pattern indicated that the overall phase of the material was not altered and the XPS results indicated surface oxidation. From the S 2p high-resolution XPS spectrum, it is evident that the peak corresponding to oxidized sulfur increased in intensity (Figure 164l). The Ni 2p high-resolution spectra also indicated that Ni at the surface had undergone oxidation. This surface modification was then confirmed using HRTEM, which indicated the presence of an amorphous Ni oxide/hydroxide layer based on observed lattice fringes (Figure 164k). Thus, as in the previous example, the surface of the material was transformed during the course of OER testing, solidifying, as many reports have done, the inevitable *in situ* oxidation of Ni sulfide surfaces at oxidizing potentials for the OER.

In situ oxidation of Ni sulfides, and metal sulfides more generally, has been so prevalently reported and accepted that authors have begun to take advantage of this *in situ* oxidation to prepare their initial OER electrocatalysts.[691,718,724] In 2018, Wang and co-workers used *in situ* oxidation to prepare their NiFe (oxy)hydroxides using S residues. They prepared NiFe disulfide samples that had undergone 0, 2, 6, and 24 h hydrogen peroxide oxidation treatments labeled as $Ni_{6/7}Fe_{1/7}$-OH, $Ni_{6/7}Fe_{1/7}$-OH-2, $Ni_{6/7}Fe_{1/7}$-OH-6, and $Ni_{6/7}Fe_{1/7}$-OH-24, respectively.[691] With longer oxidation treatment, the % S content decreased from 48.67 to 0.24% based on EDX results (not shown here). From XRD results, they observed high crystallinity in their materials, with peaks for sulfur disappearing after 24 h of the oxidation treatment. XPS results also indicated surface oxidation and simultaneous loss of sulfur, with the S 2p peak diminishing in intensity with increasing oxidation time and then disappearing at 24 h of oxidation. With increasing oxidation treatment time, the ratio of Ni^{3+}:Ni^{2+} and Fe^{3+}:Fe^{2+} also increased, indicating oxidation at the surface. The composition of the bulk of the catalysts was determined using X-ray absorption spectroscopy. The Ni K-edge X-ray absorption near edge structure (XANES) spectra indicated that Ni primarily existed in the Ni^{2+} valence state in the bulk given the similarities in the spectra of the $Ni_{6/7}Fe_{1/7}$-OH and $Ni_{6/7}Fe_{1/7}$-OH-6 samples to that of NiO and the $Ni_{6/7}Fe_{1/7}$-OH-2 sample's peak at 8353 eV in contrast to the spectra for $Ni_{6/7}Fe_{1/7}S_2$. This finding supported that Ni^{3+} was primarily present at the surface of the electrocatalyst, as indicated by XPS. The K-edge k^3-weighted EXAFS spectra of the $Ni_{6/7}Fe_{1/7}$-OH, $Ni_{6/7}Fe_{1/7}$-OH-2, and $Ni_{6/7}Fe_{1/7}$-OH-6 samples (Figure 165c) confirmed the presence of Ni−O and Ni−S bonds in the 2 h sample, but not the 6 h sample, indicating low S content in the bulk for the 6 h sample. A similar result was observed in EXAFS of Fe (Figure 165d). Differences were detected in the bond lengths of the as-prepared and 6 h oxidation sample for which the Ni−O bond length had decreased, likely due to Ni^{3+} formation at the surface, and the Fe−O bond length had increased, likely due to S being less electronegative than oxygen, as indicated by Figure 165d. Thus, for oxidation treatment times less than 24 h, the as-prepared catalysts were almost entirely transformed to the oxy(hydroxide) with only some S residues still present prior to any OER testing.

Another group found that Ni sulfides could undergo CV activation to transform the material's surface to $Ni(OH)_2$/NiOOH using only 10 CV cycles between 0.9 and 1.6 V_{RHE}.[718] Following electrochemical activation, cracking of the as-prepared Ni sulfide (sample name: H_2S_NF) electrocatalyst

https://doi.org/10.1021/acs.chemrev.3c00005
Chem. Rev. 2023, 123, 12795−13208

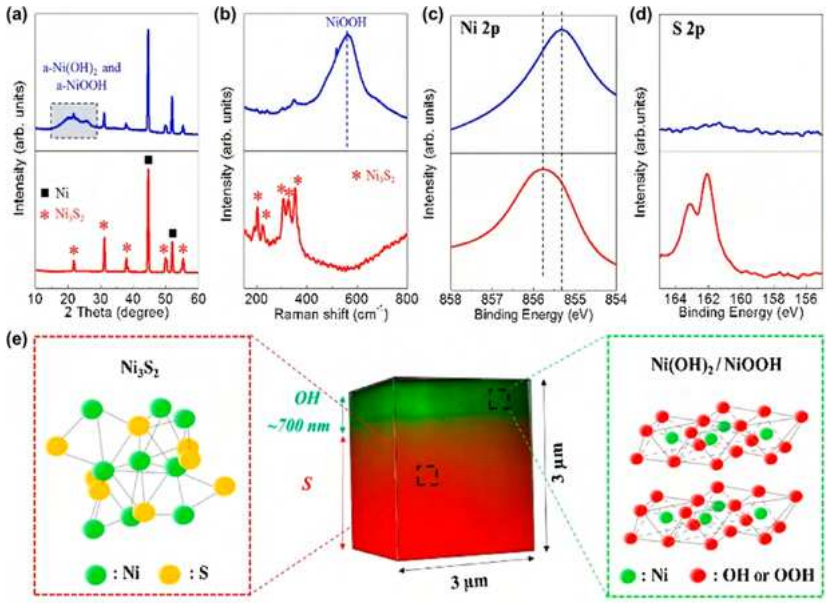


Figure 166. Characterization of CV-activated Ni sulfide for the OER. (a) GIXRD patterns, (b) Raman spectra, (c) and Ni 2p and (d) S 2p XPS spectra of Ni sulfide precursor and CV-activated Ni sulfide. (e) TOF-SIMS depth profile of CV-activated Ni sulfide with crystal structures of the core Ni_3S_2 and surface $Ni(OH)_2$/NiOOH layer. Reprinted with permission from ref 718. Copyright 2018 Elsevier.

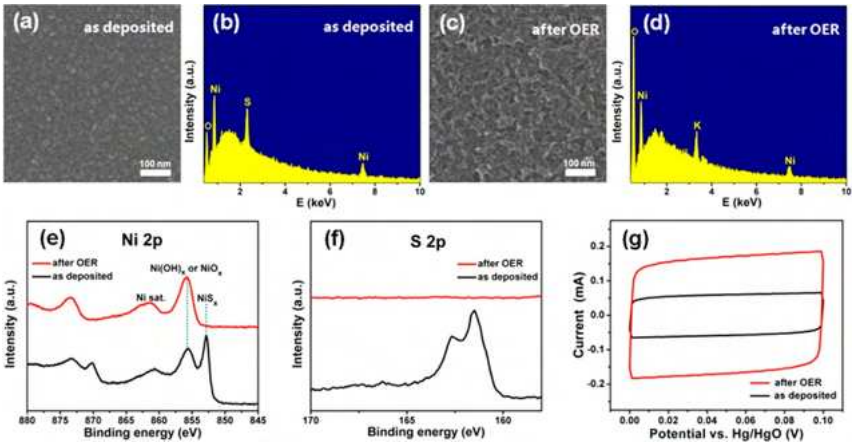


Figure 167. NiS_x film characterization after long-term stability testing. (a, c) SEM images of the NiS_x film (a) before and (c) after the OER. (b, d) EDX spectra of the NiS_x film (b) before and (d) after the OER. (e, f) High-resolution (e) Ni 2p and (f) S 2p XPS spectra of the NiS_x film before and after the OER. (g) CV profiles of the NiS_x film in the non-faradaic region before and after the OER. Reprinted with permission from ref 734. Copyright 2016 American Chemical Society.

surface was observed using SEM. This cracking is indicative of swelling of the material, which is linked to the formation of NiOOH. TEM and elemental mapping of a cross section of the activated material confirmed the formation of NiOOH at the surface, as the 0.67−0.7 nm lattice fringes corresponding to a γ-NiOOH phase were detected and little sulfur was detected for the outermost layer of the material while oxygen was detected in greater abundance in comparison to the innermost layer of the material analyzed. Characterization of the as-prepared and CV activated material using GIXRD, Raman spectroscopy, XPS, and time-of-flight secondary ion mass spectrometry (TOF-SIMS) further confirmed the formation of a $Ni(OH)_2$/NiOOH surface layer. Figure 166a shows the GIXRD patterns of the as-prepared (bottom) and CV-activated (top) samples. The GIXRD pattern of the CV-activated sample revealed a broad peak around 20° with a small peak emerging near its center at 26°, indicative of the $Ni(OH)_2$ and γ-NiOOH phases. These peaks, coupled with the drop-in intensity of those associated with the Ni_3S_2 phase, signify that partial surface oxidation had occurred due to CV activation. This partial oxidation is further evidenced by the Raman spectra before (bottom) and after activation (top), as the after-activation spectra reveal a broad peak at 560 cm^{-1} corresponding to NiOOH and very weak Ni-S peaks that were quite distinct prior to activation (Figure 166b). Figure 166c shows the high-resolution Ni 2p XPS spectra from before and after activation. There is a clear negative shift in the binding energy of the main Ni $2p_{3/2}$ peak indicating a higher Ni oxidation state and the presence of NiOOH at the surface. The S $2p_{1/2}$ and S $2p_{3/2}$ peaks also went undetected on the S 2p high-resolution spectra, further indicating that surface oxidation has occurred (Figure 166d). To gauge the extent of the oxidized layer on the CV activated sample, the authors used TOF-SIMS and determined that the oxide layer consisted

https://doi.org/10.1021/acs.chemrev.3c00005
Chem. Rev. 2023, 123, 12795−13208

of $Ni(OH)_2$ and NiOOH and that it was 700 nm deep. Under 700 nm, the material was composed of Ni_3S_2 (Figure 166e). At high oxidizing potentials during the OER, it was determined that the surface became NiOOH completely, as $Ni(OH)_2$ was oxidized to NiOOH at 1.3−1.5 V_{RHE}, as indicated by a peak in the CV spectra. This process, however, was reversible when cycling back to more reducing potentials.

The oxidation of Ni sulfides has also, of course, been reported for materials that have not undergone pre-OER oxidation steps before OER testing. For instance, Li and co-workers observed that, after only four CV cycles, the overpotential at a given current density increased when using their ALD NiS_x films as OER electrocatalysts.[734] As a result, they performed CP for 10 h at ∼1.60 V_{RHE}. For the first 2 h, there was a distinct increase in current density until the current density stabilized at ∼15 $mA{\cdot}cm^{-2}$. Following CP, there was a clear roughening of the surface and generation of the porous structure, as indicated by the SEM images taken before and after the long-term testing (Figures 167a and c). This roughening, along with the loss of the sulfur peak and intensification of the oxygen peak from the EDX spectra (Figures 167b and d), indicated that oxidation had occurred. This oxidation was further confirmed by XPS given no peaks associated with Ni−S bonds were present in the Ni 2p spectra and no sulfur peaks were detected in the S 2p spectra following long-term OER testing. Given the above findings and the presence of a $Ni(OH)_x/NiO_x$ peak on the Ni 2p high-resolution XPS spectrum, it was determined that the NiS_x film had been fully oxidized to nickel (oxy)hydrate ($Ni(OH)_2$/NiOOH). The bulk conversion of the material is evident from the loss of the sulfur peak from the EDX spectrum but also from the emergence of a potassium peak after the OER (Figures 167b and d). Potassium ions were detected because γ-NiOOH has a layered structure into which potassium ions can intercalate. The transformation of the material was further implicated by the change in the CV in the non-Faradaic region after long-term OER testing. The curve had broadened over the current scale, indicating a higher surface area material, which was confirmed by C_{dl} calculations. Unlike in the previously discussed articles, the NiS_x films underwent complete oxidation rather than simply surface oxidation. This result, however, should come as no surprise given the TOF-SIMs results previously discussed (Figure 167e), as the NiS_x films were only ∼10 nm thick based on TEM results, much thinner than the 700 nm oxidation layer formed on pre-oxidized Ni sulfide.[718] Thus, depending on initial Ni sulfide thickness, Ni sulfide-based electrocatalysts could be prepared with or without a Ni sulfide core/base and the ratio of Ni sulfide core/base to $Ni(OH)_2$/NiOOH layer could be tuned such that the electron conductivity and other properties of the material could be optimized. Thus, *in situ* oxidation is an option for preparing materials with a Ni oxide/(oxy)hydroxide layer that could serve as a protective layer against oxidation for a Ni sulfide core as has been prepared *ex situ*.[640]

Given the overwhelming evidence that Ni sulfides will be oxidized to a Ni oxide/(oxy)hydroxide phase and inevitably to the actual active site, NiOOH, at the surface, it is imperative that all Ni sulfides undergo full activation to the NiOOH phase before they are tested for the OER to determine the true performance of the stable material. If possible, extensive post-activation material characterization including techniques such as XRD, XPS, SEM, EDX, TEM, and HRTEM should also be performed to confirm the final form of the electrocatalyst has been attained.

Beyond Co sulfides and Ni sulfides, other notable precatalysts that have been studied in recent years are a copper sulfide and an iron sulfide-amine hybrid material ($FeS_{1.4}(Dmim)_{0.5}$ where Dmim = 1-*n*-butyl-2,3-dimethylimidazolium cation). Zuo and co-workers performed an in-depth study of the *in situ* oxidation of Cu_2S to CuO and the oxidized product's effectiveness as an OER electrocatalyst.[672] To prepare the Cu_2S material as an electrocatalyst for the OER, CV activation was used. The SEM images in Figures 168a−d showed that the copper sulfide on copper mesh

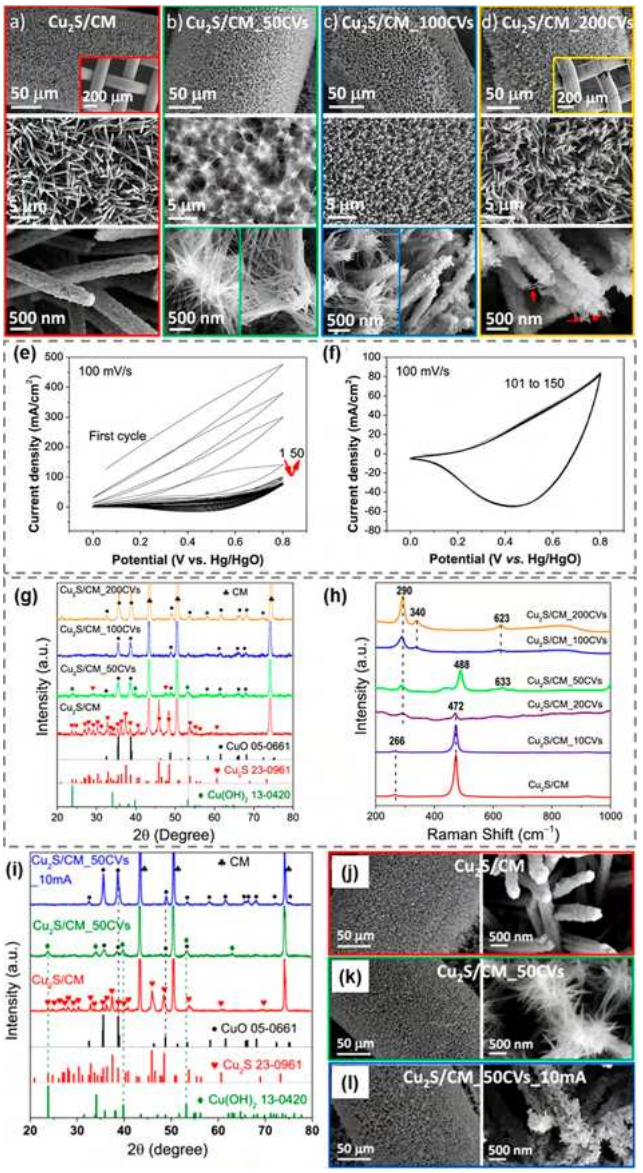


Figure 168. Material characterization for observing the transformation of Cu_2S/CM to CoO. (a−d) SEM images of Cu_2S/CM after (a) 0, (b) 50, (c) 100, and (d) 200 CV cycles. (e) First 50 CV and (f) 101st to 105th CV profiles of Cu_2S/CM. (g) XRD patterns and (h) Raman spectra of Cu_2S/CM after 0, 50, 100, and 200 CV cycles. (i) XRD patterns and (j−l) SEM images of as-prepared Cu_2S/CM, Cu_2S/CM after 50 CV cycles, and Cu_2S/CM after 50 CV cycles and subsequent stability testing, respectively. Reprinted with permission from ref 672. Copyright 2019 American Chemical Society.

https://doi.org/10.1021/acs.chemrev.3c00005
Chem. Rev. 2023, 123, 12795−13208

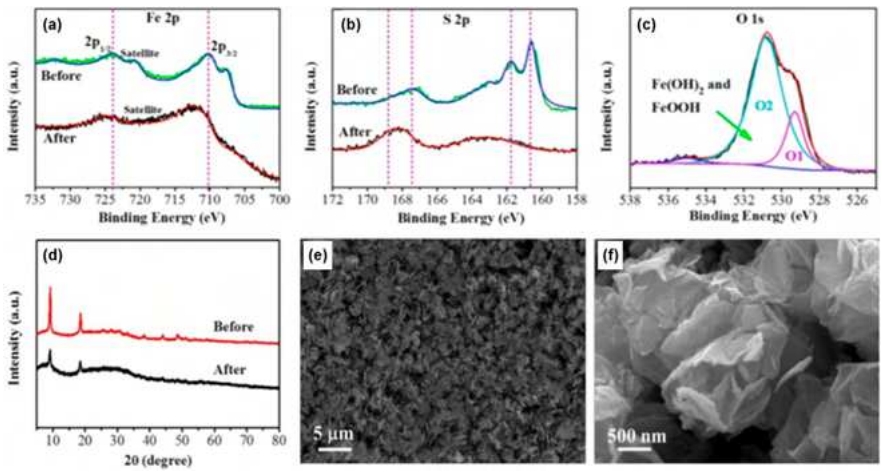


Figure 169. Pre- and post-OER characterization of Fe-sulfide-amine hybrid precatalyst ($FeS_{1.4}(Dmim)_{0.5}$). (a–c) High-resolution (a) Fe 2p, (b) S 2p, and (c) O 1s XPS spectra, (d) XRD patterns, and (e, f) SEM images of $FeS_{1.4}(Dmim)_{0.5}$ before and after long-term OER. Reprinted with permission from ref 698. Copyright 2018 Royal Society of Chemistry.

(Cu_2S/CM) underwent extensive morphological transformations at 50, 100, and 200 CV cycles from 0 to 0.8 $V_{Hg/HgO}$ at a scan rate of 100 $mV{\cdot}s^{-1}$. This observation is expected given the successive change in current density of the first 50 CV activation scans as observed in Figure 168e. CV activation scans taken at a slower scan rate of 5 $mV{\cdot}s^{-1}$ provided further evidence of material transformation, as the 0, 50, 100, and 200 CV scans had observable differences (not shown). A reproducible CV scan was only observed after 100 CV cycles were performed (Figure 168f). After 50 CV cycles, the XRD pattern indicated that the CuO and $Cu(OH)_2$ phases were present in addition to the Cu_2S phase. The Cu_2S phase was no longer present in the XRD pattern after 100 CV cycles, and only the CuO phase was observed after 200 CV cycles (Figure 168g). *In situ* Raman spectroscopy provided further evidence of the material transformation, as the peaks at 266 and 472 cm^{-1}, which correspond to the Cu–S and S–S bonds, respectively, disappeared after 50 CV cycles. Instead, peaks at 290 and 488 cm^{-1}, indicating the formation of $Cu(OH)_2$, and a peak at 633 cm^{-1}, corresponding to CuO, were observed. After 100 CV cycles, only peaks at 290, 340, and 633 cm^{-1} were observed, indicating that only CuO is present. Thus, as the authors concluded, the oxidation of Cu_2S proceeds as follows: $Cu_2S \rightarrow Cu(OH)_2 \rightarrow CuO$ (Figure 168h). XPS confirmed this finding, as the initial Cu_2S material consisted of 90% Cu_2S (Cu^+) and 10% CuO (Cu^{2+}) due to exposure to the atmosphere, while the 50 CV cycled material consisted of 18.1% Cu_2S (Cu^+), 69.6% $Cu(OH)_2$ (Cu^{2+}), and 12.3% CuO (Cu^{2+}), and a 50 CV cycled + long-term tested version of the material consisted of 100% CuO (Cu^{2+}). For the long-term OER test, the 50 CV cycled material was held at 10 $mA{\cdot}cm^{-2}$ in 1 M KOH for 10000 s. SEM images and XRD patterns confirmed that the as-prepared Cu_2S was fully transformed to CuO for the 50 CV cycles + operation at 10 $mA{\cdot}cm^{-2}$ for the 10000 s case compared to that of only 50 CV cycles for activation and the as-prepared material (Figures 168i and j–l).

Besides Cu sulfide, another monometallic sulfide that has not been extensively explored is Fe sulfide. While Fe is often doped into transition metal sulfides for improved OER performance or stability, it is rarely used as the singular metal in metal sulfides for the OER due to poor activity. Zhang and co-workers, however, were able to prepare a Fe-sulfide-amine hybrid material ($FeS_{1.4}(Dmim)_{0.5}$ where Dmim = 1-*n*-butyl-2,3-dimethylimidazolium cation) with comparable activity to other transition metal sulfides. And like other transition metal sulfides, $FeS_{1.4}(Dmim)_{0.5}$ acted as a precatalyst, as the initial material's surface was transformed to $Fe(OH)_2$/FeOOH under alkaline conditions during the OER. The surface oxidation was evident from post-OER characterization using XPS, XRD, and SEM following long-term OER testing for 12 h (see Table 5). From the Fe 2p XPS spectrum from before and after the OER (Figure 169a), there was a clear drop in intensity of lower oxidation state Fe while the peaks for oxidized Fe shifted to higher energy, indicating the presence of $Fe(OH)_2$ and FeOOH at the surface. Surface transformation to $Fe(OH)_2$/FeOOH was further confirmed by the S 2p and O 1s high-resolution spectra, as the sulfur peak intensities drastically decreased and the O 1s peaks indicated the presence of metal–O bonds (Figures 169b and c). XRD and SEM results indicated that the oxidation of the initial Fe sulfide to $Fe(OH)_2$/FeOOH was confined to the surface, as the major peaks were retained in the XRD pattern and only the surface of the Fe sulfide nanosheets was roughened with no bulk morphological changes occurring following long-term OER testing (Figures 169d–f). From their initial CV scan taken at a scan rate of 50 $mV{\cdot}s^{-1}$, it was also evident that the surface consisted of $Fe(OH)_2$/FeOOH, as two redox peaks were present, an anodic peak at ~1.34 V_{RHE} and a cathodic peak at ~1.22 V_{RHE}. The anodic peak corresponded to the oxidation of $Fe(OH)_2$ to FeOOH. Thus, if the initial material was held at sufficient oxidizing potential for longer than 12 h, it is possible that only FeOOH would reside on the surface. More work should be done to determine if $Fe(OH)_2$ and FeOOH act as the active site or if FeOOH alone is the real active site for OER electrocatalysis. More generally, Fe sulfides should be explored further given their potential for enhanced OER performance at a lower cost as Zhang and co-workers demonstrated in their work.

In recent years, multimetal precatalysts have been explored, as the incorporation of additional metals has been shown to result in improved catalytic performance towards the OER. This improved activity is a result of intrinsic synergistic effects due to the incorporation of more than one metal. These synergistic effects, however, have rarely been investigated at a

https://doi.org/10.1021/acs.chemrev.3c00005
Chem. Rev. 2023, 123, 12795–13208

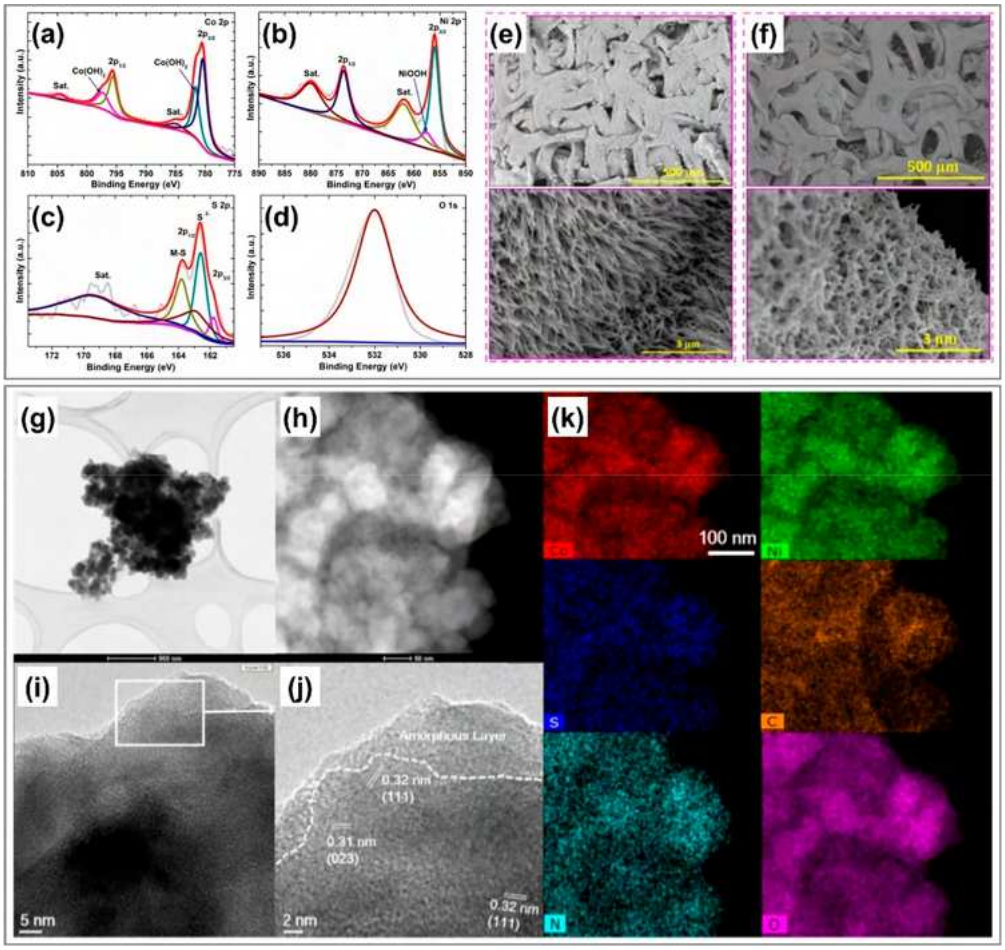


Figure 170. Characterization of Ni-Co sulfides. (a–d) High-resolution (a) Co 2p, (b) Ni 2p, (c) S 2p, and (d) O 1s XPS spectra of $NiCo_2S_4$/NF after the OER. (e, f) SEM images of $NiCo_2S_4$/NF (e) before and (f) after long-term OER testing. Reprinted with permission from ref 741. Copyright 2016 Wiley. (g, h) TEM, (i, j) HRTEM, and (k) elemental mapping images of CNS-NGA after the OER. Reprinted with permission from ref 715. Copyright 2018 American Chemical Society.

fundamental level to understand the root of these effects and why they occur. Herein, bimetal and trimetal sulfide precatalysts will be discussed.

Of the bimetal sulfides, those incorporating Co and Ni are most prevalently reported in the literature. These materials are quite common since Co and Ni sulfides are known to be active for the electrocatalysis of the OER independently. These Co-Ni sulfides have been prepared via the incorporation of Co or Ni into the same metal-sulfide crystal structure or via the preparation of a composite material. One Ni-Co sulfide material that has been explored is spinel structured $NiCo_2S_4$. Sivanantham and co-workers prepared a spinel $NiCo_2S_4$/NF electrocatalyst for the OER, as the spinel structure is thought to impart greater stability to materials under alkaline conditions (1 M KOH).[741] From the XRD pattern of the as-prepared $NiCo_2S_4$/NF, the $NiCo_2S_4$ spinel phase was clearly present with only a small Ni_3S_2 impurity also present. The as-prepared material consisted of a nanowire array morphology, which was maintained overall following 50 h of long-term OER testing with only a slight roughening of the surface observed (Figures 170e and f). This roughening indicated that oxidation only occurred at the surface of the material, as did post-OER XRD results, which indicated no alteration to the bulk crystal structure of the material. After long-term OER, the Co 2p high-resolution XPS spectrum contained all peaks, as seen in the spectrum for the as-prepared material with the addition of two peaks at 785.4 and 795.7 eV, which correspond to the $2p_{3/2}$ and $2p_{1/2}$ peaks of $Co(OH)_2$, respectively (Figure 170a). The Ni 2p XPS spectrum indicated that NiOOH was present on the surface of the material, which is the known active material formed *in situ* for prepared Ni sulfides (Figure 170b). The emergence of these new peaks along with the high-intensity peak from the O 1s high-resolution XPS spectrum supports the conclusion that the as-prepared $NiCo_2S_4$/NF is a precatalyst that undergoes partial oxidation (Figure 170d). Interestingly, however, all sulfur peaks were retained following long-term OER and the intensity of the sulfate ion peak at ~169 eV appeared to diminish relative to the metal sulfide peak (Figure 170c), which contrasts with the results for monometallic Co sulfides and Ni sulfides. Nevertheless, post-characterization results showed that the $NiCo_2S_4$/NF material underwent surface oxidation, and the identified active sites of NiOOH and $Co(OH)_2$ are in accordance with additional reports on spinel $NiCo_2S_4$ as a precatalyst for the OER.

In contrast, when Han *et al.* prepared a Ni-doped CoS_2-nitrogen-doped reduced graphene oxide aerogel nanocomposite (CNS-NGA or $Co_{1-x}Ni_xS_2$-graphene composite), they determined that CoOOH/NiOOH was the active site for the OER after long-term testing (see Table 5). TEM and HRTEM images following OER testing indicated a change to the surface

https://doi.org/10.1021/acs.chemrev.3c00005
Chem. Rev. 2023, 123, 12795–13208

of the material, specifically the formation of an amorphous layer atop the crystalline CNS-NGA (Figures 170g–i). The retention of the crystalline CNS core was confirmed by the presence of the 0.32 and 0.31 nm lattice fringes, which correspond to the (111) and (023) lattice planes of CNS (Figure 170j). Elemental mapping, in conjunction with EDX results, indicated that Co, Ni, N, S, and O were present in the material, with O content increasing from 5.61 to 22.95 at % following OER testing (Figure 170k). This increase in O content and the retained sulfur thus indicated that the surface and not the entire catalyst material underwent oxidation, as there was no indication of the oxidation of the CNS NPs prior to OER testing.[715] Additionally, the XRD pattern, which indicated the presence of cubic $CoNiS_4$ phase in the as-prepared material, was maintained with only a slight loss in peak intensity and peak broadening. These drops in peak intensity and the broadening of peaks indicated some amorphous character to the material, with this amorphous character being a CoOOH/NiOOH layer formed at the surface during OER testing. It is likely that CoOOH/NiOOH was formed after long-term OER, rather than $Co(OH)_2$ or CoO in addition to CoOOH and NiOOH, as has been reported elsewhere for Ni-doped CoS_2 because pre-OER XAS and XPS characterization only indicated the presence of Co^{2+}, making oxidation to Co^{3+} impossible.[748] An anodic peak at 1.35 V_{RHE} present in a polarization curve following long-term testing further supported the *in situ* formation of the CoOOH/NiOOH active sites, as this peak could be assigned to the reaction of $Co(OH)_2/Ni(OH)_2 + OH^- \rightarrow$ CoOOH/NiOOH + $H_2O + e^-$. Thus, at sufficiently positive potentials for the OER, the surface would be oxidized from Co^{2+}/Ni^{2+} to Co^{3+}/Ni^{3+} to form Co and Ni oxyhydroxide. The increase in double-layer capacitance following the OER, from 10.25 to 21.28 mF·cm^{-2}, also indicated the formation of this CoOOH/NiOOH layer, as the transformation of Ni sulfides to NiOOH is known to be accompanied by volume expansion of the material, as discussed earlier in this section. The charge transfer resistance (R_{ct}) of CNS-NGA, as determined from EIS, was nearly unchanged before and after long-term OER testing at 30 and 32 Ω, respectively. The stability of the R_{ct} value of CNS-NGA further confirmed that the material was only partially oxidized, as the more conducting CNS nanoparticles must be present in addition to CoOOH/NiOOH for electrical conductivity to remain essentially unchanged, as oxides/(oxy)hydroxides suffer from poor conductivity as compared to metal sulfides. Thus, the CNS nanoparticles are protected by the amorphous CoOOH/NiOOH layer, and the electrical conductivity of the as-prepared metal sulfide is preserved. The ability of metal oxide/(oxy)hydroxide layers to protect metal sulfide cores has been reported extensively in the literature for both *in situ* and *ex situ* generated oxide/(oxy)hydroxide layers including for a Ni_3S_2/Co_9S_8 subjected to long-term OER testing.[640,707,711,785]

This Ni_3S_2/Co_9S_8 electrocatalyst was prepared on Ni foam (NF), resulting in a core@branch Ni_3S_2-Co_9S_8 structure that could be modulated based on the concentration of the sulfur source during hydrothermal synthesis. The overall morphology of their most active material for the OER, Ni_3S_2/Co_9S_8 prepared using a 0.5 M sulfur source on Ni foam (NCS-0.5/NF), was essentially unaltered following 12 h of chronoamperometry at 100 mA·cm^{-2}, as nanosheets were still present on the initial Co_9S_8 branches (Figures 171a and b). Additionally, there was no observable change to the XRD pattern. There were, however, stark differences between XPS spectra taken

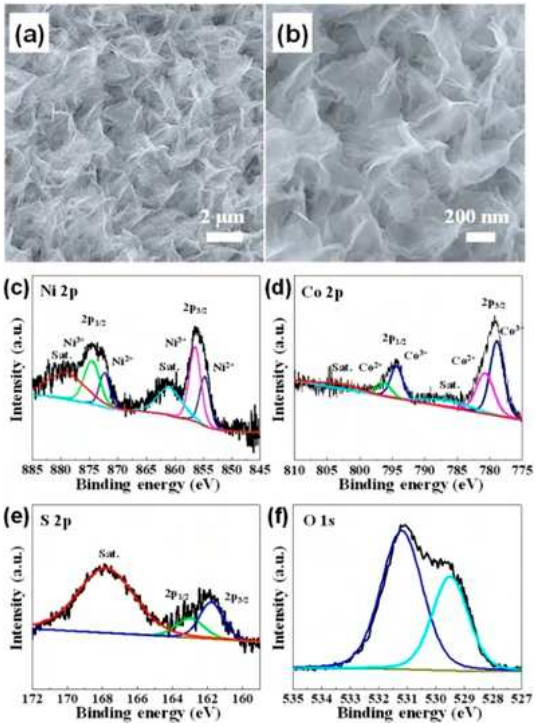


Figure 171. Post-OER characterization of NCS-0.5/NF: (a, b) SEM images and (c) Ni 2p, (d) Co 2p, (e) S 2p, and (f) O 1s XPS spectra. Reprinted with permission from ref 707. Copyright 2018 Elsevier.

before and after OER testing with both the high-resolution Ni 2p and Co 2p spectra indicating a greater ratio of Ni^{3+} to Ni^{2+} and Co^{3+} and Co^{2+} present on the surface after OER testing, respectively (Figures 171c and d). This observation implies that NiOOH and CoOOH could be at the surface and be the actual active sites for the OER, as other work on Ni sulfides and Co sulfides indicates (see Ni and Co sulfide sections). The O 1s XPS spectrum also indicates that surface oxidation has occurred, as peaks corresponding to lattice oxygen and surface hydroxyls at binding energies of 529.5 and 531.2 eV, respectively, were found (Figure 171f). The increase in the intensity of the sulfate peak at ∼169 eV and the drop in intensity of the peaks corresponding to metal–sulfide bonds in the S 2p XPS spectrum further support that the surface had been oxidized (Figure 171e). The fact that the overall morphology and diffraction pattern remain unaltered, however, indicates that once the surface is oxidized, the Ni_3S_2/Co_9S_8 phase is preserved beneath, indicating the formation of a protective oxide layer for as-prepared Ni sulfide/Co sulfide materials during OER testing.

Bimetal and multimetal sulfides have been explored as electrocatalysts for the OER because the incorporation of two or more metals has been shown to lead to synergistic effects that result in improved electrocatalytic performance and/or stability. The incorporation of multiple metals can also impart bifunctionality onto the electrocatalyst, making it useful for the electrocatalysis of other reactions such as the HER and ORR in addition to the OER. Many Mo sulfide/Ni or Co sulfide composites and heterostructures have been prepared for constructing a bifunctional electrocatalyst for overall water splitting, as MoS_2 is known to perform well for the HER and Ni/Co sulfides have shown promise for the OER. One example of such an electrocatalyst is the MoS_2/Ni_3S_2 heterostructures prepared on Ni foam by Zhang and co-workers. These

https://doi.org/10.1021/acs.chemrev.3c00005
Chem. Rev. 2023, 123, 12795–13208

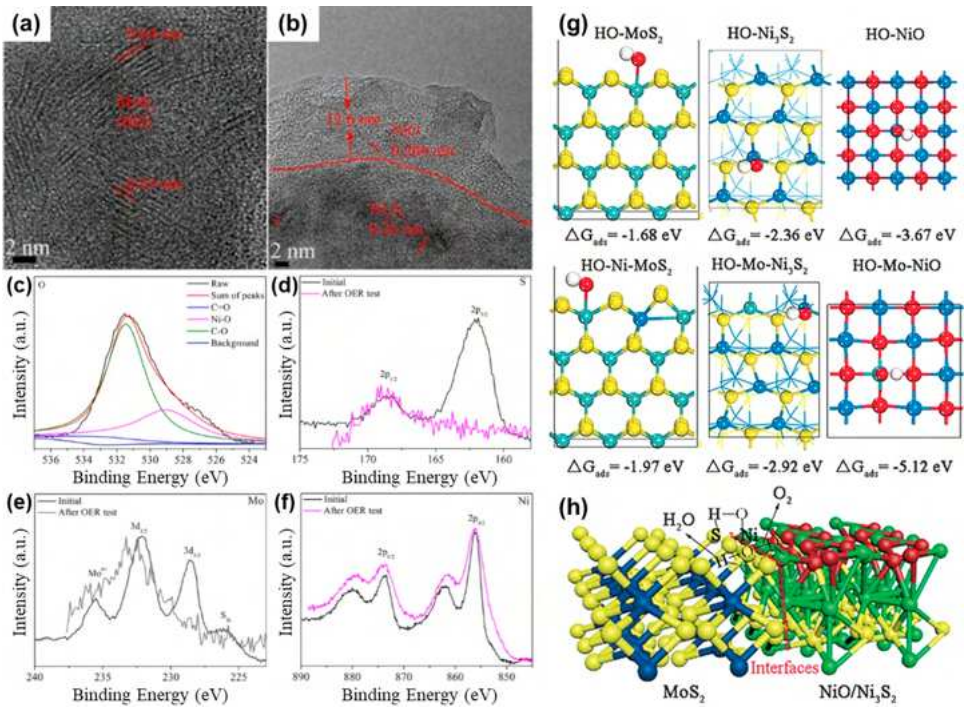


Figure 172. Post-OER characterization and mechanistic considerations of MoS_2/Ni_3S_2 heterostructure: (a, b) HRTEM images, (c–f) high-resolution (c) O 1s, (d) S 2p, (e) Mo 3d, and (f) Ni 2p XPS spectra, (g) chemisorption models for OH^-, and (h) proposed OER mechanism at the $MoS_2/NiO/Ni_3S_2$ interface. Reprinted with permission from ref 738. Copyright 2016 Wiley.

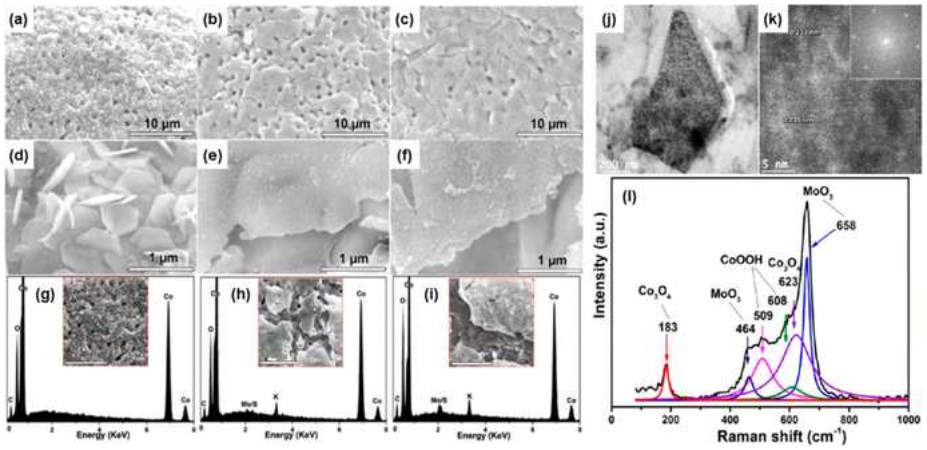


Figure 173. Post-OER characterization of Co@MoS_2 samples and bare Co foam. (a–f) Low- and high-magnification SEM images of (a, d) bare Co foam, (b, e) Co@MoS_2-500, and (c, f) Co@MoS_2-1000. (g–i) EDX spectra of (g) bare Co foam, (h) Co@MoS_2-500, and (i) Co@MoS_2-1000. (j, k) HRTEM images of bare Co foam. (l) Raman spectrum of Co@MoS_2-1000. Reprinted with permission from ref 746. Copyright 2017 Royal Society of Chemistry.

heterostructures consisted of MoS_2 decorated on Ni_3S_2 NPs and led to improved OER performance as compared to Ni_3S_2 NPs alone, achieving a current density of 94.8 $mA{\cdot}cm^{-2}$ as compared to 5.0 $mA{\cdot}cm^{-2}$ for the Ni_3S_2 NPs at 1.53 V_{RHE} in 1.0 M KOH.[738] The heterostructure also maintained stable potential during 10 h of long-term testing when held at 10 $mA{\cdot}cm^{-2}$. From post-OER characterization, it was evident that the surface of the material had been oxidized during the OER given the clear roughening of the surface from SEM images, the detection of the 0.206 nm lattice fringe corresponding to the (010) plane of NiO at the surface of the material from HRTEM images, and the XPS results (Figures 172a–f). From the O 1s and S 2p spectra, it was clear that oxides had formed on the surface, as metal–O bonds were found in the O 1s spectrum and the metal-sulfide peak disappeared after the OER testing (Figures 172c and d). The Mo spectrum was quite noisy as compared to its spectrum before long-term OER, further emphasizing the formation of NiO at the surface, as Mo was more difficult to detect via XPS. In the Mo high-resolution XPS spectra there is also a slight shift toward the Mo^{6+} peak, indicating that, of the Mo present, it was oxidized at the surface (Figure 172e). After OER testing, the MoS_2 phase was also detected in the material via HRTEM (Figures 172a and e). As in previous cases, the Ni sulfide was oxidized during OER testing to the NiO phase, the active site for OER catalysis; however, in the case of this heterostructure, the NiO phase alone was not responsible for the overall OER performance, which outdid that of Ni_3S_2 NPs alone. From DFT calculations,

https://doi.org/10.1021/acs.chemrev.3c00005
Chem. Rev. 2023, 123, 12795–13208

it was determined that the NiO-MoS_2 interface was responsible for catalyzing the OER, as OH^- adsorption was found to be most favorable at the Mo-NiO sites, as it exhibited the lowest Gibbs free energy for OH^- adsorption of the considered sites (Figure 172g). From these results, Zhang and co-workers proposed an OER mechanism at the interface of their as-prepared heterostructure material, as shown in Figure 172f. Another study on Ni sulfides/Mo sulfides, specifically Ni_3S_2/MoS_2 nanosheets on Ni foam, made similar conclusions: under OER conditions in alkaline media, the Ni-sulfide component was oxidized, resulting in a NiOOH layer on the surface during the OER while the Mo sulfide was retained.[732] In other reports, however, post-characterization results have indicated that Mo in addition to Ni has undergone oxidation during the OER in Mo sulfide/Ni sulfide and Mo-doped Ni_3S_2.[710,742] Yan and co-workers found that their MoS_2 microspheres on Ni foam underwent oxidation to form MoO_3 and NiOOH after 500 cycles of stability testing (see Table 5). The presence of MoO_3 was indicated by the decay in current density with cycle number, as MoO_3 is an insulating material. Its presence was also further confirmed using XRD and Raman spectroscopy.[742] More work needs to be done to deconvolute the interplay between Mo sulfide and Ni sulfide for the OER and whether or not Mo sulfide or Ni sulfide each contribute to OER electrocatalysis and to what extent.

In the case of Co sulfides/Mo sulfides, when MoS_2 was deposited on Co foam (Co@MoS_2) via atomic layer deposition (ALD), the surface was transformed to MoO_3 and CoOOH, similarly to the MoS_2 microsphere on Ni foam case.[742,746] Following 100 h of a CP stability test, cracks on the surface of Co@MoS_2 prepared using 500 and 1000 ALD cycles (denoted Co@MoS_2-500 and Co@MoS_2-1000, respectively) were observed with the cracks being more severe for the Co@MoS_2-1000 material (Figures 173b, c, e, and f). Unlike the bare Co foam, there was no formation of nanosheets at the surface (Figures 173a and d). The EDX spectrum for the bare Co foam denoted Co@MoS_2-500, and Co@MoS_2-1000 had increased oxygen peaks, indicating surface oxidation, as did the reduction in Mo and S peaks for Co@MoS_2-500 and Co@MoS_2-1000 (Figures 173g–i). HRTEM of the bare Co foam also indicated oxidation had occurred, as lattice fringes for CoOOH were observed from HRTEM images (Figures 173j and k). From the Raman spectrum of the post-OER catalyst, both MoO_3 and CoOOH were detected, once again indicating surface oxidation had occurred (Figure 173l). Transformation of MoS_2 to insulating MoO_3, as aforementioned, could account for the decreased activity observed after 100 h of stability testing. This loss of activity could, however, also have resulted from the loss of contact of MoS_2 from the Co foam substrate.

Bimetal-incorporated sulfides have also been prepared using metals such as Mn, Au, and Ti in addition to Co or Ni. Jadhav and co-workers investigated $MnCo_2S_4$ nanoflakes on stainless steel mesh (SS) as an electrocatalyst for the OER owing to its high electrical conductivity as a result of its spinel structure and known optical properties.[673] The XRD pattern of the as-prepared $MnCo_2S_4$ nanoflakes on SS only had observable peaks related to the SS substrate (Figure 174a). Initial XPS results revealed the presence of both Co^{2+} and Co^{3+} from the Co 2p spectrum and S^{2-} and metal–S bonds from the S 2p spectrum (Figures 174c and d). Following 100 h of chronoamperometry at 1.54 V_{RHE}, the formation of MnOOH was indicated by the presence of peaks in the Mn 2p spectrum at 641.8 and 653.6 eV, the Mn $2p_{3/2}$ and Mn $2p_{1/2}$ peaks,

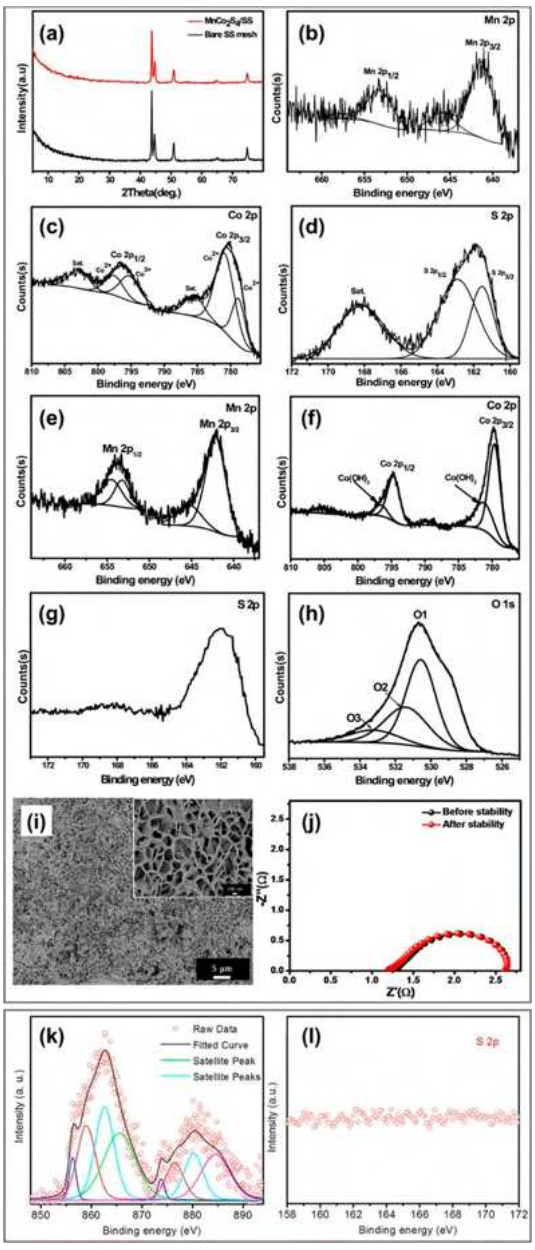


Figure 174. Characterization of bimetal sulfides. (a) XRD patterns of as-prepared spinel $MnCo_2S_4$/SS and SS substrate. (b–d) High-resolution (b) Mn 3d, (c) Co 2p, and (d) S 2p XPS spectra of the as-prepared $MnCo_2S_4$/SS. (e–h) High-resolution (e) Mn 2p, (f) Co 2p, (g) S 2p, and (h) O 1s XPS spectra and (i) SEM image of $MnCo_2S_4$/SS after the OER. (j) Nyquist plots of $MnCo_2S_4$/SS before and after long-term OER testing. Reprinted with permission from ref 673. Copyright 2019 Elsevier. (k, l) High-resolution S 2p XPS spectra of 3DG-Au-Ni_3S_2 (k) before and (l) after the OER. Reprinted with permission from ref 678. Copyright 2019 American Chemical Society.

respectively (Figure 174e). From the Co 2p spectrum, it was evident that $Co(OH)_2$ had formed on the surface given the presence of peaks at binding energies of 781.6 and 797 eV, which correspond to Co $2p_{3/2}$ and Co $2p_{1/2}$, respectively (Figure 174f). From the post-long-term OER, the O1, O2, and O3 peaks indicate that oxide, hydroxide or Mn-OH and adsorbed water are present, respectively (Figure 174h). Given these results and the loss of two sulfur peaks from the S 2p spectrum, it was clear that the as-prepared spinel had undergone partial oxidation (Figure 174g). The retention of

https://doi.org/10.1021/acs.chemrev.3c00005
Chem. Rev. 2023, 123, 12795–13208

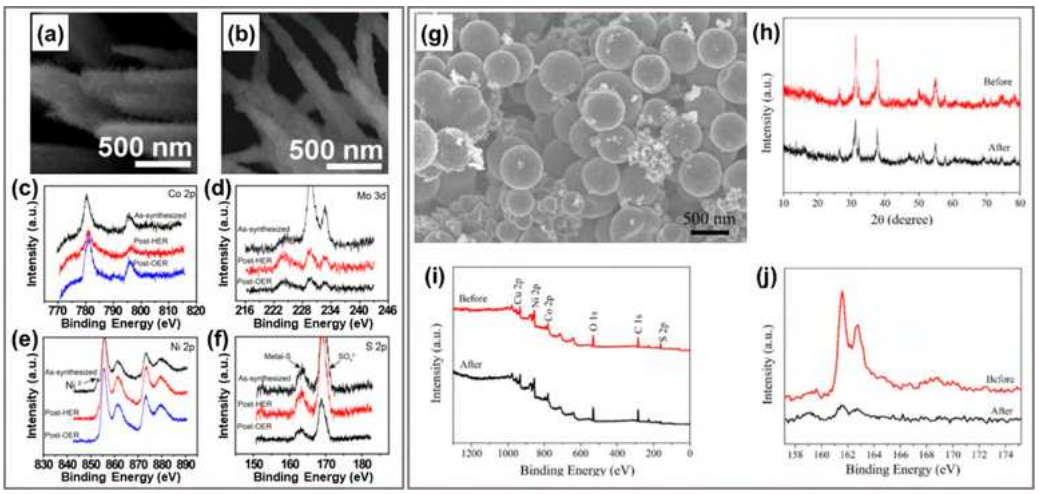


Figure 175. Pre- and post-OER characterization of multimetal sulfides. (a, b) SEM images of CoMoNiS-NF-31 (a) before and (b) after the OER. (c–f) High-resolution XPS spectra of CoMoNiS-NF-31 before and after the OER and HER: (c) Co 2p, (d) Mo 3d, (e) Ni 2p, and (f) S 2p. Reprinted with permission from ref 688. Copyright 2019 American Chemical Society. (g) SEM image of post-OER NiCuCo-sulfide. (h) XRD patterns of NiCuCo-sulfide before and after the OER. (i) Survey and (j) high-resolution S 2p XPS spectra of NiCuCo-sulfide before and after the OER. Reprinted with permission from ref 683. Copyright 2019 American Chemical Society.

the overall morphology, including the porous structure, and the EDX results after the OER indicated that the bulk of the material was unaltered (Figure 174i). The Nyquist plots recorded before and after long-term OER were also nearly identical, indicating little change to the electrical conductivity of the initial material as a result of OER testing in an alkaline environment (Figure 174j). Thus, the spinel structure imparts some stability as with the previously discussed $NiCo_2S_4$ spinel case.[741] Interestingly, the A-position metal in the spinel of general form AB_2C_4, for both the $NiCo_2S_4$ and $MnCo_2S_4$ cases, formed the oxyhydroxide following long-term OER testing while the B-position metal, Co, only formed $Co(OH)_2$. The formation of $Co(OH)_2$ and not CoOOH at the surface following OER contrasts with mechanistic studies for single-metal Co sulfide materials, which have indicated that CoOOH is the actual active site for the OER in many cases. Further investigations are needed to determine why one metal center may undergo further oxidation than another. It would be interesting to determine the extent of oxidation at each metal center. If the spinel structure could lead to the oxidation of the A-position metal of Ni or Mn instead of Co at the B-position, then the overall conductivity of the material could be well maintained despite strongly alkaline conditions, as Co is more conductive than Mn and Ni. The sacrifice of Mn sites for the preservation of Co sites could, for instance, explain the nearly identical Nyquist plot from before and after long-term OER testing (Figure 174j). Additional study of the initial spinel structure could also determine whether it also imparts stability in regard to sulfur retention, as the sulfate peak seemed to disappear from the surface while the metal-S peak was maintained in the S 2p XPS spectrum.

Unlike in the case of the as-prepared spinel electrocatalysts prepared for the OER, other as-prepared materials have an observable loss of metal-S bonds at the surface of the material, as indicated by XPS. For example, Tsai and co-workers found that their Ni_3S_2 nanosheets electrodeposited on Au dendrites on 3D-graphene (3DG-Au-Ni_3S_2) underwent surface oxidation. From the Ni 2p peak following the OER, there was a shift in peak positions to higher binding energies, indicating oxidation, as did the presence of peaks at 856.3 and 859 eV, which correspond to $Ni(OH)_2$ and NiOOH, respectively (Figure 174k).[678] Of the two peaks, the NiOOH peak was more intense, which is expected given NiOOH has been shown to be the real active site for single-metal Ni sulfides (see above discussion about nickel sulfides). Then, there was no detectable sulfur at the surface of the material, as indicated by the post-OER S 2p spectrum (Figure 174l). For a CoS_2-TiO_2 hybrid, it was also found that sulfur was not retained well at the surface, as only a sulfate peak was observed following long-term testing—the metal–S peak had completely disappeared.[725] In this case, CoOOH and $Co(OH)_2$ were detected at the surface following the OER, while no change was observed in the Ti 2p XPS spectrum. Thus, the initial structure of bimetallic sulfides has a great effect on their overall stability and which incorporated metal suffers the most from oxidation and/or dominates as the real active site.

In addition to bimetallic sulfides, trimetallic sulfides have also been reported, leading to more complex materials that require in-depth study to determine the actual active sites and why one metal may dominate as the active site following OER testing rather than another within the same as-prepared material. Yang and co-workers found that their CoMoNiS-NF-31 composite (where 3:1 is Co:Mo), consisting of MoS_2 and Co_9S_8 nanosheets on Ni_3S_2 nanorod arrays using a Ni foam (NF) support, underwent surface oxidation following 24 h of stability testing using CP (see Table 5).[688] No changes to the morphology of the composite were observed from SEM images taken before and after long-term stability testing in alkaline media (Figures 175a and b). Unlike after HER testing, there were some noticeable changes to the high-resolution XPS spectra after OER testing. In the Ni 2p spectrum, the metallic Ni peak was completely lost, while no drastic changes in the Co 2p and Mo 3d spectra were observed (Figures 175c–e). The decreased intensity of the metal–S peak from the S 2p spectrum indicated overall surface oxidation, likely to metal (oxy)hydroxide sites (Figure 175f). Given the Co_9S_8/Ni_3S_2/NF and MoS_2/Ni_3S_2/NF control samples did not perform nearly as well as CoMoNiS-NF-31 for the OER (or for the HER), it was concluded that the enhanced activity of their CoMoNiS-NF-31 composite was a result of synergistic effects

https://doi.org/10.1021/acs.chemrev.3c00005
Chem. Rev. 2023, 123, 12795–13208

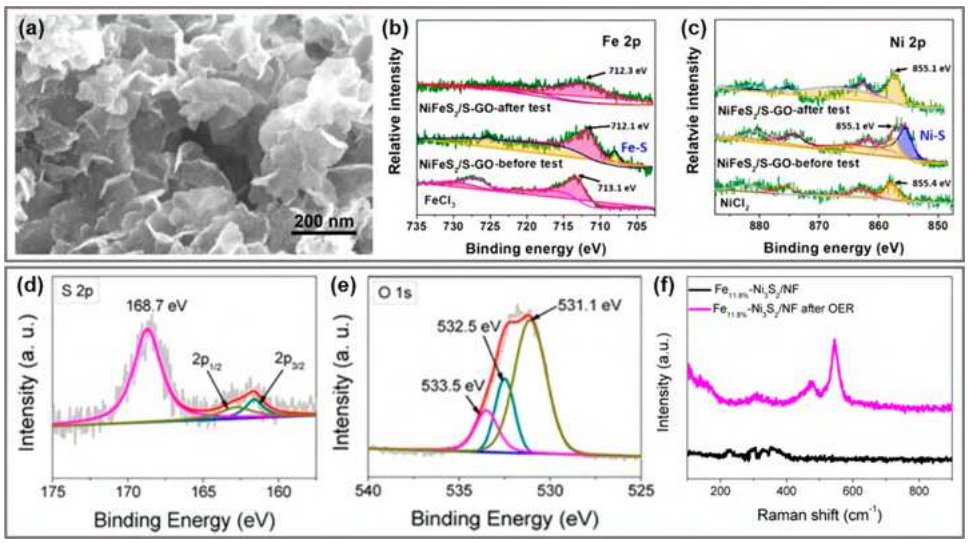


Figure 176. Pre- and post-OER characterization of Ni-Fe sulfides. (a) SEM image of post-OER $NiFeS_2$/S-GO. (b, c) High-resolution (b) Fe 2p and (c) Ni 2p XPS spectra of $FeCl_3$ and $NiFeS_2$/S-GO before and after OER stability testing. Reprinted with permission from ref 704. Copyright 2018 Royal Society of Chemistry. (d, e) High-resolution (d) S 2p and (e) O 1s XPS spectra of post-OER Fe-doped Ni_3S_2/NF. (f) Raman spectra of the as-prepared and post-OER Fe-doped Ni_3S_2/NF. Reprinted with permission from ref 753. Copyright 2015 Royal Society of Chemistry.

from the incorporation of the Co_9S_8 and MoS_2 phases within the material. DFT calculations indicated that electron transfer from Co in Co_9S_8 to Mo in MoS_2 at the interface of the material resulted in a drop-in Gibbs free energy for the intermediate steps and lower overpotentials for the OER when MoS_2 nanosheets were perpendicular to Co-terminated Co_8S_9 (see more in Section 5.1.3). Such synergistic effects have also been reported for OER electrocatalysts combining other phases such as $NiCo_2S_4$ and $CuCo_2S_4$, which Wu has done to prepare Ni, Cu, Co-based mixed sulfide nanospheres for the OER and ORR.[683] Following OER stability testing, the nanosphere morphology was maintained in addition to the overall crystal structure, as indicated by the XRD patterns from before and after OER testing (Figures 175g and h). The high-resolution XPS spectrum indicated that surface oxidation of the metal sulfides to metal (oxy)hydroxides had occurred, as the metal−S peak was greatly diminished following OER testing (Figure 175j). Whether NiOOH or CoOOH or CuO is formed or dominates in terms of electrocatalysis for the OER, however, remains unknown. In the future, extensive work should be done to decouple the effect each metal has on a material's overall structure, its activity toward the OER, and the role of each metal species in the electrocatalysis of the OER.

Metal sulfides, such as Ni sulfides, are also known to undergo a marked improvement in performance due to Fe incorporation from impure KOH electrolyte, the most common electrolyte used for testing OER electrocatalysts.[200] Thus, it comes as no surprise that Fe-doping and Fe incorporation into metal sulfides have led to improved materials for the electrocatalysis of the OER and have been extensively studied in recent years. The majority of these mixed metal sulfides consist of either Ni and Fe, Co and Fe, or Ni, Co, and Fe.

Several metal sulfides incorporating Ni and Fe have been reported, with the pyrite $NiFeS_2$ phase being the most extensively studied (refs 704, 709, 716, 722, 728, 736, and 753). For example, Zhou and co-workers prepared a NiFe sulfide with S-doped graphene oxide ($NiFeS_2$/S-GO) on glassy carbon as an OER and ORR electrocatalyst.[704] After stability testing was performed (see Table 5), they found that the material's nanosheets had become rough at the surface, possibly due to $NiFeO_x$ formation (Figure 176a). The high-resolution XPS spectra for Fe 2p and Ni 2p also indicated that oxidation occurred at the material's surface. The metal−sulfur peaks for both the Fe 2p and Ni 2p spectra disappeared following stability testing. There was also a clear shift to higher binding energies for the peaks present in both spectra, indicating the oxidation of surface $NiFeS_2$ to $NiFe(OOH)_x$ (Figures 176b and c). Similarly, Cheng *et al.* found that NiOOH and FeOOH were formed on the surface of their Fe-doped Ni_3S_2 film for the OER.[753] The presence of these species on the surface was confirmed by XPS, wherein a peak at 858.1 eV in the high-resolution Ni 2p spectrum after OER stability testing corresponded to NiOOH and peaks at 711.4 and 724.9 eV and their satellite peaks in the high-resolution Fe 2p spectrum after OER stability testing corresponded to FeOOH. The formation of these species was also confirmed by the high-resolution S 2p and O 1s spectra (Figures 176d and e). In the S 2p spectrum after OER stability testing, the $2p_{1/2}$ and $2p_{3/2}$ peaks corresponding to S^{2-} in Ni_3S_2 are greatly diminished in intensity while the Ni−O−S peak at 168.7 eV increased in intensity, implying surface oxidation had occurred. The emergence of the peak at 533.5 eV in the high-resolution O 1s spectrum also indicated NiOOH formation at the surface. The transformation of the sulfide to NiOOH and FeOOH at the surface was further confirmed by Raman spectroscopy. Figure 176f shows the Raman spectrum of the post-OER material, with three clear peaks—the 305 cm^{-1} peak corresponding to FeOOH and the other two at higher wavenumber corresponding to NiOOH. By incorporating Fe, the active site FeOOH emerges in addition to NiOOH.

A Ni-Fe disulfide@oxyhydroxide heterostructure prepared *via in situ* oxidation also indicated that a hybrid active site was formed at the surface of the material.[728] The Ni-Fe disulfide@oxyhydroxide heterostructure consisted of a 20 at % Fe-substituted Ni pyrite disulfide core ($Ni(Fe)S_2$) and a γ-Ni(Fe)OOH shell. After 1 CV cycle (Figure 177a) for

https://doi.org/10.1021/acs.chemrev.3c00005
Chem. Rev. 2023, 123, 12795−13208

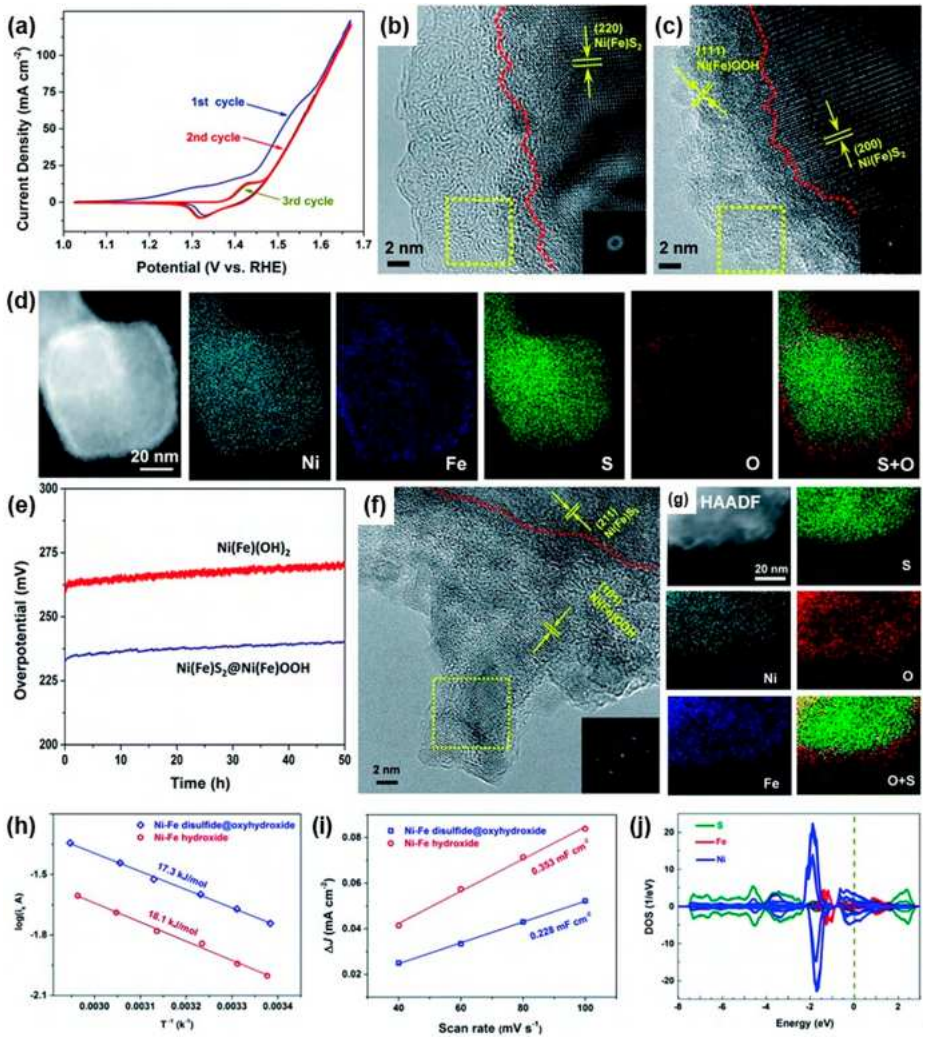


Figure 177. CV activation and post-OER characterization and analysis of Ni-Fe disulfide@oxyhydroxide heterostructure. (a) First 3 CV activation cycles of Ni-Fe disulfide. (b, c) TEM images of Ni-Fe disulfide after (b) 1 CV activation cycle and (c) 100 CV activation cycles. (d) Elemental mapping images of Ni-Fe disulfide after 100 CV activation cycles. (e) Chronopotentiometry stability test of *in situ*-prepared Ni(Fe)S_2OOH and as-prepared Ni(Fe)OH_2 at 10 mA·cm^{-2} for 50 h. (f) TEM image of Ni(Fe)S_2OOH after 24 h CA at 1.60 V_{RHE}. (g) Elemental mapping images of Ni(Fe)S_2OOH after 24 h CA at 1.60 V_{RHE}. (h) Arrhenius plots and (i) C_{dl} plots of Ni(Fe)S_2OOH and as-prepared Ni(Fe)OH_2. (j) Calculated DOS of Ni-Fe disulfide. Reprinted with permission from ref 728. Copyright 2017 Royal Society of Chemistry.

activation of the initial metal disulfide to the heterostructured metal sulfide@oxyhydroxide in 1 M KOH, it was clear that an amorphous layer with a thickness of 2−10 nm had formed on the surface from HRTEM images (Figure 177b). This amorphous layer was considered to be the intermediate Fe/Ni$(OH)_2$ state, as the material underwent an irreversible oxidation process, as indicated by the difference in the shape of CV 1 to CV 2 during the activation process. With increasing CV cycle number, the amorphous phase was converted to polycrystalline γ-Ni(Fe)OOH, as indicated by the lattice spacing of 0.213 nm corresponding to the (111) plane of γ-Ni(Fe)OOH in the HRTEM image (Figure 177c). The inset FFT pattern in Figure 177c also indicated that a crystalline phase was formed at the surface. Elemental mapping of the material after the 100 CV cycles also clearly indicated that oxidation had occurred (Figure 177d). XRD and XPS results further confirmed the formation of the γ-Ni(Fe)OOH shell at the material's surface. After long-term CP at 10 mA·cm^{-2} (Figure 177e), the overpotential of the *in situ*-prepared material only increased by ∼10 mV after 50 h. After performing 24 h of CA at 1.60 V_{RHE}, the material was characterized to gauge its stability under alkaline conditions. From the HRTEM image in Figure 177f taken after CA, it was clear that the γ-Ni(Fe)OOH shell had been maintained in terms of composition and thickness (∼10 nm). This result, along with elemental mapping (Figure 177g), confirmed that the ∼10 nm thick hydroxide phase formed after the 1 CV activation cycle was completely converted to the oxyhydroxide phase after several additional cycles and was maintained even after long-term testing. The stability of the prepared Ni-Fe disulfide@oxyhydroxide heterostructure was attributed to the incorporation of Fe, as the synonymous Ni disulfide experienced complete oxidation after the 24 h CA test. To probe the kinetics of the prepared Ni-Fe disulfide@oxyhydroxide heterostructure in comparison to its Ni-Fe hydroxide counterpart, Arrhenius plots were prepared from temperature-dependent LSV data to calculate the activation energy of each material for OER catalysis (Figure 177h). The activation energies were quite close at 17.3 and 18.1 kJ·mol^{-1} for the Ni-Fe disulfide@oxyhydroxide heterostructure and Ni-

https://doi.org/10.1021/acs.chemrev.3c00005
Chem. Rev. 2023, 123, 12795−13208

Fe hydroxide, respectively, implying that they contained the same active site, γ-Ni(Fe)OOH. The two materials also did not differ significantly regarding C_{dl} values and, in turn, ECSA values (Figure 177i). DFT calculations determined that a continuous density of states (DOS) was present at the Fermi level of the Ni(Fe)S_2 core in the Ni-Fe disulfide@oxyhydroxide heterostructure, meaning it provided the material with enhanced conductivity as compared to the Ni-Fe hydroxide. This enhanced conductivity enabled easier charge transfer, making the *in situ*-prepared Ni-Fe sulfide@oxyhydroxide superior in terms of OER performance to its corresponding hydroxide (Figure 177j). Thus, the stability afforded to the prepared material via the incorporation of Fe also led to improved OER performance.

In addition to Ni-Fe sulfides, Co-Fe sulfides and CoNiFe sulfides have also been prepared although they are not as prevalently reported in the literature.[460,729,743,894] Of the Co-Fe and CoNiFe sulfides studied, a NiCoFeS/Ni foam (NF) which underwent a second Fe electrodeposition process [via potentiostatic deposition (at −1.0 $V_{Ag/AgCl}$ for 300 s) in 3 mM $Fe(NO_3)_3$], hereafter referred to as NiCoFeS-Fe/NF, also experienced improved stability in alkaline media during the OER as a result of Fe incorporation.[743] The initial NiCoFeS-Fe/NF material was prepared by (1) electrodepositing Fe and Co onto Ni foam, (2) sulfurizing the material via a solvothermal process to produce NiCoFeS/NF, and (3) performing an additional Fe electrodeposition. Once the material underwent sulfurization, the NiS, Ni_3S_2, and Co_3O_4 phases were detected via XRD in addition to metallic nickel peaks characteristic of Ni foam. These phases were also observed in the XRD pattern for NiCoFeS-Fe/NF. No peaks associated with Fe oxides were present in the NiCoFeS-Fe/NF diffraction or that of its precursors (Figure 178a). After OER stability testing (see Table 5), the Co_3O_4 could not be distinguished in the NiCoFeS/NF XRD pattern, whereas it was still present in the NiCoFeS-Fe/NF XRD pattern (Figure 178b). Thus, additional Fe-incorporation imparted some protection onto the material. From post-OER XPS results and SEM images, however, it was clear that both NiCoFeS/NF and NiCoFeS-Fe/NF underwent surface oxidation, as Ni^{3+} and Co^{3+} peak intensities increased in the Ni 2p and Co 2p spectra, indicating NiOOH and CoOOH formation, peaks at 711.4 and 724.9 eV in the Fe 2p implied the formation of FeOOH, and roughening of the surface was clear, as shown in Figures 178c–h.

In addition to the aforementioned electro-precatalysts, a unique Fe-incorporated material, c-Ti-Fe-S nanoboxes, has also been reported.[712] These as-prepared c-Ti-Fe-S nanoboxes consisted of Ti_3S_4 and FeS_2 phases, as determined by XRD. The nanoboxes retained the box-like morphology of the Ti-Fe PBAs used to prepare them, as observed by TEM (Figures 179a and b). The nanoboxes were also completely hollow, as anticipated from the synthetic process (see Section 5.1.1.4). From XPS measurements of the as-prepared material, it was determined that Fe existed in the 2+ and 3+ states from the Fe 2p spectrum and Ti in the 2+ and 4+ states from the Ti 2p spectrum (Figures 179c and d). From the S 2p spectrum, it was clear that Ti−S and Fe−S bonds were present but also that the surface was oxidized to some degree (Figure 179e). Initial oxidation was also indicated by the O 1s spectrum (Figure 179f). Following OER stability testing (see Table 5), it was clear that the surface was predominantly populated with oxidized Fe and Ti species, as indicated by the drop-in

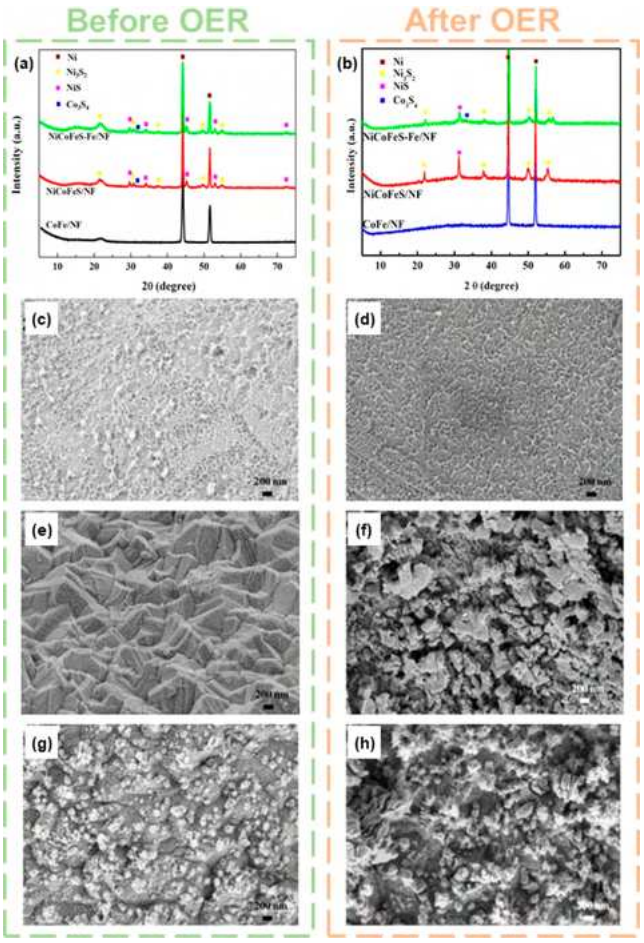


Figure 178. Pre- and post-OER characterization of CoFe/NF, NiCoFeS/NF, and NiCoFeS-Fe/NF. (a, b) XRD patterns of (a) as-prepared and (b) post-OER materials. (c–h) SEM images of (c, d) CoFe/NF, (e, f) NiCoFeS/NF, and (g, h) NiCoFeS-Fe/NF before and after the OER testing. Reprinted with permission from ref 743. Copyright 2017 Elsevier.

intensity of the Fe−S peak and the increase in the Fe−O peaks in the Fe 2p spectrum and the loss of the Ti−S peak in the Ti 2p spectrum (Figures 179j and k). There was also a large drop-in intensity of the metal−sulfide peaks and an increase in the metal−sulfate peaks in the S 2p spectrum, indicating surface oxidation (Figure 179l). The high-resolution O 1s spectrum provides further evidence of surface oxidation (Figure 179m). SEM images also support partial oxidation of the initial c-Ti-Fe-S nanoboxes given the overall morphology is maintained with only slight alteration to the material's surface (Figures 179h and i). While surface oxidation is confirmed, further investigations are required to reveal the actual active sites of this material and to expand upon its potential practical application as an electrocatalyst for the OER. Titanium is one of the lightest and most inexpensive metals, making its integration into energy storage as a catalytic material advantageous.[895] The TiS_2 phase, which has been studied as a cathode material for battery applications and hydrogen energy storage, is known to suffer from poor electrical conductivity, however, which is detrimental for electrocatalytic applications. The incorporation of an additional metal, such as Fe, could result in improved conductivity and, as a result, electrocatalytic performance for the OER and other reactions.

https://doi.org/10.1021/acs.chemrev.3c00005
Chem. Rev. 2023, 123, 12795−13208

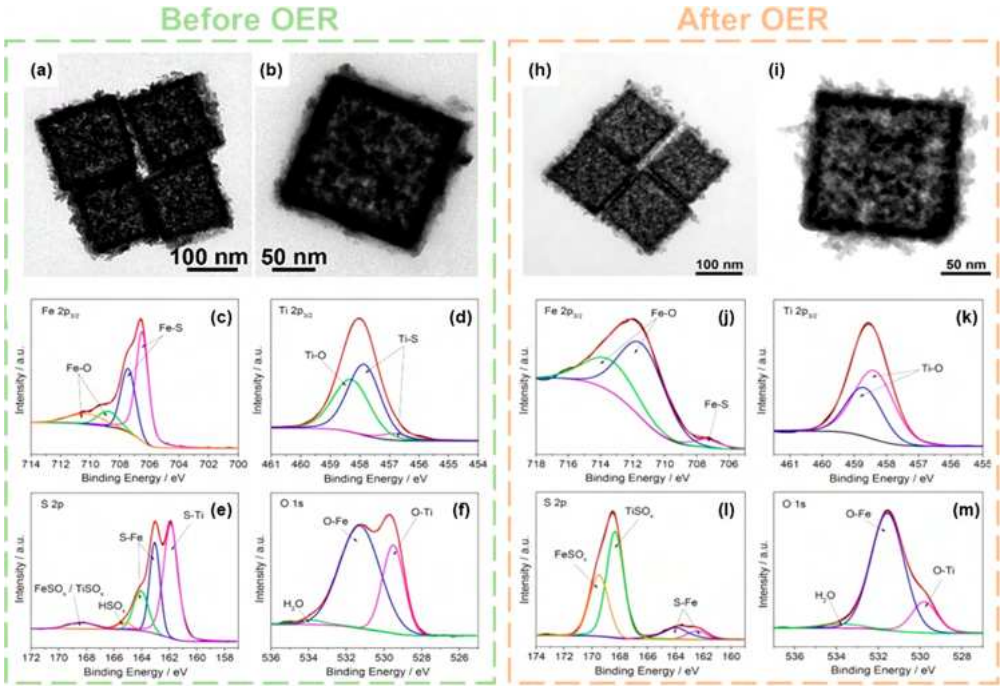


Figure 179. Pre- and post-OER characterization of c-Ti-Fe-S nanoboxes. (a, b) TEM images and (c) Fe $2p_{3/2}$, (d) Ti $2p_{3/2}$, (e) S 2p, and (f) O 1s XPS spectra of as-prepared c−Ti−Fe-S nanoboxes. (h, i) TEM images and (j) Fe $2p_{3/2}$, (k) Ti $2p_{3/2}$, (l) S 2p, and (m) O 1s XPS spectra of post-OER c-Ti-Fe-S nanoboxes. Reprinted with permission from ref 712. Copyright 2018 Royal Society of Chemistry.

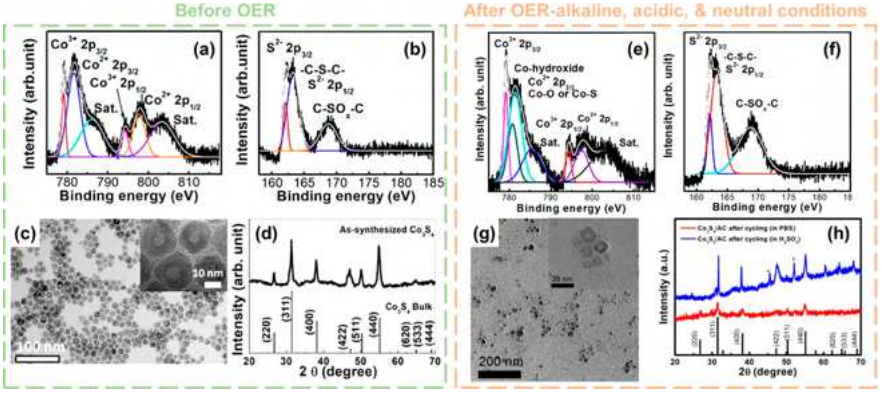


Figure 180. Stability of Co_3S_4 hollow NPs on carbon activated in alkaline media. (a, b) High-resolution (a) Co 2p and (b) S 2p XPS spectra, (c) TEM images, and (d) XRD pattern of as-prepared Co_3S_4 hollow NPs on carbon. (e, f) High-resolution (e) Co 2p and (f) S 2p XPS spectra and (g) TEM images of Co_3S_4 hollow NPs on carbon after 10000 cycles in alkaline electrolyte. (h) XRD patterns of Co_3S_4 hollow NPs on carbon after 500 LSV cycles in acidic and neutral electrolytes. Reprinted with permission from ref 676. Copyright 2020 American Chemical Society.

The majority of transition metal sulfide OER precatalysts have been studied in alkaline electrolytes with only a handful of reports studying their respective materials in neutral and acid electrolytes. Of these reports, the OER performance of the precatalysts is often reduced when used for electrocatalysis in neutral and/or acidic media. There is a need to develop OER electrocatalysts that can operate over a large pH range to make energy storage capabilities, such as overall water splitting which entails both the OER and HER, a reality. Chauhan and Deka have recently reported such a material, specifically Co_3S_4 hollow NPs supported on activated carbon.[676] The Co_3S_4 hollow NPs on carbon were activated in alkaline media prior to OER testing in alkaline (1.0 M KOH), acidic (0.5 M H_2SO_4), and neutral (1.0 M phosphate buffer) electrolytes. The activation of the material in alkaline media resulted in oxidation of the surface and generation of the real active sites for the OER, which would bind OH^- during the activation step, making the material predisposed to performing the OER in acidic and neutral conditions. Experimental results supported this hypothesis, as overpotential decreased for the activated Co_3S_4 hollow NPs in acidic and neutral electrolytes as compared to their inactivated counterparts—from 420 to 330 mV at 10 $mA{\cdot}cm^{-2}$ for the acidic case as an example. Post-OER XPS of Co_3S_4 hollow NPs in alkaline revealed that the surface of the material had been converted to a $Co(OH)_2$/CoOOH layer given the increased abundance of Co^{3+} in comparison to Co^{2+}, as indicated by the pre- and post-OER Co 2p spectra (Figures 180a and e). This layer forms in an alkaline electrolyte during the OER and acts as the real active site(s) for Co sulfides. Interestingly, no drastic change to the high-resolution S 2p XPS spectra occurs following the OER in an alkaline electrolyte (Figures 180b and f). TEM images, in

https://doi.org/10.1021/acs.chemrev.3c00005
Chem. Rev. 2023, 123, 12795−13208

addition to other post-characterization results such as FTIR spectra (not shown here) indicated that the overall morphology was maintained for the Co_3S_4 hollow NPs on activated carbon studied in an alkaline electrolyte (Figures 180c and g). Post-OER XRD characterization of the Co_3S_4 hollow NPs on activated carbon studied in acidic and neutral electrolytes also indicated little change to the material, as the overall XRD pattern was maintained even after 500 LSV cycles of the OER (Figures 180d and h). Despite the overall pattern being maintained, however, two additional peaks emerged in the XRD pattern of the Co_3S_4 hollow NPs studied in acidic electrolyte and diffraction peak intensities were greatly diminished for the neutral electrolyte case (Figure 180h). It would be beneficial to further explore the identity of the new peaks (starred in Figure 180h) for the Co_3S_4 hollow NPs studied in acidic media to further reveal the effect of pre-activation in alkaline electrolyte on the surface chemistry of the material, which could aid in understanding why pre-activation led to better electrocatalytic performance. Additionally, characterization of the pre-activated material before being studied in alkaline, acidic, and neutral electrolytes could also provide more information regarding the changes the material undergoes following long-term testing in different pH environments. It is likely that the material studied in alkaline media underwent further oxidation than those studied in acidic or neutral media, which likely contributed to its overall lower overpotential at 10 $mA{\cdot}cm^{-2}$ (270 mV) than those of its acidic (330 mV) and neutral (370 mV) counterparts. In the future, it would be advantageous to activate the Co sulfide fully to form the Co oxide/(oxy)hydroxide layer and then to study the fully activated material in acidic and neutral media to determine if the extent of activation has an effect on OER performance at different pH. Another work examining OER electrocatalyst performance, specifically CoMoNiS-NF-3:1 composite (3:1 is the ratio of Co:Mo), at different pH has reported even lower overpotentials of 166, 228, and 405 mV at 10 $mA{\cdot}cm^{-2}$ in alkaline, acidic, and neutral electrolyte; however, the reason for this improved performance in different pH environments still warrants further explanation.[688] In general, the stability and performance of OER electrocatalysts beyond alkaline conditions is an essentially unchartered territory ripe for future exploration that could lead to the development of more stable and multifunctional electrocatalysts.

5.1.3. Structural and Chemical Compositional Effects towards OER Activity. In this section, different parameters affecting the OER activity of metal sulfides will be described, such as structural and compositional modifications, as well as the *in situ* reconstruction process at the surface, that allow the understanding of their performance toward water oxidation in alkaline media. Some of these parameters include morphology, metal−sulfur ratio, doping, oxygen vacancies, the effect of pH, and others.

5.1.3.1. Morphological Effects. Strategies such as doping, phase modification, defect/vacancy engineering, interface engineering, and heterostructure formation have been used to improve the properties of metal sulfides to obtain more efficient electrocatalysts. Notably, the physical properties such as surface area and novel size effects of nanostructured materials have attracted remarkable attention for developing highly active OER electrocatalysts. Toward this aim, this section mainly focuses on the structure/morphology effects regarding the OER performance of 1D, 2D, and 3D transition metal sulfide electrocatalysts.

Typically, one-dimensional (1D) nanostructures include nanorods, nanotubes, and nanowires with only one characteristic structural feature, providing a singularly oriented electronic/ionic transport pathway that reduces the electrical resistance of the material and leads to a favorable improvement in OER performance. Significant benefits of this 1D structure include more reactive sites by tuning the grain boundaries, as well as the open interspace in the structure. These features facilitate the charge transfer process, mass transport, and easy bubble formation and release, preventing generated gas bubbles from blocking redox reaction sites.[896]

Regarding 1D nanowire structures, Du *et al.*[710] reported the *in situ* growth of a Mo-doped Ni_3S_2 precatalyst nanowire network on Ni foam (NF) by the two-step hydrothermal and sulfurization synthesis process. The opened hierarchical nanowire networks exhibited high exposure of active sites by numerous hierarchical pores (3−10 nm size range), which could facilitate mass/charge transfer and the release of evolved gas during OER electrocatalysis in basic media. Given a low overpotential of 213 mV at 10 $mA{\cdot}cm^{-2}$ and a Tafel slope of only 35.1 $mV{\cdot}dec^{-1}$, it is likely that the aforementioned benefits were achieved due to the porous structure of the 1D nanowire material. In addition, the Mo-doping positively affected the Ni_2S_3 electronic structure, specifically the binding energy of hydrogen/oxygen intermediates during the water-splitting process, increasing the conductivity and the charge transfer capability.

In the case of nanorod nanostructures, Li *et al.* fabricated $NiCo_2S_4$ nanorod array precatalysts via a one-step hydrothermal process using self-sacrificial Ni foam as the Ni source and substrate.[804] This growth strategy improved the material's conductivity, stability, and electron transport, as indicated by the material's excellent OER activity: a low overpotential of only 220 mV at 30 $mA{\cdot}cm^{-2}$ was achieved, much lower than those of Ni_3S_2 (310 mV) and $NiCo_2O_4$ (370 mV). Moreover, due to its unique *in situ* growth structure and large specific surface area, the $NiCo_2S_4$ precatalyst showed superior electrocatalytic activity for the OER, as its lower Tafel slope of 88.6 $mV{\cdot}dec^{-1}$ in comparison with those of Ni_3S_2 (183.8 $mV{\cdot}dec^{-1}$) and $NiCo_2O_4$ (166.8 $mV{\cdot}dec^{-1}$) indicated superior OER kinetics. In another report, Liu *et al.*[780] reported the facile molybdate-directed synthesis of Mo-doped Ni_3S_2 nanorod arrays via a hydrothermal process. The resulting Mo-doped Ni_3S_2 precatalyst presented an enhanced electrocatalytic activity for the OER with an overpotential of 350 mV at 100 $mA{\cdot}cm^{-2}$. Additionally, as the Mo content increased, a significant effect on the morphological properties and electrocatalytic activity was also observed. The surface of these nanorods consisted of decorated vertical-intersected nanosheets, which provided abundant active sites, accelerated charge transfer, and increased fast diffusion of generated gas products.

In regard to reports on metal sulfides with nanotube morphology, Li *et al.*[694] synthesized ternary Fe, Co, Ni-based layered double hydroxide in combination with MoS_2 nanotube array precatalyst (denoted as FeCoNi-HNTAs) from Fe, Co, Ni-based layered double hydroxide nanowire arrays supported on Ni foam (FeCoNi-LDH-NWAs). First, the FeCoNi-LDH nanowires were prepared via hydrolysis and used as a self-sacrificing template to be converted into nanotubes by hydrothermal treatment at 200 °C for 10 h. From the LSV curves, FeCoNi-HNTAs demonstrated an overpotential of 184 mV at a current density of 10 $mA{\cdot}cm^{-2}$, lower than those of

https://doi.org/10.1021/acs.chemrev.3c00005
Chem. Rev. 2023, 123, 12795−13208

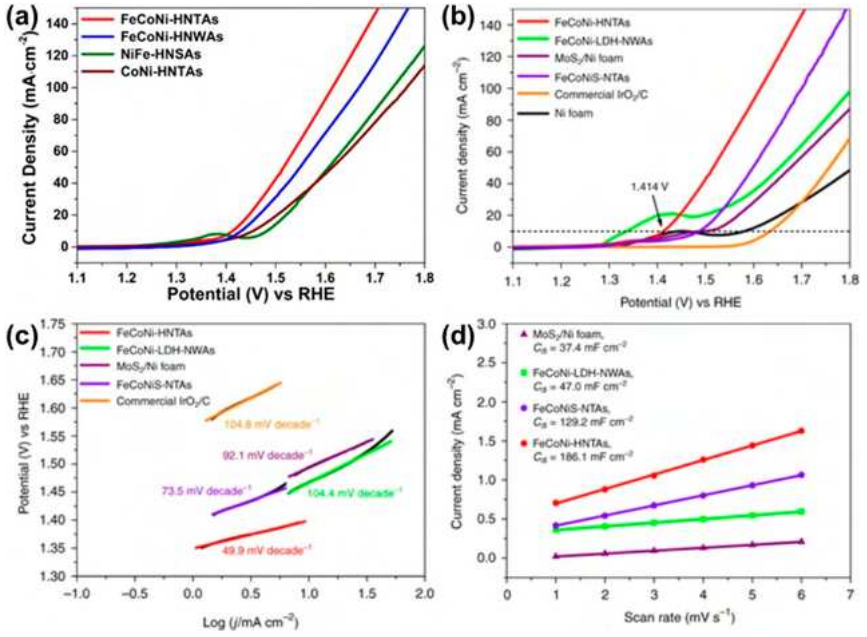


Figure 181. (a, b) Comparison of polarization curves for the OER of as-synthesized sulfide nanoarrays, MoS_2/Ni foam, commercial IrO_2/C, and Ni form electrodes measured at a scan rate of 1 mV·s^{-1} in 1 M KOH solution. (c) Tafel plots of as-prepared sulfide nanoarrays, MoS_2/Ni foam, and commercial IrO_2/C for the OER. (d) C_{dl} measurements of as-prepared sulfide nanoarrays. Reprinted with permission from ref 694. Copyright 2018 Springer Nature.

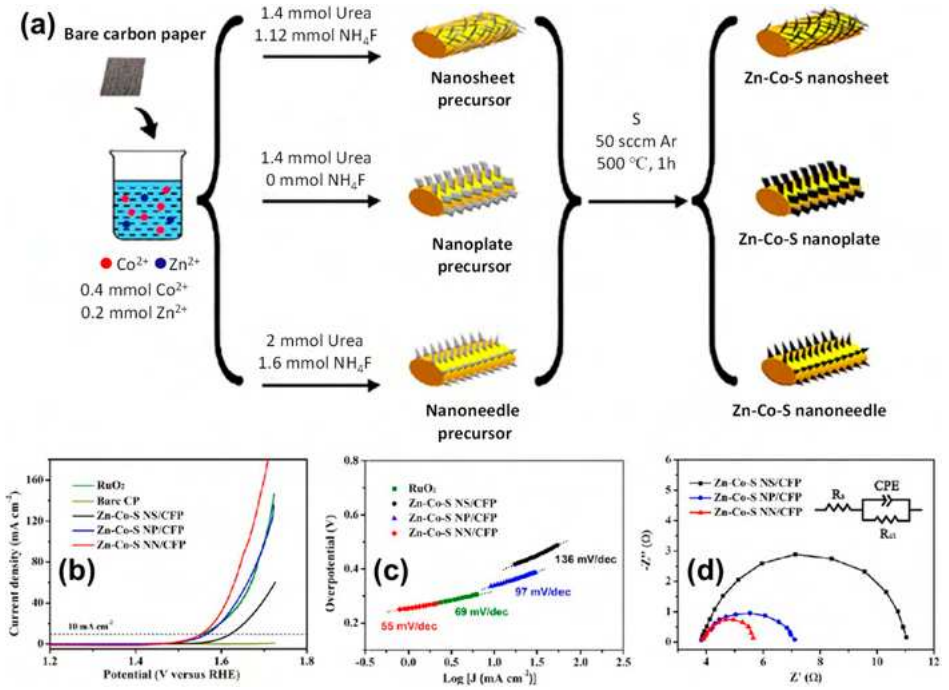


Figure 182. (a) Schematic illustration of the preparation of Zn-Co-S nanosheets, nanoplates, and nanoneedles on CFP. (b) OER polarization curves of commercial RuO_2, bare CFP, and Zn-Co-S NSs, NPs, and NN/CFP at a scan rate of 5 mV·s^{-1} in 1.0 M KOH. (c) Corresponding Tafel plots of commercial RuO_2 and Zn-Co-S NSs, NPs, and NN/CFP. (d) Nyquist plots of Zn-Co-S NSs, NPs, and NN/CFP. Inset of (d) shows the simplified Randles equivalent circuit used for fitting where R_s, CPE, and R_{ct} are the electrolyte resistance, double layer capacity, and charge transfer resistance, respectively. Reprinted with permission from ref 832. Copyright 2017 American Chemical Society.

the commercial IrO_2/C electrocatalyst (400 mV) and the other intermediate/transition samples (Figures 181a and b). A faster electrocatalytic reaction and overall improved performance were also indicated by the prepared material's low Tafel slope (49.9 mV·dec^{-1}), low transfer resistance (≈ 1 Ω), and higher ECSA (4652.5 cm^2) compared to those of other studied materials. The nanotube morphology and the trimetallic components of the FeCoNi-LDH-HNTAs provided the material with advantageous structural and compositional features for OER electrocatalysis (Figures 181c and d).

As discussed above, 1D nanostructured metal sulfides have demonstrated suitable properties for the OER, in particular the

https://doi.org/10.1021/acs.chemrev.3c00005
Chem. Rev. 2023, 123, 12795−13208

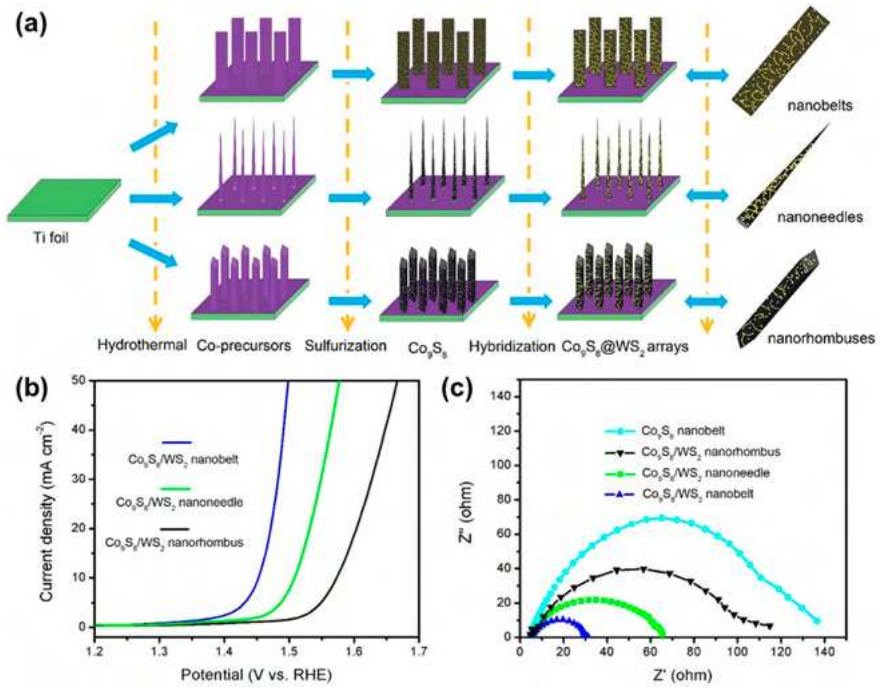


Figure 183. (a) Schematic illustration for the fabrication process of the Co_9S_8/WS_2 composites with nanoneedles, nanobelts, and nanorhombus arrays. (b) OER polarization curves of Co_9S_8/WS_2 nanobelts, nanoneedles, and nanorhombuses in 1 M KOH. (c) Nyquist plots of Co_9S_8/WS_2 nanobelts, nanoneedles, and nanorhombuses and Co_9S_8 nanobelts in 1 M KOH. Reprinted with permission from ref 837. Copyright 2017 Royal Society of Chemistry.

morphology and surface area that generate an electron mobility enhancement. Nevertheless, this strategy can be improved by combining additional modifications such as metallic nanoparticle decoration, heterostructures, doping, and others that will be discussed in the compositional effects section (Section 5.1.3.2).

As well as 1D, 2D nanostructured materials have been extensively studied as transition metal sulfide electrocatalysts for environmental and sustainable energy applications due to their unique structure-dependent features to confine electrons in their atomic layers. The 2D nanostructured materials have their surface atoms exposed and exhibit high surface areas, beneficial for tuning their functionalities at the atomic level by surface modification, doping, and defect engineering.[896] Moreover, the shorter diffusion pathways in these 2D nanostructures can accelerate the electron charge transfer, making them promising materials for energy storage and conversion technologies.[897] Among the different types of 2D nanostructured sulfides that have been investigated for the electrocatalysis of the OER, nanosheets (refs 832, 833, 711, 787, 827, 696, 806, 693, 713, 714, 466, 781, 807, 808, 784, 822, and 727), nanoplates,[832,713] nanoneedles,[832,837,711] and nanobelts[837] are the most reported in the literature. In addition, there are also reports that directly studied the effect of 2D vs 1D nanostructured sulfides on OER performance. These reports and some examples of 2D transition metal sulfides for the OER will be discussed below.

Wu *et al.* reported a comparative study on the morphology-controllable synthesis and electrochemical water splitting efficiency of a zinc cobalt mixed sulfide (Zn-Co-S) precatalyst.[832] By tailoring the amount of urea and NH_4F added to a carbon fiber paper (CFP) substrate prior to hydrothermal reaction, the morphology of the Zn-Co-S precatalyst was tuned, resulting in 2D nanosheets (NSs), 2D nanoplates (NPs), and 1D nanoneedles (NNs). The synthesis was carried out by a hydrothermal step at 100 °C for 12 h, followed by a thermal sulfurization step employing sulfur powder at 500 °C for 1 h under an Ar atmosphere (Figure 182a). They stated that the urea amount gradually enhanced the etching effect of NH_4F, whereas a large amount of NH_4F led to agglomerations, approaching the "coalescence growth". The electrocatalytic activity of the Zn-Co-S nanostructures toward the OER was studied in alkaline media (1 M KOH), as shown in Figure 182b. Among these three different nanostructures, the Zn-Co-S NNs achieved a current density of 10 mA·cm^{-2} at an overpotential of 320 mV, which outperformed those of Zn-Co-S NPs (330 mV) and Zn-Co-S NSs (390 mV). The morphology of the electrocatalysts played an essential role in determining their OER activities. This effect was further emphasized from double-layer capacitance values, which were determined to be 35.47, 32.23, and 9.99 mF·cm^{-2} for Zn-Co-S NNs, NPs, and NSs, respectively. Additionally, the charge transfer resistance (R_{ct}) values were 1.8, 3.3, and 7.2 Ω for the Zn-Co-S NNs, NPs, and NSs precatalysts, respectively (Figure 182d). These results indicated that the 1D nanoneedle structure provided a large ECSA with numerous electrocatalytic active sites and faster OER kinetics, as indicated by its low Tafel slope (55, 136, and 97 mV·dec^{-1} for NNs, NSs, and NPs, respectively) compared to the 2D nanosheet and nanoplate precatalysts.

Another comparative study has been reported by Peng *et al.*[837] in which they presented a Co_9S_8/WS_2 precatalyst with array structures supported on a conductive Ti plate as an electrocatalyst for overall water splitting. The final morphologies of the Co_9S_8 precatalysts were easily controlled using cobalt precursors of specific morphologies and Kirkendall reactions. The resulting Co_9S_8 structures were nanobelts, nanoneedles, and nanorhombuses (Figure 183a). Extra

https://doi.org/10.1021/acs.chemrev.3c00005
Chem. Rev. 2023, 123, 12795−13208

parameters such as the reaction temperature, the reactant amount, and the incorporation of NH_4F were also modified for this purpose. The capacitances of the Co_9S_8/WS_2 nanobelts, nanoneedles, and nanorhombus arrays were 65.2, 46.1, and 33.5 mF·cm^{-2}, respectively. This trend in capacitance indicated that the ECSA was the highest for the nanobelts and the lowest for the nanorhombus array. The measured BET specific surface area also confirmed these results, as the surface areas for the nanobelts, nanoneedles, and nanorhombus were 78.9, 26.9, and 38.6 $m^2 \cdot g^{-1}$, respectively. The high surface area of the Co_9S_8/WS_2 nanobelt array was attributed to the considerable nanocrystalline boundaries and the generation of new quasi-pores or micropores after coupling with WS_2, which may favor the increase of the number of exposed active electrocatalytic sites during the OER. The vertical WS_2 nanosheets of several layers grown uniformly on Co_9S_8 substrates also produced abundant exposed edge sites essential for the OER, as the larger the number of electroactive sites is, the more electrocatalytically active the material is (Figure 183b). Furthermore, the EIS measurements indicated that the Co_9S_8/WS_2 nanobelt array had lower impedance in comparison to the nanoneedles and nanorhombus arrays and thus accelerated the OER kinetics (Figure 183c). Finally, the hybridization between Co_9S_8 and WS_2 at the interface likely provided a strong electronic interaction. This synergistic effect could facilitate the electrostatic affinity to OH^- by the alkaline media, the generation of active sites, and fast catalytic kinetics, improving the OER activity.

The combination of 1D and 2D nanostructured electrocatalysts is another approach that has been used to enhance the electrocatalytic OER activities of different transition metal sulfides. These types of nanostructured materials have different structural arrangements, including core@shell, core@branch, nanosheet/nanoneedle arrays, or sandwich-like structures. Du *et al.*[711] reported a unique hierarchical precatalyst synthesized via direct growth on a porous and conductive Ni foam (NF) substrate, by coating Ni_3S_2 nanosheets on $NiCo_2O_4$ nanoneedle arrays via co-precipitation and sulfurization as a standard two-step method. Lin *et al.*[707] proposed a novel and facile synthetic strategy to rationally design core@branch Ni_3S_2/Co_9S_8 precatalyst arrays directly on nickel foam for use as a bifunctional electrocatalyst for overall water splitting. The unique core@branch Ni_3S_2/Co_9S_8 arrays provided a large surface-active area for electrochemical reactions, opened channels for effective gas release, and allowed intimate contact of the material with Ni foam for fast electron transport. Qin *et al.*[815] designed and fabricated heteroatom (nitrogen or oxygen)-doped edge-enriched 3D rivet graphene (H-3DRG) films with ultralow weight, high flexibility, and conductivity for the deposition of vertically aligned NiCo-LDH and hierarchical $NiCo_2S_4$ nanostructured precatalysts via a further anion exchange process without destroying the vertical architecture. Lin *et al.*[713] studied the synthesis of hierarchical cobalt sulfide nanocomposites (HCSNs), with the vertical growth of Co_9S_8 nanosheets on horizontal $Co_{1-x}S$ nanoplates fabricated via a simple one-pot synthesis method, which exhibited remarkable OER activity with an overpotential of 275 mV at a current density of 10 mA·cm^{-2} and a Tafel slope as low as 30 mV·dec^{-1}. Wang *et al.*[691] developed the NiFe (oxy)hydroxide precatalyst with residual S, denoted as Ni_xFe_{1-x}-OH (x = 1, 6/7, 3/4), which exhibited an extraordinarily low OER overpotential of 190 mV at the current density of 10 mA·cm^{-2} after coupling with carbon nanotubes. The NiFe (oxy)hydroxides with different amounts of S residues were prepared by controlling the oxidation degree of the sulfide precursor. As mentioned above, the rational design of 2D nanostructures is a commonly used strategy to boost the OER performance of metal sulfides, in particular the versatility of combining with 1D nanostructures of a different nature, which provides a specific orientation or hierarchical morphology that benefits the OER.

3D nanostructured metal sulfides have attracted intensive research interest because of their high surface area and, in turn, the high number of exposed absorption sites within a small volume. These characteristics serve to maximize the ion-accessible active sites for catalysis and improve ion and electron transport, facilitating the reaction kinetics. Different electrochemical energy conversion fields, such as photo-electrochemical water splitting (PEC), photo-electrocatalytic conversion of CO_2 to chemical fuels, rechargeable metal-ion batteries, and supercapacitors, have utilized those characteristics. 3D nanostructures mainly consist of 3D spatial arrangements, including arrayed 1D/2D nanostructures (i.e., nanowires, nanotubes, nanopyramids, and nanocones), 3D nanoporous structures, and 3D hierarchical nanostructures. For instance, one of the most attractive features of 3D nanoporous materials is the structural versatility for optimization of electrocatalytic performance, such as improving electrolyte permeation/penetration into the material by creating a shorter charge transport distance.[898] However, the synthesis of highly ordered nanostructures still remains a challenge with only some papers reporting specific 3D hierarchical morphologies, including nanocubes[460,719,565] and nanoboxes.[712,818] These nanostructures are of great interest because they can provide exposed facets, edges, and vertices containing electrocatalytically active sites favorable for energy applications.

In this respect, a work related to porous structure controlled by temperature and its' effect on the OER performance is presented by Zhang *et al.*[835] They designed and synthesized multifunctional hierarchical Co_9S_8 hollow microsphere precatalysts via a hydrothermal reaction using three different temperatures: 140, 80, and 60 °C. The temperature-dependent experiments showed a transition process of solid microspheres into hollow microspheres. As the hydrothermal temperature increased to 140 °C, the solid microsphere cores completely disappeared and converted into rough hollow microspheres of 800 nm in diameter. This new hollow structure facilitated more electrocatalytic site formation, as shown by the BET specific surface area results. The Co_9S_8 HMs-140 precatalyst exhibited a 45-fold surface area increase compared to Co_9S_8 HMs-80 and a 90-times increment with respect to Co_9S_8 HMs-60. Thus, the electrocatalytic sites provided by the high surface area, pore volume, and hierarchical mesoporous structure assured better electrocatalytic performance toward the OER, as shown in Figure 184a. The overpotential at 10 mA·cm^{-2} for the Co_9S_8 HMs-140 precatalyst was 420 mV, smaller than those of Co_9S_8 HMs-80 (460 mV), Co_9S_8 HMs-60 (490 mV), and RuO_2 (500 mV). Moreover, the Tafel plots indicated better OER kinetics for the Co_9S_8 HMs-140 precatalyst given it had the smallest Tafel slope value, 113 mV·dec^{-1}, among the precatalysts prepared at different temperatures (Figure 184b). Benefiting from this hierarchical hollow structure, the Co_9S_8 OER activity was enhanced in comparison to that of solid Co_9S_8 microspheres.

https://doi.org/10.1021/acs.chemrev.3c00005
Chem. Rev. 2023, 123, 12795−13208

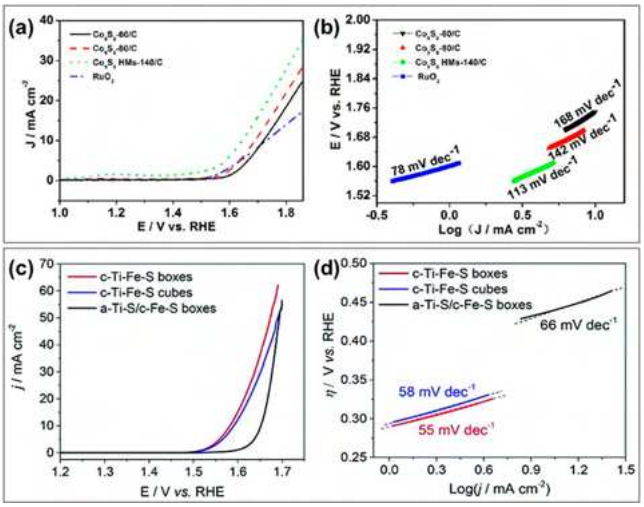


Figure 184. (a) OER polarization curves and (b) corresponding Tafel plots of the Co_9S_8-60/C, Co_9S_8-80/C, Co_9S_8 HMs-140/C, and commercial RuO_2 electrocatalysts, which were obtained with 95% *iR* compensation at 5 mV·s^{-1} in N_2-saturated 0.1 M KOH solution. Reprinted with permission from ref 835. Copyright 2017 Elsevier. (c) LSV curves and (d) corresponding Tafel slopes of the Ti-Fe mixed sulfide nanobox electrocatalysts. Reprinted with permission from ref 712. Copyright 2018 Royal Society of Chemistry.

Another example of improved electrocatalytic performance due to hierarchical structure is provided by Nai *et al.*[712] They reported the synthesis of Ti-Fe mixed sulfide (Ti-Fe-S) precatalyst nanoboxes for the OER. The Ti-Fe-S nanoboxes were prepared from a sulfurization treatment of Ti-Fe nanoboxes using sulfur powder as the S source. These Ti-Fe nanoboxes were derived from the PBA nanoboxes, firstly obtained by hollowing the nanocube PBA precursor with a solvothermal-engaged etching process. For comparison, Ti-Fe nanocubes were also converted into Ti-Fe-S nanocubes by a similar annealing route. The Ti-Fe-S nanoboxes presented a slightly higher OER activity (350 mV at 10 mA·cm^{-2}) than the Ti-Fe-S nanocubes (360 mV at 10 mA·cm^{-2}) in 1 M KOH solution, as presented in Figure 184c. Additionally, the Ti-Fe-S nanoboxes exhibited improved kinetics for the OER, as can be appreciated by the lower Tafel slope of 55 mV·dec^{-1} compared with that of the Ti−Fe−S nanocubes (58 mV·dec^{-1}) (Figure 184d), along with higher ECSA and a smaller charge transfer resistance. The OER activity was higher for Ti-Fe-S nanoboxes due to their larger ECSA as a result of the 3D nanostructure, which enabled greater electrocatalyst−electrolyte contact and improved electrocatalytic performance.

In some cases, a very particular strategy is used to develop a unique hierarchical hollow structure consisting of a core@shell form. For instance, a Co_3S_4@MoS_2 heterostructure was prepared by an *in situ* MoS_2 nanosheet growth onto the surface of Co_3S_4 nanoboxes using a two-step temperature-raising hydrothermal reaction and thermal annealing process, providing a different insight into the design of an alternative 3D nanostructured electrocatalyst for water splitting.[818] Alternatively, morphological changes can also be observed by changing the metal/sulfur ratio during the synthesis procedure. Zhu *et al.*[847] reported the preparation of *in situ* grown Ni_3S_2 superstructure precatalysts on Ni foam (NF) via a one-step ICE approach. By changing the solvent (water and ethanol) and the sulfur concentration (0.18 and 0.36 g of thioacetamide), the material morphology transformed from needle arrays to leaf patterns. From SEM images, it was evidenced that by using water, a 3D superstructure of nanoneedle arrays (NNs) was formed, while the leaf patterns (NLs) were formed at the microscale using ethanol. Decreasing the thioacetamide amount, shorter leaf patterns of 2.5 μm in length are formed in ethanol solvent (denoted as NL@NF-1). These samples were tested in 1 M KOH for the OER. The NL@NF-1 electrocatalyst exhibited a lower overpotential of 340 mV at 10 mA·cm^{-2} than NN@NF-1 (370 mV). The higher OER activity was attributed to the large specific surface area of the ultrathin sheets in NL@NF-1, which allowed more active sites for the electrocatalytic reaction. Additionally, this electrocatalyst displayed favorable hydrophilicity, which facilitated the diffusion of the electrolyte into the Ni_3S_2 nanostructure and hence promoted oxygen evolution. Thus, by tuning the solvent and the sulfur concentration, the manipulation of the sulfide morphology was enabled to improve the OER activity.

Indisputably, researchers have demonstrated the benefits and advantages of rational design for the development of highly active electrocatalysts for the OER through the consideration of surface area, the number of active sites, pore volume, and/or efficient electron/ion transport routes and through the establishment of different relationships among nanoscale effects and hierarchical organization to improve their electrochemical activities and kinetics. For the next generation of high-performance OER electrocatalysts, all of these properties/characteristics should be taken into consideration for metal sulfide preparation, as it would lead to more efficient precatalysts and accelerate the time scale of fundamental electrocatalysis research reaching practical application.

5.1.3.2. Metal/Sulfur Composition Effects. In addition to the thermodynamics and kinetic requirements for efficient OER electrocatalysis strongly influenced by the bulk, surface, structural, and electronic properties, it is important to highlight some strategies employed to achieve this aim. Among the strategies, tuning the metal sulfide *M*/S ratio can provide different OER performance since different crystalline phases, electronic structures, and morphologies can be obtained that strongly affect the active sites for the reaction. For instance, Li *et al.*[840] proposed an anionic regulation approach in which anions serve as electron donors to modulate the electronic structure of NiFe (oxy)sulfide precatalytic materials (denoted as NiFeS). The anionic regulated NiFeS electrocatalysts were synthesized via a solvothermal process using ethanol as the solvent and thioacetamide as the vulcanization reagent at 140 °C for 12 h using a gradual variation of S:O atomic ratios. The product was denoted as NiFeS-*x* (where *x* is the mass ratio of thioacetamide:NiFeLDH). The material characterization of the anionic regulated NiFeS electrocatalysts was carried out by XPS and EDX analyses and is shown in Figure 185a. The Ni:Fe atomic ratio was stable (close to 3) after the vulcanization process. On the other hand, the S:O ratio exhibited variation with the addition of thioacetamide. Sulfur gradually substituted for the oxygen in the material, rising from 0.025 (NiFeS-0) to 2.35 (NiFeS-8), as confirmed by both techniques. These compositional variations exhibited an effect over the OER performance in 0.1 M KOH, as displayed in Figure 185b. The polarization curves showed an active response for the NiFeS-0.5 and NiFeS-2 samples. The overpotential at 10 mA·cm^{-2} decreased from 329 to 286 mV for NiFeS-0 and NiFeS-2, respectively. The OER activity exhibited a volcano plot under anionic regulation, in which the

https://doi.org/10.1021/acs.chemrev.3c00005
Chem. Rev. 2023, 123, 12795−13208

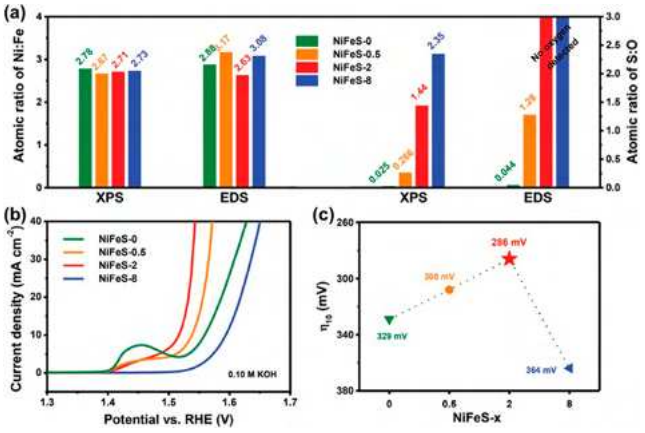


Figure 185. Elemental compositional analysis of NiFeS-X electrocatalysts and corresponding OER activity. (a) Atomic ratios of Ni:Fe and S:O for NiFeS-X electrocatalysts determined by XPS and EDX. (b) 95% *i*R-compensated LSV profiles of NiFeS-X electrocatalysts at a scan rate of 10 mV·s^{-1} in O_2-saturated 0.1 M KOH. (c) Volcano plots for the OER activity of the NiFeS-X electrocatalyst characterized by the overpotential at 10 mA·cm^{-2} against the vulcanization degree under anionic regulation. Reprinted with permission from ref 840. Copyright 2017 Wiley.

NiFeS-2 electrocatalyst provided the optimal S:O composition (Figure 185c). The mechanism behind the anionic regulation was supported by XPS analysis. With the substitution of sulfur, the S 2p spectra showed high sulfur content, while the O 2p spectra exhibited a shift to lower binding energy induced by the polarization effect of sulfur. Interestingly, the Fe 2p spectra remained identical despite variation in the S:O ratio. On the other hand, the Ni 2p spectra showed a lower binding energy shifting, suggesting a lower oxidative state by receiving more electrons under anionic regulation. With more electrons provided, the cationic nickel sites afforded a less positive electronic field and became more difficult to undergo oxidization. Thus, the Ni-Fe component serves as an active site toward water oxidation. The nonpolarized oxygen anions hold their electrons tightly, rendering high ionicity and an intense positive electric field (coming from cations) unfavorable for oxygen desorption. In contrast, the polarized sulfur ions tended to give their dispersive electrons to the empty orbits of the Ni-Fe sites and promoted the covalency of the interaction between the cations and anions. When both effects are balanced (NiFeS-2 sample), the overall active domain affords an optimized electronic structure and exhibits superior reactivity toward water oxidation.

Additionally, another notable effect of controlling the amount of sulfur has been the crystallization of different phases.[850,692] Shang *et al.*[850] reported the synthesis of Ni_xS_y with different crystalline phases via a solvothermal sulfurization of nickel foam substrates (0.1 × 1 × 2 cm^2) using ethanol (60 mL) as the solvent and thiourea as the sulfur source in varying amounts from 1 to 3 g, controlling the samples' sulfurization degree. The XRD results demonstrated that the crystalline

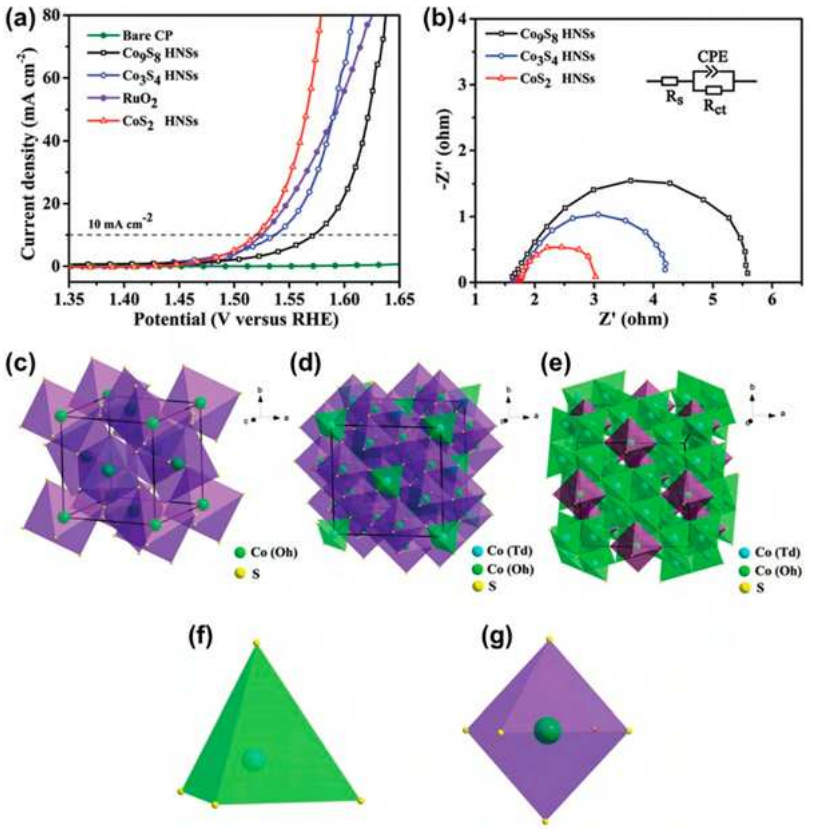


Figure 186. (a) OER LSV curves of commercial RuO_2, bare CP, Co_9S_8, Co_3S_4, and CoS_2 HNSs in 1 M KOH at a scanning rate of 5 mV·s^{-1}. (b) Nyquist plots of Co_9S_8, Co_3S_4, and CoS_2 HNSs at the applied potential of 1.567 V_{RHE}. Inset of (b) shows the simplified Randles equivalent circuit used for fitting (R_s, R_{ct}, and CPE stand for the electrolyte resistance, charge transfer resistance, and double layer capacity, respectively). (c–g) Crystal structures of (c) CoS_2, (d) Co_3S_4, (e) Co_9S_8, (f) CoS_4 tetrahedron, and (g) CoS_6 octahedron. Reprinted with permission from ref 723. Copyright 2018 Royal Society of Chemistry.

https://doi.org/10.1021/acs.chemrev.3c00005
Chem. Rev. 2023, 123, 12795−13208

phase of the as-prepared Ni_xS_y layer on nickel foam (denoted as Ni_xS_y/NF precatalyst) was strongly influenced by the degree of sulfurization. When 1 or 1.5 g of thiourea was used, the Ni_xS_y mixture was mainly composed of the NiS_2 and Ni_3S_2 phases. With a slight increase of thiourea to 2 g, more facets of Ni_3S_2 were identified and the NiS phase was also detected, whereas the NiS_2 phase disappeared. A pure single phase of Ni_3S_2 was indexed for the sample with 2.5 g of thiourea. As thiourea increased to 3 g, the Ni_3S_2 planes were retained along with the presence of the NiS_2 phase. These phase transformations were accompanied by morphological variations from small and uniform nanosheets (using 1 g of thiourea) to vertical flower-like structures (3 g of thiourea). The OER performance was also affected by these changes. The sample with 2 g of thiourea exhibited the earliest onset potential (1.24 V_{RHE}) as well as the highest current density after 1.25 V_{RHE}. The Tafel slope was determined to be 116 mV·dec^{-1}, which was smaller than those of the other samples, suggesting better OER kinetics. Moreover, the EIS data showed that this sample possessed the smallest charge transport impedances, favorable for the OER. These results suggested that a NiS phase may be a superior crystalline phase for OER performance compared to NiS_2 and Ni_3S_2. A similar approach was presented by Ma *et al.*[723] They synthesized Co_9S_8, Co_3S_4, and CoS_2 hollow nanospheres (HNSs) via a one-step facile hydrothermal method using carbon disulfide (CS_2) as a soft and sacrificial template. The CoS_x HNS precatalysts with different phases and compositions were obtained by changing the molar ratio of CS_2 to $Co(AC)_2$ using 0.065, 0.15, and 0.4 mL·mmol^{-1} $Co(AC)_2$ solutions. As the molar ratio of CS_2 to $Co(AC)_2$ increased, the phase evolved from Co_9S_8 to Co_3S_4 and finally to CoS_2. Moreover, the spherical structure of the hollow nanospheres became looser (i.e., more distorted), and the surface nanosheets became thinner. The BET specific surface areas were determined to be 49.8, 53.7, and 71.2 m^2·g^{-1} for Co_9S_8, Co_3S_4, and CoS_2, respectively. The enhanced area of CoS_2 could provide more electroactive sites and facilitate electrolyte diffusion during the electrocatalytic process. The electrochemical results showed that pyrite-type CoS_2 hollow spheres exhibited superior electrocatalytic activity with an overpotential of 290 mV to achieve 10 mA·cm^{-2} and a Tafel slope of 57 mV·dec^{-1} for the OER (Figure 186a). The EIS corroborated that the CoS_2 material afforded the fastest OER kinetics, with a lower charge transfer resistance of 1.35 Ω, compared to Co_9S_8 (3.96 Ω) and Co_3S_4 (2.57 Ω), as presented in Figure 186b. This superior activity was related to the crystal structure, chemical composition, and oxidation states. In the pyrite-type CoS_2, all cobalt ions were arranged in the form of CoS_6 octahedra with the partial oxidation of Co^{2+} to Co^{3+} (confirmed by XPS analysis). For Co_3S_4, two-thirds of the cobalt sites are in the center of the CoS_6 octahedra, while the ratio decreased to one-ninth in the Co_9S_8 phase. Since these octahedrally coordinated Co^{n+} (n = 2, 3) sites are more active than the tetrahedrally coordinated Co^{2+} sites ($Co^{2+}{}_{Td}$) for the OER, the greater amount of CoS_6 octahedra in the CoS_2 phase allowed a superior intrinsic activity (Figure 186c−g). Therefore, the surface morphology, crystal structure, and coordination environment of Co^{n+} active sites collectively influenced the OER performance of the CoS_x materials.

The sulfur dosage can also tune the chemical environment at the sulfide surface. Ju *et al.* demonstrated this concept with a novel route to *in situ* modulate the surface chemistry of cobalt sulfide precatalyst materials, improving the electrocatalytic OER activity.[685] For this purpose, thin nanosheet-like cobalt sulfide materials were synthesized by a small molecular amine-mediated process. In these experiments, the sulfur powder amounts used were 0.19, 0.15, 0.13, 0.06, and 0.016 g, corresponding to Co-S-190, Co-S-150, Co-S-130, Co-S-60, and Co-S-16 samples, respectively. The Raman spectra revealed more structural disorder or defects in the Co-S-130 and Co-S-60 samples. The FTIR results showed a band around 1097 cm^{-1} related to the S═O bond, surface oxidation of the Co-S-190 sample. Additionally, it was confirmed that the Co^{2+} and Co^{3+} states were present at the surface of the Co-S-60, Co-S-130, and Co-S-150 samples by XPS analysis. The Co^{3+} species on the surface were assigned to a high-spin state ($t_{2g}{}^4e_g{}^2$), which is beneficial for the OER, since they can optimize the adsorption, activation, and desorption of oxygen species.[899] Furthermore, oxygen bands were identified corresponding to adsorbed oxygen species, such as surface S−O, absorbed OH^-, and/or molecularly adsorbed water. In particular, the Co-S-130 sample exhibited a high concentration of surface defects and strong absorption ability for water. The XPS results confirmed that the obtained cobalt sulfide materials possessed a surface layer containing Co−S−O species (oxidized cobalt sulfide), and this chemical environment was modified by varying the sulfur content. Using large sulfur content in the synthesis, a surface with more lattice sulfur species was obtained. Thus, more oxygen species would locate on the surface due to the oxidation of surface sulfur species (S−O species), which are proposed to be the electrocatalytic active sites. Finally, the OER activity showed that the Co-S-190 required only an overpotential of 338 mV to achieve a current density of 10 mA·cm^{-2}, which is the lowest among all tested samples. The smallest Tafel slope of 69 mV·dec^{-1} suggested a fast four-electron transfer reaction for the Co-S-190 sample. All these results confirmed the unique surface state by controlling the sulfur content, which strongly affected the absorption of the oxygen species and allowed the enhancement of the electrocatalytic OER activity of cobalt sulfide.

5.1.3.3. Multi-cation Effects. Some reports have shown that binary/ternary transition metal electrocatalysts prepared via metal substitution engineering can significantly enhance electrocatalytic water oxidation due to the unique morphologies that facilitate electron transfer, interfaces created for adsorption/desorption of intermediates, and the metallic synergistic effects.[900] For instance, a large number of bimetallic compounds or hybrids, including Ni-Co (refs 861, 641, 860, 804, 820, 815, 787, and 812), Cu-Co,[744] Ni-Fe (refs 845, 735, 565, 693, 466, 809, 716, 805, and 691), Mo-Co,[673] Co-Fe,[460] and Ti-Fe[712] sulfides, have been extensively used to enhance the electrochemical activity for the OER. As an example, Liu *et al.* reported the synthesis of a Ni-Co bimetallic sulfide grown onto N and S co-doped reduced graphene oxide (denoted as $NiCo_2S_4$@N/S-rGO precatalyst) using the solvothermal method.[861] The XPS characterization confirmed the presence of Co^{3+}/Co^{2+} and Ni^{2+}/Ni^{3+} species in the bimetallic sulfide composite, attributed to the Co_3S_4 and Ni_3S_4 phases, respectively. It has been reported that transition metals with mixed valences could provide donor−acceptor chemisorption sites for the reversible adsorption of oxygen and realize high electrical conductivity for electron hopping between cations with different valence states, giving potentially high electrocatalytic activity to the $NiCo_2S_4$ hybrid. From the OER performance of the hybrid material in 0.1 M KOH and 0.1 M PBS electrolytes, it was possible to corroborate the effect of the

https://doi.org/10.1021/acs.chemrev.3c00005
Chem. Rev. 2023, 123, 12795−13208

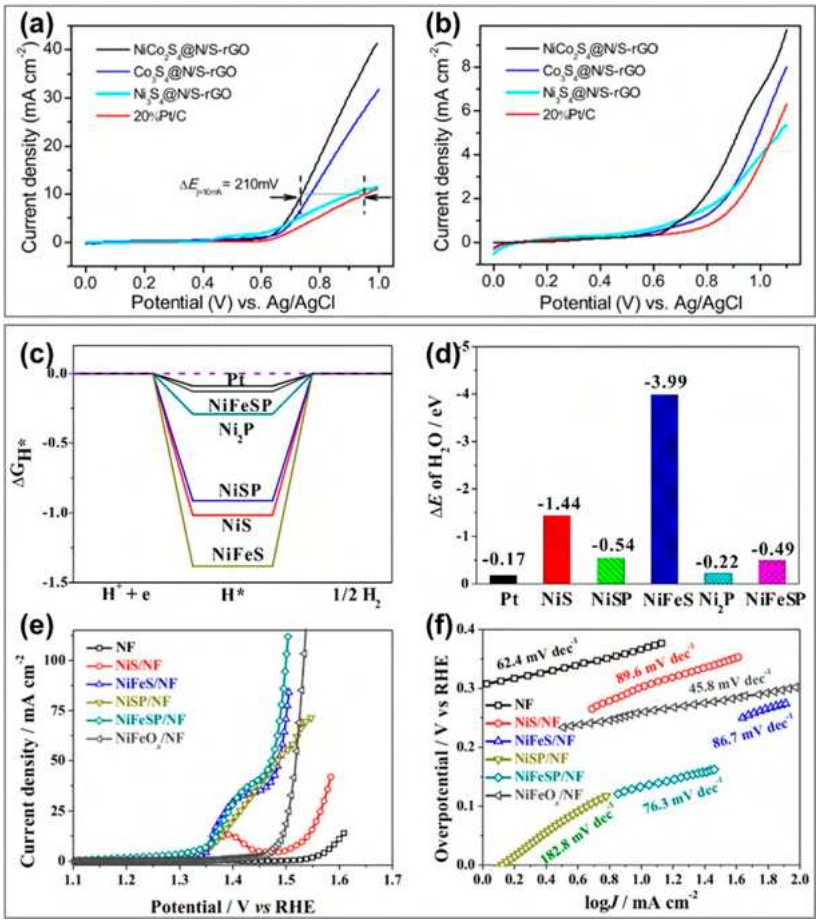


Figure 187. (a, b) OER LSV curves of $NiCo_2S_4$@N/S-rGO, Co_3S_4@N/S-rGO, Ni_3S_4@N/S-rGO, and commercial 20% Pt/C with a sweep rate of 10 $mV{\cdot}s^{-1}$ in (a) 0.1 M KOH (pH ∼ 13) and (b) 0.1 M PBS7.0. Reprinted with permission from ref 861. Copyright 2013 American Chemical Society. (c) Calculated Gibbs free energy diagrams of NiS, NiFeS, NiSP, Ni_2P, NiFeSP, and Pt for the HER. (d) H_2O adsorption energies on the NiS, NiFeS, NiSP, Ni_2P, NiFeSP, and Pt surfaces. (e) *iR*-corrected OER polarization curves and (f) Tafel plots of Ni foam (NF), NiS/NF, NiFeS/NF, NiSP/NF, NiFeSP/NF, and $NiFeO_x$. Reprinted with permission from ref 845. Copyright 2017 American Chemical Society.

bimetallic compound (Figures 187a and b). In both pH environments, the bimetallic Ni-Co sulfide exhibited higher OER performance compared to the individual Co and Ni sulfide components, suggesting a synergistic effect between both metals. Therefore, the combination of two cations with mixed valences is a useful strategy for increasing the OER activity of metal sulfides.

On the other hand, the morphology effect caused by the incorporation of more than one metal in sulfide compounds also has an impact on their OER performance, as reported for the Ni-Fe bimetallic sulfide by Gao *et al.*[565] They prepared P-S-NiFe precatalyst nanocubes through a phosphorization and a sulfurization process. This unique cubic morphology exposed rich edge active sites for the OER, contributing to a small resistance and fast reaction kinetics due to large surface areas and the metal composition synergy. In another study, a heterogeneous bimetallic phosphide/sulfide electrocatalyst on Ni foam (denoted as NiFeSP/NF precatalyst) was synthesized by Xin *et al.*[845] Through the design of this electrocatalyst, the metal−P and metal−S bonds optimized the electronic structure, as well as the Gibbs free energy for reactant adsorption or desorption, enhancing the OER activity. Using DFT calculations, the Fe and P co-doping was determined to decrease the Gibbs free energy and the H_2O adsorption energy of the NiS, making H and H_2O molecule adsorption more thermodynamically favorable (Figures 187c and d). The OER tests corroborated this synergistic effect. The P-doped bimetallic Ni-Fe sulfide showed a higher and faster performance toward water oxidation, with an overpotential of 240 mV to achieve 50 $mA{\cdot}cm^{-2}$ (Figures 187e and f). As different papers have described, the enhanced OER activity attributed to the bimetallic sulfide allowed better electron transfer and faster kinetics during the oxidation of water molecules. However, the details of the interaction between the two metals that contribute to this enhanced activity remain unknown, requiring more efforts for the unraveling of the mechanism of water oxidation as it relates to the bimetallic synergistic effect.

Trimetallic sulfide electrocatalysts have also been reported in the literature. In particular, ternary Ni-Co-Fe-based sulfides have been studied in depth.[694,827,743,765] For instance, Zhao *et al.* reported the synthesis of a ternary Ni-Co-Fe sulfide on nickel foam (denoted as NiCoFeS/NF precatalyst) using an electrodeposition-solvothermal process.[743] In the synthesis methodology, a uniform film of Co-Fe oxides was electrodeposited on the surface of the nickel foam utilizing iron and cobalt nitrate solution (denoted as CoFe/NF). After that, sulfurization was carried out by a solvothermal treatment at 140 °C for 12 h with thiourea as the sulfur source, converting the oxides into a ternary mixed sulfide precatalyst (NiCoFeS/NF). The XRD characterization revealed an amorphous phase

https://doi.org/10.1021/acs.chemrev.3c00005
Chem. Rev. 2023, 123, 12795−13208

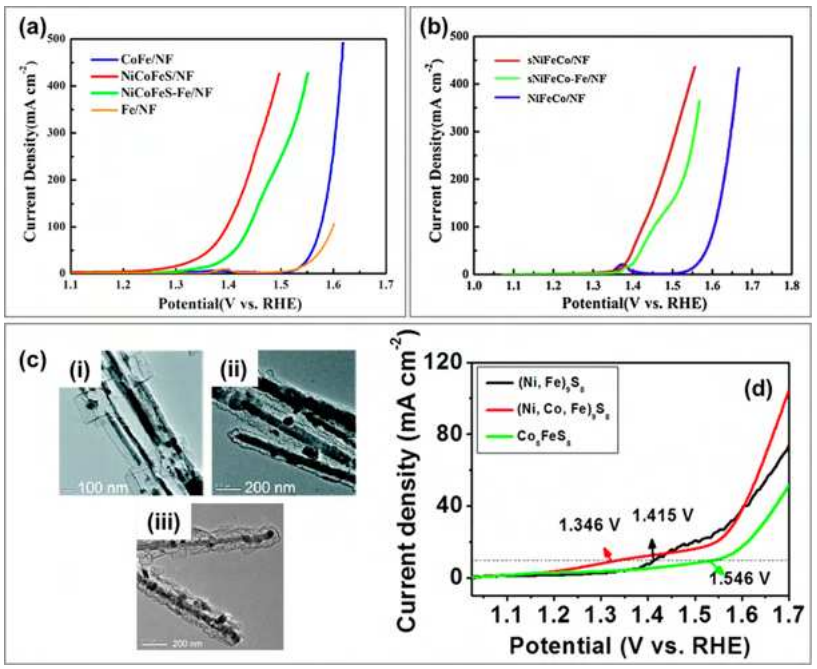


Figure 188. (a) Polarization curves of Fe/NF, CoFe/NF, NiCoFeS/NF, and NiCoFeS-Fe/NF measured in 1.0 M KOH. Reprinted with permission from ref 743. Copyright 2017 Elsevier. (b) Polarization curves of sNiFeCo/NF, sNiFeCo-Fe/NF, and NiFeCo/NF evaluated in 1 M KOH. Reprinted with permission from ref 827. Copyright 2018 Elsevier. (c) TEM images of carbon hybrids with the doping of nitrogen and the hybridization of multimetal chalcogenides: (c, i) $(Ni, Fe)_9S_8$ embedded N-doped carbon, (c, ii) $(Ni, Co, Fe)_9S_8$ embedded N-doped carbon, and (c, iii) Co_8FeS_8 embedded N-doped carbon. (d) LSV curves of $(Ni, Fe)_9S_8$/N-doped carbon, $(Ni, Co, Fe)_9S_8$/N-doped carbon, and Co_8FeS_8/N-doped carbon samples in an O_2-saturated 1.0 M KOH solution (scan rate: 5 $mV{\cdot}s^{-1}$). Reprinted with permission from ref 765. Copyright 2019 Royal Society of Chemistry.

for the CoFe/NF sample after the electrodeposition. After the sulfurization, a mixed structure was identified in which the NiS, Ni_3S_2, and Co_3S_4 phases were present in the NiCoFeS/NF sample with no crystalline Fe-based materials. However, from XPS analysis, the presence of Fe^{3+} species after both processes was confirmed (specifically Co^{2+} and Fe^{3+} hydroxides by electrodeposition). The electrocatalytic OER performance was evaluated in alkaline media and is presented in Figure 188a. As expected, the trimetallic sulfide showed an improved activity derived from the sulfurization of CoFe/NF, with a low overpotential of 40 mV to achieve 10 $mA{\cdot}cm^{-2}$ and an enhanced conductivity due to a lower charge transfer resistance caused by Co and Fe elements. Following this strategy, Chai *et al.* reported the trimetallic Ni-Fe-Co sulfide precatalyst (denoted as sNiFeCo/NF), showing a superior OER activity over the trimetallic Ni-Fe-Co oxide/hydroxide electrocatalyst (denoted as NiFeCo/Fe) attributed to the intrinsic electroconductivity of sulfides compared to metal oxides (Figure 188b).[827] On the other hand, Wang *et al.*[765] showed a multimetal Ni-Co-Fe precatalyst sulfide hybridization using metal-organic framework (MOF) precursors. The hybridization products included $(Ni, Fe)_9S_8$/N-doped carbon, $(Ni, Co, Fe)_9S_8$/N-doped carbon, and Co_8FeS_8/N-doped carbon composites, and their TEM images are illustrated in Figure 188c. Their OER performance in 1 M KOH is displayed in Figure 188d. The $(Ni, Co, Fe)_9S_8$/N-doped carbon exhibited an overpotential of 116 mV at 10 $mA{\cdot}cm^{-2}$, lower than those of the other multimetal compounds. Compared to the single-phase Ni or Co electrocatalyst, the Ni-Co-Fe electrocatalyst possessed higher conductivity due to synergistic effects induced by the multiple metals in the material, resulting in stronger electrocatalytic activity. Additionally, by the N doping of the carbon support, the nitrogen electronegativity could have changed the chemical environment of Ni^{2+} and Co^{2+} in the sample, leading to a higher electrocatalytic performance.

Li *et al.* performed an even more in-depth analysis of a FeCoNi-based precatalyst by using L-edge xXAS analysis of the Fe, Co, and Ni elements, which found that the Fe^{3+} amount increased in the trimetallic compound compared with the bimetallic NiFe-based compound.[694] This phenomenon indicates that Co ions can adjust the electronic state of Fe to favor the high valence state, which has been reported as a highly active species for the OER due to the low adsorption Gibbs free energy of intermediates on Fe sites. Moreover, the Fe ions tuned the crystal-field coordination of Co^{3+} ions located at octahedral sites in the structure, which are also considered as active sites for the OER rather than Co^{2+} ions in tetrahedral sites. The local electronic structure of Ni cations was also affected by the presence of Fe and Co ions, showing the presence of Ni^{3+}, which is regarded as an electrocatalytic site for the OER with higher activity than Ni^{2+}. Thus, the interaction between Fe, Co, and Ni ions improved the intrinsic activity of the precatalyst for the OER and affected the chemical and structural states of the FeCoNi-based precatalysts. As can be seen, the synergistic effects vary among different transition metals. Nevertheless, an extensive study regarding the metal interactions in bimetallic and trimetallic sulfides is critical to gaining an understanding of the boosted OER activity that results when multiple metals are incorporated into the material and to improving the future rational design of these highly active electrocatalysts.

5.1.3.4. Metal-Doping Effects. Many works have shown that tuning the local electronic structure of the metal sulfides by incorporating different transition metals, including Fe (refs

https://doi.org/10.1021/acs.chemrev.3c00005
Chem. Rev. 2023, 123, 12795−13208

639, 99, 97, 753, 819, 722, and 700), Zn,[841] Ni,[819,748,812] Mo,[780] and V,[680] effectively boosts the OER activity of the sulfide electrocatalyst. As an example of Fe-doping, Yuan *et al.* presented the direct growth of Fe-doped Ni_3S_2 nanosheet arrays on a conductive FeNi alloy foil (denoted as Fe-Ni_3S_2/FeNi precatalyst) via a one-step solvothermal method.[639] The HRTEM image of the Fe-Ni_3S_2 showed well-resolved lattice fringes indexed to Ni_3S_2 planes. The XRD analysis exhibited a similar result in which the peaks were attributed to Ni_3S_2, with no other impurity phases indicating that Fe-doped Ni sulfide was successfully synthesized. From the XPS analysis, it was observed that iron existed in the form of Fe^{3+} in the electrocatalyst and that some sulfate species likely formed by sulfur oxidation upon air exposure. The Fe-doped Ni_3S_2 demonstrated superior OER performance with a low overpotential of 282 mV needed to achieve a current density of 10 $mA{\cdot}cm^{-2}$, lower than those of all the other tested samples (Figure 189a). It was also suggested that the highly charged

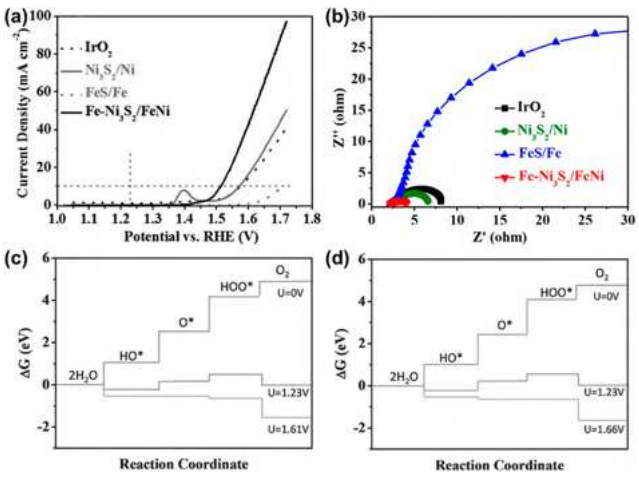


Figure 189. (a) LSV curves for Fe-Ni_3S_2/FeNi, Ni_3S_2/Ni, FeS/Fe, and IrO_2 in 1 M KOH solution. (b) EIS plots of Fe-Ni_3S_2/FeNi, Ni_3S_2/Ni, FeS/Fe, and IrO_2 recorded at 1.56 V_{RHE}. (c, d) Free energy profiles for (c) Fe-Ni_3S_2 and (d) Ni_3S_2 at zero potential (U = 0 V), equilibrium potential for oxygen evolution (U = 1.23 V), and minimum potential where all steps are downhill (U = 1.61 and 1.66 V). Reprinted with permission from ref 639. Copyright 2017 Wiley.

Fe^{3+} ions occupying the surrounding positions in the Ni_3S_2 lattice could retard the conversion of Ni^{2+} to Ni^{3+} and improve the stability of the electrocatalyst. Moreover, the larger ECSA, the faster kinetics, and the smaller charge transfer resistance of this precatalyst that made it favorable for OER electrocatalysis were attributed to Fe incorporation (Figure 189b). Using DFT calculations, it was determined that the adsorption of a water molecule over the surface Ni site in Fe-Ni_3S_2 required higher adsorption energy (E_{ads}) (−0.41 eV) compared to that over the surface Ni site in Ni_3S_2 (−0.35 eV). The strong and increased adsorption ability for a water molecule at the surface of Fe-Ni_2S_3/FeNi originates from the Fe dopant centers, which serve as electron active sites to increase the charge carrier concentration. On the other hand, oxygen molecule desorption from the surface Ni site in Fe-Ni_3S_2 is easier than that from the surface Ni site in Ni_3S_2 due to its smaller bond length (i.e., R_{O-Ni} = 2.18 and 2.16 Å for Ni_3S_2 and Fe-Ni_3S_2, respectively), resulting in an improved electrocatalytic OER performance (Figures 189c and d). These results demonstrate that Fe incorporation has an influence on the efficiency of the Ni_3S_2 electrocatalysts for the OER.

There are also similar strategies reported by other authors, including the Fe-doped Ni_3S_2 with 11.8% Fe content hydrothermally grown on nickel foam ($Fe_{11.8\%}$-Ni_3S_2/NF) from Cheng *et al.*[753] and the nitrogen-decorated iron-nickel sulfide nanosheet arrays on a conductive Ni-Fe alloy foam (N-$(Ni,Fe)_3S_2$/NIF) discussed by Jin *et al.*[819] However, it is essential to identify the complete scenario of the active sites related to Fe incorporation toward the OER. As demonstrated by Zhu *et al.*,[700] despite the retention of the crystalline Ni_3S_2 phase after the OER tests, amorphous substances derived from the surface of the Fe-Ni_3S_2 were identified, such as NiOOH and Fe species with a higher valence state of 4+, which has also been observed by Mossbauer spectroscopy in a NiFe-hydroxide-based electrocatalyst.[901] Therefore, it can be speculated that the active sites in these Fe-doped Ni-based sulfides may be attributed to Fe-NiOOH/Fe-Ni_3S_2, where the doped ferric iron could enhance the conductivity and alter the electronic structure of both NiOOH and Ni_3S_2.

In general terms, the metal-doping strategy has different effects on metal sulfide properties, including the electronic and crystalline structure modification that can result in boosted OER activity via the generation of more active sites, improvement in electron mobility, and limiting charge transfer resistance. It has also been found that the introduction of a doping agent can facilitate water molecule adsorption to produce different intermediate active species that play an important role during the OER, such as the (oxy)hydroxide-based compounds. Nevertheless, further studies are still needed for a major understanding of the metal-doping effects in metal sulfides and their relationship with their OER performance to design more efficient electrocatalysts.

5.1.3.5. Solid Solutions Effects. As the dopant concentration rises above 0.1−1%, it is common practice to refer to the materials as solid solutions rather than doped materials.[902] An example of a metal sulfide solid solution is presented by Cao *et al.*[460] They reported the synthesis of a $Co_{0.37}Fe_{0.26}S$ precatalyst solid solution synthesized by sulfurization using heat treatment under Ar flow. A CoFe-PBA precursor was first prepared via a simple chemical precipitation method. Then, the precursor was calcined with sulfur powder at 350 °C for 2 h to obtain the $Co_{0.37}Fe_{0.26}S$ precatalyst. XRD analysis revealed that the diffraction patterns of the as-obtained CoFe-based sample corresponded to the pure phase of cobalt sulfide (CoS_2). However, a slight peak shift in the XRD pattern was observed, indicating the partial Fe atom incorporation into the crystal lattice (Figure 190a). To further confirm this Fe incorporation, a high-magnification TEM analysis was carried out. The images exhibited the structure of the $Co_{0.37}Fe_{0.26}S$ precatalyst with some oriented crystallites and amorphous regions. The EELS elemental mapping showed a homogenous distribution of Co, Fe, and S elements throughout the observed sample, suggesting a uniform chemical composition and solid solution formation since the average CoS_2 structure represents the specific $Co_{0.37}Fe_{0.26}S$ composition. To understand the effect of Fe incorporation, an OER evaluation compared to CoS_2 was performed in 1 M KOH solution (Figure 190b). As observed in Figure 190b, CoS_2 demonstrated inferior OER activity compared to $Co_{0.37}Fe_{0.26}S$, indicating that the heterogeneous solid solution improved the intrinsic electrocatalytic activity. The contribution of the Fe incorporation to the enhanced OER activity can also result from the CoFe-based hydroxide

https://doi.org/10.1021/acs.chemrev.3c00005
Chem. Rev. 2023, 123, 12795−13208

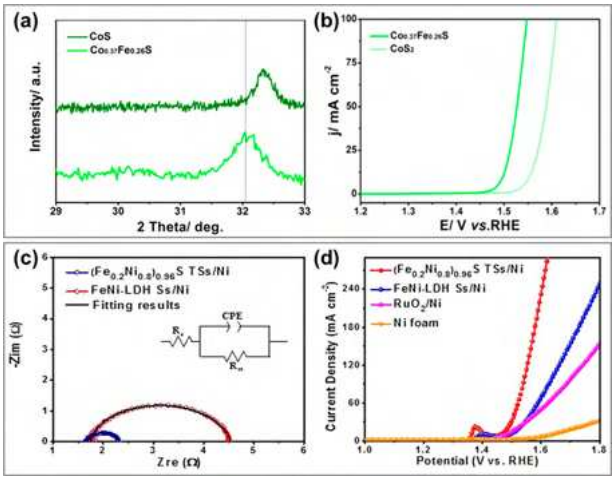


Figure 190. (a) XRD patterns of CoS_2 and $Co_{0.37}Fe_{0.26}S$. (b) LSV curves of CoS_2 and $Co_{0.37}Fe_{0.26}S$ in an O_2-saturated 1 M KOH solution. Reprinted with permission from ref 460. Copyright 2018 Elsevier. (c) Nyquist plots of $(Fe_{0.2}Ni_{0.8})_{0.96}S$ TSs/Ni and FeNi-LDH Ss/Ni. (d) Polarization curves of $(Fe_{0.2}Ni_{0.8})_{0.96}S$ TSs/Ni, FeNi-LDH Ss/Ni, RuO_2/Ni, and Ni foam. Reprinted with permission from ref 709. Copyright 2018 Springer Nature.

formation, which positively affects the electronic structure, creating more active sites, and is favorable for O and OH adsorption compared to the Co-based materials (sulfide and hydroxide).

Xu *et al.* reported a similar strategy in which they prepared the $(Fe_{0.2}Ni_{0.8})_{0.96}S$ precatalyst solid solution via vulcanizing FeNi-LDH spheres grown onto Ni foam at 140 °C for 4 h.[709] After the synthesis, the XRD results confirmed the hexagonal phase of the FeNi-based sulfide. Moreover, the HRTEM characterization showed lattice fringe spacings of the (110) and (102) planes for the $(Fe_{0.2}Ni_{0.8})_{0.96}S$ precatalyst. Compared to the FeNi-LDH, abundant defects were observed in the HRTEM image of $(Fe_{0.2}Ni_{0.8})_{0.96}S$, which may provide more active sites for the OER. The evaluation of the charge transfer kinetics was performed via EIS (Figure 190c). The $(Fe_{0.2}Ni_{0.8})_{0.96}S$ precatalyst exhibited a lower charge transfer resistance value (R_{ct}) of 0.65 Ω compared to that of FeNi-LDH (2.19 Ω), suggesting better charge transfer kinetics for the electrochemical process for the sulfide material. From polarization curves for the OER displayed in Figure 190d, it is evident that the $(Fe_{0.2}Ni_{0.8})_{0.96}S$ precatalyst outperformed all studied samples. Specifically, the $(Fe_{0.2}Ni_{0.8})_{0.96}S$ sample exhibited a lower overpotential of 233 mV at a current density of 10 mA·cm^{-2} than that of FeNi-LDH (263 mV), suggesting it is more favorable for OER electrocatalysis.

5.1.3.6. Oxygen Vacancy Effects. It has been reported that the electrocatalytic activity for the OER on metal sulfides can be significantly improved by tuning the structure of its electronic states by generating exposed planes.[830] These findings imply that designing an electrocatalyst with a plentiful disordered metal−sulfur structure is a promising strategy for the development of highly active materials. Cai *et al.*[830] reported the synthesis of oxygen-incorporated amorphous CoS_x porous nanocubes (A-$CoS_{4.6}O_{0.6}$ PNCs) by ionic exchange reaction on Prussian blue analogue (PBA), which allowed for porous structure formation consisting of a large number of defects/vacancies. By XPS analysis, it was confirmed that oxygen is doped into CoS_x hosts. Additionally, the XANES spectral shapes of the A-$CoS_{4.6}O_{0.6}$ PNCs were similar to the those of the CoS_2 compound rather than CoO, indicating an analogous Co−S octahedral structure to the CoS_2. The introduction of O atoms around Co center atoms could generate more locally disordered structures, as confirmed by XANES curves. The electrocatalytic activity towards the OER in 1.0 M KOH solution is shown in Figure 191a. The A-

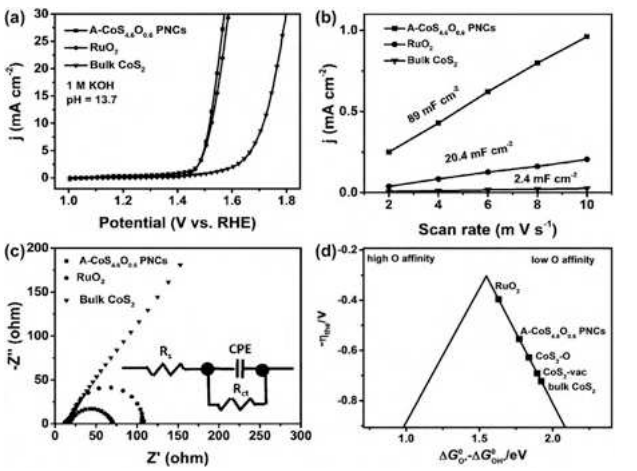


Figure 191. (a) Polarization curves and (b) corresponding Tafel plots of A-$CoS_{4.6}O_{0.6}$ PNCs, bulk CoS_2, and RuO_2 for the OER in 1 M KOH (pH = 13.7). (c) EIS plots of A-$CoS_{4.6}O_{0.6}$ PNCs, bulk CoS_2, and RuO_2 recorded at 1.505 V_{RHE} and (inset) corresponding equivalent circuit. (d) Theoretical volcano plots for RuO_2, bulk CoS_2 (no vacancy and O replacement), CoS_2-vac (only vacancy), CoS_2-O (only O replacement), and A-$CoS_{4.6}O_{0.6}$ PNCs (both vacancy and O replacement). Reprinted with permission from ref 830. Copyright 2017 Wiley.

$CoS_{4.6}O_{0.6}$ PNCs delivered a current density of 10 mA·cm^{-2} at 1.52 V_{RHE}, lower than that of RuO_2 (1.53 V_{RHE}) and that of bulk CoS_2 (1.71 V_{RHE}) as a reference. Furthermore, the EIS and C_{dl} measurements indicated that A-$CoS_{4.6}O_{0.6}$ PNCs showed smaller charge transfer resistance and larger electrochemical surface area (ECSA) compared to those of bulk CoS_2 (Figures 191b and c). DFT calculations determined the role of the incorporated O atom and the Co−S dangling bonds. The A-$CoS_{4.6}O_{0.6}$ PNCs possessed higher O affinity than bulk CoS, leading to significantly improved activity (Figure 191d) due to higher O* adsorption. Based on these results, when vacancies were introduced into CoS_2 to produce CoS_2-O, the activity was enhanced, suggesting that the vacancy sites may assist in strengthening the O* adsorption that can promote water oxidation while achieving higher OER activity.

Yin *et al.*[831] reported a similar strategy for making oxygen vacancy-dominated cobalt-nickel sulfide interface porous nanowires (NiS_2/CoS_2-O NWs) as highly active precatalysts for the OER. This precatalyst was made by first calcinating $NiCo_2O_4$ NW using sulfur powder under a nitrogen atmosphere at 300 °C for 2 h, followed by electrochemical leaching at 1.6 V_{RHE} for more than 6 h in 1 M KOH. XPS was used to investigate the surface composition after the synthesis procedure. The O 1s spectrum of the NiS_2/CoS_2-O NWs shown in Figure 192a confirmed that three oxide species were formed at the surface (denoted as O1, O2, and O3). The O1 peak was assigned to the metal−oxygen bond, the O2 peak to oxygen vacancies, and the O3 to hydroxyl species of adsorbed water molecules. Compared to the NiS_2/CoS_2 NWs, the NiS_2/

https://doi.org/10.1021/acs.chemrev.3c00005
Chem. Rev. 2023, 123, 12795−13208

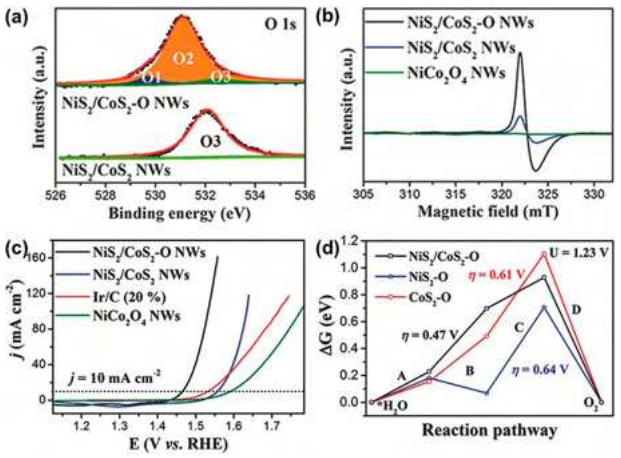


Figure 192. (a) O 1s XPS spectra of NiS_2/CoS_2 NWs and NiS_2/CoS_2-O NWs. (b) ESR spectra of NiS_2/CoS_2 NWs, NiS_2/CoS_2-O NWs, and $NiCo_2O_4$ NWs. (c) *iR*-corrected LSV curves (scan rate: 2 $mV{\cdot}s^{-1}$) of NiS_2/CoS_2-O NWs, NiS_2/CoS_2 NWs, $NiCo_2O_4$ NWs, and commercial Ir/C for the OER in 1.0 M KOH. (d) OER energetic profiles on CoS_2-O, NiS_2-O, and NiS_2/CoS_2-O. Reprinted with permission from ref 831. Copyright 2017 Wiley.

CoS_2-O NWs showed a stronger O2 peak which is smaller than the O1 and O3 peaks, confirming that the abundant oxygen vacancies were created during the electrochemical leaching. Furthermore, the electron spin resonance (ESR) signals were recorded and further confirmed the presence of oxygen vacancies in the as-obtained NiS_2/CoS_2-O NWs (Figure 192b). To be specific, the NiS_2/CoS_2-O NWs exhibited a much stronger oxygen vacancy-related signal than the negligible response of the NiS_2/CoS_2 NWs, abundant oxygen vacancies, which were formed in the surface oxide layers at the NiS_2/CoS_2-O NWs surface. The OER tests were carried out in 1 M KOH electrolyte and are presented in Figure 192c. The NiS_2/CoS_2-O NWs with abundant oxygen vacancies showed the best electrocatalytic OER activity with a low overpotential of 235 mV at 10 $mA{\cdot}cm^{-2}$, which is smaller than those of NiS_2/CoS_2 NWs (320 mV) and commercial Ir/C (300 mV). DFT calculations were also performed to estimate the energetic profile and the intermediate states of the OER on the materials (Figure 192d). The NiS_2/CoS_2-O displayed the lowest OER overpotential (0.47 V) compared to those of CoS_2-O (0.61 V) and NiS_2-O (0.64 V) and even pristine CoS_2 (0.75 V) and NiS_2 (0.94 V), indicating its lower energy barrier in the OER mechanism. These calculations were consistent with the experimental results and demonstrated that an enhanced electrocatalytic activity could be achieved by abundant oxygen vacancies providing an excess of active sites for the OER.

5.1.3.7. Composite Materials Effects. Composites or hybrid materials are an alternative strategy used for the development of highly active OER electrocatalysts. Such composites can provide good conductivity, mechanical stability, and a more catalytically active surface area for water oxidation. This section describes heterostructure formation and co-catalyst loading as a composite strategy to enhance the OER electrocatalytic activity of different sulfides.

5.1.3.7.1. Heterostructures. Heterostructures have received increasing attention because of their many advantages toward OER electrocatalysis such as the exposure of active sites from the created interface, the specific surface area and electrocatalytic sites that can be improved by designing hierarchical porous structures, and the charge transfer and electrocatalytic efficiency enhancement due to the synergistic effect between the materials in the heterostructure.[903] In particular, the electrons can be transferred from one material to another through the boundary interface. This electron transfer can modulate the current density around the active sites, leading to a higher efficiency during OER performance due to a barrier energy decrement for the formation of intermediates (*OOH) that facilitates the OER.[904] In the literature, different heterostructures have been synthesized to improve the electrocatalytic OER by metal sulfides, which typically include sulfide/sulfide-, sulfide/oxide-, and sulfide/carbon-based materials. These heterostructures will be discussed in detail in the following sections.

Metal sulfides are attractive electrocatalysts for overall water splitting. However, regarding the electrocatalytic activity of pure metal sulfides, including their different polymorphs, there is a need to improve their long-term stability and efficiency that prevent the practical application of these materials for large overall water-splitting applications. It has been demonstrated that by combining two or more metal sulfides to create a highly ordered heterostructure, the electrocatalytic activity has been improved compared to the performance of every single-metal or pure-metal sulfide. In regard to this phenomenon, many reports describe the synergy of the sulfide/sulfide heterostructure using different metal combinations, including Co-Ni,[707,786,852] Ni-Mo,[738,732,785] Co-Mo,[854,779] Ti-Fe,[712] and others,[677,816,683,701] as the root cause of the improved performance. Shit *et al.*[786] reported a CoS_x/Ni_3S_2 heterostructure as an efficient precatalyst for overall water splitting in alkaline medium. The heterostructure was synthesized by a one-step hydrothermal route at 120 °C for 12 h using Ni foam as a conductive substrate. The formation of the CoS_x/Ni_3S_2 heterostructure showed high OER activity (Figure 193a) with an overpotential of 280 mV to achieve 20 $mA{\cdot}cm^{-2}$, which is lower compared to those of Ni_3S_2 (347

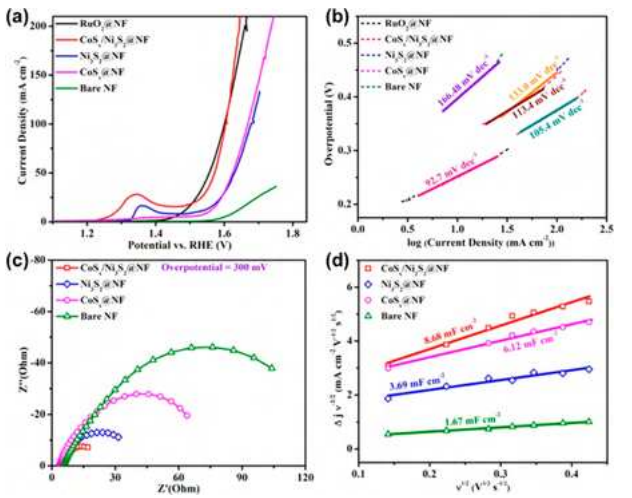


Figure 193. (a) OER polarization curves and (b) corresponding Tafel plots of CoS_x/Ni_3S_2@NF, Ni_3S_2@NF, CoS_x@NF, bare NF, and RuO_2@NF in 1.0 M KOH (with *iR* correction). (c) Nyquist plots (at an overpotential of 300 mV) and (d) $\Delta j{\cdot}\nu^{-1/2}$ vs $\nu^{1/2}$ plots of CoS_x/Ni_3S_2@NF, Ni_3S_2@NF, CoS_x@NF, and bare Ni foam (NF). Reprinted with permission from ref 786. Copyright 2018 American Chemical Society.

https://doi.org/10.1021/acs.chemrev.3c00005
Chem. Rev. 2023, 123, 12795−13208

mV) and CoS_x (353 mV). Regarding the OER kinetics, the CoS_x/Ni_3S_2 heterostructure exhibited faster kinetics than each single-metal sulfide also tested, with a lower Tafel slope of 105.4 mV·dec^{-1} compared to those of Ni_3S_2 (133 mV·dec^{-1}) and CoS_x (113.4 mV·dec^{-1}) (Figure 193b). To achieve a better understanding of this improved performance, the charge transfer resistance (R_{ct}) was determined from Nyquist plots to be 19.3, 35.2, and 82 Ω for the CoS_x/Ni_3S_2 heterostructures, Ni_3S_2, and CoS_x, respectively (Figure 193c). Additionally, the number of active sites was calculated from the C_{dl}, exhibiting a value of 8.68 mF·cm^{-2} for the heterostructure, which was ~2.35 times higher than that for Ni_3S_2 (Figure 193d). These results indicate the superior activity of the CoS_x/Ni_3S_2 heterostructure toward the OER due to the creation of more active sites, which facilitated and boosted charge transfer for the splitting of water molecules with less energy input.

It has been reported that the interfaces created in the heterostructure play an important role in the enhanced electrocatalytic activity demonstrated by these materials toward the OER. One work reported by Zhu *et al.*[854] using a core@shell precatalyst heterostructure composed of a cubic cobalt sulfide layer as the core surrounded by a shell of fullerene-like molybdenum disulfide layers formed onto carbon nanofibers (Co_9S_8@MoS_2/CNFs). The synthesis procedure was carried out by a simple S vapor assisted graphitization of polyacrylonitrile (PAN) nanofibers containing cobalt nitrate and ammonium tetrathiomolybdate. After the S vapor assisted graphitization, a large amount of Co_9S_8@MoS_2 nanocrystals with hexagonal morphology grown on the CNF was detected, as confirmed by the FESEM and TEM characterization. According to the STEM-EDX elemental mapping, the Co signal area was encapsulated in the center of the hexagon by the Mo signal area, revealing the Co_9S_8@MoS_2 core@shell structure and the direct interaction between the Co_9S_8 and MoS_2 phases (inset of Figure 194a). The polarization curve of Co_9S_8@MoS_2/CNFs showed an earlier OER onset potential of 1.580 V_{RHE} and a smaller overpotential of 430 mV at 10 mA·cm^{-2} compared to those of the Co_9S_8 and MoS_2 materials (Figure 194a). In the Tafel plots presented in Figure 194b, favorable intrinsic OER kinetics for the Co_9S_8@MoS_2/CNFs heterostructure were observed (61 mV·dec^{-1}), which are faster than those of the MoS_2/CNFs (80 mV·dec^{-1}) and Co_9S_8/CNFs (78 mV·dec^{-1}). The faster kinetics of the heterostructure were supported by the dramatic decrease in the charge transfer resistance measured (R_{ct}), exhibiting more facile electron mobility to enhance the electrocatalytic activity. This enhanced electrocatalytic activity for the OER was attributed to the synergistic effect between Co and Mo at the localized nanointerface region between MoS_2 and Co_9S_8. The nanointerface led to the creation of open latent vacancy sites on Mo atoms interacting with Co and the formation of direct Mo−Co bonds, facilitating a strong electron transfer between both metallic elements through the intermediate S atoms bonded to both metals. These synergistic effects from the nanointerface were investigated by the hydrogen evolution pathway by first-principle calculations, in which the Co_9S_8@MoS_2/CNFs showed a smaller hydrogen molecule adsorption surface energy and lower hydrogen molecule desorption energy compared to MoS_2, demonstrating the highly active nature in stabilizing the HER intermediate, promoting the H−H bond formation and releasing H_2 gas, all favorable for the water-splitting process (Figure 194c).

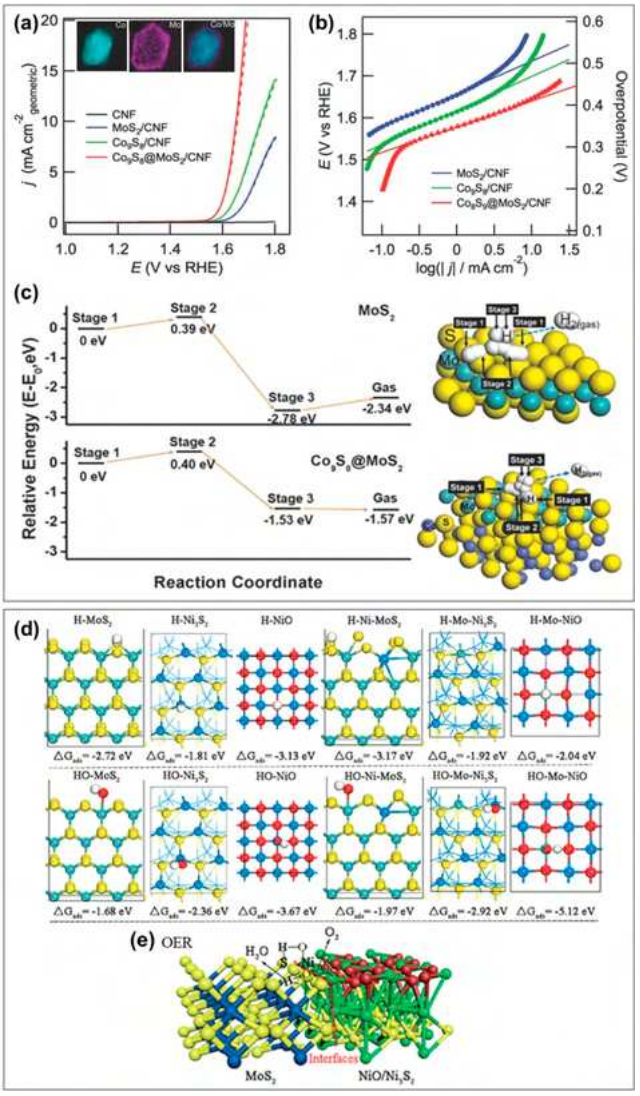


Figure 194. (a) Polarization curves and (b) corresponding Tafel plots (*iR* corrected) of Co_9S_8@MoS_2/CNF, MoS_2/CNF, Co_9S_8/CNF, and CNF at 2 mV·s^{-1} in 1 M KOH. Insets of (a) indicate STEM-EDX element mapping images. (c) Kinetic energy barrier profiles of the HER on the MoS_2 (top) and Co_9S_8@MoS_2 (down) electrocatalysts. Right side of (c) shows the diffusion paths of H_2 on the MoS_2 and Co_9S_8@MoS_2 surfaces. Reprinted with permission from ref 854. Copyright 2015 Wiley. (d) Chemisorption models of H and OH intermediates on the surfaces of MoS_2, Ni_3S_2, NiO, the MoS_2/Ni_3S_2 heterostructure (Ni-MoS_2 and Mo-Ni_3S_2 models), and the MoS_2/NiO heterostructure (Ni-MoS_2 and Mo-NiO models), respectively. (e) Proposed mechanisms for the dissociation of H_2O, OH, and OOH intermediates on the MoS_2/Ni_3S_2 heterostructure. Reprinted with permission from ref 738. Copyright 2016 Wiley.

Complementarily, Zhang *et al.*[738] established that the *in situ* generated interfaces between Ni_3S_2 and MoS_2 heterostructure precatalysts, and the additional electrochemically oxidized NiO at the surface during the OER, facilitated the synchronous chemisorption of hydrogen and oxygen-containing intermediates improving the overall electrochemical water splitting activity. They used DFT calculations to clarify the effect of these interfaces and obtain the chemisorption free energies of hydrogen (ΔG_H) and hydroxide (ΔG_{OH}) on the (101) surface of Ni_3S_2, the (010) surface of NiO, and the (002) surface of MoS_2. The results showed that the surface undercoordinated

https://doi.org/10.1021/acs.chemrev.3c00005
Chem. Rev. 2023, 123, 12795−13208

Ni sites of the Ni_3S_2/MoS_2 heterostructure model (denoted as Mo-Ni_3S_2) have an HO-chemisorption energy of −2.92 eV, which is lower than those for MoS_2 (−1.68 eV) and Ni_3S_2 (−2.36 eV), allowing superior binding activity toward oxygen-containing groups. Moreover, considering the extra formed interfaces between MoS_2 and NiO during the OER, the Mo sites of the Mo-doped NiO model (denoted as Mo-NiO) exhibited a significantly increased HO chemisorption energy up to −5.12 eV (Figure 194d). Thus, it was confirmed that the constructed interfaces decreased the Gibbs free energies of the corresponding intermediates, facilitating the dissociation of the O−H bonds of the water molecule and the OH and OOH intermediates (Figure 194e).

Another interesting strategy reported in the literature is the combination of two metal sulfide polymorphs into a heterostructure. Lin *et al.* reported the hierarchical cobalt sulfide nanocomposite (HCSN) precatalyst heterostructure, prepared by vertically growing Co_9S_8 nanosheets on horizontal $Co_{1-x}S$ nanoplates by one-pot hydrothermal synthesis at 160 °C for 12 h.[713] By adjusting the solvent mixture of ethylene glycol:water, different morphological and structural characteristics were obtained. With the increase in ethylene glycol, in-plane vertical nanosheets tended to protrude while the Co_9S_8 content of HCSN in XRD also increased, indicating that vertical nanosheets with high exposed surface area belong to Co_9S_8 and are grown onto the horizontal $Co_{1-x}S$ nanoplates. This 3D structure can be specially observed in the sample denoted as 11 EW (1:1 ethylene glycol:water ratio). This heterostructure exhibited a superior OER performance in 1 M KOH with a lower overpotential of 275 mV at a current density of 10 mA·cm^{-2} and a smaller Tafel slope of 30 mV·dec^{-1}, compared to those of a RuO_2 reference sample (overpotential: 389 mV; Tafel slope: 80 mV·dec^{-1}). Such low overpotential was attributed to the special surface morphology of the HCSN, in which more defects are on the edge and in-plane of $Co_{1-x}S$ nanoplates. Following a similar approach, Luo *et al.* presented the fabrication of a tree-like array of NiS/Ni_3S_2 heterostructure precatalysts via an epitaxial growth strategy of Ni sulfide onto Ni foam using a one-step hydrothermal process at 180 °C for 24 h[703] in which Ni_3S_2 nanorods arrays were grown on nickel foam. During the synthesis, the heterostructure was constructed by the epitaxial growth of NiS nanosheets onto the Ni_3S_2 nanorods using acetic acid as a surface activator to control the obtained morphology. As expected, the tree-like NiS/Ni_3S_2 heterostructure exhibited better OER performance (overpotential: 269 mV at 10 mA·cm^{-2}) than Ni_3S_2 in alkaline media. The electronic modulation of the heterostructure induced the transfer of electrons from metallic Ni_3S_2 to NiS, achieving a synergistic effect between NiS and Ni_3S_2, which is supported by its low overpotential and small Tafel slope of 119 mV·dec^{-1}. Therefore, such tree-like NiS/Ni_3S_2 heterostructure improved the electrical conductivity of the sample and the kinetics for the OER.

Lastly, the final approach regarding the sulfide/sulfide heterostructure used for the OER is that reported by the combination of three different metal sulfides, such as $MoS_2/Co_9S_8/Ni_3S_2/NF$[688] and Co_9S_8-CuS-FeS.[636] The $MoS_2/Co_9S_8/Ni_3S_2/NF$ precatalyst heterostructure reported by Yang *et al.*[688] was made by a 3D porous conductive nickel foam covered with Ni_3S_2 nanorods, which were then decorated with ultrathin MoS_2 and Co_9S_8 nanosheets. The strong interaction between Co_9S_8 and MoS_2 originating from the interfacial areas between the phases allowed for a remarkable OER activity to be achieved due to the complete use of active sites of the electrocatalyst and efficient electron and mass transfer. The results showed a low overpotential of 166 mV to achieve 10 mA·cm^{-2} in 1 M KOH for the ternary $MoS_2/Co_9S_8/Ni_3S_2$ heterostructure, compared to the binary Co_9S_8/Ni_3S_2 (192 mV) and MoS_2/Ni_3S_2 (239 mV). This trend was confirmed by DOS calculations which determined that the Fermi level decreased upon binding Co_9S_8 to MoS_2, indicating that electrons were withdrawn from Co to MoS_2. This process led to slight oxidation of Co and reduction of Mo in the heterostructure, which resulted in enhanced OER performance. Meanwhile, in the DFT calculations without the MoS_2, the formation of an O−O bond in OOH* was the rate-limiting step (calculated overpotential: 1.45 V), whereas the overpotential required for the same step decreased dramatically to 0.86 V using the Co_9S_8/MoS_2 structure. As Co_9S_8 loses electrons to MoS_2, the binding energies of adsorbed species change, and the overpotential decreases. This suggests that the Co_9S_8 and MoS_2 phases make the main contribution to the OER activity, while the role of Ni_3S_2 may be to create the binder between them and act as a current collector. These results indicated that the Co_9S_8 activity for the OER was dependent on the presence of interfaces to other transition metal sulfides. Another approach to demonstrate the synergistic effect of the three metal sulfides in their heterostructure was the experimental and theoretical analysis provided for the Co_9S_8-CuS-FeS heterostructure precatalyst reported by Zhang *et al.*[636] In this report, Zhang and co-workers incorporated FeS and CuS into Co_9S_8 and found that these additions were beneficial for the formation of the cobalt sulfide, increased the conductivity of the electrocatalyst, and decreased the Gibbs free energy of absorption of the oxygen atoms on Co atoms, leading to excellent OER performance. The CoCuFe-S heterostructure exhibited lower OER overpotential (300 mV at 10 mA cm^{-2}) compared to those of individual FeS (520 mV at 10 mA cm^{-2}), Co_9S_8 (380 mV at 10 mA cm^{-2}), and CuS (570 mV at 10 mA cm^{-2}). From the XPS analysis, it was concluded that after the addition of CuS and FeS, the electrons of CuS and FeS were continuously transferred to Co_9S_8 during the OER process. According to their density functional theory calculations, the Gibbs free energy of adsorbing oxygen atoms ($\Delta G_{*O} - \Delta G_{*OH}$) for Co_9S_8 was determined to be 0.73 eV, lower than the 1.6 eV optimal value. This strong absorption of oxygen atoms onto pure Co_9S_8 represents a lower OER reaction rate. Nevertheless, after the introduction of FeS and CuS, the electron-rich Co atoms promoted the breaking of Co−O bonds. The weak adsorption of the oxygen atoms with Co atoms allowed a faster reaction rate for the OER, as shown in Figure 195.

Since metal sulfides are not intrinsically suitable OER electrocatalysts because of their poor stability under oxidizing conditions, one alternative to improve their performance for the OER is through the combination of metal sulfides with metal oxides, which are highly stable at high anodic overpotentials. The combination of metal sulfides with metal oxides to create heterostructure materials is widely reported. The synergy between metal sulfides and simple metal oxides (M_xO_y, M = metal) (e.g., Co_9S_8/Co_3O_4,[839] Fe_3O_4/Co_9S_8,[848] CoS_2/TiO_2,[725] Co_3O_4/CoS_2,[720] Ni_3S_2/MnO_2,[684] NiO/Ni_3S_2[772]) as well as complex oxides ($M_xN_yO_z$, M, N = metal) (e.g., $NiCo_2O_4/Ni_3S_2$[711] and $Co_{1.2}MoO_{4.2}\cdot 1.3H_2O)/Ni_3S_2$[784]) will be discussed in detail below. Guo *et al.*[720] have

https://doi.org/10.1021/acs.chemrev.3c00005
Chem. Rev. 2023, 123, 12795−13208

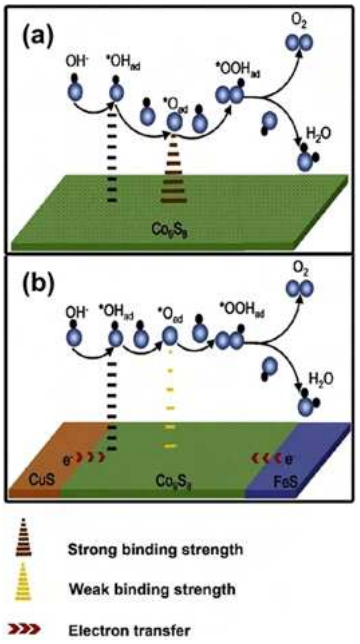


Figure 195. Schematic illustrations of the OER processes: (a) Co_9S_8 showing a strong interaction with adsorbed O atom, and (b) Co_9S_8-CuS-FeS heterostructure showing that the electron transfer from Cu and Fe to Co may enhance the electrocatalytic performance. Reprinted with permission from ref 636. Copyright 2018 Elsevier.

reported a highly active Co_3O_4/CoS_2 precatalyst heterostructure for the OER prepared via a facile solvothermal method followed by a partial phase sulfurization of the Co_3O_4. From experimental results, it was revealed that the metal sulfide/oxide heterostructure experienced enhanced conductivity, improved surface diffusion and mass transfer, an increase in the number of active sites, and a synergistic couple between the sulfide and the oxide that facilitated the electrocatalysis of the OER as compared to the CoS_2 and Co_3O_4 reference samples. The specific heterostructure feature was observed by the lattice fringes of Co_3O_4 and CoS_2 from the TEM and HRTEM images (Figure 196a), in which the interplanar spacing revealed that there were contact areas between both electrocatalytic materials that could provide numerous active sites for the OER. This was further confirmed by the polarization curves illustrated in Figure 196b, where the Co_3O_4/CoS_2 heterostructure exhibited a more negative OER onset potential (1.41 V_{RHE}) than the CoS_2 (1.48 V_{RHE}) and Co_3O_4 (1.50 V_{RHE}). The Co_3O_4/CoS_2 heterostructure also achieved a current density of 10 $mA{\cdot}cm^{-2}$ at a lower overpotential of 280 mV. Additionally, it can be seen that the Co_3O_4/CoS_2 heterostructure showed a lower Tafel slope of 63 $mV{\cdot}dec^{-1}$ compared with those of CoS_2 (92 $mV{\cdot}dec^{-1}$) and Co_3O_4 (86 $mV{\cdot}dec^{-1}$), implying its fast OER kinetics (Figure 196c). It has been reported that the introduction of CoS_2 should accelerate the breaking of the Co−O bond because of facile electron transfer from CoS_2 to Co_3O_4 and also the generation of more active oxidized Co species [$Co^{IV}(-O)$] during the OER that might further enhance its OER performance, as was confirmed by post-OER characterization. Similar observations were reported by Xiong *et al.*[684] for their Ni_3S_2/MnO_2 precatalyst heterostructure prepared via a simple two-step hydrothermal conversion of nickel foam using $KMnO_4$ and thioacetamide. The OER performance of the Ni_3S_2/MnO_2 heterostructure afforded a current density of 10

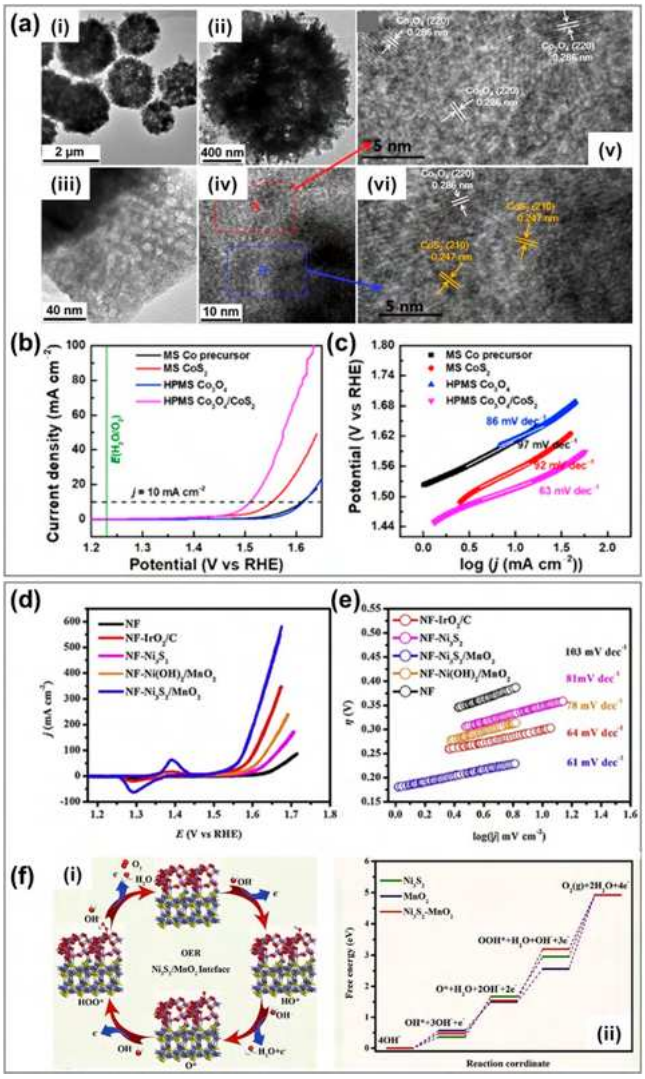


Figure 196. (a) TEM (i–iii) and HR-TEM images (iv–vi) of the HPMS Co_3O_4/CoS_2. (b) Polarization curves and (c) Tafel plots of the MS Co precursor, MS CoS_2, HPMS Co_3O_4, and HPMS Co_3O_4/CoS_2 in 1 M KOH at a potential sweep rate of 2 $mV{\cdot}s^{-1}$. Reprinted with permission from ref 720. Copyright 2018 Elsevier. (d) CV curves and (e) Tafel plots of Ni foam (NF), NF-Ni_3S_2, NF-$Ni(OH)_2/MnO_2$, NF-Ni_3S_2/MnO_2, and NF-IrO_2/C for the OER in 1.0 M KOH. (f, i) Schematic illustration of OH^- activation, OH*/O*/OOH* generation, and oxygen formation processes on Ni_3S_2/MnO_2 hybrid electrocatalyst in 1.0 M KOH. (f, ii) Calculated reaction energy diagrams of Ni_3S_2, MnO_2, and Ni_3S_2-MnO_2 at different stages of H_2O oxidation toward H_2 and O_2 generation in 1.0 M KOH. Reprinted with permission from ref 684. Copyright 2019 Elsevier.

$mA{\cdot}cm^{-2}$ at a relatively low overpotential of 260 mV, along with a Tafel slope of 61 $mV{\cdot}dec^{-1}$ (Figures 196d and e) in 1 M KOH aqueous electrolyte. Generally, the alkaline OER pathways include four-electron transfer steps and the rate-limiting step is related to the generation of *O from *OH ($\Delta G3$) or the production of *OOH from *O ($\Delta G4$). Here, a proposed mechanism by DOS calculations was provided for the Ni_3S_2/MnO_2 heterostructure during the OER (Figure 196f), in which the $\Delta G4$ energy was greatly reduced to 0.49 eV compared with those of Ni_3S_2 (0.74 eV) and MnO_2 (1.12 eV). These theoretical results indicate that the effective adsorption and cleavage of H_2O molecules on the electrocatalyst surface due to the presence of Ni_3S_2/MnO_2 heterostructure interfaces

https://doi.org/10.1021/acs.chemrev.3c00005
Chem. Rev. 2023, 123, 12795−13208

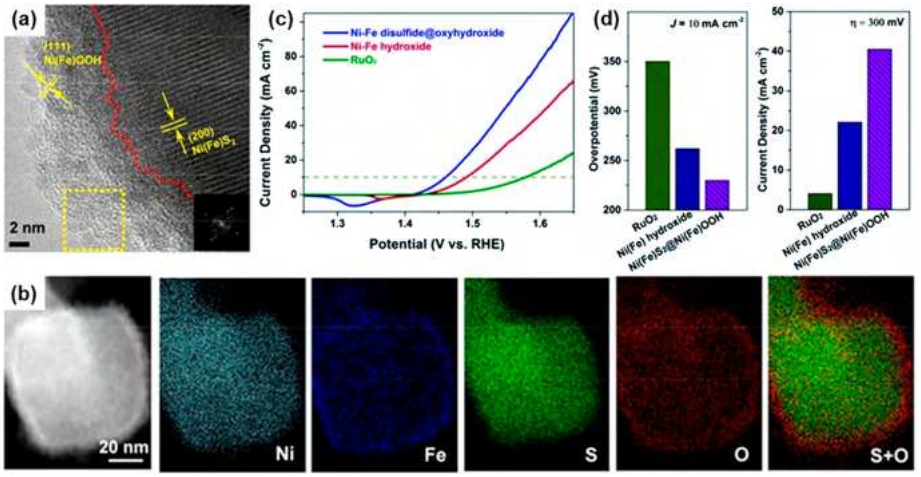


Figure 197. *In situ* electrochemical conversion process of Ni-Fe disulfide surface into Ni-Fe (oxy)hydroxide surface. (a) HRTEM image and (b) elemental mapping images of the electrocatalyst after the 100 OER cycles. (c) Normalized LSV polarization curves and (d) as-recorded overpotentials (left, j = 10 mA·cm^{-2}) and current densities (right, η = 300 mV) of Ni-Fe disulfide@(oxy)hydroxide, Ni-Fe hydroxide, and RuO_2 recorded using glassy carbon electrodes (conductive substrates). Reprinted with permission from ref 728. Copyright 2017 Royal Society of Chemistry.

might improve the OER process. This assumption is further supported by the Ni_3S_2 conversion to the (oxy)hydroxide active species on the as-prepared material's surface during electrochemical testing. Accordingly, the combination of a transition metal sulfide and a simple metal oxide favored the formation of a highly efficient OER electrocatalyst in alkaline solution.

It has also been demonstrated that the incorporation of a simple metal oxide into a sulfide/sulfide heterostructure can lead to an improvement in OER performance, as was reported by Hu *et al.*[787] In their work, MnO_2 nanoparticles were *in situ* anchored onto cubic Co_4S_3 and rhombohedral Ni_3S_2 with nanosheet morphology denoted as U-CoNi-S-NSA/MnO_2. Fast electron and mass transport were achieved by the heterostructure material prepared via the *in situ* anchoring process, which led to excellent water-splitting performance. During OER testing, U-CoNi-S-NSA/MnO_2 exhibited higher activity than other prepared samples (CoNi-S-LDH-NSA and CoNi-S-NSA), requiring an overpotential of 170 mV to achieve 10 mA·cm^{-2}, which is 40 mV smaller than that of the sulfide/sulfide heterostructure, denoted as CoNi-S-NSA (210 mV). The MnO_2 *in situ* synthesis also led to improved electrochemical surface area based on the double-layer capacitance estimations, exhibiting a four times increase in the C_{dl} value with respect to the sulfide/sulfide heterostructure. Moreover, based on the XPS results, the electron transfer from CoNi-sulfide nanosheets to MnO_2 nanoparticles enhanced the acidity (Lewis acidity) of the CoNi-sulfides, meaning these nanoparticles were posed to adsorb and activate the water molecules quickly, thereby boosting the OER performance. In addition to this approach, Wang *et al.*[822] reported a strategy using the *in situ* growth of the precatalyst heterostructure for MoS_2 nanosheet arrays and transition metal disulfide nanocubes (TS_2, T = Fe, Co, and Ni) onto the surface of transition metal molybdate solid-solution (TMO_4, T = Ni/Co, Ni/Fe, Ni/Co/Fe) that strongly affected the synergy between sulfide/oxide components, with the exposed active sites and its superaerophobic features accelerating the oxygen evolution rates. The OER results evidenced that the Fe/Co/Ni-sulfide-MoS_2-Fe/Co/Ni-MoO_x heterostructure (denoted as FCNMS) exhibited an anodic current density of 10 mA·cm^{-2} at the relatively low overpotential of 300 mV in 1 M KOH due to the strong interaction between the transitions sulfides and the metal oxide confirmed by TEM and HRTEM. The molybdate interaction was beneficial for the epitaxial growth of MoS_2, having a crucial role in the catalytic reaction due to the presence of Mo^{4+} (FCNMS) and Mo^{6+} (FCNMO) species in the heterostructure.

It has been mentioned that some active oxidized species from the transition sulfides were formed during the OER tests, such as (oxy)hydroxides (see Section 5.1.2).[738,684] Zhou *et al.*[728] found that crystalline (oxy)hydroxides species [γ-Ni(Fe)OOH] were *in situ* electrochemically formed on the surface of conductive Ni-Fe disulfide nanostructures [Ni(Fe)-S_2] as core@shell precatalyst heterostructures. From SEM and HRTEM images, it was observed that the thickness of the amorphous hydroxide intermediate was determined to be around 2−10 nm after the first OER activation cycle and then converted into a crystalline (oxy)hydroxide layer after 100 cycles without an increase in the (oxy)hydroxide layer's thickness (Figures 197a and b). The γ-Ni(Fe)OOH/Ni(Fe)S_2 heterostructure exhibited high OER electrocatalytic activity with a relatively low overpotential of 230 mV to reach 10 mA·cm^{-2} compared to those of Ni-Fe hydroxides (262 mV) and RuO_2 (350 mV), as shown in Figures 197c and d. These results indicated that the heterostructure displayed faster and improved charge transfer capabilities during the OER process compared to those of Ni-Fe hydroxide. Moreover, the crystalline (oxy)hydroxide layer prevented the Ni-Fe disulfide core from undergoing oxidation. The (oxy)hydroxide layer hindered the electrolyte diffusion to the metal sulfide core due to its low porosity and long-range crystal order. The kinetic barriers involved in the OER were determined by the temperature-dependent activation energy (E_a) calculations in which the activation energies for the Ni(Fe)OOH/Ni(Fe)S_2 heterostructure and the Ni-Fe hydroxide were 17.3 and 18.1 kJ·mol^{-1}, respectively. A similar value demonstrated the similar activation energies of the heterostructure and the as-prepared Ni-Fe hydroxide, indicating that Ni(Fe)OOH was the active species in the heterostructure material. Therefore, the

https://doi.org/10.1021/acs.chemrev.3c00005
Chem. Rev. 2023, 123, 12795−13208

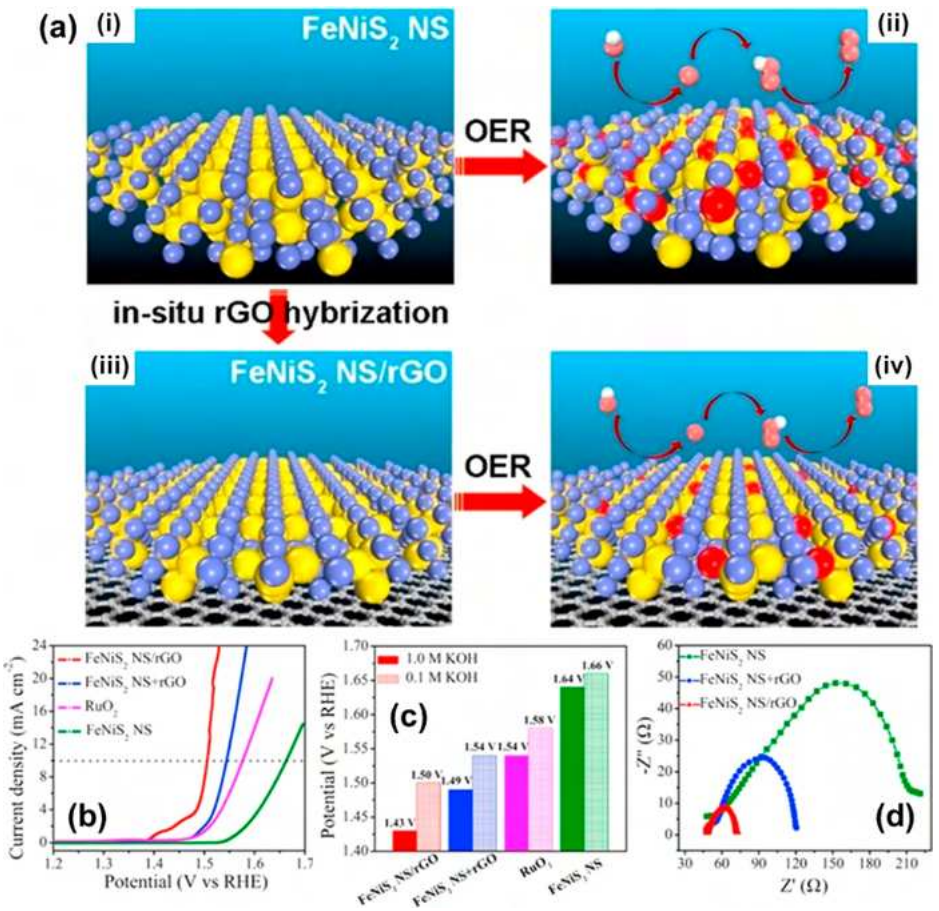


Figure 198. (a) Schematic illustration of the optimization strategy for the OER performance of $FeNiS_2$ NS by *in situ* rGO hybridization. (b) LSV curves of $FeNiS_2$ NS/rGO, $FeNiS_2$ NS + rGO, RuO_2, and $FeNiS_2$ NS in 0.1 M KOH. (c) Required overpotentials to achieve a current density of 10 $mA{\cdot}cm^{-2}$ for $FeNiS_2$ NS/rGO, $FeNiS_2$ NS + rGO, RuO_2, and $FeNiS_2$ NS in 0.1 and 1.0 M KOH. (d) Nyquist plots of $FeNiS_2$ NS/rGO, $FeNiS_2$ NS + rGO, and $FeNiS_2$ NS at a potential of 0.6 $V_{Ag/AgCl}$ in 0.1 M KOH. Reprinted with permission from ref 693. Copyright 2018 Elsevier.

combination of metal sulfide/(oxy)hydroxides can be an alternative approach for the development of highly efficient and stable OER electrocatalysts.

Significant efforts have been made to combine highly conductive supporting materials, such as carbon (C-based) materials and their derivatives, especially heteroatom doped-carbon materials such as S-doped carbon,[704] N-doped carbon (refs 851, 859, 719, 705, 715, 893, and 675), N,S-codoped carbon (refs 638, 836, 857, 846, 858, 800, 821, 803, 811, 273, and 768), and B,S-codoped carbon.[791] C-based support materials provide high surface area, electronic conductivity, and mechanical and chemical stability to improve the metal sulfide's electrocatalytic activity through heterostructure formation. Many C-based compounds, such as reduced graphene oxide (rGO),[802,693,546] carbon nanotubes (CNT's),[691] graphene,[805,678] graphite,[674] activated carbon,[676] and others,[682] have been explored as supporting materials for metal sulfide OER electrocatalysts. For instance, Jiang *et al.* reported the $FeNiS_2$ nanosheet *in situ* hybridization with reduced graphene oxide (denoted as $FeNiS_2$ NS/rGO) via a one-pot colloidal method to produce a precatalyst for the OER.[693] This procedure enabled uniform homogeneous dispersion and strong coupling of $FeNiS_2$ NS onto the rGO (Figure 198a). For comparison, a physical mixture of $FeNiS_2$ NS with rGO was also prepared (denoted as $FeNiS_2$ + rGO). The electrocatalytic OER activity of the prepared $FeNiS_2$ NS/rGO electrocatalysts was evaluated in different alkaline electrolytes, as shown in Figures 198b and c. As can be seen, the rGO-containing $FeNiS_2$ NS precatalysts either *in situ* hybridized or physically mixed possessed onset overpotentials that were much lower than that of the pure $FeNiS_2$ NS (1.55 V_{RHE}) and were even lower than that of commercial RuO_2 (1.50 V_{RHE}). Especially, the onset potential comparison between $FeNiS_2$ NS/rGO and $FeNiS_2$ NS + rGO exhibited a substantial difference, as evidenced by 1.40 vs 1.48 V_{RHE}, respectively. These results indicated that the *in situ* $FeNiS_2$ NS/rGO hybridization resulted in a material with higher electrocatalytic activity for the OER than the physical mixture of the $FeNiS_2$ NS and rGO components. For a comprehensive comparison of their OER performance, the overpotentials of the precatalysts were compared at a 10 $mA{\cdot}cm^{-2}$ current density (Figure 198c). The $FeNiS_2$ NS/rGO exhibited the lowest overpotential in both 0.1 and 1 M KOH electrolytes. Additionally, the Nyquist plots (Figure 198d) revealed a remarkable decrease in the charge transfer resistance (R_{ct}) of the $FeNiS_2$ NS/rGO, which was attributed to the enhancement of the interdomain conductivity by the hybridization with rGO, indicating the best electron transport in the composite due to the rGO connected 3D structure. Therefore, the $FeNiS_2$ NS/rGO precatalysts possessed both high overall conductivity and rich active sites (confirmed by the C_{dl} results), resulting in superior OER performance. The use of rGO as the supporting

https://doi.org/10.1021/acs.chemrev.3c00005
Chem. Rev. 2023, 123, 12795−13208

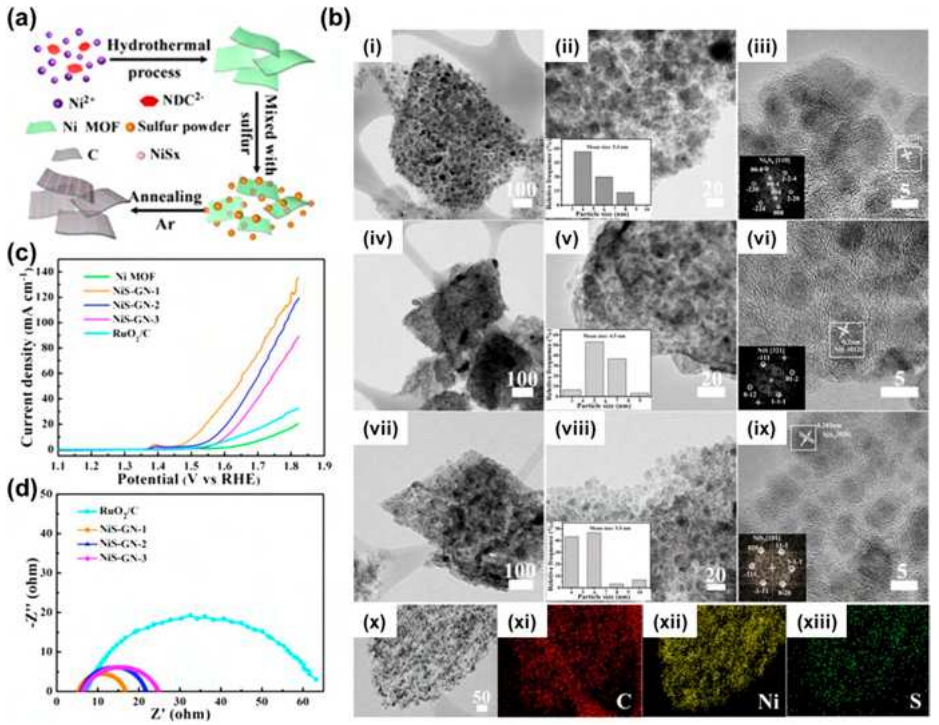


Figure 199. (a) Schematic illustration for the synthetic process of NiS_x. (b) TEM images of (i–iii) NiS-GN-1, (iv–vi) NiS-GN-2, and NiS-GN-3 (vii–ix). (b, x–xiii) EDX element mapping images of NiS-GN-1 (the unit of the scale bar is nm). The insets in ii, v, and viii show the corresponding particle size distribution histograms. The insets in iii, vi, and ix show the corresponding FFT patterns of the squares. (c) LSV curves of Ni-MOF, NiS-GN-1, NiS-GN-2, NiS-GN-3, and RuO_2/C. (d) Nyquist plots of NiS-GN-1, NiS-GN-2, NiS-GN-3, and RuO_2/C from 10^6 to 0.1 Hz. Reprinted with permission from ref 674. Copyright 2019 Elsevier.

material boosted the electrocatalytic activity of the $FeNiS_2$ NS when the components were physically mixed and *in situ* hybridized. A similar electrocatalytic effect has also been observed by other research groups using carbon nanotubes (CNT's)[691] or graphene aerogels[805] as supporting materials.

An additional example is that reported by Ma *et al.*,[674] in which different 2D nanocomposites of NiS_x were uniformly embedded in layered graphite (denoted as NiS_x@graphite precatalyst) through the sulfurization of nickel naphthalene dicarboxylic acid framework MOF nanosheets (Figure 199a). The NiS-GN-1, NiS-GN-2, and NiS-GN-3 samples were prepared using Ni-MOF and sulfur powder mass ratios of 1:0.5, 1:1, and 1:2, respectively. According to the XRD results, different phases were identified in the samples; tetragonal Ni_9S_8 for the NiS-GN-1, hexagonal NiS in the NiS-GN-2, and cubic NiS_2 in the NiS-GN-3 sample. In all cases, the formed NiS_x was observed as nanoparticles orderly embedded in the graphite nanosheets with a 5 nm size, which was favorable in enhancing the electrocatalyst's stability (Figure 199b). The electrocatalytic OER performance was evaluated in a 1 M KOH electrolyte, where RuO_2/C was used for comparison. As can be seen in Figure 199c, the NiS-GN-1 exhibited the best OER activity among the samples, with an overpotential of 278 mV at 10 mA·cm^{-2}, smaller than those of NiS-GN-2 (339 mV), NiS-GN-3 (374 mV), and even RuO_2/C (408 mV). The turnover frequency (TOF) per active site was determined to estimate the intrinsic performance of each sample for oxygen production. These results showed that the TOF per site of O_2 production for the NiS-GN-1 was the largest compared to those of NiS-GN-2 and NiS-GN-3, indicating that the Ni_9S_8 phase possessed the highest intrinsic activity for the OER among the Ni_9S_8, NiS, and NiS_2 phases found in the aforementioned samples. Electrochemical impedance spectroscopy (EIS) was used to further confirm this finding, as the NiS-GN-1 material showed the smallest charge transfer resistance (R_{ct}) and contact resistance (R_s) of the studied samples, as presented in Figure 199d. Thus, the carbon nanosheets with crooked structure as supporting material allowed the enhancement of the electron/charge transfer at the interface between the electrolyte and the electrode and of the electrochemical reaction kinetics.

Using some heteroatom doped-carbon materials as a support is another heterostructure strategy commonly employed. In this context, Chen *et al.*[719] designed nanocomposites consisting of Co_9S_8 nanoparticles embedded within N-doped porous carbon (denoted as Co_9S_8@NC), with tunable electronic coupling through a simultaneous sulfurization and carbonization process of a cobalt-based Prussian blue analogue (Co-PBA) at controlled temperatures. By increasing the thermal treatment temperature from 500 to 800 °C, the N-doped porous carbon evolved from N-doped amorphous carbon (N-AC) and N-doped graphitic carbon (N-GC) to N-doped carbon nanotubes (N-CNTs), generating a varied interaction strength with the Co_9S_8 nanoparticles in the composites. As a result, the total relative amount of the graphitic N and pyrrolic N gradually increased from the Co_9S_8@NC-500 to Co_9S_8@NC-800 samples, whereas that of the pyridinic N decreased. Thus, the work function of the N-doped carbon decreased, leading to an increased ability to donate electrons to Co_9S_8. Concisely, the N dopant provides an *n*-doping effect inducing spin redistribution near the Fermi level, decreasing the energy barrier for the *OOH species formation. This effect can be observed in the OER performance tests presented in Figure 200a. The Co_9S_8@NC-800

https://doi.org/10.1021/acs.chemrev.3c00005
Chem. Rev. 2023, 123, 12795–13208

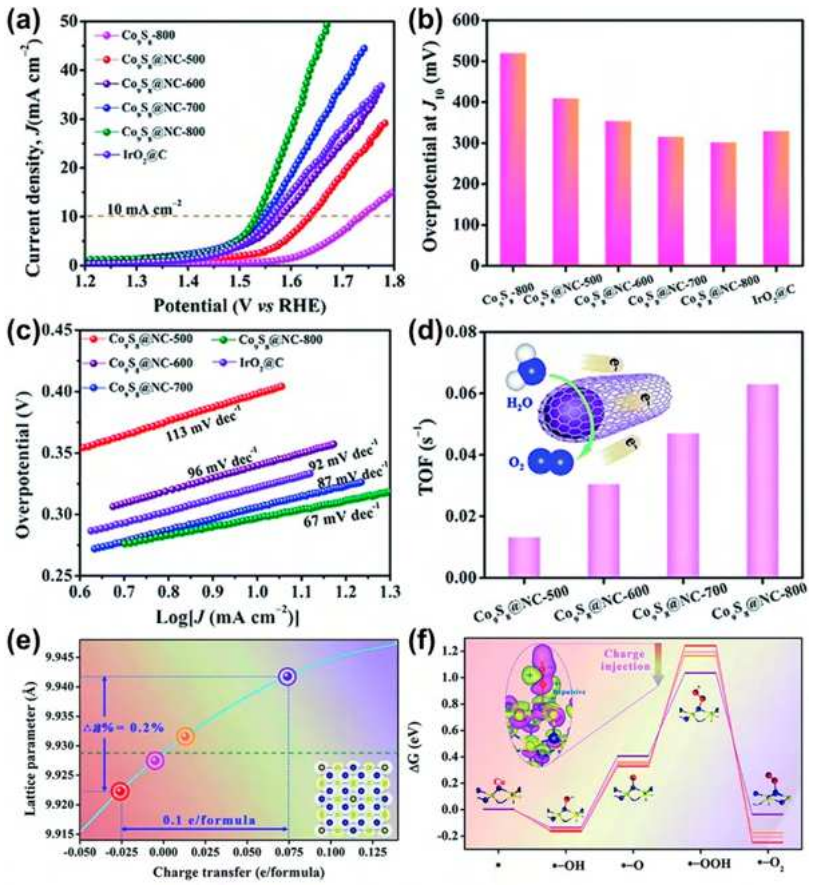


Figure 200. Electrochemical performance of Co_9S_8-800, Co_9S_8@NC-500, Co_9S_8@NC-600, Co_9S_8@NC-700, and Co_9S_8@NC-800: (a) LSV curves; (b) overpotentials required at a current density of 10 mA·cm^{-2}; (c) Tafel slopes; and (d) TOF values. (e) DFT analysis of the dependence of the lattice parameter of Co_9S_8 on the variation of injected charge transfer. (f) DFT calculated free energy landscape for the OER at 1.23 V_{RHE} on the Co_9S_8 (100) surface at different charging states. Inset of (e) indicates structural model of the Co_9S_8 crystal. Inset of (f) shows the absorption structure and charge density redistribution at different charging states (atoms with blue, yellow, red, and white colors represent Co, S, O, and H atoms, respectively). Reprinted with permission from ref 719. Copyright 2018 Royal Society of Chemistry.

delivered a much smaller overpotential (302 mV) at a current density of 10 mA·cm^{-2} compared to the Co_9S_8-800 sample without the N-doped carbon, indicating that the coupling between the sulfide and N-doped carbon support can effectively enhance the electrocatalytic activity toward the OER (Figure 200b). In Figures 200c and d, the lower Tafel slope of the Co_9S_8@NC-800 (67 mV·dec^{-1}) revealed favorable kinetics for the OER as well as higher intrinsic OER activity (0.063 s^{-1}) from turnover frequency (TOF) analysis. Additionally, the charge doping state of the Co_9S_8 and N-doped carbon system was evaluated by the lattice parameter variation based on DFT calculations. With the doping level of the relative contents of graphitic N and pyrrolic N in carbon increasing from 500 to 800 °C, the tendency of electron transfer from N-doped carbon to Co_9S_8 nanoparticles became stronger (Figure 200e). According to these results, in the calculated OER free energy pathways on the Co_9S_8 (100) surface (Figure 200f), the charge injection decreased the reaction energy for the *OOH formation, facilitating O_2 formation. Therefore, the OER barrier decreased from Co_9S_8@NC-500 to Co_9S_8@NC-800, which confirms the enhanced electrocatalytic performance from the interaction between the N-doped carbon support and cobalt sulfide nanoparticles.

Another remarkable paper reported by Han *et al.*[715] provides a comprehensive study of the origin of the high electrocatalytic activity and charge transfer mechanisms of the junction between Ni-doped CoS_2 and 3D porous N-doped reduced graphene oxide aerogel (denoted as CNS-NGA precatalyst). The CNS-NGA material was synthesized by a facile one-step hydrothermal process. The structural characterization by SEM and TEM showed diamond-like CNS nanoparticles that grew within the interconnected 3D porous NGA network. Without NGA as a supporting material, the CoS_2 nanoparticles underwent severe agglomeration, demonstrating the critical role of the N-doped graphene for obtaining homogeneously dispersed CNS clusters. This CNS-NGA porous structure facilitated the mass transfer of the electrolyte and the oxygen degassing process at the anode. On the other hand, the Ni incorporation into CoS_2 was also confirmed by the XRD analysis and the incorporation of Co or Ni atoms into defective sites in the N-doped graphene layer by Raman spectroscopy. The electrocatalytic performance of CNS-NGA for the OER is illustrated in Figure 201a. The material only required an overpotential of 330 mV to achieve a current density of 10 mA·cm^{-2}, which is lower than the overpotential for commercial RuO_2 (350 mV). Additionally, the NGA support showed a negligible OER activity, which corroborated the significant OER activity enhancement that occurred with the incorpo-

https://doi.org/10.1021/acs.chemrev.3c00005
Chem. Rev. 2023, 123, 12795−13208

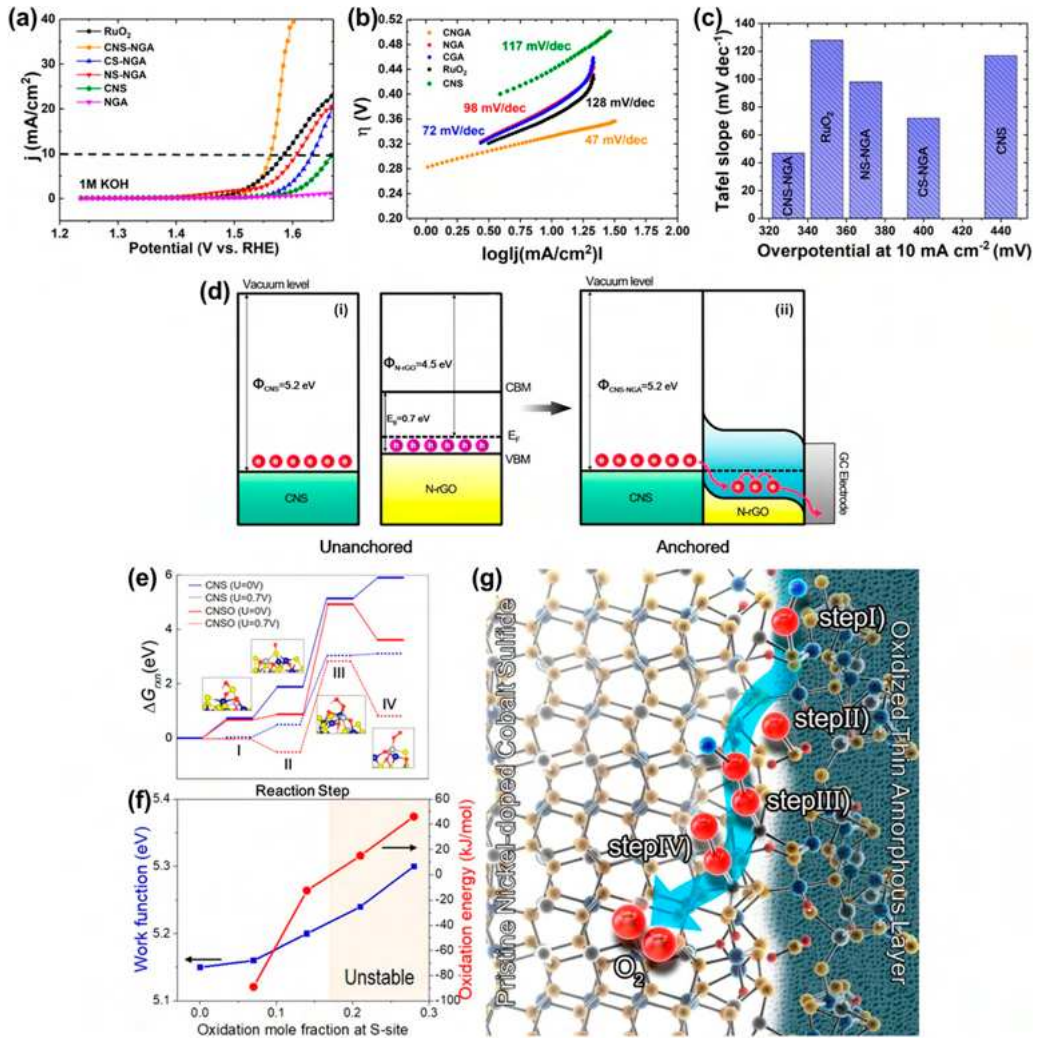


Figure 201. (a) OER polarization curves (scan rate: 0.5 mV·s^{-1}) and (b) corresponding Tafel plots of the NGA, CNS, NS-NGA, CS-NGA, CNS-NGA, and commercial RuO_2 electrocatalysts loaded on the rotating disk electrode (2000 rpm) in an O_2-saturated 1.0 M KOH solution. (c) Comparisons of the η^{10} values and Tafel slopes of the tested samples. (d) Band diagram for the CNS-NGA composite (i) before and (ii) after the junction formation. (e) Calculated energy landscapes for the NGA, CNS, and CNS-NGA systems with U = 0 and 0.7 V. (f) Work function and oxidation energy of CNS as a function of oxidation mole fraction at S sites. (g) Schematic illustration of OER pathways at CNS and CNSO boundaries. Reprinted with permission from ref 715. Copyright 2018 American Chemical Society.

ration of the CNS clusters. Moreover, the estimated Tafel slope for the CNS-NGA (47 mV·dec^{-1}) was smaller than that for the other tested materials, implying faster reaction kinetics for the oxygen evolution reaction with this CNS-NGA precatalyst (Figure 201b). The Tafel slope as a function of the overpotential for the materials is presented in Figure 201c, and this analysis indicates a synergistic effect between the CNS clusters and the conductive NGA supporting material, which led to the enhanced OER activity. The formation of covalent bonds between anchored Co and pyridinic N atoms significantly facilitated charge transport in the CNS-NGA via the reduction of the contact resistance. From DFT calculations, a proposed band diagram as shown in Figure 201d was presented to corroborate this effect. When Co atoms were anchored on the N-doped reduced graphene oxide layer, covalent bonds were formed between the Co atoms and the pyridinic N atoms, and band bending occurred at the conduction band maximum (CBM) and valence band maximum (VBM) of NGA. In this band structure, free electrons in CNS are transferred to the VBM of NGA, which has a high concentration of holes. The transferred electrons hop with holes in the VBM of NGA and further conduct through the GC electrode. Therefore, bonding between Co atoms and the pyridinic N sites in the CNS-NGA system acts as an electron sink for OH^- ions during the OER process; the OH^- electrons, adsorbed onto the surface of CNS clusters, effectively spread over the conductive NGA support and sink toward the GC electrode. To further elucidate the adsorption energies of OH, O, OOH, and O_2 in the CNS-NGA and its degree of oxidation (CNSO stands for partially oxidized CNS after long-term OER), DFT calculations were performed as illustrated in Figure 201e. The adsorption energies of all intermediates were stronger on CNSO compared with CNS, especially in step I and step II of the OER process (corresponding to OH and O adsorption, respectively). Additionally, the work function calculations of CNS were used to determine the electrocatalytic activity of the material. It was found that this value gradually increased with the oxidation mole fraction. The increased work function in CNS after oxidation might facilitate the electron transfer from CNS to

https://doi.org/10.1021/acs.chemrev.3c00005
Chem. Rev. 2023, 123, 12795−13208

NGA, allowing the bending at the interface between CNS and NGA to be more significant (Figure 201f). After all these results, the OER performance of the CNS-NGA can be interpreted as a parallelized reaction pathway: reaction steps I and II dominantly take place at the top layer oxidized region, which may facilitate the adsorption and desorption of OH and H atoms due to the amorphized structure of thin oxide layers. In contrast, reaction steps III and IV occur at CNS, exhibiting high conductivity (Figure 201g) due to Co while the Ni atoms are the electrocatalytic sites for the OER. These results showed the important role at the interface between the metal sulfides and the carbon supports, that facilitates the OER performance.

The above-discussed reports emphasize the potential of constructing heterostructures as an efficient strategy to increase the OER activity of metal sulfides. These metal sulfide-based heterostructures, however, still require further investigation to elucidate mechanism information related to the transition metal sulfides at the generated interface of different heterostructures, such as metal bonding, the adsorption−desorption of the intermediates (including the unavoidable oxidized species formed in alkaline solutions), and the formation of the active sites that allows a boosted OER activity. For all heterostructures, much in-depth study is imperative, as the material increases in complexity with the addition of interfaces between two or more different material components.

5.1.3.7.2. Co-catalysts. The loading of additional material in small and controlled amounts onto an electrocatalyst to improve its OER activity and reaction rates can be referred to as a co-catalyst.[905] It is worth mentioning that co-catalyst loading is carried out without introducing it into the crystalline structure. Additionally, the co-catalyst material is not acting like the electroactive active site during the OER reaction by itself, as it has been reported by Gao *et al.*[905] Their main functions are the creation of reaction sites, minimizing the necessary overpotential to drive the OER, and decreasing the activation energy for oxygen evolution facilitating water adsorption and conversion of intermediates.[906] For instance, metal nanoparticles were loaded into some transition metal sulfides to improve the electrocatalytic performance toward the OER. Li *et al.*[777] demonstrate that metallic Ag improved the electrocatalytic performance of cobalt iron sulfides embedded in nitrogen-doped carbon (Fe-Co-S/N-doped carbon precatalyst composites). Metallic silver was loaded on the composite by a simple dipping method using $AgNO_3$ solution in different ratios 0.02, 0.1, 3, and 5%. From the XRD characterization, a mixture of three sulfides related to Co_9S_8, FeS, and CoS phases was detected. ICP-OES was used to confirm the presence and the molar ratios of metallic Ag. From the XPS characterization, it was suggested that the Ag species loading was on the Co species and the pyridinic N sites of the composite. Regarding this last loading site, pyridinic N species may serve as a reducing agent for the conversion of Ag^+ to Ag^0 during the synthesis process. Additionally, due to the strong oxidation ability of Ag ions, it was also found that the Ag loading onto Fe-Co-S/N-doped carbon composites promoted the sulfur specie's oxidation. The OER activities of the as-prepared electrocatalysts were evaluated in 1 M KOH solution, as shown in Figure 202a. With the increase of Ag loading from 0.02 to 3%, the overpotentials at a current density of 10 mA·cm^{-2} for all the samples gradually decreased, indicating improved OER activity. The lowest overpotential was exhibited for the 3% Ag loading sample with 329 mV. However, a further increment in

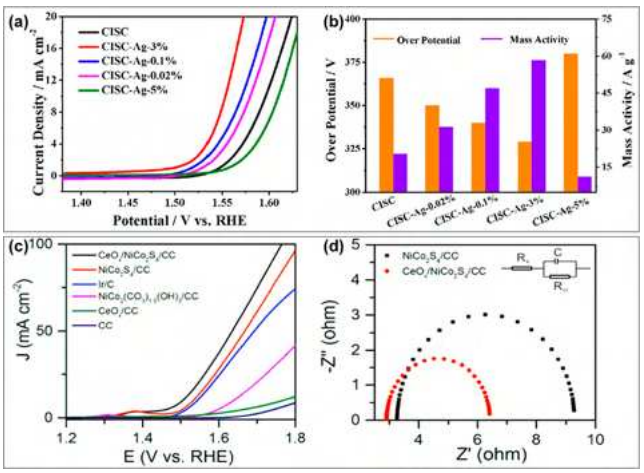


Figure 202. (a) OER LSV polarization curves and (b) comparison of overpotentials (at 10 mA·cm^{-2}) and mass activity (at the overpotential of 350 mV) of Fe-Co-S/N-doped carbon composite (CISC) and CISC-Ag samples. Reprinted with permission from ref 777. Copyright 2019 Elsevier. (c) OER LSV polarization curves of CeO$_x$/NiCo$_2$S$_4$/CC, NiCo$_2$S$_4$/CC, NiCo$_2$(CO$_3$)$_{1.5}$(OH)$_3$/CC, Ir/C, and bare carbon cloth. (d) Nyquist plots of CeO$_x$/NiCo$_2$S$_4$/CC and NiCo$_2$S$_4$/CC. Reprinted with permission from ref 671. Copyright 2019 American Chemical Society.

the silver loading content from 3 to 5% displayed decreased OER performance. The mass activity of the electrocatalysts at an overpotential of 350 mV was also compared (Figure 202b). The optimized 3% Ag-loaded electrocatalyst showed a mass activity of 58.4 A·g^{-1}, higher than those of the Fe-Co-S/N-doped carbon composites and the other materials prepared with different Ag loading ratios. Thus, the improved OER activity after the optimal 3% Ag loading as co-catalyst was attributed to the creation of more active sites, as further confirmed by the highest C_{dl} value (5.16 mF·cm^{-2}).

Alternatively, not only metal nanoparticles have been utilized as co-catalysts in the electrocatalytic OER of metal sulfides. The use of metal oxides has also been reported. Wu *et al.*[671] presented the synthesis of $NiCo_2S_4$ hollow nanotubes decorated with CeO_x nanoparticles grown onto carbon cloth ($CeO_x/NiCo_2S_4/CC$ precatalyst), through a facile sulfurization and CeO_x nanoparticle *in situ* generation process using a hydrothermal treatment at 180 °C for 6 h and $Ce(NO_3)_3 \cdot 6H_2O$ salt as Ce source. ICP-OES analysis determined that the Ce content was 6.19% in the $CeO_x/NiCo_2S_4/CC$ electrocatalyst. The crystal structure of CeO_x nanoparticles was confirmed by XRD. These CeO_x nanoparticles were uniformly deposited on the surface of $NiCo_2S_4$ under thermal reduction owing to the abundance of amino groups during the synthesis, which acted as nucleation sites and dispersing agents. The electrochemical OER testing results are presented in Figure 202c. The $CeO_x/NiCo_2S_4/CC$ electrocatalyst had the lowest overpotential of 270 mV to achieve a 10 mA·cm^{-2} current density, of all the tested samples. It also exhibited excellent kinetics for the OER with a smaller Tafel slope of 126 mV·dec^{-1} compared to that of $NiCo_2S_4/CC$ (133 mV·dec^{-1}), as corroborated by the smaller value of the charge transfer resistance (R_{ct}) illustrated in Figure 202d. These results suggested that the CeO_x nanoparticle loading improved the electrocatalytic activity of the $NiCo_2S_4$ material, leading to faster electron transfer via the turning of the surface states to generate more active sites.

https://doi.org/10.1021/acs.chemrev.3c00005
Chem. Rev. 2023, 123, 12795−13208

5.1.3.8. pH Effects. The OER is mainly considered the bottleneck for overall water splitting due to its slow kinetics. It is widely accepted that the OER mechanism is a pH-sensitive process consisting of a four-electron/proton complex multistep reaction. In acidic conditions, the water molecules are oxidized, and O_2 molecules and $H^+ + e^-$ pairs are released. In contrast, in alkaline conditions, the hydroxyl groups (OH^-) are oxidized to O_2 and water with e^- releasing.[907] Although most of the experimental OER studies have been performed in alkaline media, some other studies have also been carried out in acidic and neutral media to get a better understanding of the OER activity for metal sulfides over a wide pH range. For example, Ray *et al.*[825] compared the OER performance of the phosphorus-incorporated and unincorporated cobalt molybdenum sulfide precatalysts grown on carbon cloth substrates (denoted as P-CoMoS/CC and CoMoS/CC, respectively) in acidic (0.5 M H_2SO_4, pH = 1.0) and neutral media [1.0 M phosphate-buffered saline (PBS), pH = 6.8], as shown in Figure 203a. The required overpotential for the P-CoMoS

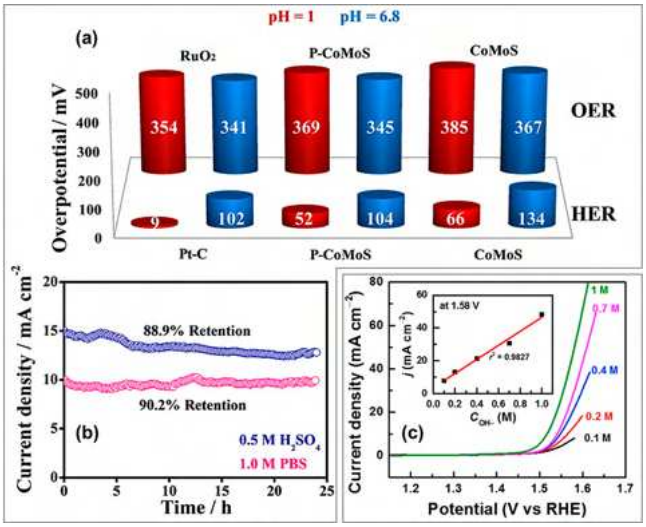


Figure 203. (a) Comparative accounts of the overpotentials of RuO_2, P-CoMoS, and CoMoS for the HER and OER in 0.5 M H_2SO_4 and 1.0 M PBS; (b) OER stability testing results of P-CoMoS in 0.5 M H_2SO_4 and 1.0 M PBS. Reprinted with permission from ref 825. Copyright 2017 American Chemical Society. (c) Polarization curves of HPMS Co_3S_4/CoS_2 at 2 mV·s^{-1} in different concentrations of KOH solution. Reprinted with permission from ref 720. Copyright 2018 Elsevier.

electrocatalyst to achieve a current density of 10 mA·cm^{-2} was slightly lower in neutral media (345 mV) compared to acidic media (369 mV). Here, the CoMoS electrocatalyst also showed a similar trend in the OER activity. It can be inferred that the OER mechanism could be intrinsically more difficult in the acidic media than in neutral media. By lowering the pH, protons are generated at the surface, depolarizing the OER and also affecting the sample stability and performance in acidic media.[908] Additionally, the P-CoMoS showed a relatively good OER stability under both conditions after 24 h of electrolysis, with around 90% retention of the initial current density (Figure 203b). A similar comparative analysis was provided by Liu *et al.*[721] in which the OER performance of the 1T-$Co_{1-x}S$ precatalyst microplates was evaluated in neutral (1 M PBS) and alkaline media (1 M KOH). As expected, the OER performance of 1T-$Co_{1-x}S$ in neutral solution was inferior to the performance (overpotential: 311 mV at 10 mA·cm^{-2}) in 1 M KOH solution. However, more research on the electrocatalytic activity difference using both environments needs to be discussed in detail to further gain an OER mechanism understanding. On the other hand, the OER activity of the sulfide-based electrocatalyst has also been examined in the KOH electrolytes at different concentrations. Guo *et al.*[720] reported on the OER polarization curves of the hierarchical porous nanosheet-assembled microsphere sulfide (HPMS Co_3S_4/CoS_2) precatalyst. The OER activity of the HPMS Co_3S_4/CoS_2 increased significantly with increasing the KOH concentration, as illustrated in Figure 203c. Here, the higher KOH concentration provided a greater electrolyte conductivity due to more reactants such as OH^-, benefiting the OER activity.[693,676,640]

Additionally, some reports have investigated the OER activity over a wide pH range, as reported by Yang *et al.*[688] They evaluated the electrocatalytic activity of the Ni_3S_2/NF precatalyst under alkaline, neutral, and acidic conditions, as presented in Figure 204. The as-obtained electrochemical test

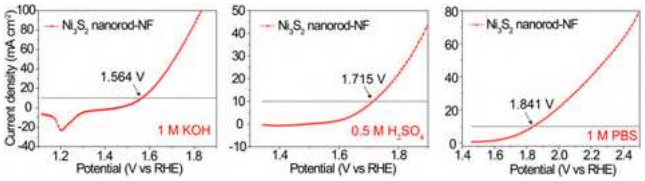


Figure 204. OER polarization curves of Ni_3S_2 nanorod-NF in different electrolytes. Reprinted with permission from ref 688. Copyright 2019 American Chemical Society.

result exhibited different overpotentials of Ni_3S_2/NF at 10 mA·cm^{-2} in alkaline (242 mV), acid (291 mV), and neutral (395 mV) electrolytes, in which the highest performance was obtained in alkaline media. To understand this behavior, the activity and stability factor (denoted ASF) using the ratio of hydrogen/oxygen production rate (current density, J) and metal dissolution rate during the HER/OER (equivalent dissolution current density, S) was used to compare the performance of the material in three different pH environments. The larger ASF value in the alkaline media (1.741×10^3) suggested the best balance between HER/OER activity and stability compared with the neutral (0.055×10^3) and acidic (0.014×10^3) environments. The lowest ASF value under acidic conditions may be due to the poor stability of the material under oxidizing potentials during the OER. On the other hand, the alkaline environment allowed the *in situ* formation of the oxide/hydroxide, highly active intermediates facilitating the OER activity as well. Therefore, the overall performance mechanism under a wide range of environments, especially alkaline, needs to consider the metal−OH bond interactions and the active species formed due to the oxidizing conditions along with the OH^- species for obtaining a complete perspective of the pH effects.

5.1.3.9. Surface Treatment Effects. The exposure of metal sulfide crystal phases active for the OER can be achieved by performing surface treatments, making this strategy preferential in attaining materials with enhanced OER performance, as reported by Shang *et al.*[750] In their work, the *in situ* growth of a Ni_xS_y precatalyst with different crystal phases was executed by performing surface pretreatment (acidification or oxidation) of nickel foam (NF) and a subsequent facile solvothermal

https://doi.org/10.1021/acs.chemrev.3c00005
Chem. Rev. 2023, 123, 12795−13208

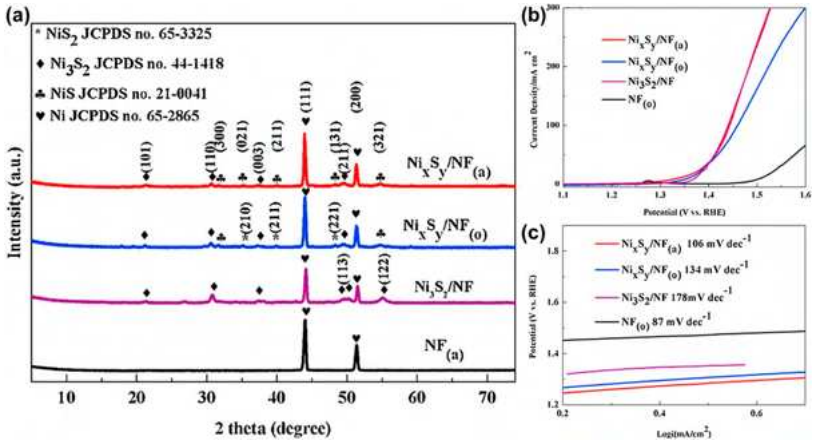


Figure 205. (a) XRD patterns, (b) linear sweep voltammograms, and (c) Tafel plots of $Ni_xS_y/NF_{(a)}$, $Ni_xS_y/NF_{(o)}$, Ni_3S_2/NF, and $NF_{(a)}$. Reprinted with permission from ref 750. Copyright 2016 Elsevier.

process. The NF was treated in acid, acetone, and ethanol under sonication, resulting in acidified NF, denoted as $NF_{(a)}$. The oxidized NF was prepared by immersion in a mixture of $(NH_4)_2S_2O_8$ and NaOH for 6 h, denoted as $NF_{(o)}$. According to the XRD results, different crystal phases of Ni_xS_y were obtained for the acidified and oxidized nickel foams. The acid-treated nickel foam [$Ni_xS_y/NF_{(a)}$] showed Ni_3S_2 and NiS phases, whereas the oxidized nickel foam [$Ni_xS_y/NF_{(o)}$] exhibited Ni_3S_2 and NiS_2 phases (Figure 205a). The electrochemical measurements for the OER showed an enhanced performance of $Ni_xS_y/NF_{(a)}$ compared to $Ni_xS_y/NF_{(o)}$ and pure Ni_3S_2/NF, indicating that NiS in the Ni_xS_y mixture contributed to its enhanced electrocatalytic activity (Figure 205b). In agreement with LSV results, the Tafel slope of $Ni_xS_y/NF_{(a)}$ (106 mV·dec^{-1}) is much smaller than those of $Ni_xS_y/NF_{(o)}$ (134 mV·dec^{-1}) and Ni_3S_2/NF (178 mV·dec^{-1}), illustrating its faster OER kinetics (Figure 205c). Therefore, it can be seen that control of crystal phases by a surface treatment during the synthesis of metal sulfides can provide an easy route to obtain improved OER properties and to probe the more active phases of Ni sulfide for the OER.

5.1.4. Challenges. From the literature discussed above, it is evident that most of the as-prepared transition metal sulfides act as precatalysts. These OER electrocatalysts undergo oxidation, resulting in the corresponding transition metal oxides/(oxy)hydroxides. This transformation often occurs on the surface; however, some studies confirm the complete oxidation of the metal sulfide electrocatalyst.[672,691,718,721,724,728,734] Still, the evidence suggests that the material will only be oxidized to a certain extent before the transformation stops.[718] Therefore, the resulting transition metal oxides/(oxy)hydroxides could be regarded as the actual electrocatalytically active sites for the OER, rather than the initial metal sulfide.[691,718,721,724,734] Nevertheless, it is still unclear how the reconstruction process occurs and how certain variables define the oxidation extent. Furthermore, the fate of sulfur species remains ambiguous, and it is uncertain if these species play a crucial role in the OER or not. Here, we review different studies examining the reconstruction process and the role of particular species during the oxidation of transition metal sulfide electrocatalysts. These examples represent significant questions that need to be answered to fully unveil the role of the *in situ* transformation of metal sulfides in improving the OER performance.

Among different species that have been detected after the reconstruction process, the sulfate (SO_4^{2-}) anion has been regarded as the main oxidized sulfur compound. Interestingly, while some studies have detected sulfate anions on the electrocatalyst's surface after the OER,[688,714,721] other reports, however, have only detected sulfate dissolved in the electrolyte.[87,673,686,705,730,734,739] According to the Pourbaix diagram of sulfur (Figure 206), the SO_4^{2-} ion is expected to exist in the

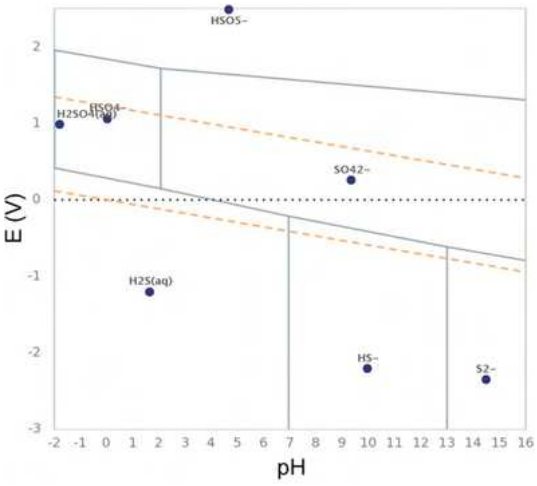


Figure 206. Pourbaix diagram for sulfur. Orange broken lines represent the thermodynamic potentials for the HER and OER at different pH values. The diagram is representative of an S ion concentration of 10^{-8} M (default) by using the Materials Project.[87−89]

liquid phase at the oxidizing potentials necessary for the OER under neutral and alkaline conditions. In contrast, bisulfite ions (HSO_4^-) are expected at acidic conditions due to sulfur speciation depending on the pH.[909,910] Moreover, the peroxymonosulfate ion (HSO_5^-) can be seen at more oxidative potentials in Figure 206. Given that most transition metal sulfides are studied in alkaline electrolytes and that potentials often lie close to the thermodynamic OER potential, it is expected that sulfate ions will be produced if metal sulfides are oxidized. Then, these ions can leach out from the material, explaining why sulfate ions have been detected in the electrolyte. However, it is still unclear why sulfate ions have been detected on the material's surface, as confirmed via post-

https://doi.org/10.1021/acs.chemrev.3c00005
Chem. Rev. 2023, 123, 12795−13208

OER XPS characterizations.[49,705,718,730] Thus, why do oxidized sulfur species remain on the surface? And intriguingly, does sulfate play a role during the OER?

Several studies have tried to answer these questions by examining the sulfate ion's effects on the OER activity. Shi *et al.* performed *in situ* Raman spectroscopy measurements to probe sulfate ions generated from as-prepared NiS_2 precatalysts.[613] Initially, sulfite (SO_3^{2-}) ions were formed after sweeping the potential from 0.93 to 1.43 V_{RHE}. Then, sulfite ions were oxidized into sulfate when sweeping at higher potentials. As a result, the Ni redox peak area increased with successive LSV scans, activating the precatalyst. Furthermore, sulfate ions were spiked into the electrolyte using $Ni(OH)_2$ as an electrocatalyst. As the sulfate concentration increased, the overpotential at 50 mA·cm^{-2} decreased from ~530 to ~440 mV. The authors theorized that SO_4^{2-} ions could adsorb onto oxide layers generated during the reconstruction process, improving the OER activity, as depicted in Figure 207.

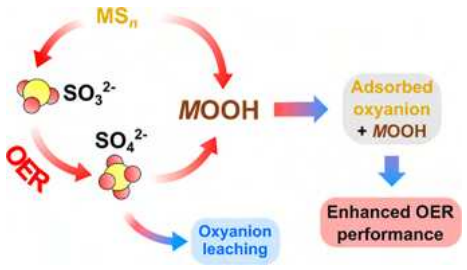


Figure 207. Formation of oxidized sulfur species ions during the OER and their contribution to OER performance. (Adapted from ref 613.).

Recently, our group also confirmed the presence of sulfate ions from Ni-S-O and Ni-S-P-O precatalysts within the nanoporous oxide/hydroxide layer formed during the OER.[273] As described previously in Section 4.2.4, we proposed a surface reconstruction model where S and P atoms within the as-prepared nickel sulfide/nickel phosphide precatalyst were oxidized during the OER, facilitating the formation of vacancies and defects, enhancing the reconstruction process as a result. Then, some *in situ* generated species (i.e., sulfates and phosphates) stayed within the porous layer, stabilizing Ni active centers and probably increasing the electrolyte conductivity. Yet, some oxidized species migrated into the bulk electrolyte, as confirmed by total-reflectance X-ray fluorescence (TXRF) elemental analysis. These two case studies suggest that oxidized sulfur species that remain on the electrocatalyst surface might play a significant role. Further studies are necessary to unveil their specific contributions to enhancing the OER performance.

Sulfate detection after OER tests is often done through XPS. However, as shown in Table 5, several studies lack proper XPS post-analysis, which might explain why sulfur oxidation is sometimes omitted in the literature. Moreover, the sulfate ion could have gone unnoticed because of the likelihood of its dissolution into the electrolyte, complicating the characterization after long-term OER tests. Another reason for the lack of consistency among different studies could be the misinterpretation of high-resolution S 2p XPS spectra taken after OER-testing.[673,707,739,741,743,850] The correct interpretation of the S 2p XPS spectra regarding the presence of sulfate ion is displayed in Figure 208. The peak at 168−170 eV can confirm the sulfate ion.[911] Therefore, care should be taken when

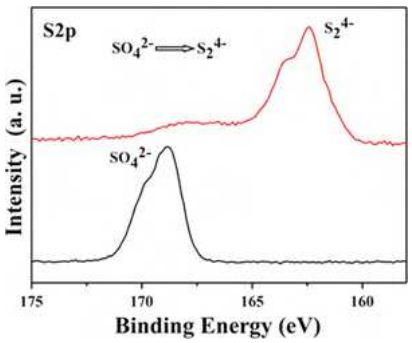


Figure 208. Correct interpretation of S 2p XPS spectra. Sulfide and sulfate species exhibit similar peaks in the 160−170 eV range. Reprinted with permission from ref 911. Copyright 2016 Royal Society of Chemistry.

analyzing XPS spectra in the S 2p region to assess sulfur oxidation from metal sulfide precatalysts properly. Finally, we encourage further studies to examine the electrolytes before and after electrochemical tests via multielemental analysis techniques as demonstrated by previous studies.[49,294] More details about these techniques are provided in Section 7.

Sulfur incorporation into the metal oxide/(oxy)hydroxide layer can also be examined by carefully monitoring the materials before and after OER tests. Ni *et al.* found that although $(NiFe)S_2$ pyrite mesocrystals were converted into metal oxyhydroxides during the OER, a relatively high amount of S remained, especially when the Fe content was high.[722] The authors attributed this change to the stabilization of sulfur by Fe dopants. They also found that spiking the electrolyte with S^{2-} (600 ppm) changed the shape of CV curves and increased the overpotential during cycling, which was attributed to the competitive oxidation of S^{2-}, decreasing the OER activity. Overall, the authors concluded that instead of S^{2-} incorporation from the electrolyte, the superior OER activity resulted from Fe and S dopants that stabilized high-valent Ni sites. These results contrast those of Shi *et al.* where SO_4^{2-} incorporation led to a net positive effect on the OER.[613] Thus, this opens a debate regarding the actual role of soluble sulfur species on the OER performance. It is worth mentioning that sulfur could also be incorporated from other sources such as Nafion, an ionomer containing sulfonic acid groups, utilized as a binder for electrocatalyst inks.[460] Furthermore, it has been shown that sulfur electrochemistry in aqueous media can be complex, as other sulfur species such as dithionate ($S_2O_6^{2-}$) could also be generated from sulfite anions.[909,910,912] Thus, the effects of sulfur species on the OER, either generated by the *in situ* reconstruction or incorporated from external sources, require further exploration. Importantly, it is necessary to unveil the incorporation mechanism, which could come from *in situ* oxidation of sulfide species, adsorption from dissolved anions in the electrolyte, or metal-mediated doping. Finally, the relevance and impact of each one of these mechanisms on the OER activity should be addressed since this could open new strategies to boost the OER activity of transition metal-based sulfide electrocatalysts.

The oxidation extent varies considerably among reported metal sulfides. Even when they consist of the same composition and are studied in the same electrolyte environments, differences have been reported. For example, two Ni sulfide materials, NiS_x and NiS/NF, have been reported to undergo surface modification during the OER; however, the

https://doi.org/10.1021/acs.chemrev.3c00005
Chem. Rev. 2023, 123, 12795−13208

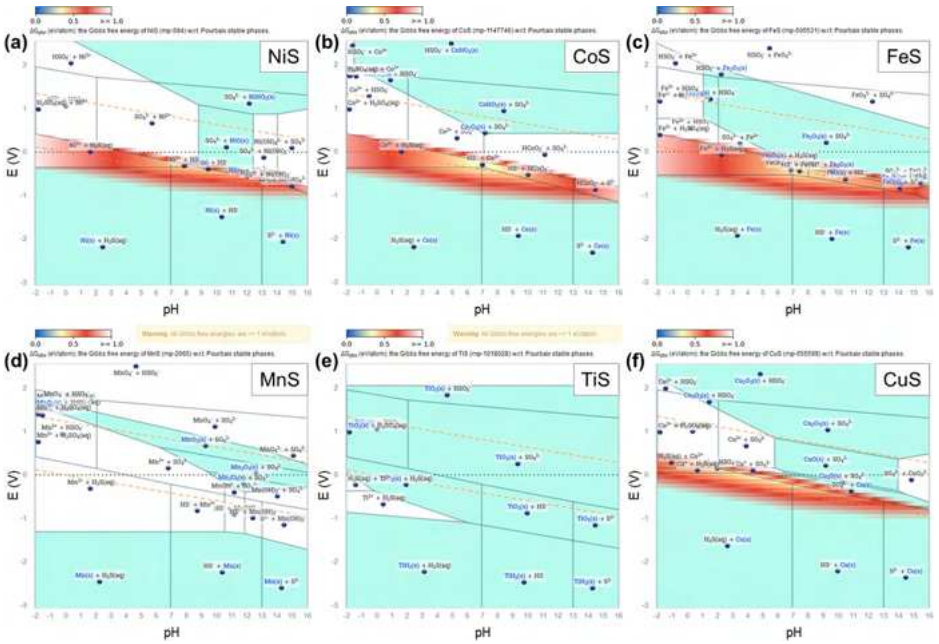


Figure 209. Electrochemical stability maps (Pourbaix diagram and Gibbs free energy overlay) for (a) NiS, (b) CoS, (c) FeS, (d) MnS, (e) TiS, and (f) CuS. The Gibbs free energy overlay indicates areas of aqueous stability for the compound, with blue regions the most stable and red/uncolored regions the least stable. Orange broken lines represent the thermodynamic potentials for the HER and OER at different pH. The diagrams were produced by using the Materials Project.[87−89]

reported materials did not transform in the same way. Instead, the as-prepared amorphous NiS_x was transformed to a crystalline oxide phase, while the surface of the as-prepared NiS/NF electrocatalyst was transformed to an amorphous oxide/hydroxide phase (see Section 5.1.2).[448,724] Thus, more fundamental studies are required to understand why either an amorphous or a crystalline oxidation layer forms on the surface of as-prepared metal sulfides. Such studies could potentially reveal the effect of the as-prepared material's crystallinity on the oxidation degree and, potentially, lead to an understanding of how to prepare less oxidation-prone transition metal sulfide electrocatalysts. Future studies could also determine if the oxidation layer changes the material's crystallinity as the OER proceeds with time. Finally, specific changes in the crystal structure could be performed to improve the stability of the material. For instance, spinel $NiCo_2S_4$ and $MnCo_2S_4$ exhibit preferential oxidation at Ni and Mn centers over Co, which oxidizes into Co hydroxide and not Co oxyhydroxide.[673,741] Thus, the spinel structure could serve as an avenue of inquiry toward developing more stable transition metal sulfide electrocatalysts, given that the metal center geometry could control the degree of oxidation. Studies on normal vs inverse spinel could also provide further insights into engineering more stable metal sulfides.

To this end, the degree of oxidation also warrants further investigation regarding the depth/thickness of the formed oxide/oxyhydroxide layer. Lee *et al.* showed that their as-prepared Ni_3S_2 was transformed to a $NiOOH/Ni_3S_2$ composite, as CV activation resulted in the surface undergoing oxidation.[718] This oxidation layer was 700 nm thick as determined by TOF-SIMS. In contrast, Zhou *et al.* electrochemically prepared a Ni-Fe disulfide@oxyhydroxide electrocatalyst containing only a Ni-Fe oxyhydroxide layer 10 nm in thickness after stability testing for 50 h.[728] These results raise questions over what affects the depth of oxidation of an as-prepared metal sulfide, such as preparation method, stability testing technique (CV vs CP), the incorporation of additional metal atoms, etc. To further understand the transition metal sulfide's oxidation extent, the electrocatalyst should be probed at several intervals during the OER using various techniques (e.g., XPS, XRD, TEM, SEM, etc.) and electrochemical tests (ECSA and TOF estimation). Samples prepared following the same method with only the addition of another metal could also shed light on the effect of metal incorporation on oxidation layer thickness. Such a study could enable more informed decisions for material preparation, such as ensuring the initial, as-prepared material is sufficiently thick such that an oxyhydroxide layer forms and a metal sulfide core is retained. More work needs to be done to unravel the underlying mechanism of oxidation and how the as-prepared material may enhance or detract from the extent of oxidation in an alkaline electrolyte/environment.

Most studies on transition metal sulfides as electrocatalysts for the OER have only been performed in alkaline electrolytes. Of the few reports of these materials in acidic and neutral media, usually only decreased overpotentials in these electrolytes vs in alkaline media have been reported (see Sections 5.1.2.2 and 5.1.3.8). Acidic and neutral media have been considerably underinvestigated, likely owing to the instability of Ni and Co sulfides, arguably the most explored metal sulfides, at oxidizing potentials in these pH ranges. From the Pourbaix diagram of Ni sulfide, for example, it can be seen that at neutral pH and oxidizing potential for the OER, Ni sulfide will detach from the electrode surface and be present as soluble Ni^{2+} and SO_4^{2-} species in the electrolyte (Figures 155b and 209a). The literature also supports the instability of these materials. For example, after long-term testing of NiS_xP_y and Ni_3S_2 in a neutral electrolyte (0.5 M $KHCO_3$), Fu *et al.* observed the formation of a green precipitate at the electrode surface.[564] They hypothesized that this green precipitant was $NiCO_3$, indicating the dissolution of Ni in neutral electrolyte had occurred as predicted by Figures 155b and 209a. Yang *et*

https://doi.org/10.1021/acs.chemrev.3c00005
Chem. Rev. 2023, 123, 12795−13208

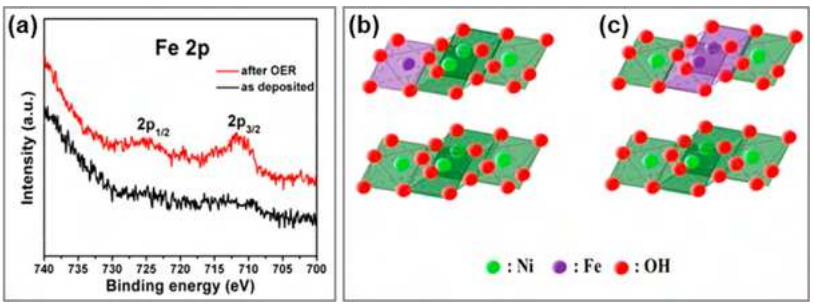


Figure 210. (a) Comparison showing the change of Fe 2p XPS peaks for the ALD NiS_x film before and after the OER. Since the Fe content was expected to be in trace amount and the main Fe peaks (i.e., Fe 2p) overlap with the Ni Auger peaks, a non-monochromated Mg Kα radiation source was used instead. Reprinted with permission from ref 734. Copyright 2016 American Chemical Society. (b, c) Schematic illustrations of Fe incorporated into γ-NiOOH: (b) Fe (edge) γ-NiOOH and (c) Fe (bridge) γ-NiOOH. Reprinted with permission from ref 718. Copyright 2018 Elsevier.

al. studied a $MoS_2/Co_9S_8/Ni_3S_2/Ni$ electrocatalyst in acidic, neutral, and alkaline electrolytes, and dissolution of the material only occurred in acidic and neutral electrolytes (0.5 M H_2SO_4 and 1 M PBS, respectively).[688] For their material, they found that at oxidizing potentials and acidic pH, the equivalent dissolution current density (S) was two orders of magnitude higher than that at alkaline pH. Additionally, the S values for the $MoS_2/Co_9S_8/Ni_3S_2/Ni$ at oxidizing potentials was one order of magnitude higher at neutral pH than at alkaline pH. The instability of this electrocatalyst comes as no surprise when consulting the Pourbaix diagrams for Ni and Co sulfide (Figures 155a and b). Thus, to develop electrocatalysts for the OER that are stable over a wide pH range, metals beyond Ni and Co should be considered, and Pourbaix diagrams must be consulted. Furthermore, more Pourbaix diagrams for common transition metal sulfides should be prepared to provide further stability information.

If we only consider developing a metal sulfide for the OER in neutral electrolytes, the Pourbaix diagrams in Figure 209 suggest that CoS, FeS, MnS, TiS, and CuS will be stable, preventing sulfide dissolution into the electrolyte. Under oxidizing OER potentials at neutral pH, CoS, FeS, MnS, TiS, and CuS can create their oxide counterparts as passivation layers on their surfaces, making the material's surface more stable in solution, preventing corrosion of the core of the prepared metal sulfide material. Furthermore, of the materials above that would be stable at neutral pH and oxidizing potentials, only one would also be stable in acidic media: TiS. At acidic pH, TiS would form TiO_2 and H_2SO_4/HSO_4^- at its surface, creating a passivation layer while impeding sulfur dissolution more than CoS, FeS, MnS, and CuS under these conditions (Figure 209). Given that titanium is less expensive than the more commonly used Ni and Co for transition metal sulfides and could also impose greater stability over a larger pH range, it stands as a more reasonable choice for developing more stable and versatile electrocatalysts for the OER. Of course, titanium comes with its own set of challenges for integration into a metal sulfide as electrocatalysts for the OER, primarily that it suffers from poor conductivity.[895] Thus, to make an OER electrocatalyst that can function at any pH using titanium sulfide, this conductivity barrier must be overcome. This issue could be overcome by incorporating another metal, such as Fe, into the TiS, as demonstrated by Nai *et al.* with their Ti-Fe mixed sulfide nanoboxes.[712] With the incorporation of an additional metal, however, special care must be taken to ensure that such an addition does not lead to destabilization/dissolution of the material at a given pH. As a result, for studies involving OER electrocatalysts in acidic or neutral environments, it is recommended that samples of the electrolyte be examined for metal and sulfur content following long-term stability testing using either total reflection X-ray fluorescence (TXRF) or ICP-MS to determine whether or not dissolution has occurred (see Section 7).

Recent findings have also shown that extrinsic iron cations in alkali electrolytes significantly influence the OER activity, especially on Ni-based oxide and chalcogenide electrocatalysts.[913] In the case of metal sulfides, Li *et al.* have shown that Fe impurities in the electrolyte contributed to the high electrocatalytic activity of nickel (oxy)hydrate [$Ni(OH)_2$/NiOOH] derived from NiS_x oxidation during the OER.[734] Fe cations from the unpurified electrolyte incorporated themselves into the γ-NiOOH structure, forming electrocatalytically active sites in addition to the NiOOH sites already present. According to XPS results, around 4% Fe was detected in the sample after OER testing in 1 M KOH electrolyte (Figure 210). Therefore, incorporating such Fe impurities into γ-NiOOH can significantly improve the OER activity, as the Fe sites have an increased affinity for OH^- compared to Ni sites. Lee *et al.* also found that a large number of defects present in the amorphous $Ni(OH)_2$/NiOOH surface layer of a transformed Ni sulfide led to an increased number of edge sites available for Fe incorporation from impure KOH, enabling improved OER performance.[718] The infiltration of Fe into the Ni (oxy)hydroxide phase was confirmed from post-OER XPS, which indicated the presence of Fe^{3+} in the material. Theoretical computation analysis also revealed that the impact of Fe incorporation might depend on the position of the Fe cations in the crystalline structure. After all, edge-positioned Fe^{3+} in octahedral coordination is a more efficient active site for the OER than bridge-positioned Fe^{3+} due to higher adsorbed O* intermediate affinity (Figure 210b).[609]

Thus, the role of Fe incorporation from the unpurified electrolyte has a similar effect on OER performance to Fe-doping, with incorporated Fe acting as active sites while also enhancing the conductivity of NiOOH.[200] This phenomenon is often not considered, and the purified electrolyte is also rarely used in the literature. To ensure that the electrocatalytic activity of transition metal sulfides is the result of the prepared material and not from unintentional Fe-incorporation from the unpurified electrolyte, researchers are encouraged to use purified electrolyte and/or to study the electrocatalytic activity of their materials in both Fe-free and presumably Fe-

https://doi.org/10.1021/acs.chemrev.3c00005
Chem. Rev. 2023, 123, 12795−13208

contaminated electrolyte. KOH electrolyte purification is described elsewhere.[200]

In conclusion, while many reports on transition metal sulfides have been performed thorough post-OER material characterization, some authors still fail to conduct these post-OER characterizations or use an insufficient number of techniques to probe the transformation of their materials during the OER. To understand this transformation, it is recommended that, at the very least, XRD, XPS, and SEM/EDX are used to characterize post-OER transition metal sulfides to reveal their real active sites. Moreover, we encourage using multielemental analysis techniques such as TXRF and ICP-MS to evaluate the post-OER electrolyte to examine the presence of dissolved species, particularly sulfate ions or Fe impurities. Additionally, evaluation of the oxide layer thickness, given partial oxidation has occurred, and the determination of essential parameters such as the ECSA and TOF before and after long-term OER testing are recommended. These techniques would provide greater insight into the material properties of metal sulfides before, during, and after the OER. Overall, these strategies could pave the way to answer remaining questions surrounding transition metal sulfide electrocatalysts.

5.2. Transition Metal Selenides

5.2.1. Electrode Preparation Methods. Transition metal selenide electrodes are primarily fabricated in one of two ways: (i) as powder-coated electrodes and (ii) as self-supported electrodes (Table 6). Thus far, several approaches have been used to prepare selenide-based electrodes, such as the hydrothermal method (refs 669, 844, 977, 1006, 1011, 1015, 1055, 1068, and 1077), solvothermal method (refs 894, 987, 990, 1047, 1079, 1087, and 1089−1091), electrodeposition (refs 95, 918, 920, 925, 994, 1008, 1023, 1067, and 1069), solid-state reaction,[969,1079,1092] gas-solid reaction (refs 967, 1002, 1019, 1048, and 1085) [also known as chemical vapor deposition (CVD)],[922] and so forth. Through these synthetic approaches, electrocatalysts are obtained by either a one-step, two-step, or multistep reaction process. Among these methods, the hydrothermal and solvothermal methods are the most popular for transition metal selenide electrocatalyst synthesis. Electrocatalysts are prepared via these methods by mixing an aqueous/organic solution containing different cations, such as Co^{2+}, Ni^{2+}, Fe^{2+}, etc., with different selenium sources, such as NaHSe and Se powder, in an autoclave. The mixture is then ramped to a target temperature to induce a reaction. For hydrothermal/solvothermal reactions, selenization occurs in the autoclave at relatively low temperatures (∼100−200 °C). The hydrothermal/solvothermal method also has the benefit of enabling self-supported electrode preparation because selenides can be grown directly onto substrates such as Ni foam, Ti foil, carbon fiber cloth, etc. In addition to the hydrothermal method, the electrodeposition method is also attractive. To electrodeposit selenides, conductive substrates/electrodes are submerged in a solution containing raw materials of interest while a constant voltage is applied. This constant voltage can either induce selenization at the electrode surface or enable precursor synthesis in the preparation of a transition metal selenide. Electrodeposition has many advantages, including that it is a straightforward method and, like hydrothermal synthesis, self-supported electrodes can be prepared and directly used as electrodes for the OER. In addition, a more uniform film may be produced, as, under the control of constant voltage, reactants grow on the surface of the substrate(s) evenly and, as such, expose more surface area to the electrolyte, resulting in improved electrocatalytic performance. Other than the hydrothermal and solvothermal methods and electrodeposition, the solid-state/gas-solid reaction approach is also widely used to synthesize transition metal selenides and is applied for the selenization of precursors, as typified by MOFs, in most of the cases. In the literature, several transition metal selenides have been prepared via mixing precursors and Se powder or other Se sources together in a tube furnace or oven at relatively high temperatures (∼400−1000 °C).[969,1079,1092] In the gas-solid reaction/selenization, the Se powder and precursor(s) have also been put in the tube furnace separately, in which Se powder/shots upstream of the precursor(s) would flow down to the precursor(s), causing a reaction to occur.[922,967,1002,1085] To ensure the volatilized Se species and precursor(s) react thoroughly, these gas-solid reactions are also carried out at relatively high temperatures (e.g., 350,[967,1002] 400,[1019] 500,[1048,1085] and 700 °C[922]). Importantly, the solid-state and gas-solid reactions, electrodeposition, and hydrothermal and solvothermal methods have also been combined with one another to prepare selenides with different characteristics and electrocatalytic activities that might not be achieved via one method alone. In this section, the aforementioned methods and more novel approaches for the synthesis of transition metal selenides are discussed in detail.

5.2.1.1. Hydrothermal Methods. Among all of the aforementioned methods, the hydrothermal method is the most popular for transition metal selenide electrocatalyst synthesis. Through this method, electrocatalysts are prepared by heating an aqueous solution containing various cations (e.g., Co^{2+}, Ni^{2+}, Fe^{2+}, etc.) with different selenium sources (e.g., NaHSe, Se powder) in an autoclave at relatively low temperatures: ∼100−200 °C, which is environmentally friendly. The hydrothermal method also enables the preparation of self-supported electrodes because selenides are able to be grown directly onto conductive substrates. By using the hydrothermal method, more complete selenization is also possible as compared to gas-solid phase reactions because of improved interactions between reagents in the liquid phase. In addition, this method allows for material tunability, as a variety of morphologies can be achieved by changing reaction time and heating temperature selections. The hydrothermal method has been employed in one-step and multistep syntheses to prepare highly porous transition metal selenides for improved OER electrocatalysis. When used for one-step synthesis, the transition metal selenide electrocatalyst is often grown *in situ* on a conductive substrate. As the transition metal selenide can be synthesized directly at the surface of a conductive substrate, self-supported electrodes can be prepared via hydrothermal synthesis as aforementioned, eliminating issues such as electrocatalyst peel-off midcatalysis. So far, transition metal selenides have been grown on a variety of substrates, including Ni foam (refs 208, 844, 947, 999, 1006, and 1015), carbon paper (refs 210, 556, 921, 957, 958, 963, 1005, 1022, and 1082), Ti foil,[955,1077] and so on. For instance, Wang *et al.* fabricated "Cuju"-structured $FeSe_2$ layers directly on Ni foam via one-pot synthesis.[1015] A solution of $FeSO_4{\cdot}7H_2O$, Se powder, and fresh Ni foam was heated at 120 °C for 12 h in an autoclave to obtain the $FeSe_2$/Ni foam electrode (Figure 211a). The hollow structure of "Cuju" balls can be observed from the SEM image (Figure 211b). As shown in the image,

https://doi.org/10.1021/acs.chemrev.3c00005
Chem. Rev. 2023, 123, 12795−13208

Table 6. Summary of the Electrocatalytic Properties, Electrochemical Testing Conditions, And Physicochemical Pre- and Post-analyses of Transition Metal Selenides Used for Alkaline/Neutral OER and of the Final Type of Electrocatalyst after OER Testing[a−e]

Initial Electrocatalyst	Substrate	Shape of Electro-catalyst	Deposi-tion Type	Specific Loading / $mg \cdot cm^{-2}_{geo}$	η@10 $mA \cdot cm^{-2}_{geo}$ / mV	C_{dl} / $mF \cdot cm^{-2}_{geo}$	TOF / s^{-1} (@η or j)	Tafel Slope / $mV \cdot dec^{-1}$	Electro-lyte	Pre-analysis	Post-analysis	Long-Term OER Test Conditions	Post-OER Electrocatalyst	Final Type of Electrocatalyst	Ref.
Fe@Co/Se_2	GC	Nanorods	S	~0.25	200	-	0.611 at 250 $mA \cdot cm^{-2}_{geo}$	35	1 M KOH	FESEM, TEM, SAED, XRD, HAADF-STEM, XANES, EXAFS, XPS, ICP-MS, N_2 ISO (BET, PSD)	FESEM, XPS, XRD	2000 CV cycles 20 h CP (10 $mA \cdot cm^{-2}_{geo}$)	$CoSe_2$, $FeSe_2$	Catalyst	914
Fe-Se_2	GC	-	S	~0.25	360	-	0.242 at 250 $mA \cdot cm^{-2}_{geo}$	105		XPS, N_2 ISO (BET, PSD)	-	-	-	-	
Co-Se_2	GC	-	S	~0.25	250	-	0.534 at 250 $mA \cdot cm^{-2}_{geo}$	65		XPS, N_2 ISO (BET, PSD)	-	-	-	-	
MnSe@MWCNT	CC	Nanoparticles	P	0.283	290	0.4192	-	54.76	1 M KOH	XRD, Raman, XPS, SEM, TEM	XPS, Raman, XRD	25 h multistep CA 12 h CP (10 $mA \cdot cm^{-2}_{geo}$) 12 h CP (50 $mA \cdot cm^{-2}_{geo}$)	MnSe [mixed anionic (hydroxy)chalco-genide]	Catalyst	915
MnSe	CC	Nanoparticles	P	0.283	310	0.772	-	61.43		XRD, Raman, SEM, TEM	-	-	-	-	
$NiSe_2$@CNT	Graphite	Nanotubes	S	0.283	260	0.273	0.39 at 350 mV	82.54	1 M KOH	XRD, Raman, XPS, TEM	Raman, XPS	45 h multistep CA ~42 h multistep CA (1.40 to 1.63 V_{RHE})	$NiSe_2$, SeO_x	Catalyst	916
NiO_x@Ni_3Se_2	Au glass	Granules	P	~1.27 (NiO_x + Ni_3Se_2)	280 355 (@50 $mA \cdot cm^{-2}_{geo}$)	0.3348	-	118.8	1 M KOH	XRD, SEM, EDX, XPS	-	100 CV cycles (50 $mV \cdot s^{-1}$, 0.0–0.5 V_{RHE}) 10 h CA (1.52 V_{RHE})	-	-	917
Ni_3Se_2	Au glass	Granules	P	0.81	290 360 (@50 $mA \cdot cm^{-2}_{geo}$)	0.1012	-	84.3		XRD, SEM, EDX, XPS	XPS	100 CV cycles (50 $mV \cdot s^{-1}$, 0.0–0.5 V_{RHE}) 10 h CA (1.51 V_{RHE})	Ni_3Se_2 [mixed anionic (hydroxo)chalco-genide]	Catalyst	
$(Co_{0.21}Ni_{0.72}Cu_{0.54})_3Se_2$/ $Ni_{16}Cu_{13.1}Co_{13.1}Se_{57}$	Au glass	Nanosheets	S	-	272	0.1472	-	53.3	1 M KOH	XRD, SEM, EDX, XPS	XRD, SEM, EDX, XPS	12 h CA (1.505 V_{RHE})	$(Co_{0.21}Ni_{0.72}Cu_{0.54})_3Se_2$/ $Ni_{16}Cu_{13.1}Co_{13.1}Se_{57}$, SeO_x	Catalyst	918
$NiSe/Co_9Ni_{50.5}Cu_9Se_{49.5}$	Au glass	Nanosheets	S	-	335	-	-	66.2		XRD, EDX	-	-	-	-	
$Cu_3Se_2/Ni_6Cu_{63.8}Co_9Se_{36.2}$	Au glass	Nanosheets	S	-	326	-	-	82.9		XRD, EDX	-	-	-	-	
$CoSe/Ni_6Cu_9Co_{47}Se_{53}$	Au glass	Nanosheets	S	-	308	-	-	177.4		XRD, EDX	-	-	-	-	
$Ni_{3.4}Cu_{56.1}Co_9Se_{40.3}$	Au glass	Nanosheets	S	-	373	-	-	85.5		EDX	-	-	-	-	
$Ni_{7.4}Cu_{33.2}Co_9Se_{39.4}$	Au glass	Nanosheets	S	-	356	-	-	115.6		EDX	-	-	-	-	
$Ni_{14.4}Cu_{69.1}Co_9Se_{36.4}$	Au glass	Nanosheets	S	-	337	-	-	96.4		EDX	-	-	-	-	
$Ni_{18.2}Cu_{46.8}Co_9Se_{35}$	Au glass	Nanosheets	S	-	363	-	-	111.2		EDX	-	-	-	-	
$Ni_{23.7}Cu_{43.3}Co_9Se_{33}$	Au glass	Nanosheets	S	-	311	-	-	98		EDX	-	-	-	-	
$Ni_{28.5}Cu_{33.4}Co_9Se_{28.1}$	Au glass	Nanosheets	S	-	359	-	-	141.7		EDX	-	-	-	-	
$Ni_{32.7}Cu_{30.8}Co_9Se_{36.5}$	Au glass	Nanosheets	S	-	306	-	-	89.4		EDX	-	-	-	-	
$Ni_{35.4}Cu_{15.1}Co_9Se_{49.5}$	Au glass	Nanosheets	S	-	369	-	-	67.1		EDX	-	-	-	-	
$(Ni_{6.77}Cu_{6.23})_3Se_2$/ $Ni_{47.4}Cu_{14.1}Co_9Se_{38.3}$	Au glass	Nanosheets	S	-	299	-	-	90.4		EDX	-	-	-	-	
$Ni_9Cu_{57.6}Co_{24.6}Se_{39.8}$	Au glass	Nanosheets	S	-	323	-	-	88.4		EDX	-	-	-	-	
$Ni_9Cu_{48.9}Co_{10.1}Se_{41.0}$	Au glass	Nanosheets	S	-	284	-	-	77		EDX	-	-	-	-	
$Ni_9Cu_{36}Co_{15.6}Se_{39.4}$	Au glass	Nanosheets	S	-	290	-	-	60.2		EDX	-	-	-	-	
$Ni_9Cu_{45.2}Co_{18.3}Se_{36.5}$	Au glass	Nanosheets	S	-	302	-	-	91.2		EDX	-	-	-	-	
$(Co_{0.40}Cu_{0.60})_3Se_2$/ $Ni_9Cu_{38.3}Co_{24.9}Se_{38.8}$	Au glass	Nanosheets	S	-	278	-	-	72.5		EDX	-	-	-	-	
$Ni_9Cu_{31.2}Co_{27.7}Se_{41.1}$	Au glass	Nanosheets	S	-	299	-	-	68.7		EDX	-	-	-	-	
$Ni_9Cu_{31}Co_{31.4}Se_{37.3}$	Au glass	Nanosheets	S	-	299	-	-	78.2		EDX	-	-	-	-	
$Ni_9Cu_{16.2}Co_{44.6}Se_{39.2}$	Au glass	Nanosheets	S	-	315	-	-	66.6		EDX	-	-	-	-	
$Ni_9Cu_{9.6}Co_{44.5}Se_{45.7}$	Au glass	Nanosheets	S	-	312	-	-	87		EDX	-	-	-	-	
$Ni_{6.2}Cu_9Co_{40.2}Se_{44.7}$	Au glass	Nanosheets	S	-	292	-	-	71.5		EDX	-	-	-	-	
$Ni_{9.8}Cu_9Co_{41.1}Se_{40.1}$	Au glass	Nanosheets	S	-	298	-	-	58.1		EDX	-	-	-	-	
$Ni_{16.3}Cu_9Co_{34.6}Se_{40.2}$	Au glass	Nanosheets	S	-	306	-	-	74.3		EDX	-	-	-	-	
$Ni_{22.3}Cu_9Co_{31.2}Se_{46.5}$	Au glass	Nanosheets	S	-	325	-	-	72.9		EDX	-	-	-	-	
$(Ni_{9.5}Co_{9.49})Se$/ $Ni_{26.9}Cu_9Co_{25.7}Se_{47.3}$	Au glass	Nanosheets	S	-	289	-	-	60.7		EDX	-	-	-	-	
$Ni_{28.4}Cu_9Co_{17.4}Se_{54.2}$	Au glass	Nanosheets	S	-	318	-	-	60.3		EDX	-	-	-	-	
$Ni_{38.1}Cu_9Co_{15.2}Se_{36.7}$	Au glass	Nanosheets	S	-	315	-	-	60.4		EDX	-	-	-	-	
$Ni_{47.1}Cu_9Co_{15.8}Se_{27.1}$	Au glass	Nanosheets	S	-	339	-	-	59.9		EDX	-	-	-	-	
$Ni_{33.2}Cu_9Co_{6.2}Se_{40.6}$	Au glass	Nanosheets	S	-	346	-	-	51.2		EDX	-	-	-	-	
$Ni_{5.7}Cu_{11.3}Co_{36.9}Se_{45.8}$	Au glass	Nanosheets	S	-	299	-	-	59.8		EDX	-	-	-	-	
$Ni_{3.9}Cu_{11.5}Co_{35.4}Se_{43.2}$	Au glass	Nanosheets	S	-	310	-	-	63.4		EDX	-	-	-	-	
$Ni_{6.1}Cu_{10.6}Co_{33.8}Se_{49.5}$	Au glass	Nanosheets	S	-	289	-	-	58.3		EDX	-	-	-	-	
$Ni_{4.5}Cu_{36.9}Co_{22.9}Se_{35.7}$	Au glass	Nanosheets	S	-	284	-	-	67.5		EDX	-	-	-	-	
$Ni_{4.9}Cu_{38.6}Co_{19.7}Se_{36.8}$	Au glass	Nanosheets	S	-	282	-	-	57		EDX	-	-	-	-	
$Ni_{5.5}Cu_{44.4}Co_{10.7}Se_{39.4}$	Au glass	Nanosheets	S	-	298	-	-	56.3		EDX	-	-	-	-	
$Ni_9Cu_{53.5}Co_{4.4}Se_{39.2}$	Au glass	Nanosheets	S	-	287	-	-	65.5		EDX	-	-	-	-	
$Ni_9Cu_{56.7}Co_{2.8}Se_{37.6}$	Au glass	Nanosheets	S	-	296	-	-	102.9		EDX	-	-	-	-	
$Ni_{11.5}Cu_{11.1}Co_{34.9}Se_{42.5}$	Au glass	Nanosheets	S	-	327	-	-	74.1		EDX	-	-	-	-	
$Ni_{11.8}Cu_{19.9}Co_{32.7}Se_{36.2}$	Au glass	Nanosheets	S	-	311	-	-	60		EDX	-	-	-	-	
$Ni_{9.7}Cu_9Co_{24}Se_{37.3}$	Au glass	Nanosheets	S	-	304	-	-	61.3		EDX	-	-	-	-	

https://doi.org/10.1021/acs.chemrev.3c00005
Chem. Rev. 2023, 123, 12795−13208

Table 6. continued

Initial Electrocatalyst	Substrate	Shape of Electro-catalyst	Deposi-tion Type	Specific Loading / $mg \cdot cm^{-2}_{geo}$	η@10 $mA \cdot cm^{-2}_{geo}$ / mV	C_{dl} / $mF \cdot cm^{-2}_{geo}$	TOF / s^{-1} (@η or j)	Tafel Slope / $mV \cdot dec^{-1}$	Electro-lyte	Pre-analysis	Post-analysis	Long-Term OER Test Conditions	Post-OER Electrocatalyst	Final Type of Electrocatalyst	Ref.
$Ni_{9.7}Cu_{28.8}Co_{20.2}Se_{41.3}$	Au glass	Nanosheets	S	-	283	-	-	69.6		EDX	-	-	-	-	
$Ni_{11.1}Cu_{40.2}Co_{13.3}Se_{33.3}$	Au glass	Nanosheets	S	-	288	-	-	83.6		EDX	-	-	-	-	
$Ni_{9.6}Cu_{45.4}Co_{9.8}Se_{35}$	Au glass	Nanosheets	S	-	283	-	-	71.3		EDX	-	-	-	-	
$Ni_{8.4}Cu_{52.2}Co_{5.8}Se_{34.4}$	Au glass	Nanosheets	S	-	288	-	-	67.6		EDX	-	-	-	-	
$Ni_{15.4}Cu_{32.9}Co_{8.3}Se_{43.1}$	Au glass	Nanosheets	S	-	313	-	-	67.2		EDX	-	-	-	-	
$Ni_{13.4}Cu_{21.2}Co_{19.4}Se_{43.9}$	Au glass	Nanosheets	S	-	293	-	-	57.9		EDX	-	-	-	-	
$Ni_{14.4}Cu_{28.9}Co_{19.2}Se_{37.5}$	Au glass	Nanosheets	S	-	280	-	-	78.9		EDX	-	-	-	-	
$Ni_{14.9}Cu_{43.8}Co_{8.8}Se_{32.4}$	Au glass	Nanosheets	S	-	298	-	-	56.2		EDX	-	-	-	-	
$Ni_{14.9}Cu_{40.1}Co_{8.3}Se_{36.7}$	Au glass	Nanosheets	S	-	298	-	-	74.2		EDX	-	-	-	-	
$Ni_{22.2}Cu_{14.4}Co_{22.2}Se_{41.2}$	Au glass	Nanosheets	S	-	287	-	-	55.3		EDX	-	-	-	-	
$Ni_{20.4}Cu_{17.7}Co_{19.5}Se_{42.8}$	Au glass	Nanosheets	S	-	308	-	-	51.9		EDX	-	-	-	-	
$Ni_{17.6}Cu_{32}Co_{13.3}Se_{37.1}$	Au glass	Nanosheets	S	-	293	-	-	53.6		EDX	-	-	-	-	918
$Ni_{17.1}Cu_{38.5}Co_{10.1}Se_{34.3}$	Au glass	Nanosheets	S	-	278	-	-	93.9		EDX	-	-	-	-	
$Ni_{19.2}Cu_{43.8}Co_{5.6}Se_{30.9}$	Au glass	Nanosheets	S	-	287	-	-	74.3		EDX	-	-	-	-	
$Ni_{26.3}Cu_{23.2}Co_{16.3}Se_{33.9}$	Au glass	Nanosheets	S	-	317	-	-	73.7		EDX	-	-	-	-	
$Ni_{21.5}Cu_{23.4}Co_{12}Se_{42.9}$	Au glass	Nanosheets	S	-	294	-	-	114.2		EDX	-	-	-	-	
$Ni_{18.2}Cu_{30.6}Co_{10}Se_{41.2}$	Au glass	Nanosheets	S	-	291	-	-	87.2		EDX	-	-	-	-	
$Ni_{22.1}Cu_{38.4}Co_{4.8}Se_{34.7}$	Au glass	Nanosheets	S	-	299	-	-	82.2		EDX	-	-	-	-	
$Ni_{34.8}Cu_{14.4}Co_{12.6}Se_{38.2}$	Au glass	Nanosheets	S	-	309	-	-	69		EDX	-	-	-	-	
$Ni_{32.4}Cu_{21.2}Co_{7.3}Se_{38.6}$	Au glass	Nanosheets	S	-	305	-	-	78.3		EDX	-	-	-	-	
$Ni_{29}Cu_{27.1}Co_{4.5}Se_{39.2}$	Au glass	Nanosheets	S	-	307	-	-	64.9		EDX	-	-	-	-	
$Ni_{43.1}Cu_{6.7}Co_{10.8}Se_{39.4}$	Au glass	Nanosheets	S	-	332	-	-	71.7		EDX	-	-	-	-	
$Ni_{39.2}Cu_{14.8}Co_{7.5}Se_{38.2}$	Au glass	Nanosheets	S	-	315	-	-	78		EDX	-	-	-	-	
$Ni_{46.8}Cu_{6.5}Co_5Se_{36.7}$	Au glass	Nanosheets	S	-	315	-	-	91.1		EDX	-	-	-	-	
ZIF-900-3 ($CoSe_2$@C-CNT)	CC	3D structure + Nanotubes	P	0.3	306	53.8	-	46	1 M KOH	XRD, SEM, EDX, Raman, TEM, XPS, N_2 ISO (BET)	XRD, SEM, XPS	30000 s CA (1.536 V_{RHE}) 1000 CV cycles (1.23−1.53 V_{RHE})	$CoSe_2$, SeO_x	Catalyst	919
ZIF-700-1	CC	3D structure + Nanotubes	P	0.3	-	-	-	-		XRD, SEM	-	-	-	-	
ZIF-800-1	CC	3D structure + Nanotubes	P	0.3	354	-	-	-		XRD, SEM	-	-	-	-	
ZIF-900-1	CC	3D structure + Nanotubes	P	0.3	352	47.9	-	46.7		XRD, N_2 ISO (BET)	-	-	-	-	
ZIF-900-0.5	CC	3D structure + Nanotubes	P	0.3	359	41.2	-	51.8		XRD, N_2 ISO (BET)	-	-	-	-	
ZIF-900-5	CC	3D structure + Nanotubes	P	0.3	358	45.2	-	50.4		XRD, N_2 ISO (BET)	-	-	-	-	
$(Co_{0.38}Fe_{0.48}Cu_{0.14})Se$	Au glass	Nanosheets	S	-	256	-	-	40.8	1 M KOH	SEM, EDX, XPS	SEM, EDX, XPS	18 h CP (10 $mA \cdot cm^{-2}_{geo}$)	$(Co_{0.38}Fe_{0.48}Cu_{0.14})Se$, SeO_x	Catalyst	920
(CoSe)/ $(Fe_9Co_{59.6}Cu_6)Se_{25.4}$	Au glass	Nanosheets	S	-	298	-	-	62.9		EDX	-	-	-	-	
(FeSe)/ $(Co_3Fe_{49.7}Cu_6)Se_{41.3}$	Au glass	Nanosheets	S	-	393	-	-	103.5		EDX	-	-	-	-	
(Cu_2Se)/ $(Co_3Fe_9Cu_{43.8})Se_{41.2}$	Au glass	Nanosheets	S	-	330	-	-	93.4		EDX	-	-	-	-	
$(Co_{11.2}Fe_{35.5}Cu_6)Se_{47.3}$	Au glass	Nanosheets	S	-	338	-	-	56.6		EDX	-	-	-	-	
$(Co_{14.5}Fe_{29.5}Cu_6)Se_{49.8}$	Au glass	Nanosheets	S	-	313	-	-	91.6		EDX	-	-	-	-	
$(Co_{20}Fe_{22.2}Cu_6)Se_{51.8}$	Au glass	Nanosheets	S	-	320	-	-	69.9		EDX	-	-	-	-	
$(Co_{21.4}Fe_{13.1}Cu_6)Se_{59.5}$	Au glass	Nanosheets	S	-	315	-	-	79.3		EDX	-	-	-	-	
$(Co_{27.4}Fe_{14.7}Cu_6)Se_{51.9}$	Au glass	Nanosheets	S	-	300	-	-	58.6		EDX	-	-	-	-	
$(Co_{29.1}Fe_9Cu_6)Se_{55.8}$	Au glass	Nanosheets	S	-	316	-	-	63.2		EDX	-	-	-	-	
$(Co_{34.4}Fe_{22.5}Cu_6)Se_{52.9}$	Au glass	Nanosheets	S	-	333	-	-	91.7		EDX	-	-	-	-	
$(Co_{38.8}Fe_{8.4}Cu_6)Se_{52.8}$	Au glass	Nanosheets	S	-	332	-	-	79.7		EDX	-	-	-	-	
$(Co_{40.3}Fe_{8.4}Cu_6)Se_{55.3}$	Au glass	Nanosheets	S	-	295	-	-	57.6		EDX	-	-	-	-	
$(Co_9Fe_{29.9}Cu_{4.9})Se_{56.1}$	Au glass	Nanosheets	S	-	388	-	-	67.9		EDX	-	-	-	-	
$(Co_9Fe_{35.5}Cu_{10})Se_{44.6}$	Au glass	Nanosheets	S	-	347	-	-	86.4		EDX	-	-	-	-	
$(Co_9Fe_{33.1}Cu_{14.4})Se_{43.5}$	Au glass	Nanosheets	S	-	379	-	-	64		EDX	-	-	-	-	
$(Co_9Fe_{35.5}Cu_{14.6})Se_{40.9}$	Au glass	Nanosheets	S	-	374	-	-	65.7		EDX	-	-	-	-	
$(Co_9Fe_{28.6}Cu_{20.4})Se_{50.7}$	Au glass	Nanosheets	S	-	367	-	-	63.8		EDX	-	-	-	-	
$(Co_9Fe_{20.8}Cu_{20.7})Se_{49.5}$	Au glass	Nanosheets	S	-	376	-	-	73.5		EDX	-	-	-	-	
$(Co_9Fe_{16.6}Cu_{25.1})Se_{49.3}$	Au glass	Nanosheets	S	-	361	-	-	58.9		EDX	-	-	-	-	
$(Co_9Fe_{10.9}Cu_{42})Se_{48.2}$	Au glass	Nanosheets	S	-	381	-	-	77.6		EDX	-	-	-	-	
$(Co_9Fe_{5.3}Cu_{33.8})Se_{38.9}$	Au glass	Nanosheets	S	-	356	-	-	68.5		EDX	-	-	-	-	
$(Co_{7.2}Fe_6Cu_{33.8})Se_{39.1}$	Au glass	Nanosheets	S	-	337	-	-	84.4		EDX	-	-	-	-	
$(Co_{13.1}Fe_6Cu_{30.9})Se_{36.1}$	Au glass	Nanosheets	S	-	325	-	-	71		EDX	-	-	-	-	
$(Co_{17.9}Fe_6Cu_{46})Se_{36.1}$	Au glass	Nanosheets	S	-	308	-	-	81.1		EDX	-	-	-	-	
$(Co_{24.4}Fe_6Cu_{29.9})Se_{35.3}$	Au glass	Nanosheets	S	-	296	-	-	92		EDX	-	-	-	-	
$(Co_{26.6}Fe_6Cu_{28.3})Se_{34.1}$	Au glass	Nanosheets	S	-	301	-	-	73.3		EDX	-	-	-	-	
$(Co_{40}Fe_6Cu_{20.4})Se_{29.5}$	Au glass	Nanosheets	S	-	311	-	-	74.9		EDX	-	-	-	-	
$(Co_{36.1}Fe_6Cu_{21.9})Se_{37.8}$	Au glass	Nanosheets	S	-	325	-	-	60.5		EDX	-	-	-	-	
$(Co_{37}Fe_6Cu_{21.9})Se_{41}$	Au glass	Nanosheets	S	-	291	-	-	84.7		EDX	-	-	-	-	
$(Co_{51.3}Fe_6Cu_{13.8})Se_{45}$	Au glass	Nanosheets	S	-	272	-	-	106.9		EDX	-	-	-	-	
$(Co_{4.2}Fe_{1.4}Cu_{31.9})Se_{38.5}$	Au glass	Nanosheets	S	-	288	-	-	60.6		EDX	-	-	-	-	
$(Co_{4.5}Fe_{0.5}Cu_{43.2})Se_{43.9}$	Au glass	Nanosheets	S	-	300	-	-	57.6		EDX	-	-	-	-	
$(Co_{3.3}Fe_{0.9}Cu_{40.4})Se_{55.4}$	Au glass	Nanosheets	S	-	295	-	-	57.4		EDX	-	-	-	-	
$(Co_{4.3}Fe_{12.3}Cu_{33.1})Se_{48.9}$	Au glass	Nanosheets	S	-	286	-	-	43.8		EDX	-	-	-	-	
$(Co_{5.8}Fe_{22}Cu_{20})Se_{52.2}$	Au glass	Nanosheets	S	-	286	-	-	43.2		EDX	-	-	-	-	
$(Co_6Fe_{25.7}Cu_{15.7})Se_{52.6}$	Au glass	Nanosheets	S	-	290	-	-	44.1		EDX	-	-	-	-	
$(Co_{6.3}Fe_{28.8}Cu_{14.7})Se_{50.3}$	Au glass	Nanosheets	S	-	285	-	-	48.3		EDX	-	-	-	-	
$(Co_9Fe_{31.3}Cu_{7.1})Se_{51.7}$	Au glass	Nanosheets	S	-	295	-	-	45.1		EDX	-	-	-	-	

https://doi.org/10.1021/acs.chemrev.3c00005
Chem. Rev. 2023, 123, 12795−13208

Table 6. continued

Initial Electrocatalyst	Substrate	Shape of Electro-catalyst	Deposi-tion Type	Specific Loading / $mg \cdot cm^{-2}_{geo}$	η@10 $mA \cdot cm^{-2}_{geo}$ / mV	C_{dl} / $mF \cdot cm^{-2}_{geo}$	TOF / s^{-1} (@η or j)	Tafel Slope / $mV \cdot dec^{-1}$	Electro-lyte	Pre-analysis	Post-analysis	Long-Term OER Test Conditions	Post-OER Electrocatalyst	Final Type of Electrocatalyst	Ref.
$(Co_{0.9}Fe_{13.2}Cu_{40.1})Se_{41}$	Au glass	Nanosheets	S	-	313	-	-	60.7		EDX	-	-	-	-	
$(Co_{1}Fe_{4.4}Cu_{44.3})Se_{43}$	Au glass	Nanosheets	S	-	306	-	-	56.7		EDX	-	-	-	-	
$(Co_{10}Fe_{10.2}Cu_{34.7})Se_{45.1}$	Au glass	Nanosheets	S	-	295	-	-	77.9		EDX	-	-	-	-	
$(Co_{13.7}Fe_{15.6}Cu_{25})Se_{45.7}$	Au glass	Nanosheets	S	-	289	-	-	43.3		EDX	-	-	-	-	920
$(Co_{12.8}Fe_{25.7}Cu_{17.3})Se_{44.2}$	Au glass	Nanosheets	S	-	267	-	-	51		EDX	-	-	-	-	
$(Co_{13.4}Fe_{27.8}Cu_{9.3})Se_{49.6}$	Au glass	Nanosheets	S	-	276	-	-	45.2		EDX	-	-	-	-	
$(Co_{7.7}Fe_{31.3}Cu_{8.1})Se_{42.6}$	Au glass	Nanosheets	S	-	291	-	-	54.1		EDX	-	-	-	-	
$(Co_{14.5}Fe_{2.5}Cu_{43.8})Se_{39.2}$	Au glass	Nanosheets	S	-	297	-	-	50.2		EDX	-	-	-	-	
Ni_3Se_4@NiFe LDH	CF	Nanosheets	S	-	223	6.1	-	55.5	1 M KOH	SEM, TEM, EDX, XPS	SEM, EDX, XRD, XPS	100 h CP (1.687 V_{RHE}) 3000 CV cycles	NiFe LDH	Catalyst (substrate)	921
Ni_3Se_4	CF	Nanosheets	S	-	330 (@50 $mA \cdot cm^{-2}_{geo}$)	1.3	-	121.2		XRD, SEM, EDX, TEM	-	-	-	-	
Cu_2Se (ED-1)	Cu substrate	Nanosheets	S	0.8	320	-	-	48.1	1 M KOH	XRD, Raman, EDX, SEM, TEM, XPS, SAED	SEM, XRD, XPS	6 h CP (10 $mA \cdot cm^{-2}_{geo}$)	Cu_2Se, Oxidized Se	Catalyst	922
Cu_2Se (CVD)	Cu substrate	Nanosheets	S	2.0	300	-	-	90.9		XRD, SEM, TEM, EDX, Raman, SAED, XPS	SEM, XRD, XPS	6 h CP (10 $mA \cdot cm^{-2}_{geo}$)	Cu_2Se, Oxidized Se	Catalyst	
Cu_2Se (ED-2)	Cu substrate	Nanosheets	S	0.7	270	-	-	107.6		XRD, SEM, TEM, EDX	-	-	-	-	
Cu_2Se (HD)	Cu substrate	Nanosheets	P	45.0	290	-	-	136.7		XRD, EDX, SEM, TEM, XPS	-	-	-	-	
(9:1)$CoSe_2$/DG - composite	GC	Nanosheets	P	0.196	270	28.1	0.024 at 270 mV	64	1 M KOH	XRD, TEM, EDX, XPS, TGA, Raman	XRD, TEM, EDX, XPS	10 h CA (1.535 V_{RHE})	$CoSe_2$	Catalyst	923
E-$CoSe_2$	GC	Nanosheets	P	0.196	292	9.3	0.0077 at 270 mV	66		XRD, XPS, TEM, Raman	-	-	-	-	
$CoSe_2$/DG - mixture	GC	Nanosheets	P	0.196	290	-	-	66		-	-	-	-	-	
(6:1)$CoSe_2$/DG - composite	GC	Nanosheets	P	0.196	290	-	-	67		TEM	-	-	-	-	
(3:1)$CoSe_2$/DG - composite	GC	Nanosheets	P	0.196	325	-	-	69		TEM	-	-	-	-	
(9:1)$CoSe_2$/G - composite	GC	Nanosheets	P	0.196	376	-	0.0022 at 270 mV	92		TEM, EDX, TGA	-	-	-	-	
(9:1)$CoSe_2$/NG - composite	GC	Nanosheets	P	0.196	353	-	0.0025 at 270 mV	83		TEM, EDX, TGA	-	-	-	-	
$Fe_{4.4}Ni_{17.6}Se_{16}$/NiSe	FeNi foam	Nanoparticles	S	-	242 (@100 $mA \cdot cm^{-2}_{geo}$)	4.92	-	61.3	1 M KOH	XRD, SEM, TEM, EDX, XPS	SEM, XRD, XPS	12 h CP (100 $mA \cdot cm^{-2}_{geo}$) 1000 CV cycles	$Fe_{4.4}Ni_{17.6}Se_{16}$/NiSe	Catalyst	924
$Fe_{4.4}Ni_{17.6}Se_{16}$	FeNi foam	Nanoparticles	S	-	296 (@100 $mA \cdot cm^{-2}_{geo}$)	2.57	-	76		XRD	-	12 h CP (100 $mA \cdot cm^{-2}_{geo}$)	-	-	
NiSe	Ni foam	Nanoparticles	S	-	340 (@100 $mA \cdot cm^{-2}_{geo}$)	1.63	-	130.4		XRD, XPS	-	-	-	-	
$(Ni_{0.25}Fe_{0.68}Co_{0.07})_3Se_4$	Au glass	Nanoflake	S	-	240	0.069	-	41.7	0.3 M KOH	SEM, TEM, EDX, XPS	SEM, XPS, EDX	8 h CA (1.73 V_{RHE})	$(Ni_{0.25}Fe_{0.68}Co_{0.07})_3Se_4$	Catalyst	925
$CoNi_2Se_4$	CFP	Nanoflake	S	4.7	160	0.432	-	72	1 M KOH	XRD, XPS, SEM, EDX, TEM	EDX, XPS	10 h CA (1.38 V_{RHE})	$CoNi_2Se_4$	Catalyst	926
Ni-Fe-Se Cages	Pt sheet	Nanocages	P	0.1	270 (@100 $mA \cdot cm^{-2}_{geo}$)	4.055×10^{-4}	0.58 at 270 mV	24	1 M KOH	SEM, XRD, EDX, TEM, FTIR, XPS	SEM, XRD, EDX, TEM	22 h CP (5 $mA \cdot cm^{-2}_{geo}$) 500 CV cycles (1.177−1.277 V_{RHE})	Ni-Fe diselenide	Catalyst	927
Ni-Fe-Se Disks	Pt sheet	Nanodisks	P	0.1	280 (@100 $mA \cdot cm^{-2}_{geo}$)	3.47×10^{-4}	0.38 at 270 mV	26		SEM, XRD, EDX, TEM	-	22 h CP (5 $mA \cdot cm^{-2}_{geo}$)	-	-	
Ni-Fe-Se Cubes	Pt sheet	Nanocubes	P	0.1	330 (@100 $mA \cdot cm^{-2}_{geo}$)	2.175×10^{-4}	0.07 at 270 mV	59		SEM, XRD, EDX, TEM	-	22 h CP (5 $mA \cdot cm^{-2}_{geo}$)	-	-	
Ni_3Se_2/300 s	GC	-	S	0.217	310	0.092	-	97.1	0.3 M KOH	XRD, EDX, SEM, TEM, Raman, HAADF, XPS	XRD, XPS, Raman	18 and 42 h CA	Ni_3Se_2	Catalyst	100
Ni_3Se_2/40 s	GC	-	S	0.0283	370	0.1	-	99.6		XRD, EDX, SEM, TEM	-	-	-	-	
Ni_3Se_2/130 s	GC	-	S	0.111	330	0.092	-	98.8		XRD, EDX, SEM, TEM	-	-	-	-	
Ni_3Se_2/600 s	GC	-	S	0.435	360	0.72	-	100.2		XRD, EDX, SEM, TEM	-	-	-	-	
Co_7Se_8/GC/Deposition 1 min	GC	Nanoflake	S	-	310	0.044	0.077 at 300 mV	36.2	1 M KOH	XRD, SEM, EDX, XPS, Raman	SEM, EDX, XPS, XRD	-	Co_7Se_8	Catalyst	928
Co_7Se_8/GC/Deposition 2.5 min	GC	Nanoflake	S	-	290	0.06	0.083 at 300 mV	32.6		XRD, SEM, EDX, XPS, Raman	SEM, EDX, XPS, XRD	15 h CA	Co_7Se_8	Catalyst	
Co_7Se_8/GC/Deposition 5 min	GC	Nanoflake	S	-	290	0.064	0.047 at 300 mV	34.1		XRD, SEM, EDX, XPS, Raman	SEM, EDX, XPS, XRD	-	Co_7Se_8	Catalyst	
Co_7Se_8/GC	GC	Nanotubes	S	-	310 (@880 $mA \cdot cm^{-2}_{geo}$)	-	-	45.3		SEM, EDX	-	1 h CA	-	-	
Co_7Se_8/GC	GC	Nanorods	S	-	310 (@590 $mA \cdot cm^{-2}_{geo}$)	-	-	53.5		SEM, EDX	-	1 h CA	-	-	
Co_7Se_8/AGS/ Deposition 5 min	Au glass	-	S	-	260	-	-	-		-	-	-	-	-	
$CoSe_2$	GC	Nanosheets	P	0.142	320	-	0.33 at 500 mV	44	0.1 M KOH	XRD, SEM, TEM, XPS, AFM, Raman, FTIR, TGA, HAADF-STEM, EXAFS	TEM, XPS, HAADF, Raman	1000 CV cycles	$CoSe_2$	Catalyst	929
B-$CoSe_2$@CoNi LDH HNA	CC	Nanotubes/ Nanosheets	P	-	250	5.87	-	55	1 M KOH	SEM, TEM, EDX, XRD, XPS, XANES, EXAFS, N_2 ISO (BET)	XRD, SEM, XPS, *In-Situ* Raman	~ 48 h OER test 30 h CP (10 $mA \cdot cm^{-2}_{geo}$, OWS)	CoOOH, NiOOH SeO_x	Precatalyst (partial oxidation)	930

https://doi.org/10.1021/acs.chemrev.3c00005
Chem. Rev. 2023, 123, 12795−13208

Table 6. continued

Initial Electrocatalyst	Substrate	Shape of Electro-catalyst	Deposi-tion Type	Specific Loading / $mg \cdot cm^{-2}_{geo}$	η@10 $mA \cdot cm^{-2}_{geo}$ / mV	C_{dl} / $mF \cdot cm^{-2}_{geo}$	TOF / s^{-1} (@η or j)	Tafel Slope / $mV \cdot dec^{-1}$	Electro-lyte	Pre-analysis	Post-analysis	Long-Term OER Test Conditions	Post-OER Electrocatalyst	Final Type of Electrocatalyst	Ref.
V-$CoSe_2$@CoNi LDH HNA	CC	Nanotubes/ Nanosheets	P	-	~ 280	1.92	-	58		SEM, TEM, XRD, N_2 ISO (BET)	-	-	-	-	930
B-$CoSe_2$	CC	Nanotubes/ Nanosheets	P	-	~ 300	0.95	-	73		SEM, TEM, XPS, XANES, EXAFS, N_2 ISO (BET)	-	-	-	-	
V-$CoSe_2$	CC	Nanotubes/ Nanosheets	P	-	~ 290	2.96	-	86		SEM, TEM, XRD, N_2 ISO (BET)	-	-	-	-	
Ni_3Se_4/UCL-1	GC	Flower-like microspheres	P	-	490	-	-	279.1	0.1 M KOH	XRD, XPS, SEM, N_2 ISO (BET, PSD), CAM	-	-	-	-	931
Ni_3Se_4/UCL-2	GC	Flower-like microspheres	P	-	420	-	-	112.0		XRD, XPS, SEM, N_2 ISO (BET, PSD), CAM	-	-	-	-	
Ni_3Se_4/UCL-3	GC	Flower-like microspheres	P	-	350	2.23	0.614 at 10 $mA \cdot cm^{-2}_{geo}$	89.4		XRD, XPS, TEM, SEM, EDX, N_2 ISO (BET, PSD), CAM	SEM, *In-Situ* XRD, XPS	1000 CV cycles (1.0–2.0 V_{RHE}) 20 h CA (1.6 V_{RHE})	NiO_x, NiOOH, $NiSeO_3$	Precatalyst (partial oxidation)	
Ni_3Se_4/UCL-4	GC	Flower-like microspheres	P	-	450	-	-	100.7		XRD, XPS, SEM, N_2 ISO (BET, PSD), CAM	-	-	-	-	
Ni_3Se_4/UCL-5	GC	Flower-like microspheres	P	-	390	-	-	140.4		XRD, XPS, SEM, N_2 ISO (BET, PSD), CAM	-	-	-	-	
$NiSe_2$/Ni_3Se_4/NF-1	Ni foam	Nanosheets	S	7.4	309 (@100 $mA \cdot cm^{-2}_{geo}$)	40.3	-	71.9	1 M KOH	XRD, XPS, TEM, SEM	XRD, SEM, XPS	2000 CV cycles 60 h CA (1.518 V_{RHE}) 9000 s multistep CA	Ni_3Se_4	Precatalyst [transformation ($NiSe_2$ to Ni_3Se_4)]	932
$NiSe_2$/Ni_3Se_4/NF-4	Ni foam	Nanoparticles/ Nanosheets	S	7.4	444 (@100 $mA \cdot cm^{-2}_{geo}$)	32.7	-	104.3		XRD, XPS, TEM, SEM	-	-	-	-	
$Ni_{0.2}Fe_{0.8}Se$–Se	Ni foam	Nanoflowers	S	-	200	11.6	-	57.7	1 M KOH	SEM, EDX, XRD, XPS	XPS, SEM	26 h CA (1.43 V_{RHE})	NiOOH, FeOOH, SeO_x	Precatalyst (partial oxidation)	933
FeSe	Ni foam	Nanoflowers	S	-	222	8.5	-	80.6		SEM	-	-	-	-	
$Ni_{0.8}Fe_{0.2}Se_2$	CC	Nanoarrays	S	0.56	257	-	-	43	1 M KOH	XRD, SEM, TEM, EDX	XPS, XRD, SEM, TEM	15 h CA (1.487 V_{RHE})	NiFe (oxy)hydroxides	Precatalyst (partial oxidation)	934
$Ni_{0.9}Fe_{0.1}Se_2$	CC	Nanowires	S	0.60	268	-	-	61		SEM, XRD	-	15 h CA (1.498 V_{RHE})	-	-	
$Ni_{0.8}Fe_{0.4}Se_2$	CC	Nanosheets	S	0.52	261	-	-	49		SEM, XRD	-	15 h CA (1.491 V_{RHE})	-	-	
$NiSe_2$	CC	Nanosheets	S	1.58	296	-	-	71		SEM, XRD, XPS	-	15 h CA (1.426 V_{RHE})	-	-	
Ni-MOF-Fe-Se-400 (Ni_3Se_4/$NiSe_2$)	GC	Nanoparticles	P	~ 0.28	242	10.35	-	41.25	1 M KOH	XRD, Raman, FTIR, SEM, TEM, HAADF-STEM, EDX, XPS, N_2 ISO (BET)	SEM, XRD, XPS, Raman	2000 CV cycles 75 h CA (1.49 V_{RHE})	Ni–OOH/Ni–Fe–OOH, SeO_x	Precatalyst (partial oxidation)	935
$NiFe_{0.2}$-MOF-Se-400	GC	Nanoparticles	P	~ 0.28	294	7.15	-	49.02		XRD, Raman, FTIR, XPS, SEM, N_2 ISO (BET)	-	-	-	-	
Ni-MOF-Se-400	GC	Nanoparticles	P	~ 0.28	299	9.14	-	54.45		XRD, Raman, SEM, XPS	-	-	-	-	
Fe-doped MOF CuCoSe	CP	Nanostructure	P	4.5	260 (@20 $mA \cdot cm^{-2}_{geo}$)	17.2	-	57	1 M KOH	XRD, Raman, SEM, EDX, TEM, AFM, XPS, N_2 ISO (BET, PSD)	XPS, XRD, FeSEM, EDX, TEM, SAED (after OWS)	50 h CA (1.49 V_{RHE}) 1000 CV cycles 30 h CA (cell voltage: 1.57 V, OWS)	Metal (oxy)hydroxide, SeO_x	Precatalyst (partial oxidation)	936
MOF CoCuSe	CP	-	P	4.5	320 (@20 $mA \cdot cm^{-2}_{geo}$)	-	-	76		XPS	-	-	-	-	
$Fe_{0.4}Co_{0.6}Se_2$	GC	Nanoframes	P	0.5	270	0.87	1.23 at 300 mV	36	1 M KOH	SEM, TEM, EDX, Raman, XRD, XPS, EPR, XANES, EXAFS	XRD, TEM, SAED, EDX, XPS, EPR, Raman	24 h CP (10 $mA \cdot cm^{-2}_{geo}$)	$Fe_{0.4}Co_{0.6}OOH$	Precatalyst (partial oxidation)	937
$Fe_{0.2}Co_{0.8}Se_2$	GC	Nanoframes	P	0.5	287	0.21	0.36 at 300 mV	45		XPS, Raman	Raman	-	-	-	
$Fe_{0.6}Co_{0.4}Se_2$	GC	Nanoframes	P	0.5	313	0.19	0.015 at 300 mV	52		XPS, Raman	Raman	-	-	-	
$CoSe_2$	GC	Nanoframes	P	0.5	346	0.14	0.003 at 300 mV	69		SEM, XRD, XPS. XANES, EXAFS	XPS, EPR, Raman	-	-	-	
$Co_{0.85}Se_{1-x}$@C (x = 0.49)	GC	Nanocages	P	0.796	231	325	1.46 at 300 mV	57	1 M KOH	XRD, XPS, Raman, EPR, TEM, SAED, HAADF-STEM, TG, SEM, ICP-AES, N_2 ISO (BET)	SEM, EDX, XPS, XRD, TEM, ICP-AES	5000 CV cycles 50 h CA	CoOOH	Precatalyst (full oxidation)	938
$Co_{0.85}Se$@C	GC	-	P	0.796	291	-	0.59 at 300 mV	75		XRD, XPS, Raman, EPR	XPS	-	-	-	
$FeSe_{2-x}$@C	GC	Nanoneedles	P	0.796	242	6	-	42		EPR, SEM, XRD	-	-	-	-	
$NiSe_{2-x}$@C	GC	Microspheres	P	0.796	270	16.5	-	92		EPR, SEM, XRD	-	-	-	-	
$NiSe_2$/$FeSe_2$	CC	Nanoparticles	P	0.3	256	18.3	-	50	1 M KOH	SEM, TEM, HAADF-STEM, EDX, XPS, XRD, N_2 ISO (BET, PSD)	SEM, XRD, XPS, TEM, Raman	15 h CA	Ni-Fe oxides/hydroxides, Se-O species	Precatalyst (partial oxidation)	939
$FeSe_2$	CC	Nanoparticles	P	0.3	338	18.9	-	139		XRD, SEM, TEM, XPS, N_2 ISO (BET, PSD)	-	-	-	-	
$CoSe_2$	CC	Nanoparticles	P	0.3	346	23.9	-	65		XRD, SEM, TEM, XPS, N_2 ISO (BET, PSD)	-	-	-	-	

https://doi.org/10.1021/acs.chemrev.3c00005
Chem. Rev. 2023, 123, 12795−13208

Table 6. continued

Initial Electrocatalyst	Substrate	Shape of Electro-catalyst	Deposi-tion Type	Specific Loading / $mg \cdot cm^{-2}_{geo}$	η@10 $mA \cdot cm^{-2}_{geo}$ / mV	C_{dl} / $mF \cdot cm^{-2}_{geo}$	TOF / s^{-1} (@η or j)	Tafel Slope / $mV \cdot dec^{-1}$	Electro-lyte	Pre-analysis	Post-analysis	Long-Term OER Test Conditions	Post-OER Electrocatalyst	Final Type of Electrocatalyst	Ref.
$NiSe_2$	CC	Nanoparticles	P	0.3	308	18	-	91	1 M KOH	XRD, SEM, TEM, XPS, N_2 ISO (BET, PSD)	-	-	-	-	939
$NiSe_2/CoSe_2$	CC	Nanoparticles	P	0.3	304	18.7	-	69		XRD, SEM, TEM, XPS, N_2 ISO (BET, PSD)	-	-	-	-	
NiFe-Se ($NiSe_2/Fe_2NiSe_4$)	CFP	Nanoparticles	P	0.5	281	0.41	-	40.93	1 M KOH	XRD, XPS, SEM, TEM, HAADF-STEM, EDX	XRD, XPS, SEM, TEM, HAADF-STEM	1000 CV cycles (1.2–1.9 V_{RHE}) 20 h CA	Ni-Fe (oxy)hydroxides, SeO_x	Precatalyst (partial oxidation)	940
$FeSe_2$	CFP	Nanoparticles	P	0.5	396	0.36	-	84.18		XRD, SEM	-	20 h CA	-	-	
$NiFe(OH)_x/(Ni, Fe)Se_2$	CC	Nanosheets	P	4.18	180	7.08	-	42	1 M KOH	XRD, Raman, SEM, TEM, EDX, HAADF-STEM	XRD, EDX, SEM, TEM	3000 CV cycles (1.1–1.8 V_{RHE}) 20 h CP (10 $mA \cdot cm^{-2}_{geo}$)	-	-	941
$(Ni, Fe)Se_2$	CC	Nanosheets	P	-	240	4.26	-	48		XPS, XRD, SEM, EDX	XRD, EDX, SEM, TEM	20 h CP (10 $mA \cdot cm^{-2}_{geo}$)	$NiFe(OH)_x$	Precatalyst (partial oxidation)	
Co–NiSe-1	Ni foam	-	S	-	~ 420 (@100 $mA \cdot cm^{-2}_{geo}$)	-	-	162.6	1 M KOH	XRD	-	-	-	-	942
Co–NiSe-2	Ni foam	Nanoflowers	S	-	380 (@100 $mA \cdot cm^{-2}_{geo}$)	-	-	111.0		XRD, SEM, Raman, TEM, EDX, XPS	Raman	2000 CV cycles 10 h CA (1.58 V_{RHE}) 11 h CA (1.55 V_{RHE})	-	Precatalyst	
Co–NiSe-3	Ni foam	-	S	-	~ 428 (@100 $mA \cdot cm^{-2}_{geo}$)	-	-	140.5		XRD	-	-	-	-	
NiSe	Ni foam	-	S	-	~ 443 (@100 $mA \cdot cm^{-2}_{geo}$)	-	-	239.0		XRD, Raman	-	-	-	-	
$CuCo_2Se_4$	CFP	Nanocorals	P	0.57	320 (@50 $mA \cdot cm^{-2}_{geo}$)	0.213	0.041 at 300 mV	66.5	1 M KOH	SEM, XPS, XRD	XRD, XPS, SEM	8 h CA (1.47 V_{RHE})	$M(OH)Se$, SeO_2	Precatalyst (partial oxidation)	943
$NiSe_2/CoSe_2$-N	CC	Nanohybrid	P	-	286	38.6	-	53	1 M KOH	EDX, TEM, HAADF-STEM, XAS, EXAFS	TEM, HETEM, XAS, EXAFS, XPS, XRD	1000 CV cycles (1.1–1.8 V_{RHE}) 15 h CP (10 $mA \cdot cm^{-2}_{geo}$) 15 h electrooxidation (2.0 V_{RHE}) 1 h electrooxidation (1.4 V_{RHE}) 1 h electrooxidation (1.3 V_{RHE})	NiOOH, CoOOH	Precatalyst (full & partial oxidation)	944
$NiSe_2/CoSe_2$-T	CC	Nanohybrid	P	-	337	26.1	-	65		TEM	XAS, EXAFS	-	-	-	
$NiSe_2$ -U	CC	Nanoparticles	P	-	389	-	-	83		XPS, TEM	XAS	-	-	-	
CuSe	Ni foam	Nanocorals	P	5.0	297	1.45	-	89	1 M KOH	SEM, EDX, TEM, SAED, XRD, XPS, ICP-AES	TEM, SAED, XPS	11 h CP (10 $mA \cdot cm^{-2}_{geo}$)	$Cu(OH)_2$, SeO_x	Precatalyst (partial oxidation)	945
$NiSe_2/NiFe_2Se_4$	NiFe alloy	Nanowrinkles	S	5	300 (@500 $mA \cdot cm^{-2}_{geo}$)	33.67	-	52.7	1 M KOH	XRD, XPS, SEM, EDX, TEM, SAED	*In-Situ* Raman, Raman, XPS, TEM, SEM	11 h CP (500 $mA \cdot cm^{-2}_{geo}$) 11 h CA (1.46 V_{RHE})	NiOOH, FeOOH	Precatalyst (partial oxidation)	946
$Ni_{0.7}Fe_{0.3}$–Se	NiFe alloy	-	S	5	340 (@500 $mA \cdot cm^{-2}_{geo}$)	-	-	-		-	-	-	-	-	
$Ni_{0.5}Fe_{0.5}$–Se	NiFe alloy	-	S	5	360 (@500 $mA \cdot cm^{-2}_{geo}$)	-	-	-		-	-	-	-	-	
NF-Se	Ni foam	-	S	4.7	270	16.48	-	105.7		-	-	-	-	-	
IF-Se	Fe foam	-	S	4.0	320	5.09	-	119.6		-	-	-	-	-	
$NiSe_{100}$	GC	Spherical particles	P	0.24	386	-	-	-	1 M KOH	XRD, SEM, XPS, Kr ISO (BET)	ICP-MS	6 h CP (10 $mA \cdot cm^{-2}_{geo}$)	-	Precatalyst	47
$NiSe@NiO_x$	Ni foam	Nanorods	S	4.25	243	10.96	-	128	1 M KOH	SEM, TEM, XRD, EDX, XPS, SAED, ICP-OES	-	40 h CP (16 $mA \cdot cm^{-2}_{geo}$)	NiO_x	Precatalyst (surface oxidized before the OER)	947
$NiSe_2$-$Ni(OH)_2$	CC	Nanotubes	S	-	190	-	1 at 250 mV	52.8	1 M KOH	XANES, TEM, EXAFS, EDX, XPS, SEM	-	100 h CP (10 $mA \cdot cm^{-2}_{geo}$)	NiOOH	Precatalyst (full oxidation)	948
$NiSe_2$@CNA	CC	Nanotubes	S	-	-	3.25	-	-		SEM, XRD, TEM, XAFS, EDX, XPS	SEM, TEM, XANES, EDX, XPS	15 h CP (10 $mA \cdot cm^{-2}_{geo}$)	NiOOH	Precatalyst (full oxidation)	
$NiSe_2$-$Ni(OH)_2$	GC	Nanotubes	P	3.12	310	-	-	-		-	-	-	-	-	
Fe-Ni_3Se_2	Ni foam	Spheres	S	1.2	225	1.9	-	35.3	1 M KOH	SEM, EDX, XRD, XPS	XRD, SEM, EDX	12 h CP (20 $mA \cdot cm^{-2}_{geo}$)	Metal oxides, Metal hydroxides	Precatalyst (partial oxidation)	949
Ni_3Se_2	Ni foam	Spheres	S	1.1	280	0.85	-	44.1		-	-	-	-	-	
$NiFe_{10}Se_{10}$	Ni foam	Nanosheets	S	-	199	6.11	-	40	1 M KOH	XRD, SEM, TEM, EDX, AFM, XPS	SEM, XPS, TEM, EDX	10 h CP (10 $mA \cdot cm^{-2}_{geo}$)	Metal oxides, Metal hydroxides	Precatalyst (partial oxidation)	950
$NiFe_5Se_{10}$	Ni foam	Nanosheets	S	-	260 (@50 $mA \cdot cm^{-2}_{geo}$)	-	-	-		SEM	-	-	-	-	
$NiFe_{10}Se_5$	Ni foam	Nanosheets	S	-	280 (@50 $mA \cdot cm^{-2}_{geo}$)	-	-	-		SEM	-	-	-	-	
$NiFe_{10}Se_{15}$	Ni foam	Nanosheets	S	-	245 (@50 $mA \cdot cm^{-2}_{geo}$)	-	-	-		SEM	-	-	-	-	
$NiSe_{10}$	Ni foam	Nanosheets	S	-	300	-	-	-		SEM	-	-	-	-	
NiSe	Ni foam	Nanoparticles	S	-	329 (@30 $mA \cdot cm^{-2}_{geo}$)	3.28	-	203.7	1 M KOH	XRD, Raman, SEM	SEM, Raman	50 h CP (100 $mA \cdot cm^{-2}_{geo}$)	NiOOH	Precatalyst (partial oxidation)	669
NiSSe	Ni foam	Nanoparticles	S	-	247 (@30 $mA \cdot cm^{-2}_{geo}$)	5.75	-	175.7		XRD, Raman, SEM, XPS	SEM, Raman	50 h CP (100 $mA \cdot cm^{-2}_{geo}$)	Ni_3S_2	Precatalyst	
$Ni_{0.85}Se$	CC	Nanosheets	P	-	500	-	-	120	1 M KOH	XRD, XPS, TEM	Raman	500 CV cycles (200 $mV \cdot s^{-1}$)	$NiSeO_3$, NiO	Precatalyst (full oxidation)	951
Ni_3Se_4	CC	Nanosheets	P	-	370	-	-	30		XRD, XPS, TEM, HAADF	Raman, TEM	500 CV cycles (200 $mV \cdot s^{-1}$)	$NiSeO_3$, NiO	Precatalyst (full oxidation)	
$NiSe_2$	CC	Nanosheets	P	-	400	-	-	90		XRD, XPS, TEM, HAADF	Raman	500 CV cycles (200 $mV \cdot s^{-1}$)	$NiSeO_3$, NiO	Precatalyst (full oxidation)	
$Fe_{7.4\%}$-NiSe	Ni foam	Nanorods + Nanosheets	S	3.1	231 (@50 $mA \cdot cm^{-2}_{geo}$)	9.5	-	43	1 M KOH	XRD, Raman, SEM, TEM, XPS, EDX	XRD, SEM, Raman, XPS	22 h CA (1.447 V_{RHE})	NiOOH	Precatalyst	952
$Fe_{10.1\%}$-NiSe	Ni foam	Nanorods + Nanosheets	S	-	250 (@50 $mA \cdot cm^{-2}_{geo}$)	-	-	-		XRD, SEM, EDX	-	-	-	-	

https://doi.org/10.1021/acs.chemrev.3c00005
Chem. Rev. 2023, 123, 12795−13208

Table 6. continued

Initial Electrocatalyst	Substrate	Shape of Electro-catalyst	Deposi-tion Type	Specific Loading / $mg \cdot cm^{-2}_{geo}$	η@10 $mA \cdot cm^{-2}_{geo}$ / mV	C_{dl} / $mF \cdot cm^{-2}_{geo}$	TOF / s^{-1} (@η or j)	Tafel Slope / $mV \cdot dec^{-1}$	Electro-lyte	Pre-analysis	Post-analysis	Long-Term OER Test Conditions	Post-OER Electrocatalyst	Final Type of Electrocatalyst	Ref.
NiSe	Ni foam	Nanorods	S	2.9	328 (@50 $mA \cdot cm^{-2}_{geo}$)	6.4	-	72.2	1 M KOH	XRD, Raman, SEM	-	-	-	-	952
$Fe_{3.2\%}$-NiSe	Ni foam	Nanorods + Nanosheets	S	-	290 (@50 $mA \cdot cm^{-2}_{geo}$)	-	-	-		XRD, SEM, EDX	-	-	-	-	
$CoSe_2$ UNM_{VAC}	GC	Nanosheets	P	0.28	284	-	2.27 at 300 mV	46.3	1 M KOH	TEM, AFM, EDX, XRD, EPR, XPS, FTIR	TEM, XPS	20 h CA (1.53 V_{RHE}) 2000 CV cycles	CoOOH	Precatalyst (partial oxidation)	953
$CoSe_2$ NS	GC	Nanosheets	P	0.28	343	-	0.51 at 300 mV	97.7		EPR, XPS, TEM, FTIR	-	2000 CV cycles	-	-	
$CoSe_2$ NP	GC	Nanoparticles	P	0.28	466	-	0.39 at 300 mV	111.1		SEM, XRD	-	2000 CV cycles	-	-	
NiFeSe@NiSe|O	CC	Nanosheets	S	-	270	43.7	2.88 at 350 mV	63.2	1 M KOH	SEM, XRD, TEM, XPS	XRD, XPS, SEM, TEM	50 h CA	Ni and Fe oxyhydroxides, Se-O species	Precatalyst (partial oxidation)	954
NiFeSe nanocubes	CC	Nanosheet + Nanocubes	S	-	310	14.2	2.19 at 350 mV	138		TEM	-	50 h CA	-	-	
NiSe|O	CC	Nanosheet	S	-	330	9.3	1.78 at 350 mV	140		XRD	-	50 h CA	-	-	
$Ti@Ni_{0.85}Se$-3 (better)	Ti mesh	Hierarchy architecture triple	S	2.55	270 (@30 $mA \cdot cm^{-2}_{geo}$)	44.6	-	102	1 M KOH	TEM, EDX, XPS, SEM, XRD	SEM, XPS, Raman, XRD	20 h CA (1.66 V_{RHE})	NiOOH	Precatalyst (partial oxidation)	955
$Ti@Ni_{0.85}Se$-4	Ti mesh	Hierarchy architecture triple	S	-	-	-	-	-		SEM	-	-	-	-	
$Ti+Ni_{0.85}Se$	Ti mesh	Nanoparticles	P	10	366 (@30 $mA \cdot cm^{-2}_{geo}$)	-	-	200		-	-	-	-	-	
$Ti@Ni_{0.85}Se$-1	Ti mesh	Nanosheets array triple	S	-	-	-	-	-		SEM	-	-	-	-	
$Ti@Ni_{0.85}Se$-2	Ti mesh	Hierarchy architecture triple	S	-	-	-	-	-		SEM	-	-	-	-	
$Ni_{0.35}Co_{0.65}Se_2$/CNW	Cu mesh	Nanowires + Nanosheets	S	-	193	3.6	0.015 at 300 mV	58	1 M KOH	XRD, SEM, TEM, XPS, EDX, FTIR	XRD, SEM, XPS	100 h CA (1.423 V_{RHE})	Ni and Co oxide/hydroxide species, SeO_x	Precatalyst (partial oxidation)	956
$NiSe_2$/CNW	Cu mesh	Nanowires + Nanosheets	S	-	340	1.7	0.0019 at 300 mV	147		XRD, SEM	-	-	-	-	
$CoSe_2$/CNW	Cu mesh	Nanowires + Nanosheets	S	-	293	1.8	0.0042 at 300 mV	196		XRD, SEM	-	-	-	-	
$Ni_{0.35}Co_{0.65}Se_2$/CONW	Cu mesh	Nanowires + Nanosheets	S	-	229	3.1	0.0099 at 300 mV	64		-	-	-	-	-	
$Ni_{0.5}Co_{0.5}Se_2$/CNW	Cu mesh	Nanowires + Nanosheets	S	-	267	2.2	0.0056 at 300 mV	104		XRD, SEM	-	-	-	-	
$Ni_{0.65}Co_{0.35}Se_2$/CNW	Cu mesh	Nanowires + Nanosheets	S	-	250	2.3	0.0069 at 300 mV	84		XRD, SEM	-	-	-	-	
$(Ni_{0.77}Fe_{0.23})Se_2$	CC	Nanosheets	S	-	228	-	-	69	1 M KOH	SEM, TEM, SAED, XPS, XRD, EDX	SEM, XPS	10 h CP (10 $mA \cdot cm^{-2}_{geo}$)	Metal oxides, Metal hydroxides	Precatalyst (partial oxidation)	957
$Ni_{1-x}Fe_xSe_2$	CFP	Nanowires	S	3.2	230	0.562	-	30	1 M KOH	SEM, EDX, TEM, XRD	TEM	-	Metal oxides, Metal hydroxides	Precatalyst (partial oxidation)	958
$Ni_{1-x}Co_xSe_2$	CFP	Nanowires	S	2.4	264	0.569	-	90		SEM, EDX, TEM, XRD	TEM	-	Metal oxides, Metal hydroxides	Precatalyst (partial oxidation)	
$Ni_{1-x}Cu_xSe_2$	CFP	Nanowires	S	2	334	0.705	-	93		SEM, EDX, TEM, XRD	TEM	-	Metal oxides, Metal hydroxides	Precatalyst (partial oxidation)	
$NiSe_2$	CFP	Nanowires	S	-	330	0.771	-	91		SEM, TEM, XRD	-	-	-	-	
$Ni_{1-y}Fe_ySe_{2-y}$-OOH	CFP	Nanosheets	S	-	211	0.936	-	21		SEM, TEM, AFM, XRD, EDX, ICP-AES, XPS	TEM	120 h CP (100 $mA \cdot cm^{-2}_{geo}$)	-	-	
$Ni_{1-y}Co_ySe_{2-y}$-OOH	CFP	Nanosheets	S	-	233	1.01	-	56		SEM, TEM, AFM, XRD, XPS	TEM	-	-	-	
$Ni_{1-y}Cu_ySe_{2-y}$-OOH	CFP	Nanosheets	S	-	256	1.05	-	67		SEM, TEM, AFM, XRD, XPS	TEM	-	-	-	
$NiSe_{2-y}$-OOH	CFP	Nanosheets	S	-	321	0.985	-	71		XRD, TEM	-	-	-	-	
$Co_1Ni_{0.5}Se$ NBs	GC	Nano Bundles	P	-	250	15.6	-	48	1 M KOH	TEM, EDX, XRD, XPS	TEM, EDX, XPS	35 h CP (10 $mA \cdot cm^{-2}_{geo}$) 3000 CV cycles (−0.05–0.05 $V_{Ag/AgCl}$)	Metal oxides, Metal hydroxides	Precatalyst (partial oxidation)	959
$Co_1Ni_{0.5}Se$ NBs	GC	Nano Bundles	P	-	274	7.3	-	62		XRD, TEM, EDX	-	-	-	-	
Co_1Ni_1Se NBs	GC	Nano Bundles	P	-	315	14.7	-	79.2		XRD, TEM, EDX	-	-	-	-	
CoSe@NiFe-LDH/NF	Ni foam	Nanotubes + Nanosheets	S	1.5	201	15.7	-	39	1 M KOH	XRD, SEM, TEM, SAED, XPS	SEM, XPS	18 h CP (10 $mA \cdot cm^{-2}_{geo}$)	Metal oxides, Metal hydroxides	Precatalyst (partial oxidation)	960
CoSe/NF	Ni foam	Nanotubes	S	-	265	6.75	-	65		XRD, SEM	SEM	-	-	-	
Cu_2Se	CF	Intersecting nanosheet into nanotubes	S	10.5	200	17.09	-	150	1 M KOH	XRD, XPS, SEM, TEM	SEM, XRD, XPS, TEM	12 h CP (10 $mA \cdot cm^{-2}_{geo}$)	CuO	Precatalyst (full oxidation)	961
$(Ni,Co)Se_2$	Ni foam	Nanocubes	P	3	278	-	-	65	3 M KOH	XRD, SEM, TEM, XPS, EDX	SEM, XRD	20 h CP (10 $mA \cdot cm^{-2}_{geo}$)	(Ni,Co)OOH	Precatalyst (full oxidation)	962
$CoSe_2$	Ni foam	Nanocubes	P	3	325	-	-	91		XRD, SEM, TEM	-	-	-	-	
Co_7Se_8/MXene	CC	Nanoparticles + Nanosheets	P	1.5	291	2.5	0.0013 at 300 mV	81.5	1 M KOH	TEM, SEM, XPS, EDX, ICP-OES, XRD	XPS, TEM, EDX, ICP-OES	24 h CP (50 $mA \cdot cm^{-2}_{geo}$)	CoOOH	Precatalyst (full oxidation)	963
Co_7Se_8	CC	Nanoparticles	P	1.5	325	1.4	0.00053 at 300 mV	97		SEM	-	-	-	-	
CoNiSe/NC-3	CC	Nanospheres	P	0.24	270	0.0386	-	60.5	1 M KOH	SEM, TEM, XPS	SEM, XRD, XPS	6 h CA (1.5 V_{RHE})	Metal oxides, Metal hydroxides	Precatalyst (partial oxidation)	964

https://doi.org/10.1021/acs.chemrev.3c00005
Chem. Rev. 2023, 123, 12795−13208

Table 6. continued

Initial Electrocatalyst	Substrate	Shape of Electro-catalyst	Deposi-tion Type	Specific Loading / $mg \cdot cm^{-2}_{geo}$	η@10 $mA \cdot cm^{-2}_{geo}$ / mV	C_{dl} / $mF \cdot cm^{-2}_{geo}$	TOF / s^{-1} (@η or j)	Tafel Slope / $mV \cdot dec^{-1}$	Electro-lyte	Pre-analysis	Post-analysis	Long-Term OER Test Conditions	Post-OER Electrocatalyst	Final Type of Electrocatalyst	Ref.
CoSe/NC-1	CC	Nanospheres	P	0.24	350	0.0103	-	98		-	-	-	-	-	
CoNiSe/NC-2	CC	Nanospheres	P	0.24	320	0.0175	-	78.7		-	-	-	-	-	964
CoNiSe/NC-4	CC	Nanospheres	P	0.24	330	0.0175	-	85		-	-	-	-	-	
NiSe/NC-5	CC	Nanospheres	P	0.24	340	0.077	-	103		-	-	-	-	-	
$Co_{0.85}Se$-hyd	CC	Nanoparticles (agglomerated) + chain	P	0.205	354	0.92 μF	-	65	1 M KOH	XRD, TEM, XPS	XRD, Raman, TEM, HAADF	24 h CA (1.724 V_{RHE})	Metal oxides, Metal hydroxides	Precatalyst (partial oxidation)	965
CoSe-DNA	CC	Nanoparticles + chain	P	0.205	383	0.5 μF	-	71		XRD, TEM, HAADF, XPS	-	24 h CA (1.674 V_{RHE})	-	-	
CoSe	CC	Nanoparticles	P	0.205	382	0.3 μF	-	80		XRD, TEM	-	24 h CA (1.674 V_{RHE})	-	-	
5% Fe-$NiSe_2$	GC	Nanosphere	P	0.2	231	-	0.052 at 270 mV	83	1 M KOH	SEM, XRD, XPS, TEM, SAED, EDX, Raman	XRD, EDX, XPS	20 h CP (15 $mA \cdot cm^{-2}_{geo}$)	Metal oxides, Metal hydroxides	Precatalyst (partial oxidation)	966
1% Fe-$NiSe_2$	GC	Nanosphere	P	0.2	280	-	0.025 at 270 mV	99		SEM, XRD, XPS, TEM, Raman	-	-	-	-	
3% Fe-NiSe	GC	Nanosphere	P	0.2	260	-	0.03 at 270 mV	89		SEM, XRD, XPS, TEM, Raman	-	-	-	-	
7% Fe-$NiSe_2$	GC	Nanosphere	P	0.2	280	-	0.016 at 270 mV	88		SEM, XRD, XPS, TEM, Raman	-	-	-	-	
$NiSe_2$	GC	Nanosphere	P	0.2	324	-	0.013 at 270 mV	114		SEM, XRD, XPS, TEM, Raman	-	-	-	-	
$Fe_{0.125}Ni_{0.875}Se_2$	GC	Nanotubes	P	0.35	250	1.07	0.063 at 320 mV	49	1 M KOH	SEM, TEM, SAED, ICP-MS, XRD, Raman, XPS	SEM, TEM, EDX, ICP-MS	10 h CP (10 $mA \cdot cm^{-2}_{geo}$) 1000 CV cycles	Metal oxides, Metal hydroxides	Precatalyst (partial oxidation)	967
$Fe_{0.25}Ni_{0.75}Se_2$	GC	Nanotubes	P	0.35	290	0.75	0.025 at 320 mV	73		-			-	-	
$Fe_{0.5}Ni_{0.5}Se_2$	GC	Nanotubes	P	0.35	405	0.41	0.005 at 320 mV	93		-			-	-	
$Fe_{0.063}Ni_{0.937}Se_2$	GC	Nanotubes	P	0.35	327	0.62	0.013 at 320 mV	87		-			-	-	
$NiSe_2$	GC	Nanoparticles	P	0.35	425	0.21	0.003 at 320 mV	121		XRD, Raman, XPS			-	-	
Cu-14-Co_3Se_4/GC	GC	Nano tubes + sheets	P	0.51	280	-	-	111	1 M KOH	XRD, N_2 ISO (BET, PSD), XPS, SEM, TEM, EDX	SEM, TEM, XPS, EDX	3.5 h CP (100 $mA \cdot cm^{-2}_{geo}$)	Metal oxides, Metal hydroxides	Precatalyst (partial oxidation)	968
$CoSe_2$/GC	GC	Nano tubes + sheets	P	0.51	340	-	-	128		XRD, N_2 ISO (BET, PSD), XPS	-	-	-	-	
$CoSe_2$	GC	Nano tubes + sheets	P	0.51	370	-	-	221		XRD, N_2 ISO (BET, PSD), XPS	-	-	-	-	
EG/(Co, Ni)Se_2-NC	GF	Nanoparticles (core@shell)	S	-	258	53.8	-	73.3	1 M KOH	SEM, EDX, XRD, XPS, TEM	Raman, XPS, TEM, SEM	10 h CP (20 $mA \cdot cm^{-2}_{geo}$)	CoO_2/CoOOH	Precatalyst (partial oxidation)	969
EG/(Co, Ni)Se_2	GF	Nanoparticles	S	-	285	53.1	-	87.2		-	-	10 h CP (20 $mA \cdot cm^{-2}_{geo}$)	-	-	
EG/CoSe-NC	GF	Nanoparticles	S	-	310	48.5	-	90.7		-	-	10 h CP (20 $mA \cdot cm^{-2}_{geo}$)	-	-	
EG/Ni_3Se_2	GF	Nanoparticles	S	-	394	45.5	-	230		-	-	10 h CP (20 $mA \cdot cm^{-2}_{geo}$)	-	-	
CuCoSe-12h	Ni foam	Nanowires	S	-	238	4.95	-	62	1 M KOH	SEM, TEM, EDX, SAED, XPS, Raman	XPS, Raman, TEM, SAED, XRD	20 h CP (10 $mA \cdot cm^{-2}_{geo}$)	CoOOH	Precatalyst (full oxidation)	970
CuCoSe-24h	Ni foam	Nanotube	S	-	250	3.89	-	90		XRD, SEM	-	-	-	-	
CuSe-12h	Ni foam	Nanosheet	S	-	370 (@40 $mA \cdot cm^{-2}_{geo}$)	-	-	-		SEM	-	-	-	-	
CoSe-12h	Ni foam	Nanowire	S	-	300 (@40 $mA \cdot cm^{-2}_{geo}$)	-	-	-		SEM	-	-	-	-	
NiSe-PANI	Ni foam	Microspheres	S	-	280	-	-	-	1 M KOH	SEM, TEM, XRD, Raman, XPS, EDX	SEM, XRD, XPS, TEM	70 h CP (30 $mA \cdot cm^{-2}_{geo}$)	Ni-oxides, Ni-hydroxides	Precatalyst	971
NiSe	Ni foam	Microspheres	S	-	180	-	-	-		XRD, Raman, XPS	-	-	-	-	
p-NiSe/NGr	GC	Nanosheets	P	0.18	311	2.56	0.132 at 300 mV	44	1 M KOH	XRD, N_2 ISO (BET, PSD), SEM, TEM, Raman, EDX, XPS, TGA	XRD, TEM	10 h CP (10 $mA \cdot cm^{-2}_{geo}$)	$NiOOH/\alpha$-$Ni(OH)_2$	Precatalyst (partial oxidation)	972
ZnNiSe/NGr	GC	Nanosheets	P	0.18	330	-	-	-		TEM	-	-	-	-	

https://doi.org/10.1021/acs.chemrev.3c00005
Chem. Rev. 2023, 123, 12795−13208

Table 6. continued

Initial Electrocatalyst	Substrate	Shape of Electrocatalyst	Deposition Type	Specific Loading/ $mg \cdot cm^{-2}_{geo}$	η@10 $mA \cdot cm^{-2}_{geo}$/ mV	C_{dl}/ $mF \cdot cm^{-2}_{geo}$	TOF/s^{-1} (@η or f)	Tafel Slope/ $mV \cdot dec^{-1}$	Electrolyte	Pre-analysis	Post-analysis	Long-Term OER Test Conditions	Post-OER Electrocatalyst	Final Type of Electrocatalyst	Ref.
Mn-Co-Se	Ni foam	Microsphere (egg yolk)	P	0.9	243	57	-	62	1 M KOH	XRD, XPS, SEM, TEM, EDX, ICP-MS, SAED, HAADF	XPS	3000 CV cycles (1.07−1.17 V_{RHE})	MnCo oxides	Precatalyst	973
Co-Se1	Ni foam	Nanoparticles	P	-	280 (@100 $mA \cdot cm^{-2}_{geo}$)	-	-	40.4	1 M KOH	SEM, TEM, XPS, XRD, EDX, SAED, XANES, EXAFS	XRD, SEM, EDX	12 h CP (20 $mA \cdot cm^{-2}_{geo}$)	CoOOH	Precatalyst (partial oxidation)	974
Co-Se2	Ni foam	Nanoparticles	P	-	380 (@100 $mA \cdot cm^{-2}_{geo}$)	-	-	-		-	-	-	-	-	
Co-Se3	Ni foam	Nanoparticles	P	-	400 (@100 $mA \cdot cm^{-2}_{geo}$)	-	-	-		-	-	-	-	-	
Co-Se4	Ni foam	Nanoparticles	P	-	410 (@100 $mA \cdot cm^{-2}_{geo}$)	-	-	70.9		SEM, TEM, XPS, XRD, EDX, SAED, XANES, EXAFS	-	-	-	-	
Co-Se5	Ni foam	Nanoparticles	P	-	407 (@100 $mA \cdot cm^{-2}_{geo}$)	-	-	-		-	-	-	-	-	
Ni-Fe-$Se_{1:1}$-180	GC	Nanoparticles	P	0.42	216	-	-	36	1 M KOH	XRD, FTIR, SEM, TEM, XPS, N_2 ISO (BET), TGA, XRF	XPS, XRD	12 h CP (20 $mA \cdot cm^{-2}_{geo}$)	Metal oxides, Metal hydroxides	Precatalyst (partial oxidation)	975
Ni-Fe-$Se_{1:3}$-180	GC	Nanoparticles	P	0.42	260	-	-	-		XRD, FTIR	-	-	-	-	
Ni-Fe-$Se_{1:3}$-180	GC	Nanoparticles	P	0.42	275	-	-	-		XRD, FTIR	-	-	-	-	
Ni-Fe-$Se_{1:1}$-140	GC	Nanoparticles	P	0.42	255	-	-	-		XRD, FTIR	-	-	-	-	
Ni-Fe-$Se_{1:1}$-160	GC	Nanoparticles	P	0.42	250	-	-	-		XRD, FTIR	-	-	-	-	
Ni-Fe-$Se_{1:1}$-200	GC	Nanoparticles	P	0.42	225	-	-	-		XRD, FTIR	-	-	-	-	
$NiCoSe_2$@NiO@ $CoNi_2S_4$@CoS_2	Ni foam	Nanosheets	S	-	310 (@30 $mA \cdot cm^{-2}_{geo}$)	126.1	-	159.1	1 M KOH	XRD, XPS, SEM, TEM, EDX	SEM, XRD, XPS	24 h CP (10 $mA \cdot cm^{-2}_{geo}$)	FeOOH, Co-based oxides, hydroxides, and oxyhydroxides	Precatalyst (partial oxidation)	782
$NiCoSe_2$@NiO	Ni foam	Nanosheets	S	-	369 (@30 $mA \cdot cm^{-2}_{geo}$)	58.3	-	232.3		-	-	-	-	-	
$CoNi_2S_4$@CoS_2	Ni foam	Nanosheets	S	-	365 (@30 $mA \cdot cm^{-2}_{geo}$)	66.1	-	237.6		SEM	-	-	-	-	
Fe_2O_3@Ni_3Se_4 ($I_{Ni:Fe}$ = 1:10)	GC	Nanotubes	P	-	246	-	-	51	1 M KOH	XRD, SEM, TEM, XPS, EDX	XPS	15 h CP (20 $mA \cdot cm^{-2}_{geo}$)	Metal oxides, Metal hydroxides	Precatalyst (partial oxidation)	976
Fe_2O_3@Ni_3Se_4 ($I_{Ni:Fe}$ = 11:50)	GC	Nanotubes	P	-	267	-	-	59		XRD, SEM, TEM	-	-	-	-	
Fe_2O_3@Ni_3Se_4 ($I_{Ni:Fe}$ = 2:25)	GC	Nanotubes	P	-	332	-	-	145		XRD, SEM, TEM	-	-	-	-	
Ni_3Se_4	GC	Nanoparticles	P	-	292	-	-	72		XRD	-	-	-	-	
$Co_{0.75}Fe_{0.25}$-Se	Ni foam	Nanoparticles	P	2.9	246	2.1	0.017 at 300 mV	41.4	1 M KOH	XRD, ICP-AES, TEM, EDX, XPS	XPS	40 h CP (10 $mA \cdot cm^{-2}_{geo}$)	Co/Fe oxo/hydroxide	Precatalyst (partial oxidation)	977
$Co_{0.69}Fe_{0.31}$-Se	Ni foam	Nanoparticles	P	2.9	247	1.7	0.013 at 300 mV	44.6		XRD, ICP-AES	-	-	-	-	
$Co_{0.51}Fe_{0.49}$-Se	Ni foam	Nanoparticles	P	2.9	261	1.5	0.0073 at 300 mV	46.9		XRD, ICP-AES	-	-	-	-	
$FeSe_2$	GC	Nanoparticles	P	2.9	286	1.2	0.0038 at 300 mV	47.7		XRD, ICP-AES, TEM	-	-	-	-	
CoSe	Ni foam	Nanoparticles	P	2.9	303	1.7	0.0012 at 300 mV	74.4		XRD, XPS, TEM, ICP-AES	-	-	-	-	
$Co_{0.93}Fe_{0.07}$-Se	Ni foam	Nanoparticles	P	2.9	264	1.5	0.0061 at 300 mV	50.7		XRD, ICP-AES	-	-	-	-	
$Co_{0.85}Fe_{0.15}$-Se	Ni foam	Nanoparticles	P	2.9	248	1.5	0.012 at 300 mV	46.7		XRD, ICP-AES	-	-	-	-	
$Co_4Mn_1Se_2$	-	Nanosheets	P	0.2	274	50.5	-	39	1 M KOH	XRD, Raman, XPS, TEM, EDX, AFM, ICP-AES	TEM, XRD, XPS	7 h CP (10 $mA \cdot cm^{-2}_{geo}$)	Metal oxides, Metal hydroxides	Precatalyst (partial oxidation)	978
$Co_1Mn_1Se_2$	-	Nanosheets	P	0.2	330	-	-	-		XRD, Raman, XPS, TEM, ICP-AES	-	-	-	-	
$Co_2Mn_1Se_2$	-	Nanosheets	P	0.2	317	-	-	-		XRD, Raman, XPS, TEM, ICP-AES	-	-	-	-	
$CoSe_2$	-	Nanosheets	P	0.2	317	43.6	-	48		XRD, Raman, XPS, TEM	-	-	-	-	
Fe-NiSe-3	Ni foam	Nanoparticles	P	-	220	7.6	-	43	1 M KOH	XRD, SEM, TEM, EDX, XPS, N_2 ISO (BET), ICP-AES, Raman	XPS, SEM	20 h CP (10 $mA \cdot cm^{-2}_{geo}$) 1000 CV cycles (1.2−1.7 V_{RHE})	NiOOH	Precatalyst (partial oxidation)	979
Fe-NiSe-1	Ni foam	Nanoparticles	P	-	250	-	-	-		ICP-AES	-	-	-	-	
Fe-NiSe-5	Ni foam	Nanoparticles	P	-	255	-	-	-		ICP-AES	-	-	-	-	
NiSe	Ni foam	Nanoparticles	P	-	255	3.1	-	54		SEM, EDX, XPS, XRD	-	-	-	-	
(1:1)(Ni, $Co)_{0.85}$Se-8h	Ni foam	Nanosheets	S	-	355 (@100 $mA \cdot cm^{-2}_{geo}$)	3.55	-	86.75	1 M KOH	SEM, XRD, TEM, EDX, XPS,	SEM, XRD, XPS	12 h CP (72 $mA \cdot cm^{-2}_{geo}$) 2000 CV cycles (−0.3−0.3 V_{RHE})	NiOOH/CoOOH	Precatalyst (partial oxidation)	980
(1:1)(Ni, $Co)_{0.85}$Se-1h	Ni foam	Nanosheets	S	-	390 (@100 $mA \cdot cm^{-2}_{geo}$)	-	-	-		SEM	-	-	-	-	
(1:1)(Ni, $Co)_{0.85}$Se-2h	Ni foam	Nanosheets	S	-	372 (@100 $mA \cdot cm^{-2}_{geo}$)	-	-	-		SEM	-	-	-	-	
(1:1)(Ni, $Co)_{0.85}$Se-24h	Ni foam	Nanosheets	S	-	403 (@100 $mA \cdot cm^{-2}_{geo}$)	-	-	-		SEM	-	-	-	-	
(2:1)(Ni, $Co)_{0.85}$Se-8h	Ni foam	Nanosheets	S	-	400 (@100 $mA \cdot cm^{-2}_{geo}$)	-	-	-		SEM, XRD	-	-	-	-	
(1:2)(Ni, $Co)_{0.85}$Se-8h	Ni foam	Nanosheets	S	-	380 (@100 $mA \cdot cm^{-2}_{geo}$)	-	-	-		SEM, XRD	-	-	-	-	

https://doi.org/10.1021/acs.chemrev.3c00005
Chem. Rev. 2023, 123, 12795−13208

Table 6. continued

Initial Electrocatalyst	Substrate	Shape of Electrocatalyst	Deposition Type	Specific Loading/ $mg \cdot cm^{-2}_{geo}$	η@10 $mA \cdot cm^{-2}_{geo}$/ mV	C_{dl}/ $mF \cdot cm^{-2}_{geo}$	TOF/s^{-1} (@η or j)	Tafel Slope/ $mV \cdot dec^{-1}$	Electrolyte	Pre-analysis	Post-analysis	Long-Term OER Test Conditions	Post-OER Electrocatalyst	Final Type of Electrocatalyst	Ref.
$Co_{0.85}Se$/NF	Ni foam	Nanosheets + Nanotubes	S	0.6	232	-	-	78.9	1 M KOH	XRD, SEM, TEM, EDX, XPS	SEM, TEM, XPS, XRD	160 h CP (20 $mA \cdot cm^{-2}_{geo}$)	SeO_x	Precatalyst (partial oxidation)	981
$(Ni, Fe)_3Se_4$	GC	Nanosheets	P	0.673	250	5.94	0.044 at 300 mV	41	1 M KOH	XRD, TEM, AFM, SEM, XPS, EDX, N_2 ISO (BET, PSD)	EDX, TEM, XPS	26 h CP (10 $mA \cdot cm^{-2}_{geo}$)	Metal oxides, Metal hydroxides	Precatalyst (partial oxidation)	982
$(Ni, Fe)_3Se_4$	Ni foam	Nanosheets	P	1.5	225	-	-	-		XRD, TEM, AFM, SEM, XPS, EDX, N_2 ISO (BET, PSD)	-	-	-	-	
Ni_3Se_4	GC	Nanosheets	P	0.673	320	2.74	0.003 at 300 mV	140		XRD, TEM, SEM	-	-	-	-	
$FeSe_2$/rGO	GC	Nanosheet + Nanoparticles	P	0.14	475	0.05	0.0023(Fe) at 350 mV	87.77	1 M KOH	XRD, XPS, Raman, SEM, TEM, N_2 ISO (BET)	XPS, XRD	-	Metal oxides, Metal hydroxides	Precatalyst (partial oxidation)	983
$FeSe_2$@$CoSe_2$/ rGO-2	GC	Nanosheet + Nanoparticles	P	0.14	260	1.15	0.661(Co), 0.588(Fe) at 350 mV	36.3		XRD, XPS, TEM, EDX, SEM, Raman, N_2 ISO (BET)	XPS, XRD	6 h CA (1.59 V_{RHE}) 1000 CV cycles (0.2–0.7 $V_{Ag/AgCl}$)	Metal oxides, Metal hydroxides [$Co_{1-x}Fe_x(OOH)$ likely]	Precatalyst (partial oxidation)	
$CoSe_2$/rGO	GC	Nanosheet + Nanoparticles	P	0.14	370	0.75	0.028(Co) at 350 mV	85		XRD, XPS, Raman, N_2 ISO (BET)	XPS, XRD	-	Metal oxides, Metal hydroxides	Precatalyst (partial oxidation)	
$FeSe_2$@$CoSe_2$/ rGO-1	GC	Nanosheet + Nanoparticles	P	0.14	278	0.42	0.865(Co), 0.351(Fe) at 350 mV	38.2		XRD, XPS, Raman, N_2 ISO (BET)	-	-	-	-	
$FeSe_2$@$CoSe_2$/ rGO-3	GC	Nanosheet + Nanoparticles	P	0.14	312	0.35	0.128(Co), 0.135(Fe) at 350 mV	51.5		XRD, XPS, Raman, N_2 ISO (BET)	-	-	-	-	
$FeSe_2$@$CoSe_2$/ rGO-2	GC	Nanosheet + Nanoparticles	P	0.14	336	-	-	57.7	0.1 M KOH	XRD, XPS, Raman, N_2 ISO (BET)	-	-	-	-	
CoSe	FTO	Nanocrystals	P	-	425	-	0.00346 at 350 mV	67	1 M KOH	XRD, TEM	XRD, ICP-OES	-	Metal oxides, Metal hydroxides	Precatalyst (full oxidation)	984
$Ni_{0.3}Co_{0.74}Se$	FTO	Nanocrystals	P	-	397	-	0.01009 at 350 mV	76		XRD, TEM, EDX, XPS, FTIR	XRD, ICP-OES, TEM, XPS, FTIR, EDX	-	Ni-Co oxides and hydroxides	Precatalyst (full oxidation)	
NiSe	FTO	Nanocrystals	P	-	-	-	0.00004 at 350 mV	286		XRD, TEM	XRD, ICP-OES	-	Ni-Co oxides and hydroxides	Precatalyst (partial oxidation)	
$Ni_{0.25}Co_{0.65}S_{0.4}Se_{0.6}$	FTO	Nanocrystals	P	-	358	-	0.02484 at 350 mV	64		XRD, TEM, EDX, XPS	TEM, XPS, XRD, EDX	8 h CP (10 $mA \cdot cm^{-2}_{geo}$)	Metal oxides, Metal hydroxides	Precatalyst	
$Ni_{0.52}Co_{0.56}Se$	FTO	Nanocrystals	P	-	520	-	0.00045 at 350 mV	83		XRD, TEM	-	-	-	-	
$Ni_{0.78}Co_{0.28}Se$	FTO	Nanocrystals	P	-	-	-	0.00023 at 350 mV	184		XRD, TEM	-	-	-	-	
$Ni_{0.78}Co_{0.28}S_{0.2}Se_{0.8}$	FTO	Nanocrystals	P	-	373	-	0.01588 at 350 mV	64		XRD, TEM	-	-	-	-	
$NiCoSe_{2-x}$/NC	CF	Mushroom like core/shell nanorods	S	8.40741	215	-	-	75	1 M KOH	XRD, Raman, SEM, TEM, XPS, EDX	XPS, SEM, TEM, EDX	10 h CP (100 $mA \cdot cm^{-2}_{geo}$)	Metal oxides, Metal hydroxides	Precatalyst (partial oxidation)	985
Ni_3Se_4	CF	Nanoparticles	S	8.40741	443	-	-	90		XRD, Raman, SEM, EDX	SEM, EDX	10 h CP (2 $mA \cdot cm^{-2}_{geo}$)	Metal oxides, Metal hydroxides	Precatalyst (partial oxidation)	
CoSe	CF	Nanoparticles	S	8.40741	338	-	-	85		XRD, Raman, SEM	SEM, EDX	10 h CP (5 $mA \cdot cm^{-2}_{geo}$)	Metal oxides, Metal hydroxides	Precatalyst (partial oxidation)	
NiSe-$NiSe_{0.85}$/CP	CP	Nanoflakes	S	1.68	300	35.9	0.0135 at 300 mV	98	1 M KOH	XRD, XPS, SEM, TEM	SEM, XPS, XRD	48 h CP (200 $mA \cdot cm^{-2}_{geo}$) 3000 CV cycles	Ni oxides and hydroxides	Precatalyst (partial oxidation)	986
NiSe/CP	CP	Nanoflakes	S	1.63	390	9.5	-	138		XRD, SEM	-	-	-	-	
$NiSe_{0.85}$/CP	CP	Nanoflakes	S	1.7	420	5.9	-	210		XRD, SEM	-	-	-	-	
Fe-Ni-Se	Ni foam	Nanorods	S	3	290 (@60 $mA \cdot cm^{-2}_{geo}$)	14.1	-	61	1 M KOH	XRD, SEM, TEM, EDX	TEM, EDX	30 h CA (1.49 V_{RHE})	Ni/Fe oxides and hydroxides	Precatalyst (partial oxidation)	987
Ni-Se	Ni foam	Nanorods	S	3	360 (@60 $mA \cdot cm^{-2}_{geo}$)	11.2	-	73		XRD, SEM, TEM	-	-	-	-	
$CoSe_2$	CC	Nanorods	S	-	170	91.34	-	107	1 M KOH	XRD, XPS, SEM, TEM	TEM, XPS	10 h CP (15 $mA \cdot cm^{-2}_{geo}$) 10 h CA (1.42 V_{RHE})	$Co(OH)_2$/CoOOH	Precatalyst (full oxidation)	988
$Fe_{0.09}Co_{0.13}$-$NiSe_2$	CFC	Nanosheets	S	-	251	4.29	-	63	1 M KOH	SEM, XRD, TEM, XPS, N_2 ISO (BET, PSD), EDX, Raman	TEM, XRD, SEM, Raman, XPS, ICP-AES	50 h CP (10 $mA \cdot cm^{-2}_{geo}$) 3000 CV cycles	Ni(Co, Fe)O_xH_y/ $Fe_{0.09}Co_{0.13}$-$NiSe_2$	Precatalyst (partial oxidation)	989
$NiSe_2$	CFC	Nanosheets	S	-	320	1.42	-	105		XPS, XRD	-	-	-	-	
$Fe_{0.2}$-$NiSe_2$	CFC	Nanosheets	S	-	280	3.36	-	88		XPS, SEM, XRD, EDX	-	-	-	-	
$Co_{0.2}$-$NiSe_2$	CFC	Nanosheets	S	-	295	2.41	-	95		XPS, SEM, XRD, EDX	-	-	-	-	
$Fe_{0.16}Co_{0.06}$-$NiSe_2$	CFC	Nanosheets	S	-	285	-	-	-		SEM, XRD, EDX	-	-	-	-	
$Fe_{0.04}Co_{0.17}$-$NiSe_2$	CFC	Nanosheets	S	-	291	-	-	-		SEM, XRD, EDX	-	-	-	-	
$Ni_{0.75}Fe_{0.25}Se_2$	GC	Nanochains	P	0.255	286 (@20 $mA \cdot cm^{-2}_{geo}$)	1.23	0.7 at 500 mV	67	1 M KOH	XRD, SEM, TEM, EDX, XPS, N_2 ISO (BET, PSD)	SEM, EDX, XRD, XPS, TEM	12 h CP (10 $mA \cdot cm^{-2}_{geo}$)	NiFe oxy-hydroxides	Precatalyst (full oxidation)	990
$Ni_{0.5}Fe_{0.5}Se_2$	GC	Nanochains	P	0.255	340 (@50 $mA \cdot cm^{-2}_{geo}$)	-	-	-		XRD	-	-	-	-	
$Ni_{0.25}Fe_{0.75}Se_2$	GC	Nanochains	P	0.255	390 (@50 $mA \cdot cm^{-2}_{geo}$)	-	-	-		XRD	-	-	-	-	
$NiSe_2$	GC	Nanochains	P	0.255	356 (@20 $mA \cdot cm^{-2}_{geo}$)	0.82	0.31 at 500 mV	91		XRD, SEM, EDX, XPS	-	-	-	-	

https://doi.org/10.1021/acs.chemrev.3c00005
Chem. Rev. 2023, 123, 12795−13208

Table 6. continued

Initial Electrocatalyst	Substrate	Shape of Electrocatalyst	Deposition Type	Specific Loading/ $mg \cdot cm^{-2}_{geo}$	η@10 $mA \cdot cm^{-2}_{geo}$/ mV	C_{dl}/ $mF \cdot cm^{-2}_{geo}$	TOF/s^{-1} (@η or j)	Tafel Slope/ $mV \cdot dec^{-1}$	Electrolyte	Pre-analysis	Post-analysis	Long-Term OER Test Conditions	Post-OER Electrocatalyst	Final Type of Electrocatalyst	Ref.
2-tier NiSe	Ni foam	Nanosheets	S	0.69	290	32.8	1.87 at 470 mV	77.1	1 M NaOH	SEM, TEM, EDX, XRD, AFM, XPS	SEM, XPS	30 h CP (10, 20, 10 $mA \cdot cm^{-2}_{geo}$)	NiOOH	Precatalyst	991
$Ni_{0.76}Fe_{0.24}Se$	Ni foam	Nanosheets	S	-	197	17.4	-	56	1 M KOH	XRD, SEM, TEM, EDX, ICP-AES, XPS, N_2 ISO (BET, PSD)	SEM, XRD, XPS	60000 s CP (10 $mA \cdot cm^{-2}_{geo}$) 500 CV cycles (0.3−0.9 $V_{Hg/HgO}$)	Ni(Fe) oxo/hydroxide	Precatalyst (partial oxidation)	992
$Ni_{0.82}Fe_{0.18}Se$	Ni foam	Nanosheets/ Nanoclusters	S	-	205	-	-	62		ICP-AES	-	-	-	-	
$Ni_{0.5}Fe_{0.5}Se$	Ni foam	Nanosheets/ Nanoclusters	S	-	205	-	-	60		ICP-AES	-	-	-	-	
NiSe	Ni foam	Nanosheets	S	-	217	13.5	-	73		XRD, N_2 ISO (BET, PSD), SEM, XPS	-	-	-	-	
$NiCoSe_2$/NF	Ni foam	Nanosheets	S	-	183	4.32	-	97	1 M KOH	SEM, EDX, XPS, XRD, TEM, ICP-AES	SEM, XPS, EDX	50 h CA (1.63 V_{RHE})	NiOOH/CoOOH	Precatalyst (partial oxidation)	993
Cu_2Se-Cu_2O/TF	Ti foil	Nanoparticles	S	-	465	51	-	140	0.2 M carbonate buffer (pH = 11.0)	XRD, SEM, EDX, TEM, XPS,	SEM, XRD, TEM, XPS	20 h CP (10 $mA \cdot cm^{-2}_{geo}$)	CuO	Precatalyst (partial oxidation)	994
$CoNiSe_2$	Ni foam	Nanorods	S	1.84	307 (@100 $mA \cdot cm^{-2}_{geo}$)	9.3	-	79	1 M KOH	SEM, TEM, XRD, EDX, XPS, SAED, ICP-AES	XRD, SEM, XPS	20 h CP (100 $mA \cdot cm^{-2}_{geo}$) 3000 CV cycles	Ni(III) species	Precatalyst (partial oxidation)	995
$NiSe_2$ UNWs/NiO_x (NSWANs)	CFP	Nanowire	S	-	266	83.78	-	53.4	1 M KOH	TEM, XRD, XPS, EDX, EXAFS, ICP-AES	XPS, TEM, XRD, EDX, ICP-AES	24 h CP (20 $mA \cdot cm^{-2}_{geo}$)	NiO_x, $NiSe_2$, SeO_x	Precatalyst (partial oxidation)	996
$NiSe_2$ UNWs	CFP	Nanowire	S	-	287	60.76	-	65.3		XRD, XPS, EXAFS, TEM, ICP-AES, EDX	XPS, ICP-AES	-	-	-	
NiSe/NF	Ni foam	Nanowire	S	21.5	271	40.4	-	80	1 M KOH	XRD, SEM, TEM, XPS	-	20 h CA (1.52 V_{RHE})	NiOOH	Precatalyst (partial oxidation)	844
Ni_3S_2/NF	Ni foam	Nanowire	S	19.3	222	80.8	-	60		XRD, SEM, TEM, XPS	-	20 h CA (1.47 V_{RHE})	NiOOH	Precatalyst (partial oxidation)	
$Ni_{0.5}Fe_{0.5}Se_2$	GC	Nanodendrite	P	0.45	235	0.320	-	34.7	1 M KOH	ICP-AES, XRD, TEM, EDX, XPS	XRD, TEM, XPS	16 h CP (10 $mA \cdot cm^{-2}_{geo}$) 500 CV cycles (1.23−1.5 V_{RHE})	Ni(Fe)OOH	Precatalyst (partial oxidation)	997
$Ni_{0.75}Fe_{0.25}Se_2$	GC	Nanodendrite	P	0.45	250	0.308	-	45.8		XRD, TEM, ICP-AES	-	-	-	-	
$Ni_{0.25}Fe_{0.75}Se_2$	GC	Nanodendrite	P	0.45	271	0.254	-	53.8		XRD, TEM, ICP-AES	-	-	-	-	
$Ni_{0.4}Fe_{0.6}Se_2$	Ni foam	Nanoflake	S	2.1	217	3.1	-	41	1 M KOH	XRD, SEM, TEM, EDX, XPS	SEM, TEM, XPS	72 h CP (10 $mA \cdot cm^{-2}_{geo}$)	Co-Fe-Se-based oxide/hydroxide	Precatalyst (partial oxidation)	998
NiFe LDH-NiSe/NF	Ni foam	Nanosheets	S	2.12	240 (@100 $mA \cdot cm^{-2}_{geo}$)	3.81	-	65.6	1 M KOH	XRD, XPS, SEM, TEM, EDX	XPS, TEM, EDX	12 h CA (1.56 V_{RHE}) 1000 CV cycles	NiOOH	Precatalyst (partial oxidation)	999
$NiSe_x$/NF	Ni foam	Nanosheets	S	2.01	303	1.47	-	85.8		SEM, XRD, EDX, TEM	-	-	-	-	
$Ni_{0.67}Co_{0.33}Se_2$/ C-HRD (Carbon Hollow Rhombic Dodecahedra)	Ni foam	Nanosheets	P	1.5	245	54.4	-	70	1 M KOH	XRD, SEM, TEM, Raman, XPS, ICP-MS, EDX	SEM, TEM, XRD, XPS	36 h CP (20 $mA \cdot cm^{-2}_{geo}$)	NiCo oxyhydroxides	Precatalyst (partial oxidation)	1000
$CoSe_2$/C-HRD	Ni foam	Nanosheets	P	1.5	295	12.9	-	72		XRD, XPS, EDX, SEM, TEM	-	-	-	-	
$CoSe_2$/NC-SRD	Ni foam	Nanosheets	P	1.5	300	9.7	-	98		XRD, XPS, EDX, SEM, TEM	-	-	-	-	
$NiCo_2Se_4$	GC	Holey nanosheets	P	0.285	295	0.000765	0.016 at 300 mV	53	1 M KOH	XRD, TEM, SEM, EDX, XPS	XRD, SEM, EDX	36 h CP (10 $mA \cdot cm^{-2}_{geo}$) 2000 CV cycles (0−0.8 $V_{Ag/AgCl}$)	NiO_x/CoO_x	Precatalyst (partial oxidation)	1001
$NiCo_2Se_4$	GC	Nanoparticles	P	-	380	-	-	97		XRD, SEM	-	-	-	-	
$NiCo_2Se_4$	GC	Nanosheets	P	-	-	-	-	149		XRD, SEM	-	-	-	-	
(Ni,Co)Se_2-GA (Graphene Aerogel)	Ni foam	Nanocages	P	2.5-2.8	250	16.0	-	70	1 M KOH	SEM, TEM, EDX, ICP-MS, XRD, XPS, HAADF	XPS, XRD, Raman	20 h CA (1.522 V_{RHE}) 5000 CV cycles (1.0−1.6 V_{RHE})	Ni/Co hydroxides	Precatalyst (partial oxidation)	1002
(Ni,Co)Se_2	Ni foam	Nanocages	P	2.5-2.8	320	10.4	-	89		SEM, TEM, XRD	-	-	-	-	
Fe-NiSe/NF	Ni foam	Nanowire	S	-	233	0.99	-	48	1 M KOH	XRD, SEM, TEM, EDX, XPS, SAED	SEM, XRD, EDX, XPS	24 h CA (1.464 V_{RHE}) 24 h CP (10 $mA \cdot cm^{-2}_{geo}$)	NiOOH	Precatalyst (partial oxidation)	1003
$Ni_{1.12}Fe_{0.49}Se_2$	GC	Nanorods	P	0.45	227	-	-	37.9	1 M KOH	ICP-AES, TEM, EDX, XRD, XPS	XPS, XRD, TEM	10 h CP (10 $mA \cdot cm^{-2}_{geo}$) 1000 CV cycles (0.3−0.8 $V_{Hg/HgO}$)	Ni(Fe)OOH	Precatalyst (partial oxidation)	1004
$Ni_{1.06}Fe_{0.58}Se_2$	GC	Urchin-like	P	0.45	238	-	-	44.3		TEM, XRD	-	-	-	-	
$Ni_{1.02}Fe_{0.88}Se_2$	GC	Urchin-like	P	0.45	248	-	-	46.3		TEM, XRD	-	-	-	-	
$Ni_{1.16}Fe_{0.27}Se_2$	GC	Urchin-like	P	0.45	258	-	-	55.7		TEM, XRD	-	-	-	-	
$Ni_{0.5}Fe_{0.5}Se_2$	CFC	Nanoparticles	S	-	-	53	-	63	1 M KOH	XRD, XPS, SEM, EDX, TEM, SAED	-	500 CV cycles (0.45−0.55 V_{SCE})	NiOOH	Precatalyst	1005
$FeSe_2$	CFC	Nanoparticles	S	-	-	0.13	-	199		-	-	-	-	-	
$Ni_{0.2}Fe_{0.8}Se_2$	CFC	Nanoparticles	S	-	-	22	-	86		-	-	-	-	-	
$Ni_{0.8}Fe_{0.2}Se_2$	CFC	Nanoparticles	S	-	-	44	-	83		-	-	-	-	-	
$NiSe_2$	CFC	Nanoparticles	S	-	-	4.4	-	175		-	-	-	-	-	
Ni_3Se_2/NF	Ni foam	Cauliflower-shape	S	-	315 (@100 $mA \cdot cm^{-2}_{geo}$)	3.3	-	40.2	1 M KOH	XRD, SEM, XPS, TEM	XRD, SEM, XPS	285 h CP (100 $mA \cdot cm^{-2}_{geo}$)	NiOOH	Precatalyst (partial oxidation)	1006
Ni_3Se_4/NF	Ni foam	Nano-assemblies	S	2.4	231	16.6	-	33	3 M KOH	XRD, TEM, EDX, XPS, SEM, SAED	XRD, Raman, SEM, TEM, XPS, EDX	1000 min CA (1.46 V_{RHE}) 1000 CV cycles	NiO, $NiSeO_3$	Precatalyst (partial oxidation)	1007
Ni_3Se_4/NF	Ni foam	Nano-assemblies	S	2.4	243	-	-	30	1 M KOH	XRD, TEM, EDX, XPS, SEM, SAED	XRD, Raman, SEM, TEM, XPS, EDX	1000 CV cycles	NiO, $NiSeO_3$	Precatalyst (partial oxidation)	
Ni_3Se_4/NF	Ni foam	Nano-assemblies	S	2.4	309	-	-	40	0.1 M KOH	XRD, TEM, EDX, XPS, SEM, SAED	XRD, Raman, SEM, TEM, XPS, EDX	1000 CV cycles	NiO, $NiSeO_3$	Precatalyst (partial oxidation)	
NG/$NiSe_2$/NF	Ni foam	Nanofilm	S	2.5	307 (@20 $mA \cdot cm^{-2}_{geo}$)	3.68	-	89	0.1 M KOH	XPS, EDX, XRD, SEM, TEM, Raman, SAED, HAADF	SEM, XPS, XRD	100 h CA (1.55 V_{RHE})	NiO_x	Precatalyst (partial oxidation)	1008
$NiSe_2$/NF	Ni foam	Nanofilm	S	2.5	358 (@20 $mA \cdot cm^{-2}_{geo}$)	0.89	-	109		XPS, EDX, XRD, SEM, TEM, Raman	-	-	-	-	

https://doi.org/10.1021/acs.chemrev.3c00005
Chem. Rev. 2023, 123, 12795−13208

Table 6. continued

Initial Electrocatalyst	Substrate	Shape of Electrocatalyst	Deposition Type	Specific Loading/ $mg \cdot cm^{-2}_{geo}$	η@10 $mA \cdot cm^{-2}_{geo}$/ mV	C_{dl}/ $mF \cdot cm^{-2}_{geo}$	TOF/s^{-1} (@η or j)	Tafel Slope/ $mV \cdot dec^{-1}$	Electrolyte	Pre-analysis	Post-analysis	Long-Term OER Test Conditions	Post-OER Electrocatalyst	Final Type of Electrocatalyst	Ref.
G/$NiSe_2$/NF	Ni foam	Nanofilm	S	2.5	337 (@20 $mA \cdot cm^{-2}_{geo}$)	2.54	-	95	1 M KOH	XPS, EDX, XRD, SEM, TEM, Raman	-	-	-	-	1008
NiSe/NF	Ni foam	-	S	0.01	136 (@100 $mA \cdot cm^{-2}_{geo}$)	-	-	112.3		XRD, SEM, TEM, Raman, XPS	SEM, TEM, Raman, XPS	12 h CP (100 $mA \cdot cm^{-2}_{geo}$)	Ni oxyhydroxide and selenite species	Precatalyst (partial oxidation)	1009
Ni_3Se_2	GC	Nanoparticles	P	0.2	-	22.1×10^{-3}	11.3 at 450 mV	46	0.1 M KOH	XRD, TEM, SEM, EXAFS, N_2 ISO (BET)	XPS, XANES, TEM	-	NiO_x	Precatalyst (partial oxidation)	1010
NiSe	GC	Nanoparticles	P	0.2	-	19.1×10^{-3}	6.7 at 450 mV	72		XRD, TEM, SEM, N_2 ISO (BET)	XPS, XANES, TEM	-	NiO_x	Precatalyst (partial oxidation)	
$FeSe_2$	Ni piece	Nanoplatelets	P	-	330	1.09	-	48.1	1 M KOH	XRD, SEM, EDX, TEM, AFM, XPS, EDX	XRD, EDX	70 h CA (1.67 V_{RHE})	Metal oxide	Precatalyst (partial oxidation)	1011
$CuSe_2$	Ni piece	Nanoplatelets	P	-	580	0.48	-	214.8		SEM, TEM, XRD, EDX	-	-	-	-	
$CoSe_2$-DETA (diethylenetriamine)	GC	Nanobelt	P	0.2	-	5.4	-	79	0.1 M KOH	XRD, Raman, TEM, HAADF	-	-	-	-	1012
Ag-$CoSe_2$	GC	Nanobelt	P	0.2	320	5.1	-	56		TEM, EDX, XRD, Raman, ICP-AES, HAADF, XPS	TEM, XRD	1000 CV cycles (1.24–1.34 V_{RHE})	-	Precatalyst	
$FeSe_2$/NF	Ni foam	Nanoparticles	S	-	245	-	-	-	1 M KOH	XRD, SEM, TEM, XPS, ICP-AES, FTIR, Mössbauer	TEM, FTIR, ICP-AES, XPS	18 h CP (10 $mA \cdot cm^{-2}_{geo}$)	$Fe(OH)_2$/FeOOH	Precatalyst (partial oxidation)	1013
$FeSe_2$/FTO	FTO	Nanoparticles	S	-	292	-	-	-		-	-	-	-	-	
Co_3Se_4/CF	Co foam	Nanowire	S	2.6	320 (@397 $mA \cdot cm^{-2}_{geo}$)	30.26	0.0644 at 320 mV	44	1 M KOH	SEM, XRD, EDX, Raman, TEM, XPS, ICP-AES, HAADF	XRD, ICP-AES, SEM, EDX, TEM, XPS	12 h CP (10 $mA \cdot cm^{-2}_{geo}$)	CoOOH	Precatalyst (full oxidation)	1014
$FeSe_2$/NF	Ni foam	Microspheres	S	2.6	226	7	495 at 707 mV	41	1 M KOH	XRD, TEM, XPS, SEM, EDX	SEM, TEM, EDX, XPS	36 h CP (10 $mA \cdot cm^{-2}_{geo}$)	Fe-SDO (diselenide-derived oxide)	Precatalyst (partial oxidation)	1015
MnSe/NF	Ni foam	-	S	2.6	339	-	-	117		XRD, SEM	SEM	36 h CP (10 $mA \cdot cm^{-2}_{geo}$)	-	-	
$NiSe_2$/NF	Ni foam	-	S	2.6	338	2.6	-	86		XRD, SEM	SEM	36 h CP (10 $mA \cdot cm^{-2}_{geo}$)	-	-	
$NiCoSe_2$/NF	Ni foam	Nanobrush	S	8.5	274	18.9	-	61.2	1 M KOH	XRD, SEM, TEM, EDX, XPS	XRD, SEM	24 h CP (30 $mA \cdot cm^{-2}_{geo}$) 5000 CV cycles	NiOOH/CoOOH	Precatalyst (partial oxidation)	1016
$NiCoSe_2$/NF	Ni foam	Nanorods	S	8.5	288	13.3	-	64.6		TEM	-	-	-	-	
$NiCoSe_2$/NF	Ni foam	Nanosheets	S	8.5	290	7.5	-	79.5		TEM	-	-	-	-	
$Co_{0.85}Se$/NF	Ni foam	-	S	8.5	297	-	-	-		-	-	-	-	-	
$Ni_{0.85}Se$/NF	Ni foam	-	S	8.5	310	-	-	-		-	-	-	-	-	
$NiSe_2$	Au glass	-	S	0.13	140	0.188	-	48.7	1 M KOH	XRD, SEM, TEM, EDX, XPS, Raman	XRD, XPS, EDX	24 h CP (10 $mA \cdot cm^{-2}_{geo}$)	$NiSe_2$, $Ni_{0.85}Se$	Precatalyst	1017
$NiSe_2$	CFP	-	S	1.4	220	-	-	56.6		XRD, SEM, TEM, EDX, XPS, Raman	-	-	-	-	
$FeNi_2Se_4$-NrGO (nitrogen doped reduced graphene oxide)	CFP	Nanoparticles	S	0.55	170	0.332	0.05 at 250 mV	62.1	1 M KOH	XRD, XPS, EDX, TEM, SEM	XPS, XRD	12 h CA (1.40 V_{RHE})	$FeNi_2Se_4$, SeO_x	Precatalyst (partial oxidation)	210
$FeNi_2Se_4$	CFP	Nanoparticles	S	0.55	210	0.212	0.044 at 250 mV	87.8		XRD, EDX, TEM, SEM	-	-	-	-	
NiSe NWs/NF	Ni foam	Nanowire	S	-	336 (@100 $mA \cdot cm^{-2}_{geo}$)	-	-	78	1 M KOH	XRD, SEM, TEM, XPS, EDX	SEM, TEM, XPS	12 h CP (100 $mA \cdot cm^{-2}_{geo}$) 100 CV cycles (1.1–1.7 V_{RHE})	CoOOH	Precatalyst (partial oxidation)	1018
NiSe NWs/NF@Co	Ni foam	Nanowire	S	-	283 (@100 $mA \cdot cm^{-2}_{geo}$)	-	-	63		XRD, SEM, TEM, XPS, EDX, EDX	SEM, TEM, XPS	12 h CP (100 $mA \cdot cm^{-2}_{geo}$) 100 CV cycles (1.1–1.7 V_{RHE})	Ni(Co)OOH	Precatalyst (partial oxidation)	
$NiSe_2$/Ni_3Se_4/C/NF	Ni foam	Nanofilm	S	-	275 (@30 $mA \cdot cm^{-2}_{geo}$)	45.1	-	63	1 M KOH	XRD, SEM, TEM, EDX, ICP-MS, HAADF, XPS	XPS, Raman, SEM, EDX	24 h CA (1.5 V_{RHE}) 2000 CV cycles	NiOOH	Precatalyst (partial oxidation)	1019
NiSe	Graphene/ Ni	Nanowalls	S	-	-	6.17	-	83.4	1 M KOH	XRD, SEM, TEM, Raman, XPS, SAED	XRD, SEM, XPS	12 h CA (1.72 V_{RHE})	$Ni(OH)_2$, NiOOH	Precatalyst	1020
CoSe	Graphene/ Ni	Nanowalls	S	-	-	6.88	-	74.7		XRD, SEM, TEM, Raman, XPS, SAED	XRD, SEM, XPS	12 h CA (1.68 V_{RHE})	$Co(OH)_2$, CoOOH	Precatalyst	
Ni_3Se_2/ Dissoluted 30 s	Au glass	Nanofilm	S	-	190	0.196	-	48.9	1 M NaOH	XRD, SEM, TEM, EDX, XPS, SAED	XRD	24 h CA (1.65 V_{RHE})	$Ni(OH)_2$	Precatalyst (partial oxidation)	1021
Ni_3Se_2/ Dissoluted 15 s	Au glass	Nanofilm	S	-	230	-	-	54.6		-	-	-	-	-	
Ni_3Se_2	Au glass	Nanofilm	S	-	260	0.06	-	87.1		XRD, SEM, TEM, EDX, XPS, SAED	-	-	-	-	
NiSe	Ni foam	-	S	-	253	-	-	54	1 M KOH	TEM, XRD, SAED, EDX	TEM, SAED, EDX	-	$Ni(OH)_2$	Precatalyst	98
$Ni_xFe_{1-x}Se_2$	Ni foam	Nanoplates	S	-	195	3.3	-	28		XPS, XRD, SEM, TEM, EDX	XPS, XRD, SEM, TEM, EDX, N_2 ISO (BET, PSD)	24 h CP (10 $mA \cdot cm^{-2}_{geo}$)	$NiFeO_x$	Precatalyst (full oxidation)	
$(Ni_{0.75}Fe_{0.25})Se_2$	CF	Nanosheets	S	1.5	255 (@35 $mA \cdot cm^{-2}_{geo}$)	30.2	-	47.2	1 M KOH	XRD, SEM, TEM, XPS, EDX, N_2 ISO (BET), ICP, SAED	XRD, SEM, XPS, EDX, ICP	28 h CP (35 $mA \cdot cm^{-2}_{geo}$)	$Ni_{1-x}Fe_xOOH$	Precatalyst (partial oxidation)	1022
$NiSe_2$	CF	Nanosheets	S	1.4	323	4.1	-	83.6		XRD, SEM, TEM, EDX, XPS, ICP	XRD	12 h CP (15 $mA \cdot cm^{-2}_{geo}$)	-	-	
$Ni_{0.85}Se$/GS	Graphite	Porous film	S	-	302	-	-	62	1 M NaOH	SEM, TEM, XRD, XPS	XRD, XPS	48 h CP (10 $mA \cdot cm^{-2}_{geo}$)	NiOOH	Precatalyst (partial oxidation)	1023
CoO_x-CoSe/NF	Ni foam	Film	S	1.7	300 (@100 $mA \cdot cm^{-2}_{geo}$)	-	-	68	1 M KOH	XPS, SEM, EDX, XRD	SEM, XPS	48 h CP (50 $mA \cdot cm^{-2}_{geo}$)	CoOOH, Co_3O_4, NiOOH	Precatalyst (full oxidation)	1024
Ni_3Se_2/NF	Ni foam	Nanoforest	S	8.87	353 (@100 $mA \cdot cm^{-2}_{geo}$)	-	-	144	1 M KOH	SEM, TEM, XRD, EDX, XPS, HAADF	XPS	17 h CA	NiOOH	Precatalyst (partial oxidation)	1025

https://doi.org/10.1021/acs.chemrev.3c00005
Chem. Rev. 2023, 123, 12795−13208

Table 6. continued

Initial Electrocatalyst	Substrate	Shape of Electrocatalyst	Deposition Type	Specific Loading/ $mg \cdot cm^{-2}_{geo}$	η@10 $mA \cdot cm^{-2}_{geo}$/ mV	C_{dl}/ $mF \cdot cm^{-2}_{geo}$	TOF/s^{-1} (@η or j)	Tafel Slope/ $mV \cdot dec^{-1}$	Electrolyte	Pre-analysis	Post-analysis	Long-Term OER Test Conditions	Post-OER Electrocatalyst	Final Type of Electrocatalyst	Ref.
Fe-NiSe/FeNi	FeNi foam	Nanoflake	S	4.8	245 (@50 mA/cm^2_{geo})	-	-	64	1 M KOH	SEM, EDX, XRD, TEM, XPS, ICP-MS, SAED	SEM, TEM, XPS, Raman, SAED, ICP-MS	24 h CP (500 $mA \cdot cm^{-2}_{geo}$)	Ni(Fe)OOH	Precatalyst (full oxidation)	1026
CoSe	GC	Coral-like	P	0.28	295	6.104	-	40	1 M KOH	XRD, SEM, XPS, TEM	XRD, SEM, XPS	10000 s CA (1.58 V_{RHE})	$CoOOH/CoO_x$	Precatalyst (partial oxidation)	1027
CoSe	GC	Nanoparticles	P	0.28	350	1.610	-	49		XRD, SEM	-	-	-	-	
NiSe	Ni foam	Nanowire	S	-	-	-	-	54	1 M KOH	SEM, TEM, XRD, XPS, EDX, HAADF-STEM	XPS, XRD	15 h CA (1.58 V_{RHE})	NiO	Precatalyst (partial oxidation)	1028
$(Ni, Co)_{0.85}Se$	CFC	Nanotube arrays	S	5	255	22.99	0.003 at 300 mV	79	1 M KOH	XRD, SEM, TEM, XPS, EDX	XRD, SEM, TEM, XPS	24 h CP (10 $mA \cdot cm^{-2}_{geo}$)	γ-NiOOH	Precatalyst (partial oxidation)	1029
$Co_{0.85}Se$	CFC	Nanotube arrays	S	4.3	324	14.405	0.0012 at 300 mV	85		XPS, TEM	-	-	-	-	
$(Ni, Co)_{0.85}Se$@NiCo-LDH	CFC	Nanotube arrays	S	6	216	28.41	-	77		SEM, TEM, AFM, XRD	-	24 h CP (10 $mA \cdot cm^{-2}_{geo}$)	-	-	
$CoSe_2$ (ECT-Se-CoO)	CFC	Nanosheets	S	-	324	121	-	63.1	1 M KOH	SEM, TEM, EDX, XRD, XPS	SEM, TEM, EDX, XRD, XPS (after CV activation)	> 75 h CP (20 $mA \cdot cm^{-2}_{geo}$)	CoOOH, SeO_x	Precatalyst (full oxidation)	97
$Co_{0.5}Fe_{0.5}Se_2$ (ECT-Se-$Co_{0.5}Fe_{0.5}O$)	CFC	Nanosheets	S	-	270	-	-	36.2		SEM	SEM (after CV activation)	100 h CP (20 $mA \cdot cm^{-2}_{geo}$)	-	-	
$Co_{0.37}Ni_{0.26}Fe_{0.37}Se_2$ (ECT-Se-$Co_{0.37}Ni_{0.26}Fe_{0.37}O_4$)	CFC	Nanosheets	S	-	243	-	-	35.1		TEM	SEM, TEM	200 h CP (20 $mA \cdot cm^{-2}_{geo}$)	-	-	
NiSe/NF	Ni foam	Nanowires	S	2.8	270 (@20 mA/cm^2_{geo})	-	-	64	1 M KOH	XRD, TEM, XPS, SEM, EDX, Raman	TEM, Raman, XPS	12 h CP (100 $mA \cdot cm^{-2}_{geo}$)	NiOOH	Precatalyst (partial oxidation)	208
Ni_3Se_2/CF	Cu foam	Film	S	3.0	340 (@50 mA/cm^2_{geo})	-	-	80	1 M KOH	SEM, TEM, XRD, XPS	SEM, XPS	10 h CA (1.59 V_{RHE})	NiOOH	Precatalyst (partial oxidation)	1030
(Amorphous CoSe) α-CoSe/Ti	Ti mesh	Nanoparticles	S	3.8	292	-	-	69	1 M KOH	XRD, XPS, SEM, TEM, Raman, ICP-MS	SEM, Raman, XPS, ICP-MS	27 h CA (1.385 V_{RHE}) 1000 CV cycles (1.26–1.76 V_{RHE})	CoOOH	Precatalyst (partial oxidation)	1031
$Ni_{0.85}Se$	Ni foam	Plane film	S	-	350	0.80	-	72.5	1 M KOH	XRD, SEM, XPS	-	-	-	-	1032
$MoSe_2$ (MS1.6)	Ni foam	-	P	6	370	1.71	-	53.5	1 M NaOH	XRD, Raman	-	5000 CV cycles (100 $mV \cdot s^{-1}$)	-	-	1033
$MoSe_2$ (MS1.8)	Ni foam	Nanoflakes	P	6	320	5.85	-	43.5		XRD, TEM, SAED, XPS, Raman	-	5000 CV cycles (100 $mV \cdot s^{-1}$)	-	-	
$MoSe_2$ (MS2.0)	Ni foam	-	P	6	373	3.36	-	77.1		XRD, Raman	-	5000 CV cycles (100 $mV \cdot s^{-1}$)	-	-	
$MoSe_2$ (MS2.2)	Ni foam	-	P	6	390	2.56	-	77.5		XRD, Raman	-	5000 CV cycles (100 $mV \cdot s^{-1}$)	-	-	
Ni_xSe_y 40 min	Ni belt	Nanoparticles	S	-	485 (@50 mA/cm^2_{geo})	2.67	-	-	1 M KOH	XRD, SEM, XPS	-	-	-	-	915
Ni_xSe_y 60 min	Ni belt	Nanoparticles	S	-	332 (@50 mA/cm^2_{geo})	7.48	-	-		XRD, SEM, XPS	-	-	-	-	
Ni_xSe_y 80 min	Ni belt	Nanodendrites	S	-	309 (@50 mA/cm^2_{geo})	15.87	-	-		XRD, SEM, XPS	-	-	-	-	
Ni_xSe_y 120 min	Ni belt	Nanodendrites	S	-	346 (@50 mA/cm^2_{geo})	3.74	-	-		XRD, SEM, XPS	-	-	-	-	
$V_{0.03}Ni_{0.97}Se$	Ni belt	-	S	-	324 (@50 mA/cm^2_{geo})	16.16	-	-		XRD, XPS	-	-	-	-	
$Mn_{0.2}Ni_{0.8}Se$	Ni belt	-	S	-	281 (@50 mA/cm^2_{geo})	19.04	-	-		XRD, XPS	-	-	-	-	
$Fe_{0.2}Ni_{0.8}Se$	Ni belt	Nanocorals	S	-	255 (@50 mA/cm^2_{geo})	23.97	-	-		XRD, XPS, SEM, TEM, EDX	-	-	-	-	
$Ni_{0.75}Fe_{0.25}Se_2$	Ni foam	Nanosheet	S	1.33	183	2.45	0.03 at 250 mV	26.5	1 M KOH	XRD, SEM, XPS	-	-	-	-	1034
$Ni_{0.75}Fe_{0.25}Se_2$	CC	Interlinked nanosheet structure	S	0.76	235	4.13	0.06 at 500 mV	43.7	1 M KOH	XRD, SEM, XPS, Mössbauer, XAS (XANES, XAFS)	-	-	-	-	1035
$Cu_{0.41}Fe_{0.60}Se_{1.99}$	Cu foam	Nanowires	S	-	200	0.271	-	46	1 M KOH	SEM, EDX, TEM, HAADF-STEM, XRD, XPS, N_2 ISO (BET, PSD)	-	2000 CV cycles (1.0–1.8 V_{RHE}) 70 h CP (100 $mA \cdot cm^{-2}_{geo}$)	-	-	1036
S-0.01 (NiSe)	Ni foam	Nanoparticles	S	-	306 (@100 mA/cm^2_{geo}) 318 (@150 mA/cm^2_{geo}) 330 (@200 mA/cm^2_{geo})	59.3	-	61	1 M KOH	XRD, SEM, EDX	-	500 CV cycles	-	-	1037
S-0.1 (NiSe)	Ni foam	Nanoparticles	S	-	328 (@100 mA/cm^2_{geo}) 343 (@150 mA/cm^2_{geo}) 357 (@200 mA/cm^2_{geo})	46.8	-	87		XRD, SEM	-	-	-	-	
S-1 (NiSe)	Ni foam	Nanoparticles	S	-	344 (@100 mA/cm^2_{geo}) 365 (@150 mA/cm^2_{geo}) 386 (@200 mA/cm^2_{geo})	22	-	93		XRD, SEM	-	-	-	-	
S-10 (NiSe)	Ni foam	Nanoparticles	S	-	342 (@100 mA/cm^2_{geo}) 363 (@150 mA/cm^2_{geo}) 386 (@200 mA/cm^2_{geo})	25.6	-	125		XRD, SEM	-	-	-	-	
$NiSe_2$	GC	-	P	~ 0.136	461 (@20 mA/cm^2_{geo}) 590 (@50 mA/cm^2_{geo})	0.61	0.0098 at 300 mV	165	1 M KOH	XRD, Raman, XPS	-	-	-	-	762

https://doi.org/10.1021/acs.chemrev.3c00005
Chem. Rev. 2023, 123, 12795−13208

Table 6. continued

Initial Electrocatalyst	Substrate	Shape of Electrocatalyst	Deposition Type	Specific Loading/ $mg \cdot cm^{-2}_{geo}$	η@10 $mA \cdot cm^{-2}_{geo}$/ mV	C_{dl}/ $mF \cdot cm^{-2}_{geo}$	TOF/s^{-1} (@η or j)	Tafel Slope/ $mV \cdot dec^{-1}$	Electrolyte	Pre-analysis	Post-analysis	Long-Term OER Test Conditions	Post-OER Electrocatalyst	Final Type of Electrocatalyst	Ref.
$NiCoSe_2$	CC	Nanosheets	S	-	302	2.9	-	60	1 M KOH	XRD, SEM	-	-	-	-	537
c-$CoSe_2$	CC	Nanosturcture	S	-	290	13.05	-	90	1 M KOH	XRD, SEM, TEM, Raman, ICP-MS	ICP-MS	-	-	-	48
ZnSe@MOF-5	Ni foam	Nanoparticles	P	-	134 (@2 $mA \cdot cm^{-2}_{geo}$)	-	-	-	1 M KOH	XRD, FTIR, SEM, EDX, Raman	-	-	-	-	1038
CuSe@MOF-6	Ni foam	Nanoparticles	P	-	154 (@2 $mA \cdot cm^{-2}_{geo}$)	-	-	-		XRD, FTIR, SEM, EDX, Raman	-	-	-	-	
NiSe@MOF-7	Ni foam	Nanoparticles	P	-	164 (@2 $mA \cdot cm^{-2}_{geo}$)	-	-	-		XRD, FTIR, SEM, EDX, Raman	-	-	-	-	
CoSe@MOF-8	Ni foam	Nanoparticles	P	-	130 (@2 $mA \cdot cm^{-2}_{geo}$)	-	-	-		XRD, FTIR, SEM, EDX, Raman	-	-	-	-	
FeSe@MOF-9	Ni foam	Nanoparticles	P	-	124 (@2 $mA \cdot cm^{-2}_{geo}$)	-	-	-		XRD, FTIR, SEM, EDX, Raman	-	-	-	-	
MnSe@MOF-10	Ni foam	Nanoparticles	P	-	170 (@10 $mA \cdot cm^{-2}_{geo}$)	-	-	61		XRD, FTIR, SEM, EDX, Raman	-	10 min CP (1.5 V_{RHE})	-	-	
NiSe/NC	GC	Nanosheets	P	0.204	406	-	-	102	1 M KOH	XRD, XPS, SEM, TEM, N_2 ISO (BET, PSD), EDX	-	-	-	-	1039
NiSe/Ni/NC	GC	Nanosheets	P	0.204	321	-	-	54		XRD, XPS, SEM, TEM, N_2 ISO (BET, PSD), EDX	-	25 h CP (10 $mA \cdot cm^{-2}_{geo}$) 3000 CV cycles	-	-	
CoZn-Se	GC	Nanosheets	P	-	320	11.8	0.022 at 320 mV	66	1 M KOH	XRD, SEM, TEM, XPS, EXAFS	TEM	15h CA (1.55 V_{RHE}) 2000 CV cycles (1.10–1.65 V_{RHE})	-	-	1040
$CoSe_2$	GC	Nanosheets	P	-	424	4.9	-	52		XRD, SEM, EXAFS	-	-	-	-	
ZnSe	GC	Nanosheets	P	-	408	4.7	-	64		XRD, SEM, EXAFS	-	-	-	-	
$CoTe_2$@CdTe	Graphite	Nanowires	P	33.3333	140	0.071	-	68	1 M KOH	XRD, SEM, TEM, EDX, SAED, N_2 ISO (BET)	-	8.33 h bulk electrolysis	-	-	1041
$CoSe_2$@CdSe	Graphite	Nanoparticles	P	33.3333	329	0.0435	-	128		XRD, SEM, EDX, N_2 ISO (BET)	-	-	-	-	
$NiSe_2$ -413-2h-tetralin	GC	Dendrite	P	0.114	295	-	-	71	1 M KOH	XRD, SEM, TEM, XPS	-	10000 CV cycles (−0.16–0.05 $V_{Ag/AgCl}$)	-	-	1042
$NiSe_2$ -413-2h-DMF	GC	Dendrite	P	0.114	320	-	-	73		XRD, SEM	-	-	-	-	
$NiSe_2$ -413-2h-EMF	GC	Dendrite	P	0.114	344	-	-	64		XRD, SEM	-	-	-	-	
$NiSe_2$ -393-2h-tetralin	GC	Nanorods	P	0.114	440	-	-	73		XRD, TEM	-	-	-	-	
$NiSe_2$ -433-2h-tetralin	GC	Dendrite	P	0.114	345	-	-	71		XRD, TEM	-	-	-	-	
$NiSe_2$ -453-2h-tetralin	GC	Dendrite	P	0.114	320	-	-	68		XRD, TEM	-	-	-	-	
$NiSe_2$ -473-2h-tetralin	GC	Dendrite	P	0.114	340	-	-	71		XRD, TEM	-	-	-	-	
$NiSe_2$ -413-4h-tetralin	GC	Dendrite	P	0.114	315	-	-	-		XRD, TEM	-	-	-	-	
$NiSe_2$ -413-8h-tetralin	GC	Dendrite	P	0.114	330	-	-	-		XRD, TEM	-	-	-	-	
$Fe_{0.08}Co_{0.09}Ni_{0.83}Se_2$	GC	Nanoparticles	P	-	268	0.256	-	57.53	1 M KOH	XRD, SEM, EDX, TEM, XPS	-	2 h CP (10 $mA \cdot cm^{-2}_{geo}$)	-	-	1043
$Fe_{0.09}Ni_{0.91}Se_2$	GC	Nanoparticles	P	-	325	0.231	-	54.78		XRD, SEM, EDX, TEM, XPS	-	2 h CP (10 $mA \cdot cm^{-2}_{geo}$)	-	-	
$NiSe_2$	GC	Nanoparticles	P	-	375	0.157	-	89.36		XRD, SEM, EDX, TEM, XPS	-	2 h CP (10 $mA \cdot cm^{-2}_{geo}$)	-	-	
$Cu_{2-x}Se$@CuO	CF	Nanoparticles + Nanocrystals	S	-	253	-	-	73	1 M KOH	XRD, XPS, SEM, TEM	-	24 h CP (20 $mA \cdot cm^{-2}_{geo}$)	-	-	1044
$NiSe_2$/g-C_3N_4	Ni foam	Nanocoral	P	4	290 (@40 $mA \cdot cm^{-2}_{geo}$)	-	-	143	1 M KOH	XRD, FTIR, SEM, EDX, Raman	-	10 h CA (1.42 V_{RHE})	-	-	1045
$NiSe_2$	Ni foam	Nanoparticles	P	-	400 (@40 $mA \cdot cm^{-2}_{geo}$)	-	-	299		XRD, FTIR, SEM	-	-	-	-	
Co_3Se_4	GC	Nanosheets	P	-	328	23	-	66	1 M KOH	XRD, XPS, SEM	-	-	-	-	1046
$FeSe_2$	GC	Nanosheets	P	-	-	-	-	-		XRD, XPS	-	-	-	-	
Co_3Se_4 & $FeSe_2$	GC	Nanosheets	P	-	280	28.6	-	51		XRD, SEM, TEM, EDX, XPS	-	24 h CA	-	-	
$(Ni_xCo)Se_2$	CC	Triangular array	S	-	256	38	-	74	1 M KOH	XRD, SEM, TEM, SAED, XPS, EDX	XRD, SEM	20 h CA (1.5 V_{RHE})	-	-	1047
$Co_{0.85}Se$	GC	Nanoparticles + Nanofibers	P	0.225	350	10.3	-	61	0.1 M KOH	XRD, SEM, TEM, EDX, XPS	-	-	-	-	1048
$Cu_{1.8}Se$	CC	Nanotubes	S	1.6	-	-	-	393.2	1 M KOH	XRD, FTIR	-	-	-	-	1049
$CoSe_2$/$Cu_{1.8}Se$	CC	Nanotubes	S	2.2	275 (@20 $mA \cdot cm^{-2}_{geo}$)	-	-	154.9		XRD	-	-	-	-	
$NiCoSe_2$/$Cu_{1.8}Se$	CC	Nanotubes	S	2.5	265 (@20 $mA \cdot cm^{-2}_{geo}$)	-	-	146.2		-	-	-	-	-	
$ZnNi_{0.5}Co_{0.5}Se_2$/ $Cu_{1.8}Se$	CC	Mutli-dimensional	S	2.3	167 (@20 $mA \cdot cm^{-2}_{geo}$)	-	-	72		SEM, EDX, TEM, SAED, XRD, XPS, FTIR	SEM	20 h CP (50 $mA \cdot cm^{-2}_{geo}$)	-	-	
$Ni_{0.75}Fe_{0.25}Se_2$ (12h)	Ni foam	Nanocrystals	S	-	227	-	-	49.6	1 M KOH	SEM, XRD	-	-	-	-	1050
$Ni_{0.75}Fe_{0.25}Se_2$ (6h)	Ni foam	Nanocrystals	S	2.3	210	16.52	-	39.4		SEM, TEM, XRD, XPS	SEM	30 h CP (10, 50, 100 $mA \cdot cm^{-2}_{geo}$)	-	-	
$Ni_{0.75}Fe_{0.25}Se_2$ (3h)	Ni foam	Nanocrystals	S	-	230	-	-	48.9		SEM, XRD	-	-	-	-	
(Co, Ni)Se_2@NiFe-LDH	GC	Rhombic Nanocages	P	-	277	0.41	-	75	1 M KOH	TEM, SEM, EDX, XRD, XPS, Raman	-	17 h CP (10 $mA \cdot cm^{-2}_{geo}$)	-	-	1051
(Co, Ni)Se_2	GC	Rhombic Nanocages	P	-	356	0.66	-	90		TEM, XRD, EDX, XPS	-	-	-	-	
(Co,Ni)Se_2/ NiFe-LDH (1:1)	GC	Nanosheets + Rhombic Nanocages	P	-	343	-	-	89		-	-	-	-	-	
$Co_{0.75}Ni_{0.25}Se$	Ni foam	Nanorods	S	-	269 (@50 $mA \cdot cm^{-2}_{geo}$)	66.5	-	74	1 M KOH	SEM, TEM, XRD, XPS	-	22 h CP (1.65 V_{RHE})	-	-	1052

https://doi.org/10.1021/acs.chemrev.3c00005
Chem. Rev. 2023, 123, 12795−13208

Table 6. continued

Initial Electrocatalyst	Substrate	Shape of Electrocatalyst	Deposition Type	Specific Loading/ $mg \cdot cm^{-2}_{geo}$	η@10 $mA \cdot cm^{-2}_{geo}$/ mV	C_{dl}/ $mF \cdot cm^{-2}_{geo}$	TOF/s^{-1} (@η or j)	Tafel Slope/ $mV \cdot dec^{-1}$	Electrolyte	Pre-analysis	Post-analysis	Long-Term OER Test Conditions	Post-OER Electrocatalyst	Final Type of Electrocatalyst	Ref.
NiSe	Ni foam	Nanorods	S	-	353 (@50 $mA \cdot cm^{-2}_{geo}$)	13.05	-	109	1 M KOH	XRD	-	-	-	-	1052
$Fe_{40}Ni_{40}Se_{20}$ - 308K	CFP	Nanosheets	P	-	330	17.5	-	50		XRD, DSC, XPS, SEM	XRD, EDX	10 h CA 1000 CV cycles	-	-	1053
$Fe_{40}Ni_{40}Se_{20}$ - 393K	CFP	Nanosheets	P	-	307	26.53	-	35		XRD, DSC, XPS, SEM	XRD, EDX	10 h CA 1000 CV cycles	-	-	
$Fe_{40}Ni_{40}Se_{20}$ - 573K	CFP	Nanosheets	P	-	332	37.13	-	33		XRD, DSC, XPS, SEM	EDX	10 h CA	-	-	
Zn-Co-Te	PGE	Nanorods	P	-	221	-	-	91	5 M KOH	SEM, XRD	-	1000 CV cycles (0.91−3.3 V_{RHE})	-	-	1054
Zn-Co-Se	PGE	Nanorods	P	-	560	-	-	135.9		SEM	-	-	-	-	
$Ni_{0.85}Se$-NHCS	GC	Hollow sphere	P	0.11905	353	5.09	-	91.95	1 M KOH	XRD, XPS, Raman, SEM, TEM, SAED	-	500 CV cycles	-	-	1055
$Ni_{0.95}Se$-NHCS	GC	Hollow sphere	P	0.11905	370	3.91	-	95.27		XRD, XPS, SEM	-	-	-	-	
NiSe-NHCS	GC	Hollow sphere	P	0.11905	375	3.51	-	96.04		XRD, XPS, SEM	-	-	-	-	
NiSe	GC	Nanoparticles	P	-	-	-	-	-	1 M KOH	XRD, SEM, EDAX	-	-	-	-	1056
$Ni_{0.5}Mo_{0.5}Se$	GC	Nanoparticles	P	-	-	-	-	-		XRD, SEM, TEM, EDAX	-	-	-	-	
NiSe-0	Ni foam	Nanorods	S	-	840 (@100 $mA \cdot cm^{-2}_{geo}$)	10.2	-	316.5	1 M KOH	XRD, SEM, XPS, TEM	-	-	-	-	1057
NiSe-0.5	Ni foam	Nanorods	S	-	763 (@100 $mA \cdot cm^{-2}_{geo}$)	17.9	-	265.2		XRD, SEM, XPS	-	-	-	-	
NiSe-1	Ni foam	Nanorods	S	-	711 (@100 $mA \cdot cm^{-2}_{geo}$)	18.2	-	253.1		XRD, SEM, XPS	-	-	-	-	
NiSe-2	Ni foam	Nanorods	S	-	504 (@100 $mA \cdot cm^{-2}_{geo}$)	32.2	-	104.6		XRD, SEM, XPS	-	-	-	-	
NiSe-4	Ni foam	Nanorods	S	-	370 (@100 $mA \cdot cm^{-2}_{geo}$)	50.9	-	95.3		XRD, SEM, XPS, TEM	SEM	12h CP (100 $mA \cdot cm^{-2}_{geo}$)	-	-	
NiSe-8	Ni foam	Nanorods	S	-	414 (@100 $mA \cdot cm^{-2}_{geo}$)	74.1	-	102.1		XRD, SEM, XPS	-	-	-	-	
Pt-Ni_3Se_2@ NiOOH/NF (PNOF)	Ni foam	Nanosheets + Nanoparticles	S	-	310 (@50 $mA \cdot cm^{-2}_{geo}$)	43.3	-	31	1 M KOH	XRD, TEM, XPS, SEM	XRD, TEM	1000 CV cycles (1.067−1.167 V_{RHE}) 12 h multistep CP (OWS)	-	-	1058
Ni_3Se_2@ NiOOH/NF (NOF)	Ni foam	Nanosheets	S	-	320 (@50 $mA \cdot cm^{-2}_{geo}$)	41.2	-	35		XRD, TEM, XPS, SEM	TEM	1000 CV cycles (1.067−1.167 V_{RHE})	-	-	
Ni_3Se_2	Ni foam	Dendrite like arrays	S	-	400 (@50 $mA \cdot cm^{-2}_{geo}$)	28.7	-	75		XRD, TEM, EDX	-	-	-	-	
$FeSe_2$	-	Nanocubes	P	-	330	5.85	-	87.6	1 M KOH	SEM	-	-	-	-	1059
$CoSe_2$	-	Nanocubes	P	-	300	8.56	-	80.1		SEM, XRD	-	-	-	-	
(Fe-Co)Se_2	-	Nanospheres	P	-	251	12.49	-	47.6		SEM, TEM, EDX	SEM, TEM	24 h CP (10 $mA \cdot cm^{-2}_{geo}$)	-	-	
$Co_{0.85}Se/Ni_{0.85}Se$	CFP	Nanocages	S	0.65	300	-	-	87	1 M KOH	SEM, TEM, XRD, EDX, XPS, FTIR	-	20 h CA (1.63 V_{RHE}) 1000 CV cycles (0.1−0.2 V_{RHE})	-	-	1060
porous CoFe-Se	GC	Nanocubes	P	-	310	-	-	135	0.1 M KOH	XRD, XPS, SEM, TEM	-	-	-	-	566
$CoSe_2$	CFP	Nanosheets	S	2.47	350	8.5	-	52.3	Fe-purified 1 M KOH	XRD, EDX, Raman, XPS, SEM, TEM	-	-	-	-	556
$CoSe_2$_1D	Ni foam	Nanorods	P	0.6	377 (@50 $mA \cdot cm^{-2}_{geo}$)	-	0.56 at 370 mV	88	1 M KOH	SEM, TEM, XRD	-	8 h CP (50 $mA \cdot cm^{-2}_{geo}$) 2000 CV cycles (1.00−1.10 V_{RHE})	-	-	1061
$CoSe_2$_2D	Ni foam	Nanosheets	P	0.6	372 (@50 $mA \cdot cm^{-2}_{geo}$)	11.9	0.656 at 370 mV	74		SEM, TEM, XRD, XPS	-	8 h CP (50 $mA \cdot cm^{-2}_{geo}$) 2000 CV cycles (1.00−1.10 V_{RHE})	-	-	
NiSe/Ni_3Se_2/NF-4	Ni foam	Nanoneedles	S	4.4	330 (@20 $mA \cdot cm^{-2}_{geo}$)	1.18	-	144.5	1 M KOH	XRD, SEM	-	-	-	-	1062
NiSe/Ni_3Se_2/NF-8	Ni foam	Nanosheets	S	5.3	325 (@20 $mA \cdot cm^{-2}_{geo}$)	1.42	-	74.9		XRD, SEM	-	-	-	-	
NiSe/Ni_3Se_2/NF-12	Ni foam	Nanosheets	S	5.7	260 (@20 $mA \cdot cm^{-2}_{geo}$)	1.72	-	69.2		XRD, SEM, TEM, EDX, XPS	XRD, SEM, XPS	50000 s CP (10 $mA \cdot cm^{-2}_{geo}$)	-	-	
NiSe/Ni_3Se_2/NF-16	Ni foam	Nanostructure	S	5.9	333 (@20 $mA \cdot cm^{-2}_{geo}$)	1.57	-	112.5		XRD, SEM	-	-	-	-	
NiSe/Ni_3Se_2/NF-20	Ni foam	Nanostructure	S	6.2	335 (@20 $mA \cdot cm^{-2}_{geo}$)	1.23	-	130.5		XRD, SEM	-	-	-	-	
160-NiSe/Ni_3Se_2/ NF-12	Ni foam	Nanowires	S	5.9	280 (@20 $mA \cdot cm^{-2}_{geo}$)	1.58	-	105.1		XRD, SEM	-	-	-	-	
200-NiSe/Ni_3Se_2/ NF-12	Ni foam	Nanostructure	S	7.3	353 (@20 $mA \cdot cm^{-2}_{geo}$)	1.16	-	109.5		XRD, SEM	-	-	-	-	
FeCoSe@CNT	GC	Nanotubes	P	-	330	86.1	-	74	1 M KOH	XRD, TGA, SEM, TEM, XPS	-	500 CV cycles (1.3−1.7 V_{RHE})	-	-	1063
CoSe@CNT	GC	Nanotubes	P	-	350	68.4	-	99		XRD, TGA, N_2 ISO (BET, PSD), SEM, TEM, XPS	-	-	-	-	
CoSe	GC	Nanoparticles	P	-	391	10.8	-	106		XRD, N_2 ISO (BET, PSD), SEM	-	-	-	-	
$NiSe_2$ NSs/CC-120	CC	Nansheets	S	-	332 (@40 $mA \cdot cm^{-2}_{geo}$)	11	-	109.4	1 M KOH	XRD, SEM	-	-	-	-	1064
$NiSe_2$ NSs/CC-150	CC	Nansheets	S	-	314 (@40 $mA \cdot cm^{-2}_{geo}$)	27	-	119.1		XRD, SEM	-	-	-	-	
$NiSe_2$ NSs/CC-180	CC	Nansheets	S	-	301 (@40 $mA \cdot cm^{-2}_{geo}$)	80	-	94.8		XRD, SEM, N_2 ISO (BET), TEM, EDX	SEM	12 h CA (1.286 V_{RHE})	-	-	
$NiSe_2$ NSs/CC-210	CC	Nansheets	S	-	340 (@40 $mA \cdot cm^{-2}_{geo}$)	20	-	164.4		XRD, SEM	-	-	-	-	
$NiCo_2Se_4$-H	Carbon electrode	Microspheres	P	0.01	300	-	-	72	0.1 M KOH	XRD, TEM, XPS, SEM, EDX	-	-	-	-	1065
$NiCo_2Se_4$-S	Carbon electrode	Microspheres	P	0.01	-	-	-	-		XRD, TEM	-	-	-	-	
$Co_{0.85}Se$	Carbon electrode	Microspheres	P	0.01	-	-	-	-		XRD, TEM, XPS	-	-	-	-	

https://doi.org/10.1021/acs.chemrev.3c00005
Chem. Rev. 2023, 123, 12795−13208

Table 6. continued

Initial Electrocatalyst	Substrate	Shape of Electrocatalyst	Deposition Type	Specific Loading/ $mg \cdot cm^{-2}_{geo}$	η@10 $mA \cdot cm^{-2}_{geo}$/ mV	C_{dl}/ $mF \cdot cm^{-2}_{geo}$	TOF/s^{-1} (@η or j)	Tafel Slope/ $mV \cdot dec^{-1}$	Electrolyte	Pre-analysis	Post-analysis	Long-Term OER Test Conditions	Post-OER Electrocatalyst	Final Type of Electrocatalyst	Ref.
$Ni_{0.85}Se$	Carbon electrode	Microspheres	P	0.01	-	-	-	-		XRD, TEM, XPS	-	-	-	-	1065
Ni_3Se_4	Ni foam	Nanorods	S	-	243	11.2	-	40	1 M KOH	XRD, SEM, TEM, EDX, XPS, Raman	-	24 h CP (10 $mA \cdot cm^{-2}_{geo}$)	-	-	1066
(Nanosheet) $NiCoSe_2$	CC	Nanosheets	S	1.6	255.8	-	6.6 at 330 mV	71		EDX, SEM, TEM, XPS, XRD	SEM, XPS	200 h CA (1.52 V_{RHE}) 5000 CV cycles	-	-	
NiSe	CC	Nanosheets	S	2.1	331.4	-	3.7 at 330 mV	143		EDX, SEM	-	-	-	-	
CoSe	CC	Nanosheets	S	1.7	313.1	-	4.7 at 330 mV	92		EDX, SEM	-	-	-	-	
(Pyramids) $NiCoSe_2$	CC	Pyramid	S	-	300.3	-	-	111	1 M KOH	EDX	-	-	-	-	1067
$Ni_{1.5}Co_{0.5}Se_2$	CC	Nanosheets	S	-	340 (@25 mA/cm^2_{geo})	-	-	-		EDX	-	-	-	-	
$Ni_{1.34}Co_{0.66}Se_2$	CC	Nanosheets	S	-	310 (@25 mA/cm^2_{geo})	-	-	-		EDX	-	-	-	-	
$Ni_{0.66}Co_{1.34}Se_2$	CC	Nanosheets	S	-	320 (@25 mA/cm^2_{geo})	-	-	-		EDX	-	-	-	-	
$Ni_{0.5}Co_{1.5}Se_2$	CC	Nanosheets	S	-	330 (@25 mA/cm^2_{geo})	-	-	-		EDX	-	-	-	-	
P-$NiSe_2$ (p:polyvinyl-pyrrolidone)	GC	Hollow nanoparticles	P	0.255	379 (@20 mA/cm^2_{geo})	-	-	-		XRD	-	-	-	-	
P-$Ni_{0.75}Fe_{0.25}Se_2$	GC	Hollow nanoparticles	P	0.255	272 (@20 mA/cm^2_{geo})	1.7	0.099 at 300 mV	56		XRD, SEM, TEM, EDX, XPS, N_2 ISO (BET, PSD)	SEM	12 h CP (10 $mA \cdot cm^{-2}_{geo}$)	-	-	
P-$Ni_{0.5}Fe_{0.5}Se_2$	GC	Hollow nanoparticles	P	0.255	338 (@20 mA/cm^2_{geo})	-	-	-		XRD, SEM	-	-	-	-	
P-$Ni_{0.25}Fe_{0.75}Se_2$	GC	Hollow nanoparticles	P	0.255	344 (@20 mA/cm^2_{geo})	-	-	-	1 M KOH	XRD, SEM	-	-	-	-	1068
P-$FeSe_2$	GC	Hollow nanoparticles	P	0.255	372 (@20 mA/cm^2_{geo})	-	-	-		XRD	-	-	-	-	
$Ni_{0.75}Fe_{0.25}Se_2$	GC	Hollow nanoparticles	P	0.255	301 (@20 mA/cm^2_{geo})	1.04	0.042 at 300 mV	80		N_2 ISO (BET, PSD)	SEM	-	-	-	
P0.5-$Ni_{0.75}Fe_{0.25}Se_2$	GC	Hollow nanoparticles	P	0.255	276 (@20 mA/cm^2_{geo})	-	-	73		-	-	-	-	-	
P2-$Ni_{0.75}Fe_{0.25}Se_2$	GC	Hollow nanoparticles	P	0.255	331 (@20 mA/cm^2_{geo})	-	-	64		-	-	-	-	-	
$NiSe_2$/NF	Ni foam	Nanosheets	S	-	274 (@20 mA/cm^2_{geo})	4.65	-	97		XRD, XPS, SEM, EDX	-	20 h CA	-	-	
Ni_3Se_2/NF	Ni foam	Nanosheets	S	-	287 (@20 mA/cm^2_{geo})	1.93	-	107	1 M KOH	XRD, XPS, SEM, EDX	-	20 h CA	-	-	1069
NiSe/NF	Ni foam	Nanosheets	S	-	329 (@20 mA/cm^2_{geo})	1.21	-	110		XRD, XPS, SEM, EDX	-	20 h CA	-	-	
$CoSe_2$	GC	Nanocubes	P	0.21	335	20.21	-	54.2	1 M KOH	TEM, SEM, XRD, XPS, N_2 ISO (BET, PSD), EDX	SEM	4 h CA (1.59 V_{RHE}) 1000 CV cycles (1.19−1.29 V_{RHE})	-	-	1070
$CoSe_2$ -NH_4OH	CC	Amorphous	P	-	670	-	-	-		TEM, XRD, EDX	-	-	-	-	
$CoSe_2$ -$C_2H_4N_2$	CC	Nanoparticles	P	-	340	-	-	-	0.1 M KOH	TEM, XRD, EDX	-	-	-	-	1071
$CoSe_2$ -$C_3H_{13}NO_3$	CC	Nanosheets	P	-	550	-	-	-		TEM, XRD, EDX	-	-	-	-	
$CoSe_2$ -N_2H_4	CC	Nanobulks	P	-	600	-	-	-		TEM, XRD, EDX	-	-	-	-	
NC-PoSe	GC	3D framework	P	-	430	-	-	157		TEM, XRD, Raman, N_2 ISO (BET, PSD), XPS, SEM	-	-	-	-	
FeSe/NC-PoFeSe Fe/Se = 1:0.5	GC	3D framework	P	-	450	-	-	-		-	-	-	-	-	
FeSe/NC-PoFeSe Fe/Se = 1:1	GC	3D framework	P	-	360	-	-	-	0.1 M KOH	SEM, TEM, XRD, Raman, N_2 ISO (BET, PSD), XPS, EDX	-	5000 s CA (1.6 V_{RHE})	-	-	1072
FeSe/NC-PoFeSe Fe/Se = 1:2	GC	3D framework	P	-	330	-	-	76		-	-	-	-	-	
FeSe/NC-PoFeSe Fe/Se = 1:4	GC	3D framework	P	-	350	-	-	-		-	-	-	-	-	
NiSe	GC	Nanoparticles	P	0.2	389	0.05	-	93		XRD, SEM, TEM, EDX, XPS	-	-	-	-	
$NiSe_2$	GC	Nanoparticles	P	0.2	427	-	-	136		XRD, SEM	-	-	-	-	
Ni_3Se_2	GC	Nanoparticles	P	0.2	469		-	120		XRD, SEM	-	-	-	-	
NiSe/MWCNTs	GC	Nanoparticles	P	0.2	336	1.10	-	78	1 M KOH	XRD, SEM, TEM, XPS, EDX, XPS	-	24 h CA (1.57 V_{RHE})	-	-	1073
$NiSe_2$/MWCNTs	GC	Nanoparticles	P	0.2	388	-	-	116		-	-	-	-	-	
Ni_3Se_2/MWCNTs	GC	Nanoparticles	P	0.2	361	-	-	67		-	-	-	-	-	
$CoSe_2$	CC	Nanoarray	S	1.7	-	12.01	-	62.5	1 M KOH	XRD, XPS, Raman, TEM, SEM, EDX, SAED	-	24 h CP (10 $mA \cdot cm^{-2}_{geo}$) 1000 CV cycles (1.35−1.55 V_{RHE})	-	-	1074
$Fe_{0.5}Co_{0.5}Se_2$	CFC	Nanospheres	S	-	290	-	-	64	1 M KOH	XRD, SEM, EDX, XPS	XRD	1000 CV cycles (0.45−0.55 V_{SCE})	-	-	1075
NiSe@CoOOH NWs/NF	Ni foam	Nanowire	S	4.8	217	-	-	65	1 M KOH	SEM, TEM, XRD, EDX, XPS, N_2 ISO (BET)	-	12 h CP (100 $mA \cdot cm^{-2}_{geo}$)	-	-	1076
Ti@$Co_{0.85}Se$	Ti mesh	Nanosheets	S	0.067	530	-	162 h^{-1} at 530 mV	153	1 M PBS (pH = 7.0)	SEM, EDX, TEM, XRD, XPS	-	30 h CA (1.75 V_{RHE}) 1000 CV cycles (0.2−1.6 V_{SCE})	-	-	1077
$Zn_{0.1}Co_{0.9}Se_2$	GC	Nanoparticles	P	0.285	340	8.57	-	43.2	1 M KOH	SEM, TEM, EDX, XRD, XPS, HAADF	SEM	30 h CA (1.57 V_{RHE}) 5000 CV cycles (1.30−1.70 V_{RHE})	-	-	1078

https://doi.org/10.1021/acs.chemrev.3c00005
Chem. Rev. 2023, 123, 12795−13208

Table 6. continued

Initial Electrocatalyst	Substrate	Shape of Electrocatalyst	Deposition Type	Specific Loading/ $mg \cdot cm^{-2}_{geo}$	η@10 $mA \cdot cm^{-2}_{geo}$/ mV	C_{dl}/ $mF \cdot cm^{-2}_{geo}$	TOF/s^{-1} (@η or j)	Tafel Slope/ $mV \cdot dec^{-1}$	Electrolyte	Pre-analysis	Post-analysis	Long-Term OER Test Conditions	Post-OER Electrocatalyst	Final Type of Electrocatalyst	Ref.
$Zn_{0.3}Co_{0.7}Se_2$	GC	Nanoparticles	P	0.285	-	5.74	-	68.9		XRD	-	-	-	-	1078
$Zn_{0.5}Co_{0.5}Se_2$	GC	Nanoparticles	P	0.285	-	5.01	-	84.2		XRD	-	-	-	-	
$CoSe_2$ ($CoSe_2$-450)	GC	Microsphere	P	0.354	330	7.8	0.016 at 330 mV	79	1 M KOH	XRD, SEM, EDX, XPS, TEM, N_2 ISO (BET)	-	5000 s CA (1.56 V_{RHE}) 1000 CV cycles (0.2–0.6 $V_{Hg/HgO}$)	-	-	1079
$NiFeCoSe_x$	CFC	Nanoparticles	S	-	150	200	-	85	1 M KOH	XRD, XPS, SEM, EDX	-	500 CV cycles (0.3–0.4 V_{SCE})	-	-	894
c-$CoSe_2$ (cubic phase)	GC	Nanocubes	P	0.27	230	40.41	-	83	1 M KOH	XRD, XPS, SEM, TEM, Raman, EDX, N_2 ISO (BET)	-	20 h CA (1.46 V_{RHE})	-	-	1080
o-$CoSe_2$ (orthorhombic phase)	GC	Nanocubes	P	0.27	310	28.77	-	124	1 M KOH	XRD, SEM, N_2 ISO (BET)	-	20 h CA (1.46 V_{RHE})	-	-	
$Co_{0.85}Se$@NC	GC	Nanocrystals	P	0.4	-	3.2	-	75	1 M KOH	XRD, TG, XPS, XANES, EXAFS, SEM, TEM, EDX, Raman	TEM	12 h CA (1.55 V_{RHE}) 12 h CP (10 $mA \cdot cm^{-2}_{geo}$) 1000 CV cycles (1.15–1.19 V_{RHE})	-	-	1081
$Ni_{0.7}Co_{0.3}Se_2$/CC	CC	Nanosheets	S	2.8	258	40.8×10^{-3}	-	42.3	1 M KOH	SEM, EDX, TEM, XPS, XRD, N_2 ISO (BET, PSD), ICP-AES, SAED	-	50 h CP (10 $mA \cdot cm^{-2}_{geo}$)	-	-	1082
$CoSe_2$/CC	CC	Nanosheets	S	2.2	267	16.6×10^{-3}	-	51.6		TEM, SEM, XRD, XPS, ICP-AES, N_2 ISO (BET, PSD)	-	-	-	-	
$NiSe_2$/CC	CC	Nanosheets	S	2.4	288	21.2×10^{-3}	-	55.8		TEM, SEM, XRD, XPS, ICP-AES, N_2 ISO (BET, PSD)	-	-	-	-	
ZIF-$Co_{0.85}Se$	GC	Nanoparticles	P	0.14	360	-	-	62	1 M KOH	XRD, TEM, EDX, XPS, N_2 ISO (BET)	-	10000 s CA (1.60 V_{RHE})	-	-	1083
PBA-$Co_{0.85}Se$	GC	Nanoparticles	P	0.14	520	-	-	115		XRD, XPS, SEM, TEM, N_2 ISO (BET)	-	10000 s CA (1.60 V_{RHE})	-	-	
$Co_{0.85}Se$	GC	Nanoparticles	P	0.14	450	-	-	133		XPS, SEM, TEM, N_2 ISO (BET)	-	10000 s CA (1.60 V_{RHE})	-	-	
CeO_2/$CoSe_2$	GC	Nanoparticles/ Nanobelts	S	0.2	288	-	-	44	0.1 M KOH	SEM, TEM, STEM-EDX, XRD, XPS, FTIR, Raman	-	10 h CP (10 $mA \cdot cm^{-2}_{geo}$)	-	-	1084
$CoSe_2$/CF	CF	Nanoparticles	S	2.9	297	-	-	41	1 M KOH	XRD, SEM, TEM, XPS, FTIR, UV-Vis, EDX	-	20 h CP (1.57 V_{RHE}) 5000 CV cycles (1.20–1.70 V_{RHE})	-	-	1085
$NiSe_2$/$Ni(O_x)$	Ni foam (oxidized)	Pyramids	S	-	-	-	-	96	1 M KOH	XRD, XPS, TEM, SEM	-	-	-	-	1086
NiSe/NF	Ni foam	Nanorods, Nanowires	S	-	-	-	-	153		XRD, XPS, TEM	-	-	-	-	
$CoSe_2$/Ni_3Se_2	CFP	Microsphere	S	0.2	393	-	-	89	0.1 M KOH	XRD, SEM, EDX, XPS	SEM	10 h CA (1.65 V_{RHE})	-	-	1087
EG/$Co_{0.85}Se$/ NiFe-LDH	EG	Nanoarray	S	-	270 (@150 $mA \cdot cm^{-2}_{geo}$) 280 (@150 $mA \cdot cm^{-2}_{geo}$)	-	-	57	1 M KOH	SEM, FTIR, XPS, EDX, TEM, XRD, Raman, ICP-OES, SAED	XRD, XPS	10 h CP (200 $mA \cdot cm^{-2}_{geo}$)	-	-	1088
EG/$Co_{0.85}Se$	EG	Nanosheets	S	-	-	-	-	73		-	-	-	-	-	
GaSe	GC	Layered structure	P	-	-	-	-	-	0.1 M KOH	SEM, EDX, Raman, XRD, XPS	-	-	-	-	853

[a]Some values (i.e., "specific loading", "η", and "C_{dl}") were calculated or obtained from the descriptions and figures in the previous papers. "Post-OER Electrocatalyst" and "Final Type of Electrocatalyst" were determined based on the experimental results and descriptions provided in the previous papers. [b]η, overpotential; j, current density; C_{dl}, double layer capacitance; TOF, turnover frequency; P, powder-coated electrode; S, self-supported electrode; CV, cyclic voltammetry; CA, chronoamperometry; CP, chronopotentiometry; OWS, overall water splitting. [c]Substrate abbreviations: GC (glassy carbon); CC (carbon cloth); CP (carbon paper); CFC (carbon fiber cloth); CF (carbon fiber); FTO (fluorine-doped tin oxide); EG (exfoliated graphite); PGE (pencil graphite electrode). [d]Electrolyte abbreviation: PBS (phosphate buffer solution). [e]Analysis abbreviations (minor terms only): ISO (isotherm); PSD (pore size distribution); CAM (contact angle measurement).

https://doi.org/10.1021/acs.chemrev.3c00005
Chem. Rev. 2023, 123, 12795−13208

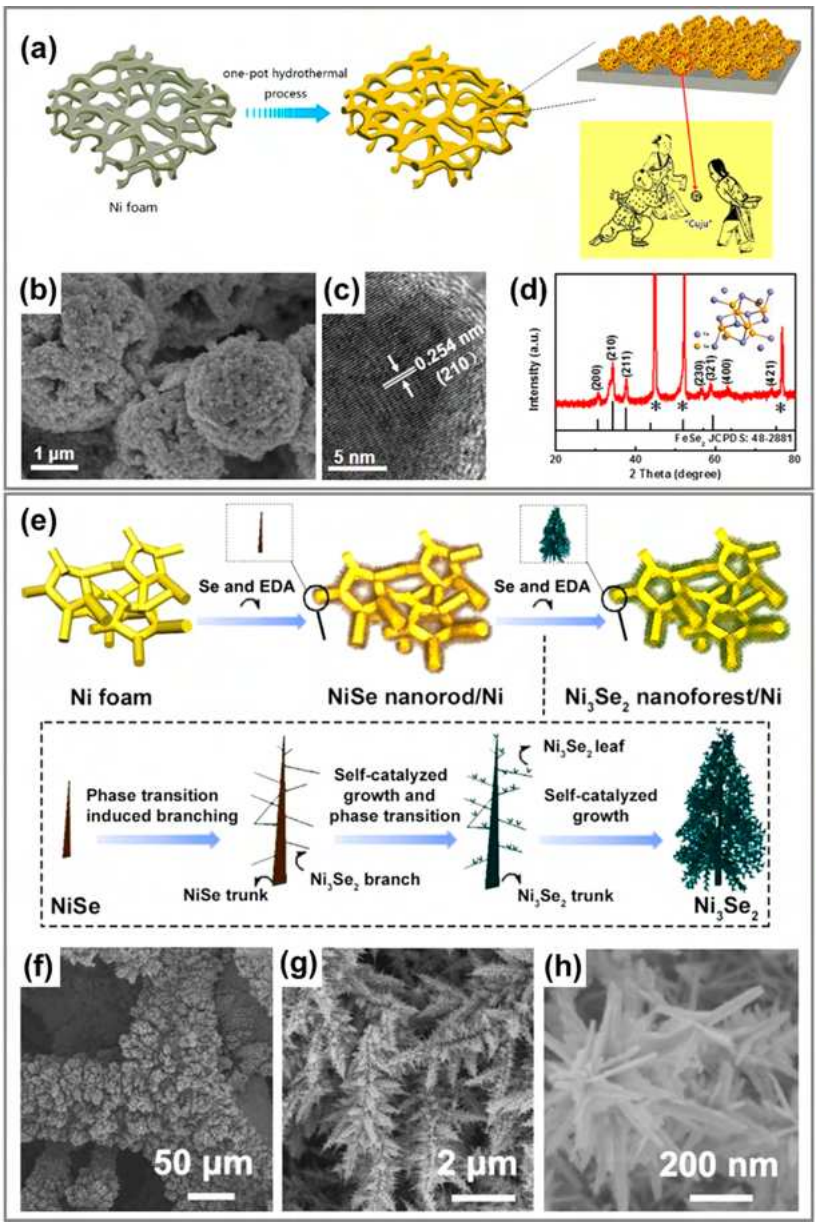


Figure 211. (a) Schematic illustration of the synthesis process of "Cuju-balls-like" $FeSe_2$ on Ni foam. (b) SEM image of $FeSe_2$ grown on the surface of Ni foam. (c) TEM image of $FeSe_2$. (d) XRD pattern of the $FeSe_2$ on Ni foam (inset: the crystal structure of $FeSe_2$). Reproduced with permission from ref 1015. Copyright 2017 American Chemical Society. (e) Schematic illustration for the formation process of Ni_2Se_3 nanoforest on Ni foam. (f–h) SEM images of the as-synthesized Ni_3Se_2 nanoforest supported on Ni foam. Reproduced with permission from ref 1025. Copyright 2016 Elsevier.

this hydrothermal synthesis produced a high-surface-area metal selenide, resulting in an increased number of exposed active sites for the OER. The porosity of the electrocatalyst induced vacancy defects and lattice distortion in the internal structure, which contributed to the enhanced electrochemical performance of $FeSe_2$. In the high-magnification TEM image and XRD pattern (Figures 211c and d), the lattice fringe and peak corresponding to the (210) plane of $FeSe_2$ were observed, respectively. Moreover, the diffraction peaks in the XRD pattern also showed the crystal structure of the iron diselenide without any crystalline impurity phases (see Figure 211d). Similarly, Shanmugam *et al.* grew crystalline Ni_3Se_2 directly on Ni foam via hydrothermal synthesis using Ni foam and Se powder as Ni and Se sources, respectively.[1006] The fabricated Ni_3Se_2 had a rhombohedral crystal structure, and the rough surface of the porous electrocatalyst led to increased surface area and paths for evolved gas to escape during the OER. The two works discussed show that the hydrothermal method can be used to prepare highly crystalline selenide structures with large surface areas for enhanced OER electrocatalysis.

During one-step hydrothermal synthesis, the morphologies of transition metal selenides can be regulated by adding a chelating agent to the reaction solution. For example, Zhang *et al.* used the one-step hydrothermal method to synthesize nanoforest-like Ni_3Se_2 on Ni foam using the chelating agent ethylenediamine (EDA).[1025] The unique mechanism of Ni_3Se_2 growth is shown in Figure 211e. At first, under the assistance of EDA acting as a shape modifier,[1093] the self-catalyzed growth of NiSe nanowires on the Ni foam surface occurred. Then, the phase-induced branching led to the amine-assisted growth of

https://doi.org/10.1021/acs.chemrev.3c00005
Chem. Rev. 2023, 123, 12795−13208

Ni_3Se_2 on NiSe nanowires. Finally, the phase transformed from hexagonal NiSe to rhombohedral Ni_3Se_2 by sequential self-catalyzed growth, and the Ni_3Se_2 hierarchical branches and leaves grew mainly on the Ni_3Se_2 trunk. As shown in the SEM images, a nanoforest-like morphology was obtained capable of improved catalysis via large surface area (a large number of exposed active sites for the OER) (Figures 211f–h). In addition, the surfaces of the nanoforest branches and leaves were hydrophilic and aerophobic in nature, leading to efficient electrolyte penetration and bubble release during the OER.

By using the one-step hydrothermal method, transition metal selenide powders can also be prepared. A typical one-step hydrothermal process is illustrated in Figure 212a: the Se source and metal ions are mixed in an autoclave and then heated to generate the final product. Yan *et al.* synthesized crystalline $FeSe_2$ nanoplatelets, as displayed in Figure 212a, and then deposited the $FeSe_2$ nanoplatelets onto Ni foam.[1011] Figures 212b–e show the structure and morphology of the as-obtained selenide powder. The XRD pattern revealed a highly crystalline structure for orthorhombic $FeSe_2$ (Figure 212b), and the SEM and TEM images showed the platelet-like morphology (Figures 212c and d). From HRTEM, a lattice fringe corresponding to the (210) plane of $FeSe_2$ was observed, which matches with the results from XRD (Figure 212e). The authors found that the unique 2D nanostructure of $FeSe_2$ enhanced the kinetics of water oxidation and that the exposed (210) crystal facet guaranteed long-term electrocatalysis of the OER without significant activity decay. They also showcased the ability to obtain a variety of morphologies for a given material using hydrothermal synthesis, as $FeSe_2$ nanorods were obtained at 120 °C, bulk $FeSe_2$ at 210 °C, and $FeSe_2$ nanoplatelets at 180 °C, respectively. Of the three morphologies, the $FeSe_2$ nanoplatelet morphology was the most advantageous for OER electrocatalysis, as it led to more exposed surface area and, therefore, active sites. In another work, Xu *et al.* employed a simple one-step hydrothermal method to synthesize a CoSe/$FeSe_2$ nanohybrid electrocatalyst and then transferred it onto Ni foam.[977] The crystalline $Co_{0.75}Fe_{0.25}$-Se had a nanohybrid structure consisting of $FeSe_2$ and CoSe with defects. The abundant heterointerface sites and synergistic effect between $FeSe_2$ and CoSe led to improved OER electrocatalysis, as did the present defects via increased surface area. The above two examples show that the hydrothermal method can be used to synthesize selenide powder samples of a variety of structures and morphologies in one step.

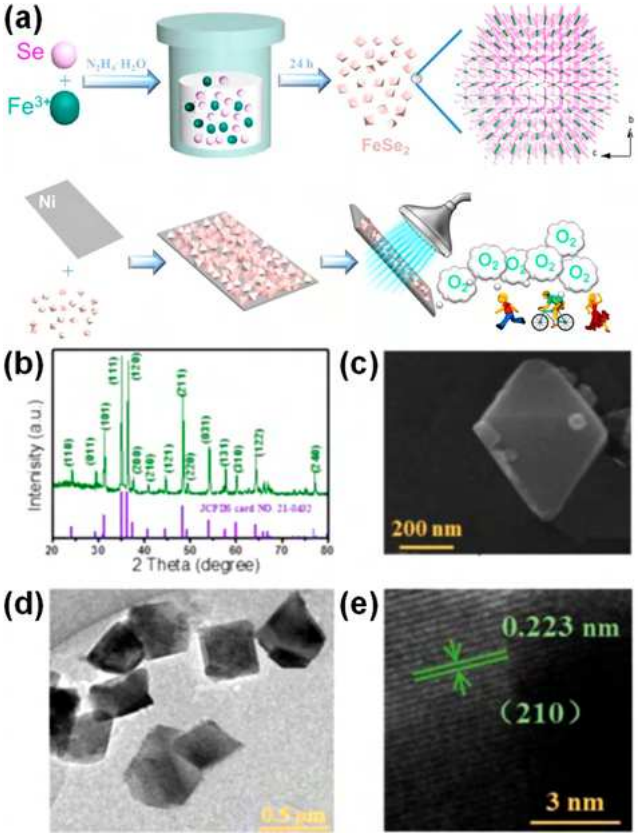


Figure 212. (a) Schematic illustration for the synthesis process of $FeSe_2$ nanoplatelets and its application for the OER. (b) XRD pattern and (c) SEM, (d) TEM, and (e) HRTEM images of $FeSe_2$-180 °C nanoplatelets. Reproduced with permission from ref 1011. Copyright 2017 Elsevier.

The hydrothermal process can also be carried out in two steps, wherein the first step is the synthesis of precursors [e.g., $Co(CO_3)_{0.5}OH$, CoO, NiFe layered double hydroxide (LDH), etc.] with well-defined morphologies (e.g., nanosheet, nanoarray, etc.) and the second step is the selenization step for the incorporation of selenium into the nanostructures and roughening of the material surface.[1022,1052] By using two steps to prepare metal selenides, it becomes easier to synthesize these materials with set morphologies, as they can be pre-determined using the precursors prepared in step one, while also imparting greater surface area unto the material via surface roughening in the selenization step. For example, Mai *et al.* grew crystalline $(Ni_{0.75}Fe_{0.25})Se_2$ nanosheets *in situ* on carbon fiber cloth via a two-step hydrothermal method (Figure 213a).[1022] In the first step, $Ni(NO_3)_2{\cdot}6H_2O$, $Fe(NO_3)_3{\cdot}9H_2O$, NH_4F, and $CO(NH_2)_2$ were mixed in deionized water and then transferred into an autoclave to generate a nanosheet-like NiFe-based precursor, $Ni_{0.75}Fe_{0.25}(CO_3)_{0.125}(OH)_2{\cdot}0.38H_2O$ (Figures 213b). In the second step, the NiFe-based precursor was hydrothermally selenized into highly crystalline $(Ni_{0.75}Fe_{0.25})Se_2$, as signified by the XRD pattern (Figure 213e). The SEM and TEM images show that the $(Ni_{0.75}Fe_{0.25})$-Se_2 electrocatalyst consisted of porous nanosheets, which indicates clear retention of the overall shape of the precursor (Figures 213c–d and f–g). During the hydrothermal selenization process (second step), due to the removal of carbonate and hydroxyl groups, there was a drastic phase shift from the rhombohedral phase (precursor) to the cubic phase (selenide). This phase transformation led to the highly porous nature of the metal selenide and additional surface area. Fang *et al.* synthesized selenides of $CoSe_2$ with core-branch morphology (Figure 213h) using a two-step process, wherein the hydrothermal method was employed to generate a nanoarray structure to maximize the surface area exposed to the electrolyte for enhanced electrochemical performance.[988] First, the hydrothermal method and annealing were used to synthesize a CoO nanocones precursor. Then a Na_2SeO_3-assisted selenization was carried out via the hydrothermal method to transform CoO nanocones into hollow core-branch $CoSe_2$ (see Figures 213i and j). The hollow core-branch $CoSe_2$ had a rougher surface compared to the CoO precursor, as shown in Figure 213k. The as-prepared $CoSe_2$ had a highly crystalline structure, as indicated by the HRTEM images (Figures 213l and m) and XRD pattern (Figure 213n). Liu *et*

https://doi.org/10.1021/acs.chemrev.3c00005
Chem. Rev. 2023, 123, 12795–13208

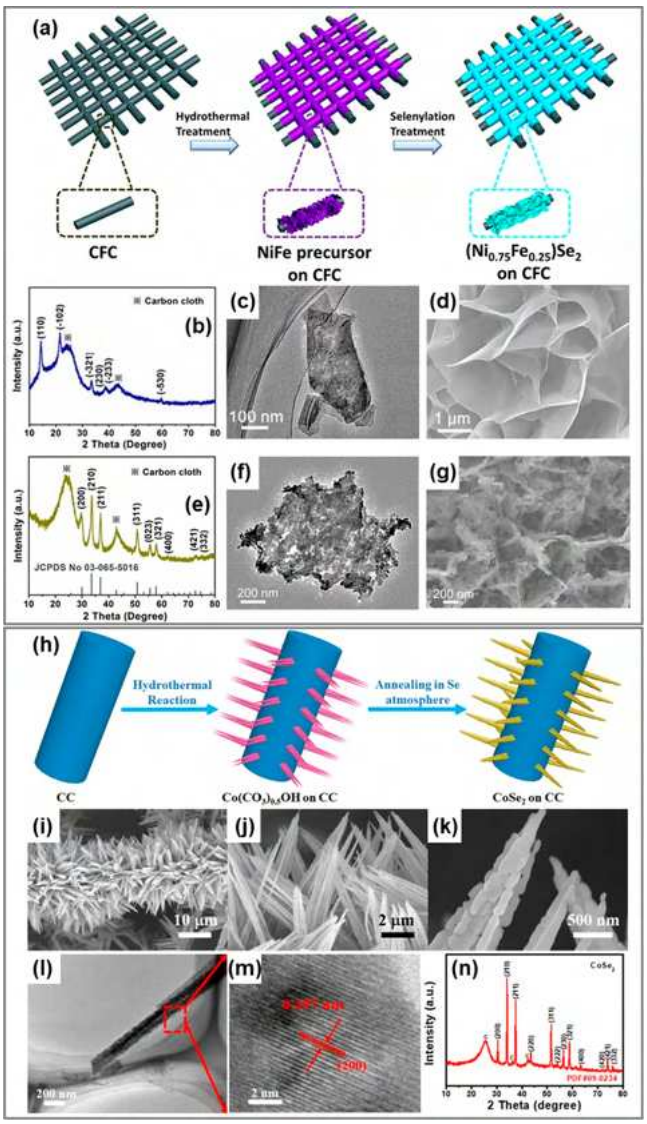


Figure 213. (a) Schematic illustration of the synthesis procedures for porous $(Ni_{0.75}Fe_{0.25})Se_2$ nanosheets on CFC. (b) XRD pattern and (c) TEM and (d) SEM images of a NiFe-based precursor. (e) XRD pattern and (f) TEM and (g) SEM images of porous $(Ni_{0.75}Fe_{0.25})Se_2$ nanosheets on CFC. Reproduced with permission from ref 1022. Copyright 2016 American Chemical Society. (h) Schematic illustration for the formation of bamboo-like $CoSe_2$ on carbon cloth. (i–k) SEM and (l, m) HRTEM images and (n) XRD pattern of $CoSe_2$. Reproduced with permission from ref 1074. Copyright 2018 IOP Publishing.

al. also fabricated $Co_{0.75}Ni_{0.25}Se$ nanorods on Ni foam using a two-step hydrothermal procedure.[1052] They used the hydrothermal method to prepare a Co-based precursor on Ni foam consisting of nanoclusters. This nanocluster precursor was then used to prepare a bimetallic selenide, $Co_{0.75}Ni_{0.25}Se$, that retained the precursor morphology with only additional roughening at the surface. The Co-based precursor was converted into the bimetallic selenide via an anion exchange reaction. Thus, as these examples show, the hydrothermal method is advantageous, as it enables control over the resulting metal selenide morphology—by carefully selecting a precursor with a morphology favorable for OER electrocatalysis (i.e., large surface area for an abundance of exposed active sites), the electrocatalytic performance of metal selenides can be optimized, as the selenization step will impart additional surface area via roughening.

Regarding two-step synthesis, several researchers have used other methods (e.g., electrodeposition, solution-based method, electrospinning, etc.) to synthesize precursors and reserved the hydrothermal method for the selenization step using Se sources such as Se powder or NaHSe.[1005,1025,1045,1047,1088] For instance, Zheng *et al.* designed a self-regulated acidic etching method to synthesize a $Ni(OH)_2$ precursor and then applied topotactic selenization (a structural change to a crystalline solid) to convert layered $Ni(OH)_2$ into ultrathin 2D nonlayered NiSe nanosheets using the hydrothermal method (Figures 214a).[991] In the first step, they placed Ni foam in an HCl solution and held the solution at 80 °C while stirring for 20 h to *in situ* etch Ni foam and generate $Ni(OH)_2$. The $Ni(OH)_2$ precursor formed as a result of the consumption of H^+ from HCl which enabled hydrolysis to occur at Ni sites. The as-prepared $Ni(OH)_2$ exhibited a two-tiered morphology consisting of nanosheets of relatively large size and low thickness (0.96 nm), as shown in Figures 214b and c. To prepare NiSe, the 2D layered $Ni(OH)_2$ precursor was mixed with NaHSe and heated in an autoclave at 180 °C for 4 h. The SEM image of NiSe indicated that the two-tiered structure was maintained (Figure 214d). The XRD patterns of the samples before and after hydrothermal selenization revealed the complete phase conversion from hexagonal β-$Ni(OH)_2$ to hexagonal NiSe (Figure 214e). In another example, Liu *et al.* grew $Ni_{0.5}Fe_{0.5}Se_2$ on carbon fiber cloth (CFC) *in situ* via electrodeposition followed by hydrothermal selenization.[1005] They first electrodeposited NiFe hydroxide on the CFC. Then, the $Ni_{0.75}Fe_{0.25}Se_2$ was synthesized by mixing NaHSe with the as-prepared NiFe hydroxide and heating the solution at 140 °C for 12 h in an autoclave (Figure 214f). From XRD (Figure 214g), it is evident that via hydrothermal selenization, an amorphous NiFe hydroxide was converted into a crystalline transition metal selenide (i.e., cubic pyrite-type metal diselenide), as sharp peaks emerged in the diffraction pattern. Additionally, changes in morphology from vertical NiFe hydroxide nanosheets to pyrite-type octahedral structured $Ni_{0.75}Fe_{0.25}Se_2$ before and after the hydrothermal process were observed, as shown by SEM and TEM images (Figures 214f, h, and i). Thus, transition metal selenide electrocatalysts can be generated using two-step processes in which the hydrothermal method is used for the selenization step.

The hydrothermal method has also been used to prepare selenide/other material(s) composites (i.e., selenide/hydroxide, selenide/carbon-based material, and selenide/hydroxide/carbon-based material) as OER electrocatalysts. For the preparation of selenide/hydroxide composites, hydroxides are usually coated on the surfaces of the selenides to boost electrochemical performance by providing increased surface area and active sites for catalysis. For instance, Wang *et al.* synthesized CoSe/NiFe layered double hydroxide nanotube arrays on Ni foam (CoSe@NiFe-LDH/NF) through a three-step hydrothermal process (Figure 215a).[960] First, they sealed and heated $Co(NO_3)_2{\cdot}6H_2O$, $CO(NH_2)_2$, NH_4F, and deionized water with pre-treated Ni foam in an autoclave to prepare a cobalt carbonate hydroxide precursor. Then, for hydrothermal selenization, which seems to be solvothermal selenization from our best knowledge, the precursor was mixed with Se powder, NaOH, DMF, and hydrazine hydrate, and the mixture was heated in an autoclave to generate CoSe nanotubes consisting of plicated nanosheets on Ni foam.

https://doi.org/10.1021/acs.chemrev.3c00005
Chem. Rev. 2023, 123, 12795−13208

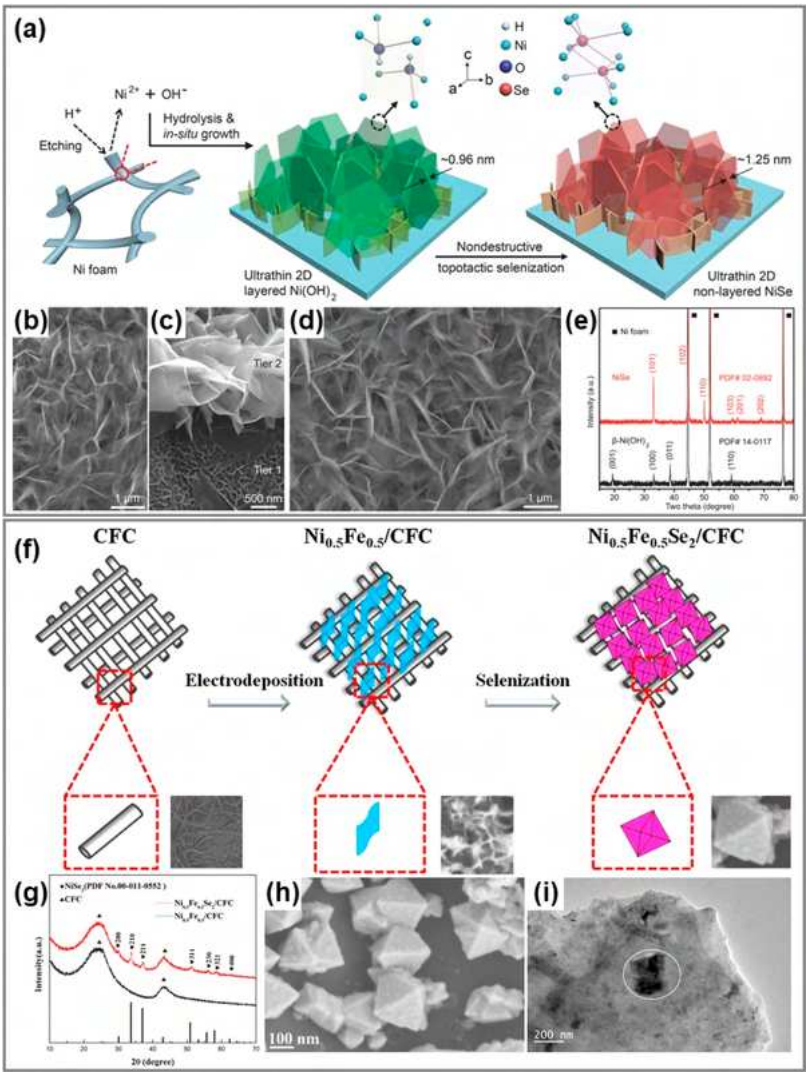


Figure 214. (a) Schematic illustration for the formation of an NiSe electrode. (b, c) SEM images of a $Ni(OH)_2$ precursor. (d) SEM image and (e) XRD pattern of NiSe. Reproduced with permission from ref 991. Copyright 2018 Wiley. (f) Schematic illustration of the fabrication procedure for pyrite-type octahedral $Ni_{0.5}Fe_{0.5}Se_2$ on CFC. (g) XRD patterns of $Ni_{0.5}Fe_{0.5}$ hydroxide and $Ni_{0.5}Fe_{0.5}Se_2$ on CFC. (h) SEM and (i) TEM images of pyrite-type octahedral $Ni_{0.5}Fe_{0.5}Se_2$ on CFC. Reproduced with permission from ref 1005. Copyright 2017 Elsevier.

During this process, the inner carbonate hydroxide diffused outward, while Se^{2-} species released from the Se powder moved inward. Owing to the difference in the diffusion rates ($d_{Co} > d_{Se}$) (i.e., the Kirkendall effect), the nanowires of the precursor were gradually transformed into the hollow nanotubes of the selenide during selenization. Finally, the as-obtained CoSe/NF was put in an aqueous solution containing $Fe(NO_3)_2{\cdot}9H_2O$, $Ni(NO_3)_2{\cdot}6H_2O$, and urea, and the mixture was heated in an autoclave to obtain NiFe-LDH coated on the surface of the CoSe/NF. The resultant CoSe@NiFe-LDH/NF inherited the hollow nanotube structure from CoSe/NF, which was indicated by TEM results (Figure 215b). From the HRTEM image and XRD pattern, both the NiSe and NiFe-LDH phase were observed (Figure 215c and d). The SEM images revealed the rough surface of the layered structure NiSe@NiFe-LDH, which provided an open 3D structure for electrolyte contact and improved bubble release (Figure 215e). Thus, composite metal selenide/hydroxide materials can be prepared via the hydrothermal method for improved OER electrocatalysis.

Metal selenide/carbon-based material composites have also been prepared owing to carbon-based material's rough surfaces and high conductivity. Carbon materials composed of conjugated sp^2 carbon networks, such as graphitic carbon nitride ($g\text{-}C_3N_4$), enable fast charge transfer between electrocatalysts and substrates owing to their large degree of electron delocalization. This fast charge transfer results in short charge carrier paths to active sites in the metal selenide, resulting in improved electrocatalytic efficiency. He *et al.* prepared a nickel selenide ($NiSe_2$) on $g\text{-}C_3N_4$ using a one-step hydrothermal process (Figure 215f).[1045] The Ni source $NiCl_2{\cdot}6H_2O$, Se powder, and $NaBH_4$ were mixed together in deionized water and stirred for 1 h and then mixed with $g\text{-}C_3N_4$-containing aqueous suspension and transferred to an autoclave to undergo hydrothermal synthesis (160 °C, 12 h) and produce $NiSe_2/g\text{-}C_3N_4$. SEM images showed that $NiSe_2$ nanoparticles were anchored onto the rough surface of $g\text{-}C_3N_4$, resulting in a nanocoral-like structure (Figure 215g). The XRD pattern indicated that the crystalline structure of $NiSe_2/g\text{-}C_3N_4$ did not differ from that of $NiSe_2$ (Figure 215h), which further indicated the successful formation of $NiSe_2$ on $g\text{-}C_3N_4$. Feng

https://doi.org/10.1021/acs.chemrev.3c00005
Chem. Rev. 2023, 123, 12795−13208

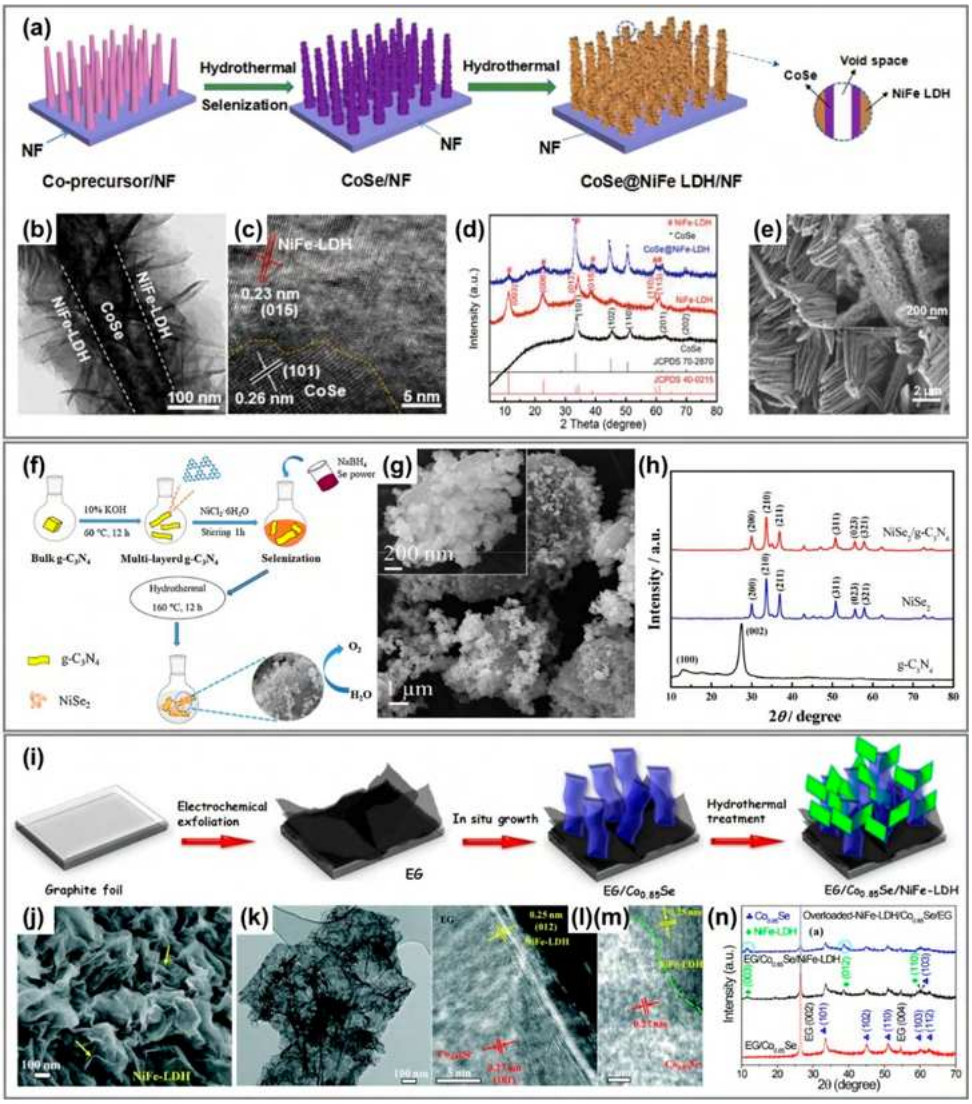


Figure 215. (a) Schematic representation for the formation process of CoSe@NiFe-LDH/NF. (b) TEM and (c) HRTEM images, (d) XRD pattern, and (e) SEM image of the CoSe@NiFe-LDH/NF. Reproduced with permission from ref 960. Copyright 2019 Elsevier. (f) Schematic illustration for the synthesis procedure of $NiSe_2/g\text{-}C_3N_4$ composite electrocatalyst. (g) SEM images of $NiSe_2/g\text{-}C_3N_4$ nanocoral composite. (h) XRD patterns of as-prepared $g\text{-}C_3N_4$, $NiSe_2$, and $NiSe_2/g\text{-}C_3N_4$ samples. Reproduced with permission from ref 1045. Copyright 2019 Elsevier. (i) Schematic illustration for the synthesis process of $EG/Co_{0.85}Se$/NiFe-LDH. (j) FESEM, (k) TEM, and (l, m) HRTEM images of $EG/Co_{0.85}Se$/NiFe-LDH. (n) XRD patterns of $EG/Co_{0.85}Se$, $EG/Co_{0.85}Se$/NiFe-LDH, and overloaded-NiFe-LDH/$Co_{0.85}Se$/EG. Reproduced with permission from ref 1088. Copyright 2016 Royal Society of Chemistry.

et al. also prepared a composite material using a carbon-based substrate. Specifically, they grew $Co_{0.85}Se$ and NiFe layered double hydroxide (NiFe-LDH) on exfoliated graphite (EG) foil *in situ* via a two-step hydrothermal process.[1088] First, graphite foil was exfoliated though anodization. Second, $Co_{0.85}Se$ was *in situ* grown on the EG foil, generating nanosheet-like structures. Then, NiFe-LDH was generated on the surface hydrothermally, resulting in a roughened surface, as depicted in Figure 215j. A schematic illustration of this process is displayed in Figure 215i. From the TEM and HRTEM images, the presence of NiFe-LDH and $Co_{0.85}Se$ was confirmed, as the top NiFe-LDH layer was visible (Figure 215k) and the observed lattice fringes corresponded to the (012) plane of NiFe-LDH and to the (101) plane of $Co_{0.85}Se$ (Figures 215l and m). Additionally, these crystal planes were also detected via XRD (Figure 215n). Notably, a high-surface-area 3D nanostructured hybrid metal selenide capable of promoting oxygen diffusion and contact between electrocatalytic material and electrolyte was prepared, resulting in decent OER performance (see Table 6). Thus, metal selenides prepared on carbon-based substrates enabled improved OER electrocatalysis owing to their high conductivity and potential to increase the electrochemically active surface area (ECSA).

5.2.1.2. Solvothermal Methods. The solvothermal method, like the hydrothermal method, involves solution-based synthesis in a temperature-controlled autoclave; however, instead of water as the solvent, other organic solvents [e.g., ethanol, ethylene glycol (EG), $N_2H_4{\cdot}H_2O$, etc.] are used. In the literature, the solvothermal method has been used for the preparation of metal selenides, owing to the variety of crystal structures and morphologies that can be obtained.[987,990,1047,1079,1087] For instance, Chen *et al.* used a three-step approach to synthesize triangle-like hollow (Ni,Co)-Se_2 arrays on carbon cloth by using the solvothermal method

https://doi.org/10.1021/acs.chemrev.3c00005
Chem. Rev. 2023, 123, 12795−13208

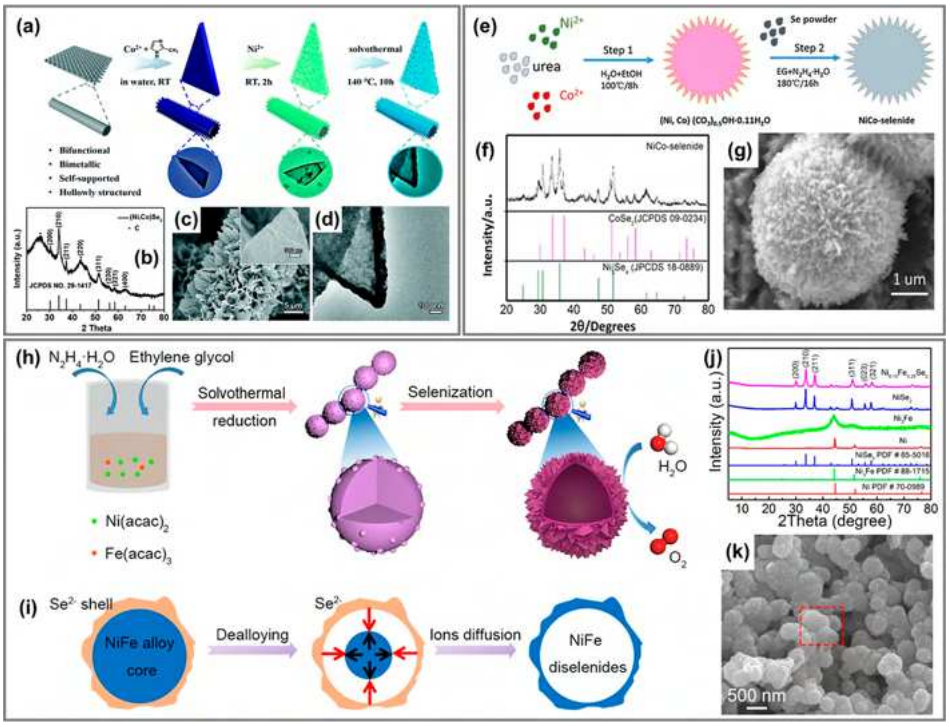


Figure 216. (a) Schematic illustration for the fabrication process of triangle-like hollow (Ni,Co)Se_2 arrays on carbon cloth. (b) XRD pattern and (c) SEM and (d) TEM images of the hollow (Ni,Co)Se_2 plate. Reproduced with permission from ref 1047. Copyright 2019 Royal Society of Chemistry. (e) Schematic illustration for the formation process of the NiCo-selenide nanocomposite. (f) XRD pattern and (g) SEM image of NiCo-selenide. Reproduced with permission from ref 1087. Copyright 2016 Springer Nature. (h, i) Schematic illustrations for the synthetic process of NiFe diselenide hollow nanochains (h) and the formation of hollow structure (i). (j) XRD patterns of Ni_3Fe, $NiSe_2$, and $Ni_{0.75}Fe_{0.25}Se_2$. (k) SEM image of NFSHNCs. Reproduced with permission from ref 990. Copyright 2018 Elsevier.

for the selenization step (Figure 216a).[1047] First, they grew MOF-Co onto carbon cloth as a template via the solution-based method. Then, the MOF-Co template was converted to NiCo-LDH through an etching reaction with $Ni(NO_3)_2$. The NiCo-LDH was sealed with NaHSe and N_2-saturated ethanol in an autoclave and solvothermally selenized to (Ni,Co)Se_2 at 140 °C for 10 h. The crystalline structure of (Ni,Co)Se_2 was confirmed via XRD (Figure 216b). SEM and TEM results indicated that the final selenide retained the hollow triangle morphology originating from the precursor, enabling a high-surface-area material for electrocatalysis (Figures 216c and d). After the solvothermal selenization, the wall of the hollow selenides became thicker. Although the resulting selenide had thicker walls than its precursor, it retained the overall triangle-like hollow structure, enabling a higher surface area for improved electrocatalysis. Other than *in situ* growth of selenides on substrates, researchers have synthesized various selenide powder samples with different morphologies through the solvothermal method and then deposited them onto glassy carbon electrodes as an ink via drop casting. Xiao *et al.* employed a two-step solvothermal method to prepare a NiCo-selenide nanocomposite with a nanosphere-like structure for OER electrocatalysis (Figure 216e).[1087] Initially, $Co(NO_3)_2 \cdot 6H_2O$, $Ni(NO_3)_2 \cdot 6H_2O$, and urea were dissolved in deionized water and absolute ethanol and then transferred into an autoclave to be heated at 100 °C for 8 h to prepare a NiCo-percursor. Then, the as-synthesized precursor was mixed with Se powder, $N_2H_4 \cdot H_2O$, and EG in the autoclave and heated to 180 °C for 16 h. The XRD patterns showed the composition of the NiCo-precursor and NiCo-selenide and revealed that the NiCo-selenide consisted of two selenide phases (Figure 216f). A comparison of the SEM images of the NiCo-precursor and produced N-Co selenides indicate retention of the initial urchin-like microsphere morphology following solvothermal synthesis (Figure 216g). Wang *et al.* also used a two-step solvothermal method to synthesize NiFe diselenide hollow nanochains (NFSHNCs) (Figure 216h).[990] First, they used the solvothermal method to prepare a nickel−iron alloy nanochain precursor by mixing $Ni(acac)_2$ and $Fe(acac)_3$ into EG and $N_2H_4 \cdot H_2O$ to be heated at 160 °C for 10 h. Then, the precursor was transferred into another autoclave, submerged in an as-prepared solution containing Se^{2-} and Se species, and brought to 180 °C for 1 h to produce NFSHNCs. Figure 216i displays the formation of the hollow structured NFSHNCs; during synthesis, the NiFe alloy core was gradually consumed by Se^{2-} ions, resulting in a hollow NiFe selenide. This resulting hollow microsphere-like structure was confirmed via SEM and TEM (Figure 216k). In addition, XRD results indicated the NFSHNCs were crystalline in nature with peaks corresponding to Ni_3Fe and $NiSe_2$ (Figure 216j). Therefore, the solvothermal method has a similar mechanism and function as the hydrothermal method. The main difference between hydrothermal and solvothermal methods is that the solvothermal method uses organic liquid as a solvent, while the hydrothermal method uses water as a solvent. Like the hydrothermal method, the solvothermal method can be used to fabricate synthetic precursors and for selenization in the preparation of crystalline metal selenides for OER catalysis.

5.2.1.3. Electrodeposition. Electrodeposition enables the facile growth of transition metal selenides onto conductive substrates for enhanced conductivity and film uniformity. This growth is controlled using an electric field, enabling even

https://doi.org/10.1021/acs.chemrev.3c00005
Chem. Rev. 2023, 123, 12795−13208

coating of the metal selenide across the substrate surface for the generation of self-supported electrodes. Compared with other methods, such as chemical vapor deposition (CVD), electrodeposition is a much more user-friendly synthesis method and much less dangerous. Like the hydrothermal method, electrodeposition has been used to prepare transition metal selenides using one- and two-step processes.[925,980,994,1008,1020,1023,1067]

Regarding the one-step process, the preparation of selenide electrocatalysts on various substrate surfaces has been achieved by *in situ* electrodeposition at constant potential.[925,994,1008,1023,1067] For example, Wang *et al.* synthesized $NiCoSe_2$ on a carbon cloth substrate via electrodeposition.[1067] First, an electrodeposition solution containing $NiCl_2{\cdot}6H_2O$, $CoCl_2{\cdot}6H_2O$, and SeO_2 was prepared. Then, the electrodeposition was performed at a potential of −0.8 V_{SCE} for 600 s. A schematic illustration of this process is shown in Figure 217a. The SEM images revealed that $NiCoSe_2$ had a crimped nanosheet morphology with macroporous structure, which was confirmed via TEM (Figures 217b−d). Additionally, HRTEM images showed lattice distortion and rich defects in the $NiCoSe_2$ nanosheet structure, which likely contributed to additional active site exposure for enhanced electrocatalysis (Figure 217e). The XRD pattern indicated that crystalline $NiCoSe_2$ was prepared, which matched well with HRTEM results—the (002) facet corresponding to the $NiCoSe_2$ phase was observed (Figure 217f). In another report, Zhang *et al.* directly grew a $Ni_{0.85}Se$ film on a graphite substrate (GS) via electrodeposition and subsequent N_2-annealing.[1023] First, the authors performed electrodeposition at −0.7 V_{SCE} for 60 min to synthesize an amorphous $NiSe_x$ precursor (Figure 217g). The deposition process proceeded via the following reactions:

$$SeO_2 + H_2O \rightarrow H_2SeO_3$$

$$H_2SeO_3 + 4H^+ + 4e^- \rightarrow Se(s) + 3H_2O$$

$$Se(s) + xe^- \rightarrow Se_x^{2-}$$

$$Se_x^{2-} + Ni^{2+} \rightarrow NiSe_x(s)$$

After the $NiSe_x$ precursor film was formed, a post-annealing treatment was conducted to produce a crystalline $Ni_{0.85}Se$ film on the GS ($Ni_{0.85}Se$/GS). The XRD pattern of the $Ni_{0.85}Se$/GS showed a highly crystalline structure (Figure 217h). The $Ni_{0.85}Se$ (101) plane was also observed in the TEM image (Figures 217k). The SEM and TEM images revealed that the $Ni_{0.85}Se$/GS sample had a rough, porous surface, resulting in a large surface area beneficial for OER electrocatalysis (Figures 217i and j). Thus, electrodeposition is both an effective and facile method for one-step synthesis of transition metal selenides as electrocatalysts for the OER.

Electrodeposition has also been used to fabricate selenide/carbon-based materials and selenide/oxide composites to serve as electrocatalysts for the OER. For instance, Wu *et al.* coated N-doped graphene on the surface of Ni foam as a substrate for the electrodeposition of $NiSe_2$ (Figure 218a).[1008] The $NiSe_2$ electrocatalyst was prepared by immersing N-graphene-coated Ni foam (NG/NF) into an electrolyte solution containing $NiCl_2$, SeO_2, and LiCl. A potential of −0.5 V_{SCE} was then applied to the electrode for 1 h and $NiSe_2$ was electrodeposited onto NG/NF. XRD results indicated that crystalline $NiSe_2$ was formed and that the substrate did not lead to changes in the crystallinity of $NiSe_2$ (Figure 218b). SEM (Figure 218c) revealed that $NiSe_2$ had a pyramid-like morphology, which was verified by TEM results (Figure 218d). By using the NG/NF substrate, the $NiSe_2$ film grew vertically and exhibited a rough surface. The electrodeposited $NiSe_2$ exhibited fast reaction kinetics owing to the improved adhesion between the substrate and the electrocatalyst via the N-graphene coating, which reduced electrical resistance at the contact/interface. Sun *et al.* used cathodic electrolysis at a constant potential of −0.65 $V_{Ag/AgCl}$ for 600 s in an aqueous solution containing Cu^{2+} and SeO_2 to *in situ* coat a Cu_2Se−Cu_2O composite film onto Ti foil (TF) (Figure 218e).[994] The XRD pattern revealed a highly crystalline structure of the Cu_2Se−Cu_2O composite (Figure 218f), and the SEM image showed that the as-prepared electrocatalyst had a nanoparticle-like morphology with a smooth surface (Figures 218g and h). Lattice fringes corresponding to both Cu_2Se and Cu_2O phases were also found via TEM (Figure 218i). As shown by these examples,

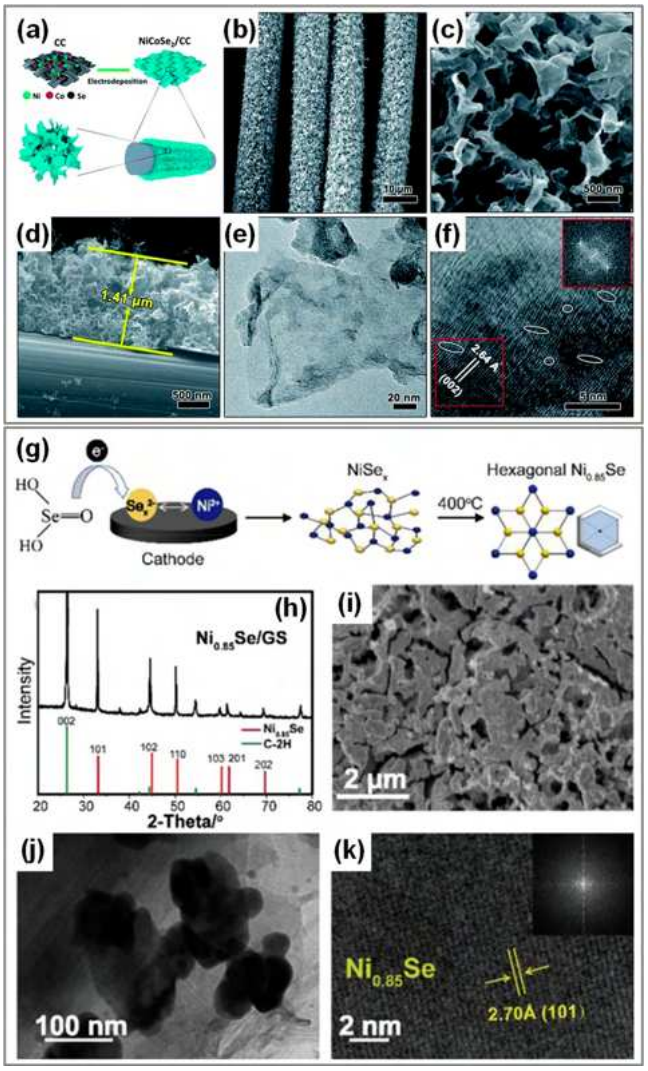


Figure 217. (a) Schematic illustration for the construction of the $NiCoSe_2$ nanosheet network. (b, c) SEM, (d) TEM, and (e, f) HRTEM images of $NiCoSe_2$ nanosheets. Reproduced with permission from ref 1067. Copyright 2018 Royal Society of Chemistry. (g) Schematic illustration for the synthesis of $Ni_{0.85}Se$ on graphite substrate (GS). (h) XRD pattern and (i) SEM and (j, k) TEM images of $Ni_{0.85}Se$ grown on GS. Reproduced with permission from ref 1023. Copyright 2016 Elsevier.

https://doi.org/10.1021/acs.chemrev.3c00005
Chem. Rev. 2023, 123, 12795−13208

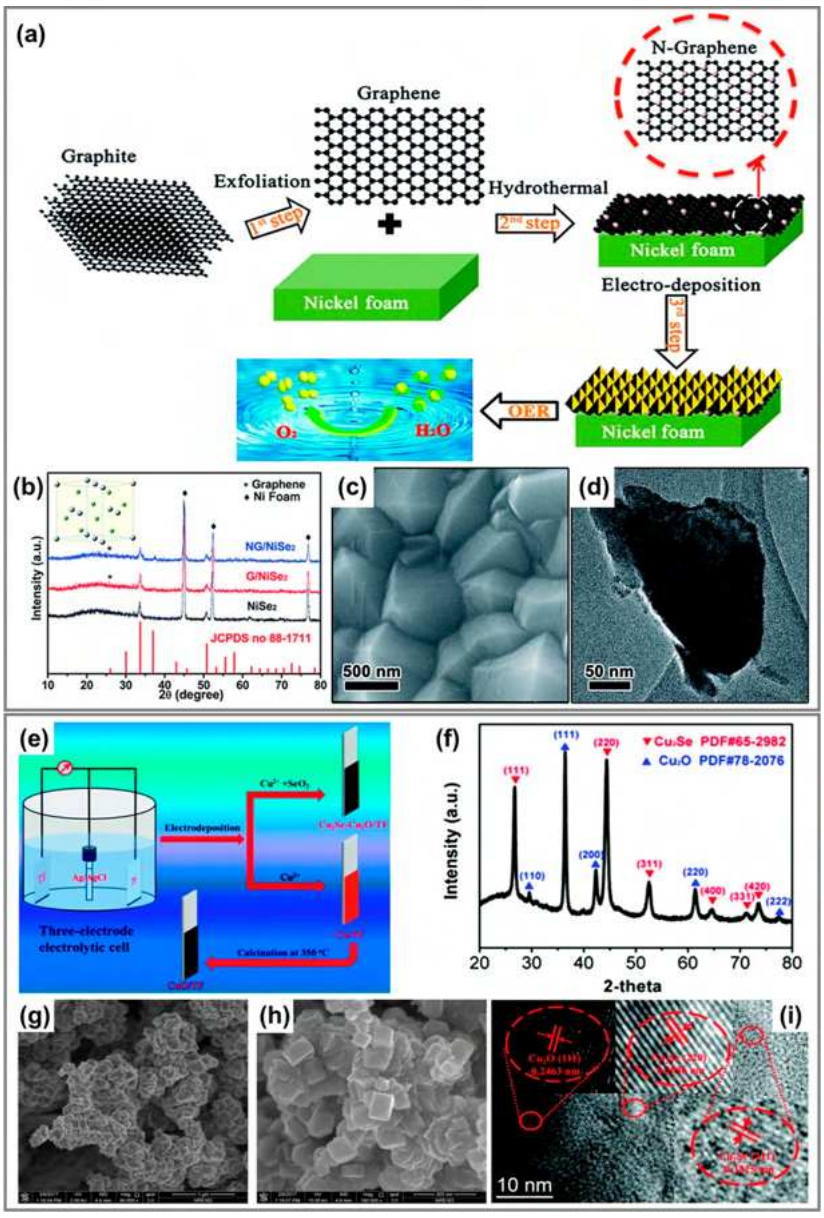


Figure 218. (a) Schematic illustration for the construction of $NG/NiSe_2/NF$ hybrid electrocatalyst. (b) XRD patterns of as-prepared $NiSe_2$, $G/NiSe_2$, and $NG/NiSe_2$ on Ni foam. Inset of (b) is the crystal structure of cubic $NiSe_2$. (c) SEM and (d) TEM images of $NiSe_2$ on the N-doped graphene-encapsulated Ni foam ($NG/NiSe_2/NF$). Reproduced with permission from ref 1008. Copyright 2017 Royal Society of Chemistry. (e) Schematic illustration of the fabrication of the Cu_2Se-Cu_2O/TF electrode. (f) XRD pattern and (g) TEM and (h, i) SEM images of Cu_2Se-Cu_2O/TF. Reproduced with permission from ref 994. Copyright 2018 Royal Society of Chemistry.

the electrodeposition method can be used to prepare uniform, highly crystalline materials, whose final composition and structure depend on the cation, Se source, and applied voltage used.

Like the hydrothermal method, electrodeposition can also be used in two-step synthesis, wherein electrodeposition is used in the first step to prepare a precursor that will later be converted into a transition metal selenide. Zhu *et al.* used CVD to coat graphene on the surface of the Ni foam and then employed electrodeposition to synthesize $Co(OH)_2$ hydroxide nanowalls as a precursor, which was subsequently converted to CoSe through thermal selenization (Figure 219a).[1020] The as-prepared CoSe exhibited a nanowall-like morphology, as shown in the SEM image in Figure 219b. These selenide nanowalls enabled a greater number of exposed active sites for OER electrocatalysis. In addition to having a nanowall structure, the CoSe was also highly crystalline, as indicated by XRD (Figure 219c). The as-deposited CoSe also demonstrated high electrical conductivity, leading to enhanced electron transfer for OER catalysis. Shao *et al.* grew $(Ni,Co)_{0.85}Se$ nanosheet arrays on Ni foam through electrodeposition and subsequent hydrothermal selenization (Figure 219d).[980] They first synthesized Ni-Co layered double hydroxides (NiCo-LDHs) on the Ni foam via electrodeposition at a constant potential of -1.2 V_{SCE} for 400 s. Then the NiCo-LDH precursor was treated with NaHSe by the hydrothermal method to obtain the final selenide $(Ni,Co)_{0.85}Se$ nanosheet arrays (NSAs). The XRD results showed that the $(Ni,Co)_{0.85}Se$ NSAs overshadowed the crystalline structure of NiCo-LDH, indicating transformation

https://doi.org/10.1021/acs.chemrev.3c00005
Chem. Rev. 2023, 123, 12795−13208

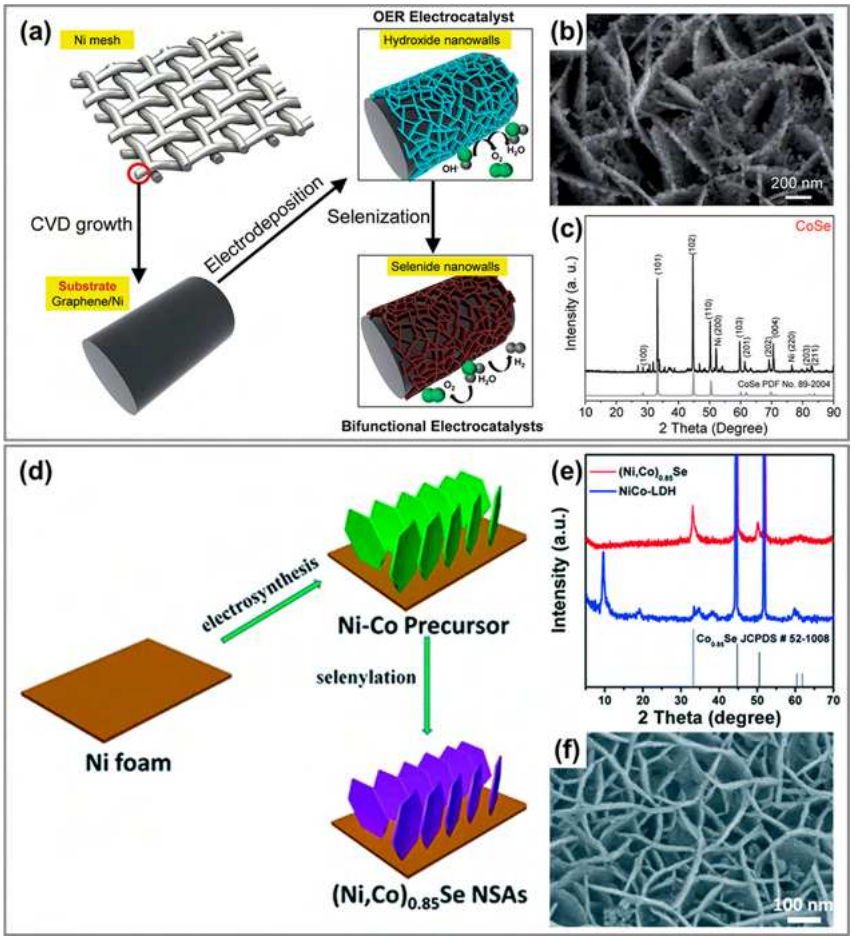


Figure 219. (a) Schematic illustration for the synthetic process of hydroxide nanowalls as OER electrocatalysts and selenide nanowalls as bifunctional electrocatalysts. (b) SEM image and (c) XRD pattern of CoSe. Reproduced with permission from ref 1020. Copyright 2016 Royal Society of Chemistry. (d) Schematic illustration of the synthesis of $(Ni,Co)_{0.85}Se$ NSAs. (e) XRD patterns of NiCo-LDH and $(Ni,Co)_{0.85}Se$ NSAs. (f) SEM image of $(Ni,Co)_{0.85}Se$ NSAs. Reproduced with permission from ref 980. Copyright 2018 Royal Society of Chemistry.

of the material to a NiCo selenide (Figure 219e). SEM showed that the $(Ni,Co)_{0.85}Se$ NSAs had a nanosheet-like morphology (Figure 219f). The layered nanosheet-like morphology of the electrodeposited NiCo-LDH precursor was maintained well after the follow-up selenization process. Thus, in two-step synthesis of transition metal selenides, the electrodeposition method can be used in the first step to control the morphology of the final product.

5.2.1.4. MOF-Derived Methods. Metal-organic frameworks (MOFs) are crystalline, three-dimensional nanostructures formed by coordination bonding between metal ions and organic linkers. Recently, MOFs have been employed as sacrificial templates to synthesize electrocatalysts. By using MOFs as synthetic precursors, transition metal selenides can be prepared that retain characteristics of the initial MOFs. For instance, a highly porous MOF can be used as a template to produce an electrocatalyst with high porosity for improved electrocatalysis via a greater number of exposure active sites and improved mass transfer. In addition, under different reaction conditions [acid etching and high temperatures (~400−600 °C)], the electrocatalysts can also be grown directly on the MOF framework to obtain electrocatalysts with predetermined structural properties.

To obtain selenides using MOF precursors, Dong *et al.* synthesized a MOF (zeolitic imidazolate framework-67, ZIF-67) on carbon fiber (CF) by mixing $Co(NO_3)_2$ and 2-methylimidazole methanol (MelM). Then, the ZIF-67 was placed into a tube furnace downstream of Se powder and heated under Ar atmosphere at 500 °C for 60 min to convert ZIF-67 into $CoSe_2$ (Figure 220a) (i.e., gas-solid selenization).[1085] XRD results indicated that the as-prepared $CoSe_2$ consisted of a cubic pyrite structure (p-$CoSe_2$) and a marcasite structure (m-$CoSe_2$) (Figure 220b), as confirmed by TEM and HRTEM (Figures 220d and e). SEM showed that the $CoSe_2$ electrocatalyst consisted of nanoparticles with rough surfaces (Figure 220c). Liang *et al.* also used ZIF-67 on Ni foam (ZIF-67/NF) to synthesize a NiCo layered double hydroxide (NiCo LDH/C/NF) precursor and then transformed the material to Co-Ni-Se/C/NF via thermal (gas-solid) selenization (Figure 220f).[1019] First, they prepared ZIF-67/NF by immersing Ni foam into a solution containing 2-methylimidazole, $Co(NO_3)_2 \cdot 6H_2O$, and methanol for 24 h. Then, the ZIF-67/NF was converted into porous NiCo LDH/C/NF via a reaction with $Ni(NO_3)_2$ in ethanol. Then, a tube furnace was used to prepare the final Co-Ni-Se/C/NF electrocatalyst by placing Se powder upstream of the NiCo LDH/C/NF at 400 °C. The high temperature enabled selenization of the precursor, resulting in metal selenide nanoparticles. From the XRD pattern, the diffraction peaks of Co-Ni-Se/C/NF corresponded to two selenide phases: Ni_3Se_4 and $NiSe_2$. Also, from XRD, it was

https://doi.org/10.1021/acs.chemrev.3c00005
Chem. Rev. 2023, 123, 12795−13208

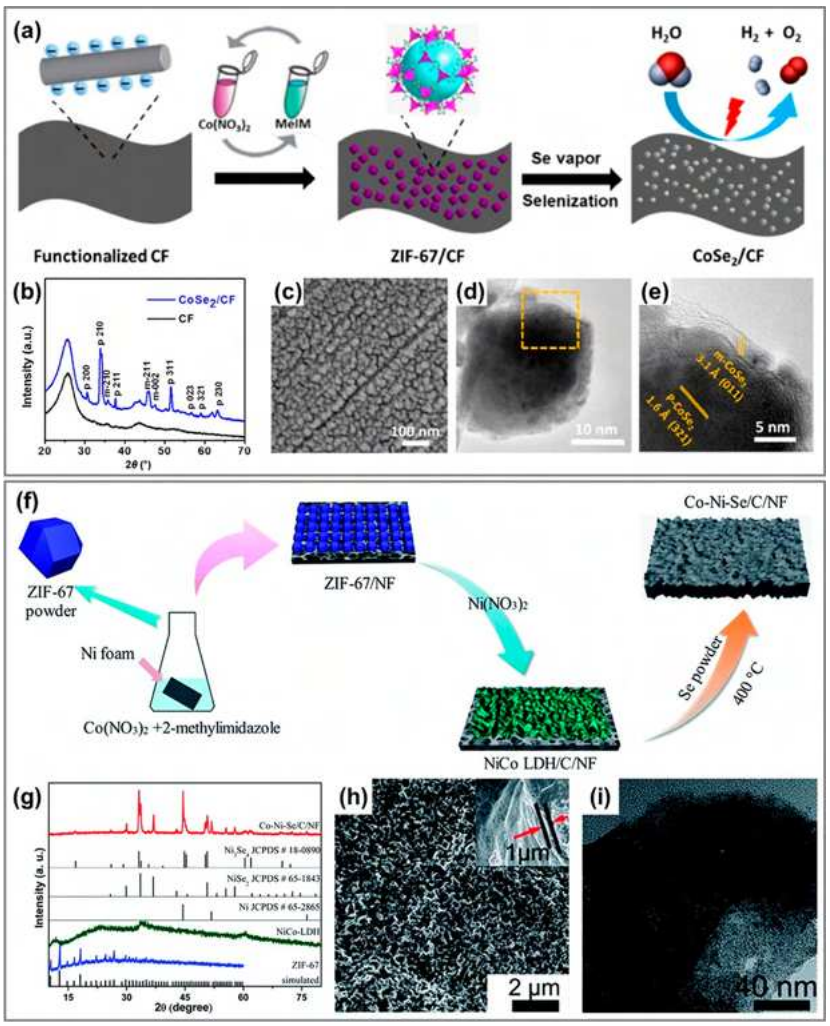


Figure 220. (a) Schematic illustration for the synthesis of $CoSe_2$ nanoparticles on CFs. (b) XRD patterns of $CoSe_2$/CF and CF. (c) SEM, (d) TEM, and (e) HRTEM images of $CoSe_2$ nanoparticles. Reproduced with permission from ref 1085. Copyright 2016 Springer Nature. (f) Schematic illustration for the synthetic route of Co-Ni−Se/C/NF. (g) XRD patterns of Co-Ni-Se/C/NF, NiCo-LDH, and ZIF-67. (h) SEM and (i) TEM images of Co-Ni-Se/C/NF. Reproduced with permission from ref 1019. Copyright 2016 Royal Society of Chemistry.

evident that the initial crystal structure of ZIF-67 and the NiCo LDH precursor were lost following selenization (Figure 220g). SEM showed a porous surface of the as-obtained selenides, and TEM indicated that metal selenide nanoparticles were embedded within a carbon matrix (Figures 220h and i). The rough surfaces observed via SEM and TEM images were attributed to the etching of the ZIF-67 cubes by $Ni(NO_3)_2$ during the first synthetic step (precursor preparation step). Thus, as demonstrated by both Dong *et al.* and Liang *et al.*, by using a MOF, such as ZIF-67, and converting it to a metal selenide via pyrolysis under inert atmosphere with Se powder, nanoparticle-like morphologies with high surface areas can be obtained for the benefit of OER electrocatalysis.

Similarly, Fan *et al.* synthesized $CoSe_2$ microspheres with a Co-MOF precursor using a tube furnace (Figure 221a).[1079] First, they used the solvothermal method to synthesize a Co-MOF precursor. Then, the Co-MOF and Se powder were mixed together in a mass ratio of 1:1 in a porcelain boat and ramped to 450 °C under Ar atmosphere (i.e., solid-state selenization). During the annealing process, cobalt ions separated from the Co-MOF and reacted with Se powder to produce $CoSe_2$. From the XRD pattern (Figure 221b), the $CoSe_2$ composite consisted of m-$CoSe_2$ (orthorhombic marcasite structure) and p-$CoSe_2$ (cubic pyrite structure), and the narrow full-width at half-maximum (FWHM) of the observed diffraction peaks implied high crystallinity of the product. From SEM and TEM images, a hollow microsphere-like structure of the $CoSe_2$ was observed (Figures 221c and d). Liang *et al.* grew (Ni, Co)Se_2 nanocages *in situ* on a graphene aerogel (GA) substrate with the help of Prussian blue analogs (PBAs) (Figure 221e).[1002] First, they synthesized NiCo-PBA anchored on reduced graphene aerogel (NiCo PBA-GA) nanocubes as precursors through the hydrothermal method. Then, (Ni,Co)Se_2-GA was fabricated by selenizing NiCo PBA-GA via annealing in a tube furnace with Se powder at 350 °C under an Ar atmosphere (i.e., gas-solid selenization). The annealing process not only allowed the selenization to occur but also led to the generation of porous structure, as verified by SEM and TEM results (Figures 221f and g). Here, we assume that the emergence of the porous nanocages might occur due to the volatilization of carbon species from the MOF precursor and the drastic crystal-structural transformation from the MOF into the selenide. Furthermore, the XRD patterns indicated the successful transformation of NiCo PBA to (Ni,Co)Se_2 (Figure 221h). From these examples, it is clear that the use of MOF-

https://doi.org/10.1021/acs.chemrev.3c00005
Chem. Rev. 2023, 123, 12795−13208

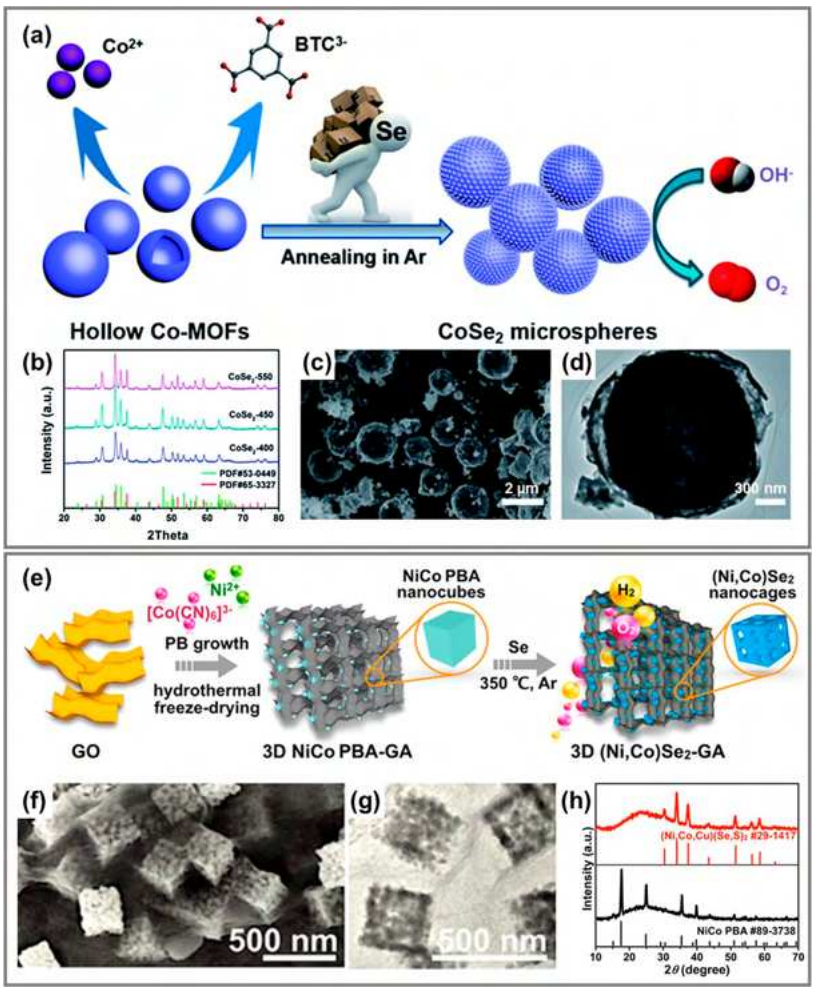


Figure 221. (a) Schematic illustration for the synthetic strategy of the $CoSe_2$ microspheres. (b) XRD patterns of the $CoSe_2$ microspheres prepared with different selenization temperatures (450, 500, and 550 °C). (c) SEM and (d) TEM images of the $CoSe_2$ microspheres prepared at the selenization temperature of 450 °C. Reproduced with permission from ref 1079. Copyright 2016 Royal Society of Chemistry. (e) Schematic illustration for the synthesis process of $(Ni,Co)Se_2$-GA for water splitting electrocatalysis. (f) SEM and (g) TEM images of $(Ni,Co)Se_2$-GA. (h) XRD patterns of NiCo PBA and $(Ni,Co)Se_2$-GA. Reproduced with permission from ref 1002. Copyright 2017 American Chemical Society.

derived materials as precursor is beneficial for controlling the morphologies of the final transition metal selenides.

In addition to one- and two-step synthesis cases, MOF-involved multistep preparation methods have also been used to synthesize selenides. Hou *et al.* employed a MOF-based multistep synthesis to obtain electrochemically exfoliated graphite (EG) foil-supported bimetallic selenide encased in N-doped carbon (EG/$(Co,Ni)Se_2$-NC).[969] First, graphite foil was exfoliated in a 0.05 M $(NH_4)_2SO_4$ solution at 10 V for 3 min. Then the CoNi-LDH was coated on the surface of EG under −1.2 $V_{Ag/AgCl}$ for 150 s via electrodeposition followed by application of ZIF-67 at the surface via a thermal strategy. The resulting MOF-based precursor, EG/CoNi-LDH/ZIF-67, was mixed with Se powder and annealed under Ar atmosphere to produce the final product, EG/$(Co,Ni)Se_2$-NC (Figure 222a). The XRD pattern revealed the successful conversion of the precursor into $(Co,Ni)Se_2$ via thermal (solid-state) selenization (Figure 222b). SEM images showed the nanoparticle-like cluster morphology of the electrocatalyst, and TEM images indicated that the electrocatalyst consisted of a core@shell structure composed of a N-doped carbon shell and $(Co,Ni)Se_2$ core (Figures 222c and d). The core@shell morphology generated by the MOF structure might lead to increased contact between the electrocatalytic material and the electrolyte during the OER.

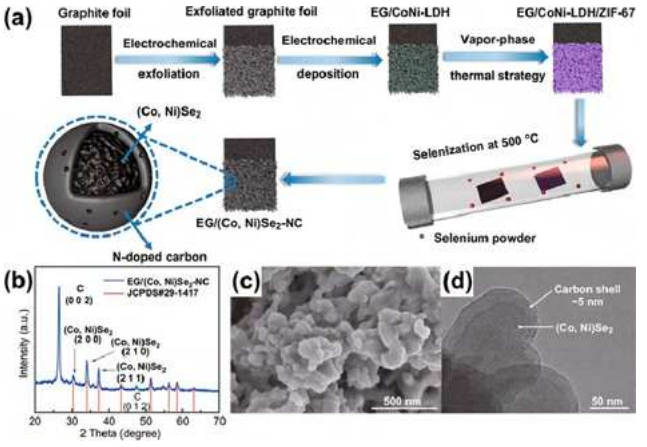


Figure 222. (a) Synthetic scheme of the EG/$(Co,Ni)Se_2$-NC hybrid. (b) XRD pattern and (c) SEM and (d) TEM images of EG/$(Co,Ni)Se_2$-NC. Reproduced with permission from ref 969. Copyright 2019 Springer Nature.

https://doi.org/10.1021/acs.chemrev.3c00005
Chem. Rev. 2023, 123, 12795−13208

5.2.1.5. Solution-Based Methods. Mixing two different solvents together (i) to synthesize a precursor for later selenization or (ii) to directly prepare the desired transition metal selenide has been performed extensively.[961,984,1071,1084] Compared to the hydrothermal and electrodeposition methods, solution-based methods enable more facile and direct synthesis because they circumvent the need for complicated equipment like an autoclave or a three-electrode system. The typical solution-based synthesis of transition metal selenide powders requires a transition metal and selenium precursor. These precursor species are dissolved into a solvent and heated under inert atmosphere to induce the formation reaction for the metal selenide. For example, Manna *et al.* used a one-step solution-based method to synthesize Ni-Co-Se nanocrystals (NCs).[984] Specifically, Ni and Co salts were mixed with 1-octadecene in a three-neck flask under vacuum at 120 °C. Then, Se-oleylamine, the Se source, was injected into the flask under Ar atmosphere at 250 °C. After 5 min, the reaction was cooled and quenched using toluene, resulting in the formation of the Ni-Co-Se alloy NCs (Figure 223a). The

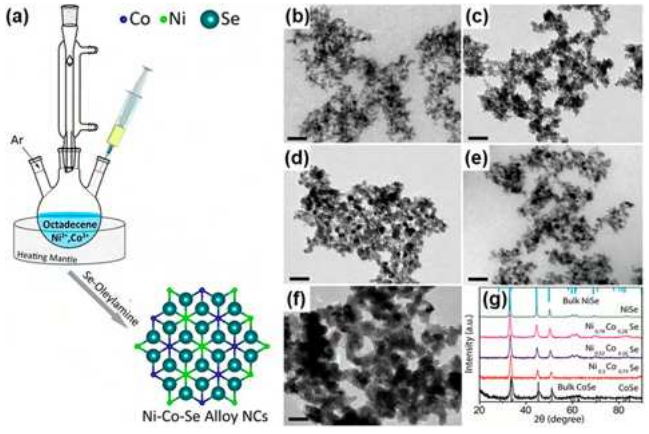


Figure 223. (a) Sketch of the colloidal synthesis of ternary Ni-Co-Se NCs having a hexagonal crystal structure. (b–f) TEM images and (g) XRD patterns of CoSe, $Ni_{0.3}Co_{0.74}Se$, $Ni_{0.52}Co_{0.56}Se$, $Ni_{0.78}Co_{0.28}Se$, and NiSe NCs. Reproduced with permission from ref 984. Copyright 2018 American Chemical Society.

nanoparticle-like cluster morphology of the Ni-Co-Se electrocatalysts was observed via TEM (Figures 223b–f). XRD indicated that the product had high crystalline purity, as only one hexagonal *M*Se-type crystal structure (*M* = Ni, Co) was observed for the Ni-Co-Se samples (Figure 223g). Additionally, the authors varied the ratio of Ni to Co salts during synthesis. From the diffraction peaks of all the as-synthesized Ni-Co-Se clusters at different Ni/Co ratios, all detected peaks were located between those for the pure NiSe and CoSe phases—the increase of Ni content led to the shift of diffraction peaks to a lower 2θ value, indicative of expansion of the lattice spacing. Wang *et al.* also employed a similar solution-based synthesis method to prepare $CoSe_2$.[1071] First, they prepared Co- and Se-precursor solutions separately at ambient atmosphere and in a three-neck flask under a N_2 atmosphere, respectively. Then, the above two solutions were mixed to obtain $CoSe_2$ nanocrystals at 240 °C. To modulate the morphology of the final $CoSe_2$, Co-precursor solutions were prepared using several different additive species: ammonium hydroxide, ethylenediamine, triethanolamine, and hydrazine hydrate. They hypothesized that different selenide morphologies would emerge because of the differing reducing capabilities between the additives, meaning Se powders would be reduced to varying degrees. When ammonium hydroxide was used as an additive, an amorphous $CoSe_2$ morphology was observed, while $CoSe_2$ nanoparticles (5–8 nm), nanosheets, and nanobulks (side lengths of 40 nm) were observed when ethylenediamine, triethanolamine, and hydrazine hydrate were used, respectively. Thus, the additive used during solution-based synthesis of metal selenides will have a direct impact on the resulting morphology. And, more generally, by changing the composition of the reacting solution, the final product can easily be transformed. It should be noted, however, that this facile method tends to only produce metal selenides with clustered nanoparticle-like morphology unlike the open, porous structures that have been observed from hydrothermal and electrodeposition-based syntheses.

The solution-based method can also be used to prepare powder composites composed of selenides and oxides. For example, Yu *et al.* coated CeO_2 onto the surface of $CoSe_2$/diethylenetriamine (DETA) nanobelts (NBs) via a solution-based reaction under N_2 atmosphere, resulting in $CoSe_2$@CeO_2 composite electrocatalysts (Figure 224a).[1084] Due to the abundance of amino groups on the surface of $CoSe_2$, CeO_2 was anchored on the surface via the interaction between amino groups and Ce atoms. In this composite, $CoSe_2$ enabled electrocatalysis while CeO_2 aided hydroperoxyl (OOH) formation on the surface of the hybrid material. The CeO_2 sites aided OOH formation because of the oxygen vacancies on CeO_2, which enabled much stronger adsorbate binding compared to normal oxide sites. The presence of both $CoSe_2$ and CeO_2 was confirmed via XRD and SAED. Specifically, the XRD pattern exhibited peaks corresponding to the lattice fringes of both cubic $CoSe_2$ and cubic CeO_2 (Figure 224b). In the SAED pattern (inset of Figure 224d), the $CoSe_2$ (521) and (400) and CeO_2 (311) crystal planes were detected. From SEM and TEM images, a porous belt-like morphology was observed. During OER testing, this porous structure likely led to beneficial gas evolution and mass transfer (Figures 224c and d). The successful anchoring of CeO_2 nanoparticles onto $CoSe_2$ nanobelts (see Figure 224a) via solution-based synthesis illustrates the capability of this method to produce highly porous composite metal oxide/metal selenide materials for enhanced OER activity with ease.

The solution-based method has also been used for the direct fabrication of transition metal selenide films onto conductive substrates. For instance, the Lian group employed a two-step solution-based reaction to synthesize a Cu_2Se electrocatalyst film on Cu foam.[961] In the first step, a $Cu(OH)_2$ precursor film with a nanoarray-like morphology was prepared by immersing Cu foam into an aqueous solution containing NaOH and $(NH_4)_2S_2O_8$ at room temperature for 20 min. Then, the as-prepared precursor film was immersed with Se powder, $NaBH_4$, and NaOH in water for 30 min to obtain Cu_2Se fluffy intersected-nanosheet decorated nanotubes on Cu foam (Figure 224e). The XRD patterns revealed that $Cu(OH)_2$ was successfully converted into Cu_2Se through the second-step solution-based reaction (selenization) (Figure 224f). The SEM and TEM images further confirmed that Cu_2Se with a nanowire-like morphology and porous surface was prepared (Figures 224g and h). From their results, the Liam group found that the solution-based method can be used to prepare a Cu_2Se film on Cu foam without complex equipment, pressure and temperature assistance, and long synthetic times. Thus,

https://doi.org/10.1021/acs.chemrev.3c00005
Chem. Rev. 2023, 123, 12795–13208

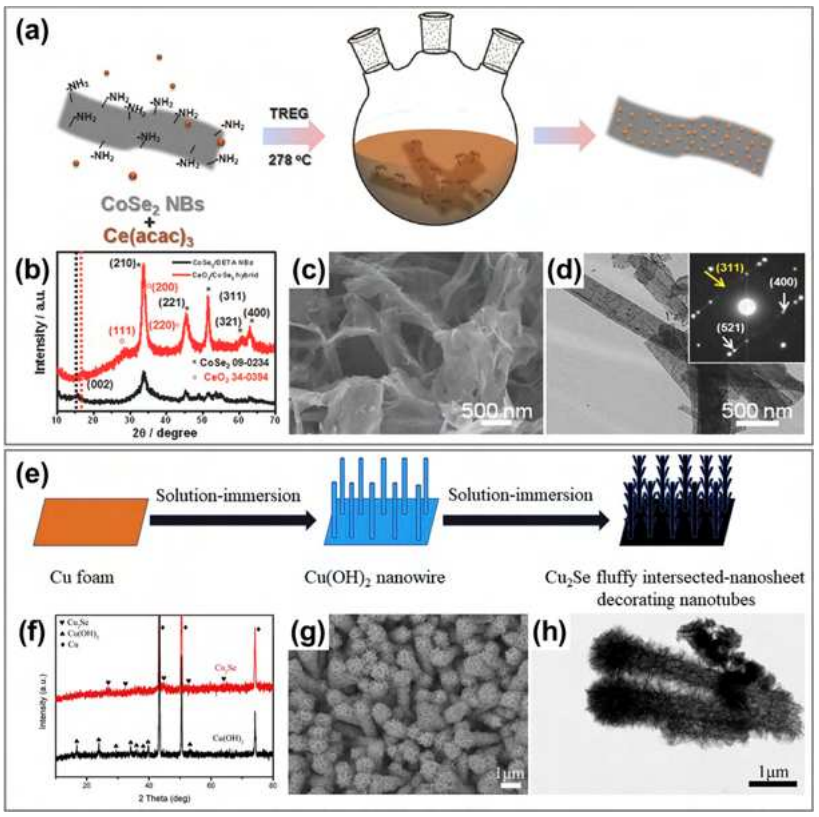


Figure 224. (a) Schematic illustration for the synthesis of the $CeO_2/CoSe_2$ nanobelt composite by a facile polyol reduction method at 278 °C for 1 h. (b) XRD patterns of $CoSe_2$/DETA NBs and $CeO_2/CoSe_2$ hybrid nanobelt. (c) SEM and (d) TEM images of the $CeO_2/CoSe_2$ hybrid nanobelt. The inset in (d) shows the corresponding SAED pattern. Reproduced with permission from ref 1084. Copyright 2015 Wiley. (e) Schematic illustration for the synthesis process of Cu_2Se fluffy intersected nanosheets decorated with nanotubes arrays. (f) XRD patterns of $Cu(OH)_2$ and Cu_2Se. (g) SEM and (h) TEM images of Cu_2Se. Reproduced with permission from ref 961. Copyright 2019 Elsevier.

this method has merits for further use in the synthetic preparation of metal selenide electrocatalysts for the OER. In addition to the facile nature of solution-based synthesis, it is also, in many cases, more environmentally friendly as compared to the hydrothermal and electrodeposition methods, uniquely posing it as a more sustainable means for producing electrocatalysts for green energy applications.

5.2.1.6. Other Methods. Some unique strategies have also been used to synthesize high-performance transition metal selenide electrocatalysts. These strategies include the solution-liquid-solid method,[1028] electrospinning method,[1048] magnetron sputtering method,[1053] microwave-assisted method,[1007] and more. Furthermore, post-annealing treatment(s) have been performed to achieve higher crystallinity and changes in morphology for improved OER performance.

5.2.1.6.1. Solution-Liquid-Solid Methods. The solution-liquid-solid (SLS) method offers many advantages for the preparation of metal selenides, as it only requires a simple experimental setup (e.g., autoclaves) and enables material tunability via changes in synthetic conditions. For example, Wu *et al.* synthesized NiSe nanowire arrays using the SLS approach by randomly depositing Se droplets onto the surface of Ni foam. (Figure 225e).[1028] For the first step, $NaBH_4$ and Se powder were mixed in deionized water to form a clear, colorless solution. Then, the solution was mixed with ethanol under N_2 flow to obtain a milk-like liquid. Finally, the as-prepared liquid was transferred into an autoclave with a piece of Ni foam and heated at 140 °C for 3 h to obtain the NiSe nanowires. During the reaction, the Se droplets deposited on

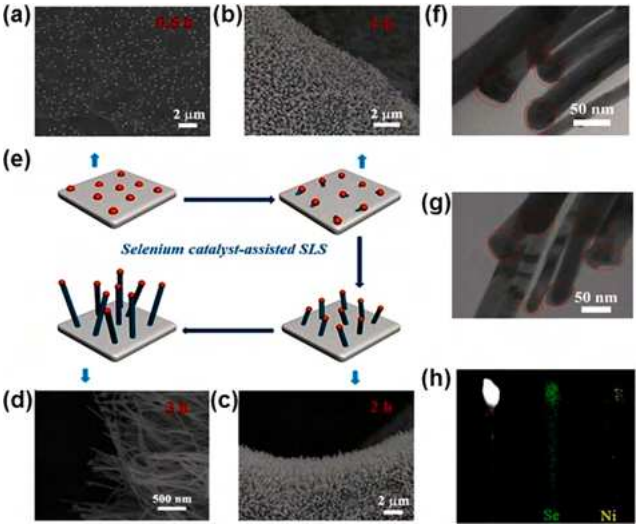


Figure 225. SEM images of the intermediate products at different reaction stages: (a) 0.5, (b) 1, (c) 2, and (d) 3 h. (e) Schematic illustration for the growth of NiSe nanowires by using a nonmetallic molecular crystal (Se) as a synthetic catalyst. (f, g) TEM images of the intermediate products. (h) HAADF-STEM image of the intermediate product (NiSe) and corresponding elemental mapping. Reproduced with permission from ref 1028. Copyright 2016 Wiley.

the surface of Ni foam catalyzed the growth of NiSe nanowires, wherein the nanowire growth occurred between the Se droplet and Ni substrate (Figure 225a–d). The reaction was carried

https://doi.org/10.1021/acs.chemrev.3c00005
Chem. Rev. 2023, 123, 12795−13208

out at low temperature to ensure this nanowire growth occurred because, at higher temperatures, the weak interactions between Se and the Ni substrate would be disturbed (nonmetals have much lower melting points compared to metals). From SEM and TEM images, Se droplets could easily be seen on the top of the nanowires, as further evidenced by the HAADF-STEM (Figures 225f–h). Additionally, the SLS method enabled tunability of nanowire length with reaction time, as depicted by SEM images (Figure 225a–d). Thus, the SLS method offers a facile and novel approach to the preparation of high surface area transition metal sulfide materials owing to the produced nanowire morphology.

5.2.1.6.2. Electrospinning Methods. The electrospinning method has been used to synthesize 1D carbon nanofibers (CNFs) with encapsulated transition metal selenides as electrocatalysts.[1094] Specifically, Zhao *et al.* synthesized $Co_{0.85}Se$ nanoparticles in carbon nanofibers ($Co_{0.85}Se$@CNFs) using a two-step process: (1) electrospinning and (2) subsequent gas-solid selenization.[1048] The electrospinning method was used to obtain a Co-containing nanofiber-structured precursor. First, a solution was prepared containing $Co(NO_3)_2{\cdot}6H_2O$, DMF (solvent), and polyvinylpyrrolidone. Then, the solution was transferred into a plastic syringe and a voltage of 20 kV was applied between the syringe needle and a rolling collector (Figure 226a). Because of the applied voltage,

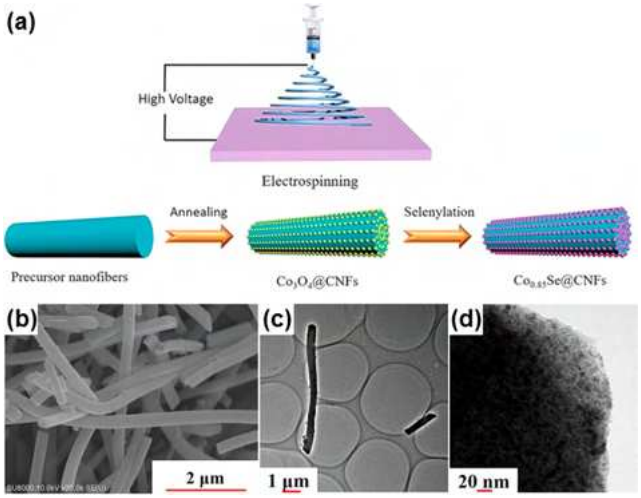


Figure 226. (a) Schematic illustration for the synthesis of $Co_{0.85}Se$@CNFs by an electrospinning strategy. (b) SEM, (c) TEM, and (d) high-magnification bright-field TEM images of $Co_{0.85}Se$@CNFs. Reproduced with permission from ref 1048. Copyright 2020 Wiley.

a silk-like Co-containing nanofiber was deposited onto the surface of the collector. The deposited nanofiber was annealed under an Ar atmosphere at 500 °C for 3 h to form the Co_3O_4@CNFs precursor. For the selenization step, a gas-solid method was used, wherein the solid precursor (Co_3O_4@CNFs) reacted with H_2Se gas, which was generated from the reaction between H_2 gas and Se powder, at 500 °C for 3 h to produce $Co_{0.85}Se$@CNFs. SEM and TEM results depicted a nanofiber-like morphology for the $Co_{0.85}Se$@CNFs, and the high-magnification bright-field TEM image showed a distribution of tiny $Co_{0.85}Se$ nanoparticles within the nanofibers (Figures 226b–d). Given the initially prepared nanofiber morphology is carried through to the final product, electrospinning offers a means by which to produce high surface area materials with short electron transfer paths and structural stability[1094]—all desirable characteristics for high performance OER electrocatalysts.

5.2.1.6.3. Magnetron Sputtering Methods. Magnetron sputtering has been widely used for the deposition of films at scale. In the sputtering process, films are formed via the bombardment of a target with ions. Specifically, a deposition chamber is filled with sputtering gas and high vacuum is established. Then, a plasma is ignited by applying a voltage between a cathode and anode. This plasma causes ionization of gas atoms, resulting in energetic, positive ions hitting a target material via their attraction to the cathode (located at the target). When these positive ions hit the target, atoms from the target are ejected and can then deposit onto a substrate material. Zhang *et al.* used magnetron-sputtering to deposit metal selenides, $Fe_{40}Co_{40}Se_{20}$, onto carbon fiber paper (CFP) and to investigate deposition temperature effects on electrocatalytic performance.[1053] They performed magnetron deposition of the bimetallic selenide at 308, 393, and 573 K for 4 h using Ar gas. The target used was $Fe_{40}Co_{40}Se_{20}$ (attached to a power source at 100 W), and the substrate, CFP, was rotated 120 mm above the target at 40 rpm. Before each deposition, a chamber pressure of $<3.0 \times 10^{-4}$ Pa was established. They found that samples prepared at 308 and 393 K were amorphous, while films prepared at 573 K were crystalline from XRD diffraction patterns and differential scanning calorimetry data (not shown here). Of the samples, the amorphous films outperformed the crystalline film prepared at 573 K (i.e., decreased overpotential for the OER), with the $Fe_{40}Co_{40}Se_{20}$ film deposited at 393 K showing the best performance (overpotential of 307 mV). This difference in performance was attributed to the increased charge transfer resistance exhibited by the 573 K film as compared to the 308 and 393 K films. The increased charge transfer resistance of the 573 K was hypothesized to be the result of increased grain boundaries, as XPS results indicated the presence of additional phases in the film that were not present in its amorphous counterparts. The amorphous 393 K film outperformed the 308 K film owing to its larger double layer capacitance of 26.53 $mF{\cdot}cm^{-2}$ as compared to 17.50 $mF{\cdot}cm^{-2}$. With their $Fe_{40}Co_{40}Se_{20}$ thin films, Zhang *et al.* showed that uniform metal selenide films can be obtained via magnetron sputtering but also that deposition temperature will affect the structure of the prepared film and, in turn, its electrocatalytic performance for the OER.

5.2.1.6.4. Microwave-Assisted Methods. Compared with other time-consuming methods (e.g., hydrothermal method, MOF-derived method, and solution-based method), the microwave-based method is simpler, time-saving, and cheaper for large-scale synthesis, as it does not require high temperatures and high pressure. Kundu *et al.* used a microwave-assisted method to fabricate Ni_3Se_4 for the OER.[1007] As shown in Figure 227a, NaHSe and Ni foam were mixed in N_2-purged deionized water and irradiated in a microwave at 20 s intervals for a total of 3 min at 300 W of power. The mixture was then cooled to room temperature for 5 h, allowing nickel selenide growth to go to completion. The FESEM image of the as-prepared Ni_3Se_4/Ni foam showed needle-like structures on the Ni foam surface (Figure 227b). Figure 227c shows that the selenide nanoassemblies on the surface of the Ni foam resulted in a hierarchical array morphology. From the TEM image and SAED pattern, the observed hierarchical nanostructures consisted of ultrathin

https://doi.org/10.1021/acs.chemrev.3c00005
Chem. Rev. 2023, 123, 12795–13208

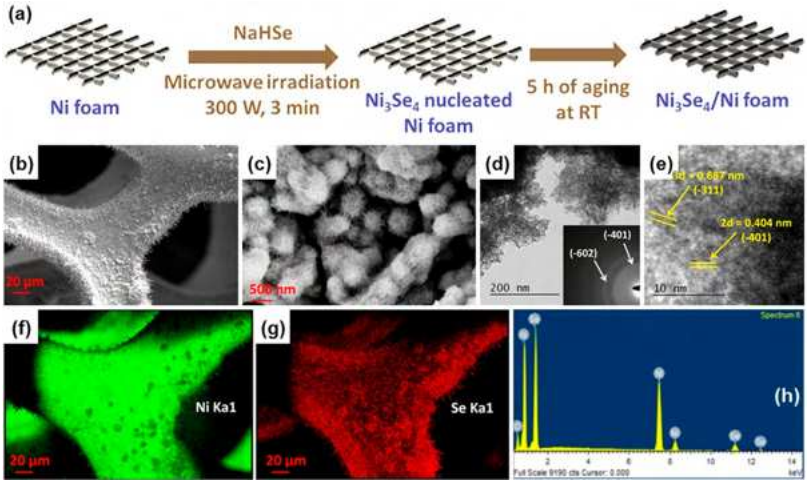


Figure 227. (a) Schematic illustration for the microwave-initiated facile formation of Ni_3Se_4 nanoassemblies on Ni foam (Ni_3Se_4/Ni). (b, c) FESEM, (d, e) HRTEM, (f, g) EDX elemental mapping images, and (h) corresponding EDX spectrum of the Ni_3Se_4/Ni. Reproduced with permission from ref 1007. Copyright 2017 American Chemical Society.

sheets of Ni_3Se_4 (Figure 227d). In the HRTEM image, the lattice fringes corresponding to the Ni_3Se_4 (−401) and (−311) planes were observed (Figure 227e). EDX results indicated that Ni, Se, and O were present within the material, with Ni and Se being evenly distributed throughout and the detected O likely being due to Ni-oxides/hydroxides generated on the sample surface (Figures 227f–h). By using microwave-assisted methods, metal selenides like Kundu *et al.*'s Ni_3Se_4 material can be prepared at lower overall energy costs and with reduced hazards for OER electrocatalysis.

5.2.1.6.5. Chemical Vapor Deposition. Chemical vapor deposition (CVD) is a synthetic method used for the preparation of thin films via the reaction of gases on the surface of a substrate, which was briefly discussed in the beginning of the selenide electrode preparation section (Section 5.2.1). This method has many advantages. For example, it results in more uniform films than physical vapor deposition and impurity contamination is rare. Typically, metal selenides prepared via CVD, such as $MoSe_2$, have been primarily applied to hydrogen evolution electrocatalysis and/or batteries.[1095−1097] While reports exist on the preparation of metal selenides with metals besides Mo,[1098,1099] few have been applied as OER electrocatalysts. One example is Masud *et al.*'s preparation of Cu_2Se via CVD.[922] Specifically, they placed Cu coated silicon wafers (1 cm × 2 cm) at the center of a tube furnace as the substrate. The Se source was kept at the inlet of the tube, and the ceramic tube liner shifted such that it was outside the heating zone until 700 °C was reached at the center of the tube. This step of shifting the equipment was taken owing to Se sublimation occurring at lower temperatures than 700 °C. At 700 °C, the Se vaporized and reacted with the Cu surface of the substrate, producing the final Cu_2Se film. The carrier gas used for the CVD was N_2 (120 sccm), and the tube was held at 700 °C for 30 min. From XRD, Cu_2Se was confirmed as the major phase with minor peaks corresponding to the Cu_3Se phase (diffraction patterns not shown here). The CVD-prepared Cu_2Se exhibited an overpotential of 300 mV at 10 mA·cm^{-2}, underperforming other Cu_2Se materials prepared via the hydrothermal method and electrodeposition method that were also prepared by Masud *et al.* This difference in activity was believed to be the result of the CVD-prepared electrocatalysts' granular morphology, less-open porous structure, higher degree of crystallinity, and larger grain sizes, especially in comparison to the Cu_2Se samples prepared via electrodeposition. It is likely that classic CVD (i.e., the reaction between a transition metal film and gaseous Se species) is underused to prepare metal selenides as OER electrocatalysts because it generates more crystalline and compact materials, which results in inferior OER electrocatalytic performance as compared to highly porous and amorphous materials.

5.2.1.6.6. Anion Exchange Reactions. Metal selenides have also been prepared via anion exchange reactions, wherein a metal hydroxide precursor is mixed with a selenium precursor under low temperature conditions. An example of this reaction was mentioned in the hydrothermal method section (Section 5.2.1.1) above;[1052] however, more detail on this underlying process will be discussed here. Specifically, during the anion exchange reaction, the oxygen anion in a metal hydroxide is replaced by Se anions. Whether or not the anion exchange occurs is dependent on thermodynamics, which can be approximated by comparing the solubility of the products and reactions, wherein the reaction is favorable if the solubility of the reactant precursor (metal hydroxide) is greater than the solubility of the product (metal selenide or other metal chalcogenide).[1100,1101] This method is advantageous because it can be performed at low temperature, solubility can easily be tuned using complexation agents to drive a reaction forward, and this method can lead to the generation of porous, hollow structures for promoted OER electrocatalysis. For example, Zhao *et al.* prepared nanoporous, hollow $CoSe_2$ nanosheets in addition to Co_3S_4, $CoTe_2$, CdS, and NiS using the anion exchange method under hydrothermal conditions.[1100] Specifically, they prepared a homogeneous $Co(OH)_2$ solution (0.1 mmol of $Co(OH)_2$ precursor stirred in 12 mL of DI water) and combined it with a Se powder (0.2 mmol) and $NaBH_4$ (0.6 mmol). The corresponding solution was transferred to a Teflon-lined autoclave, and synthesis was performed at 180°C for 15 h. SEM results before and after anion-exchange indicated that the hexagonal nanosheet structure of the $Co(OH)_2$ precursor was maintained while the material became hollow and porous, as indicated by TEM results for $CoSe_2$ (not shown here). Thus, the anion exchange method can be used to obtain large surface area metal selenides of a pre-selected

https://doi.org/10.1021/acs.chemrev.3c00005
Chem. Rev. 2023, 123, 12795−13208

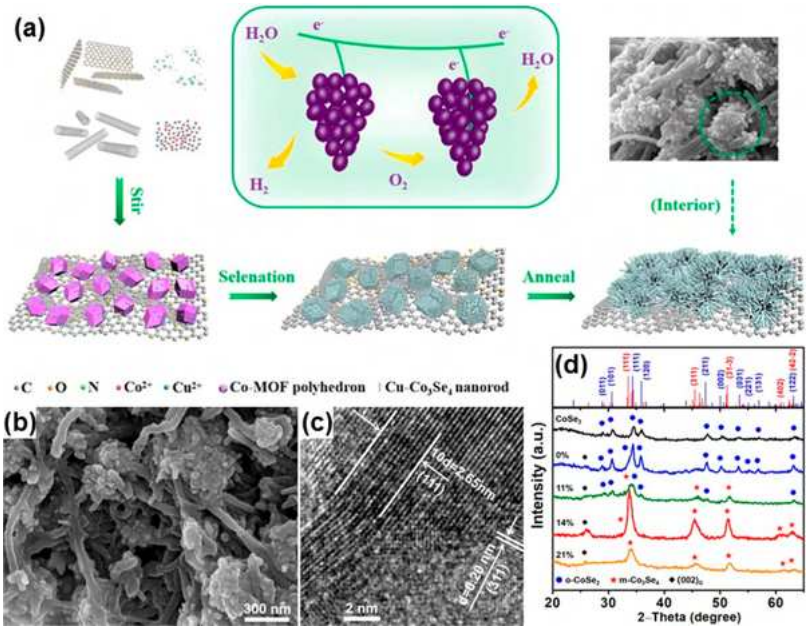


Figure 228. (a) Schematic illustration for the preparation process of Cu-Co_3Se_4/GC composites. (b) SEM and (c) HRTEM images of Cu-14-Co_3Se_4/GC. (d) XRD patterns of Co_3Se_4/GC, Cu-11-Co_3Se_4/GC, Cu-14-Co_3Se_4/GC, and Cu-21-Co_3Se_4/GC. Reproduced with permission from ref 968. Copyright 2019 American Chemical Society.

morphology via metal hydroxide precursor choice for improved OER performance.

5.2.1.6.7. Post-Annealing Treatment. In addition to the methods discussed above, it has also been found that annealing as-prepared metal selenides can enhance their crystallinity and modify their morphology, making them more suitable for electrocatalysis. Li *et al.* used post-annealing treatment to synthesize Cu-Co_3Se_4 electrocatalysts (Figure 228a).[968] Initially, they synthesized precursors containing Co^{2+} and Cu^{2+} on reduced graphene oxide (GO) and carbon nanotubes (CNTs) (GC). Then, they mixed the as-prepared precursors with Na_2SeO_3 and performed hydrothermal selenization to produce metal selenides. Then, they annealed the selenides at 300 °C for 2 h under an Ar atmosphere to obtain the final Cu-Co_3Se_4/GC electrocatalysts. The additional annealing step roughened the surface of the as-prepared selenides, exposing more active sites for electrocatalysis via the generation of nanocavities (Figure 228b). The open-channel nanocavities, which can be seen from the SEM image (Figure 228b), facilitated mass transfer and electrolyte penetration into the selenide material for improved electrocatalysis. The lattice fringes detected via TEM and XRD indicated that, while there was a change in morphology, the cobalt selenide crystal structure was maintained even after the post-annealing step (Figures 228c and d). Thus, a post-annealing step can change the morphology of an as-prepared metal selenide electrocatalyst for enhanced water oxidation.

5.2.2. Final Types of Selenide-Based Electrocatalysts. As seen in Table 6, post-OER electrocatalysts can be classified as either catalysts or precatalysts. In general, transition metal selenides classified as "catalysts" experience no change in the valence state of Se or their morphologies following OER testing (i.e., no oxidation, no reconstruction, etc.) (see Figure 229a). These catalysts can be pure metal selenides or metal selenides with a surface layer of metal oxides/(oxy)hydroxides. The surface oxides/(oxy)hydroxides of metal oxides/(oxy)-hydroxides/metal sulfide composite materials act as the active

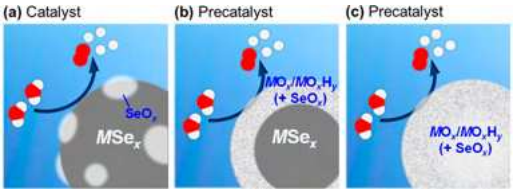


Figure 229. Schematic illustrations of suggested final types of transition metal selenide-based electrocatalysts after long-term OER testing.

sites, while the metal sulfide core enables improved conductivity compared to pure metal oxide/(oxy)hydroxide electrocatalysts. As shown in Table 6, despite some transition metal sulfides being reported as "catalysts", the majority of transition metal selenide electrocatalysts are described as "precatalysts". Generally, during the OER process, selenide "precatalysts" are partially/fully oxidized into metal oxides/(oxy)hydroxides (Figures 229b and c). The newly formed oxides/(oxy)hydroxides act as the real catalytically active phases for the OER.[208,921,953,955,1014,1030] In addition, other oxide species such as SeO_x have sometimes been observed on the surface of metal selenides after OER testing; however, whether they contribute to electrocatalysis warrants further investigation.[97,210,918−920,956,981,996] In the majority of cases, the metal selenide will be partially oxidized at the surface, leaving behind an unoxidized selenium core. This core enables improved conductivity as compared to its hydroxide/oxyhydroxide counterparts, leading to improved electron transfer to and from the surface active sites (i.e., oxides/(oxy)-hydroxides).[921,1030,1076] In the following section, we will discuss both selenide catalysts and precatalysts in detail with regard to their ability to perform as OER electrocatalysts.

5.2.2.1. Catalysts. Several metal selenides [i.e., Co_7Se_8,[928] Ni_3Se_2,[100,917] $CoNi_2Se_4$,[926] $(Ni_{0.25}Fe_{0.68}Co_{0.07})_3Se_4$,[925] $(Fe_{0.48}Co_{0.38}Cu_{0.14})Se$,[920] $NiSe_2$@multi-walled carbon nanotubes (MWCNTs),[916] MnSe@MWCNTs[915]] have been

https://doi.org/10.1021/acs.chemrev.3c00005
Chem. Rev. 2023, 123, 12795−13208

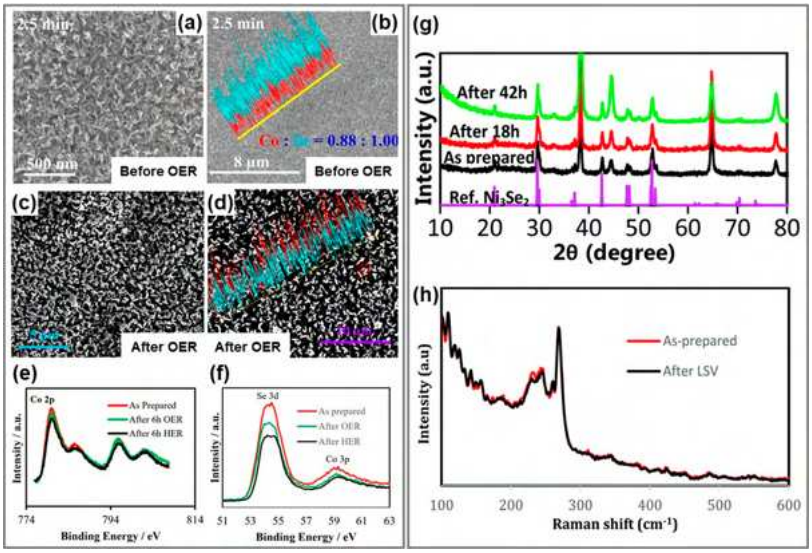


Figure 230. SEM images and EDX line-scan profiles of Co_7Se_8 (a, b) before and (c, d) after a 6 h OER process. (e) Co 2p and (f) Se 3d XPS spectra of Co_7Se_8 before and after 6 h OER and HER processes. Reproduced with permission from ref 928. Copyright 2016 American Chemical Society. (g) XRD patterns of Ni_3Se_2 before and after the long-term chronoamperometric tests. (h) Raman spectra of Ni_3Se_2 before long-time cycling and after LSV that was after a 18 h continuous OER test. Reproduced with permission from ref 100. Copyright 2016 Royal Society of Chemistry.

reported as OER catalysts by the Nath group. For example, for a Co_7Se_8 catalyst film prepared on a glassy carbon electrode via electrodeposition, they observed no compositional changes in the material following OER testing.[928] To examine the film for its OER durability, a 6 h chronoamperometric test was employed at a constant current density of 10 mA·cm^{-2} in 0.1 M KOH and post-OER characterization was completed. The techniques used for post-OER characterization were SEM, EDX, XRD, and XPS. From the pre- and post-OER SEM images, an increase in porosity was observed for the Co_7Se_8 film (Figures 230a and c). Additionally, EDX line-scan analysis showed that the atomic ratio of Co:Se increased (0.88:1 → 0.91:1) after the OER test, though Co and Se remained evenly distributed on the surface (Figures 230b and d). The authors hypothesized that the decrease in Co:Se was the result of the dissolution of Se species into the electrolyte. Despite the possible loss of Se, no change to the bulk of the material was observed, as there were no changes to the XRD pattern before and after the OER. Additionally, after OER testing, no changes were observed in the Co 2p and Se 3d high-resolution XPS spectra, indicating that the surface composition of the catalyst did not change after long-term OER testing (Figures 230e and f). The Nath group came to similar conclusions for their Ni_3Se_2 film on an Au-coated glass substrate prepared via electrodeposition.[100] The as-prepared Ni_3Se_2 electrode exhibited an OER overpotential of 290 mV at 10 mA·cm^{-2} and long-term electrochemical stability in N_2 saturated 0.3 M KOH. Specifically, an 18 h chronoamperometric measurement was carried out at an overpotential where the current density was around 10 mA·cm^{-2}. After long-term testing, various characterization techniques such as XRD, XPS, and Raman spectroscopy indicated that the composition of Ni_3Se_2 remained unchanged, suggesting that the Ni_3Se_2 acted as a catalyst for the OER. To be specific, from XRD patterns, there were essentially no changes in peak position or intensity (Figure 230g). No obvious changes were observed in the Ni 2p XPS spectra before and after the OER. The high-resolution O 1s or Se 3d spectra also showed negligible changes. In addition, no peaks corresponding to Ni-oxide/hydroxide were detected from Raman spectra (Figure 230h). Even though the Se content decreased slightly after long-term testing, the structure and composition of the Ni_3Se_2 film remained unchanged, indicating that their Ni_3Se_2 film acted as a catalyst for the OER. However, given that these results conflict with other reports[1030,1058] (see precatalyst section), further work needs to be done to understand why such stable materials resulted in this case.

The Nath group also came to a similar finding for their bimetallic Co-Ni selenide ($CoNi_2Se_4$) catalyst film prepared on a Au-coated glass substrate via electrodeposition.[926] After a 10 h chronoamperometry stability test (applied bias: 1.38 V_{RHE}) in 1 M KOH, no drastic changes were observed in the XRD pattern for $CoNi_2Se_4$ (Figure 231a), indicating that there was not a change to the bulk of the material. In addition, no morphological changes were observed from SEM images, and EDX analysis indicated almost no compositional changes to the bulk of the electrocatalyst (Figures 231b and c). No compositional changes were observed at the surface of the material either, as there were only negligible changes in the binding energies of Ni, Co, and Se in all high-resolution XPS spectra (Figures 231d and e). According to these characterization results, the authors concluded that the $CoNi_2Se_4$ was a stable catalyst for the OER, much like their monometallic selenide films.

Furthermore, a trimetallic Ni-Fe-Co selenide [$(Ni_{0.25}Fe_{0.68}Co_{0.07})_3Se_4$] catalyst film fabricated on an Au-coated glass substrate also experienced no compositional changes following OER testing.[925] The $(Ni_{0.25}Fe_{0.68}Co_{0.07})_3Se_4$ catalyst exhibited an OER overpotential of 230 mV at 10 mA·cm^{-2} and demonstrated relatively high electrochemical durability according to an 8 h chronoamperometric test (applied bias: 0.50 $V_{Ag/AgCl}$) in 0.3 M KOH. Post-OER characterization using SEM, XPS, and EDX also indicated that the material had high durability. According to the pre- and post-OER SEM images (Figures 232a and b), there was only slight surface roughing after the OER, which could have only

https://doi.org/10.1021/acs.chemrev.3c00005
Chem. Rev. 2023, 123, 12795−13208

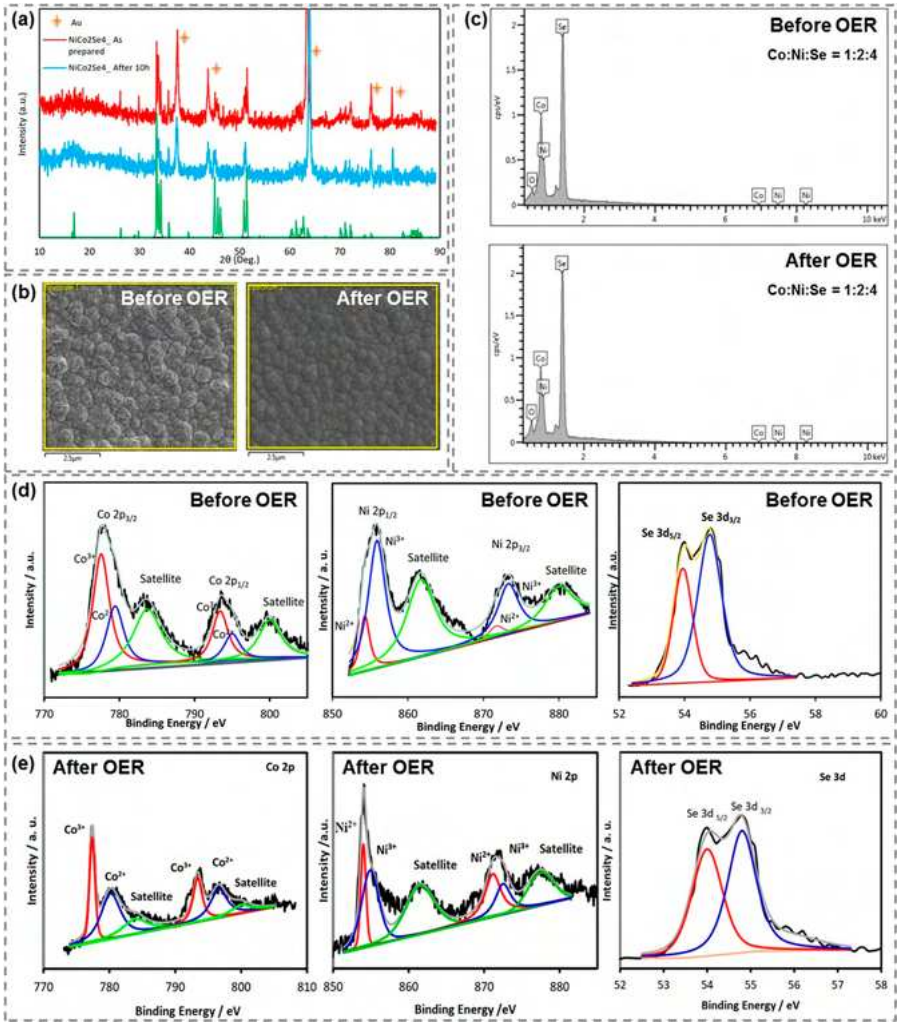


Figure 231. (a) XRD patterns, (b) SEM images, and (c) corresponding EDX spectra of $CoNi_2Se_4$ before and after the long-term OER process. Ni 2p, Co 2p, and Se 3d XPS spectra of $CoNi_2Se_4$ (d) before and (e) after chronoamperometry for 10 h. Reproduced with permission from ref 926. Copyright 2017 Royal Society of Chemistry.

been caused by the generation and release of O_2 bubbles. XPS and EDX results indicated high compositional integrity after OER testing [the ratio of Ni:Fe:Co only changed from 11.4:31.7:3.3 to 14.1:35.9:5.4 (from EDX)], implying that almost no oxidation occurred at the selenide surface during OER testing (Figures 232c and d). Similarly, a $(Fe_{0.48}Co_{0.38}Cu_{0.14})Se$ catalyst film on Au-coated glass also exhibited high durability after stability testing.[920] SEM images indicated roughening of the surface due to O_2 bubble formation after the OER, but little to no change in peak positions in high-resolution XPS spectra as in the previous example (Figures 232e–h). Also, from EDX analysis, the relative elemental ratio of Co:Fe:Cu (18.5:23.7:6.6 → 17.3:24.5:9.5) experienced little change after long-time OER testing, indicating, once again, that the $(Fe_{0.48}Co_{0.38}Cu_{0.14})Se$ sample is catalytic, rather than precatalytic. The authors mention that the stability of these materials could possibly be the result of using a quaternary mixed metal selenide with multiple material phases.

Meanwhile, (oxy)hydroxides serving as an outer protective layer in core@shell (core: selenide; shell: oxide/(oxy)-hydroxide) structured selenide catalysts also experienced high durability, as the outer layer participated in the OER directly instead of the selenide core. The shell oxide/(oxy)hydroxide provides active sites for *OH, *OOH, and *O adsorption, facilitating the OER. The selenide core then acts as a conductive substrate for efficient electron transfer. For example, Li *et al.* observed high stability for their Ni_3Se_4@NiFe LDH core@shell catalyst synthesized on carbon fiber cloth.[921] After 100 h of a chronoamperometric stability test at 1.687 V_{RHE}, the initial morphology had not changed according to SEM images (Figures 233a and d). The bulk composition also went unchanged, as EDX and XRD results indicated that the composition and crystal structure of the Ni_3Se_4@NiFe LDH catalyst were essentially the same before and after testing (Figures 233b and e). From the XPS spectra, the Ni 2p and Fe 2p peaks were virtually the same before and after the OER, which indicates that the surface composition was almost constant during the OER (Figures 233c and f). Thus, transition metal selenides with an outer shell of hydroxides/oxyhydroxides act as catalysts owing to their protective oxidative layer.

5.2.2.2. Precatalysts. As seen in Table 6, most of the available studies regarding transition metal selenides reported material changes (i.e., morphology, composition, structure) after long-term OER tests. Typically, the selenide precatalysts

https://doi.org/10.1021/acs.chemrev.3c00005
Chem. Rev. 2023, 123, 12795−13208

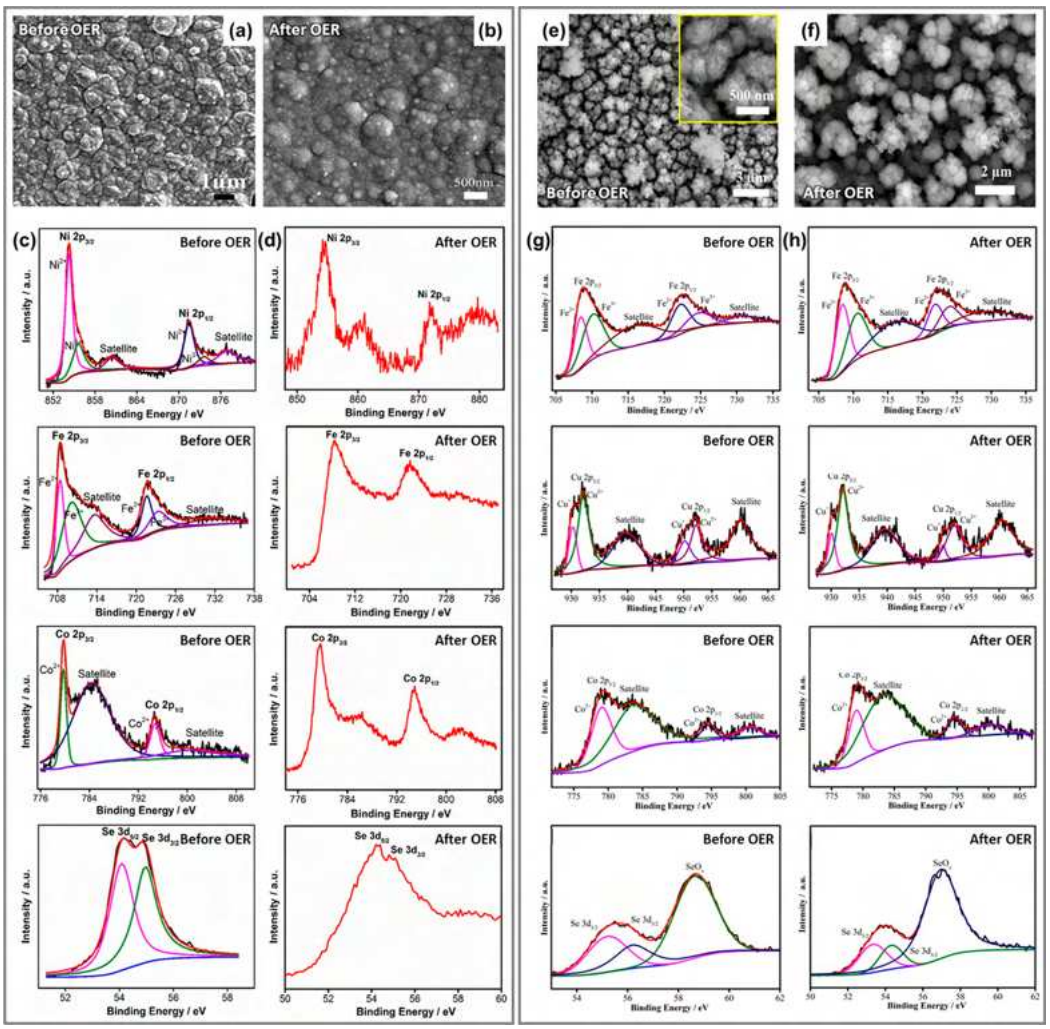


Figure 232. (a, b) SEM images of $(Ni_{0.25}Fe_{0.68}Co_{0.07})_3Se_4$ (a) before and (b) after chronoamperometry. (c, d) XPS spectra of $(Ni_{0.25}Fe_{0.68}Co_{0.07})_3Se_4$ (c) before and (d) after chronoamperometry. Reproduced with permission from ref 925. Copyright 2018 American Chemical Society. (e, f) SEM images of $(Fe_{0.48}Co_{0.38}Cu_{0.14})Se$ (e) before and (f) after chronoamperometry. (g, h) XPS spectra of $(Fe_{0.48}Co_{0.38}Cu_{0.14})Se$ (g) before and (h) after chronoamperometry. Reproduced with permission from ref 920. Copyright 2019 American Chemical Society.

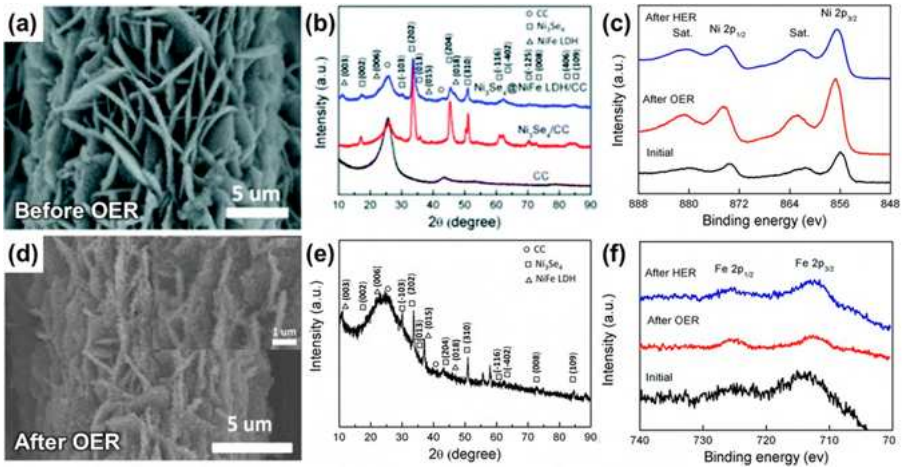


Figure 233. (a, d) SEM images of the hierarchical hetero-Ni_3Se_4@NiFe LDH/CC micro/nanosheets (a) before and (d) after the OER process. (b) XRD patterns of CC, Ni_3Se_2/CC, and Ni_3Se_4@NiFe LDH/CC before the OER. (e) XRD pattern of Ni_3Se_4@NiFe LDH/CC after the OER. (c) Ni 2p and (f) Fe 2p XPS spectra of the Ni_3Se_4@NiFe LDH/CC electrode before and after the OER and HER. Reproduced with permission from ref 921. Copyright 2019 Royal Society of Chemistry.

https://doi.org/10.1021/acs.chemrev.3c00005
Chem. Rev. 2023, 123, 12795−13208

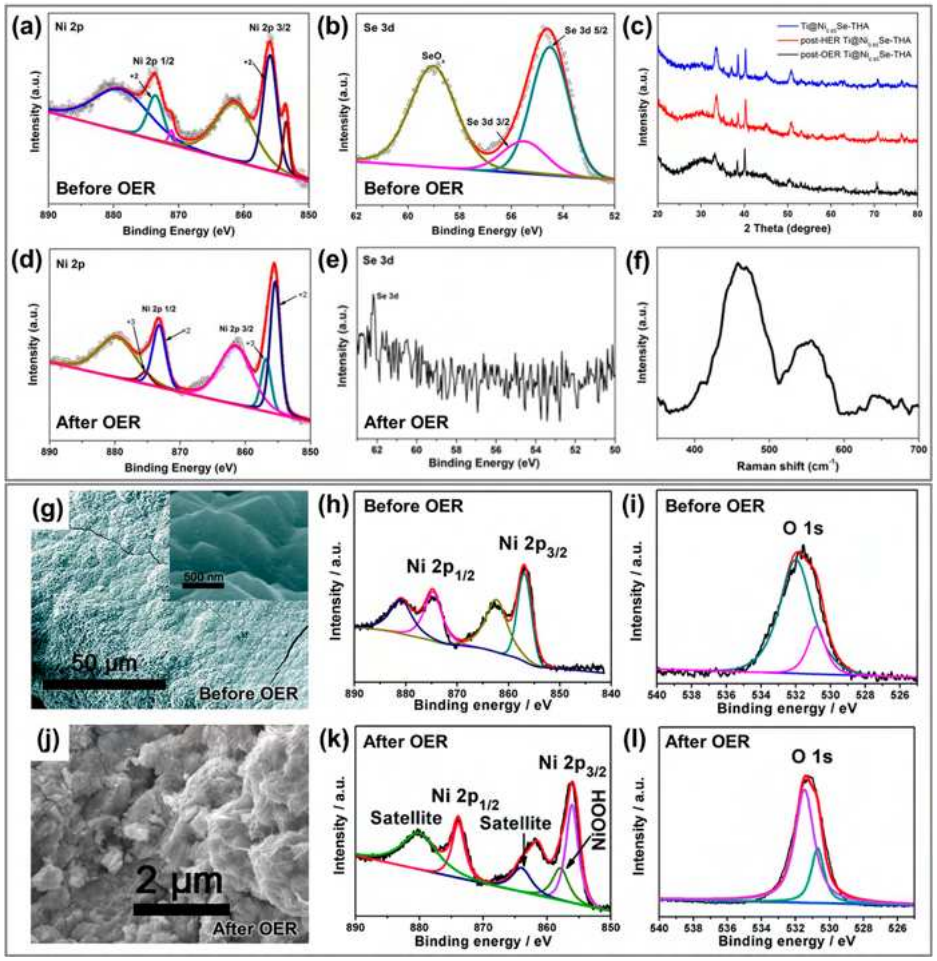


Figure 234. (a, d) Ni 2p XPS spectra of the Ti@$Ni_{0.85}Se$-THA (a) before and (d) after OER test. (b, e) Se 3d XPS spectra of the Ti@$Ni_{0.85}Se$-THA (b) before and (e) after the OER test. (c) XRD patterns of the Ti@$Ni_{0.85}Se$-THA before and after the OER and HER. (f) Raman spectrum of the Ti@$Ni_{0.85}Se$-THA after the OER. Reproduced with permission from ref 955. Copyright 2019 Wiley. (g, j) SEM images of Ni_3Se_2 (g) before and (j) after OER testing. (h, k) Ni 2p XPS spectra of Ni_3Se_2 before (h) and after (k) OER testing. (i, l) O 1s XPS spectra of Ni_3Se_2 before (i) and after (l) OER testing. Reproduced with permission from ref 1030. Copyright 2015 Royal Society of Chemistry.

are oxidized during the OER and transformed into their oxide/(oxy)hydroxide counterparts and/or SeO_x, which serve as actual electroactive sites for the OER. In this section, we will introduce several metal selenide precatalysts with different compositions and morphologies. Additionally, the *in situ* electrochemical transformations of the selenide precatalysts during OER testing will be discussed in detail to gain a better understanding of these phenomena and to identify the real OER active species based on the reported data.

Nickel-based selenides have garnered much attention for the OER and HER due to their low cost, easy preparation, facile accessibility, and abundant reserves.[202,605] Nickel selenides can be prepared using Ni foam, wherein Ni foam acts as both the substrate and Ni source, leading to enhanced electron transfer for improved electrocatalysis.[1102] For nickel selenides, different valence states of Ni result in various material compositions (i.e., $NiSe_2$,[947,950,1006,1015] NiSe (refs 208, 949, 983, 995, 1007, 1008, 1018, 1020, 1027, and 1083), $Ni_{0.85}Se$,[950,953,1022] Ni_3Se_4,[950,984,1005] and Ni_3Se_2,[1004,1008,1024,1030]). Herein, we will introduce some typical nickel selenide precatalysts for the OER.

During the OER, the majority of reported nickel selenides undergo partial oxidation at the surface, resulting in transformation of the surface to the real electrocatalytically active sites—NiOOH. For example, Wang *et al.* grew $Ni_{0.85}Se$ with a triple hierarchy architecture directly on Ti mesh (Ti@$Ni_{0.85}Se$-THA).[955] A long-term stability test was performed for 30 h using chronoamperometry at an applied potential of 1.574 V_{RHE} in 1.0 M KOH electrolyte. The XPS results showed the formation of Ni^{3+} and loss of Se 3d (no signal) after the OER, implying the transformation of $Ni_{0.85}Se$ into NiOOH (Figures 234a, b, d, and e). Compared with the pre-OER XRD pattern of $Ni_{0.85}Se$, the intensity of post-OER XRD peaks was weakened, which indicated that NiOOH formed on the surface of $Ni_{0.85}Se$ (Figure 234c). However, the peaks of NiOOH cannot be found in the XRD pattern, likely owing to the small amount of NiOOH formed. Moreover, Raman analysis also indicated the formation of NiOOH after the OER (Figure 234f). The coexistence of NiOOH and $Ni_{0.85}Se$ after the OER indicated that partial oxidation of $Ni_{0.85}Se$ had occurred. Additionally, Sun *et al.* deposited a Ni_3Se_2 precatalyst on Cu foam.[1030] The electrochemical stability of the Ni_3Se_2 electrode was tested using a chronopotentiometric test at a current density of 70 $mA{\cdot}cm^{-2}$ for 10 h in 1.0 M KOH. The SEM images of the post-OER sample showed a newly generated thin layer on the surface, different from the as-prepared electrode (Figures 234g and j). Additionally, the XPS spectra exhibited a peak in the Ni 2p region, which

https://doi.org/10.1021/acs.chemrev.3c00005
Chem. Rev. 2023, 123, 12795−13208

corresponded to NiOOH species (Figures 234h and k), while a peak in the O 1s region confirmed partial oxidation during the OER (Figures 234i and l). Notably, the authors concluded that while the NiOOH acted as the active species, Ni_3Se_2 served as a conductive substrate, promoting electron transfer to the surface OER active sites. Similarly, Sun *et al.* synthesized a NiSe precatalyst directly on Ni foam and found that partial oxidation had occurred following long-term OER stability testing.[208] Specifically, chronopotentiometry was employed to test the as-prepared electrocatalyst at a current density of 100 $mA{\cdot}cm^{-2}$ for 12 h in 1.0 M KOH electrolyte. The pre- and post-OER Raman spectra revealed that NiOOH was present in the post-OER sample, suggesting the partial oxidation of the nickel selenide during OER testing. In addition, the XPS spectra showed the formation of Ni^{III}, confirming the presence of NiOOH on the surface, which was regarded as the OER active species (data not shown here).

In addition to partial oxidation at their surfaces, nickel selenides can also undergo material transformation during the OER through the dissolution of Se into the electrolyte. For example, the Nath group found that their $NiSe_2$ film on Au-coated glass lost Se following OER stability testing for 24 h using chronoamperometry (applied bias: 1.37 V_{RHE}; electrolyte: 1.0 M KOH).[1017] The XRD pattern of the post-OER material indicated that, while the $NiSe_2$ phase was primarily maintained, an overall reduction in diffraction peak intensity for the $Ni_{0.85}Se$ phase was observed, signifying a loss of Se from the structure (Figure 235a, wherein the diffraction pattern corresponding to PDF # 00-041-1495 is for the cubic $NiSe_2$ phase). The loss of selenium was further confirmed by EDX, which detected a change in the Ni to Se ratio from 1:2 to 1:1.75 after long-term OER testing (Figures 235c and d). While XRD and EDX indicated the dissolution of Se, the Ni 2p XPS spectra (Figure 235b) indicated that no oxidation had occurred, as there were no changes to the peaks after OER testing. Thus, metal selenide transformation is also possible via the loss of Se.

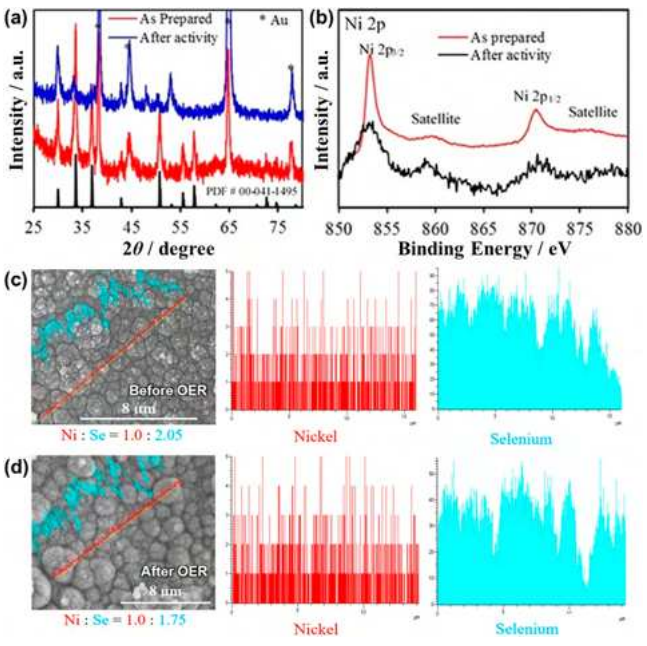


Figure 235. (a) XRD patterns of $NiSe_2$ before and after the current transient experiment for 24 h. (b) Ni 2p XPS spectra of $NiSe_2$ before and after OER testing. (c, d) SEM images and EDX line-scan profiles of $NiSe_2$ (c) before and (d) after OER testing. Reproduced with permission from ref 1017. Copyright 2017 Springer Nature.

In addition to nickel selenides, cobalt selenides have also been frequently used as precatalysts for the OER. Because of the unique electronic configuration and metallic behavior of cobalt, cobalt selenides are regarded as ideal candidates for the OER.[981,1103] Depending on the selenium content, cobalt selenides will exhibit different crystal structures, morphologies, and properties (e.g., $CoSe_2$,[923,988,1070,1071,1074,1079,1085] Co_3Se_4,[1014,1046] $Co_{0.85}Se$,[981,1048,1077,1081] CoSe,[960,965,1027] etc.). For instance, Zhang *et al.* reported $CoSe_2$ ultrathin nanomeshes ($CoSe_2$ UNM_{vac}) with Se vacancies as a precatalyst for the OER.[953] The stability of the $CoSe_2$ precatalyst was tested in 1.0 M KOH at a current density of 10 $mA{\cdot}cm^{-2}$ for 20 h. Pre- and post-OER EDX mapping confirmed the presence of oxygen in the post-OER precatalyst, indicating $CoSe_2$ had undergone oxidation during the OER (Figures 236a and b). Post-XPS spectra revealed that only partial oxidation occurred as a Co−O peak, indicative the formation of CoOOH, and a Co−Se peak were both observed following the OER (Figures 236c and d). Notably, the authors proposed that a CoOOH layer at the surface might provide numerous OER active sites and that the remaining $CoSe_2$ might promote efficient electron transfer to the surface CoOOH species. The authors also claimed that the Se vacancies might promote the formation of CoOOH species on the selenide precatalyst surface. Following stability testing, post-OER ECSA increased by 97.12% compared with the pre-OER material. This increased ECSA resulted in high contact area between the precatalyst surface covered with CoOOH species and the electrolyte, providing more OER active species (i.e., CoOOH) for catalysis.

Similarly, Liu *et al.* reported a Co_3Se_4 precatalyst *in situ* grown on Co foam via the hydrothermal method.[1014] Long-term OER testing was performed at a current density of 10 $mA{\cdot}cm^{-2}$ for 12 h in 1.0 M KOH. From pre- and post-OER SEM images of the Co_3Se_4 precatalyst, the nanowire morphology of Co_3Se_4 was transformed into a nanosheet-like morphology (Figures 236e and f). EDX results revealed a sharp decrease in Se content, while oxygen increased significantly, suggesting oxidation occurred at the selenide surface (Figure 236g). The post-OER XRD and TEM results also confirmed the formation of CoOOH via oxidation of the as-prepared Co_3Se_4 (Figures 236h−j). Moreover, the XPS results revealed shifts in the Co $2p_{3/2}$ peak position toward higher energies, matching the Co $2p_{3/2}$ peak corresponding to CoOOH (Figures 236o). In addition, the metal−Se peak disappeared in the Se 3d XPS spectra while additional peaks emerged in the O 1s spectra, indicating oxidation of the surface (Figures 236p and q). Even though there is no signal for metal selenides in the XRD pattern and XPS spectra of the post-OER product, there was a tiny Se signal in the HAADF (Figures 236k−n). Here, we assume that the detected Se was presumably from (i) the residual oxidized Se species and/or (ii) the Se species dissolved in the electrolyte that adsorbed on the post-OER product. Notably, at a constant current density of 10 $mA{\cdot}cm^{-2}$, the electrocatalytic performance was maintained for 3500 h, which is thus far the longest stability testing among reported cobalt selenides.

Xiao *et al.* prepared a coral-like CoSe precatalyst on carbon fiber paper via a two-step solvothermal method.[1027] They carried out chronoamperometry at an applied potential of 1.58

https://doi.org/10.1021/acs.chemrev.3c00005
Chem. Rev. 2023, 123, 12795−13208

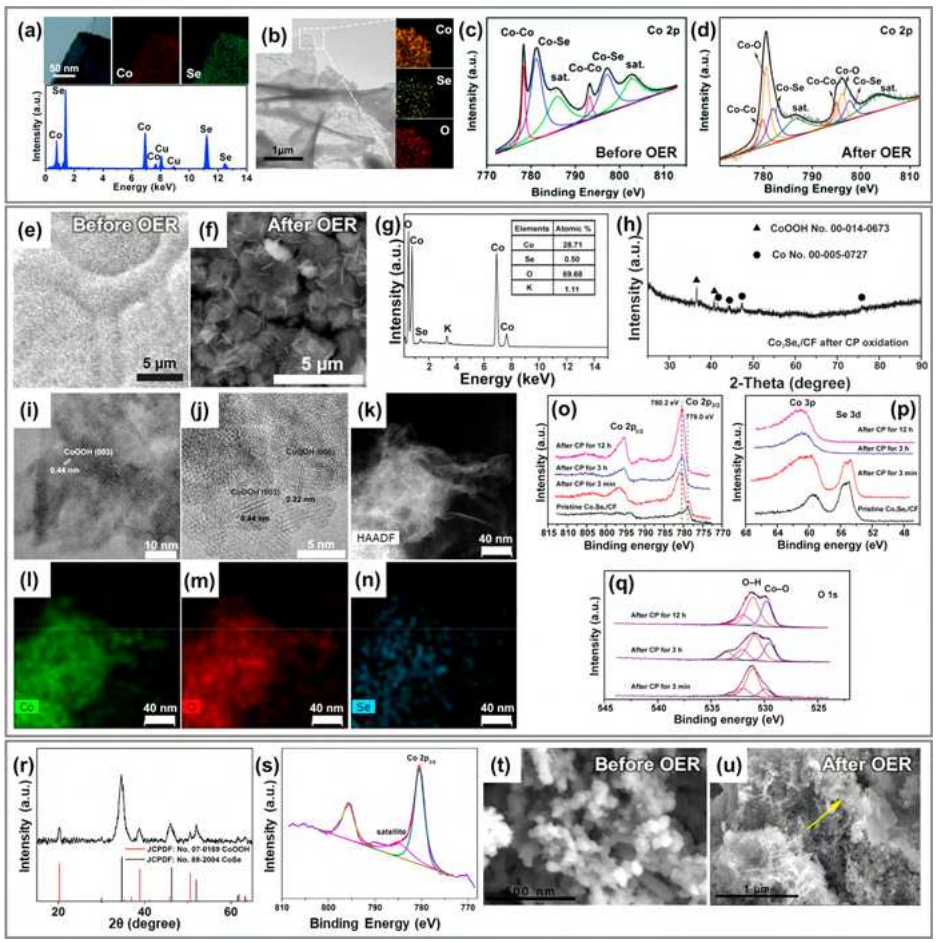


Figure 236. (a) STEM-EDX mapping images and EDX spectrum of $CoSe_2$ UNM_{vac} before the OER. (b) TEM and STEM-EDX mapping images of $CoSe_2$ UNM_{vac} after the OER. (c, d) Co 2p XPS spectra of $CoSe_2$ UNM_{vac} (c) before and (d) after the OER process. Reproduced with permission from ref 953. Copyright 2019 Royal Society of Chemistry. (e, f) SEM images of Co_3Se_4/CF (e) before and (f) after 12 h long-term stability test. (g) EDX spectrum and (h) XRD pattern of the Co_3Se_4/CF electrode after the 12 h CP. (i–n) TEM analysis results of Co_3Se_4/CF after the stability: (i, j) HRTEM images, (k) HAADF-STEM image, and elemental mapping images of Co (l), O (m), and Se (n). (o) Co 2p, (p) Co 3p-Se 3d, and (q) O 1s XPS spectra of Co_3Se_4/CF before and after CP tests at 10 $mA{\cdot}cm^{-2}$ for different testing times. Reproduced with permission from ref 1014. Copyright 2017 Wiley. (r) XRD pattern of the coral-like CoSe after 30 cycles of continuous cyclic voltammetry. (s) Co 2p XPS spectra of coral-like CoSe after the OER test. (t, u) SEM images of the coral-like CoSe (t) before and (u) after the OER test. Reproduced with permission from ref 1027. Copyright 2016 Elsevier.

V_{RHE} to test the precatalyst's stability for 10000 s in 1.0 M KOH. Subsequently, they characterized the post-OER material after 30 cycles of continuous cyclic voltammetry. The post-OER XRD pattern confirmed the presence of both CoSe and CoOOH phases (Figure 236r). Moreover, the post-OER Co 2p XPS peak at 780.4 eV suggested the presence of Co^{III} species, and thereby the presence of newly formed CoOOH surface species (Figure 236s). From SEM (Figures 236t and u), the thin layer formed on the CoSe surface further confirmed CoOOH formation during the OER. According to the authors, a possible OER mechanism could be described as follows:

$$Co^{(II)} + 3OH^- \leftrightarrow Co^{(III)}OOH + H_2O + e^-$$

$$Co^{(III)}OOH + OH^- \leftrightarrow Co^{(IV)}O(OH)_2 + e^-$$

$$Co^{(IV)}O(OOH)_2 + 2OH^- \leftrightarrow Co^{(IV)}OO_2 + 2H_2O + 2e^-$$

$$Co^{(IV)}OO_2 + OH^- \leftrightarrow Co^{(III)}OOH + O_2 + e^-$$

Accordingly, CoSe acted as a conductive substrate rather than an electrocatalyst during the OER, and the oxidized CoSe surface provided numerous active species (i.e., CoOOH) for electrocatalysis.

Recent studies have discussed the *in situ* transformation of iron and copper selenides to their oxide/(oxy)hydroxide counterparts during the OER as well. For example, Driess *et al.* synthesized a $FeSe_2$ precatalyst on Ni foam from a molecular 2Fe-2Se precursor.[1013] After long-term stability testing (chronopotentiometry at 10 $mA{\cdot}cm^{-2}$ in 1.0 M KOH for 18 h), TEM and HRTEM images revealed a thin amorphous shell on the $FeSe_2$ surface, implying surface transformation (i.e., oxidation) during the OER (Figure 237a). Fourier transform infrared (FTIR) spectra also indicated surface oxidation, as broad hydroxyl bands at 3300 and 1644 cm^{-1} were observed (Figure 237b). Furthermore, ICP-AES analysis of post-OER $FeSe_2$ revealed the loss of Se after the OER, providing further evidence of the transformation of $FeSe_2$ during the OER process. From XPS results (Figure 237c), the peaks in the Fe 2p region were slightly shifted after OER testing, suggesting an increase in the

https://doi.org/10.1021/acs.chemrev.3c00005
Chem. Rev. 2023, 123, 12795–13208

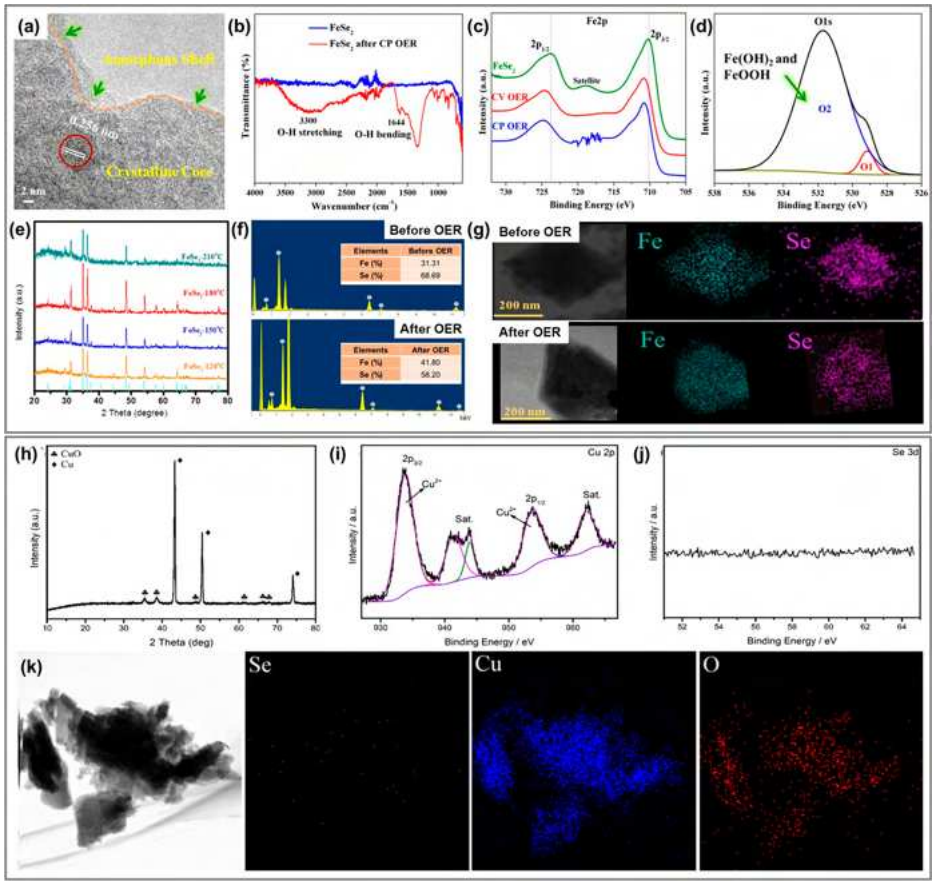


Figure 237. (a) TEM image of $FeSe_2$ after the OER CP measurements in 1.0 M KOH for 18 h. (b) FTIR transmission spectra of as-prepared $FeSe_2$ and $FeSe_2$ after the OER CP experiment. (c) Fe 2p XPS spectra of $FeSe_2$ before and after the OER CV and CP tests. (d) O 1s XPS spectrum of $FeSe_2$ after the OER. Reproduced with permission from ref 1013. Copyright 2017 Wiley. (e) XRD patterns of $FeSe_2$ samples after 70 h OER testing. (f) STEM-EDX elemental mapping images and (g) EDX spectra of $FeSe_2$-180 °C before and after the OER. Reproduced with permission from ref 1011. Copyright 2017 Elsevier. (h) XRD pattern, (i) Cu 2p and (j) Se 3d XPS spectra, and (k) element mapping images of Cu_2Se on Cu foam after the OER. Reproduced with permission from ref 961. Copyright 2019 Elsevier.

oxidation states of Fe (i.e., from mixed Fe^{2+}/Fe^{3+} to Fe^{3+}) indicative of surface oxidation. Moreover, the XPS spectra in the O 1s region confirmed the formation of FeO_x (O1) and the presence of oxyhydroxide/hydroxides (O2) (Figure 237d). Therefore, the $FeSe_2$ precatalyst was partially transformed into FeO_x and FeOOH during OER testing, the real active species for the OER. Similarly, Yan *et al.* synthesized 2D $FeSe_2$ nanoplatelet powder via the hydrothermal method and found that the material underwent an *in situ* surface transformation during the OER.[1011] After durability testing (1.67 V_{RHE} for 70 h), XRD patterns for $FeSe_2$ samples prepared at different temperatures indicated retention of the as-prepared material's crystal structure, signifying no changes to the bulk structure following OER testing (Figure 237e). STEM-EDX elemental mapping results showed the morphology of the electrocatalyst remained as well; however, there was a decrease in Se content indicative of material transformation during the OER (Figures 237f and g). Based on a previous report,[98] the authors hypothesized that $FeSe_2$ was partially oxidized into oxides and/or (oxy)hydroxides at its surface, resulting in the generation of the real electrocatalytic active sites.

Lian *et al.* also observed material transformation for their crystalline Cu_2Se precatalyst on Cu foam prepared via a simple solution-immersion method.[961] The electrochemical durability of the Cu_2Se precatalyst was tested at a constant current density of 10 $mA{\cdot}cm^{-2}$ for 12 h in 1 M KOH. Post-OER XRD analysis revealed the formation of CuO and the absence of the Cu_2Se phase (Figure 237h). The Cu 2p XPS spectra exhibited an increase in the oxidation state of Cu (i.e., $Cu^{+} \rightarrow Cu^{2+}$) after OER testing (Figure 237i). XPS results also revealed a loss of Se at the precatalyst's surface (Figure 237j), indicating Se dissolution, which was further confirmed by elemental mapping (Figure 237k). Based on the above analyses, the authors concluded that Cu_2Se could be almost completely transformed into CuO species, which might act as OER active sites.

Similarly, bimetallic, trimetallic, and multimetallic selenide precatalysts have been extensively studied and found to undergo oxidation during the OER (see Table 6). In comparison to their monometallic counterparts, these multimetal selenides have demonstrated improved electrocatalytic performance owing to synergistic effects between different metal ions. Additionally, because of the mismatch in the Jahn-Teller distortion degree induced by the presence of multiple metal ions, incorporating/doping foreign transition metal(s) into a monometallic selenide may create vacancies in its crystal lattice, facilitating the *in situ* electrochemical oxidation of the precatalyst during the OER and leading to a greater number of exposed active sites for electrocatalysis.[980,1104]

Nickel-cobalt selenide is one of the most common bimetallic selenide precatalysts used for the OER. Here, we introduce examples of nickel-cobalt selenides with different Se content:

https://doi.org/10.1021/acs.chemrev.3c00005
Chem. Rev. 2023, 123, 12795−13208

Se-poor $M_{0.85}Se$ and Se-rich MSe_2 (M = Ni + Co). For the example of the Se-poor Ni-Co selenide, Shao *et al.* synthesized a $(Ni,Co)_{0.85}Se$ precatalyst on Ni foam and tested its long-term electrochemical durability at a constant current density of 30 mA·cm^{-2} for 12 h in 1 M KOH.[980] Ni 2p and Co 2p XPS spectra exhibited new, weak peaks after OER testing, attributed to the formation of NiOOH and CoOOH on the surface (Figures 238a and b). However, no peaks were detected in the

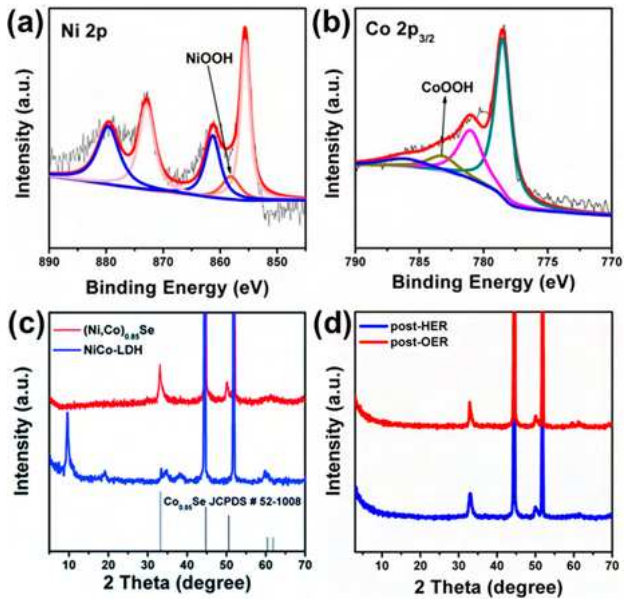


Figure 238. (a) Ni 2p and (b) Co 2p XPS spectra of $(Ni,Co)_{0.85}Se$ after OER testing. (c) XRD patterns of $(Ni,Co)_{0.85}Se$ and NiCo-LDH. (d) XRD patterns of $(Ni,Co)_{0.85}Se$ after OER and HER testing. Reproduced with permission from ref 980. Copyright 2018 Royal Society of Chemistry.

post-OER XRD pattern corresponding to NiOOH or CoOOH, indicating that oxidation was confined to the surface of the as-prepared material (Figures 238c and d). The authors concluded that the *in situ*-formed nickel and cobalt oxyhydroxides acted as the active sites for the OER. According to previous reports,[1002,1105] these oxyhydroxide species can promote the deprotonation of OOH_{ad}, which adheres to the selenide surface and facilitates the production of O_2 gas via an electron-withdrawing inductive effect. In another instance, Alshareef *et al.* doped Ni into $Co_{0.85}Se$ to obtain a bimetallic $(Ni, Co)_{0.85}Se$ precatalyst on a carbon fabric substrate for the OER.[1029] After long-term stability testing (at 10 mA·cm^{-2} for 24 h in 1.0 M KOH), a Ni^{3+} peak at 857.78 eV was observed in the XPS spectra corresponding to the formation of NiOOH on the selenide surface. Moreover, Co^{3+} was also detected at 778.88 eV in post-OER high-resolution XPS spectra, indicative of cobalt oxyhydroxide formation during OER testing. The partial oxidation of $(Ni, Co)_{0.85}Se$ was then further confirmed by the post-OER O 1s XPS spectrum, indicating metal-oxyhydroxide formation. Thus, in Se-poor multimetal selenide electrocatalysts, material transformation during the OER appears to be confined to the surface and results in (oxy)hydroxide species formation for all metal ions (Ni and Co).

As for the Se-rich Ni-Co selenide, surface oxidation was also observed. For example, Wang *et al.* prepared a bimetallic selenide [$(Ni,Co)Se_2$] precatalyst on Ni foam.[1000] The stability of the $(Ni,Co)Se_2$ precatalyst was tested at a constant current density of 20 mA·cm^{-2} for 36 h in 1 M KOH electrolyte. Although the morphology remained unchanged according to SEM images taken before and after the OER (Figures 239a and d), new peaks emerged in the XPS spectra assigned to Co−O and Ni−O bonds (i.e., CoOOH and NiOOH), suggesting the partial oxidation of the precatalyst during the OER (Figure 239b, c, e, and f). Chun *et al.* had similar results for their $NiCoSe_2$ precatalyst on Ni foam.[993] After stability testing (10 mA·cm^{-2} for 50 h in 1.0 M KOH), no morphological changes were detected via SEM (Figure 239g and j), while peaks corresponding to CoOOH and NiOOH were detected in post-OER XPS spectra (Figure 239h, i, k, and l). Thus, while $NiCoSe_2$ experiences no changes to its morphology, its surface composition is transformed during the OER, resulting in the emergence of Ni and Co oxyhydroxide species as active sites for electrocatalysis. Hou *et al.* also synthesized a bimetallic selenide, specifically, $(Co,Ni)Se_2$ covered by N-doped carbon and supported on exfoliated graphite (EG) foil (EG/$(Co,Ni)Se_2$-NC).[969] Notably, by using *in situ* Raman spectroscopy, the authors thoroughly investigated the electrochemical reconstruction of the EG/$(Co,Ni)Se_2$-NC material during OER testing in 1 M KOH. As depicted in the *in situ* Raman spectra (Figure 239m), the formation of CoOOH during the OER process was confirmed. Specifically, at a potential of 1.2 V_{RHE}, a peak corresponding to Co−Se bonds at 202 cm^{-1} was observed. With an increase of the potential from 1.2 to 1.4 V_{RHE}, the Raman peak shifted from 202 to 206 cm^{-1}. At the potential of 1.4 V_{RHE}, another peak located at 210 cm^{-1} appeared corresponding to Co-OOH species. By further increasing the potential, the intensity of the peak at 210 cm^{-1} decreased gradually. At a potential greater than 1.5 V_{RHE}, this peak diminished, which can be explained by the newly generated active species CoO_2. For long-term OER testing, the chronoamperometric measurement was employed for 10 h at a current density of 20 mA·cm^{-2} in 1 M KOH. The authors then performed *ex situ* XPS analysis on the EG/$(Co,Ni)Se_2$-NC material before and after OER testing, as depicted in Figures 239n−q. They found that the content of Ni^{3+} decreased while the Co^{3+} content increased, suggesting that CoOOH species mainly act as the OER active sites rather than NiOOH species. Additionally, the increase in Co^{3+} species confirmed selenide oxidation during OER testing. However, the decrease of Ni^{3+} and increase of Ni^{2+} indicated that the introduction of Ni in $CoSe_2$ would promote the electron transfer process. The XPS and Raman results showed that the initial bimetallic selenide's surface transformed into CoOOH and CoO_2 via oxidation and that this oxidation was facilitated by the fast electron transfer at Ni sites during the OER. Thus, by incorporating two metals into selenide-rich materials, oxide and oxyhydroxide active species might be generated without sacrificing electrical conductivity and oxidation may be tuned.

In addition to nickel-cobalt selenides, nickel-iron selenides have also been reported as OER precatalysts. Chai *et al.* synthesized bimetallic Ni-Fe selenides ($Fe_{0.125}Ni_{0.875}Se_2$) through a gas-solid reaction at 350 °C for 2 h.[967] To test the long-term stability of the selenides, chronopotentiometric measurements were performed at a constant current density of 10 mA·cm^{-2} for 10 h in 1 M KOH. Even though the SEM image showed no change in the morphology after long-term cycling (Figures 240a and c), TEM results confirmed the formation of a thin oxidation layer on the surface of the original selenides (Figures 240b and d). Furthermore,

https://doi.org/10.1021/acs.chemrev.3c00005
Chem. Rev. 2023, 123, 12795−13208

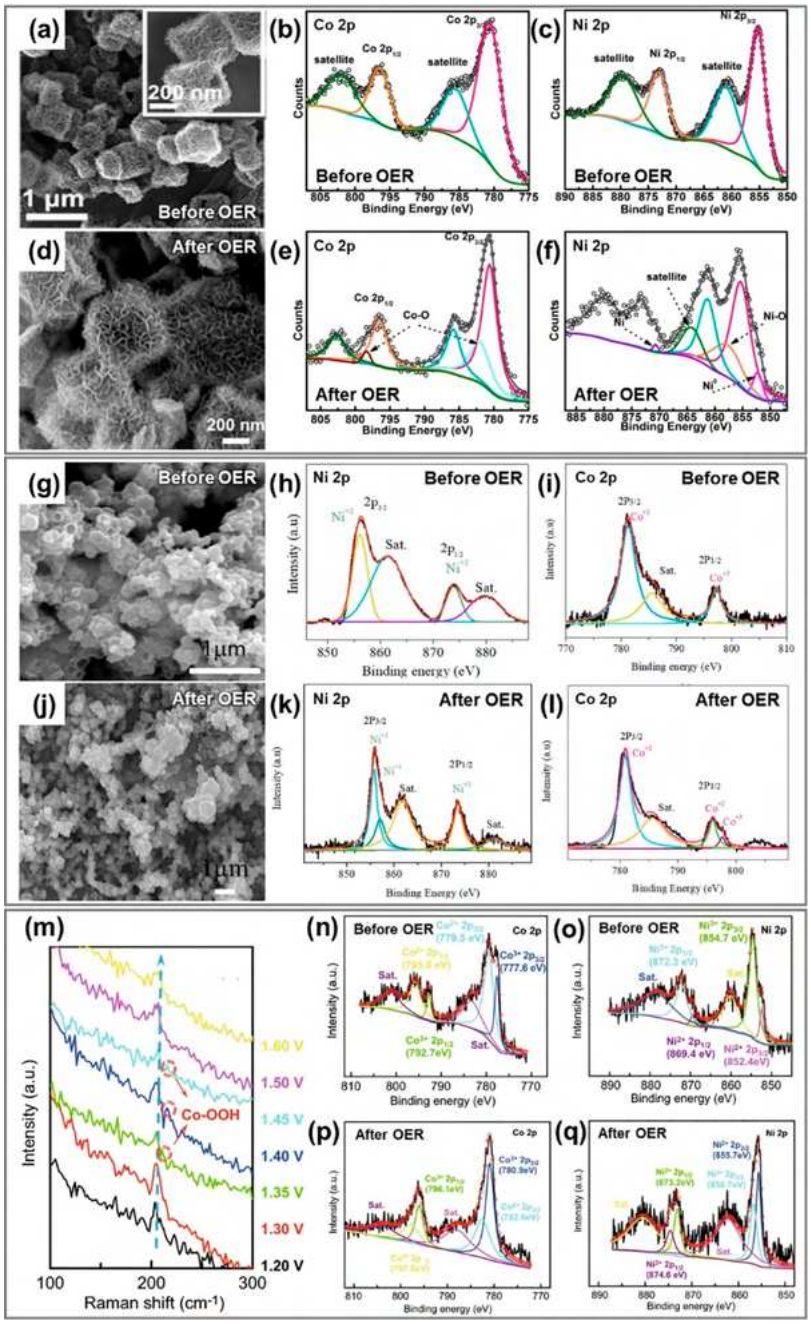


Figure 239. (a, d) SEM images of $(Ni,Co)Se_2$ (a) before and (d) after the OER. (b, e) Co 2p XPS spectra of $(Ni,Co)Se_2$ (b) before and (e) after the OER. (c, f) Ni 2p XPS spectra of $(Ni,Co)Se_2$ (c) before and (f) after the OER. Reproduced with permission from ref 1000. Copyright 2017 Elsevier. (g, j) SEM images of $NiCoSe_2$/NF (g) before and (j) after the OER. (h, k) Ni 2p XPS spectra of $NiCoSe_2$/NF (h) before and (k) after the OER. (i, l) Co 2p XPS spectra of $NiCoSe_2$/NF (i) before and (l) after the OER. Reproduced with permission from ref 993. Copyright 2018 American Chemical Society. (m) *In situ* Raman spectra of EG/$(Co, Ni)Se_2$-NC under applied potentials ranging from 1.20 to 1.60 V_{RHE}. (n, p) Co 2p XPS spectra of EG/$(Co, Ni)Se_2$−NC (n) before and (p) after the OER. (o, q) Ni 2p XPS spectra of EG/$(Co, Ni)Se_2$−NC (o) before and (q) after the OER. Reproduced with permission from ref 969. Copyright 2019 Springer Nature.

HRTEM and HAADF-STEM mapping revealed the existence of O in the selenide precatalyst after OER testing, indicating that partial oxidation of the selenide had occurred (Figures 240e and f). In another case, Li *et al.* fabricated a Fe-doped nickel selenide (Fe-NiSe) film covered by porous carbon on Ni foam.[979] The long-term stability of the material was tested using chronoamperometry at a constant potential (i.e., the potential at the current density of 10 $mA{\cdot}cm^{-2}$) for 20 h in alkaline media (1 M KOH). From SEM images before and after OER testing, the morphology remained unchanged, which the authors attributed to the porous carbon layer preventing the aggregation of the particulate Fe-NiSe (Figure 240g). However, the Ni 2p peak at 856.8 eV shown in the post-OER XPS spectrum indicated that NiOOH formed on the surface (Figures 240h and i). Note that the as-formed NiOOH may be the real OER active species.

There are also under-reported bimetallic selenides that have been used as OER electrocatalysts, such as Mn-Co diselenide and Cu-Co selenide. Zeng *et al.* fabricated a bimetallic Mn-Co selenide [e.g., $(Co_4Mn_1)Se_2$] with a relatively high degree of

https://doi.org/10.1021/acs.chemrev.3c00005
Chem. Rev. 2023, 123, 12795−13208

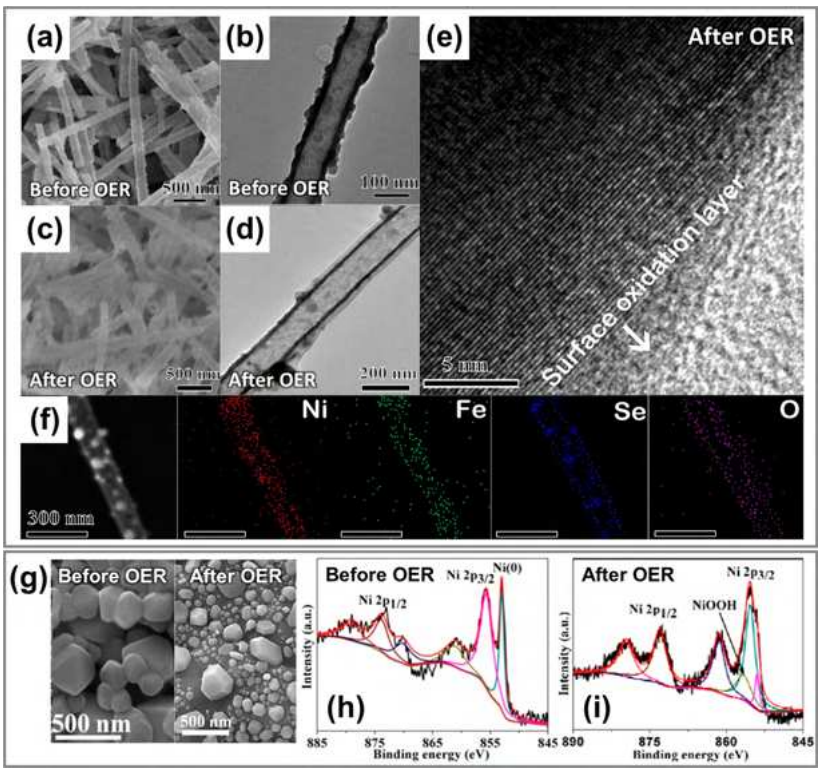


Figure 240. (a, c) SEM images of $Fe_{0.125}Ni_{0.875}Se_2$ (a) before and (c) after the OER. (b, d) TEM images of $Fe_{0.125}Ni_{0.875}Se_2$ (b) before and (d) after the OER. (e) HRTEM image and (f) HAADF-STEM elemental mapping images of $Fe_{0.125}Ni_{0.875}Se_2$ after the 10 h cycling test. Reproduced with permission from ref 967. Copyright 2019 Elsevier. (g) SEM images of Fe-NiSe before and after the OER. (h, i) Ni 2p XPS spectra of Fe-NiSe (h) before and (i) after the OER. Reproduced with permission from ref 979. Copyright 2018 Royal Society of Chemistry.

structural disorder and improved electronic structure to promote electron transfer for electrocatalysis.[978] They performed a long-term stability test at a constant current density of 10 $mA{\cdot}cm^{-2}$ for 7 h in 1 M KOH. Post-OER XPS spectra in the Co 2p region revealed the presence of Co^{3+} cations (Figure 241a), and the binding energies in the O 1s region suggested the presence of metal−oxygen bonds (Figure 241b), surface-absorbed SeO_2, and oxygen as -OH groups, indicating the formation of CoOOH, which agrees with the Co 2p XPS result. In the post-OER TEM image, the authors found the lattice spacing of 2.6 Å, corresponding to the orthorhombic $CoSe_2$ (111) planes, indicating the preservation of some Mn-Co selenide species even after long-term OER testing. Moreover, from the pre- and post-OER XRD results, the formation of amorphous species (i.e., CoOOH) was also confirmed as a dominant component due to the partial oxidation of the Mn-Co selenide during the OER (Figure 241c). In this report, information about post-OER Mn species (e.g., Mn oxide, Mn hydroxide, etc.) was not provided. However, since there are several reports about the Co-Mn hydroxides as stable OER electrocatalysts in alkaline media,[1106,1107] oxidized Mn species derived from the Mn-Co selenide may also be stable and insoluble in the electrolyte. Thus, we assume that the post-OER-formed CoOOH might not be a pure phase and that Mn species could be incorporated into the CoOOH structure. Accordingly, Mn-incorporated CoOOH can be regarded as the possible real OER active species. Regarding another example of a poorly-studied bimetallic selenide, Mai *et al.* synthesized a bimetallic Cu-Co selenide precatalyst consisting of Cu_2Se and Co_3Se_4 on Ni foam.[970] A long-term stability test was carried out in 1.0 M KOH at a current density of 10 $mA{\cdot}cm^{-2}$ for 20 h. In the XPS spectra, the intensity of the Cu^{2+} peak increased, whereas the Cu^{+} peak intensity decreased after OER testing, implying that Cu_2Se oxidation occurred (Figure 241d). As a result, $Cu(OH)_2$

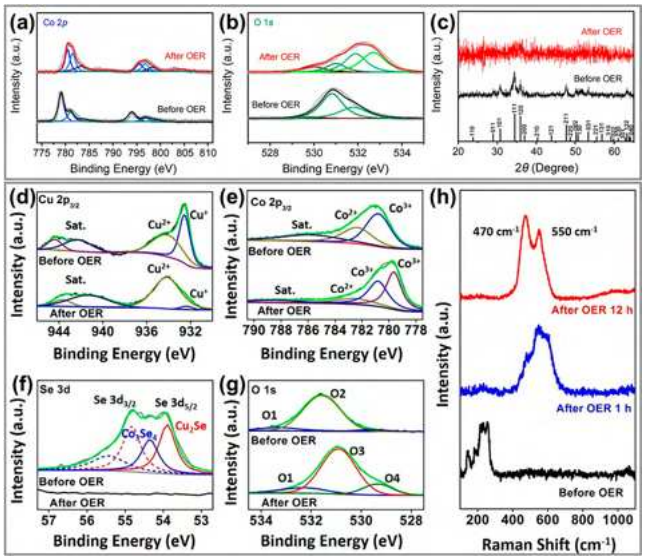


Figure 241. (a) Co 2p and (b) O 1s XPS spectra of $(Co_4Mn_1)Se_2$ before and after OER testing. (c) XRD patterns of $(Co_4Mn_1)Se_2$ before and after OER testing. Reproduced with permission from ref 978. Copyright 2018 Elsevier. (d) Cu $2p_{3/2}$, (e) Co $2p_{3/2}$, (f) Se 3d, and (g) O 1s XPS spectra of CuCoSe before and after the OER. (h) Raman spectra of CuCoSe-12h before and after OER testing. Reproduced with permission from ref 970. Copyright 2019 Wiley.

https://doi.org/10.1021/acs.chemrev.3c00005
Chem. Rev. 2023, 123, 12795−13208

species were generated on the electrocatalyst surface. After OER testing, the oxidation state of Co also changed: a new XPS peak at 779.5 eV confirmed the formation of Co^{3+}, corresponding to CoOOH (Figure 241e). The absence of Se species was also confirmed by XPS (Figure 241f). In the pre-OER O 1s spectrum (Figure 241g), only O1 and O2 peaks corresponding to adsorbed water molecules and defect sites with low oxygen coordination were detected, respectively. After OER testing, the O2 component disappeared owing to oxidation of the material. Moreover, in the post-OER O 1s XPS spectrum, the O3 and O4 peaks appeared, representative of hydroxyl groups and metal−oxygen bonds, respectively (see Figure 241g). Elemental mappings confirmed the Se signal decrease and O signal increase. TEM analysis also confirmed the formation of metal (oxy)hydroxides during OER testing. Raman spectroscopy further provided evidence for the *in situ* oxidation of Cu-Co selenide. As shown in Figure 241h, the bands corresponding to selenides (100−300 cm^{-1}) and (oxy)hydroxides (470 and 550 cm^{-1}) gradually became weak and strong, respectively, with further OER testing. According to the above experimental observations, we can conclude that, after OER testing, the Cu/Co (oxy)hydroxides (i.e., CoOOH and $Cu(OH)_2$) derived from the Cu-Co selenide could be the actual OER electroactive species.

Doping dual metal cations into monometallic nickel selenides has been reported as a means to prepare high-performance precatalysts (i.e., FeCoNi diselenide,[1108] FeCo-Mo diselenide,[1109] etc.). This improved performance compared to monometal selenides results because the co-doped cations improve electronic interactions within the material and because they induce strain that leads to lattice distortion, resulting in an increased number of exposed active sites for OER electrocatalysis. For example, Fan *et al.* prepared Fe- and Co-co-doped $NiSe_2$ ($Fe_{0.09}Co_{0.13}$-$NiSe_2$) porous nanosheets on carbon fiber cloth.[989] The long-term stability test of $Fe_{0.09}Co_{0.13}$-$NiSe_2$ was carried out at a constant current density of 10 $mA{\cdot}cm^{-2}$ for 50 h in 1 M KOH. After OER testing, SEM and XRD results showed no obvious changes in the morphology and crystal structure of $Fe_{0.09}Co_{0.13}$-$NiSe_2$ (Figures 242a, b, and e). The induced lattice distortions were confirmed by both pre- and post-OER TEM analysis, and a thin layer of nickel (cobalt, iron) oxide/hydroxide was observed on the $Fe_{0.09}Co_{0.13}$-$NiSe_2$ surface in the post-OER TEM image, which provided evidence of the partial oxidation of the as-prepared multimetal selenide (Figures 242c and d). EDX elemental mapping images showed the distribution of Co, Fe, Ni, Se, and O throughout the post-OER product, which, again, indicates the partial oxidation of the metal selenide. Moreover, after OER testing, two Raman bands (at 541.3 and 710 cm^{-1}), corresponding to NiO, were found, signifying that surface oxidation occurred during OER testing (Figure 242f). Notably, the post-OER XPS spectra showed the appearance of Ni^{3+} peaks (857.3 and 876.2 eV), which are evidence of the formation of an oxide/oxyhydroxide layer on the selenide surface, as implicated by Raman and other characterization techniques (Figure 242g). Also, in the post-OER Se 3d XPS spectrum, the intensity of the metal−selenium peak became weaker than in the pre-OER spectrum, indicating the transformation from selenide to oxide/hydroxide at its surface (Figure 242h). Additionally, after the OER stability test, ICP-AES analysis also detected a loss of Se and an increase of O. Based on the above evidence, the authors concluded that the real OER electrocatalyst was $Ni(Co, Fe)O_xH_y$/

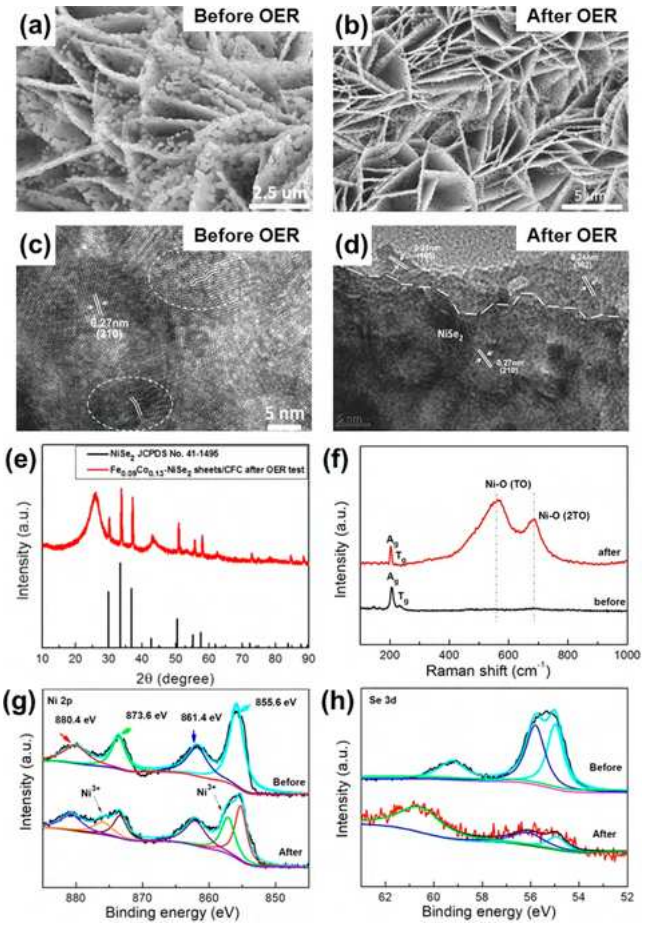


Figure 242. (a, b) SEM images of the $Fe_{0.09}Co_{0.13}$-$NiSe_2$ nanosheets/CFC (a) before and (b) after OER testing. (c, d) TEM images of $Fe_{0.09}Co_{0.13}$-$NiSe_2$ nanosheets/CFC (c) before and (d) after OER testing. (e) XRD pattern of $Fe_{0.09}Co_{0.13}$-$NiSe_2$ nanosheets/CFC after OER. (f) Raman spectra of $Fe_{0.09}Co_{0.13}$-$NiSe_2$ nanosheets/CFC before and after OER. (g) Ni 2p and (h) Se 3d XPS spectra of $Fe_{0.09}Co_{0.13}$-$NiSe_2$ nanosheets/CFC before and after OER testing. Reproduced with permission from ref 989. Copyright 2018 Wiley.

$Fe_{0.09}Co_{0.13}NiSe_2$. Note that despite the clear surface oxidation, the overall lattice distortion arising from the dual Fe and Co co-doping that led to enhanced performance was maintained (see aforementioned TEM results). Thus, co-doped metal selenide precatalysts such as $Fe_{0.09}Co_{0.13}$-$NiSe_2$ can lead to improved OER electrocatalysis that persists with time owing to lattice distortions and enhanced electronic interactions.

Selenide-based composites, including selenide/selenide, selenide/carbon-based material, and selenide/oxide, have been synthesized and employed as electrocatalysts for the OER. Herein, we provide several examples of these composite systems and discuss conclusive evidence of their status as precatalysts. For instance, Tian *et al.* synthesized a NiSe-$Ni_{0.85}Se$ heterostructure precatalyst on carbon paper through the hydrothermal selenization of a NiO precursor.[986] According to the authors, the synergistic effect of heterostructure interfaces between NiSe and $Ni_{0.85}Se$ phases provided more active sites for the OER and decreased the OH^- adsorption energy, resulting in a higher electrochemical OER performance compared with NiSe and $Ni_{0.85}Se$ nanostructures. Several characterizations of the NiSe-$Ni_{0.85}Se$ electrocatalyst were conducted after chronopotentiometric stability testing (at

https://doi.org/10.1021/acs.chemrev.3c00005
Chem. Rev. 2023, 123, 12795−13208

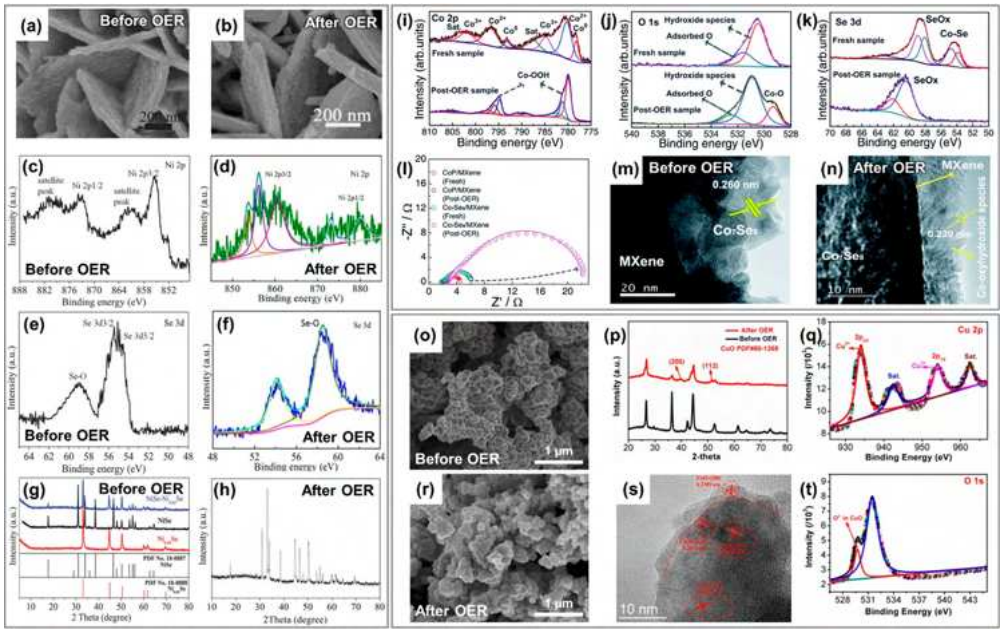


Figure 243. (a, b) SEM images of the NiSe-$Ni_{0.85}Se$/CP before (a) and after (b) OER testing. (c–f) XPS spectra of NiSe-$Ni_{0.85}Se$/CP before (c, e) and after (d, f) OER testing. (g) XRD patterns of NiSe-$Ni_{0.85}Se$/CP, NiSe/CP, and $Ni_{0.85}Se$/CP. (h) XRD pattern of NiSe-$Ni_{0.85}Se$/CP after OER testing. Reproduced with permission from ref 986. Copyright 2018 Wiley. (i) Co 2p, (j) O 1s, and (k) Se 3d XPS spectra of Co_7Se_8/Mxene before and after the OER. (l) Nyquist plots for various samples (measured at 1.63 V_{RHE}) in the frequency range from 0.1 Hz to 100 kHz. (m, n) HRTEM images of Co_7Se_8/MXene (m) before and (n) after the OER. Reproduced with permission from ref 963. Copyright 2019 Royal Society of Chemistry. (o, r) SEM images of Cu_2Se–Cu_2O on Ti foil (o) before and (r) after the OER. (p) XRD patterns of Cu_2Se-Cu_2O on Ti foil before and after the OER. (q) Cu 2p XPS spectra and (s) TEM image of the post-OER Cu_2Se-Cu_2O sample scraped from the Ti foil substrate. (t) O 1s XPS spectra of Cu_2Se-Cu_2O on Ti foil after the OER. Reproduced with permission from ref 994. Copyright 2018 Royal Society of Chemistry.

a constant current density of 200 mA·cm^{-2} for 48 h in 1 M KOH) to determine if material transformation had occurred during OER testing. The pre- and post-OER SEM images showed that the morphology of the NiSe-$Ni_{0.85}Se$ sample did not change drastically during OER testing (Figures 243a and b), while the pre- and post-OER XPS results confirmed the formation of SeO_x (Se 3d) and Ni oxide/hydroxide species (peaks at 861.7 and 879.6 eV) after OER testing (Figures 243c–f). Note that XRD analysis confirmed the retention of the selenide phases after OER testing but was unable to detect the formation of oxyhydroxide species (Figures 243g and h), indicating that the bulk material remained unchanged, while the surface was modified. These findings confirmed the partial oxidation of NiSe-$Ni_{0.85}Se$ into Ni oxide/hydroxide (likely the OER active species) and SeO_x. Yoo *et al.* also observed surface oxidation post-OER for their as-prepared cobalt selenide (Co_7Se_8) film on a MXene layer ($Ti_3C_2T_x$; T = -O, -OH, -F), which acted as a conductive substrate matrix.[963] Here, the MXene substrate formed a strong heterojunction with the Co_7Se_8 precatalyst beneficial for electron transfer via enhanced electrical conductivity. For long-term OER testing, chronoamperometry (applied bias: 1.69 V_{RHE}) was employed for 24 h in 1 M KOH. EDX analysis confirmed the increase in O-content and decrease in Se-content in the sample after the OER (Co:Se:O = 7.0:8.0:8.5 → 7.0:0.2:3.0), suggesting partial oxidation of the selenide had occurred. From Co 2p XPS results (Figure 243i), the Co–Se peaks disappeared after the OER, while several new peaks (at 780.2, 781.5, 795.4, and 796.5 eV) corresponding to CoOOH species were observed. As shown in the pre- and post-OER O 1s XPS spectra (Figure 243j), the generation of a new peak at 529.3 eV implied the formation of Co–O bonds, such as those in CoOOH. Additionally, in the Se 3d XPS spectra, a single peak at 60 eV after OER testing confirmed the oxidation of Se to SeO_x, a by-product that might decrease the activity and stability of the electrocatalyst (Figure 243k). In fact, the CoOOH/Co_7Se_8 electrocatalyst with SeO_x species deposited at the surface (i.e., a post-OER Co_7Se_8/MXene) exhibited remarkably higher charge transfer resistance (16.2 Ω) than the fresh Co_7Se_8/MXene material (3.35 Ω) (Figure 243l), implying that the SeO_x species at the electrocatalyst surface had an adverse impact on the conductivity, which comes as no surprise given the Se–O bond is more ionic in nature. However, the increase in charge transfer resistance is likely also a result of the formed CoOOH on the surface, as it is known to be poorly electron conducting due to a lack of bond covalency (i.e., poor electron delocalization). Moreover, HRTEM images confirmed the presence of characteristic lattice fringes for CoOOH (Figures 243m and n). Notably, the surface CoOOH derived from the selenide can act as the OER active species. To give another example, Sun *et al.* also observed post-OER oxidation of their Cu_2Se-Cu_2O composite material. Their Cu_2Se-Cu_2O composite film was electrodeposited onto Ti foil, and long-term stability testing was performed at a constant current density of 10 mA·cm^{-2} for 20 h.[994] SEM images revealed that the surface roughness increased after OER testing, implying surface oxidation had occurred (Figures 243o and r). The pre-OER XRD pattern confirmed that the diffraction peaks corresponded to both the Cu_2Se and Cu_2O phases. After OER testing, the Cu_2Se phase's peaks weakened in intensity compared to the pristine composite sample (Figure 243p). Moreover, in the post-OER XRD pattern, the diffraction peaks at 39.0 and 51.4° indicated that formation of CuO on the surface of the composite precatalyst had occurred. TEM

https://doi.org/10.1021/acs.chemrev.3c00005
Chem. Rev. 2023, 123, 12795–13208

images confirmed the existence of CuO as a layer on the surface of the Cu_2Se-Cu_2O film after OER testing (Figure 243s). Moreover, the XPS peaks at 933.9 and 953.6 eV in the Cu 2p region revealed an increase in the oxidation state of copper (Cu^0 to Cu^{2+}), and the peak at 529.6 eV in the O 1s spectrum verified the presence of O^{2-} in the electrocatalyst film after OER testing, again implying that formation of CuO had occurred (Figures 243q and t). According to the authors, the as-formed CuO layer might not only act as OER active species but could also suppress further oxidation of the Cu_2Se-Cu_2O film during OER testing.

Some researchers have begun to take advantage of the fact that a preformed oxidation layer on the surface of metal selenides can protect the material's core and prevent further oxidation. Wang *et al.* decorated $NiSe_2$ ultrathin nanowires (UNWs) deposited on carbon fiber paper with amorphous NiO_x nanoparticles to prepare selenide@oxide core@shell composite electrocatalysts (NSWANs) for the HER and OER in alkaline media (1 M KOH).[996] After 1000 OER cycles, XPS spectra indicated no change in surface composition, as the peak positions for Ni 2p and Se 3d peaks at 853.2 and 54.6 eV, respectively, were consistent with the as-prepared material, which was not the case for the $NiSe_2$ UNWs prepared without the NiO_x layer (Figures 244a and b). The pre- and post-OER

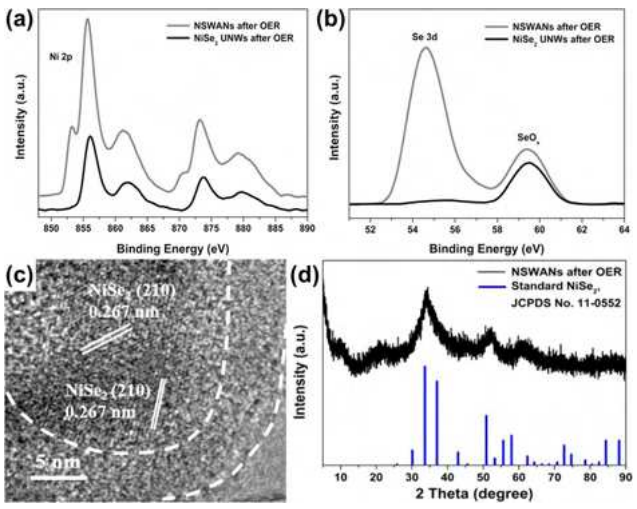


Figure 244. (a) Ni 2p and (b) Se 3d XPS spectra of the core@shell NSWANs and $NiSe_2$ UNWs after 1000 OER cycles. (c) HRTEM image and (d) XRD pattern of the NSWANs after the OER cycles. Reproduced with permission from ref 996. Copyright 2017 Wiley.

XPS results did, however, indicate that SeO_x formed after the OER tests, which may be attributed to slight oxidation of the $NiSe_2$ core, meaning the amorphous NiO_x nanoparticles may not have been sufficient as a protective shell. Nevertheless, HRTEM indicated that the core@shell structure was maintained with the (210) lattice plane for $NiSe_2$ being detected at the core and an amorphous layer representative of NiO_x being observed at the "shell" (Figure 244c). In addition, XRD results still indicated that the $NiSe_2$ phase persisted with no peaks being attributed to NiO_x or newly generated oxide species (Figure 244d). No peaks corresponding to NiO_x were observed because of the low overall content of NiO_x in comparison to the Ni selenide component of the material and the amorphous nature of the NiO_x nanoparticles. From ICP-AES, the ratio of Ni and Se from before and after OER testing did not change, suggesting that Se might be retained in the material and may not undergo dissolution into the electrolyte. Because SeO_x was detected via XPS after OER testing, partial oxidation of the material did occur, however, to a much lesser extent than for a pure metal selenide. Thus, oxidation can be circumvented, at least to some extent, by preparing core@shell metal selenide@oxide materials. In addition, a pre-formed oxidation layer also means active sites are present initially and do not have to be formed during the OER. Here, specifically, the $NiSe_2$ cores with a thin, amorphous NiO_x shell (i.e., $NiSe_2$@NiO_x core@shell structures) were the active species for the OER.

In addition to preparing metal selenide@oxides for protection of the metal selenide core using *ex situ* methods such as electrodeposition, these materials can be prepared by intentionally oxidizing a metal selenide under OER conditions.[947] For example, Zou *et al.* reported a NiSe@NiO_x core@shell structure electrocatalyst prepared by synthesizng a NiSe precatalyst and then performing oxidation via potentiostatic electrolysis at a potential of 1.5 V_{RHE} for 60 h in 1 M KOH. The oxidation of the material was carried out to completion (until no further deselenization was observed) (see Figure 245). Newly generated NiO_x was coated on the surface

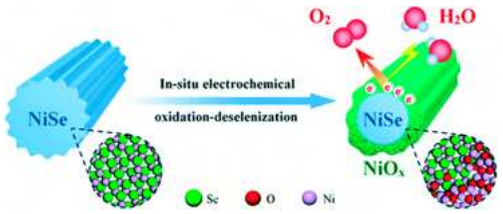


Figure 245. Schematic illustration for the oxidation−deselenization of NiSe nanorods during the OER. Reproduced with permission from ref 947. Copyright 2016 Royal Society of Chemistry.

of NiSe to form a core@shell structure. The superficial NiO_x with an amorphous structure served as a protective layer for the NiSe core, preventing further oxidation during the OER, and exhibited a rough surface, while the NiSe served as the scaffold of the structure. During OER testing, the NiO_x shell was the actual active phase for the OER, and the NiSe core provided good electrical conductivity and support. As a result, the combination of NiO_x and NiSe led to fast charge transfer kinetics and an overall stable electrocatalytic material for OER electrocatalysis.

5.2.3. Structural and Chemical Compositional Effects toward OER Activity. Numerous studies have focused on tuning parameters and features to prepare transition metal selenides for optimal performance as OER electrocatalysts. Material properties, including the type of cation(s) (M) in selenides (MSe_x), the M/Se ratio, the crystal structure, the exposed crystal facets, the amount of defects/vacancies, etc., have been shown to increase conductivity, increase the number of exposed active sites, and lower adsorption energy, for improved OER electrocatalyst performance.[953,978,979,1005,1072,1084] In addition, synthetic conditions, conductive substrates (current collector), and electrochemical testing conditions have also been shown to impact metal selenide electrocatalytic OER performance.[100,928,975,1042] In this section, the influence and effects of the above variables are discussed to elucidate possible relationships between the

https://doi.org/10.1021/acs.chemrev.3c00005
Chem. Rev. 2023, 123, 12795−13208

inherent properties of metal selenides and their resultant OER performance.

5.2.3.1. Morphology Effects. As OER electrocatalysis is a surface-sensitive process, nanostructures with high surface areas have attracted more attention than traditional thin films due to the increased exposure of active sites.[928] Various morphologies such as nanobelts, nanospheres, nanoparticles, etc. have been attributed to improved OER electrocatalytic performance (see Table 6). An electrocatalyst's morphology can influence mass transport, the contact area between the electrode surface/electrolyte interface, and the number of OER active sites, which strongly affect the electrocatalytic performance. As a result, the precise control of one-dimensional (1D), two-dimensional (2D), and three-dimensional (3D) morphologies has received increased attention in recent years.

The majority of 1D and 2D electrocatalytic materials have a simple structure that facilitates mass transfer for efficient OER electrolysis. For instance, Li *et al.* found that both 1D and 2D cobalt selenides led to improved OER performance, with the 2D cobalt selenides slightly outperforming their 1D counterparts.[1061] They prepared their 1D and 2D cobalt selenides (1D $CoSe_2$ nanorods and 2D $CoSe_2$ nanosheets) via a three-step process, wherein a hydrothermal reaction and O_2-annealing were used to prepare Co_3O_4 precursors with different morphologies followed by selenization. The morphology of the Co_3O_4 precursors was tuned using the hydrothermal reaction time (1 and 11 h). Material characterization, specifically TEM images, confirmed that the selenization step did not cause changes to the morphology and that it was set based on the prepared precursor (Figures 246a–e). The 1D $CoSe_2$ nanorods and 2D $CoSe_2$ nanosheets exhibited OER overpotentials of 377 and 372 mV at 50 mA·cm^{-2}, respectively (Figure 246g). The 2D $CoSe_2$ had a smaller Tafel slope (74 mV·dec^{-1}) than the 1D $CoSe_2$ (88 mV·dec^{-1}) (Figure 246h). These results suggested that 2D nanosheets have improved electrocatalytic performance in comparison to 1D nanorods. It is likely that the 2D $CoSe_2$ nanosheets outperformed the 1D $CoSe_2$ nanorods because atoms in ultrathin 2D nanosheets have lower coordination numbers due to the higher surface-to-volume atom ratio, resulting in an increased number of exposed active sites as a result of their morphology.[1110−1112] These conclusions are further supported by the 2D $CoSe_2$ electrocatalyst's C_{dl} value of 11.90 mF·cm^{-2}, which is higher than that of the 1D $CoSe_2$ (see Figure 246f).

While 2D materials have been shown to improve electrocatalytic performance in comparison to 1D materials due to their higher surface area, these 2D materials can be limited by the stacking of their sheets, which leads to less active site exposure.[1113,1114] To avoid this issue, Yu *et al.* fabricated 2D ultrathin $CoSe_2$ nanomeshes with abundant selenium vacancies (UNM_{vac}) using a plasma-exfoliation method (Figure 247a).[953] The TEM images show that the layered porous nanomesh structure provided more tunnels for the electrolyte to pass through the electrocatalyst, increasing the contact with the electrolyte and enhancing the electrocatalytic activity (Figures 247b and c). The selenium vacancies also provided an increased number of exposed active sites for improved performance. To explore the influence of the morphology, the authors also prepared $CoSe_2$ nanosheets ($CoSe_2$ NS) and $CoSe_2$ nanoparticles ($CoSe_2$ NP) as control samples (Figures 247d and e). The $CoSe_2$ UNM_{vac} exhibited the lowest OER overpotential of 284 mV at 10 mA·cm^{-2} in 1 M KOH, compared with $CoSe_2$ NS (343 mV) and $CoSe_2$ NP (466 mV)

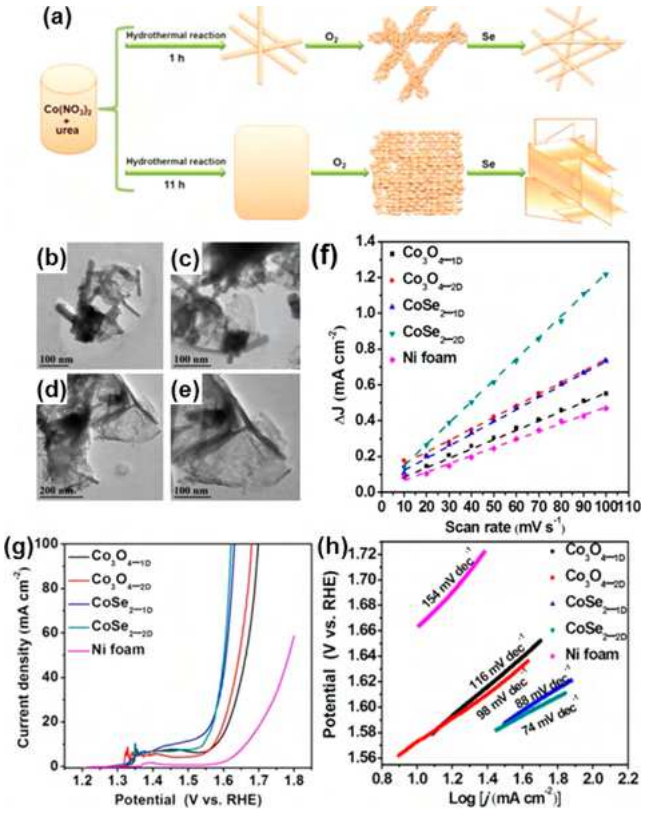


Figure 246. (a) Schematic illustration for the synthesis of cobalt-based catalysts. (b–e) Typical low- and high-magnification TEM images of the as-prepared (b, c) 1D nanorods and (d, e) 2D nanosheets of $CoSe_2$. (f) The differences in current density variation ($\Delta J = j_a - j_c$) at 1.05 V_{RHE} as a function of scan rate, which was fitted to evaluate the C_{dl} for as-produced cobalt-based electrocatalysts. (g) Polarization curves and (h) Tafel plots of the cobalt-based electrocatalysts. Reproduced with permission from ref 1061. Copyright 2018 Wiley.

(Figure 247f). The $CoSe_2$ UNM_{vac} also had the lowest Tafel slope of 46.3 mV·dec^{-1} as compared to the $CoSe_2$ NS and NP samples (97.7 and 111.1 mV·dec^{-1}, respectively) (Figure 247g). Remarkably, the ECSA of the $CoSe_2$ UNM_{vac} increased 97.12% (137 → 270 cm^2) after a long-term stability test, suggesting that the nanomesh structure with abundant pores and structural vacancies induced the formation of more CoOOH active sites during OER testing. Moreover, the porous nanomesh structure provided transport tunnels to compensate for the decreased penetration of the electrolyte caused by the stacking of the nanosheets. Combining the above results, the $CoSe_2$ UNM_{vac} exhibited excellent OER activity due to the abundant active sites provided by the ultrathin nanomesh structure and anion vacancies, which improved the exposure of the electrocatalytic surface to the electrolyte and increased the inherent activity of low-coordination Co atoms.

Compared to 1D and 2D materials, 3D materials can further benefit OER electrocatalysis owing to their larger surface areas and open structures, which lead to an increased number of active sites.[946,1088] For example, Luo *et al.* prepared a $Ni_{0.76}Fe_{0.24}Se$ electrocatalyst with a 3D rose-like hierarchical architecture and compared its electrochemical performance to the 2D-structured materials NiSe and NiFe LDH.[992] The $Ni_{0.76}Fe_{0.24}Se$ electrocatalyst exhibited a low OER over-

https://doi.org/10.1021/acs.chemrev.3c00005
Chem. Rev. 2023, 123, 12795−13208

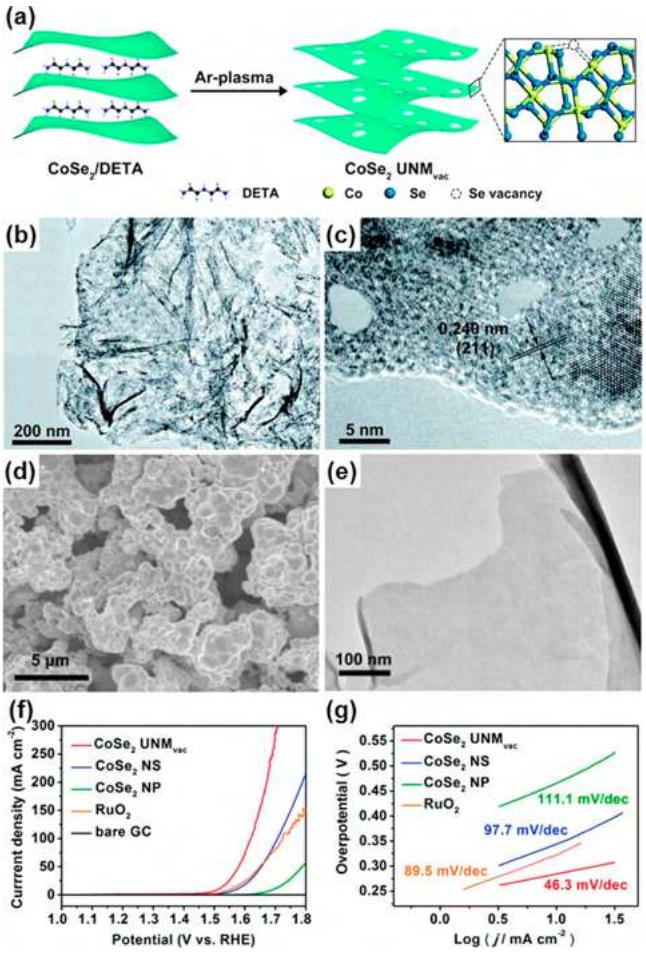


Figure 247. (a) Scheme for the preparation of $CoSe_2$ UNM_{vac}. (b) Low-magnification TEM image and (c) HRTEM image of $CoSe_2$ UNM_{vac}. (d) SEM image of $CoSe_2$ NP and (e) TEM image of $CoSe_2$ NS. (f) *IR*-corrected polarization curves and (g) the corresponding Tafel plots of $CoSe_2$-based samples and RuO_2 for the OER in 1 M KOH at a scan rate of 5 $mV{\cdot}s^{-1}$. Reproduced with permission from ref 953. Copyright 2019 Royal Society of Chemistry.

potential of 197 mV at a current density of 10 $mA{\cdot}cm^{-2}$ and a small Tafel slope of 62 $mV{\cdot}dec^{-1}$ in 1 M KOH, outperforming both 2D NiSe (217 mV overpotential, 73 $mV{\cdot}dec^{-1}$ Tafel slope) and NiFe LDH (220 mV overpotential, 61 $mV{\cdot}dec^{-1}$ Tafel slope). The superior OER performance of this electrocatalyst can be attributed to its unique 3D structure enabling good contact with the electrolyte and an abundance of exposed sites, as observed via SEM (not shown here). In addition, the C_{dl} value of the 3D $Ni_{0.76}Fe_{0.24}Se$ was 17.4 $mF{\cdot}cm^{-2}$, which was higher than those of 2D NiSe (13.5 $mF{\cdot}cm^{-2}$) and 2D NiFe LDH (3.2 $mF{\cdot}cm^{-2}$), indicating that the 3D $Ni_{0.76}Fe_{0.24}Se$ had a larger surface area and more active sites than the 2D samples. Overall, the open structure provided more accessible pathways for improved mass transfer to active sites for electrocatalysis. The porous structure also accelerated the release of O_2 bubbles into the bulk electrolyte. Thus, 3D morphologies have the potential to enhance OER electrocatalysis via improved mass transfer and bubble release as compared to 1D and 2D structures.

5.2.3.2. Metal/Selenium Composition Effects. Fabricating transition metal selenides with different *M*/Se ratios is a common way to tune the intrinsic OER activity of selenide electrocatalysts. By changing the *M*/Se ratio, the resulting product can exhibit different crystal structures, leading to changes in the surface electronic structure and OER performance.[951,974,1010,1069,1073] Mi *et al.* investigated these phenomena by studying $NiSe_2$, NiSe, and Ni_3Se_2 electrocatalysts to determine which Ni/Se ratio exhibited the best OER performance under alkaline conditions (1.0 M KOH).[1073] Using the Scherrer equation to fit XRD peaks, they calculated the crystallite sizes of the three nickel selenide samples (Figures 248a–c). The crystallite size of $NiSe_2$ was 33 nm,

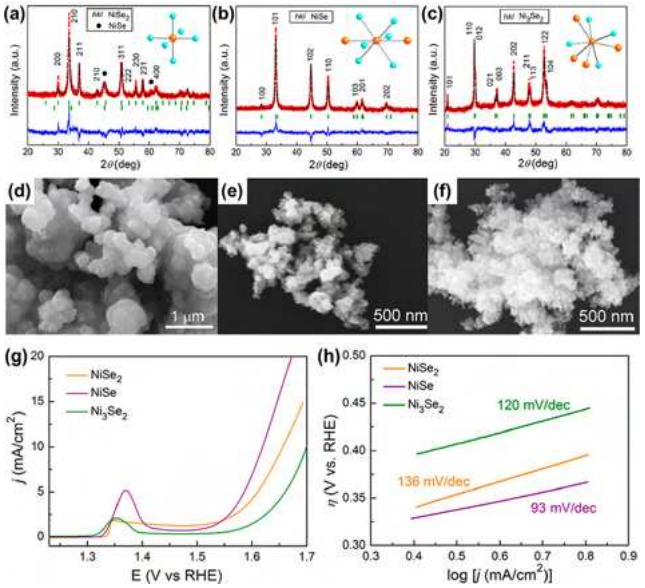


Figure 248. (a–c) Rietveld refinement of XRD data for $NiSe_2$, NiSe, and Ni_3Se_2, respectively, showing the observed and calculated intensities and their difference. (d–f) SEM images of $NiSe_2$, NiSe, and Ni_3Se_2, respectively. (g) Polarization curves of $NiSe_2$, NiSe, and Ni_3Se_2 under 1 M KOH at a scan rate of 10 $mV{\cdot}s^{-1}$ and (h) the corresponding Tafel plots. Reproduced with permission from ref 1073. Copyright 2018 American Chemical Society.

which was relatively larger than those of NiSe (25 nm) and Ni_3Se_2 (26 nm). While SEM images indicated larger particle sizes than the above-calculated values (likely due to crystallite aggregation and/or differences in synthetic conditions), the $NiSe_2$ electrocatalyst still exhibited a larger overall particle size than NiSe and Ni_3Se_2, matching with XRD results (Figures 248d–f). As shown in Figures 248g and h, NiSe exhibited the lowest overpotential of 389 mV at 10 $mA{\cdot}cm^{-2}$ and the smallest Tafel slope of 93 $mV{\cdot}dec^{-1}$. This result contradicted the author's hypothesis that Se-rich $NiSe_2$ would enable faster dioxygen molecule transfer for enhanced OER owing to the greater abundance of 3d-2p repulsion between the Ni d-band and Se d-band centers that would come with an increased number of Ni–Se bonds.[72,1115] As a result, the authors concluded that, while the *M*/Se ratio could alter the surface electronic structure, other variables besides the electronic structure can greatly influence OER performance, such as surface area, which scaled with improved OER electrocatalysis in this case. Thus, while the electronics of metal selenides can be tuned using the metal:selenium ratio, how the surface area of materials changes in tandem with this electronic tuning must also be considered, and the role of electronic structure vs morphology may merit deconvolution in future studies.

https://doi.org/10.1021/acs.chemrev.3c00005
Chem. Rev. 2023, 123, 12795–13208

5.2.3.3. Multi-cation Effects. Multi-cation incorporated selenides always demonstrate improved electrochemical OER performance in comparison to their mono-cationic counterparts. This performance is often attributed to synergistic effects between the metal ions. The multimetallic selenides with various metal/metal ratios (e.g., $Co_{1-x}Mn_xSe$, Fe-Co-Cu-Se, Co-Ni-Cu-Se, etc.)[978,918,920] exhibit different electrocatalytic activities owing to their diverse crystal and electronic structures obtained via metal-mixing. As an example, Zeng *et al.* prepared a bimetallic selenide by incorporating Mn into Co selenides and evaluated how the Mn/Co ratio (i.e., 1:1, 1:2, and 1:4) influenced electrochemical performance.[978] The overpotential of the best-performing bimetallic selenide, $(Co_4Mn_1)Se_2$, was only 274 mV at 10 mA·cm^{-2} in 1 M KOH, which was smaller than that of $CoSe_2$ (317 mV). Additionally, the Tafel slope for $(Co_4Mn_1)Se_2$ (39 mV·dec^{-1}) was also less than $CoSe_2$ (48 mV·dec^{-1}). The authors assumed the enhanced electrochemical performance was attributed to the incorporation of Mn. From TEM images (Figure 249a), the cobalt selenides with higher Mn content had more lattice distortion, implying higher disorder in the crystal structure. In the Raman spectra of $CoSe_2$ and Mn-incorporated $CoSe_2$ with different Mn/Co ratios, the full-width at half-maximum (FWHM) of the peak at 173.5 cm^{-1}, which corresponds to the orthorhombic $CoSe_2$ phase, was found to increase with the increasing Mn/Co ratio, indicating that greater Mn-incorporation led to greater structural disorder (Figure 249c). Moreover, XPS results showed gradual shifts for Co 2p to lower energy after the introduction of Mn, indicating the modulated electronic structure of Co centers (Figure 249b). At the temperature of 300 K, the electrical resistivity of $(Co_4Mn_1)Se_2$ nanosheets (1.3×10^{-5} Ω·m) was an order of magnitude lower than that of $CoSe_2$ nanosheets (2.16×10^{-4} Ω·m), verifying that the incorporation of Mn into cobalt selenides led to increased conductivity and, as a result improved electron transfer and electrocatalytic performance (Figure 249d). The authors did observe, however, that as the Mn-incorporation increased further, higher resistivities and lower conductivities were found, likely as a result of too much disorder to the structure, resulting in deficient electron transport. Accordingly, to maximize OER activity, appropriate Mn/Co ratios must be obtained in the Mn-incorporated $CoSe_2$ system, and it should be noted that there is a threshold for metal-incorporation, past which OER electrocatalytic performance diminishes.

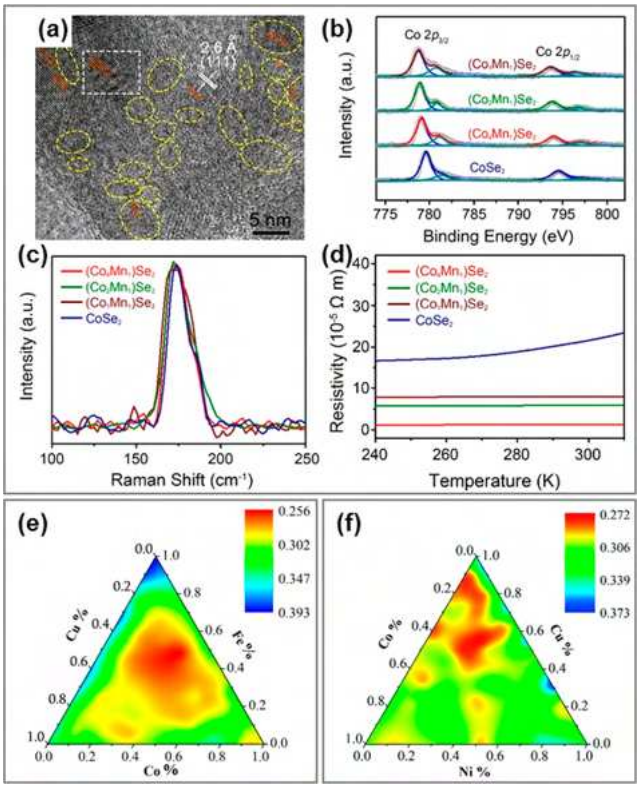


Figure 249. (a) HRTEM image of $(Co_4Mn_1)Se_2$ nanosheets. The yellow dashed lines represent the detached ultrasmall nanoparticles. The lattice distortion is marked by the orange lines. (b) Co 2p XPS spectra of $(CoMn)Se_2$ and $CoSe_2$ nanosheets. (c) Raman spectra of $(Co_4Mn_1)Se_2$, $(Co_2Mn_1)Se_2$, $(Co_1Mn_1)Se_2$, and $CoSe_2$ nanosheets. (d) Temperature-dependent electrical resistivity of $(CoMn)Se_2$ and $CoSe_2$ nanosheets. Reproduced with permission from ref 978. Copyright 2018 Elsevier. (e) Mapping of OER overpotential η (in units of V) at a current density of 10 mA·cm^{-2} for Fe-Co-Cu-Se. Reproduced with permission from ref 920. Copyright 2019 American Chemical Society. (f) Mapping of overpotential [η (in units of V)] at a current density of 10 mA·cm^{-2} for Co-Ni-Cu-Se. Reproduced with permission from ref 918. Copyright 2019 Wiley.

In addition to bimetallic selenides, there are reports of trimetallic selenides that emphasize the importance of metal:metal:metal ratio control for maximized OER performance. Nath *et al.* mapped the influence of different transition metal ions toward OER activity in alkaline media (1.0 M KOH) by producing phase diagrams of quaternary selenides using the three transition metal ions Cu, Co, and Fe.[920] From their constructed phase diagram (Figure 249e), they were able to pinpoint a region of optimal performance, wherein the lowest overpotentials were observed for quaternary selenides with metal incorporation at 10−50% Cu, 15−50% Co, and 30−70% Fe. Of the quaternary selenides in this region, $(Fe_{0.48}Co_{0.38}Cu_{0.14})Se$ showed the lowest overpotential of 235 mV at 10 mA·cm^{-2} and the smallest Tafel slope of 40.8 mV·dec^{-1} (Figure 249e). Additionally, the Nath group explored the composition effect of Co-Ni-Cu selenides.[918] They employed the same phase diagram approach to determine the best ratio of Co/Ni/Cu in the quaternary selenide for optimal OER electrocatalysis (Figure 249f). From their study, they found that $(Co_{0.21}Ni_{0.25}Cu_{0.54})_3Se_2$ exhibited the best electrocatalytic activity with an overpotential of 272 mV at 10 mA·cm^{-2} in 1.0 M KOH. These studies revealed that quaternary selenides with optimized metal ratios could exhibit superior electrochemical OER performance compared to their binary and ternary counterparts. Because these studies suggest that transition metal selenide OER performance is highly dependent on the metal composition, the use of phase diagrams provides a straightforward strategy for the material design of OER electrocatalysts.

5.2.3.4. Metal Doping Effects. Doping metal ions into metal selenides is a strategy to improve their electrochemical performance. By introducing a small quantity of transition metal ions (i.e., Fe, Co, Ni, etc.) into the selenides, enhancements in the electron transfer and electrical conductivity leading to improved OER performance have been observed.[952,966,979,989,1026,1043] In addition, metal doping can tune the adsorption energy of generated intermediates (e.g., *O, *OH, and *OOH), accelerating the formation of O_2 gas.[943,967,979,990,1116] In this section, several works are discussed that have studied the influence of metal dopants on OER activity from experimental and theoretical perspectives.

https://doi.org/10.1021/acs.chemrev.3c00005
Chem. Rev. 2023, 123, 12795−13208

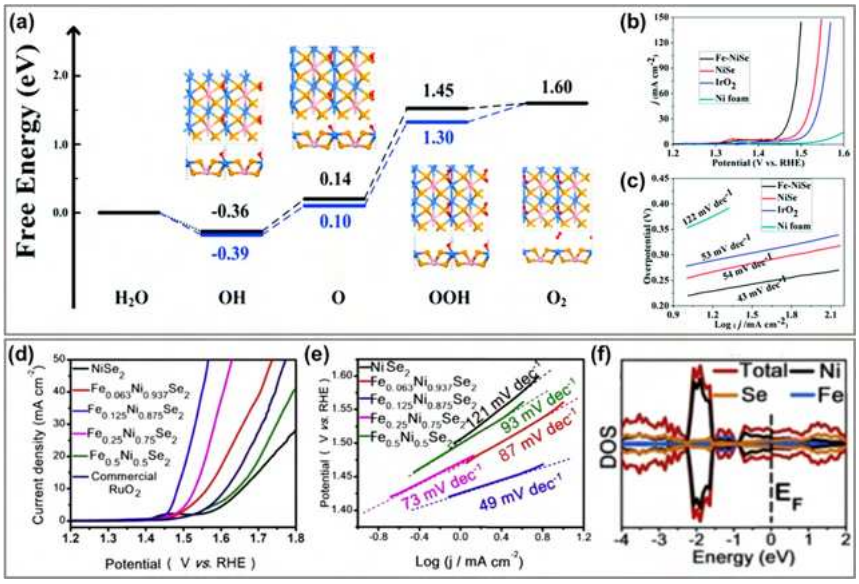


Figure 250. (a) Free energy profile (in eV) of the OER pathway on NiSe(110) (black line) and Fe-modified NiSe(110) (blue line) surfaces. (b) Polarization curves and (c) Tafel plots of NiSe and Fe-NiSe. Reproduced with permission from ref 979. Copyright 2018 Wiley. (d) Polarization curves and (e) Tafel slopes of various selenide electrocatalysts. (f) Density of states (DOS) of the $Fe_{0.125}Ni_{0.875}Se_2$ electrocatalyst. Reproduced with permission from ref 967. Copyright 2019 Elsevier.

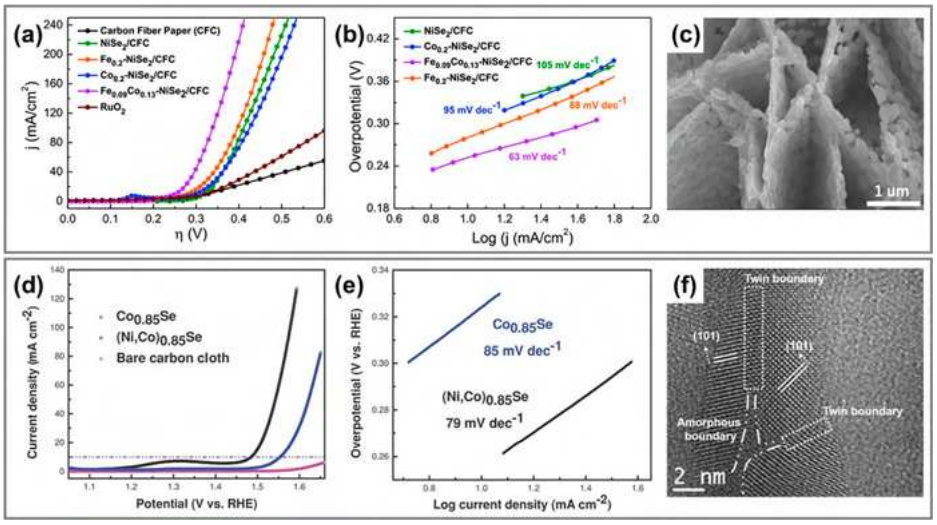


Figure 251. (a) Polarization curves and (b) Tafel plots of $Fe_{0.09}Co_{0.13}$-$NiSe_2$ nanosheet arrays, $Fe_{0.2}$-$NiSe_2$ nanosheet arrays, $Co_{0.2}$-$NiSe_2$ nanosheet arrays, pure $NiSe_2$ nanosheet arrays, carbon fiber paper, and RuO_2. (c) SEM image of $Fe_{0.09}Co_{0.13}$-$NiSe_2$ dual-cation-doped $NiSe_2$. Reproduced with permission from ref 989. Copyright 2018 Wiley. (d) *IR*-corrected LSV curves and (e) Tafel plots of $Co_{0.85}Se$, $(Ni, Co)_{0.85}Se$, and bare carbon cloth substrate. (f) The aberration-corrected HRTEM image of as-obtained $(Ni, Co)_{0.85}Se$ nanotubes. Reproduced with permission from ref 1029. Copyright 2016 Wiley.

Within the literature, iron has been indicated as a highly efficient dopant for nickel- and cobalt-based selenides for promoting electrocatalytic OER activity. For example, Li *et al.* observed that by doping Fe into a NiSe precatalyst on porous carbon-derived substrates (Fe-NiSe), a reduction in both overpotential and Tafel slope was possible.[979] From DFT calculations (Figure 250a), it was found that Fe doping decreased the adsorption-free energies of intermediates during the OER [i.e., *OH (−0.36 → −0.39 eV), *O (0.14 → −0.10 eV), and *OOH (1.45 → 1.30 eV)]. From the density of states diagrams, it was found that Fe atoms shifted the d-band of surface Ni atoms toward the Fermi level, resulting in much stronger Fe−Se bonds. The strengthening of the Fe−Se bonds led to a decrease in Ni−Se bond strength, thus enhancing the interaction of Ni centers with OER intermediates during the OER. Observations from DFT matched well with experimental results. After doping Fe into the NiSe, the OER overpotential decreased from 255 to 220 mV at 10 mA·cm^{-2}, and the Tafel slope was reduced from 54 to 43 mV·dec^{-1} in 1.0 M KOH (Figures 250b and c). By performing low-temperature selenization of sacrificial templates (i.e., MOFs), Chai *et al.* also prepared Fe-doped nickel selenide electrocatalysts with different Fe doping levels.[967] Among the as-prepared samples, the $Fe_{0.125}Ni_{0.875}Se_2$ electrocatalyst on glassy carbon exhibited the best OER performance in alkaline media (1 M KOH), exhibiting the lowest overpotential and reaching a mass-normalized current density of 115.7 A·g^{-1} at an overpotential of 320 mV at 10 mA·cm^{-2} (see Figure 250d). Moreover, the

https://doi.org/10.1021/acs.chemrev.3c00005
Chem. Rev. 2023, 123, 12795−13208

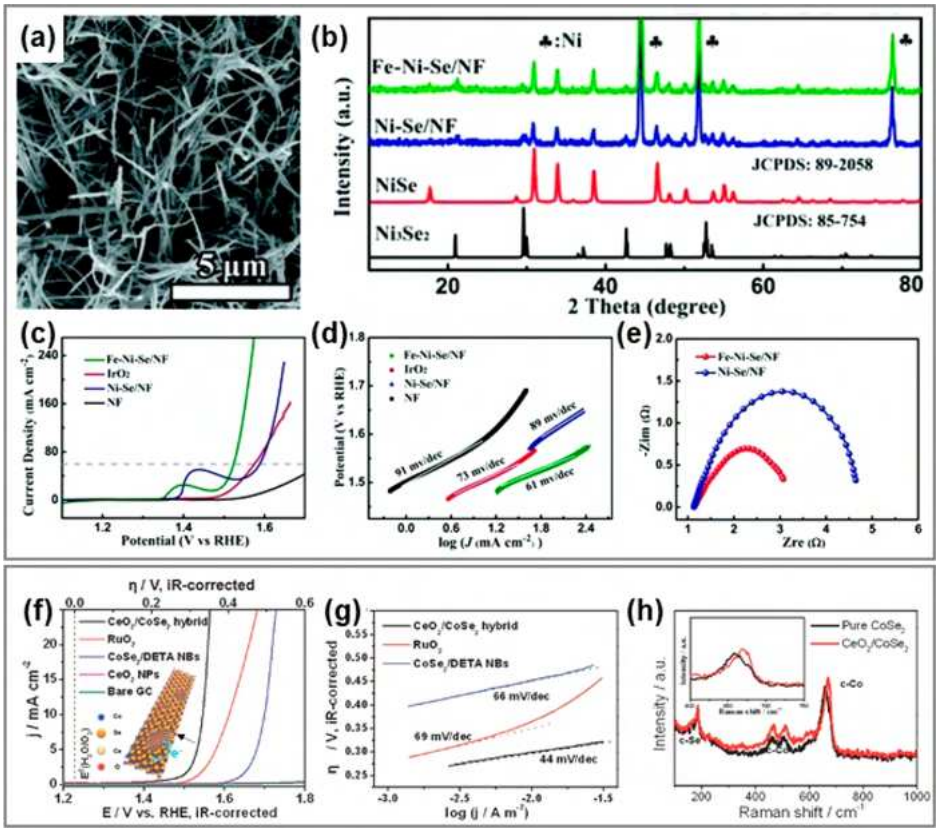


Figure 252. (a) SEM image and (b) XRD patterns of Fe-Ni-Se/NF. (c) *IR*-corrected polarization curves of different electrocatalysts in 1 M KOH solution at a scan rate of 5 mV·s^{-1} and (d) corresponding Tafel plots. (e) Nyquist plots of Fe-Ni-Se/NF and Ni-Se/NF. Reproduced with permission from ref 987. Copyright 2018 Royal Society of Chemistry. (f) *IR*-corrected polarization curves and (g) Tafel plots of $CeO_2/CoSe_2$, RuO_2, and $CoSe_2$/DETA NBs, CeO_2 NPs, and bare GC. (h) Raman spectra of $CeO_2/CoSe_2$ and pure $CoSe_2$. Reproduced with permission from ref 1084. Copyright 2015 Wiley.

$Fe_{0.125}Ni_{0.875}Se_2$ also had the lowest Tafel slope of 49 mV·dec^{-1} (Figure 250e). According to the density of states (DOS), the $Fe_{0.125}Ni_{0.875}Se_2$ electrocatalyst showed no energetic band gap, suggesting improved charge transport and conductivity (Figure 250f). This lack of a band gap was confirmed by the high density of electron-occupied states near the Fermi level for $Fe_{0.125}Ni_{0.875}Se_2$ (from −1.5 to 1.0 eV). Furthermore, the d-band center energy of Ni was upshifted after Fe-doping, thus facilitating the adsorption of OER intermediates [i.e., *OH (−2.11 → −2.80 eV), *O (−4.56 → −4.58 eV), and *OOH (−0.92 → −1.34 eV)]. Overall, these results confirmed that Fe doping can promote the OER performance of transition metal selenide electrocatalysts.

Other than mono-cation doping, simultaneously doping Fe and another foreign cation into a monometallic selenide has been shown to enable lattice structure and electronic interaction tuning via synergistic effects between multi-cations for improved OER electrocatalysis. For example, Fan *et al.* reported Co and Fe co-doped nickel selenide ($Fe_{0.09}Co_{0.13}$-$NiSe_2$) with a 3D nanosheet-like morphology.[989] This sample exhibited an OER overpotential of 251 mV at 10 mA·cm^{-2} and a Tafel slope of 63 mV·dec^{-1} in 1.0 M KOH (Figures 251a and b). Moreover, the value of R_{ct} of the $Fe_{0.09}Co_{0.13}$-$NiSe_2$ was much smaller than that for $Fe_{0.2}$-$NiSe_2$, $Co_{0.2}$-$NiSe_2$, and $NiSe_2$. The authors attributed the excellent electrochemical performance of $Fe_{0.09}Co_{0.13}$-$NiSe_2$ to the dual-cation doping and the 3D nanosheet morphology (Figure 251c). DFT calculations confirmed that the metal doping reduced the adsorption energy for OER intermediates and enhanced the intrinsic electrocatalytic OER activity. Furthermore, the 3D nanosheet morphology exposed numerous active sites for enhanced activity when combined with the effects of the lattice distortions caused by Fe and Co doping. Furthermore, the 3D nanosheets provided abundant channels for electrolyte penetration and promoted the release of evolved O_2 bubbles.

In addition to the doping of Fe and Co, another common transition metal, nickel, has also been incorporated into selenides to boost their OER activity. For instance, Alshareef *et al.* reported Ni-doped $Co_{0.85}Se$ with numerous defects (i.e., planar extended defects, stacking faults, and twin boundaries) and a 3D structure.[1029] As a result, the Ni-doped $Co_{0.85}Se$ exhibited improved performance (i.e., overpotential of 255 mV to reach 10 mA·cm^{-2} and a Tafel slope of 79 mV·dec^{-1} in 1 M KOH) compared to undoped $Co_{0.85}Se$ (Figures 251d and e). The enhanced electrochemical performance can be attributed to the defects introduced by Ni dopants (Figure 251f). These defects are hypothesized to create extra dangling bonds (a dangling bond is an unsatisfied valence on an immobilized atom) that lead to a decreased surface adsorption energy for *OOH and improved OER activity. The 3D structure and abundant defects resulting from cation-doping offered sufficient active sites for the OER and accelerated the release of evolved O_2 gas from the electrocatalyst surface for overall improved performance for the doped vs. undoped selenide electrocatalyst.

https://doi.org/10.1021/acs.chemrev.3c00005
Chem. Rev. 2023, 123, 12795−13208

5.2.3.5. Composite Materials Effects. Composite materials (i.e., selenide/selenide, selenide/oxide, and selenide/carbon-based material) have shown extraordinary electrochemical performance due to synergistic effects between composite components. The heterogeneous structure of composite materials provides abundant boundaries and vacancies, exposing more active sites for the electrocatalysis of the OER. Additionally, the synergistic effects between the two components in the composite may facilitate the needed change (i.e., boosting charge transfer, enhancing ionic and electronic conductivity, optimizing electrolyte penetration, etc.) to further improve the electrochemical performance. In this section, different composites are discussed to evaluate the effect(s) of heterogeneity on electrocatalytic OER performance.

In designing a heterogeneous selenide/selenide composite,[986,1019,1041,1049,1087] Xu *et al.* synthesized a 1D Fe-doped nickel selenide (Fe-Ni-Se) composite consisting of NiSe and Ni_3Se_2 nanorods prepared via a one-pot solvothermal method.[987] An SEM image of the Fe-Ni-Se composite showed the nanorod-like morphology (Figure 252a). The XRD results indicated the coexistence of the two nickel selenide phases NiSe and Ni_3Se_2 (Figure 252b). The Fe-Ni-Se composite exhibited an OER overpotential of 290 mV at 60 $mA{\cdot}cm^{-2}$ and a Tafel slope of 61 $mV{\cdot}dec^{-1}$ in 1 M KOH (Figures 252c and d). The outstanding performance of the Fe-Ni-Se sample resulted because the nanorod-like morphology and boundaries and vacancies created by the coexistence of the two phases in the material (i.e., NiSe and Ni_3Se_2) provided abundant active sites on the surface, which are believed to enable more electrolyte penetration into the electrocatalytic material for promoted OER. Additionally, the Fe-Ni-Se electrocatalyst exhibited a relatively large ECSA of 353 cm^2 and an electron-transfer resistance lower than that of Ni-Se, indicating faster electron transfer for facilitated OER (Figure 252e). Therefore, the enhanced OER performance resulted from the high surface area and defects imposed by the composite structure of the electrocatalyst.

In addition to selenide/selenide composites, oxide/selenide composites have also been prepared to generate more high-performing OER electrocatalysts.[1084,1117,1118] For example, Yu *et al.* coated CeO_2 on the surface of $CoSe_2$/diethylenetriamine (DETA) nanobelts (NBs) via a solution-based reaction to prepare the $CoSe_2@CeO_2$ nanobelt composite.[1084] The $CoSe_2@CeO_2$ composite showed enhanced electrochemical performance as compared to the $CoSe_2$/DETA NBs alone. Specifically, the $CoSe_2@CeO_2$ composite had a lower OER overpotential of 288 mV at 10 $mA{\cdot}cm^{-2}$ and a smaller Tafel slope of 44 $mV{\cdot}dec^{-1}$ compared with the $CoSe_2$/DETA NBs (overpotential: ∼465 mV; Tafel slope: 66 $mV{\cdot}dec^{-1}$) in 0.1 M KOH electrolyte (Figures 252f and g). A large amount of oxygen vacancies in the CeO_2 presumably facilitated the formation of intermediate hydroperoxyl species (*OOH) on the composite surface. The CeO_2, however, has no electrocatalytic activity toward the OER process (see Figure 252f). The Raman spectra showed that both the $CoSe_2$/DETA NBs and $CeO_2/CoSe_2$ composite exhibited four characteristic peaks corresponding to cubic $CoSe_2$. The Raman peak at 657 cm^{-1} of the $CoSe_2$/DETA NBs (inset in Figure 252h) shifted to a higher wavelength after coating it with CeO_2 NPs, implying that electron transfer between the CeO_2 NPs and $CoSe_2$ NB components was occurring. This modification of the electronic structure as a result of material heterogeneity made CeO_2 more acidic (Lewis acid), facilitating the activation (dissociation) of H_2O molecules (Lewis base) for improved OER electrocatalysis. Furthermore, the current−voltage ($I-V$) response analysis (not shown here) of $CoSe_2$/DETA NBs and the $CeO_2/CoSe_2$ composite indicated that the electrical conductivity of the $CeO_2/CoSe_2$ composite was increased due to the improved charge transfer due to the CeO_2 coating, which positively affected electrocatalytic performance.

As aforementioned, selenide/carbon-based material composites have been prepared in addition to selenide/selenide and selenide/oxide composites (refs 915, 916, 983, 1000, 1008, 1045, 1063, 1072, 1119, and 1120). For example, Liao *et al.* synthesized 3D FeSe nanoparticles grown on a 3D carbon-based material derived from ripe pollen grains (RPGs).[1072] The 3D porous structure of conductive pollen provided a more exposed surface and enhanced electrical conductivity of the resultant electrode (Figures 253a and b). The FeSe with N-doped carbon and pollen grains (FeSe/NC-PoFeSe) electrocatalyst exhibited an overpotential of 330 mV at 10 $mA{\cdot}cm^{-2}$ and a Tafel slope of 76 $mV{\cdot}dec^{-1}$ in 0.1 M KOH electrolyte (Figures 253c and d). The OER activity of FeSe/NC-PoFeSe can be attributed to the effective combination of FeSe and pollen [i.e., heteroatom (e.g., N, S, P, and B)-doped nanocarbon materials (HCMs)]. FeSe nanoparticles distributed uniformly on HCMs promoted the charge transfer from metal ions to carbon. For FeSe/NC-PoFeSe, the carbon actually leads to an impairment of the electron density around the Fe atoms, resulting in the metal ions becoming electrophilic and, as a result, probably posed for OH^- adsorption. Additionally, the 3D porous structure facilitated the diffusion of the electrolyte and the release of O_2 bubbles. Wu *et al.* have also reported a selenide/carbon-based material composite for the OER. Specifically, they deposited N-doped graphene on Ni foam (NG/NF) and used this as-prepared NG/NF as a conductive substrate for a $NiSe_2$ electrocatalyst (Figure 253e).[1008] The $NiSe_2$ loaded on NG/NF ($NG/NiSe_2$/NF) exhibited better electrochemical OER performance than $NiSe_2$ on bare Ni foam ($NiSe_2$/NF) and graphene-coated Ni foam ($G/NiSe_2$/NF) (Figures 253f and g). The authors found that there was a synergistic effect between the N-doped graphene support and the $NiSe_2$ electrocatalyst. Due to the metallic property of the support, the diffusion and transfer of electrons were significantly enhanced for accelerated OER. In addition, the bonding force between the $NiSe_2$ and N-doped graphene support reduced the possibility of the material peeling off from the substrate, resulting in high mechanical stability. Also, the layered structure of N-doped graphene had a more flexible structure to buffer the volume change during the OER process without negative effects on the electrocatalytic performance. They also hypothesized that the electron donation from the N-graphene layer to $NiSe_2$ can potentially reduce the surface−oxygen interaction strength, resulting in a moderate bond strength and, consequently, an acceleration of OER kinetics..

5.2.3.6. Synthetic Parameter Effects. As discussed above, certain properties of selenide electrocatalysts will affect their OER performance, and such properties can be tuned by controlling the synthetic parameters (i.e., electrodeposition time, post-annealing time, selenization time, selenization temperature, etc.). Different synthetic conditions will result in as-prepared materials with different crystalline structures, various morphologies, and different compositions, which are key factors that influence the electrochemical performance

https://doi.org/10.1021/acs.chemrev.3c00005
Chem. Rev. 2023, 123, 12795−13208

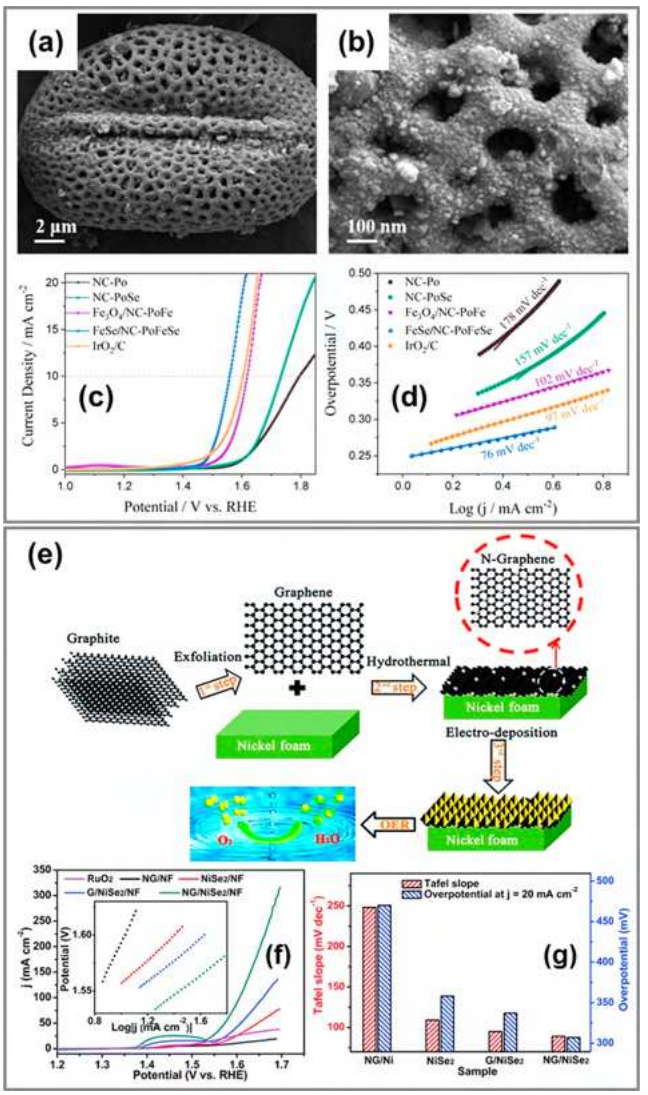


Figure 253. (a, b) SEM images of FeSe/NC-PoFeSe. (c) LSV curves and (d) Tafel plots of RPGs on their own (NC-Po), RPGs with selenium powder (NC-PoSe), RPGs with $NH_4Fe(SO_4)_2$ (Fe_3O_4/NC-PoFe), FeSe/NC-PoFeSe, and commercial IrO_2/C. Reproduced with permission from ref 1072. Copyright 2018 American Chemical Society. (e) Schematic illustration for the construction of the NG/$NiSe_2$/NF hybrid electrocatalyst. (f) LSV polarization curves of NG/$NiSe_2$/NF with a sweep rate of 2 $mV{\cdot}s^{-1}$. Inset: corresponding Tafel plots. (g) Corresponding Tafel slopes and overpotentials at 20 $mA{\cdot}cm^{-2}$. Reproduced with permission from ref 1008. Copyright 2017 Royal Society of Chemistry.

directly. Herein, we discuss the effect of synthetic parameters on metal selenide OER activity.

One method that has been used extensively to tune the morphology of selenides is the varying of the reaction time during synthesis. For example, Nath *et al.* studied the effect of electrodeposition and annealing times and their influence on the electrochemical performance of Ni_3Se_2.[100] First, Ni_3Se_2 was electrodeposited on Au-coated glass substrates by mixing 10 mM $Ni(CH_3CO_2)_2{\cdot}4H_2O$, 10 mM SeO_2, and 25 mM LiCl at −0.80 $V_{Ag/AgCl}$ for 40, 130, 300, and 600 s at room temperature. With increasing deposition time, the coated films grew thicker, and the surface became smoother. Of all the samples prepared, the Ni_3Se_2 sample prepared with a 300 s deposition time exhibited the best OER performance (i.e., overpotential of 310 mV at 10 $mA{\cdot}cm^{-2}$ and Tafel slope of 97.1 $mV{\cdot}dec^{-1}$) in 0.3 M KOH (Figures 254a–e). It was found

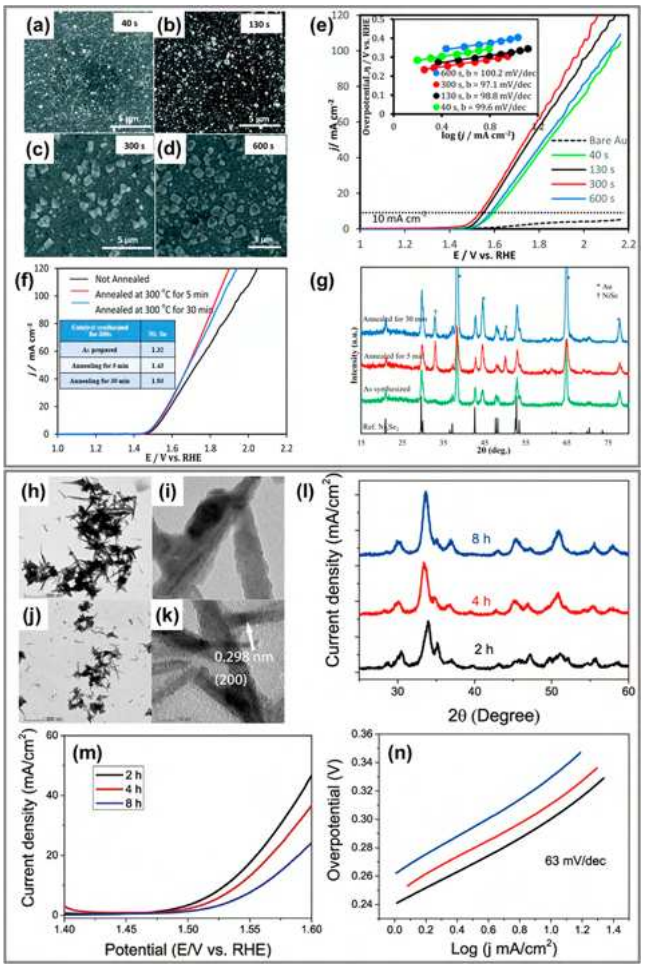


Figure 254. Ni_3Se_2 samples electrodeposited with different deposition times: (a) 40, (b) 130, (c) 300, and (d) 600 s. (e) Polarization curves and Tafel plots of Ni_3Se_2 samples electrodeposited for different deposition times. (f) LSV curves before and after annealing at 300 °C for 5 and 30 min of the catalysts in 0.3 M KOH solution at 0.01 V s^{-1}. (g) XRD patterns of catalysts deposited for 300 s without and with post-annealing for 5 and 30 min. Reproduced with permission from ref 100. Copyright 2016 Royal Society of Chemistry. (h) TEM image of Ni-Fe-Se synthesized at 413 K aged for 4 h. (i) Bright-field high-magnification TEM image of the sample after 4 h aging. (j) TEM images of Ni-Fe-Se synthesized at 413 K aged for 8 h. (k) Bright-field high-magnification TEM image of the sample for aging 8 h. (l) Polarization curves of Ni-Fe-Se aged for different times. (m) Polarization curves and (n) Tafel plots of Ni-Se samples synthesized at 413 K for different aging times. Reproduced with permission from ref 1042. Copyright 2019 Elsevier.

that when the deposition time increased above 600 s, several active sites were buried underneath the thicker layer, and, as a result, the overpotential became higher. In addition, the thicker layer also influenced the mobility of electrons, decreasing the electrical conductivity of the electrode as layer thickness increased with deposition time. Furthermore, it was found that shorter deposition times produced rougher surfaces, exposing more active sites for electrocatalysis. Nath and co-workers then examined the effect of annealing time (i.e., 5 and 30 min) at 300 °C post-electrodeposition of Ni_3Se_2. Comparing the LSV curves of the Ni_3Se_2 before and after annealing with different

https://doi.org/10.1021/acs.chemrev.3c00005
Chem. Rev. 2023, 123, 12795−13208

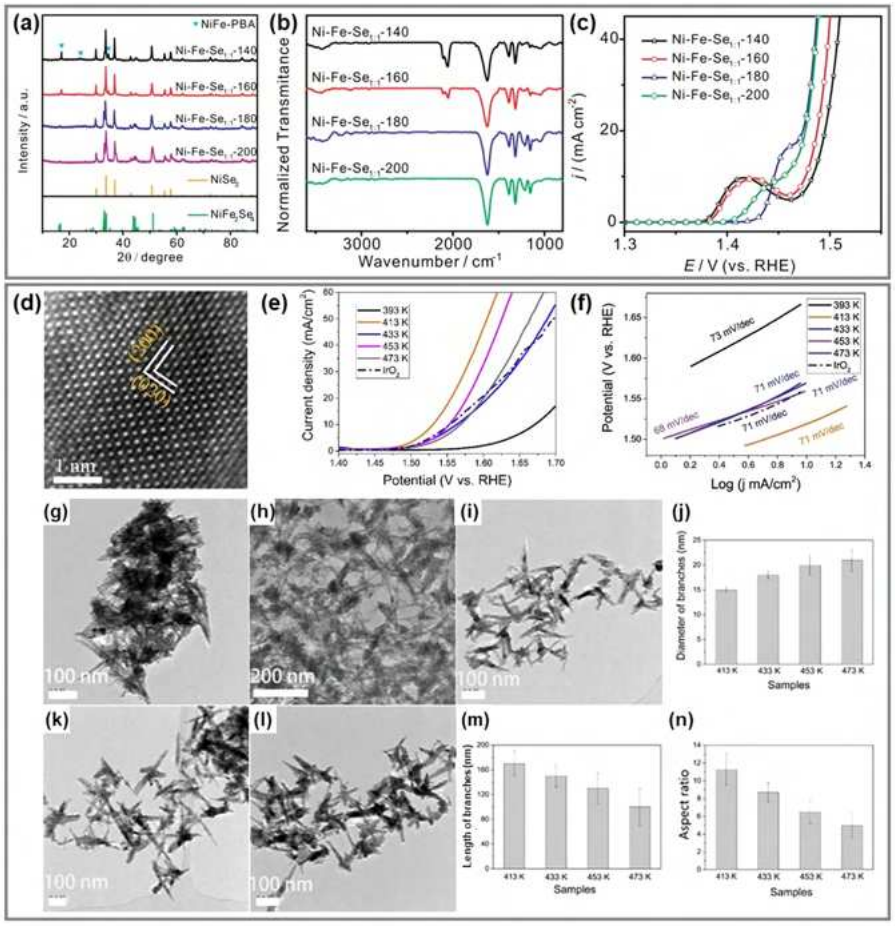


Figure 255. (a) XRD patterns, (b) FT-IR spectra, and (c) polarization curves of Ni-Fe-Se samples prepared under different hydrothermal temperatures. Reproduced with permission from ref 975. Copyright 2018 Elsevier. (d) High-magnification bright-field TEM image of $NiSe_2$ DLNs. The growth axis of the $NiSe_2$ DLNs is ⟨200⟩. (e) Polarization curves and (f) Tafel plots of $NiSe_2$ samples synthesized at different temperatures. (g–i, k–l) Low-magnification bright-field TEM images of $NiSe_2$ samples synthesized at (g) 393 K, (h) 413 K, (i) 433 K, (k) 453 K, and (l) 473 K. (m, j, and n) are comparisons of length statistics, diameter statistics, and length/diameter ratio statistics of DLNs, respectively. Reproduced with permission from ref 1042. Copyright 2019 Elsevier.

holding times, the authors found that both the samples after 5 and 30 min of annealing exhibited a low overpotential of 290 mV at 10 mA·cm^{-2} (Figure 254f). Moreover, the EDS results showed that the ratio of Ni to Se increased following the increased annealing time, and XRD results indicated a higher crystallinity after thermal treatment as well (Figure 254g). Therefore, it was verified that the longer annealing time would endow the selenides with a more stable crystalline structure and more Se content. Overall, this work demonstrates that adjusting both the electrodeposition and annealing time during synthesis can effectively tune the structure of the transition metal selenides to further improve OER performance.

Similarly, Zu *et al.* synthesized $NiSe_2$ dendrite-like nanostructures (DLNs) by heating a mixture of starting materials [$Ni(acac)_2$, oleylamine, tetralin, and Se powder] in solution.[1042] In order to investigate the stability of the nanostructure, the authors prolonged the aging (reaction) time from 2 to 4 and then 8 h at 413 K to destroy the DLNs (Figures 254h–k). XRD patterns showed that the prolonged aging time did not change the crystallinity of the $NiSe_2$ (Figure 254l). However, with increased aging time, the regular and well-organized morphology was destroyed, resulting in a mixture of DLNs and nanorods. The LSV curves of the samples prepared with different aging times indicated that the broken DLNs exhibited higher overpotentials at 10 mA·cm^{-2} in an alkaline electrolyte (1 M KOH). Of the aged samples, the 2 h sample had the lowest overpotential at 10 mV less than that of the 4 h sample and 30 mV less than that of the 8 h sample (Figure 254m). Similar Tafel slopes (63 mV·dec^{-1}) of all the tested samples indicated that the destruction of the structure did not influence the intrinsic chemical and ionic properties of the electrocatalysts (Figure 254n). Instead, the destruction of the structure with aging likely contributed to an increase in surface area, which would lead to an increase in exposed active sites for electrocatalysis. Of course, as shown by the results of Zu and co-workers, this destruction positively influenced performance up to 2 h, as decreased activity was observed for the 4 and 8 h samples.

Selenization temperature has also been shown to affect the electrocatalytic performance of metal selenides. Wang *et al.* synthesized Ni-Fe-Se electrocatalysts via hydrothermal selenization of NiFe-PBA precursors at different temperatures (i.e., 140, 160, 180, and 200 °C).[975] From XRD measurements, it was found that NiFe-based selenides showed similar XRD patterns with characteristic diffraction peaks for $NiSe_2$ and $NiFe_2Se_4$ and that the intensity of the diffraction peaks corresponding to $NiFe_2Se_4$ increased gradually with increased selenization temperature (Figure 255a). At the lower

https://doi.org/10.1021/acs.chemrev.3c00005
Chem. Rev. 2023, 123, 12795–13208

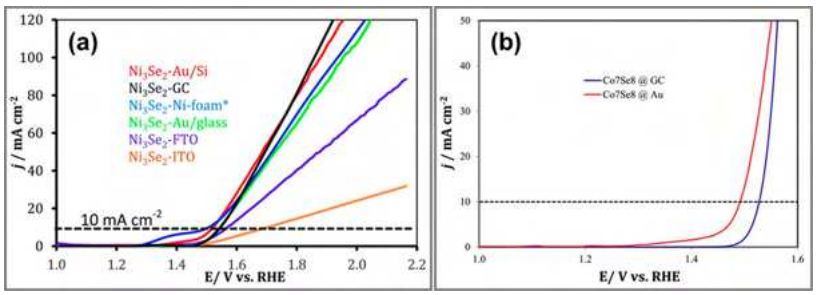


Figure 256. (a) OER activities of Ni_3Se_2 catalysts electrodeposited on various substrates, which were measured in 0.3 M KOH. Reproduced with permission from ref 100. Copyright 2016 Royal Society of Chemistry. (b) Current−voltage plots for Co_7Se_8 electrocatalysts deposited on different substrates (Au and GC) in N_2-saturated 1.0 M KOH solution at a scan rate of 5 mV·s^{-1}. Reproduced with permission from ref 928. Copyright 2016 American Chemical Society.

selenization temperatures of 140 and 160 °C, some weak diffraction peaks for $Ni_3[Fe(CN)_6]\cdot 10H_2O$ were found in the XRD patterns, indicating the incomplete decomposition of the NiFe-PBA precursor. At the higher temperatures of 180 and 200 °C, the as-prepared selenides showed high intensities of diffraction peaks of $NiFe_2Se_4$ without any impurity peaks, suggesting that the crystalline structure of $NiFe_2Se_4$ can be easily formed. FT-IR measurements further confirmed that, after the selenization, the samples obtained at 140 and 160 °C (Ni-Fe-Se1:1-140 and -160) still showed the existence of a CN^- group from the NiFe-PBA precursor, once again indicating the incomplete selenization of the precursor at the lower temperatures. In contrast, the typical peaks for the NiFe-PBA precursor were not observed in the FT-IR spectra of the samples selenized at 180 and 200 °C (Ni-Fe-Se1:1-180 and -200), as expected based on XRD results (Figure 255b). In alkaline media (1 M KOH), both the Ni-Fe-Se1:1-180 and -200 electrocatalysts exhibited low overpotential (~249 mV at 30 mA·cm^{-2} for both materials) and small Tafel slope (36 mV·dec^{-1} for the Ni-Fe-Se1:1-180) compared with the samples prepared at the lower temperatures (Figure 255c). Their excellent OER performance was attributed to the complete conversion from the NiFe-PBA to the Ni-Fe-Se selenides. Similarly, Zu *et al.* found that the exposed lattice planes of $NiSe_2$ electrocatalysts can be controlled by adjusting the selenization temperature (i.e., 393, 413, 433, 453, and 473 K).[1042] They hypothesized that the exposed (200) facet could improve the OER performance of the $NiSe_2$ electrocatalyst. After all, the assumed active sites of the $NiSe_2$ electrocatalyst are considered to be the undercoordinated surface atoms on its (200) plane instead of the basal planes in this study. From a typical HRTEM image of the $NiSe_2$ sample, the as-prepared sample had dendrite-like nanostructures (DLNs) and was grown along the ⟨200⟩ direction, which aided the exposure of the {200} planes (Figure 255d). To further expose the (200) facet, they changed the selenization temperature with the goal of growing relatively long $NiSe_2$ dendrites (Figures 255g−i and k−l). Ni-Se nanorods were formed at the low temperature of 393 K. When the temperature was increased to 413 K, the product exhibited an ordered cuboid dendrite with a relatively high exposure ratio of the (200) plane, indicating the formation of the DLNs. Statistical analysis results of the DLN branches showed that the product obtained at 413 K possessed the longest branches and smallest diameter of branches, suggesting a larger aspect ratio (i.e., the ratio of length to diameter) among all the DLNs synthesized at different temperatures (Figures 255j and m). At a higher temperature, above 433 K, the length of branches, as well as the aspect ratio, decreased, likely owing to a fast nucleation rate (Figures 255m and n). The $NiSe_2$ DLNs with preferable exposed lattice planes successfully provided more vacancies and active sites for the OER. Here, the $NiSe_2$ synthesized at 413 K showed the lowest overpotential of 299 mV at 10 mA·cm^{-2} and Tafel slope of 71 mV·dec^{-1} in 1 M KOH.

5.2.3.7. Substrate Effects. Conductive materials (i.e., glassy carbon, carbon fibers, Ni foam, Ti foil, etc.) normally serve as substrates for OER electrocatalysts. These substrate materials facilitate electron transfer to the electrocatalysts, improving electrical conductivity and overall electrocatalytic performance. Thus, the substrate is an important factor in influencing the electrochemical performance of transition metal selenides. Herein, we briefly discuss reports on substrate effects on metal selenide OER electrocatalytic activity.

Gold metal coated on a glass substrate has been reported as a promoter to enhance the electrochemical performance of OER electrocatalysts. The Nath group has coated Ni_3Se_2 catalysts on Au-coated glass, Au-coated Si, indium tin oxide (ITO)-coated glass, fluorine-doped tin oxide (FTO)-coated glass, glassy carbon electrodes, and Ni foam to investigate their influence on OER performance in 0.3 M KOH.[100] From electrochemical measurements (Figure 256a), it was found that the Au-coated glass, Au-coated Si, and glassy carbon electrode exhibited relatively smaller overpotentials of 320, 300, and 310 mV at 10 mA·cm^{-2}, respectively, than those of ITO-coated glass (450 mV) and FTO-coated glass (340 mV). Considering Au-coated glass, Au-coated Si, and glassy carbon electrodes, all these substrates have smoother and more uniform surfaces and topologies than ITO- and FTO-coated glass substrates, suggesting that the planar and even substrates can efficiently improve the OER performance of deposited electrocatalysts. In addition, they also determined that Ni foam with its porous structure provided more surface area with more active sites for the OER than the planar substrates. The Ni_3Se_2 coated on the Ni foam exhibited the lowest overpotential of 270 mV at 10 mA·cm^{-2}. Similarly, the Nath group also studied the influence of glassy carbon electrodes and Au-coated glass substrates for a Co_7Se_8 electrocatalyst in 1 M KOH.[928] Of these two substrates, the cobalt selenide electrocatalyst deposited onto Au-coated glass exhibited a lower overpotential of 260 mV at 10 mA·cm^{-2} than that of glassy carbon (290 mV) (Figure 256b). They proposed that the better electrochemical performance was attributed to the properties of the Au-coated substrate. Specifically, the higher conductivity, roughness, and texturing of the Au-coated substrate were thought to promote charge transfer between substrate and electrocatalyst to further enhance the efficiency of electron transfer. Notably, according

https://doi.org/10.1021/acs.chemrev.3c00005
Chem. Rev. 2023, 123, 12795−13208

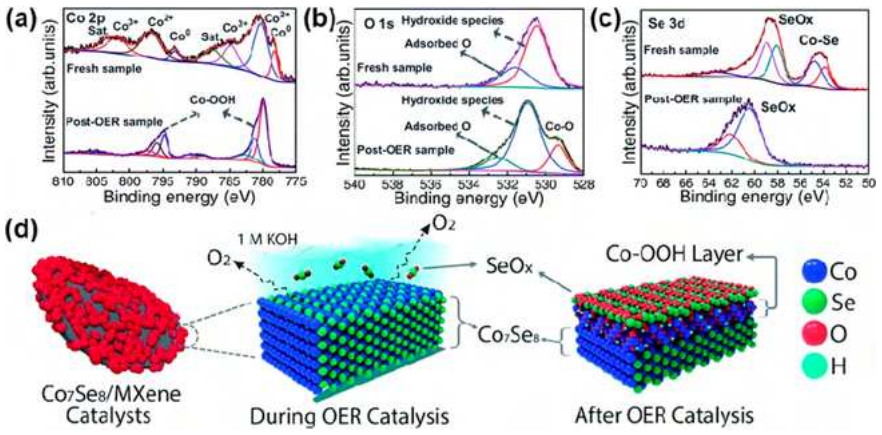


Figure 257. OER post-analysis of a Co_7Se_8/MXene electrocatalyst: comparison of XPS spectra before and after OER testing for (a) Co 2p, (b) O 1s, and (c) Se 3d regions; and (d) schematic illustration of the *in situ* reconstruction of the Co_7Se_8/MXene electrocatalyst during the OER. Reprinted with permission from ref 963. Copyright 2019 Royal Society of Chemistry.

to a previous report regarding a Ni (oxy)hydroxide/Au electrode, Au species on the electrode surface were determined to be beneficial to the electrochemical performance.[1121] It was found that the enhanced activity was attributed to partial electron transfer from the Ni (oxy)hydroxides to the more electronegative Au substrate to facilitate the formation of Ni^{4+} species. Additionally, Frydendal *et al.* employed DFT calculations to conclude that the hydrogen acceptor role of Au−O contributes to enhanced OER activity.[1122] Accordingly, Au-based substrates may also influence the selenide electronic structure as well as participate in the OER process and, as such, warrant further experimental and computational investigations.

5.2.4. Challenges. Like the metal sulfide trends described in Section 5.1, most studies on transition metal selenide electrocatalysts suggest that surface reconstruction occurs during OER testing. However, some studies still claim that transition metal selenides can be stable during the OER without undergoing significant transformation or oxidation. Hence, there is an ongoing debate over whether oxidation truly happens. Furthermore, it is not fully understood how different properties affect surface oxidation. Generally, this surface oxidation mainly occurs because the selenides are thermodynamically unstable as compared to their oxide counterparts.[85] From Section 5.2.3, introduced defects and lattice distortion,[953,987,1011,1015,1029] transition metal dopants,[967,978,979,989,1029] synthetic conditions,[100,928,1042] etc. can also act as triggers for this surface oxidation. However, it is still unclear how certain processes and mechanisms occur during selenide surface oxidation and if they can be controlled. In this section, we highlight studies related to four main topics that are not fully understood and remain elusive in the transition metal selenide field: (i) surface oxidation evidence, (ii) the role of SeO_x species, (iii) Se dissolution, and (iv) pH-dependent stability. We consider the most critical challenges that future studies must address for understanding transition metal selenide electrocatalysts.

Although most of the studies in the literature agree that surface oxidation during the OER occurs, some reports claim that transition metal selenides are indeed stable under oxidative potentials (refs 100, 844, 920, 925, 926, 928, 1016, 1048, 1050−1052, 1075, and 1087). Li *et al.* carried out an extensive evaluation for the electrocatalytic properties of a (Co,Ni)Se_2@NiFe LDH electrocatalyst and tested the long-term stability for 17 h using chronopotentiometry at 10 mA·cm^{-2}.[1051] The authors claimed that the bimetallic selenide was stable since only a slight activity loss of 6 mV was observed. Moreover, varying the current density (5−100 mA·cm^{-2}) resulted in constant overpotentials. Similarly, Zhao *et al.* monitored the steady-state OER current density of a NiCo-selenide ($Ni_3Se_4/CoSe_2$) electrocatalyst, registering a ∼10% anodic current loss after 10 h.[1087] Additionally, the authors characterized the morphology before and after electrode stability tests using SEM. Although the surface was somewhat damaged, the NiCo-selenide nanorods within the urchin-like morphology were still observed. So far, SEM has also been utilized to examine morphological stability after OER stability testing by other studies.[844,1016,1050] Additionally, Chi *et al.* utilized XRD post-analysis to assess the stability of a $Fe_{0.5}Co_{0.5}Se_2$/CFC after accelerated degradation tests through CV (1000 cycles).[1075] Notably, there was no significant difference between XRD patterns before and after CV testing, confirming the stability of crystalline $CoSe_2$ during the OER.

The above studies have provided solid evidence of electrochemical, morphological, and structural stability. It is, however, still hard to categorize these metal selenide electrocatalysts as "stable". We consider that future studies should carefully address specific considerations when examining the OER stability of transition metal selenides. First, stability tests should be carried out for extended periods, if possible, using uniform time scales (e.g., 24, 48, or 72 h) to favor comparing materials in the field. Second, stability should be confirmed by using complementary post-analysis techniques. We recommend that authors not report only one stability type (i.e., structural, morphological, chemical). We provide more guidelines and suggest a standard post-analysis testing procedure in Sections 1.4 and 7.9. Third, the authors should confirm that the initial metal selenide remains after the OER by checking its crystal structure (XRD, TEM, SAED) and chemical composition through XPS. EDX, while also a powerful tool in determining chemical composition, is more questionable. Thus, while EDX can be used for post-analysis characterization, it should also be accompanied by a more sensitive technique such as XPS. *In situ*/*operando* techniques capable of monitoring specific signals are highly recommended (more details in Section 7.9). We emphasize that true stability and proof of oxidation/surface reconstruction can only be confirmed when complementary techniques are utilized after sufficient and standardized OER testing periods.

https://doi.org/10.1021/acs.chemrev.3c00005
Chem. Rev. 2023, 123, 12795−13208

Notably, there are conflicting reports in the literature that reflect contradictory results regarding the transformation of transition metal selenides with the same composition. For instance, the Nath group examined a Co_7Se_8 electrocatalyst with 3D rod-like and tubular nanostructures.[928] The material exhibited no noticeable degradation during controlled potential (1.52 V_{RHE}, 6 h) and controlled current (10 mA·cm^{-2}, 15 h) electrolysis. Furthermore, the authors carried out SEM, EDX, XRD, and XPS post-analyses to examine physicochemical stability. XRD results suggested no change in the crystalline structure. SEM images revealed increased porosity, which was also confirmed by ECSA measurements after OER tests. EDX mappings revealed a uniform distribution of Co and Se on the surface, although the relative Co:Se ratio increased to 0.91:1. The authors claimed that the O content was constant, suggesting no oxidation during the OER. XPS also confirmed this claim, as Co 2p and 3d peaks remained unchanged. Thus, the authors concluded that Co_7Se_8 acted as a "catalyst", showing no oxidation/reconstruction. However, the authors suggested that the slight change in the Co:Se ratio could be attributed to the partial leaching of Se during the OER, although this hypothesis was not verified. The Yoo group also studied a Co_7Se_8 electrocatalyst deposited on exfoliated MXene sheets.[963] Similarly, stability was examined through chronoamperometric runs at 50 mA·cm^{-2} for over 10 h, with moderate degradation (~30% current decay). Moreover, the authors also performed XPS post-analysis to examine the material's chemical stability and surface oxidation after OER testing. Figure 257a shows that the post-OER sample exhibited only peaks for the CoOOH phase, while Co−Se peaks disappeared. Moreover, the O 1s spectra confirmed the retention of hydroxide species and Co−O bond formation after the OER (Figure 257b). Moreover, the Se 3d confirmed the complete transformation of pristine Co−Se species into the SeO_x phase (Figure 257c). HRTEM images further confirmed the presence of CoOOH in the post-OER sample. Additional EDX and ICP-OES analysis confirmed the decrease of Se from ~45 to 5 wt %, indicating the dissolution of Se species into the electrolyte. Finally, the authors performed post-OER EIS analysis to evaluate the conductivity of the final electrocatalyst. Notably, the charge transfer resistance increased from 3.35 to 16.2 Ω. The authors hypothesized that the presence of the SeO_x phase within the oxyhydroxide layer probably deteriorates the electrocatalyst's performance, thus explaining the moderate stability degradation (Figure 257d).

Differing results have also been reported for Ni-Se electrocatalysts. Regarding the $NiSe_2$ composition, Swesi *et al.* found that the sample was not oxidized and that no NiO was detected after the OER. However, although Ni and Se remained after OER stability tests of $NiSe_2$ electrocatalysts, some $Ni_{0.85}Se$ was found from post-OER XRD measurements.[1017] This finding suggests that Se-deficient phases could be produced during the OER, although drastic decomposition might not be visible through XPS. Hence, this suggests that the leaching of Se could arise from processes other than surface oxidation. This contradicts the results from Shi *et al.*[613] where the formation of selenites/selenates and the NiOOH phase was observed using the same composition ($NiSe_2$). Li *et al.* also found evidence of NiO after testing $NiSe_2$ precatalysts.[994] Hence, it is difficult to conclude if the $NiSe_2$ composition can be safely regarded as a "catalyst" rather than a "precatalyst".

Nath *et al.* examined the stability of electrocatalytic Ni_3Se_2 films deposited on Au-coated Si substrates.[100] The authors claimed that the Ni_3Se_2 was stable during chronoamperometric tests (at ~1.52 V_{RHE}) for over 42 h in 0.3 M KOH since no evident degradation was observed, and LSV scans before and after the OER were similar. Moreover, powder XRD, XPS, and Raman spectroscopy were utilized to examine the structural and chemical stability of the electrocatalytic film after long-term OER tests. XRD patterns of pristine Ni_3Se_2 and after 18 and 42 h were almost identical, and XPS spectra showed minimal changes to the O 1s and Se 3d peaks after the OER. Notably, Raman spectroscopy results confirmed the absence of Ni−O and Ni−OH bands, suggesting that the surface was not oxidized under anodic potentials. Nevertheless, the authors claimed that the Se content decreased after stability tests, although further compositional evidence and experimental procedures were not disclosed. Zhang *et al.* reported that eutectic $NiSe/Ni_3Se_2$ electrocatalysts on Ni foam retained their structural and chemical composition after 50000 s of continuous operation at 10 mA·cm^{-2}.[1062] Similarly, SEM and XRD analyses confirmed negligible morphological and structural changes. Nevertheless, detailed XPS deconvolutions were not disclosed, preventing further discussion of the chemical transformation during OER testing.

In contrast, Anantharaj *et al.* confirmed the reconstruction of Ni_3Se_4 nanoassemblies deposited on Ni foam during OER tests in neutral and alkaline media.[1007] Stability was examined by accelerated degradation tests using sequential CV cycling (1000 cycles, 200 mV·s^{-1}) and LSV scans before and after testing. Anodic overpotential shifts in alkaline (pH = 14) and neutral (pH = 7) media were 24 and 44 mV, respectively, demonstrating high electrochemical stability. Moreover, the authors utilized XRD, Raman spectroscopy, SEM, HRTEM, and XPS post-analysis to examine the integrity of the materials after the OER and HER in alkaline media. Notably, XRD suggested the formation of NiO and $NiSeO_3$, although the signal-to-noise ratio was low because of the metallic peaks coming from the Ni foam substrate. Additional Raman spectra confirmed the presence of the NiO and $NiSeO_3$ phases, as depicted in Figure 258a. Bands at 443, 238, and 139 cm^{-1} were attributed to Ni−Se before testing. However, bands ascribable to NiO (813 and 1575 cm^{-1}) and $NiSeO_3$ (1360 and 1222 cm^{-1}) emerged after anodic polarization. Nevertheless, the presence of Ni−Se bands suggested that these three phases coexisted after OER testing. Regarding morphological integrity, SEM/EDX analyses revealed negligible degradation of the electrocatalyst. Moving forward, the authors examined structural stability through HRTEM and SAED (Figure 258b−d). Although the sheet-like nanostructures remained unchanged (Figure 258b), HRTEM images revealed lattice fringes ascribable to Ni_3Se_4, NiO, and $NiSeO_3$ (Figure 258c). These three phases were also found in the SAED pattern (Figure 258d). Finally, XPS analyses revealed the presence of Ni_3Se_4, NiO, and Se^{4+}, confirming that partial oxidation of Ni_3Se_4/Ni occurred.

These studies show that it is still unclear if transition metal selenides undergo partial/full oxidation during the OER. Overall, we contemplate two divergent schemes for future analysis regarding the stability of transition metal selenides. These are not mutually exclusive, but more rigorous studies are necessary to fully understand what happens to transition metal selenides during the OER. The first scheme questions those studies classifying transition metal selenides as "catalysts" based on insufficient post-OER characterization. Reports resorting to various complementary techniques have provided

https://doi.org/10.1021/acs.chemrev.3c00005
Chem. Rev. 2023, 123, 12795−13208

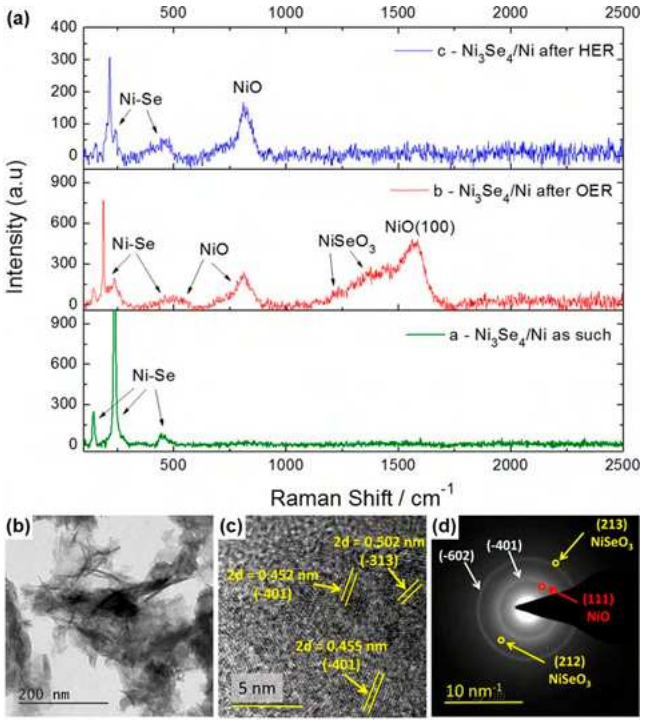


Figure 258. OER post-analysis of a Ni_3Se_4/Ni electrocatalyst after OER testing in alkaline electrolyte: (a) Raman spectra before and after electrochemical stability tests; (b, c) HRTEM images at low (b) and high (c) magnifications after the OER; and (d) corresponding SAED pattern. Reprinted with permission from ref 1007. Copyright 2017 American Chemical Society.

significant evidence of surface reconstruction/oxidation and chemical changes (refs 929, 948, 950, 952, 963, 965, 970, 984, 996, 1007, and 1019). Notice that some studies claiming electrocatalytic stability have utilized only certain techniques (e.g., SEM, XRD) for analyzing the post-OER samples, which could be inadequate for making generalities about electrocatalytic stability. In this sense, we consider that more rigorous studies focused on evaluating the surface reconstruction (e.g., oxidation, dissolution, etc.) of transition metal selenides are needed. Also, we encourage future studies to consistently confirm stability through complementary post-OER analysis techniques and extend testing periods to expose the materials to harsh OER conditions. Furthermore, confirming chemical, structural, and morphological stability is essential. Notice that, for instance, the morphology could remain unchanged according to SEM. However, chemical and structural changes could be revealed through XPS, TEM, SAED, and Raman spectroscopy, as Anantharaj *et al.* found for Ni_3Se_4 electrocatalysts.[1007] Notice that XPS should also be supported by additional techniques to evaluate other processes, such as elemental dissolution via elemental analysis of the electrolyte. For instance, Shi and Lian found that Cu_2Se precatalysts were transformed into CuO/Cu_2Se films through XPS.[961] The authors proposed that Se dissolution occurred because of the absence of XPS characteristic peaks. However, there was no further evidence from multi-elemental analysis techniques (e.g., ICP-OES, ICP-MS, TXRF). Therefore, authors should consider examining different stability aspects through complementary techniques before concluding that the material is truly stable.

In contrast, the second scheme involves acknowledging that certain transition metal selenides are indeed stable. However, if oxidation does not occur for certain materials, what is the reason behind different behaviors? We theorize that specific effects (e.g., type of substrate) could enhance or suppress the oxidation degree. For instance, some studies from the Nath group claiming long-term stability of transition metal selenide electrocatalysts have utilized Au-coated substrates (refs 100, 920, 925, 926, and 928), while others based on more common substrates (e.g., Ni foam) have confirmed surface oxidation.[963,1007,1010,1021,1025,1030] In particular, notice the Co_7Se_8 comparison between the Nath and Yoo groups, where Au-coated Si and exfoliated MXene sheet substrates were utilized for the same transition metal selenide but resulted in different oxidation trends. Understanding substrate effects is critical because electrocatalysts might change their stability during scale-up procedures (e.g., when migrating from glassy carbon electrodes to 3D porous electrodes), and therefore they would become useless for large-scale water electrolysis. Thus, rather than finding the most stable electrocatalyst, this field should aim to understand the real driving forces behind OER activity and stability.

Another aspect that remains elusive is the role of SeO_x anions in the OER. As shown in the Pourbaix diagram of selenium (Figure 259), selenium can be oxidized into SeO_4^{2-}

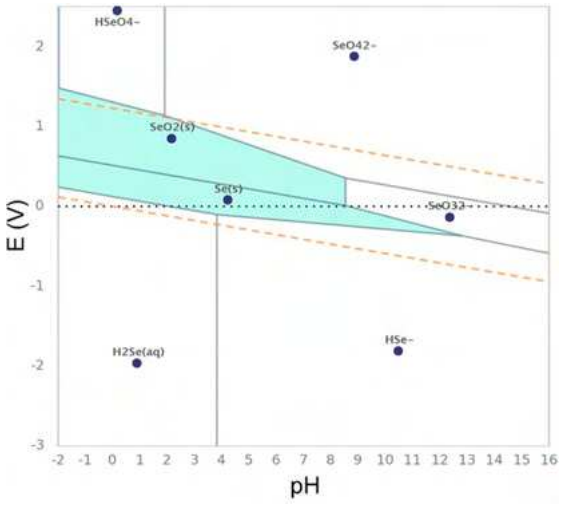


Figure 259. Pourbaix diagram for selenium. Orange broken lines represent the thermodynamic potentials for the HER and OER at different pH values. The diagram is produced at the Se ion concentration of 10^{-8} M (default) by using the Materials Project.[87−89]

(mildly acidic to alkaline pH) and SeO_2 + $HSeO_4^-$ (acidic pH) near the thermodynamic OER potentials. Thus, we can intuitively understand that, from the selenide precatalyst surfaces, similar Se species may appear during the OER. Recently, inspired by the significant amount of evidence regarding the dissolution of transition metal chalcogenides during the OER, Shi *et al.* carried out a comprehensive study of the effect of dissolved selenites (SeO_3^{2-}) and selenates (SeO_4^{2-}) on the OER activity of $NiSe_2$ electrocatalysts.[613] The authors examined the transformation of Se−Se species into selenite and selenate anions and their surface adsorption on *M*OOH sites generated during the OER (Figure 260a). First, successive LSV scans suggested the transformation of $NiSe_2$ electrocatalysts, and after 10 scans, the shape stabilized

https://doi.org/10.1021/acs.chemrev.3c00005
Chem. Rev. 2023, 123, 12795−13208

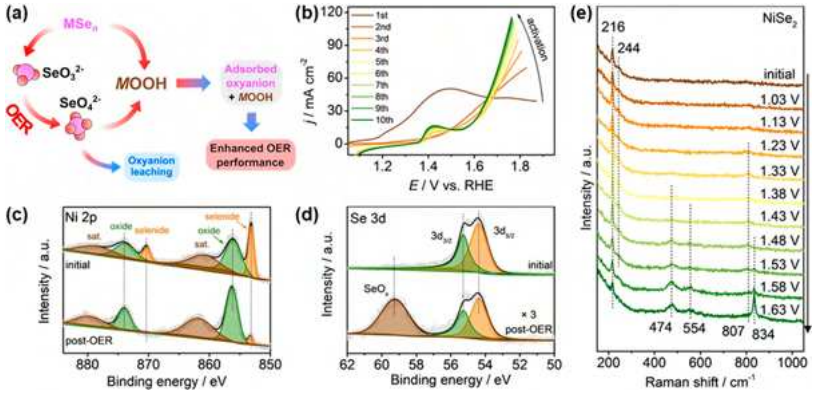


Figure 260. Transformation of $NiSe_2$ precatalysts during the OER: (a) schematic illustration of the sequential oxidation process of Se species and their interaction with the *M*OOH phase; (b) sequential LSV scans during electrocatalytic activation; (c) Ni 2p and (d) Se 3d XPS spectra of the $NiSe_2$ precatalyst before and after OER testing; and (e) *in situ* Raman spectroscopy measurements during OER potential scans. Reprinted and reprinted with permission from ref 613. Copyright 2020 Wiley.

(Figure 260b). Next, XPS measurements confirmed the *in situ* transformation of $NiSe_2$. Figure 260c shows that Ni−Se peaks at 853.2 and 870.4 eV weakened, while Ni−O peaks at 856.2 and 874.0 eV became more apparent. Moreover, the Se 3d spectra (Figure 260d) confirmed the formation of oxidized Se at 59.3 eV. Additional ICP-MS measurements confirmed the leaching of Se into the electrolyte, and further C_{dl} measurements also suggested the enlargement of the ECSA. Furthermore, the authors utilized *in situ* Raman spectroscopy to track down the oxidation of Se during OER testing (Figure 260e). Notably, the bands associated with Se−Se stretching modes (216 and 244 cm^{-1}) decreased as the potential increased from 1.03 to 1.63 V_{RHE}, while corresponding bands confirmed the formation of NiOOH at 474 and 554 cm^{-1}. Notably, specific signals were assigned to selenite (807 cm^{-1}, from 1.23 to 1.53 V) and selenate (834 cm^{-1}, starting at 1.53 V) species. These results suggest that Se species are oxidized through sequential steps, and the final phase after the OER corresponds to SeO_4^{2-}.

Moving forward, the authors examined the effect of oxidized Se species dissolved in the electrolyte. The OER activity of a $Ni(OH)_2$ electrocatalytic film was evaluated when different amounts of selenites were added to the electrolyte, as depicted in Figure 261a. The current density increased from 47 (pure KOH) to 221 $mA{\cdot}cm^{-2}$ (0.1 M SeO_3^{2-}) at a constant overpotential of 500 mV, confirming the activity improvement due to the adsorption of oxidized Se species. Notably, the addition of selenite species did not modify the pH significantly, and further addition of selenites up to 0.5 M decreased the activity slightly. Moreover, the Tafel slope also decreased from 153 to 96 $mV{\cdot}dec^{-1}$ by adding 0.1 M SeO_3^{2-}, and EIS measurements suggested improved charge transfer as well (Figure 261b). Moreover, Faradaic efficiencies around 96% were attributed to the oxidation of SeO_3^{2-} to SeO_4^{2-}. Finally, *in situ* Raman spectroscopy tests during potential scans confirmed the oxidation of $Ni(OH)_2$ into NiOOH (bands at 475 and 555 cm^{-1}), as well as the signals at 807 and 834 cm^{-1} attributed to selenite and selenate species, respectively (Figure 261c).

Additional DFT calculations revealed that the Gibbs free energy of the OER intermediates is indeed lower when SeO_4^{2-} anions are adsorbed on NiOOH, also increasing the electron density on Ni and favoring the adsorption of O*. In combination with the experimental results discussed above,

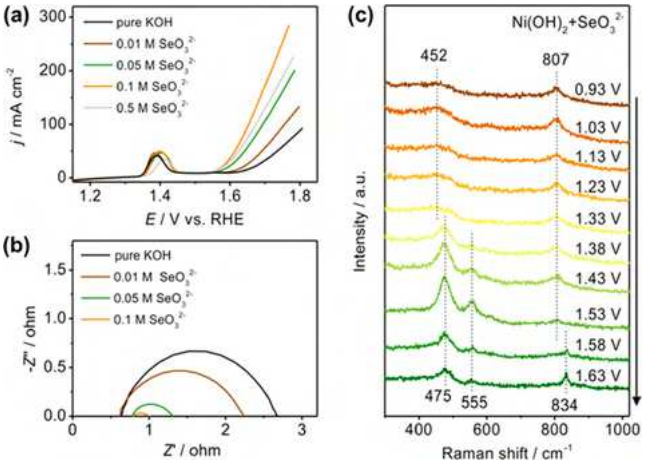


Figure 261. Effect of dissolved selenite species on the OER activity of $Ni(OH)_2$ electrocatalytic films: (a) LSV scans and (b) Nyquist plots of $Ni(OH)_2$ at different selenite concentrations in 1 M KOH; (c) potential-dependent *in situ* Raman spectra of $Ni(OH)_2$ in 0.1 M SeO_3^{2-}. Reprinted with permission from ref 613. Copyright 2020 Wiley.

the authors concluded that the adsorption of oxidized Se species enhanced the OER activity. Similar to the reconstruction process proposed for transition metal sulfides (Section 5.1.4) and based on the findings by Shi *et al.*, we theorize that transition metal selenides also suffer from an *in situ* oxidation mechanism, where Se species are oxidized sequentially, as depicted in Figure 260a. Thus, while some anions are dissolved into the electrolyte, others could be adsorbed into the *M*OOH phase, improving the OER activity.

Despite these findings, however, it is still unclear if oxidized Se species are solely responsible for the activity enhancement or if a series of material transformations promote it during the OER. Shi *et al.* found that the addition of selenites to the electrolyte did not affect the ECSA of $Ni(OH)_2$ and that the stability of the $NiSe_2$ precatalyst was better than that for the $Ni(OH)_2$ + SeO_3^{2-} scenario. Thus, it seems that the OER activity enhancement in the $NiSe_2$ precatalyst might also be coming from the ECSA enhancement due to Se leaching. Our group also suggested a similar reconstruction process for nickel sulfide and phosphide precatalysts,[49] where oxidation and subsequent leaching of S and P species promoted the creation

https://doi.org/10.1021/acs.chemrev.3c00005
Chem. Rev. 2023, 123, 12795−13208

of defects and vacancies, resulting in ECSA enlargement and improving the OER activity. Shi *et al.* found that the $NiSe_2$ precatalyst also contained more oxidized Se in the NiOOH phase after the OER than in the $Ni(OH)_2$ film in the presence of selenites. This result suggests that *in situ* activation from transition metal selenide precatalysts could favor the OER performance from ECSA enlargement and anion adsorption. In contrast, immersing the *M*OOH phase in the electrolyte might only improve the activity from anion adsorption.

In addition, we must also emphasize that other studies have found contradictory results regarding the benefits of incorporating oxidized Se species into the *M*OOH phase. As previously discussed, the Yoo group found that the SeO_x phase increased the charge-transfer resistance, decreased the conductivity, and deteriorated the stability of Co_7Se_8 electrocatalysts on exfoliated MXene sheets.[963] Finally, some studies have only confirmed the presence of oxidized Se species after the OER in precatalysts with high activity and stability, without further discussing the specific role of such species in the OER performance.[986,1007] Thus, more comprehensive studies regarding the true OER improvement from incorporating oxidized Se species are necessary.

Finally, the stability and dissolution of transition metal selenides at different electrolyte pH values demand more attention. Only a few reports have studied the performance of transition metal selenides in neutral[1007,1077] and mild alkaline electrolytes,[994] while the acidic environment has not been studied to date. As previously mentioned, Anantharaj *et al.* tested the OER performance of Ni_3Se_4/NF electrocatalysts in neutral media (PBS, pH = 7).[1007] Notably, Ni_3Se_4 required an overpotential of 480 mV at 10 $mA{\cdot}cm^{-2}$ in PBS electrolyte, while pristine Ni foam and RuO_2/NF could not reach the same current density even at 2.0 V_{RHE}. Regarding its stability, the electrocatalyst sustained a constant current density during chronoamperometric runs (1.73 V_{RHE}) for over 16 h and a slight overpotential shift of 44 mV after accelerated CV degradation tests. However, the authors did not report any post-OER analysis to check the material's chemical, structural, or morphological stability in neutral conditions. Moreover, Zhang *et al.* examined the interface of a cobalt selenide ($Co_{0.85}Se$) electrocatalyst in contact with Ti mesh in a neutral electrolyte (1 M PBS, pH = 7). The Ti@$Co_{0.85}Se$ electrocatalyst exhibited an overpotential of ∼500 mV at 10 $mA{\cdot}cm^{-2}$, and a Tafel slope of 153 $mV{\cdot}dec^{-1}$. The material was also stable after 1000 CV cycles, and the anodic current decreased ∼15% after a chronoamperometric test for over 30 h. Notably, the authors mentioned that some cobalt selenide nanosheets could have been released into the electrolyte, although more details and experimental evidence regarding post-OER stability were not provided. However, the authors emphasized that providing a robust ohmic contact between the metal selenide electrocatalyst and the Ti mesh is essential for promoting the OER activity in neutral media.

Additionally, Chen *et al.* examined a Cu_2Se-Cu_2O electrocatalyst deposited on Ti foil in 0.2 M carbonate buffer (pH = 11).[994] The Cu_2Se-Cu_2O/TF electrode exhibited an overpotential of 465 mV at 10 $mA{\cdot}cm^{-2}$, and a Tafel slope of 140 $mV{\cdot}dec^{-1}$. Moving forward, the stability of the material was confirmed for over 20 h at 10 $mA{\cdot}cm^{-2}$, without noticeable attenuation of the current. Notably, the authors provided post-OER characterization to support the durability of the material. SEM images showed a rougher surface after stability tests. Next, XRD and TEM measurements suggested the presence of crystalline CuO. Finally, XPS analysis confirmed the *in situ* formation of CuO on the surface of the material. The authors proposed that the protective CuO layer prevented further oxidation of the precatalyst, resulting in long-term durability in mild alkaline conditions. Although the study from Chen *et al.* confirmed that Cu_2Se-Cu_2O acted as a precatalyst in mild alkaline media, the studies in neutral electrolytes at pH = 7 also need to include post-OER characterization to examine the surface reconstruction of their materials. Furthermore, as discussed in previous *X*-ides sections, the elemental dissolution and leaching should be carefully assessed through multi-elemental analysis techniques (e.g., ICP-OES, TXRF) by probing the electrolyte.

In summary, certain aspects of the study of transition metal selenides remain elusive in the literature. First, future studies need to be performed thorough post-OER material characterization with complementary techniques since a significant number of studies claim that transition metal selenides act as "catalysts" rather than "precatalysts". Second, contradictions about the reconstruction (i.e., oxidation) of certain metal selenide compositions (e.g., Co_7Se_8, $NiSe_2$) must be clarified in the future by conducting systematic and precise experiments. Special attention should be paid to specific species such as selenites and selenates, which are regarded by some studies as beneficial for the OER. In contrast, others claim these species are detrimental and decrease the conductivity and OER kinetics. Therefore, we need to understand the role of these species in the OER and if they induce other changes during the reconstruction process, such as creating more vacancies, defects, and ECSA enlargement overall. Finally, future studies including neutral, acidic, and mild alkaline electrolytes also need to provide detailed post-OER examinations to confirm (i) if the materials are genuinely stable and (ii) if the reconstruction process occurs in the same way as in typical alkaline conditions. Moreover, the dissolution of certain species should also be addressed, and its impact on activity (e.g., anion adsorption) and stability (Se content decrease, degradation) should be carefully examined. Overall, solving these challenges will improve our understanding of transition metal selenides to realize better performing materials for the electrocatalytic OER.

5.3. Transition Metal Tellurides

5.3.1. Electrode Preparation Methods. As shown in Table 7, two types of transition metal telluride electrodes have been fabricated: (1) powder-coated electrodes (P) and (2) self-supported electrodes (S). Regardless of the type of electrodes, transition metal telluride electrocatalysts were typically prepared through either a two-step approach (starting materials → precursor → final product) (refs 97, 682, 1128−1130, 1132, 1144, 1147, 1149, 1150, and 1156−1162) or a one-step approach (starting materials → final product) (refs 101, 177, 184, 763, 1041, 1054, 1127, 1130, 1133, 1145, 1146, and 1148, 1156). In the two-step approaches, transition metal telluride OER electrocatalysts are mainly synthesized via the common synthetic approach−tellurization. Transition metal tellurides are synthesized in tellurization by reacting transition metal-based precursors (metal oxide,[97] metal hydroxide,[1149,1158,1161] metal hydroxyl-fluoride,[1132,1147] metal hydroxy-carbonate,[1160,1162] metal organic framework (MOF),[682,1128,1159] and so forth), which were synthesized by the hydrothermal method,[1132,1147,1149,1158,1160,1161] solvothermal method,[1157] solution-based method,[682,1128,1159,1162] and

https://doi.org/10.1021/acs.chemrev.3c00005
Chem. Rev. 2023, 123, 12795−13208

Table 7. Summary of the Electrocatalytic Properties, Electrochemical Testing Conditions, and Physicochemical Pre- and Post-analyses of Transition Metal Tellurides Used for Alkaline/Neutral OER and of the Final Type of Electrocatalyst after OER Testing[a−d]

Initial Electrocatalyst	Substrate	Shape of Electrocatalyst	Deposition Type	Specific Loading / $mg \cdot cm^{-2}_{geo}$	η@10 $mA \cdot cm^{-2}_{geo}$ / mV	C_{dl} / $mF \cdot cm^{-2}_{geo}$	TOF / s^{-1} (@η or j)	Tafel Slope / $mV \cdot dec^{-1}$	Electrolyte	Pre-analysis	Post-analysis	Long-Term OER Test Conditions	Post-OER Electrocatalyst	Final Type of Electrocatalyst	Ref.
NiO_x@Ni_3Te_2	Au glass	Irregularly shaped granules	S	~0.87 (NiO_x + Ni_3Te_2)	270 330 (@50 mA/cm^2_{geo})	~9.37	-	92.9	1 M KOH	XRD, SEM, EDX, XPS	-	100 CV cycles (50 $mV \cdot s^{-1}$, 0.0–0.5 V_{RHE}) 10 h CA (1.50 V_{RHE})	-	-	917
Ni_3Te_2	Au glass	Irregularly shaped granules	S	0.41	230 310 (@50 mA/cm^2_{geo})	~24.0	-	52.8		XRD, SEM, EDX, XPS, sXAS	XPS, sXAS	100 CV cycles (50 $mV \cdot s^{-1}$, 0.0–0.5 V_{RHE}) 10 h CA (1.46 V_{RHE})	Ni_3Te_2 [mixed anionic (hydroxo)chalcogenide]	Catalyst	
Cu_7Te_4-CF	Cu foam	Nanowire	P	12.73	277	26.55	2.57 at 350 mV	33	1 M KOH	XRD, SEM, EDX, TEM, SAED, XPS, ISO (BET, PSD)	XRD, SEM, XPS	1000 CV cycles (50 $mV \cdot s^{-1}$, 1.0–2.0 V_{RHE}) 100 h CA (1.66 V_{RHE})	Cu_7Te_4, TeO_4	Catalyst	1123
Cu_7Te_4-GC	GC	Nanowire	P	0.8983	321	-	-	56.7			-	100 h CA (1.66 V_{RHE})	-	-	
ED-CoTe	Au glass	Fluffy nanoball-like shape	S	-	200	-	-	43.8	Fe-purified 1 M KOH	SEM, EDX, XPS	-	24 h CA (1.43 V_{RHE})	-	-	1124
HD-CoTe	Carbon cloth	Nanorod	P	-	270	-	-	67.7		XRD, SEM, EDX, XPS, TEM	XRD, XPS, TEM, ICP-MS	24 h CA	CoTe, TeO_3	Catalyst	
ED-$CoTe_2$	Au glass	Fluffy nanostructure with rough edges	S	-	240	-	-	44.8		SEM, EDX, XPS	-	24 h CA (1.44 V_{RHE})	-	-	
HD-$CoTe_2$	Carbon cloth	Irregular nanostructure	P	-	320	-	-	111.8		XRD, SEM, EDX, XPS	XRD, XPS, ICP-MS	24 h CA	$CoTe_2$, TeO_3	Catalyst	
NiFe LDH/NiTe-1	Ni foam	Nanorod covered by nanosheets	S	-	246 (@50 mA/cm^2_{geo})	13.18	-	78.65	1 M KOH	SEM, TEM	-	-	-	-	1125
NiFe LDH/NiTe-2	Ni foam	Nanorod covered by nanosheets	S	-	228 (@50 mA/cm^2_{geo})	17.94	0.031 at 300 mV	51.04		XRD, SEM, TEM, EDX, SAED, XPS	XRD, SEM, XPS	4500 s multistep CA 30 h CA	NiFe LDH	Catalyst (substrate)	
NiFe LDH/NiTe-3	Ni foam	Nanorod covered by nanosheets	S	-	251 (@50 mA/cm^2_{geo})	10.97	-	64		SEM, TEM	-	-	-	-	
NiFe LDH/NiTe-4	Ni foam	Nanorod covered by nanosheets	S	-	275 (@50 mA/cm^2_{geo})	8.62	-	94.09		SEM, TEM	-	-	-	-	
NiTe	Ni foam	Rod-like nanoarray	S	-	350 (@50 mA/cm^2_{geo})	7.13	0.003 at 300 mV	109.09		SEM, TEM	-	-	-	-	
CoTe-NF	Ni foam	Nanoflake	S	2.34	241 402 (@100 mA/cm^2_{geo})	20.625	1.03 at 241 mV	66	1 M KOH	XRD, SEM, EDX, XPS	XRD, SEM, XPS (after 17 h CA)	17 h CA (1.89 V_{RHE}) 1000 CV cycles (50 $mV \cdot s^{-1}$) 18 h CA (cell voltage: 1.52 V, OWS)	CoTe, TeO_2	Catalyst	1126
ZnTe	Ni foam	Nanosphere	P	0.5	210	24	0.25 (@10 mA/cm^2_{geo})	62	1 M KOH	XRD, SEM, EDX, TEM, XPS	XRD, SEM, XPS (after more than 24 h CA)	> 24 h CA (1.58 V_{RHE}) 100 CV cycles (0.0–2.0 V_{RHE})	ZnTe (hydroxo-telluride) + TeO_x	Catalyst	1127
ZnTe	GC	Nanosphere	P	0.07	287	-	0.035 (@10 mA/cm^2_{geo})	67			-	> 10 h CA (1.53 V_{RHE})	-	-	
$CoTe_2$@CdTe	Pencil graphite	Nanowire array	P	2	140	0.071 (in 1.0 M KCl)	-	68	1 M KOH	XRD, FESEM, EDX, TEM	EDX	500 CV cycles (1.0–2.8 V_{RHE}) 3 month storage test (no bias) 8.33 h CA	$CoTe_2$@CdTe	Catalyst	1041
Ni_3Te_2	Au glass	Nanoflake	S	4.1	210	-	0.023 (@270 mV)	54.2	1 M KOH (and Fe-purified 1 M KOH)	XRD, SEM, TEM, EDX, XPS, Raman	XRD, SEM, EDX, XPS	24 h CA (1.44 V_{RHE})	Ni_3Te_2 (hydroxo-telluride)	Catalyst	101
Ni_3Te_2	GC			4.9	180	-	0.01 (@270 mV)	64.3		-	-	-	-	-	
Ni_3Te_2	Ni foam			40.8	230	-	-	-		-	-	-	-	-	
Ni_3Te_2	Au glass	Nanoflake	P	4.9	220	-	0.01 (@270 mV)	61.5		XRD, SEM, TEM, EDX	XRD	24 h CA (1.45 V_{RHE})	Ni_3Te_2 (hydroxo-telluride)	Catalyst	
$CoTe_2$@N-GC	CP	Nanocrystal	P	1	300	56.4	-	90	1 M KOH	XRD, SEM, EDX, TEM, XPS, TGA	XRD, TEM (after 2000 CV)	20 h CA (1.55 V_{RHE}) 2000 CV cycles (1.45–1.65 V_{RHE})	$CoTe_2$	Catalyst	1128
$CoTe_2$@N-rGO	CP	Nanocrystal	P	1	390	-	-	115		XRD, EDX, TEM	-	-	-	-	
$CoTe_2$	CP	Nanocrystal	P	1	360	39.8	-	102		XRD, TEM	-	-	-	-	
CoTe	GC	Nanofleece	P	0.25	365	0.266	0.20 (@350 mV)	73	0.1 M KOH	XRD, SEM, EDX, TEM, XPS, HAADF-STEM, XANES	XRD, SEM, XPS (after 2000 CV)	3000 CV cycles [0.3–0.8 $V_{Ag/AgCl\ (4\ M\ KCl)}$]	CoTe + TeO_2	Catalyst	1129
$CoTe_2$	GC	Nanofleece	P	0.25	357	0.357	0.12 (@350 mV)	32					$CoTe_2$ + TeO_2	Catalyst	
CoTe	CFP	Nanofleece	P	1	-	-	-	-			-	24 h CP (10 $mA \cdot cm^{-2}_{geo}$)	-	-	
$CoTe_2$	CFP	Nanofleece	P	1	-	-	-	-			-		-	-	
Cu_7Te_4	GC	Nanosheet	P	0.2	460	-	-	103	0.1 M KOH	XRD, SEM, EDX, TEM, AFM, FTIR	SEM, XRD (after 2000 CV)	7 h CP (10 $mA \cdot cm^{-2}_{geo}$) 2000 CV cycles (1.16–2.36 V_{RHE})	Cu_7Te_4	Catalyst	1130
Cu_7Te_4	GC	Bulk	P	0.2	610	-	-	149		XRD, SEM	-	-	-	-	
O_V@Fe-NiTe [O vacancy (O_V)-rich TeO_2 layer on Fe-NiTe]	Ni foam	Microsphere consisting of nanosheets	S	-	245 (@100 mA/cm^2_{geo})	71.3	-	35.5	1 M KOH	XRD, SEM, TEM, EDX, Raman, XPS, XAS, (XANES)	XRD, SEM, TEM, Raman, XPS	2 h CA (1.585 V_{RHE}) 100 h CA (1.63 V_{RHE}) 100 h CA (1.525 V_{RHE})	O vacancy-rich TeO_2	Catalyst (substrate)	1131

https://doi.org/10.1021/acs.chemrev.3c00005
Chem. Rev. 2023, 123, 12795−13208

Table 7. continued

Initial Electrocatalyst	Substrate	Shape of Electrocatalyst	Deposition Type	Specific Loading / $mg \cdot cm^{-2}_{geo}$	η@10 $mA \cdot cm^{-2}_{geo}$ / mV	C_{dl} / $mF \cdot cm^{-2}_{geo}$	TOF / s^{-1} (@η or f)	Tafel Slope / $mV \cdot dec^{-1}$	Electrolyte	Pre-analysis	Post-analysis	Long-Term OER Test Conditions	Post-OER Electrocatalyst	Final Type of Electrocatalyst	Ref.
Fe-NiTe	Ni foam	Microsphere consisting of nanosheets	S	-	340 (@100 $mA \cdot cm^{-2}_{geo}$)	43.2	-	81.6		XRD, SEM, TEM, EDX, Raman, XPS, XAS (XANES)	Raman, XPS	2 h CA (1.585 V_{RHE})	$NiTe, TeO_2$	Precatalyst (Fe dissolution)	1131
NiTe	Ni foam	Microsphere consisting of nanoplates	S	-	407 (@100 $mA \cdot cm^{-2}_{geo}$)	15.5	-	131.98		XRD, SEM, TEM, XPS	-	-	-	-	
$CoTe_2$	GC	Nanowire	P	0.405	323	15.99	-	85.1	1 M KOH	XRD, EDX, TEM, XANES	*In-Situ* XANES	24 h CA (1.52 V_{RHE}) 1000 CV cycles (1.10–1.70 V_{RHE})	$CoTe_2$	Catalyst	1132
$CoTe_2$/CNT-0.50	GC	Nanoparticle (on CNT)	P	0.405	291	25.61	-	44.2			-		-	-	
$CoTe_2$/CNT-0.75	GC	Nanoparticle (on CNT)	P	-	301	24.52	-	48.9			*In-Situ* XANES		CoOOH	Precatalyst	
$CoTe_2$/CNT-1.00	GC	Nanoparticle (on CNT)	P	-	313	24.40	-	70.4			-		-	-	
$NiCo_2Te_4$/PTCDA	CC	Nanocluster	P	-	120 [240 (@100 $mA \cdot cm^{-2}_{geo}$)]	-	-	50 (ECSA-based)	1 M PBS (pH = 7)	XRD, EDX, TEM, XPS, FTIR	XPS	20 h CA (η@10 $mA \cdot cm^{-2}_{geo}$)	$NiCo_2Te_4$, TeO_x	Catalyst	1133
$NiCo_2Te_4$	CC	Nanocluster	P	-	150	-	-	30 (ECSA-based)		XRD, EDX, TEM, XPS	XPS		Oxidized Ni and Co species, TeO_x	Precatalyst	
3CNT/CNF-240C ($CoTe_2$–$NiTe_2$)	CoNi foam	Nanorod covered by agminated nanoparticles	S	8.23	280	26.0	-	19.4	1 M KOH	XRD, SEM, TEM, EDX, XPS	XRD, SEM, TEM, EDX, XPS	18 h CP [10 (15 h), 20 $mA \cdot cm^{-2}_{geo}$ (3 h)]	CoOOH, Ni (oxy)hydroxide, Te oxide	Precatalyst (partial oxidation)	1134
3CNT/CNF-220C ($CoTe_2$–$NiTe_2$)	CoNi foam	Nanorod covered by agminated nanoparticles	S	8.16	320	-	-	22.7		XRD, SEM	-	-	-	-	
3CNT/CNF-180C ($CoTe_2$–$NiTe_2$)	CoNi foam	Nanoparticle	S	5.12	420	-	-	23.4		XRD, SEM	-	-	-	-	
4CNT/CNF-200C ($CoTe_2$–$NiTe_2$)	CoNi foam	Nanorod covered by agminated nanoparticles	S	5.26	430	-	-	29.3		XRD, SEM	-	-	-	-	
3CNT/CNF-200C ($CoTe_2$–$NiTe_2$)	CoNi foam	Nanorod covered by agminated nanoparticles	S	5.70	350	-	-	23.1		XRD, SEM	-	-	-	-	
2CNT/CNF-200C ($CoTe_2$–$NiTe_2$)	CoNi foam	Nanoparticle	S	5.43	400	-	-	30.6		XRD, SEM	-	-	-	-	
1CNT/CNF-200C ($CoTe_2$–$NiTe_2$)	CoNi foam	Nanoparticle	S	5.38	410	-	-	27.9		XRD, SEM	-	-	-	-	
3CT/CF-240C ($CoTe_2$)	CoNi foam	Nanorod	S	3.85	390	3.9	-	39.6		XRD, SEM, XPS	-	18 h CP [10 (15 h), 20 $mA \cdot cm^{-2}_{geo}$ (3 h)]	-	-	
Co/CoTe	GC	Microcube with rough surfaces	P	~0.28	~239 400 (@50 $mA \cdot cm^{-2}_{geo}$)	25.0	0.01 at 470 mV	94.1	1 M KOH	XRD, SEM, TEM, EDX, XPS, Raman	XRD, SEM, XRD, Raman	50 h CP (50 $mA \cdot cm^{-2}_{geo}$) 1000 LSV sweeps	CoOOH, Oxidized Te species (Te^{4+})	Precatalyst (partial oxidation)	1135
CoTe	GC	Microcube with rough surfaces	P	~0.28	~281 450 (@50 $mA \cdot cm^{-2}_{geo}$)	11.5	0.005 at 470 mV	180.2		XRD, SEM, XPS	-	-	-	-	
0.1CoNi LDH@Te-180C	Ni foam	Nanosheets coated with nanoparticles	S	0.93	400	1.1	-	77.3	1 M KOH	SEM, XRD	-	-	-	-	1136
0.2CoNi LDH@Te-180C	Ni foam	Nanosheets coated with nanoparticles	S	0.82	390	8.6	-	75.7		SEM, XRD	-	-	-	-	
0.3CoNi LDH@Te-180C	Ni foam	Nanosheets coated with nanoparticles	S	0.89	360	2.3	-	63.4		SEM, XRD	-	-	-	-	
0.4CoNi LDH@Te-180C (CoNi LDH, $Ni_{0.35}Te_{0.9}$, NiTe)	Ni foam	Nanosheets coated with nanoparticles	S	0.91	360	11.6	0.0027 at 350 mV 0.0179 at 400 mV	56.6		SEM, XRD, AFM, XPS, TEM, EDX, ICP-OES	SEM, XRD, XPS, TEM, EDX, ICP-OES	18 h CP [10 (15 h), 20 $mA \cdot cm^{-2}_{geo}$ (3 h)]	CoOOH, NiOOH, Telluroxide	Precatalyst (partial oxidation)	
0.4CoNi LDH@Te-160C	Ni foam	Nanoparticle	S	0.75	490	1.8	-	75.7		SEM, XRD	-	-	-	-	
0.4CoNi LDH@Te-200C	Ni foam	Nanosheets coated with nanoparticles	S	0.95	380	4.3	-	65.2		SEM, XRD	-	-	-	-	
Ni-Te-180C ($Ni_{0.35}Te_{0.9}$, NiTe)	Ni foam	Nanosheet	S	0.63	423	2.1	0.0025 at 400 mV	65.1		SEM, XRD	-	18 h CP [10 (15 h), 20 $mA \cdot cm^{-2}_{geo}$ (3 h)]	-	-	
ED-$FeTe_x$	Fe foam	Nanosheet	S	-	264.4 330.4 (@100 $mA \cdot cm^{-2}_{geo}$)	7.53	-	54.2	1 M KOH	XRD, SEM, EDX, TEM, SAED, XPS	SEM, XPS	50 h CP (10 $mA \cdot cm^{-2}_{geo}$)	$FeTe_x$, Likely oxidized $FeTe_x$ species (surface Te partially oxidized)	Precatalyst (partial oxidation)	1137
CVD-$FeTe_x$ ($FeTe_{1.1}$)	Fe foam	Nanosheet	S	-	295.4 371.4 (@100 $mA \cdot cm^{-2}_{geo}$)	1.57	-	69.9		XRD, SEM, EDX, TEM, XPS	XPS	50 h CP (10 $mA \cdot cm^{-2}_{geo}$)	Likely oxidized $FeTe_x$ species (surface Te fully oxidized)	Precatalyst	
Co@0.1gNiCoTe2-240	Co foam	Nanosheet	S	-	320	-	-	-	1 M KOH	XRD, SEM	-	-	-	-	1138
Co@0.2gNiCoTe2-240 (Ni-doped $CoTe_2$)	Co foam	Nanosheet	S	-	280	16.9	-	34		XRD, SEM, TEM, HAADF, EDX, XPS	XRD, SEM, TEM, EDX, XPS	18 h CP [10 (15 h), 20 $mA \cdot cm^{-2}_{geo}$ (3 h)]	CoOOH, NiOOH, TeO_2	Precatalyst (partial oxidation)	

https://doi.org/10.1021/acs.chemrev.3c00005
Chem. Rev. 2023, 123, 12795−13208

Table 7. continued

Initial Electrocatalyst	Substrate	Shape of Electrocatalyst	Deposition Type	Specific Loading / $mg \cdot cm^{-2}_{geo}$	η@10 $mA \cdot cm^{-2}_{geo}$ / mV	C_{dl} / $mF \cdot cm^{-2}_{geo}$	TOF / s^{-1} (@η or f)	Tafel Slope / $mV \cdot dec^{-1}$	Electrolyte	Pre-analysis	Post-analysis	Long-Term OER Test Conditions	Post-OER Electrocatalyst	Final Type of Electrocatalyst	Ref.
Co@0.3gNiCoTe$_2$-240	Co foam	Nanosheet	S	-	370	-	-	-		XRD, SEM	-	-	-	-	
Co@0.4gNiCoTe$_2$-240	Co foam	Nanosheet	S	-	380	-	-	-		XRD, SEM	-	-	-	-	
Co@0.2gNiCoTe$_2$-200	Co foam	Nanoparticle	S	-	310	-	-	-		XRD, SEM	-	-	-	-	1138
Co@0.2gNiCoTe$_2$-160	Co foam	Nanoparticle	S	-	410	-	-	-		XRD, SEM	-	-	-	-	
Co@CoTe$_2$-240	Co foam	Nanoparticle	S	-	330	12.6	-	42		XRD, SEM	-	18 h CP [10 (15 h), 20 $mA \cdot cm^{-2}_{geo}$ (3 h)]	-	-	
$NiTe_2$	Ni foam	Nanosheet	S	4.110	440	5.1	0.012 at 320 mV	102		XRD, SEM	-	10 h CA (1.48 V_{RHE})	-	-	
$Ni_{0.8}Fe_{0.2}Te_2$	Ni foam	Nanoflake	S	4.505	320	6.3	0.026 at 320 mV	53		XRD, SEM, EDX	-	-	-	-	
$Ni_{0.4}Fe_{0.6}Te_2$	Ni foam	Nanoflake	S	5.51	190	20.5	2.830 at 320 mV	26	1 M KOH	XRD, SEM, TEM, SAED, EDX, XPS	XRD, SEM, EDX, TEM, XPS (after 30 h CA)	1000 CV cycles (100 $mV \cdot s^{-1}$) 30 h CA (1.48 V_{RHE})	NiFeOOH(Te)	Precatalyst (partial oxidation)	1139
$Ni_{0.2}Fe_{0.8}Te_2$	Ni foam	Nanoflake	S	4.194	340	5.7	0.017 at 320 mV	71		XRD, SEM, EDX	-	-	-	-	
$FeTe_2$	Ni foam	Nano-/microparticle	S	3.710	360	4.5	0.028 at 320 mV	48		XRD, SEM, EDX	-	-	-	-	
NiTe@NiFe-LDH_{60s}	Ni foam	Furry T-shaped hierarchical nanorod	S	-	218	29.11	1.79×10^{-3} at 300 mV	32		XRD, SEM, EDX, TEM, SAED, XPS	XRD, SEM, EDX, XPS	2000 CV cycles 26 h CA (1.448 V_{RHE}) 27 h CP (10 $mA \cdot cm^{-2}_{geo}$, OWS)	NiFe-LDH, Te oxide	Precatalyst (partial oxidation)	
NiTe@RuO_2	Ni foam	Furry T-shaped hierarchical nanorod	S	-	274	19.97	3.33×10^{-4} at 300 mV	65		XRD, SEM, EDX, TEM, SAED, HAADF-STEM, XPS	-	15 h (1.504 V_{RHE})	-	-	
NiTe	Ni foam	Furry T-shaped hierarchical nanorod	S	-	387	2.06	1.51×10^{-5} at 300 mV	98		XRD, SEM, EDX	-	-	-	-	
NiTe@NiFe-LDH_{40s}	Ni foam	Furry T-shaped hierarchical nanorod	S	-	~237	-	-	43	1 M KOH	SEM	-	-	-	-	1140
NiTe@NiFe-LDH_{50s}	Ni foam	Furry T-shaped hierarchical nanorod	S	-	~237	-	-	36		SEM	-	-	-	-	
NiTe@NiFe-LDH_{90s}	Ni foam	Furry T-shaped hierarchical nanorod	S	-	~239	-	-	41		SEM	-	-	-	-	
NiTe@NiFe-LDH_{120s}	Ni foam	Furry nanorod	S	-	~246	-	-	45		SEM	-	-	-	-	
NiTe@NiFe-LDH_{150s}	Ni foam	Furry nanorod	S	-	~264	-	-	59		SEM	-	-	-	-	
$NiTe_2/Ni(OH)_2$-0.05	CFC	-	S	-	~323	-	-	-		-	-	-	-	-	
$NiTe_2/Ni(OH)_2$-0.1	CFC	3D interconnected nanosheet	S	1.38	267	4.29	-	75	1 M KOH	XRD, SEM, TEM, STEM, EDX, XPS	XRD, SEM, XPS	3000 CV cycles 30 h CA (1.497 V_{RHE})	$Ni(OH)_2$, Te oxide	Precatalyst (partial oxidation)	1141
$NiTe_2/Ni(OH)_2$-0.15	CFC	-	S	-	~291	-	-	-		-	-	-	-	-	
$NiTe_2$	CFC	3D interconnected nanosheet	S	-	~470	1.42	-	356		SEM	-	-	-	-	
Co@CoTe$_2$-200	Co foam	Ultrafine particle	S	1.01	286 318 (@50 mA/cm^{-2}_{geo}) 334 (@100 mA/cm^{-2}_{geo})	66.3	-	40.8	1 M KOH	XRD, SEM, TEM, EDX, HAADF-STEM	-	16 h CP [10 (15 h), 20 $mA \cdot cm^{-2}_{geo}$ (3 h)]	-	-	1142
Co@CoTe$_2$-240	Co foam	Ultrafine particle	S	4.76	284 317 (@50 mA/cm^{-2}_{geo}) 335 (@100 mA/cm^{-2}_{geo})	29.8	-	42.0		XRD, SEM, TEM, EDX, HAADF-STEM, XPS	XRD, SEM, TEM, EDX, XPS	16 h CP [10 (15 h), 20 $mA \cdot cm^{-2}_{geo}$ (3 h)]	CoOOH, TeO_2	Precatalyst (partial oxidation)	
CoTe	Ni foam	Nanorod array	S	1.3	350 (@100 mA/cm^{-2}_{geo})	16	-	75	1 M KOH	XRD, SEM, TEM, EDX, XPS, XANES	XRD, TEM, XPS, XANES	12 h CA (1.53 V_{RHE}) 12 h CA (1.70 V_{RHE})	CoOOH	Precatalyst (partial oxidation)	1143
NiTe	Ni foam	Nanorod array	S	-	430 (@100 mA/cm^{-2}_{geo})	10	-	122		XRD, SEM, TEM, EDX, XPS, XANES	XPS, XANES	12 h CA (1.53 V_{RHE})	NiOOH	Precatalyst	
CoTe:Fe (0.4 at.% Fe)	GC	-	P	~0.71	~370	1.39	-	84.3		XRD, XPS, ICP-AES	-	-	-	-	
CoTe:Fe (2.6 at.% Fe)	GC	Nanoparticle	P	~0.71	300	2.33	0.064 (@320 mV)	45	1 M KOH	XRD, EDX, TEM, XPS, ICP-AES	XRD, XPS	12 h CA (1.54 V_{RHE}) 1000 CV cycles (1.0–1.6 V_{RHE})	Fe-doped CoOOH, TeO_2	Precatalyst (partial oxidation)	1144
CoTe:Fe (5.3 at.% Fe)	GC	-	P	~0.71	~327	1.86	-	49.5		XRD, XPS, ICP-AES	-	-	-	-	
CoTe	GC	-	P	~0.71	445	0.77	0.003 (@320 mV)	93.1		XRD, XPS, ICP-AES	-	-	-	-	
Ni_3Te_2-CoTe	CC	Nanosheet	S	~0.25	~320 [392 (@100 mA/cm^{-2}_{geo}), 454 (@300 mA/cm^{-2}_{geo})]	7.47	-	68	1 M KOH	XRD, SEM, TEM, XPS	XPS	1000 CV cycles	NiOOH, CoOOH, TeO_2	Precatalyst	1145
Ni_3Te_2	CC	-	S	-	~336 [~461 (@100 mA/cm^{-2}_{geo})]	0.4	-	106		XRD	-	-	-	-	

https://doi.org/10.1021/acs.chemrev.3c00005
Chem. Rev. 2023, 123, 12795−13208

Table 7. continued

Initial Electrocatalyst	Substrate	Shape of Electrocatalyst	Deposition Type	Specific Loading / $mg \cdot cm^{-2}_{geo}$	η@10 $mA \cdot cm^{-2}_{geo}$ / mV	C_{dl} / $mF \cdot cm^{-2}_{geo}$	TOF / s^{-1} (@η or j)	Tafel Slope / $mV \cdot dec^{-1}$	Electrolyte	Pre-analysis	Post-analysis	Long-Term OER Test Conditions	Post-OER Electrocatalyst	Final Type of Electrocatalyst	Ref.
CoTe	CC	-	S	-	~395	21	-	91		XRD	-	-	-	-	1145
$CoTe_2$	Ni foam	Nanoparticle	S	1.24 ± 0.19	310	4.2	-	54	1 M KOH	XRD, SEM, EDX, XPS	SEM, XPS (after 40 h CA)	40 h CA (1.60 V_{RHE}) 2000 CV cycles (1.0–1.6 V_{RHE})	Oxidized Co species (maybe CoOOH), TeO_x	Precatalyst	1146
$CoTe_2$	Ti mesh	Nanowire array	S	1.45	~300 [340 (@50 $mA \cdot cm^{-2}_{geo}$)]	247.8	-	67	1 M KOH	XRD, SEM, EDX, TEM, XPS	XRD, SEM, XPS	25 h CA (1.55 V_{RHE})	Oxidized Co species (maybe CoOOH), TeO_x	Precatalyst (partial oxidation)	1147
NiTe	Ni foam	Nanosheet array	S	2.8	262	29.3	0.324 (@400 mV)	74	1 M KOH	XRD, SEM, TEM, XPS, ICP-OES	XRD, SEM, TEM, XPS, ICP-OES	35 h CA (1.59 V_{RHE}) 1000 CV cycles	NiOOH, TeO_x	Precatalyst (partial oxidation)	1148
$NiTe_2$	Ti mesh	Nanosheet array	S	0.95	315	32.2	-	82	1 M KOH	XRD, SEM, EDX, TEM, XPS, Raman, ICP-OES	XRD, SEM TEM, XPS, Raman, ICP-OES	24 h CA (1.571 V_{RHE})	NiOOH, TeO_x	Precatalyst (partial oxidation)	1149
$CoTe_2$ (ECT-Te-CoO)	CFC	Nanosheet	S	-	343	58	-	64.2	1 M KOH	XRD, SEM, EDX, TEM	XRD, SEM, EDX, TEM, XPS (after CV oxidation)	~25 h CP (20 $mA \cdot cm^{-2}_{geo}$)	CoOOH	Precatalyst (partial oxidation)	97
$Co_{0.5}Fe_{0.5}Te_2$ (ECT-Te-$Co_{0.5}Fe_{0.5}O$)	CFC	Nanosheet	S	-	326	-	-	39.3		-	-	~20 h CP (20 $mA \cdot cm^{-2}_{geo}$)	-	-	
$Co_{0.37}Ni_{0.26}Fe_{0.37}Te_2$ (ECT-Te-$Co_{0.37}Ni_{0.26}Fe_{0.37}O$)	CFC	Nanosheet	S	-	276	-	-	49.6		TEM	SEM, TEM (after CV oxidation)	~40 h CP (20 $mA \cdot cm^{-2}_{geo}$)	-	-	
$CoTe_2$	GC	Nanocrystalline	P	0.28	380	-	0.021 (@300 mV)	58	1 M KOH	XRD, SEM, EDX, TEM, UV-Vis, XPS, Raman, ICP-OES	XPS (after 2 and 100 CV), ICP-OES (during 4 h CA)	24 h CP (0.5 $mg \cdot cm^{-2}_{geo}$) 1000 CV cycles	CoO_x	Precatalyst	1150
NiTe@NF	Ni foam	Nanosheet	S	1.2	199.5	-	-	84.4	1 M KOH	XRD, SEM, EDX, XPS	-	-	-	-	1151
NiTe	Ni foam	Nanorod array	S	-	339	13.8	0.005 at 300 mV	124.9	1 M KOH	XRD, SEM, TEM, CAM	-	-	-	-	363
					~317	-	-	-	1 M KOH + Seawater		-	-	-	-	
Fe-NiTe	Ni foam	Nanosheet array	S	-	437 (@50 $mA \cdot cm^{-2}_{geo}$)	3.0	-	135	1 M KOH	XRD, SEM, TEM, XPS	-	-	-	-	1152
NiTe	Ni foam	Nanosheet array	S	-	472 (@50 $mA \cdot cm^{-2}_{geo}$)	1.6	-	196		XRD, SEM	-	-	-	-	
Fe-$NiTe_2$	Ni foam	-	S	-	270	8.3	-	173	1 M KOH	-	-	-	-	-	529
NiTe	Ni foam	Rod-shaped nanoarray	S	-	389	2.83	-	131	1 M KOH	XRD, SEM, TEM, HAADF, EDX, XPS	-	-	-	-	1032
$CoTe_2$	CP	Nanowire	P	2	362	-	~0.0014 at 350 mV	~50	1 M NaOH	XRD, SEM, XPS, TEM, EDX, HAADF-STEM	-	15 h CP (10 $mA \cdot cm^{-2}_{geo}$)	-	-	532
CoTe	CC	Nanorod	S	-	315 400 (@100 $mA \cdot cm^{-2}_{geo}$)	35.95	-	87	1 M KOH	XRD, SEM, TEM, EDX, XANES, XPS	-	-	-	-	1153
Fe/Ni-CoTe@NCF	GC	Nanoparticles	P	-	287	11.12	-	52.3	1 M KOH	XRD, SEM, TEM, EDX, N_2 ISO (BET, PSD), XPS	-	-	-	-	1154
Fe-CoTe@NCF	GC	-	P	-	351	2.16	-	62.2		-	-	-	-	-	
CoTe	GC	-	P	-	390	1.15	-	107.4		-	-	-	-	-	
o-$CoTe_2$@HPC/CNTs	GC	-	P	-	361	3.1	~0.0015 at 295 mV	93	1 M KOH	XRD, XPS, N_2 ISO (BET)	-	CV activation (50 $mV \cdot s^{-1}$)	-	-	1155
h-$CoTe_2$@HPC/CNTs	GC	Rambutan-like structure	P	-	308	5.7	~0.004 at 295 mV	62		XRD, EPR, XPS, XAS (XANES, EXAFS), FESEM, TEM, HAADF, EDX, Raman, N_2 ISO (BET)	-	CV activation (50 $mV \cdot s^{-1}$)	-	-	
NiTe	CC	-	P	0.21	400	-	0.010 ($s^{-1} \cdot mol^{-1}$) metal loading, 0.269 ($s^{-1} \cdot mol^{-1}$) Ni^{2+}/Ni^{3+}	66	1 M KOH	XRD, EDX, XPS, ICP-MS	-	100 CV cycles (1.0–1.6 V_{RHE})	-	-	177
CoTe@NC	Ni foam	Nanoparticle	P	0.5	356	0.00032	-	112	1 M KOH	XRD, EDX, TEM, XPS	-	15 h CP (10 $mA \cdot cm^{-2}_{geo}$)	-	-	682
NiTe/rGO	Ni foam	Plate + Particle + Rod	S	~3	410 (@50 $mA \cdot cm^{-2}_{geo}$)	33.1 (in 1 M KOH + 0.33 M urea)	-	-	1 M KOH	XRD, SEM, EDX, TEM, XPS, Raman	-	-	-	-	1156
$NiTe_2$	Ni foam	Plate + Particle + Rod	S	~3	450 (@50 $mA \cdot cm^{-2}_{geo}$)	6.9 (in 1 M KOH + 0.33 M urea)	-	-		XRD, SEM, TEM, XPS	-	-	-	-	
NiTe	Ni foam	Nanoarray	S	1.5	403 (@100 $mA \cdot cm^{-2}_{geo}$)	7.9	0.005 (@300 mV)	130	1 M KOH	XRD, FESEM, TEM, XPS, XANES	-	-	-	-	763
NiTe	Cu foil	Nanorod	P	-	516	0.46	-	155	1 M KOH	XRD, SEM, TEM, EDX, FTIR, XPS	-	-	-	-	1157
PdTe	Cu foil	Nanocube	P	-	-	-	-	270				-	-	-	
NiTe-PbNiTe (1.0 g)	Cu foil	Nanorod	P	-	387	1.17	-	96				12 h CP (10 $mA \cdot cm^{-2}_{geo}$) 1000 CV cycles (1.16–2.36 V_{RHE})	-	-	
Zn-Co-Te ($CoTe_2$-ZnTe)	Pencil graphite	Nanorod	P	1.280	221	-	-	91	5 M KOH (pH = 15.14)	XRD, FESEM	-	1000 CV cycles 3 month storage test (no bias)	-	-	1054
$CoTe_2$-$MnTe_2$	Ti mesh	Nanowire array	S	1.96	310 (@50 $mA \cdot cm^{-2}_{geo}$)	73	-	118	1 M KOH	XRD, SEM, EDX, TEM, XPS, ICP-AES	SEM (after 1000 CV)	60 h CA (1.55 V_{RHE}) 1000 CV cycles	-	-	1158
$CoTe_2$-$MnTe_2$	CC	Nanowire array	S	-	317 (@50 $mA \cdot cm^{-2}_{geo}$)	-	-	-		SEM	-	-	-	-	
$MnTe_2$	Ti mesh	Poor nanoarray	S	-	417 (@50 $mA \cdot cm^{-2}_{geo}$)	-	-	-		SEM	-	-	-	-	

https://doi.org/10.1021/acs.chemrev.3c00005
Chem. Rev. 2023, 123, 12795−13208

Table 7. continued

Initial Electrocatalyst	Substrate	Shape of Electrocatalyst	Deposition Type	Specific Loading / mg·cm$^{-2}_{geo}$	η@10 mA·cm$^{-2}_{geo}$ / mV	C_{dl} / mF·cm$^{-2}_{geo}$	TOF / s^{-1} (@η or j)	Tafel Slope / mV·dec^{-1}	Electrolyte	Pre-analysis	Post-analysis	Long-Term OER Test Conditions	Post-OER Electrocatalyst	Final Type of Electrocatalyst	Ref.
$CoTe_2$	Ti mesh	Nanowire array	S	-	490 (@50 mA·cm$^{-2}_{geo}$)	-	-	-	1 M KOH	SEM	-	-	-	-	1158
CoTe	Ni disk	-	P	0.21	330 (@1 mA·cm$^{-2}_{geo}$)	-	-	-		XRD	-	-	-	-	184
CoTe$_2$@NCNTFs	GC	Nanoparticle	P	0.285	330	25.73	-	82.8		XRD, SEM, EDX, TEM, XPS, Raman	-	35 h CP 2000 CV cycles (1.10–1.70 V_{RHE})	-	-	1159
CoTe$_2$@NC	GC	Nanoparticle	P	0.285	350	14.74	-	94.9		XRD, Raman	-	-	-	-	
$CoTe_2$	GC	Bulk	P	0.285	460	4.21	-	153.1		XRD, SEM	-	-	-	-	
CoTe	FTO	Nanotube	S	0.9	420	-	-	-		XRD, SEM, XPS	-	-	-	-	
CoTe-100	FTO	Nanotube	S	1.09	380	-	-	-		XRD, SEM	-	-	-	-	
CoTe-200 (TeO_2 exists on the surface.)	FTO	Nanotube	S	0.7	370	-	-	-	1 M KOH	XRD, SEM, TEM, XPS	-	5 h CP (10 mA·cm$^{-2}_{geo}$)	-	-	1160
CoTe-300	FTO	Nanotube	S	1.18	430	-	-	-		XRD, SEM	-	-	-	-	
CoTe-400	FTO	Nanotube	S	0.81	480	-	-	-		XRD, SEM	-	-	-	-	
NiTe-$NiTe_2$-$Ni(OH)_2$	Graphite rod	Nanosheet	P	~0.49	679	-	-	115	1 M KOH	XRD, SEM, EDX, TEM, XPS	-	2 h CP (+50 mA)	-	-	1161
CoTe	Ti foil	Nanotubular	S	-	370	-	-	-	1 M KOH	XRD, SEM, EDX, TEM, UV-Vis, XPS	-	5 h CA (1.60 V_{RHE})	-	-	1162

[a]Some values (i.e., "specific loading", "η", and "C_{dl}") were calculated or obtained from the descriptions and figures in the previous papers. "Post-OER Electrocatalyst" and "Final Type of Electrocatalyst" were determined based on the experimental results and descriptions provided in the previous papers. [b]η, overpotential; j, current density; C_{dl}, double layer capacitance; TOF, turnover frequency; P, powder-coated electrode; S, self-supported electrode; CV, cyclic voltammetry; CA, chronoamperometry; CP, chronopotentiometry; OWS, overall water splitting. [c]Substrate abbreviations: GC (glassy carbon); CC (carbon cloth); CP (carbon paper); CFC (carbon fiber cloth); CFP (carbon fiber paper); FTO (fluorine-doped tin oxide). [d]Analysis abbreviations (minor terms only): ISO (isotherm); PSD (pore size distribution); sXAS (soft X-ray absorption spectroscopy).

electrodeposition,[97] with various tellurium sources, resulting in the formation of transition metal tellurides. Besides the above-described transition metal-based precursors, Te precursors prepared by the hydrothermal method,[1129,1130] solvothermal method,[1157] and solution-based method[1144] were also used in the two-step fabrication processes.[1129,1130,1144,1157] Importantly, both the metal-based and Te precursors tend to act as self-sacrificed templates, and the resultant metal tellurides maintain the geometry of their precursors to some extent. Furthermore, to avoid the laborious procedures of two-step approaches, transition metal telluride OER electrocatalysts were also synthesized through several one-step approaches such as the hydrothermal method (refs 101, 763, 1041, 1054, 1127, 1145, 1146, and 1148), solid-state reaction,[177,184] gas-solid reaction,[1156] electrodeposition,[101] solution-based method,[1133] and solvothermal method.[1130] In this section, we briefly discuss the typical strategies used to synthesize transition metal tellurides and introduce examples of transition metal tellurides prepared via these methods.

5.3.1.1. Hydrothermal Methods. The hydrothermal method has been involved in both the two-step and one-step approaches, which are suited for the preparation of transition metal tellurides with nanostructures. So far, in the two-step approaches, the hydrothermal preparation of the transition-metal-based precursors has been the most popular.[1132,1147,1149,1158,1160,1161] For example, Bhat *et al.* reported the fabrication of $NiTe/NiTe_2$ nanosheets through the hydrothermal anion exchange transformation (tellurization) of hydrothermally grown hexagonal $Ni(OH)_2$ nanosheets (Figure 262a).[1161] $Ni(OH)_2$ powder (Figure 262b) reacted with Te^{2-} in a Teflon-lined stainless steel autoclave with NaHTe aqueous solution (solute: Te powder and $NaBH_4$) and $Ni(OH)_2$@$NiTe/NiTe_2$ core@shell powder with hollow interiors formed (Figure 262c).[1100] Notably, the as-formed $NiTe/NiTe_2$ nanosheets were porous, providing a relatively large catalytic surface for the OER.[1161] Recently, Wang *et al.* developed a similar two-step hydrothermal approach to fabricate 3D porous $NiTe_2$ nanosheet arrays anchored on Ti mesh through topotactic transformation from $Ni(OH)_2$ nanoarrays (Figure 262d), which may produce more electrocatalytic OER active sites and provide fast mass transfer pathways. Metal hydroxyl-fluoride can also be used instead of metal hydroxide as a precursor in the two-step hydrothermal process.[1132,1147] As seen in Figure 262e, hollow $CoTe_2$ nanowire arrays were also fabricated directly on Ti mesh through topotactical conversion from hydrothermally grown Co(OH)F nanoarrays through hydrothermal tellurization.[1147]

In addition to the transition metal-based precursors, Te precursors were also prepared via the hydrothermal method.[1129,1130] Gao *et al.* synthesized ultrathin Te nanowires (precursor/template) via a hydrothermal method. Subsequently, the Te nanowires were converted into hierarchical $CoTe_2$ nanofleeces through a polyol reduction approach (see Figure 263a–e); $CoTe_2$ hierarchical structures uniformly formed from Te wires (see Figure 263f). Furthermore, by changing the polyol reduction conditions (i.e., heating temperature and Co source concentration), CoTe nanofleeces can also be fabricated (see Figure 263g). Similarly, Qin *et al.* also prepared Te nanorods (precursor) using a hydrothermal method.[1130] As illustrated in Figure 263h, ultrathin Cu_7Te_4 nanosheets with 2.1 nm thickness were formed from the Te nanorod surface through an ionic liquid-assisted ionothermal route. This process can be divided into two stages: (1)

https://doi.org/10.1021/acs.chemrev.3c00005
Chem. Rev. 2023, 123, 12795−13208

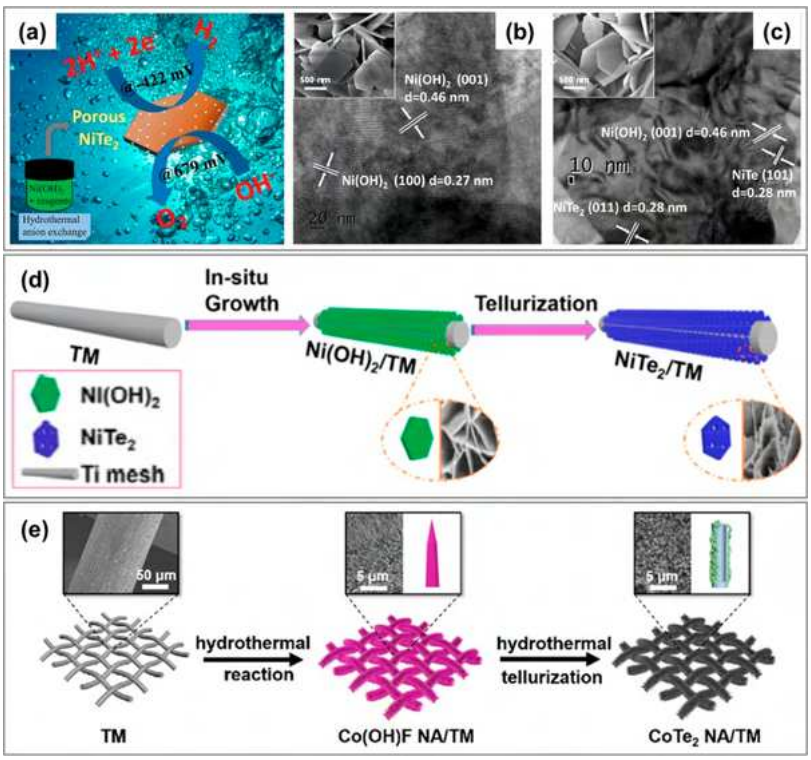


Figure 262. (a) Schematic illustration for the fabrication process of porous nickel telluride hexagonal nanosheets. (b, c) Corresponding (inset) FESEM and TEM images of (b) nickel hydroxide and (c) nickel telluride nanosheets. Reproduced with permission from ref 1161. Copyright 2017 Elsevier. (d) Schematic illustration for the direct growth of a porous $NiTe_2$ nanosheet array on Ti mesh. Reproduced with permission from ref 1149. Copyright 2018 Wiley. (e) Schematic illustration of the direct growth of a hierarchical $CoTe_2$ nanowire array on Ti mesh. Reprinted with permission from ref 1147. Copyright 2018 American Chemical Society.

transformation of Te nanorods into Cu_7Te_4 nanoplates via a dissolution−recrystallization process and (2) ionic liquid-assisted exfoliation of Cu_7Te_4 nanoplates to Cu_7Te_4 nanosheets and their dispersion.

In most of the reports using one-step approaches, the metal tellurides were synthesized through hydrothermal methods using different Te sources (i.e., $NaTeO_3$,[763,1145,1146] TeO_2,[101] and Te[1041,1054,1127,1148]). As illustrated in Figure 264a, a $CoTe_2$ nanofilm was directly introduced onto Ni foam through a one-step hydrothermal process using Na_2TeO_3 and $Co(NO_3)_2$ as Te and Co sources, respectively.[1146] In this process, hydrazine hydrate acts as the reducing agent to produce Te ions. The as-obtained $CoTe_2$ nanofilm had a random particulate shape (see Figures 264b and c). Xue *et al.* also reported the direct growth of NiTe nanoarrays on Ni foam via a similar one-step hydrothermal reaction (Ni source: Ni foam; Te source: Na_2TeO_3).[763] Furthermore, a Ni_3Te_2-CoTe composite film was grown directly on carbon cloth by a one-step hydrothermal method (see Figures 264d and e). Figure 264f shows that the as-grown Ni_3Te_2-CoTe composite possessed nanosheet structures. Accordingly, in the one-step hydrothermal method using Na_2TeO_3, Ni-based tellurides may be more favorable for obtaining ordered shapes (i.e., nanoarrays, nanosheets, etc.) than Co tellurides. Recently, it was revealed that the use of electrodes with ordered shapes is effective for achieving high activity for electrochemical water splitting. For example, according to previous studies,[1163,1164] nanoarray structures can facilitate the electrolyte penetration as well as the diffusion of ionic species. Moreover, as reported by Qin and co-workers,[1130] nanosheet structures are more advantageous for efficient oxygen evolution than bulk structures, possibly due to their larger specific surface area. Presumably, nanosheet structures can also provide sufficient space for mass transfer and gas bubbles.[1130] However, in the one-step hydrothermal process, the relationship between final structure, synthetic conditions, and metal telluride properties (i.e., used transition metal(s) and final crystal structure) is still elusive. For future electrode design, systematic studies about the one-step hydrothermal method are much desired.

5.3.1.2. Solution-Based Methods. One of the most facile and environmentally friendly routes for fabricating transition metal telluride films is a solution-based approach.[1133,1162] Patil *et al.* reported the two-step solution-based direct growth of nanostructured CoTe films on FTO glass and Ti foil substrates using less hazardous chemicals.[1162] First, Co hydroxy-carbonate precursor films were prepared from an aqueous solution containing Co precursor [i.e., $Co(NO_3)_2$, $CoCl_2$, or $Co(C_5H_7O_2)_2$] and urea through the solution-based chemical reaction:

$$NH_2CONH_2 + 3H_2O + Co^{2+} \rightarrow Co(OH)_x(CO_3)_y + 2NH_4^+ \quad (8)$$

As displayed in Figure 265a, the as-prepared Co hydroxy-carbonate films were immersed in the tellurium precursor solution (solute: Te powder, NaOH, and rongalite). In this solution, the hydroxy-carbonate films were transformed into nanostructured CoTe films at room temperature, as described below:

$$Co(OH)_x(CO_3)_y + Te^{2-} \rightarrow CoTe + xH_2O + yCO_2 \quad (9)$$

https://doi.org/10.1021/acs.chemrev.3c00005
Chem. Rev. 2023, 123, 12795−13208

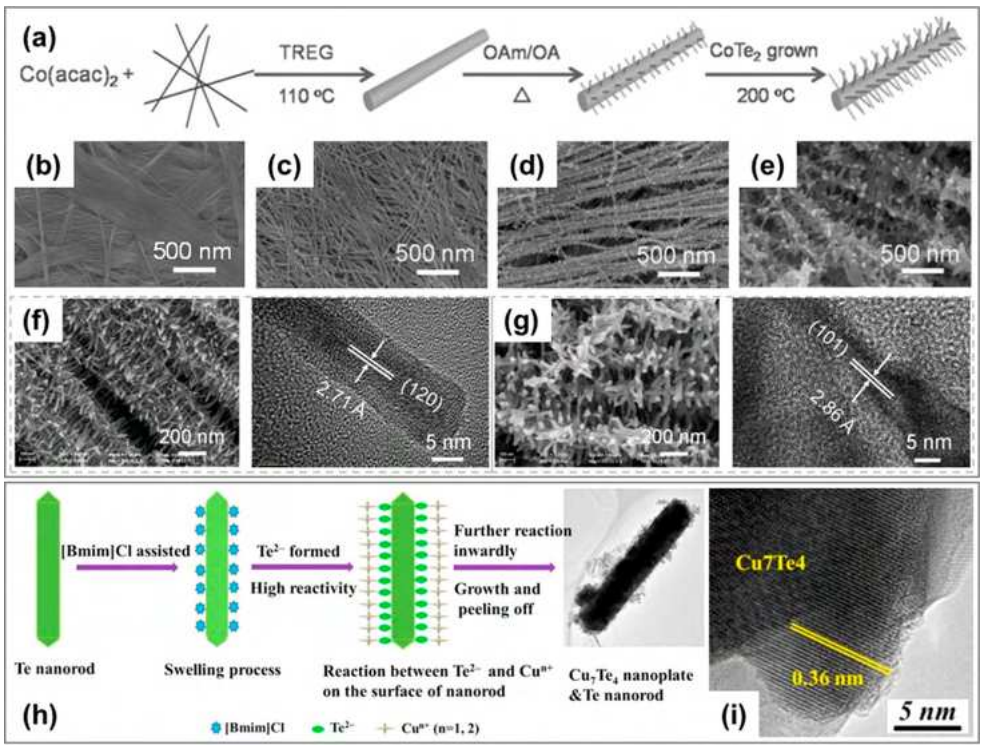


Figure 263. (a) Schematic illustration for the proposed mechanism of hierarchical $CoTe_2$ nanostructure growth. (b–d) SEM images of (b) ultrathin Te nanowires and the products obtained at (c) 110 °C for 60 min and 200 °C for (d) 0 and (e) 120 min. (f, g) SEM and HRTEM images of hierarchical $CoTe_2$ (f) and CoTe (g) nanostructures. Reproduced with permission from ref 1129. Copyright 2017 Wiley. (h) Schematic illustration for the formation of Cu_7Te_4 nanoparticles on the surface of Te nanorods through a dissolution–recrystallization mechanism. (i) HRTEM image of the intermediate product obtained at the reaction time of 2 h. Reproduced with permission from ref 1130. Copyright 2017 Elsevier.

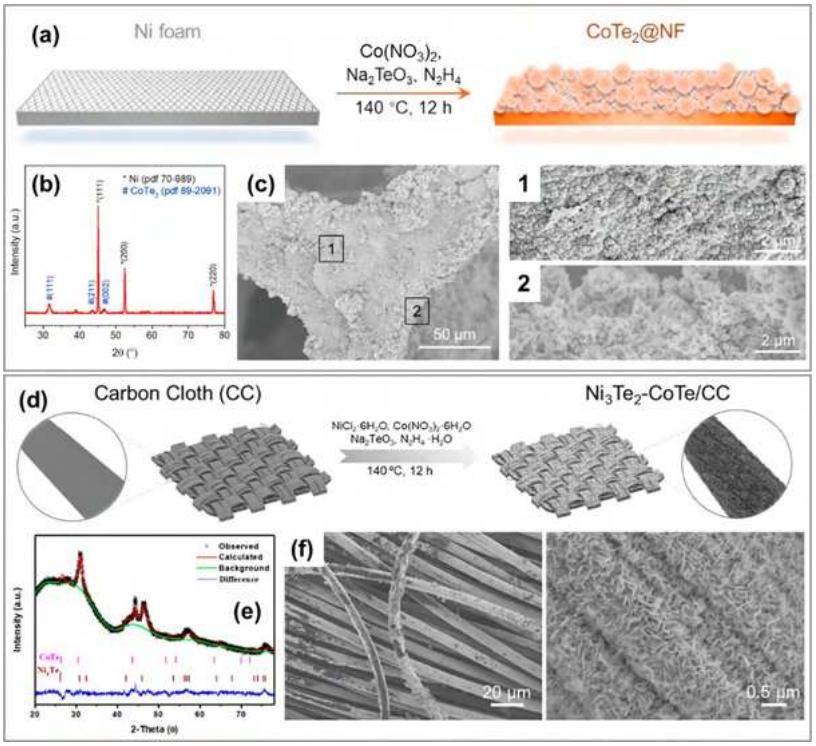


Figure 264. (a) Schematic illustration for the direct growth of $CoTe_2$ nanofilm on Ni foam. (b) XRD pattern and (c) SEM images of $CoTe_2$ on Ni foam. (d) Schematic illustration for the direct growth of the Ni_3Te_2-CoTe nanosheet structure on carbon cloth. (e) XRD pattern and (f) SEM images of Ni_3Te_2-CoTe on carbon cloth. Reproduced with permission from refs 1146 1145. Copyright 2019 Elsevier.

https://doi.org/10.1021/acs.chemrev.3c00005
Chem. Rev. 2023, 123, 12795–13208

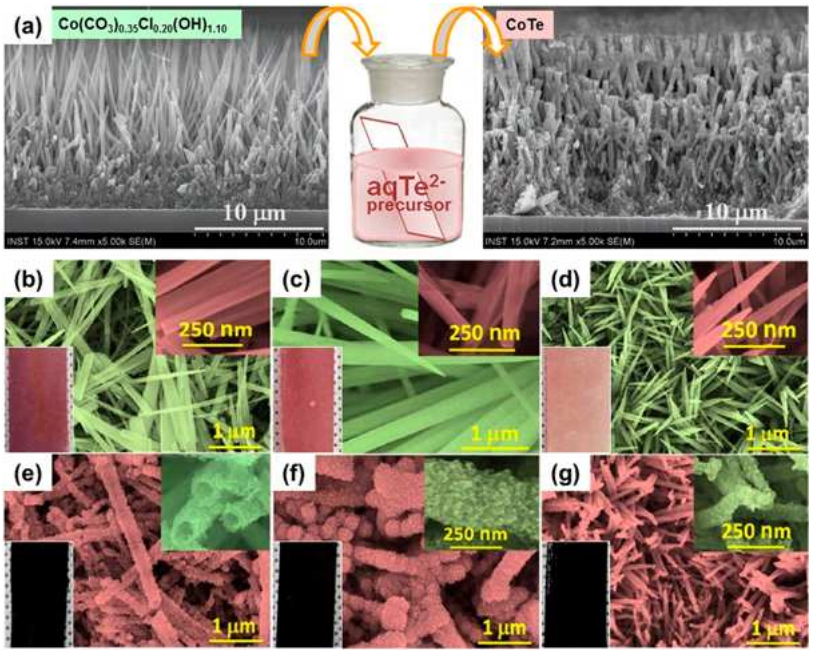


Figure 265. (a) Cross-sectional SEM images of cobalt hydroxycarbonate film (fabricated using $CoCl_2$ precursor) and nanotubular CoTe film after their anion exchange transformation reactions. (b–g) FESEM images and optical views of cobalt hydroxycarbonate films on FTO glass substrates from (b) $CoCl_2$, (c) $CoNO_3$, and (d) $Co(C_5H_7O_2)_2$ precursors and (e–g) corresponding CoTe nanotubes. Reproduced with permission from ref 1162. Copyright 2015 American Chemical Society.

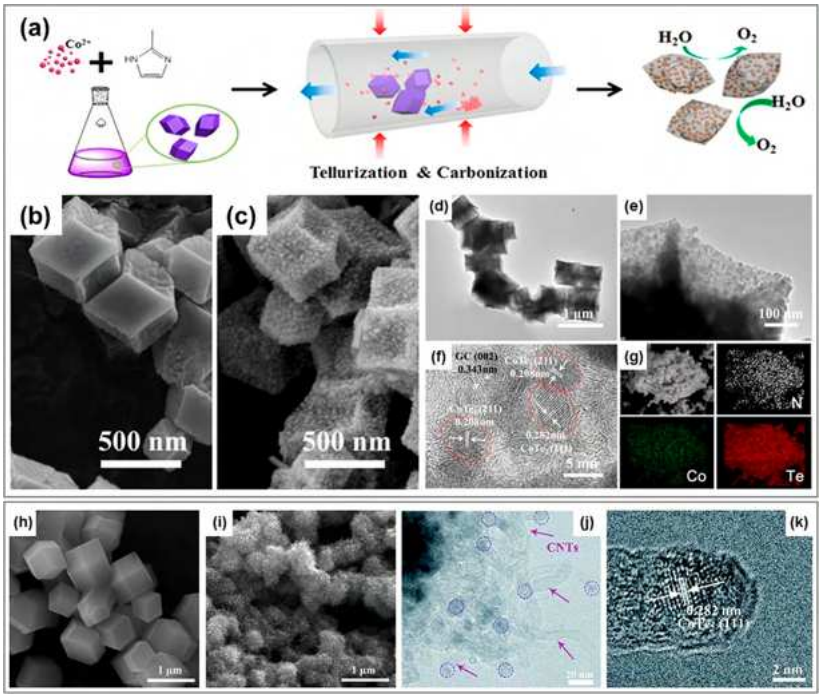


Figure 266. (a) Schematic illustration for the fabrication of $CoTe_2$ nanocrystals embedded in an N-doped graphitic carbon matrix ($CoTe_2$@N-GC). (b, c) SEM images of (b) ZIF-67 and (c) $CoTe_2$@N-GC. (d, e) TEM, (f) HRTEM, and (g) SEM-EDX elemental mapping images of $CoTe_2$@N-GC. Reproduced with permission from ref 1128. Copyright 2017 American Chemical Society. (h, i) SEM images of (h) ZIF-67 and (i) $CoTe_2$ nanoparticles encapsulated in N-doped carbon nanotube frameworks ($CoTe_2$@NCNTFs). (j) TEM and (k) HRTEM images of $CoTe_2$@NCNTFs. Reproduced with permission from ref 1159. Copyright 2018 Royal Society of Chemistry.

Interestingly, the resultant morphologies of the hydroxycarbonate films depend on the different cobalt precursors. For example, when using $CoCl_2$, a nanobeam-like structure was obtained (Figure 265b). On the other hand, nanobelt-like structures were observed when using $CoNO_3$ and $Co(C_5H_7O_2)_2$ (Figures 265c and d). These morphological differences can be explained by variation in the affinities of different counterions to Co ions in Co precursors (i.e., Cl^- > NO^{3-} > $C_5H_7O^{2-}$),[1165] which may change the local concentration of Co ions available for the reaction (eq

https://doi.org/10.1021/acs.chemrev.3c00005
Chem. Rev. 2023, 123, 12795–13208

8).[1162] After tellurization, all the CoTe films showed hollow tube-like nanostructures with rough surfaces (see Figures 265e–g), which took over the outward appearance of their hydroxy-carbonate precursors to some extent. Accordingly, by following the as-presented solution-based method, we may be able to precisely tailor the resultant metal telluride film's morphologies by (1) further exploring potential metal precursors and (2) mixing the known metal precursors for synthesizing their metal hydroxy-carbonate precursor films, which need to be studied in the future.

Additionally, Tao *et al.* prepared $NiCo_2Te_4$ nanoclusters via a one-pot solution-based approach.[1133] $Ni(C_5H_7O_2)_3$, $Co(C_5H_7O_2)_3$, oleic acid, oleylamine, and benzyl ether were mixed by magnetic stirrer in a three-necked flask under N_2 flow. The mixture-containing flask was heated to 200 °C for 30 min. Subsequently, trioctylphosphine telluride with oleic acid was quickly added in the mixture heated at 275 °C. Then, the as-prepared mixture was further heated at 265 °C for 10 min and cooled down to room temperature. After washing and centrifuging, the $NiCo_2Te_4$ nanocluster sample was obtained as a precipitate.

5.3.1.3. MOF-Derived Methods. The use of metal-organic frameworks (MOFs) as precursors is a strategy to fabricate composites of metal telluride nanomaterials and carbon materials,[682,1128,1159] which may be able to enhance the specific surface areas of metal tellurides. For instance, 2-methylimidazole cobalt salt [zeolitic imidazolate framework-67 (ZIF-67)] was used as a precursor in $CoTe_2$ nanoparticle fabrication. Specifically, ZIF-67 was thermally tellurized into $CoTe_2$ nanocrystals embedded in an N-doped graphitic carbon matrix ($CoTe_2$@N-GC). ZIF-67 and Te powder were placed in two separate boats in a tube furnace and were heated at 450 °C for 6 h under mixed H_2 and Ar (5% H_2) (see Figure 266a). As seen in Figures 266b and c, after the thermal tellurization, the as-obtained $CoTe_2$@N-GC maintained the outward appearance of ZIF-67. From the TEM and SEM-EDX elemental mapping images (Figures 266d–g), it was confirmed that $CoTe_2$ nanocrystals with a diameter of 10–30 nm were evenly dispersed in the 3D matrix of N-GC. Wang and co-workers, on the other hand, observed a change in electrocatalyst morphology when synthesizing $CoTe_2$ nanoparticles encapsulated in N-doped carbon nanotube frameworks ($CoTe_2$@NCNTFs) by using a ZIF-67 precursor (see Figure 266h) under different thermal tellurization conditions [700 °C for 2 h under a mixed H_2 and Ar (10% H_2)].[1159] As demonstrated in Figures 266i–k, the resultant product possesses an urchin-like polyhedral shape that consists of short carbon nanotubes (*ca.* 20 nm in length) connected to carbon-coated $CoTe_2$ nanoparticles. The use of a different MOF precursor results in a different shape of the metal telluride and carbon composite. Sivanantham *et al.* tellurized a Co-based Prussian blue analogue (PBA) precursor using Te powder in a Swagelok reactor (500 °C for 3 h) and obtained CoTe@nanocarbon core@shell particles with a core size of ~25 nm and carbon shell thickness of ~3 nm.[682] Taken together, the use of MOFs emerges as one of the effective ways to fabricate metal telluride and carbon material composites with unique shapes. More MOF precursors and tellurization conditions should be explored to further understand how these experimental choices can effectively be used to tune composite morphology.

5.3.1.4. Solvothermal Methods. The solvothermal method was used in both the two- and one-step approaches.[1130,1157] For instance, Wang *et al.* fabricated bimetallic telluride (NiTe-PbNiTe) via chemical conversion from solvothermally grown Te nanorods (see Figures 267a and b).[1157] In the first step, Te

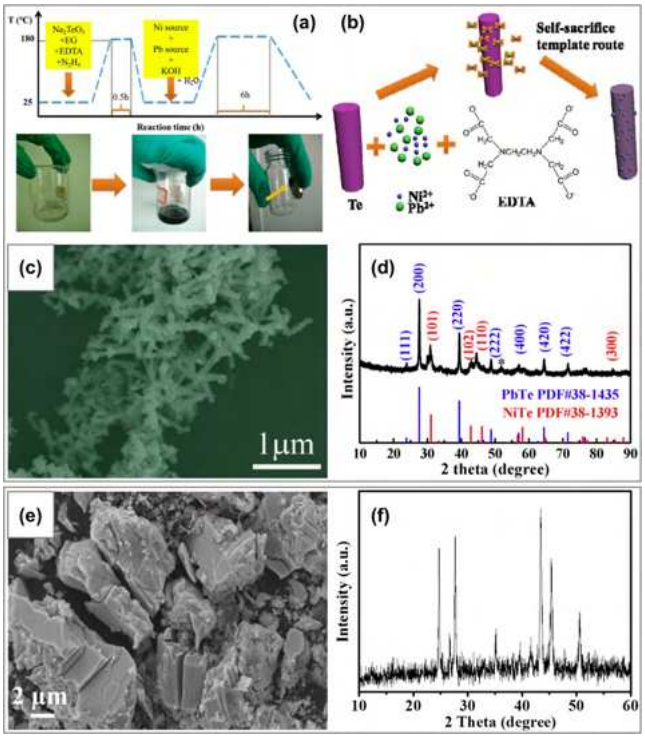


Figure 267. (a) Preparation scheme of NiTe-PbNiTe nanorods. (b) Schematic illustration of the proposed mechanism of NiTe-PbNiTe nanorod growth. (c) SEM image and (d) XRD pattern of NiTe-PdNiTe nanorods (atomic ratio $I_{Ni:Pd}$ = 4.8:1). Reproduced with permission from ref 1157. Copyright 2019 Elsevier. (e) SEM image and (f) XRD pattern of bulk Cu_7Te_4. Reproduced with permission from ref 1130. Copyright 2017 Elsevier.

nanorods with smooth surfaces were synthesized by a solvothermal method. In the second step, Pd^{2+} and Ni^{2+} ions from the added Pd and Ni sources were reduced into Pd and Ni on the Te nanorod surface as the reaction mixture was heated and hydrazine was added. Ni and Pb sources also reacted with ligand ethylenediaminetetraacetic acid (EDTA), forming $[Pb(EDTA)]^{2-}$ and $[Ni(EDTA)]^{2-}$ complexes. At the holding temperature (180 °C), these complexes could accelerate the formation of Pd and Ni ions. Then, the as-formed Pd and Ni ions diffused into the Te template matrix, forming NiTe and PdTe. Consequently, as shown in Figures 267c and d, NiTe-PbNiTe nanorods with rough surfaces, which contain minor amounts of Ni (marked by *), were obtained via the Te template process. Qin *et al.* reported the simple solvothermal synthesis of bulk Cu_7Te_4.[1130] Cu powder and Te powder were added into the mixture of deionized water and ethylene glycol. The as-prepared solution was transferred into a stainless-steel autoclave, heated to 200 °C for 24 h, and cooled to room temperature. After washing and drying, bulk Cu_7Te_4 was obtained. The SEM image of the as-obtained sample confirmed relatively large particles with undefined shapes (see Figure 267e). As shown in Figure 267f, XRD analysis revealed the formation of hexagonal Cu_7Te_4 as a main phase.

5.3.1.5. Solid-State/Gas-Solid Reactions. Solid-state and gas-solid reactions are quite simple one-step approaches, since

https://doi.org/10.1021/acs.chemrev.3c00005
Chem. Rev. 2023, 123, 12795–13208

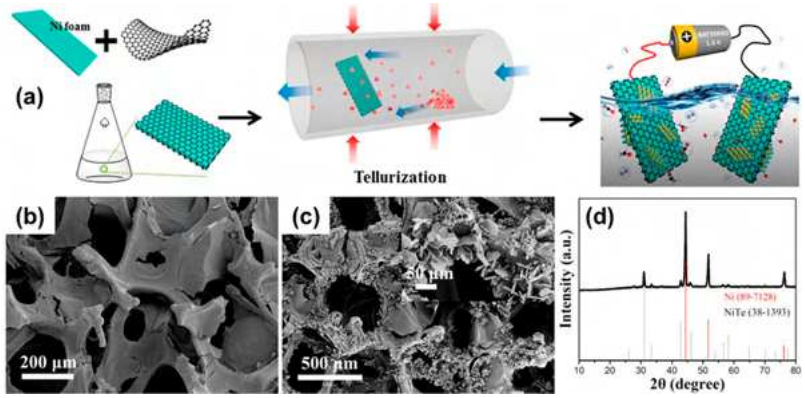


Figure 268. (a) Schematic illustration for the direct fabrication of NiTe composited with reduced graphene oxide (NiTe/rGO) on Ni foam. (b, c) SEM images of (b) graphene oxide (GO) coated Ni foam and (c) NiTe/rGO on Ni foam. (d) XRD pattern of NiTe/rGO on Ni foam. Reproduced with permission from ref 1156. Copyright 2019 American Chemical Society.

the as-purchased chemicals or substrates can be used as transition metal-based precursors. Notably, in the one-step approaches, the second most common approach is solid-state reaction.[177,184] In the method reported by the Schuhmann group,[177,184] transition metal powder and Te powder are installed in an ampoule. The as-prepared ampoule was heated to 800 °C and held at this temperature for 2 h. Subsequently, the preheated ample was further heated to 1100 °C, held at this temperature for 15 h, and then cooled to room temperature. Consequently, one can obtain the metal telluride product in the form of a metallic ingot. To use the as-obtained sample as an electrocatalyst, the ingot was finely ground into a powder. Through this process, CoTe and NiTe were prepared as OER electrocatalysts.[177,184]

The gas-solid reaction approach is an advanced variation of the solid-state reaction method. Wang *et al.* fabricated $NiTe_2$ on Ni foam by using a thermal gas-solid tellurization process.[1156] For this process, Te powder was placed upstream of a piece of Ni foam in a tube furnace. The products were heated to 450 °C and kept at this temperature for 8 h under 5% H_2 and 95% Ar gas flow. During the heating, the upstream Te powder reacted with H_2 gas, forming active H_2Te gas. The as-formed H_2Te gas further reacted with the Ni foam surface, resulting in $NiTe_2$ nanocrystals on the Ni foam. As seen in Figure 268, Wang *et al.* also used graphene oxide (GO) coated Ni foam, which was prepared by a modified Hummers method with an additional minor modification,[1166] for this thermal tellurization process.[1156] As a result, NiTe composited with reduced GO (rGO) was introduced onto Ni foam.

5.3.1.6. Electrodeposition. Binder-free transition metal telluride electrodes with well-interconnected structures and abundant structural space for the OER can be obtained through two- and one-step approaches involving electrodeposition.[97,101] Chen *et al.* prepared transition metal ditellurides (MTe_2, M = Co, Ni, Fe) on carbon fiber cloth through the electrodeposition of transition metal oxide precursors and their subsequent tellurization.[97] In the first step, the electrodeposition of the oxide precursor on carbon fiber cloth was conducted under a constant potential of −1 V_{SCE} for 90 s in an aqueous solution containing transition metal salt(s) [i.e., $Co(NO_3)_2{\cdot}6H_2O$, $Ni(NO_3)_2{\cdot}6H_2O$, $(NH_4)_2Fe(SO_4)_2{\cdot}6H_2O$] at room temperature (counter electrode: Pt mesh). In the second step, the as-deposited oxide precursor on carbon fiber cloth was tellurized in a horizontal quartz tube furnace under Ar flow. Here, the oxide precursor and Te powder were installed in the downstream and center of the tube furnace, respectively. During the tellurization, the tube center and downstream were heated to 500 and ∼350 °C, respectively. Interestingly, the as-obtained MTe_2 samples maintained the nanosheet morphologies of their oxide precursors and exhibited nanoporous structures possibly due to the high-temperature tellurization accompanied by the crystal structural change (e.g., CoO → $CoTe_2$). Recently, Silva *et al.* also fabricated crystalline Ni_3Te_2 films on various conductive substrates (i.e., Au coated glass, glassy carbon, Ni foam, carbon fiber paper, carbon cloth) via one-step electrodeposition in an aqueous solution (Ni source: $NiSO_4{\cdot}6H_2O$; Te source: TeO_2) under an applied potential of −1.05 $V_{Ag/AgCl}$ at 80 °C. The as-deposited Ni_3Te_2 film surface mainly consisted of randomly oriented nanoflakes (thickness: ∼8 nm).

As discussed above, in many cases, the metal tellurides synthesized using two-step approaches exhibited rough surfaces and/or porous structures, which can enhance the number of OER active sites. These complex morphologies probably originate from the drastic crystal structural change from the precursor to telluride. Accordingly, we may be able to intentionally create high-performance transition metal telluride OER electrocatalysts with desired shapes by (1) controlling precursor morphology and (2) selecting appropriate conversion treatments. On the other hand, for one-step approaches, although several groups reported the hydrothermal methods (refs 101, 763, 1041, 1054, 1127, 1145, 1146, and 1148), there are a few reports of alternate synthetic approaches (i.e., solid-state reaction,[177,184] gas-solid reaction,[1156] electrodeposition,[101] solution-based reaction,[1133] and solvothermal reaction[1130]). Further studies are necessary to gain a better understanding of how each of the synthetic methods impact or effect the electrocatalyst structure, composition, and, in turn, OER activity.

5.3.2. Final Types of Telluride-Based Electrocatalysts. Compared with other transition metal chalcogenides (i.e., transition metal sulfides and selenides), the total number of reports about transition metal tellurides as OER electrocatalysts is much smaller. However, as shown in Table 7, the share of the reports concluding "catalyst" to be the final electrocatalyst type in the metal tellurides is greater than that of the metal sulfides and selenides. Since the electronegativity of Te (χ_{Te} = 2.1) is lower than those of S (χ_S = 2.58) and Se (χ_{Se} = 2.55), the covalency of the M−Te bonds in a transition metal telluride may increase, resulting in its superior oxidation

https://doi.org/10.1021/acs.chemrev.3c00005
Chem. Rev. 2023, 123, 12795−13208

resistance. Under the reported OER testing conditions, the transition metal tellurides were predominantly classified as one of two final types of electrocatalysts: "catalyst" ("almost" no oxidation, Figure 269a) and "precatalyst" (partial oxidation, see Figure 269b). With a focus on the papers with post-OER analysis results, we herein introduce the notable examples for each final type in the following Sections.

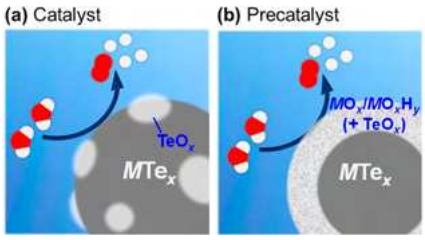


Figure 269. Schematic illustrations of suggested final types of transition metal telluride-based electrocatalysts after long-term OER testing.

5.3.2.1. Catalysts. Of the reported metal telluride-based OER electrocatalysts, mono-metal tellurides (CoTe (refs 1124, 1126, and 1129), $CoTe_2$,[1124,1129,1132] Ni_3Te_2,[101,917] Cu_7Te_4,[1123,1130] and ZnTe[1127]), a bimetal telluride (Fe-doped NiTe with an oxygen vacancy-rich TeO_2 layer on its surface[1131]), a metal telluride composite ($CoTe_2$@CdTe[1041]), and mono- and bi-metal tellurides modified with carbon-based materials ($CoTe_2$@N-GC[1128] and $NiCo_2Te_4$/PTCDA[1133]) were reported as "catalyst". Importantly, as indicated in Figure 269a, most of the as-prepared and post-OER metal telluride catalysts showed the presence of oxidized Te species (i.e., TeO_x). The amount of Te oxides formed during the OER may vary depending on the oxidation resistance of tellurium species in the metal telluride. Since there is no report mentioning the electrocatalytic OER activity of Te oxides, many electrochemists regard the metal telluride surface, not the surface Te oxides, as the main OER active sites in metal telluride catalysts. (Concerns about the surface Te oxide formation will be discussed in detail later in Section 5.3.3.)

Recently, a Ni_3Te_2 electrocatalyst electrodeposited on Au glass (Ni_3Te_2/Au) exhibited a remarkably high oxidation resistance during OER testing.[101] Figures 270a–f show the physiochemical characterization results of the Ni_3Te_2/Au before and after the 24 h OER CA tests at the applied potential of 1.44 V_{RHE} in 1 M KOH. From the pre- and post-OER SEM images, significant changes in morphology were not observed (see Figures 270a and b). In the pre- and post-OER XRD patterns, there were almost no changes in diffraction peak positions, indicating that the bulk composition of Ni_3Te_2 was maintained during the OER test (see Figure 270c). Additionally, XPS was employed to examine the surface chemical states (Figures 270d–f). The Ni 2p spectrum contains the first doublet at 853.5 and 871.4 eV, which correspond to Ni^{2+} in Ni tellurides,[1167,1168] and the satellite doublet before and after the OER test. The pre- and post-OER Te 3d spectra demonstrated only one doublet at 572.3 and 582.5 eV, assignable to Te^{2-} in nickel tellurides.[1167,1168] In the O 1s region, the components corresponding to surface adsorbed O_2 and traces of Te oxides were confirmed before and after OER testing. Accordingly, the Ni_3Te_2 surface is quite stable under OER conditions, probably due to its unique crystal structure (Ni_3Te_2). The electrochemical stability of Ni_3Te_2/Au was also investigated via a continuous OER CV test (Figure 270g). In Ni-based electrocatalysts, changes in the chemical coordination around the surface Ni atoms generally lead to potential shifts and intensity changes of the Ni redox peaks during OER CV testing.[101] In addition, surface oxidation of Ni chalcogenides causes the formation of Ni oxide/oxyhydroxide, resulting in the gradual increase of the Ni redox peak intensity with time.[177] As shown in Figure 270g, the Ni redox peaks of the Ni_3Te_2/Au did not show any potential shifts or intensity increases (i.e., increases in current response) within the 100 OER CV cycles. Therefore, it was demonstrated that Ni_3Te_2 has a high oxidation resistance under OER conditions. Here, the as-observed Ni redox peaks may be assigned to the partial hydroxylation, which forms a hydroxo-telluride surface, without any changes in the telluride coordination. Hence, in the Ni_3Te_2/Au electrode, the real active sites might be the Ni_3Te_2 surface. This allows coordination expansion at its Ni sites during the OER. Incidentally, in order to check the effect of Fe impurity from the KOH aqueous electrolyte, the OER activity of the Ni_3Te_2/Au was also confirmed in purified 1 M KOH. Since there was almost no change in electrocatalytic OER activity between purified and unpurified KOH aqueous media, it was concluded that the influence of the Fe incorporation was negligible in the Ni_3Te_2 OER catalyst.

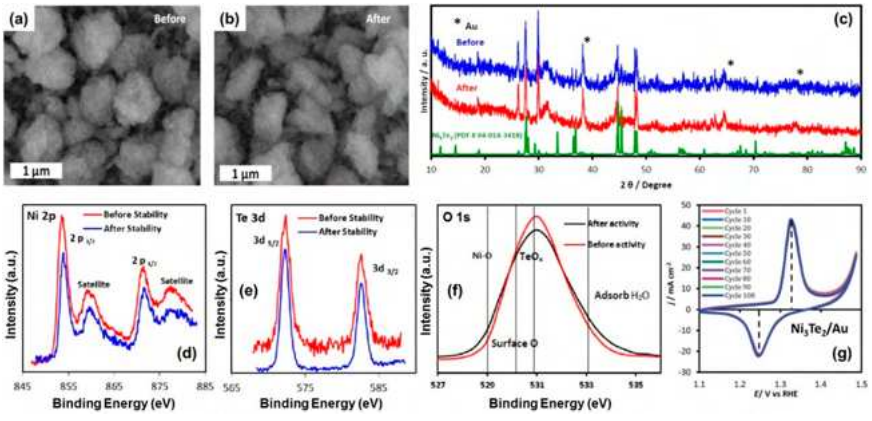


Figure 270. (a, b) SEM image, (c) XRD patterns, and (d–f) XPS spectra of Ni_3Te_2 catalyst electrodeposited on Au glass before and after 24 h OER CA test (applied potential: 1.44 V_{RHE}) in 1 M KOH media. (g) CV curves of Ni_3Te_2 catalyst on Au glass for 100 cycles indicating the Ni redox peaks ($Ni^{2+} \leftrightarrow Ni^{3+}$). Reproduced with permission from ref 101. Copyright 2018 Royal Society of Chemistry.

https://doi.org/10.1021/acs.chemrev.3c00005
Chem. Rev. 2023, 123, 12795–13208

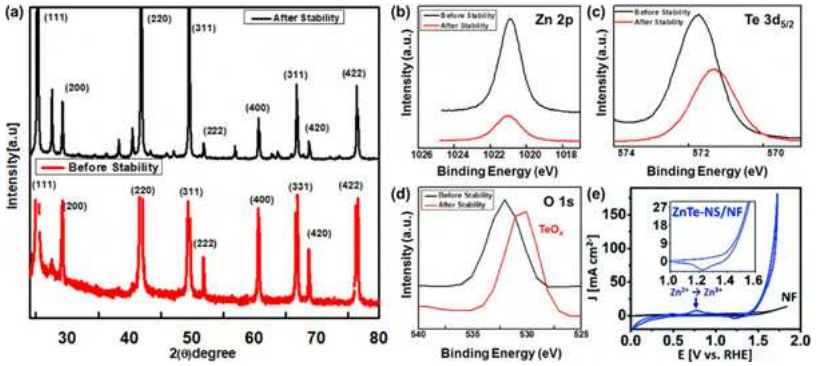


Figure 271. (a) XRD patterns and (b–d) XPS spectra of ZnTe nanosphere (ZnTe-NS) catalyst on Ni foam before and after a 24 h OER CA test (applied potential: 1.58 V_{RHE}) in 1 M KOH media. (e) CV curves of ZnTe-NS/Ni foam and bare Ni foam in 1 M KOH media. Reproduced with permission from ref 1127. Copyright 2019 Royal Society of Chemistry.

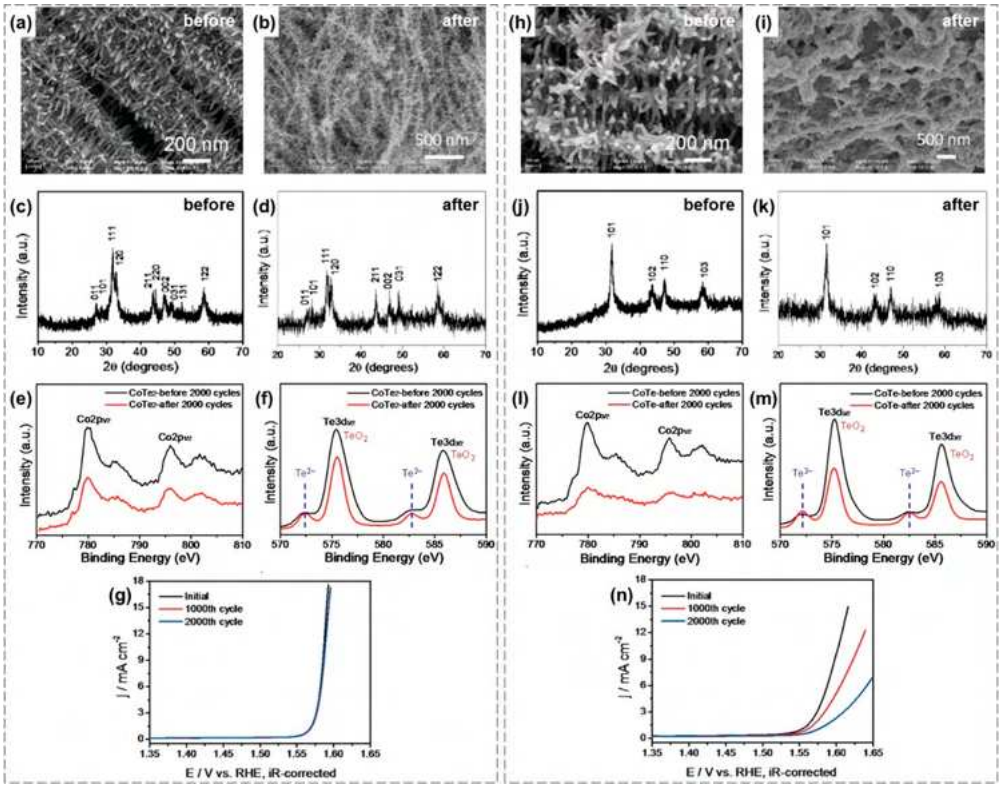


Figure 272. (a, b, h, i) SEM images, (c, d, j, k) XRD patterns, and (e, f, l, m) XPS spectra of (left column) $CoTe_2$ and (right column) CoTe nanofleeces before and after 2000 OER CV cycles (potential range: 0.3–0.8 $V_{Ag/AgCl}$). (g, n) LSV curves of (g) $CoTe_2$ and (n) CoTe nanofleeces before and after different cycles of the OER CV tests. Reproduced with permission from ref 1129. Copyright 2017 Wiley.

ZnTe nanospheres deposited on Ni foam (ZnTe-NS/Ni foam) were also reported as a "catalyst" that generates traces of Te oxides during the OER process.[1127] Sadaqat *et al.* examined the stability of the ZnTe-NS electrocatalyst through a 24 h OER CA test at an applied potential of 1.58 V_{RHE} in 1 M KOH. After a 24 h OER CA test, compositional and morphological changes of the ZnTe-NS were studied via several analytical techniques such as SEM, XRD, and XPS. The pre- and post-OER SEM results confirmed that there were no morphological alterations.[1127] As seen from the XRD results (Figure 271a), the bulk composition of ZnTe remained intact after OER testing. Figures 271b–d show the Zn 2p, Te $3d_{3/2}$, and O 1s XPS spectra. In the Zn 2p region, the XPS peak did not show a significant shift after OER testing, indicating the absence of Zn oxides. A slight peak shift was observed in the Te $3d_{5/2}$ region. Possibly because of Te oxide formation and O_2 adsorption, the O 1s XPS peak was also slightly shifted. Thus, the ZnTe surface was maintained to some extent even after long-term OER testing. Even though traces of Te oxides formed during OER testing, the OER activity of the ZnTe-NS/Ni foam was sustained for 24 h. The CV profile of the ZnTe-NS/Ni foam showed the anodic peak assignable to the Zn oxidation ($Zn^{2+} \rightarrow Zn^{3+}$) (see Figure 271e). Similarly, the ZnTe-NS surface may experience a change/alteration in its electronic structure via Zn oxidation, which forms hydroxo-telluride intermediates. Accordingly, it was suggested that the ZnTe surface mainly acts as an OER active site in the ZnTe-NS/Ni foam. The role of as-formed Te oxides still needs to be further examined in the future.

https://doi.org/10.1021/acs.chemrev.3c00005
Chem. Rev. 2023, 123, 12795–13208

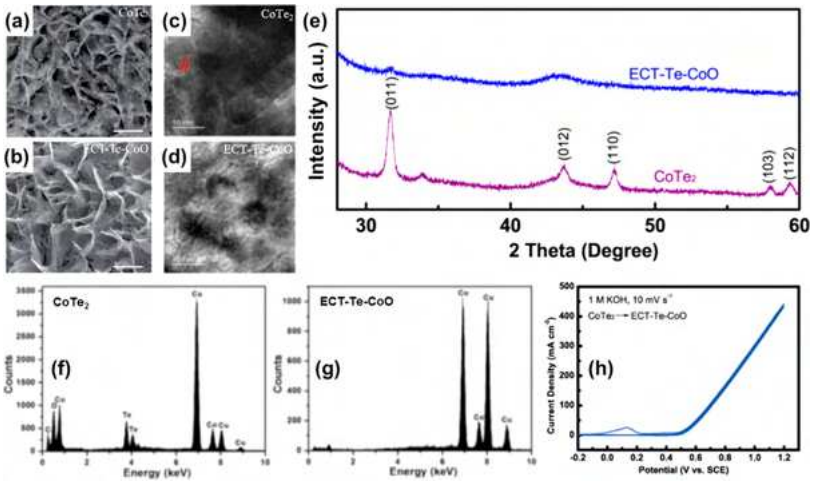


Figure 273. (a, b) SEM and (c, d) HRTEM images, (e) XRD patterns, and (f, g) EDX spectra of a porous $CoTe_2$ nanosheet film on carbon fiber cloth before and after *in situ* electrochemical oxidation. (h) Electrochemical tuning process of $CoTe_2$ at the scan rate of 10 $mV{\cdot}s^{-1}$ in 1 M KOH media. Reproduced with permission from ref 97. Copyright 2016 American Chemical Society.

The crystal structure of a metal telluride is one of the most important parameters for determining its electrochemical stability. Gao *et al.* investigated the OER performances of two Co tellurides with different crystal structures (i.e., $CoTe_2$ and CoTe) in 0.1 M KOH.[1129] To determine the stabilities of hierarchical $CoTe_2$ and CoTe nanofleeces on glassy carbon electrodes, 2000 OER CV cycles (0.3−0.8 $V_{Ag/AgCl}$) were performed. After the OER test, changes in the chemical composition and morphology of the electrocatalysts after the OER test were checked through XRD, SEM, and XPS analyses (see Figure 272). As shown in Figures 272a, b, h, and i, the original shape of the $CoTe_2$ material remained after the OER test, whereas morphological destruction of CoTe occurred. This morphological change in CoTe might have been caused by the dissolution of Co and Te species in the electrolyte.[1150] The pre- and post-OER XRD and XPS measurements demonstrated that there were almost no obvious bulk- and surface-compositional changes for both $CoTe_2$ and CoTe. However, with careful attention to the Te 3d spectra of $CoTe_2$ and CoTe, the XPS doublet intensities of Te^{2-} in Co tellurides relative to those of TeO_4 were visually increased after the OER test, which may imply that surface Te and/or Co species dissolved into the electrolyte.[60,1150] Furthermore, $CoTe_2$ exhibited higher electrochemical stability than CoTe in the OER CV test (see Figures 272g and n). This is presumably because the dissolution rate of CoTe was faster than that of $CoTe_2$, and this relatively fast dissolution of CoTe decreases its total loading amount and the number of OER active sites.[115] Taken together, the OER active sites in $CoTe_2$ and CoTe may be fresh telluride surfaces that are maintained through their continuous dissolution during the OER. Moreover, McKendry *et al.* also revealed that the $CoTe_2$ nanowire electrocatalyst on a glassy carbon electrode is stable under OER potentials in 1 M KOH, as determined using *in situ* XANES.[1132]

Of the other catalysts mentioned, Cu_7Te_4, $CoTe_2$@N-GC, and $CoTe_2$@CdTe also act as surface-stable OER electrocatalysts in alkaline media. However, to investigate the change of electrocatalyst surface, pre- and post-OER XPS and HRTEM analyses are necessary.[57] Hence, further surface analyses may need to be applied to these reported electrocatalysts to thoroughly identify their surface OER active species.

5.3.2.2. Precatalysts. Generally, transition metal telluride-based precatalysts (NiTe,[177,1143,1148] $NiTe_2$,[1149] CoTe,[1143] $CoTe_2$,[97,1146,1147,1150] $NiCo_2Te_4$,[1133] Ni_3Te_2-CoTe,[1145] $CoTe_2$/CNT,[1132] and Fe-doped CoTe[1144]) undergo oxidation during the OER, forming metal oxides/oxyhydroxides and/or Te oxides. Notably, the formed metal oxide/oxyhydroxide has been identified as the surface OER active site. As with the catalyst case, little is known about the contribution of Te oxides to electrochemical water oxidation activity. According to reports that studied the degree of oxidation following long-term OER tests,[97,1144,1147−1149] metal telluride precatalysts undergo partial oxidation under OER conditions, revealing their status as precatalysts for the OER (see Figure 269b).

So far, a number of studies have focused on $CoTe_2$-based precatalysts.[97,1132,1146,1147,1150] For example, Chen *et al.* prepared a porous $CoTe_2$ nanosheet film on a conductive carbon fiber substrate.[97] The as-prepared $CoTe_2$ precatalyst was activated through an *in situ* electrochemical oxidation tuning process,[96] in which the $CoTe_2$ was electro-oxidized into its oxide counterpart (ECT-Te-CoO) by a positive scan (scan rate: 10 $mV{\cdot}s^{-1}$) from its open circuit voltage to 1.2 V_{SCE} for 2−3 min in 1 M KOH.[97] Figures 273a−g show the characterization results of the $CoTe_2$ before and after the *in situ* electrochemical oxidation. As seen in Figures 273a and b, the oxidized product maintained the nanosheet shape of $CoTe_2$, while a large number of nanopores evolved after the oxidation.[97] In the HRTEM images, the small crystallites that existed before the oxidation (see red lines in Figure 273c) disappeared after the oxidation (see Figure 273d). Additionally, the XRD results revealed that the *in situ* electrochemical oxidation changed the crystal structure of the $CoTe_2$ from crystalline to nearly amorphous. This structural change might have occurred due to the drastic changes in bonding and structure from the replacement of Te^- to O^{2-}. Here, the $CoTe_2$ (011) diffraction peak with weak intensity can also be observed after the oxidation, which might serve as evidence for the partial oxidation (almost full oxidation) of the electrocatalyst. In Figures 273f and g, the EDX measurements confirmed the absence of Te signals in the oxidized product owing to the full oxidation of the $CoTe_2$. Furthermore, in the post-OER XPS spectrum for Co 2p, the doublet signal corresponding to Co^{3+} was confirmed, which suggests that the

https://doi.org/10.1021/acs.chemrev.3c00005
Chem. Rev. 2023, 123, 12795−13208

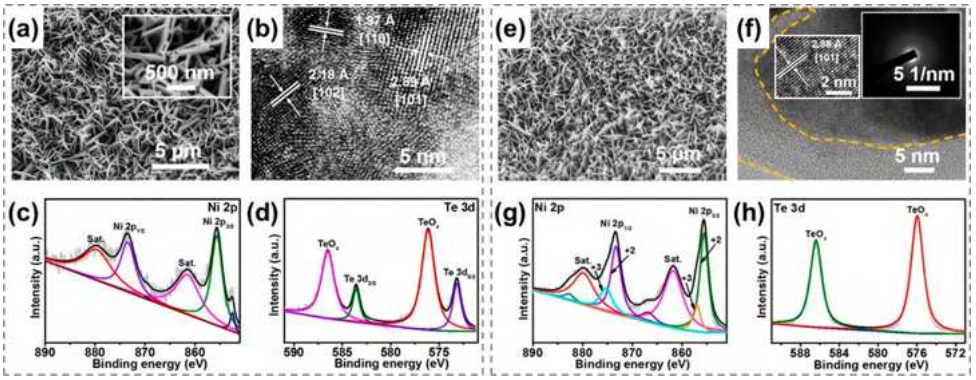


Figure 274. (a, e) SEM and (b, f) HRTEM images, (c, d, g, h) XPS spectra, and (f, inset) corresponding SAED pattern of NiTe nanosheet array on Ni foam before and after a 35 h OER CA test (applied potential: 1.59 V_{RHE}) in 1 M KOH media. Reproduced with permission from ref 1148. Copyright 2018 Elsevier.

oxidized product is CoOOH.[1169] The CV curves for the *in situ* electrochemical oxidation process are shown in Figure 273f. Importantly, an irreversible oxidation peak appeared in the very first oxidation scan and disappeared completely in the following CV scans. This irreversible oxidation may be assignable to the transformation of $CoTe_2$ into CoOOH. A similar irreversible oxidation peak in the CV curve was also observed for the $CoTe_2$ particulate film on glassy carbon electrode in 1 M KOH.[1150] The pre- and post-OER XPS analysis found the formation of the Co^{3+} species after the OER CV test, which also suggests the formation of CoOOH or CoO_x.[1150,1169] In addition, ICP-OES analysis on the electrolyte was conducted during the 4 h OER CA test, indicating that small amounts of Co (0.1 μM) and Te (1 μM) were released from the $CoTe_2$ surface. Zhichao *et al.* also discussed the formation of TeO_x and partial dissolution of Te species during electrochemical water oxidation over the hierarchical $CoTe_2$ nanowire array on Ti mesh.[1147] From the pre-OER XPS analysis, the as-prepared $CoTe_2$ sample contained two different components of Te oxides: TeO_2 and TeO_3. After a 25 h OER CA test (applied potential: 1.55 V_{RHE}), TeO_3 disappeared and only TeO_2 remained. Accordingly, it can be suggested that the $CoTe_2$ precatalyst is generally transformed into its oxide counterparts (probably CoOOH and TeO_2) via the partial oxidation and subsequent dissolution process after long-term OER testing, and the as-formed CoOOH likely acts as the OER active site.

Nickel mono- and ditellurides (i.e., NiTe, $NiTe_2$) have also exhibited similar oxidation behavior to their cobalt counterparts during the long-term OER tests.[177,1148,1149] A NiTe nanosheet array on Ni foam was prepared via a facile tellurization treatment and was subjected to a 35 h OER CA test at the applied potential of 1.59 V_{RHE} in 1 M KOH.[1148] The XRD measurement confirmed that the NiTe bulk structure remained and that TeO_2 formed after the OER test.[1148] As shown in Figures 274a and e, the nanosheet array feature of NiTe was kept, even after the OER test. The HRTEM image of the as-prepared NiTe sample (Figure 274b) displays lattice fringes with 2.89, 2.18, and 1.97 Å spacings, which correspond to the (101), (102), and (110) interplanar distances of NiTe, respectively. After OER testing, the crystalline part as well as the amorphous NiOOH layer on the NiTe nanosheet surface can be observed from the HRTEM images (Figure 274f). The SAED pattern also indicates the formation of amorphous species. In Figures 274c, d, g, and h, the XPS results suggest that the post-OER surface mainly consists of NiOOH and Te oxides. Here, the newly formed NiOOH layer on the NiTe may be the active OER species. Furthermore, the ICP-OES analysis of the pre- and post-OER NiTe samples was performed. After the OER test, the Ni:Te molar ratio in the sample was changed from 1:1.02 to 1:0.67, implying the dissolution of Te species into the electrolyte during the OER process. Recently, Masa *et al.* also reported the electrooxidation of a NiTe particulate film on carbon cloth via 100 OER CV cycles (1.0−1.6 V_{RHE}) in 1 M KOH.[177] The peak intensity of the Ni^{2+} to Ni^{3+} oxidation in the NiTe CV curve significantly increased during the OER CV cycling, which is attributed to the growth of a Ni oxide/hydroxide shell over the NiTe. Accordingly, by checking the peak intensity of the Ni^{2+} to Ni^{3+} oxidation, one can predict the oxidation degree of nickel telluride precatalysts. Apart from the NiTe precatalysts, characterization of the $NiTe_2$ nanosheet array on Ti mesh before and after a 24 h OER CA test (applied potential: 1.571 V_{RHE}) in 1 M KOH also demonstrated remarkable surface oxidation. SEM, XRD, and HRTEM measurements showed that the nanosheet array feature and bulk structure of the $NiTe_2$ were well preserved after OER testing. The formation of amorphous NiOOH on the $NiTe_2$ surface was confirmed by HRTEM, XPS, and Raman analyses. The XPS analysis further indicated the existence of surface TeO_x species after OER testing. The reduced atomic ratio of Ni:Te in the electrocatalyst sample after OER testing was revealed by ICP-OES, implying that Te species dissolved into the electrolyte during OER testing. These intensive structure and composition investigations suggest that NiTe and $NiTe_2$ undergo partial oxidation and form NiOOH (OER active species) and TeO_x species on their surfaces.

As observed above, in the cobalt- and nickel-containing tellurides, there is a high chance that the Co^{3+} and Ni^{3+} signal evolution/increase in the XPS spectra indicates the formation of oxidized Co and Ni species (e.g., CoOOH and NiOOH) on their surfaces. From this standpoint, Ni_3Te_2-CoTe[1145] and Fe-doped CoTe[1144] might be transformed into "NiOOH + CoOOH + TeO_2" and "Fe-doped CoOOH + TeO_2" in 1 M KOH, respectively. Additionally, the effect of the formation of Te oxides on OER activity needs further investigation.

5.3.3. Structural and Chemical Compositional Effects toward OER Activity. In this section, we briefly discuss the compositional and morphological effects of transition metal telluride electrocatalysts on their OER activity. Herein, we also

https://doi.org/10.1021/acs.chemrev.3c00005
Chem. Rev. 2023, 123, 12795−13208

introduce some strategies for improving the OER performance of the transition metal tellurides.

5.3.3.1. Metal/Tellurium Composition Effects. Figure 275 shows the reported OER overpotentials of various mono-metal

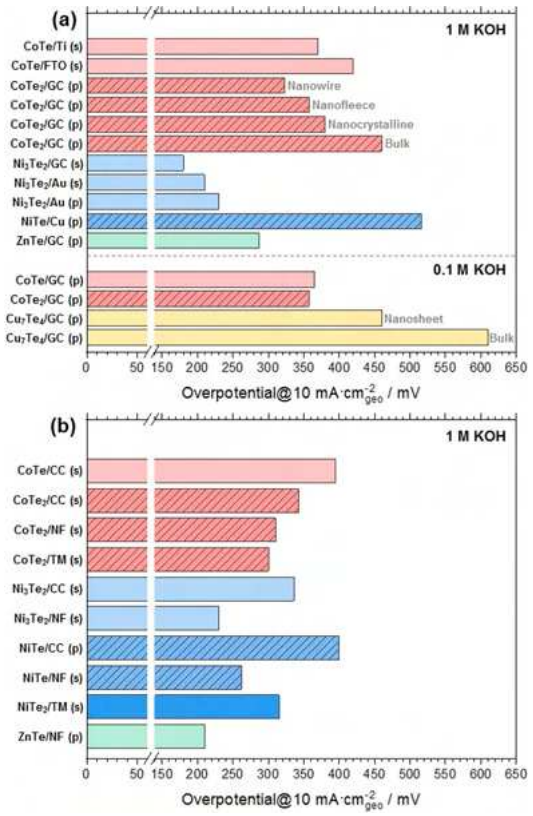


Figure 275. Comparison of electrocatalytic OER activity for various mono-metal tellurides on (a) 2D- and (b) 3D-structured conductive substrates in alkaline electrolytes. Abbreviations—Ti: titanium foil; FTO: fluorine-doped tin oxide glass substrate; GC: glassy carbon substrate; Au: gold glass; Cu; Cu foil; CC: carbon (fiber) paper; NF: nickel foam; TM: titanium mesh.

tellurides (reported from 2015 to 2019) at a current density of 10 mA·cm^{-2} in alkaline electrolytes. To make fair comparisons, we divided these electrocatalysts into two groups: (a) 2D- and (b) 3D-structured electrodes. In most cases, the 3D-structured electrodes showed higher OER activities than the 2D-structured ones because of their higher number of electrolyte-accessible OER active sites. In the 2D-electrode group, the lowest OER overpotential was reported for the Ni_3Te_2 catalyst with an overpotential of 180 mV in 1 M KOH.[101] The ZnTe catalyst achieved the lowest OER overpotential of the 3D-electrode group, 210 mV in 1 M KOH.[1127] As shown in Figure 275a, nanostructured $CoTe_2$ and Cu_7Te_4 achieved much higher electrocatalytic water oxidation activities than bulk $CoTe_2$ and Cu_7Te_4.[1129,1130,1132,1150,1159] Thus, especially in the 2D-structured electrodes, the morphology of the loaded electrocatalyst is one of the key factors to determine its geometric OER activity. Furthermore, when the loaded electrocatalytic materials are the same in the 3D-structured electrodes (Figure 275b), the OER activities of the carbon-based substrates (i.e., NiTe/CC, Ni_3Te_2/CC, $CoTe_2$/CC) are relatively lower than those of the transition metal-based ones (i.e., NiTe/NF, Ni_3Te_2/NF, $CoTe_2$/NF, $CoTe_2$/TM). These higher OER activities of the transition metal-based electrodes may be obtained because of their excellent electrical conductivities.

5.3.3.2. Metal Telluride Coupling Effects. To further improve the OER activity, some groups reported bimetallic transition metal telluride composites such as $CoTe_2$@CdTe nanowires,[1041] Ni_3Te_2-CoTe nanosheet structures,[1145] NiTe-PbNiTe (i.e., NiTe + PdTe) nanorods,[1157] Zn-Co-Te (i.e., $CoTe_2$ + ZnTe) nanorods,[1054] and $CoTe_2$-$MnTe_2$ nanowire arrays[1158] due probably to their modified band structures. Among all the reported metal telluride-metal telluride electrodes, the $CoTe_2$@CdTe nanowire array-like film on a pencil graphite electrode gave the lowest OER overpotential (140 mV) at a current density of 10 mA·cm^{-2} with a relatively low Tafel slope value of 68 mV·dec^{-1} in 1 M KOH (see Table 7).[1041] Interestingly, as shown in Figures 276a and b, the

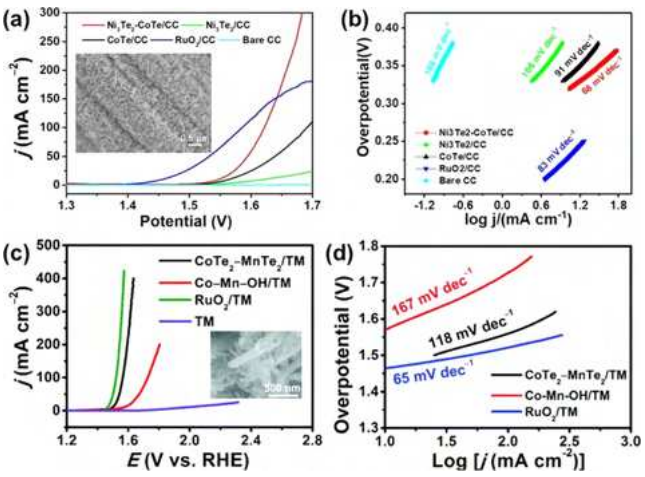


Figure 276. (a) LSV curves and (b) corresponding OER Tafel slope plots of Ni_3Te_2-CoTe (see inset SEM image), Ni_3Te_2, CoTe, and RuO_2 on carbon cloth in 1 M KOH. Reproduced with permission from ref 1145. Copyright 2019 Elsevier. (c) LSV curves and (d) corresponding OER Tafel slope plots of $CoTe_2$-$MnTe_2$ (see inset SEM image) and Co-Mn-OH on Ti mesh in 1 M KOH. Reproduced with permission from ref 1158. Copyright 2018 Royal Society of Chemistry.

Ni_3Te_2-CoTe composite electrocatalyst achieved a higher OER performance than its mono-metal telluride components (Ni_3Te_2 and CoTe) in 1 M KOH.[1145] According to DFT results, the Ni_3Te_2 component in this composite possesses a d-band center close to the Fermi level of Ni_3Te_2, achieving a high conductivity and possibly forming stronger interactions between the electrocatalyst surface and OER intermediates. Hence, the Ni_3Te_2-CoTe composite demonstrated improved OER performance. Furthermore, the $CoTe_2$-$MnTe_2$ composite synthesized by Wang *et al.* was able to show enhanced electrocatalytic OER activity (η: 310 mV at 50 mA·cm^{-2}) compared to its oxide counterpart Co-Mn-OH (η: 440 mV at 50 mA·cm^{-2}), which might be ascribed to its larger number of active sites and higher conductivity (Figures 276c and d).[1158]

5.3.3.3. Metal-Doping/Substitution Effects. Foreign metal substitution and doping on mono-metal tellurides (e.g., $CoTe_2$) can also boost their electrochemical OER activity.[97,1144] Chen *et al.* synthesized $CoTe_2$, $Co_{0.5}Fe_{0.5}Te_2$, and $Co_{0.37}Ni_{0.26}Fe_{0.37}Te_2$ films on carbon fiber cloth substrates.[97] Mono-, bi-, and multi-metal tellurides were oxidized in 1 M KOH, resulting in nanoporous transition metal oxides with increased surface areas. The OER overpotentials of the

https://doi.org/10.1021/acs.chemrev.3c00005
Chem. Rev. 2023, 123, 12795−13208

resultant oxides are ordered as follows: 276 mV (oxidized $Co_{0.37}Ni_{0.26}Fe_{0.37}Te_2$) < 326 mV (oxidized $Co_{0.5}Fe_{0.5}Te_2$) < 343 mV (oxidized $CoTe_2$). Moreover, Zhong *et al.* prepared Fe-doped $CoTe_2$ precatalysts with different Fe-doping levels (0.4−5.3 at %).[1144] In Figure 277a, the best-performing Fe-doped $CoTe_2$ (sample name: Fe-CoTe-2; Fe-doping level: 2.6 at %) showed higher OER performance (η: 300 mV at 10 mA·cm^{-2}; Tafel slope: 45 mV·dec^{-1}) than the undoped $CoTe_2$ (η: 445 mV at 10 mA·cm^{-2}; Tafel slope: 93.1 mV·dec^{-1}) in 1 M KOH. At an OER overpotential of 320 mV, the intrinsic activity based on the ECSA of the $CoTe_2$ was enhanced by 14 times and the turnover frequency (TOF) was increased by a factor of 21 through the Fe doping. Previously, Zhu *et al.* reported that, in P-substituted $CoSe_2$, P substitution introduced more vacancies/defects, allowing the Co cations to be easily oxidized into CoOOH during OER testing in alkaline media.[48] As seen in Figure 277b, the formation of defects was present in the Fe-doped $CoTe_2$. Therefore, as suggested by Zhong *et al.*, the superior OER performance of the Fe-doped $CoTe_2$ might be achieved via the surface structure change (oxidation) induced by Fe doping, resulting in the formation of Co^{3+}.

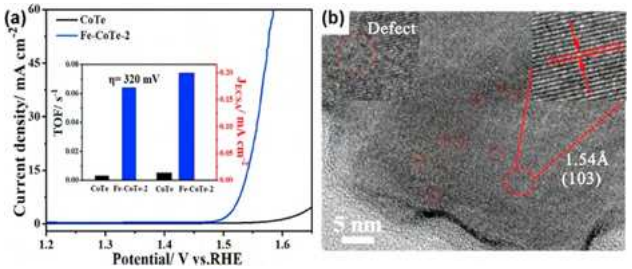


Figure 277. (a) LSV curves of bare and Fe-doped $CoTe_2$ on glassy carbon electrodes in 1 M KOH. (inset) Corresponding ECSA-based intrinsic OER activities and TOFs. (b) HRTEM image of Fe-doped $CoTe_2$. Reproduced with permission from ref 1144. Copyright 2019 Elsevier.

5.3.3.4. Composite Materials Effects. The OER performance of metal telluride can also be improved through hybridizing with conductive carbon-based materials.[682,1128,1132,1133,1156,1159] Generally, the composite of the metal telluride and carbon-based material may enhance the OER active material (i.e., metal telluride) utilization, possibly resulting in high mass activity, since metal tellurides in carbon-based materials tend to form nanoparticles that are dispersed/encapsulated in the carbon-based matrix (see Figures 278a, e, and i).[1128,1132,1133,1159] For example, Liu *et al.* successfully prepared $CoTe_2$ nanoparticles encapsulated in an N-doped graphitic carbon matrix ($CoTe_2$@N-GC) by tellurization of a MOF template precursor (ZIF-67) under a hydrogen atmosphere.[1128] The high surface area $CoTe_2$@N-GC drove a current density of 10 mA·cm^{-2} at a small overpotential of 300 mV, which is much lower than that of $CoTe_2$ powder (360 mV) in 1 M KOH (see Figures 278a−d). By using a different MOF precursor [Co-based Prussian blue analogue (PBA) precursor], CoTe@nanocarbon core@shell (CoTe@NC) was successfully synthesized.[682] The CoTe@NC exhibited good OER performance (η: 356 mV at 10 mA·cm^{-2}; Tafel slope: 112 mV·dec^{-1}) and excellent stability during long-term OER testing (15 h CP at a current density of 10 mA·cm^{-2}). In this structure, the nanocarbon shell acts as a good electron conductor as well as an active site protector. Additionally, the carbon-based materials can also control the oxidation of the metal telluride during the OER. As shown in Figures 278e−g, Lu *et al.* prepared composites of $CoTe_2$ nanoparticles and multiwalled carbon nanotubes ($CoTe_2$/CNT) as well as

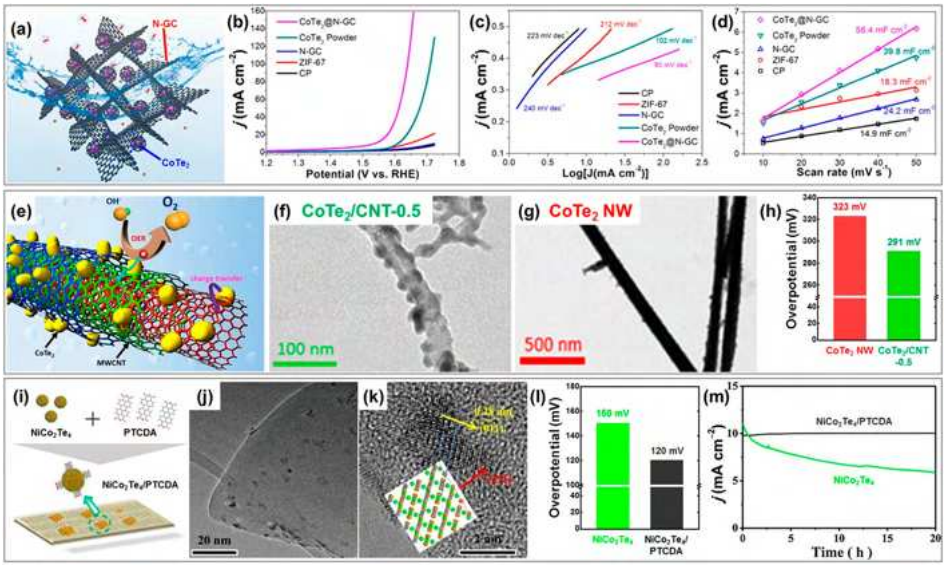


Figure 278. (a) Schematic illustration of $CoTe_2$ nanocrystals embedded in an N-doped graphitic carbon matrix ($CoTe_2$@N-GC). (b) LSV curves, (c) corresponding Tafel slope plots, and (d) double-layer capacitances of $CoTe_2$@N-GC, $CoTe_2$ powder, N-GC, and ZIF-67 on carbon paper electrodes in 1 M KOH. Reproduced with permission from ref 1128. Copyright 2017 American Chemical Society. (e) Schematic illustration of a $CoTe_2$ nanoparticles hybridized multiwalled carbon nanotube ($CoTe_2$/CNT). (f, g) TEM images of (f) $CoTe_2$/CNT hybrid material and (g) $CoTe_2$ nanowire (NW). (h) OER overpotentials of $CoTe_2$ NW and $CoTe_2$/CNT in 1 M KOH. Reproduced with permission from ref 1132. Copyright 2016 American Chemical Society. (i) Schematic illustration of $NiCo_2Te_4$ clusters modified with perylene-3,4,9,10-tetracarboxylic dianhydride ($NiCo_2Te_4$/PTCDA). (j) TEM and (k) HRTEM images of $NiCo_2Te_4$/PTCDA. (l) OER overpotentials and (m) 24 h CA responses of $NiCo_2Te_4$ and $NiCo_2Te_4$/PTCDA in 1 M PBS (pH = 7). Reproduced with permission from ref 1133. Copyright 2019 Elsevier.

https://doi.org/10.1021/acs.chemrev.3c00005
Chem. Rev. 2023, 123, 12795−13208

$CoTe_2$ nanowires ($CoTe_2$ NW).[1132] The $CoTe_2$/CNT demonstrated better OER activity than the $CoTe_2$ NW's in 1 M KOH (see Figure 278h). To search for the superior OER activity recorded by the $CoTe_2$/CNT, *in situ* XANES was used to compare the electrochemical behaviors of the $CoTe_2$/CNT and $CoTe_2$ NW samples during the OER. It confirmed that the $CoTe_2$/CNT more easily formed CoOOH (transition state), which enhanced the OER efficiency, when compared to the $CoTe_2$ NW during the OER. On the other hand, Tao *et al.* reported that the neutral OER durability (i.e., oxidation resistance) of $NiCo_2Te_4$ nanocluster electrocatalysts can be improved by surface modification with perylene-3,4,9,10-tetracarboxylic dianhydride (PTCDA).[1133] As a result, the OER overpotential of the $NiCo_2Te_4$/PTCDA is lower than that of the $NiCo_2Te_4$ (see Figure 278l), and the $NiCo_2Te_4$/PTCDA was able to deliver a stable OER current density of around 10 mA·cm^{-2} during the OER CA test. Taken together, these studies demonstrate a possibility that one could control the metal telluride oxidation during the OER by adding an appropriate carbon-based material. Further screening for other carbon-based materials regarding (1) their oxidation and (2) the OER activity and stability of the metal tellurides is required to truly determine the synergetic effects between metal tellurides and carbon-based materials, which will provide guidelines to tailor metal telluride/carbon-based material composites.

5.3.4. Challenges. In the realm of transition metal telluride electrocatalysts, several challenges still exist. First, in both the catalyst and precatalyst cases, TeO_x species tend to form during the telluride preparation process (refs 682, 763, 1129, 1133, 1144−1147, 1156, and 1160) as well as during OER testing.[101,1127,1129,1133,1144−1150] To predict the electrochemical stability of the TeO_x species, the Pourbaix diagram of Te species is shown in Figure 279. Te species are converted into

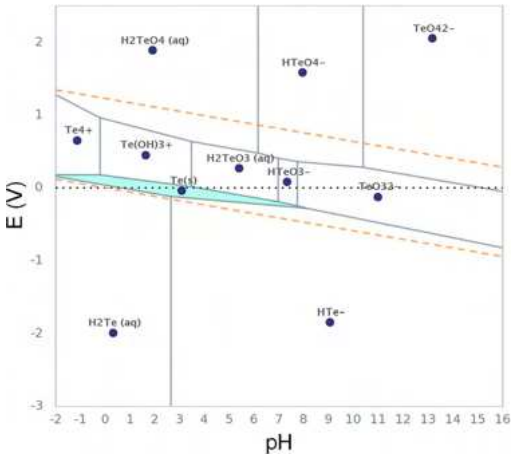


Figure 279. Pourbaix diagram for tellurium. Orange broken lines represent the thermodynamic potentials for the HER and OER at different pH values. The diagram is produced at the Te ion concentration of 10^{-8} M (default) by using the Materials Project.[87−89]

soluble species (i.e., H_2TeO_4, $HTeO_4^-$, and TeO_4^{2-}) at the thermodynamic OER potential or higher over a wide range of pH values. However, there seems to be great variability among the reported solubilities of different types of Te oxides (e.g., TeO, Te_2O_3, TeO_2, and Te_2O_5).[1170] For example, as multiple reports suggest,[1129,1144,1145,1147−1149] TeO_2 exists after the long-term OER tests, implying that TeO_2 is relatively stable in the reported conditions. In contrast, TeO_3 may be soluble in the electrolyte.[1147] Although it is predicted that the Te species may be dissolved into the electrolyte, only a few studies actually confirmed this dissolution behavior thorough ICP-OES.[1148−1150] For example, the $CoTe_2$ precatalyst underwent the dissolution of Te species as well as Co species. Therefore, an important recommendation for future studies is to examine the cationic and anionic species released from metal tellurides by analyzing the electrolytes before and after the OER test through appropriate techniques (e.g., ICP-OES, ICP-AES, TXRF, etc.).

As discussed before, TeO_x on metal telluride electrocatalysts is considered unlikely to be the electroactive species toward the OER.[1146] However, the coexistence of TeO_x may still affect the electron transfer, surface hydrophilicity, and electrochemical stability of the metal telluride electrocatalyst during the OER process. Recently, Kim *et al.* fabricated a CoTe nanotube film deposited on FTO. Subsequently, a CoTe and TeO_2 composite film was also prepared by annealing the as-prepared CoTe film at 200 °C in ambient air for 1 h. As shown in Figure 280a, the surface HRTEM image revealed the

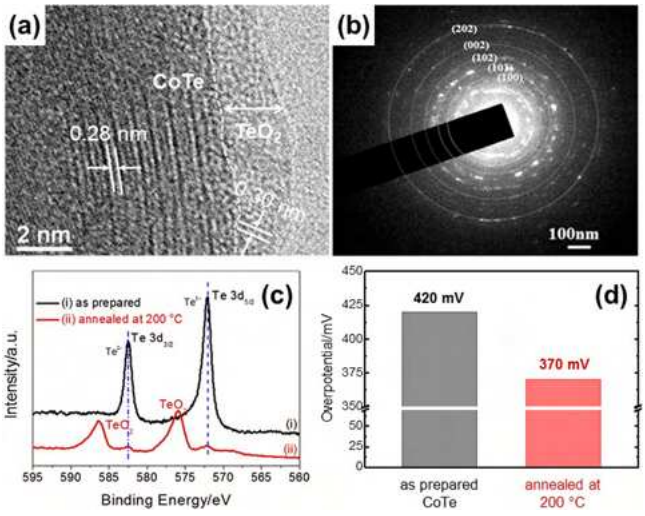


Figure 280. (a) HRTEM image and (b) SAED pattern of a 200 °C-annealed CoTe nanotube film on FTO. (c) Te 3d core level XPS spectra of the as-prepared and 200 °C-annealed CoTe films. (d) Bar graph showing the OER overpotentials of the as-prepared and 200 °C-annealed CoTe films at a current density of 10 mA·cm^{-2} in 1 M KOH. Reproduced with permission from ref 1160. Copyright 2018 Elsevier.

presence of a 3-nm-thick layer covering the inner core structure. The as-observed interplanar spacings of 0.28 and 0.30 nm correspond to the CoTe (101) and TeO_2 (102) planes. Furthermore, the SAED pattern indicated the polycrystalline nature of the CoTe core (Figure 280b). The XPS analysis showed the formation of a TeO_2 surface after annealing (Figure 280c). Accordingly, the 200 °C-annealed CoTe film possessed the CoTe@TeO_2 core@shell structure. Surprisingly, although the 200 °C-annealed CoTe film showed the TeO_2 surface, it recorded a lower OER overpotential of 370 mV at a current density of 10 mA·cm^{-2} compared to the as-prepared film (420 mV) in 1 M KOH (Figure 280d). Kim *et al.* suggested that the superior OER activity of the 200 °C-annealed CoTe is achieved because of its enhanced ECSA and electrical conductivity obtained by improving the intergranular

https://doi.org/10.1021/acs.chemrev.3c00005
Chem. Rev. 2023, 123, 12795−13208

connectivity. However, the TeO_2 skin may also contribute to the resultant OER activity, either positively or negatively. If the effect is positive, the surface TeO_2 may act as (i) a modulator to tune the surface electronic structure, optimizing the binding energy for each OER intermediate, and (ii) a passivation layer to suppress the oxidation and dissolution of CoTe to some extent. If it is negative, TeO_2 may become an obstacle that prevents the surface OER active species (i.e., CoOOH) from participating in the OER. Either way, future work must focus on investigating the effect of Te oxides on water oxidation electrocatalysis over metal tellurides.

Recently, Lee *et al.* synthesized Te-incorporated NiCo layered double hydroxide (LDH) samples with different Te incorporation levels on Ni foam [χTe-NiCo LDH (χ = 0.2, 0.4, 0.6, and 0.8), where χ denotes the stoichiometric ratios of Te to Co from the synthesis] using the one-step hydrothermal method and examined the Te incorporation effect on their material properties and OER performance.[1171] The material characterization results for the 0.6Te-NiCo LDH sample as a representative case are displayed in Figure 281. Figure 281a

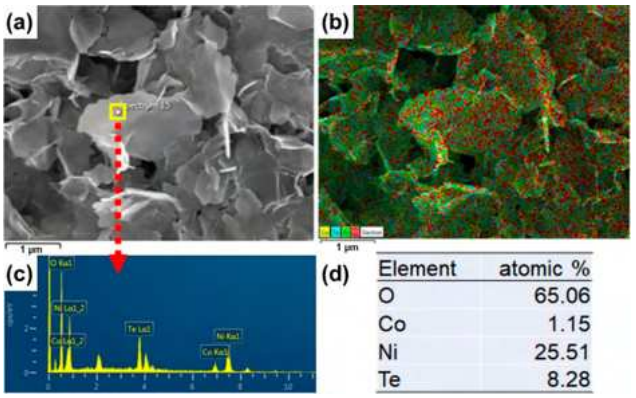


Figure 281. (a) FESEM and (b) EDX elemental mapping images, (c) EDX spectrum, and (d) corresponding quantitative result of Te-incorporated NiCo LTH layered double hydroxides (0.6Te-NiCo LDH) on Ni foam. Reproduced with permission from ref 1171. Copyright 2021 The Korean Institute of Metals and Materials.

shows the formation of a uniform nanosheet structure on Ni foam. EDX analyses revealed the homogeneous distribution of Co, Ni, Te, and O elements throughout the 0.6Te-NiCo LDH and the Co:Ni:Te:O atomic ratio of 1.15:25.51:8.28:65.06 (see Figure 281b–d). The 0.6Te-NiCo LDH sample exhibited the highest OER performance compared with the prepared Te-NiCo LDH samples. Importantly, the 0.6Te-NiCo LDH sample recorded an OER overpotential of 290 mV at 10 $mA{\cdot}cm^{-2}$ and a Tafel slope of 45.4 $mV{\cdot}dec^{-1}$ in 1 M KOH, which are lower than those of the NiCo LDH (350 mV and 110.3 $mV{\cdot}dec^{-1}$). Moreover, the 0.6Te-NiCo LDH showed lower charge transfer resistance (from EIS data) and higher double layer capacitance (17.86 $mF{\cdot}cm^{-2}$) than the NiCo LDH (5.9 $mF{\cdot}cm^{-2}$). According to these results, the authors claimed that the Te incorporation into the NiCoLDH can enhance both its electrical conductivity and number of active sites. This Te-incorporated NiCo LDH study also provides the possibility that the oxidized Te species in the telluride-derived metal oxide/(oxy)hydroxide formed after the OER can also contribute positively for facilitating the OER. However, as for the Te-incorporated NiCo LDH study, further investigations for revealing Te species (i.e., chemical composition) and checking specific OER activity may be necessary to understand the details regarding the role of Te species in the NiCo LDH and evaluate whether Te species truly enhance the intrinsic activity of the NiCo LDH or not.

Unfortunately, there are conflicting reports on the degree of oxidation of the $CoTe_2$ electrocatalysts in alkaline media: a few reports suggest that the $CoTe_2$ surface is stable during the OER,[1128,1129,1132] but several other reports observed the oxidation of $CoTe_2$ into its oxide counterparts (i.e., Co and Te oxides).[97,1132,1146,1147,1150] In general, these discrepancies are attributed to differences in electrochemical testing conditions [i.e., applied potentials, electrolyte concentrations, electrochemical techniques (e.g., CV, CP, and CA), etc.], compatibility of metal tellurides and supports/substrates, crystallinity and morphology of metal tellurides, and so forth. For instance, Lu *et al.* found that the use of multiwalled CNT to support $CoTe_2$ allows easier formation of its oxide counterpart CoOOH during the alkaline OER process in comparison to pure $CoTe_2$.[1132] Further systematic investigations are still necessary to find the universal factors that govern the oxidation of $CoTe_2$ under OER conditions. Findings from such studies would enable control over the oxidation of $CoTe_2$ and other metal tellurides and, hopefully, lead to the development of more stable and efficient catalysts for the OER.

6. TRANSITION METAL-BASED POLYANION COMPOUNDS/COMPOSITES

In recent years, transition metal-based polyanion compounds/composites have also been studied for the electrocatalytic OER and successfully outshined their monoanionic/single-phase counterparts, while becoming the center of attention in this field. Figure 282 shows schematic illustrations of a transition

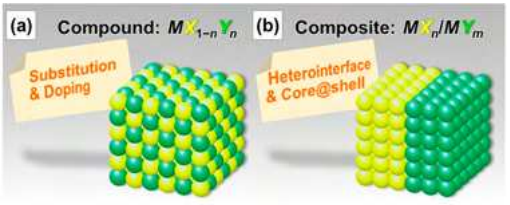


Figure 282. Schematic illustrations of a transition metal-based dual-anion compound ($MX_{1-n}Y_n$) (a) and a composite (MX_n/MY_m) (b). *M* = transition metal(s) (e.g., Ni, Co, Fe, etc.), *X* and *Y* = B, C, N, P, S, Se, or Te ($X \neq Y$).

metal-based dual-anion compound and a composite as simple example systems. Herein, we classify the reported metal-based polyanion *X*-ide electrocatalysts into two groups, "compounds" and "composites", and we briefly introduce some representative "catalyst" and "precatalyst" examples for each group and highlight their electrocatalytic OER activities and electrochemical behaviors during long-term OER testing. For each example, we also provide recommendations or challenges related to the unclear points that need further research. Incidentally, there are also a few exceptional reports about polyanion compound-containing composites [i.e., P-S-NiFe ($FeNi_2S_3$ + $NiPS_3$ + FeS + Fe + C)[845] and O,N-$NiFeC_x$ (likely Ni_3C:N + Fe_3C:N + Fe_2O_3:N)[1179]], which are determined as "classification not possible" and not discussed in the following Sections.

https://doi.org/10.1021/acs.chemrev.3c00005
Chem. Rev. 2023, 123, 12795−13208

6.1. Compounds

In this review, the transition metal-based polyanion compound is defined as a foreign anion(s)-doped/substituted monoanionic metal *X*-ide with a crystalline or amorphous structure (see Figure 282a) (refs 48, 50, 169, 170, 179, 182, 269, 270, 272, 292, 330, 372, 383, 466, 554, 669, 697, 781, 806, 819, 824, 825, 843, 849, 893, 984, 1034, 1035, 1153, 1155, 1172−1175, 1177, 1178, and 1180−1182). As shown in Table 8, in this material group, most of the reported samples showed partial/full oxidation during OER testing (refs 48, 50, 169, 170, 182, 269, 270, 272, 330, 372, 466, 554, 669, 781, 825, 893, 984, 1034, 1035, 1153, 1175, 1177, 1178, and 1180). So far, only a few studies reported their polyanion compounds as stable "catalysts".[1155,1172−1174]

6.1.1. Catalysts. There have been three reports about nickel- and cobalt-selenide-based dual/multiple-anion compound catalysts for the OER.[1155,1172,1174] In one instance, Zuo *et al.* reported a dual-cation- and boron-doped pyrite-type nickel selenide ($Fe_5Co_4Ni_{20}Se_{36}B_x$) as an alkaline OER catalyst.[1172] As shown in Figure 283a, the $Fe_5Co_4Ni_{20}Se_{36}B_x$ nanoparticles were prepared through a two-step process. First, an amorphous membrane (FeCoNi-B) was prepared via a wet-chemical process, involving the aqueous reaction between $NaBH_4$ (as reducing agent) and metal ions (Ni^{2+}, Co^{2+}, Fe^{3+}) from $Ni(NO_3)_2$, $Co(NO_3)_2$, and $FeCl_3$. Subsequently, the as-prepared FeCoNi-B precursor was converted into $Fe_5Co_4Ni_{20}Se_{36}B_x$ through gas-solid selenization (selenium source: selenium powder) at 450 °C for 2 h under N_2 gas flow. Importantly, note that the as-obtained sample was in nanoscale powder form. For comparison, $NiSe_2B_x$, $FeNi_3Se_8B_x$, and $CoNi_3Se_8B_x$ were also prepared by using the same synthetic process with different transition metal-based starting materials. As displayed in Figure 283b, i, the XRD pattern of the $Fe_5Co_4Ni_{20}Se_{36}B_x$ sample can be indexed as the nickel diselenide-type crystal structure. From the Rietveld refinement analysis, it was revealed that Fe, Co, and Ni atoms might co-occupy the same sites in the crystal structure with the Ni:(Fe + Co) and Fe:Co ratios of 2:1 and 1:1, respectively. The refinement analysis further confirmed that B atoms were incorporated in the interstitial sites of the crystal structure (see Figure 283a). Some of the incorporated B atoms formed *M*−B bonding (*M* = Fe, Co, and Ni), while others made B−Se bonding. TEM analysis found that the as-prepared $Fe_5Co_4Ni_{20}Se_{36}B_x$ nanoparticles with relatively uniform sizes were dispersed on the FeCoNi-B membrane (Figure 283b, ii). In the SAED pattern of the $Fe_5Co_4Ni_{20}Se_{36}B_x$ nanoparticle, bright diffraction dots were observed, which indicates its high crystallinity (Figure 283b, iii). On the other hand, the FFT pattern of the FeCoNi-B membrane showed its amorphous nature (Figure 283b, iv). Figure 283c shows the OER LSV curves of all the prepared samples tested in alkaline media (1.0 M KOH). $Fe_5Co_4Ni_{20}Se_{36}B_x$ exhibited a lower overpotential of 279.8 mV at the current density of 10 $mA{\cdot}cm^{-2}$ than $FeNi_3Se_8B_x$ (335 mV), $CoNi_3Se_8B_x$ (453 mV), and $NiSe_2B_x$ (543 mV). In Figure 283d, the corresponding Tafel slopes also followed the same trend as the LSV curves, also indicating that $Fe_5Co_4Ni_{20}Se_{36}B_x$ had more favorable OER kinetics. To investigate the reasons behind this superior OER activity of $Fe_5Co_4Ni_{20}Se_{36}B_x$, the authors also obtained the ECSA-normalized LSV curves and conducted EIS measurement for all the samples. In the ECSA-normalized LSV measurement, among the tested samples, $Fe_5Co_4Ni_{20}Se_{36}B_x$ again showed the highest current densities over the tested potential window, which implies its higher intrinsic activity. The EIS results were similar for all the samples. Furthermore, to examine the effects of cation (Fe and Co) and boron dopants on the OER activity, DFT calculations were performed for the OER free energy pathways on the (111) facets of $Fe_{0.25}Ni_{0.75}Se_2$, $Fe_{0.25}Ni_{0.75}Se_2B_{0.2}$, $Co_{0.25}Ni_{0.75}Se_2$, $Co_{0.25}Ni_{0.75}Se_2B_{0.2}$, $Fe_{0.125}Co_{0.125}Ni_{0.75}Se_2$, and $Fe_{0.125}Co_{0.125}Ni_{0.75}Se_2B_{0.2}$ models. In short, $Fe_{0.125}Co_{0.125}Ni_{0.75}Se_2B_{0.2}$ had a lower theoretical OER overpotential (0.472 V) than $Fe_{0.25}Ni_{0.75}Se_2$ (1.630 V), $Fe_{0.25}Ni_{0.75}Se_2B_{0.2}$ (0.977 V), $Co_{0.25}Ni_{0.75}Se_2$ (1.361 V), $Co_{0.25}Ni_{0.75}Se_2B_{0.2}$ (0.679 V), and $Fe_{0.125}Co_{0.125}Ni_{0.75}Se_2$ (0.581 V). Here, the B-doped models could achieve lower overpotentials than undoped models, an indication of the positive effect of boron dopants on the OER activity. Moreover, from computational studies, the authors proposed OER mechanisms for the pyrite-type multi-metal selenides with and without boron dopants. As seen in Figures 283e and f, boron dopants can weaken the interaction between the electrocatalyst (*) and the -OOH group, reducing the Gibbs free energy (ΔG) for the bottleneck step: $*OOH \rightarrow * + O_2 + H^+ + e^-$. Additionally, Figure 283g indicates the projected density of states (PDOS) of d orbitals of metal atoms (active sites). The redistribution of d electrons in metals happens due to boron doping. The authors also calculated the number of d electrons around active metal sites, showing that boron doping can decrease the total d electron number of metals. Thus, the d electrons are redistributed because of the d electron migration from metals to boron. Based on the experimental and theoretical results, the authors concluded that dual-cation and boron doping could modulate the special atomic and electronic structures of the pyrite-type nickel selenide, thereby enhancing its OER activity. Finally, the stability of the $Fe_5Co_4Ni_{20}Se_{36}B_x$ sample was evaluated by a 10 h chronoamperometric test followed by TEM and STEM elemental mapping analyses. Since the $Fe_5Co_4Ni_{20}Se_{36}B_x$ sample could maintain an OER current density of 10 $mA{\cdot}cm^{-2}$ for 10 h and its pre- and post-OER elemental mapping images showed similar elemental distributions, the authors suggested that the sample was structurally and compositionally stable during the OER. However, the particle size of the $Fe_5Co_4Ni_{20}Se_{36}B_x$ sample was increased after long-term OER testing, the reason for which is still unknown. For this point, we recommend that the authors conduct post-OER XPS analysis to clarify whether an unwanted surface reconstruction (e.g., oxidation, dissolution, decomposition, etc.) occurred or not.

In another instance, the Nath group reported a nickel-selenide-based coordination complex $[Ni\{(SeP^iPr_2)_2N\}_2]$ as an OER catalyst in alkaline media.[1174] The $Ni\{(SeP^iPr_2)_2N\}_2$ ($Ni^{II}Se_4$) was prepared by using a standard Schlenk technique under Ar atmosphere.[1185] Figure 284a shows the crystal structure of the $Ni^{II}Se_4$ complex with a tetrahedral coordination geometry around Ni^{II} ions. To measure the OER activity, the $Ni^{II}Se_4$ complex and Nafion were drop-cast on the various conductive substrates [i.e., Au-coated glass, carbon fiber paper (CFP), and glassy carbon (GC)], resulting in the fabrication of the $Ni^{II}Se_4$@Au, $Ni^{II}Se_4$@CFP, and $Ni^{II}Se_4$@GC electrodes, respectively. First, the authors investigated the Ni oxidation ($Ni^{II} \rightarrow Ni^{III}$) potentials for the $Ni^{II}Se_4$ complex and $Ni(OH)_2$ samples (see Figure 284b). Incidentally, the Ni^{III} can be the actual electrocatalytic center for the OER. Here, the $Ni^{II}Se_4$ complex exhibited a lower Ni^{II} oxidation potential (1.34 V_{RHE}) than the $Ni(OH)_2$ (1.40 V_{RHE}) because Ni^{II}-coordinating Se

https://doi.org/10.1021/acs.chemrev.3c00005
Chem. Rev. 2023, 123, 12795−13208

Table 8. Summary of the Electrocatalytic Properties, Electrochemical Testing Conditions, and Physicochemical Pre- And Post-analyses of Transition Metal-Based Polyanion Compounds/Composites Used for Alkaline/Neutral/Acidic OER and of the Final Type of Electrocatalyst after OER Testing[a−e]

Initial Electrocatalyst	Substrate	Shape of Electrocatalyst	Deposition Type	Specific Loading / $mg \cdot cm^{-2}_{geo}$	η@10 $mA \cdot cm^{-2}_{geo}$ / mV	C_{dl} / $mF \cdot cm^{-2}_{geo}$	TOF / s^{-1} (@η or j)	Tafel Slope / $mV \cdot dec^{-1}$	Electrolyte	Pre-analysis	Post-analysis	Long-Term OER Test Conditions	Post-OER Electrocatalyst	Final Type of Electrocatalyst	Ref.
o-$CoTe_2$|P@HPC/CNTs	GC or CC	Rambutan-like structure	P	-	241	6.6	0.0086 at 245 mV 0.0244 at 270 mV 0.0889 at 295 mV	46	1 M KOH	XRD, EPR, XPS, XAS (XANES, EXAFS), FESEM, TEM, HAADF, EDX, Raman, N_2 ISO (BET)	XRD, TEM, FESEM, EDX	CV activation (50 $mV \cdot s^{-1}$) 24 h CA (the potential at 10 $mA \cdot cm^{-2}_{geo}$) 24 h CA (the potential at 250 $mA \cdot cm^{-2}_{geo}$) 24 h CA (cell voltate: 250 $mA \cdot cm^{-2}_{geo}$, OWS)	*o*-$CoTe_2$|P, CNT	Catalyst	1155
o-$CoTe_2$|S@HPC/CNTs	GC	Rambutan-like structure	P	-	282	-	-	51		XRD, FESEM, TEM, EDX	-	CV activation (50 $mV \cdot s^{-1}$)	-	-	
o-$CoTe_2$|Se@HPC/CNTs	GC	Rambutan-like structure	P	-	~ 276	-	-	62		XRD, FESEM, TEM, EDX	-	CV activation (50 $mV \cdot s^{-1}$)	-	-	
o-$CoTe_2$|P'@HPC/CNTs	GC	-	P	-	326	4.2	~ 0.0025 at 295 mV	71		XRD, XPS, N_2 ISO (BET)	-	CV activation (50 $mV \cdot s^{-1}$)	-	-	
$NiSe_2B_x$	GC	Nanoparticle	P	~ 0.25	543	0.067	-	161	1 M KOH	XRD, SEM, EDX, XPS	-	-	-	-	1172
$FeNi_3Se_6B_x$	GC	Nanoparticle	P	~ 0.25	335	0.081	-	86.3		XRD, SEM, EDX	-	-	-	-	
$CoNi_3Se_6B_x$	GC	Nanoparticle	P	~ 0.25	453	0.063	-	121		XRD, SEM, EDX	-	-	-	-	
$Fe_5Co_4Ni_{20}Se_{36}B_x$	GC	Nanoparticle	P	~ 0.25	279.8	0.055	-	59.5		XRD, SEM, EDX, TEM, STEM, HAADF-STEM-EELS, XPS	TEM, HAADF-STEM, EDX	10 h CA (~ 1.51 V_{RHE})	-	Catalyst	
NiTe/NiS	Ni foam	Nanoarray and quantum-dots	S	~ 1.50	257 (@100 $mA \cdot cm^{-2}_{geo}$)	16.9	0.178 at 300 mV	49	1 M KOH	SEM, TEM, EDX, STEM, XRD, XPS, XANES	XRD, SEM, XPS	50 h CP (50 $mA \cdot cm^{-2}_{geo}$)	NiTe, NiS	Catalyst	763
$(BO_3)_{1.08}$−Ni_3S_4	GC	Nanosheets	P	0.306	306	0.146 mF	-	36.5	1 M KOH	XRD, SEM, TEM, XPS, AFM	TEM, XPS	10 h CP (10 $mA \cdot cm^{-2}_{geo}$) 2000 CV cycles	Borate-doped Ni sulfide	Catalyst	1173
$(BO_3)_{0.78}$−Ni_3S_4	GC	Nanosheets	P	0.306	~ 333	-	-	54.8		XRD, TEM	-	-	-	-	
$(BO_3)_{0.57}$−Ni_3S_4	GC	Nanosheets	P	0.306	~ 322	-	-	49.3		XRD, TEM	-	-	-	-	
porous CoFe-Se-P	GC	Nanocubes	P	0.14	210	-	-	108	0.1 M KOH	XRD, XPS, SEM, TEM, EDX, N_2 ISO (BET)	XRD, SEM, EDX, XPS	40 h CA (1.44 V_{RHE}) 1000 CV cycles	(Co,Fe)Se_2, (Co,Fe)P, $(Co,Fe)_3O_4$	Catalyst	566
solid CoFe-Se-P	GC	Nanocubes	P	0.14	280	-	-	112		XRD, XPS, SEM	-	-	-	-	
NiSP/NF	Ni foam	-	S	4.5	280 (@50 $mA \cdot cm^{-2}_{geo}$)	-	-	182.8	1 M KOH	N_2 ISO (BET)	-	-	-	-	845
NiFeSP/NF	Ni foam	Graphene-like nanosheets	S	4.2	240 (@50 $mA \cdot cm^{-2}_{geo}$)	-	-	76.3		XRD, SEM, TEM, HAADF-STEM, EDX, XPS, N_2 ISO (BET)	SEM, XRD, XPS	25 h CP (50 $mA \cdot cm^{-2}_{geo}$)	NiS, Ni_2P, FeS, $Fe_2P_4O_{12}$	Catalyst	
$[Ni\{(SeP^iPr_2)_2N\}_2]$@Au	Au glass	-	P	0.7	250 390 (@100 $mA \cdot cm^{-2}_{geo}$)	-	0.10 at 300 mV	90.6	1 M KOH	-	-	-	-	-	1174
$[Ni\{(SeP^iPr_2)_2N\}_2]$@CFP	CFP	Particulate	P	0.7	200 310 (@100 $mA \cdot cm^{-2}_{geo}$)	-	0.26 at 300 mV	89.5		SEM, EDX, XRD, XPS	SEM, EDX, XRD, XPS	> 12 h CA (1.44 V_{RHE})	$[Ni\{(SeP^iPr_2)_2N\}_2]$	Catalyst	
$[Ni\{(SeP^iPr_2)_2N\}_2]$@GC	GC	-	P	-	270	-	0.08 at 300 mV	88.7		-	-	-	-	-	
NiTe-NiCoN	Ni foam	3D nanoarray	S	-	~ 255	38.5	-	95	1 M KOH	XRD, SEM, TEM, SAED, HAADF-STEM, EDX, XPS, XANES, CAM	-	-	-	-	363
NiTe-NiFeN	Ni foam	3D nanoarray	S	-	211 294 (@400 $mA \cdot cm^{-2}_{geo}$)	37.4	0.225 at 300 mV	39.9		XRD, SEM, TEM, SAED, HAADF-STEM, EDX, XPS, XANES, CAM	SEM, XPS, TEM, *In-Situ* Raman	40 h multistep CP (10, 20, 50, 100 $mA \cdot cm^{-2}_{geo}$) 100 h CP (10 $mA \cdot cm^{-2}_{geo}$, OWS) 100 h CP (100 $mA \cdot cm^{-2}_{geo}$, OWS)	NiFe (oxy)hydroxide	Precatalyst (partial oxidation)	
					~ 210	-	-	-	1 M KOH + 0.5 M NaCl		UV-Vis, XPS	-	-	-	
					~ 231	-	-	-	1 M KOH + Seawater		EDX	40 h multistep CP (10, 20, 50, 100 $mA \cdot cm^{-2}_{geo}$) 100 h CP (10 $mA \cdot cm^{-2}_{geo}$, OWS) 100 h CP (100 $mA \cdot cm^{-2}_{geo}$, OWS)	-	-	
NiTe-NiFeN (425 °C NH_3 treatment)	Ni foam	3D nanoarray	S	-	~ 211	-	-	-	1 M KOH + 0.5 M NaCl	SEM, AFM	-	-	-	-	
NiTe-NiFeN (500 °C NH_3 treatment)	Ni foam	3D nanoarray	S	-	~ 215	35.5	-	-		SEM, AFM	-	-	-	-	
Fe-NiTe–$Ni_{12}P_5$	Ni foam	Nanosheet array with rough and irregular particles	S	-	275 (@20 $mA \cdot cm^{-2}_{geo}$) 303 (@50 $mA \cdot cm^{-2}_{geo}$) 340 (@100 $mA \cdot cm^{-2}_{geo}$)	10.0	-	66	1 M KOH	XRD, SEM, EDX, TEM, XPS	XRD, SEM, EDX, TEM, XPS	5000 CV cycles 60 h CP (50 $mA \cdot cm^{-2}_{geo}$)	NiOOH (likely with Fe dopant), TeO_x, PO_x	Precatalyst (partial oxidation)	1152

https://doi.org/10.1021/acs.chemrev.3c00005
Chem. Rev. 2023, 123, 12795−13208

Table 8. continued

Initial Electrocatalyst	Substrate	Shape of Electrocatalyst	Deposition Type	Specific Loading / $mg \cdot cm^{-2}_{geo}$	η@10 $mA \cdot cm^{-2}_{geo}$ / mV	C_{dl} / $mF \cdot cm^{-2}_{geo}$	TOF / s^{-1} (@η or j)	Tafel Slope / $mV \cdot dec^{-1}$	Electrolyte	Pre-analysis	Post-analysis	Long-Term OER Test Conditions	Post-OER Electrocatalyst	Final Type of Electrocatalyst	Ref.
NiTe–$Ni_{12}P_5$	Ni foam	Nanosheet array with micro-sized particles	S	-	385 (@50 $mA \cdot cm^{-2}_{geo}$)	7.3	-	105		XRD, SEM, TEM	-	-	-	-	1152
N-Co_2C HS/EC	GC	3D hierarchical structure	P	0.10	278	-	-	77	1 M KOH	XRD, SEM, TEM, EDX, Raman, XPS, XANES, HAADF-STEM	*In-Situ* Raman	-	$CoOOH$, $Co(OH)_2$	Precatalyst	1175
					~ 356	5.9	-	-	0.1 M KOH		-	-	-	-	
Fe-$NiTe_2$/Ni_2P	Ni foam	Loose and porous biscuit-like shape	S	-	190	26.5	-	102	1 M KOH	XRD, SEM, TEM, EDX, XPS	SEM, XPS	1000 CV cycles 22 h CP (10 $mA \cdot cm^{-2}_{geo}$)	$NiFeOOH$, TeO_x, PO_x	Precatalyst	529
$NiTe_2$/Ni_2P	Ni foam	Loose and porous biscuit-like shape	S	-	300	8.6	-	215		SEM	-	-	-	-	
$Ni_{0.85}Se$/NiTe-600	Ni foam	Rod-shaped nanoarray	S	-	251	4.93	-	70.5	1 M KOH	SEM	-	-	-	-	1032
$Ni_{0.85}Se$/NiTe-1200	Ni foam	Rod-shaped nanoarray	S	-	212	7.06	-	53.4		SEM	-	-	-	-	
$Ni_{0.85}Se$/NiTe-1800	Ni foam	Rod-shaped nanoarray	S	-	200	7.49	-	49.7		XRD, SEM, TEM, SAED, EDX, XPS	XRD, SEM, EDX, TEM, XPS, ICP-MS	72 h multistep CA	$NiOOH$, TeO_x, SeO_x	Precatalyst (partial oxidation & Ni dissolution)	
$Ni_{0.85}Se$/NiTe-2400	Ni foam	Rod-shaped nanoarray	S	-	221	6.33	-	54.3		SEM	-	-	-	-	
NiSP/NF	Ni foam	Honey-comb structure with nanoparticles	S	-	281	71.43	2.0781	68.51	1 M KOH	XRD, SEM, EDX, TEM, SAED, XPS	XRD, SEM, XPS	60 h multistep CP (10, 50, 100 $mA \cdot cm^{-2}_{geo}$) 3000 CV cycles (100 $mV \cdot s^{-1}$)	NiS, Ni_2P, $Ni(OH)_2$, NiOOH, Oxidized S species, Oxidized P species	Precatalyst (partial oxidation)	754
NiSP/NF	Ni foam	Numerous grains covered with nanosheets	S	~ 4.8	259 341 (@50 $mA \cdot cm^{-2}_{geo}$) 395 (@100 $mA \cdot cm^{-2}_{geo}$)	3.36	-	99	Fe-purified 1 M KOH	XRD, SEM, EDX, TEM, SAED, XPS, TXRF	XRD, SEM, EDX, XPS, TXRF	20 h CP (20 $mA \cdot cm^{-2}_{geo}$)	NiO_xH_y, Sulfate (SO_4^{2-})	Precatalyst	49
CoP-$CoTe_2$	CP	Nanowire	P	2	346	-	~ 0.0022 at 350 mV	44	1 M NaOH	XRD, SEM, XPS, TEM, EDX, HAADF-STEM	XRD, SEM, XPS, TEM, EDX, HAADF-STEM	14 h CP (10 $mA \cdot cm^{-2}_{geo}$) 100 h CP (10 $mA \cdot cm^{-2}_{geo}$, OWS)	$Co_3(TeO_3)_2(OH)_2$, $Co(OH)_2$	Precatalyst (full oxidation)	532
S-CoTe 15 min	CC	-	S	-	~ 283	-	-	-	1 M KOH	-	-	-	-	-	1153
S-CoTe 20 min	CC	Cross-linked 1D nanorods	S	-	257 318 (@100 $mA \cdot cm^{-2}_{geo}$)	48.9	-	63		XRD, SEM, TEM, SAED, HAADF-STEM, XANES, XPS	TEM, EDX, HAADF-STEM, XANES, XPS, Raman	50 & 1500 CV cycles 20 h CA	$CoOOH$, SO_x, TeO_x	Precatalyst (partial oxidation)	
S-CoTe 25 min	CC	-	S	-	~ 270	-	-	-		-	-	-	-	-	
P-$Ni_{0.75}Fe_{0.25}Se_2$	Ni foam	Nanosheet with particles	S	1.32	156	3.29	0.18 at 250 mV	19.5	1 M KOH	XRD, SEM, TEM, EDX, XPS	XRD, SEM, XPS	48 h multistep CP (10, 50, 100, 300 $mA \cdot cm^{-2}_{geo}$) 1000 h CP (300 $mA \cdot cm^{-2}_{geo}$)1000 h CP (100 $mA \cdot cm^{-2}_{geo}$, OWS)	NiFe oxide/hydroxide species, P-O species, Se-O species	Precatalyst (partial oxidation)	1034
	CC	-	S	-	~ 187	-	-	-		-	-	-	-	-	
P-$Ni_{0.75}Fe_{0.25}Se_2$	CC	Interlinked nanosheet structure with nanoparticles	S	0.72	192 185 (with iR correction)	6.25	0.18 at 500 mV	31.5 27.2 (with iR correction)	1 M KOH	XRD, SEM, TEM, STEM, EDX, Mössbauer, XAS (XANES, XAFS), ICP-OES	XRD, XPS	120 h CP (100 $mA \cdot cm^{-2}_{geo}$) 5000 CV cycles (50 $mV \cdot s^{-1}$)	NiFe oxide/hydroxide species, P-O species, Se-O species	Precatalyst (partial oxidation)	1035
CoC_x/ $(Co_{0.55}Fe_{1.945})_2P$@C	GC	Spherical nanoparticle aggregate	P	~ 0.3	390	-	-	65	1 M KOH	XRD, SEM, EDX, TEM, XPS, Raman, N_2 ISO (BET), UV-Vis, ICP-OES	XRD, SEM, XPS	1000 CV cycles 2 h CP	$CoOOH$, P-C species	Precatalyst (partial oxidation)	245
Co_xP@Ni-Co-S/NF (3 min)	Ni foam	Nanosheet	S	-	~ 372 (@100 $mA \cdot cm^{-2}_{geo}$)	-	-	-	1 M KOH	SEM	-	-	-	-	759
Co_xP@Ni-Co-S/NF (6 min)	Ni foam	Nanosheet with rough surface	S	-	~ 366 (@100 $mA \cdot cm^{-2}_{geo}$)	-	-	-		SEM	-	-	-	-	
Co_xP@Ni-Co-S/NF (9 min)	Ni foam	2D/2D hierarchical porous structure	S	-	271 (@50 $mA \cdot cm^{-2}_{geo}$) 289 (@100 $mA \cdot cm^{-2}_{geo}$)	2.513	-	62		XRD, SEM, EDX, XPS, Raman, ICP-AES	XRD, SEM, XPS	32.5 h CP (50 $mA \cdot cm^{-2}_{geo}$)	NiOOH, CoOOH	Precatalyst (partial oxidation)	
Co_xP@Ni-Co-S/NF (12 min)	Ni foam	2D/2D hierarchical porous structure	S	-	~ 346 (@100 $mA \cdot cm^{-2}_{geo}$)	-	-	-		SEM	-	-	-	-	
Co_xP@Ni-Co-S/NF (15 min)	Ni foam	2D/2D hierarchical porous structure	S	-	~ 370 (@100 $mA \cdot cm^{-2}_{geo}$)	-	-	-		SEM	-	-	-	-	
CoP/Mo_2CT_x	GC	Stacked layers covered with nanoarrays	P	1.428	260	10.39	~ 37 at 300 mV	51	1 M KOH	XRD, SEM, TEM, HAADF-STEM, EDX, XPS, N_2 ISO (BET), ICP-OES	XRD, SEM, EDX, TEM, Raman, XPS	50 h CP (10 $mA \cdot cm^{-2}_{geo}$) 3000 CV cycles	$CoOOH$, PO_x	Precatalyst (partial oxidation)	246
	CC		P	0.4	-	-	-	-			-	50 h CA (cell voltage: 1.56 V, OWS)	-	-	
CBPC-1 (Co–B–P/BCCNF)	Ni foam	3D nanofiber networks covered with nanocotton clusters	P	4.0	291	5.79	-	185	1 M KOH	SEM	-	-	-	-	169

https://doi.org/10.1021/acs.chemrev.3c00005
Chem. Rev. 2023, 123, 12795−13208

Table 8. continued

Initial Electrocatalyst	Substrate	Shape of Electrocatalyst	Deposition Type	Specific Loading / $mg \cdot cm^{-2}_{geo}$	η@10 $mA \cdot cm^{-2}_{geo}$ / mV	C_{dl} / $mF \cdot cm^{-2}_{geo}$	TOF / s^{-1} (@η or j)	Tafel Slope / $mV \cdot dec^{-1}$	Electrolyte	Pre-analysis	Post-analysis	Long-Term OER Test Conditions	Post-OER Electrocatalyst	Final Type of Electrocatalyst	Ref.
CBPC-2 (Co–B–P/BCCNF)	Ni foam	3D nanofiber networks covered with nanocotton clusters	P	4.0	262	14.51	-	164		XRD, SEM, EDX, TEM, SAED, XPS, Raman	XPS	24 h CA (1.492 V_{RHE})	Co oxide/hydroxide, BO_x, PO_x	Precatalyst	169
CBPC-3 (Co–B–P/BCCNF)	Ni foam	3D nanofiber networks covered with nanocotton clusters	P	4.0	279	11.38	-	170		SEM	-	-	-	-	
CBPC-4 (Co–B–P/BCCNF)	Ni foam	3D nanofiber networks covered with nanocotton clusters	P	4.0	289	6.28	-	173		SEM	-	-	-	-	
Co-Mo-P (3)/ Zn-Co-S	GC	Nanoneedles (flower-like structure)	S	0.17	273	5.0	0.119 at 340 mV	41	1 M KOH	FESEM, EDX, XRD, XPS, FTIR	FESEM, EDX, XRD, XPS	10 h CA (1.55 V_{RHE}) 500 CV cycles 3000 s multistep CP (10, 50, 100, 150, 200 $mA \cdot cm^{-2}_{geo}$)	Metal (oxy)hydroxides, Sulfates, Phosphates	Precatalyst (partial oxidation)	530
W,P-FeB	Ni foam	3D nano-forest structure	P	-	209 246 (@50 $mA \cdot cm^{-2}_{geo}$) 259 (@100 $mA \cdot cm^{-2}_{geo}$)	8.57	-	39.87	1 M KOH	XRD, SEM, EDX, TEM, SAED, XPS, Raman	XRD, TEM, XPS, Raman, ICP-MS	25 h CA (1.458 V_{RHE})	W-doped FeOOH	Precatalyst (full oxidation)	170
P-FeB	Ni foam	-	P	-	228 256 (@50 $mA \cdot cm^{-2}_{geo}$) 268 (@100 $mA \cdot cm^{-2}_{geo}$)	8.06	-	45.41		XRD	-	-	-	-	
Cu_3N–Cu_3P/NPSC NWs@NF	Ni foam	Nanowall array consisting of nanoplates	S	0.82	240	6.53	-	53.8	1 M KOH	XRD, SEM, TEM, SAED, EDX, XPS	EDX (after OWS)	36 h CP (10 $mA \cdot cm^{-2}_{geo}$) 24 h CP (10 $mA \cdot cm^{-2}_{geo}$, OWS)	Cu oxides/hydroxides, C oxides	Precatalyst	1176
8% $FeNi_3N$-Ni_3S_2	GC	-	P	0.425	~ 237	-	~ 0.29 at 270 mV	39	1 M KOH	XRD	-	-	-	-	369
12% $FeNi_3N$-Ni_3S_2	GC	Semihexagonal-shaped particle	P	0.425	230	-	0.33 at 270 mV	38		XRD, SEM, EDX, TEM, XPS	XRD, TEM, XPS	40000 s CP (10 $mA \cdot cm^{-2}_{geo}$)	$Ni(OH)_2$, NiOOH	Precatalyst (partial oxidation)	
	Ni foam		P	2	-	-	-	-			-	-	-	-	
18% $FeNi_3N$-Ni_3S_2	GC	-	P	0.425	~ 247	-	~ 0.13 at 270 mV	27		XRD	-	-	-	-	
26% $FeNi_3N$-Ni_3S_2	GC	-	P	0.425	~ 245	-	~ 0.12 at 270 mV	23		XRD	-	-	-	-	
$NiS_{90}Se_{10}$	GC	Spherical particles	P	0.24	318	-	-	-	1 M KOH	XRD, SEM, TEM, EDX, XPS, Kr ISO (BET)	TEM, EDX, HAADF, ICP-MS	6 and ~ 22 h CP (10 $mA \cdot cm^{-2}_{geo}$)	NiO_xH_y, NiO	Precatalyst (partial oxidation)	47
$NiS_{75}Se_{25}$	GC	Spherical particles	P	0.24	324	-	-	-		XRD, SEM, XPS, Kr ISO (BET)	-	-	-	-	
$NiS_{50}Se_{50}$	GC	Spherical particles	P	0.24	412	-	-	-		XRD, SEM, XPS, Kr ISO (BET)	-	-	-	-	
NiCoP-$NiCoSe_2$ (activated)	CC	Nanoparticles and nanosheets	S	0.073 (before activation) 0.035 (after activation)	243	5.5	-	52	1 M KOH	XRD, SEM, XPS, TEM, EDX	SEM, XPS	200 CV cycles (50 $mV \cdot s^{-1}$, −0.2–0.8 V_{SCE}, activation) 80 h CA (1.56 V_{RHE}) 1000 CV cycles	NiCo (oxy)hydroxides	Precatalyst (surface oxidized before the OER)	537
CoP_2-CoSe (activated)	CC	Nanoparticles and nanosheets	S	-	340	-	-	-		-	-	200 CV cycles (50 $mV \cdot s^{-1}$, −0.2–0.8 V_{SCE}, activation)	-	-	
NiP_2-NiSe (activated)	CC	Nanoparticles and nanosheets	S	-	270	-	-	-		-	-	200 CV cycles (50 $mV \cdot s^{-1}$, −0.2–0.8 V_{SCE}, activation)	-	-	
Ni_1Co_9P-$Ni_1Co_9Se_2$ (activated)	CC	Nanoparticles and nanosheets	S	-	309	-	-	-		-	-	200 CV cycles (50 $mV \cdot s^{-1}$, −0.2–0.8 V_{SCE}, activation)	-	-	
Ni_3Co_7P-$Ni_3Co_7Se_2$ (activated)	CC	Nanoparticles and nanosheets	S	-	260	-	-	-		-	-	200 CV cycles (50 $mV \cdot s^{-1}$, −0.2–0.8 V_{SCE}, activation)	-	-	
Ni_7Co_3P-$Ni_7Co_3Se_2$ (activated)	CC	Nanoparticles and nanosheets	S	-	278	-	-	-		-	-	200 CV cycles (50 $mV \cdot s^{-1}$, −0.2–0.8 V_{SCE}, activation)	-	-	
Ni_9Co_1P-$Ni_9Co_1Se_2$ (activated)	CC	Nanoparticles and nanosheets	S	-	313	-	-	-		-	-	200 CV cycles (50 $mV \cdot s^{-1}$, −0.2–0.8 V_{SCE}, activation)	-	-	
$CoSe_{1.26}P_{1.42}$	CC	Nanostructure	S	-	255.00	118.39	-	87	1 M KOH	XRD, SEM, TEM, Raman, EDX, XPS, ICP-MS	ICP-MS, XPS, EDX, TEM	15 h CA (1.322 V_{RHE})	CoOOH	Precatalyst (almost full oxidation)	48
$CoSe_{0.45}P_{1.18}$	CC	Nanostructure	S	-	263	105.38	-	89		XRD, SEM, ICP-MS	-	-	-	-	
$CoSe_{2.01}P_{0.49}$	CC	Nanostructure	S	-	280	26.39	-	91		XRD, SEM, ICP-MS	-	-	-	-	
$CoSe_{1.61}P_{0.54}$	CC	Nanostructure	S	-	268	111.1	-	90		XRD, SEM, ICP-MS	-	-	-	-	
VN-Co-P	GC	Nanowire	P	-	335	-	-	-	1 M KOH	XRD, SEM, EDX, XPS, TEM, Raman	TEM	-	Amorphous oxide/hydroxide	Precatalyst (partial oxidation)	372
VN-P	GC	Nanowire	P	-	401	-	-	-		XRD, SEM	-	-	-	-	
N0-MoS_2	-	Flower-like structure	P	0.36	> 570 (@5 $mA \cdot cm^{-2}_{geo}$)	-	-	-	1 M KOH	XRD, Raman, XPS, SEM, ESR	-	5 min CV cycles (5 $mV \cdot s^{-1}$, 0–0.9 $V_{Hg/HgO}$)	-	-	1177
N1-MoS_2	-	Flower-like structure	P	0.36	~ 514	-	-	-		XRD, Raman, XPS, SEM, ESR	-	5 min CV cycles (5 $mV \cdot s^{-1}$, 0–0.9 $V_{Hg/HgO}$)	-	-	
N2-MoS_2	-	Flower-like structure	P	0.36	~ 396	-	-	-		XRD, Raman, XPS, SEM, ESR	-	5 min CV cycles (5 $mV \cdot s^{-1}$, 0–0.9 $V_{Hg/HgO}$)	-	-	

https://doi.org/10.1021/acs.chemrev.3c00005
Chem. Rev. 2023, 123, 12795−13208

Table 8. continued

Initial Electrocatalyst	Substrate	Shape of Electrocatalyst	Deposition Type	Specific Loading / $mg \cdot cm^{-2}_{geo}$	η@10 $mA \cdot cm^{-2}_{geo}$ / mV	C_{dl} / $mF \cdot cm^{-2}_{geo}$	TOF / s^{-1} (@η or f)	Tafel Slope / $mV \cdot dec^{-1}$	Electrolyte	Pre-analysis	Post-analysis	Long-Term OER Test Conditions	Post-OER Electrocatalyst	Final Type of Electrocatalyst	Ref.
N3-MoS_2	-	Flower-like structure	P	0.36	~329	10.9	-	-		XRD, Raman, XPS, SEM, TEM, EDX, ESR, N_2 ISO (BET)	XRD, Raman, XPS, TEM, EDX, N_2 ISO (BET)	5 min CV cycles (5 $mV \cdot s^{-1}$, 0–0.9 $V_{Hg/HgO}$)	Amorphous MoO_x	Precatalyst (partial oxidation)	1177
MoO_x@N0-doped MoS_{2-x}	-	-	P	0.36	480	8.6	-	116		-	-	-	-	-	
MoO_x@N1-doped MoS_{2-x}	-	-	P	0.36	390	11.5	-	66		-	-	-	-	-	
MoO_x@N2-doped MoS_{2-x}	-	-	P	0.36	350	12.5	-	67		-	-	-	-	-	
MoO_x@N3-doped MoS_{2-x}	-	-	P	0.36	270	15	-	61		XRD, Raman, XPS, TEM, EDX, N_2 ISO (BET)	XRD, Raman, XPS	2000 CV cycles (50 $mV \cdot s^{-1}$) 72000 s CA (1.6 V_{RHE})	Amorphous MoO_x	Precatalyst (partial oxidation)	
MoO_y/N3-MoS_{2-x}	-	-	P	0.36	420	-	-	-		XRD	-	-	-	-	
$(MoS_2)_{0.06}Mo_2C$	GC	Core@shell nanoparticles	P	~0.18	310	1.10	-	233	0.1 M KOH	XRD, SEM, EDX, TEM, XPS, Raman	-	-	-	-	255
$(MoS_2)_{0.125}Mo_2C$	GC	Core@shell nanoparticles	P	~0.18	280	1.92	-	209			TEM, XRD, XPS	12 h CA (1.54 V_{RHE})	-	Precatalyst (partial oxidation)	
$(MoS_2)_{0.25}Mo_2C$	GC	Core@shell nanoparticles	P	~0.18	360	0.60	-	293			-	-	-	-	
P-$NiMo_4N_5$@Ni-1	Ni foam	Twist braid nanorod arrays	S	~2.5	297 (@100 $mA \cdot cm^{-2}_{geo}$)	30.1	-	33.6	1 M KOH	XRD, SEM, TEM, EDX, XPS, FTIR	XRD, SEM, TEM, EDX, XPS, FTIR	24 h CA (1.47 V_{RHE})	$NiOOH, MoO_x$	Precatalyst (partial oxidation)	330
P-$NiMo_4N_5$@Ni-2	Ni foam	Nanoflower arrays	S	-	370 (@100 $mA \cdot cm^{-2}_{geo}$)	17.9	-	44.1		XRD, SEM, TEM, HAADF-STEM, EDX	SEM	-	-	-	
P-$NiMo_4N_5$@Ni-3	Ni foam	Tremella-like thin nanosheet arrays	S	-	420 (@100 $mA \cdot cm^{-2}_{geo}$)	14.3	-	59.9		XRD, SEM, TEM, HAADF-STEM, EDX	SEM	-	-	-	
P-$NiMo_4N_5$@Ni-4	Ni foam	Irregular nanorod arrays shape	S	-	403 (@100 $mA \cdot cm^{-2}_{geo}$)	-	-	49.4		XRD, SEM	-	-	-	-	
P-$NiMo_4N_5$@Ni-5	Ni foam	Irregular bulk shape	S	-	426 (@100 $mA \cdot cm^{-2}_{geo}$)	-	-	58.2		XRD, SEM	-	-	-	-	
$Ni_{33.3}B_{14.7}O_{52.0}$	GC	Nanosheets	P	0.2264	335	0.251	-	90.8	1 M KOH	XRD, SEM, XAS (XANES), ICP-OES	-	-	-	-	50
$Ni_{33.4}P_{1.5}B_{12.6}O_{52.4}$	GC	Nanocages	P	0.2264	330	-	-	80.9		XRD, TEM, ICP-OES	-	-	-	-	
$Ni_{35.0}P_{2.7}B_{9.8}O_{52.5}$	GC	Nanocages	P	0.2264	308	-	-	81.7		XRD, TEM, ICP-OES	-	-	-	-	
$Ni_{33.7}P_{3.2}B_{10.2}O_{52.9}$	GC	Nanocages	P	0.2264	300	0.416	-	67.4		XRD, TEM, XAS (XANES), ICP-OES	-	-	-	-	
$Ni_{34.0}P_{3.4}B_{9.8}O_{52.9}$	GC	Nanocages	P	0.2264	328	-	-	66.7		XRD, TEM, ICP-OES	-	-	-	-	
$Ni_{31.2}P_{6.8}B_{7.6}O_{54.5}$	GC	Nanocages	P	0.2264	313	-	-	124		XRD, TEM, ICP-OES	-	-	-	-	
$Fe_{0.3}Ni_{28.6}P_{6.8}B_{8.7}O_{55.6}$	GC	Nanocages	P	0.2264	297	0.224	-	67		XRD, SEM, TEM, ICP-OES	-	-	-	-	
$Fe_{4.0}Ni_{20.8}P_{11.6}P_{4.3}O_{58.9}$	GC	Nanocages	P	0.2264	263	0.520	-	50		XRD, SEM, TEM, ICP-OES	-	-	-	-	
$Fe_{6.4}Ni_{16.1}P_{12.9}B_{4.3}O_{60.2}$	GC	Nanocages	P	0.2264	236	0.240	-	39		XRD, SEM, TEM, SAED, EDX, ICP-OES, XAS (XANES, FT-EXAFS), XPS, STEM	XRD, SEM, TEM, SAED, STEM, EDX, XPS, XAS (XANES, FT-EXAFS)	50 h CA (1.466 V_{RHE}) 30 h CP (10 $mA \cdot cm^{-2}_{geo}$) 40 h CA (1.52 V_{RHE})	Metal oxides/(oxy)hydroxides, Oxidized P and B species	Precatalyst (partial oxidation)	
$Fe_{10.2}Ni_{12.0}P_{12.3}B_{4.5}O_{60.6}$	GC	Nanocages	P	0.2264	253	0.256	-	73		XRD, SEM, TEM, ICP-OES	-	-	-	-	
$Fe_{10.0}Ni_{5.5}P_{15.5}B_{5.5}O_{63.1}$	GC	Nanosheets	P	0.2264	326	0.395	-	80		XRD, SEM, TEM, ICP-OES	-	-	-	-	
$Fe_{16.8}Ni_{6.1}P_{9.3}B_{7.7}O_{60.1}$	GC	Nanosheets	P	0.2264	344	0.463	-	67		XRD, SEM, TEM, ICP-OES	-	-	-	-	
$Fe_{23.3}Ni_{3.3}P_{3.1}B_{9.8}O_{58.5}$	GC	Nanosheets	P	0.2264	383	0.420	-	69		XRD, SEM, TEM, ICP-OES	-	-	-	-	
Co_3C-NB	GC, CC	Nanosheets	P	0.353	358	-	0.05 at 354 mV	90	0.1 M KOH	XRD, SEM, EDX, TEM, SAED, XPS, N_2 ISO (BET)	XRD, SEM	24 h CP (50 $mA \cdot cm^{-2}_{geo}$) 4 h CP (100 $mA \cdot cm^{-2}_{geo}$)	$Co(OH)_2$, CoO	Precatalyst (partial oxidation)	270
Co_3C-N	GC, CC	Nanoparticles	P	0.353	435	-	0.05 at 450 mV	97			-	24 h CP (50 $mA \cdot cm^{-2}_{geo}$)	-	-	
Co_3C-B	GC, CC	Nanosheets	P	0.353	439	-	0.05 at 460 mV	92.2			-	24 h CP (50 $mA \cdot cm^{-2}_{geo}$)	-	-	
Mo_2C-Mo_2N (h-TMCN)	Ni foam	Nanosheets	P	1	230	185.4	0.189 at 300 mV	82	1 M KOH	XRD, SEM, EDX, TEM, TGA, N_2 ISO (BET, PSD), XAFS, XPS	SEM, EDX, TEM, XPS	40 h CA [1.47 (20 h), 1.495 (10 h), 1.51 V_{RHE} (10 h)]	MoO_x (Mo^{6+} species)	Precatalyst (partial oxidation)	256
untreated NiFePB	-	-	S	-	-	45.67 × 10^{-3}	-	-	1 M NaOH	-	-	-	-	-	1178
a-NiFePB (activated NiFePB)	-	Porous skeleton structure	S	-	197 217 (@100 $mA \cdot cm^{-2}_{geo}$)	358 × 10^{-3}	-	34		XRD, SAED, TEM, EDX, XPS, XAS (XANES, EXAFS)	XRD, TEM, XPS, ICP-MS	1400 h CP (100 $mA \cdot cm^{-2}_{geo}$) 12 h CP (10 $mA \cdot cm^{-2}_{geo}$) 3 CV cycles (0–0.85 V) > 50 h multistep CP (10, 20, 40, 100, 200 $mA \cdot cm^{-2}_{geo}$)	$NiFeO_xH_y$, Borate	Precatalyst (surface oxidized before the OER)	
O,N-$NiFeC_x$-350 (O,N-codoped Ni-Fe carbides)	GC	Nanocubes	P	~0.28	270	-	0.025 at 300 mV 0.082 at 350 mV	43	1 M KOH	XRD, FESEM, TEM, SAED, HAADF, EDX, XPS, N_2 ISO, Raman	FESEM, TEM, SAED, HAADF, EDX, XPS, *In-Situ* Raman	25000 s CP (10 $mA \cdot cm^{-2}_{geo}$) 10 CV cycles (5 $mV \cdot s^{-1}$, 1.2–1.6 V_{RHE}) 800 s CP (1 $mA \cdot cm^{-2}_{geo}$, *In-Situ* Raman)	$NiFeO_xH_y$	Precatalyst (partial oxidation)	1179
NiSSe (NiS + NiSe)	Ni foam	Nanograins	S	-	247 (@30 $mA \cdot cm^{-2}_{geo}$)	5.75 mF	-	175.7	1 M KOH	XRD, SEM, TEM, XPS, Raman	FESEM, Raman	50 h CP (100 $mA \cdot cm^{-2}_{geo}$)	Ni_3S_2	Precatalyst (unique transformation)	669

https://doi.org/10.1021/acs.chemrev.3c00005
Chem. Rev. 2023, 123, 12795−13208

Table 8. continued

Initial Electrocatalyst	Substrate	Shape of Electrocatalyst	Deposition Type	Specific Loading / $mg \cdot cm_{geo}^{-2}$	η@10 $mA \cdot cm_{geo}^{-2}$ / mV	C_{dl} / $mF \cdot cm_{geo}^{-2}$	TOF / s^{-1} (@η or j)	Tafel Slope / $mV \cdot dec^{-1}$	Electrolyte	Pre-analysis	Post-analysis	Long-Term OER Test Conditions	Post-OER Electrocatalyst	Final Type of Electrocatalyst	Ref.
Co-P-B-5	GC	Nanoparticles	P	0.30	290	0.067	0.1747 $atom^{-1} \cdot s^{-1}$ at 500 mV	42	1 M NaOH	XRD, XPS, TEM, SAED, N_2 ISO (BET)	TEM, XPS	20 h CA (1.53 V_{RHE}) 500 CV cycles	CoOOH, Oxidized P, Oxidized B	Precatalyst (partial oxidation)	182
$NiCoS/Ti_3C_2T_x$	GC	Nanosheets	P	~0.21	365	2.4	0.009 at 350 mV 0.036 at 400 mV	58.2	1 M KOH	Raman, TEM, EDX, SEM, N_2 ISO (BET), XRD, XPS	XPS, SEM, TEM, EDX	20000 s CP (10 $mA \cdot cm_{geo}^{-2}$)	NiCoOOH	Precatalyst (partial oxidation)	274
$NiCoSe_2$@NiO@ $CoNi_2S_4$@CoS_2	Ni foam	Nanosheets	S	-	310 (@30 $mA \cdot cm_{geo}^{-2}$)	126.1	-	159.1	1 M KOH	XRD, XPS, SEM, TEM, STEM, EDX	SEM, XRD, XPS	24 h CP (10 $mA \cdot cm_{geo}^{-2}$)	FeOOH, Co-based oxides, hydroxides, oxyhydroxides, SeO_x	Precatalyst (partial oxidation)	782
$Ni_{0.25}Co_{0.65}S_{0.4}Se_{0.6}$	FTO	Nanocrystals	P	-	358	-	0.02484 at 350 mV	64	1 M KOH	XRD, TEM, STEM, EDX, XPS, ICP	XRD, TEM, STEM, EDX, XPS, ICP	8 h CP (10 $mA \cdot cm_{geo}^{-2}$)	Ni-Co oxides and hydroxides	Precatalyst (full oxidation)	984
$Ni_{0.75}Co_{0.28}S_{0.2}Se_{0.8}$	FTO	Nanocrystals	P	-	373	-	0.01588 at 350 mV	64		XRD, TEM, ICP	-	-	-	-	
rGO–few-layer $FePSe_3$	GC	Nanosheets	P	0.150	430	-	-	117	0.5 M KOH	XRD, Raman, XPS, TEM, TPM	XRD, XPS	7 h CA (1.7 V_{RHE})	α-Fe_2O_3	Precatalyst (partial oxidation)	1180
few-layer $FePSe_3$	GC	Ultrathin sheets	P	0.150	~752	-	-	209		XRD, Raman, SEM, DEX, XPS, AFM, TPM	-	-	-	-	
bulk $FePSe_3$	GC	Bulk	P	0.150	~888 (@5 $mA \cdot cm_{geo}^{-2}$)	-	-	221		XRD, Raman, VDP, CL, SEM, EDX	-	-	-	-	
Co_9S_8-NSC@Mo_2C	GC	Polyhedral nanoparticles with rough surface	P	0.425	293	17.5	-	~59.7	1 M KOH	XRD, Raman, XPS, SEM, TEM, STEM, N_2 ISO (BET)	SEM, XPS	20 h CA (1.53 V_{RHE}) 2500 CV cycles (1.0–1.8 V_{RHE})	-	Precatalyst	273
(NiFe)PS_3	GC	Nanosheets	P	-	275	-	-	41.7	1 M KOH	SEM, TEM, EDX, XRD, XPS, FTIR	XPS, TEM, Raman	2000 CV cycles	(NiFe)OOH, $(NiFe)(OH)_2$, Oxidized S and P species	Precatalyst (partial oxidation)	466
(NiFe)PS_3	Ni foam		P	-	223	-	-	-		SEM, TEM, EDX, XRD, XPS, FTIR	-	-	-	-	
Ni_3S_2|P (P-decorated Ni_3S_2)	Ni foam	Nanosheet arrays	S	~0.92	420 (@100 $mA \cdot cm_{geo}^{-2}$)	-	-	224	1 M KOH	SEM, TEM, AFM, STEM, EDX, XRD, Raman, XPS	SEM, TEM, Raman, XPS	-	NiOOH, S-O species	Precatalyst (partial oxidation)	781
O-N-Co_9S_8/N-RGO (O,N-co-doped Co_9S_8 on N-doped reduce graphite oxide)	GC	Distorted cubic crystals	P	0.40	350	-	-	-	0.1 M KOH	XRD, SEM, TEM, EELS, XPS	XRD, XPS, TEM	20 h CA (1.60 V_{RHE}) 2000 CV cycles (50 $mV \cdot s^{-1}$, 0.9–1.7 V_{RHE})	Co_3O_4, SO_4^{2-}	Precatalyst (almost full oxidation)	893
O-N-Co_9S_8	GC	-	P	0.40	~390	-	-	-		-	-	-	-	-	
N-WC@CFP	CFP	Nanoarray	P	10	245	50.5	-	-	0.5 M H_2SO_4	XRD, SEM, EDX, TEM, XPS	XRD	1 h CP (10 $mA \cdot cm_{geo}^{-2}$)	W oxide ($WO_{2.92}$)	Precatalyst (partial oxidation)	269
NiS_xP_y (Ni_3S_2/$Ni_{12}P_5$)	Ni foam	Nanowires on nanorods	S	~6	178 192 (FE correction)	14.46 mF	-	95	1 M KOH	SEM, EDX, TEM, STEM, XRD, Raman, XPS, XAS, (XANES, EXAFS)	XRD, Raman, XPS, XAS, (XANES, EXAFS), SEM	135 h CA (1.43 V_{RHE}) ~45 h CP (20 and 30 $mA \cdot cm_{geo}^{-2}$)	NiOOH, SO_4^{2-}, PO_4^{3-}	Precatalyst (partial oxidation)	564
NiS_xP_y (Ni_3S_2/$Ni_{12}P_5$)	Ni foam	Nanowires on nanorods	S	~6	241 315 (FE correction)	458.3 μF	-	211.7	0.5 M $KHCO_3$ (pH = 8.54)	SEM, EDX, TEM, STEM, XRD, Raman, XPS, XAS, (XANES, EXAFS)	-	-	Green precipitation (maybe $NiCO_3$) observed on electrode surface after the long-term OER test	Precatalyst	
CoSe$_2$|CoP	CFP	Nanosheets	S	2.14	240	13.1	-	46.6	Fe-purified 1 M KOH	XRD, EDX, Raman, XPS, SEM, TEM	XPS, SEM, TEM, EDX	120 h CA (1.47 V_{RHE})	$Co(OH)_2$/CoOOH	Precatalyst (full oxidation)	556
S:CoP NPs	GC	Nanoparticle	P	0.4–0.5	300	14.59	0.23 at 350 mV	107	1 M KOH	SEM	-	-	-	-	554
S:CoP@NG	GC	Nanoparticle	P	0.4–0.5	260	43.09	-	108		XRD, SEM	-	-	-	-	
S:CoP@CC	CC	Nanoparticle	S	~1.2	290	186.27	-	94		XRD, TEM, STEM-EDX, XPS, ICP-OES	TEM, STEM-EDX, XPS, ICP-OES	20 h CA (1.58 V_{RHE})	S- and P-doped CoO_x (CoO, Co_3O_4), P–O species	Precatalyst (partial oxidation)	
S:CoP@NF	Ni foam	Nanoparticles	S	~1.2	270	218.02	0.12 at 350 mV	82		SEM	-	20 h CA (1.58 V_{RHE})	-	-	
B,N:Mo_2C@BCN-2	GC	Nanoparticles	P	1	290	20.51	-	61	1 M KOH	XRD, SEM, EDX, TEM, XPS, ICP	TEM, XPS, EA	20 h CA (1.58 V_{RHE})	MoO_x, -CO_x, -NO_x, -B–O	Precatalyst (partial oxidation)	272
N:Mo_2C@NC	GC	Nanoparticles	P	1	303	5.08	-	66		XRD, SEM	-	-	-	-	
P-CoMoS/CC	CC	Nanoflake	S	2.19	260	34.9	-	70.2	1 M KOH	XRD, XPS, FESEM, TEM, STEM-EDX, ICP-OES, N_2 ISO (BET)	XPS, XRD	24 h CA (1.55 V_{RHE}) 2000 CV cycles (1.3–1.8 V_{RHE})	Co- or Mo-oxide/hydroxide species, SO_4^{2-}, PO_x	Precatalyst (partial oxidation)	825
P-CoS/CC	CC	Micro-particulate	S	2.56	390	14.1	-	96.5		XRD, FESEM, N_2 ISO (BET)	-	-	-	-	
P-MoS/CC	CC	Nanoflake	S	2.54	432	17.8	-	124.7		XRD, FESEM, N_2 ISO (BET)	-	-	-	-	
P-CoMoS/CC	CC	Nanoflake	S	2.19	369	-	-	-	1 M PBS (pH = 6.8)	XRD, XPS, FESEM, TEM, STEM-EDX, ICP-OES, N_2 ISO (BET)	-	24 h CA	-	-	
P-CoMoS/CC	CC	Nanoflake	S	2.19	345	-	-	-	0.5 M H_2SO_4	XRD, XPS, FESEM, TEM, STEM-EDX, ICP-OES, N_2 ISO (BET)	-	24 h CA	-	-	

https://doi.org/10.1021/acs.chemrev.3c00005
Chem. Rev. 2023, 123, 12795−13208

Table 8. continued

Initial Electrocatalyst	Substrate	Shape of Electrocatalyst	Deposition Type	Specific Loading / $mg \cdot cm^{-2}_{geo}$	η@10 $mA \cdot cm^{-2}_{geo}$ / mV	C_{dl} / $mF \cdot cm^{-2}_{geo}$	TOF / s^{-1} (@η or j)	Tafel Slope / $mV \cdot dec^{-1}$	Electrolyte	Pre-analysis	Post-analysis	Long-Term OER Test Conditions	Post-OER Electrocatalyst	Final Type of Electrocatalyst	Ref.
EG/Ni_3Se_2/Co_9S_8	Graphite foil	Nanosheet	S	~2.5	330 (@25 $mA \cdot cm^{-2}_{geo}$) 390 (@50 $mA \cdot cm^{-2}_{geo}$) 440 (@100 $mA \cdot cm^{-2}_{geo}$)	-	-	131	1 M KOH	FESEM, EDX, TEM, XPS, N_2 ISO (BET), Raman, AFM, XRD, ICP-OES, CAM	XPS, TEM, ICP-OES	10 h CP (100 $mA \cdot cm^{-2}_{geo}$) 1 h CP (100 $mA \cdot cm^{-2}_{geo}$, FE)	Ni oxo/hydroxy species, Co oxo/hydroxy species, SeO_x, SO_4^{2-}	Precatalyst (partial oxidation)	826
N, P-Co_9S_8/CoS_2/$Co_{1-x}S$	CP	Nanosheet	P	0.2	285	33.13	-	70.1	1 M KOH	XRD, SEM, Raman, N_2 ISO (BET), TEM, EDX, XPS	-	1000 CV cycles 10 h CP	-	-	1181
N-Co_9S_8/CoS_2	CP	-	P	0.2	307	8.82	-	89.5		XRD, Raman, XPS	-	-	-	-	
N-Co_9S_8	CP	-	P	0.2	318	7.61	-	80.0		XRD, Raman, XPS	-	-	-	-	
NiFeCuP@Ni_3S_2/NiF	Ni foam	Wrinkled nanosheet	S	~20	230 282 (@50 $mA \cdot cm^{-2}_{geo}$) 351 (@100 $mA \cdot cm^{-2}_{geo}$)	12.52	-	42	1 M KOH	XRD, SEM, EDX, TEM, SAED, XPS, N_2 ISO (BET, PSD)	-	18 h CP (20 $mA \cdot cm^{-2}_{geo}$) 2000 CV cycles	-	-	761
NiFeP@Ni_3S_2/NiF	Ni foam	Wrinkled nanosheet	S	~20	236 318 (@50 $mA \cdot cm^{-2}_{geo}$) 400 (@100 $mA \cdot cm^{-2}_{geo}$)	6.17	-	54		XRD, SEM, TEM, XPS, N_2 ISO (BET)	-	11.5 h CP	-	-	
NiP@Ni_3S_2/NiF	Ni foam	-	S	~20	280 374 (@50 $mA \cdot cm^{-2}_{geo}$) 463 (@100 $mA \cdot cm^{-2}_{geo}$)	-	-	63		-	-	-	-	-	
NiS_2/$NiSe_2$	GC	Hollow nanocage	P	~0.136	290 (@20 $mA \cdot cm^{-2}_{geo}$) 345 (@50 $mA \cdot cm^{-2}_{geo}$)	2.99	0.0656 at 300 mV	119	1 M KOH	XRD, SEM, TEM, EDX, Raman, XPS, N_2 ISO (BET, PSD)	TEM	5000 CV cycles 20 h CA (1.63 V_{RHE})	-	-	762
Physical mixture of NiS/NiS_2 and $NiSe_2$	GC	-	P	~0.136	366 (@20 $mA \cdot cm^{-2}_{geo}$)	-	-	-		-	-	-	-	-	
NiNS (Ni_3N/Ni_3S_2)	Ni foam	-	S	20	300 404 (@100 $mA \cdot cm^{-2}_{geo}$)	9.51	-	112	1 M KOH	XRD, SEM, EDX, TEM, XPS, EA	XRD	5000 CV cycles 12 h CA (1.62 V_{RHE})	-	-	405
MNiNS (Mechanically mixed Ni_3N and Ni_3S_2)	Ni foam	-	S	20	-	0.6	-	308.2			-	-	-	-	
Co1-Fe1-B-P (*M*:P = 1:10)	Ni foam	-	P	0.46	297	-	-	-	1 M KOH	-	-	-	-	-	179
Co1-Fe1-B-P (*M*:P = 1:15)	Ni foam	Nanochains	P	0.46	253	6	-	40		XRD, XPS, SEM, TEM, EDX	SEM	4500 s multistep CA (0 → 60 → 0 $mA \cdot cm^{-2}_{geo}$, 15 $mA \cdot cm^{-2}_{geo}$ per 500 s) 11 h CA (1.455 V_{RHE})	-	-	
Co1-Fe1-B-P (*M*:P = 1:20)	Ni foam	-	P	0.46	274	-	-	-		-	-	-	-	-	
CoNiSSe-0.1 ($Co_{0.9}Ni_{0.1}S_{0.5}Se_{1.5}$)	GC	Aggregated nanosheets	P	~0.96	~403	0.116	-	122.9	1 M KOH	XRD, Raman, SEM, ICP-OES	-	-	-	-	1182
CoNiSSe-0.2 ($Co_{0.8}Ni_{0.2}S_{0.5}Se_{1.5}$)	GC	Aggregated nanosheets	P	~0.96	~393	0.132	-	93.7		XRD, Raman, SEM, ICP-OES	-	-	-	-	
CoNiSSe-0.3 ($Co_{0.7}Ni_{0.3}S_{0.5}Se_{1.5}$)	GC	3D flower-like structure	P	~0.96	370	0.317	-	65.5		XRD, Raman, XPS, SEM, TEM, STEM, EDX, ICP-OES	-	1000 CV cycles (100 $mV \cdot s^{-1}$, 1.02−1.58 V_{RHE}) 5000 s CP (1.56 V_{RHE})	-	-	
CoNiSSe-0.4 ($Co_{0.6}Ni_{0.4}S_{0.5}Se_{1.5}$)	GC	Aggregated nanosheets	P	~0.96	~397	0.163	-	88.1		XRD, Raman, SEM, ICP-OES	-	-	-	-	
N-Ni_3S_2	Ni foam	Nanoparticles	S	-	320	-	-	71.9	1 M KOH	SEM, TEM, XPS	-	-	-	-	697
N-Ni_3S_2/VS_2	Ni foam	Nanosheets	S	-	297	-	-	70.5		FESEM, EDX, TEM, XRD, XPS, N_2 ISO (BET), Raman	-	-	-	-	
[d]Ni-cdc (Ni-S-P-O)	GC	Aggregated particles	P	1.3	251	0.01142 mF	35.28 × 10^{-5} at 300 mV 57.82 × 10^{-5} at 500 mV	44.2	0.1 M KOH	XRD, SEM, EDX	-	500 CV cycles (1.164−1.764 V_{RHE})	-	-	1183
[d]Ni-ecda (Ni-S-P-O)	GC	Aggregated particles	P	1.3	732	0.00995 mF	4.33 × 10^{-5} at 300 mV 6.60 × 10^{-5} at 500 mV	60.9		XRD, SEM, EDX	-	-	-	-	
[d]Ni *i*-mnt (Ni-S-P-O)	GC	Aggregated particles	P	1.3	609	0.00782 mF	5.20 × 10^{-5} at 300 mV 8.88 × 10^{-5} at 500 mV	65.1		XRD, SEM, EDX	-	-	-	-	
[d]Ni-NED (Ni-S-P-O)	GC	Aggregated particles	P	1.3	702	0.00588 mF	5.36 × 10^{-5} at 300 mV 7.09 × 10^{-5} at 500 mV	67.1		XRD, SEM, EDX	-	-	-	-	
N-$(Ni,Fe)_3S_2$/NIF	NiFe alloy foam (Fe 15%)	Nanosheets	S	-	167	~17.7	-	33	1 M KOH	TG-IR, SEM, XRD, TEM, EDX, XPS	XRD, EDX	50 h CP (10 $mA \cdot cm^{-2}_{geo}$) 20 h CP (10 $mA \cdot cm^{-2}_{geo}$)	-	-	819
N-Ni_3S_2/NF	Ni foam	Particulate	S	-	242	-	-	76		TG-IR, SEM, XRD, TEM	-	20 h CP (10 $mA \cdot cm^{-2}_{geo}$)	-	-	

https://doi.org/10.1021/acs.chemrev.3c00005
Chem. Rev. 2023, 123, 12795−13208

Table 8. continued

Initial Electrocatalyst	Substrate	Shape of Electrocatalyst	Deposition Type	Specific Loading / $mg \cdot cm^{-2}_{geo}$	η@10 $mA \cdot cm^{-2}_{geo}$ / mV	C_{dl} / $mF \cdot cm^{-2}_{geo}$	TOF / s^{-1} (@η or j)	Tafel Slope / $mV \cdot dec^{-1}$	Electrolyte	Pre-analysis	Post-analysis	Long-Term OER Test Conditions	Post-OER Electrocatalyst	Final Type of Electrocatalyst	Ref.
H:N-$(Ni,Fe)_3S_2$/NIF	NiFe alloy foam (Fe 15%)	Particulate	S	-	172	-	-	32		TG-IR, SEM, XRD, TEM	-	20 h CP (10 $mA \cdot cm^{-2}_{geo}$)	-	-	819
N-(Ni,Fe)S/NIF	NiFe alloy foam (Fe 15%)	Particulate	S	-	189	~ 6.6	-	57		SEM, XRD, TEM	-	20 h CP (10 $mA \cdot cm^{-2}_{geo}$)	-	-	
N-$(Ni,Fe)_9S_8$/NIF	NiFe alloy foam (Fe 50%)	-	S	-	~ 195	-	-	-		XRD	-	-	-	-	
Co_2P/CoN-in-NCNTs	GC	Nanoparticles encapsulated nanotubes	P	0.10	420	-	-	-	0.1 M KOH	XRD, SEM, STEM, TEM, EDX, XPS, N_2 ISO (BET), TGA, Raman	-	-	-	-	1184
P-S-NiFe NCs	GC	Nanocube	P	-	270	0.26407	-	35	1 M KOH	XRD, SEM, XPS, EDX, N_2 ISO (BET)	-	12 h CA 1000 CV cycles	-	-	565
S-P-NiFe NCs	GC	Irregular shape	P	-	~ 400	0.21713	-	68		XRD, SEM	-	-	-	-	
Pni_3S_2/NF (P-doped Ni_3S_2)	Ni foam	Nanosheets	S	-	306 (@100 $mA \cdot cm^{-2}_{geo}$)	-	-	99	1 M KOH	FESEM, TEM, EDX, XPS, XRD, ICP-ES, N_2 ISO (BET)	-	10 h CA (1.54 V_{RHE})	-	-	806
Fe_4N/Fe_3C	GC	Microparticle	P	0.57	451	-	-	54	1 M KOH	XRD, TEM, XPS, VSM	-	1000 CV cycles	-	-	277
N_1–NiS_2-500	CP	Nanosheets	S	-	~ 364 (@40 $mA \cdot cm^{-2}_{geo}$)	-	~ 0.27 at 370 mV ~ 0.83 at 470 mV	-	1 M KOH	XRD, SEM, XPS	-	-	-	-	824
N_2–NiS_2-500	CP	Nanoellipses	S	-	270 ~352 (@40 $mA \cdot cm^{-2}_{geo}$)	-	0.39 at 370 mV 1.78 at 470 mV	-		XRD, SEM, XPS	-	1000 CV cycles (100 $mV \cdot s^{-1}$) 40 h CA (1.5 V_{RHE}) 600 s CA (1.53 V_{RHE}, FE)	-	-	
N_3–NiS_2-500	CP	Nanosheets	S	-	~ 390 (@40 $mA \cdot cm^{-2}_{geo}$)	-	~ 0.20 at 370 mV ~ 0.64 at 470 mV	-		XRD, SEM, XPS	-	-	-	-	
N-Ni_3S_2/NF	Ni foam	Nanopore	S	-	-	37.5	-	70	1 M KOH	SEM, XRD, TEM, XPS	-	10000 s CA (1.55 V_{RHE})	-	-	843
NIN (PF/$Ni_{1.5}Co_{1.5}N$)	GC	Nanorods	P	0.25	280 380 470	14.0	1.4×10^{-3} at 350 mV	66.1	1 M KOH	XRD, XPS, SEM, EDX, TEM, HAADF-STEM, ISO (BET)	SEM, EDX	1000 CV cycles	-	-	383
	Ni foam			-	-	-	-	-			-	20 h CA (1.51 V_{RHE})	-	-	
NIA (P,F-doped Ni-Co nitride/oxide hybrids)	GC	-	P	0.25	310	8.25	0.8×10^{-3} at 350 mV	67.2		XRD, XPS, ISO (BET)	-	-	-	-	
P/$Co_{1.5}Ni_{1.5}N$	GC	Nanorods	P	0.25	320	-	-	79.0		SEM, EDX	-	-	-	-	
F/$Co_{1.5}Ni_{1.5}N$	GC	Aggregated particles	P	0.25	340	-	-	74.2		SEM, EDX	-	-	-	-	
PF/$Ni_{0.75}Co_{2.25}N$	GC	-	P	0.25	290	-	-	77.5		XRD	-	-	-	-	
PF/$Ni_{2.25}Co_{0.75}N$	GC	-	P	0.25	340	-	-	109.2		XRD	-	-	-	-	
PF/Ni_3N	GC	-	P	0.25	300	-	-	81.0		XRD	-	-	-	-	
PF/Co_3N	GC	-	P	0.25	310	-	-	86.2		XRD	-	-	-	-	
CoNP@NC/NG-700	GC	Core@shell nanoparticles	P	0.08	390	5.9	-	78	0.1 M KOH	XRD, SEM, EDX, TEM, XPS, TGA, Raman	TEM	1000 CV cycles (0–1.2 $V_{Ag/AgCl}$) 5000 s CA (1.565 V_{RHE})	-	-	404
CoNP/NG-700	GC	Nanoparticle	P	0.08	480	1.9	-	98		XRD, XPS	-	5000 s CA (1.565 V_{RHE})	-	-	
N-Co_9S_8/G	GC	Nanoparticle	P	0.2	409	-	-	82.7	0.1 M KOH	TEM, SEM, Raman, XRD, TGA	-	2000 CV cycles (100 $mV \cdot s^{-1}$, 1.4–1.7 V_{RHE})	-	-	849
NA-Co_9S_8/G	GC	-	P	0.2	433	-	-	83		-	-	-	-	-	
N-Co_9S_8	GC	-	P	0.2	548	-	-	241		-	-	-	-	-	
N-Fe_3C@CNT/PC (FeNC-800)	GC	Nanoparticles	P	0.9	410	-	-	137	0.1 M KOH	XRD, SEM, EDX, TEM, XPS, Raman, N_2 ISO (BET, PSD), TGA	-	5000 s CP (10 $mA \cdot cm^{-2}_{geo}$)	-	-	292

[a]Some values (i.e., "specific loading", "η", and "C_{dl}") were calculated or obtained from the descriptions and figures in the previous papers. "Post-OER Electrocatalyst" and "Final Type of Electrocatalyst" were determined based on the experimental results and descriptions provided in the previous papers. [b]η, overpotential; j, current density; C_{dl}, double layer capacitance; TOF, turnover frequency; P, powder-coated electrode; S, self-supported electrode; CV, cyclic voltammetry; CA, chronoamperometry; CP, chronopotentiometry; OWS, overall water splitting. [c]Electrolyte abbreviation: PBS (phosphate buffer solution). [d]Substrate abbreviations: GC (glassy carbon); CC (carbon cloth); CP (carbon paper); CFP (carbon fiber paper); FTO (fluorine-doped tin oxide). [e]Analysis abbreviations (minor terms only): ISO (isotherm); PSD (pore size distribution); CAM (contact angle measurement); TG-IR (infrared spectroscopy); EA (elemental analysis); TPM (two-probe measurement); CL (cathodoluminescence); ESR (electron spin resonance measurement); VSM (vibrating sample magnetometry).

https://doi.org/10.1021/acs.chemrev.3c00005
Chem. Rev. 2023, 123, 12795−13208

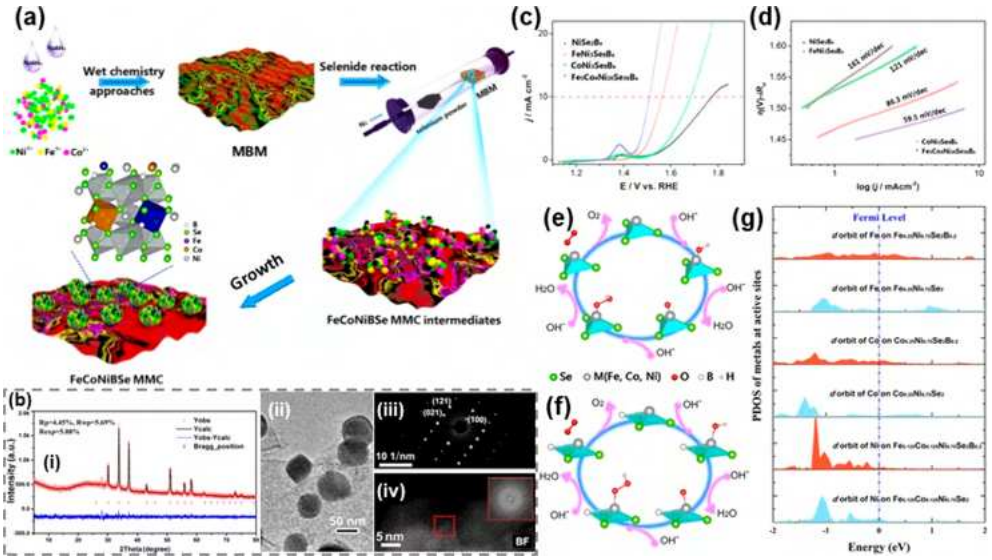


Figure 283. (a) Schematic illustration of the synthesis of $Fe_5Co_4Ni_{20}Se_{36}B_x$ nanoparticles on amorphous FeCoNiB membrane (MBM). (b) XRD pattern and Rietveld refinement results (i), HRTEM image (ii), and SAED pattern (iii) of $Fe_5Co_4Ni_{20}Se_{36}B_x$ nanoparticles, and (iv) STEM image of the supporting membrane. (c) *iR*-corrected polarization curves and (d) corresponding Tafel slopes of $NiSe_2B_x$, $FeNi_3Se_8B_x$, $CoNi_3Se_8B_x$, and $Fe_5Co_4Ni_{20}Se_{36}B_x$ obtained in 1.0 M KOH. (e, f) Proposed OER mechanisms for (e) B-doped and (f) undoped pyrite selenides. (g) Projected density of states (PDOS) of transition metal atoms at active sites. Reproduced with permission from ref 1172. Copyright 2019 American Chemical Society.

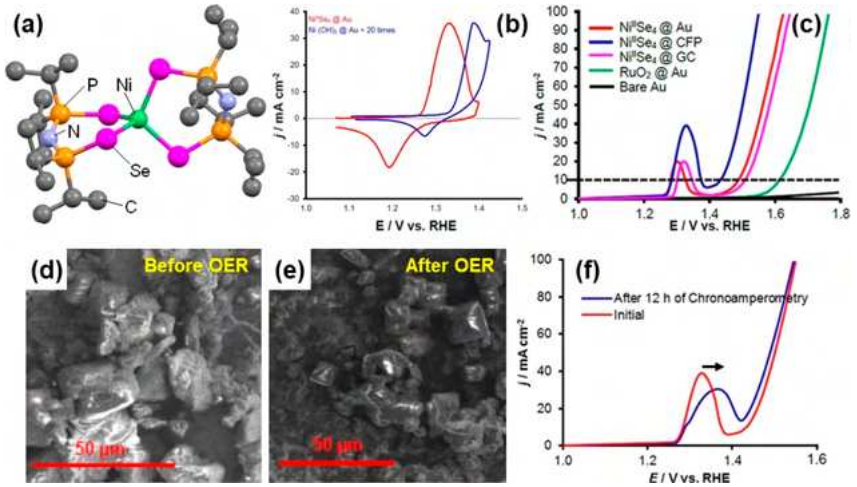


Figure 284. (a) Molecular structure of the $[Ni\{(SeP^iPr_2)_2N\}_2]$ complex ($Ni^{II}Se_4$) with the tetrahedral seleno-coordination of Ni^{II}. (b) Cyclic voltammograms (scan rate: 10 mV·s^{-1}) of $Ni^{II}Se_4$@ Au and $Ni(OH)_2$@Au electrodes. (c) Linear sweep voltammograms (scan rate: 10 mV·s^{-1}) of $Ni^{II}Se_4$@Au, $Ni^{II}Se_4$@CFP, $Ni^{II}Se_4$@GC, RuO_2@Au, and bare Au electrodes. (d, e) SEM images of $Ni^{II}Se_4$@CFP (d) before and (e) after the 12 h OER chronoamperometric test (applied potential: 1.44 V_{RHE}). (f) Linear sweep voltammograms of $Ni^{II}Se_4$@CFP before and after the 12 h OER test. Reproduced with permission from ref 1174. Copyright 2016 Wiley.

atoms in the $Ni^{II}Se_4$ have a lower electronegativity than Ni^{II}-coordinating O atoms in the $Ni(OH)_2$. This low electronegativity of ligands (O → Se) can increase the covalence of the Ni^{II}–ligand bonding. A similar trend in transition metal oxidation potential was also previously observed in iron-selenide-based complexes $[Fe\{(EP^iPr_2)_2N\}_2]$ (E = S, Se).[1186] Second, the authors evaluated the electrocatalytic OER performance of the $Ni^{II}Se_4$@Au, $Ni^{II}Se_4$@CFP, and $Ni^{II}Se_4$@GC electrodes in 1.0 M KOH. RuO_2@Au and bare Au electrodes were also tested for comparison. As indicated in Figure 284c, the $Ni^{II}Se_4$-based electrodes showed better OER performance compared with the RuO_2@Au and bare Au electrodes. Especially, the $Ni^{II}Se_4$@CFP recorded the lowest OER overpotential of 200 mV at the current density of 10 mA·cm^{-2} among all the $Ni^{II}Se_4$-based electrodes. This may be because CFP possesses a highly porous three-dimensional structure, realizing efficient charge transfer throughout the electrode. Finally, the authors further investigated the electrochemical, compositional, and structural stability of $Ni^{II}Se_4$@CFP by performing a 12 h chronoamperometric test (applied potential: 1.44 V_{RHE}) and subsequent SEM, EDX, XRD, and XPS analyses. $Ni^{II}Se_4$@CFP exhibited a stable current density with continuous oxygen generation for 12 h, indicating its high electrochemical stability. Figures 284d and e show the pre- and post-OER SEM images of the $Ni^{II}Se_4$, which confirm that its original surface morphology was maintained even after a 12 h OER test. In both the pre- and post-OER EDX spectra, nickel, phosphorous, and selenium signals were present with similar

https://doi.org/10.1021/acs.chemrev.3c00005
Chem. Rev. 2023, 123, 12795−13208

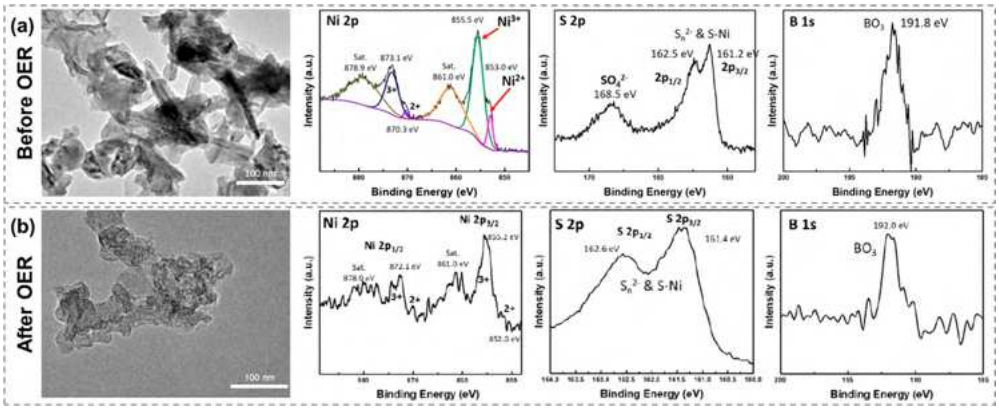


Figure 285. TEM images and Ni 2p, S 2p, and B 1s XPS spectra of a borate-doped nickel sulfide catalyst [$(BO_3)_{1.08}$-Ni_3S_4] (a) before and (b) after long-term OER testing in 1 M KOH. Reproduced with permission from ref 1173. Copyright 2019 Wiley.

relative ratios of Ni:P:Se (= ~1:3:4). The XRD patterns of the $Ni^{II}Se_4$ before and after the OER showed a similar position for each diffraction peak. Furthermore, for the Ni 2p and Se 3d XPS spectra before and after the OER, the authors claimed that the peaks were of a similar nature. From these characterization results, the authors concluded that the $Ni^{II}Se_4$ is compositionally and structurally stable under the tested OER condition. However, as seen in Figure 284f, the Ni^{II} oxidation potential was anodically shifted, which possibly implies a change in the environment around Ni ions in the complex. So far, it is well-known that the anodic shift of Ni redox peaks in Ni (oxy)hydroxide can occur due to incidental Fe incorporation from the unpurified KOH electrolyte.[200] Thus, we guess that similar Fe incorporation into the $Ni^{II}Se_4$ complex could happen during the OER process, which needs to be clarified in the future.

In addition to the selenide-based dual/multiple-anion compounds, one example has also been reported regarding a nickel-sulfide-based multiple-anion compound as a stable OER catalyst. Zhang *et al.* synthesized borate-doped nickel sulfide nanosheets [$(BO_3)_x$-Ni_3S_4, x = 0.57, 0.78, and 1.08] via a simple hydrothermal process and tested them for the electrocatalytic OER in 1 M KOH.[1173] The optimal borate-doped nickel sulfide [$(BO_3)_{1.08}$-Ni_3S_4] exhibited a lower OER overpotential (306 mV) at 10 mA·cm^{-2} and a smaller Tafel slope (36 mV·dec^{-1}) than borate-free Ni_3S_4 (338 mV, 57 mV·dec^{-1}), indicating the positive effect of borate dopants on OER activity. The $(BO_3)_{1.08}$-Ni_3S_4 sample maintained a potential of ~1.56 V_{RHE} at a constant current density of 10 mA·cm^{-2} for 10 h, indicating its high electrochemical stability. To examine the morphological and compositional stability, TEM and XPS analyses were performed for $(BO_3)_{1.08}$-Ni_3S_4 before and after the OER. As seen in Figure 285, the initial morphology and characteristic Ni 2p, S 2p, and B 1s XPS signals were preserved after OER testing, from which the authors concluded that the constitution of $(BO_3)_{1.08}$-Ni_3S_4 was stable even after long-term OER testing.

6.1.2. Precatalysts. As mentioned above, most of the crystalline and amorphous polyanion compounds can be classified as "precatalysts" for the OER (see Table 8). To begin, we will discuss the polyanion compound precatalysts undergoing almost complete oxidation during the OER. Wang *et al.* synthesized quaternary Ni-Co-S-Se alloy nanocrystals through a solution-based method and investigated the specific roles of Ni, Co, S, and Se elements on OER activity as well as the compositional and structural transformations during the OER.[984] The authors also prepared NiSe, CoSe, and Ni-Co-Se nanocrystals by using a similar method without a sulfur source (1-dodecanethiol), in which the amounts of $Ni(acac)_2$ and $Co(acac)_2$ were controlled. The as-prepared NiSe, CoSe, Ni-Co-Se, and Ni-Co-S-Se samples possessed the same hexagonal crystal structure. All the as-prepared nanocrystals, which were loaded on FTO substrates, were tested for OER electrolysis in 1 M KOH. As seen in Figure 286a, the Ni-Co-S-Se ($Ni_{0.25}Co_{0.65}S_{0.4}Se_{0.6}$) sample showed a lower OER overpotential (358 mV) at 10 mA·cm^{-2} and a smaller Tafel slope (64 mV·dec^{-1}) than the NiSe, CoSe, and Ni-Co-Se ($Ni_{0.3}Co_{0.74}Se$) samples. The TOF of the Ni-Co-S-Se sample was 24.84 × 10^{-3} s^{-1} at an overpotential of 350 mV, which was higher than those of the NiSe (0.04 × 10^{-3} s^{-1}), CoSe (3.46 × 10^{-3} s^{-1}), and Ni−Co−Se (10.05 × 10^{-3} s^{-1}) samples, suggesting the highest intrinsic OER activity of the Ni-Co-S-Se samples tested. To investigate the actual OER active sites, the authors conducted post-OER characterization (XRD, ICP, TEM, STEM, EDX, XPS, etc.) of the tested samples. According to the characterization results, NiSe did not experience the compositional and structural transformation (no formation of Ni oxide or hydroxide species) during the OER. In contrast, CoSe was completely transformed into amorphous CoO_x and $Co(OH)_x$ species during OER testing. Similarly, after the OER, the Ni-Co-Se sample was turned into amorphous Ni-Co oxides/hydroxides and a small fraction of tiny CoO/NiO nanocrystals. Interestingly, the Ni-Co-S-Se showed a slightly different OER transformation compared with the Ni-Co-Se sample. As shown in Figures 286b−l, the Ni-Co-S-Se sample underwent almost full oxidation during OER testing, resulting in the generation of more crystalline products: small Ni-Co oxide nanocrystals (~1−2 nm in diameter), crystalline $Co(OH)_2$ nanosheets, and amorphous Ni-Co oxide/hydroxide. The authors assumed that the defects (Figure 286d) and boundaries (Figures 286c, e, and f) in the Ni-Co-S-Se sample could become preferential nucleation sites for the crystalline oxide/hydroxide species and that the superior OER activity of the Ni-Co-S-Se sample might mainly result from the crystalline oxide/hydroxide species formed during the OER. Note that, according to the post-OER ICP and/or XPS results, no residual Se and/or S was detected in the Ni-Co, Ni-Co-Se, and Ni-Co-S-Se samples, implying that the Se and S species in the initial selenides might be dissolved into the electrolyte by forming SeO_x and SO_x species.

https://doi.org/10.1021/acs.chemrev.3c00005
Chem. Rev. 2023, 123, 12795−13208

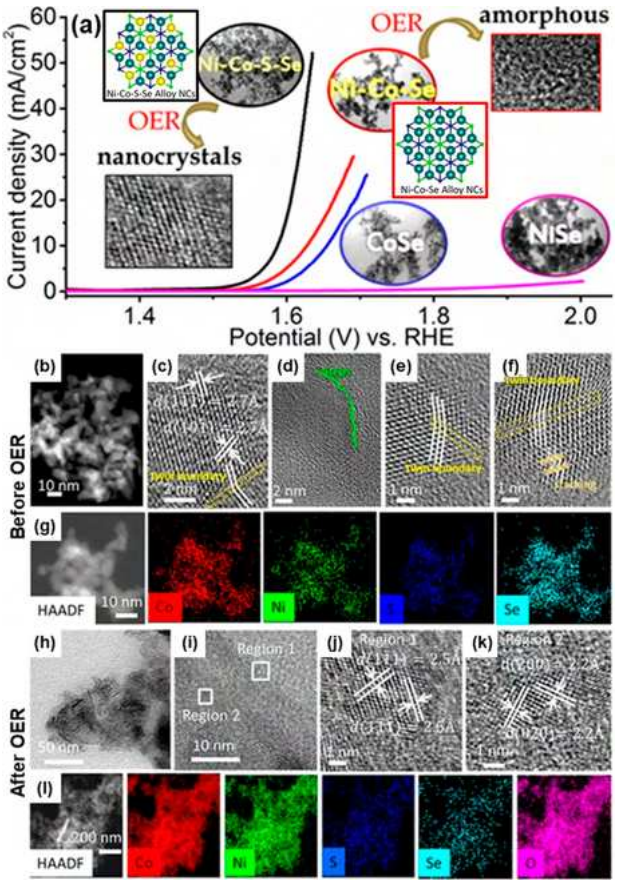


Figure 286. (a) LSV curves of Ni-Co-S-Se, Ni-Co-Se, CoSe, and NiSe on FTO substrates in 1 M KOH. (b) HAADF-STEM, (c–f) HRTEM, and (g) EDX elemental mapping images of $Ni_{0.25}Co_{0.65}S_{0.4}Se_{0.6}$ NCs before the OER. (h) TEM, (i–k) HRTEM, and (l) EDX elemental mapping images of $Ni_{0.25}Co_{0.65}S_{0.4}Se_{0.6}$ NCs after the OER. Reproduced with permission from ref 984. Copyright 2018 American Chemical Society.

From the Ni-Co-S-Se case, it was suggested that the insertion of a foreign anion into the *X*-ide may alter its oxidation behavior during the OER. Recently, Zuo *et al.* also found that the oxidation resistance of cobalt selenide under OER conditions can be altered by partial P-substitution. In this report, the authors prepared P-substituted $CoSe_2$ (P-$CoSe_2$) nanostructure samples through the thermal phosphoselenization of cobalt hydroxide carbonate hydrate precursors $[Co(OH)(CO_3)_{0.5}{\cdot}xH_2O]$. In alkaline media (1 M KOH), the best-performing P-$CoSe_2$ ($Co_{1.26}Se_{1.42}$) sample recorded an OER overpotential of 255 mV at 10 mA·cm^{-2}, which is smaller than that of the phosphorous-free $CoSe_2$. To reveal the behavior of the $CoSe_2$ and $CoSe_{1.26}P_{1.42}$ samples when they contact alkaline electrolytes, liquid-phase TEM measurements were performed. Specifically, the authors took *in situ* STEM images of $CoSe_2$ and $CoSe_{1.26}P_{1.42}$ after immersion in 1 M KOH. 150 s after immersion, the $CoSe_2$ sample maintained the initial morphology (Figures 287a and b), whereas the $CoSe_{1.26}P_{1.42}$ bulk was transformed into numerous nanoparticles (Figures 287e and f). From the corresponding HRTEM images (Figures 287c and d), the $CoSe_2$ surface was preserved after contact with the alkaline electrolyte. However, as shown in Figures 287g and h, $Co(OH)_2$ was formed on the $CoSe_{1.26}P_{1.42}$ surface after immersion in the alkaline electrolyte. These results indicate that $CoSe_{1.26}P_{1.42}$ is more unstable compared with $CoSe_2$ in 1 M KOH. Furthermore, the authors also investigated the stability of $CoSe_2$ and $CoSe_{1.26}P_{1.42}$ under potentials characteristic of the OER. For both the $CoSe_2$ and $CoSe_{1.26}P_{1.42}$ samples, the almost complete oxidation into CoOOH during the OER was confirmed by post-OER ICP-MS (Co:Se:P = 1:1.26:1.42 → 1:0.03:0.11, Co:Se = 1:2.13 → 1:0.08). *In situ* electrospectroscopic analyses, importantly, revealed that the P-substitution could generate more vacancies or defects in $CoSe_2$ and facilitate the compositional and structural transformation into CoOOH species during the OER (see Figure 287i). Incidentally, XPS analysis found that P and Se species disappeared from the $CoSe_{1.26}P_{1.42}$ surface after the OER, suggesting that the *in situ*-formed CoOOH species may act as dominant, real OER active sites.

Similarly, Li *et al.* studied the oxidation behavior of mildly oxidized, N-doped Co_9S_8 crystals on N-doped graphene oxide (O-N-Co_9S_8@N-RGO) during the OER process in 0.1 M KOH.[893] In this study, the O-N-Co_9S_8@N-RGO sample was prepared through the thermal nitridation of a Co, S, N and RGO-containing precursor. Toward the OER, O-N-Co_9S_8@N-RGO showed an overpotential of ∼350 mV at 10 mA·cm^{-2}. When comparing TEM, HRTEM, and elemental mapping images before and after 9 h of amperometric OER testing at 1.60 V_{RHE} (Figures 287j–l and Figures 287m and n, respectively), there is a clear change in morphology, replacement of Co_9S_8 lattice fringes with those of Co_3O_4, and an almost complete loss of sulfur from the initial material. These results implied an almost complete transformation of the initial material, whose phase, Co_3O_4, was confirmed by the ratio of Co^{3+}/Co^{2+} from XPS results, as was the near-complete substitution of S for O (XPS results not shown here). The authors claimed that this significant phase transformation might be facilitated by the imperfect crystallization nature of O-N-Co_9S_8 due to the N doping (confirmed by XRD). Notably, the presence of sulfate SO_4^{2-} on the post-OER precatalyst surface was confirmed even after the OER test. However, post-OER characterization results also indicated a complete loss of N from the initial material following the OER testing [i.e., no N signal in the elemental mapping (Figure 287n)]. Based on the above results, it was concluded that the *in situ*-generated Co_3O_4 species might be the active sites for the OER. However, it is still questionable whether the surface SO_4^{2-} species have some influence on the OER process or not, which needs to be examined in the future.

Besides the above-mentioned cases about the polyanion compounds experiencing almost complete oxidation during the OER, there are also many reports regarding partial oxidation cases (see Table 8). For example, Liu *et al.* reported a three-dimensional (3D) integrated monometallic phosphosulfide electrode, P-incorporated Ni_3S_2 nanosheet arrays (Ni_3S_2|P) on Ni foam, prepared via a hydrothermal process (i.e., Ni_3S_2 preparation) and subsequent, thermal phosphorylation (see Figure 288a).[781] Through DFT calculations, it was established that electron clouds around Ni–P bonds in the Ni_3S_2|P structure were more delocalized, making them favorable to activate and enrich the electrically connected active sites (i.e., Ni), resulting in the further acceleration of the water-splitting process. Especially, the Ni sites in the Ni_3S_2|P theoretically had a higher adsorption energy for water molecules than those in the pure Ni_3S_2, suggesting that the Ni_3S_2|P is more suitable for the water decomposition reaction. In Ni_3S_2|P, the presence of the Ni–P bonds was confirmed by XPS analysis, in which the

https://doi.org/10.1021/acs.chemrev.3c00005
Chem. Rev. 2023, 123, 12795–13208

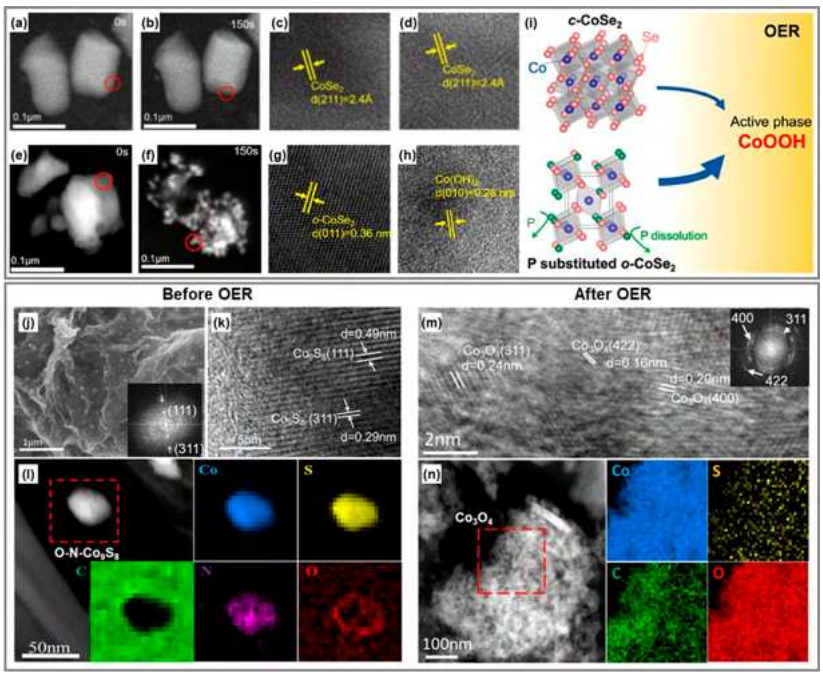


Figure 287. (a, b, e, f) *In situ* STEM images of (a, b) cubic $CoSe_2$ (*c*-$CoSe_2$) and (e, f) orthorhombic $CoSe_{1.26}P_{1.42}$ (*o*-$CoSe_{1.26}P_{1.42}$) obtained at different times (0 and 150 s) after immersion in 1 M KOH. (c, d, g, h) HRTEM images for the selected regions of the (c, g) initial and (d, h) final states of *c*-$CoSe_2$ and *o*-$CoSe_{1.26}P_{1.42}$, respectively. (i) Schematic models for the transformations of *c*-$CoSe_2$ and *o*-$CoSe_{1.26}P_{1.42}$, during the OER in alkaline electrolyte. Reproduced with permission from ref 48. Copyright 2019 American Chemical Society. (j) TEM, (k) HRTEM, and (l) elemental mapping images of O-N-Co_9S_8@N-RGO before the OER. (m) HRTEM and (n) elemental mapping images of O-N-Co_9S_8@N-RGO after the OER. Reproduced with permission from ref 893. Copyright 2018 Elsevier.

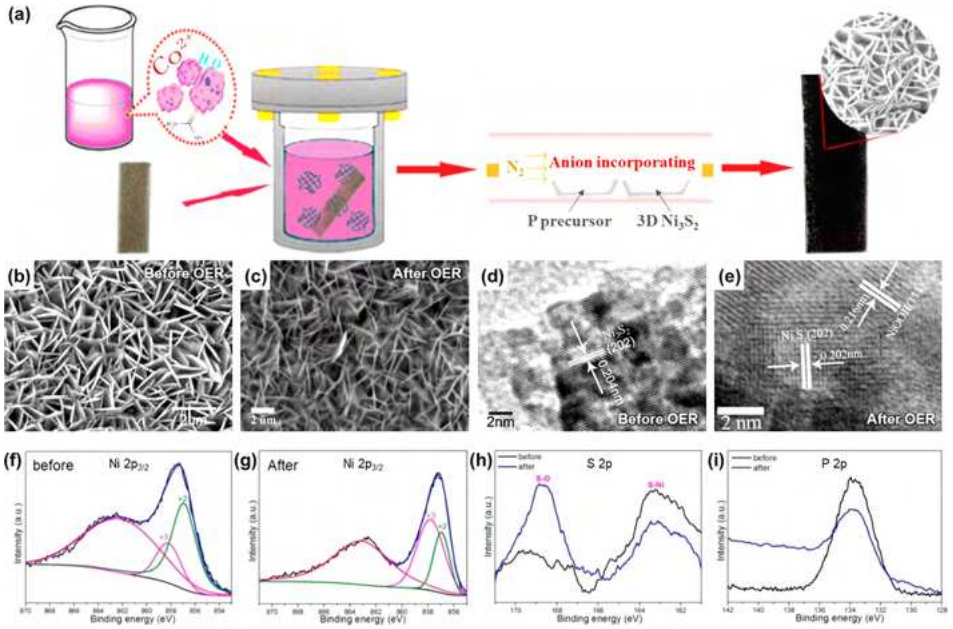


Figure 288. (a) Schematic illustration for the two-step fabrication of P-decorated Ni_3S_2 nanosheet arrays (Ni_3S_2|P) on Ni foam. (b, c) SEM images of the Ni_3S_2|P (b) before and (c) after the OER. (d, e) HRTEM images of the Ni_3S_2|P (d) before and (e) after the OER. (f, g) Ni $2p_{3/2}$, (h) S 2p, and (i) P 2p XPS spectra of the Ni_3S_2|P before and after the OER. Reproduced with permission from ref 781. Copyright 2018 American Chemical Society.

main Ni 2p peaks of the Ni_3S_2|P became broader than those of the pure Ni_3S_2 due to the formation of the Ni−P bonds. The OER performance was evaluated in alkaline media (1 M KOH), showing that the best Ni_3S_2|P sample (P/S atomic ratio: 0.54) recorded an overpotential of 420 mV at 100 mA·cm^{-2} and a Tafel slope of 224 mV·dec^{-1}, which was smaller than those of the pure Ni_3S_2 (> 500 mV; 286 mV·dec^{-1}). This excellent performance was related to not only the P incorporation but also the facilitated NiOOH formation on the Ni_3S_2|P surface during OER testing. Figures 288f and g show the SEM images of the Ni_3S_2|P sample before and after the OER, indicating that the sample maintained the nanosheet-

https://doi.org/10.1021/acs.chemrev.3c00005
Chem. Rev. 2023, 123, 12795−13208

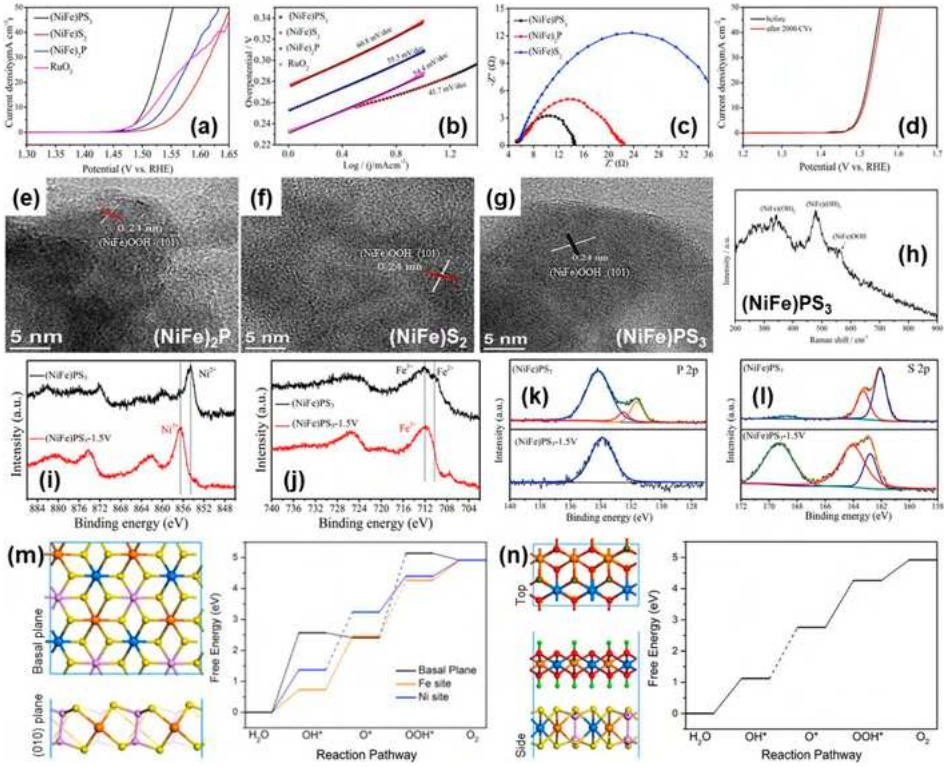


Figure 289. (a) Linear sweep voltammograms and (b) corresponding Tafel plots of $(NiFe)PS_3$, $(NiFe)S_2$, $(NiFe)_2P$, and RuO_2 on glassy carbon electrodes in 1 M KOH. (c) EIS spectra of $(NiFe)PS_3$, $(NiFe)S_2$, and $(NiFe)_2P$ at 1.55 V_{RHE}. (d) Linear sweep voltammograms of $(NiFe)PS_3$ before and after 2000 CV cycles. (e−g) HRTEM images of (e) $(NiFe)_2P$, (f) $(NiFe)S_2$, and (g) $(NiFe)PS_3$ after the OER test. (h) Raman spectrum of $(NiFe)PS_3$ after the OER test. (i) Ni 2p, (j) Fe 2p, (k) P 2p, and (l) S 2p XPS spectra of $(NiFe)PS_3$ before and after the OER test (i.e., electrochemical scan to 1.5 V_{RHE}). (m) Basal and (010) planes of the 2D $(NiFe)PS_3$ monolayer and OER free-energy diagrams for the basal plane and unsaturated Fe and Ni sites of the (010) plane. (n) Top and side views of the $(NiFe)OOH/(NiFe)PS_3$ heterobilayer and its OER free energy diagram. Blue, orange, pink, yellow, red, and green spheres represent Ni, Fe, P, S, O, and H, respectively. In the OER free energy diagrams, dashed lines indicate rate-determining steps. Reproduced with permission from ref 466. Copyright 2018 Elsevier.

like morphology after OER testing. TEM observations confirmed NiOOH formation after OER testing owing to the partial oxidation of the $Ni_3S_2|P$ sample (see Figures 288d and e). As seen in Figures 288f−i, XPS analysis further revealed the partial oxidation of $Ni_3S_2|P$ into NiOOH from the intensity increase of the Ni^{3+} and S−O peaks after OER testing. A post-OER Raman spectroscopy test also disclosed NiOOH formation. However, the contribution of the S-O species generated on the $Ni_3S_2|P$ surface due to its OER activity was not elucidated clearly.

Liu *et al.* synthesized a similar dual-anion compound, a crystalline bimetallic phosphosulfide $(NiFe)PS_3$, via a one-pot phosphosulfidation of a NiFe Prussian blue analogue (PBA) precursor.[466] During this conversion process, the sample morphology varied from nanocubes (NiFe PBA) to flower-like nanosheets [$(NiFe)PS_3$], providing more exposed active sites to facilitate the OER in 1 M KOH electrolyte. As shown in Figure 289a, the $(NiFe)PS_3$ exhibited superior activity for water oxidation, requiring an overpotential of 275 mV to achieve a current density of 10 $mA{\cdot}cm^{-2}$, which is lower than those of $(NiFe)_2P$ (308 mV) and $(NiFe)S_2$ (338 mV). This superior performance was accompanied by fast kinetics (Figure 289b) and a small charge transfer resistance (Figure 289c), which is attributed to the optimized electron modulation due to the dual-anion P and S in the structure. Furthermore, after 2000 CV cycles, the $(NiFe)PS_3$ exhibited only a slight potential increase of 4 mV, which implies its relatively high electrochemical stability (see Figure 289d). To gain a deeper understanding of the OER mechanisms for the tested samples, the authors also conducted post-OER analyses (i.e., TEM, XPS, and Raman). As observed in Figures 289e−g, the formation of (NiFe)OOH was found in the post-OER analysis of the $(NiFe)_2P$, $(NiFe)S_2$, and $(NiFe)PS_3$ samples. The post-OER Raman spectroscopy result of $(NiFe)PS_3$ also indicate the generation of (NiFe)OOH and $(NiFe)(OH)_2$ after OER testing (Figure 289h). XPS analysis further revealed the oxidation state increases for surface Ni and Fe species and the peak intensity increases of the oxidized P and S species after the OER (see Figures 289i−l), from which the authors suggested the *in situ* formation of the (NiFe)OOH layer on the $(NiFe)PS_3$ surface during the OER. Accordingly, the *in situ*-formed (NiFe)OOH species during the OER process might act as the OER active sites. In a different analysis via DFT calculations (Figure 289m), it was confirmed that the theoretical OER overpotentials were 0.58, 0.64, and 1.50 V for the Fe and Ni sites on the $(NiFe)PS_3(010)$ surface and its basal plane, respectively. These DFT results imply that the basal plane of $(NiFe)PS_3$ is almost inactive toward the OER, whereas only the Fe and Ni sites on the $(NiFe)PS_3(010)$ plane are relatively active for the OER. However, as discussed above, the (NiFe)OOH and $(NiFe)(OH)_2$ species were *in situ*-formed during the OER at the surface of $(NiFe)PS_3$. Thus, the authors also performed DFT calculations for a new model, a $(NiFe)OOH/(NiFe)PS_3$ heterobilayer (Figure 289n). This heterobilayer achieved a lower theoretical OER overpotential of 0.41 V compared with the $(NiFe)PS_3$, which clarifies that

https://doi.org/10.1021/acs.chemrev.3c00005
Chem. Rev. 2023, 123, 12795−13208

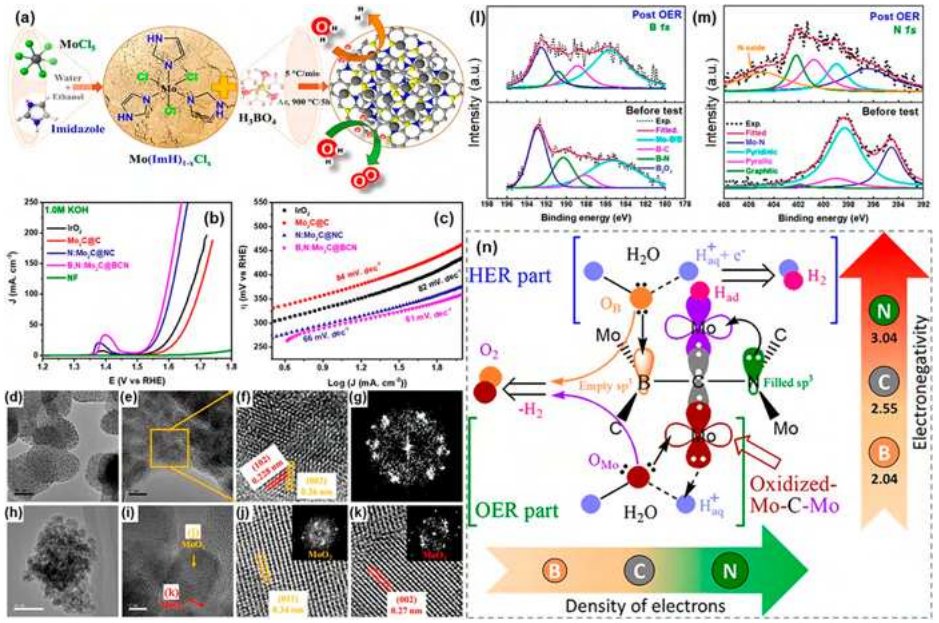


Figure 290. (a) Schematic illustration for the synthesis of B, N co-doped Mo_2C nanoparticles embedded in a B, N co-doped carbon network (B,N:Mo_2C@BCN) from a $[Mo(ImH)_{1-x}Cl_x]$ complex. (b) *iR*-corrected polarization curves and (c) corresponding Tafel slopes of Mo_2C@C, N:Mo_2C@NC, and B,N:Mo_2C@BCN on Ni foam and a commercial IrO_2 electrode in 1.0 M KOH. (d) TEM and (e, f) HRTEM images and (g) corresponding FFT pattern of B,N:Mo_2C@BCN. (h) TEM and (i) HRTEM images of *in situ* oxidized B,N:Mo_2C@BCN after the 20 h OER test. (j, k) Corresponding HRTEM images and FFT patterns (insets) of (j) MoO_2 and (k) MoO_3. (l) B 1s and (m) N 1s XPS spectra of B,N:Mo_2C@BCN before and after the OER. (n) Proposed mechanism of the overall water splitting over the B,N:Mo_2C@BCN electrocatalyst. Reproduced with permission from ref 272. Copyright 2018 American Chemical Society.

the oxyhydroxide formation on the $(NiFe)PS_3$ is the key to significantly boosting its OER activity. In this report, there are still two questionable points: (i) the oxidation degree of the $(NiFe)PS_3$ after the OER and (ii) the roles and synergistic effect of oxidized P and S species for the OER process. Especially for the first point, we recommend that the authors conduct analyses for checking the bulk composition and structure (e.g., XRD, EDX, ICP, etc.).

In addition to the reports dealing with the mono-anion incorporation into the monoanionic *X*-ide, there are a few reports about dual-anion incorporation (e.g., B, N co-doped Co_3C,[270] B, N co-doped Mo_2C,[272] etc.). For instance, Anjum *et al.* synthesized boron and nitrogen co-doped molybdenum carbide nanoparticles imbedded in a boron and nitrogen co-doped carbon network (B,N:Mo_2C@BCN) and observed the partial oxidation of B,N:Mo_2C to form the composite of B,N:Mo_2C and MoO_x after OER testing in alkaline media (1.0 M KOH).[272] The synthetic scheme for the B,N:Mo_2C@BCN is shown in Figure 290a. As a precursor for carburization, the organometallic complex of Mo-imidazole $[Mo(ImH)_{1-x}Cl_x]$ was synthesized by aging the imidazole monomer with $MoCl_5$ in ethanol at 80 °C for 24 h. Then, the complex was annealed along with boric acid at 900 °C under an Ar atmosphere, leading to *in situ* carburization/doping reactions between the Mo-imidazole complex and boric acid, resulting in the B,N:Mo_2C@BCN. Figures 290b and c show the electrocatalytic OER performances of commercial IrO_2, pure Mo_2C@C, N:Mo_2C@NC, and B,N:Mo_2C@BCN in 1.0 M KOH. The B,N:Mo_2C@BCN exhibited a lower OER overpotential (360 mV) at 100 mA·cm^{-2} and a smaller Tafel slope (61 mV·dec^{-1}) than the IrO_2 (435 mV; 82 mV·dec^{-1}), Mo_2C@C (464 mV; 84 mV·dec^{-1}), and N:Mo_2C@NC (380 mV; 64 mV·dec^{-1}). To examine the reason behind this superior OER activity, the authors characterized the B,N:Mo_2C@BCN before and after 20 h of OER CA testing (applied potential: 1.58 V_{RHE}). As shown in Figures 290d–g, TEM and HRTEM images for the B,N:Mo_2C@BCN before OER testing show that crystalline nanoparticles with an average size of ∼5 nm were embedded in the BCN network and exhibit lattice fringes of 0.228 and 0.226 nm corresponding to the (102) and (002) facets of orthorhombic *β*-Mo_2C. However, the TEM and HRTEM images for the B,N:Mo_2C@BCN after the OER test in Figures 290h–k exhibit lattice fringes of 0.34 and 0.27 nm for the MoO_2(011) and MoO_3(002) facets, respectively. TEM analysis also revealed the formation of the composite of MoO_2, MoO_3, and B,N:Mo_2C after OER testing (corresponding HRTEM images and FFT patterns were not provided here), indicating the partial oxidation of B,N:Mo_2C into MoO_2 and MoO_3 during OER testing. Importantly, as seen in Figures 290l and m, B and N species were still present in the B,N:Mo_2C that was partially oxidized after OER testing. Based on the experimental results, the authors also proposed possible HER and OER mechanisms for the B,N:Mo_2C@BCN, as displayed in Figure 290n. Since nitrogen is more electronegative than carbon and boron, nitrogen in the B,N:Mo_2C withdraws electrons from C−B bonding through C−N bonding. Then, lone pair electrons in nitrogen are donated to a vacant Mo 3d orbital through a N sp^3 hybrid orbital, resulting in an oxidation state decrease for Mo. For the HER, water molecules are adsorbed on electron-deficient boron sites, which weakens the O−H bonds in water molecules. Subsequently, protons freed from Mo sites (H_{ad}) combine with aqueous protons (H_{aq}^+), generating H_2 molecules. For the OER, water molecules are adsorbed on Mo sites, forming hydroxyl anions (OH^-_{Mo}). These hydroxyl anions react with hydroxyl anions at the boron sites (OH^-_B) to produce O_2 molecules and protons. However, as discussed above, the B,N:Mo_2C underwent partial oxidation during the OER,

https://doi.org/10.1021/acs.chemrev.3c00005
Chem. Rev. 2023, 123, 12795−13208

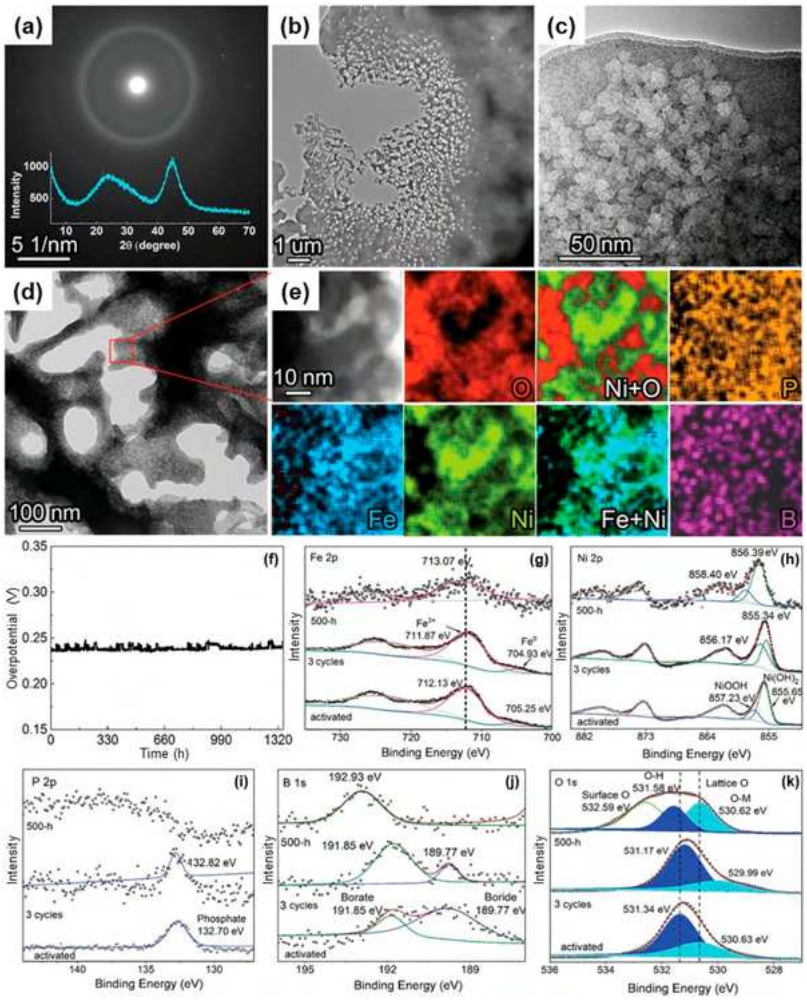


Figure 291. (a) SAED and XRD patterns and (b) TEM image of amorphous metallic NiFePB. (c, d) HRTEM images and (e) EDX elemental mapping profiles of activated NiFePB. (f) Chronopotentiometric test of the activated NiFePB under the constant current density of 100 mA·cm^{-2} in 1.0 M NaOH. (g) Ni 2p, (h) Fe 2p, (i) P 2p, (j) B 1s, and (k) O 1s XPS spectra for the activated NiFePB before and after the OER tests (3 CV cycles and 500 h CP). Reproduced with permission from ref 1178. Copyright 2019 Wiley.

forming B,N:Mo_2C, MoO_2, and MoO_3 with -CO_x, -NO_x, and -B−O species. To investigate the impacts of the *in situ*-formed Mo oxides and oxidized anion species on the OER activity, the authors further compared the OER performance of B,N:Mo_2C@BCN with those of control samples: as-synthesized MoO_2, a physical mixture of Mo_2C + MoO_2, and Mo_2C@C, in which the B,N:Mo_2C@BCN surpassed all the control samples. Accordingly, the authors concluded that the superior OER activity of the B,N:Mo_2C@BCN might result from the synergistic effect of B- and N-doping. Additionally, since the post-OER B,N:Mo_2C@BCN possessed defects and a polycrystalline nature (confirmed by TEM), we guess that these unique structural properties of the post-OER B,N:Mo_2C@BCN might also contribute to its relatively high OER activity.

So far, we have discussed only examples regarding the polyanion compound precatalyst with crystalline nature. Herein, we also introduce the polyanion compound precatalyst having an amorphous nature. Hu *et al.* reported a porous, amorphous, metallic NiFePB precatalyst, which experienced partial oxidation under OER testing, and they thoroughly investigated its electrochemical, compositional, and structural stability for long-term OER testing.[1178] The authors prepared the NiFePB strip electrodes by melting spinning and rapidly quenching NiFePB ingots in an Ar atmosphere. Subsequently, the NiFePB surface was activated by immersing the as-prepared strip in an acidic solution for 10 min, forming metal oxides/hydroxides [$MO_x/M(OH)_x$] as active species for the OER. Figure 291a shows the XRD and FFT patterns of the activated NiFePB (a-NiFePB) sample, indicating its amorphous feature. TEM analysis revealed that the a-NiFePB had a porous surface (pore size: 50−300 nm) (Figure 291b) and a porous skeleton (Figures 291c and d). From the elemental mapping images (Figure 291e), it was confirmed that the a-NiFePB possessed a core@shell structure and that the shell (thickness: <10 nm) had oxygen-containing functional species (i.e., an oxide/hydroxide layer). Here, this shell might also protect the NiFePB core from oxidation. In an alkaline electrolyte (1.0 M NaOH), the a-NiFePB strip electrode achieved a relatively low OER overpotential of 217 mV to reach 100 mA·cm^{-2} and a corresponding Tafel slope of 34 mV·dec^{-1}. This relatively high OER activity might be realized by (i) the unique porous amorphous structure and (ii) the P and B coupling. Especially, the coupling of P and B could moderate the electronic structure of active sites and the electrical conductivity of the electrocatalyst toward the OER. Notably,

https://doi.org/10.1021/acs.chemrev.3c00005
Chem. Rev. 2023, 123, 12795−13208

during 1400 h of OER CP testing at the constant current density of 100 mA·cm^{-2} (see Figure 291f), the a-NiFePB demonstrated somewhat stable OER overpotentials, implying its relatively high electrochemical stability. Furthermore, as shown in Figures 291g–k, XPS analysis was conducted on the a-NiFePB before and after the OER tests (3 CV cycles and 500 h CP). The XPS results of the fresh and 3 CV cycled a-NiFePB samples were similar, and their surfaces mainly consisted of $NiFeO_xH_y$, boron species, and phosphorous species. However, after 500 h of CP testing, boride and phosphate species disappeared, and $NiFeO_xH_y$ and borate remained. Accordingly, the authors made the conclusion that the $NiFeO_xH_y$ species might be the electrocatalytically active sites after the long-term OER testing. Here, we also assume that the disappearance of surface phosphate species might cause a slight activity decay during OER testing (Figure 291f). Additionally, there is a possibility that the remaining borate species in the $NiFeO_xH_y$ layer can positively affect the OER activity.[140,141] The role of the borate species in the $NiFeO_xH_y$@NiFePB during the OER process needs to be further investigated in the future.

6.2. Composites

As shown in Figure 282, the transition metal-based polyanion composite consists of more than two *X*-ide compounds [i.e., $MX_n + MY_m$ ($X \neq Y$)] (refs 47, 49, 245, 246, 255, 256, 273, 274, 277, 363, 369, 404, 405, 529, 532, 537, 556, 564, 566, 754, 759, 761–763, 782, 826, 845, 1032, 1152, 1176, 1183, and 1184), forming unique lateral and/or vertical heterostructures (see Figure 292). As is the case for the polyanion

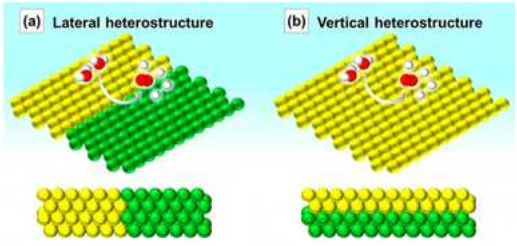


Figure 292. Schematic illustrations of (a) lateral and (b) vertical heterostructures of transition metal-based dual-anion composites (MX_n/MY_m). Yellow and green spheres represent MX_n and MY_m species, respectively. *M* = transition metal(s) (e.g., Ni, Co, Fe, etc.), *X* and *Y* = B, C, N, P, S, Se, or Te ($X \neq Y$).

compounds, most of the polyanion compounds experienced surface reconstruction (e.g., oxidation) during the OER process (refs 47,49, 245, 246, 255, 256, 273, 274, 363, 369, 529, 532, 537, 556, 564, 754, 759, 782, 826, 1032, 1152, 1176, and 1179), whereas there are only a few polyanion compounds that exhibited superior stability and could almost maintain their initial surface during and after the OER.[566,763,845]

6.2.1. Catalysts. As of 2022, three types of dual-anion nanocomposite systems such as monometallic telluride/sulfide (NiTe/NiS),[763] bimetallic phosphide/selenide (CoFe-Se-P),[566] and bimetallic phosphide/sulfide (NiFeSP)[845] have been reported to be stable during OER testing. Herein, we introduce two representative examples. As one example, Xue and co-workers have reported a high-stability NiTe/NiS nanoarray catalyst for the OER.[763] The NiTe/NiS catalyst was prepared via the growth of NiTe columns on Ni foam and the subsequent decoration of them with NiS nanodots through a two-step hydrothermal approach (see Figure 293a). The NiTe columnar morphology is maintained following the decoration of the NiTe columns with NiS nanodots, as confirmed by SEM (Figure 293b). The presence of the NiS nanodots on the surface of the NiTe columns was then confirmed via TEM and HRTEM (Figures 293c and d). The presence of Ni, Te, and S was also confirmed from STEM and elemental mapping (not provided here). The XRD results indicated the presence of the NiTe and NiS phases prior to OER testing (Figure 293e). Following a long-term stability test (see Table 8), the NiTe and NiS phases were once again confirmed using XRD (Figure 293e). The as-prepared columnar morphology was also maintained, and no binding energy shifts were detected in the Ni 2p XPS spectrum following OER testing (Figure 293f), indicating that the Ni^{2+} valence state was maintained and no oxidation occurred at the Ni-metal sites. It is possible that this enhanced compositional stability of the as-prepared electrocatalyst could be the result of tellurium incorporation given its improved stability compared to sulfur, making the NiTe/NiS nanoarray a catalyst instead of the anticipated precatalyst. Furthermore, the NiTe/NiS sample also maintained the nanoarray morphology even after OER testing (Figures 293g and h), indicating its good physical stability. As shown in Figures 293i–l, the DFT calculations demonstrated that the incorporation of NiS nanodots on NiTe nanoarrays modulated the electronic structure of the d-band center of Ni by triggering electron transfer from NiTe to S, decreasing the binding strength of *OOH intermediates, which resulted in low reaction barriers [ΔG = 3.48 (site 1), 3.15 (site 2), and 3.13 eV (site 3)] of the OER rate-limiting step compared with that for NiTe (ΔG = 3.67 eV), thus improving the OER performance. This effect was evidenced by the OER activity in alkaline media (1.0 M KOH). Significantly, as seen in Figure 293m, the NiTe/NiS nanoarrays exhibited better electrocatalytic OER performance with a lower overpotential of 257 mV at 100 mA·cm^{-2} than those of NiS (362 mV) and NiTe (403 mV). Moreover, the synergy of the NiTe/NiS interface showed faster electronic transport with small charge transfer resistance and Tafel slope (49 mV·dec^{-1}) (Figure 293n), which also shows good agreement with the DFT results.

As another example, Zhang *et al.* reported a mesoporous cobalt/iron phosphide-selenide nanocomposite (CoFe-Se-P) as a bifunctional catalyst for water splitting.[566] In this work, the authors employed hydrothermal synthesis and subsequent HCl etching to produce a hollow CoFe-PBA precursor. Afterward, the thermal phosphosulfidation of the as-produced hollow CoFe-PBA precursor was performed (Figure 294a), resulting in the formation of a hollow CoFe-Se-P sample. Importantly, a 1 M HCl aqueous solution was used to further etch the as-prepared CoFe-Se-P cubic-like skeleton to obtain a porous CoFe-Se-P nanocomposite (denoted as CoFe-Se-P-HCl in Figure 294a). Through this acid etching, the hollow nanobox structure of the CoFe-Se-P sample was broken into small pieces, as shown in the SEM and TEM images (Figures 294b and c). Notably, the use of the acid for etching the hollow structure into the porous nanostructure might provide more OER active sites. The HRTEM image of CoFe-Se-P-HCl is shown in Figure 294d, indicating that the resultant CoFe-Se-P-HCl material mainly consisted of $(Co,Fe)Se_2$, (Co,Fe)P, and $(Co,Fe)_3O_4$ species. To confirm the effect of the coexistence of selenide and phosphide on the OER activity, the porous CoFe-Se-P, CoFe-Se, and CoFe-P composites were tested for the OER in 0.1 M KOH. Among all the tested samples, the porous CoFe-Se-P exhibited the lowest OER overpotential of 230 mV

https://doi.org/10.1021/acs.chemrev.3c00005
Chem. Rev. 2023, 123, 12795–13208

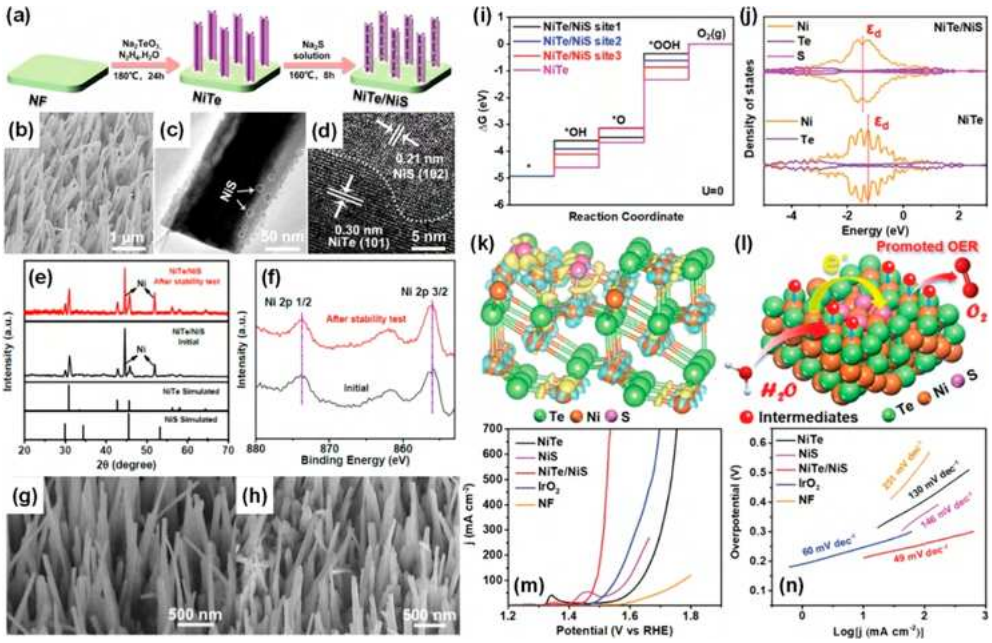


Figure 293. (a) Schematic illustration for the fabrication of NiTe/NiS heterojunction nanoarrays on Ni foam. (b) FESEM, (c) TEM, and (d) HRTEM images of the NiTe/NiS composite. (e) XRD patterns and (f) Ni 2p XPS spectra of the NiTe/NiS composite before and after the salability test. (g, h) SEM images of the NiTe/NiS composite (g) before and (h) after the stability test. (i) Calculated OER free energy diagrams on the NiTe and NiTe/NiS surfaces ($U = 0$). (j) DOSs of the NiTe and NiTe/NiS. (k) Charge density difference in the NiTe/NiS interface, in which yellow and blue regions denote electron accumulation and depletion, respectively. (l) Schematic illustration for the mechanism of the OER activity enhancement in the NiTe/NiS. (m) LSV curves and (n) Tafel slopes of NiTe, NiS, NiTe/NiS, IrO_2, and bare Ni foam. Reproduced with permission from ref 763. Copyright 2019 Wiley.

at 10 mA·cm^{-2} and the smallest Tafel slope of 108 mV·dec^{-1} (Figures 294e and f), implying a positive synergy between selenide and phosphide toward the OER. As shown in Figure 294g, the porous CoFe-Se-P nanocomposite could also be electrochemically stable during the long-term OER tests (i.e., 1000 CV cycles and 40 h of CA testing). Furthermore, the authors carried out the XRD, XPS, EDX, and SEM measurements of the porous CoFe-Se-P nanocomposite after the 40 h CA test. As seen in Figure 294h, there was no significant difference between the pre- and post-OER XRD patterns. The post-OER sample also showed XPS peaks in the Co 2p, Fe 2p, Se 3d, and P 2p regions similar to those of the fresh sample. Moreover, the features in the post-OER EDX spectrum were similar to those of the fresh sample. In the pre- and post-OER SEM images, obvious morphological change was not observed. Accordingly, the surface and bulk composition and morphology of the porous CoFe-Se-P nanocomposite seemed to be stable under the OER conditions used in this study, suggesting that the porous CoFe-Se-P nanocomposite is a stable catalyst rather than a precatalyst. Interestingly, oxidized phosphorous species exist on the catalyst surface before and after OER testing, and their impacts on the OER activity are still unknown. Further investigation for this point is desired.

6.2.2. Precatalysts. Similar to the polyanion compound precatalysts, most of the polyanion composite precatalysts also underwent complete or partial oxidation during the OER process (see Table 8). In this Section we introduce five representative examples with the dual-anion composite precatalysts having various interesting architectures such as 2D hetero-nanostructures,[256,556] 3D hetero-nanostructures (i.e., 1D/1D hierarchical hetero-nanostructures,[564] 2D/2D hierarchical hetero-nanostructures[826]), and core@shell structure.[255] Bose *et al.* reported a 2D lateral hetero-nanostructure, a $CoSe_2$|CoP hybrid precatalyst layer, on carbon fiber paper and revealed its complete oxidation during the long-term OER process.[556] For the preparation of the $CoSe_2$|CoP sample, the authors first synthesized a $CoSe_2$ layer on carbon fiber paper through a solvothermal process. Then, the as-synthesized $CoSe_2$ on carbon fiber paper was subjected to a thermal phosphidation treatment (see Figure 295a), resulting in the $CoSe_2$|CoP sample. The resultant sample possessed a nanosheet morphology, and nanoblisters (size: 10−18 nm) were formed on the nanosheet surface, which was observed by FESEM. In the resultant sample, the coexistence of $CoSe_2$ and CoP was confirmed (Figures 295b−d). In the elemental mapping images (Figures 295e−h), Co, Se, and P were homogeneously distributed throughout the composite. The authors investigated the OER performance of the $CoSe_2$|CoP in a Fe-purified 1 M KOH electrolyte. Here, $CoSe_2$ and CoP samples were also prepared as comparisons and tested for the OER under the same conditions. Prior to the OER performance measurement, CV cycling from 1.05 to 1.65 V_{RHE} for about 10 h was applied for the as-prepared samples to record stable voltammograms, generating the as-prepared sample-derived oxides (DOs). As shown in Figures 295i and j, the $CoSe_2$|CoP-DO achieved a higher OER performance (overpotential: 240 mV at 10 mA·cm^{-2}; Tafel slope: 46.6 mV·dec^{-1}) than the $CoSe_2$-DO (350 mV; 52.3 mV·dec^{-1}) and CoP-DO (339 mV; 77.7 mV·dec^{-1}). From the EIS and double-layer capacitance (C_{dl}) measurements, this superior OER activity of the $CoSe_2$|CoP-DO might mainly result from its lower charge transfer resistance (R_{ct}) of 1.04 Ω and higher ECSA (C_{dl}: 13.1 mF·cm^{-2}) compared with those of the $CoSe_2$-DO (1.25 Ω; 8.5 mF·cm^{-2}) and CoP-DO (1.45 Ω; 9.8 mF·cm^{-2}). Furthermore, the transformation of the $CoSe_2$|CoP

https://doi.org/10.1021/acs.chemrev.3c00005
Chem. Rev. 2023, 123, 12795−13208

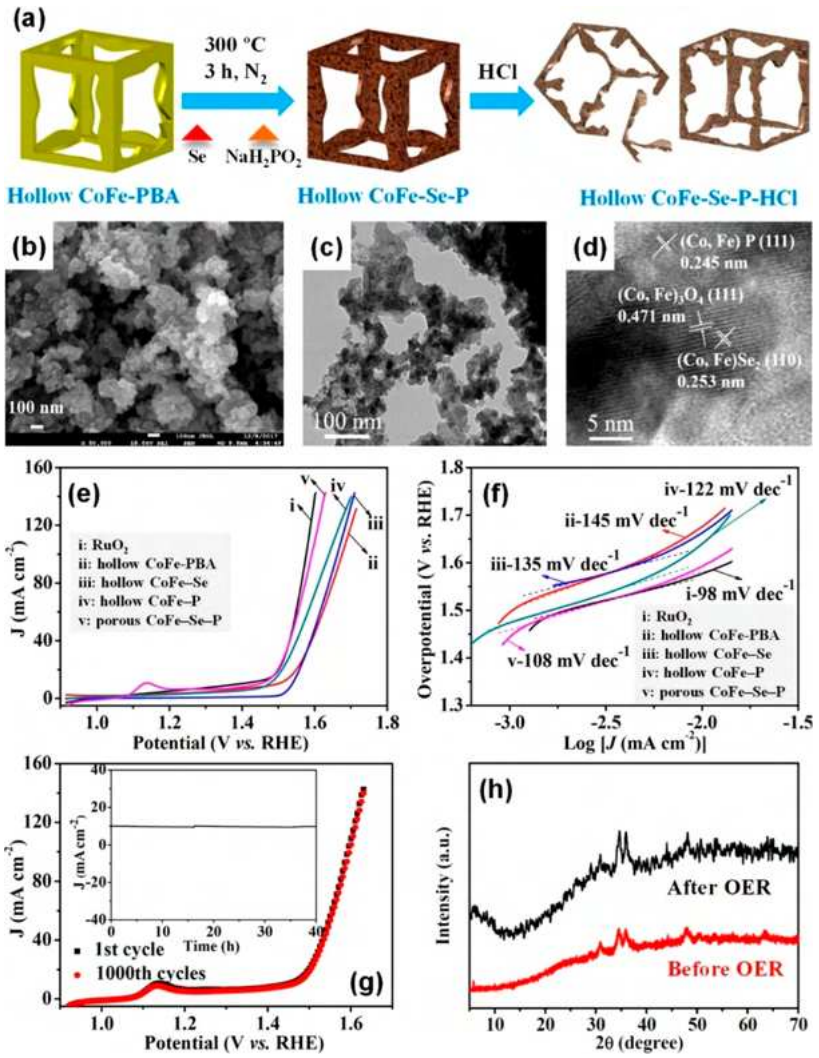


Figure 294. (a) Schematic illustration of the preparation of a HCl-treated porous CoFe-Se-P nanocomposite and its application as a bifunctional electrocatalyst for water splitting. (b) SEM and (c, d) TEM images of the porous CoFe-Se-P nanocomposite. (e) LSV curves and (f) Tafel plots of RuO_2, hollow CoFe-PBA, hollow CoFe-Se, hollow CoFe-P, and porous CoFe-Se-P nanocomposites on glassy carbon electrodes. (g) LSV curves (scan rate: 10 $mV{\cdot}s^{-1}$) of the porous CoFe-Se-P nanocomposite before and after 1000 CV cycles. (h) 40 h chronoamperometric test (at the applied potential of 1.44 V_{RHE}) of the porous CoFe-Se-P nanocomposite. All the electrochemical tests were performed in 0.1 M KOH. Reproduced with permission from ref 566. Copyright 2018 American Chemical Society.

precatalyst during the 10 h OER CV cycles and following the 120 h CA test at 1.47 V_{RHE} was investigated through various post-OER characterizations (i.e., XPS, SEM, EDX, TEM, and Raman). After the 10 h CV cycling, the complete and slight oxidation of $CoSe_2$ and CoP into CoO_x, $Co(OH)_2$, and CoOOH occurred, respectively (see Figure 295k). From the XPS analysis, it was confirmed that surface selenium species disappeared while phosphate (PO_4^{3-}) species were generated after the OER CV cycling. The author assumed that the generated phosphate species might affect the kinetics of surface deprotonation for facilitating the OER.[106] After the following 120 h CA test, the precatalyst was completely oxidized into cobalt oxides, oxyhydroxides, and hydroxides (see Figures 295k and l) and the phosphate species disappeared from the precatalyst surface. The post-OER precatalyst experienced a slight OER overpotential increase (~30 mV); however, it exhibited no change in the Tafel slope. According to the XPS results, CoO_x and CoOOH species existed on the post-OER precatalyst surface and might act as the actual OER active sites. Notably, the authors also emphasized that the cobalt oxo/hydroxo species derived from the $CoSe_2$|CoP can provide nanostructures with an enlarged surface area enhancing the OER performance, which is one of the main advantages for the use of unstable *X*-ides as OER electrocatalysts.[91]

For another example regarding a 2D lateral heteronanostructure, Kou *et al.* synthesized holey 2D nonlayered molybdenum-based transition metal carbide/nitride heterostructure nanosheets (h-TMCN) through the thermal pyrolysis of Mo/Zn bimetal imidazolate frameworks (Mo/Zn BIFs) (see Figure 296a) and confirmed their partial oxidation during OER testing.[256] As shown in Figure 296b, the as-prepared sample was in the shape of holey nanosheets with even thicknesses of around 45 nm. In Figure 296c, the HRTEM image of the h-TMCN displays *d*-spacings of ~2.3 and ~2.2 Å, corresponding to the (121) and (200) planes of the Mo_2C and Mo_2N, respectively, indicating the successful formation of the Mo_2C/Mo_2N composite with heterointerfaces. This point is also supported by the corresponding SAED pattern (inset of Figure 296c) that contains the diffraction spots for both Mo_2C and Mo_2N. For the electrocatalytic OER, the h-TMCN was

https://doi.org/10.1021/acs.chemrev.3c00005
Chem. Rev. 2023, 123, 12795−13208

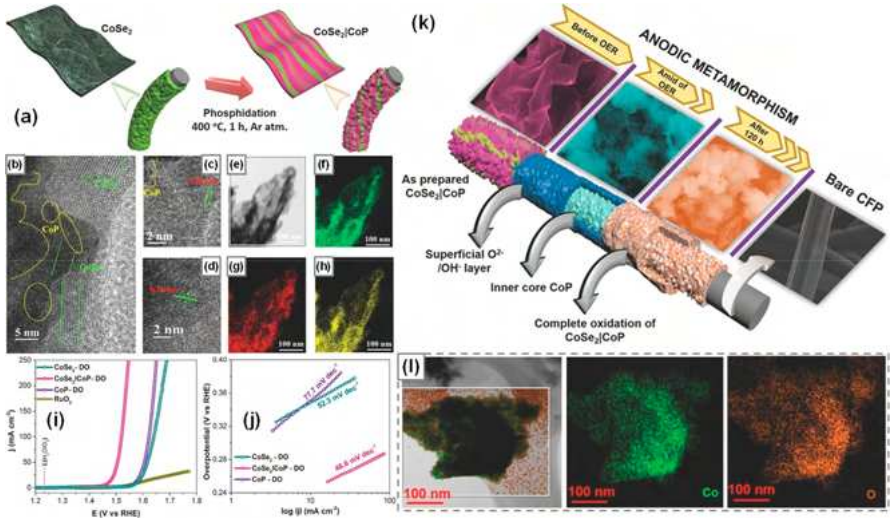


Figure 295. (a) Schematic illustration for the preparation of a $CoSe_2$|CoP hybrid precatalyst. (b–d) HRTEM and (e–h) elemental mapping images of the $CoSe_2$|CoP. (i) Polarization curves and (j) Tafel slopes of $CoSe_2$-DO, CoP-DO, $CoSe_2$|CoP-DO, and RuO_2 (derived oxides denoted as DO). (k) Schematic illustration for the transformation of $CoSe_2$|CoP into $CoSe_2$|CoP-DO during the OER process. (l) Elemental mapping images of the $CoSe_2$|CoP-DO (after 120 h of the CA test at 1.47 V_{RHE}), in which green and orange signals represent cobalt and oxygen, respectively. Reproduced with permission from ref 556. Copyright 2018 Wiley.

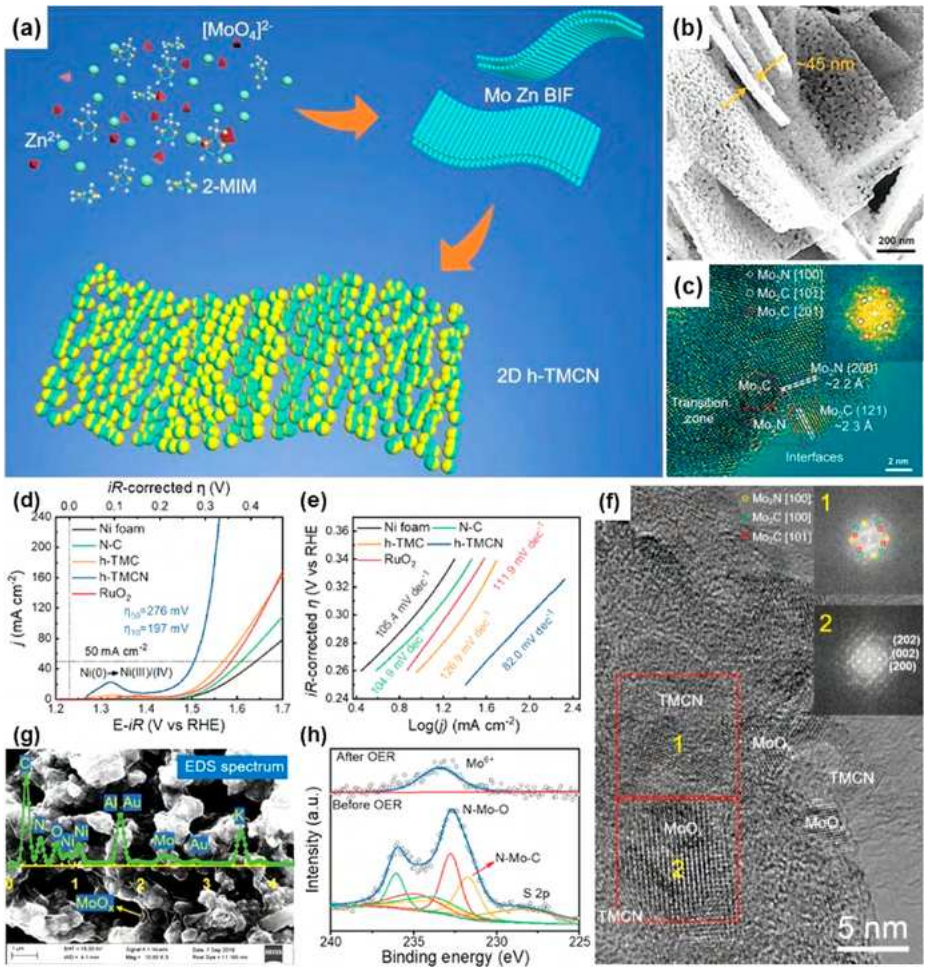


Figure 296. (a) Schematic illustration for the preparation of holey 2D nonlayered transition metal carbide/nitride (h-TMCN) heterostructure nanosheets. (b) SEM and (c) HRTEM images and corresponding SAED pattern of h-TMCN nanosheets. (d) LSV curves and (e) Tafel slopes of h-TMCN, h-TMC, N-C (dense TMC), RuO_2, and Ni foam electrodes. (f) HRTEM image and corresponding FFT patterns of the h-TMCN after long-term OER testing. (g) SEM image and EDX spectrum of the h-TMCN after long-term OER testing. (h) Mo 3d XPS spectra of the h-TMCN before and after long-term OER testing. Reproduced with permission from ref 256. Copyright 2019 Wiley.

https://doi.org/10.1021/acs.chemrev.3c00005
Chem. Rev. 2023, 123, 12795–13208

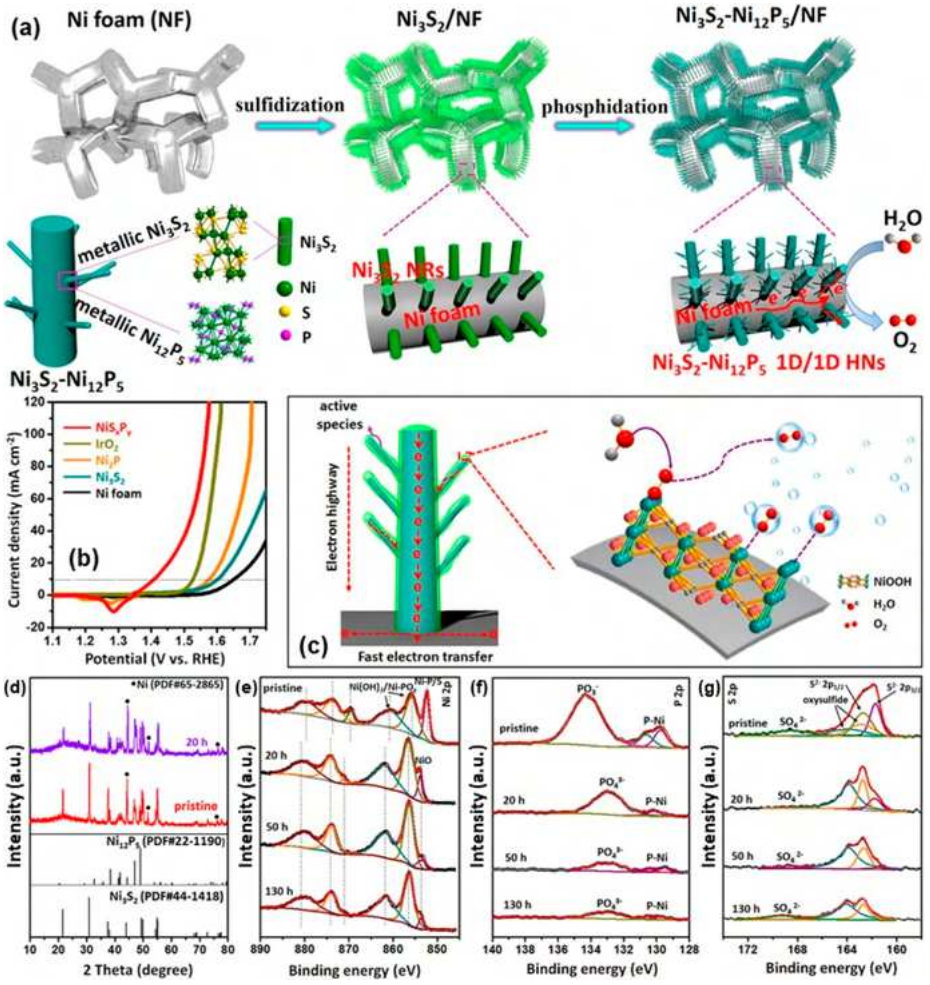


Figure 297. (a) Schematic illustrations for the fabrication of 1D/1D hierarchical NiS_xP_y nanostructures on Ni foam. (b) LSV curves of NiS_xP_y-O, Ni_3S_2-O, Ni_2P-O, and commercial IrO_2 on Ni foam and bare Ni foam, which were recorded at a scan rate of 1 mV·s^{-1} in 1.0 M KOH. (c) Schematic illustration of the fast electron transport in the 1D/1D hierarchical NiS_xP_y nanostructures for the OER. (d) XRD patterns of the NiS_xP_y composite of Ni foam before and after the 20 h OER CA test. (e) Ni 2p, (f) P 2p, and (g) S 2p XPS spectra of the NiS_xP_y composite of Ni foam before, during, and after the 130 h OER CA test. Reprinted with permission from ref 564. Copyright 2018 American Chemical Society.

compared with noncomposite 2D holey transition metal carbide nanosheets (h-TMC: hexagonal Mo_2C) in 1 M KOH. The OER LSV curves in Figure 296d show that h-TMCN exhibited a higher OER activity (overpotential: 276 mV at 50 mA·cm^{-2}) than the h-TMC (340 mV). Additionally, Figure 296e displays that the h-TMCN and h-TMC samples had Tafel slopes of 82.0 and 126.9 mV·dec^{-1}, respectively. Moreover, at the OER overpotential of 300 mV, the h-TMCN achieved a significantly higher TOF value of 0.189 s^{-1} compared with the h-TMC (0.019 s^{-1}), suggesting the greater intrinsic OER activity of the h-TMCN. From the EIS measurement, the charge transfer resistance (R_{ct}) of h-TMCN was smaller than that of the h-TMC. Furthermore, the h-TMCN demonstrated a greater double-layer capacitance value (C_{dl}) of 185.4 mF·cm^{-2} than the h-TMC (155.0 mF·cm^{-2}), implying a higher ECSA for the h-TMCN. Based on these electrochemical results, it can be safely speculated that the superior OER activity of the h-TMCN might mainly arise from its unique microstructure as well as high intrinsic OER activity due to N-Mo-C heterointerface sites exposed on the nanosheets. The authors also performed DFT calculations to further confirm the effect of the heterointerface toward the OER. The calculated total density of states at the Mo_2N/Mo_2C heterointerface is much higher than those at the Mo_2C and Mo_2N surfaces at their Fermi levels. These theoretical results indicate that the electron mobility at the Mo_2N/Mo_2C heterointerface is enhanced, possibly resulting in superior OER activity. The stability of the h-TMCN was investigated by performing 40 h of the chronoamperometric test (see details in Table 8) and subsequent post-OER analyses. During 40 h of the OER testing, the h-TMCN showed a stable current density. Interestingly, after 40 h of OER testing, the OER overpotential of the h-TMCN at 50 mA·cm^{-2} decreased by 23 mV. TEM analysis confirmed the formation of MoOx species on the h-TMCN surface after OER testing. From the post-OER SEM-EDX result (Figure 296g), the authors found the formation of sheet-like oxidized layers on the h-TMCN surfaces and a significant size increase of the holes. As seen in the pre- and post-OER Mo 3d spectra, Mo^{6+} species were generated on the post-OER h-TMCN surface. From these analytical results, the authors concluded that the severe surface oxidation of h-TMCN during the OER generated more active MoO_x species, which might cause OER activity improvement after the long-term OER testing.

The dual-anion composites with 3D architectures can also be constructed with two different *X*-ide components having 1D

https://doi.org/10.1021/acs.chemrev.3c00005
Chem. Rev. 2023, 123, 12795−13208

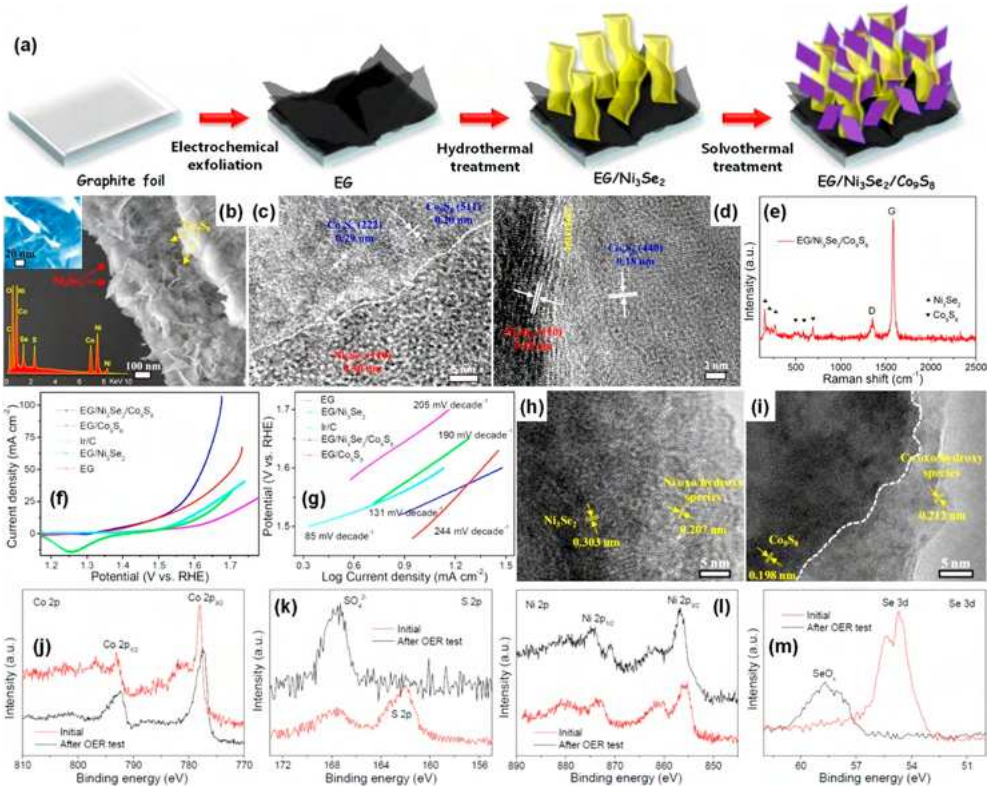


Figure 298. (a) Schematic illustration for the fabrication process of a 3D EG/Ni_3Se_2/Co_9S_8 electrode. (b) FESEM images, [inset of (b)] corresponding EDX spectrum, (c, d) HRTEM images, and (e) XRD pattern of the EG/Ni_3Se_2/Co_9S_8 electrode. (f, g) Polarization curves and corresponding Tafel slopes of EG, EG/Ni_3Se_2, EG/Co_9S_8, EG/Ni_3Se_2/Co_9S_8, and Ir/C in 1.0 M KOH. (h, i) HRTEM images and (j) Co 2p, (k) S 2p, (l) Ni 2p, and (m) Se 3d XPS spectra of the EG/Ni_3Se_2/Co_9S_8 electrode after 10 h of the OER CA test. Reprinted with permission from ref 826. Copyright 2017 American Chemical Society.

or 2D structures, which is beneficial for increasing the number of OER active sites per unit geometric area. For instance, Fu *et al.* synthesized 1D/1D hierarchical nanostructures of the metallic NiS_xP_y composite precatalyst consisting of crystalline Ni_3S_2 nanorods and crystalline $Ni_{12}P_5$ nanowires (see Figure 297a) and revealed their surface oxidation under alkaline OER conditions.[564] Here, the NiS_xP_y composite was fabricated via a two-step approach: hydrothermal sulfidation and subsequent gas-solid phosphidation. In the initial step, the Ni_3S_2 nanorods were grown on Ni foam. In the second step, the dense $Ni_{12}P_5$ nanowires were vertically grown on the as-grown Ni_2S_3 nanorod surfaces under a strongly reductive PH_3 atmosphere. The resultant NiS_xP_y composite was tested for the OER in alkaline media (1.0 M KOH). The authors also compared the OER activity of the NiS_xP_y composite with those of the Ni_3S_2 and Ni_2P control samples (see Figure 297b). Since all the tested sulfide- and phosphide-based precatalysts might experience their oxidation during the OER (Figure 297c), the authors named the oxidized NiS_xP_y, Ni_3S_2, and Ni_2P samples as NiS_xP_y-O, Ni_3S_2-O, and Ni_2P-O, respectively. The NiS_xP_y-O sample showed the lowest OER overpotential of 178 mV at 10 mA·cm^{-2} [without correction by Faradaic efficiency (the corrected value is 192 mV)] and the smallest Tafel slope of 95.0 mV·dec^{-1} among the tested samples. Moreover, the NiS_xP_y-O sample recorded a smaller charge transfer resistance, determined by EIS, and a higher ECSA, estimated by the double layer capacitance (14.46 mF), compared with the Ni_3S_2-O (8.45 mF) and Ni_2P-O (6.51 mF) samples. Therefore, the fast OER kinetics and larger surface area of the NiS_xP_y-O sample might mainly result in its superior OER performance.

The authors further examined the stability of the NiS_xP_y composite during the OER by performing a 135 h CA test (at the constant potential of 1.43 V_{RHE}) and following post-OER characterizations. For 135 h, the NiS_xP_y composite could deliver current densities of about 10 mA·cm^{-2}, indicating its excellent electrochemical stability. The pre- and post-OER results showed similar diffraction peaks and the presence of Ni_3S_2 and $Ni_{12}P_5$ phases, confirming the relatively high bulk stability of the NiS_xP_y composite under the long-term OER testing conduction used in this study. The XPS results during the 130 h OER test are also shown in Figures 297e–g. As the OER CA test proceeded, Ni-S and Ni-P species disappeared, while the emergence of $Ni(OH)_2$, Ni-PO_x, oxysulfide, SO_4^{2-}, and PO_4^{3-} species was observed. From the XPS quantitative analysis, the authors found the gradual decrease of P and S and the gradual increase of O over 130 h of the OER test, implying the *in situ* formation of oxide/oxyhydroxide. Furthermore, XAS and Raman spectroscopic results also indicated the formation of NiOOH on the NiS_xP_y composite surface after the OER. Accordingly, the as-observed superior OER activity of the NiS_xP_y composite was also induced by *in situ*-formed surface NiOOH species, which may act as real OER active sites (Figure 297c). Here, the authors still observed the Ni-PO_x, oxysulfide, SO_4^{2-}, and PO_4^{3-} species on the post-OER NiS_xP_y composite surface (see Figures 297e–g). Their (synergistic) contributions to the OER process also need to be investigated in the future.

As another example, the work of Hou *et al.* integrated Co_9S_8 nanosheets with vertically aligned Ni_3Se_2 nanosheets on electrochemically exfoliated graphene (EG) foil to construct

https://doi.org/10.1021/acs.chemrev.3c00005
Chem. Rev. 2023, 123, 12795−13208

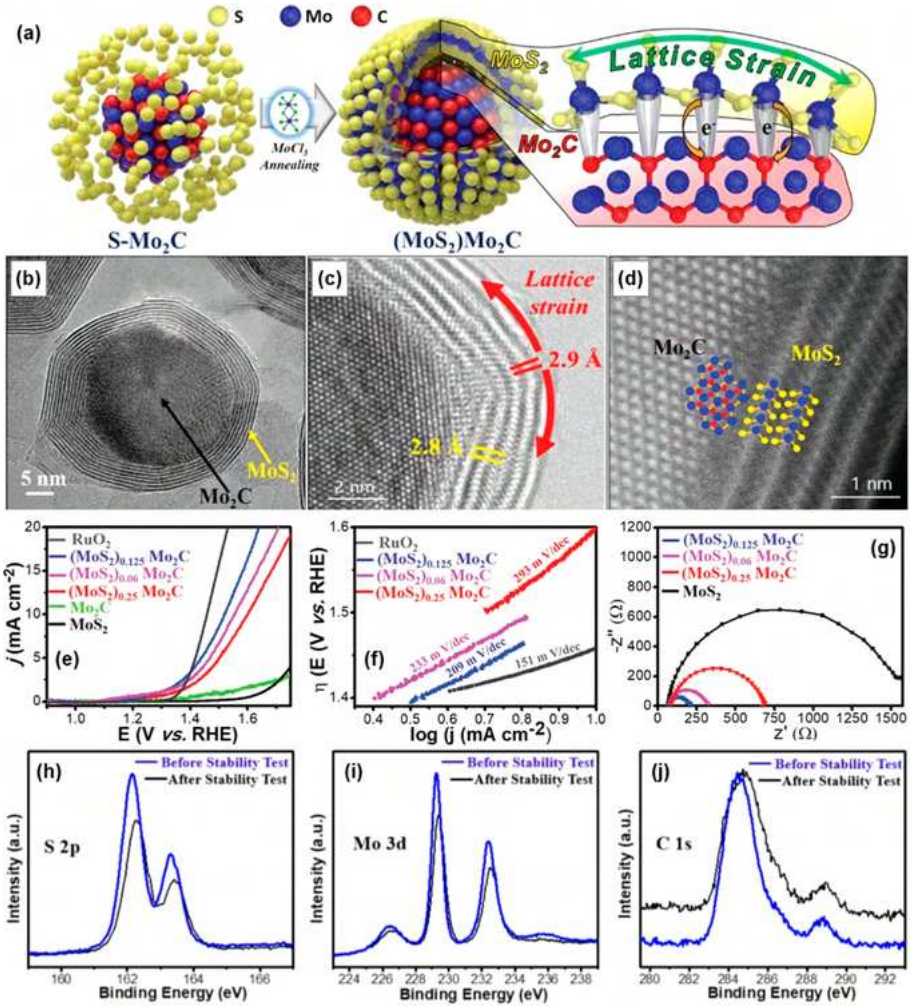


Figure 299. (a) Schematic illustration for the synthetic process of a MoS_2@Mo_2C core@shell structure exhibiting lattice strain and spin coupling effects. (b, c) HRTEM and (d) STEM images of the $(MoS_2)_{0.125}Mo_2C$ sample. (e) LSV curves, (f) Tafel slopes, and (g) EIS spectra of $(MoS_2)_{0.125}Mo_2C$, $(MoS_2)_{0.06}Mo_2C$, $(MoS_2)_{0.25}Mo_2C$, Mo_2C, MoS_2, and RuO_2 in 0.1 M KOH. The EIS spectra were recorded at 1.44 V_{RHE}. (h) S 2p, (i) Mo 3d, and (j) C 1s XPS spectra of the $(MoS_2)_{0.125}Mo_2C$ sample before and after the OER test. Reprinted with permission from ref 255. Copyright 2019 Wiley.

the 3D hybrid electrode, denoted as EG/Ni_3Se_2/Co_9S_8, through a hydrothermal and solvothermal process (Figure 298a).[826] This 2D/2D hierarchical structure ensured an efficient exposure and better utilization of electroactive sites, facilitated electrolyte penetration/diffusion, and underwent partial oxidation during the OER. As shown in Figure 298b, Ni_3Se_2/Co_9S_8 nanosheets were uniformly grown on the EG foil surface. From the EDX spectrum (inset of Figure 298b) and elemental mapping images (not shown here), it was confirmed that Co, S, Ni, Se, C, and O elements were evenly distributed throughout the hybrid structure. From the HRTEM images in Figures 298c and d, the presence of interfaces between Ni_3Se_2 and Co_9S_8 was verified. The XRD pattern of EG/Ni_3Se_2/Co_9S_8 further revealed the coexistence of crystalline Ni_3Se_2 and Co_9S_8 phases in the hybrid structure. As seen in Figure 298e, the hybrid electrocatalyst showed an enhanced OER activity in alkaline media (1.0 M KOH), requiring overpotentials of 330, 390, and 440 mV at current densities of 25, 50, and 100 mA·cm^{-2}, respectively, which were smaller than those of EG/Co_9S_8 and EG/Ni_3Se_2. Moreover, among the tested samples, EG/Ni_3Se_2/Co_9S_8 also exhibited the smallest Tafel slope (Figure 298f). Importantly, EG/Ni_3Se_2/Co_9S_8 showed a much higher BET specific surface area of 83 $m^2 \cdot g^{-1}$ than EG/Ni_3Se_2 (29 $m^2 \cdot g^{-1}$) and EG/Co_9S_8 (37 $m^2 \cdot g^{-1}$). This high surface area might contribute to the superior OER activity of EG/Ni_3Se_2/Co_9S_8. For the OER CP stability test (at a constant current density of 100 mA·cm^{-2}), EG/Ni_3Se_2/Co_9S_8 could maintain its OER activity for 10 h without showing significant decay. To understand the OER mechanism over EG/Ni_3Se_2/Co_9S_8, post-OER TEM, XPS, ICP-MS, and ion chromatographic analyses were also conducted. As displayed in Figures 298h and i, layers of Ni and Co oxo/hydroxy species with thicknesses of 5.3 and 9.26 nm were formed on the Ni_3Se_2 and Co_9S_8 surfaces after OER testing, respectively. After testing, the Co 2p XPS spectrum was shifted toward negative binding energy (Figures 298j), indicating an increase in Co oxidation states. In the S 2p XPS spectra (Figures 298k), the disappearance and emergence of surface sulfide (Co_9S_8) and sulfate species (SO_4^{2-}) were found after OER testing. The pre- and post-OER Ni 2p XPS spectra also indicated a shift toward positive binding energy, which might correspond to the formation of Ni oxides/hydroxides (Figures 298l). From the Se 3d XPS spectra (Figures 298m), it was also revealed that the selenide components disappeared and that SeO_x species were generated

https://doi.org/10.1021/acs.chemrev.3c00005
Chem. Rev. 2023, 123, 12795−13208

on the hybrid surface after OER testing. Additionally, the dissolution of S and Se species in the post-OER electrolyte was confirmed by ICP-OES and ion chromatography. These post-OER characterizations revealed the partial oxidation of the EG/Ni_3Se_2/Co_9S_8 sample after the OER, resulting in the formation of oxidized Ni and Co species as OER active sites. Moreover, the authors also claimed that the EG/Ni_3Se_2/Co_9S_8 surpassed the EG/Ni_3Se_2 and EG/Co_9S_8 in the OER activity because of the synergistic effects between the different metal (Ni and Co) oxides/hydroxides *in situ* formed on the EG/Ni_3Se_2/Co_9S_8 surface. However, the impacts of residual surface SO_4^{2-} and SeO_x species on the OER activity are still not clear and need to be examined further.

Finally, we introduce the dual *X*-ide-based core@shell structure as a representative example of vertical heterostructures (see Figure 292). Tiwari and co-workers reported a MoS_2@Mo_2C core@shell structure and its surface oxidation during OER testing in alkaline media (0.1 M KOH).[255] As indicated in Figure 299a, S-coated Mo_2C nanoparticles (S-Mo_2C) were first prepared by stirring the CS_2 solution, which contained Mo_2C and sulfur, for 3 h. Then, the mixture of the as-prepared S-Mo_2C and $MoCl_5$ was annealed with sulfur in an Ar atmosphere at 700 °C for 30 min, resulting in a core@shell structure [$(MoS_2)Mo_2C$]. To change the number of MoS_2 sheets on the Mo_2C nanoparticle cores (average particle size: 15 nm), the core@shell structures were prepared with different amounts of $MoCl_5$ (i.e., 0.06, 0.125, and 0.25 mmol), forming three core@shell samples: $(MoS_2)_{0.06}Mo_2C$, $(MoS_2)_{0.125}Mo_2C$, and $(MoS_2)_{0.25}Mo_2C$. Figure 299b shows the HRTEM image of the $(MoS_2)_{0.125}Mo_2C$ as a representative sample, indicating the formation of well-stacked MoS_2 sheets on the Mo_2C nanoparticles. As seen in Figure 299c, there was 3.45% tensile strain in the MoS_2 lattice of the $(MoS_2)_{0.125}Mo_2C$ sample, whereas residual strain was not present in the Mo_2C lattice. For the $(MoS_2)_{0.06}Mo_2C$ and $(MoS_2)_{0.25}Mo_2C$ samples, 1.78 and 0.05% tensile strains were found in the MoS_2 lattices, respectively. Additionally, lattice mismatch was not confirmed along the Mo_2C and MoS_2 (100) planes at the $(MoS_2)_{0.125}Mo_2C$ core@shell interface (see Figure 299d). This observation suggests that a certain extent of van der Waals epitaxy is formed along the MoS_2 and Mo_2C (100) crystal facets. Moreover, a decrease in the $MoCl_5$ amount (0.125 → 0.06 mmol) decreased the MoS_2 shell thickness, while an increase in the $MoCl_5$ amount (0.125 → 0.25 mmol) induced the collapse of the core@shell structure. The as-synthesized composite samples, Mo_2C, MoS_2, and RuO_2 were tested for the OER in 0.1 M KOH (see Figures 299e and f). Compared with the pristine Mo_2C and MoS_2 samples, the composite samples showed better activity. Among the tested transition metal-based samples, the $(MoS_2)_{0.125}Mo_2C$ sample recorded the lowest OER overpotential of 280 mV at 10 mA·cm^{-2} and the smallest Tafel slope of 209 mV·dec^{-1}. The authors also examined the intrinsic OER activities of the as-prepared composites by checking their ECSA-normalized LSV curves. The as-obtained curves indicated that $(MoS_2)_{0.125}Mo_2C$ had the highest intrinsic OER activity among them. Figure 299g shows the EIS plots of the as-prepared composites and MoS_2, indicating that the pristine MoS_2 had a much higher charge transfer resistance (R_{ct}) compared with the composites. Notably, the $(MoS_2)_{0.125}Mo_2C$ sample showed a lower R_{ct} (148 Ω) than the $(MoS_2)_{0.06}Mo_2C$ (275 Ω) and $(MoS_2)_{0.25}Mo_2C$ (597 Ω) samples. Furthermore, the electrochemical stability of $(MoS_2)_{0.125}Mo_2C$ was examined by performing 12 h of the CA test at a constant potential of 1.54 V_{RHE}. After the 12 h OER test, $(MoS_2)_{0.125}Mo_2C$ could maintain an overpotential that was similar to the initial one for a given current density. Additionally, the physicochemical stability of $(MoS_2)_{0.125}Mo_2C$ was confirmed by TEM, XRD, and XPS. The post-OER TEM and XRD results were similar to the pre-OER results even after OER testing, which indicates the high structural stability of $(MoS_2)_{0.125}Mo_2C$ under the tested OER condition. As shown in Figures 299h–j, the S 2p, Mo 3d, and C 1s XPS peaks, however, shifted slightly after the OER test, for which the authors assumed that these peak shifts occurred possibly due to (i) the partial oxidation of the MoS_2 shell surface and (ii) the partial diffusion of the electrolyte to the interface of the core@shell structure during the OER test. Here, the authors also claimed that, the as-prepared core@shell structure which possessed van der Waals layers of MoS_2 might induce spin coupling between Mo atoms (d orbital) and C atoms (p orbital) of MoS_2 and Mo_2C, respectively, which can accelerate the electron transfer and improve the stability for efficient OER electrolysis.[1187]

7. IDENTIFYING ACTIVE SPECIES/SITES USING SPECIAL CHARACTERIZATION TECHNIQUES

As previously discussed, most of the reports related to transition metal *X*-ides have demonstrated significant material transformations during the OER. There is a need to determine the driving forces behind these transformations and the identity of the real active species/sites and the electrocatalytic mechanisms. Deciphering these unknowns will benefit the future design and development of novel and robust electrocatalysts with enhanced activity and stability.[61,1188] Hence, research in this field must incorporate appropriate tools and strategies to solve this debate effectively. In this sense, research on transition metal *X*-ides should apply advanced characterization techniques that have been implemented in other fields to unveil the true electrocatalytic processes of several materials. Numerous techniques have provided key findings about structural reconstruction during electrochemical water splitting, including novel *in situ* and *operando* approaches used to track structural or electronic transformations and analyze chemical species.[1188−1190] We highlight special characterization techniques that can capture precise information beyond typical characterization methods and play a pivotal role in studying electrocatalytic materials, particularly transition metal *X*-ides.

This Section focuses on the relevance of several unique characterization approaches to comprehend the structural, morphological, and electronic reconstruction processes of different electrocatalytic materials. First, we briefly describe the capabilities and limitations of each technique. Then, through past applications and case studies, we illustrate the significance of these techniques in understanding the electrocatalytic transformations of *X*-ide and metal-oxide electrocatalysts for the OER and HER. Finally, we discuss some critical remarks that need to be considered for future research on *X*-ides, and we provide a characterization workflow to establish rational guidelines for the proper characterization of the materials. We expect to expand the "OER toolbox", as depicted in Figure 300, by complementing typical electrochemical methods with special characterization techniques. Overall, we hope to offer valuable insights on how to find the electrocatalytically active species/sites of next-generation transition metal *X*-ides. Finally, we also outline key requirements for successful *X*-ide OER electrocatalysts in practical water electrolysis. Additionally, we

https://doi.org/10.1021/acs.chemrev.3c00005
Chem. Rev. 2023, 123, 12795−13208

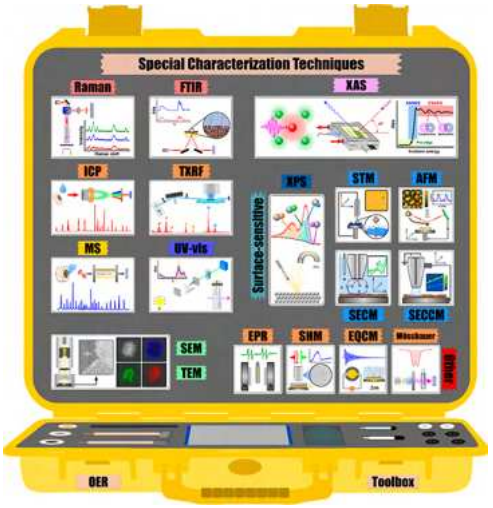


Figure 300. Schematic illustration of representative characterization techniques for active site elucidation in electrochemical water splitting.

explore the potential of artificial intelligence/machine learning-based approaches to advance *X*-ide OER electrocatalyst research.

7.1. Vibrational Spectroscopy

Analyzing chemical bonds and examining molecular structure are essential to understanding electrocatalytically active surfaces. Vibrational modes of functional groups can be monitored to track the electrocatalytic cycle and detect reaction sites and intermediates.[608,1190,1191] Two techniques can provide such information: Fourier-transform infrared (FTIR) spectroscopy and Raman spectroscopy. Although both techniques can provide information on chemical bonds, these techniques differ in some fundamental ways. While FTIR measures the absorbance, transmittance, or reflectance of infrared (IR) radiation, Raman spectroscopy relies upon the inelastic scattering of photons and polarizable molecules.[1192] Nevertheless, both techniques are powerful tools to probe chemical reactions, and their significance to the study of electrocatalytic processes has been proven in recent years.[1189] Here, we summarize some case studies which relied on vibrational spectroscopy to detect and characterize electrocatalytically active species/sites.

An effective way to evaluate the stability of the electrocatalyst and provide evidence of chemical transformation is to monitor critical absorption bands with FTIR spectroscopy. Fan *et al.* performed *in situ* FTIR measurements of a CoS_x electrocatalyst during chronopotentiometric runs.[705] Figure 301a depicts the spectra collected at different times, offering

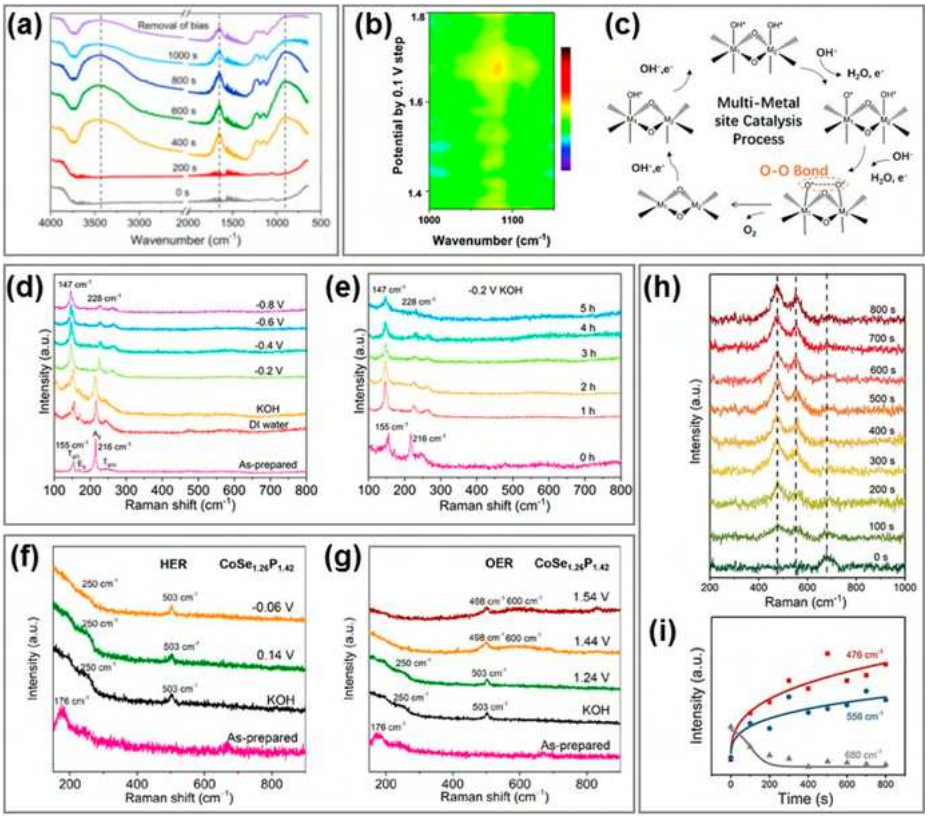


Figure 301. (a) *In situ* FTIR spectra of the CoS_x electrocatalyst during the OER at 1 mA. Reprinted with permission from ref 705. Copyright 2018 American Chemical Society. (b) Contour map of *operando* ATR-FTIR measurements of the O−O bond using a DMsA electrocatalyst; (c) Schematic illustration of the proposed multimetal site mechanism. Reprinted with permission from ref 1193. Copyright 2020 Royal Society of Chemistry. (d, e) *Operando* Raman spectra of the $NiSe_2$ electrocatalyst during the HER at (d) different potentials and (e) during the stability test. Reprinted with permission from ref 1194. Copyright 2020 American Chemical Society. (f, g) *In situ* Raman spectra of the $CoSe_{1.26}P_{1.42}$ electrocatalyst for (f) the HER and (g) OER. Reprinted with permission from ref 48. Copyright 2019 American Chemical Society. (h) *In situ* Raman spectra of the O,N-$NiFeC_x$ electrocatalyst during the OER at 1 $mA{\cdot}cm^{-2}$; (i) Peak intensity changes. Reprinted with permission from ref 1179. Copyright 2019 Wiley.

https://doi.org/10.1021/acs.chemrev.3c00005
Chem. Rev. 2023, 123, 12795−13208

convincing proof of chemical transformation during the OER. Notably, the bands at 3350 and 1630 cm^{-1}, assigned to the stretching and bending modes of the H-bonded hydroxyl group on the surface, respectively, increased and then stabilized during the reaction. Furthermore, an intense band at 892 cm^{-1}, assigned to the O−H bending mode of structural hydroxyls, suggested that hydroxide species were formed on the surface during the OER. Using FTIR alongside other characterization techniques, it was concluded that CoOOH was the active site for the OER and that the CoS_x electrocatalyst underwent a structural and chemical transformation. A more sophisticated approach consists of monitoring the reaction to track critical reaction steps or find intermediates. Wang *et al.* carried out *operando* attenuated total reflectance (ATR) FTIR measurements on a dealloyed multimetal site alloy (DMsA) electrocatalyst to monitor the OER on Ni, Fe, and Cu.[1193] This approach was able to capture the formation of the O−O bond at 1078 cm^{-1}, as depicted in the contour image in Figure 301b. Furthermore, by coupling isotopic experiments in $H_2{}^{18}O$ and complementary Raman and XPS evidence of the oxidation of the metals into metal oxyhydroxide counterparts, the authors proposed that the OER occurred through a direct oxygen evolution mechanism, as depicted in Figure 301c. The authors concluded that the multimetal sites exhibited a synergic effect that accelerated the O−O bond formation. Similarly, Zhang *et al.* employed rapid-scan ATR FTIR spectroscopy to observe intermediates during photochemical water oxidation on a Co_3O_4 electrocatalyst at pH 8.[608] Notably, two intermediates were detected, a superoxide at 1013 cm^{-1} and a Co(IV)-oxo site at 840 cm^{-1}, which exhibited different kinetic behavior. Despite its scarcity in the field, these studies demonstrate that FTIR can be effectively used to monitor the OER and capture critical reaction steps.

On the other hand, Raman spectroscopy has been extensively used for the characterization of water-splitting electrocatalysts. This technique has been able to track surface reconstruction processes during the HER. Zhai *et al.* demonstrated the decomposition of a $NiSe_2$ electrocatalyst during the HER using *operando* measurements.[1194] As depicted in Figure 301d, the intensities of several bands in the range 150−250 cm^{-1} varied with the applied potential. Furthermore, a remarkable decrease in intensity was observed during the chronopotentiometric test (Figure 301e). Alongside other characterization results, the authors concluded that the electrocatalyst was transformed from cubic $NiSe_2$ into hexagonal NiSe. Similarly, from the study regarding NiMo electrocatalysts,[1195] Raman spectroscopy revealed unexpected processes, such as the redeposition of MoO_x oxides on NiMo electrocatalysts from trace amounts of Mo ions in the electrolyte under XAS or visible-light irradiation, which may explain erroneous conclusions about the role of oxides during the HER. Raman spectroscopy has also been applied to unveil the HER mechanism. For instance, the S−H stretching vibration was detected in a MoS_x electrocatalyst, while Mo−H vibrations were absent, thus ruling out metallic Mo as the electrocatalytically active site.[1196]

Several studies have demonstrated that Raman spectroscopy is a suitable technique to detect the presence of surface oxides, hydroxides, and oxyhydroxides during the OER due to its high sensitivity in the low-frequency range.[1192,1197] Species commonly debated as OER active phases, such as NiOOH and CoOOH, have been thoroughly examined using Raman spectroscopy (refs 202, 204, 212, 564, 1191, and 1198−1205). In the case of transition metal *X*-ides, several studies in the literature have reported the transformation of the initial materials into oxidized species. The transformation of the $CoSe_{1.26}P_{1.42}$ electrocatalyst during the HER and OER was monitored through *in situ* Raman tests by Zhu *et al.*[48] Before the electrochemical tests, the electrocatalyst was transformed into $Co(OH)_2$ once in contact with the KOH electrolyte, demonstrated by the presence of new bands at 250 and 503 cm^{-1} and the reduction of the Se−Se stretching mode at 176 cm^{-1}. For the HER (Figure 301f), the decrease of the band at 250 cm^{-1} was attributed to the transformation of Co cations into metallic Co. On the other hand, peaks at 498 and 600 cm^{-1} were attributed to the formation of CoOOH during the OER (Figure 301g). Therefore, metallic Co and CoOOH were proposed as the real active species for the HER and OER, respectively. The reconstruction of oxygen- and nitrogen-doped NiFe carbide during the OER was tracked through *in situ* Raman tests by He *et al.*[1179] As displayed in Figure 301h when a low current density of 1 $mA{\cdot}cm^{-2}$ was applied, two peaks emerged at 476 and 556 cm^{-1}, which represent the bending and stretching modes of Ni−O in NiO_xH_y species. At the same time, the peak at 680 cm^{-1} assigned to the Ni−O−Fe vibration decreased. Note that peak intensities gradually stabilized, as displayed in Figure 301i. Therefore, *in situ* Raman spectroscopy demonstrated the irreversible self-reconstruction of the metallic carbide into electrocatalytically active $NiFeO_xH_y$ species. Fu *et al.* also concluded that *in situ*-generated NiOOH was the electrocatalytically- active site of a nickel sulfide/phosphide hybrid (NiS_xP_y) electrocatalyst after detecting the Ni−O band at 540 cm^{-1}.[564] Raman spectroscopy has also been applied to detect elusive intermediates. For example, the Co-superoxide intermediate (1013 cm^{-1}) was also found during the OER on CoOOH active species in the electrocatalyst.[1191] Finally, Raman spectroscopy has been used to study structural and substrate effects, such as the impact of film edges on the activation of cobalt manganese oxyhydroxides,[1206] the differences in vibrational modes between basal and edge planes of MoS_2 crystals,[1207] or the activity enhancement due to Au-promoted oxidation of Co(II) and Co(III) into Co(IV).[1204]

Vibrational spectroscopy offers encouraging capabilities to characterize OER electrocatalysts, assess the stability of the materials, and identify active species/sites and intermediates. In addition, we note that Raman and FTIR offer advantages that should be considered when characterizing the electrocatalysts. Remarkably, both methods rely on relatively affordable and easy-to-operate instruments compared to complex characterization approaches such as XAS. These techniques usually require little to no sample preparation, and relatively simple electrochemical setups can be made for *in situ*/*operando* measurements.[1190] Moreover, Raman spectroscopy benefits from the non-interference of water and the enhancement of the inelastic scattering process when metallic Pt, Au, or Ag substrates are present, which allows for surface-enhanced Raman spectroscopy (SERS).[1192,1204,1206] Raman spectroscopy can also complement XRD characterization by detecting crystalline nanoparticles (<4 nm) and amorphous phases, the latter being critical to provide evidence of surface reconstruction after/during the OER.[1201] On the other hand, certain limitations must be considered. Fluorescence of the sample, weak signals, or intense gas evolution might compromise data collection in Raman spectroscopy.[1196,1206]

https://doi.org/10.1021/acs.chemrev.3c00005
Chem. Rev. 2023, 123, 12795−13208

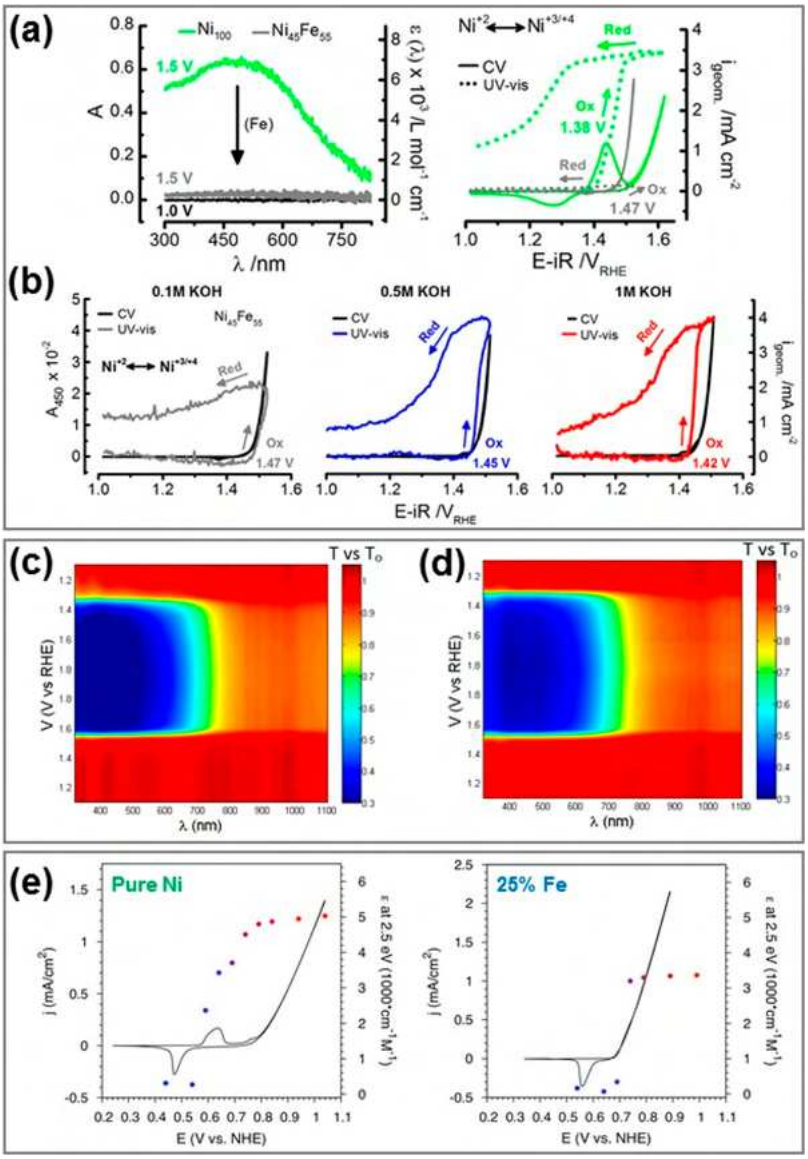


Figure 302. (a) *In situ* UV−vis spectra of NiOOH and $Ni_{45}Fe_{55}OOH$ electrocatalysts at different potentials in 0.1 M KOH; (b) UV−vis spectra at A_{450} during potential cycling of $Ni_{45}Fe_{55}$ electrocatalysts in different concentrations. Reprinted with permission from ref 611. Copyright 2017 American Chemical Society. (c, d) Contour plots of normalized transmission at different potentials and wavelengths using (c) Ni(Fe)-B_i and (d) Ni(Fe)OOH electrocatalysts. Reprinted with permission from ref 204. Copyright 2015 American Chemical Society. (e) CVs and corresponding UV−vis absorbance at 2.5 eV of pure Ni and 25% Fe-doped Ni films obtained during potentiostatic tests. Reprinted with permission from ref 1209. Copyright 2017 National Academy of Sciences.

More specific limitations may depend on the instrumental setup, such as the higher resistance due to water-immersion objectives.[202] Fluorescence is not a problem in FTIR, but water interference could be a problem depending on the studied frequencies. Moreover, FTIR may demand precise control of different properties, such as the thickness of the sample or the interface with the electrolyte.[1189,1190] Nevertheless, these limitations can be overcome when Raman and FTIR spectroscopy techniques are combined, becoming a formidable characterization tool.

7.2. UV−vis Spectroscopy

UV−vis spectroscopy is a well-established technique capable of acquiring useful information from the electronic transitions of bonding and nonbonding electrons. For instance, UV−vis is highly sensitive to transition metal ions or conjugated organic compounds.[1205] These analytes can be present in different materials for electrochemical water splitting, not only as the intended electrocatalyst but also as conductive supports, binders, dopants, dissolved species, or even impurities in the electrolyte. When spectrophotometry is performed simultaneously with electrochemical tests (i.e., UV−vis spectroelectrochemistry), electronic transitions can be captured in real-time and linked to concurrent processes at the electrode interface.[204] For instance, *in situ* spectroelectrochemistry can be used to quantify the optical absorption of several metal oxides, hydroxides, and oxyhydroxides at OER potentials, as these materials usually exhibit electrochromism (i.e., color changes when voltage is applied).[1208] Therefore, this technique could be applied to monitor the formation of oxides on transition metal *X*-ides during the OER.

Although specific applications of UV−vis spectroscopy are scarce in the field, certain studies have demonstrated the

https://doi.org/10.1021/acs.chemrev.3c00005
Chem. Rev. 2023, 123, 12795−13208

robustness of this technique to unveil critical aspects of electrocatalytically active species/sites. Notably, UV−vis spectroscopy has played a vital role in identifying the active species of Ni-Fe oxyhydroxide electrocatalysts. Understanding the local environments is essential to explaining the variation of Ni and Fe oxidation states, which are debated as the real OER active sites in Ni-Fe oxyhydroxides. Therefore, *operando* UV−vis measurements were performed by Görlin *et al.* to examine the number of oxidized $Ni^{+3/+4}$ in Ni-Fe centers.[611] As displayed in Figure 302a, Ni centers display a spectral absorption band at ∼450 nm (A_{450}), which represents the characteristic coloration of NiOOH, while the $Ni_{45}Fe_{55}$ electrocatalyst exhibited a reduced absorption intensity. Moreover, simultaneous UV−vis spectra and CVs demonstrated that the absorption started at more anodic potentials for the $Ni_{45}Fe_{55}$ electrocatalyst. This confirmed that Fe suppressed the oxidation of Ni sites and shifted the oxidation onset closer to the onset potential of the OER. Furthermore, the Ni redox peak shifted cathodically, and the absorption intensified with increasing pH during *operando* UV−vis tests at different KOH concentrations (Figure 302b), suggesting that larger numbers of Ni centers were oxidized at a higher pH. Similarly, Trześniewski *et al.* correlated the spectral properties of Ni-Fe electrocatalysts during Ni activation.[204] Contour plots showing the normalized transmission as a function of the wavelength and potential during CVs are shown in Figure 302c for Ni(Fe)-B_i and Figure 302d for Ni(Fe)OOH electrocatalysts. Strong and broad absorption features were seen at wavelengths below 800 nm, between 1.4−1.6 V_{RHE} (i.e., blue regions in the contour plots), which coincide with the Ni oxidation and reduction waves. As these redox waves correspond to the catalyst activation, this implies that light absorption is inherent to the electrocatalytically active site of these materials. Since no significant differences in the electrochemical and spectral features of the studied materials were seen, UV−vis measurements suggested that the active site for Ni(Fe)-B_i and Ni(Fe)OOH electrocatalysts was NiOOH. The correlation of optical and redox changes of thin-film Ni-Fe electrocatalysts was also verified by Goldsmith *et al.*[1209] As depicted in Figure 302e, absorption intensified upon increasing the potential in both pure Ni and Fe-doped Ni electrocatalysts. However, the absorption onset shifted toward anodic potentials in the 25% Fe-doped Ni electrocatalyst. Using additional first-principles calculations, the authors proposed that absorbance changes were observed only after the electrocatalytic wave because electrocatalytically active sites with higher oxidation states (i.e., Ni^{4+}, Fe^{4+}) were necessary to boost the OER.

UV−vis spectroscopy is a well-established, affordable, and robust characterization technique that can be easily employed in most laboratories. Measurements demand UV-transparent materials such as quartz windows, and electrocatalysts are usually drop-cast on transparent FTO or ITO electrodes.[611,1208,1209] Moreover, typical three-electrode electrochemical cells can be made using cuvettes, but aspects such as the optical path length, thickness of the electrocatalytic film, and even gas bubbles (i.e., operating current densities) should be carefully addressed.[1208] UV−vis should always be complemented with additional characterization techniques, as discussed at the end of this Section. Nevertheless, these case studies demonstrate the utilization of UV−vis spectroscopy to monitor redox state changes of electrochromic electrocatalysts during the OER.

7.3. X-ray Absorption Spectroscopy

XAS is one of the most versatile and powerful characterization techniques due to the considerable amount of information obtained from the studied material. Notably, the oxidation states, the bond distances, the coordination numbers (CNs), the degree of disorder, and the identity of neighboring atoms are usually inferred. Liquid and solid materials, either crystalline or amorphous, can be characterized at different scales.[1210,1211] Furthermore, this technique is compatible with *in situ* and *operando* measurements. These features demonstrate that XAS is a formidable tool for examining the electronic and structural reconstruction of materials during reactive conditions.[1188,1190,1211]

XAS measurements rely on the excitation of core electrons to unoccupied states from incident X-rays. The XAS spectrum can be roughly split into three regions, as depicted in Figure 303: the pre-edge (i.e., below the ionization threshold), the X-ray absorption near edge structure (XANES), and the extended X-ray absorption fine structure (EXAFS). The sharp rise in absorption (i.e., absorption edge) in the XANES region is caused by the strong absorption of the X-rays. In the EXAFS region, the electrons are further excited to the continuum, where scattering waves of the outgoing electron cause constructive or destructive interference with adjacent atoms and produce characteristic wiggles in the spectrum. The resultant edges depend on the excited core electron: K-, L-, and M-edges for n = 1, 2, and 3, respectively.[1211] For instance, the K-edge transition (1s to np) is found around 5−10 keV (hard X-rays) for 3d transition metals. Unfavored transitions (e.g., 1s to 3d in transition metals) may appear as pre-edge peaks.[1210] Overall, information about the oxidation states and electronic structure of the target atoms can be inferred from the XANES, while the EXAFS provides information related to the coordination geometry and bond distances of neighboring atoms.[1190,1210,1212] Furthermore, the versatility of XAS resides in a large number of operation modes and the tunability of X-rays, which expand the capabilities of the technique. More aspects of the fundamentals and applications of XAS can be found in specialized reviews.[1210,1211]

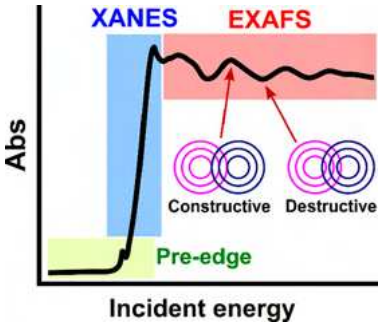


Figure 303. Schematic illustration of the X-ray absorption spectrum showing the pre-edge, XANES, and EXAFS regions, as well as the resulting interference in the latter.

XAS has been extensively used in the past to identify the active species/sites and monitor the electronic and structural properties of different OER electrocatalysts, particularly in the debate about the real active sites in several metal oxides, hydroxides, and oxyhydroxides. Zhang *et al.* studied the reconstruction of iridium-incorporated cobalt-based hydroxide nanosheets during the OER.[1213] After an OER stability test for

https://doi.org/10.1021/acs.chemrev.3c00005
Chem. Rev. 2023, 123, 12795−13208

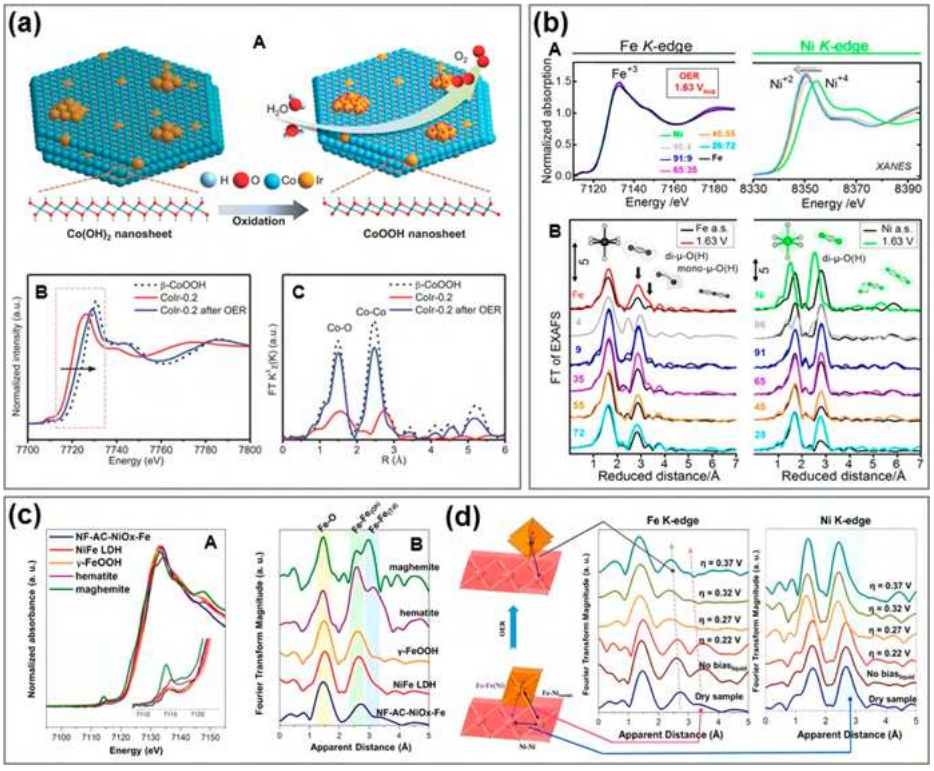


Figure 304. (a) XAS characterization of the CoIr-0.2 electrocatalyst: schematic illustration of the transformation of the α-Co(OH)$_2$ to β-CoOOH phase (A), Co K-edge XANES spectra (B) with corresponding FT curves (C). Reprinted with permission from ref 1213. Copyright 2018 Wiley. (b) XAS spectra of Ni-Fe electrocatalysts at different compositions (Ni$_{100-x}$Fe$_x$) after the OER (A) and corresponding Ni and Fe K-edge FT-EXAFS oscillations (B). Reprinted with permission from ref 610. Copyright 2016 American Chemical Society. (c) XAS spectra of the NF-AC-NiO$_x$-Fe electrocatalyst and references: pre-edge/XANES (A) and Fe K-edge FT-EXAFS spectra (B); (d) *In situ* Ni and Fe K-edge FT-EXAFS spectra of the Au-NiO$_x$-Fe electrocatalyst during the OER. Reprinted with permission from ref 1203. Copyright 2019 American Chemical Society.

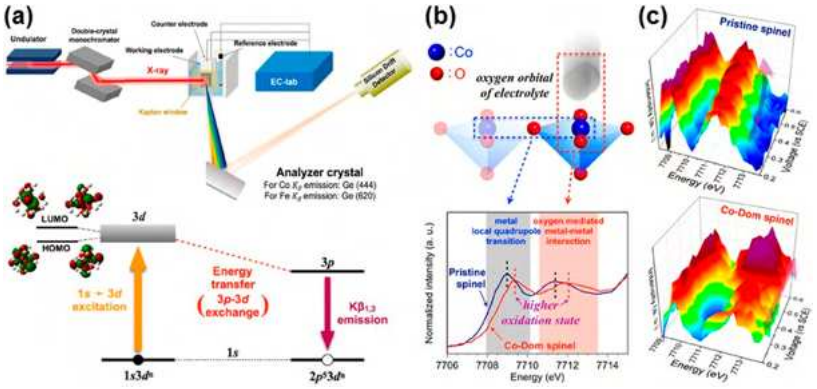


Figure 305. (a) Schematic illustration of *operando* HERFD-XAS and energy diagram for the 3p−3d exchange; (b) Schematic illustration of the Co 3d orbital interaction with O 2p and corresponding HERFD-XAS spectra at the Co K-edge for pristine and Co-Dom spinel; (c) *Operando* HERFD-XAS spectra at different potentials. Reprinted with permission from ref 1218. Copyright 2018 American Chemical Society.

10 h, XAS measurements revealed that both Co and Ir were oxidized. As depicted in Figure 304a, the Co K-edge XANES spectrum was shifted toward higher energies after the OER, implying a higher oxidation state for Co. Moreover, the Fourier transform (FT) curve exhibited peaks corresponding to the Co−O and Co−Co bonds in β-CoOOH. This demonstrated that initially disordered Co(OH)$_2$ was transformed into stable β-CoOOH nanosheets. Notably, XAS has been extensively used to unveil the role of Fe centers in NiFeOOH and CoFeOOH electrocatalysts, as the identity of the real active sites has been under debate.[609,611,1214,1215] An interesting study by Görlin *et al.* employed XAS to evaluate the role of the Ni:Fe stoichiometry on Ni-Fe electrocatalysts during the OER.[610] *Quasi in situ* XAS was used to analyze the Ni and Fe K-edges of the electrocatalysts with different compositions, as displayed in Figure 304b. The XANES spectra showed that the Fe centers remained mainly as Fe^{3+} after 30 min of conditioning at 1.63 V_{RHE}, independent of the composition. At the Ni K-edge, a shift of 2.7 eV was attributed to the Ni^{2+}/Ni^{4+} transition. The Fe−O, Fe−M, Ni−O, and Ni−Ni distances from FT-EXAFS confirmed that a fraction of the Ni centers remained as Ni^{2+}, while the Fe centers adapted to the Ni lattice without changing their oxidation state. Octahedrally coordinated [MO$_6$] units were proposed as the dominant structures with Ni and Fe

https://doi.org/10.1021/acs.chemrev.3c00005
Chem. Rev. 2023, 123, 12795−13208

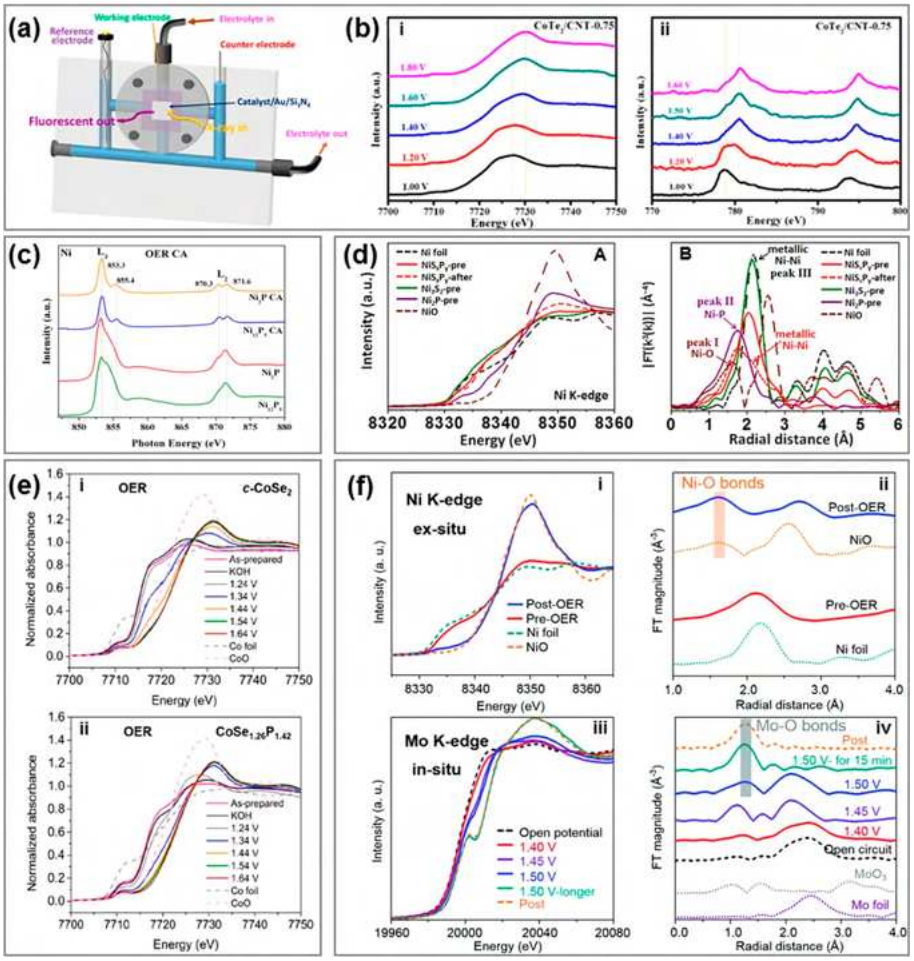


Figure 306. (a) Schematic illustration of a substrate-film-sample holder for *in situ* XANES tests; (b) *In situ* XANES spectra at the Co K-edge (i) and Co L-edge (ii) for the $CoTe_2$ electrocatalyst during the OER. Reprinted with permission from ref 1132. Copyright 2016 American Chemical Society. (c) Ni $L_{2,3}$-edge XAS spectra for $Ni_{12}P_5$ and Ni_2P electrocatalysts before and after chronoamperometric OER measurements. Reprinted with permission from ref 494. Copyright 2017 American Chemical Society. (d) Comparison of Ni K-edge XANES spectra (A) and Ni EXAFS data (B) in R-space collected on Ni-based samples. Reprinted with permission from ref 564. Copyright 2018 American Chemical Society. (e) *In situ* Co K-edge XANES spectra of *c*-$CoSe_2$ (i) and $CoSe_{1.26}P_{1.42}$ (ii) electrocatalysts at different potentials during the OER. Reprinted with permission from ref 48. Copyright 2019 American Chemical Society. (f) XAFS measurements of the Mo_6Ni_6C electrocatalyst and references during the OER: Ni K-edge XANES spectra (i), FT of Ni K-edge EXAFS (ii), Mo K-edge XANES spectra (iii), and FT of Mo K-edge EXAFS (iv). Reprinted with permission from ref 224. Copyright 2019 Royal Society of Chemistry.

atoms connected by μ-O(H) bridges. Notably, Fe's addition caused a higher distortion of the metal center, which implies that the high activity can be associated with the high amorphicity of the electrocatalyst. Recently, Song *et al.* found that nanoclusters of γ-FeOOH were covalently linked to γ-NiOOH after incorporating Fe during the potential cycling of acid-cleaned Ni foam (NF-AC) in commercial KOH.[1203] From Figure 304c, the Fe K-edge XANES spectra revealed an oxidation state of 3+ for Fe, and peaks from the FT-EXAFS spectra were associated with Fe−Fe bonds with octahedrally coordinated Fe atoms. Also, a long Fe−Ni path and small coordination numbers were found, which indicated the presence of discrete γ-FeOOH nanoclusters linked to the NiO_x support via bridging oxygen. Furthermore, *in situ* XAS measurements (Figure 304d) revealed that the Ni−Ni distances were reduced during the OER, demonstrating the oxidation of Ni centers. Notably, the Fe−Ni path was reduced drastically during the OER, attributed to a structural tilting of the FeO_6 octahedron.

Hard X-ray XAS measurements based on the K-edge transition are relatively insensitive to electronic or structural features of transition metals since d orbitals mainly contribute to the frontier orbitals.[1189] On the other hand, the L-edge transition (2p to *n*d) allows for examining the electronic structure of *n*d orbitals, which are directly linked to the intermediates during the electrocatalytic process.[1216,1217] In this sense, Hung *et al.* demonstrated that *operando* K$\beta_{1,3}$ high-energy resolution fluorescence-detected X-ray absorption spectroscopy (HERFD-XAS) could be used to directly measure the interaction between the 3d orbitals of Co ions and oxygen during the OER at ambient conditions.[1218] As depicted in Figure 305a, collection of the K$\beta_{1,3}$ emission at a small incident angle can capture the interaction of metal ions at the surface. Pristine spinel [i.e., CoO(OH)] and Fe-doped, Co-dominated (Co-Dom) spinel (i.e., $Co_{2/3}Fe_{1/3}O(OH)$) were used as target electrocatalysts for the OER. From Figure 305b, the peak shift at the Co K-edge in both the metal local quadrupole transition and the O-mediated metal−metal interaction suggested that the Fe ions in the Co-Dom spinel

https://doi.org/10.1021/acs.chemrev.3c00005
Chem. Rev. 2023, 123, 12795−13208

stabilized the Co ions with higher oxidation states and facilitated the formation of intermediates during the OER. From *operando* HERFD results (Figure 305c), the peak for the O-mediated metal−metal interaction shifted toward lower energies for the pristine spinel, while the peak for the Co-Dom spinel intensified with increasing potentials but stayed at the same energy. This revealed that the chemical state of the Co center in the Co-Dom spinel was different, enabling a stronger Co−O orbital interaction. By complementing these results with electrochemical information and first-principle calculations, Co centers, rather than Fe centers, were determined to be the true active sites. Additionally, *in situ* HERFD-XAS has been used to evaluate the electronic environment of Fe-doped NiO_x electrocatalysts during the OER, providing insights on the role of Fe^{3+} during the OER.[609]

Finally, recent studies have examined transition metal *X*-ides using XAS. The effect of CNT substrates on the transformation of $CoTe_2$ electrocatalysts was studied by Lu *et al.*[1132] *In situ* XANES was carried out in a custom substrate-film-sample holder assembly (Figure 306a). From Figure 306b, the Co K-edge and L-edge XANES spectra exhibited peak shifts toward higher energies with increasing potential, which suggested the oxidation of Co^{2+} into Co^{3+}. Since there were no energy shifts in the XANES of $CoTe_2$ nanowires, it was suggested that the CNTs favored the transformation of $CoTe_2$ into CoOOH during the OER. Similar results were observed for the CoS_x electrocatalyst using *ex-situ* XANES (i.e., $CoS_x \rightarrow$ CoOOH).[705] To gather insights on the transformation of nickel phosphides during the OER, Menezes *et al.* complemented post-OER TEM and XPS analysis with XAS tests at the Ni $L_{2,3}$-edge.[494] As shown in Figure 306c, the peak at ∼858 eV, assigned to Ni−P, diminished after chronoamperometric OER tests, whereas a peak attributed to $Ni(OH)_2$ at ∼855 eV intensified. Moreover, the L_2-edge peak split, which suggested the formation of Ni^{2+} and phosphate species. The authors concluded that the nickel phosphides were partially oxidized and transformed into nickel phosphates and $Ni(OH)_2$. Fu *et al.* employed XAS to determine the oxidation states of NiS_xP_y electrocatalysts before and after the OER.[564] From Figure 306d, the Ni K-edge XANES spectra revealed that Ni increased its oxidation state compared to the pristine sample, which confirmed its oxidation. Moreover, the peaks from EXAFS spectra were assigned to Ni−O, Ni−P, and Ni−Ni bonds. Partial oxidation was verified by the presence of predominant peaks assigned to Ni−O and Ni-PO_x after the OER. The transformation of $CoSe_2$ and P-substituted $CoSe_2$ precatalysts during the OER and HER was studied using *in situ* XAS by Zhu *et al.*[48] During the OER, peaks intensified and shifted toward higher energies, as shown in the Co K-edge XANES spectra (Figure 306e), which confirmed the oxidation of Co. Furthermore, the chemical state of Co^{3+} was achieved at lower potentials in the $CoSe_{1.26}P_{1.42}$ electrocatalyst, which suggests that the lattice distortion caused by the phosphorous promoted the transformation during the OER. This was confirmed by EXAFS curve fitting, as the CN of the Co−Co path in the $CoSe_{1.26}P_{1.42}$ electrocatalyst was larger, suggesting a more significant amount of CoOOH. On the other hand, the chemical state of the $CoSe_{1.26}P_{1.42}$ electrocatalyst after the HER resembled that of Co foil, confirming metallic Co as the electrocatalytically active site. Finally, XAS played an essential role in characterizing a Mo_6Ni_6C electrocatalyst and its reconstruction during the OER.[224] Ni K-edge and Mo K-edge XANES and EXAFS spectra are displayed in Figure 306f. The Ni center in the initial carbide exhibited a chemical state similar to the Ni foil, whereas the as-reconstructed O-MoNi-C resembled NiO. The Ni−Ni bonds disappeared from the *ex situ* EXAFS spectra, while the Ni−O peak emerged. *In situ* Mo K-edge XANES revealed that the chemical states of Mo increased with the applied potential, whereas *in situ* EXAFS confirmed the presence of Mo−O bonds and the disappearance of Mo−Mo bonds. These findings corroborated the pre-oxidation process and reconstruction of the bimetallic carbide surface (i.e., $Mo_6Ni_6C \rightarrow MoO_x$ + NiOOH).

XAS has played a critical role in the study of the interesting properties of water-splitting electrocatalysts, such as the effect of Co incorporation from the substrate onto NiFe LDHs,[1219] the formation of dominant Ir oxides and their dissolution trends,[293] the redeposition of Mo^{4+} oxides during the HER,[1195] the effect of $NiFeO_x$ loading on Au-substrates and the population of Fe edge-sites atoms,[1220] the impact of film thickness on the OER and ORR activity of Mn oxide electrocatalysts,[1221] and the role of metallic Ni as the electrocatalytically active site for the HER,[1222] among others. Overall, these case studies demonstrate the broad applicability of XAS in the study of water-splitting electrocatalysts. Certain advantages further support the use of XAS. Remarkably, sample preparation is minimal, and only low amounts of materials are required. Some emerging modes, such as ultrafast XAS, can provide time-resolved measurements, whereas fluorescence modes are appropriate to study analytes in low concentrations.[1210] As previously mentioned, the HERFD-XAS approach allows for direct registering of metal−oxygen interactions and is suitable to study 1s to 3d transitions at the pre-edge.[1211,1218] On the other hand, certain limitations must be taken into account. Importantly, XAS is a bulk-sensitive technique and therefore only provides averaged information on the materials at the thermodynamic steady state.[1190,1211] Most of the *in situ* XAS measurements rely on hard X-rays, which are not surface sensitive. Still, this can be overcome with other approaches, such as the electron yield mode.[1210] Although it is not a ubiquitous issue, X-ray-induced damage of the sample or reduction of certain species should always be verified.[1220] Other considerations, which should be carefully addressed, include the potential interference of strong background Ni signals when Ni foam is used[1203] or irregular oscillations due to gas bubbles.[1223] Evidently, the complexity of the technique is a paramount concern. XAS experiments are usually performed in synchrotron facilities, capable of providing tunable X-ray beams with adequate intensities.[1210] Depending on the instrumental setup, issues like poor spatial resolution[1189] or limited probe depth can be found in *operando* measurements. Therefore, strategies such as using highly nanoporous electrocatalysts might be required to guarantee penetration of the electrolyte.[1217] Finally, when making custom electrochemical cells, windows transparent to X-rays such as Si_3N_4 membranes must be employed.[1132] Although these aspects illustrate the complexity of XAS, fundamental studies focused on understanding intricate processes should consider XAS due to its powerful capabilities, especially when it is challenging to capture structural and compositional transformations in real-time using other techniques.

7.4. Electron Microscopy

The electrocatalytic activity and stability of materials strongly rely on structural, compositional, and morphological features, such as particle sizes, structural defects, exposed crystalline

https://doi.org/10.1021/acs.chemrev.3c00005
Chem. Rev. 2023, 123, 12795−13208

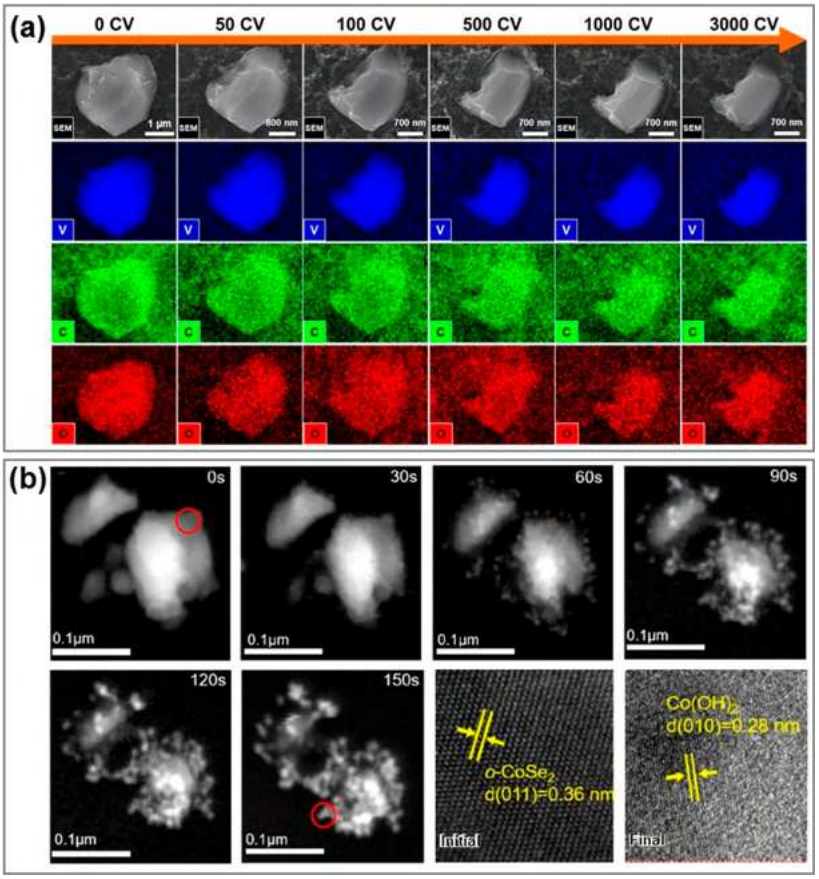


Figure 307. (a) *Quasi in situ* IL-SEM/EDX elemental mapping of the V_8C_7 particulate electrocatalyst during the OER at several CVs. Reprinted with permission from ref 221. Copyright 2020 American Chemical Society. (b) *In situ* STEM images of the $CoSe_{1.26}P_{1.42}$ electrocatalyst immersed in KOH at different times; HRTEM images show regions circled in red. Reprinted with permission from ref 48. Copyright 2019 American Chemical Society.

facets, surface roughness, and micro-/nanostructures with high surface area.[1224,1225] Electron microscopy (EM) technologies are ideal methods to examine the materials and provide precise information on these features. These techniques directly capture high-resolution images at the nanoscale or atomic resolution by using a focused beam of electrons that interact with the material. There are two main types of EM techniques: scanning electron microscopy (SEM) and transmission electron microscopy (TEM). SEM mainly relies on secondary and backscattered electrons, which are emitted when the surface is scanned with a finely focused beam of electrons. Emitted electrons are collected with different detectors, and the positions and intensities of the signals are linked to the topography and composition of the material. In contrast, the electrons are transmitted through the sample in TEM, generating a projected view. Like SEM, in the scanning TEM (STEM) mode, a fine electron beam scans the material, allowing the surface to be mapped and collecting secondary and backscattered electrons.[1226] Additionally, EM technologies are greatly complemented by other advantageous techniques and modes, such as energy-dispersive X-ray spectroscopy (EDX), electron energy loss spectroscopy (EELS), high-angle annular dark-field imaging (HAADF), and selected area electron diffraction (SAED), which provide nanoscale-resolved spatial and spectroscopic information.[1190,1225]

Morphological and compositional characterization of the material before and after the OER to detect significant changes is indispensable.[224,1179,1215] However, some studies have exploited the capabilities of EM technologies to study water-splitting electrocatalysts in interesting ways, a formidable example being the monitoring of precise locations. Recently, our group utilized identical-location (IL) *quasi in situ* SEM coupled to EDX to capture the morphological transformation of V_8C_7 microparticles during OER degradation tests.[221] As displayed in Figure 307a, the size of the V_8C_7 microparticle was gradually reduced as the CV cycles continued until stabilization above 500 CV cycles. Notably, the shape of the particle changed from a rounded initial structure into a well-faceted cuboid-like shape. This transformation was attributed to the partial oxidation of the initial carbide into V_2O_5, which subsequently was dissolved into the electrolyte as VO_4^{3-}. By using complementary DFT studies, it was proposed that a selective dissolution process exposed stable (100), (010), and (001) surfaces, where VOOH was formed as the active species for the OER. Zhu *et al.* employed liquid-phase (LP) TEM to monitor the structural stability of the $CoSe_{1.26}P_{1.42}$ electrocatalyst when immersed in KOH.[48] Figure 307b shows sequential IL-STEM images of the electrocatalyst at different times after immersion in the electrolyte. Interestingly, the initially smooth particles with irregular shapes were transformed into several nanoparticles. By measuring the lattice spacing with HRTEM images before and after immersion, it was revealed that the initial *o*-$CoSe_2$ was transformed into $Co(OH)_2$. This confirmed that the electrocatalyst was unstable in the KOH electrolyte, and the notorious and fast transformation was attributed to the preferential dissolution of P.

https://doi.org/10.1021/acs.chemrev.3c00005
Chem. Rev. 2023, 123, 12795−13208

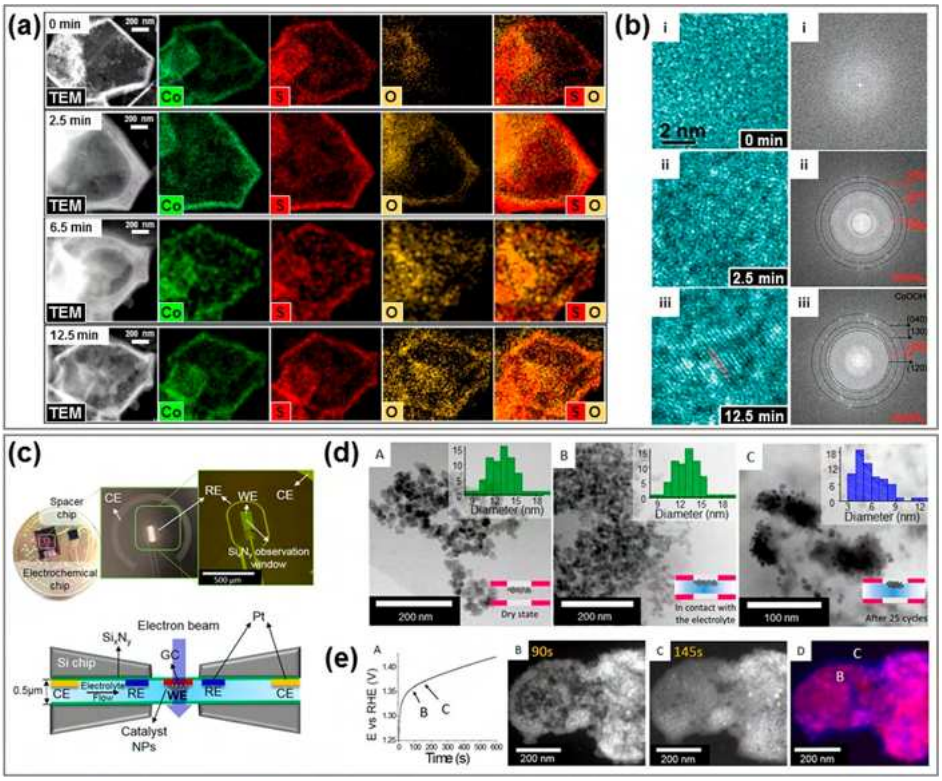


Figure 308. (a) *In situ* TEM-HAADF images and EDX elemental maps of the CoS_x electrocatalyst during the OER; (b) *In situ* HRTEM images with corresponding SAED patterns proving the transition from amorphous CoS_x to crystalline CoOOH. Reprinted with permission from ref 705. Copyright 2018 American Chemical Society. (c) Photos and schematic views of the holder for *in situ* EC-TEM tests; (d) *In situ* STEM images of Co_3O_4 nanoparticles on the EC-TEM sample holder in the dry state (A), immersed in 0.1 M KOH (B), and after CV cycling (C). Insets depict the size distributions; (e) *In situ* EC-TEM test at 10 $mA{\cdot}cm^{-2}$: CP curve (A), STEM-HAADF images at 90 (B) and 145 s (C), superposition of B (red) and C (blue) (D). Reprinted with permission from ref 1230. Copyright 2019 American Chemical Society.

IL-EM approaches have been applied to evaluate other processes such as the degradation of Pt/Ni,[1227] Ru, and RuO_2 nanoparticles (NPs),[1228] the stability of NiFe NPs during the OER,[1229] and the effects of aging in KOH electrolyte and electrochemical cycling on $Ni(OH)_2$ films.[200] Evidently, IL-EM examinations provide valuable insights into the structural and morphological transformations and complement other techniques.

To circumvent the classical *ex situ* TEM characterization in ultra-high vacuum (UHV), electrochemical *in situ* LP-TEM can be done to capture degradation processes in real-time.[1225,1230] Fan *et al.* monitored the transformation of amorphous CoS_x electrocatalyst into crystalline CoOOH during the OER using *in situ* TEM.[705] Images taken at different anodization times showed that the surface shell thickened, while EDX mapping indicated an increase of the oxygen content at the inner shell (Figure 308a). *In situ* IL-HRTEM images (Figure 308b) revealed that the initially amorphous CoS_x was transformed into crystalline CoOOH, and further SAED and EELS measurements confirmed this result. Moreover, the observed lattice fringes revealed that the mechanism was mediated by $Co(OH)_2$. Ortiz Peña *et al.* demonstrated an *in situ* electrochemical TEM (EC-TEM) methodology using Co_3O_4 NPs as the OER electrocatalyst.[1230] A typical three-electrode cell was conceived, which employed disposable electrochemical chips at the tip of TEM sample holders (Figure 308c). *In situ* TEM revealed that the NPs were stable after being immersed in the electrolyte, but after 25 CV cycles, their diameter was reduced (Figure 308d). Subsequent *in situ* HRTEM results suggested the formation of an amorphous matrix. Then, the morphological transformation was captured during CP tests for 10 min (Figure 308e), which confirmed the partial amorphization process, where smaller crystalline NPs were embedded inside an amorphous CoOOH-like phase exposed to the electrolyte.

EM techniques offer encouraging capabilities that demonstrate their applicability in the study of transition metal *X*-ides. EM technologies can be non-destructive, allowing *quasi in situ* and IL studies depending on the measurement conditions.[1225] Even relatively "simple" approaches like IL-SEM/EDX can effectively assist in the understanding of essential processes such as selective dissolution or metal incorporation.[200,221,1228,1229] More robust techniques such as TEM and its complementary techniques (e.g., HAADF, SAED, EELS) offer a robust set of tools to confirm the transformations, even when *ex situ* measurements are used before and after the OER. Notably, HRTEM is extremely useful in evaluating changes in the crystal structure, and SAED can be used to confirm processes such as the amorphization of the materials.[1230] Furthermore, STEM provides excellent spatial resolution and improves the signal-to-noise ratio.[1230] Finally, *in situ* EM is highly recommended, especially for fundamental studies, since these approaches allow researchers to readily capture the morphological and compositional transformation of the electrocatalyst in real-time under reactive conditions. In contrast, *ex situ* measurements cannot thoroughly verify the real state of the materials.[1226,1230] However, EM techniques have some limitations. EM technologies rely on delicate

https://doi.org/10.1021/acs.chemrev.3c00005
Chem. Rev. 2023, 123, 12795−13208

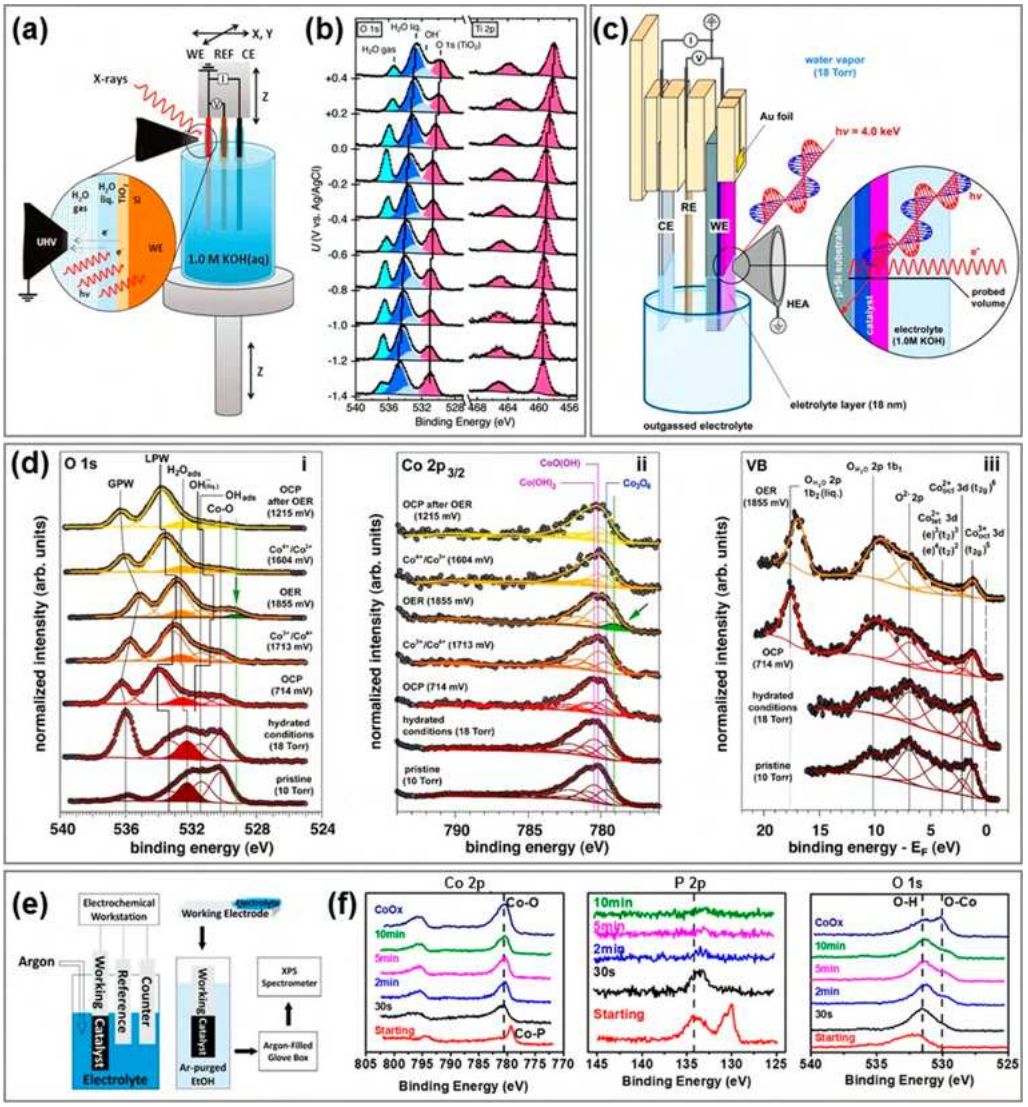


Figure 309. (a) Schematic illustration of a PEC cell for *operando* AP-XPS analysis of the semiconductor/liquid junction; (b) O 1s and Ti 2p peaks from AP-XPS measurements at different potentials for a bare p^+-Si/TiO_2 electrode Reprinted with permission from ref 1231. Copyright 2015 Royal Society of Chemistry. (c) Schematic illustration of the electrochemical setup for *operando* AP-XPS tests during the OER; (d) AP-XPS analysis of a biphasic CoO_x electrocatalyst: evolution of the O 1s peak (i), the Co $2p_{3/2}$ peak (ii), and the valence band (iii) at different conditions. Note: new features in (i) and (ii) are highlighted in green. Reprinted with permission from ref 1233. Copyright 2017 American Chemical Society. (e) Schematic illustration of the protective sample transfer procedure for *quasi in situ* XPS tests; (f) Co 2p, P 2p, and O 1s core-level XPS spectra of CoP nanoparticles at different stages of the OER (at 1.67 V_{RHE}) in 1 M KOH. Reprinted with permission from ref 470. Copyright 2018 American Chemical Society.

instruments, and their use could be limited by experimental conditions.[1190] Conventional EM approaches require UHV. Therefore, it is evident that *ex-situ* SEM and TEM analyses are performed outside the material environment. *In situ* TEM involves extremely demanding technical challenges, such as using robust and transparent membranes to comply with the UHV conditions as well as the fabrication of robust electrochemical cells.[1225,1226] Sealed liquid cells may also exhibit low resolution.[1226] TEM and STEM require thin samples (<100 nm), which restricts the size and handling of materials such as Ni foam. Finally, the most critical limitation of *in situ* TEM measurements is the effect of electron beam irradiation on the chemical properties of the materials, which may also interfere with electrochemical measurements.[1225,1230] SEM does not lead to substantial damage like TEM if electron beams with moderate energies are used.[1226] Still, it is always necessary to address if the materials are sensitive to electron beams without ignoring the trade-off between energy intensity and resolution. Nevertheless, EM technologies have improved tremendously in recent years, and it is expected that new approaches like *in situ* TEM will be broadly available in the near future.[1190]

7.5. Surface-Sensitive Techniques

Probing the electrocatalytic surface is essential to understand the real active species/sites during electrocatalytic reactions, as processes like adsorption, activation, and desorption occur at the electrode/electrolyte interface.[1188] Furthermore, evidence suggests that transition metal *X*-ides undergo significant surface reconstruction during the OER, which impacts their activity and stability.[61] Therefore, surface-sensitive characterization techniques must first be employed to confirm the electrocatalyst self-reconstruction and ultimately unveil the

https://doi.org/10.1021/acs.chemrev.3c00005
Chem. Rev. 2023, 123, 12795−13208

driving forces behind these changes. This Section summarizes the unique capabilities of different surface-sensitive techniques and their role in the characterization of water-splitting electrocatalysts.

7.5.1. X-ray Photoelectron Spectroscopy. In XPS, the sample is irradiated with high-energy X-rays, causing the emission of photoelectrons near the surface. These photoelectrons exhibit different energies depending on their chemical environment. As a result, XPS provides valuable information related to the surface elemental composition and electronic states of the materials.[1205,1231] This feature has increased the reputation of XPS for the chemical characterization of numerous classes of materials in different fields. Notably, this technique has been routinely used to characterize transition metal *X*-ide electrocatalysts in the literature. In fact, post-OER XPS analysis has been considered a decisive measurement to confirm the reconstruction of non-oxide electrocatalysts.[61] Other relevant aspects, such as Fe incorporation, have been precisely examined by XPS.[200,212] Since the role of XPS in conventional pre- and post-analysis has already been discussed in previous Sections of this review, we now emphasize studies relying on novel and advanced XPS approaches.

Operando and *in situ* measurements can be done using ambient-pressure XPS (AP-XPS), allowing researchers to capture surface structural and chemical changes in real-time.[61,1205,1232] Lichterman *et al.* demonstrated the robustness of AP-XPS to characterize semiconductor/liquid junctions in real-time under ambient conditions.[1231] After placing a three-electrode photoelectrochemical cell inside the experimental chamber (Figure 309a), the solid/liquid interface was probed at 20−27 mbar through a thin electrolyte film that covered the working electrode surface. As depicted in Figure 309b, AP-XPS captured the shift in O 1s and Ti 2p binding energies for a p^+-Si/TiO_2 electrode as a function of the electrode potential, revealing the nature of ohmic and rectifying junctions. *Operando* AP-XPS was also employed by Favaro *et al.* to examine biphasic CoO_x electrocatalysts under OER conditions.[1233] Similarly, a "dip-and-pull" method covered the working electrode surface with a thin (∼19 nm) electrolyte layer using the electrochemical setup in Figure 309c. *Operando* measurements were performed in a reduced pressure (∼24 mbar), H_2O-saturated environment at 298 K. Spectra were taken at the Co 2p and O 1s core-level regions as a function of the applied potential (Figure 309d). Notably, the formation of a CoOOH phase was confirmed. First, the upward shift of the binding energy for H_2O_{ads} in the O 1s core-level region demonstrated that the adsorption occurred on CoOOH with increasing potential. The Co 2p region indicated a $Co(OH)_2$ overlayer on the top of a Co_3O_4 phase, and the evolution of the Co $2p_{3/2}$ peak suggested that thin surface layers of Co_3O_4 were converted into CoOOH. The valence band revealed the transformation of the $Co(OH)_2$ overlayer into CoOOH as the intensity of the Co^{2+} 3d band increased. This oxidative conversion was seen at potentials below the OER onset, demonstrating that $Co(OH)_2$ promoted the highly active CoOOH phase. Finally, new spectral features at low binding energies were seen for both regions when CoOOH emerged, theorized to be highly active Co^{4+} sites. Similar results were observed by Xiao *et al.* by using quasi *operando* XPS, where oxygen vacancies facilitated the oxidation of Co_3O_4 into CoOOH.[1197] Furthermore, AP-XPS has been used to examine Ni-Fe oxyhydroxides and confirmed the presence of $Ni^{2+/3+}$ and Fe^{3+} species by monitoring the Ni and Fe 2p regions during the OER.[1232] These case studies show that AP-XPS enables direct examination of insightful spectral features of the electrocatalytic surfaces under operating conditions.

In a remarkable study on transition metal *X*-ides by Wu *et al.*, CoP NPs were examined by *quasi in situ* XPS.[470] A protective sample transfer procedure was employed to transfer the air-sensitive CoP NPs from the electrochemical cell to the XPS spectrometer (Figure 309e). This method revealed that the CoP NPs were oxidized upon immersion in the KOH electrolyte and that hydroxide ions replaced polyphosphate anions. Moreover, it was found that under HER potentials, the oxidized species were electrochemically reduced and that phosphate ions were dissolved into the electrolyte. Regarding the OER (Figure 309f), the Co−P peak was replaced by Co−O in the Co 2p region. Furthermore, in the P 2p region, the Co−P peak rapidly disappeared, whereas the P−O peak only decreased somewhat, suggesting that some phosphide-derived oxide remained after the dissolution process. Finally, the O 1s region revealed hydroxide and Co−O features, which confirmed the strong oxidation of the CoP electrocatalyst.

XPS is a formidable tool for examining the oxidation states and chemical environments of electrocatalytic materials. Certainly, XPS post-analysis has been extremely useful for confirming the electrocatalytic materials' surface oxidation during the OER.[61,448] We encourage using *ex-situ* XPS characterization before and after the OER as a modest way to verify the oxidation degree. Additionally, XPS can be used to estimate and monitor metal contents in electrocatalytic films effectively.[200] Additionally, XPS is a powerful technique to characterize carbon-based materials.[1234] Regarding new approaches, it should be mentioned that other techniques or modes such as ion-beam profiling can be employed. Lastly, AP-XPS is encouraged to reveal the chemical environments of transition metal *X*-ides during the OER. Interestingly, this approach could be applied to verify if the reconstruction of *X*-ides occurs similarly to metal oxides. Furthermore, after the reconstruction, this technique could unveil the outcome of oxidation products (e.g., phosphates, sulfates, etc.). Although XPS is a robust technique, certain limitations must be considered. Notably, a Mg X-ray source should be used when measuring low concentrations of Fe, as a conventional Al source interferes with the Fe 2p peaks.[200] Care should be taken when performing *ex situ* measurements, as air-sensitive compounds could be oxidized after the reaction.[470] Indeed, precious information related to the reaction environment may be lost in *ex situ* measurements, as XPS demands UHV conditions.[1205,1231,1233] However, AP-XPS could also involve technical challenges which should be carefully examined. Notably, AP-XPS is restricted to synchrotron radiation sources, which impedes its large-scale implementation.[1205] Pressure in AP-XPS is limited by the photoelectron collection efficiency and the vapor pressure of water.[1231,1232] Moreover, electrochemical measurements at current densities of interest (0.1−10 $mA{\cdot}cm^{-2}$) are constrained by the ohmic losses in the thin electrolyte film.[1232] Finally, *operando* AP-XPS probes 10 to 30 nm of the liquid phase and 2 to 10 nm of the solid phase on average.[1233] Still, AP-XPS can be used to confirm relevant transformations or new spectral features at low current densities, especially in fundamental studies. Strategies to allow higher current densities include the use of higher electrolyte concentrations or the use of interdigitated electrode

https://doi.org/10.1021/acs.chemrev.3c00005
Chem. Rev. 2023, 123, 12795−13208

arrays.[1232] We expect that novel approaches on XPS will enable the examination of new electrocatalytic features in the future.

7.5.2. Scanning Probe Microscopy. In scanning probe microscopy (SPM) techniques, surfaces are directly probed by micro-to-nano-level tips that react to specific responses, creating spatially resolved images when the tip scans a section of the sample.[1226,1235] Depending on the technique, morphological, topographical, compositional, and chemical information at the micro- or nanoscale level can be retrieved, which has proved extremely valuable in the characterization of electrocatalysts. Herein, we summarize insightful case studies in which SPM revealed critical information on electrocatalytic surfaces. The SPM techniques described in this Section are depicted in Figure 310.

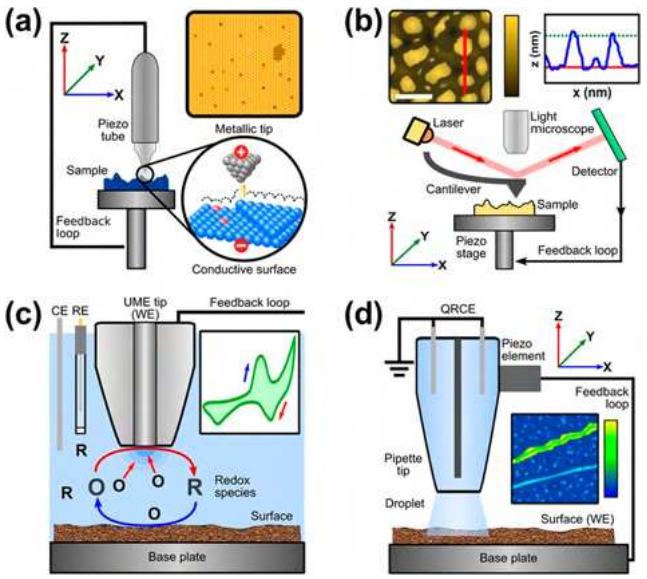


Figure 310. Schematic illustrations of representative SPM techniques: (a) scanning tunneling microscopy, (b) atomic force microscopy, (c) scanning electrochemical microscopy, and (d) scanning electrochemical cell microscopy.

In scanning tunneling microscopy (STM), an atomically sharp, conductive tip is brought very close to a conductive surface (Figure 310a). Due to a bias between the tip and surface, electron tunneling occurs depending on the surface−tip separation. The height of the tip is adjusted through a piezoelectric controller to keep a constant current. Hence, topographical images are produced as the tip scans the surface.[1235,1236] STM has demonstrated exciting capabilities for the study of electrocatalytic materials. Notably, Jaramillo *et al.* used STM coupled to electrochemical measurements to study the HER activity of edge sites on MoS_2 electrocatalysts.[1237] The fractions of edge sites were varied and characterized by STM, and then HER activity was measured. As the activity increased with the number of edge sites, it was concluded that these are the real active sites in MoS_2. Furthermore, Pfisterer *et al.* revealed that relative changes in the tunneling current noise can be used to accurately distinguish active sites under reaction conditions.[1236] Despite its decline in interest due to novel techniques like *in situ* TEM, these approaches demonstrate that STM offers interesting capabilities as a complementary surface-sensitive technique for the study of electrocatalytically active sites.

Another technique capable of providing topographical images is atomic force microscopy (AFM). In this technique, a sharp tip at the end of a cantilever is brought near the surface. As the tip interacts with the surface, the cantilever deflection produces a 3D topographical image (Figure 310b).[1226,1238] By coupling AFM with electrochemical measurements, several features of the electrocatalytic surfaces can be spatially resolved. AFM has been routinely utilized to characterize micro- and nanostructures, such as transition metal LDH nanosheets, nanoclusters, or platelets.[204,1202,1239] So far, AFM has been employed in more insightful studies that found interesting outcomes. The morphological evolution of $Ni(OH)_2$ nanosheets was studied by Deng *et al.*[1240] As displayed in Figure 311a, *in situ* electrochemical AFM (EC-AFM) revealed that $Ni(OH)_2$ nanosheets were transformed into disordered NPs during CV and CP measurements. Interestingly, by monitoring the mean height of the sample, it was found that morphology changes occurred during the $Ni(OH)_2$ oxidation and accelerated with the onset of OER current. Furthermore, the insertion of Fe cations from the electrolyte into the nanosheets as a function of the potential was examined by EC-AFM (Figure 311b). The results revealed that Fe incorporated into NiO_xH_y NPs expanded the volume proportionally to the concentration of Fe added to the electrolyte. Moreover, it was suggested that part of the Fe was deposited as a secondary FeOOH phase. This study demonstrated that dramatic morphology changes occur during the electrochemical activation of $Ni(OH)_2$, increasing the effective surface area and apparent volume.

Similarly, Dette *et al.* evaluated the structural transformation of $Ni_{1-\delta}Co_\delta O_xH_y$ nanosheets using *operando* AFM during CV cycling.[1241] As displayed in Figure 311c, nanosheets with a high Ni content exhibited a ripening process that transformed the 2D nanosheet into 3D NPs. However, the porosity, height, and roughness were increased at high Co contents without cracking the nanosheets. A more detailed view of the structural evolution during cycling is depicted in Figure 311d. It was suggested that Co provided stronger Co−O bonds and much more porous sheets, which effectively reduced the mechanical strain during cycling. Finally, samples with Fe cations were also studied (Figure 311e). Notably, the rough $Ni_{0.8}Fe_{0.2}O_xH_y$ nanosheet stayed intact during CV cycling, consistent with the porosity's proposed role in the ripening process. Furthermore, an interesting interaction between NiFe LDH electrocatalysts and the support was examined by Gu *et al.*[1219] *Ex situ* AFM was used to track the morphological transformation of NiFe LDH nanosheets at different potentials (Figure 311f). AFM images revealed that the nanosheets collapsed and transformed into disordered NPs with increasing potential. Moreover, the Co support was roughened, and an amorphous layer was formed on the NiFe LDH. As displayed in Figure 311g, it was found from AFM and other characterization techniques that Co from the support was incorporated into the porous $NiFeCoO_xH_y$ layer, which explained the improvement of the OER activity. Additionally, AFM has played a crucial role in the evaluation of nanoscale semiconductor/electrocatalyst interfaces,[1242] mass loading effects on the electrode coverage,[1239] surface electrochemical potentials in heterogeneous systems,[1238] and morphologies of edge and basal planes of layered structural crystals (e.g., MoS_2).[1207,1243]

Spatially resolved electrochemical activity (i.e., electrochemical imaging) can be measured by scanning electro-

https://doi.org/10.1021/acs.chemrev.3c00005
Chem. Rev. 2023, 123, 12795−13208

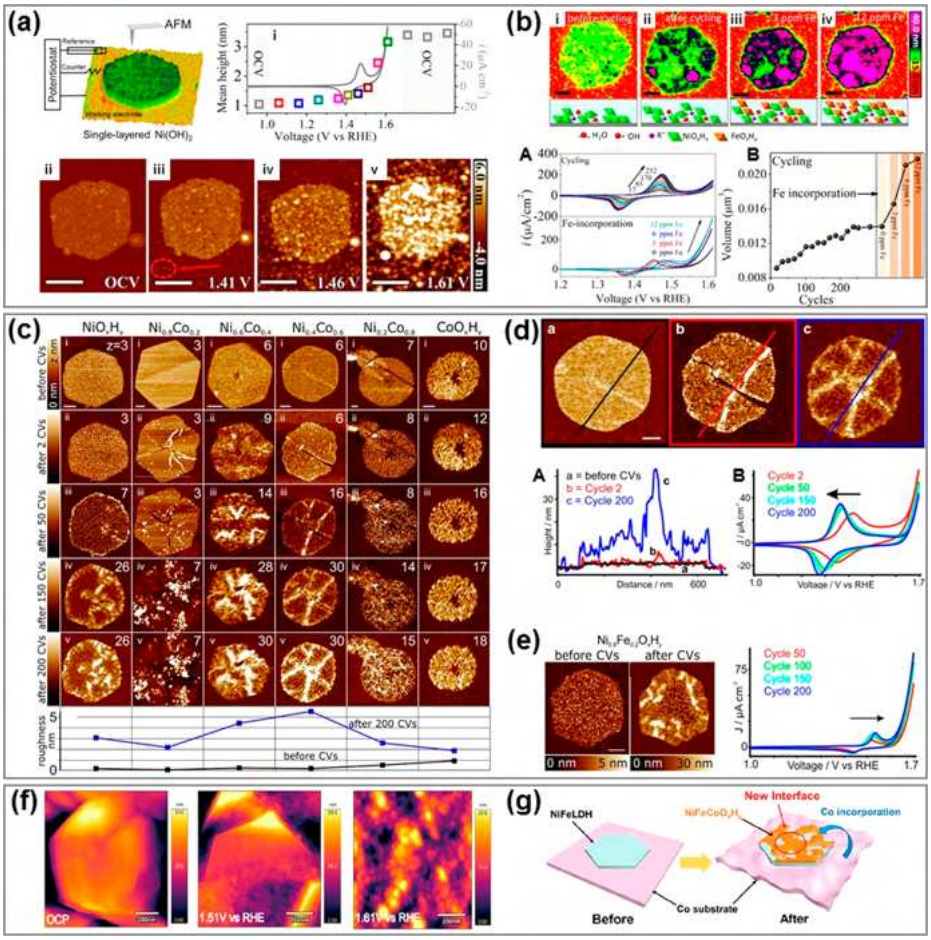


Figure 311. (a) *In situ* EC-AFM monitoring of $Ni(OH)_2$ nanosheets during the OER: nanosheet height at varying potentials (i), AFM images at the open-circuit voltage (OCV) and after chronopotentiometric runs for 500 s (ii–v); (b) EC-AFM monitoring of $Ni(OH)_2$ nanosheets in the presence of Fe in 0.1 M KOH: AFM images and structural schematic illustrations at different conditions (i–iv), CVs at different cycling stages and amounts of Fe (A), volume variation during cycling and subsequent addition of Fe (B). Reprinted with permission from ref 1240. Copyright 2017 American Chemical Society. (c) AFM images of the evolution of $Ni_{1-\delta}Co_\delta O_xH_y$ nanosheets at different compositions and cycling stages, with corresponding evolution of the mean roughness; (d) Ripening process of a $Ni_{0.4}Co_{0.6}O_xH_y$ nanosheet (a–c) with corresponding line scans (A) and CVs (B); (e) Topographical evolution of a $Ni_{0.8}Co_{0.2}O_xH_y$ nanosheet with associated CVs. Reprinted with permission from ref 1241. Copyright 2019 American Chemical Society. (f) AFM images of NiFe LDHs at different potential conditions; (g) Schematic illustration of the Co incorporation into NiFe LDHs. Reprinted with permission from ref 1219. Copyright 2020 American Chemical Society.

chemical probe microscopy (SEPM) techniques. These methods rely on small-scale electrodes that map the interfacial reactivity.[1226,1235,1244] Scanning electrochemical microscopy (SECM) is the most popular SEPM technique, which relies on the use of ultramicroelectrodes (UMEs) and, most recently, nanoelectrodes to measure the topography or electrochemical activity of surfaces immersed in an electrolyte (Figure 310c). Notably, the electrode can be employed to measure the local fluxes of chemical species and estimate heterogeneous reaction rates at the nanoscale by titrating redox species. These are usually produced via a substrate generation/tip collection (SG/TC) mode, where species are generated over the substrate surface and collected at the tip.[1245,1246] Several studies have demonstrated the ability of SECM to probe surface active sites and intermediates directly. For instance, Ahn and Bard utilized SECM to characterize a CoP_i electrocatalyst during the OER.[1247] Through amperometric surface titrations of Co^{3+} and Co^{4+} oxidation states, the density of water-accessible Co sites and pseudo-first-order reaction rate constants were accurately estimated. Similarly, SECM was used to evaluate the surface OER kinetics of Ni^{4+} and Fe^{4+} in $Ni_{1-x}Fe_xOOH$ electrocatalysts using redox titrations (Figure 312a).[1248] This approach detected which sites exhibited slow or fast kinetics and revealed that the number of electrocatalytically active "fast" sites was proportional to the Fe content. Moreover, an unusually high density of active sites was attributed to the contribution of atoms from layers underneath the interface layer. Active sites with different OER rates were also identified in MnO_x electrocatalysts through this approach.[1246] Finally, SECM was employed by Sun *et al.* to image the local OER activity of NiO nanosheets with a sub-20-nm lateral resolution.[1245] As displayed in Figure 312b, the SG/TC mode allowed for the imaging of defect sites by reducing the generated O_2 over the substrate. Interestingly, a 10–20% current increase over the nanosheet edge suggested that the NiO edges exhibited significantly higher OER activity than the basal plane. By using complementary TEM and *ab initio* calculations, the authors demonstrated that the (100) nanofacets of NiO were responsible for the increased activity at the edge.

A notable example of nanoscale SEPM is scanning electrochemical cell microscopy (SECCM).[1226] Unlike

https://doi.org/10.1021/acs.chemrev.3c00005
Chem. Rev. 2023, 123, 12795–13208

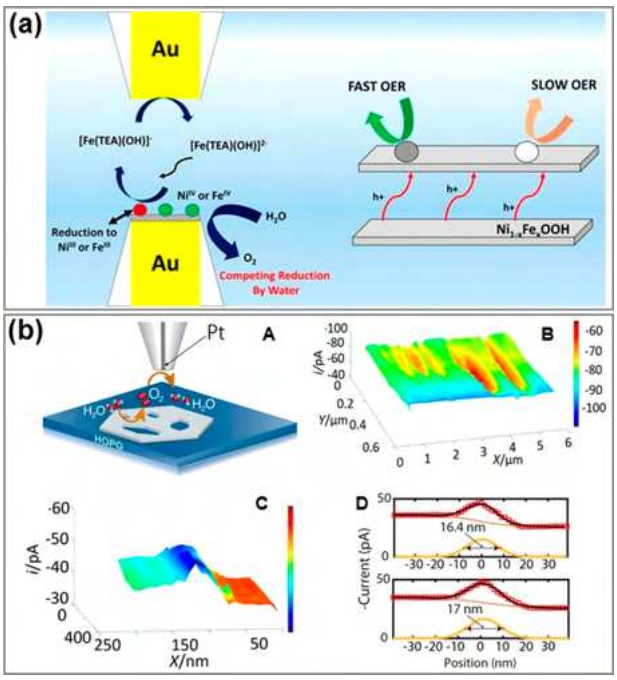


Figure 312. Case studies on SECM: (a) SECM study of $Ni_{1-x}Fe_xOOH$ electrocatalysts with "slow" and "fast" OER active sites using redox titrations. Reprinted with permission from ref 1248. Copyright 2016 American Chemical Society. (b) Topography and local OER activity mapping of NiO nanosheets using SECM: schematic illustration of the SG/TC measurement (A), SG/TC images exposing defect holes (B), and NiO edge (C) and line scans across edges (D). Reprinted with permission from ref 1245. Copyright 2019 National Academy of Sciences.

SECM, SECCM employs a nanopipette filled with electrolyte, which generates a droplet at the tip covering the surface (Figure 310d). Electrochemical measurements are carried out by applying a bias between the tip of a *quasi* reference counter electrode (QRCE) and the substrate (i.e., working electrode). This means that electrochemical processes are confined to a precise spot on the working electrode surface, which enables the examination of characteristic surface features.[1235,1249−1251] SECCM has been used to unveil the structural and compositional effects of different electrocatalysts. Bentley *et al.* studied local activity differences on bulk iron-nickel sulfide HER electrocatalysts.[1252] SECCM measurements were performed in a typical hopping mode (Figure 313a). As shown in Figure 313b, LSV scans were recorded at predefined macroscopic features of $Fe_{4.5}Ni_{4.5}S_8$ (111) crystals (basal and defect) and two areas of platelet-shaped crystals. Interestingly, the defect sites exhibited increased HER activities compared to basal sites. The measurements followed a normal distribution, which demonstrated the reproducibility of the technique. The platelet-shaped crystals exhibited enhanced HER activity as well. However, CVs and EDX measurements confirmed that this enhancement was caused by Fe-rich sites prone to corrosion, demonstrating that electrocatalytic activity strongly depends on structural and compositional features. Similarly, Yule *et al.* employed SECCM combined with SEM/EDX to examine the effect of structure and composition on the HER using low-carbon steel (Figure 312c).[1253] Notably, the HER activity was enhanced at grain boundaries and MnS inclusions (HER "hot spots"), and even low index grains exhibited different activities (Figure 312d).

Transition metal dichalcogenides such as MoS_2 have been studied by SECCM to unveil the structure−activity relationship during the HER. Tao *et al.* performed nm-resolved SECCM experiments to characterize the edge and basal planes of exfoliated MoS_2 crystals.[1254] As depicted in Figure 314a, a line of high activity corresponding to an edge plane was seen, and the basal surface consisted of two regions with different activity without any enhancement at the border. Moreover, the edge activity deteriorated more than the basal plane activity during aging experiments. Similarly, the local voltammetric response of the basal and edge planes of bulk MoS_2 was examined by SECCM and AFM.[1243] As shown in Figure 314b, all of the six surface defects exhibited increased current densities, and the relative enhancement was proportional to the height of the steps, as confirmed by AFM. Indeed, these

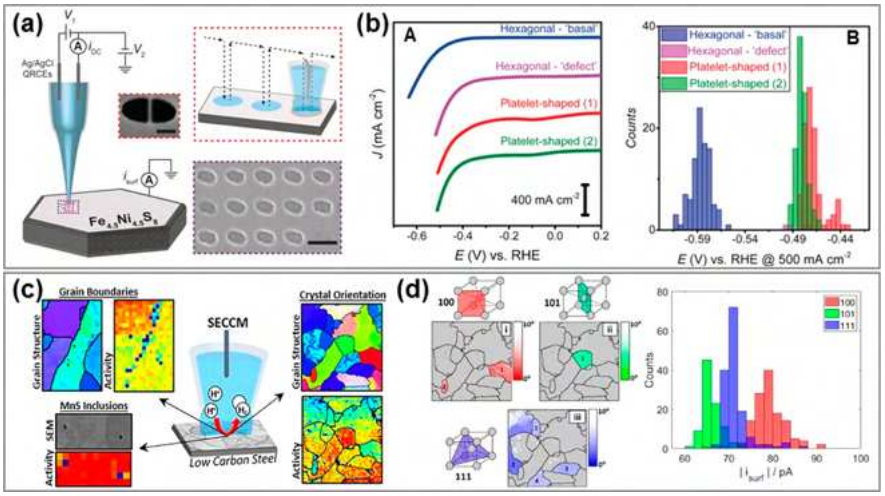


Figure 313. Representative case studies on SECCM: (a) Schematic illustration of the voltammetric hopping mode in SECCM; (b) SECCM study of the $Fe_{4.5}Ni_{4.5}S_8$ electrocatalyst during the HER: averaged LSVs from different regions (A), distribution of the potential at 500 mA·cm^{-2} (B). Reprinted with permission from ref 1252. Copyright 2018 Wiley. (c) SECCM study of nanoscale HER active sites on low-carbon steel at different index orientations; (d) Low-index orientations at different grains with the corresponding histogram of the average surface currents. Reprinted with permission from ref 1253. Copyright 2019 American Chemical Society.

https://doi.org/10.1021/acs.chemrev.3c00005
Chem. Rev. 2023, 123, 12795−13208

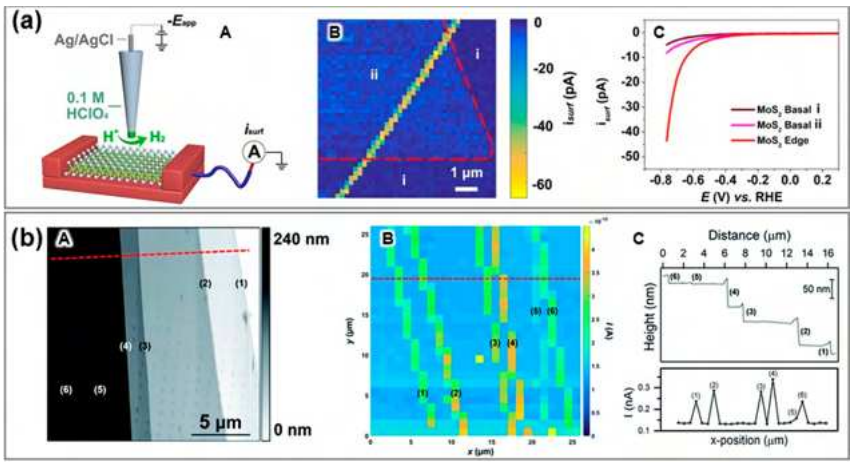


Figure 314. HER activity of basal and edge sites on MoS_2 electrocatalysts using SECCM: (a) schematic illustration of the setup used for nanoscale measurements (A), spatially resolved HER activity at −0.766 V_{RHE} (B), and average LSVs from two distinct areas of basal and edge planes (C). Reprinted with permission from ref 1254. Copyright 2020 American Chemical Society. (b) HER activity on natural crystals of MoS_2: AFM topographical map (A), spatially resolved SECCM current map at −0.85 V_{RHE} (B), AFM and surface current profiles from the dashed red line (C). Reprinted with permission from ref 1243. Copyright 2017 Royal Society of Chemistry.

results demonstrate that surface activity cannot be considered uniform, even for well-defined crystals, and that surface defects serve as important active sites.

Because of the wide variety of techniques, SPM techniques offer encouraging capabilities to examine the surface heterogeneity of transition metal *X*-ides and its effect on electrocatalytic processes.[1242] Notably, AFM is a formidable technique that can be used to track morphological changes of electrocatalytic materials during/after the OER, as previously demonstrated by the Boettcher group.[1240,1241] Depth histograms, height profiles, mean roughness, coverages, surface areas, and volumes can be utilized to assess nanostructure transformation and surface defects quantitatively (refs 1202, 1239−1241, and 1243). Moreover, AFM is a relatively simple technique that can be conducted in ambient air or liquid environments,[1226] and more advanced applications such as potential-sensing EC-AFM can readily capture the local electrochemical potential of electrocatalytic surfaces in *operando*.[1238] SECM is a relatively simple technique with tremendous potential for the elucidation of active sites. SECM can measure reaction rates because it is an in-solvent technique, meaning it operates under realistic conditions.[1247] Importantly, as the accessible electrocatalytic sites can be directly measured in SECM, this technique can be used to estimate electrocatalytic parameters (e.g., TOF) accurately.[1247,1248] Furthermore, SECM can be used to detect elusive oxidation states, complementing other spectroscopic techniques.[1246] Compared to other SPM techniques, SECCM can perform thousands of spatially resolved measurements in particular electrode regions (i.e., spot wetted by the droplet).[1235,1252] In this regard, one key advantage of SECCM over SECM is that the surface may change during the scanning procedure since the sample must be fully immersed in the electrolyte, whereas SECCM only probes targeted locations.[1243] It should be noted that SEPM techniques can be complemented by following a correlative multi-microscopy approach, where other spectroscopic/microscopic techniques can examine the probe position before or after the measurements.[1235,1249,1253] Additionally, this approach has been demonstrated to be an excellent way to evaluate the mobility and poisoning of NPs[1255] and localized corrosion processes.[1256] Moreover, SPM techniques can be combined to provide more robust approaches. For instance, AFM-SECM and STM-SECM can be used to enhance electrochemical and topographical imaging.[1235] Finally, since SPM techniques are usually automated, regions of interest can be mapped more accurately and reproducibly.[1235] However, SPM methods involve certain limitations depending on the technique. Compared to the other techniques, STM is restricted by different operational and instrumental considerations, and more improvements are necessary to enable its application in the study of active sites. The selection of a technique will depend on important considerations, such as the conductivity of the electrocatalytic species, the spatial resolution, measurement times, and sample and probe preparation.[1242,1245] Since SPM techniques utilize physical probes, it might be challenging to examine rough surfaces with steep trenches and walls effectively.[1226,1238] Furthermore, open-cell configurations must be used, which restricts some experimental conditions.[1226] Depending on the mode, AFM has a higher risk of damaging the sample, as the tip may scrap the surface if the measurement is not performed correctly.[1226] Complex imaging studies, such as spatiotemporally resolved measurements, generate large volumes of data that can be limited by storage capabilities. Finally, analyzing and interpreting massive amounts of spatially resolved images may require statistical methods and big data mining protocols.[1249]

7.6. Multi-elemental Analysis

The identification and quantification of chemical elements has significant implications in the study of electrocatalytic materials. Essential metrics such as mass activities or TOFs usually rely on metal loadings and elemental compositions, routinely estimated during the pre-analysis stages by multi-elemental analysis techniques (refs 212, 610, 611, 705, 1198, 1206, 1219, and 1257). Furthermore, recent studies have demonstrated the importance of measuring elemental contents during or after electrocatalytic reactions. Notably, the dissolution, redeposition, and localized corrosion of several species from electrocatalysts under operating conditions has been reported, including noble metals (refs 293, 294, 1227,

https://doi.org/10.1021/acs.chemrev.3c00005
Chem. Rev. 2023, 123, 12795−13208

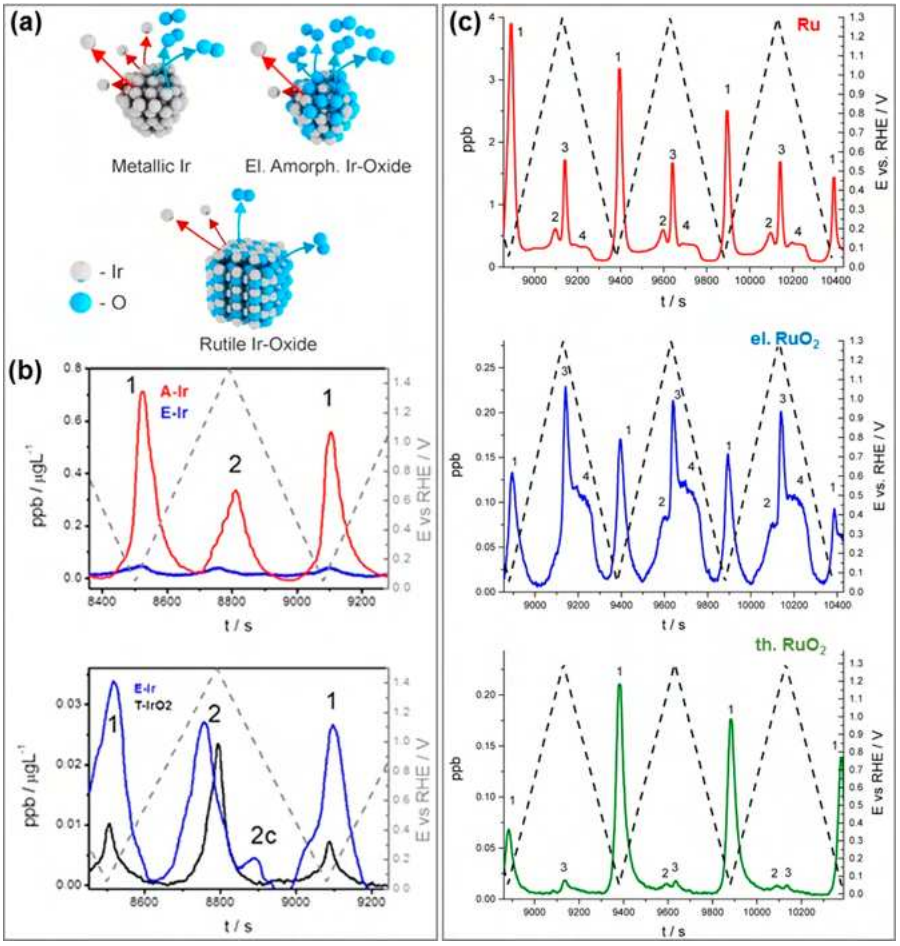


Figure 315. (a) Schematic illustration of the electrochemical dissolution of pure iridium (A-Ir), electrochemically pretreated IrO_2 (E-Ir), and thermally prepared IrO_2 (T-IrO2); (b) Potential-resolved dissolution profiles of Ir-based particles during CV to an upper potential limit of 1.5 V_{RHE}. Reprinted with permission from ref 293. Copyright 2017 American Chemical Society. (c) Potential-resolved dissolution profiles of as-synthesized Ru, electrochemically prepared RuO_2 (el. RuO_2), and thermally prepared RuO_2 (th. RuO_2) during CV to an upper potential limit of 1.3 V_{RHE}. Reprinted with permission from ref 1228. Copyright 2015 American Chemical Society.

1228, and 1258−1261), transition metals (refs 221, 294, 614, and 1252), and non-metals such as Se and P.[48,100,470,1194] Another concern is the incorporation of metals from the electrolyte or the substrate into the electrocatalyst, which has proved to be critical for understanding the activity enhancement of metal oxide-based OER electrocatalysts.[200,212,1219,1262] Therefore, it is evident that these processes have tremendous implications on the activity and stability of electrocatalytic materials, and powerful multi-elemental analysis techniques are necessary to detect and monitor the species involved in such processes. This Section highlights two types of multi-elemental analysis techniques with the potential for studying electrocatalytic materials: inductively coupled plasma (ICP) and X-ray fluorescence (XRF). Other popular techniques with elemental analysis capabilities are omitted, such as XPS (see Section 7.5.1) and EDX (see Section 7.4).

In ICP-based techniques, the plasma produced from a frequency generator and an appropriate gas (e.g., Ar) is used as the atomization/ionization source. Then, the identity of the produced ions is elucidated by two main approaches: atomic emission spectroscopy (AES) or mass spectrometry (MS). AES relies on the characteristic emission wavelengths of the elements, while MS separates and detects the ions (details in Section 7.7). Both methods have interesting capabilities and have been used in the past to study electrocatalytic materials. Due to its simplicity, ICP-AES is usually employed to analyze elemental compositions and metal contents.[610,611,705,1198] On the other hand, ICP-MS has been extensively used to measure dissolution and corrosion processes accurately. Jovanovič *et al.* studied the dissolution of Ir and IrO_2 particles using ICP-MS under OER conditions (Figure 315a).[293] Time- and potential-resolved dissolution profiles were accurately measured during CVs, as displayed in Figure 315b. Remarkably, it was found that surface redox transitions triggered the electrochemical dissolution of Ir particles and the severity depending on the potential limits. By complementing the study with IL-SEM and IL-TEM measurements, it was found that electrochemically pretreated IrO_2 particles were relatively stable and active during the OER. This was attributed to the nature of the initial oxide, as the amount of Ir(III) induced a different dissolution route. Following the same approach, Hodnik *et al.* studied the dissolution trends of Ru and RuO_2 NPs.[1228] Interestingly, Ru dissolution occurred at potentials below the OER onset, and dissolution profiles comparing as-prepared Ru with electrochemically and thermally prepared Ru (Figure 315c) revealed that the latter was more stable. It was suggested that the increased stability could be caused by the reduced amount of defects, meaning that stability and activity followed an inverse

https://doi.org/10.1021/acs.chemrev.3c00005
Chem. Rev. 2023, 123, 12795−13208

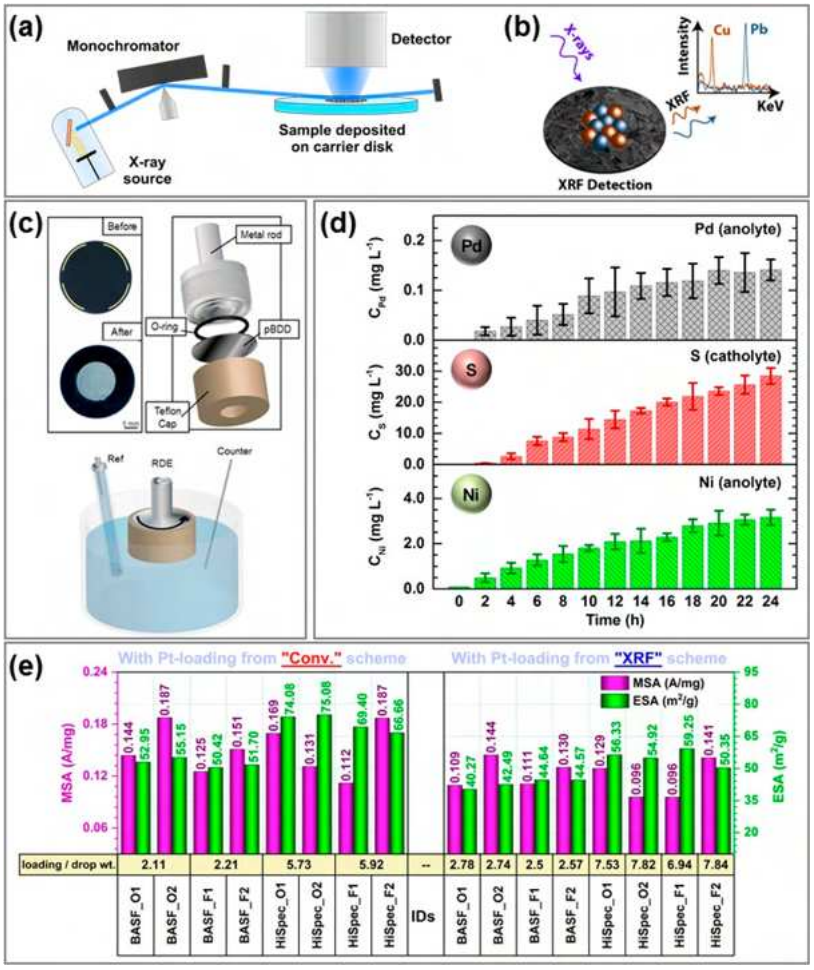


Figure 316. (a) Schematic illustration of the working principle and principal components of TXRF. (b) Detection of preconcentrated metals using EC-XRF; (c) Schematic views of the pBDD electrode used for electrodeposition of heavy metals in solution. Reprinted with permission from ref 1265. Copyright 2014 American Chemical Society. (d) Concentration profiles of dissolved Pd, S, and Ni from Ni foam-based electrodes during the HER (cathode) and sulfite electrolysis (anode). Reprinted with permission from ref 294. Copyright 2020 American Chemical Society. (e) Calculated electrochemical surface area (ESA) and mass-specific activity (MSA) of different inks, based on Pt loadings estimated using conventional and XRF-based schemes. Reprinted with permission from ref 1266. Copyright 2018 American Chemical Society.

relationship. These trends invite further exploration of transition metal OER electrocatalysts, as highly active materials with large surface areas and numerous defect sites are usually targeted, although sometimes without accurate stability examination.

Another multi-elemental analysis method, which has received attention, is XRF. This technique relies on the characteristic radiation emitted by the target material when high-energy X-rays excite it. Among different available modes of operation, total-reflection X-ray fluorescence (TXRF) uses the total reflection of incident beams at glancing angles, which effectively reduces the absorption and scattering of the radiation on the sample surface.[1263,1264] Figure 316a shows the working principle and main components of this technique. TXRF is similar to EDX because an energy-dispersive detector collects the characteristic fluorescence, but the special geometry improves the sensitivity and reduces the matrix effect. This means that bulk elemental composition can be determined accurately, which has been exploited by recent studies to estimate the metal loadings and even to address losses after experiments.[610,611,1214]

Recent studies have highlighted the applicability of XRF to the study of trace species and dissolution processes. Hutton *et al.* demonstrated the robustness of a novel electrochemical XRF (EC-XRF) approach in which dissolved species can be electrochemically pre-concentrated on a target polycrystalline boron-doped diamond (pBDD) electrode and subsequently detected by XRF (Figure 316b).[1265] The reusable electrode is compatible with a rotating disk electrode (RDE) configuration, which improves the pre-concentration process (Figure 316c). As target species, Pb^{2+} and Cu^{2+} exhibited low limits of detection (~0.05 ppb). This provides interesting capabilities for the study of dissolved metals in electrochemical experiments. In a more specific application, our group employed an electrochemical flow cell coupled with TXRF analysis to precisely monitor the dissolution of metals from the anode (Pd/NF) and cathode (Ni/NiO/NF) during sulfite oxidation and hydrogen evolution reactions, respectively.[294] As displayed in Figure 316d, time-resolved dissolution profiles during stability tests confirmed the presence of Ni and Pd in the electrolyte as the reaction progressed. Concentrations stabilized after ca. 18 h, implying that a reconstruction process regulated the dissolution rates. Complementary SEM/EDX and XPS characterizations indicated that the electrodes experienced a surface transformation where unstable oxides were dissolved until electrocatalytic sites were exposed. TXRF

https://doi.org/10.1021/acs.chemrev.3c00005
Chem. Rev. 2023, 123, 12795−13208

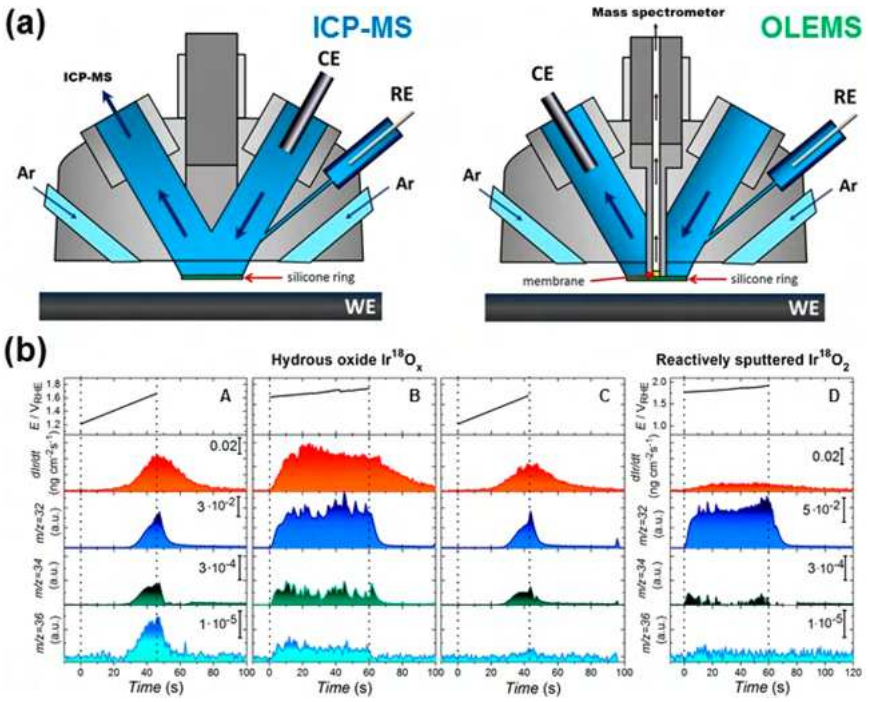


Figure 317. (a) Schematic illustrations of SFC-MS techniques; (b) On-line monitoring of lattice oxygen production and dissolution of hydrous $Ir^{18}O_x$ (A–C) and reactively sputtered $Ir^{18}O_2$ (D) during the OER. Electrochemical protocol: anodic scan from 1.2 V_{RHE} until a current of 20 mA·cm^{-2} was reached (A), galvanostatic polarization at 15 mA·cm^{-2} for 60 s (B), anodic scan of A repeated after B (C), galvanostatic polarization at 25 mA·cm^{-2} for 60 s (D). Reprinted with permission from ref 1260. Copyright 2019 Royal Society of Chemistry.

was also capable of monitoring the crossover of sulfite/sulfate species across the membrane. Finally, Chourashiya *et al.* devised a novel and reproducible XRF approach to estimate the Pt loadings on GCEs for RDE experiments.[1266] As depicted in Figure 316e, two estimation schemes using different inks were compared: the conventional method relying on the electrocatalyst weight and the XRF-based approach where the GCE was directly exposed to quantitative XRF. The electrochemical surface area (ESA) and mass-specific activity (MSA) were estimated from CV and LSV scans. Interestingly, although the conventional scheme suggested that the electrocatalyst density of the ink was constant, the XRF approach demonstrated that the electrocatalyst density varied even for the same inks, proving that the associated MSA and ESA values depend not only on the quality of the coating but also on the real Pt loading. This XRF scheme was also used to determine the relative loss of Pt from the GCE after ORR tests.

Multi-elemental analysis techniques are formidable methods for detecting and quantifying chemical elements in deposited materials and dissolved species. Typical metal content estimations should be performed before measurements and after stability tests to detect possible dissolution processes under operating conditions. Moreover, while noble metals have been extensively investigated, more studies are necessary to examine the evident dissolution and redeposition processes on OER electrocatalysts.[48,221,470,1194,1195] To satisfy these needs, both ICP- and XRF-based techniques offer encouraging strengths. ICP enables the uninterrupted sampling of the analyte, an approach known as online flow electrochemistry.[293,1228,1259] This can be used to obtain dissolution profiles during operating conditions. On the other hand, XRF techniques can be used to estimate metal leaching, either directly on as-deposited electrocatalysts over the GCE[1266] or by dissolving the electrocatalysts in acid.[610,611] Instrumental and operability features should be considered as well. ICP techniques are highly sensitive, with low limits of detection and large dynamic ranges. ICP-MS is more precise and sensitive than ICP-AES, but the latter is usually more affordable. TXRF is also an affordable and accessible technique, and one single instrument is capable of detecting a wide variety of elements, ranging from boron to uranium.[1264] Because of the total reflection condition, background noise is significantly reduced, which means that TXRF is particularly useful for analyzing samples with intricate matrices and requires small amounts of the sample.[1264] Quantitative TXRF can be performed rapidly by adding an internal standard with a known concentration. Limits of detection at the ppb level can be easily achieved, and some portable instruments are commercially available.[1263] Finally, more advanced applications like synchrotron radiation-induced TXRF are extremely powerful and can be used to reach lower detection limits.[1264] Multi-elemental analysis techniques also exhibit certain limitations. Notably, sample preparation is essential, mainly when trace analysis is performed.[1263,1264] Studies should validate the reproducibility of their protocols, as results strongly depend on the operator and the experimental procedure. Multi-elemental analysis techniques may exhibit typical spectroscopic concerns such as poor spectral resolution or overlapping peaks, depending on the experimental conditions and studied materials. This is important, as low concentrations can be over- or under-estimated.[1263] Limits of detection for ICP-AES are relatively high, and background emission is considerable. As ICP-MS is highly sensitive, its cost is significantly increased, and carryover effects are prone to occur. Regarding XRF, it can be difficult to measure some elements. While Mo cannot be detected due to its use as an X-ray source, As, Pb, Cd, and Sb suffer from interferences or low-intensity lines.[1263] Strong K-lines from K and Ca in the electrolyte could be problematic for the study of

https://doi.org/10.1021/acs.chemrev.3c00005
Chem. Rev. 2023, 123, 12795–13208

electrocatalysts in alkaline or neutral electrolytes. Finally, these techniques are not able to distinguish between different oxidation states, which means that complementary techniques such as XPS may be required to verify the chemical state of dissolved species.[909]

7.7. Mass Spectrometry

Mass spectrometry (MS) is a high-throughput analytical technique that enables the separation of ions based on their mass-to-charge (m/z) ratios. The resultant plot of intensity against m/z (i.e., mass spectrum) represents the distribution of the ions by their masses and provides valuable information on the elemental or isotopic fingerprint of the sampled species. Remarkably, mechanistic studies are enabled in MS by using isotope labeling methods.[1267] Different MS techniques have been employed in electrocatalysis to provide time-resolved analysis of reaction products, intermediates, and adsorbates during operating conditions.[1268−1271] Without considering ICP-MS, two main MS approaches have been used for this purpose: online electrochemical mass spectrometry (OLEMS) and differential electrochemical mass spectrometry (DEMS). Both techniques have been used to detect and monitor volatile products formed under electrochemical experiments by coupling the cell to a mass spectrometer through a gas-permeable interface.[1268,1272] Interestingly, this strategy can be used to characterize electrocatalytically active sites and gain insights into electrocatalytic reactions. In OLEMS, the inlet of the mass spectrometer is brought into proximity to the working electrode, and a permeable membrane prevents the electrolyte from getting into the vacuum line.[1270,1273] Kasian *et al.* evaluated the extent of lattice oxygen participation on reactively sputtered IrO_2 and hydrous iridium oxide electrocatalysts during the OER using OLEMS and ICP-MS.[1260] As depicted in Figure 317a, a scanning flow cell (SFC) approach was used to couple ICP-MS and OLEMS with electrochemical tests. By using ^{18}O-labelled IrO_2 samples and $H_2{}^{16}O$ in the electrolyte, three types of lattice O_2 production mechanisms were expected: without lattice exchange ($^{16}O^{16}O$, m/z = 32), with O atoms from water and oxide lattice ($^{16}O^{18}O$, m/z = 34), and with two lattice O atoms ($^{18}O^{18}O$, m/z = 36). As displayed in Figure 317b, the evolution of different O_2 signals with time was captured by OLEMS, while time-resolved dissolution profiles were measured by ICP-MS. Notably, the dissolution of Ir decreased at the second anodic scan, which suggested that lattice defects were dissolved during the first scan and stabilized during the galvanostatic run. Although O_2 was produced by lattice oxygen (m/z = 34 and 36) from hydrous $Ir^{18}O_2$ in the first scan, these signals decreased after the galvanostatic run. In the case of reactively sputtered $Ir^{18}O_2$, both the dissolution and participation of Ir and lattice oxygen were insignificant, respectively. This behavior was attributed to -Ir^{III}OOH species, which served as OER active sites in hydrous $Ir^{18}O_2$. Lattice oxygen sites were not involved in the reactively sputtered oxide due to its OH-free structure. Furthermore, the increased dissolution of Ir from the hydrous oxide was attributed to the structural differences caused by the -Ir^{III}OOH species. These results reveal the importance of structural features to the activity and stability of OER electrocatalysts.

Unlike OLEMS, DEMS utilizes a flow cell and a Teflon membrane permeable to volatile analytes. Notably, the flow of the electrolyte improves the mass transfer, which closely resembles RDE experiments.[1268,1270] In this technique, the ion current produced by the detected species is simultaneously recorded with the electrode current, resulting in plots known as MS cyclic voltammograms (MSCVs).[1269,1271] DEMS has been used to evaluate faradaic efficiency (FE) during O_2 production using NiFe oxyhydroxide electrocatalysts.[611] FE was estimated from DEMS-derived faradaic current (i.e., O_2 detected by MS), the integral charge of which was then divided by the total faradaic charge obtained from CV. Notably, as the FEs are directly related to the redox activity, it was possible to uncover the apparent redox charge associated with processes other than the OER. As shown in Figure 318a, the FEs varied at different KOH electrolyte concentrations and between supported and unsupported Ni-Fe electrocatalysts. When the pH (i.e., the KOH concentration) was increased and the electrocatalyst was supported on carbon, more charge was used

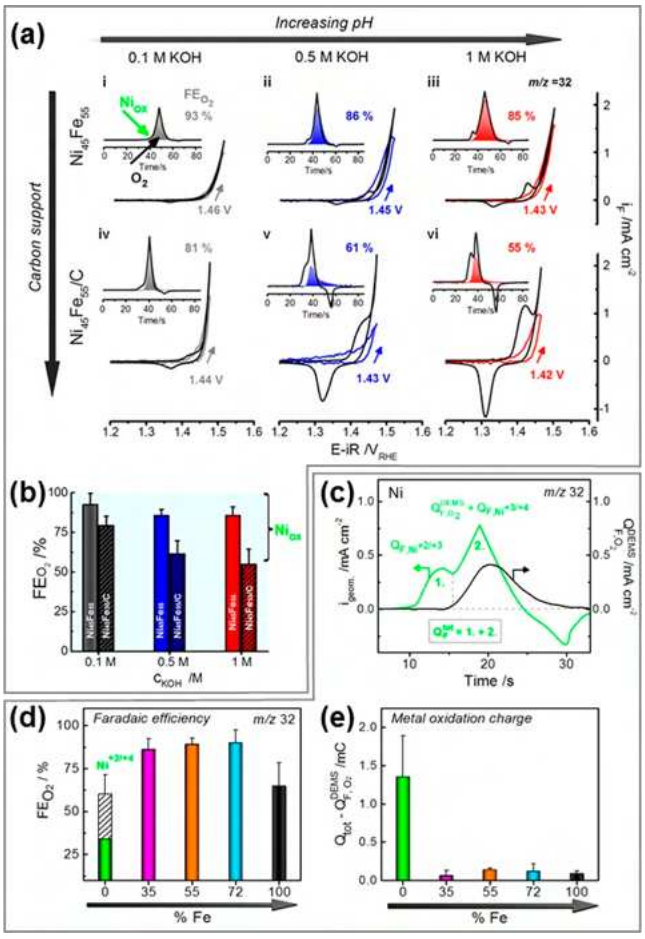


Figure 318. (a, b) *Operando* DEMS study of the effects of conductive supports and the electrolyte pH on Ni-Fe electrocatalysts during the OER: (a) DEMS results using different KOH concentrations using unsupported $Ni_{45}Fe_{55}$ (i−iii) and $Ni_{45}Fe_{55}$/C (iv−vi) electrocatalysts. CVs are shown as black curves, mass spectrometric faradaic ion currents of O_2 (m/z = 32) are shown as colored lines/areas, and the insets show the CVs in the time domain; (b) FEs estimated from entire redox peak (Ni_{OX}) areas. Reprinted with permission from ref 611. Copyright 2017 American Chemical Society. (c−e) *Operando* DEMS results during the OER: (c) CV scan (green) and corresponding faradaic ion current of O_2 (black curve) of Ni electrocatalyst; (d) FEs of different NiFeOOH electrocatalysts as a function of atomic%Fe; (e) absolute faradaic charge injected into the electrocatalyst layer for changing metal oxidation states. Reprinted with permission from ref 610. Copyright 2016 American Chemical Society.

https://doi.org/10.1021/acs.chemrev.3c00005
Chem. Rev. 2023, 123, 12795−13208

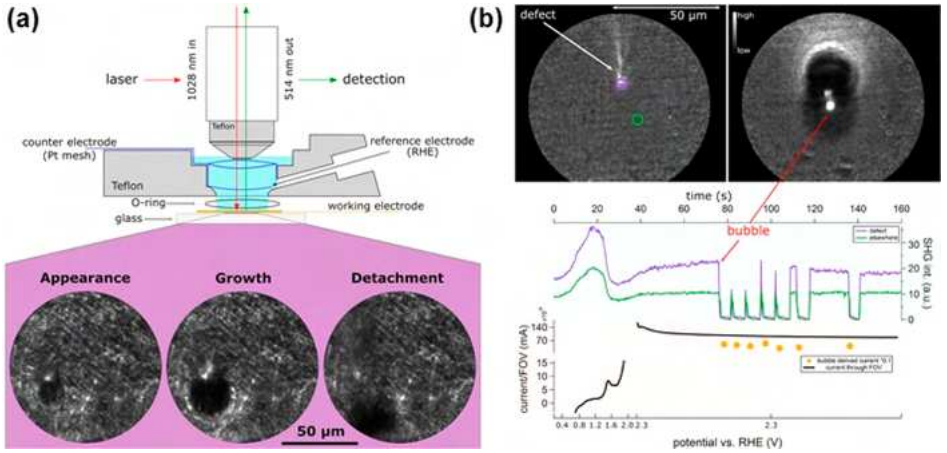


Figure 319. (a) Schematic illustration of the SHM experiment; (b) evolution of O_2 bubbles: circular FOVs of the Au electrode at 2.3 V_{RHE} with corresponding SHG intensity and current versus potential curves. Reprinted with permission from ref 1275. Copyright 2020 American Chemical Society.

for the electrocatalytic redox processes and less charge was used for O_2 evolution (Figure 318b). The electrocatalytic redox activity influences the OER activity, as more active sites are generated. Therefore, these results demonstrate that higher pH and electrocatalyst dispersion enhance electrocatalytic redox activity by improving charge transport and increasing the number of OER active sites. The same strategy was implemented to examine the charge efficiency at different Fe contents.[610] As depicted in Figure 318c for the Ni electrocatalyst, the area under the voltammetric curve equals the total faradaic charge, while the DEMS-derived charge represents the O_2 detected by MS. Figure 318d shows the variation of the FEs with the Fe content, while Figure 318e displays the faradaic charge injected to the electrocatalyst to change the metal oxidation states. Interestingly, the FE increased with increasing Fe content (but drastically dropped for pure Fe), suggesting that the faradaic contribution to the electrocatalytic redox activity (i.e., the injected charge to change the oxidation states) decreased relative to the O_2 evolution charge. This showed that Fe reduced the detectable amount of high-valent Ni, which remained at a lower oxidation state than pure Ni. By using complementary XAS measurements, it was confirmed that the Ni oxidation state was highly dependent on the Ni:Fe stoichiometry. These case studies demonstrate the crucial roles of the pH, electrocatalytic supports, and metal stoichiometry on the OER activity.

These case studies demonstrate that MS techniques can effectively assist with the characterization of electrocatalytically active sites. MS techniques are great methods to measure electrocatalytic O_2 gas production and accurately estimate FEs.[1269] In this regard, MS techniques are highly sensitive compared to other gas detection methods like gas chromatography.[1268] As the signals of volatile products are proportional to their production rates, kinetic studies can be performed.[1268] Other gases such as CO, CO_2, H_2, volatile organic compounds, and even some adsorbates can be measured as well.[1271] Moreover, isotope labeling allows for qualitative monitoring of intermediates and estimation of reaction yields, both of which have been particularly useful for studying electrochemical water oxidation.[1267] Among the described techniques, DEMS offers better collection efficiency than OLEMS.[1274] Furthermore, DEMS enables measurements through electrochemical quartz crystal microbalance (EQCM) and FTIR,[1268,1269,1272] and both MS methods can be coupled with techniques such as ICP-MS or EM to correlate corrosion measurements.[1269] Nevertheless, certain challenges should be considered. As previously mentioned, the high sensitivity of MS techniques involves increased capital costs. Moreover, when isotope labeling experiments are performed, care should be taken, as isotope exchange between the labeled species and the solvent or other surfaces may occur.[1267] Regarding instrumental limitations, DEMS and OLEMS systems are constrained by the design of customized cells, as commercial setups are not widely available.[1271,1274] The geometry of the DEMS cell may induce a large IR drop, and two counter electrodes are needed.[1268] Part of the volatile products may be lost due to the continuous electrolyte flow, especially if the electrochemical cell is not properly designed.[1268] The collection efficiency of OLEMS can be extremely low, and it is highly sensitive to the distance between the tip and the electrode.[1274] Finally, to enable FE measurements, electrocatalyst-specific calibration factors must be obtained from steady-state measurements.[610,611] Nevertheless, the tremendous development of novel approaches in MS is expected to improve the availability of these methods in the near future. More instrumental specifications and applications of MS techniques in electrochemistry can be found elsewhere.[611,1268,1270,1271]

7.8. Other Advanced Characterization Techniques

Interesting studies using novel techniques and unusual approaches to characterize electrocatalytically active species/sites have been reported in recent years. Zwaschka *et al.* coupled second harmonic microscopy (SHM) with electrochemical experiments to examine the role of spatial heterogeneity on the OER activity of Au surfaces.[1275] The surface specificity of SHM is based on symmetry selection rules, making it highly sensitive for detecting and monitoring the surface dielectric function. As depicted in Figure 319a, bubble generation at defect sites during the OER was captured on Au electrodes through SHM imaging in real-time. As displayed by the circular fields of view (FOVs) in Figure 319b, O_2 bubbles evolved at the defect site for 30 s after a constant potential at 2.3 V_{RHE} was established. The local second harmonic generation (SHG) signal fluctuated at this point due to the formation and diffusion of the bubble. Interestingly, bubble evolution was not steady, and the SHG signal decreased

https://doi.org/10.1021/acs.chemrev.3c00005
Chem. Rev. 2023, 123, 12795−13208

after the fifth bubble, which suggested that the partially oxidized active sites were consumed. Further measurements also revealed that metastable active sites produced O_2 gas at potentials below the OER onset, which suggested that dynamic, oxidized sites are a prerequisite for the OER. Overall, the OER activity was dominated by ∼1% of the surface area, demonstrating that the OER is highly localized and needs structural defects or oxidized sites to proceed. SHM enables precise time-resolved measurements, making it a formidable technique to directly capture active sites and bubble evolution in *operando*.

Another technique with interesting capabilities is Mössbauer spectroscopy. This technique provides insightful information on Fe sites, such as oxidation state, symmetry, electron-spin configuration, and magnetic properties.[1189,1205] Mössbauer spectroscopy has been used to determine the relative site residence of Fe atoms in tetrahedral and pyramidal sites in NiFe phosphides,[1276] as well as to characterize iron phosphides.[480] In the OER field, Chen *et al.* reported the direct evidence of Fe^{4+} sites in NiFe oxyhydroxides.[901] As depicted in Figure 320, *operando* Mössbauer spectroscopy

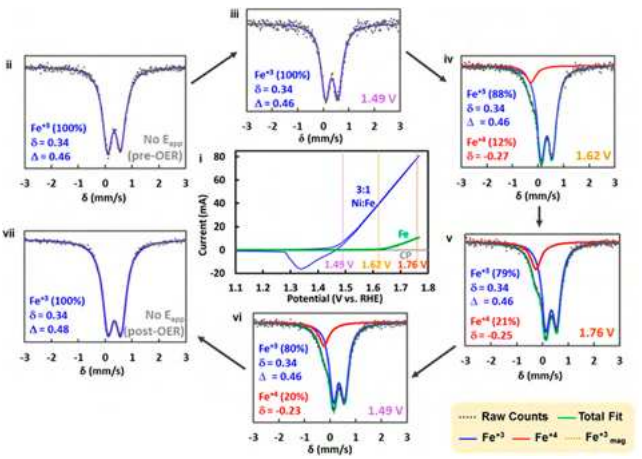


Figure 320. *Operando* Mössbauer results during the OER: (i) CVs of NiFeOOH (blue) and hydrous Fe oxide (green) electrocatalysts, (ii–vii) Mössbauer spectra collected at different stages. Reprinted with permission from ref 901. Copyright 2015 American Chemical Society.

measurements captured the evolution of Fe^{3+} species during CV. Notably, a shoulder emerged at high potentials, which denoted the oxidation of Fe^{3+} sites into Fe^{4+}. However, even after lowering the potential, the persistence of a substantial Fe^{4+} amount suggested that these were not directly related to the electrocatalytic activity. Furthermore, no Fe^{4+} was found in the hydrous Fe oxide, which confirms the stabilizing effect of Fe in the NiOOH lattice. Thus, although it was impossible to distinguish between Ni and Fe active sites, Mössbauer spectroscopy provided critical evidence of the role of Fe in NiFe oxyhydroxide electrocatalysts.

Electron paramagnetic resonance (EPR) spectroscopy is a powerful technique that has been used to examine the coordination environment and the electronic structure of paramagnetic centers in different electrocatalysts such as Co-based oxides and phosphates.[1197,1277,1278] Although it is generally not possible to study materials with a high density of magnetic centers (e.g., NiFe LDHs), Sayler *et al.* devised an interesting approach in which nonmagnetic [ZnAl] LDHs were doped with Ni and Fe to unveil their coordination environment.[1279] As depicted in Figure 321a, edge and interstitial Ni and Fe sites in [ZnAl] LDHs were studied as OER

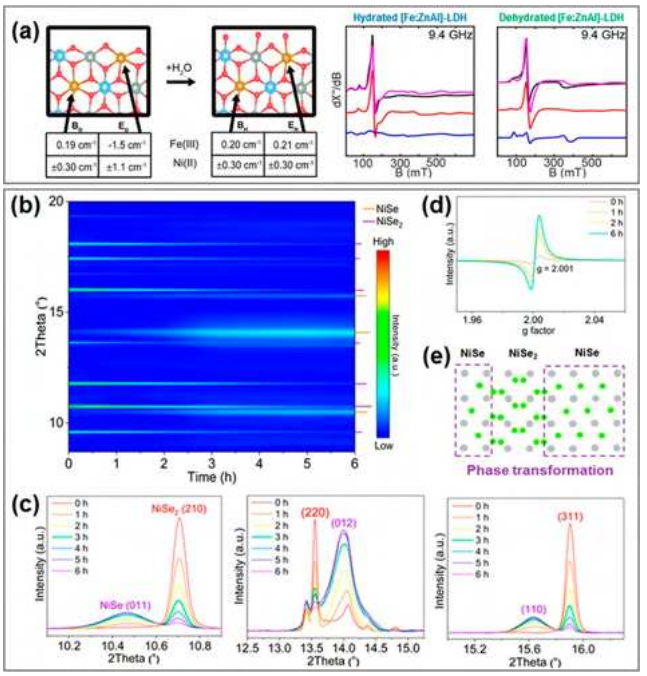


Figure 321. (a) EPR study of Ni,Fe-doped [ZnAl] LDHs: depiction of edge (E) and interstitial (B) sites under hydrated and dehydrated conditions with corresponding ZFS parameters and continuous-wave spectra. B_D (dehydrated) and B_H (hydrated) sites are shown in red, E_D (dehydrated) and E_H (hydrated) sites are shown in blue, and the sum of components is shown in magenta. Reprinted with permission from ref 1279. Copyright 2020 American Chemical Society. (b) Contour plot of the time-resolved SXRD pattern evolution of the $NiSe_2$ electrocatalyst during the HER; (c) Intensity changes of $NiSe_2$ and NiSe phases; (d) EPR spectral evolution with time; (e) Schematic illustration of the NiSe transformation. Reprinted with permission from ref 1194. Copyright 2020 American Chemical Society.

electrocatalysts under hydrated and dehydrated conditions. From continuous wave and pulsed spin spectra at the studied conditions, it was possible to estimate the Ni and Fe sites' zero-field splitting (ZFS) magnetic parameters. Overall, results suggested that both Ni and Fe edge sites are coordinated by water and hydroxide ligands in an octahedral ligand field, where high-valent metal-oxo centers are likely involved. This demonstrates how EPR can be used as a complementary technique in fundamental studies on electrocatalytically active sites.

X-ray diffraction (XRD) is an advantageous technique to characterize crystalline features of transition metal *X*-ides in the pre- and post-analysis stages. Although XRD has mostly been used in a typical *ex situ* approach, recent interesting *in situ* experiments have been reported. Notably, Zhai *et al.* employed *operando* synchrotron-based XRD (SXRD) to characterize the crystalline phase transformation of $NiSe_2$ electrocatalysts during the HER.[1194] As depicted in Figure 321b, *operando* SXRD enabled the time-resolved changes in the diffraction patterns during CA tests. The (210), (220), and (311) indices of $NiSe_2$ gradually decreased, whereas the (011), (012), and (110) indices of NiSe increased with time (Figure 321c). Complementary EPR measurements verified the increase of Se vacancies with time (Figure 321d). From additional character-

https://doi.org/10.1021/acs.chemrev.3c00005
Chem. Rev. 2023, 123, 12795−13208

izations and theoretical computations, the reconstruction of cubic $NiSe_2$ into hexagonal NiSe was confirmed (Figure 321e), and the latter was considered the real active site during the HER. Similarly, Tung *et al.* employed *in situ* grazing-angle XRD to monitor the structural transformation of single-crystal Co_3O_4 during the OER.[1223] Notably, the formation of CoOOH as the active phase under OER potentials was directly seen. These case studies demonstrate that *in situ* XRD can provide clear evidence of the reconstruction processes by directly capturing the crystal transformation.

Finally, we highlight the use of electrochemical microgravimetry through the electrochemical quartz crystal microbalance (EQCM) technique. This technique precisely measures the electrode mass changes through the oscillation frequency of a quartz crystal.[1272] Notably, Klaus *et al.* used EQCM to evaluate the $Ni(OH)_2$/NiOOH redox transformations in Fe-free and unpurified KOH electrolytes (Figure 322a).[212] As shown in Figure 322b, after aging Ni films for 6 days in 1 M KOH, the mass density decreased during the oxidation (Ni^{2+} to Ni^{3+}) in both unpurified and purified KOH, with the decrease being significantly greater in the latter. The mass decrease was linked to the α- to β-$Ni(OH)_2$ transformation. Furthermore, compared to the film aged in Fe-free KOH, there was minimal mass change before and after overcharging the film aged in unpurified KOH (Figure 322c), suggesting that overcharging reversed the effects of aging only in Fe-free KOH. Both experiments demonstrated that Fe impurities inhibited the aging formation of β-$Ni(OH)_2$/β-NiOOH and the overcharging conversion of β- to γ-NiOOH. Alongside Raman and XPS measurements, these results led to the conclusion that Fe impurities induced structural changes in the $Ni(OH)_2$ films due to the incorporation of the Fe impurity. This example reveals that EQCM can be used to monitor the transformations of OER electrocatalysts. Additionally, EQCM can be used to precisely track mass activity changes or dissolution processes, and combining both DEMS and EQCM would enable the simultaneous detection of volatile adsorbates such as CO.[1272] These capabilities demonstrate the potential of EQCM to complement other special techniques in this field.

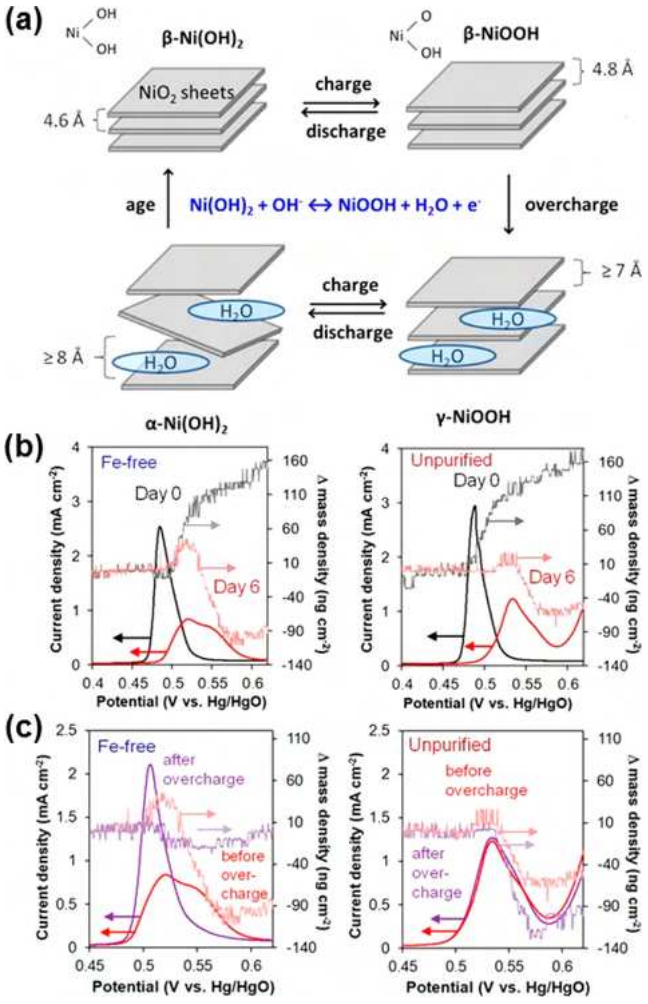


Figure 322. (a) Scheme for the $Ni(OH)_2$/NiOOH redox transformation; QCM mass density changes and concurrent potential scans for $Ni(OH)_2$ films on Au/Ti quartz crystals in Fe-free and unpurified 0.1 M KOH: (b) before and after 6 days of aging in 1 M KOH and (c) before and after the 10 $mV \cdot s^{-1}$ overcharge scan to 0.85 $V_{Hg/HgO}$. Reprinted with permission from ref 212. Copyright 2015 American Chemical Society.

7.9. Important Remarks and Guidelines for Selecting Special Characterization Techniques

The evaluation of transition metal *X*-ides necessitates the selection of appropriate characterization techniques. As previously discussed, each technique offers unique capabilities, advantages, and limitations that should be carefully judged. This Section offers critical observations and recommendations to improve and, ultimately, to systematize the characterization of transition metal *X*-ides.

The studies discussed previously revealed that electrocatalytic activity is highly local and strongly influenced by surface heterogeneity, structural defects, elemental composition, oxidation states, etc. In most cases, these findings were achieved only through *in situ* and *operando* techniques, which implies that capturing the reconstruction processes in real-time is essential.[1194,1212,1223,1226] Therefore, more fundamental studies, relying mainly on *in situ*/*operando* techniques, are necessary to unveil the real nature of the transformation observed in transition metal *X*-ides during the OER. However, we note that *ex situ* and *quasi in situ* measurements should not be considered obsolete or useless. Although traditional *ex situ* characterization protocols cannot capture the dynamic changes during operating conditions, these methods provide the first evidence about the reconstruction process. Moreover, *in situ*/*operando* techniques are subject to instrumental and experimental constraints, which hinder their use. Nevertheless, *ex situ* measurements should be carefully executed, following an organized and well-established protocol to allow a fair comparison with other materials. This can be done, for instance, with novel materials or when the synthesis of the electrocatalyst is improved. Still, *in situ*/*operando* techniques should be used to expand the characterization whenever possible.

Remarkably, numerous advanced techniques have used customized cells due to limited commercial availability. For example, devices have been specifically fabricated or adapted to enable characterization with FTIR,[1193] Raman (refs 48, 212, 1191, 1198, 1202, and 1204), XAS (refs 609, 1132, 1216, 1217, 1219, 1223, 1280, and 1281), AFM,[1238,1240,1241] ICP,[1260] DEMS,[610,611,1274] and other advanced techniques.[901,1194] Some interesting designs are shown in Figure 323. Lee *et al.* utilized a customized electrochemical cell to apply a water immersion objective during *in situ* Raman experiments (Figure 323a).[1202]

https://doi.org/10.1021/acs.chemrev.3c00005
Chem. Rev. 2023, 123, 12795−13208

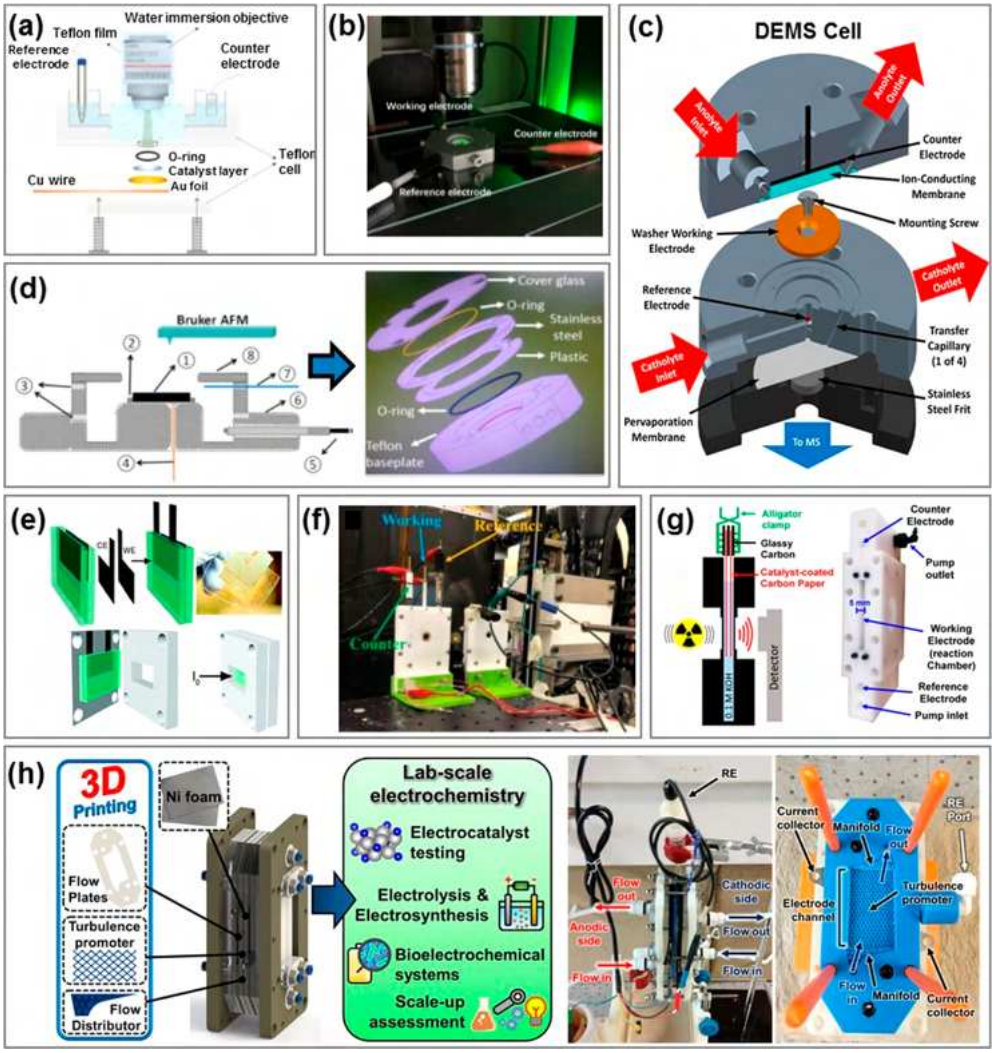


Figure 323. Representative examples of customized cells for special characterization: (a) Experimental setup for *in situ* Raman measurements using a water immersion objective. Reprinted with permission from ref 1202. Copyright 2019 Wiley. (b) Three-electrode cell for *in situ* Raman spectroscopy. Reprinted with permission from ref 48. Copyright 2019 American Chemical Society. (c) Schematic illustration of DEMS cell components. Reprinted with permission from ref 1274. Copyright 2015 American Chemical Society. (d) Homemade cell for EC-AFM tests. Reprinted with permission from ref 1240. Copyright 2017 American Chemical Society. (e) Electrochemical cell for *in situ* XAS. Reprinted with permission from ref 1282. Copyright 2012 American Chemical Society. (f) Experimental setup for *operando* SXRD. Reprinted with permission from ref 1194. Copyright 2020 American Chemical Society. (g) Electrochemical cell for *operando* Mössbauer tests. Reprinted with permission from ref 901. Copyright 2015 American Chemical Society. (h) 3D-printed electrochemical flow cell for realistic stability tests and preliminary scale-up. Reprinted with permission from ref 1283. Copyright 2020 American Chemical Society.

In situ Raman measurements were performed in a specifically designed setup devised by Zhu *et al.* (Figure 323b).[48] As displayed in Figure 323c, Clark *et al.* fabricated a DEMS cell to detect volatile species in real-time.[1274] For *in situ* EC-AFM measurements, Deng *et al.* employed the customized electrochemical cell shown in Figure 323d.[1240] Erickson *et al.* fabricated a cell with a thin polydimethylsiloxane window to enable *in situ* XAS tests (Figure 323e).[1282] Figure 323f shows the experimental setup used for *operando* SXRD measurements of $NiSe_2$ electrocatalysts by Zhai *et al.*[1194] An electrochemical cell for *operando* Mössbauer tests was fabricated by Chen *et al.* using Delrin, an inexpensive material with minimal γ-ray absorption that can be easily machined (Figure 323g).[901] A robust 3D-printed electrochemical flow cell was designed and characterized by Márquez-Montes *et al.*, which enables the realistic testing of different electrochemical processes (Figure 323h).[1283] These devices depend on important design features. Applications such as 3D printing have been used for fast prototyping and fabrication of custom geometries. Notably, the use of a flowing electrolyte has proven to be necessary to remove bubbles,[100,1225,1230] homogenize the electrolyte,[1211] or take samples on-line (e.g., DEMS, SFC-ICP).[294,1228,1259−1261] Other important factors include the reproducibility[1268] and properties of the material (e.g., X-ray transparency, mechanical resistance to vacuum).[1217,1274,1282] Furthermore, testing of the electrocatalysts under realistic and reproducible conditions at the lab scale can be done by using 3D-printed cells with tailored designs.[294,1283] Overall, until more sophisticated systems are available, special characterization will rely on customized systems. Future studies should be careful when formulating experimental conditions to enable reliable and reproducible results.

While the techniques mentioned above provide us with tools to observe the changes in the chemical or physical

https://doi.org/10.1021/acs.chemrev.3c00005
Chem. Rev. 2023, 123, 12795−13208

Table 9. Comparison Chart Showing the Complementary Capabilities and Reported Applications of Different Special Characterization Techniques for Water-Splitting Electrocatalysts[a]

Capability / Application	FTIR	Raman	UV-Vis	XAS	SEM*	TEM*	XPS	STM	AFM	SECM	SECCM	ICP (MS/AES)	XRF	DEMS/OLEMS	XRD	Mössbauer	EPR
Functional groups / chemical bonds	●	●	○	●	○	○	●	○	○	○	○	○	○	○	○	○	○
Oxidation states	○	○	○	●	○	○	●	○	○	●	⊙	○	○	○	○	●	●
Crystallinity (amorphicity)	○	●	○	●	○	●	○	○	○	○	○	○	○	○	●	⊙	○
Atomic structural changes	○	●	○	●	○	●	○	⊙	○	○	○	○	○	○	●	●	●
Detection of oxides	●	●	●	●	●	●	●	⊙	○	○	○	○	○	○	●	○	○
Bond distance	○	○	○	●	○	●	○	○	○	○	○	○	○	○	●	○	●
Coordination number	○	⊙	○	●	○	○	○	○	○	○	○	○	○	○	○	○	●
Study of defect sites/vacancies	○	●	○	○	●	●	●	●	●	●	●	○	○	○	○	○	●
Electrochemical imaging	○	○	○	○	○	○	○	⊙	⊙	●	●	○	○	○	○	○	○
Local electrocatalytic activity	○	○	○	○	○	○	○	●	●	●	●	○	○	○	○	○	○
Morphology change	○	○	○	○	●	●	○	●	●	●	●	○	○	○	○	○	○
Elemental content	○	○	○	⊙	●	●	●	○	○	○	○	●	●	○	○	○	○
Estimation of metal loadings	○	○	○	○	○	○	○	○	○	○	○	●	●	○	○	○	○
Dissolution assessment	○	○	⊙	●	●	●	○	○	⊙	⊙	●	●	●	○	○	○	○
Metal incorporation	⊙	●	●	●	●	●	●	⊙	●	⊙	⊙	●	⊙	⊙	●	⊙	○
Detection of products and FEs	○	○	○	○	○	○	○	○	○	●	⊙	○	○	●	○	○	○
Isotope labeling	●	⊙	○	⊙	○	○	○	○	○	○	○	●	○	●	○	○	⊙
Detection of intermediates species	●	●	⊙	●	○	○	●	○	○	●	⊙	○	○	●	○	●	⊙

[a]● = applicable; ⊙ = possible/not directly confirmed in the field; ○ = not applicable. *Considers additional modes (e.g., EDX, SAED, EELS, etc.).

compositions of electrocatalysts, it is also crucial to monitor the charge transfer kinetics and electrical conductivity of the electrocatalyst during the OER process. Furthermore, the temperature variation greatly impacts the electrochemical process during the OER. For instance, the charge transfer kinetics, electrode's electrical conductivity, and electrolyte ionic conductivity (i.e., solution resistance) depend on operating temperature.[138,177,1284,1285] The electrocatalyst performance at different temperatures is also crucial for its practical applications.[1286] However, very few studies in the past have discussed the variation in the *X*-ide-based electrocatalyst's performance at different temperatures.

For instance, Masa *et al.* observed the OER overpotentials of Ni-based metalloids at different temperatures; then, experimentally obtained results were used to calculate the apparent activation energy of the OER.[138,177] While this method shows the direct way to observe the electrocatalyst performance at varying temperatures, it does not consider the effects of temperatures on different electrochemical processes that happened during the OER. For example, the proton conductivity of Nafion membranes, generally used as a proton exchange membrane and a binder for the powder-based electrode, is highly dependent on the operating temperature.[1287] Hence the total cell voltage of a water electrolyzer might also vary due to the change in proton conductivity.[1287] Here, we could deconvolute such resistance contributions from other components/events, happening during the electrochemical process, by using electrochemical impedance spectroscopy (EIS). For instance, Stühmeier *et al.* have studied the pressure and temperature dependence of the hydrogen oxidation and evolution reaction kinetics on Pt electrocatalysts.[1284] Here, they could subtract the resistance induced

https://doi.org/10.1021/acs.chemrev.3c00005
Chem. Rev. 2023, 123, 12795−13208

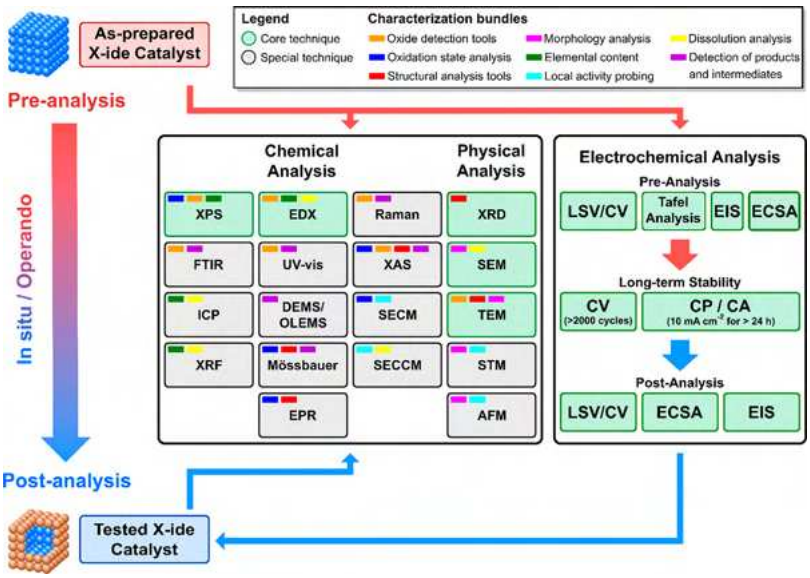


Figure 324. Characterization workflow for systematized evaluation of transition metal *X*-ide OER electrocatalysts. The electrochemical analysis section is adapted from ref 57. Characterization techniques for chemical and physical analysis are divided into two main groups: "core" techniques, which should be consistently used in all the reports (pre- and post-analysis), and unique methods to complement the analysis. Techniques are categorized in "characterization bundles", which can perform certain types of analysis or complement results. Whenever is possible, *in situ*/*operando* approaches using these characterization techniques should be employed.

by the proton exchange membrane by obtaining high-frequency resistance through EIS. However, the material conductivity could also be part of the resistance; hence, to observe the effects of temperature on electrocatalyst conductivity, we could utilize a 4-point probe instrument.[1288−1290] Accordingly, the 4-point probe and impedance at high frequency in EIS could help elucidate the effects of temperature on electrocatalytic material conductivity and solution resistance, respectively.

Furthermore, the EIS analysis can also provide the charge transfer resistance of an electrochemical process of interest, which should be useful for studies related to *X*-ide OER electrocatalysts.[564,1291] While the Nyquist plot obtained from impedance spectra helps us understand different processes like charge and mass transfer during the OER, the time constants of different electrochemical processes are often close. Since the Nyquist plot is a frequency-domain measurement, it cannot separate processes at different time domains. Here, unlike equivalent circuit models and physicochemical models used in EIS, distribution of relaxation times (DRT) analysis does not require a specific definition of discrete impedance contributions; instead, the impedance is assumed to arise from an infinite series of resistive−capacitive relaxations, which can be represented by a distribution function in the time domain. The DRT analysis reveals the presence of a process as characteristic peaks in the distribution; hence, by performing DRT analysis on impedance spectra, we can obtain higher frequency resolution, which helps separate and identify different electrochemical processes and their dependence on the electrolyzer operating temperature.[1292,1293]

To summarize, we can see that it is crucial to investigate the temperature dependence of the electrocatalytic activity of *X*-ide-based electrocatalysts for their practical applications. Here EIS has been a very reliable technique in the past to observe the effects of temperature on the different processes in the OER. However, we might need additional analytical techniques to elucidate the impact of operating temperature on the *X*-ide-based electrocatalysts in more detail. Here we believe that utilizing EIS, DRT, and a 4-point probe provides us with the tools to effectively understand the impacts of temperature on the *X*-ide OER electrocatalyst's performance.

The importance of complementing special techniques should also be summarized and highlighted. As previously shown in this Section, several studies employed different characterization techniques to address different unknowns, correlating each particular finding to formulate the main conclusions of the study. Complementary methods can be used to confirm observed trends using different approaches. Furthermore, knowing complementary techniques can be very useful when planning experiments, as more accessible techniques (e.g., Raman) can be used instead of more complex ones (e.g., XAS) to tackle a particular property. Notably, computational studies are valuable tools to complement the study of electrocatalytic materials. Theoretical approaches have been used to explain complex results by simulating different reaction scenarios or calculating parameters from experimental data. Notable reports in the literature have coupled computational approaches with special characterization techniques, providing exceptional comprehension of the electrocatalytically active sites (refs 221, 609, 1194, 1196, 1203, 1218, 1220, and 1245). From this perspective, a comparative chart depicting the most relevant capabilities of the techniques described in this Section is shown in Table 9. We believe that this tool will aid in selecting complementary techniques for studying electrocatalytic materials, mainly transition metal *X*-ides. Notably, the capabilities included in Table 9 are based solely on direct measurements reported for water-splitting electrocatalysts. We understand that highly versatile techniques such as Raman spectroscopy or XAS could find other properties by using additional correlations or computations. Other techniques such as SHM and EQCM are not included due to the scarcity of applications. Still, we expect that new capabilities will be developed in the following years, improving this chart in the future.

https://doi.org/10.1021/acs.chemrev.3c00005
Chem. Rev. 2023, 123, 12795−13208

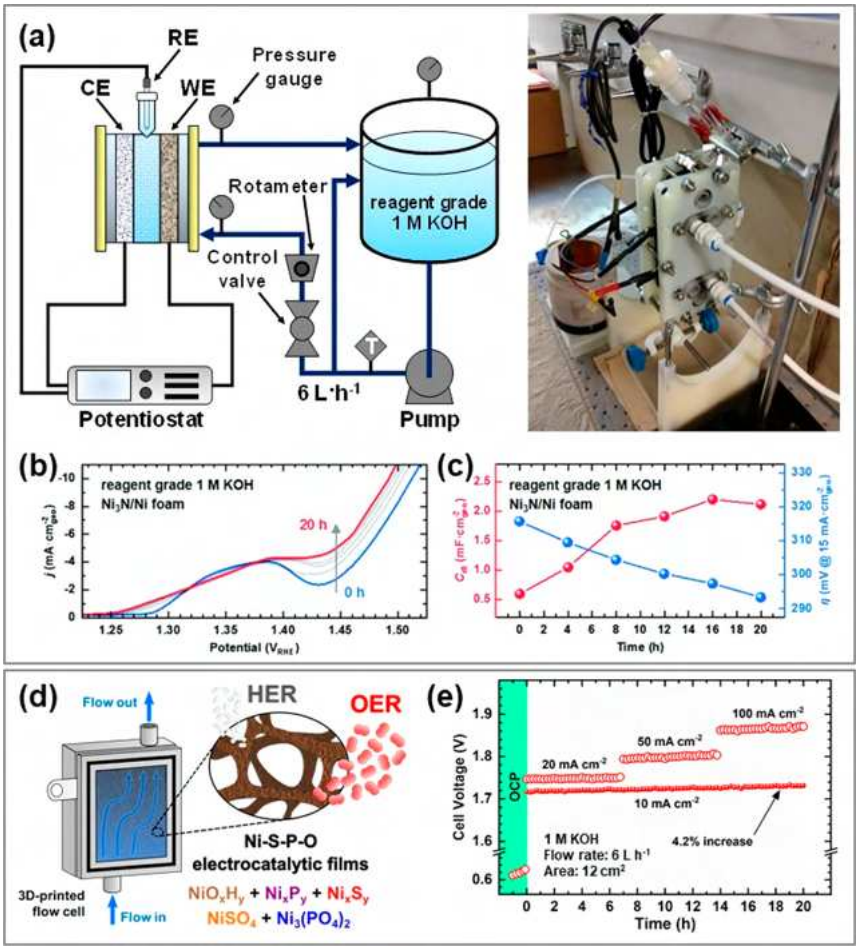


Figure 325. Examining practical application aspects of *X*-ide OER electrocatalysts: (a) experimental flow cell setup for testing nickel nitride (Ni_3N) electrocatalysts in unpurified KOH electrolyte; (b) Polarization curves recorded at different times during galvanostatic stability tests; (c) Double-layer capacitance (C_{dl}) and OER overpotential changes during electrochemical flow cell tests. Reprinted with permission from ref 90. Copyright 2021 Royal Society of Chemistry. (d) Examining Ni-S-P-O electrocatalytic films using a 3D-printed electrochemical flow cell; (e) Multistep current stability analysis of Ni-S-P-O electrodes. Reprinted with permission from ref 49. Copyright 2021 Royal Society of Chemistry.

Finally, the lack of consistency when reporting characterization results of transition metal *X*-ides is a major concern in the literature. Therefore, materials should be characterized in a more organized way to allow for an objective comparison between electrocatalysts. Inspired by the preliminary characterization workflow recommended by our group in the past,[57] we propose an updated version in Figure 324, which includes a "core" characterization set plus different particular characterization "bundles". Based on the main capabilities of each technique, these special characterization bundles are predefined approaches that future studies can use to examine particular insights. We recommend this workflow in the transition metal *X*-ide field to systematize the study and comparison of upcoming electrocatalysts. Evidently, due to the wide variety of electrocatalytic materials, it is challenging to control variations in experimental conditions, such as substrates, electrochemical conditions, electrolytes, stability periods, surface areas, electrocatalyst loadings, etc. Still, we expect these guidelines will facilitate and standardize the characterization of transition metal *X*-ide electrocatalysts.

7.10. Lab-Scale Electrochemical Testing toward Practical Application

Up to this point, we have reviewed studies of *X*-ide OER electrocatalysts relying on conventional three-electrode cell setups at the laboratory scale. Note, however, that these electrocatalysts need to meet practical water electrolysis requirements. Therefore, it is crucial to consider industrial operating conditions even in the laboratory.[1286] Although many fundamental studies use other conditions to understand critical phenomena (e.g., active site/phase elucidation) or demonstrate the feasibility of new approaches at early stages of development, many studies still claim outstanding properties with potential for large-scale implementation without testing under appropriate practical conditions. Hence, researchers need to consider the challenges and current limitations of water electrolysis technologies so that *X*-ide OER electrocatalysts are synthesized and evaluated accordingly. Herein, we summarize the most important practical considerations to ease the scale-up and application of water-splitting electrocatalysts.

Overall, electrocatalytic materials in practical water electrolysis are mainly limited by (1) the high capital costs, (2) low activity/efficiency, (3) stability issues, and (4) limited scalability and complexity.[1294,1295] Although most of the studies typically claim to satisfy points (1) and (2), addressing stability and scalability is often disregarded or improperly assessed. Stability is essential to guarantee the long-term operation of water electrolyzers and reduce maintenance costs.[1294] Hence, even if the activity of an *X*-ide electrocatalyst

https://doi.org/10.1021/acs.chemrev.3c00005
Chem. Rev. 2023, 123, 12795−13208

is higher than that of a commercial benchmark, it is not relevant for industrial scale if it needs to be replaced continuously. Therefore, *X*-ide electrocatalyst research needs to consider more specific requirements. Regarding proton exchange membrane (PEM) electrolysis, electrocatalysts must withstand high temperatures (between 50 and 80 °C) and acidic environments.[1294] Electrocatalysts designed for alkaline electrolysis must withstand harsh alkaline environments and, most importantly, high temperatures (between 70 and 100 °C) and electrolyte concentrations (∼34 wt % or ∼6 M).[1286,1294,1296,1297] For both systems, high temperatures and corrosive environments might accelerate one critical concern: electrocatalyst degradation. Therefore, studies must carefully examine degradation during prolonged tests, not only the potential or current drift over time.[1296] For instance, chemical dissolution can be examined through electrolyte inspection via ICP-MS or TXRF and post-mortem surface examination using XPS. However, physical effects, such as intense bubble evolution under practical conditions, could also cause degradation.[1298] Other components can also be compromised, such as membranes or gaskets.[1299] Finally, researchers are encouraged to examine the temperature dependence of the electrocatalytic activity, as some materials could exhibit a different performance at high temperatures.[1286]

Understanding the effect of impurities is also critical, especially for those studies proposing "metal-free" electrocatalysts with superior performance. Although it is impractical to completely remove impurities from commercial feedstocks in a large-scale scenario,[1286] this procedure is essential at the early stages of scale-up because it reveals if the electrocatalytic performance is determined by the electrocatalyst itself or the experimental conditions. For example, our group examined the effects of Fe incorporation into nickel nitride (Ni_3N) electrocatalysts in conventional three-electrode and flow cell configurations using an unpurified 1 M KOH electrolyte.[90,324] The flow electrolyzer configuration (Figure 325a) enabled uniform incorporation of Fe impurities from the KOH electrolyte into the nitride film, which was directly grown on large Ni foam electrodes (projected geometric area: 12 cm^2). As shown in Figure 325b, polarization curves taken during galvanostatic tests (10 $mA{\cdot}cm^{-2}$ for 20 h) reveal a shift of the $Ni^{2+/3+}$ redox peak and a significant decrease of the OER overpotential, which are clear signs of Fe incorporation.[200,1300] Moreover, Figure 325c correlates the gradual decrease in the OER overpotential as the double-layer capacitance (C_{dl}) increases, suggesting that more Fe impurities are absorbed as the surface area increases due to NiOOH formation during the OER. Therefore, intrinsic OER activity changes caused by Fe impurities are also present in larger cell configurations with enhanced mass transfer. Note that impurities present in the electrolyte can also degrade other cell components, such as the membrane, leading to erroneous conclusions about electrocatalytic stability and deactivation processes.[1294,1300] Therefore, we urge the community to follow recent guidelines to remove impurities effectively.[200,1300]

It is often believed that the longer the testing period without noticeable drift in potential or current, the more stable the material is. Recent studies have examined the performance of *X*-ide electrocatalysts using membrane electrode assemblies (MEAs) and operating at higher current densities for several tens of hours, including FeNiCo||FeNiCoP (500 $mA{\cdot}cm^{-2}$ at 1.72 V during 40 h),[1301] bifunctional NiCoP@NiFeP (1 $A{\cdot}cm^{-2}$ at 1.93 V during 100 h),[1302] and bifunctional NiFeS@Ti_3C_2 (∼400 $mA{\cdot}cm^{-2}$ at 1.85 V during 35 h) electrocatalysts.[1303] Although the authors have confirmed the stability of these materials during prolonged operation, this may not guarantee complete stability in a realistic scenario. For example, incorporating water electrolyzers into renewable solar and wind power sources results in intermittent operation and causes undesirable reverse currents that can deteriorate the materials.[1286,1304] Hence, targeting higher current densities while simulating intermittency or multistep outputs during galvanostatic or potentiostatic tests is recommended. Our group examined the performance of Ni-S-P-O electrocatalytic films on Ni foam electrodes (projected geometric area: 12 cm^2) in a zero-gap MEA configuration using an electrochemical flow cell (Figure 325d).[49] Multistep galvanostatic tests from 10 to 100 $mA{\cdot}cm^{-2}$ showed a voltage increase of 4.2% in 20 h (Figure 325e). Similarly, an additional test at 100 $mA{\cdot}cm^{-2}$ during 48 h showed an increase of 3.6%. Postmortem XPS analysis showed that the initial Ni-S-P-O precatalyst suffered from continuous oxidation into sulfate and phosphate oxyanions, which dissolved into the electrolyte, resulting in the constant potential increase. Although this degradation rate could be considered negligible for laboratory standards, it is not for industrial requirements (< 0.1% over 24 h).[1286] Thus, future studies must carefully examine the impact of industrial operating conditions on *X*-ide OER electrocatalysts.

We note that integrating transition metal *X*-ides into commercial-scale electrolyzer configurations is still scarce in the literature. Although these previous examples have examined the effect of factors and conditions relevant to industrial water electrolysis, the number of studies comparing traditional electrocatalytic materials and transition metal *X*-ides strictly under the same commercial-scale configurations is limited. Additionally, note that there are numerous studies claiming that electrocatalysts are tested using "water electrolyzers"; however, such cell configurations are rather simple and lack the components of commercial electrolyzers (e.g., separators, current collectors, electrolyte recirculation). Moreover, several studies did not consider industrially relevant conditions, and therefore, the alleged excellent performance may not be applicable when scaled up.

Nevertheless, it is possible to compare transition metal *X*-ides and traditional electrocatalysts in a commercial scenario. One of the best examples so far is the application of a cobalt phosphide (CoP) HER electrocatalyst to a commercial-scale 86 cm^2 polymer electrolyte membrane (PEM) electrolyzer by the Jaramillo group.[1305] In this study, the authors not only prepared a CoP electrocatalyst on a commercial gas diffusion electrode (GDE) and tested it under relevant operating conditions (1.86 $A{\cdot}cm^{-2}$, 400 psi, 50 °C) in a commercial PEM-electrolyzer cell stack but also compared its performance using the same cell configuration and identical conditions with a platinum black-based GDE. The CoP cathode produced about 10.1 kg of H_2 over 1700 h with 12−18% greater power density than that of the Pt cathode. Although the CoP electrocatalyst exhibited remarkable stability, the authors suggest that CoP dissolution was responsible for two abrupt increases in potential when the electrolyzer briefly lost power (< 1 min). Furthermore, the authors employed IrO_x as the OER electrocatalyst to limit the performance assessment to the cathode. Hence, the OER performance of the CoP electrocatalyst under such conditions has not been reported yet. Nonetheless, this study reflects how a transition metal *X*-ide

https://doi.org/10.1021/acs.chemrev.3c00005
Chem. Rev. 2023, 123, 12795−13208

electrocatalyst needs to be adequately tested and compared with commercial standards.

In summary, we urge the community to adopt fair and systematic procedures to explore the application of transition metal *X*-ides in commercial alkaline water electrolyzers. Future research can focus on (1) studying the impact of industrially relevant conditions to unveil how specific electrode processes occur (e.g., electrocatalyst dissolution, inactivation), (2) engineering electrocatalysts to withstand such adverse effects (e.g., passivation layers, self-healing mechanisms), and (3) comparing transition metal *X*-ide electrocatalysts with commercial materials, strictly operating under relevant conditions and using commercial electrolyzer configurations (e.g., flow cells, stacks, GDEs, membranes, and separators). Specifically, there is a need for more research on transition metal *X*-ide OER electrocatalysts in alkaline media, which is currently limited to the laboratory scale and prevents fair comparison with traditional electrocatalytic materials. Hence, we encourage researchers to take the next step to achieve commercial water electrolysis requirements.

7.11. Advanced Technologies for Further Developing *X*-ide Electrocatalyst Research

Using artificial intelligence (AI) through machine learning (ML) is another exciting and promising avenue for accelerating the optimization of transition metal *X*-ide electrocatalysts and examining their stability more systematically.[1306,1307] Robust ML models can help to identify structure−activity and stability relationships without requiring extenuating laboratory experiments and computation resources, thereby accelerating the discovery of new materials and providing the most efficient pathways to achieve electrocatalyst development goals.[1308] ML can also link electrocatalytic properties with synthesis conditions, predict specific morphologies and structures, or maximize properties such as surface area.[1306] Furthermore, ML is extremely useful for automating the physical and chemical characterizations of electrocatalytic materials, thus enabling rapid detection of compositional and structural differences before and after testing. This approach is advantageous when large quantities of data are acquired by some analytical techniques (e.g., mass spectrometry, scanning probe microscopy, and image analysis).

ML also offers significant advantages for computational electrocatalysis. For instance, ML potentials can be constructed by training a model with different atomic configurations and their corresponding forces and energies. Then, the model learns the underlying potential energy surface to predict the energies and forces of new configurations and describe the interactions between electrocatalysts and reactants.[1309] Therefore, ML models are powerful alternatives to expensive and time-consuming DFT calculations.

Previous studies have employed ML to examine OER electrocatalysts, mainly nonprecious oxides and 2D materials.[1310,1311] ML models designed for OER electrocatalysts have been trained with compositional, geometrical/structural, and electronic descriptors so that predictions of the OER activity are made. For example, Ge and coauthors employed the least absolute shrinkage and selection operator (LASSO) process together with DFT to train ML models with structural descriptors (e.g., rotational angle, bond length, distance between layers) of Mo and W chalcogenides to estimate the HER and OER overpotentials.[1312] This LASSO method predicted that the best sample, $MoTe_2/WTe_2$ with rotation of 300°, would exhibit overpotentials of 30 and 170 mV for the HER and the OER, respectively.

ML has been extensively used in other electrochemical applications, such as batteries, to screen materials libraries through high-throughput experimentation and to predict the cost and performance of the resulting battery architectures.[1313,1314] Moreover, battery informatics research has resulted in extensive databases containing crystalline, electronic, and structural properties, kinetic and transport parameters, and battery cycling data, which are readily available online.[1313,1314] Besides accessing these libraries to retrieve essential data, high-quality libraries enable easy comparison and cross-validation within research institutes and companies.

Recent advances in robotics, lab automation, and AI are reshaping the way experimental sciences work, and the convergence of these areas has resulted in the development of automated laboratories. Using robotics and AI for high-throughput synthesis and testing of electrocatalysts offers promising advantages, including (1) increased productivity and efficiency, (2) better reproducibility and higher data quality, (3) improved safety, and (4) potential for self-driven labs (SDLs) and ML-coupled approaches.[1315] Coupling autonomous high-throughput testing with machine learning enables the optimization of material compositions when robotics and instruments can handle samples, start experiments, and automate characterization. SDLs are expected to improve as significant advances in hardware development, module engineering, remote operation, and online characterization are made.[1316] These improvements would be extremely valuable for performing robust testing and characterization of OER electrocatalysts.

Although the implementation of these advanced methods in transition metal *X*-ide research is still starting to rise, we devise specific applications that would be extremely helpful for this field. First, SDLs coupled with ML could rapidly screen several transition metal *X*-ide combinations. Next, the generated libraries could establish relationships with activity and stability metrics, including electrocatalytic activity, turnover frequencies, surface area, or dissolution rates.[1308] Importantly, these libraries should be made available to the public and used to determine future directions or cross-validation. Other promising approaches include (i) examining different crystalline phases, compositions, or morphologies of the same transition metal *X*-ide to determine activity and stability trends, (ii) optimizing synthetic conditions based on activity and stability descriptors, and (iii) determining optimal operating conditions to minimize electrocatalytic deactivation or dissolution. SDLs and ML approaches also enable more reproducible and systematic *in situ*/*operando* measurements for examining the chemical and structural transformations of transition metal *X*-ides during the OER. Electrocatalytic degradation processes could be resolved in real-time by coupling techniques online (e.g., ICP-MS), and ML models could be used to readjust operating conditions and revert deactivation processes. Furthermore, SDLs enable examining long-term stability tests remotely or under specific experimental conditions that may not be safe or practical for human operators.

Nevertheless, these advanced strategies are still limited by critical challenges, mainly: (1) acquiring sufficient and high-quality data, (2) determining descriptors properly, (3) analyzing outliers, statistical significance, and reproducibility carefully, (4) considering realistic conditions and experimental parameters, and (5) improving hardware and software

https://doi.org/10.1021/acs.chemrev.3c00005
Chem. Rev. 2023, 123, 12795−13208

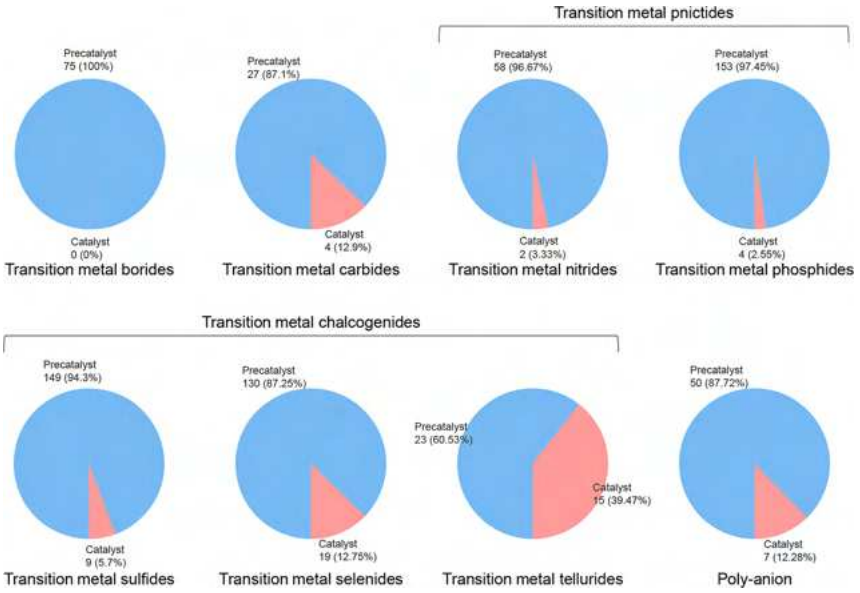


Figure 326. Pie charts showing the sample numbers and percentages of "catalysts" and "precatalysts" reported in each material group. All the pie charts were drawn using the publications cited in this review (for details about the corresponding references, see Tables 1−8). From the pie charts, we excluded the samples with "Catalyst (substrate)" labels, in which passivation layers were introduced prior to the OER testing.

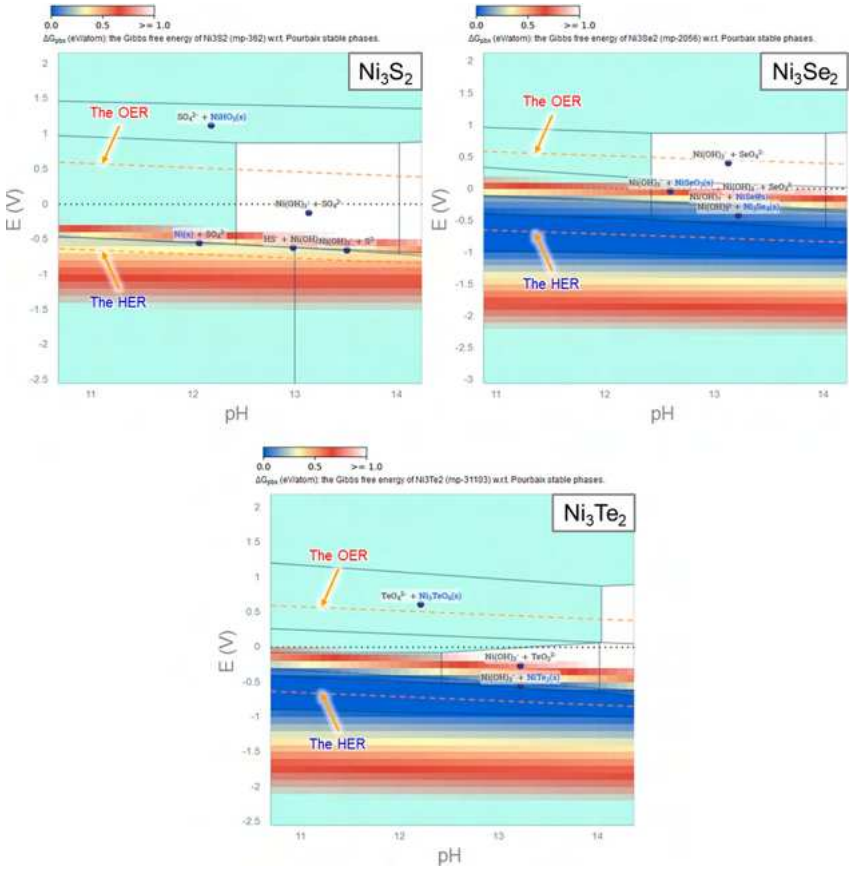


Figure 327. Electrochemical stability maps (Pourbaix diagram and Gibbs free energy overlay) of Ni_3S_2, Ni_3Se_2, and Ni_3Te_2 in alkaline pH regions. The Gibbs free energy overlays indicate areas of aqueous stability for Ni_3S_2, Ni_3Se_2, and Ni_3Te_2, with blue regions being the most stable and red/uncolored regions being the least stable. The diagrams were generated using the Materials Project.[87−89]

accessibility.[1307] For example, high-throughput electrocatalyst design is limited by the availability of high-quality libraries and standard datasets needed for training ML modules.[1310] Importantly, these libraries must be highly consistent and reliable, avoiding common experimental issues highlighted by recent studies in the literature, such as Fe incorporation.[200,1300] Furthermore, ML applications require systematic guidance to determine correct descriptors and reliable approaches to

https://doi.org/10.1021/acs.chemrev.3c00005
Chem. Rev. 2023, 123, 12795−13208

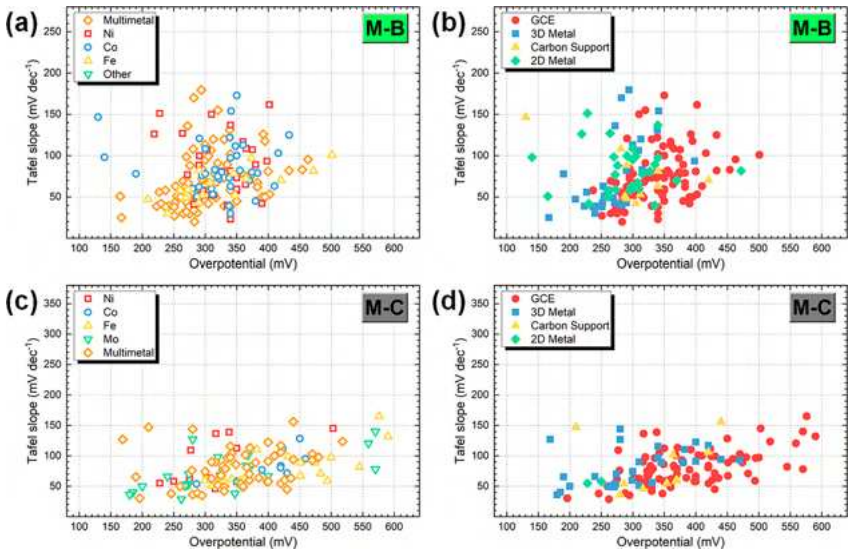


Figure 328. Electrocatalytic activity mappings for transition metal borides (a, b) and carbides (c, d). Mappings are categorized based on the transition metal (a, c) and conductive substrate (b, d).

estimate outputs, like correctly estimating the electrochemical surface area or Tafel slopes.[113,1317,1318] As evidenced in this review, specific descriptors used for traditional electrocatalysts might not be completely reliable when applied to transition metal *X*-ides because these materials will likely transform during the OER process. Hence, special care must be taken when selecting these descriptors in materials that are unstable or change during testing. Cross-validation, obtaining electrochemical data under real environments, and considering important effects (e.g., solvation effects) and experimental conditions are critical aspects that must be considered when training ML models.[1310] SDLs and robotics are mainly limited by challenges in cognition and motor functions, limited sensitivity and resolution, lack of cost-effective hardware, and accessible, user-friendly software.[1315,1316,1319] Therefore, using these advanced methods in electrocatalysis still requires precise human guidance to obtain reliable predictions and accelerate the development of high-performance electrocatalytic materials.

8. CONCLUSIONS AND GENERAL RECOMMENDATIONS

8.1. Overview and Summary of *X*-ide Electrocatalysts

In this review, we comprehensively summarized the recent advances (mainly from 2013 to 2022) of the transition metal *X*-ide-based OER electrocatalysts and proposed approaches for revealing their real OER electroactive sites/species/phases. We have categorized the reported *X*-ide-based electrocatalysts into three groups: "precatalyst", "catalyst", and "unknown". Focusing on the "precatalyst" and "catalyst" groups, as summarized in Figure 326, most of the reported *X*-ide-based electrocatalysts can be classified as precatalysts, which undergo a surface/bulk reconstruction (i.e., oxidation, dissolution, decomposition, etc.) under OER conditions. The most frequently reported reconstruction process is oxidation, in which the *X*-ides are partially/fully converted into their counterpart oxides/(oxy)hydroxides, likely becoming real OER active sites/species/phases. In addition, the oxidized anion species (e.g., BO_2^-, PO_4^{3-}, SO_4^{2-}, etc.) often remained on the post-OER *X*-ide precatalyst surfaces as well. The role of oxidized anion species in the OER process is still an open problem to discuss and should be studied more carefully in the future. On the other hand, for each material group (i.e., boride, carbide, pnictide, chalcogenide, and polyanion compound/composite), there are still a few/some reports claiming that the *X*-ides could act as stable catalysts during the OER. However, the reasons behind their superior oxidation resistance are still unknown. Here, Ni_3X_2-based electrocatalysts (X = S, Se, Te) can be cited as specific examples,[100,101,543] and they could maintain their surface chemical compositions even after long-term OER tests in alkaline media (1 M KOH). However, according to the theoretically calculated Pourbaix diagrams of Ni_3X_2 (see Figure 327), they are least stable near the OER potentials at pH ≈ 14. So, we may still need to elucidate the main factor(s) [e.g., applied potentials and potential windows (for the OER testing), OER testing time, electrolyte concentrations, electrocatalytic material dimensions, types of conductive substrates, etc.] for emerging the exceptional oxidation resistances of certain *X*-ides under OER conditions. Additionally, on the post-OER *X*-ide catalyst surfaces, the existence of oxidized anion species, possibly generated during the *X*-ide synthesis, could often be observed. Thus, as is for the *X*-ide precatalysts, it is still necessary to examine whether oxidized anion species can affect the OER performance of the *X*-ide catalysts or not. Nevertheless, note that conducting consistent physical and chemical characterizations of *X*-ide electrocatalysts before and after the OER is mandatory to verify and discuss their real active species and associated OER mechanisms.

Herein, we also provide a summary of the OER activities of different transition metal *X*-ide-based electrocatalysts. To provide an intuitive comparison of their OER activities, we categorized the electrocatalytic data from Tables 1−8 based on their type of metal (e.g., Ni, Co, Fe, multimetal) and the supports: glassy carbon electrode (GC), 3D metal substrates (e.g., Ni foam, Cu foam, mesh electrodes, etc.), 2D metal substrates (e.g., Ni foil, Ti foil, etc.), and carbon-based substrates (e.g., carbon paper, carbon fibers, etc.). These distribution mappings depict the overpotential (i.e., *x*-axis) at 10 $mA{\cdot}cm_{geo}^{-2}$ and Tafel slope (i.e., *y*-axis) for each reported electrocatalyst from the corresponding *X*-ide group. Moreover,

https://doi.org/10.1021/acs.chemrev.3c00005
Chem. Rev. 2023, 123, 12795−13208

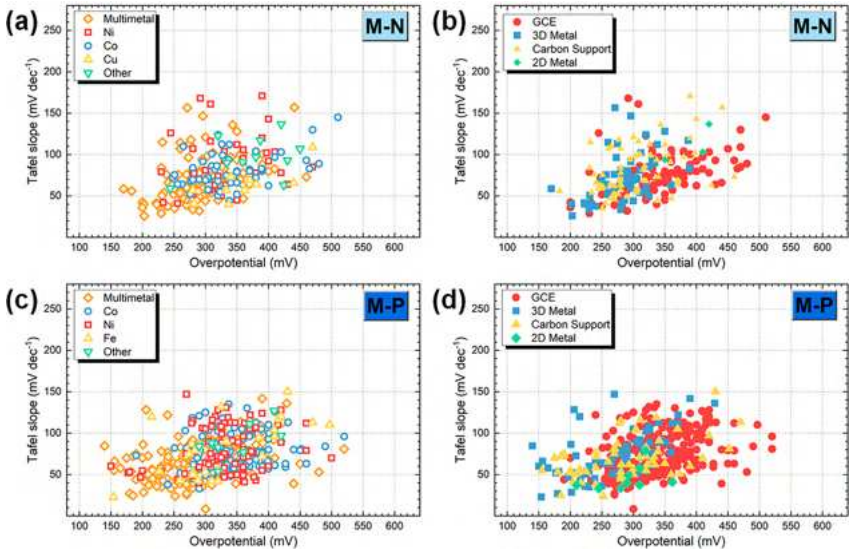


Figure 329. Electrocatalytic activity mappings for transition metal nitrides (a, b) and phosphides (c, d). Mappings are categorized based on the transition metal (a, c) and conductive substrate (b, d).

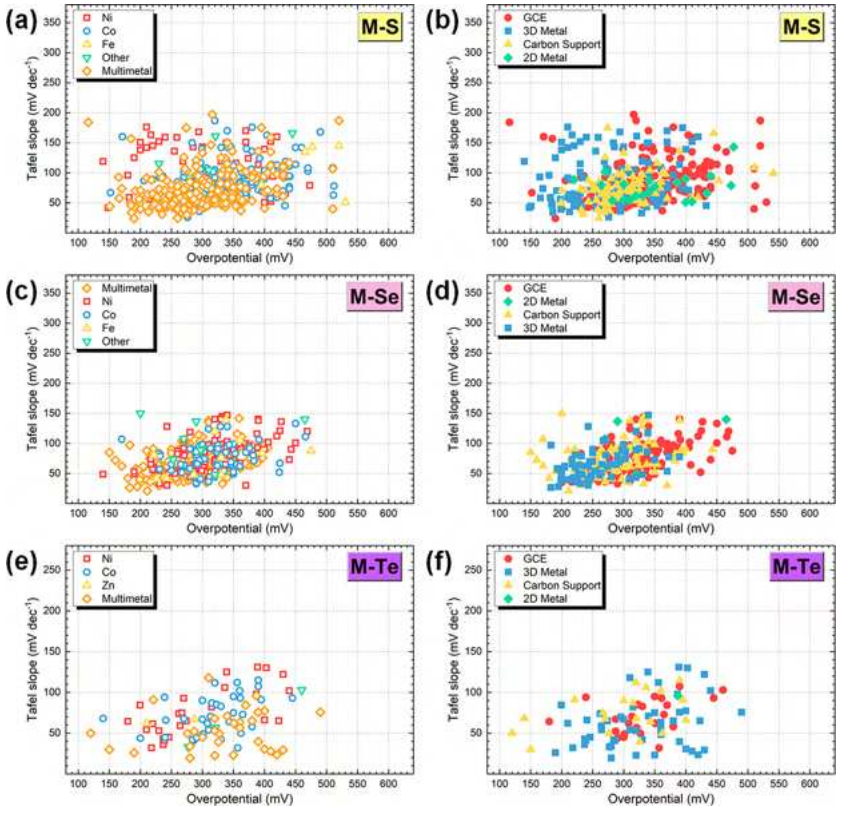


Figure 330. Electrocatalytic activity mappings for transition metal sulfides (a, b), selenides (c, d), and tellurides (e, f). Mappings are categorized based on the transition metal (a, c, e) and conductive substrate (b, d, f).

we included data only reported in 1 M KOH to provide a reasonable comparison. Figures 328−331 show the activity mappings for transition metal borides (*M*-B) and carbides (*M*-C), pnictides (*M*-N and *M*-P), chalcogenides (*M*-S, *M*-Se, and *M*-Te), and polyanion compounds/composites (*M*-Mix), respectively. Notably, these figures depict the data scattering for *X*-ide-based electrocatalysts reported in the literature from 2013 to 2022. As shown in each figure, a highly dense area where most of the points reside represents the most common overpotentials and Tafel slopes reported so far. Furthermore, we can find possible outliers or data points that deviate from most studies. Thus, these graphs provide a simple way to roughly compare the resulting OER activity of the *X*-ide-based electrocatalysts with the average trends reported so far.

Notice, however, that it is difficult to compare different transition metal *X*-ide trends more precisely. Therefore, we statistically examined the overpotential at 10 mA·cm$_{geo}^{-2}$ and Tafel slope differences between *X*-ide groups. First, we

https://doi.org/10.1021/acs.chemrev.3c00005
Chem. Rev. 2023, 123, 12795−13208

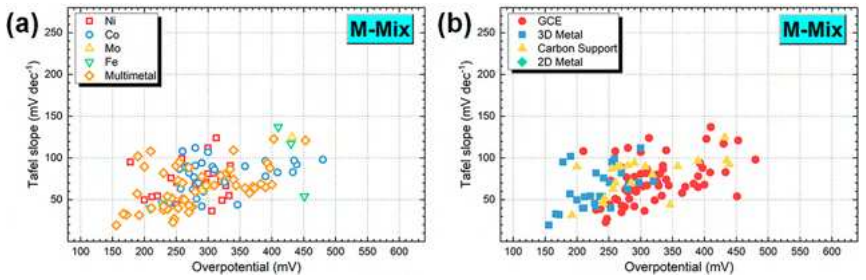


Figure 331. Electrocatalytic activity mappings for polyanion compound/composite electrocatalysts. Mappings are categorized based on the transition metal (a) and conductive substrate (b).

calculated the average and standard deviations for each dataset and excluded those data points considered as outliers based on the Grubbs test (0.05 significance level). Next, analysis of variance (ANOVA) with a Tukey's range test was used to detect any significant difference between *X*-ides. For this analysis, we again used a significance level of 0.05. ANOVA and Tukey tests were performed using the Minitab® 17 statistical analysis package. Figure 332 depicts a bar plot

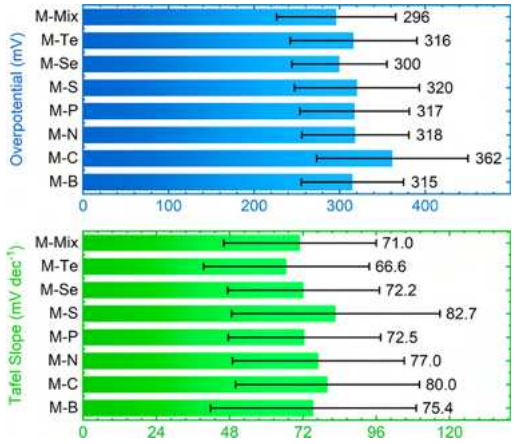


Figure 332. Comparison of OER activity parameters for different *X*-ide-based electrocatalysts. Values shown to the right represent the average value, while error bars show the standard deviation.

showing the averages for overpotentials at 10 $mA{\cdot}cm_{geo}^{-2}$ and Tafel slopes among different *X*-ides. Notably, no statistically significant differences were found among the categorized datasets, suggesting that the electrocatalytic activities of these *X*-ides are roughly the same. This trend can be attributed to the large standard deviations, which in turn might arise from the wide diversity of substrates, dopants, heterostructures, morphologies, etc. However, it is still possible to see some remarkable trends based solely on the average values. For instance, the *M*-Se and *M*-B electrocatalysts show the narrowest overpotential dispersion, while the *M*-C, *M*-S, and *M*-Te electrocatalysts show a wide range of overpotentials at 10 $mA{\cdot}cm_{geo}^{-2}$. Furthermore, the *M*-Se, *M*-B, and *M*-Mix electrocatalysts display relatively lower average overpotentials at 10 $mA{\cdot}cm_{geo}^{-2}$ than the others. Regarding the Tafel slopes, almost all the *X*-ides show very similar averages and standard deviations around 80 $mV{\cdot}dec^{-1}$, suggesting that the kinetics is roughly the same among these transition metal *X*-ides. Nevertheless, this should not be considered a definitive comparison. More systematic studies comparing different *X*-ides using the same experimental conditions (e.g., conductive substrate, electrocatalyst morphology, electrocatalyst mass loading, electrolyte concentration, electrochemical cell, electrochemical testing parameters, etc.) are needed to provide an objective comparison in the future.

8.2. Best Practices for Studying *X*-ide Precatalysts

Worthy of special attention, according to the OER activity discussion, is that there have so far been reports arguing that the enhanced OER activity of transition metal *X*-ide precatalysts compared to their counterpart (oxy)hydroxides (MO_xH_y) is attributed to their superb intrinsic OER activity, which originates from the material properties of the *in situ*-formed oxide/(oxy)hydroxide layer during the OER, enhanced conductivity by transition metal *X*-ides, or electronic effects (or other synergistic effects) between the transition metal *X*-ide and the *in situ*-formed oxide/(oxy)hydroxide layers on its surface. However, these arguments are often simply based on the enhanced geometric OER activity (e.g., overpotential at 10 $mA{\cdot}cm_{geo}^{-2}$) and pre-OER material characterizations, which are not sufficient for the correct interpretation of the intrinsic OER activity of transition *X*-ide electrocatalysts that undergo *in situ* reconstruction (e.g., oxidation, decomposition, dissolution, etc.) during the OER. In this regard, to better clarify whether there exists any intrinsic activity enhancement for transition metal *X*-ide precatalysts, it is critical to perform proper and accurate analyses. Furthermore, in general, the geometric OER activity can be enhanced by (i) tuning the morphologies of the electrocatalyst and electrode to maximize the number of active sites per unit projected area and minimize the transport limitation of electron and mass and (ii) selecting electrocatalytic material possessing the best intrinsic OER activity.[45,1224] So, to examine only the intrinsic OER activity using the geometric OER activity, we may need to cancel out the contributions of electrocatalyst and electrode morphological properties. Herein, we describe the concerns and suggestions for discussing both the geometric and intrinsic OER activity of the *X*-ide precatalysts as follows.

First, to discuss the intrinsic OER activity of transition metal *X*-ide precatalysts, it is indispensable to provide the intrinsic activity-related parameters, including ECSA-normalized specific activity, TOF, or Tafel slopes. Considering the fact that the number of active sites of transition metal *X*-ide precatalysts increases during the OER by *in situ* oxidation (or any other types of reconstructions) and can significantly affect the geometric OER activity, it is crucial to decouple the effects of the increased number of active sites on the OER activity from those of intrinsic activity to reasonably discuss the intrinsic activity.

For the ECSA-normalized specific activity, the ECSA value can be measured by non-faradaic double-layer capacitance

https://doi.org/10.1021/acs.chemrev.3c00005
Chem. Rev. 2023, 123, 12795−13208

(C_{dl}) or coulombic charge for faradaic redox reaction of transition metals (Q_{redox}) using CV or AC EIS techniques. However, to measure the correct ECSA for intrinsic activity estimation, it is crucial to choose proper parameters (C_{dl} or Q_{redox}) and analysis techniques (CV or EIS) depending on the characteristics (e.g., morphology, composition, etc.) of the electrocatalysts of interest.

As to C_{dl}, C_{dl} can be measured by two different analysis techniques: (i) C_{dl} measured by scan-rate-dependent CV analysis in a non-faradaic potential region ($C_{dl,CV}$) and (ii) C_{dl} measured by EIS analysis in the faradaic potential region ($C_{dl,EIS}$). For transition metal (oxy)hydroxides that are electrolyte-permeable and poorly electrically conductive (e.g., NiO_xH_y, FeO_xH_y, MnO_xH_y, etc.), it is recommended to employ $C_{dl,EIS}$ measured at potentials more positive than their redox peak (M^{2+}/M^{3+}, M = transition metal) instead of $C_{dl,CV}$. This is because $C_{dl,CV}$ under non-faradaic potential regions can detect the C_{dl} of the conductive substrate instead of that of the actual electrocatalyst with poor electrical conductivity, while $C_{dl,EIS}$ can detect the actual C_{dl} of the electrocatalyst layer due to the improved electrical conductivity of transition metal (oxy)hydroxides under potential regions more positive than their anodic redox peak.[31,1320] On the other hand, for thin films of transition metal compounds or those with a core@shell structure (conductive transition metal *X*-ide core and thin *in situ* oxidized shell), which are expected to have negligible electrical conductivity issues through the electrocatalyst layer, it is acceptable to use both $C_{dl,CV}$ and $C_{dl,EIS}$. Nevertheless, note that the estimation of ECSA from C_{dl} still has several limitations in terms of accuracy. For example, the measured C_{dl} value can be complicated by ion transfer reactions at the interface, such as specific adsorption of H^+/OH^-, intercalation, and corrosion.[1321] Also, conversion of C_{dl} to ECSA using specific capacitance (C_s) values, which vary with material properties (e.g., chemical composition, crystallinity, and facet orientation), surface structure, and electrode potential, can lead to inaccuracy in the obtained ECSA values.[113]

In addition to C_{dl}, Q_{redox} under the CV redox peak (M^{2+}/M^{3+}) can be used to measure the ECSA for most transition metal-based compound OER electrocatalysts, except for FeO_xH_y and MnO_xH_y, which have too low electrical conductivity and give a resulting low electrochemical reversibility for the faradaic redox reaction.[46] Especially for the composites of OER-active transition metal (e.g., Ni, Co)-based *X*-ides and OER-nonactive materials (e.g., carbonaceous materials, OER-nonactive transition metal compounds), the ECSA from Q_{redox} has the advantage of selectively reflecting the ECSA of OER-active materials, while the ECSA from C_{dl} can reflect C_{dl} from both OER-active and OER-nonactive materials. However, it is to be noted that the estimation of ECSA from Q_{redox} has limitations in that the number of electrons transferred for the redox reaction can be ambiguous and that some portion of Q_{redox} cannot be revealed due to the trapping of a portion of the electrocatalyst layer in the oxidized state due to a low-conductivity issue.[1320]

For the TOF, there have been attempts to obtain the TOF by normalizing OER activity with the mass loading of the electrocatalyst.[31,40,113] Although this approach can be used to measure the TOF of ideal, thin electrocatalyst layers that meet the condition that all atoms within the electrocatalyst layer are exposed to the electrolyte and become active sites, it usually does not work for real electrocatalyst layers that have the limitation of utilizing whole active metals due to blocking of active sites by overlying layers or mass transport limitations.

The Tafel slope can also be used as a parameter to compare the intrinsic activities of different electrocatalysts. The Tafel slope has an advantage over ECSA-normalized specific activity and the TOF in that the Tafel slope can be simply calculated using geometric area-normalized current density, which is especially helpful for the case where it is challenging to measure an accurate ECSA for the electrocatalyst. However, in comparing the intrinsic activity using the Tafel slope, one should be careful because the Tafel slope value can be easily altered depending on the potential range, which affects the surface coverage of reactants on the electrocatalyst,[1322] and current density scale, which determines the degree of electron and mass transport limitation during the OER.[213] Thus, for a fair comparison of intrinsic activities of different electrocatalysts, it is recommended to compare the Tafel slopes of different electrocatalysts in a similar potential range and current density scale, if possible.

Second, for the study of compositional effects on the OER activity of Ni, Co-based transition metal *X*-ide precatalysts, it is necessary to control the unintentional incorporation of Fe-impurities from alkaline electrolytes. It has been reported that Fe-impurities, which exist in commercial alkaline electrolytes (e.g., KOH and NaOH) at ppm scale,[1300] can be spontaneously (or unintentionally) incorporated into Ni, Co-based oxides and (oxy)hydroxides, forming NiFe- or CoFe-based electrocatalysts and enhancing their OER activity significantly.[200,207] There is a possibility that different amounts of Fe-impurities are incorporated into different Ni, Co-based electrocatalysts, resulting in measurable/decent OER activity regardless of the initial compositions. Thus, to study the compositional effects for objective comparison of OER activities of different electrocatalysts, it would be better to use a Fe-purified alkaline electrolyte for the OER test or to analyze the Fe composition after the OER test in Fe-unpurified electrolyte so that any uncontrolled effects from different Fe-incorporation can be excluded or minimized. Incidentally, in the previous studies, most of the *X*-ide precatalysts were examined in Fe-unpurified alkaline media and might thereby experience the incidental Fe-uptake, enhancing their OER activity *in situ*.

Third, the degree of electrochemical activation of transition metal *X*-ide precatalysts prior to the OER test should be considered for an objective comparison of OER activity. Specifically, Kim *et al.* reported that the intrinsic OER activity of the Co_3C precatalyst could vary a lot depending on the degree of *in situ* oxidation of Co_3C.[91] For example, after two LSV sweeps of the OER with Co_3C samples, which had the core@shell structure of $Co_3C@CoO_x$, they exhibited ECSA-normalized specific activity higher than that of fully oxidized Co_3C after 350 LSV sweeps of the OER. Also, Son *et al.* identified that depending on the type of electrochemical conditioning techniques (e.g., CP and CV), the degree of electrochemical activation (i.e., *in situ* oxidation of and Fe-incorporation into *X*-ide precatalysts) can change significantly, resulting in different material properties and electrochemical characteristics.[95]

Lastly, it is indispensable to conduct post-OER material characterizations together with pre-OER characterizations for both main and control samples to understand the origin of the different intrinsic activities correctly. This is because there is a high possibility that the advantageous material properties (e.g.,

https://doi.org/10.1021/acs.chemrev.3c00005
Chem. Rev. 2023, 123, 12795−13208

composition, structure, morphology, etc.) and electronic effects that are observed before the OER noticeably change or even disappear after OER testing due to severe *in situ* oxidation and reconstruction of transition metal *X*-ide precatalysts during the OER. This point indicates that pre-OER material characterizations are not sufficient to explain the origin of the distinct intrinsic activity of transition metal *X*-ide precatalysts.

8.3. Current Stage of *X*-ide Studies and Developments and Future Directions

Despite their potential as high-performance OER electrocatalysts, the current stage of *X*-ide OER electrocatalysts development remains immature to the extent that it simply reports decent OER performance and explains why based on the observed material properties and electrochemical characteristics. It still lacks a fundamental understanding of the material properties of as-prepared *X*-ides and their correlation with *in situ*-formed (oxy)hydroxides, which is necessary to design the benchmark OER electrocatalyst/electrode using *X*-ides. The benchmark OER electrocatalyst/electrode needs to be designed by balancing the trade-off relations between (1) intrinsic activity, (2) active surface area, (3) electron transport, and (4) mass transport.[95,1323] Here, intrinsic activity is determined by the crystal structure and defect ratio of the *in situ* metal (oxy)hydroxide and the synergistic effect between the *X*-ide core and the *in situ*-formed metal (oxy)hydroxide shell. Active surface area is determined by the thickness and porous structure of the *in situ*-formed metal (oxy)hydroxide layer. Electron transport is determined by the electrical conductivity of *X*-ides and the *in situ*-formed metal oxyhydroxide and the thickness and porous structure of the *in situ*-formed metal (oxy)hydroxide layer. Mass transport is determined by the thickness and porous structure of the *in situ*-formed metal (oxy)hydroxide layer.

For an in-depth understanding of the transformation principle of *X*-ides and the material properties of *in situ*-formed metal (oxy)hydroxides, it is critical to understand the distinct role of each anion in *X*-ide precatalysts as follows: (1) distinct resistance to oxidation of *X*-ides with different anion compositions for predicting the thickness of the *in situ* oxidized layer on a grain or electrode film, (2) effects of size and ratio of anion in *X*-ides on the porous structure (i.e., size and distribution of nanopores) of the *in situ*-formed metal (oxy)hydroxide, (3) effect of composition of *X*-ides on the crystal structure and crystallinity (i.e., ratio of defect sites) of the *in situ*-formed metal (oxy)hydroxide, (4) comparison of the different electrical conductivity of each *X*-ide, and (5) any change in type of active species and OER reaction mechanism (i.e., adsorbate evolution mechanism, lattice oxidation mechanism) and driving force (i.e., electrostatic potential and chemical potential) of *in situ*-formed metal (oxy)-hydroxides from different *X*-ides compared to as-prepared metal (oxy)hydroxide.[1324] Identifying the role of each anion in *X*-ides would enable us to find the optimal composition of each anion in *X*-ides for achieving desirable material properties as OER electrocatalysts.

In addition, to develop the benchmark *X*-ide catalytic electrode, the morphology of the as-prepared *X*-ide precatalyst layer should also be properly designed to achieve the best balance of electrocatalytic properties (i.e., intrinsic activity, active surface area, electron transport, and mass transport) by considering the characteristics of each *X*-ide and *in situ* variation of its material properties. For example, the optimal grain size of the as-prepared *X*-ide precatalyst can be selected by considering its resistance to oxidation depending on the target grain structure (i.e., either partially oxidized core@shell structure or fully oxidized layer). The morphology and thickness of the as-prepared *X*-ide precatalyst layer can be designed by reflecting the synergy with the *in situ*-formed nanoporous structure in terms of active surface area and transport of electron and mass.

We hope that this review will provide future electrochemistry-oriented guidelines to effectively assess the physical and chemical transformations of electrocatalytic materials for the OER as well as clues to design future electrocatalytic materials for highly efficient, robust, and economical energy conversion systems toward a sustainable hydrogen society.

AUTHOR INFORMATION

Corresponding Author

C. Buddie Mullins − *Department of Chemistry, The University of Texas at Austin, Austin, Texas 78712, United States; McKetta Department of Chemical Engineering, Center for Electrochemistry, and H2@UT, The University of Texas at Austin, Austin, Texas 78712, United States;* orcid.org/0000-0003-1030-4801; Email: mullins@che.utexas.edu

Authors

Kenta Kawashima − *Department of Chemistry, The University of Texas at Austin, Austin, Texas 78712, United States;* orcid.org/0000-0001-7318-6115

Raúl A. Márquez − *Department of Chemistry, The University of Texas at Austin, Austin, Texas 78712, United States;* orcid.org/0000-0003-3885-5007

Lettie A. Smith − *Department of Chemistry, The University of Texas at Austin, Austin, Texas 78712, United States;* orcid.org/0000-0003-0378-072X

Rinish Reddy Vaidyula − *Department of Chemistry, The University of Texas at Austin, Austin, Texas 78712, United States;* orcid.org/0000-0002-1767-0575

Omar A. Carrasco-Jaim − *McKetta Department of Chemical Engineering, The University of Texas at Austin, Austin, Texas 78712, United States;* orcid.org/0000-0001-9850-217X

Ziqing Wang − *Department of Chemistry, The University of Texas at Austin, Austin, Texas 78712, United States;* orcid.org/0000-0001-7746-0409

Yoon Jun Son − *McKetta Department of Chemical Engineering, The University of Texas at Austin, Austin, Texas 78712, United States;* orcid.org/0000-0003-1704-2314

Chi L. Cao − *McKetta Department of Chemical Engineering, The University of Texas at Austin, Austin, Texas 78712, United States*

Complete contact information is available at: https://pubs.acs.org/10.1021/acs.chemrev.3c00005

Author Contributions

†K.K. and R.A.M. contributed equally to this work. K.K., R.A.M., L.A.S., R.R.V., O.A.C.-J., Z.W., Y.J.S., and C.B.M. composed the manuscript, and all authors edited the written work. All authors have given approval for the final version of the manuscript. CRediT: **Kenta Kawashima** conceptualization, data curation, formal analysis, investigation, methodology, software, validation, visualization, writing-original draft, writing-review & editing; **Raul A. Marquez** data curation, formal

https://doi.org/10.1021/acs.chemrev.3c00005
Chem. Rev. 2023, 123, 12795−13208

analysis, investigation, methodology, software, validation, visualization, writing-original draft, writing-review & editing; **Lettie A Smith** data curation, formal analysis, investigation, software, validation, visualization, writing-original draft, writing-review & editing; **Rinish Reddy Vaidyula** data curation, formal analysis, investigation, software, validation, visualization, writing-original draft, writing-review & editing; **Omar Ali Carrasco Jaim** data curation, formal analysis, investigation, software, validation, visualization, writing-original draft, writing-review & editing; **Ziqing Wang** data curation, formal analysis, investigation, software, validation, visualization, writing-original draft, writing-review & editing; **Yoon Jun Son** data curation, formal analysis, investigation, software, validation, visualization, writing-original draft, writing-review & editing; **Chi L. Cao** writing-review & editing; **C. Buddie Mullins** conceptualization, funding acquisition, resources, supervision, validation, visualization, writing-review & editing.

Notes

The authors declare no competing financial interest.

Biographies

Kenta Kawashima received his B.Eng. (2014) and M.Eng. (2016) from Shinshu University and is currently a Ph.D. candidate (Chemistry) at UT Austin. His research focuses on developing highly active electrocatalysts and photoelectrocatalysts for efficient water splitting and the application of a molten-salt synthesis method for studying crystal growth.

Raúl A. Márquez received his B.Eng. in Chemical Engineering (2017) and M.Sc. in Chemistry (2020) from Universidad Autonoma de Chihuahua, Mexico. He is currently a Ph.D. student (Chemistry) at UT Austin. His research focuses on using novel approaches, such as 3D printing, electrochemical flow reactors, and *in situ/operando* techniques for developing and characterizing advanced materials for various electrocatalytic processes.

Lettie A. Smith received her B.S. in Chemistry from the University of North Carolina at Chapel Hill in Spring 2020. She began graduate school at UT Austin in Fall 2020 under the supervision of Prof. C. Buddie Mullins. Her research focuses on electrocatalysis for the ORR, HER, and OER.

Rinish Reddy Vaidyula received his integrated dual degree in Industrial Chemistry from the Indian Institute of Technology Varanasi (BHU) in 2020. He started a Ph.D. degree in the Department of Chemistry at UT Austin in 2021 under the supervision of Prof. C. Buddie Mullins. His research interest is in sodium-ion battery systems and battery recycling.

Omar A. Carrasco-Jaim received his M.S. in Environmental Engineering from Universidad Autónoma de Nuevo León, Mexico, in 2015 and his Ph.D. in Materials Science and Engineering from Universidad Autónoma de San Luis Potosí, Mexico, in 2020. He currently works in the McKetta Department of Chemical Engineering at UT Austin as a postdoctoral fellow within the ConTex Program 2020. His research focuses on solar energy conversion using photocatalysis and photoelectrocatalysis.

Ziqing Wang received his bachelor's degree from the School of Materials Science and Engineering at Central South University in 2020. He is currently a Ph.D. student at UT Austin. His research interests are aqueous zinc-ion batteries, high-performance electrodes and electrolytes, and drug delivery systems.

Yoon Jun Son received his B.S. in Chemical and Biological Engineering from Korea University in 2015 and his M.S. in Chemical and Biological Engineering from Seoul National University in 2017 under the supervision of Prof. Yung-Eun Sung. He then started a Ph.D. degree in Chemical Engineering at UT Austin in 2018 under the supervision of Prof. C. Buddie Mullins. His research interests are electrocatalysis for clean energy conversion and storage.

Chi L. Cao received her B.S. in Chemical Engineering from UT Austin in 2021. She is currently an engineer at W. L. Gore.

C. Buddie Mullins received a Ph.D. from the California Institute of Technology and was a postdoc at IBM Almaden Research Center. He is currently a Professor in the Departments of Chemical Engineering and Chemistry at UT Austin. His interests include surface chemistry, photocatalytic processes, and materials/architectures for advanced batteries.

ACKNOWLEDGMENTS

The authors gratefully acknowledge the support of the National Science Foundation via grants CHE-1664941 and CHE-2102307. We also acknowledge the Welch Foundation for its generous support through grant F-1436. The authors would like to thank Prof. Víctor H. Ramos-Sánchez for his fruitful advice on guidelines for selecting characterization techniques.

REFERENCES

(1) Van Bavel, J. The World Population Explosion: Causes, Backgrounds and Projections for the Future. *Facts Views Vis. Obgyn* **2013**, *5*, 281−291.
(2) Mont, O.; Power, K. The Role of Formal and Informal Forces in Shaping Consumption and Implications for a Sustainable Society. Part I. *Sustainability* **2010**, *2*, 2232−2252.
(3) *BP Statistical Review of World Energy 2021 | 70th Edition*; BP p.l.c., 2021. https://www.bp.com/content/dam/bp/business-sites/en/global/corporate/pdfs/energy-economics/statistical-review/bp-stats-review-2021-full-report.pdf (accessed 2022-12-21).
(4) Nicoletti, G.; Arcuri, N.; Nicoletti, G.; Bruno, R. A Technical and Environmental Comparison between Hydrogen and Some Fossil Fuels. *Energy Convers. Manag.* **2015**, *89*, 205−213.
(5) *BP Energy Outlook 2022 Edition*; BP p.l.c., 2022. https://www.bp.com/content/dam/bp/business-sites/en/global/corporate/pdfs/energy-economics/energy-outlook/bp-energy-outlook-2022.pdf (accessed 2022-12-21).
(6) Sharma, S.; Ghoshal, S. K. Hydrogen the Future Transportation Fuel: From Production to Applications. *Renew. Sustain. Energy Rev.* **2015**, *43*, 1151−1158.
(7) Yan, Y.; Xia, B. Y.; Zhao, B.; Wang, X. A Review on Noble-Metal-Free Bifunctional Heterogeneous Catalysts for Overall Electrochemical Water Splitting. *J. Mater. Chem. A* **2016**, *4*, 17587−17603.
(8) Harris, D. C. *Quantitative Chemical Analysis*; Macmillan, 2010; pp AP20−AP27.
(9) Osselin, F.; Soulaine, C.; Fauguerolles, C.; Gaucher, E. C.; Scaillet, B.; Pichavant, M. Orange Hydrogen Is the New Green. *Nat. Geosci.* **2022**, *15*, 765−769.
(10) Bhandari, R.; Shah, R. R. Hydrogen as Energy Carrier: Techno-Economic Assessment of Decentralized Hydrogen Production in Germany. *Renewable Energy* **2021**, *177*, 915−931.
(11) Bhaskar, A.; Assadi, M.; Nikpey Somehsaraei, H. Decarbonization of the Iron and Steel Industry with Direct Reduction of Iron Ore with Green Hydrogen. *Energies* **2020**, *13*, 758.
(12) Nhuchhen, D. R.; Sit, S. P.; Layzell, D. B. Decarbonization of Cement Production in a Hydrogen Economy. *Appl. Energy* **2022**, *317*, 119180.
(13) Frenette, G.; Forthoffer, D. Economic & Commercial Viability of Hydrogen Fuel Cell Vehicles from an Automotive Manufacturer Perspective. *Int. J. Hydrog. Energy* **2009**, *34*, 3578−3588.

https://doi.org/10.1021/acs.chemrev.3c00005
Chem. Rev. 2023, 123, 12795−13208

(14) International Energy Agency, (IEA). *Future of Hydrogen - Seizing Today's Opportunities*; Full Report; IEA: Paris, 2019. https://www.iea.org/reports/the-future-of-hydrogen.
(15) Hosseini, S. E.; Butler, B. An Overview of Development and Challenges in Hydrogen Powered Vehicles. *Int. J. Green Energy* **2020**, *17*, 13−37.
(16) Office of Energy Efficiency & Renewable Energy, (EERE). *Hydrogen's Role in Transportation*; Vehicle Technologies Office, https://www.energy.gov/eere/vehicles/articles/hydrogens-role-transportation (accessed 2023-04-24).
(17) Sapountzi, F. M.; Gracia, J. M.; Weststrate, C. J.; Fredriksson, H. O. A.; Niemantsverdriet, J. W. Electrocatalysts for the Generation of Hydrogen, Oxygen and Synthesis Gas. *Progress in Energy and Combustion Science* **2017**, *58*, 1−35.
(18) Tenhumberg, N.; Büker, K. Ecological and Economic Evaluation of Hydrogen Production by Different Water Electrolysis Technologies. *Chemie Ingenieur Technik* **2020**, *92*, 1586−1595.
(19) Terlouw, T.; Bauer, C.; McKenna, R.; Mazzotti, M. Large-Scale Hydrogen Production *via* Water Electrolysis: A Techno-Economic and Environmental Assessment. *Energy Environ. Sci.* **2022**, *15*, 3583−3602.
(20) Office of Energy Efficiency & Renewable Energy, (EERE). *Technical Targets for Proton Exchange Membrane Electrolysis*; Hydrogen and Fuel Cell Technologies Office, https://www.energy.gov/eere/fuelcells/technical-targets-proton-exchange-membrane-electrolysis (accessed 2023-04-24).
(21) Cook, T. R.; Dogutan, D. K.; Reece, S. Y.; Surendranath, Y.; Teets, T. S.; Nocera, D. G. Solar Energy Supply and Storage for the Legacy and Nonlegacy Worlds. *Chem. Rev.* **2010**, *110*, 6474−6502.
(22) Zou, X.; Zhang, Y. Noble Metal-Free Hydrogen Evolution Catalysts for Water Splitting. *Chem. Soc. Rev.* **2015**, *44*, 5148−5180.
(23) Wang, Y.; Kong, B.; Zhao, D.; Wang, H.; Selomulya, C. Strategies for Developing Transition Metal Phosphides as Heterogeneous Electrocatalysts for Water Splitting. *Nano Today* **2017**, *15*, 26−55.
(24) Yagi, M.; Kaneko, M. Molecular Catalysts for Water Oxidation. *Chem. Rev.* **2001**, *101*, 21−36.
(25) Dau, H.; Limberg, C.; Reier, T.; Risch, M.; Roggan, S.; Strasser, P. The Mechanism of Water Oxidation: From Electrolysis via Homogeneous to Biological Catalysis. *ChemCatChem* **2010**, *2*, 724−761.
(26) Koper, M. T. M. Thermodynamic Theory of Multi-Electron Transfer Reactions: Implications for Electrocatalysis. *J. Electroanal. Chem.* **2011**, *660*, 254−260.
(27) McCrory, C. C. L.; Jung, S.; Ferrer, I. M.; Chatman, S. M.; Peters, J. C.; Jaramillo, T. F. Benchmarking Hydrogen Evolving Reaction and Oxygen Evolving Reaction Electrocatalysts for Solar Water Splitting Devices. *J. Am. Chem. Soc.* **2015**, *137*, 4347−4357.
(28) Cherevko, S.; Geiger, S.; Kasian, O.; Kulyk, N.; Grote, J.-P.; Savan, A.; Shrestha, B. R.; Merzlikin, S.; Breitbach, B.; Ludwig, A.; et al. Oxygen and Hydrogen Evolution Reactions on Ru, RuO_2, Ir, and IrO_2 Thin Film Electrodes in Acidic and Alkaline Electrolytes: A Comparative Study on Activity and Stability. *Catal. Today* **2016**, *262*, 170−180.
(29) Fabbri, E.; Habereder, A.; Waltar, K.; Kötz, R.; Schmidt, T. J. Developments and Perspectives of Oxide-Based Catalysts for the Oxygen Evolution Reaction. *Catal. Sci. Technol.* **2014**, *4*, 3800−3821.
(30) Burke, M. S.; Zou, S.; Enman, L. J.; Kellon, J. E.; Gabor, C. A.; Pledger, E.; Boettcher, S. W. Revised Oxygen Evolution Reaction Activity Trends for First-Row Transition-Metal (Oxy)Hydroxides in Alkaline Media. *J. Phys. Chem. Lett.* **2015**, *6*, 3737−3742.
(31) Burke, M. S.; Enman, L. J.; Batchellor, A. S.; Zou, S.; Boettcher, S. W. Oxygen Evolution Reaction Electrocatalysis on Transition Metal Oxides and (Oxy)Hydroxides: Activity Trends and Design Principles. *Chem. Mater.* **2015**, *27*, 7549−7558.
(32) Gao, M.; Sheng, W.; Zhuang, Z.; Fang, Q.; Gu, S.; Jiang, J.; Yan, Y. Efficient Water Oxidation Using Nanostructured α-Nickel-Hydroxide as an Electrocatalyst. *J. Am. Chem. Soc.* **2014**, *136*, 7077−7084.
(33) Kim, J.-H.; Youn, D. H.; Kawashima, K.; Lin, J.; Lim, H.; Mullins, C. B. An Active Nanoporous Ni(Fe) OER Electrocatalyst via Selective Dissolution of Cd in Alkaline Media. *Appl. Catal. B: Environ.* **2018**, *225*, 1−7.
(34) Meng, Y.; Song, W.; Huang, H.; Ren, Z.; Chen, S.-Y.; Suib, S. L. Structure-Property Relationship of Bifunctional MnO_2 Nanostructures: Highly Efficient, Ultra-Stable Electrochemical Water Oxidation and Oxygen Reduction Reaction Catalysts Identified in Alkaline Media. *J. Am. Chem. Soc.* **2014**, *136*, 11452−11464.
(35) Wygant, B. R.; Jarvis, K. A.; Chemelewski, W. D.; Mabayoje, O.; Celio, H.; Mullins, C. B. Structural and Catalytic Effects of Iron- and Scandium-Doping on a Strontium Cobalt Oxide Electrocatalyst for Water Oxidation. *ACS Catal.* **2016**, *6*, 1122−1133.
(36) Smith, R. D. L.; Prévot, M. S.; Fagan, R. D.; Trudel, S.; Berlinguette, C. P. Water Oxidation Catalysis: Electrocatalytic Response to Metal Stoichiometry in Amorphous Metal Oxide Films Containing Iron, Cobalt, and Nickel. *J. Am. Chem. Soc.* **2013**, *135*, 11580−11586.
(37) Zhang, B.; Zheng, X.; Voznyy, O.; Comin, R.; Bajdich, M.; García-Melchor, M.; Han, L.; Xu, J.; Liu, M.; Zheng, L.; et al. Homogeneously Dispersed Multimetal Oxygen-Evolving Catalysts. *Science* **2016**, *352*, 333−337.
(38) Zhao, B.; Ke, X.-K.; Bao, J.-H.; Wang, C.-L.; Dong, L.; Chen, Y.-W.; Chen, H.-L. Synthesis of Flower-Like NiO and Effects of Morphology on Its Catalytic Properties. *J. Phys. Chem. C* **2009**, *113*, 14440−14447.
(39) Tang, D.; Mabayoje, O.; Lai, Y.; Liu, Y.; Mullins, C. B. In Situ Growth of Fe(Ni)OOH Catalyst on Stainless Steel for Water Oxidation. *ChemistrySelect* **2017**, *2*, 2230−2234.
(40) Trotochaud, L.; Ranney, J. K.; Williams, K. N.; Boettcher, S. W. Solution-Cast Metal Oxide Thin Film Electrocatalysts for Oxygen Evolution. *J. Am. Chem. Soc.* **2012**, *134*, 17253−17261.
(41) Chemelewski, W. D.; Rosenstock, J. R.; Mullins, C. B. Electrodeposition of Ni-Doped FeOOH Oxygen Evolution Reaction Catalyst for Photoelectrochemical Water Splitting. *J. Mater. Chem. A* **2014**, *2*, 14957−14962.
(42) Chemelewski, W. D.; Lee, H.-C.; Lin, J.-F.; Bard, A. J.; Mullins, C. B. Amorphous FeOOH Oxygen Evolution Reaction Catalyst for Photoelectrochemical Water Splitting. *J. Am. Chem. Soc.* **2014**, *136*, 2843−2850.
(43) Kim, J.-H.; Shin, K.; Kawashima, K.; Youn, D. H.; Lin, J.; Hong, T. E.; Liu, Y.; Wygant, B. R.; Wang, J.; Henkelman, G.; et al. Enhanced Activity Promoted by CeO_x on a CoO_x Electrocatalyst for the Oxygen Evolution Reaction. *ACS Catal.* **2018**, *8*, 4257−4265.
(44) Lim, H.; Kim, J. Y.; Evans, E. J.; Rai, A.; Kim, J.-H.; Wygant, B. R.; Mullins, C. B. Activation of a Nickel-Based Oxygen Evolution Reaction Catalyst on a Hematite Photoanode via Incorporation of Cerium for Photoelectrochemical Water Oxidation. *ACS Appl. Mater. Interfaces* **2017**, *9*, 30654−30661.
(45) Morales-Guio, C. G.; Liardet, L.; Hu, X. Oxidatively Electrodeposited Thin-Film Transition Metal (Oxy)Hydroxides as Oxygen Evolution Catalysts. *J. Am. Chem. Soc.* **2016**, *138*, 8946−8957.
(46) Zou, S.; Burke, M. S.; Kast, M. G.; Fan, J.; Danilovic, N.; Boettcher, S. W. Fe (Oxy)Hydroxide Oxygen Evolution Reaction Electrocatalysis: Intrinsic Activity and the Roles of Electrical Conductivity, Substrate, and Dissolution. *Chem. Mater.* **2015**, *27*, 8011−8020.
(47) Wygant, B. R.; Poterek, A. H.; Burrow, J. N.; Mullins, C. B. Effect of Selenium Content on Nickel Sulfoselenide-Derived Nickel (Oxy)Hydroxide Electrocatalysts for Water Oxidation. *ACS Appl. Mater. Interfaces* **2020**, *12*, 20366−20375.
(48) Zhu, Y.; Chen, H.-C.; Hsu, C.-S.; Lin, T.-S.; Chang, C.-J.; Chang, S.-C.; Tsai, L.-D.; Chen, H. M. Operando Unraveling of the Structural and Chemical Stability of P-Substituted $CoSe_2$ Electrocatalysts toward Hydrogen and Oxygen Evolution Reactions in Alkaline Electrolyte. *ACS Energy Lett.* **2019**, *4*, 987−994.
(49) Marquez-Montes, R. A.; Kawashima, K.; Son, Y. J.; Weeks, J. A.; Sun, H. H.; Celio, H.; Ramos-Sánchez, V. H.; Mullins, C. B. Mass Transport-Enhanced Electrodeposition of Ni-S-P-O Films on Nickel

Foam for Electrochemical Water Splitting. *J. Mater. Chem. A* **2021**, *9*, 7736−7749.
(50) Ren, H.; Sun, X.; Du, C.; Zhao, J.; Liu, D.; Fang, W.; Kumar, S.; Chua, R.; Meng, S.; Kidkhunthod, P.; et al. Amorphous Fe-Ni-P-B-O Nanocages as Efficient Electrocatalysts for Oxygen Evolution Reaction. *ACS Nano* **2019**, *13*, 12969−12979.
(51) Lin, J.; Wang, H.; Yan, Y.; Cao, J.; Qu, C.; Zheng, X.; Feng, J.; Qi, J. Sandwich-like Structured $NiSe_2$/Ni_2P@FeP Interface Nanosheets with Rich Defects for Efficient Electrocatalytic Water Splitting. *J. Power Sources* **2020**, *445*, 227294.
(52) Masa, J.; Schuhmann, W. The Role of Non-Metallic and Metalloid Elements on the Electrocatalytic Activity of Cobalt and Nickel Catalysts for the Oxygen Evolution Reaction. *ChemCatChem* **2019**, *11*, 5842−5854.
(53) Han, N.; Liu, P.; Jiang, J.; Ai, L.; Shao, Z.; Liu, S. Recent Advances in Nanostructured Metal Nitrides for Water Splitting. *J. Mater. Chem. A* **2018**, *6*, 19912−19933.
(54) Wang, J.; Liu, Z.; Zheng, Y.; Cui, L.; Yang, W.; Liu, J. Recent Advances in Cobalt Phosphide Based Materials for Energy-Related Applications. *J. Mater. Chem. A* **2017**, *5*, 22913−22932.
(55) Lv, Y.; Wang, X. Nonprecious Metal Phosphides as Catalysts for Hydrogen Evolution, Oxygen Reduction and Evolution Reactions. *Catal. Sci. Technol.* **2017**, *7*, 3676−3691.
(56) Peng, L.; Shah, S. S. A.; Wei, Z. Recent Developments in Metal Phosphide and Sulfide Electrocatalysts for Oxygen Evolution Reaction. *Chin. J. Catal.* **2018**, *39*, 1575−1593.
(57) Wygant, B. R.; Kawashima, K.; Mullins, C. B. Catalyst or Precatalyst? The Effect of Oxidation on Transition Metal Carbide, Pnictide, and Chalcogenide Oxygen Evolution Catalysts. *ACS Energy Lett.* **2018**, *3*, 2956−2966.
(58) Jamesh, M.-I.; Sun, X. Recent Progress on Earth Abundant Electrocatalysts for Oxygen Evolution Reaction (OER) in Alkaline Medium to Achieve Efficient Water Splitting - A Review. *J. Power Sources* **2018**, *400*, 31−68.
(59) Li, Y.; Du, X.; Huang, J.; Wu, C.; Sun, Y.; Zou, G.; Yang, C.; Xiong, J. Recent Progress on Surface Reconstruction of Earth-Abundant Electrocatalysts for Water Oxidation. *Small* **2019**, *15*, 1901980.
(60) Li, W.; Xiong, D.; Gao, X.; Liu, L. The Oxygen Evolution Reaction Enabled by Transition Metal Phosphide and Chalcogenide Pre-Catalysts with Dynamic Changes. *Chem. Commun.* **2019**, *55*, 8744−8763.
(61) Sivanantham, A.; Ganesan, P.; Vinu, A.; Shanmugam, S. Surface Activation and Reconstruction of Non-Oxide-Based Catalysts Through in Situ Electrochemical Tuning for Oxygen Evolution Reactions in Alkaline Media. *ACS Catal.* **2020**, *10*, 463−493.
(62) Dinh, K. N.; Liang, Q.; Du, C.-F.; Zhao, J.; Tok, A. I. Y.; Mao, H.; Yan, Q. Nanostructured Metallic Transition Metal Carbides, Nitrides, Phosphides, and Borides for Energy Storage and Conversion. *Nano Today* **2019**, *25*, 99−121.
(63) Jin, J.; Yin, J.; Liu, H.; Lu, M.; Li, J.; Tian, M.; Xi, P. Transition Metal (Fe, Co and Ni)-Carbide-Nitride (M-C-N) Nanocatalysts: Structure and Electrocatalytic Applications. *ChemCatChem* **2019**, *11*, 2780−2792.
(64) Joo, J.; Kim, T.; Lee, J.; Choi, S.-I.; Lee, K. Morphology-Controlled Metal Sulfides and Phosphides for Electrochemical Water Splitting. *Adv. Mater.* **2019**, *31*, 1806682.
(65) Tareen, A. K.; Priyanga, G. S.; Khan, K.; Pervaiz, E.; Thomas, T.; Yang, M. Nickel-Based Transition Metal Nitride Electrocatalysts for the Oxygen Evolution Reaction. *ChemSusChem* **2019**, *12*, 3941−3954.
(66) Chen, Z.; Duan, X.; Wei, W.; Wang, S.; Zhang, Z.; Ni, B.-J. Boride-Based Electrocatalysts: Emerging Candidates for Water Splitting. *Nano Res.* **2020**, *13*, 293−314.
(67) Jiang, Y.; Lu, Y. Designing Transition-Metal-Boride-Based Electrocatalysts for Applications in Electrochemical Water Splitting. *Nanoscale* **2020**, *12*, 9327−9351.
(68) Wang, H.; Zhu, S.; Deng, J.; Zhang, W.; Feng, Y.; Ma, J. Transition Metal Carbides in Electrocatalytic Oxygen Evolution Reaction. *Chin. Chem. Lett.* **2021**, *32*, 291−298.
(69) Luo, R.; Qian, Z.; Xing, L.; Du, C.; Yin, G.; Zhao, S.; Du, L. Re-Looking into the Active Moieties of Metal X-Ides (X- = Phosph-, Sulf-, Nitr-, and Carb-) Toward Oxygen Evolution Reaction. *Adv. Funct. Mater.* **2021**, *31*, 2102918.
(70) Liu, X.; Meng, J.; Zhu, J.; Huang, M.; Wen, B.; Guo, R.; Mai, L. Comprehensive Understandings into Complete Reconstruction of Precatalysts: Synthesis, Applications, and Characterizations. *Adv. Mater.* **2021**, *33*, 2007344.
(71) Ding, H.; Liu, H.; Chu, W.; Wu, C.; Xie, Y. Structural Transformation of Heterogeneous Materials for Electrocatalytic Oxygen Evolution Reaction. *Chem. Rev.* **2021**, *121*, 13174−13212.
(72) Anantharaj, S.; Ede, S. R.; Sakthikumar, K.; Karthick, K.; Mishra, S.; Kundu, S. Recent Trends and Perspectives in Electrochemical Water Splitting with an Emphasis on Sulfide, Selenide, and Phosphide Catalysts of Fe, Co, and Ni: A Review. *ACS Catal.* **2016**, *6*, 8069−8097.
(73) Gupta, S.; Patel, M. K.; Miotello, A.; Patel, N. Metal Boride-Based Catalysts for Electrochemical Water-Splitting: A Review. *Adv. Funct. Mater.* **2020**, *30*, 1906481.
(74) Hausmann, J. N.; Menezes, P. W. Why Should Transition Metal Chalcogenides Be Investigated as Water Splitting Precatalysts Even Though They Transform into (Oxyhydr)Oxides? *Curr. Opin. Electrochem.* **2022**, *34*, 100991.
(75) Nath, M.; Singh, H.; Saxena, A. Progress of Transition Metal Chalcogenides as Efficient Electrocatalysts for Energy Conversion. *Curr. Opin. Electrochem.* **2022**, *34*, 100993.
(76) Su, H.; Jiang, J.; Song, S.; An, B.; Li, N.; Gao, Y.; Ge, L. Recent Progress on Design and Applications of Transition Metal Chalcogenide-Associated Electrocatalysts for the Overall Water Splitting. *Chin. J. Catal.* **2023**, *44*, 7−49.
(77) Yao, Y.; Zhang, Z.; Jiao, L. Development Strategies in Transition Metal Borides for Electrochemical Water Splitting. *Energy Environ. Mater.* **2022**, *5*, 470−485.
(78) Amorim, I.; Liu, L. Transition Metal Tellurides as Emerging Catalysts for Electrochemical Water Splitting. *Curr. Opin. Electrochem.* **2022**, *34*, 101031.
(79) Zhang, T.; Sun, J.; Guan, J. Self-Supported Transition Metal Chalcogenides for Oxygen Evolution. *Nano Res.* **2023**, *16*, 8684−8711.
(80) Yu, F.; Zhou, H.; Huang, Y.; Sun, J.; Qin, F.; Bao, J.; Goddard, W. A.; Chen, S.; Ren, Z. High-Performance Bifunctional Porous Non-Noble Metal Phosphide Catalyst for Overall Water Splitting. *Nat. Commun.* **2018**, *9*, 1−9.
(81) Jin, S. Are Metal Chalcogenides, Nitrides, and Phosphides Oxygen Evolution Catalysts or Bifunctional Catalysts? *ACS Energy Lett.* **2017**, *2*, 1937−1938.
(82) Liu, H.; Jia, X.; Cao, A.; Wei, L.; D'agostino, C.; Li, H. The Surface States of Transition Metal X-Ides under Electrocatalytic Conditions. *J. Chem. Phys.* **2023**, *158*, 124705.
(83) Niessen, A. K.; De Boer, F. R. The Enthalpy of Formation of Solid Borides, Carbides, Nitrides, Silicides and Phosphides of Transition and Noble Metals. *J. Less Common Met.* **1981**, *82*, 75−80.
(84) Stevanović, V.; Lany, S.; Zhang, X.; Zunger, A. Correcting Density Functional Theory for Accurate Predictions of Compound Enthalpies of Formation: Fitted Elemental-Phase Reference Energies. *Phys. Rev. B* **2012**, *85*, 115104.
(85) Rasmussen, F. A.; Thygesen, K. S. Computational 2D Materials Database: Electronic Structure of Transition-Metal Dichalcogenides and Oxides. *J. Phys. Chem. C* **2015**, *119*, 13169−13183.
(86) Ataca, C.; Şahin, H.; Ciraci, S. Stable, Single-Layer MX_2 Transition-Metal Oxides and Dichalcogenides in a Honeycomb-Like Structure. *J. Phys. Chem. C* **2012**, *116*, 8983−8999.
(87) Persson, K. A.; Waldwick, B.; Lazic, P.; Ceder, G. Prediction of Solid-Aqueous Equilibria: Scheme to Combine First-Principles Calculations of Solids with Experimental Aqueous States. *Phys. Rev. B* **2012**, *85*, 235438.

https://doi.org/10.1021/acs.chemrev.3c00005
Chem. Rev. 2023, 123, 12795−13208

(88) Singh, A. K.; Zhou, L.; Shinde, A.; Suram, S. K.; Montoya, J. H.; Winston, D.; Gregoire, J. M.; Persson, K. A. Electrochemical Stability of Metastable Materials. *Chem. Mater.* **2017**, *29*, 10159−10167.
(89) Jain, A.; Ong, S. P.; Hautier, G.; Chen, W.; Richards, W. D.; Dacek, S.; Cholia, S.; Gunter, D.; Skinner, D.; Ceder, G.; et al. Commentary: The Materials Project: A Materials Genome Approach to Accelerating Materials Innovation. *APL Mater.* **2013**, *1*, 011002.
(90) Kawashima, K.; Márquez-Montes, R. A.; Li, H.; Shin, K.; Cao, C. L.; Vo, K. M.; Son, Y. J.; Wygant, B. R.; Chunangad, A.; Youn, D. H.; Henkelman, G.; et al. Electrochemical Behavior of a Ni_3N OER Precatalyst in Fe-Purified Alkaline Media: The Impact of Self-Oxidation and Fe Incorporation. *Mater. Adv.* **2021**, *2*, 2299−2309.
(91) Kim, J.-H.; Kawashima, K.; Wygant, B. R.; Mabayoje, O.; Liu, Y.; Wang, J. H.; Mullins, C. B. Transformation of a Cobalt Carbide (Co_3C) Oxygen Evolution Precatalyst. *ACS Appl. Energy Mater.* **2018**, *1*, 5145−5150.
(92) Cong, Y.; Park, H. S.; Dang, H. X.; Fan, F.-R. F.; Bard, A. J.; Mullins, C. B. Tantalum Cobalt Nitride Photocatalysts for Water Oxidation under Visible Light. *Chem. Mater.* **2012**, *24*, 579−586.
(93) Xu, J.; Li, J.; Xiong, D.; Zhang, B.; Liu, Y.; Wu, K.-H.; Amorim, I.; Li, W.; Liu, L. Trends in Activity for the Oxygen Evolution Reaction on Transition Metal (M = Fe, Co, Ni) Phosphide Pre-Catalysts. *Chem. Sci.* **2018**, *9*, 3470−3476.
(94) Mabayoje, O.; Shoola, A.; Wygant, B. R.; Mullins, C. B. The Role of Anions in Metal Chalcogenide Oxygen Evolution Catalysis: Electrodeposited Thin Films of Nickel Sulfide as "Pre-Catalysts. *ACS Energy Lett.* **2016**, *1*, 195−201.
(95) Son, Y. J.; Kim, S.; Leung, V.; Kawashima, K.; Noh, J.; Kim, K.; Marquez, R. A.; Carrasco-Jaim, O. A.; Smith, L. A.; Celio, H.; et al. Effects of Electrochemical Conditioning on Nickel-Based Oxygen Evolution Electrocatalysts. *ACS Catal.* **2022**, *12*, 10384−10399.
(96) Chen, W.; Wang, H.; Li, Y.; Liu, Y.; Sun, J.; Lee, S.; Lee, J.-S.; Cui, Y. In Situ Electrochemical Oxidation Tuning of Transition Metal Disulfides to Oxides for Enhanced Water Oxidation. *ACS Cent. Sci.* **2015**, *1*, 244−251.
(97) Chen, W.; Liu, Y.; Li, Y.; Sun, J.; Qiu, Y.; Liu, C.; Zhou, G.; Cui, Y. In Situ Electrochemically Derived Nanoporous Oxides from Transition Metal Dichalcogenides for Active Oxygen Evolution Catalysts. *Nano Lett.* **2016**, *16*, 7588−7596.
(98) Xu, X.; Song, F.; Hu, X. A Nickel Iron Diselenide-Derived Efficient Oxygen-Evolution Catalyst. *Nat. Commun.* **2016**, *7*, 1−7.
(99) Yu, J.; Cheng, G.; Luo, W. Ternary Nickel-Iron Sulfide Microflowers as a Robust Electrocatalyst for Bifunctional Water Splitting. *J. Mater. Chem. A* **2017**, *5*, 15838−15844.
(100) Swesi, A. T.; Masud, J.; Nath, M. Nickel Selenide as a High-Efficiency Catalyst for Oxygen Evolution Reaction. *Energy Environ. Sci.* **2016**, *9*, 1771−1782.
(101) De Silva, U.; Masud, J.; Zhang, N.; Hong, Y.; Liyanage, W. P. R.; Zaeem, M. A.; Nath, M. Nickel Telluride as a Bifunctional Electrocatalyst for Efficient Water Splitting in Alkaline Medium. *J. Mater. Chem. A* **2018**, *6*, 7608−7622.
(102) Chen, P.; Xu, K.; Fang, Z.; Tong, Y.; Wu, J.; Lu, X.; Peng, X.; Ding, H.; Wu, C.; Xie, Y. Metallic Co_4N Porous Nanowire Arrays Activated by Surface Oxidation as Electrocatalysts for the Oxygen Evolution Reaction. *Angew. Chem. Int. Ed.* **2015**, *54*, 14710−14714.
(103) Stern, L.-A.; Feng, L.; Song, F.; Hu, X. Ni_2P as a Janus Catalyst for Water Splitting: The Oxygen Evolution Activity of Ni_2P Nanoparticles. *Energy Environ. Sci.* **2015**, *8*, 2347−2351.
(104) Li, X.; Han, G.-Q.; Liu, Y.-R.; Dong, B.; Hu, W.-H.; Shang, X.; Chai, Y.-M.; Liu, C.-G. NiSe@NiOOH Core-Shell Hyacinth-like Nanostructures on Nickel Foam Synthesized by in Situ Electrochemical Oxidation as an Efficient Electrocatalyst for the Oxygen Evolution Reaction. *ACS Appl. Mater. Interfaces* **2016**, *8*, 20057−20066.
(105) Masa, J.; Sinev, I.; Mistry, H.; Ventosa, E.; de la Mata, M.; Arbiol, J.; Muhler, M.; Cuenya, B. R.; Schuhmann, W. Ultrathin High Surface Area Nickel Boride (Ni_xB) Nanosheets as Highly Efficient Electrocatalyst for Oxygen Evolution. *Adv. Energy Mater.* **2017**, *7*, 1700381.
(106) Dutta, A.; Pradhan, N. Developments of Metal Phosphides as Efficient OER Precatalysts. *J. Phys. Chem. Lett.* **2017**, *8*, 144−152.
(107) Masa, J.; Barwe, S.; Andronescu, C.; Sinev, I.; Ruff, A.; Jayaramulu, K.; Elumeeva, K.; Konkena, B.; Roldan Cuenya, B.; Schuhmann, W. Low Overpotential Water Splitting Using Cobalt-Cobalt Phosphide Nanoparticles Supported on Nickel Foam. *ACS Energy Lett.* **2016**, *1*, 1192−1198.
(108) Buttler, A.; Spliethoff, H. Current Status of Water Electrolysis for Energy Storage, Grid Balancing and Sector Coupling via Power-to-Gas and Power-to-Liquids: A Review. *Renewable Sustainable Energy Rev.* **2018**, *82*, 2440−2454.
(109) Niu, S.; Li, S.; Du, Y.; Han, X.; Xu, P. How to Reliably Report the Overpotential of an Electrocatalyst. *ACS Energy Lett.* **2020**, *5*, 1083−1087.
(110) Kawashima, K.; Márquez, R. A.; Son, Y. J.; Guo, C.; Vaidyula, R. R.; Smith, L. A.; Chukwuneke, C. E.; Mullins, C. B. Accurate Potentials of Hg/HgO Electrodes: Practical Parameters for Reporting Alkaline Water Electrolysis Overpotentials. *ACS Catal.* **2023**, *13*, 1893−1898.
(111) Anantharaj, S.; Sagayaraj, P. J.; Yesupatham, M. S.; Arulraj, R.; Eswaran, K.; Sekar, K.; Noda, S. The Reference Electrode Dilemma in Energy Conversion Electrocatalysis: "Right vs Okay vs Wrong. *J. Mater. Chem. A* **2023**, DOI: 10.1039/D3TA03145D.
(112) *Electrochemical Dictionary*, 2nd ed.; Bard, A. J., Inzelt, G., Scholz, F., Eds.; Springer-Verlag: Berlin Heidelberg, 2012. DOI: 10.1007/978-3-642-29551-5.
(113) Wei, C.; Sun, S.; Mandler, D.; Wang, X.; Qiao, S. Z.; Xu, Z. J. Approaches for Measuring the Surface Areas of Metal Oxide Electrocatalysts for Determining Their Intrinsic Electrocatalytic Activity. *Chem. Soc. Rev.* **2019**, *48*, 2518−2534.
(114) Montoya, J. H.; Seitz, L. C.; Chakthranont, P.; Vojvodic, A.; Jaramillo, T. F.; Nørskov, J. K. Materials for Solar Fuels and Chemicals. *Nat. Mater.* **2017**, *16*, 70−81.
(115) Wei, C.; Xu, Z. J. The Comprehensive Understanding of as an Evaluation Parameter for Electrochemical Water Splitting. *Small Methods* **2018**, *2*, 1800168.
(116) McCrory, C. C. L.; Jung, S.; Peters, J. C.; Jaramillo, T. F. Benchmarking Heterogeneous Electrocatalysts for the Oxygen Evolution Reaction. *J. Am. Chem. Soc.* **2013**, *135*, 16977−16987.
(117) Franklin, T. C.; Nnodimele, R.; Adeniyi, W. K. The Anodic Oxidation of Iron Pyrite Powder in a Cationic Surfactant-Styrene-Aqueous Sodium Hydroxide Emulsion. *J. Electrochem. Soc.* **1987**, *134*, 2150−2153.
(118) Franklin, T. C.; Nnodimele, R.; Adeniyi, W. K.; Hunt, D. The Anodic Oxidation of Galena in a Cationic Surfactant-Aqueous Sodium Hydroxide Emulsion. *J. Electrochem. Soc.* **1988**, *135*, 1944−1947.
(119) Franklin, T. C.; Adeniyi, W. K. Cationic Surfactants in Electrochemical Determination of Sulfide Minerals. *Anal. Chim. Acta* **1988**, *207*, 311−317.
(120) Franklin, T. C.; Adeniyi, W. K.; Nnodimele, R. The Electro-oxidation of Some Insoluble Inorganic Sulfides, Selenides, and Tellurides in Cationic Surfactant-Aqueous Sodium Hydroxide Systems. *J. Electrochem. Soc.* **1990**, *137*, 480−484.
(121) Zou, X.; Zhang, W.; Zhou, X.; Song, K.; Ge, X.; Zheng, W. The Surface of Metal Boride Tinted by Oxygen Evolution Reaction for Enhanced Water Electrolysis. *J. Energy Chem.* **2022**, *72*, 509−515.
(122) Wang, X.; Zuo, Y.; Horta, S.; He, R.; Yang, L.; Ostovari Moghaddam, A.; Ibáñez, M.; Qi, X.; Cabot, A. CoFeNiMnZnB as a High-Entropy Metal Boride to Boost the Oxygen Evolution Reaction. *ACS Appl. Mater. Interfaces* **2022**, *14*, 48212−48219.
(123) Zhao, S.; Xu, S.; Yao, J.; Chen, N.; Gong, Y.; Zhang, X.; Hao, X.; Zhang, L.; Pei, C.; Tian, R.; et al. Elucidating the Reaction Pathway of Crystalline Multimetal Borides for Highly Efficient Oxygen-Evolving Electrocatalysts. *J. Mater. Chem. A* **2022**, *10*, 1569−1578.
(124) Tripathy, R. K.; Samantara, A. K.; Behera, J. N. Electrochemically Activated Co-Prussian Blue Analogue Derived Amorphous CoB Nanostructures: An Efficient Electrocatalyst for the Oxygen Evolution Reaction. *Dalton Trans.* **2022**, *51*, 2782−2788.

(125) Zhao, Y.; Ma, F.; Wang, Z.; Wang, P.; Liu, Y.; Cheng, H.; Dai, Y.; Zheng, Z.; Huang, B. Borate-Modulated Amorphous NiFeB Nanocatalysts as Highly Active and Stable Electrocatalysts for Oxygen Evolution Reaction. *J. Alloys Compd.* **2022**, *903*, 163741.
(126) Sun, Y.; Zhao, Y.; Deng, X.; Dai, D.; Gao, H. An Efficient Amorphous Ternary Transition Metal Boride (WFeNiB) Electrocatalyst for Oxygen Evolution from Water. *Sustain. Energy Fuels* **2022**, *6*, 1345−1352.
(127) Patil, K.; Babar, P.; Li, X.; Karade, V.; Kim, S.; Jang, S. Y.; Bhoite, P.; Kim, J. H. Co-Fe-B Nanochain Electrocatalysts for Oxygen Evolution at High Current Density. *ACS Appl. Nano Mater.* **2022**, *5*, 6260−6267.
(128) Wang, S.; Zhao, R.; Zheng, T.; Fang, Y.; Wang, W.; Xue, W. Metal-Organic Framework-Derived Self-Supporting Metal Boride for Efficient Electrocatalytic Oxygen Evolution Reaction. *J. Colloid. Interface Sci.* **2022**, *618*, 34−43.
(129) Wang, N.; Xu, A.; Ou, P.; Hung, S.-F.; Ozden, A.; Lu, Y.-R.; Abed, J.; Wang, Z.; Yan, Y.; Sun, M.-J.; et al. Boride-Derived Oxygen-Evolution Catalysts. *Nat. Commun.* **2021**, *12*, 6089.
(130) Schuch, J.; Klemenz, S.; Schuldt, P.; Zieschang, A.-M.; Dolique, S.; Connor, P.; Kaiser, B.; Kramm, U. I.; Albert, B.; Jaegermann, W. Efficient Oxygen Evolution Electrocatalyst by Incorporation of Nickel into Nanoscale Dicobalt Boride. *ChemCatChem* **2021**, *13*, 1772−1780.
(131) Hong, Y.-R.; Kim, K. M.; Ryu, J. H.; Mhin, S.; Kim, J.; Ali, G.; Chung, K. Y.; Kang, S.; Han, H. Dual-Phase Engineering of Nickel Boride-Hydroxide Nanoparticles toward High-Performance Water Oxidation Electrocatalysts. *Adv. Funct. Mater.* **2020**, *30*, 2004330.
(132) Liu, Q.; Zhao, H.; Jiang, M.; Kang, Q.; Zhou, W.; Wang, P.; Zhou, F. Boron Enhances Oxygen Evolution Reaction Activity over Ni Foam-Supported Iron Boride Nanowires. *J. Mater. Chem. A* **2020**, *8*, 13638−13645.
(133) ul Haq, T.; Mansour, S. A.; Munir, A.; Haik, Y. Gold-Supported Gadolinium Doped CoB Amorphous Sheet: A New Benchmark Electrocatalyst for Water Oxidation with High Turnover Frequency. *Adv. Funct. Mater.* **2020**, *30*, 1910309.
(134) Lao, J.; Li, D.; Jiang, C.; Luo, R.; Peng, H.; Qi, R.; Lin, H.; Huang, R.; Waterhouse, G. I. N.; Luo, C. Efficient Overall Water Splitting Using Nickel Boride-Based Electrocatalysts. *Int. J. Hydrog. Energy* **2020**, *45*, 28616−28625.
(135) Yuan, H.; Wei, S.; Tang, B.; Ma, Z.; Li, J.; Kundu, M.; Wang, X. Self-Supported 3 D Ultrathin Cobalt-Nickel-Boron Nanoflakes as an Efficient Electrocatalyst for the Oxygen Evolution Reaction. *ChemSusChem* **2020**, *13*, 3662−3670.
(136) Han, P.; Tan, T.; Wu, F.; Cai, P.; Cheng, G.; Luo, W. Nickel-Iron Borate Coated Nickel-Iron Boride Hybrid for Highly Stable and Active Oxygen Evolution Electrocatalysis. *Chin. Chem. Lett.* **2020**, *31*, 2469−2472.
(137) Chen, X.; Yu, Z.; Wei, L.; Zhou, Z.; Zhai, S.; Chen, J.; Wang, Y.; Huang, Q.; Karahan, H. E.; Liao, X.; et al. Ultrathin Nickel Boride Nanosheets Anchored on Functionalized Carbon Nanotubes as Bifunctional Electrocatalysts for Overall Water Splitting. *J. Mater. Chem. A* **2019**, *7*, 764−774.
(138) Masa, J.; Andronescu, C.; Antoni, H.; Sinev, I.; Seisel, S.; Elumeeva, K.; Barwe, S.; Marti-Sanchez, S.; Arbiol, J.; Roldan Cuenya, B.; Muhler, M.; Schuhmann, W. Role of Boron and Phosphorus in Enhanced Electrocatalytic Oxygen Evolution by Nickel Borides and Nickel Phosphides. *ChemElectroChem* **2019**, *6*, 235−240.
(139) Sun, J.; Zhang, W.; Wang, S.; Ren, Y.; Liu, Q.; Sun, Y.; Tang, L.; Guo, J.; Zhang, X. Ni-Co-B Nanosheets Coupled with Reduced Graphene Oxide towards Enhanced Electrochemical Oxygen Evolution. *J. Alloys Compd.* **2019**, *776*, 511−518.
(140) Li, J.; Chen, H.; Liu, Y.; Gao, R.; Zou, X. In Situ Structural Evolution of a Nickel Boride Catalyst: Synergistic Geometric and Electronic Optimization for the Oxygen Evolution Reaction. *J. Mater. Chem. A* **2019**, *7*, 5288−5294.
(141) Guo, F.; Wu, Y.; Chen, H.; Liu, Y.; Yang, L.; Ai, X.; Zou, X. High-Performance Oxygen Evolution Electrocatalysis by Boronized Metal Sheets with Self-Functionalized Surfaces. *Energy Environ. Sci.* **2019**, *12*, 684−692.
(142) Han, H.; Hong, Y.-R.; Woo, J.; Mhin, S.; Kim, K. M.; Kwon, J.; Choi, H.; Chung, Y.-C.; Song, T. Electronically Double-Layered Metal Boride Hollow Nanoprism as an Excellent and Robust Water Oxidation Electrocatalysts. *Adv. Energy Mater.* **2019**, *9*, 1803799.
(143) Zieschang, A.-M.; Bocarsly, J. D.; Schuch, J.; Reichel, C. V.; Kaiser, B.; Jaegermann, W.; Seshadri, R.; Albert, B. Magnetic and Electrocatalytic Properties of Nanoscale Cobalt Boride, Co_3B. *Inorg. Chem.* **2019**, *58*, 16609−16617.
(144) Yuan, H.; Wang, S.; Gu, X.; Tang, B.; Li, J.; Wang, X. One-Step Solid-Phase Boronation to Fabricate Self-Supported Porous FeNiB/FeNi Foam for Efficient Electrocatalytic Oxygen Evolution and Overall Water Splitting. *J. Mater. Chem. A* **2019**, *7*, 19554−19564.
(145) Nsanzimana, J. M. V.; Dangol, R.; Reddu, V.; Duo, S.; Peng, Y.; Dinh, K. N.; Huang, Z.; Yan, Q.; Wang, X. Facile Synthesis of Amorphous Ternary Metal Borides-Reduced Graphene Oxide Hybrid with Superior Oxygen Evolution Activity. *ACS Appl. Mater. Interfaces* **2019**, *11*, 846−855.
(146) Kirshenbaum, M. J.; Richter, M. H.; Dasog, M. Electrochemical Water Oxidation in Acidic Solution Using Titanium Diboride (TiB_2) Catalyst. *ChemCatChem* **2019**, *11*, 3877−3881.
(147) Gupta, S.; Jadhav, H.; Sinha, S.; Miotello, A.; Patel, M. K.; Sarkar, A.; Patel, N. Cobalt-Boride Nanostructured Thin Films with High Performance and Stability for Alkaline Water Oxidation. *ACS Sustainable Chem. Eng.* **2019**, *7*, 16651−16658.
(148) Zhang, J.; Li, X.; Liu, Y.; Zeng, Z.; Cheng, X.; Wang, Y.; Tu, W.; Pan, M. Bimetallic Boride Electrocatalysts with Enhanced Activity for the Oxygen Evolution Reaction. *Nanoscale* **2018**, *10*, 11997−12002.
(149) Nsanzimana, J. M. V.; Reddu, V.; Peng, Y.; Huang, Z.; Wang, C.; Wang, X. Ultrathin Amorphous Iron-Nickel Boride Nanosheets for Highly Efficient Electrocatalytic Oxygen Production. *Chem.—Eur. J.* **2018**, *24*, 18502−18511.
(150) Nsanzimana, J. M. V.; Peng, Y.; Xu, Y. Y.; Thia, L.; Wang, C.; Xia, B. Y.; Wang, X. An Efficient and Earth-Abundant Oxygen-Evolving Electrocatalyst Based on Amorphous Metal Borides. *Adv. Energy Mater.* **2018**, *8*, 1701475.
(151) Liang, X.; Dong, R.; Li, D.; Bu, X.; Li, F.; Shu, L.; Wei, R.; Ho, J. C. Coupling of Nickel Boride and $Ni(OH)_2$ Nanosheets with Hierarchical Interconnected Conductive Porous Structure Synergizes the Oxygen Evolution Reaction. *ChemCatChem* **2018**, *10*, 4555−4561.
(152) Klemenz, S.; Schuch, J.; Hawel, S.; Zieschang, A.-M.; Kaiser, B.; Jaegermann, W.; Albert, B. Synthesis of a Highly Efficient Oxygen-Evolution Electrocatalyst by Incorporation of Iron into Nanoscale Cobalt Borides. *ChemSusChem* **2018**, *11*, 3150−3156.
(153) Hao, W.; Wu, R.; Zhang, R.; Ha, Y.; Chen, Z.; Wang, L.; Yang, Y.; Ma, X.; Sun, D.; Fang, F.; et al. Electroless Plating of Highly Efficient Bifunctional Boride-Based Electrodes toward Practical Overall Water Splitting. *Adv. Energy Mater.* **2018**, *8*, 1801372.
(154) Chen, Z.; Kang, Q.; Cao, G.; Xu, N.; Dai, H.; Wang, P. Study of Cobalt Boride-Derived Electrocatalysts for Overall Water Splitting. *Int. J. Hydrog. Energy* **2018**, *43*, 6076−6087.
(155) Xu, N.; Cao, G.; Chen, Z.; Kang, Q.; Dai, H.; Wang, P. Cobalt Nickel Boride as an Active Electrocatalyst for Water Splitting. *J. Mater. Chem. A* **2017**, *5*, 12379−12384.
(156) Ma, X.; Wen, J.; Zhang, S.; Yuan, H.; Li, K.; Yan, F.; Zhang, X.; Chen, Y. Crystal Co_xB (x = 1-3) Synthesized by a Ball-Milling Method as High-Performance Electrocatalysts for the Oxygen Evolution Reaction. *ACS Sustainable Chem. Eng.* **2017**, *5*, 10266−10274.
(157) Lu, W.; Liu, T.; Xie, L.; Tang, C.; Liu, D.; Hao, S.; Qu, F.; Du, G.; Ma, Y.; Asiri, A. M.; et al. In Situ Derived Co-B Nanoarray: A High-Efficiency and Durable 3D Bifunctional Electrocatalyst for Overall Alkaline Water Splitting. *Small* **2017**, *13*, 1700805.
(158) Li, H.; Wen, P.; Li, Q.; Dun, C.; Xing, J.; Lu, C.; Adhikari, S.; Jiang, L.; Carroll, D. L.; Geyer, S. M. Earth-Abundant Iron Diboride

https://doi.org/10.1021/acs.chemrev.3c00005
Chem. Rev. 2023, 123, 12795−13208

(FeB_2) Nanoparticles as Highly Active Bifunctional Electrocatalysts for Overall Water Splitting. *Adv. Energy Mater.* **2017**, *7*, 1700513.
(159) Jiang, J.; Wang, M.; Yan, W.; Liu, X.; Liu, J.; Yang, J.; Sun, L. Highly Active and Durable Electrocatalytic Water Oxidation by a $NiB_{0.45}/NiO_x$ Core-Shell Heterostructured Nanoparticulate Film. *Nano Energy* **2017**, *38*, 175−184.
(160) Gupta, S.; Patel, N.; Fernandes, R.; Hanchate, S.; Miotello, A.; Kothari, D. C. Co-Mo-B Nanoparticles as a Non-Precious and Efficient Bifunctional Electrocatalyst for Hydrogen and Oxygen Evolution. *Electrochim. Acta* **2017**, *232*, 64−71.
(161) Elumeeva, K.; Masa, J.; Medina, D.; Ventosa, E.; Seisel, S.; Kayran, Y. U.; Genç, A.; Bobrowski, T.; Weide, P.; Arbiol, J.; et al. Cobalt Boride Modified with N-Doped Carbon Nanotubes as a High-Performance Bifunctional Oxygen Electrocatalyst. *J. Mater. Chem. A* **2017**, *5*, 21122−21129.
(162) Chen, H.; Ouyang, S.; Zhao, M.; Li, Y.; Ye, J. Synergistic Activity of Co and Fe in Amorphous Cox-Fe-B Catalyst for Efficient Oxygen Evolution Reaction. *ACS Appl. Mater. Interfaces* **2017**, *9*, 40333−40343.
(163) Masa, J.; Weide, P.; Peeters, D.; Sinev, I.; Xia, W.; Sun, Z.; Somsen, C.; Muhler, M.; Schuhmann, W. Amorphous Cobalt Boride (Co_2B) as a Highly Efficient Nonprecious Catalyst for Electrochemical Water Splitting: Oxygen and Hydrogen Evolution. *Adv. Energy Mater.* **2016**, *6*, 1502313.
(164) Wang, L.; Li, J.; Zhao, X.; Hao, W.; Ma, X.; Li, S.; Guo, Y. Surface-Activated Amorphous Iron Borides (Fe_xB) as Efficient Electrocatalysts for Oxygen Evolution Reaction. *Adv. Mater. Interfaces* **2019**, *6*, 1801690.
(165) Yuan, W.; Zhao, X.; Hao, W.; Li, J.; Wang, L.; Ma, X.; Guo, Y. Performance of Surface-Oxidized Ni_3B, Ni_2B, and NiB_2 Electrocatalysts for Overall Water Splitting. *ChemElectroChem* **2019**, *6*, 764−770.
(166) Tan, T.; Han, P.; Cong, H.; Cheng, G.; Luo, W. An Amorphous Cobalt Borate Nanosheet-Coated Cobalt Boride Hybrid for Highly Efficient Alkaline Water Oxidation Reaction. *ACS Sustainable Chem. Eng.* **2019**, *7*, 5620−5625.
(167) Jiang, W.-J.; Niu, S.; Tang, T.; Zhang, Q.-H.; Liu, X.-Z.; Zhang, Y.; Chen, Y.-Y.; Li, J.-H.; Gu, L.; Wan, L.-J.; Hu, J.-S. Crystallinity-Modulated Electrocatalytic Activity of a Nickel(II) Borate Thin Layer on Ni_3B for Efficient Water Oxidation. *Angew. Chem. Int. Ed.* **2017**, *56*, 6572−6577.
(168) Ding, J.; Yue, R.; Zhu, X.; Liu, W.; Pei, H.; He, S.; Mo, Z. Flower-like Co3Ni1B Nanosheets Based on Reduced Graphene Oxide (RGO) as an Efficient Electrocatalyst for the Oxygen Evolution Reaction. *New J. Chem.* **2022**, *46*, 13524−13532.
(169) Wang, X.; He, Q.; Ge, Q.; Fu, T.; Chen, S.; Zhou, P.; Xiao, F.; He, P.; Jia, L.; Jia, B.; et al. Self-Assembled Nanocotton-like Co-B-P/Bacterial Cellulose Based Carbon Nanofiber as Highly Efficient Electrocatalyst for Oxygen Evolution Reaction. *Int. J. Hydrog. Energy* **2021**, *46*, 20930−20940.
(170) Chen, Z.; Zheng, R.; Graś, M.; Wei, W.; Lota, G.; Chen, H.; Ni, B.-J. Tuning Electronic Property and Surface Reconstruction of Amorphous Iron Borides via W-P Co-Doping for Highly Efficient Oxygen Evolution. *Appl. Catal. B: Environ.* **2021**, *288*, 120037.
(171) Jokar, A.; Toghraei, A.; Maleki, M.; Barati Darband, Gh. Facile Electrochemical Synthesis of Ni-Co-B Film on Cu Sheet for Dual-Electrocatalysis of Hydrogen and Oxygen Evolution Reactions. *Electrochim. Acta* **2021**, *389*, 138691.
(172) Li, Y.; Jiang, X.; Tang, M.; Zheng, Q.; Huo, Y.; Xie, F.; Lin, D. A High-Performance Oxygen Evolution Electrocatalyst Based on Partially Amorphous Bimetallic Cobalt Iron Boride Nanosheet. *Int. J. Hydrog. Energy* **2020**, *45*, 28586−28597.
(173) Wang, X.; Zhou, L.; Yang, T.; Gao, J.; He, P.; Jia, L.; Dong, F.; Jia, B.; Zhang, H. Facile One-Step Synthesis of Tunable Nanochain-like Fe-Mo-B: A Highly Efficient and Stable Catalyst for Oxygen Evolution Reaction. *J. Alloys Compd.* **2020**, *822*, 153517.
(174) Sukanya, R.; Chen, S.-M. Amorphous Cobalt Boride Nanosheets Anchored Surface-Functionalized Carbon Nanofiber: An Bifunctional and Efficient Catalyst for Electrochemical Sensing and Oxygen Evolution Reaction. *J. Colloid. Interface Sci.* **2020**, *580*, 318−331.
(175) Wang, S.; He, P.; Xie, Z.; Jia, L.; He, M.; Zhang, X.; Dong, F.; Liu, H.; Zhang, Y.; Li, C. Tunable Nanocotton-like Amorphous Ternary Ni-Co-B: A Highly Efficient Catalyst for Enhanced Oxygen Evolution Reaction. *Electrochim. Acta* **2019**, *296*, 644−652.
(176) Nsanzimana, J. M. V.; Gong, L.; Dangol, R.; Reddu, V.; Jose, V.; Xia, B. Y.; Yan, Q.; Lee, J.-M.; Wang, X. Tailoring of Metal Boride Morphology via Anion for Efficient Water Oxidation. *Adv. Energy Mater.* **2019**, *9*, 1901503.
(177) Masa, J.; Piontek, S.; Wilde, P.; Antoni, H.; Eckhard, T.; Chen, Y.-T.; Muhler, M.; Apfel, U.-P.; Schuhmann, W. Ni-Metalloid (B, Si, P, As, and Te) Alloys as Water Oxidation Electrocatalysts. *Adv. Energy Mater.* **2019**, *9*, 1900796.
(178) Li, Y.; Huang, B.; Sun, Y.; Luo, M.; Yang, Y.; Qin, Y.; Wang, L.; Li, C.; Lv, F.; Zhang, W.; et al. Multimetal Borides Nanochains as Efficient Electrocatalysts for Overall Water Splitting. *Small* **2019**, *15*, 1804212.
(179) Wu, Z.; Nie, D.; Song, M.; Jiao, T.; Fu, G.; Liu, X. Facile Synthesis of Co-Fe-B-P Nanochains as an Efficient Bifunctional Electrocatalyst for Overall Water-Splitting. *Nanoscale* **2019**, *11*, 7506−7512.
(180) Mann, D. K.; Xu, J.; Mordvinova, N. E.; Yannello, V.; Ziouani, Y.; González-Ballesteros, N.; Sousa, J. P.; Lebedev, O. I.; Kolen'ko, Y. V.; Shatruk, M. Electrocatalytic Water Oxidation over $AlFe_2B_2$. *Chem. Sci.* **2019**, *10*, 2796−2804.
(181) Jiang, Y.; Fang, Y.; Chen, C.; Ni, P.; Kong, B.; Song, Z.; Lu, Y.; Niu, L. Amorphous Cobalt Boride Nanosheets Directly Grown on Nickel Foam: Controllable Alternately Dipping Deposition for Efficient Oxygen Evolution. *ChemElectroChem* **2019**, *6*, 3684−3689.
(182) Chunduri, A.; Gupta, S.; Bapat, O.; Bhide, A.; Fernandes, R.; Patel, M. K.; Bambole, V.; Miotello, A.; Patel, N. A Unique Amorphous Cobalt-Phosphide-Boride Bifunctional Electrocatalyst for Enhanced Alkaline Water-Splitting. *Appl. Catal. B: Environ.* **2019**, *259*, 118051.
(183) Barwe, S.; Andronescu, C.; Engels, R.; Conzuelo, F.; Seisel, S.; Wilde, P.; Chen, Y.-T.; Masa, J.; Schuhmann, W. Cobalt Metalloid and Polybenzoxazine Derived Composites for Bifunctional Oxygen Electrocatalysis. *Electrochim. Acta* **2019**, *297*, 1042−1051.
(184) Weidner, J.; Barwe, S.; Sliozberg, K.; Piontek, S.; Masa, J.; Apfel, U.-P.; Schuhmann, W. Cobalt-Metalloid Alloys for Electrochemical Oxidation of 5-Hydroxymethylfurfural as an Alternative Anode Reaction in Lieu of Oxygen Evolution during Water Splitting. *Beilstein J. Org. Chem.* **2018**, *14*, 1436−1445.
(185) Li, Y.; Xu, H.; Huang, H.; Gao, L.; Zhao, Y.; Ma, T. Synthesis of Co-B in Porous Carbon Using a Metal-Organic Framework (MOF) Precursor: A Highly Efficient Catalyst for the Oxygen Evolution Reaction. *Electrochem. Commun.* **2018**, *86*, 140−144.
(186) Arivu, M.; Masud, J.; Umapathi, S.; Nath, M. Facile Synthesis of Ni_3B/RGO Nanocomposite as an Efficient Electrocatalyst for the Oxygen Evolution Reaction in Alkaline Media. *Electrochem. Commun.* **2018**, *86*, 121−125.
(187) An, L.; Sun, Y.; Zong, Y.; Liu, Q.; Guo, J.; Zhang, X. Nickel Iron Boride Nanosheets on RGO for Active Electrochemical Water Oxidation. *J. Solid State Chem.* **2018**, *265*, 135−139.
(188) Yang, Y.; Zhuang, L.; Rufford, T. E.; Wang, S.; Zhu, Z. Efficient Water Oxidation with Amorphous Transition Metal Boride Catalysts Synthesized by Chemical Reduction of Metal Nitrate Salts at Room Temperature. *RSC Adv.* **2017**, *7*, 32923−32930.
(189) Xu, S.; Chen, Y.; Li, Y.; Lu, A.; Yao, Y.; Dai, J.; Wang, Y.; Liu, B.; Lacey, S. D.; Pastel, G. R.; et al. Universal, In Situ Transformation of Bulky Compounds into Nanoscale Catalysts by High-Temperature Pulse. *Nano Lett.* **2017**, *17*, 5817−5822.
(190) Cao, G.-X.; Xu, N.; Chen, Z.-J.; Kang, Q.; Dai, H.-B.; Wang, P. Cobalt-Tungsten-Boron as an Active Electrocatalyst for Water Electrolysis. *ChemistrySelect* **2017**, *2*, 6187−6193.
(191) Eßmann, V.; Barwe, S.; Masa, J.; Schuhmann, W. Bipolar Electrochemistry for Concurrently Evaluating the Stability of Anode and Cathode Electrocatalysts and the Overall Cell Performance

https://doi.org/10.1021/acs.chemrev.3c00005
Chem. Rev. 2023, 123, 12795−13208

during Long-Term Water Electrolysis. *Anal. Chem.* **2016**, *88*, 8835−8840.
(192) Lavrenko, V. A.; Yagupol'skaya, L. N.; Kuznetsova, L. I. Kinetics of Electrolytic Hydrogen Evolution at Some Transition Metal Borides. *Ehlektrokhimiya* **1974**, *10*, 1078−1081.
(193) Osaka, T.; Ishibashi, H.; Endo, T.; Yoshida, T. Oxygen Evolution Reaction on Transition Metal Borides. *Electrochim. Acta* **1981**, *26*, 339−343.
(194) Osaka, T.; Iwase, Y.; Kitayama, H.; Ichino, T. Oxygen Evolution Reaction on Composite Cobalt Borides. *BCSJ.* **1983**, *56*, 2106−2111.
(195) Tripathy, R. K.; Samantara, A. K.; Behera, J. N. Metal-Organic Framework (MOF)-Derived Amorphous Nickel Boride: An Electroactive Material for Electrochemical Energy Conversion and Storage Application. *Sustain. Energy Fuels* **2021**, *5*, 1184−1193.
(196) Koczkur, K. M.; Mourdikoudis, S.; Polavarapu, L.; Skrabalak, S. E. Polyvinylpyrrolidone (PVP) in Nanoparticle Synthesis. *Dalton Trans.* **2015**, *44*, 17883−17905.
(197) Arzac, G. M.; Rojas, T. C.; Fernández, A. Boron Compounds as Stabilizers of a Complex Microstructure in a Co-B-Based Catalyst for $NaBH_4$ Hydrolysis. *ChemCatChem* **2011**, *3*, 1305−1313.
(198) Liang, Y.; Wang, H.; Diao, P.; Chang, W.; Hong, G.; Li, Y.; Gong, M.; Xie, L.; Zhou, J.; Wang, J.; et al. Oxygen Reduction Electrocatalyst Based on Strongly Coupled Cobalt Oxide Nanocrystals and Carbon Nanotubes. *J. Am. Chem. Soc.* **2012**, *134*, 15849−15857.
(199) Lončarević, D.; Čupić, Ž. The Perspective of Using Nanocatalysts in the Environmental Requirements and Energy Needs of Industry. In *Industrial Applications of Nanomaterials*; Thomas, S., Grohens, Y., Pottathara, Y. B., Eds.; Micro and Nano Technologies; Elsevier, 2019; Chapter 4, pp 91−122. DOI: 10.1016/B978-0-12-815749-7.00004-9.
(200) Trotochaud, L.; Young, S. L.; Ranney, J. K.; Boettcher, S. W. Nickel-Iron Oxyhydroxide Oxygen-Evolution Electrocatalysts: The Role of Intentional and Incidental Iron Incorporation. *J. Am. Chem. Soc.* **2014**, *136*, 6744−6753.
(201) Fidelsky, V.; Toroker, M. C. Enhanced Water Oxidation Catalysis of Nickel Oxyhydroxide through the Addition of Vacancies. *J. Phys. Chem. C* **2016**, *120*, 25405−25410.
(202) Louie, M. W.; Bell, A. T. An Investigation of Thin-Film Ni-Fe Oxide Catalysts for the Electrochemical Evolution of Oxygen. *J. Am. Chem. Soc.* **2013**, *135*, 12329−12337.
(203) Jiang, J.; Sun, F.; Zhou, S.; Hu, W.; Zhang, H.; Dong, J.; Jiang, Z.; Zhao, J.; Li, J.; Yan, W.; et al. Atomic-Level Insight into Super-Efficient Electrocatalytic Oxygen Evolution on Iron and Vanadium Co-Doped Nickel (Oxy)Hydroxide. *Nat. Commun.* **2018**, *9*, 2885.
(204) Trześniewski, B. J.; Diaz-Morales, O.; Vermaas, D. A.; Longo, A.; Bras, W.; Koper, M. T. M.; Smith, W. A. In Situ Observation of Active Oxygen Species in Fe-Containing Ni-Based Oxygen Evolution Catalysts: The Effect of pH on Electrochemical Activity. *J. Am. Chem. Soc.* **2015**, *137*, 15112−15121.
(205) Subbaraman, R.; Tripkovic, D.; Chang, K.-C.; Strmcnik, D.; Paulikas, A. P.; Hirunsit, P.; Chan, M.; Greeley, J.; Stamenkovic, V.; Markovic, N. M. Trends in Activity for the Water Electrolyser Reactions on 3 d M(Ni,Co,Fe,Mn) Hydr(Oxy)Oxide Catalysts. *Nat. Mater.* **2012**, *11*, 550−557.
(206) Lu, S.; Cao, D.; Xu, X.; Wang, H.; Xiang, Y. Study of Carbon Black Supported Amorphous Ni-B Nano-Catalyst for Hydrazine Electrooxidation in Alkaline Media. *RSC Adv.* **2014**, *4*, 26940−26945.
(207) Burke, M. S.; Kast, M. G.; Trotochaud, L.; Smith, A. M.; Boettcher, S. W. Cobalt-Iron (Oxy)Hydroxide Oxygen Evolution Electrocatalysts: The Role of Structure and Composition on Activity, Stability, and Mechanism. *J. Am. Chem. Soc.* **2015**, *137*, 3638−3648.
(208) Tang, C.; Cheng, N.; Pu, Z.; Xing, W.; Sun, X. NiSe Nanowire Film Supported on Nickel Foam: An Efficient and Stable 3D Bifunctional Electrode for Full Water Splitting. *Angew. Chem. Int. Ed.* **2015**, *54*, 9351−9355.
(209) Chen, R.; Wang, H.-Y.; Miao, J.; Yang, H.; Liu, B. A Flexible High-Performance Oxygen Evolution Electrode with Three-Dimensional $NiCo_2O_4$ Core-Shell Nanowires. *Nano Energy* **2015**, *11*, 333−340.
(210) Umapathi, S.; Masud, J.; Swesi, A. T.; Nath, M. $FeNi_2Se_4$-Reduced Graphene Oxide Nanocomposite: Enhancing Bifunctional Electrocatalytic Activity for Oxygen Evolution and Reduction through Synergistic Effects. *Adv. Sustain. Syst.* **2017**, *1*, 1700086.
(211) Ahn, I.-K.; Lee, S.-Y.; Kim, H. G.; Lee, G.-B.; Lee, J.-H.; Kim, M.; Joo, Y.-C. Electrochemical Oxidation of Boron-Doped Nickel-Iron Layered Double Hydroxide for Facile Charge Transfer in Oxygen Evolution Electrocatalysts. *RSC Adv.* **2021**, *11*, 8198−8206.
(212) Klaus, S.; Cai, Y.; Louie, M. W.; Trotochaud, L.; Bell, A. T. Effects of Fe Electrolyte Impurities on $Ni(OH)_2$/NiOOH Structure and Oxygen Evolution Activity. *J. Phys. Chem. C* **2015**, *119*, 7243−7254.
(213) Son, Y. J.; Kawashima, K.; Wygant, B. R.; Lam, C. H.; Burrow, J. N.; Celio, H.; Dolocan, A.; Ekerdt, J. G.; Mullins, C. B. Anodized Nickel Foam for Oxygen Evolution Reaction in Fe-Free and Unpurified Alkaline Electrolytes at High Current Densities. *ACS Nano* **2021**, *15*, 3468−3480.
(214) Zhang, Y.; Liu, Z.; Guo, F.; Li, M.; Bo, X. Morphological Modulation of Iron Carbide Embedded Nitrogen-Doped Hierarchically Porous Carbon by Manganese Doping as Highly Efficient Bifunctional Electrocatalysts for Overall Water Splitting. *J. Colloid. Interface Sci.* **2022**, *618*, 149−160.
(215) Zhang, J.; Yang, L.; Yuan, W.; Yang, S.; Zhang, W.; Cao, R. CoO_x Supported on α-MoC for Efficient Electrocatalytic Oxygen Evolution Reaction. *ChemElectroChem* **2022**, *9*, No. e202200963.
(216) Zhu, S.; Lei, J.; Zhang, L.; Lu, L. Efficient Electrocatalytic Oxygen Evolution by Fe3C Nanosheets Perpendicularly Grown on 3D Ni Foams. *Int. J. Hydrogen Energy* **2019**, *44*, 16507−16515.
(217) Yang, H.; Luo, S.; Li, X.; Li, S.; Jin, J.; Ma, J. Controllable Orientation-Dependent Crystal Growth of High-Index Faceted Dendritic $NiC_{0.2}$ Nanosheets as High-Performance Bifunctional Electrocatalysts for Overall Water Splitting. *J. Mater. Chem. A* **2016**, *4*, 18499−18508.
(218) Zhang, H.; Geng, S.; Ouyang, M.; Yadegari, H.; Xie, F.; Riley, D. J. A Self-Reconstructed Bifunctional Electrocatalyst of Pseudo-Amorphous Nickel Carbide @ Iron Oxide Network for Seawater Splitting. *Adv. Sci.* **2022**, *9*, 2200146.
(219) Nguyen, E. T.; Bertini, I. A.; Ritz, A. J.; Lazenby, R. A.; Mao, K.; McBride, J. R.; Mattia, A. V.; Kuszynski, J. E.; Wenzel, S. F.; Bennett, S. D.; et al. A Single Source, Scalable Route for Direct Isolation of Earth-Abundant Nanometal Carbide Water-Splitting Electrocatalysts. *Inorg. Chem.* **2022**, *61*, 13836−13845.
(220) Wang, M.; Wang, Y.; Mao, S. S.; Shen, S. Transition-Metal Alloy Electrocatalysts with Active Sites Modulated by Metal-Carbide Heterophases for Efficient Oxygen Evolution. *Nano Energy* **2021**, *88*, 106216.
(221) Kawashima, K.; Cao, C. L.; Li, H.; Márquez-Montes, R. A.; Wygant, B. R.; Son, Y. J.; Guerrera, J. V.; Henkelman, G.; Mullins, C. B. Evaluation of a V_8C_7 Anode for Oxygen Evolution in Alkaline Media: Unusual Morphological Behavior. *ACS Sustainable Chem. Eng.* **2020**, *8*, 14101−14108.
(222) Chen, J.; Ren, B.; Cui, H.; Wang, C. Constructing Pure Phase Tungsten-Based Bimetallic Carbide Nanosheet as an Efficient Bifunctional Electrocatalyst for Overall Water Splitting. *Small* **2020**, *16*, 1907556.
(223) Xu, S.; Wang, M.; Saranya, G.; Chen, N.; Zhang, L.; He, Y.; Wu, L.; Gong, Y.; Yao, Z.; Wang, G.; et al. Pressure-Driven Catalyst Synthesis of Co-Doped Fe_3C@Carbon Nano-Onions for Efficient Oxygen Evolution Reaction. *Appl. Catal. B: Environ.* **2020**, *268*, 118385.
(224) Zu, M. Y.; Wang, C.; Zhang, L.; Zheng, L. R.; Yang, H. G. Reconstructing Bimetallic Carbide Mo_6Ni_6C for Carbon Interconnected MoNi Alloys to Boost Oxygen Evolution Electrocatalysis. *Mater. Horiz.* **2019**, *6*, 115−121.
(225) Xing, J.; Li, Y.; Guo, S.; Jin, T.; Li, H.; Wang, Y.; Jiao, L. Molybdenum Carbide In-Situ Embedded into Carbon Nanosheets as

Efficient Bifunctional Electrocatalysts for Overall Water Splitting. *Electrochim. Acta* **2019**, *298*, 305−312.
(226) Zhu, X.; Zhang, X.; Huang, L.; Liu, Y.; Zhang, H.; Dong, S. Cobalt Doped β-Molybdenum Carbide Nanoparticles Encapsulated within Nitrogen-Doped Carbon for Oxygen Evolution. *Chem. Commun.* **2019**, *55*, 9995−9998.
(227) Zhang, S.; Gao, G.; Hao, J.; Wang, M.; Zhu, H.; Lu, S.; Duan, F.; Dong, W.; Du, M.; Zhao, Y. Low-Electronegativity Vanadium Substitution in Cobalt Carbide Induced Enhanced Electron Transfer for Efficient Overall Water Splitting. *ACS Appl. Mater. Interfaces* **2019**, *11*, 43261−43269.
(228) Kou, Z.; Zhang, L.; Ma, Y.; Liu, X.; Zang, W.; Zhang, J.; Huang, S.; Du, Y.; Cheetham, A. K.; Wang, J. 2D Carbide Nanomeshes and Their Assembling into 3D Microflowers for Efficient Water Splitting. *Appl. Catal. B: Environ.* **2019**, *243*, 678−685.
(229) Das, D.; Santra, S.; Nanda, K. K. In Situ Fabrication of a Nickel/Molybdenum Carbide-Anchored N-Doped Graphene/CNT Hybrid: An Efficient (Pre)Catalyst for OER and HER. *ACS Appl. Mater. Interfaces* **2018**, *10*, 35025−35038.
(230) Kim, M.; Kim, S.; Song, D.; Oh, S.; Chang, K. J.; Cho, E. Promotion of Electrochemical Oxygen Evolution Reaction by Chemical Coupling of Cobalt to Molybdenum Carbide. *Appl. Catal. B: Environ.* **2018**, *227*, 340−348.
(231) Chen, C.; Wu, A.; Yan, H.; Xiao, Y.; Tian, C.; Fu, H. Trapping $[PMo_{12}O_{40}]^{3-}$ Clusters into Pre-Synthesized ZIF-67 toward Mo_xCo_xC Particles Confined in Uniform Carbon Polyhedrons for Efficient Overall Water Splitting. *Chem. Sci.* **2018**, *9*, 4746−4755.
(232) Wang, M.; Dipazir, S.; Lu, P.; Wang, Y.; Yuan, M.; Li, S.; Zhang, G. Synthesis of Polyoxometalates Derived Bifunctional Catalyst towards Efficient Overall Water Splitting in Neutral and Alkaline Medium. *J. Colloid Interface Sci.* **2018**, *532*, 774−781.
(233) Wang, Y.; Wu, W.; Rao, Y.; Li, Z.; Tsubaki, N.; Wu, M. Cation Modulating Electrocatalyst Derived from Bimetallic Metal-Organic Frameworks for Overall Water Splitting. *J. Mater. Chem. A* **2017**, *5*, 6170−6177.
(234) Fan, H.; Yu, H.; Zhang, Y.; Zheng, Y.; Luo, Y.; Dai, Z.; Li, B.; Zong, Y.; Yan, Q. Fe-Doped Ni_3C Nanodots in N-Doped Carbon Nanosheets for Efficient Hydrogen-Evolution and Oxygen-Evolution Electrocatalysis. *Angew. Chem. Int. Ed.* **2017**, *56*, 12566−12570.
(235) Yu, Z.-Y.; Duan, Y.; Gao, M.-R.; Lang, C.-C.; Zheng, Y.-R.; Yu, S.-H. A One-Dimensional Porous Carbon-Supported Ni/Mo_2C Dual Catalyst for Efficient Water Splitting. *Chem. Sci.* **2017**, *8*, 968−973.
(236) Jiang, J.; Liu, Q.; Zeng, C.; Ai, L. Cobalt/Molybdenum Carbide@N-Doped Carbon as a Bifunctional Electrocatalyst for Hydrogen and Oxygen Evolution Reactions. *J. Mater. Chem. A* **2017**, *5*, 16929−16935.
(237) Wang, H.; Cao, Y.; Sun, C.; Zou, G.; Huang, J.; Kuai, X.; Zhao, J.; Gao, L. Strongly Coupled Molybdenum Carbide on Carbon Sheets as a Bifunctional Electrocatalyst for Overall Water Splitting. *ChemSusChem* **2017**, *10*, 3540−3546.
(238) Barman, B. K.; Nanda, K. K. Prussian Blue as a Single Precursor for Synthesis of Fe/Fe_3C Encapsulated N-Doped Graphitic Nanostructures as Bi-Functional Catalysts. *Green Chem.* **2016**, *18*, 427−432.
(239) Xu, K.; Ding, H.; Lv, H.; Chen, P.; Lu, X.; Cheng, H.; Zhou, T.; Liu, S.; Wu, X.; Wu, C.; et al. Dual Electrical-Behavior Regulation on Electrocatalysts Realizing Enhanced Electrochemical Water Oxidation. *Adv. Mater.* **2016**, *28*, 3326−3332.
(240) Feng, M.; Huang, J.; Peng, Y.; Huang, C.; Yue, X.; Huang, S. Tuning Electronic Structures of Transition Metal Carbides to Boost Oxygen Evolution Reactions in Acidic Medium. *ACS Nano* **2022**, *16*, 13834−13844.
(241) Choi, M.; Lee, S.; Jang, D.; Park, S. Production of Fe_3C/N-Doped Carbon Hybrid and Its Electrocatalytic Performance for Oxygen Evolution Reactions. *Carbon Lett.* **2022**, *32*, 885−892.
(242) Lin, X.; Cao, S.; Chen, H.; Chen, X.; Wang, Z.; Zhou, S.; Xu, H.; Liu, S.; Wei, S.; Lu, X. Boosting Oxygen Evolution Reaction of Hierarchical Spongy NiFe-PBA/Ni_3C(B) Electrocatalyst: Interfacial Engineering with Matchable Structure. *Chem. Eng. J.* **2022**, *433*, 133524.
(243) Wang, B.; Ai, Y.; Yao, Y.; Jiang, M.; Yan, L.; Xu, S.; Sun, W. Electrochemical Synergy between FeNi Nanoalloy@tungsten Carbide on N-Doped Graphitized Carbon Layers as an Excellent Electrocatalyst for Oxygen Evolution Reaction. *Electrochim. Acta* **2022**, *415*, 140254.
(244) Lu, S.; Wu, J.; Hu, H.; Pan, X.; Hu, Z.; Li, H.; Zhu, H.; Duan, F.; Du, M. Boosting Oxygen Evolution through Phase and Electronic Modulation of Highly Dispersed Tungsten Carbide with Nickel Doping. *J. Colloid. Interface Sci.* **2021**, *585*, 258−266.
(245) Wu, Y.; Xiao, Z.; Jin, Z.; Li, X.; Chen, Y. The Cobalt Carbide/Bimetallic CoFe Phosphide Dispersed on Carbon Nanospheres as Advanced Bifunctional Electrocatalysts for the ORR, OER, and Rechargeable Zn-Air Batteries. *J. Colloid. Interface Sci.* **2021**, *590*, 321−329.
(246) Liu, S.; Lin, Z.; Wan, R.; Liu, Y.; Liu, Z.; Zhang, S.; Zhang, X.; Tang, Z.; Lu, X.; Tian, Y. Cobalt Phosphide Supported by Two-Dimensional Molybdenum Carbide (MXene) for the Hydrogen Evolution Reaction, Oxygen Evolution Reaction, and Overall Water Splitting. *J. Mater. Chem. A* **2021**, *9*, 21259−21269.
(247) Guo, Y.; Huang, Q.; Ding, J.; Zhong, L.; Li, T.-T.; Pan, J.; Hu, Y.; Qian, J.; Huang, S. CoMo Carbide/Nitride from Bimetallic MOF Precursors for Enhanced OER Performance. *Int. J. Hydrog. Energy* **2021**, *46*, 22268−22276.
(248) Rabi, O.; Pervaiz, E.; Ali, M.; Zahra, R. Bifunctional Molybdenum Carbide Based Hybrids for Electrocatalytic Water Splitting. *Ceram. Int.* **2021**, *47*, 24949−24958.
(249) Abbas, S. A.; Ma, A.; Seo, D.; Jung, H.; Lim, Y. J.; Mehmood, A.; Nam, K. M. Synthesis of Fe_3C@C Core-Shell Catalysts with Controlled Shell Composition for Robust Oxygen Evolution Reaction. *Appl. Surf. Sci.* **2021**, *551*, 149445.
(250) Kim, J.; Lee, D. H.; Yang, Y.; Chen, K.; Liu, C.; Kang, J.; Li, O. L. Hybrid Molybdenum Carbide/Heteroatom-Doped Carbon Electrocatalyst for Advanced Oxygen Evolution Reaction in Hydrogen Production. *Catalysts* **2020**, *10*, 1290.
(251) Zakaria, M. B.; Zheng, D.; Apfel, U.; Nagata, T.; Kenawy, E.-R. S.; Lin, J. Dual-Heteroatom-Doped Reduced Graphene Oxide Sheets Conjoined CoNi-Based Carbide and Sulfide Nanoparticles for Efficient Oxygen Evolution Reaction. *ACS Appl. Mater. Interfaces* **2020**, *12*, 40186−40193.
(252) Kohila Rani, K.; Karuppiah, C.; Wang, S.-F.; Alaswad, S. O.; Sireesha, P.; Devasenathipathy, R.; Jose, R.; Yang, C.-C. Direct Pyrolysis and Ultrasound Assisted Preparation of N, S Co-Doped Graphene/Fe_3C Nanocomposite as an Efficient Electrocatalyst for Oxygen Reduction and Oxygen Evolution Reactions. *Ultrason. Sonochem.* **2020**, *66*, 105111.
(253) Feng, X.; Bo, X.; Guo, L. An Advanced Hollow Bimetallic Carbide/Nitrogen-Doped Carbon Nanotube for Efficient Catalysis of Oxygen Reduction and Hydrogen Evolution and Oxygen Evolution Reaction. *J. Colloid. Interface Sci.* **2020**, *575*, 69−77.
(254) Dong, T.; Zhang, X.; Cao, Y.; Chen, H.-S.; Yang, P. Ni/Ni_3C Core-Shell Nanoparticles Encapsulated in N-Doped Bamboo-like Carbon Nanotubes towards Efficient Overall Water Splitting. *Inorg. Chem. Front.* **2019**, *6*, 1073−1080.
(255) Tiwari, A. P.; Yoon, Y.; Novak, T. G.; Azam, A.; Lee, M.; Lee, S. S.; Lee, G.; Srolovitz, D. J.; An, K.-S.; Jeon, S. Lattice Strain Formation through Spin-Coupled Shells of MoS_2 on Mo_2C for Bifunctional Oxygen Reduction and Oxygen Evolution Reaction Electrocatalysts. *Adv. Mater. Interfaces* **2019**, *6*, 1900948.
(256) Kou, Z.; Wang, T.; Gu, Q.; Xiong, M.; Zheng, L.; Li, X.; Pan, Z.; Chen, H.; Verpoort, F.; Cheetham, A. K.; et al. Rational Design of Holey 2D Nonlayered Transition Metal Carbide/Nitride Heterostructure Nanosheets for Highly Efficient Water Oxidation. *Adv. Energy Mater.* **2019**, *9*, 1803768.
(257) Xing, J.; Lin, F.; Huang, L.; Si, Y.; Wang, Y.; Jiao, L. Coupled Cobalt-Doped Molybdenum Carbide@N-Doped Carbon Nanosheets/Nanotubes Supported on Nickel Foam as a Binder-Free

https://doi.org/10.1021/acs.chemrev.3c00005
Chem. Rev. 2023, 123, 12795−13208

Electrode for Overall Water Splitting. *Chin. J. Catal.* **2019**, *40*, 1352−1359.
(258) Li, Z.; Gao, Q.; Liang, X.; Zhang, H.; Xiao, H.; Xu, P.; Liu, Z. Low Content of Fe_3C Anchored on Fe,N,S-Codoped Graphene-like Carbon as Bifunctional Electrocatalyst for Oxygen Reduction and Oxygen Evolution Reactions. *Carbon* **2019**, *150*, 93−100.
(259) Li, R.; Li, X.; Yu, D.; Li, L.; Yang, G.; Zhang, K.; Ramakrishna, S.; Xie, L.; Peng, S. $Ni_3ZnC_{0.7}$ Nanodots Decorating Nitrogen-Doped Carbon Nanotube Arrays as a Self-Standing Bifunctional Electrocatalyst for Water Splitting. *Carbon* **2019**, *148*, 496−503.
(260) Jia, X.; Wang, M.; Liu, G.; Wang, Y.; Yang, J.; Li, J. Mixed-Metal MOF-Derived Co-Doped Ni_3C/Ni NPs Embedded in Carbon Matrix as an Efficient Electrocatalyst for Oxygen Evolution Reaction. *Int. J. Hydrogen Energy* **2019**, *44*, 24572−24579.
(261) Fang, H.; Huang, T.; Sun, Y.; Kang, B.; Liang, D.; Yao, S.; Yu, J.; Dinesh, M. M.; Wu, S.; Lee, J. Y.; et al. Metal-Organic Framework-Derived Core-Shell-Structured Nitrogen-Doped CoC_x/FeCo@C Hybrid Supported by Reduced Graphene Oxide Sheets as High Performance Bifunctional Electrocatalysts for ORR and OER. *J. Catal.* **2019**, *371*, 185−195.
(262) Geng, S.; Yang, W.; Yu, Y. Fabrication of NiC/MoC/$NiMoO_4$ Heterostructured Nanorod Arrays as Stable Bifunctional Electrocatalysts for Efficient Overall Water Splitting. *Chem.—Asian J.* **2019**, *14*, 1013−1020.
(263) Zhao, T.; Gao, J.; Wu, J.; He, P.; Li, Y.; Yao, J. Highly Active Cobalt/Tungsten Carbide@N-Doped Porous Carbon Nanomaterials Derived from Metal-Organic Frameworks as Bifunctional Catalysts for Overall Water Splitting. *Energy Technol.* **2019**, *7*, 1800969.
(264) Chen, X.; Xu, J.; Chai, H.; Wang, Y.; Jia, D.; Zhou, W. One-Step Synthesis of Hollow Chain-like Nitrogen Doped Carbon Nanotubes/Iron Carbide as Highly Efficient Bifunctional Oxygen Electrocatalyst. *J. Electroanal. Chem.* **2019**, *838*, 16−22.
(265) Xing, X.; Liu, R.; Cao, K.; Kaiser, U.; Streb, C. Transition-Metal Oxides/Carbides@Carbon Nanotube Composites as Multifunctional Electrocatalysts for Challenging Oxidations and Reductions. *Chem.—Eur. J.* **2019**, *25*, 11098−11104.
(266) Najafi, L.; Bellani, S.; Oropesa-Nuñez, R.; Prato, M.; Martín-García, B.; Brescia, R.; Bonaccorso, F. Carbon Nanotube-Supported $MoSe_2$ Holey Flake:Mo_2C Ball Hybrids for Bifunctional pH-Universal Water Splitting. *ACS Nano* **2019**, *13*, 3162−3176.
(267) Zhang, Y.; Zai, J.; He, K.; Qian, X. Fe_3C Nanoparticles Encapsulated in Highly Crystalline Porous Graphite: Salt-Template Synthesis and Enhanced Electrocatalytic Oxygen Evolution Activity and Stability. *Chem. Commun.* **2018**, *54*, 3158−3161.
(268) Qin, Q.; Hao, J.; Zheng, W. Ni/Ni_3C Core/Shell Hierarchical Nanospheres with Enhanced Electrocatalytic Activity for Water Oxidation. *ACS Appl. Mater. Interfaces* **2018**, *10*, 17827−17834.
(269) Han, N.; Yang, K. R.; Lu, Z.; Li, Y.; Xu, W.; Gao, T.; Cai, Z.; Zhang, Y.; Batista, V. S.; Liu, W.; et al. Nitrogen-Doped Tungsten Carbide Nanoarray as an Efficient Bifunctional Electrocatalyst for Water Splitting in Acid. *Nat. Commun.* **2018**, *9*, 924.
(270) Ma, X.; Li, K.; Zhang, X.; Wei, B.; Yang, H.; Liu, L.; Zhang, M.; Zhang, X.; Chen, Y. The Surface Engineering of Cobalt Carbide Spheres through N, B Co-Doping Achieved by Room-Temperature in Situ Anchoring Effects for Active and Durable Multifunctional Electrocatalysts. *J. Mater. Chem. A* **2019**, *7*, 14904−14915.
(271) Ai, L.; Su, J.; Wang, M.; Jiang, J. Bamboo-Structured Nitrogen-Doped Carbon Nanotube Coencapsulating Cobalt and Molybdenum Carbide Nanoparticles: An Efficient Bifunctional Electrocatalyst for Overall Water Splitting. *ACS Sustain. Chem. Eng.* **2018**, *6*, 9912−9920.
(272) Anjum, M. A. R.; Lee, M. H.; Lee, J. S. Boron- and Nitrogen-Codoped Molybdenum Carbide Nanoparticles Imbedded in a BCN Network as a Bifunctional Electrocatalyst for Hydrogen and Oxygen Evolution Reactions. *ACS Catal.* **2018**, *8*, 8296−8305.
(273) Luo, X.; Zhou, Q.; Du, S.; Li, J.; Zhong, J.; Deng, X.; Liu, Y. Porous Co_9S_8/Nitrogen, Sulfur-Doped Carbon@Mo_2C Dual Catalyst for Efficient Water Splitting. *ACS Appl. Mater. Interfaces* **2018**, *10*, 22291−22302.
(274) Zou, H.; He, B.; Kuang, P.; Yu, J.; Fan, K. Metal-Organic Framework-Derived Nickel-Cobalt Sulfide on Ultrathin Mxene Nanosheets for Electrocatalytic Oxygen Evolution. *ACS Appl. Mater. Interfaces* **2018**, *10*, 22311−22319.
(275) Zhang, X.; Huang, L.; Han, Y.; Xu, M.; Dong, S. Nitrogen-Doped Carbon Encapsulating γ-MoC/Ni Heterostructures for Efficient Oxygen Evolution Electrocatalysts. *Nanoscale* **2017**, *9*, 5583−5588.
(276) Tang, Y.-J.; Liu, C.-H.; Huang, W.; Wang, X.-L.; Dong, L.-Z.; Li, S.-L.; Lan, Y.-Q. Bimetallic Carbides-Based Nanocomposite as Superior Electrocatalyst for Oxygen Evolution Reaction. *ACS Appl. Mater. Interfaces* **2017**, *9*, 16977−16985.
(277) Lei, X.; Ye, Z.; Zhao, N.; Lei, F.; Yang, H. Magnetic γ'-Fe_4N/Fe_3C, χ-Fe_5C_2, and θ-Fe_3C by a Simple Route for Application as Electrochemical Catalysts. *Chem.—Eur. J.* **2017**, *23*, 17592−17597.
(278) Zhang, Y.; Wang, Y.; Han, C.; Jia, S.; Zhou, S.; Zang, J. Tungsten-Coated Nano-Boron Carbide as a Non-Noble Metal Bifunctional Electrocatalyst for Oxygen Evolution and Hydrogen Evolution Reactions in Alkaline Media. *Nanoscale* **2017**, *9*, 19176−19182.
(279) Su, J.; Xia, G.; Li, R.; Yang, Y.; Chen, J.; Shi, R.; Jiang, P.; Chen, Q. Co_3ZnC/Co Nano Heterojunctions Encapsulated in N-Doped Graphene Layers Derived from PBAs as Highly Efficient Bi-Functional OER and ORR Electrocatalysts. *J. Mater. Chem. A* **2016**, *4*, 9204−9212.
(280) Liu, C.-H.; Tang, Y.-J.; Wang, X.-L.; Huang, W.; Li, S.-L.; Dong, L.-Z.; Lan, Y.-Q. Highly Active Co-Mo-C/NRGO Composite as an Efficient Oxygen Electrode for Water-Oxygen Redox Cycle. *J. Mater. Chem. A* **2016**, *4*, 18100−18106.
(281) Luo, Y.; Wang, Z.; Fu, Y.; Jin, C.; Wei, Q.; Yang, R. In Situ Preparation of Hollow Mo_2C-C Hybrid Microspheres as Bifunctional Electrocatalysts for Oxygen Reduction and Evolution Reactions. *J. Mater. Chem. A* **2016**, *4*, 12583−12590.
(282) Regmi, Y. N.; Wan, C.; Duffee, K. D.; Leonard, B. M. Nanocrystalline Mo_2C as a Bifunctional Water Splitting Electrocatalyst. *ChemCatChem* **2015**, *7*, 3911−3915.
(283) Jiang, H.; Yao, Y.; Zhu, Y.; Liu, Y.; Su, Y.; Yang, X.; Li, C. Iron Carbide Nanoparticles Encapsulated in Mesoporous Fe-N-Doped Graphene-Like Carbon Hybrids as Efficient Bifunctional Oxygen Electrocatalysts. *ACS Appl. Mater. Interfaces* **2015**, *7*, 21511−21520.
(284) Gao, Q.; Zhang, W.; Shi, Z.; Yang, L.; Tang, Y. Structural Design and Electronic Modulation of Transition-Metal-Carbide Electrocatalysts toward Efficient Hydrogen Evolution. *Adv. Mater.* **2019**, *31*, 1802880.
(285) Kitchin, J. R.; Nørskov, J. K.; Barteau, M. A.; Chen, J. G. Trends in the Chemical Properties of Early Transition Metal Carbide Surfaces: A Density Functional Study. *Catal. Today* **2005**, *105*, 66−73.
(286) Chen, W.-F.; Muckerman, J. T.; Fujita, E. Recent Developments in Transition Metal Carbides and Nitrides as Hydrogen Evolution Electrocatalysts. *Chem. Commun.* **2013**, *49*, 8896−8909.
(287) Kawashima, K.; Shin, K.; Wygant, B. R.; Kim, J.-H.; Cao, C. L.; Lin, J.; Son, Y. J.; Liu, Y.; Henkelman, G.; Mullins, C. B. Cobalt Metal-Cobalt Carbide Composite Microspheres for Water Reduction Electrocatalysis. *ACS Appl. Energy Mater.* **2020**, *3*, 3909−3918.
(288) Obolonchik, V. A.; Semenov-Kobzar', A. A. Hydrogen Overvoltage Study on Carbides of Transition Metals. *Powder Metall. Met. Ceram.* **1968**, *7*, 713−717.
(289) Semenov-Kobzar', A. A.; Obolonchik, V. A.; Akinina, Z. S. Stability of Transition-Metalcarbides under Anodic-Polarization Conditions. *Powder Metall. Met. Ceram.* **1969**, *8*, 399−402.
(290) Suslick, K. S.; Hyeon, T.; Fang, M. Nanostructured Materials Generated by High-Intensity Ultrasound: Sonochemical Synthesis and Catalytic Studies. *Chem. Mater.* **1996**, *8*, 2172−2179.
(291) Anantharaj, S.; Kundu, S.; Noda, S. The Fe Effect": A Review Unveiling the Critical Roles of Fe in Enhancing OER Activity of Ni and Co Based Catalysts. *Nano Energy* **2021**, *80*, 105514.
(292) Zhao, P.; Xu, W.; Hua, X.; Luo, W.; Chen, S.; Cheng, G. Facile Synthesis of a N-Doped Fe_3C@CNT/Porous Carbon Hybrid

https://doi.org/10.1021/acs.chemrev.3c00005
Chem. Rev. 2023, 123, 12795−13208

for an Advanced Oxygen Reduction and Water Oxidation Electrocatalyst. *J. Phys. Chem. C* **2016**, *120*, 11006−11013.
(293) Jovanovič, P.; Hodnik, N.; Ruiz-Zepeda, F.; Arčon, I.; Jozinović, B.; Zorko, M.; Bele, M.; Šala, M.; Šelih, V. S.; Hočevar, S.; et al. Electrochemical Dissolution of Iridium and Iridium Oxide Particles in Acidic Media: Transmission Electron Microscopy, Electrochemical Flow Cell Coupled to Inductively Coupled Plasma Mass Spectrometry, and X-Ray Absorption Spectroscopy Study. *J. Am. Chem. Soc.* **2017**, *139*, 12837−12846.
(294) Márquez-Montes, R. A.; Kawashima, K.; Vo, K. M.; Chávez-Flores, D.; Collins-Martínez, V. H.; Mullins, C. B.; Ramos-Sánchez, V. H. Simultaneous Sulfite Electrolysis and Hydrogen Production Using Ni Foam-Based Three-Dimensional Electrodes. *Environ. Sci. Technol.* **2020**, *54*, 12511−12520.
(295) Tsikas, D.; Chobanyan-Jürgens, K. Quantification of Carbonate by Gas Chromatography-Mass Spectrometry. *Anal. Chem.* **2010**, *82*, 7897−7905.
(296) Polesello, S.; Tartari, G.; Giacomotti, P.; Mosello, R.; Cavalli, S. Determination of Total Dissolved Inorganic Carbon in Freshwaters by Reagent-Free Ion Chromatography. *J. Chromatogr. A* **2006**, *1118*, 56−61.
(297) Zhu, Y.-P.; Liu, Y.-P.; Ren, T.-Z.; Yuan, Z.-Y. Self-Supported Cobalt Phosphide Mesoporous Nanorod Arrays: A Flexible and Bifunctional Electrode for Highly Active Electrocatalytic Water Reduction and Oxidation. *Adv. Funct. Mater.* **2015**, *25*, 7337−7347.
(298) Shi, Y.; Zhang, B. Recent Advances in Transition Metal Phosphide Nanomaterials: Synthesis and Applications in Hydrogen Evolution Reaction. *Chem. Soc. Rev.* **2016**, *45*, 1529−1541.
(299) Pei, Y.; Cheng, Y.; Chen, J.; Smith, W.; Dong, P.; Ajayan, P. M.; Ye, M.; Shen, J. Recent Developments of Transition Metal Phosphides as Catalysts in the Energy Conversion Field. *J. Mater. Chem. A* **2018**, *6*, 23220−23243.
(300) Xie, J.; Xie, Y. Transition Metal Nitrides for Electrocatalytic Energy Conversion: Opportunities and Challenges. *Chem.—Eur. J.* **2016**, *22*, 3588−3598.
(301) Zhong, Y.; Xia, X.; Shi, F.; Zhan, J.; Tu, J.; Fan, H. J. Transition Metal Carbides and Nitrides in Energy Storage and Conversion. *Adv. Sci.* **2016**, *3*, 1500286.
(302) Peng, X.; Pi, C.; Zhang, X.; Li, S.; Huo, K.; Chu, P. K. Recent Progress of Transition Metal Nitrides for Efficient Electrocatalytic Water Splitting. *Sustain. Energy Fuels* **2019**, *3*, 366−381.
(303) Matsuda, Y.; Inoue, M.; Morita, M.; Takasu, Y.; Mizuno, H.; Miura, H. Electrochemical Characteristics of Titanium Nitride and Vanadium Nitride in Acidic and Alkaline Solutions. *Denki Kagaku oyobi Kogyo Butsuri Kagaku* **1982**, *50*, 258−262.
(304) Morita, M.; Tachihara, F.; Matsuda, Y.; Mizuno, H. Anodic Behavior of Niobium Nitride and Tantalum Nitride in Aqueous Solutions. *Denki Kagaku oyobi Kogyo Butsuri Kagaku* **1985**, *53*, 504−507.
(305) Gorbachev, A. K.; Andryushchenko, F. K.; Nikifarov, U. V. Hydrogen Evolution on Corrosion-Resistant Cathodes in Sulfuric Acid Solutions. *J. Appl. Chem. USSR (Engl. Transl.)* **1986**, *58* (10), PT.1.
(306) Azuma, M.; Nakato, Y.; Tsubomura, H. Efficient and Stable Oxygen Evolution of Zirconium Nitride Thin Film Electrodes Prepared by the Reactive RF Sputtering Technique. *J. Electroanal. Chem. Interfacial Electrochem.* **1987**, *220*, 369−372.
(307) Budniok, A.; Kupka, J. The Evolution of Oxygen on Amorphous Ni-Co-P Alloys. *Electrochim. Acta* **1989**, *34*, 871−873.
(308) Kupka, J.; Budniok, A. Electrolytic Oxygen Evolution on Ni-Co-P Alloys. *J. Appl. Electrochem.* **1990**, *20*, 1015−1020.
(309) Podesta, J. J.; Piatti, R. C. V.; Arvia, A. J.; Ekdunge, P.; Jüttner, K.; Kreysa, G. The Behaviour of Ni-Co-P Base Amorphous Alloys for Water Electrolysis in Strongly Alkaline Solutions Prepared through Electroless Deposition. *Int. J. Hydrog. Energy* **1992**, *17*, 9−22.
(310) De Giz, M. J.; Tremiliosi-Filho, G.; Gonzalez, E. R.; Srinivasan, S.; Appleby, A. J. The Hydrogen Evolution Reaction on Amorphous Nickel and Cobalt Alloys. *Int. J. Hydrog. Energy* **1995**, *20*, 423−427.
(311) Zhu, J.; Liu, C.; Sun, J.; Xing, Y.; Quan, B.; Li, D.; Jiang, D. Interfacial Engineering of Co3FeNx Embedded N-Doped Carbon Nanoarray Derived from Metal-Organic Frameworks for Enhanced Oxygen Evolution Reaction. *Electrochim. Acta* **2020**, *354*, 136629.
(312) Hou, J.; Sun, Y.; Li, Z.; Zhang, B.; Cao, S.; Wu, Y.; Gao, Z.; Sun, L. Electrical Behavior and Electron Transfer Modulation of Nickel-Copper Nanoalloys Confined in Nickel-Copper Nitrides Nanowires Array Encapsulated in Nitrogen-Doped Carbon Framework as Robust Bifunctional Electrocatalyst for Overall Water Splitting. *Adv. Funct. Mater.* **2018**, *28*, 1803278.
(313) Chen, M.; Liu, D.; Zi, B.; Chen, Y.; Liu, D.; Du, X.; Li, F.; Zhou, P.; Ke, Y.; Li, J.; et al. Remarkable Synergistic Effect in Cobalt-Iron Nitride/Alloy Nanosheets for Robust Electrochemical Water Splitting. *J. Energy Chem.* **2022**, *65*, 405−414.
(314) Nie, Z.; Xie, R.; Wu, J.; Aruta, C.; Yang, N. Enhancing Oxygen Evolution Reaction Activity of Co4N1-x Film Electrodes through Nitrogen Deficiency. *Catal. Today* **2022**, *400-401*, 95−101.
(315) Zhang, S.; Wang, L.; Xie, T.; Chen, Q.; Peng, W.; Li, Y.; Zhang, F.; Fan, X. Heterointerface Enhanced NiFe LDH/V-Co4N Electrocatalysts for the Oxygen Evolution Reaction. *J. Mater. Chem. A* **2022**, *10*, 21523−21530.
(316) Peng, X.; Huang, C.; Dai, J.; Liu, Y. Uniform Cobalt Grafted on Vanadium Nitride as a High Efficient Oxygen Evolution Reaction Catalyst. *Int. J. Hydrog. Energy* **2022**, *47*, 4386−4393.
(317) Yuan, Y.; Adimi, S.; Thomas, T.; Wang, J.; Guo, H.; Chen, J.; Attfield, J. P.; DiSalvo, F. J.; Yang, M. Co_3Mo_3N—An Efficient Multifunctional Electrocatalyst. *Innovation* **2021**, *2*, 100096.
(318) Lu, Y.; Li, Z.; Xu, Y.; Tang, L.; Xu, S.; Li, D.; Zhu, J.; Jiang, D. Bimetallic Co-Mo Nitride Nanosheet Arrays as High-Performance Bifunctional Electrocatalysts for Overall Water Splitting. *Chem. Eng. J.* **2021**, *411*, 128433.
(319) Gao, X.; Li, X.; Yu, Y.; Kou, Z.; Wang, P.; Liu, X.; Zhang, J.; He, J.; Mu, S.; Wang, J. Synergizing Aliovalent Doping and Interface in Heterostructured NiV Nitride@oxyhydroxide Core-Shell Nanosheet Arrays Enables Efficient Oxygen Evolution. *Nano Energy* **2021**, *85*, 105961.
(320) Choi, H. W.; Jeong, D. I.; Kwon, S. B.; Woo, S.; Kim, J.; Kim, J. H.; Yang, W. S.; Lim, B.; Kang, B. K.; Yoon, D. H. Nickel-Iron Nitrides and Alloy Heterojunction with Amorphous N-Doped Carbon Shell: High-Efficiency Synergistic Electrocatalysts for Oxygen Evolution Reaction. *Appl. Surf. Sci.* **2021**, *566*, 150706.
(321) Tang, H.; Yang, D.; Lu, M.; Kong, S.; Hou, Y.; Liu, D.; Liu, D.; Yan, S.; Chen, Z.; Yu, T.; et al. Spin Unlocking Oxygen Evolution Reaction on Antiperovskite Nitrides. *J. Mater. Chem. A* **2021**, *9*, 25435−25444.
(322) Zhai, T.; Niu, H.; Yan, Y.; Yang, S.; Lu, C.; Zhou, W. Rational Hetero-Interface Design of Fe_3N@Ni_2Co-LDHs as High Efficient Electrocatalyst for Oxygen Evolution Reaction. *J. Alloys Compd.* **2021**, *853*, 157353.
(323) Xu, Y.; Cheng, Z.; Jiang, J.; Du, J.; Xu, Q. 2D Amorphous Bimetallic NiFe Nitrides for a High-Efficiency Oxygen Evolution Reaction. *Chem. Commun.* **2021**, *57*, 13170−13173.
(324) Kawashima, K.; Márquez-Montes, R. A.; Li, H.; Shin, K.; Cao, C. L.; Vo, K. M.; Son, Y. J.; Wygant, B. R.; Chunangad, A.; Youn, D. H.; et al. Transformation of a Ni_3N OER Precatalyst in Fe-Purified and Fe-Unpurified Alkaline Media: Revealing the Reason for Its Superior OER Activity. ACS Spring Meeting 2023. DOI: 10.1021/scimeetings.3c00005.
(325) Li, B.; Song, F.; Qian, Y.; Shaw, J.; Rao, Y. Boron-Doped Graphene Oxide-Supported Nickel Nitride Nanoparticles for Electrocatalytic Oxygen Evolution in Alkaline Electrolytes. *ACS Appl. Nano Mater.* **2020**, *3*, 9924−9930.
(326) Wang, J.; Cao, F.; Shen, C.; Li, G.; Li, X.; Yang, X.; Li, S.; Qin, G. Nanoscale Nickel-Iron Nitride-Derived Efficient Electrochemical Oxygen Evolution Catalysts. *Catal. Sci. Technol.* **2020**, *10*, 4458−4466.
(327) Yuan, Y.; Adimi, S.; Guo, X.; Thomas, T.; Zhu, Y.; Guo, H.; Priyanga, G. S.; Yoo, P.; Wang, J.; Chen, J.; et al. A Surface-Oxide-Rich Activation Layer (SOAL) on Ni_2Mo_3N for a Rapid and Durable

Oxygen Evolution Reaction. *Angew. Chem. Int. Ed.* **2020**, *59*, 18036−18041.
(328) Yin, Z.; Sun, Y.; Jiang, Y.; Yan, F.; Zhu, C.; Chen, Y. Hierarchical Cobalt-Doped Molybdenum-Nickel Nitride Nanowires as Multifunctional Electrocatalysts. *ACS Appl. Mater. Interfaces* **2019**, *11*, 27751−27759.
(329) Dutta, S.; Indra, A.; Feng, Y.; Han, H.; Song, T. Promoting Electrocatalytic Overall Water Splitting with Nanohybrid of Transition Metal Nitride-Oxynitride. *Appl. Catal. B: Environ.* **2019**, *241*, 521−527.
(330) Shen, F.-C.; Sun, S.-N.; Xin, Z.-F.; Li, S.-L.; Dong, L.-Z.; Huang, Q.; Wang, Y.-R.; Liu, J.; Lan, Y.-Q. Hierarchically Phosphorus Doped Bimetallic Nitrides Arrays with Unique Interfaces for Efficient Water Splitting. *Appl. Catal. B: Environ.* **2019**, *243*, 470−480.
(331) Kang, B. K.; Im, S. Y.; Lee, J.; Kwag, S. H.; Kwon, S. B.; Tiruneh, S.; Kim, M.-J.; Kim, J. H.; Yang, W. S.; Lim, B.; et al. In-Situ Formation of MOF Derived Mesoporous Co_3N/Amorphous N-Doped Carbon Nanocubes as an Efficient Electrocatalytic Oxygen Evolution Reaction. *Nano Res.* **2019**, *12*, 1605−1611.
(332) Yu, L.; Zhu, Q.; Song, S.; McElhenny, B.; Wang, D.; Wu, C.; Qin, Z.; Bao, J.; Yu, Y.; Chen, S.; et al. Non-Noble Metal-Nitride Based Electrocatalysts for High-Performance Alkaline Seawater Electrolysis. *Nat. Commun.* **2019**, *10*, 5106.
(333) Kwag, S. H.; Lee, Y. S.; Lee, J.; Jeong, D. I.; Kwon, S. B.; Yoo, J. H.; Woo, S.; Lim, B. S.; Park, W. K.; Kim, M.-J.; et al. Design of 2D Nanocrystalline Fe_2Ni_2N Coated onto Graphene Nanohybrid Sheets for Efficient Electrocatalytic Oxygen Evolution. *ACS Appl. Energy Mater.* **2019**, *2*, 8502−8510.
(334) Xue, Z.; Kang, J.; Guo, D.; Zhu, C.; Li, C.; Zhang, X.; Chen, Y. Self-Supported Cobalt Nitride Porous Nanowire Arrays as Bifunctional Electrocatalyst for Overall Water Splitting. *Electrochim. Acta* **2018**, *273*, 229−238.
(335) Chang, B.; Yang, J.; Shao, Y.; Zhang, L.; Fan, W.; Huang, B.; Wu, Y.; Hao, X. Bimetallic NiMoN Nanowires with a Preferential Reactive Facet: An Ultraefficient Bifunctional Electrocatalyst for Overall Water Splitting. *ChemSusChem* **2018**, *11*, 3198−3207.
(336) Ray, C.; Lee, S. C.; Jin, B.; Kundu, A.; Park, J. H.; Chan Jun, S. Conceptual Design of Three-Dimensional CoN/Ni_3N-Coupled Nanograsses Integrated on N-Doped Carbon to Serve as Efficient and Robust Water Splitting Electrocatalysts. *J. Mater. Chem. A* **2018**, *6*, 4466−4476.
(337) Li, J.; Kong, X.; Jiang, M.; Lei, X. Hierarchically Structured CoN/Cu_3N Nanotube Array Supported on Copper Foam as an Efficient Bifunctional Electrocatalyst for Overall Water Splitting. *Inorg. Chem. Front.* **2018**, *5*, 2906−2913.
(338) Wu, A.; Xie, Y.; Ma, H.; Tian, C.; Gu, Y.; Yan, H.; Zhang, X.; Yang, G.; Fu, H. Integrating the Active OER and HER Components as the Heterostructures for the Efficient Overall Water Splitting. *Nano Energy* **2018**, *44*, 353−363.
(339) He, G.; Han, X.; Moss, B.; Weng, Z.; Gadipelli, S.; Lai, F.; Kafizas, A. G.; Brett, D. J. L.; Guo, Z. X.; Wang, H.; et al. Solid Solution Nitride/Carbon Nanotube Hybrids Enhance Electrocatalysis of Oxygen in Zinc-Air Batteries. *Energy Stor. Mater.* **2018**, *15*, 380−387.
(340) Zhao, S.; Li, M.; Han, M.; Xu, D.; Yang, J.; Lin, Y.; Shi, N.-E.; Lu, Y.; Yang, R.; Liu, B.; et al. Defect-Rich Ni_3FeN Nanocrystals Anchored on N-Doped Graphene for Enhanced Electrocatalytic Oxygen Evolution. *Adv. Funct. Mater.* **2018**, *28*, 1706018.
(341) Chen, Z.; Ha, Y.; Liu, Y.; Wang, H.; Yang, H.; Xu, H.; Li, Y.; Wu, R. In Situ Formation of Cobalt Nitrides/Graphitic Carbon Composites as Efficient Bifunctional Electrocatalysts for Overall Water Splitting. *ACS Appl. Mater. Interfaces* **2018**, *10*, 7134−7144.
(342) Liu, T.; Li, M.; Bo, X.; Zhou, M. Comparison Study toward the Influence of the Second Metals Doping on the Oxygen Evolution Activity of Cobalt Nitrides. *ACS Sustain. Chem. Eng.* **2018**, *6*, 11457−11465.
(343) Guo, H.-P.; Ruan, B.-Y.; Luo, W.-B.; Deng, J.; Wang, J.-Z.; Liu, H.-K.; Dou, S.-X. Ultrathin and Edge-Enriched Holey Nitride Nanosheets as Bifunctional Electrocatalysts for the Oxygen and Hydrogen Evolution Reactions. *ACS Catal.* **2018**, *8*, 9686−9696.
(344) Zheng, J.; Chen, X.; Zhong, X.; Li, S.; Liu, T.; Zhuang, G.; Li, X.; Deng, S.; Mei, D.; Wang, J.-G. Hierarchical Porous NC@CuCo Nitride Nanosheet Networks: Highly Efficient Bifunctional Electrocatalyst for Overall Water Splitting and Selective Electrooxidation of Benzyl Alcohol. *Adv. Funct. Mater.* **2017**, *27*, 1704169.
(345) Yan, F.; Wang, Y.; Li, K.; Zhu, C.; Gao, P.; Li, C.; Zhang, X.; Chen, Y. Highly Stable Three-Dimensional Porous Nickel-Iron Nitride Nanosheets for Full Water Splitting at High Current Densities. *Chem.—Eur. J.* **2017**, *23*, 10187−10194.
(346) Gao, T.; Jin, Z.; Zhang, Y.; Tan, G.; Yuan, H.; Xiao, D. Coupling Cobalt-Iron Bimetallic Nitrides and N-Doped Multi-Walled Carbon Nanotubes as High-Performance Bifunctional Catalysts for Oxygen Evolution and Reduction Reaction. *Electrochim. Acta* **2017**, *258*, 51−60.
(347) Ouyang, B.; Zhang, Y.; Zhang, Z.; Fan, H. J.; Rawat, R. S. Nitrogen-Plasma-Activated Hierarchical Nickel Nitride Nanocorals for Energy Applications. *Small* **2017**, *13*, 1604265.
(348) Chen, M.; Qi, J.; Guo, D.; Lei, H.; Zhang, W.; Cao, R. Facile Synthesis of Sponge-like Ni_3N/NC for Electrocatalytic Water Oxidation. *Chem. Commun.* **2017**, *53*, 9566−9569.
(349) Yin, Z.; Sun, Y.; Zhu, C.; Li, C.; Zhang, X.; Chen, Y. Bimetallic Ni-Mo Nitride Nanotubes as Highly Active and Stable Bifunctional Electrocatalysts for Full Water Splitting. *J. Mater. Chem. A* **2017**, *5*, 13648−13658.
(350) Xie, F.; Wu, H.; Mou, J.; Lin, D.; Xu, C.; Wu, C.; Sun, X. Ni_3N@Ni-Ci Nanoarray as a Highly Active and Durable Non-Noble-Metal Electrocatalyst for Water Oxidation at near-Neutral pH. *J. Catal.* **2017**, *356*, 165−172.
(351) Fu, G.; Cui, Z.; Chen, Y.; Xu, L.; Tang, Y.; Goodenough, J. B. Hierarchically Mesoporous Nickel-Iron Nitride as a Cost-Efficient and Highly Durable Electrocatalyst for Zn-Air Battery. *Nano Energy* **2017**, *39*, 77−85.
(352) Chen, P.; Xu, K.; Tong, Y.; Li, X.; Tao, S.; Fang, Z.; Chu, W.; Wu, X.; Wu, C. Cobalt Nitrides as a Class of Metallic Electrocatalysts for the Oxygen Evolution Reaction. *Inorg. Chem. Front.* **2016**, *3*, 236−242.
(353) Zhang, Y.; Ouyang, B.; Xu, J.; Jia, G.; Chen, S.; Rawat, R. S.; Fan, H. J. Rapid Synthesis of Cobalt Nitride Nanowires: Highly Efficient and Low-Cost Catalysts for Oxygen Evolution. *Angew. Chem. Int. Ed.* **2016**, *55*, 8670−8674.
(354) Wang, Y.; Liu, D.; Liu, Z.; Xie, C.; Huo, J.; Wang, S. Porous Cobalt-Iron Nitride Nanowires as Excellent Bifunctional Electrocatalysts for Overall Water Splitting. *Chem. Commun.* **2016**, *52*, 12614−12617.
(355) Zhang, Q.; Wang, Y.; Wang, Y.; Al-Enizi, A. M.; Elzatahry, A. A.; Zheng, G. Myriophyllum-like Hierarchical TiN@Ni_3N Nanowire Arrays for Bifunctional Water Splitting Catalysts. *J. Mater. Chem. A* **2016**, *4*, 5713−5718.
(356) Shalom, M.; Ressnig, D.; Yang, X.; Clavel, G.; Fellinger, T. P.; Antonietti, M. Nickel Nitride as an Efficient Electrocatalyst for Water Splitting. *J. Mater. Chem. A* **2015**, *3*, 8171−8177.
(357) Xu, K.; Chen, P.; Li, X.; Tong, Y.; Ding, H.; Wu, X.; Chu, W.; Peng, Z.; Wu, C.; Xie, Y. Metallic Nickel Nitride Nanosheets Realizing Enhanced Electrochemical Water Oxidation. *J. Am. Chem. Soc.* **2015**, *137*, 4119−4125.
(358) Kumaresan, L.; Shanmugavelayutham, G.; Saravanan, P. Single-Phase Ferromagnetic Iron Nitride (ε-Fe_3N) Nanoparticles Synthesized by Thermal Plasma Method for Oxygen Evolution and Supercapacitor Applications. *Appl. Phys. A* **2022**, *128*, 1073.
(359) Liu, Y.; Qie, Y.; Kong, F.; Yang, Z.; Yang, H. Synthesis and Magnetism of Single-Phase γ'-Fe_4N by Non-Ammonia Route and Applied in Oxygen Evolution Reaction Electrocatalysis. *Mater. Today Commun.* **2022**, *30*, 103103.
(360) Wu, Y.; Liu, Y.; Liu, B.; Jiang, W.; Zhou, T.; Li, H.; Shang, M.; Lang, J.; Liu, C.; Che, G. Vanadium Nitride/Carbon Nanotube Vertical Nanoarrays on Iron Foam for Oxygen Evolution Reaction. *ACS Appl. Nano Mater.* **2022**, *5*, 7714−7722.

https://doi.org/10.1021/acs.chemrev.3c00005
Chem. Rev. 2023, 123, 12795−13208

(361) Chen, Q.; Gong, N.; Zhu, T.; Yang, C.; Peng, W.; Li, Y.; Zhang, F.; Fan, X. Surface Phase Engineering Modulated Iron-Nickel Nitrides/Alloy Nanospheres with Tailored d-Band Center for Efficient Oxygen Evolution Reaction. *Small* **2022**, *18*, 2105696.
(362) Luo, X.; Ma, H.; Gao, J.; Yu, L.; Gu, X.; Liu, J. Nickel-Rich Ni_3N Particles Stimulated by Defective Graphitic Carbon Nitrides for the Effective Oxygen Evolution Reaction. *Ind. Eng. Chem. Res.* **2022**, *61*, 2081−2090.
(363) Li, R.; Li, Y.; Yang, P.; Ren, P.; Wang, D.; Lu, X.; Xu, R.; Li, Y.; Xue, J.; Zhang, J.; et al. Synergistic Interface Engineering and Structural Optimization of Non-Noble Metal Telluride-Nitride Electrocatalysts for Sustainably Overall Seawater Electrolysis. *Appl. Catal. B: Environ.* **2022**, *318*, 121834.
(364) Liu, T.; Cai, S.; Mei, Z.; Zhao, G.; Xu, L.; An, Q.; Fu, Y.; Wang, H.; Li, M.; Guo, H. Boosting the Water Splitting Activity of Cobalt Nitride through Morphological Design: A Comparison of the Influence of Structure on the Hydrogen and Oxygen Evolution Reactions. *Sustain. Energy Fuels* **2021**, *5*, 3632−3639.
(365) Jiao, F.; Wang, J.; Lin, Y.; Li, J.; Jing, X.; Gong, Y. Sliver Nanoparticles Decorated Co-Mo Nitride for Efficient Water Splitting. *Appl. Surf. Sci.* **2021**, *553*, 149440.
(366) Pan, Y.; Yao, Y.; Liang, C.; Yang, Y.; Chen, J.; Li, Q. Plasma Mediated Preparation of $NiFeN_x$ Nanoparticles Anchored on Nickel Foam for Efficient Oxygen Evolution in Alkaline Solution. *Mater. Lett.* **2021**, *302*, 130371.
(367) Saad, A.; Shen, H.; Cheng, Z.; Arbi, R.; Guo, B.; Hui, L. S.; Liang, K.; Liu, S.; Attfield, J. P.; Turak, A.; et al. Mesoporous Ternary Nitrides of Earth-Abundant Metals as Oxygen Evolution Electrocatalyst. *Nano-Micro Lett.* **2020**, *12*, 79.
(368) Shu, X.; Chen, S.; Chen, S.; Pan, W.; Zhang, J. Cobalt Nitride Embedded Holey N-Doped Graphene as Advanced Bifunctional Electrocatalysts for Zn-Air Batteries and Overall Water Splitting. *Carbon* **2020**, *157*, 234−243.
(369) Liang, S.; Jing, M.; Pervaiz, E.; Guo, H.; Thomas, T.; Song, W.; Xu, J.; Saad, A.; Wang, J.; Shen, H.; et al. Nickel-Iron Nitride-Nickel Sulfide Composites for Oxygen Evolution Electrocatalysis. *ACS Appl. Mater. Interfaces* **2020**, *12*, 41464−41470.
(370) Liu, X.; Lv, X.; Wang, P.; Zhang, Q.; Huang, B.; Wang, Z.; Liu, Y.; Zheng, Z.; Dai, Y. Improving the HER Activity of Ni_3FeN to Convert the Superior OER Electrocatalyst to an Efficient Bifunctional Electrocatalyst for Overall Water Splitting by Doping with Molybdenum. *Electrochim. Acta* **2020**, *333*, 135488.
(371) Diao, J.; Qiu, Y.; Liu, S.; Wang, W.; Chen, K.; Li, H.; Yuan, W.; Qu, Y.; Guo, X. Interfacial Engineering of W_2N/WC Heterostructures Derived from Solid-State Synthesis: A Highly Efficient Trifunctional Electrocatalyst for ORR, OER, and HER. *Adv. Mater.* **2020**, *32*, 1905679.
(372) Yang, H.; Hu, Y.; Huang, D.; Xiong, T.; Li, M.; Balogun, M.-S.; Tong, Y. Efficient Hydrogen and Oxygen Evolution Electrocatalysis by Cobalt and Phosphorus Dual-Doped Vanadium Nitride Nanowires. *Mater. Today Chem.* **2019**, *11*, 1−7.
(373) Saad, A.; Cheng, Z.; Zhang, X.; Liu, S.; Shen, H.; Thomas, T.; Wang, J.; Yang, M. Ordered Mesoporous Cobalt-Nickel Nitride Prepared by Nanocasting for Oxygen Evolution Reaction Electrocatalysis. *Adv. Mater. Interfaces* **2019**, *6*, 1900960.
(374) Liu, Z.; Tan, H.; Liu, D.; Liu, X.; Xin, J.; Xie, J.; Zhao, M.; Song, L.; Dai, L.; Liu, H. Promotion of Overall Water Splitting Activity Over a Wide pH Range by Interfacial Electrical Effects of Metallic NiCo-Nitrides Nanoparticle/$NiCo_2O_4$ Nanoflake/Graphite Fibers. *Adv. Sci.* **2019**, *6*, 1801829.
(375) Lv, M.; Zhou, Y.; Rasaki, S. A.; Shen, H.; Wang, C.; Song, W.; Thomas, T.; Yang, M.; Wang, J. Gold Nanocluster-Decorated Nickel Nitride as Stable Electrocatalyst for Oxygen Evolution Reaction in Alkaline Media. *ChemElectroChem* **2019**, *6*, 5744−5749.
(376) Wang, X.; Li, Q.; Shi, P.; Fan, J.; Min, Y.; Xu, Q. Nickel Nitride Particles Supported on 2D Activated Graphene-Black Phosphorus Heterostructure: An Efficient Electrocatalyst for the Oxygen Evolution Reaction. *Small* **2019**, *15*, 1901530.
(377) Li, R.-Q.; Hu, P.; Miao, M.; Li, Y.; Jiang, X.-F.; Wu, Q.; Meng, Z.; Hu, Z.; Bando, Y.; Wang, X.-B. CoO-Modified Co_4N as a Heterostructured Electrocatalyst for Highly Efficient Overall Water Splitting in Neutral Media. *J. Mater. Chem. A* **2018**, *6*, 24767−24772.
(378) Chen, X.; Gao, P.; Liu, H.; Xu, J.; Zhang, B.; Zhang, Y.; Tang, Y.; Xiao, C. In Situ Growth of Iron-Nickel Nitrides on Carbon Nanotubes with Enhanced Stability and Activity for Oxygen Evolution Reaction. *Electrochim. Acta* **2018**, *267*, 8−14.
(379) Wan, X.; Su, J.; Guo, L. Enhanced Photoelectrochemical Water Oxidation on $BiVO_4$ with Mesoporous Cobalt Nitride Sheets as Oxygen-Evolution Cocatalysts. *Eur. J. Inorg. Chem.* **2018**, *2018*, 2557−2563.
(380) Zhu, C.; Wang, A.-L.; Xiao, W.; Chao, D.; Zhang, X.; Tiep, N. H.; Chen, S.; Kang, J.; Wang, X.; Ding, J.; et al. In Situ Grown Epitaxial Heterojunction Exhibits High-Performance Electrocatalytic Water Splitting. *Adv. Mater.* **2018**, *30*, 1705516.
(381) Wang, Y.; Zhang, B.; Pan, W.; Ma, H.; Zhang, J. 3 D Porous Nickel-Cobalt Nitrides Supported on Nickel Foam as Efficient Electrocatalysts for Overall Water Splitting. *ChemSusChem* **2017**, *10*, 4170−4177.
(382) Sun, Y.; Zhang, T.; Li, X.; Liu, D.; Liu, G.; Zhang, X.; Lyu, X.; Cai, W.; Li, Y. Mn Doped Porous Cobalt Nitride Nanowires with High Activity for Water Oxidation under Both Alkaline and Neutral Conditions. *Chem. Commun.* **2017**, *53*, 13237−13240.
(383) Bai, X.; Wang, Q.; Xu, G.; Ning, Y.; Huang, K.; He, F.; Wu, Z.; Zhang, J. Phosphorus and Fluorine Co-Doping Induced Enhancement of Oxygen Evolution Reaction in Bimetallic Nitride Nanorods Arrays: Ionic Liquid-Driven and Mechanism Clarification. *Chem.—Eur. J.* **2017**, *23*, 16862−16870.
(384) Chen, Q.; Wang, R.; Yu, M.; Zeng, Y.; Lu, F.; Kuang, X.; Lu, X. Bifunctional Iron-Nickel Nitride Nanoparticles as Flexible and Robust Electrode for Overall Water Splitting. *Electrochim. Acta* **2017**, *247*, 666−673.
(385) Han, L.; Feng, K.; Chen, Z. Self-Supported Cobalt Nickel Nitride Nanowires Electrode for Overall Electrochemical Water Splitting. *Energy Technol.* **2017**, *5*, 1908−1911.
(386) Fan, Y.; Ida, S.; Staykov, A.; Akbay, T.; Hagiwara, H.; Matsuda, J.; Kaneko, K.; Ishihara, T. Ni-Fe Nitride Nanoplates on Nitrogen-Doped Graphene as a Synergistic Catalyst for Reversible Oxygen Evolution Reaction and Rechargeable Zn-Air Battery. *Small* **2017**, *13*, 1700099.
(387) Zhang, B.; Xiao, C.; Xie, S.; Liang, J.; Chen, X.; Tang, Y. Iron-Nickel Nitride Nanostructures in Situ Grown on Surface-Redox-Etching Nickel Foam: Efficient and Ultrasustainable Electrocatalysts for Overall Water Splitting. *Chem. Mater.* **2016**, *28*, 6934−6941.
(388) Jia, X.; Zhao, Y.; Chen, G.; Shang, L.; Shi, R.; Kang, X.; Waterhouse, G. I. N.; Wu, L.-Z.; Tung, C.-H.; Zhang, T. Ni_3FeN Nanoparticles Derived from Ultrathin NiFe-Layered Double Hydroxide Nanosheets: An Efficient Overall Water Splitting Electrocatalyst. *Adv. Energy Mater.* **2016**, *6*, 1502585.
(389) Nandi, S.; Singh, S. K.; Mullangi, D.; Illathvalappil, R.; George, L.; Vinod, C. P.; Kurungot, S.; Vaidhyanathan, R. Low Band Gap Benzimidazole COF Supported Ni_3N as Highly Active OER Catalyst. *Adv. Energy Mater.* **2016**, *6*, 1601189.
(390) Jiang, M.; Li, Y.; Lu, Z.; Sun, X.; Duan, X. Binary Nickel-Iron Nitride Nanoarrays as Bifunctional Electrocatalysts for Overall Water Splitting. *Inorg. Chem. Front.* **2016**, *3*, 630−634.
(391) Wang, Y.; Xie, C.; Liu, D.; Huang, X.; Huo, J.; Wang, S. Nanoparticle-Stacked Porous Nickel-Iron Nitride Nanosheet: A Highly Efficient Bifunctional Electrocatalyst for Overall Water Splitting. *ACS Appl. Mater. Interfaces* **2016**, *8*, 18652−18657.
(392) Zhang, K.; Zhang, L.; Chen, X.; He, X.; Wang, X.; Dong, S.; Han, P.; Zhang, C.; Wang, S.; Gu, L.; et al. Mesoporous Cobalt Molybdenum Nitride: A Highly Active Bifunctional Electrocatalyst and Its Application in Lithium-O_2 Batteries. *J. Phys. Chem. C* **2013**, *117*, 858−865.
(393) Kafle, B. P. Introduction to Nanomaterials and Application of UV-Visible Spectroscopy for Their Characterization. In *Chemical Analysis and Material Characterization by Spectrophotometry*; Kafle, B.

https://doi.org/10.1021/acs.chemrev.3c00005
Chem. Rev. 2023, 123, 12795−13208

P., Ed.; Elsevier, 2020; Chapter 6, pp 147−198. DOI: 10.1016/B978-0-12-814866-2.00006-3.
(394) Chen, W.-F.; Iyer, S.; Iyer, S.; Sasaki, K.; Wang, C.-H.; Zhu, Y.; Muckerman, J. T.; Fujita, E. Biomass-Derived Electrocatalytic Composites for Hydrogen Evolution. *Energy Environ. Sci.* **2013**, *6*, 1818−1826.
(395) Vaidhyanathan, B.; Rao, K. J. Synthesis of Ti, Ga, and V Nitrides: Microwave-Assisted Carbothermal Reduction and Nitridation. *Chem. Mater.* **1997**, *9*, 1196−1200.
(396) da Silva, A. K.; Ricci, T. G.; de Toffoli, A. L.; Maciel, E. V. S.; Nazario, C. E. D.; Lanças, F. M. The Role of Magnetic Nanomaterials in Miniaturized Sample Preparation Techniques. In *Handbook on Miniaturization in Analytical Chemistry*; Hussain, C. M., Ed.; Elsevier, 2020; Chapter 4, pp 77−98. DOI: 10.1016/B978-0-12-819763-9.00004-0.
(397) Nunes, D.; Pimentel, A.; Santos, L.; Barquinha, P.; Pereira, L.; Fortunato, E.; Martins, R. Synthesis, Design, and Morphology of Metal Oxide Nanostructures. In *Metal Oxide Nanostructures*; Nunes, D., Pimentel, A., Santos, L., Barquinha, P., Pereira, L., Fortunato, E., Martins, R., Eds.; Metal Oxides; Elsevier, 2019; Chapter 2, pp 21−57. DOI: 10.1016/B978-0-12-811512-1.00002-3.
(398) Shaikh, S. F.; Ubaidullah, M.; Mane, R. S.; Al-Enizi, A. M. Types, Synthesis Methods and Applications of Ferrites. In *Spinel Ferrite Nanostructures for Energy Storage Devices*; Mane, R. S., Jadhav, V. V., Eds.; Micro and Nano Technologies; Elsevier, 2020; Chapter 4, pp 51−82. DOI: 10.1016/B978-0-12-819237-5.00004-3.
(399) Feng, S.-H.; Li, G.-H. Hydrothermal and Solvothermal Syntheses. In *Modern Inorganic Synthetic Chemistry*, 2nd ed.; Xu, R., Xu, Y., Eds.; Elsevier: Amsterdam, 2017; Chapter 4, pp 73−104. DOI: 10.1016/B978-0-444-63591-4.00004-5.
(400) Nasirpouri, F.; Alipour, K.; Daneshvar, F.; Sanaeian, M.-R. Electrodeposition of Anticorrosion Nanocoatings. In *Corrosion Protection at the Nanoscale*; Rajendran, S., Nguyen, T. A., Kakooei, S., Yeganeh, M., Li, Y., Eds.; Micro and Nano Technologies; Elsevier, 2020; Chapter 24, pp 473−497. DOI: 10.1016/B978-0-12-819359-4.00024-6.
(401) Zhang, X.; Zhang, L.; Zhu, G.-G.; Zhu, Y.-X.; Lu, S.-Y. Mixed Metal Phosphide Chainmail Catalysts Confined in N-Doped Porous Carbon Nanoboxes as Highly Efficient Water-Oxidation Electrocatalysts with Ultralow Overpotentials and Tafel Slopes. *ACS Appl. Mater. Interfaces* **2020**, *12*, 7153−7161.
(402) Yu, J.; Li, Q.; Chen, N.; Xu, C.-Y.; Zhen, L.; Wu, J.; Dravid, V. P. Carbon-Coated Nickel Phosphide Nanosheets as Efficient Dual-Electrocatalyst for Overall Water Splitting. *ACS Appl. Mater. Interfaces* **2016**, *8*, 27850−27858.
(403) Yao, Y.; Mahmood, N.; Pan, L.; Shen, G.; Zhang, R.; Gao, R.; Aleem, F.; Yuan, X.; Zhang, X.; Zou, J.-J. Iron Phosphide Encapsulated in P-Doped Graphitic Carbon as Efficient and Stable Electrocatalyst for Hydrogen and Oxygen Evolution Reactions. *Nanoscale* **2018**, *10*, 21327−21334.
(404) Zhong, X.; Jiang, Y.; Chen, X.; Wang, L.; Zhuang, G.; Li, X.; Wang, J. Integrating Cobalt Phosphide and Cobalt Nitride-Embedded Nitrogen-Rich Nanocarbons: High-Performance Bifunctional Electrocatalysts for Oxygen Reduction and Evolution. *J. Mater. Chem. A* **2016**, *4*, 10575−10584.
(405) Zhao, Y.; Jin, B.; Vasileff, A.; Jiao, Y.; Qiao, S.-Z. Interfacial Nickel Nitride/Sulfide as a Bifunctional Electrode for Highly Efficient Overall Water/Seawater Electrolysis. *J. Mater. Chem. A* **2019**, *7*, 8117−8121.
(406) Zhao, Z.; Wu, H.; He, H.; Xu, X.; Jin, Y. A High-Performance Binary Ni-Co Hydroxide-Based Water Oxidation Electrode with Three-Dimensional Coaxial Nanotube Array Structure. *Adv. Funct. Mater.* **2014**, *24*, 4698−4705.
(407) Chou, N. H.; Ross, P. N.; Bell, A. T.; Tilley, T. D. Comparison of Cobalt-Based Nanoparticles as Electrocatalysts for Water Oxidation. *ChemSusChem* **2011**, *4*, 1566−1569.
(408) Li, A.; Sun, Y.; Yao, T.; Han, H. Earth-Abundant Transition-Metal-Based Electrocatalysts for Water Electrolysis to Produce Renewable Hydrogen. *Chem.—Eur. J.* **2018**, *24*, 18334−18355.
(409) Huang, L.-F.; Hutchison, M. J.; Santucci, R. J.; Scully, J. R.; Rondinelli, J. M. Improved Electrochemical Phase Diagrams from Theory and Experiment: The Ni-Water System and Its Complex Compounds. *J. Phys. Chem. C* **2017**, *121*, 9782−9789.
(410) Cao, B.; Veith, G. M.; Diaz, R. E.; Liu, J.; Stach, E. A.; Adzic, R. R.; Khalifah, P. G. Cobalt Molybdenum Oxynitrides: Synthesis, Structural Characterization, and Catalytic Activity for the Oxygen Reduction Reaction. *Angew. Chem. Int. Ed.* **2013**, *52*, 10753−10757.
(411) Gao, W.-K.; Chi, J.-Q.; Wang, Z.-B.; Lin, J.-H.; Liu, D.-P.; Zeng, J.-B.; Yu, J.-F.; Wang, L.; Chai, Y.-M.; Dong, B. Optimized Bimetallic Nickel-Iron Phosphides with Rich Defects as Enhanced Electrocatalysts for Oxygen Evolution Reaction. *J. Colloid Interface Sci.* **2019**, *537*, 11−19.
(412) Chen, S.; Dai, J.; Ren, F.; Xu, H.; Du, Y. 3D Hollow Nanoflowers Assembled by Ultrathin Molybdenum-Nickel Phosphide Nanosheets as Robust Electrocatalysts for Oxygen Evolution Reaction. *J. Colloid Interface Sci.* **2019**, *536*, 71−79.
(413) Zhou, L.; Jiang, S.; Liu, Y.; Shao, M.; Wei, M.; Duan, X. Ultrathin CoNiP@Layered Double Hydroxides Core-Shell Nanosheets Arrays for Largely Enhanced Overall Water Splitting. *ACS Appl. Energy Mater.* **2018**, *1*, 623−631.
(414) Zhang, X.; Huang, L.; Wang, Q.; Dong, S. Transformation of Homobimetallic MOFs into Nickel-Cobalt Phosphide/Nitrogen-Doped Carbon Polyhedral Nanocages for Efficient Oxygen Evolution Electrocatalysis. *J. Mater. Chem. A* **2017**, *5*, 18839−18844.
(415) Masud, J.; Umapathi, S.; Ashokaan, N.; Nath, M. Iron Phosphide Nanoparticles as an Efficient Electrocatalyst for the OER in Alkaline Solution. *J. Mater. Chem. A* **2016**, *4*, 9750−9754.
(416) Wang, T.; Fu, X.-Z.; Wang, S. Etching Oxide Overlayers of NiFe Phosphide to Facilitate Surface Reconstruction for Oxygen Evolution Reaction. *Green Energy Environ.* **2022**, *7*, 365−371.
(417) Nguyen, T. X.; Ting, N.-H.; Ting, J.-M. Multimetal Phosphide as Bi-Functional Electrocatalyst for Enhanced Water Splitting Performance. *J. Power Sources* **2022**, *552*, 232249.
(418) Tang, H.; Qi, Y.; Feng, D.; Chen, Y.; Liu, L.; Hao, L.; Yue, K.; Li, D.; Wang, Y. Preparation of a Ni-Fe-Based Transition Metal Phosphide as an Efficient Electrocatalyst for the Oxygen Evolution Reaction. *Sustain. Energy Fuels* **2022**, *6*, 4477−4483.
(419) Yu, M.; Guo, X.; Chang, X.; Ma, X.; Zhang, M. Assembled Cobalt Phosphide Nanoparticles on Carbon Nanofibers as a Bifunctional Catalyst for Hydrogen Evolution Reaction and Oxygen Evolution Reaction. *Sustain. Energy Fuels* **2022**, *6*, 5000−5007.
(420) Wang, Y.; Xie, M.; Dai, F.; Liu, J.; Zhang, L.; Zhang, R.; Zhang, Z.; Hu, W. Iron Regulates the Interfacial Charge Distribution of Transition Metal Phosphides for Enhanced Oxygen Evolution Reaction. *J. Colloid. Interface Sci.* **2022**, *615*, 725−731.
(421) Zhao, S.; Zhao, Y.; Chen, J.; Dai, R.; Zhou, W.; Yang, J.; Zhao, X.; Chen, Z.; Zhou, Y.; Zhang, H.; et al. Crystalline and Amorphous Phases: NiFeCo Trimetal Phosphide as an Efficient Electrocatalyst to Accelerate Oxygen Evolution Reaction Kinetics. *Electrochim. Acta* **2022**, *426*, 140788.
(422) Chen, T.; Li, B.; Song, K.; Wang, C.; Ding, J.; Liu, E.; Chen, B.; He, F. Defect-Activated Surface Reconstruction: Mechanism for Triggering the Oxygen Evolution Reaction Activity of NiFe Phosphide. *J. Mater. Chem. A* **2022**, *10*, 22750−22759.
(423) Kim, D.; Park, S.; Yan, B.; Hong, H.; Cho, Y.; Kang, J.; Qin, X.; Yoo, T.; Piao, Y. Synthesis of Remarkably Thin Co-Fe Phosphide/Carbon Nanosheet for Enhanced Oxygen Evolution Reaction Electrocatalysis Driven by Readily Generated Active Oxyhydroxide. *ACS Appl. Energy Mater.* **2022**, *5*, 2400−2411.
(424) Liu, H.; Yang, S.; Ma, J.; Dou, M.; Wang, F. Surface Engineering of MOFs as a Route to Cobalt Phosphide Electrocatalysts for Efficient Oxygen Evolution Reaction. *Nano Energy* **2022**, *98*, 107315.
(425) Wu, Y.; Han, P.; Li, B.; Dang, Y.; Zhou, Y. A Novel Trimetal Phosphide with Amorphous Porous Structure for the Enhanced Electrocatalysis of Oxygen Evolution Reaction. *J. Electrochem. Soc.* **2021**, *168*, 116510.

https://doi.org/10.1021/acs.chemrev.3c00005
Chem. Rev. 2023, 123, 12795−13208

(426) Wu, D.; Kong, A.; Li, W.; Fu, Y.; Zhang, J. Facile Synthesis of Bimetallic Ni-Fe Phosphide as Robust Electrocatalyst for Oxygen Evolution Reaction in Alkaline Media. *Int. J. Hydrog. Energy* **2021**, *46*, 39844−39854.
(427) Yuan, G.; Bai, J.; Zhang, L.; Chen, X.; Ren, L. The Effect of P Vacancies on the Activity of Cobalt Phosphide Nanorods as Oxygen Evolution Electrocatalyst in Alkali. *Appl. Catal. B: Environ.* **2021**, *284*, 119693.
(428) Kumar, P.; Murthy, A. P.; Bezerra, L. S.; Martini, B. K.; Maia, G.; Madhavan, J. Carbon Supported Nickel Phosphide as Efficient Electrocatalyst for Hydrogen and Oxygen Evolution Reactions. *Int. J. Hydrog. Energy* **2021**, *46*, 622−632.
(429) Kaneti, Y. V.; Guo, Y.; Septiani, N. L. W.; Iqbal, M.; Jiang, X.; Takei, T.; Yuliarto, B.; Alothman, Z. A.; Golberg, D.; Yamauchi, Y. Self-Templated Fabrication of Hierarchical Hollow Manganese-Cobalt Phosphide Yolk-Shell Spheres for Enhanced Oxygen Evolution Reaction. *Chem. Eng. J.* **2021**, *405*, 126580.
(430) Liu, Y.; Ran, N.; Ge, R.; Liu, J.; Li, W.; Chen, Y.; Feng, L.; Che, R. Porous Mn-Doped Cobalt Phosphide Nanosheets as Highly Active Electrocatalysts for Oxygen Evolution Reaction. *Chem. Eng. J.* **2021**, *425*, 131642.
(431) Zhang, Y.; Gao, X.; Lv, L.; Xu, J.; Lin, H.; Ding, Y.; Wang, C. Tailoring π-Symmetry Electrons in Cobalt-Iron Phosphide for Highly Efficient Oxygen Evolution. *Electrochim. Acta* **2020**, *341*, 136029.
(432) Wu, J.; Wang, D.; Wan, S.; Liu, H.; Wang, C.; Wang, X. An Efficient Cobalt Phosphide Electrocatalyst Derived from Cobalt Phosphonate Complex for All-pH Hydrogen Evolution Reaction and Overall Water Splitting in Alkaline Solution. *Small* **2020**, *16*, 1900550.
(433) Zhou, L.-N.; Yu, L.; Liu, C.; Li, Y.-J. Electrocatalytic Activity Sites for the Oxygen Evolution Reaction on Binary Cobalt and Nickel Phosphides. *RSC Adv.* **2020**, *10*, 39909−39915.
(434) Wang, J.; Wang, J.; Zhang, M.; Li, S.; Liu, R.; Li, Z. Metal-Organic Frameworks-Derived Hollow-Structured Iron-Cobalt Bimetallic Phosphide Electrocatalysts for Efficient Oxygen Evolution Reaction. *J. Alloys Compd.* **2020**, *821*, 153463.
(435) Zhan, K.; Feng, C.; Feng, X.; Zhao, D.; Yue, S.; Li, Y.; Jiao, Q.; Li, H.; Zhao, Y. Iron-Doped Nickel Cobalt Phosphide Nanoarrays with Urchin-like Structures as High-Performance Electrocatalysts for Oxygen Evolution Reaction. *ACS Sustainable Chem. Eng.* **2020**, *8*, 6273−6281.
(436) Ding, X.; Uddin, W.; Sheng, H.; Li, P.; Du, Y.; Zhu, M. Porous Transition Metal Phosphides Derived from Fe-Based Prussian Blue Analogue for Oxygen Evolution Reaction. *J. Alloys Compd.* **2020**, *814*, 152332.
(437) Li, G.; Zhu, T.; Ye, Y.; Liang, S.; Duan, W.; Hong, W.; Feng, C. Transforming Ni-Coagulated Polyferriertic Sulfate Sludge into Porous Heteroatom-Doped Carbon-Supported Transition Metal Phosphide: An Efficient Catalyst for Oxygen Evolution Reaction. *Energy Technol.* **2020**, *8*, 1900995.
(438) Li, H.; Du, Y.; Fu, Y.; Wu, C.; Xiao, Z.; Liu, Y.; Sun, X.; Wang, L. Self-Supported Ni_2P Nanotubes Coated with FeP Nanoparticles Electrocatalyst (FeP@Ni_2P/NF) for Oxygen Evolution Reaction. *Int. J. Hydrogen Energy* **2020**, *45*, 565−573.
(439) Wang, Y.; Zhao, S.; Zhu, Y.; Qiu, R.; Gengenbach, T.; Liu, Y.; Zu, L.; Mao, H.; Wang, H.; Tang, J.; et al. Three-Dimensional Hierarchical Porous Nanotubes Derived from Metal-Organic Frameworks for Highly Efficient Overall Water Splitting. *iScience* **2020**, *23*, 100761.
(440) Chen, J.; Zhang, Y.; Ye, H.; Xie, J.-Q.; Li, Y.; Yan, C.; Sun, R.; Wong, C.-P. Metal-Organic Framework-Derived $Co_xFe_{1-x}P$ Nanoparticles Encapsulated in N-Doped Carbon as Efficient Bifunctional Electrocatalysts for Overall Water Splitting. *ACS Appl. Energy Mater.* **2019**, *2*, 2734−2742.
(441) Ding, S.; Cao, D.; Liu, D.; Lin, Y.; Wang, C.; Wu, C.; Zhou, Y.; Chen, S.; Song, L. Modulating Electronic Structure of Cobalt Phosphide Precatalysts via Dual-Metal Incorporation for Highly Efficient Overall Water Splitting. *ACS Appl. Energy Mater.* **2019**, *2*, 8022−8030.
(442) Hu, F.; Zhang, Y.; Shen, X.; Tao, J.; Yang, X.; Xiong, Y.; Peng, Z. Porous Amorphous $NiFeO_x$/NiFeP Framework with Dual Electrocatalytic Functions for Water Electrolysis. *J. Power Sources* **2019**, *428*, 76−81.
(443) Li, J.-S.; Kong, L.-X.; Wu, Z.; Zhang, S.; Yang, X.-Y.; Sha, J.-Q.; Liu, G.-D. Polydopamine-Assisted Construction of Cobalt Phosphide Encapsulated in N-Doped Carbon Porous Polyhedrons for Enhanced Overall Water Splitting. *Carbon* **2019**, *145*, 694−700.
(444) Li, P.; Zeng, H. C. Promoting Electrocatalytic Oxygen Evolution over Transition-Metal Phosphide-Based Nanocomposites via Architectural and Electronic Engineering. *ACS Appl. Mater. Interfaces* **2019**, *11*, 46825−46838.
(445) Li, S.; Wang, X.; Li, M.; Liu, J.; Li, C.; Wu, H.; Guo, D.; Ye, F.; Wang, S.; Cheng, L.; et al. Self-Supported Ternary $(Ni_xFe_y)_2P$ Nanoplates Arrays as an Efficient Bifunctional Electrocatalyst for Overall Water Splitting. *Electrochim. Acta* **2019**, *319*, 561−568.
(446) Lian, Y.; Sun, H.; Wang, X.; Qi, P.; Mu, Q.; Chen, Y.; Ye, J.; Zhao, X.; Deng, Z.; Peng, Y. Carved Nanoframes of Cobalt-Iron Bimetal Phosphide as a Bifunctional Electrocatalyst for Efficient Overall Water Splitting. *Chem. Sci.* **2019**, *10*, 464−474.
(447) Lv, X.; Hu, Z.; Ren, J.; Liu, Y.; Wang, Z.; Yuan, Z.-Y. Self-Supported Al-Doped Cobalt Phosphide Nanosheets Grown on Three-Dimensional Ni Foam for Highly Efficient Water Reduction and Oxidation. *Inorg. Chem. Front.* **2019**, *6*, 74−81.
(448) Sultana, U. K.; O'Mullane, A. P. Electrochemically Fabricated Ni-P, Ni-S and Ni-Se Materials for Overall Water Splitting: Investigating the Concept of Bifunctional Electrocatalysis. *ChemElectroChem* **2019**, *6*, 2630−2637.
(449) Tang, Y.-J.; Zhu, H.-J.; Dong, L.-Z.; Zhang, A.-M.; Li, S.-L.; Liu, J.; Lan, Y.-Q. Solid-Phase Hot-Pressing of POMs-ZIFs Precursor and Derived Phosphide for Overall Water Splitting. *Appl. Catal. B: Environ.* **2019**, *245*, 528−535.
(450) Teng, C.; Zhang, N.; Gao, X.; Li, X.; Wu, Z.; Wang, W.; Zhi, M.; Hong, Z. Uniform NiFe Phosphide Nanosheets Arrays on Carbon Cloth as High-Performance Oxygen Evolution Catalysts. *Mater. Today Energy* **2019**, *11*, 192−198.
(451) Wang, Y.; Ma, B.; Chen, Y. Iron Phosphides Supported on Three-Dimensional Iron Foam as an Efficient Electrocatalyst for Water Splitting Reactions. *J. Mater. Sci.* **2019**, *54*, 14872−14883.
(452) Zhang, C.; Gong, N.; Ding, C.; Li, Y.; Peng, W.; Zhang, G.; Zhang, F.; Fan, X. Plasma-Assisted Synthesis of Three-Dimensional Hierarchical $NiFeO_x$/NiFeP Electrocatalyst for Highly Enhanced Water Oxidation in Alkaline Media. *Int. J. Hydrogen Energy* **2019**, *44*, 26118−26127.
(453) Man, H.-W.; Tsang, C.-S.; Li, M. M.-J.; Mo, J.; Huang, B.; Lee, L. Y. S.; Leung, Y.; Wong, K.-Y.; Tsang, S. C. E. Tailored Transition Metal-Doped Nickel Phosphide Nanoparticles for the Electrochemical Oxygen Evolution Reaction (OER). *Chem. Commun.* **2018**, *54*, 8630−8633.
(454) Leonard, D. P.; Stickle, W. F.; Ji, X. Carbon-Supported Iron Phosphides: Highest Intrinsic Oxygen Evolution Activity of the Iron Triad. *ACS Appl. Energy Mater.* **2018**, *1*, 3593−3597.
(455) Jiang, M.; Li, J.; Cai, X.; Zhao, Y.; Pan, L.; Cao, Q.; Wang, D.; Du, Y. Ultrafine Bimetallic Phosphide Nanoparticles Embedded in Carbon Nanosheets: Two-Dimensional Metal-Organic Framework-Derived Non-Noble Electrocatalysts for the Highly Efficient Oxygen Evolution Reaction. *Nanoscale* **2018**, *10*, 19774−19780.
(456) Lei, H.; Chen, M.; Liang, Z.; Liu, C.; Zhang, W.; Cao, R. Ni_2P Hollow Microspheres for Electrocatalytic Oxygen Evolution and Reduction Reactions. *Catal. Sci. Technol.* **2018**, *8*, 2289−2293.
(457) Luo, F.; Zhang, Q.; Yu, X.; Xiao, S.; Ling, Y.; Hu, H.; Guo, L.; Yang, Z.; Huang, L.; Cai, W.; et al. Palladium Phosphide as a Stable and Efficient Electrocatalyst for Overall Water Splitting. *Angew. Chem., Int. Ed.* **2018**, *57*, 14862−14867.
(458) Li, P.; Zeng, H. C. Bimetallic Ni-Fe Phosphide Nanocomposites with a Controlled Architecture and Composition Enabling Highly Efficient Electrochemical Water Oxidation. *J. Mater. Chem. A* **2018**, *6*, 2231−2238.

(459) Xu, X.; Li, C.; Lim, J. G.; Wang, Y.; Ong, A.; Li, X.; Peng, E.; Ding, J. Hierarchical Design of NiOOH@Amorphous Ni-P Bilayer on a 3D Mesh Substrate for High-Efficiency Oxygen Evolution Reaction. *ACS Appl. Mater. Interfaces* **2018**, *10*, 30273−30282.
(460) Cao, Z.; Zhou, T.; Xi, W.; Zhao, Y. Bimetal Metal-Organic Frameworks Derived $Co_{0.4}Fe_{0.28}P$ and $Co_{0.37}Fe_{0.26}S$ Nanocubes for Enhanced Oxygen Evolution Reaction. *Electrochim. Acta* **2018**, *263*, 576−584.
(461) Dinh, K. N.; Sun, X.; Dai, Z.; Zheng, Y.; Zheng, P.; Yang, J.; Xu, J.; Wang, Z.; Yan, Q. O_2 Plasma and Cation Tuned Nickel Phosphide Nanosheets for Highly Efficient Overall Water Splitting. *Nano Energy* **2018**, *54*, 82−90.
(462) Dutta, A.; Mutyala, S.; Samantara, A. K.; Bera, S.; Jena, B. K.; Pradhan, N. Synergistic Effect of Inactive Iron Oxide Core on Active Nickel Phosphide Shell for Significant Enhancement in Oxygen Evolution Reaction Activity. *ACS Energy Lett.* **2018**, *3*, 141−148.
(463) Guo, Y.; Tang, J.; Wang, Z.; Sugahara, Y.; Yamauchi, Y. Hollow Porous Heterometallic Phosphide Nanocubes for Enhanced Electrochemical Water Splitting. *Small* **2018**, *14*, 1802442.
(464) Liu, G.; Li, N.; Zhao, Y.; Yao, R.; Wang, M.; He, D.; Li, J. Fabrication of Fe-Doped Co_2P Nanoparticles as Efficient Electrocatalyst for Electrochemical and Photoelectrochemical Water Oxidation. *Electrochim. Acta* **2018**, *283*, 1490−1497.
(465) Liu, K.; Wang, F.; He, P.; Shifa, T. A.; Wang, Z.; Cheng, Z.; Zhan, X.; He, J. The Role of Active Oxide Species for Electrochemical Water Oxidation on the Surface of 3d-Metal Phosphides. *Adv. Energy Mater.* **2018**, *8*, 1703290.
(466) Liu, Z.; Wang, Y.; Chen, R.; Chen, C.; Yang, H.; Ma, J.; Li, Y.; Wang, S. Quaternary Bimetallic Phosphosulphide Nanosheets Derived from Prussian Blue Analogues: Origin of the Ultra-High Activity for Oxygen Evolution. *J. Power Sources* **2018**, *403*, 90−96.
(467) Qiu, B.; Cai, L.; Wang, Y.; Lin, Z.; Zuo, Y.; Wang, M.; Chai, Y. Fabrication of Nickel-Cobalt Bimetal Phosphide Nanocages for Enhanced Oxygen Evolution Catalysis. *Adv. Funct. Mater.* **2018**, *28*, 1706008.
(468) Wang, L.; Zhou, Q.; Pu, Z.; Zhang, Q.; Mu, X.; Jing, H.; Liu, S.; Chen, C.; Mu, S. Surface Reconstruction Engineering of Cobalt Phosphides by Ru Inducement to Form Hollow Ru-RuP_x-Co_xP Pre-Electrocatalysts with Accelerated Oxygen Evolution Reaction. *Nano Energy* **2018**, *53*, 270−276.
(469) Wang, M.; Dong, C.-L.; Huang, Y.-C.; Li, Y.; Shen, S. Electronic Structure Evolution in Tricomponent Metal Phosphides with Reduced Activation Energy for Efficient Electrocatalytic Oxygen Evolution. *Small* **2018**, *14*, 1801756.
(470) Wu, Z.; Gan, Q.; Li, X.; Zhong, Y.; Wang, H. Elucidating Surface Restructuring-Induced Catalytic Reactivity of Cobalt Phosphide Nanoparticles under Electrochemical Conditions. *J. Phys. Chem. C* **2018**, *122*, 2848−2853.
(471) Xi, W.; Yan, G.; Lang, Z.; Ma, Y.; Tan, H.; Zhu, H.; Wang, Y.; Li, Y. Oxygen-Doped Nickel Iron Phosphide Nanocube Arrays Grown on Ni Foam for Oxygen Evolution Electrocatalysis. *Small* **2018**, *14*, 1802204.
(472) Xu, W.; Zhu, S.; Liang, Y.; Cui, Z.; Yang, X.; Inoue, A. A Nanoporous Metal Phosphide Catalyst for Bifunctional Water Splitting. *J. Mater. Chem. A* **2018**, *6*, 5574−5579.
(473) Xu, J.; Sousa, J. P. S.; Mordvinova, N. E.; Costa, J. D.; Petrovykh, D. Y.; Kovnir, K.; Lebedev, O. I.; Kolen'ko, Y. V. Al-Induced In Situ Formation of Highly Active Nanostructured Water-Oxidation Electrocatalyst Based on Ni-Phosphide. *ACS Catal.* **2018**, *8*, 2595−2600.
(474) Xu, H.; Wei, J.; Zhang, K.; Shiraishi, Y.; Du, Y. Hierarchical NiMo Phosphide Nanosheets Strongly Anchored on Carbon Nanotubes as Robust Electrocatalysts for Overall Water Splitting. *ACS Appl. Mater. Interfaces* **2018**, *10*, 29647−29655.
(475) Xu, J.; Liu, Y.; Li, J.; Amorim, I.; Zhang, B.; Xiong, D.; Zhang, N.; Thalluri, S. M.; Sousa, J. P. S.; Liu, L. Hollow Cobalt Phosphide Octahedral Pre-Catalysts with Exceptionally High Intrinsic Catalytic Activity for Electro-Oxidation of Water and Methanol. *J. Mater. Chem. A* **2018**, *6*, 20646−20652.
(476) Zhou, X.; Gao, H.; Wang, Y.; Liu, Z.; Lin, J.; Ding, Y. P Vacancies-Enriched 3D Hierarchical Reduced Cobalt Phosphide as a Precursor Template for Defect Engineering for Efficient Water Oxidation. *J. Mater. Chem. A* **2018**, *6*, 14939−14948.
(477) Zhao, Y.; Fan, G.; Yang, L.; Lin, Y.; Li, F. Assembling Ni-Co Phosphides/Carbon Hollow Nanocages and Nanosheets with Carbon Nanotubes into a Hierarchical Necklace-like Nanohybrid for Electrocatalytic Oxygen Evolution Reaction. *Nanoscale* **2018**, *10*, 13555−13564.
(478) Yang, S.; He, Q.; Wang, C.; Jiang, H.; Wu, C.; Zhang, Y.; Zhou, T.; Zhou, Y.; Song, L. Confined Bimetallic Phosphide within P, N Co-Doped Carbon Layers towards Boosted Bifunctional Oxygen Catalysis. *J. Mater. Chem. A* **2018**, *6*, 11281−11287.
(479) Zhang, C.; Xie, Y.; Deng, H.; Zhang, C.; Su, J.-W.; Dong, Y.; Lin, J. Ternary Nickel Iron Phosphide Supported on Nickel Foam as a High-Efficiency Electrocatalyst for Overall Water Splitting. *Int. J. Hydrogen Energy* **2018**, *43*, 7299−7306.
(480) Yao, S.; Forstner, V.; Menezes, P. W.; Panda, C.; Mebs, S.; Zolnhofer, E. M.; Miehlich, M. E.; Szilvási, T.; Kumar, N. A.; Haumann, M.; et al. From an Fe_2P_3 Complex to FeP Nanoparticles as Efficient Electrocatalysts for Water-Splitting. *Chem. Sci.* **2018**, *9*, 8590−8597.
(481) Zhang, Q.; Li, T.; Liang, J.; Wang, N.; Kong, X.; Wang, J.; Qian, H.; Zhou, Y.; Liu, F.; Wei, C.; et al. Highly Wettable and Metallic NiFe-Phosphate/Phosphide Catalyst Synthesized by Plasma for Highly Efficient Oxygen Evolution Reaction. *J. Mater. Chem. A* **2018**, *6*, 7509−7516.
(482) Zhang, Q.; Yan, D.; Nie, Z.; Qiu, X.; Wang, S.; Yuan, J.; Su, D.; Wang, G.; Wu, Z. Iron-Doped NiCoP Porous Nanosheet Arrays as a Highly Efficient Electrocatalyst for Oxygen Evolution Reaction. *ACS Appl. Energy Mater.* **2018**, *1*, 571−579.
(483) Xu, J.; Wei, X.-K.; Costa, J. D.; Lado, J. L.; Owens-Baird, B.; Gonçalves, L. P. L.; Fernandes, S. P. S.; Heggen, M.; Petrovykh, D. Y.; Dunin-Borkowski, R. E.; Kovnir, K.; Kolen'ko, Y. V. Interface Engineering in Nanostructured Nickel Phosphide Catalyst for Efficient and Stable Water Oxidation. *ACS Catal.* **2017**, *7*, 5450−5455.
(484) Ye, L.; Wen, Z. Reduced Graphene Oxide Supporting Hollow Bimetallic Phosphide Nanoparticle Hybrids for Electrocatalytic Oxygen Evolution. *Electrochem. Commun.* **2017**, *83*, 85−89.
(485) Zhou, H.; Yu, F.; Sun, J.; He, R.; Chen, S.; Chu, C.-W.; Ren, Z. Highly Active Catalyst Derived from a 3D Foam of $Fe(PO_3)_2/Ni_2P$ for Extremely Efficient Water Oxidation. *Proc. Natl. Acad. Sci. U.S.A.* **2017**, *114*, 5607.
(486) Yan, L.; Cao, L.; Dai, P.; Gu, X.; Liu, D.; Li, L.; Wang, Y.; Zhao, X. Metal-Organic Frameworks Derived Nanotube of Nickel-Cobalt Bimetal Phosphides as Highly Efficient Electrocatalysts for Overall Water Splitting. *Adv. Funct. Mater.* **2017**, *27*, 1703455.
(487) Ahn, S. H.; Manthiram, A. Cobalt Phosphide Coupled with Heteroatom-Doped Nanocarbon Hybrid Electroctalysts for Efficient, Long-Life Rechargeable Zinc-Air Batteries. *Small* **2017**, *13*, 1702068.
(488) Ai, L.; Niu, Z.; Jiang, J. Mechanistic Insight into Oxygen Evolution Electrocatalysis of Surface Phosphate Modified Cobalt Phosphide Nanorod Bundles and Their Superior Performance for Overall Water Splitting. *Electrochim. Acta* **2017**, *242*, 355−363.
(489) Anantharaj, S.; Reddy, P. N.; Kundu, S. Core-Oxidized Amorphous Cobalt Phosphide Nanostructures: An Advanced and Highly Efficient Oxygen Evolution Catalyst. *Inorg. Chem.* **2017**, *56*, 1742−1756.
(490) Han, A.; Zhang, H.; Yuan, R.; Ji, H.; Du, P. Crystalline Copper Phosphide Nanosheets as an Efficient Janus Catalyst for Overall Water Splitting. *ACS Appl. Mater. Interfaces* **2017**, *9*, 2240−2248.
(491) Huang, H.; Yu, C.; Zhao, C.; Han, X.; Yang, J.; Liu, Z.; Li, S.; Zhang, M.; Qiu, J. Iron-Tuned Super Nickel Phosphide Microstructures with High Activity for Electrochemical Overall Water Splitting. *Nano Energy* **2017**, *34*, 472−480.
(492) Li, D.; Baydoun, H.; Kulikowski, B.; Brock, S. L. Boosting the Catalytic Performance of Iron Phosphide Nanorods for the Oxygen

https://doi.org/10.1021/acs.chemrev.3c00005
Chem. Rev. 2023, 123, 12795−13208

Evolution Reaction by Incorporation of Manganese. *Chem. Mater.* **2017**, *29*, 3048−3054.
(493) Liao, W.; Huang, L. Improving the Oxygen Evolution Performance of Nickel Phosphide Nanoparticles with Satellite Nitrogen-Doped Carbon Quantum Dots. *Mater. Lett.* **2017**, *209*, 106−110.
(494) Menezes, P. W.; Indra, A.; Das, C.; Walter, C.; Göbel, C.; Gutkin, V.; Schmeißer, D.; Driess, M. Uncovering the Nature of Active Species of Nickel Phosphide Catalysts in High-Performance Electrochemical Overall Water Splitting. *ACS Catal.* **2017**, *7*, 103−109.
(495) Pu, Z.; Zhang, C.; Amiinu, I. S.; Li, W.; Wu, L.; Mu, S. General Strategy for the Synthesis of Transition-Metal Phosphide/N-Doped Carbon Frameworks for Hydrogen and Oxygen Evolution. *ACS Appl. Mater. Interfaces* **2017**, *9*, 16187−16193.
(496) Tang, K.; Wang, X.; Wang, M.; Xie, Y.; Zhou, J.; Yan, C. Ni/Fe Ratio Dependence of Catalytic Activity in Monodisperse Ternary Nickel Iron Phosphide for Efficient Water Oxidation. *ChemElectroChem* **2017**, *4*, 2150−2157.
(497) Wang, P.; Pu, Z.; Li, Y.; Wu, L.; Tu, Z.; Jiang, M.; Kou, Z.; Amiinu, I. S.; Mu, S. Iron-Doped Nickel Phosphide Nanosheet Arrays: An Efficient Bifunctional Electrocatalyst for Water Splitting. *ACS Appl. Mater. Interfaces* **2017**, *9*, 26001−26007.
(498) Liyanage, D. R.; Li, D.; Cheek, Q. B.; Baydoun, H.; Brock, S. L. Synthesis and Oxygen Evolution Reaction (OER) Catalytic Performance of $Ni_{2-x}Ru_xP$ Nanocrystals: Enhancing Activity by Dilution of the Noble Metal. *J. Mater. Chem. A* **2017**, *5*, 17609−17618.
(499) Wang, T.; Wang, C.; Jin, Y.; Sviripa, A.; Liang, J.; Han, J.; Huang, Y.; Li, Q.; Wu, G. Amorphous Co-Fe-P Nanospheres for Efficient Water Oxidation. *J. Mater. Chem. A* **2017**, *5*, 25378−25384.
(500) Wei, L.; Goh, K.; Birer, O.; Karahan, H. E.; Chang, J.; Zhai, S.; Chen, X.; Chen, Y. A Hierarchically Porous Nickel-Copper Phosphide Nano-Foam for Efficient Electrochemical Splitting of Water. *Nanoscale* **2017**, *9*, 4401−4408.
(501) Zhang, B.; Lui, Y. H.; Zhou, L.; Tang, X.; Hu, S. An Alkaline Electro-Activated Fe-Ni Phosphide Nanoparticle-Stack Array for High-Performance Oxygen Evolution under Alkaline and Neutral Conditions. *J. Mater. Chem. A* **2017**, *5*, 13329−13335.
(502) Zhu, C.; Fu, S.; Xu, B. Z.; Song, J.; Shi, Q.; Engelhard, M. H.; Li, X.; Beckman, S. P.; Sun, J.; Du, D.; et al. Sugar Blowing-Induced Porous Cobalt Phosphide/Nitrogen-Doped Carbon Nanostructures with Enhanced Electrochemical Oxidation Performance toward Water and Other Small Molecules. *Small* **2017**, *13*, 1700796.
(503) Zhao, Z.; Schipper, D. E.; Leitner, A. P.; Thirumalai, H.; Chen, J.-H.; Xie, L.; Qin, F.; Alam, M. K.; Grabow, L. C.; Chen, S.; et al. Bifunctional Metal Phosphide FeMnP Films from Single Source Metal Organic Chemical Vapor Deposition for Efficient Overall Water Splitting. *Nano Energy* **2017**, *39*, 444−453.
(504) Zhang, L.; Chang, C.; Hsu, C.-W.; Chang, C.-W.; Lu, S.-Y. Hollow Nanocubes Composed of Well-Dispersed Mixed Metal-Rich Phosphides in N-Doped Carbon as Highly Efficient and Durable Electrocatalysts for the Oxygen Evolution Reaction at High Current Densities. *J. Mater. Chem. A* **2017**, *5*, 19656−19663.
(505) Zhang, B.; Lui, Y. H.; Ni, H.; Hu, S. Bimetallic $(Fe_xNi_{1-x})_2P$ Nanoarrays as Exceptionally Efficient Electrocatalysts for Oxygen Evolution in Alkaline and Neutral Media. *Nano Energy* **2017**, *38*, 553−560.
(506) Yan, Y.; Zhao, B.; Yi, S. C.; Wang, X. Assembling Pore-Rich FeP Nanorods on the CNT Backbone as an Advanced Electrocatalyst for Oxygen Evolution. *J. Mater. Chem. A* **2016**, *4*, 13005−13010.
(507) Chang, J.; Liang, L.; Li, C.; Wang, M.; Ge, J.; Liu, C.; Xing, W. Ultrathin Cobalt Phosphide Nanosheets as Efficient Bifunctional Catalysts for a Water Electrolysis Cell and the Origin for Cell Performance Degradation. *Green Chem.* **2016**, *18*, 2287−2295.
(508) Li, W.; Gao, X.; Wang, X.; Xiong, D.; Huang, P.-P.; Song, W.-G.; Bao, X.; Liu, L. From Water Reduction to Oxidation: Janus Co-Ni-P Nanowires as High-Efficiency and Ultrastable Electrocatalysts for over 3000 h Water Splitting. *J. Power Sources* **2016**, *330*, 156−166.
(509) Dutta, A.; Samantara, A. K.; Dutta, S. K.; Jena, B. K.; Pradhan, N. Surface-Oxidized Dicobalt Phosphide Nanoneedles as a Nonprecious, Durable, and Efficient OER Catalyst. *ACS Energy Lett.* **2016**, *1*, 169−174.
(510) Fu, S.; Zhu, C.; Song, J.; Engelhard, M. H.; Li, X.; Du, D.; Lin, Y. Highly Ordered Mesoporous Bimetallic Phosphides as Efficient Oxygen Evolution Electrocatalysts. *ACS Energy Lett.* **2016**, *1*, 792−796.
(511) Li, J.; Li, J.; Zhou, X.; Xia, Z.; Gao, W.; Ma, Y.; Qu, Y. Highly Efficient and Robust Nickel Phosphides as Bifunctional Electrocatalysts for Overall Water-Splitting. *ACS Appl. Mater. Interfaces* **2016**, *8*, 10826−10834.
(512) Jin, Z.; Li, P.; Xiao, D. Metallic Co_2P Ultrathin Nanowires Distinguished from CoP as Robust Electrocatalysts for Overall Water-Splitting. *Green Chem.* **2016**, *18*, 1459−1464.
(513) Mendoza-Garcia, A.; Su, D.; Sun, S. Sea Urchin-like Cobalt-Iron Phosphide as an Active Catalyst for Oxygen Evolution Reaction. *Nanoscale* **2016**, *8*, 3244−3247.
(514) Read, C. G.; Callejas, J. F.; Holder, C. F.; Schaak, R. E. General Strategy for the Synthesis of Transition Metal Phosphide Films for Electrocatalytic Hydrogen and Oxygen Evolution. *ACS Appl. Mater. Interfaces* **2016**, *8*, 12798−12803.
(515) Wang, P.; Song, F.; Amal, R.; Ng, Y. H.; Hu, X. Efficient Water Splitting Catalyzed by Cobalt Phosphide-Based Nanoneedle Arrays Supported on Carbon Cloth. *ChemSusChem* **2016**, *9*, 472−477.
(516) Wang, X.; Li, W.; Xiong, D.; Petrovykh, D. Y.; Liu, L. Bifunctional Nickel Phosphide Nanocatalysts Supported on Carbon Fiber Paper for Highly Efficient and Stable Overall Water Splitting. *Adv. Funct. Mater.* **2016**, *26*, 4067−4077.
(517) Wei, S.; Qi, K.; Jin, Z.; Cao, J.; Zheng, W.; Chen, H.; Cui, X. One-Step Synthesis of a Self-Supported Copper Phosphide Nanobush for Overall Water Splitting. *ACS Omega* **2016**, *1*, 1367−1373.
(518) Wang, X.; Li, W.; Xiong, D.; Liu, L. Fast Fabrication of Self-Supported Porous Nickel Phosphide Foam for Efficient, Durable Oxygen Evolution and Overall Water Splitting. *J. Mater. Chem. A* **2016**, *4*, 5639−5646.
(519) Xiong, D.; Wang, X.; Li, W.; Liu, L. Facile Synthesis of Iron Phosphide Nanorods for Efficient and Durable Electrochemical Oxygen Evolution. *Chem. Commun.* **2016**, *52*, 8711−8714.
(520) Yu, X.-Y.; Feng, Y.; Guan, B.; Lou, X. W. D.; Paik, U. Carbon Coated Porous Nickel Phosphides Nanoplates for Highly Efficient Oxygen Evolution Reaction. *Energy Environ. Sci.* **2016**, *9*, 1246−1250.
(521) Yu, J.; Li, Q.; Li, Y.; Xu, C.-Y.; Zhen, L.; Dravid, V. P.; Wu, J. Ternary Metal Phosphide with Triple-Layered Structure as a Low-Cost and Efficient Electrocatalyst for Bifunctional Water Splitting. *Adv. Funct. Mater.* **2016**, *26*, 7644−7651.
(522) Zhang, Z.; Liu, S.; Xiao, J.; Wang, S. Fiber-Based Multifunctional Nickel Phosphide Electrodes for Flexible Energy Conversion and Storage. *J. Mater. Chem. A* **2016**, *4*, 9691−9699.
(523) Zhang, G.; Wang, G.; Liu, Y.; Liu, H.; Qu, J.; Li, J. Highly Active and Stable Catalysts of Phytic Acid-Derivative Transition Metal Phosphides for Full Water Splitting. *J. Am. Chem. Soc.* **2016**, *138*, 14686−14693.
(524) Chang, J.; Xiao, Y.; Xiao, M.; Ge, J.; Liu, C.; Xing, W. Surface Oxidized Cobalt-Phosphide Nanorods As an Advanced Oxygen Evolution Catalyst in Alkaline Solution. *ACS Catal.* **2015**, *5*, 6874−6878.
(525) Ledendecker, M.; Krick Calderón, S.; Papp, C.; Steinrück, H.-P.; Antonietti, M.; Shalom, M. The Synthesis of Nanostructured Ni_5P_4 Films and Their Use as a Non-Noble Bifunctional Electrocatalyst for Full Water Splitting. *Angew. Chem. Int. Ed.* **2015**, *54*, 12361−12365.
(526) Yan, Y.; Xia, B. Y.; Ge, X.; Liu, Z.; Fisher, A.; Wang, X. A Flexible Electrode Based on Iron Phosphide Nanotubes for Overall Water Splitting. *Chem.—Eur. J.* **2015**, *21*, 18062−18067.
(527) Han, A.; Chen, H.; Sun, Z.; Xu, J.; Du, P. High Catalytic Activity for Water Oxidation Based on Nanostructured Nickel Phosphide Precursors. *Chem. Commun.* **2015**, *51*, 11626−11629.

https://doi.org/10.1021/acs.chemrev.3c00005
Chem. Rev. 2023, 123, 12795−13208

(528) Liu, Y.; Ding, M.; Deng, X.; Zhang, Y.; Zhao, G. Bimetal Phosphide as High Efficiency and Stable Bifunctional Electrocatalysts for Hydrogen and Oxygen Evolution Reaction in Alkaline Solution. *RSC Adv.* **2022**, *12*, 9051−9057.
(529) Li, W.; Yu, X.; Luo, L.; Du, Y.; Wu, Q. Fe-Doped $NiTe_2/Ni_2P$ Grown in Situ on Ni Foam as an Efficient Electrocatalyst for Oxygen Evolution Reaction. *J. Alloys Compd.* **2022**, *917*, 165369.
(530) Shamloofard, M.; Shahrokhian, S. Dual-Electrocatalysis Behavior of Star-like Zinc-Cobalt-Sulfide Decorated with Cobalt-Molybdenum-Phosphide in Hydrogen and Oxygen Evolution Reactions. *Nanoscale* **2021**, *13*, 17576−17591.
(531) Wang, J.; Chen, C.; Cai, N.; Wang, M.; Li, H.; Yu, F. High Topological Trimetal Phosphide of CoP@FeNiP toward Enhanced Activities in Oxygen Evolution Reaction. *Nanoscale* **2021**, *13*, 1354−1363.
(532) Amorim, I.; Xu, J.; Zhang, N.; Yu, Z.; Araújo, A.; Bento, F.; Liu, L. Dual-Phase CoP-$CoTe_2$ Nanowires as an Efficient Bifunctional Electrocatalyst for Bipolar Membrane-Assisted Acid-Alkaline Water Splitting. *Chem. Eng. J.* **2021**, *420*, 130454.
(533) Wang, C.; Chen, W.; Yuan, D.; Qian, S.; Cai, D.; Jiang, J.; Zhang, S. Tailoring the Nanostructure and Electronic Configuration of Metal Phosphides for Efficient Electrocatalytic Oxygen Evolution Reactions. *Nano Energy* **2020**, *69*, 104453.
(534) Shuai, C.; Mo, Z.; Niu, X.; Zhao, P.; Dong, Q.; Chen, Y.; Liu, N.; Guo, R. Nickel/Cobalt Bimetallic Phosphides Derived Metal-Organic Frameworks as Bifunctional Electrocatalyst for Oxygen and Hydrogen Evolution Reaction. *J. Alloys Compd.* **2020**, *847*, 156514.
(535) Amorim, I.; Xu, J.; Zhang, N.; Xiong, D.; Thalluri, S. M.; Thomas, R.; Sousa, J. P. S.; Araújo, A.; Li, H.; Liu, L. Bimetallic Cobalt-Nickel Phosphide Nanowires for Electrocatalysis of the Oxygen and Hydrogen Evolution Reactions. *Catal. Today* **2020**, *358*, 196−202.
(536) Xu, Q.; Gao, W.; Wang, M.; Yuan, G.; Ren, X.; Zhao, R.; Zhao, S.; Wang, Q. Electrodeposition of NiS/Ni_2P Nanoparticles Embedded in Amorphous $Ni(OH)_2$ Nanosheets as an Efficient and Durable Dual-Functional Electrocatalyst for Overall Water Splitting. *Int. J. Hydrogen Energy* **2020**, *45*, 2546−2556.
(537) Wang, T.; Liu, X.; Yan, Z.; Teng, Y.; Li, R.; Zhang, J.; Peng, T. Facile Preparation Process of NiCoP-$NiCoSe_2$ Nano-Bilayer Films for Oxygen Evolution Reaction with High Efficiency and Long Duration. *ACS Sustainable Chem. Eng.* **2020**, *8*, 1240−1251.
(538) Ayom, G. E.; Khan, D. M.; Ingsel, T.; Lin, W.; Gupta, R.; Zamisa, S.; Zyl, W. V.; Revaprasadu, N. Flexible Molecular Precursors for Selective Decomposition to Nickel Sulfide or Nickel Phosphide for Water Splitting and Supercapacitance. *Chem.—Eur. J.* **2020**, *26*, 2693−2704.
(539) Huang, L.; Wu, H.; Zhang, Y. One-Step Synthesis of CoPSe-$CoSe_2$/CNTs as Efficient Electrocatalyst for Oxygen Evolution Reaction. *Electrochim. Acta* **2020**, *331*, 135362.
(540) Jiang, D.; Ma, W.; Yang, R.; Quan, B.; Li, D.; Meng, S.; Chen, M. Nickel-Manganese Bimetallic Phosphides Porous Nanosheet Arrays as Highly Active Bifunctional Hydrogen and Oxygen Evolution Electrocatalysts for Overall Water Splitting. *Electrochim. Acta* **2020**, *329*, 135121.
(541) Qi, Y.; Zhang, Q.; Meng, S.; Li, D.; Wei, W.; Jiang, D.; Chen, M. Iron-Doped Nickle Cobalt Ternary Phosphide Hyperbranched Hierarchical Arrays for Efficient Overall Water Splitting. *Electrochim. Acta* **2020**, *334*, 135633.
(542) Yang, S.; Chen, G.; Ricciardulli, A. G.; Zhang, P.; Zhang, Z.; Shi, H.; Ma, J.; Zhang, J.; Blom, P. W. M.; Feng, X. Topochemical Synthesis of Two-Dimensional Transition-Metal Phosphides Using Phosphorene Templates. *Angew. Chem. Int. Ed.* **2020**, *59*, 465−470.
(543) Du, X.; Fu, J.; Zhang, X. Construction of a $MnCo_2O_4$@Ni_yM_x (S and P) Crosslinked Network for Efficient Electrocatalytic Water Splitting. *CrystEngComm* **2019**, *21*, 7293−7302.
(544) Lu, Y.; Hou, W.; Yang, D.; Chen, Y. CoP Nanosheets In-Situ Grown on N-Doped Graphene as an Efficient and Stable Bifunctional Electrocatalyst for Hydrogen and Oxygen Evolution Reactions. *Electrochim. Acta* **2019**, *307*, 543−552.
(545) Lv, Z.; Zhang, Y.; Wang, K.; Yu, T.; Liu, X.; Wang, G.; Xie, G.; Jiang, L. High Performance of Co-P/NF Electrocatalyst for Oxygen Evolution Reaction. *Mater. Chem. Phys.* **2019**, *235*, 121772.
(546) Meganathan, M. D.; Huang, T.; Fang, H.; Mao, J.; Sun, G. Electrochemical Impacts of Sheet-like Hafnium Phosphide and Hafnium Disulfide Catalysts Bonded with Reduced Graphene Oxide Sheets for Bifunctional Oxygen Reactions in Alkaline Electrolytes. *RSC Adv.* **2019**, *9*, 2599−2607.
(547) Ren, J.-T.; Chen, L.; Yuan, G.-G.; Weng, C.-C.; Yuan, Z.-Y. Monolithic Ni_xM_y (M = OH, P, S, Se) Nanosheets as Efficient and Stable Electrocatalysts for Overall Water Splitting. *Electrochim. Acta* **2019**, *295*, 148−156.
(548) Pawar, S. M.; Pawar, B. S.; Babar, P. T.; Aqueel Ahmed, A. T.; Chavan, H. S.; Jo, Y.; Cho, S.; Kim, J.; Inamdar, A. I.; Kim, J. H.; et al. Electrosynthesis of Copper Phosphide Thin Films for Efficient Water Oxidation. *Mater. Lett.* **2019**, *241*, 243−247.
(549) Shanmugam, S.; Sivanantham, A.; Matsunaga, M.; Simon, U.; Osaka, T. Metal Phosphide Nanoparticles Embedded in Carbon as Efficient Electrocatalyst for Oxygen Evolution Reaction. *Electrochim. Acta* **2019**, *297*, 749−754.
(550) Sun, K.; Li, J.; Huang, L.; Ji, S.; Kannan, P.; Li, D.; Liu, L.; Liao, S. Biomass-Derived 3D Hierarchical N-Doped Porous Carbon Anchoring Cobalt-Iron Phosphide Nanodots as Bifunctional Electrocatalysts for LiO_2 Batteries. *J. Power Sources* **2019**, *412*, 433−441.
(551) Wang, X.; Ma, Z.; Chai, L.; Xu, L.; Zhu, Z.; Hu, Y.; Qian, J.; Huang, S. MOF Derived N-Doped Carbon Coated CoP Particle/Carbon Nanotube Composite for Efficient Oxygen Evolution Reaction. *Carbon* **2019**, *141*, 643−651.
(552) Yang, S.; Xie, M.; Chen, L.; Wei, W.; Lv, X.; Xu, Y.; Ullah, N.; Judith, O. C.; Adegbemiga, Y. B.; Xie, J. Cobalt Phosphide Nanoparticles Embedded in 3D N-Doped Porous Carbon for Efficient Hydrogen and Oxygen Evolution Reactions. *Int. J. Hydrogen Energy* **2019**, *44*, 4543−4552.
(553) Zheng, H.; Huang, X.; Gao, H.; Lu, G.; Li, A.; Dong, W.; Wang, G. Cobalt-Tuned Nickel Phosphide Nanoparticles for Highly Efficient Electrocatalysis. *Appl. Surf. Sci.* **2019**, *479*, 1254−1261.
(554) Anjum, M. A. R.; Okyay, M. S.; Kim, M.; Lee, M. H.; Park, N.; Lee, J. S. Bifunctional Sulfur-Doped Cobalt Phosphide Electrocatalyst Outperforms All-Noble-Metal Electrocatalysts in Alkaline Electrolyzer for Overall Water Splitting. *Nano Energy* **2018**, *53*, 286−295.
(555) Yu, L.; Zhou, H.; Sun, J.; Mishra, I. K.; Luo, D.; Yu, F.; Yu, Y.; Chen, S.; Ren, Z. Amorphous NiFe Layered Double Hydroxide Nanosheets Decorated on 3D Nickel Phosphide Nanoarrays: A Hierarchical Core-Shell Electrocatalyst for Efficient Oxygen Evolution. *J. Mater. Chem. A* **2018**, *6*, 13619−13623.
(556) Bose, R.; Jothi, V. R.; Velusamy, D. B.; Arunkumar, P.; Yi, S. C. A Highly Effective, Stable Oxygen Evolution Catalyst Derived from Transition Metal Selenides and Phosphides. *Part. Part. Syst. Charact.* **2018**, *35*, 1800135.
(557) Ma, L.; Zhang, W.; Zhao, P.; Liang, J.; Hu, Y.; Zhu, G.; Chen, R.; Tie, Z.; Liu, J.; Jin, Z. Highly Efficient Overall Water Splitting Driven by All-Inorganic Perovskite Solar Cells and Promoted by Bifunctional Bimetallic Phosphide Nanowire Arrays. *J. Mater. Chem. A* **2018**, *6*, 20076−20082.
(558) Xing, J.; Zou, Z.; Guo, K.; Xu, C. The Effect of Phosphating Time on the Electrocatalytic Activity of Nickel Phosphide Nanorod Arrays Grown on Ni Foam. *J. Mater. Res.* **2018**, *33*, 556−567.
(559) Surendran, S.; Shanmugapriya, S.; Shanmugam, S.; Vasylechko, L.; Kalai Selvan, R. Interweaved Nickel Phosphide Sponge as an Electrode for Flexible Supercapattery and Water Splitting Applications. *ACS Appl. Energy Mater.* **2018**, *1*, 78−92.
(560) Wang, J.; Liu, D.; Huang, H.; Yang, N.; Yu, B.; Wen, M.; Wang, X.; Chu, P. K.; Yu, X.-F. In-Plane Black Phosphorus/Dicobalt Phosphide Heterostructure for Efficient Electrocatalysis. *Angew. Chem. Int. Ed.* **2018**, *57*, 2600−2604.
(561) Narendra Kumar, A. V.; Li, Y.; Yu, H.; Yin, S.; Xue, H.; Xu, Y.; Li, X.; Wang, H.; Wang, L. 3D Graphene Aerogel Supported FeNi-P Derived from Electroactive Nickel Hexacyanoferrate as Efficient Oxygen Evolution Catalyst. *Electrochim. Acta* **2018**, *292*, 107−114.

https://doi.org/10.1021/acs.chemrev.3c00005
Chem. Rev. 2023, 123, 12795−13208

(562) Ren, J.-T.; Yuan, G.-G.; Weng, C.-C.; Yuan, Z.-Y. Ultrafine Metal Phosphide Nanoparticles in Situ Encapsulated in Porous N,P-Codoped Nanofibrous Carbon Coated on Carbon Paper for Effective Water Splitting. *Electrochim. Acta* **2018**, *261*, 454−463.
(563) Chen, J.; Li, Y.; Sheng, G.; Xu, L.; Ye, H.; Fu, X.-Z.; Sun, R.; Wong, C.-P. Iron-Doped Nickel Phosphide Nanosheets In Situ Grown on Nickel Submicrowires as Efficient Electrocatalysts for Oxygen Evolution Reaction. *ChemCatChem* **2018**, *10*, 2248−2253.
(564) Fu, H. Q.; Zhang, L.; Wang, C. W.; Zheng, L. R.; Liu, P. F.; Yang, H. G. 1D/1D Hierarchical Nickel Sulfide/Phosphide Nanostructures for Electrocatalytic Water Oxidation. *ACS Energy Lett.* **2018**, *3*, 2021−2029.
(565) Gao, W.-K.; Lin, J.-H.; Wang, K.; Liu, Z.-Z.; Qin, J.-F.; Xie, J.-Y.; Zhang, X.-Y.; Chai, Y.-M.; Dong, B. Controllable Phosphorsulfurization of Uniform Binary Ni-Fe Nanocubes for Enhanced Water Oxidation. *Mater. Lett.* **2018**, *229*, 248−251.
(566) He, L.; Cui, B.; Hu, B.; Liu, J.; Tian, K.; Wang, M.; Song, Y.; Fang, S.; Zhang, Z.; Jia, Q. Mesoporous Nanostructured CoFe-Se-P Composite Derived from a Prussian Blue Analogue as a Superior Electrocatalyst for Efficient Overall Water Splitting. *ACS Appl. Energy Mater.* **2018**, *1*, 3915−3928.
(567) Jia, H.; Jiang, R.; Lu, W.; Ruan, Q.; Wang, J.; Yu, J. C. Aerosol-Spray Metal Phosphide Microspheres with Bifunctional Electrocatalytic Properties for Water Splitting. *J. Mater. Chem. A* **2018**, *6*, 4783−4792.
(568) Li, H.; Ke, F.; Zhu, J. MOF-Derived Ultrathin Cobalt Phosphide Nanosheets as Efficient Bifunctional Hydrogen Evolution Reaction and Oxygen Evolution Reaction Electrocatalysts. *Nanomater.* **2018**, *8*, 89.
(569) Li, H.; Xu, S.-M.; Yan, H.; Yang, L.; Xu, S. Cobalt Phosphide Composite Encapsulated within N,P-Doped Carbon Nanotubes for Synergistic Oxygen Evolution. *Small* **2018**, *14*, 1800367.
(570) Li, J.; Liu, G.; Liu, B.; Min, Z.; Qian, D.; Jiang, J.; Li, J. An Extremely Facile Route to Co_2P Encased in N,P-Codoped Carbon Layers: Highly Efficient Bifunctional Electrocatalysts for ORR and OER. *Int. J. Hydrogen Energy* **2018**, *43*, 1365−1374.
(571) Liu, Y.; Wang, Q.; Wu, L.; Long, Y.; Li, J.; Song, S.; Zhang, H. Nanoporous Carbon-Coated Bimetallic Phosphides for Efficient Electrochemical Water Splitting. *Cryst. Growth Des.* **2018**, *18*, 3404−3410.
(572) Zhang, F.; Wei, M.; Sui, J.; Jin, C.; Luo, Y.; Bie, S.; Yang, R. Cobalt Phosphide Microsphere as an Efficient Bifunctional Oxygen Catalyst for Li-Air Batteries. *J. Alloys Compd.* **2018**, *750*, 655−658.
(573) Zhu, M.; Zhou, Y.; Sun, Y.; Zhu, C.; Hu, L.; Gao, J.; Huang, H.; Liu, Y.; Kang, Z. Cobalt Phosphide/Carbon Dots Composite as an Efficient Electrocatalyst for Oxygen Evolution Reaction. *Dalton Trans.* **2018**, *47*, 5459−5464.
(574) Xiao, X.; He, C.-T.; Zhao, S.; Li, J.; Lin, W.; Yuan, Z.; Zhang, Q.; Wang, S.; Dai, L.; Yu, D. A General Approach to Cobalt-Based Homobimetallic Phosphide Ultrathin Nanosheets for Highly Efficient Oxygen Evolution in Alkaline Media. *Energy Environ. Sci.* **2017**, *10*, 893−899.
(575) Song, J.; Zhu, C.; Xu, B. Z.; Fu, S.; Engelhard, M. H.; Ye, R.; Du, D.; Beckman, S. P.; Lin, Y. Bimetallic Cobalt-Based Phosphide Zeolitic Imidazolate Framework: CoPx Phase-Dependent Electrical Conductivity and Hydrogen Atom Adsorption Energy for Efficient Overall Water Splitting. *Adv. Energy Mater.* **2017**, *7*, 1601555.
(576) Xu, Y.; Duan, S.; Li, H.; Yang, M.; Wang, S.; Wang, X.; Wang, R. $Au/Ni_{12}P_5$ Core/Shell Single-Crystal Nanoparticles as Oxygen Evolution Reaction Catalyst. *Nano Res.* **2017**, *10*, 3103−3112.
(577) Zou, H.-H.; Yuan, C.-Z.; Zou, H.-Y.; Cheang, T.-Y.; Zhao, S.-J.; Qazi, U. Y.; Zhong, S.-L.; Wang, L.; Xu, A.-W. Bimetallic Phosphide Hollow Nanocubes Derived from a Prussian-Blue-Analog Used as High-Performance Catalysts for the Oxygen Evolution Reaction. *Catal. Sci. Technol.* **2017**, *7*, 1549−1555.
(578) Yuan, C.-Z.; Zhong, S.-L.; Jiang, Y.-F.; Yang, Z. K.; Zhao, Z.-W.; Zhao, S.-J.; Jiang, N.; Xu, A.-W. Direct Growth of Cobalt-Rich Cobalt Phosphide Catalysts on Cobalt Foil: An Efficient and Self-Supported Bifunctional Electrode for Overall Water Splitting in Alkaline Media. *J. Mater. Chem. A* **2017**, *5*, 10561−10566.
(579) Li, F.; Bu, Y.; Lv, Z.; Mahmood, J.; Han, G.-F.; Ahmad, I.; Kim, G.; Zhong, Q.; Baek, J.-B. Porous Cobalt Phosphide Polyhedrons with Iron Doping as an Efficient Bifunctional Electrocatalyst. *Small* **2017**, *13*, 1701167.
(580) Hou, J.; Sun, Y.; Cao, S.; Wu, Y.; Chen, H.; Sun, L. Graphene Dots Embedded Phosphide Nanosheet-Assembled Tubular Arrays for Efficient and Stable Overall Water Splitting. *ACS Appl. Mater. Interfaces* **2017**, *9*, 24600−24607.
(581) He, P.; Yu, X.-Y.; Lou, X. W. D. Carbon-Incorporated Nickel-Cobalt Mixed Metal Phosphide Nanoboxes with Enhanced Electrocatalytic Activity for Oxygen Evolution. *Angew. Chem. Int. Ed.* **2017**, *56*, 3897−3900.
(582) Ren, J.; Hu, Z.; Chen, C.; Liu, Y.; Yuan, Z. Integrated Ni_2P Nanosheet Arrays on Three-Dimensional Ni Foam for Highly Efficient Water Reduction and Oxidation. *J. Energy Chem.* **2017**, *26*, 1196−1202.
(583) Barwe, S.; Andronescu, C.; Vasile, E.; Masa, J.; Schuhmann, W. Influence of Ni to Co Ratio in Mixed Co and Ni Phosphides on Their Electrocatalytic Oxygen Evolution Activity. *Electrochem. Commun.* **2017**, *79*, 41−45.
(584) Li, P.; Zeng, H. C. Advanced Oxygen Evolution Catalysis by Bimetallic Ni-Fe Phosphide Nanoparticles Encapsulated in Nitrogen, Phosphorus, and Sulphur Tri-Doped Porous Carbon. *Chem. Commun.* **2017**, *53*, 6025−6028.
(585) Liang, X.; Zheng, B.; Chen, L.; Zhang, J.; Zhuang, Z.; Chen, B. MOF-Derived Formation of Ni_2P-CoP Bimetallic Phosphides with Strong Interfacial Effect toward Electrocatalytic Water Splitting. *ACS Appl. Mater. Interfaces* **2017**, *9*, 23222−23229.
(586) Zhang, T.; Du, J.; Xi, P.; Xu, C. Hybrids of Cobalt/Iron Phosphides Derived from Bimetal-Organic Frameworks as Highly Efficient Electrocatalysts for Oxygen Evolution Reaction. *ACS Appl. Mater. Interfaces* **2017**, *9*, 362−370.
(587) Zhai, M.; Wang, F.; Du, H. Transition-Metal Phosphide-Carbon Nanosheet Composites Derived from Two-Dimensional Metal-Organic Frameworks for Highly Efficient Electrocatalytic Water-Splitting. *ACS Appl. Mater. Interfaces* **2017**, *9*, 40171−40179.
(588) Hao, J.; Yang, W.; Huang, Z.; Zhang, C. Superhydrophilic and Superaerophobic Copper Phosphide Microsheets for Efficient Electrocatalytic Hydrogen and Oxygen Evolution. *Adv. Mater. Interfaces* **2016**, *3*, 1600236.
(589) Huang, H.; Yu, C.; Yang, J.; Zhao, C.; Han, X.; Liu, Z.; Qiu, J. Strongly Coupled Architectures of Cobalt Phosphide Nanoparticles Assembled on Graphene as Bifunctional Electrocatalysts for Water Splitting. *ChemElectroChem* **2016**, *3*, 719−725.
(590) Li, Z.; Dou, X.; Zhao, Y.; Wu, C. Enhanced Oxygen Evolution Reaction of Metallic Nickel Phosphide Nanosheets by Surface Modification. *Inorg. Chem. Front.* **2016**, *3*, 1021−1027.
(591) Liu, M.; Li, J. Cobalt Phosphide Hollow Polyhedron as Efficient Bifunctional Electrocatalysts for the Evolution Reaction of Hydrogen and Oxygen. *ACS Appl. Mater. Interfaces* **2016**, *8*, 2158−2165.
(592) Wu, R.; Wang, D. P.; Zhou, K.; Srikanth, N.; Wei, J.; Chen, Z. Porous Cobalt Phosphide/Graphitic Carbon Polyhedral Hybrid Composites for Efficient Oxygen Evolution Reactions. *J. Mater. Chem. A* **2016**, *4*, 13742−13745.
(593) Xiao, J.; Lv, Q.; Zhang, Y.; Zhang, Z.; Wang, S. One-Step Synthesis of Nickel Phosphide Nanowire Array Supported on Nickel Foam with Enhanced Electrocatalytic Water Splitting Performance. *RSC Adv.* **2016**, *6*, 107859−107864.
(594) Yang, L.; Qi, H.; Zhang, C.; Sun, X. An Efficient Bifunctional Electrocatalyst for Water Splitting Based on Cobalt Phosphide. *Nanotechnology* **2016**, *27*, 23LT01.
(595) Wu, T.; Pi, M.; Zhang, D.; Chen, S. 3D Structured Porous CoP_3 Nanoneedle Arrays as an Efficient Bifunctional Electrocatalyst for the Evolution Reaction of Hydrogen and Oxygen. *J. Mater. Chem. A* **2016**, *4*, 14539−14544.

https://doi.org/10.1021/acs.chemrev.3c00005
Chem. Rev. 2023, 123, 12795−13208

(596) Mendoza-Garcia, A.; Zhu, H.; Yu, Y.; Li, Q.; Zhou, L.; Su, D.; Kramer, M. J.; Sun, S. Controlled Anisotropic Growth of Co-Fe-P from Co-Fe-O Nanoparticles. *Angew. Chem. Int. Ed.* **2015**, *54*, 9642−9645.
(597) Yang, Y.; Fei, H.; Ruan, G.; Tour, J. M. Porous Cobalt-Based Thin Film as a Bifunctional Catalyst for Hydrogen Generation and Oxygen Generation. *Adv. Mater.* **2015**, *27*, 3175−3180.
(598) Son, C. Y.; Kwak, I. H.; Lim, Y. R.; Park, J. FeP and FeP_2 Nanowires for Efficient Electrocatalytic Hydrogen Evolution Reaction. *Chem. Commun.* **2016**, *52*, 2819−2822.
(599) Laoutid, F.; Bonnaud, L.; Alexandre, M.; Lopez-Cuesta, J.-M.; Dubois, Ph. New Prospects in Flame Retardant Polymer Materials: From Fundamentals to Nanocomposites. *Mater. Sci. Eng. R Rep.* **2009**, *63*, 100−125.
(600) Fu, S.; Song, P.; Liu, X. Thermal and Flame Retardancy Properties of Thermoplastics/Natural Fiber Biocomposites. In *Advanced High Strength Natural Fibre Composites in Construction*; Fan, M., Fu, F., Eds.; Woodhead Publishing, 2017; Chapter 19, pp 479−508. DOI: 10.1016/B978-0-08-100411-1.00019-4.
(601) Prins, R.; Bussell, M. E. Metal Phosphides: Preparation, Characterization and Catalytic Reactivity. *Catal. Lett.* **2012**, *142*, 1413−1436.
(602) Wu, T.; Pi, M.; Zhang, D.; Chen, S. Three-Dimensional Porous Structural MoP_2 Nanoparticles as a Novel and Superior Catalyst for Electrochemical Hydrogen Evolution. *J. Power Sources* **2016**, *328*, 551−557.
(603) Kibsgaard, J.; Jaramillo, T. F. Molybdenum Phosphosulfide: An Active, Acid-Stable, Earth-Abundant Catalyst for the Hydrogen Evolution Reaction. *Angew. Chem. Int. Ed.* **2014**, *53*, 14433−14437.
(604) Callejas, J. F.; Read, C. G.; Popczun, E. J.; McEnaney, J. M.; Schaak, R. E. Nanostructured Co_2P Electrocatalyst for the Hydrogen Evolution Reaction and Direct Comparison with Morphologically Equivalent CoP. *Chem. Mater.* **2015**, *27*, 3769−3774.
(605) Popczun, E. J.; McKone, J. R.; Read, C. G.; Biacchi, A. J.; Wiltrout, A. M.; Lewis, N. S.; Schaak, R. E. Nanostructured Nickel Phosphide as an Electrocatalyst for the Hydrogen Evolution Reaction. *J. Am. Chem. Soc.* **2013**, *135*, 9267−9270.
(606) Huang, J.; Xiong, Y.; Peng, Z.; Chen, L.; Wang, L.; Xu, Y.; Tan, L.; Yuan, K.; Chen, Y. A General Electrodeposition Strategy for Fabricating Ultrathin Nickel Cobalt Phosphate Nanosheets with Ultrahigh Capacity and Rate Performance. *ACS Nano* **2020**, *14*, 14201−14211.
(607) Surendranath, Y.; Kanan, M. W.; Nocera, D. G. Mechanistic Studies of the Oxygen Evolution Reaction by a Cobalt-Phosphate Catalyst at Neutral pH. *J. Am. Chem. Soc.* **2010**, *132*, 16501−16509.
(608) Zhang, M.; de Respinis, M.; Frei, H. Time-Resolved Observations of Water Oxidation Intermediates on a Cobalt Oxide Nanoparticle Catalyst. *Nat. Chem.* **2014**, *6*, 362−367.
(609) Friebel, D.; Louie, M. W.; Bajdich, M.; Sanwald, K. E.; Cai, Y.; Wise, A. M.; Cheng, M.-J.; Sokaras, D.; Weng, T.-C.; Alonso-Mori, R.; et al. Identification of Highly Active Fe Sites in (Ni,Fe)OOH for Electrocatalytic Water Splitting. *J. Am. Chem. Soc.* **2015**, *137*, 1305−1313.
(610) Görlin, M.; Chernev, P.; Ferreira de Araújo, J.; Reier, T.; Dresp, S.; Paul, B.; Krähnert, R.; Dau, H.; Strasser, P. Oxygen Evolution Reaction Dynamics, Faradaic Charge Efficiency, and the Active Metal Redox States of Ni-Fe Oxide Water Splitting Electrocatalysts. *J. Am. Chem. Soc.* **2016**, *138*, 5603−5614.
(611) Görlin, M.; Ferreira de Araújo, J.; Schmies, H.; Bernsmeier, D.; Dresp, S.; Gliech, M.; Jusys, Z.; Chernev, P.; Kraehnert, R.; Dau, H.; Strasser, P. Tracking Catalyst Redox States and Reaction Dynamics in Ni-Fe Oxyhydroxide Oxygen Evolution Reaction Electrocatalysts: The Role of Catalyst Support and Electrolyte pH. *J. Am. Chem. Soc.* **2017**, *139*, 2070−2082.
(612) Dai, W.; Bai, X.; Zhu, Y.; Zhang, Y.; Lu, T.; Pan, Y.; Wang, J. Surface Reconstruction Induced in Situ Phosphorus Doping in Nickel Oxides for an Enhanced Oxygen Evolution Reaction. *J. Mater. Chem. A* **2021**, *9*, 6432−6441.
(613) Shi, Y.; Du, W.; Zhou, W.; Wang, C.; Lu, S.; Lu, S.; Zhang, B. Unveiling the Promotion of Surface-Adsorbed Chalcogenate on the Electrocatalytic Oxygen Evolution Reaction. *Angew. Chem. Int. Ed.* **2020**, *59*, 22470−22474.
(614) Lutterman, D. A.; Surendranath, Y.; Nocera, D. G. A Self-Healing Oxygen-Evolving Catalyst. *J. Am. Chem. Soc.* **2009**, *131*, 3838−3839.
(615) Valizadeh, A.; Najafpour, M. M. Is Nickel Phosphide an Efficient Catalyst for the Oxygen-Evolution Reaction at Low Overpotentials? *New J. Chem.* **2020**, *44*, 19630−19641.
(616) Baresel, D.; Sarholz, W.; Scharner, P.; Schmitz, J. Transition metal chalcogenides as oxygen catalysts for fuel cells. *Ber. Bunsenges. Phys. Chem.* **1974**, *78*, 608−611.
(617) Behret, H.; Binder, H.; Sandstede, G. Electrocatalytic Oxygen Reduction with Thiospinels and Other Sulphides of Transition Metals. *Electrochim. Acta* **1975**, *20*, 111−117.
(618) Franklin, A. D. Electrocatalysis on Non-Metallic Surfaces. *Proceedings of a Workshop Held at the National Bureau of Standards*, Gaithersburg, Maryland, December 9−12, 1975; U.S. Department of Commerce, The Bureau, 1976.
(619) Vandenborre, H.; Vermeiren, Ph.; Leysen, R. Hydrogen Evolution at Nickel Sulphide Cathodes in Alkaline Medium. *Electrochim. Acta* **1984**, *29*, 297−301.
(620) Vante, N. A.; Schubert, B.; Tributsch, H.; Perrin, A. Influence of D-State Density and Chemistry of Transition Metal Cluster Selenides on Electrocatalysis. *J. Catal.* **1988**, *112*, 384−391.
(621) Kong, D.; Cha, J. J.; Wang, H.; Lee, H. R.; Cui, Y. First-Row Transition Metal Dichalcogenide Catalysts for Hydrogen Evolution Reaction. *Energy Environ. Sci.* **2013**, *6*, 3553−3558.
(622) Pandey, M.; Vojvodic, A.; Thygesen, K. S.; Jacobsen, K. W. Two-Dimensional Metal Dichalcogenides and Oxides for Hydrogen Evolution: A Computational Screening Approach. *J. Phys. Chem. Lett.* **2015**, *6*, 1577−1585.
(623) Li, Y.; Wang, H.; Xie, L.; Liang, Y.; Hong, G.; Dai, H. MoS_2 Nanoparticles Grown on Graphene: An Advanced Catalyst for the Hydrogen Evolution Reaction. *J. Am. Chem. Soc.* **2011**, *133*, 7296−7299.
(624) Gao, M.-R.; Xu, Y.-F.; Jiang, J.; Zheng, Y.-R.; Yu, S.-H. Water Oxidation Electrocatalyzed by an Efficient $Mn_3O_4/CoSe_2$ Nanocomposite. *J. Am. Chem. Soc.* **2012**, *134*, 2930−2933.
(625) Wang, F.; Shifa, T. A.; Zhan, X.; Huang, Y.; Liu, K.; Cheng, Z.; Jiang, C.; He, J. Recent Advances in Transition-Metal Dichalcogenide Based Nanomaterials for Water Splitting. *Nanoscale* **2015**, *7*, 19764−19788.
(626) Xia, X.; Wang, L.; Sui, N.; Colvin, V. L.; Yu, W. W. Recent Progress in Transition Metal Selenide Electrocatalysts for Water Splitting. *Nanoscale* **2020**, *12*, 12249−12262.
(627) Anantharaj, S.; Kundu, S.; Noda, S. Progress in Nickel Chalcogenide Electrocatalyzed Hydrogen Evolution Reaction. *J. Mater. Chem. A* **2020**, *8*, 4174−4192.
(628) Anantharaj, S.; Noda, S. Nickel Selenides as Pre-Catalysts for Electrochemical Oxygen Evolution Reaction: A Review. *Int. J. Hydrog. Energy* **2020**, *45*, 15763−15784.
(629) Huang, J.; Jiang, Y.; An, T.; Cao, M. Increasing the Active Sites and Intrinsic Activity of Transition Metal Chalcogenide Electrocatalysts for Enhanced Water Splitting. *J. Mater. Chem. A* **2020**, *8*, 25465−25498.
(630) Boppella, R.; Tan, J.; Yun, J.; Manorama, S. V.; Moon, J. Anion-Mediated Transition Metal Electrocatalysts for Efficient Water Electrolysis: Recent Advances and Future Perspectives. *Coord. Chem. Rev.* **2021**, *427*, 213552.
(631) Zhao, Y.; Wei, S.; Pan, K.; Dong, Z.; Zhang, B.; Wu, H.-H.; Zhang, Q.; Lin, J.; Pang, H. Self-Supporting Transition Metal Chalcogenides on Metal Substrates for Catalytic Water Splitting. *Chem. Eng. J.* **2021**, *421*, 129645.
(632) Zheng, W.; Lee, L. Y. S. Metal-Organic Frameworks for Electrocatalysis: Catalyst or Precatalyst? *ACS Energy Lett.* **2021**, *6*, 2838−2843.

(633) Yin, Z.; Zhang, S.; Li, J.; Ma, S.; Chen, W.; Ma, X.; Zhou, Y.; Zhang, Z.; Wang, X. In Situ Fabrication of a Ni-Fe-S Hollow Hierarchical Sphere: An Efficient (Pre)Catalyst for OER and HER. *New J. Chem.* **2021**, *45*, 12996−13003.
(634) Chinnadurai, D.; Rajendiran, R.; Kandasamy, P. Bimetallic Copper Nickel Sulfide Electrocatalyst by One Step Chemical Bath Deposition for Efficient and Stable Overall Water Splitting Applications. *J. Colloid. Interface Sci.* **2022**, *606*, 101−112.
(635) Gao, W.-K.; Qin, J.-F.; Wang, K.; Yan, K.-L.; Liu, Z.-Z.; Lin, J.-H.; Chai, Y.-M.; Liu, C.-G.; Dong, B. Facile Synthesis of Fe-Doped Co_9S_8 Nano-Microspheres Grown on Nickel Foam for Efficient Oxygen Evolution Reaction. *Appl. Surf. Sci.* **2018**, *454*, 46−53.
(636) Zhang, S.; Sun, Y.; Liao, F.; Shen, Y.; Shi, H.; Shao, M. Co_9S_8-CuS-FeS Trimetal Sulfides for Excellent Oxygen Evolution Reaction Electrocatalysis. *Electrochim. Acta* **2018**, *283*, 1695−1701.
(637) Zhang, C.; Bhoyate, S.; Kahol, P. K.; Siam, K.; Poudel, T. P.; Mishra, S. R.; Perez, F.; Gupta, A.; Gupta, G.; Gupta, R. K. Highly Efficient and Durable Electrocatalyst Based on Nanowires of Cobalt Sulfide for Overall Water Splitting. *ChemNanoMat* **2018**, *4*, 1240−1246.
(638) Qiao, X.; Jin, J.; Fan, H.; Li, Y.; Liao, S. In Situ Growth of Cobalt Sulfide Hollow Nanospheres Embedded in Nitrogen and Sulfur Co-Doped Graphene Nanoholes as a Highly Active Electrocatalyst for Oxygen Reduction and Evolution. *J. Mater. Chem. A* **2017**, *5*, 12354−12360.
(639) Yuan, C.-Z.; Sun, Z.-T.; Jiang, Y.-F.; Yang, Z.-K.; Jiang, N.; Zhao, Z.-W.; Qazi, U. Y.; Zhang, W.-H.; Xu, A.-W. One-Step In Situ Growth of Iron-Nickel Sulfide Nanosheets on FeNi Alloy Foils: High-Performance and Self-Supported Electrodes for Water Oxidation. *Small* **2017**, *13*, 1604161.
(640) Zou, X.; Liu, Y.; Li, G.-D.; Wu, Y.; Liu, D.-P.; Li, W.; Li, H.-W.; Wang, D.; Zhang, Y.; Zou, X. Ultrafast Formation of Amorphous Bimetallic Hydroxide Films on 3D Conductive Sulfide Nanoarrays for Large-Current-Density Oxygen Evolution Electrocatalysis. *Adv. Mater.* **2017**, *29*, 1700404.
(641) Yan, K.-L.; Shang, X.; Li, Z.; Dong, B.; Chi, J.-Q.; Liu, Y.-R.; Gao, W.-K.; Chai, Y.-M.; Liu, C.-G. Facile Synthesis of Binary NiCoS Nanorods Supported on Nickel Foam as Efficient Electrocatalysts for Oxygen Evolution Reaction. *Int. J. Hydrog. Energy* **2017**, *42*, 17129−17135.
(642) Cui, M.; Yang, C.; Li, B.; Dong, Q.; Wu, M.; Hwang, S.; Xie, H.; Wang, X.; Wang, G.; Hu, L. High-Entropy Metal Sulfide Nanoparticles Promise High-Performance Oxygen Evolution Reaction. *Adv. Energy Mater.* **2021**, *11*, 2002887.
(643) Wang, Y.; Chen, N.; Du, X.; Han, X.; Zhang, X. Transition Metal Atoms M (M = Mn, Fe, Cu, Zn) Doped Nickel-Cobalt Sulfides on the Ni Foam for Efficient Oxygen Evolution Reaction and Urea Oxidation Reaction. *J. Alloys Compd.* **2022**, *893*, 162269.
(644) Wu, J.; Zhang, Y.; Zhang, B.; Li, S.; Xu, P. Zn-Doped CoS_2 Nanoarrays for an Efficient Oxygen Evolution Reaction: Understanding the Doping Effect for a Precatalyst. *ACS Appl. Mater. Interfaces* **2022**, *14*, 14235−14242.
(645) Ji, Q.; Kong, Y.; Tan, H.; Duan, H.; Li, N.; Tang, B.; Wang, Y.; Feng, S.; Lv, L.; Wang, C.; et al. Operando Identification of Active Species and Intermediates on Sulfide Interfaced by Fe_3O_4 for Ultrastable Alkaline Oxygen Evolution at Large Current Density. *ACS Catal.* **2022**, *12*, 4318−4326.
(646) Zhang, N.; Hu, Y.; An, L.; Li, Q.; Yin, J.; Li, J.; Yang, R.; Lu, M.; Zhang, S.; Xi, P.; et al. Surface Activation and Ni-S Stabilization in NiO/NiS_2 for Efficient Oxygen Evolution Reaction. *Angew. Chem. Int. Ed.* **2022**, *61*, No. e202207217.
(647) Bao, T.; Xia, Y.; Lu, J.; Zhang, C.; Wang, J.; Yuan, L.; Zhang, Y.; Liu, C.; Yu, C. A Pacman-Like Titanium-Doped Cobalt Sulfide Hollow Superstructure for Electrocatalytic Oxygen Evolution. *Small* **2022**, *18*, 2103106.
(648) Lu, Q.; Wu, H.; Zheng, X.; Cao, Y.; Li, J.; Wang, Y.; Wang, H.; Zhi, C.; Deng, Y.; Han, X.; et al. Controllable Constructing Janus Homologous Heterostructures of Transition Metal Alloys/Sulfides for Efficient Oxygen Electrocatalysis. *Adv. Energy Mater.* **2022**, *12*, 2202215.
(649) Yao, N.; Wang, G.; Jia, H.; Yin, J.; Cong, H.; Chen, S.; Luo, W. Intermolecular Energy Gap-Induced Formation of High-Valent Cobalt Species in CoOOH Surface Layer on Cobalt Sulfides for Efficient Water Oxidation. *Angew. Chem. Int. Ed.* **2022**, *61*, No. e202117178.
(650) Jia, X.; Kang, H.; Yang, X.; Li, Y.; Cui, K.; Wu, X.; Qin, W.; Wu, G. Amorphous Ni(III)-Based Sulfides as Bifunctional Water and Urea Oxidation Anode Electrocatalysts for Hydrogen Generation from Urea-Containing Water. *Appl. Catal. B: Environ.* **2022**, *312*, 121389.
(651) Chhetri, K.; Muthurasu, A.; Dahal, B.; Kim, T.; Mukhiya, T.; Chae, S.-H.; Ko, T. H.; Choi, Y. C.; Kim, H. Y. Engineering the Abundant Heterointerfaces of Integrated Bimetallic Sulfide-Coupled 2D MOF-Derived Mesoporous CoS_2 Nanoarray Hybrids for Electrocatalytic Water Splitting. *Materials Today Nano* **2022**, *17*, 100146.
(652) Javaid, S.; Xu, X.; Chen, W.; Chen, J.; Hsu, H.-Y.; Wang, S.; Yang, X.; Li, Y.; Shao, Z.; Jones, F.; Jia, G. Ni^{2+}/Co^{2+} Doped Au-Fe_7S_8 Nanoplatelets with Exceptionally High Oxygen Evolution Reaction Activity. *Nano Energy* **2021**, *89*, 106463.
(653) Dai, T.; Zhang, X.; Sun, M.; Huang, B.; Zhang, N.; Da, P.; Yang, R.; He, Z.; Wang, W.; Xi, P.; et al. Uncovering the Promotion of $CeO_2/CoS_{1.97}$ Heterostructure with Specific Spatial Architectures on Oxygen Evolution Reaction. *Adv. Mater.* **2021**, *33*, 2102593.
(654) Xiao, K.; Wei, J.-X.; Han, W.-K.; Liu, Z.-Q. Bimetallic Sulfide Interfaces: Promoting Destabilization of Water Molecules for Overall Water Splitting. *J. Power Sources* **2021**, *487*, 229408.
(655) Wang, C.; Zhu, M.; Cao, Z.; Zhu, P.; Cao, Y.; Xu, X.; Xu, C.; Yin, Z. Heterogeneous Bimetallic Sulfides Based Seawater Electrolysis towards Stable Industrial-Level Large Current Density. *Appl. Catal. B: Environ.* **2021**, *291*, 120071.
(656) Nguyen, T. X.; Su, Y.-H.; Lin, C.-C.; Ting, J.-M. Self-Reconstruction of Sulfate-Containing High Entropy Sulfide for Exceptionally High-Performance Oxygen Evolution Reaction Electrocatalyst. *Adv. Funct. Mater.* **2021**, *31*, 2106229.
(657) Yang, Y.; Meng, H.; Kong, C.; Yan, S.; Ma, W.; Zhu, H.; Ma, F.; Wang, C.; Hu, Z. Heterogeneous Ni_3S_2@$FeNi_2S_4$@NF Nanosheet Arrays Directly Used as High Efficiency Bifunctional Electrocatalyst for Water Decomposition. *J. Colloid. Interface Sci.* **2021**, *599*, 300−312.
(658) Naderi, A.; Yong, X.; Karamad, M.; Cai, J.; Zang, Y.; Gates, I.; Siahrostami, S.; Wang, G. Ternary Cobalt-Iron Sulfide as a Robust Electrocatalyst for Water Oxidation: A Dual Effect from Surface Evolution and Metal Doping. *Appl. Surf. Sci.* **2021**, *542*, 148681.
(659) Jing, Z.; Zhao, Q.; Zheng, D.; Sun, L.; Geng, J.; Zhou, Q.; Lin, J. Nickel-Doped Pyrrhotite Iron Sulfide Nanosheets as a Highly Efficient Electrocatalyst for Water Splitting. *J. Mater. Chem. A* **2020**, *8*, 20323−20330.
(660) Qin, J.-F.; Yang, M.; Chen, T.-S.; Dong, B.; Hou, S.; Ma, X.; Zhou, Y.-N.; Yang, X.-L.; Nan, J.; Chai, Y.-M. Ternary Metal Sulfides MoCoNiS Derived from Metal Organic Frameworks for Efficient Oxygen Evolution. *Int. J. Hydrog. Energy* **2020**, *45*, 2745−2753.
(661) Zhao, M.; Li, W.; Li, J.; Hu, W.; Li, C. M. Strong Electronic Interaction Enhanced Electrocatalysis of Metal Sulfide Clusters Embedded Metal-Organic Framework Ultrathin Nanosheets toward Highly Efficient Overall Water Splitting. *Adv. Sci.* **2020**, *7*, 2001965.
(662) Guo, Y.; Zhou, X.; Tang, J.; Tanaka, S.; Kaneti, Y. V.; Na, J.; Jiang, B.; Yamauchi, Y.; Bando, Y.; Sugahara, Y. Multiscale Structural Optimization: Highly Efficient Hollow Iron-Doped Metal Sulfide Heterostructures as Bifunctional Electrocatalysts for Water Splitting. *Nano Energy* **2020**, *75*, 104913.
(663) Li, X.; Kou, Z.; Xi, S.; Zang, W.; Yang, T.; Zhang, L.; Wang, J. Porous $NiCo_2S_4$/FeOOH Nanowire Arrays with Rich Sulfide/Hydroxide Interfaces Enable High OER Activity. *Nano Energy* **2020**, *78*, 105230.
(664) Thangasamy, P.; Oh, S.; Nam, S.; Randriamahazaka, H.; Oh, I.-K. Ferrocene-Incorporated Cobalt Sulfide Nanoarchitecture for Superior Oxygen Evolution Reaction. *Small* **2020**, *16*, 2001665.

https://doi.org/10.1021/acs.chemrev.3c00005
Chem. Rev. 2023, 123, 12795−13208

(665) Wang, M.; Dong, C.-L.; Huang, Y.-C.; Shen, S. Operando Spectral and Electrochemical Investigation into the Heterophase Stimulated Active Species Transformation in Transition-Metal Sulfides for Efficient Electrocatalytic Oxygen Evolution. *ACS Catal.* **2020**, *10*, 1855−1864.
(666) Zhao, Y.; Mavrokefalos, C. K.; Zhang, P.; Erni, R.; Li, J.; Triana, C. A.; Patzke, G. R. Self-Templating Strategies for Transition Metal Sulfide Nanoboxes as Robust Bifunctional Electrocatalysts. *Chem. Mater.* **2020**, *32*, 1371−1383.
(667) Zhai, P.; Zhang, Y.; Wu, Y.; Gao, J.; Zhang, B.; Cao, S.; Zhang, Y.; Li, Z.; Sun, L.; Hou, J. Engineering Active Sites on Hierarchical Transition Bimetal Oxides/Sulfides Heterostructure Array Enabling Robust Overall Water Splitting. *Nat. Commun.* **2020**, *11*, 5462.
(668) Fei, B.; Chen, Z.; Liu, J.; Xu, H.; Yan, X.; Qing, H.; Chen, M.; Wu, R. Ultrathinning Nickel Sulfide with Modulated Electron Density for Efficient Water Splitting. *Adv. Energy Mater.* **2020**, *10*, 2001963.
(669) Deokate, R. J.; Mujawar, S. H.; Chavan, H. S.; Mali, S. S.; Hong, C. K.; Im, H.; Inamdar, A. I. Chalcogenide Nanocomposite Electrodes Grown by Chemical Etching of Ni-Foam as Electrocatalyst for Efficient Oxygen Evolution Reaction. *Int. J. Energy Res.* **2020**, *44*, 1233−1243.
(670) Ma, B.; Yang, Z.; Yuan, Z.; Chen, Y. Effective Surface Roughening of Three-Dimensional Copper Foam via Sulfurization Treatment as a Bifunctional Electrocatalyst for Water Splitting. *Int. J. Hydrog. Energy* **2019**, *44*, 1620−1626.
(671) Wu, X.; Yang, Y.; Zhang, T.; Wang, B.; Xu, H.; Yan, X.; Tang, Y. CeO_x-Decorated Hierarchical $NiCo_2S_4$ Hollow Nanotubes Arrays for Enhanced Oxygen Evolution Reaction Electrocatalysis. *ACS Appl. Mater. Interfaces* **2019**, *11*, 39841−39847.
(672) Zuo, Y.; Liu, Y.; Li, J.; Du, R.; Han, X.; Zhang, T.; Arbiol, J.; Divins, N. J.; Llorca, J.; Guijarro, N.; et al. In Situ Electrochemical Oxidation of Cu_2S into CuO Nanowires as a Durable and Efficient Electrocatalyst for Oxygen Evolution Reaction. *Chem. Mater.* **2019**, *31*, 7732−7743.
(673) Jadhav, H. S.; Roy, A.; Thorat, G. M.; Chung, W.-J.; Seo, J. G. Hierarchical Free-Standing Networks of $MnCo_2S_4$ as Efficient Electrocatalyst for Oxygen Evolution Reaction. *J. Ind. Eng. Chem.* **2019**, *71*, 452−459.
(674) Ma, M.; Yang, G.; Wang, H.; Lu, Y.; Zhang, B.; Cao, X.; Peng, D.; Du, X.; Liu, Y.; Huang, Y. Ordered Distributed Nickel Sulfide Nanoparticles across Graphite Nanosheets for Efficient Oxygen Evolution Reaction Electrocatalyst. *Int. J. Hydrog. Energy* **2019**, *44*, 1544−1554.
(675) Zhang, W.; Ma, X.; Zhong, C.; Ma, T.; Deng, Y.; Hu, W.; Han, X. Pyrite-Type CoS_2 Nanoparticles Supported on Nitrogen-Doped Graphene for Enhanced Water Splitting. *Front. Chem.* **2018**, *6*, 569.
(676) Chauhan, M.; Deka, S. Hollow Cobalt Sulfide Nanoparticles: A Robust and Low-Cost pH-Universal Oxygen Evolution Electrocatalyst. *ACS Appl. Energy Mater.* **2020**, *3*, 977−986.
(677) Zhou, Q.; Li, T.-T.; Wang, J.; Guo, F.; Zheng, Y.-Q. Hierarchical Cu_2S NRs@CoS Core-Shell Structure and Its Derivative towards Synergistic Electrocatalytic Water Splitting. *Electrochim. Acta* **2019**, *296*, 1035−1041.
(678) Tsai, H.-C.; Vedhanarayanan, B.; Lin, T.-W. Freestanding and Hierarchically Structured Au-Dendrites/3D-Graphene Scaffold Supports Highly Active and Stable Ni_3S_2 Electrocatalyst toward Overall Water Splitting. *ACS Appl. Energy Mater.* **2019**, *2*, 3708−3716.
(679) Wang, A.; Hu, K.; Liu, Y.; Li, R.; Ye, C.; Yi, Z.; Yan, K. Flower-like MoS_2 with Stepped Edge Structure Efficient for Electrocatalysis of Hydrogen and Oxygen Evolution. *Int. J. Hydrog. Energy* **2019**, *44*, 6573−6581.
(680) Guo, J.; Zhang, K.; Sun, Y.; Liu, Q.; Tang, L.; Zhang, X. Efficient Bifunctional Vanadium-Doped Ni_3S_2 Nanorod Array for Overall Water Splitting. *Inorg. Chem. Front.* **2019**, *6*, 443−450.
(681) Zhang, H.; Jiang, H.; Xu, Q.; Hu, Y.; Li, C. Rapid Low-Temperature Synthesis of Hollow $CuS_{0.55}$ Nanoparticles for Efficient Electrocatalytic Water Oxidation. *Chem. Eng. Sci.* **2019**, *195*, 665−670.
(682) Sivanantham, A.; Hyun, S.; Son, M.; Shanmugam, S. Nanostructured Core-Shell Cobalt Chalcogenides for Efficient Water Oxidation in Alkaline Electrolyte. *Electrochim. Acta* **2019**, *312*, 234−241.
(683) Wu, X.; Li, S.; Liu, J.; Yu, M. Mesoporous Hollow Nested Nanospheres of Ni, Cu, Co-Based Mixed Sulfides for Electrocatalytic Oxygen Reduction and Evolution. *ACS Appl. Nano Mater.* **2019**, *2*, 4921−4932.
(684) Xiong, Y.; Xu, L.; Jin, C.; Sun, Q. Interface-Engineered Atomically Thin Ni_3S_2/MnO_2 Heterogeneous Nanoarrays for Efficient Overall Water Splitting in Alkaline Media. *Appl. Catal. B: Environ.* **2019**, *254*, 329−338.
(685) Ju, S.; Liu, Y.; Chen, H.; Tan, F.; Yuan, A.; Li, X.; Zhu, G. In Situ Surface Chemistry Engineering of Cobalt-Sulfide Nanosheets for Improved Oxygen Evolution Activity. *ACS Appl. Energy Mater.* **2019**, *2*, 4439−4449.
(686) Qin, C.; Fan, A.; Ren, D.; Luan, C.; Yang, J.; Liu, Y.; Zhang, X.; Dai, X.; Wang, M. Amorphous NiMS (M: Co, Fe or Mn) Holey Nanosheets Derived from Crystal Phase Transition for Enhanced Oxygen Evolution in Water Splitting. *Electrochim. Acta* **2019**, *323*, 134756.
(687) Li, K.; Qian, Y.; Zhang, H.; Zhang, L.; Chai, Q.; Wang, Q.; Du, J.; Han, Y.; Wang, W.; Kang, D. J. Highly Efficient Oxygen Evolution Electrocatalysts Based on Nanosheet-Shaped CuS in Situ Grown on Carbon Cloth. *Ceram. Int.* **2019**, *45*, 10664−10671.
(688) Yang, Y.; Yao, H.; Yu, Z.; Islam, S. M.; He, H.; Yuan, M.; Yue, Y.; Xu, K.; Hao, W.; Sun, G.; et al. Hierarchical Nanoassembly of $MoS_2/Co_9S_8/Ni_3S_2/Ni$ as a Highly Efficient Electrocatalyst for Overall Water Splitting in a Wide pH Range. *J. Am. Chem. Soc.* **2019**, *141*, 10417−10430.
(689) Wang, J.; Zeng, H. C. A Hybrid Electrocatalyst with a Coordinatively Unsaturated Metal-Organic Framework Shell and Hollow Ni_3S_2/NiS Core for Oxygen Evolution Reaction Applications. *ACS Appl. Mater. Interfaces* **2019**, *11*, 23180−23191.
(690) Shinde, N.; Shinde, P.; Xia, Q. X.; Yun, J. M.; Mane, R.; Kim, K. H. Electrocatalytic Water Splitting through the Ni_xS_y Self-Grown Superstructures Obtained via a Wet Chemical Sulfurization Process. *ACS Omega* **2019**, *4*, 6486−6491.
(691) Wang, T.; Nam, G.; Jin, Y.; Wang, X.; Ren, P.; Kim, M. G.; Liang, J.; Wen, X.; Jang, H.; Han, J.; et al. NiFe (Oxy) Hydroxides Derived from NiFe Disulfides as an Efficient Oxygen Evolution Catalyst for Rechargeable Zn-Air Batteries: The Effect of Surface S Residues. *Adv. Mater.* **2018**, *30*, 1800757.
(692) Tiwari, A. P.; Yoon, Y.; Novak, T. G.; An, K.-S.; Jeon, S. Continuous Network of Phase-Tuned Nickel Sulfide Nanostructures for Electrocatalytic Water Splitting. *ACS Appl. Nano Mater.* **2019**, *2*, 5061−5070.
(693) Jiang, J.; Lu, S.; Wang, W.-K.; Huang, G.-X.; Huang, B.-C.; Zhang, F.; Zhang, Y.-J.; Yu, H.-Q. Ultrahigh Electrocatalytic Oxygen Evolution by Iron-Nickel Sulfide Nanosheets/Reduced Graphene Oxide Nanohybrids with an Optimized Autoxidation Process. *Nano Energy* **2018**, *43*, 300−309.
(694) Li, H.; Chen, S.; Zhang, Y.; Zhang, Q.; Jia, X.; Zhang, Q.; Gu, L.; Sun, X.; Song, L.; Wang, X. Systematic Design of Superaerophobic Nanotube-Array Electrode Comprised of Transition-Metal Sulfides for Overall Water Splitting. *Nat. Commun.* **2018**, *9*, 1−12.
(695) Kale, S. B.; Lokhande, A. C.; Pujari, R. B.; Lokhande, C. D. Cobalt Sulfide Thin Films for Electrocatalytic Oxygen Evolution Reaction and Supercapacitor Applications. *J. Colloid. Interface Sci.* **2018**, *532*, 491−499.
(696) Cheng, X.; Lei, C.; Yang, J.; Yang, B.; Li, Z.; Lu, J.; Zhang, X.; Lei, L.; Hou, Y.; Ostrikov, K. Efficient Electrocatalytic Oxygen Evolution at Extremely High Current Density over 3D Ultrasmall Zero-Valent Iron-Coupled Nickel Sulfide Nanosheets. *ChemElectroChem* **2018**, *5*, 3866−3872.
(697) Zhong, X.; Tang, J.; Wang, J.; Shao, M.; Chai, J.; Wang, S.; Yang, M.; Yang, Y.; Wang, N.; Wang, S.; et al. 3D Heterostructured Pure and N-Doped Ni_3S_2/VS_2 Nanosheets for High Efficient Overall Water Splitting. *Electrochim. Acta* **2018**, *269*, 55−61.

https://doi.org/10.1021/acs.chemrev.3c00005
Chem. Rev. 2023, 123, 12795−13208

(698) Zhang, G.; Qin, Q.; Luo, W.; Liu, Y.; Jin, C.; Hao, J.; Zhang, J.; Zheng, W. A Combination-Decomposition Method to Synthesize Two-Dimensional Metal Sulfide-Amine Hybrid Nanosheets: A Highly Efficient Fe-Based Water Oxidation Electrocatalyst. *Chem. Commun.* **2018**, *54*, 4617−4620.
(699) Yang, Y.; Yuan, M.; Li, H.; Sun, G.; Ma, S. Controllable Synthesis of Ultrathin Co_9S_8 Nanosheets as a Highly Efficient Electrocatalyst for Overall Water Splitting. *Electrochim. Acta* **2018**, *281*, 198−207.
(700) Zhu, W.; Yue, Z.; Zhang, W.; Hu, N.; Luo, Z.; Ren, M.; Xu, Z.; Wei, Z.; Suo, Y.; Wang, J. Wet-Chemistry Topotactic Synthesis of Bimetallic Iron-Nickel Sulfide Nanoarrays: An Advanced and Versatile Catalyst for Energy Efficient Overall Water and Urea Electrolysis. *J. Mater. Chem. A* **2018**, *6*, 4346−4353.
(701) Yang, H.; Wang, B.; Li, H.; Ni, B.; Wang, K.; Zhang, Q.; Wang, X. Trimetallic Sulfide Mesoporous Nanospheres as Superior Electrocatalysts for Rechargeable Zn-Air Batteries. *Adv. Energy Mater.* **2018**, *8*, 1801839.
(702) Luo, P.; Sun, F.; Deng, J.; Xu, H.; Zhang, H.; Wang, Y. Tree-Like NiS-Ni_3S_2/NF Heterostructure Array and Its Application in Oxygen Evolution Reaction. *Acta Phys. Chim. Sin.* **2018**, *34*, 1397−1404.
(703) Zhou, Y.; Luo, M.; Zhang, Z.; Li, W.; Shen, X.; Xia, W.; Zhou, M.; Zeng, X. Iron Doped Cobalt Sulfide Derived Boosted Electrocatalyst for Water Oxidation. *Appl. Surf. Sci.* **2018**, *448*, 9−15.
(704) Zhou, D.; Jia, Y.; Yang, H.; Xu, W.; Sun, K.; Zhang, J.; Wang, S.; Kuang, Y.; Liu, B.; Sun, X. Boosting Oxygen Reaction Activity by Coupling Sulfides for High-Performance Rechargeable Metal-Air Battery. *J. Mater. Chem. A* **2018**, *6*, 21162−21166.
(705) Fan, K.; Zou, H.; Lu, Y.; Chen, H.; Li, F.; Liu, J.; Sun, L.; Tong, L.; Toney, M. F.; Sui, M.; et al. Direct Observation of Structural Evolution of Metal Chalcogenide in Electrocatalytic Water Oxidation. *ACS Nano* **2018**, *12*, 12369−12379.
(706) Hu, C.; Liu, J.; Wang, J.; She, W.; Xiao, J.; Xi, J.; Bai, Z.; Wang, S. Coordination-Assisted Polymerization of Mesoporous Cobalt Sulfide/Heteroatom (N,S)-Doped Double-Layered Carbon Tubes as an Efficient Bifunctional Oxygen Electrocatalyst. *ACS Appl. Mater. Interfaces* **2018**, *10*, 33124−33134.
(707) Lin, J.; Wang, H.; Zheng, X.; Du, Y.; Zhao, C.; Qi, J.; Cao, J.; Fei, W.; Feng, J. Controllable Synthesis of Core-Branch Ni_3S_2/Co_9S_8 Directly on Nickel Foam as an Efficient Bifunctional Electrocatalyst for Overall Water Splitting. *J. Power Sources* **2018**, *401*, 329−335.
(708) Ren, G.; Hao, Q.; Mao, J.; Liang, L.; Liu, H.; Liu, C.; Zhang, J. Ultrafast Fabrication of Nickel Sulfide Film on Ni Foam for Efficient Overall Water Splitting. *Nanoscale* **2018**, *10*, 17347−17353.
(709) Xu, P.; Li, J.; Luo, J.; Wei, L.; Zhang, D.; Zhou, D.; Xu, W.; Yuan, D. $(Fe_{0.2}Ni_{0.8})_{0.96}S$ Tubular Spheres Supported on Ni Foam as an Efficient Bifunctional Electrocatalyst for Overall Water Splitting. *Sci. Rep.* **2018**, *8*, 1−9.
(710) Du, C.; Men, Y.; Hei, X.; Yu, J.; Cheng, G.; Luo, W. Mo-Doped Ni_3S_2 Nanowires as High-Performance Electrocatalysts for Overall Water Splitting. *ChemElectroChem* **2018**, *5*, 2564−2570.
(711) Du, X.; Wang, Q.; Li, Y.; Zhang, X. Oxide/Sulfide-Based Hybrid Arrays as Robust Electrocatalysts for Water Splitting. *Dalton Trans.* **2018**, *47*, 10273−10280.
(712) Nai, J.; Lu, Y.; Yu, X.-Y. Formation of Ti-Fe Mixed Sulfide Nanoboxes for Enhanced Electrocatalytic Oxygen Evolution. *J. Mater. Chem. A* **2018**, *6*, 21891−21895.
(713) Lin, R.; Lin, T.; Huang, J.; Huang, X.; Liu, Y. Hierarchical Cobalt Sulfide with Vertical In-Plane Edge Structure for Enhanced Electrocatalytic Oxygen Evolution Reaction. *Electrochim. Acta* **2018**, *281*, 348−356.
(714) Souleymen, R.; Wang, Z.; Qiao, C.; Naveed, M.; Cao, C. Microwave-Assisted Synthesis of Graphene-like Cobalt Sulfide Freestanding Sheets as an Efficient Bifunctional Electrocatalyst for Overall Water Splitting. *J. Mater. Chem. A* **2018**, *6*, 7592−7607.
(715) Han, H.; Kim, K. M.; Choi, H.; Ali, G.; Chung, K. Y.; Hong, Y.-R.; Choi, J.; Kwon, J.; Lee, S. W.; Lee, J. W.; et al. Parallelized Reaction Pathway and Stronger Internal Band Bending by Partial Oxidation of Metal Sulfide-Graphene Composites: Important Factors of Synergistic Oxygen Evolution Reaction Enhancement. *ACS Catal.* **2018**, *8*, 4091−4102.
(716) Shang, X.; Qin, J.-F.; Lin, J.-H.; Dong, B.; Chi, J.-Q.; Liu, Z.-Z.; Wang, L.; Chai, Y.-M.; Liu, C.-G. Tuning the Morphology and Fe/Ni Ratio of a Bimetallic Fe-Ni-S Film Supported on Nickel Foam for Optimized Electrolytic Water Splitting. *J. Colloid. Interface Sci.* **2018**, *523*, 121−132.
(717) Ho, T. A.; Bae, C.; Nam, H.; Kim, E.; Lee, S. Y.; Park, J. H.; Shin, H. Metallic Ni_3S_2 Films Grown by Atomic Layer Deposition as an Efficient and Stable Electrocatalyst for Overall Water Splitting. *ACS Appl. Mater. Interfaces* **2018**, *10*, 12807−12815.
(718) Lee, M.; Oh, H.-S.; Cho, M. K.; Ahn, J.-P.; Hwang, Y. J.; Min, B. K. Activation of a Ni Electrocatalyst through Spontaneous Transformation of Nickel Sulfide to Nickel Hydroxide in an Oxygen Evolution Reaction. *Appl. Catal. B: Environ.* **2018**, *233*, 130−135.
(719) Chen, Z.; Wu, R.; Liu, M.; Liu, Y.; Xu, S.; Ha, Y.; Guo, Y.; Yu, X.; Sun, D.; Fang, F. Tunable Electronic Coupling of Cobalt Sulfide/Carbon Composites for Optimizing Oxygen Evolution Reaction Activity. *J. Mater. Chem. A* **2018**, *6*, 10304−10312.
(720) Guo, M.; Xu, K.; Qu, Y.; Zeng, F.; Yuan, C. Porous Co_3O_4/CoS_2 Nanosheet-Assembled Hierarchical Microspheres as Superior Electrocatalyst towards Oxygen Evolution Reaction. *Electrochim. Acta* **2018**, *268*, 10−19.
(721) Liu, Y.; Zhang, J.; Li, Y.; Yuan, G.; Niu, X.; Zhang, X.; Wang, Q. Self-Templated Synthesis of $Co_{1-x}S$ Porous Hexagonal Microplates for Efficient Electrocatalytic Oxygen Evolution. *ChemElectroChem* **2018**, *5*, 1167−1172.
(722) Ni, B.; He, T.; Wang, J.; Zhang, S.; Ouyang, C.; Long, Y.; Zhuang, J.; Wang, X. The Formation of $(NiFe)S_2$ Pyrite Mesocrystals as Efficient Pre-Catalysts for Water Oxidation. *Chem. Sci.* **2018**, *9*, 2762−2767.
(723) Ma, X.; Zhang, W.; Deng, Y.; Zhong, C.; Hu, W.; Han, X. Phase and Composition Controlled Synthesis of Cobalt Sulfide Hollow Nanospheres for Electrocatalytic Water Splitting. *Nanoscale* **2018**, *10*, 4816−4824.
(724) Dai, W.; Pan, Y.; Wang, N.; Wu, S.; Li, X.; Zhu, Y.; Lu, T. Nanocrystalline NiS Particles Synthesized by Mechanical Alloying as a Promising Oxygen Evolution Electrocatalyst. *Mater. Lett.* **2018**, *218*, 115−118.
(725) Ganesan, P.; Sivanantham, A.; Shanmugam, S. CoS_2-TiO_2 Hybrid Nanostructures: Efficient and Durable Bifunctional Electrocatalysts for Alkaline Electrolyte Membrane Water Electrolyzers. *J. Mater. Chem. A* **2018**, *6*, 1075−1085.
(726) Shang, X.; Yan, K.-L.; Lu, S.-S.; Dong, B.; Gao, W.-K.; Chi, J.-Q.; Liu, Z.-Z.; Chai, Y.-M.; Liu, C.-G. Controlling Electrodeposited Ultrathin Amorphous Fe Hydroxides Film on V-Doped Nickel Sulfide Nanowires as Efficient Electrocatalyst for Water Oxidation. *J. Power Sources* **2017**, *363*, 44−53.
(727) Zhao, X.; Jiang, J.; Xue, Z.; Yan, C.; Mu, T. An Ambient Temperature, CO_2-Assisted Solution Processing of Amorphous Cobalt Sulfide in a Thiol/Amine Based Quasi-Ionic Liquid for Oxygen Evolution Catalysis. *Chem. Commun.* **2017**, *53*, 9418−9421.
(728) Zhou, M.; Weng, Q.; Zhang, X.; Wang, X.; Xue, Y.; Zeng, X.; Bando, Y.; Golberg, D. In Situ Electrochemical Formation of Core-Shell Nickel-Iron Disulfide and Oxyhydroxide Heterostructured Catalysts for a Stable Oxygen Evolution Reaction and the Associated Mechanisms. *J. Mater. Chem. A* **2017**, *5*, 4335−4342.
(729) Luo, P.; Zhang, H.; Liu, L.; Zhang, Y.; Deng, J.; Xu, C.; Hu, N.; Wang, Y. Targeted Synthesis of Unique Nickel Sulfide (NiS, NiS_2) Microarchitectures and the Applications for the Enhanced Water Splitting System. *ACS Appl. Mater. Interfaces* **2017**, *9*, 2500−2508.
(730) Liu, H.; Ma, F.-X.; Xu, C.-Y.; Yang, L.; Du, Y.; Wang, P.-P.; Yang, S.; Zhen, L. Sulfurizing-Induced Hollowing of Co_9S_8 Microplates with Nanosheet Units for Highly Efficient Water Oxidation. *ACS Appl. Mater. Interfaces* **2017**, *9*, 11634−11641.
(731) Xiong, D.; Zhang, Q.; Thalluri, S. M.; Xu, J.; Li, W.; Fu, X.; Liu, L. One-Step Fabrication of Monolithic Electrodes Comprising

https://doi.org/10.1021/acs.chemrev.3c00005
Chem. Rev. 2023, 123, 12795−13208

Co_9S_8 Particles Supported on Cobalt Foam for Efficient and Durable Oxygen Evolution Reaction. *Chem.—Eur. J.* **2017**, *23*, 8749−8755.
(732) Xu, Y.-Z.; Yuan, C.-Z.; Chen, X.-P. One-Pot Synthesis Nickel Sulfide/Amorphous Molybdenum Sulfide Nanosheets Array on Nickel Foam as a Robust Oxygen Evolution Reaction Electrocatalyst. *J. Solid State Chem.* **2017**, *256*, 124−129.
(733) Ren, J.-T.; Yuan, Z.-Y. Hierarchical Nickel Sulfide Nanosheets Directly Grown on Ni Foam: A Stable and Efficient Electrocatalyst for Water Reduction and Oxidation in Alkaline Medium. *ACS Sustainable Chem. Eng.* **2017**, *5*, 7203−7210.
(734) Li, H.; Shao, Y.; Su, Y.; Gao, Y.; Wang, X. Vapor-Phase Atomic Layer Deposition of Nickel Sulfide and Its Application for Efficient Oxygen-Evolution Electrocatalysis. *Chem. Mater.* **2016**, *28*, 1155−1164.
(735) Dong, B.; Zhao, X.; Han, G.-Q.; Li, X.; Shang, X.; Liu, Y.-R.; Hu, W.-H.; Chai, Y.-M.; Zhao, H.; Liu, C.-G. Two-Step Synthesis of Binary Ni-Fe Sulfides Supported on Nickel Foam as Highly Efficient Electrocatalysts for the Oxygen Evolution Reaction. *J. Mater. Chem. A* **2016**, *4*, 13499−13508.
(736) Jiang, J.; Lu, S.; Gao, H.; Zhang, X.; Yu, H.-Q. Ternary $FeNiS_2$ Ultrathin Nanosheets as an Electrocatalyst for Both Oxygen Evolution and Reduction Reactions. *Nano Energy* **2016**, *27*, 526−534.
(737) Zhu, W.; Yue, X.; Zhang, W.; Yu, S.; Zhang, Y.; Wang, J.; Wang, J. Nickel Sulfide Microsphere Film on Ni Foam as an Efficient Bifunctional Electrocatalyst for Overall Water Splitting. *Chem. Commun.* **2016**, *52*, 1486−1489.
(738) Zhang, J.; Wang, T.; Pohl, D.; Rellinghaus, B.; Dong, R.; Liu, S.; Zhuang, X.; Feng, X. Interface Engineering of MoS_2/Ni_3S_2 Heterostructures for Highly Enhanced Electrochemical Overall-Water-Splitting Activity. *Angew. Chem. Int. Ed.* **2016**, *55*, 6702−6707.
(739) Wang, J.; Zhong, H.; Wang, Z.; Meng, F.; Zhang, X. Integrated Three-Dimensional Carbon Paper/Carbon Tubes/Cobalt-Sulfide Sheets as an Efficient Electrode for Overall Water Splitting. *ACS Nano* **2016**, *10*, 2342−2348.
(740) You, B.; Sun, Y. Hierarchically Porous Nickel Sulfide Multifunctional Superstructures. *Adv. Energy Mater.* **2016**, *6*, 1502333.
(741) Sivanantham, A.; Ganesan, P.; Shanmugam, S. Hierarchical $NiCo_2S_4$ Nanowire Arrays Supported on Ni Foam: An Efficient and Durable Bifunctional Electrocatalyst for Oxygen and Hydrogen Evolution Reactions. *Adv. Funct. Mater.* **2016**, *26*, 4661−4672.
(742) Yan, K.; Lu, Y. Direct Growth of MoS_2 Microspheres on Ni Foam as a Hybrid Nanocomposite Efficient for Oxygen Evolution Reaction. *Small* **2016**, *12*, 2975−2981.
(743) Zhao, X.; Shang, X.; Quan, Y.; Dong, B.; Han, G.-Q.; Li, X.; Liu, Y.-R.; Chen, Q.; Chai, Y.-M.; Liu, C.-G. Electrodeposition-Solvothermal Access to Ternary Mixed Metal Ni-Co-Fe Sulfides for Highly Efficient Electrocatalytic Water Oxidation in Alkaline Media. *Electrochim. Acta* **2017**, *230*, 151−159.
(744) Chauhan, M.; Reddy, K. P.; Gopinath, C. S.; Deka, S. Copper Cobalt Sulfide Nanosheets Realizing a Promising Electrocatalytic Oxygen Evolution Reaction. *ACS Catal.* **2017**, *7*, 5871−5879.
(745) Li, H.; Guo, Z.; Wang, X. Atomic-Layer-Deposited Ultrathin Co_9S_8 on Carbon Nanotubes: An Efficient Bifunctional Electrocatalyst for Oxygen Evolution/Reduction Reactions and Rechargeable Zn-Air Batteries. *J. Mater. Chem. A* **2017**, *5*, 21353−21361.
(746) Xiong, D.; Zhang, Q.; Li, W.; Li, J.; Fu, X.; Cerqueira, M. F.; Alpuim, P.; Liu, L. Atomic-Layer-Deposited Ultrafine MoS_2 Nanocrystals on Cobalt Foam for Efficient and Stable Electrochemical Oxygen Evolution. *Nanoscale* **2017**, *9*, 2711−2717.
(747) Sultana, U. K.; He, T.; Du, A.; O'Mullane, A. P. An Amorphous Dual Action Electrocatalyst Based on Oxygen Doped Cobalt Sulfide for the Hydrogen and Oxygen Evolution Reactions. *RSC Adv.* **2017**, *7*, 54995−55004.
(748) Fang, W.; Liu, D.; Lu, Q.; Sun, X.; Asiri, A. M. Nickel Promoted Cobalt Disulfide Nanowire Array Supported on Carbon Cloth: An Efficient and Stable Bifunctional Electrocatalyst for Full Water Splitting. *Electrochem. Commun.* **2016**, *63*, 60−64.
(749) Chen, J. S.; Ren, J.; Shalom, M.; Fellinger, T.; Antonietti, M. Stainless Steel Mesh-Supported NiS Nanosheet Array as Highly Efficient Catalyst for Oxygen Evolution Reaction. *ACS Appl. Mater. Interfaces* **2016**, *8*, 5509−5516.
(750) Shang, X.; Li, X.; Hu, W.-H.; Dong, B.; Liu, Y.-R.; Han, G.-Q.; Chai, Y.-M.; Liu, Y.-Q.; Liu, C.-G. In Situ Growth of Ni_xS_y Controlled by Surface Treatment of Nickel Foam as Efficient Electrocatalyst for Oxygen Evolution Reaction. *Appl. Surf. Sci.* **2016**, *378*, 15−21.
(751) Liu, D.; Lu, Q.; Luo, Y.; Sun, X.; Asiri, A. M. $NiCo_2S_4$ Nanowires Array as an Efficient Bifunctional Electrocatalyst for Full Water Splitting with Superior Activity. *Nanoscale* **2015**, *7*, 15122−15126.
(752) Liu, T.; Liang, Y.; Liu, Q.; Sun, X.; He, Y.; Asiri, A. M. Electrodeposition of Cobalt-Sulfide Nanosheets Film as an Efficient Electrocatalyst for Oxygen Evolution Reaction. *Electrochem. Commun.* **2015**, *60*, 92−96.
(753) Cheng, N.; Liu, Q.; Asiri, A. M.; Xing, W.; Sun, X. A Fe-Doped Ni_3S_2 Particle Film as a High-Efficiency Robust Oxygen Evolution Electrode with Very High Current Density. *J. Mater. Chem. A* **2015**, *3*, 23207−23212.
(754) Zhang, Y.; Lin, L.; Liu, J.; Peng, J.; Chen, L. Hierarchical Sulphide - Phosphide NiSP /NF Catalyst Prepared by Gradient Electrodeposition for Oxygen Evolution Reaction. *J. Alloys Compd.* **2022**, *895*, 162675.
(755) Devarayapalli, K. C.; Lee, J.; Kang, S.; Moon, S.; Vattikuti, S. V. P.; Lee, J.; Lee, K. Nanostructured Cobalt-Based Metal-Organic Framework/Cadmium Sulfide Electrocatalyst for Enhanced Oxygen Evolution Reaction and Anion Exchange Membrane-Based Water Electrolysis: Synergistic Effect. *J. Power Sources* **2022**, *527*, 231151.
(756) Nouseen, S.; Singh, P.; Lavate, S.; Chattopadhyay, J.; Kuchkaev, A. M.; Yakhvarov, D. G.; Srivastava, R. Transition Metal Based Ternary Hierarchical Metal Sulphide Microspheres as Electrocatalyst for Splitting of Water into Hydrogen and Oxygen Fuel. *Catal. Today* **2022**, *397-399*, 618−630.
(757) Li, Y.; Guo, Q.; Jiang, Y.; Shen, W.; Li, M.; He, R. A Novel Ball-in-Ball Hollow Oxygen-Incorporating Cobalt Sulfide Spheres as High-Efficient Electrocatalyst for Oxygen Evolution Reaction. *Chin. Chem. Lett.* **2021**, *32*, 755−760.
(758) Asiri, A. M.; Adeosun, W. A.; Khan, S. B.; Alamry, K. A.; Marwani, H. M.; Zakeeruddin, S. M.; Gräetzel, M. $NiCuCoS_3$ Chalcogenide as an Efficient Electrocatalyst for Hydrogen and Oxygen Evolution. *J. Mater. Res. Technol.* **2021**, *15*, 4826−4837.
(759) Li, M.; Zheng, K.; Zhang, J.; Li, X.; Xu, C. Design and Construction of 2D/2D Sheet-on-Sheet Transition Metal Sulfide/Phosphide Heterostructure for Efficient Oxygen Evolution Reaction. *Appl. Surf. Sci.* **2021**, *565*, 150510.
(760) Li, D.; Liu, Z.; Wang, J.; Liu, B.; Qin, Y.; Yang, W.; Liu, J. Hierarchical Trimetallic Sulfide $FeCo_2S_4$-$NiCo_2S_4$ Nanosheet Arrays Supported on a Ti Mesh: An Efficient 3D Bifunctional Electrocatalyst for Full Water Splitting. *Electrochim. Acta* **2020**, *340*, 135957.
(761) Khodabakhshi, M.; Chen, S.; Ye, T.; Wu, H.; Yang, L.; Zhang, W.; Chang, H. Hierarchical Highly Wrinkled Trimetallic NiFeCu Phosphide Nanosheets on Nanodendrite Ni_3S_2/Ni Foam as an Efficient Electrocatalyst for the Oxygen Evolution Reaction. *ACS Appl. Mater. Interfaces* **2020**, *12*, 36268−36276.
(762) Yang, Y.; Kang, Y.; Zhao, H.; Dai, X.; Cui, M.; Luan, X.; Zhang, X.; Nie, F.; Ren, Z.; Song, W. An Interfacial Electron Transfer on Tetrahedral NiS_2/$NiSe_2$ Heterocages with Dual-Phase Synergy for Efficiently Triggering the Oxygen Evolution Reaction. *Small* **2020**, *16*, 1905083.
(763) Xue, Z.; Li, X.; Liu, Q.; Cai, M.; Liu, K.; Liu, M.; Ke, Z.; Liu, X.; Li, G. Interfacial Electronic Structure Modulation of NiTe Nanoarrays with NiS Nanodots Facilitates Electrocatalytic Oxygen Evolution. *Adv. Mater.* **2019**, *31*, 1900430.
(764) Ren, L.; Wang, C.; Li, W.; Dong, R.; Sun, H.; Liu, N.; Geng, B. Heterostructural NiFe-LDH@Ni_3S_2 Nanosheet Arrays as an Efficient Electrocatalyst for Overall Water Splitting. *Electrochim. Acta* **2019**, *318*, 42−50.
(765) Wang, F.; Li, K.; Li, J.; Wolf, L. M.; Liu, K.; Zhang, H. A Bifunctional Electrode Engineered by Sulfur Vacancies for Efficient Electrocatalysis. *Nanoscale* **2019**, *11*, 16658−16666.

https://doi.org/10.1021/acs.chemrev.3c00005
Chem. Rev. 2023, 123, 12795−13208

(766) Tang, S.; Wang, X.; Zhang, Y.; Courté, M.; Fan, H. J.; Fichou, D. Combining Co_3S_4 and Ni:Co_3S_4 Nanowires as Efficient Catalysts for Overall Water Splitting: An Experimental and Theoretical Study. *Nanoscale* **2019**, *11*, 2202−2210.
(767) He, D.; Wu, X.; Liu, W.; Lei, C.; Yu, C.; Zheng, G.; Pan, J.; Lei, L.; Zhang, X. $Co_{1-x}S$ Embedded in Porous Carbon Derived from Metal Organic Framework as a Highly Efficient Electrocatalyst for Oxygen Evolution Reaction. *Chin. Chem. Lett.* **2019**, *30*, 229−233.
(768) Liu, H.; Xu, C.-Y.; Du, Y.; Ma, F.-X.; Li, Y.; Yu, J.; Zhen, L. Ultrathin Co_9S_8 Nanosheets Vertically Aligned on N,S/RGO for Low Voltage Electrolytic Water in Alkaline Media. *Sci. Rep.* **2019**, *9*, 1−10.
(769) Prabakaran, K.; Lokanathan, M.; Kakade, B. Three Dimensional Flower like Cobalt Sulfide (CoS)/Functionalized MWCNT Composite Catalyst for Efficient Oxygen Evolution Reactions. *Appl. Surf. Sci.* **2019**, *466*, 830−836.
(770) Guan, Y.; Xuan, H.; Li, H.; Han, P. Synthesis of 3D Flower-like Nickel-Molybdenum-Sulfur Microspheres as Efficient and Stable Electrocatalyst for Hydrogen and Oxygen Evolution Reactions. *Electrochim. Acta* **2019**, *320*, 134614.
(771) Liu, H.; Sun, S.-C.; Xu, C.-Y.; Du, Y.; Ma, F.-X.; Zhen, L. Salt-Templated Synthesis of Co9S8 Nanoparticles Anchored on N, S Co-Doped Carbon Nanosheets towards High-Performance Water Oxidation. *J. Electroanal. Chem.* **2019**, *835*, 67−72.
(772) Peng, L.; Shen, J.; Zheng, X.; Xiang, R.; Deng, M.; Mao, Z.; Feng, Z.; Zhang, L.; Li, L.; Wei, Z. Rationally Design of Monometallic NiO-Ni_3S_2/NF Heteronanosheets as Bifunctional Electrocatalysts for Overall Water Splitting. *J. Catal.* **2019**, *369*, 345−351.
(773) Khan, N. A.; Rashid, N.; Junaid, M.; Zafar, M. N.; Faheem, M.; Ahmad, I. NiO/NiS Heterostructures: An Efficient and Stable Electrocatalyst for Oxygen Evolution Reaction. *ACS Appl. Energy Mater.* **2019**, *2*, 3587−3594.
(774) Zhao, H.; Yang, Y.; Dai, X.; Qiao, H.; Yong, J.; Luan, X.; Yu, L.; Luan, C.; Wang, Y.; Zhang, X. NiCo-DH Nanodots Anchored on Amorphous NiCo-Sulfide Sheets as Efficient Electrocatalysts for Oxygen Evolution Reaction. *Electrochim. Acta* **2019**, *295*, 1085−1092.
(775) Li, L.; Song, L.; Guo, H.; Xia, W.; Jiang, C.; Gao, B.; Wu, C.; Wang, T.; He, J. N-Doped Porous Carbon Nanosheets Decorated with Graphitized Carbon Layer Encapsulated Co_9S_8 Nanoparticles: An Efficient Bifunctional Electrocatalyst for the OER and ORR. *Nanoscale* **2019**, *11*, 901−907.
(776) Ding, J.; Ji, S.; Wang, H.; Gai, H.; Liu, F.; Linkov, V.; Wang, R. Mesoporous Nickel-Sulfide/Nickel/N-Doped Carbon as HER and OER Bifunctional Electrocatalyst for Water Electrolysis. *Int. J. Hydrog. Energy* **2019**, *44*, 2832−2840.
(777) Li, X.; Zhu, G.; Xiao, L.; Liu, Y.; Ji, Z.; Shen, X.; Kong, L.; Shah, S. A. Loading of Ag on Fe-Co-S/N-Doped Carbon Nanocomposite to Achieve Improved Electrocatalytic Activity for Oxygen Evolution Reaction. *J. Alloys Compd.* **2019**, *773*, 40−49.
(778) Guo, X.; Liang, G.; Gu, A. Designed Formation of CoS_2 Nanoboxes with Enhanced Oxygen Evolution Reaction Electrocatalytic Properties. *Int. J. Hydrog. Energy* **2019**, *44*, 31020−31028.
(779) Shit, S.; Chhetri, S.; Bolar, S.; Murmu, N. C.; Jang, W.; Koo, H.; Kuila, T. Hierarchical Cobalt Sulfide/Molybdenum Sulfide Heterostructure as Bifunctional Electrocatalyst towards Overall Water Splitting. *ChemElectroChem* **2019**, *6*, 430−438.
(780) Liu, B.; Zhang, X.-Y.; Chen, T.-S.; Zhang, L.-M.; Yang, X.-L.; Ma, X.; Liu, D. Synthesis of Mo Doped Ni_2S_3 Nanaorods Arrays for Overall Water Splitting. *Int. J. Electrochem. Sci.* **2018**, *13*, 8506−8517.
(781) Liu, Q.; Wei, L.; Liu, Q.; Chen, G.; Kong, X. Anion Engineering on 3D Ni_3S_2 Nanosheets Array toward Water Splitting. *ACS Appl. Energy Mater.* **2018**, *1*, 3488−3496.
(782) Xu, Z.; Pan, H.; Lin, Y.; Yang, Z.; Wang, J.; Gong, Y. Constructing a Hexagonal Copper-Coin-Shaped $NiCoSe_2$@NiO@$CoNi_2S_4$@CoS_2 Hybrid Nanoarray on Nickel Foam as a Robust Oxygen Evolution Reaction Electrocatalyst. *J. Mater. Chem. A* **2018**, *6*, 18641−18648.
(783) Guo, M.; Liu, Y.; Dong, S.; Jiao, X.; Wang, T.; Chen, D. Co_9S_8-Catalyzed Growth of Thin-Walled Graphite Microtubes for Robust, Efficient Overall Water Splitting. *ChemSusChem* **2018**, *11*, 4150−4155.
(784) Tao, K.; Gong, Y.; Zhou, Q.; Lin, J. Nickel Sulfide Wrapped by Porous Cobalt Molybdate Nanosheet Arrays Grown on Ni Foam for Oxygen Evolution Reaction and Supercapacitor. *Electrochim. Acta* **2018**, *286*, 65−76.
(785) Li, F.; Zhang, D.; Xu, R.-C.; Fu, W.-F.; Lv, X.-J. Superhydrophilic Heteroporous MoS_2/Ni_3S_2 for Highly Efficient Electrocatalytic Overall Water Splitting. *ACS Appl. Energy Mater.* **2018**, *1*, 3929−3936.
(786) Shit, S.; Chhetri, S.; Jang, W.; Murmu, N. C.; Koo, H.; Samanta, P.; Kuila, T. Cobalt Sulfide/Nickel Sulfide Heterostructure Directly Grown on Nickel Foam: An Efficient and Durable Electrocatalyst for Overall Water Splitting Application. *ACS Appl. Mater. Interfaces* **2018**, *10*, 27712−27722.
(787) Hu, Q.; Liu, X.; Zhu, B.; Li, G.; Fan, L.; Chai, X.; Zhang, Q.; Liu, J.; He, C. Redox Route to Ultrathin Metal Sulfides Nanosheet Arrays-Anchored MnO_2 Nanoparticles as Self-Supported Electrocatalysts for Efficient Water Splitting. *J. Power Sources* **2018**, *398*, 159−166.
(788) Yu, Z.; Bai, Y.; Zhang, S.; Liu, Y.; Zhang, N.; Sun, K. MOF-Directed Templating Synthesis of Hollow Nickel-Cobalt Sulfide with Enhanced Electrocatalytic Activity for Oxygen Evolution. *Int. J. Hydrog. Energy* **2018**, *43*, 8815−8823.
(789) Zhang, J.; Zhang, D.; Zhang, R.; Zhang, N.; Cui, C.; Zhang, J.; Jiang, B.; Yuan, B.; Wang, T.; Xie, H.; et al. Facile Synthesis of Mesoporous and Thin-Walled Ni-Co Sulfide Nanotubes as Efficient Electrocatalysts for Oxygen Evolution Reaction. *ACS Appl. Energy Mater.* **2018**, *1*, 495−502.
(790) Zhai, Z.; Li, C.; Zhang, L.; Wu, H.-C.; Zhang, L.; Tang, N.; Wang, W.; Gong, J. Dimensional Construction and Morphological Tuning of Heterogeneous MoS_2/NiS Electrocatalysts for Efficient Overall Water Splitting. *J. Mater. Chem. A* **2018**, *6*, 9833−9838.
(791) Zhang, X.; Ding, P.; Sun, Y.; Li, X.; Li, H.; Guo, J. $CoMoS_{3.13}$ Nanosheets Grafted on B, N Co-Doped Graphene Nanotubes as Bifunctional Catalyst for Efficient Water Electrolysis. *J. Alloys Compd.* **2018**, *731*, 403−410.
(792) Yang, H.; Wang, C.; Zhang, Y.; Wang, Q. Chemical Valence-Dependent Electrocatalytic Activity for Oxygen Evolution Reaction: A Case of Nickel Sulfides Hybridized with N and S Co-Doped Carbon Nanoparticles. *Small* **2018**, *14*, 1703273.
(793) Zequine, C.; Bhoyate, S.; Siam, K.; Kahol, P. K.; Kostoglou, N.; Mitterer, C.; Hinder, S. J.; Baker, M. A.; Constantinides, G.; Rebholz, C.; et al. Needle Grass Array of Nanostructured Nickel Cobalt Sulfide Electrode for Clean Energy Generation. *Surf. Coat. Technol.* **2018**, *354*, 306−312.
(794) Jiang, J.; Chen, J.; Jiang, P.; Leng, Y.; Jin, W. N-Doped Carbon-Coated Metal Sulfides/Phosphides Derived from Protic Salts for Oxygen Evolution Reaction. *ChemCatChem* **2019**, *11*, 1185−1191.
(795) Yu, Z.; Bai, Y.; Zhang, S.; Liu, Y.; Zhang, N.; Sun, K. Metal-Organic Framework-Derived $Zn_{0.975}Co_{0.025}S$/CoS_2 Embedded in N,S-Codoped Carbon Nanotube/Nanopolyhedra as an Efficient Electrocatalyst for Overall Water Splitting. *J. Mater. Chem. A* **2018**, *6*, 10441−10446.
(796) Zheng, X.; Wu, X.; Han, X.; Deng, Y.; Wang, J. In-Situ Multi-Deposition Process for Cobalt-Sulfide Synthesis with Efficient Bifunctional Catalytic Activity. *Ferroelectrics* **2018**, *523*, 119−125.
(797) Zhu, M.; Zhang, Z.; Zhang, H.; Zhang, H.; Zhang, X.; Zhang, L.; Wang, S. Hydrophilic Cobalt Sulfide Nanosheets as a Bifunctional Catalyst for Oxygen and Hydrogen Evolution in Electrolysis of Alkaline Aqueous Solution. *J. Colloid. Interface Sci.* **2018**, *509*, 522−528.
(798) Zhu, W.; Chen, R.; Yin, Y.; Zhang, J.; Wang, Q. Highly (110)-Oriented $Co_{1-x}S$ Nanosheet Arrays on Carbon Fiber Paper as High-Performance and Binder-Free Electrodes for Oxygen Production. *ChemistrySelect* **2018**, *3*, 3970−3974.
(799) Li, J.; Xu, W.; Luo, J.; Zhou, D.; Zhang, D.; Wei, L.; Xu, P.; Yuan, D. Synthesis of 3D Hexagram-Like Cobalt-Manganese Sulfides

https://doi.org/10.1021/acs.chemrev.3c00005
Chem. Rev. 2023, 123, 12795−13208

Nanosheets Grown on Nickel Foam: A Bifunctional Electrocatalyst for Overall Water Splitting. *Nano-Micro Lett.* **2018**, *10*, 6.
(800) Chen, L.; Yang, W.; Liu, X.; Long, L.; Li, D.; Jia, J. Cobalt Sulfide/N,S-Codoped Defect-Rich Carbon Nanotubes Hybrid as an Excellent Bi-Functional Oxygen Electrocatalyst. *Nanotechnology* **2019**, *30*, 075402.
(801) Singh, A.; Trivedi, M.; Singh, P.; Kociok-Köhn, G.; Azad, U. P.; Singh, A. K.; Kumar, A. Copper(I) Tertiary Phosphine Xanthate Complexes as Single Source Precursors for Copper Sulfide and Their Application in the OER. *New J. Chem.* **2018**, *42*, 18759−18764.
(802) Hong, Y.-R.; Mhin, S.; Kwon, J.; Han, W.-S.; Song, T.; Han, H. Synthesis of Transition Metal Sulfide and Reduced Graphene Oxide Hybrids as Efficient Electrocatalysts for Oxygen Evolution Reactions. *R. Soc. Open Sci.* **2018**, *5*, 180927.
(803) Li, Y.; Zhou, Y.; Wen, H.; Yang, J.; Maouche, C.; Liu, Q.; Wu, Y.; Cheng, C.; Zhu, J.; Cheng, X. N,S-Atom-Coordinated Co_9S_8 Trinary Dopants within a Porous Graphene Framework as Efficient Catalysts for Oxygen Reduction/Evolution Reactions. *Dalton Trans.* **2018**, *47*, 14992−15001.
(804) Li, X.-X.; Wang, X.-T.; Xiao, K.; Ouyang, T.; Li, N.; Liu, Z.-Q. In Situ Formation of Consubstantial $NiCo_2S_4$ Nanorod Arrays toward Self-Standing Electrode for High Activity Supercapacitors and Overall Water Splitting. *J. Power Sources* **2018**, *402*, 116−123.
(805) Wang, H.; Tang, J.; Li, Y.; Chu, H.; Ge, Y.; Baines, R.; Dong, P.; Ajayan, P. M.; Shen, J.; Ye, M. Template-Free Solvothermal Preparation of Ternary $FeNi_2S_4$ Hollow Balloons as RuO_2-like Efficient Electrocatalysts for the Oxygen Evolution Reaction with Superior Stability. *J. Mater. Chem. A* **2018**, *6*, 19417−19424.
(806) Ding, Y.; Li, H.; Hou, Y. Phosphorus-Doped Nickel Sulfides/Nickel Foam as Electrode Materials for Electrocatalytic Water Splitting. *Int. J. Hydrog. Energy* **2018**, *43*, 19002−19009.
(807) Liu, B.; Qu, S.; Kou, Y.; Liu, Z.; Chen, X.; Wu, Y.; Han, X.; Deng, Y.; Hu, W.; Zhong, C. In Situ Electrodeposition of Cobalt Sulfide Nanosheet Arrays on Carbon Cloth as a Highly Efficient Bifunctional Electrocatalyst for Oxygen Evolution and Reduction Reactions. *ACS Appl. Mater. Interfaces* **2018**, *10*, 30433−30440.
(808) Nan, K.; Du, H.; Su, L.; Li, C. M. Directly Electrodeposited Cobalt Sulfide Nanosheets as Advanced Catalyst for Oxygen Evolution Reaction. *ChemistrySelect* **2018**, *3*, 7081−7088.
(809) Liu, Y.; Yin, S.; Shen, P. K. Asymmetric 3d Electronic Structure for Enhanced Oxygen Evolution Catalysis. *ACS Appl. Mater. Interfaces* **2018**, *10*, 23131−23139.
(810) Kale, S. B.; Lokhande, A. C.; Pujari, R. B.; Lokhande, C. D. Effect of Pretreatment on Catalytic Activity of Cobalt Sulfide Thin Film for Oxygen Evolution Reaction. *Mater. Lett.* **2018**, *228*, 418−420.
(811) Ma, X.-X.; He, X.-Q. Achieving Superior Performance for Oxygen Electrode Catalyst by the Assistance of NaCl to Construct Cobalt Sulfide on Nitrogen and Sulfur Dual-Doped Graphene. *Int. J. Hydrog. Energy* **2018**, *43*, 13256−13265.
(812) Tang, Y.; Yang, H.; Sun, J.; Xia, M.; Guo, W.; Yu, L.; Yan, J.; Zheng, J.; Chang, L.; Gao, F. Phase-Pure Pentlandite $Ni_{4.3}Co_{4.7}S_8$ Binary Sulfide as an Efficient Bifunctional Electrocatalyst for Oxygen Evolution and Hydrogen Evolution. *Nanoscale* **2018**, *10*, 10459−10466.
(813) Tie, J.; Peng, S.; Diao, G.; Chen, F.; Sun, M.; Yu, L.; Zhou, J.; Li, Y. Shape-Controlled Synthesis of Nickel-Cobalt-Sulfide with Enhanced Electrochemical Activity. *J. Mater. Sci.: Mater. Electron.* **2018**, *29*, 2251−2258.
(814) Wu, L.-L.; Wang, Q.-S.; Li, J.; Long, Y.; Liu, Y.; Song, S.-Y.; Zhang, H.-J. Co_9S_8 Nanoparticles-Embedded N/S-Codoped Carbon Nanofibers Derived from Metal-Organic Framework-Wrapped CdS Nanowires for Efficient Oxygen Evolution Reaction. *Small* **2018**, *14*, 1704035.
(815) Qin, K.; Wang, L.; Wen, S.; Diao, L.; Liu, P.; Li, J.; Ma, L.; Shi, C.; Zhong, C.; Hu, W.; et al. Designed Synthesis of NiCo-LDH and Derived Sulfide on Heteroatom-Doped Edge-Enriched 3D Rivet Graphene Films for High-Performance Asymmetric Supercapacitor and Efficient OER. *J. Mater. Chem. A* **2018**, *6*, 8109−8119.
(816) Chen, Z.; Liu, M.; Wu, R. Strongly Coupling of Co_9S_8/Zn-Co-S Heterostructures Rooted in Carbon Nanocages towards Efficient Oxygen Evolution Reaction. *J. Catal.* **2018**, *361*, 322−330.
(817) Gao, Q.; Shi, Z.; Xue, K.; Ye, Z.; Hong, Z.; Yu, X.; Zhi, M. Cobalt Sulfide Aerogel Prepared by Anion Exchange Method with Enhanced Pseudocapacitive and Water Oxidation Performances. *Nanotechnology* **2018**, *29*, 215601.
(818) Guo, Y.; Tang, J.; Wang, Z.; Kang, Y.-M.; Bando, Y.; Yamauchi, Y. Elaborately Assembled Core-Shell Structured Metal Sulfides as a Bifunctional Catalyst for Highly Efficient Electrochemical Overall Water Splitting. *Nano Energy* **2018**, *47*, 494−502.
(819) Jin, Y.; Yue, X.; Du, H.; Wang, K.; Huang, S.; Shen, P. K. One-Step Growth of Nitrogen-Decorated Iron-Nickel Sulfide Nanosheets for the Oxygen Evolution Reaction. *J. Mater. Chem. A* **2018**, *6*, 5592−5597.
(820) Dong, B.; Yan, K.-L.; Liu, Z.-Z.; Chi, J.-Q.; Gao, W.-K.; Lin, J.-H.; Dai, F.-N.; Chai, Y.-M.; Liu, C.-G. Urchin-Like Nanorods of Binary NiCoS Supported on Nickel Foam for Electrocatalytic Overall Water Splitting. *J. Electrochem. Soc.* **2018**, *165*, H102−H108.
(821) Li, W.; Li, Y.; Wang, H.; Cao, Y.; Yu, H.; Peng, F. Co_9S_8-Porous Carbon Spheres as Bifunctional Electrocatalysts with High Activity and Stability for Oxygen Reduction and Evolution Reactions. *Electrochim. Acta* **2018**, *265*, 32−40.
(822) Wang, J.; Li, L.; Wang, L.; Liu, Y.; Sun, W.; Li, W.; Li, G. In Situ Growth of MoS_2 Nanosheet Arrays and TS_2 (T = Fe, Co, and Ni) Nanocubes onto Molybdate for Efficient Oxygen Evolution Reaction and Improved Hydrogen Evolution Reaction. *ACS Omega* **2018**, *3*, 464−471.
(823) Hu, C.; Yi, Z.; She, W.; Wang, J.; Xiao, J.; Wang, S. Urchin-like Non-Precious-Metal Bifunctional Oxygen Electrocatalysts: Boosting the Catalytic Activity via the In-Situ Growth of Heteroatom (N, S)-Doped Carbon Nanotube on Mesoporous Cobalt Sulfide/Carbon Spheres. *J. Colloid. Interface Sci.* **2018**, *524*, 465−474.
(824) Hao, J.; Yang, W.; Hou, J.; Mao, B.; Huang, Z.; Shi, W. Nitrogen Doped NiS_2 Nanoarrays with Enhanced Electrocatalytic Activity for Water Oxidation. *J. Mater. Chem. A* **2017**, *5*, 17811−17816.
(825) Ray, C.; Lee, S. C.; Sankar, K. V.; Jin, B.; Lee, J.; Park, J. H.; Jun, S. C. Amorphous Phosphorus-Incorporated Cobalt Molybdenum Sulfide on Carbon Cloth: An Efficient and Stable Electrocatalyst for Enhanced Overall Water Splitting over Entire pH Values. *ACS Appl. Mater. Interfaces* **2017**, *9*, 37739−37749.
(826) Hou, Y.; Qiu, M.; Nam, G.; Kim, M. G.; Zhang, T.; Liu, K.; Zhuang, X.; Cho, J.; Yuan, C.; Feng, X. Integrated Hierarchical Cobalt Sulfide/Nickel Selenide Hybrid Nanosheets as an Efficient Three-Dimensional Electrode for Electrochemical and Photoelectrochemical Water Splitting. *Nano Lett.* **2017**, *17*, 4202−4209.
(827) Chai, Y.-M.; Shang, X.; Liu, Z.-Z.; Dong, B.; Han, G.-Q.; Gao, W.-K.; Chi, J.-Q.; Yan, K.-L.; Liu, C.-G. Ripple-like NiFeCo Sulfides on Nickel Foam Derived from in-Situ Sulfurization of Precursor Oxides as Efficient Anodes for Water Oxidation. *Appl. Surf. Sci.* **2018**, *428*, 370−376.
(828) Wu, C.; Zhang, Y.; Dong, D.; Xie, H.; Li, J. Co_9S_8 Nanoparticles Anchored on Nitrogen and Sulfur Dual-Doped Carbon Nanosheets as Highly Efficient Bifunctional Electrocatalyst for Oxygen Evolution and Reduction Reactions. *Nanoscale* **2017**, *9*, 12432−12440.
(829) Guo, J.; Zhang, X.; Sun, Y.; Tang, L.; Zhang, X. Self-Template Synthesis of Hierarchical $CoMoS_3$ Nanotubes Constructed of Ultrathin Nanosheets for Robust Water Electrolysis. *J. Mater. Chem. A* **2017**, *5*, 11309−11315.
(830) Cai, P.; Huang, J.; Chen, J.; Wen, Z. Oxygen-Containing Amorphous Cobalt Sulfide Porous Nanocubes as High-Activity Electrocatalysts for the Oxygen Evolution Reaction in an Alkaline/Neutral Medium. *Angew. Chem. Int. Ed.* **2017**, *56*, 4858−4861.
(831) Yin, J.; Li, Y.; Lv, F.; Lu, M.; Sun, K.; Wang, W.; Wang, L.; Cheng, F.; Li, Y.; Xi, P.; et al. Oxygen Vacancies Dominated NiS_2/CoS_2 Interface Porous Nanowires for Portable Zn-Air Batteries Driven Water Splitting Devices. *Adv. Mater.* **2017**, *29*, 1704681.

https://doi.org/10.1021/acs.chemrev.3c00005
Chem. Rev. 2023, 123, 12795−13208

(832) Wu, X.; Han, X.; Ma, X.; Zhang, W.; Deng, Y.; Zhong, C.; Hu, W. Morphology-Controllable Synthesis of Zn-Co-Mixed Sulfide Nanostructures on Carbon Fiber Paper Toward Efficient Rechargeable Zinc-Air Batteries and Water Electrolysis. *ACS Appl. Mater. Interfaces* **2017**, *9*, 12574−12583.
(833) Chaudhari, N. K.; Oh, A.; Sa, Y. J.; Jin, H.; Baik, H.; Kim, S. G.; Lee, S. J.; Joo, S. H.; Lee, K. Morphology Controlled Synthesis of 2-D Ni-Ni_3S_2 and Ni_3S_2 Nanostructures on Ni Foam towards Oxygen Evolution Reaction. *Nano Converg.* **2017**, *4*, 7.
(834) Ganesan, V.; Ramasamy, P.; Kim, J. Hierarchical $Ni_{3.5}Co_{5.5}S_8$ Nanosheet-Assembled Hollow Nanocages: Superior Electrocatalyst towards Oxygen Evolution Reaction. *Int. J. Hydrog. Energy* **2017**, *42*, 5985−5992.
(835) Zhang, Y.; Chao, S.; Wang, X.; Han, H.; Bai, Z.; Yang, L. Hierarchical Co_9S_8 Hollow Microspheres as Multifunctional Electrocatalysts for Oxygen Reduction, Oxygen Evolution and Hydrogen Evolution Reactions. *Electrochim. Acta* **2017**, *246*, 380−390.
(836) Wang, N.; Li, L.; Zhao, D.; Kang, X.; Tang, Z.; Chen, S. Graphene Composites with Cobalt Sulfide: Efficient Trifunctional Electrocatalysts for Oxygen Reversible Catalysis and Hydrogen Production in the Same Electrolyte. *Small* **2017**, *13*, 1701025.
(837) Peng, S.; Li, L.; Zhang, J.; Tan, T. L.; Zhang, T.; Ji, D.; Han, X.; Cheng, F.; Ramakrishna, S. Engineering Co_9S_8/WS_2 Array Films as Bifunctional Electrocatalysts for Efficient Water Splitting. *J. Mater. Chem. A* **2017**, *5*, 23361−23368.
(838) Guo, P.; Wu, Y.-X.; Lau, W.-M.; Liu, H.; Liu, L.-M. CoS Nanosheet Arrays Grown on Nickel Foam as an Excellent OER Catalyst. *J. Alloys Compd.* **2017**, *723*, 772−778.
(839) Deng, S.; Shen, S.; Zhong, Y.; Zhang, K.; Wu, J.; Wang, X.; Xia, X.; Tu, J. Assembling Co_9S_8 Nanoflakes on Co_3O_4 Nanowires as Advanced Core/Shell Electrocatalysts for Oxygen Evolution Reaction. *J. Energy Chem.* **2017**, *26*, 1203−1209.
(840) Li, B.-Q.; Zhang, S.-Y.; Tang, C.; Cui, X.; Zhang, Q. Anionic Regulated NiFe (Oxy)Sulfide Electrocatalysts for Water Oxidation. *Small* **2017**, *13*, 1700610.
(841) Liu, Q.; Xie, L.; Liu, Z.; Du, G.; Asiri, A. M.; Sun, X. A Zn-Doped Ni_3S_2 Nanosheet Array as a High-Performance Electrochemical Water Oxidation Catalyst in Alkaline Solution. *Chem. Commun.* **2017**, *53*, 12446−12449.
(842) Jiang, J.; Yan, C.; Zhao, X.; Luo, H.; Xue, Z.; Mu, T. A PEGylated Deep Eutectic Solvent for Controllable Solvothermal Synthesis of Porous $NiCo_2S_4$ for Efficient Oxygen Evolution Reaction. *Green Chem.* **2017**, *19*, 3023−3031.
(843) Chen, P.; Zhou, T.; Zhang, M.; Tong, Y.; Zhong, C.; Zhang, N.; Zhang, L.; Wu, C.; Xie, Y. 3D Nitrogen-Anion-Decorated Nickel Sulfides for Highly Efficient Overall Water Splitting. *Adv. Mater.* **2017**, *29*, 1701584.
(844) Ren, H.; Huang, Z.-H.; Yang, Z.; Tang, S.; Kang, F.; Lv, R. Facile Synthesis of Free-Standing Nickel Chalcogenide Electrodes for Overall Water Splitting. *J. Energy Chem.* **2017**, *26*, 1217−1222.
(845) Xin, Y.; Kan, X.; Gan, L.-Y.; Zhang, Z. Heterogeneous Bimetallic Phosphide/Sulfide Nanocomposite for Efficient Solar-Energy-Driven Overall Water Splitting. *ACS Nano* **2017**, *11*, 10303−10312.
(846) Chen, B.; Ma, G.; Zhu, Y.; Wang, J.; Xiong, W.; Xia, Y. Metal-Organic-Framework-Derived Bimetallic Sulfide on N, S-Codoped Porous Carbon Nanocomposites as Multifunctional Electrocatalysts. *J. Power Sources* **2016**, *334*, 112−119.
(847) Zhu, T.; Zhu, L.; Wang, J.; Ho, G. W. In Situ Chemical Etching of Tunable 3D Ni_3S_2 Superstructures for Bifunctional Electrocatalysts for Overall Water Splitting. *J. Mater. Chem. A* **2016**, *4*, 13916−13922.
(848) Yang, J.; Zhu, G.; Liu, Y.; Xia, J.; Ji, Z.; Shen, X.; Wu, S. Fe_3O_4-Decorated Co_9S_8 Nanoparticles In Situ Grown on Reduced Graphene Oxide: A New and Efficient Electrocatalyst for Oxygen Evolution Reaction. *Adv. Funct. Mater.* **2016**, *26*, 4712−4721.
(849) Dou, S.; Tao, L.; Huo, J.; Wang, S.; Dai, L. Etched and Doped Co_9S_8/Graphene Hybrid for Oxygen Electrocatalysis. *Energy Environ. Sci.* **2016**, *9*, 1320−1326.
(850) Shang, X.; Hu, W.-H.; Han, G.-Q.; Liu, Z.-Z.; Dong, B.; Liu, Y.-R.; Li, X.; Chai, Y.-M.; Liu, C.-G. Crystalline Phase-Function Relationship of in Situ Growth Ni_xS_y Controlled by Sulfuration Degree for Oxygen Evolution Reaction. *Int. J. Hydrog. Energy* **2016**, *41*, 13032−13038.
(851) Cao, X.; Zheng, X.; Tian, J.; Jin, C.; Ke, K.; Yang, R. Cobalt Sulfide Embedded in Porous Nitrogen-Doped Carbon as a Bifunctional Electrocatalyst for Oxygen Reduction and Evolution Reactions. *Electrochim. Acta* **2016**, *191*, 776−783.
(852) Ma, X.-X.; He, X.-Q. $Co_4S_3/Ni_xS_6(7 \geq x \geq 6)$/NiOOH in-Situ Encapsulated Carbon-Based Hybrid as a High-Efficient Oxygen Electrode Catalyst in Alkaline Media. *Electrochim. Acta* **2016**, *213*, 163−173.
(853) Tan, S. M.; Chua, C. K.; Sedmidubský, D.; Sofer, Z.; Pumera, M. Electrochemistry of Layered GaSe and GeS: Applications to ORR, OER and HER. *Phys. Chem. Chem. Phys.* **2016**, *18*, 1699−1711.
(854) Zhu, H.; Zhang, J.; Yanzhang, R.; Du, M.; Wang, Q.; Gao, G.; Wu, J.; Wu, G.; Zhang, M.; Liu, B.; et al. When Cubic Cobalt Sulfide Meets Layered Molybdenum Disulfide: A Core-Shell System Toward Synergetic Electrocatalytic Water Splitting. *Adv. Mater.* **2015**, *27*, 4752−4759.
(855) Ouyang, C.; Wang, X.; Wang, C.; Zhang, X.; Wu, J.; Ma, Z.; Dou, S.; Wang, S. Hierarchically Porous Ni_3S_2 Nanorod Array Foam as Highly Efficient Electrocatalyst for Hydrogen Evolution Reaction and Oxygen Evolution Reaction. *Electrochim. Acta* **2015**, *174*, 297−301.
(856) Shen, M.; Ruan, C.; Chen, Y.; Jiang, C.; Ai, K.; Lu, L. Covalent Entrapment of Cobalt-Iron Sulfides in N-Doped Mesoporous Carbon: Extraordinary Bifunctional Electrocatalysts for Oxygen Reduction and Evolution Reactions. *ACS Appl. Mater. Interfaces* **2015**, *7*, 1207−1218.
(857) Ganesan, P.; Prabu, M.; Sanetuntikul, J.; Shanmugam, S. Cobalt Sulfide Nanoparticles Grown on Nitrogen and Sulfur Codoped Graphene Oxide: An Efficient Electrocatalyst for Oxygen Reduction and Evolution Reactions. *ACS Catal.* **2015**, *5*, 3625−3637.
(858) Chen, B.; Li, R.; Ma, G.; Gou, X.; Zhu, Y.; Xia, Y. Cobalt Sulfide/N,S Codoped Porous Carbon Core-Shell Nanocomposites as Superior Bifunctional Electrocatalysts for Oxygen Reduction and Evolution Reactions. *Nanoscale* **2015**, *7*, 20674−20684.
(859) Wang, H.; Li, Z.; Li, G.; Peng, F.; Yu, H. Co_3S_4/NCNTs: A Catalyst for Oxygen Evolution Reaction. *Catal. Today* **2015**, *245*, 74−78.
(860) Zhang, Z.; Wang, X.; Cui, G.; Zhang, A.; Zhou, X.; Xu, H.; Gu, L. $NiCo_2S_4$ Sub-Micron Spheres: An Efficient Non-Precious Metal Bifunctional Electrocatalyst. *Nanoscale* **2014**, *6*, 3540−3544.
(861) Liu, Q.; Jin, J.; Zhang, J. $NiCo_2S_4$@graphene as a Bifunctional Electrocatalyst for Oxygen Reduction and Evolution Reactions. *ACS Appl. Mater. Interfaces* **2013**, *5*, 5002−5008.
(862) Demazeau, G. Solvothermal and Hydrothermal Processes: The Main Physico-Chemical Factors Involved and New Trends. *Res. Chem. Intermed.* **2011**, *37*, 107−123.
(863) Yang, N.; Tang, C.; Wang, K.; Du, G.; Asiri, A. M.; Sun, X. Iron-Doped Nickel Disulfide Nanoarray: A Highly Efficient and Stable Electrocatalyst for Water Splitting. *Nano Res.* **2016**, *9*, 3346−3354.
(864) Lu, F.; Meng, F.; Wang, L.; Sang, Y.; Luo, J. Controlled Synthesis and Optical Properties of CeO_2 Nanoparticles by a $N_2H_4 \cdot H_2O$-Assisted Hydrothermal Method. *Micro Nano Lett.* **2012**, *7*, 624−627.
(865) Huang, J.; Wei, J.; Xiao, Y.; Xu, Y.; Xiao, Y.; Wang, Y.; Tan, L.; Yuan, K.; Chen, Y. When Al-Doped Cobalt Sulfide Nanosheets Meet Nickel Nanotube Arrays: A Highly Efficient and Stable Cathode for Asymmetric Supercapacitors. *ACS Nano* **2018**, *12*, 3030−3041.
(866) Penn, R. L.; Banfield, J. F. Imperfect Oriented Attachment: Dislocation Generation in Defect-Free Nanocrystals. *Science* **1998**, *281*, 969−971.
(867) Cölfen, H.; Antonietti, M. Mesocrystals: Inorganic Superstructures Made by Highly Parallel Crystallization and Controlled Alignment. *Angew. Chem. Int. Ed.* **2005**, *44*, 5576−5591.

https://doi.org/10.1021/acs.chemrev.3c00005
Chem. Rev. 2023, 123, 12795−13208

(868) Chen, W.; Li, S.; Chen, C.; Yan, L. Self-Assembly and Embedding of Nanoparticles by In Situ Reduced Graphene for Preparation of a 3D Graphene/Nanoparticle Aerogel. *Adv. Mater.* **2011**, *23*, 5679−5683.
(869) Cheng, H.; Xue, H.; Zhao, G.; Hong, C.; Zhang, X. Preparation, Characterization, and Properties of Graphene-Based Composite Aerogels via in Situ Polymerization and Three-Dimensional Self-Assembly from Graphene Oxide Solution. *RSC Adv.* **2016**, *6*, 78538−78547.
(870) Hou, Y.; Zhang, B.; Wen, Z.; Cui, S.; Guo, X.; He, Z.; Chen, J. A 3D Hybrid of Layered MoS_2/Nitrogen-Doped Graphene Nanosheet Aerogels: An Effective Catalyst for Hydrogen Evolution in Microbial Electrolysis Cells. *J. Mater. Chem. A* **2014**, *2*, 13795−13800.
(871) Maheskumar, V.; Selvaraju, T.; Vidhya, B. Influence of Solvent in Solvothermal Synthesis of Cu_3SnS_4: Morphology and Band Gap Dependant Electrocatalytic Hydrogen Evolution Reaction and Photocatalytic Dye Degradation. *Int. J. Hydrog. Energy* **2018**, *43*, 22861−22873.
(872) Huang, Z.-F.; Song, J.; Li, K.; Tahir, M.; Wang, Y.-T.; Pan, L.; Wang, L.; Zhang, X.; Zou, J.-J. Hollow Cobalt-Based Bimetallic Sulfide Polyhedra for Efficient All-pH-Value Electrochemical and Photocatalytic Hydrogen Evolution. *J. Am. Chem. Soc.* **2016**, *138*, 1359−1365.
(873) Fang, Z.; Peng, L.; Qian, Y.; Zhang, X.; Xie, Y.; Cha, J. J.; Yu, G. Dual Tuning of Ni-Co-A (A = P, Se, O) Nanosheets by Anion Substitution and Holey Engineering for Efficient Hydrogen Evolution. *J. Am. Chem. Soc.* **2018**, *140*, 5241−5247.
(874) Yang, M.; Zhang, C. H.; Li, N. W.; Luan, D. Y.; Yu, L.; Lou, X. W. Design and Synthesis of Hollow Nanostructures for Electrochemical Water Splitting. *Adv. Sci.* **2022**, *9*, 2105135.
(875) Guan, B. Y.; Yu, L.; Lou, X. W. D. General Synthesis of Multishell Mixed-Metal Oxyphosphide Particles with Enhanced Electrocatalytic Activity in the Oxygen Evolution Reaction. *Angew. Chem. Int. Ed.* **2017**, *56*, 2386−2389.
(876) Rui, X.; Tan, H.; Yan, Q. Nanostructured Metal Sulfides for Energy Storage. *Nanoscale* **2014**, *6*, 9889−9924.
(877) Xia, X.; Zhu, C.; Luo, J.; Zeng, Z.; Guan, C.; Ng, C. F.; Zhang, H.; Fan, H. J. Synthesis of Free-Standing Metal Sulfide Nanoarrays via Anion Exchange Reaction and Their Electrochemical Energy Storage Application. *Small* **2014**, *10*, 766−773.
(878) Sun, D.; Zhu, X.; Luo, B.; Zhang, Y.; Tang, Y.; Wang, H.; Wang, L. New Binder-Free Metal Phosphide-Carbon Felt Composite Anodes for Sodium-Ion Battery. *Adv. Energy Mater.* **2018**, *8*, 1801197.
(879) Hu, L.; Dai, C.; Liu, H.; Li, Y.; Shen, B.; Chen, Y.; Bao, S.-J.; Xu, M. Double-Shelled NiO-$NiCo_2O_4$ Heterostructure@Carbon Hollow Nanocages as an Efficient Sulfur Host for Advanced Lithium-Sulfur Batteries. *Adv. Energy Mater.* **2018**, *8*, 1800709.
(880) Lu, Z.; Zhu, W.; Yu, X.; Zhang, H.; Li, Y.; Sun, X.; Wang, X.; Wang, H.; Wang, J.; Luo, J.; et al. Ultrahigh Hydrogen Evolution Performance of Under-Water "Superaerophobic" MoS_2 Nanostructured Electrodes. *Adv. Mater.* **2014**, *26*, 2683−2687.
(881) Guo, M.; Qayum, A.; Dong, S.; Jiao, X.; Chen, D.; Wang, T. In Situ Conversion of Metal (Ni, Co or Fe) Foams into Metal Sulfide (Ni_3S_2, Co_9S_8 or FeS) Foams with Surface Grown N-Doped Carbon Nanotube Arrays as Efficient Superaerophobic Electrocatalysts for Overall Water Splitting. *J. Mater. Chem. A* **2020**, *8*, 9239−9247.
(882) Li, H.; Chen, S.; Jia, X.; Xu, B.; Lin, H.; Yang, H.; Song, L.; Wang, X. Amorphous Nickel-Cobalt Complexes Hybridized with 1T-Phase Molybdenum Disulfide via Hydrazine-Induced Phase Transformation for Water Splitting. *Nat. Commun.* **2017**, *8*, 15377.
(883) Park, H. K.; Ahn, H.; Lee, T. H.; Lee, J. Y.; Lee, M. G.; Lee, S. A.; Yang, J. W.; Kim, S. J.; Ahn, S. H.; Kim, S. Y.; et al. Grain Boundaries Boost Oxygen Evolution Reaction in NiFe Electrocatalysts. *Small Methods* **2021**, *5*, 2000755.
(884) Wang, H.-F.; Chen, L.; Pang, H.; Kaskel, S.; Xu, Q. MOF-Derived Electrocatalysts for Oxygen Reduction, Oxygen Evolution and Hydrogen Evolution Reactions. *Chem. Soc. Rev.* **2020**, *49*, 1414−1448.
(885) Park, K. S.; Ni, Z.; Cote, A. P.; Choi, J. Y.; Huang, R.; Uribe-Romo, F. J.; Chae, H. K.; O'Keeffe, M.; Yaghi, O. M. Exceptional Chemical and Thermal Stability of Zeolitic Imidazolate Frameworks. *Proc. Natl. Acad. Sci. U.S.A.* **2006**, *103*, 10186−10191.
(886) Hu, H.; Guan, B. Y.; Lou, X. W. D. Construction of Complex CoS Hollow Structures with Enhanced Electrochemical Properties for Hybrid Supercapacitors. *Chem.* **2016**, *1*, 102−113.
(887) Chen, L.; Wang, H.-F.; Li, C.; Xu, Q. Bimetallic Metal-Organic Frameworks and Their Derivatives. *Chem. Sci.* **2020**, *11*, 5369−5403.
(888) Zhong, H.; Wang, J.; Zhang, Y.; Xu, W.; Xing, W.; Xu, D.; Zhang, Y.; Zhang, X. ZIF-8 Derived Graphene-Based Nitrogen-Doped Porous Carbon Sheets as Highly Efficient and Durable Oxygen Reduction Electrocatalysts. *Angew. Chem. Int. Ed.* **2014**, *53*, 14235−14239.
(889) Chemical Vapor Deposition. In *The Materials Science of Semiconductors*; Rockett, A., Ed.; Springer US: Boston, MA, 2008; pp 573−609. DOI: 10.1007/978-0-387-68650-9_12.
(890) Devi, N.; Sahoo, S.; Kumar, R.; Singh, R. K. A Review of the Microwave-Assisted Synthesis of Carbon Nanomaterials, Metal Oxides/Hydroxides and Their Composites for Energy Storage Applications. *Nanoscale* **2021**, *13*, 11679−11711.
(891) Colmenares, L. C.; Wurth, A.; Jusys, Z.; Behm, R. J. Model Study on the Stability of Carbon Support Materials under Polymer Electrolyte Fuel Cell Cathode Operation Conditions. *J. Power Sources* **2009**, *190*, 14−24.
(892) Möller, S.; Barwe, S.; Masa, J.; Wintrich, D.; Seisel, S.; Baltruschat, H.; Schuhmann, W. Online Monitoring of Electrochemical Carbon Corrosion in Alkaline Electrolytes by Differential Electrochemical Mass Spectrometry. *Angew. Chem. Int. Ed.* **2020**, *59*, 1585−1589.
(893) Li, J.; Liu, G.; Fu, J.; Jiang, G.; Luo, D.; Hassan, F. M.; Zhang, J.; Deng, Y.-P.; Xu, P.; Ricardez-Sandoval, L.; et al. Surface Decorated Cobalt Sulfide as Efficient Catalyst for Oxygen Evolution Reaction and Its Intrinsic Activity. *J. Catal.* **2018**, *367*, 43−52.
(894) Chi, J.-Q.; Yan, K.-L.; Xiao, Z.; Dong, B.; Shang, X.; Gao, W.-K.; Li, X.; Chai, Y.-M.; Liu, C.-G. Trimetallic NiFeCo Selenides Nanoparticles Supported on Carbon Fiber Cloth as Efficient Electrocatalyst for Oxygen Evolution Reaction. *Int. J. Hydrog. Energy* **2017**, *42*, 20599−20607.
(895) Zang, X.; Shen, C.; Kao, E.; Warren, R.; Zhang, R.; Teh, K. S.; Zhong, J.; Wei, M.; Li, B.; Chu, Y.; et al. Titanium Disulfide Coated Carbon Nanotube Hybrid Electrodes Enable High Energy Density Symmetric Pseudocapacitors. *Adv. Mater.* **2018**, *30*, 1704754.
(896) Li, X.; Wang, J. One-dimensional and Two-dimensional Synergized Nanostructures for High-performing Energy Storage and Conversion. *InfoMat* **2020**, *2*, 3−32.
(897) He, Z.; Zhang, J.; Li, X.; Guan, S.; Dai, M.; Wang, S. 1D/2D Heterostructured Photocatalysts: From Design and Unique Properties to Their Environmental Applications. *Small* **2020**, *16*, 2005051.
(898) Wang, J.; Cui, Y.; Wang, D. Design of Hollow Nanostructures for Energy Storage, Conversion and Production. *Adv. Mater.* **2019**, *31*, 1801993.
(899) Xu, Y.; Zhang, F.; Sheng, T.; Ye, T.; Yi, D.; Yang, Y.; Liu, S.; Wang, X.; Yao, J. Clarifying the Controversial Catalytic Active Sites of Co_3O_4 for the Oxygen Evolution Reaction. *J. Mater. Chem. A* **2019**, *7*, 23191−23198.
(900) Kim, J. S.; Kim, B.; Kim, H.; Kang, K. Recent Progress on Multimetal Oxide Catalysts for the Oxygen Evolution Reaction. *Adv. Energy Mater.* **2018**, *8*, 1702774.
(901) Chen, J. Y. C.; Dang, L.; Liang, H.; Bi, W.; Gerken, J. B.; Jin, S.; Alp, E. E.; Stahl, S. S. Operando Analysis of NiFe and Fe Oxyhydroxide Electrocatalysts for Water Oxidation: Detection of Fe^{4+} by Mössbauer Spectroscopy. *J. Am. Chem. Soc.* **2015**, *137*, 15090−15093.
(902) West, A. R. Crystal Defects, Non-Stoichiometry and Solid Solutions. In *Solid State Chemistry and its Applications*, Student ed.; John Wiley & Sons Ltd: United Kingdom, 2014; pp 83−122.

(903) Zheng, D.; Yu, L.; Liu, W.; Dai, X.; Niu, X.; Fu, W.; Shi, W.; Wu, F.; Cao, X. Structural Advantages and Enhancement Strategies of Heterostructure Water-Splitting Electrocatalysts. *Cell Reports Physical Science* **2021**, *2*, 100443.
(904) Oh, N. K.; Seo, J.; Lee, S.; Kim, H.-J.; Kim, U.; Lee, J.; Han, Y.-K.; Park, H. Highly Efficient and Robust Noble-Metal Free Bifunctional Water Electrolysis Catalyst Achieved via Complementary Charge Transfer. *Nat. Commun.* **2021**, *12*, 4606.
(905) Gao, W.; Gou, W.; Ma, Y.; Wei, R.; Ho, J. C.; Qu, Y. Cerium Phosphate as a Novel Cocatalyst Promoting $NiCo_2O_4$ Nanowire Arrays for Efficient and Robust Electrocatalytic Oxygen Evolution. *ACS Appl. Energy Mater.* **2019**, *2*, 5769−5776.
(906) Xu, X.-T.; Pan, L.; Zhang, X.; Wang, L.; Zou, J.-J. Rational Design and Construction of Cocatalysts for Semiconductor-Based Photo-Electrochemical Oxygen Evolution: A Comprehensive Review. *Adv. Sci.* **2019**, *6*, 1801505.
(907) Liang, Q.; Brocks, G.; Bieberle-Hütter, A. Oxygen Evolution Reaction (OER) Mechanism under Alkaline and Acidic Conditions. *J. Phys. Energy* **2021**, *3*, 026001.
(908) Juodkazis, K.; Juodkazytė, J.; Vilkauskaitė, R.; Šebeka, B.; Jasulaitienė, V. Oxygen Evolution on Composite Ruthenium and Nickel Oxides Electrode. *CHEMIJA* **2008**, *19*, 1−6.
(909) Márquez-Montes, R. A.; Orozco-Mena, R. E.; Camacho-Dávila, A. A.; Pérez-Vega, S.; Collins-Martínez, V. H.; Ramos-Sánchez, V. H. Optimization of the Electrooxidation of Aqueous Ammonium Sulfite for Hydrogen Production at Near-Neutral pH Using Response Surface Methodology. *Int. J. Hydrogen Energy* **2020**, *45*, 13821−13831.
(910) Bouroushian, M. *Electrochemistry of Metal Chalcogenides*; Springer-Verlag Berlin Heidelberg: Berlin, 2010.
(911) Ou, X.; Luo, Z. One-Step Synthesis of Ni_3S_2 Nanoplatelets on Graphene for High Performance Supercapacitors. *RSC Adv.* **2016**, *6*, 10280−10284.
(912) Márquez-Montes, R. A.; Orozco-Mena, R. E.; Lardizábal-Gutiérrez, D.; Chávez-Flores, D.; López-Ortíz, A.; Ramos-Sánchez, V. H. Sulfur Dioxide Exploitation by Electrochemical Oxidation of Sulfite in Near-Neutral pH Electrolytes: A Kinetics and Mechanistic Study. *Electrochem. Commun.* **2019**, *104*, 106481.
(913) Spanos, I.; Masa, J.; Zeradjanin, A.; Schlögl, R. The Effect of Iron Impurities on Transition Metal Catalysts for the Oxygen Evolution Reaction in Alkaline Environment: Activity Mediators or Active Sites? *Catal. Lett.* **2021**, *151*, 1843−1856.
(914) Ibraheem, S.; Yasin, G.; Kumar, A.; Mushtaq, M. A.; Ibrahim, S.; Iqbal, R.; Tabish, M.; Ali, S.; Saad, A. Iron-Cation-Coordinated Cobalt-Bridged-Selenides Nanorods for Highly Efficient Photo/Electrochemical Water Splitting. *Appl. Catal. B: Environ.* **2022**, *304*, 120987.
(915) Singh, H.; Marley-Hines, M.; Chakravarty, S.; Nath, M. Multi-Walled Carbon Nanotube Supported Manganese Selenide as a Highly Active Bifunctional OER and ORR Electrocatalyst. *J. Mater. Chem. A* **2022**, *10*, 6772−6784.
(916) Singh, H.; Liyanage, W. P. R.; Nath, M. Carbon Nanotube Encapsulated Metal Selenide Nanostructures for Efficient Electrocatalytic Oxygen Evolution Reaction. *Chem. Commun.* **2022**, *58*, 8360−8363.
(917) De Silva, U.; See, J.; Liyanage, W. P. R.; Masud, J.; Wu, J.; Yang, W.; Chen, W.-T.; Prendergast, D.; Nath, M. Understanding the Structural Evolution of a Nickel Chalcogenide Electrocatalyst Surface for Water Oxidation. *Energy Fuels* **2021**, *35*, 4387−4403.
(918) Cao, X.; Johnson, E.; Nath, M. Identifying High-Efficiency Oxygen Evolution Electrocatalysts from Co-Ni-Cu Based Selenides through Combinatorial Electrodeposition. *J. Mater. Chem. A* **2019**, *7*, 9877−9889.
(919) Yuan, M.; Wang, M.; Lu, P.; Sun, Y.; Dipazir, S.; Zhang, J.; Li, S.; Zhang, G. Tuning Carbon Nanotube-Grafted Core-Shell-Structured Cobalt Selenide@carbon Hybrids for Efficient Oxygen Evolution Reaction. *J. Colloid. Interface Sci.* **2019**, *533*, 503−512.
(920) Cao, X.; Johnson, E.; Nath, M. Expanding Multinary Selenide Based High-Efficiency Oxygen Evolution Electrocatalysts through Combinatorial Electrodeposition: Case Study with Fe-Cu-Co Selenides. *ACS Sustainable Chem. Eng.* **2019**, *7*, 9588−9600.
(921) Zhang, T.; Hang, L.; Sun, Y.; Men, D.; Li, X.; Wen, L.; Lyu, X.; Li, Y. Hierarchical Hetero-Ni_3Se_4@NiFe LDH Micro/Nanosheets as Efficient Bifunctional Electrocatalysts with Superior Stability for Overall Water Splitting. *Nanoscale Horiz.* **2019**, *4*, 1132−1138.
(922) Masud, J.; Liyanage, W. P. R.; Cao, X.; Saxena, A.; Nath, M. Copper Selenides as High-Efficiency Electrocatalysts for Oxygen Evolution Reaction. *ACS Appl. Energy Mater.* **2018**, *1*, 4075−4083.
(923) Wang, X.; Zhuang, L.; He, T.; Jia, Y.; Zhang, L.; Yan, X.; Gao, M.; Du, A.; Zhu, Z.; Yao, X.; et al. Grafting Cobalt Diselenide on Defective Graphene for Enhanced Oxygen Evolution Reaction. *iScience* **2018**, *7*, 145−153.
(924) Ma, S.; Yuan, H.; Cai, L.; Wang, X.; Long, H.; Chai, Y.; Tsang, Y. H. One Step Synthesis of $Fe_{4.4}Ni_{17.6}Se_{16}$ Coupled NiSe Foam as Self-Supported, Highly Efficient and Durable Oxygen Evolution Electrode. *Mater. Today Chem.* **2018**, *9*, 133−139.
(925) Cao, X.; Hong, Y.; Zhang, N.; Chen, Q.; Masud, J.; Zaeem, M. A.; Nath, M. Phase Exploration and Identification of Multinary Transition-Metal Selenides as High-Efficiency Oxygen Evolution Electrocatalysts through Combinatorial Electrodeposition. *ACS Catal.* **2018**, *8*, 8273−8289.
(926) Amin, B. G.; Swesi, A. T.; Masud, J.; Nath, M. $CoNi_2Se_4$ as an Efficient Bifunctional Electrocatalyst for Overall Water Splitting. *Chem. Commun.* **2017**, *53*, 5412−5415.
(927) Nai, J.; Lu, Y.; Yu, L.; Wang, X.; Lou, X. W. D. Formation of Ni-Fe Mixed Diselenide Nanocages as a Superior Oxygen Evolution Electrocatalyst. *Adv. Mater.* **2017**, *29*, 1703870.
(928) Masud, J.; Swesi, A. T.; Liyanage, W. P. R.; Nath, M. Cobalt Selenide Nanostructures: An Efficient Bifunctional Catalyst with High Current Density at Low Coverage. *ACS Appl. Mater. Interfaces* **2016**, *8*, 17292−17302.
(929) Liu, Y.; Cheng, H.; Lyu, M.; Fan, S.; Liu, Q.; Zhang, W.; Zhi, Y.; Wang, C.; Xiao, C.; Wei, S.; et al. Low Overpotential in Vacancy-Rich Ultrathin $CoSe_2$ Nanosheets for Water Oxidation. *J. Am. Chem. Soc.* **2014**, *136*, 15670−15675.
(930) Song, J.; Chen, Y.; Huang, H.; Wang, J.; Huang, S.-C.; Liao, Y.-F.; Fetohi, A. E.; Hu, F.; Chen, H.; Li, L.; et al. Heterointerface Engineering of Hierarchically Assembling Layered Double Hydroxides on Cobalt Selenide as Efficient Trifunctional Electrocatalysts for Water Splitting and Zinc-Air Battery. *Adv. Sci.* **2022**, *9*, 2104522.
(931) Wang, R.; Liu, B.; You, S.; Li, Y.; Zhang, Y.; Wang, D.; Tang, B.; Sun, Y.; Zou, J. Three-Dimensional Ni3Se4 Flowers Integrated with Ultrathin Carbon Layer with Strong Electronic Interactions for Boosting Oxygen Reduction/Evolution Reactions. *Chem. Eng. J.* **2022**, *430*, 132720.
(932) Tan, L.; Yu, J.; Wang, H.; Gao, H.; Liu, X.; Wang, L.; She, X.; Zhan, T. Controllable Synthesis and Phase-Dependent Catalytic Performance of Dual-Phase Nickel Selenides on Ni Foam for Overall Water Splitting. *Appl. Catal. B: Environ.* **2022**, *303*, 120915.
(933) Chen, Z.; Zhou, T.; Liu, Q.; Wang, Z.; Gu, R.; Guo, L.; Liu, Y. Three-Dimensional Flower-Like Bimetallic Nickel-Iron Selenide for Efficient Oxygen Evolution Reaction. *J. Phys. Chem. C* **2022**, *126*, 5131−5137.
(934) Tian, Z.; Liu, Y.; Xu, Q.; Shi, Y.; Ma, C.; Peng, B.; Liu, G.; Yang, J.; Zheng, W. Fe Doped $NiSe_2$ Nanoarrays to Boost Electrocatalytic Oxygen Evolution Reaction. *Electrochim. Acta* **2022**, *425*, 140711.
(935) Srinivas, K.; Ma, F.; Liu, Y.; Zhang, Z.; Wu, Y.; Chen, Y. Metal-Organic Framework-Derived Fe-Doped $Ni_3Se_4/NiSe_2$ Heterostructure-Embedded Mesoporous Tubes for Boosting Oxygen Evolution Reaction. *ACS Appl. Mater. Interfaces* **2022**, *14*, 52927−52939.
(936) Chae, S.-H.; Muthurasu, A.; Kim, T.; Kim, J. S.; Khil, M.-S.; Lee, M.; Kim, H.; Lee, J. Y.; Kim, H. Y. Templated Fabrication of Perfectly Aligned Metal-Organic Framework-Supported Iron-Doped Copper-Cobalt Selenide Nanostructure on Hollow Carbon Nanofibers for an Efficient Trifunctional Electrode Material. *Appl. Catal. B: Environ.* **2021**, *293*, 120209.

https://doi.org/10.1021/acs.chemrev.3c00005
Chem. Rev. 2023, 123, 12795−13208

(937) Zhang, J.-Y.; Yan, Y.; Mei, B.; Qi, R.; He, T.; Wang, Z.; Fang, W.; Zaman, S.; Su, Y.; Ding, S.; et al. Local Spin-State Tuning of Cobalt-Iron Selenide Nanoframes for the Boosted Oxygen Evolution. *Energy Environ. Sci.* **2021**, *14*, 365−373.
(938) Zhang, L.; Lu, C.; Ye, F.; Pang, R.; Liu, Y.; Wu, Z.; Shao, Z.; Sun, Z.; Hu, L. Selenic Acid Etching Assisted Vacancy Engineering for Designing Highly Active Electrocatalysts toward the Oxygen Evolution Reaction. *Adv. Mater.* **2021**, *33*, 2007523.
(939) Ni, S.; Qu, H.; Xu, Z.; Zhu, X.; Xing, H.; Wang, L.; Yu, J.; Liu, H.; Chen, C.; Yang, L. Interfacial Engineering of the $NiSe_2/FeSe_2$ p-p Heterojunction for Promoting Oxygen Evolution Reaction and Electrocatalytic Urea Oxidation. *Appl. Catal. B: Environ.* **2021**, *299*, 120638.
(940) Guo, Y.; Zhang, C.; Zhang, J.; Dastafkan, K.; Wang, K.; Zhao, C.; Shi, Z. Metal-Organic Framework-Derived Bimetallic NiFe Selenide Electrocatalysts with Multiple Phases for Efficient Oxygen Evolution Reaction. *ACS Sustainable Chem. Eng.* **2021**, *9*, 2047−2056.
(941) Liu, C.; Han, Y.; Yao, L.; Liang, L.; He, J.; Hao, Q.; Zhang, J.; Li, Y.; Liu, H. Engineering Bimetallic NiFe-Based Hydroxides/Selenides Heterostructure Nanosheet Arrays for Highly-Efficient Oxygen Evolution Reaction. *Small* **2021**, *17*, 2007334.
(942) Liang, D.; Mao, J.; Liu, P.; Li, J.; Yan, J.; Song, W. In-Situ Doping of Co in Nickel Selenide Nanoflower for Robust Electrocatalysis towards Oxygen Evolution. *Int. J. Hydrog. Energy* **2020**, *45*, 27047−27055.
(943) Cao, X.; Medvedeva, J. E.; Nath, M. Copper Cobalt Selenide as a High-Efficiency Bifunctional Electrocatalyst for Overall Water Splitting: Combined Experimental and Theoretical Study. *ACS Appl. Energy Mater.* **2020**, *3*, 3092−3103.
(944) Zheng, X.; Han, X.; Cao, Y.; Zhang, Y.; Nordlund, D.; Wang, J.; Chou, S.; Liu, H.; Li, L.; Zhong, C.; et al. Identifying Dense $NiSe_2/CoSe_2$ Heterointerfaces Coupled with Surface High-Valence Bimetallic Sites for Synergistically Enhanced Oxygen Electrocatalysis. *Adv. Mater.* **2020**, *32*, 2000607.
(945) Chakraborty, B.; Beltrán-Suito, R.; Hlukhyy, V.; Schmidt, J.; Menezes, P. W.; Driess, M. Crystalline Copper Selenide as a Reliable Non-Noble Electro(Pre)Catalyst for Overall Water Splitting. *ChemSusChem* **2020**, *13*, 3222−3229.
(946) Yuan, J.; Cheng, X.; Wang, H.; Lei, C.; Pardiwala, S.; Yang, B.; Li, Z.; Zhang, Q.; Lei, L.; Wang, S.; Hou, Y. A Superaerophobic Bimetallic Selenides Heterostructure for Efficient Industrial-Level Oxygen Evolution at Ultra-High Current Densities. *Nano-Micro Letters* **2020**, *12*, 104.
(947) Gao, R.; Li, G.-D.; Hu, J.; Wu, Y.; Lian, X.; Wang, D.; Zou, X. In Situ Electrochemical Formation of $NiSe/NiO_x$ Core/Shell Nano-Electrocatalysts for Superior Oxygen Evolution Activity. *Catal. Sci. Technol.* **2016**, *6*, 8268−8275.
(948) Wang, L.; Wang, X.; Xi, S.; Du, Y.; Xue, J. A-$Ni(OH)_2$ Originated from Electro-Oxidation of $NiSe_2$ Supported by Carbon Nanoarray on Carbon Cloth for Efficient Water Oxidation. *Small* **2019**, *15*, 1902222.
(949) Ghaemmaghami, M.; Yamini, Y.; Saievar-Iranizad, E.; Bayat, A. Straightforward Fabrication of Robust Fe-Doped Ni_3Se_2 Supported Nickel Foam as a Highly Efficient Electrocatalyst for the Oxygen Evolution Reaction. *Sustain. Energy Fuels* **2020**, *4*, 1150−1156.
(950) Sun, Y.-Y.; Jiang, M.-Y.; Wu, L.-K.; Hou, G.-Y.; Tang, Y.-P.; Liu, M. Ultra-Thin NiFeSe Nanosheets as a Highly Efficient Bifunctional Electrocatalyst for Overall Water Splitting. *Sustain. Energy Fuels* **2020**, *4*, 582−588.
(951) Anantharaj, S.; Subhashini, E.; Swaathini, K. C.; Amarnath, T. S.; Chatterjee, S.; Karthick, K.; Kundu, S. Respective Influence of Stoichiometry and NiOOH Formation in Hydrogen and Oxygen Evolution Reactions of Nickel Selenides. *Appl. Surf. Sci.* **2019**, *487*, 1152−1158.
(952) Zou, Z.; Wang, X.; Huang, J.; Wu, Z.; Gao, F. An Fe-Doped Nickel Selenide Nanorod/Nanosheet Hierarchical Array for Efficient Overall Water Splitting. *J. Mater. Chem. A* **2019**, *7*, 2233−2241.
(953) Zhang, Y.; Zhang, C.; Guo, Y.; Liu, D.; Yu, Y.; Zhang, B. Selenium Vacancy-Rich $CoSe_2$ Ultrathin Nanomeshes with Abundant Active Sites for Electrocatalytic Oxygen Evolution. *J. Mater. Chem. A* **2019**, *7*, 2536−2540.
(954) Yilmaz, G.; Tan, C. F.; Lim, Y.-F.; Ho, G. W. Pseudomorphic Transformation of Interpenetrated Prussian Blue Analogs into Defective Nickel Iron Selenides for Enhanced Electrochemical and Photo-Electrochemical Water Splitting. *Adv. Energy Mater.* **2019**, *9*, 1802983.
(955) Yang, C.; Zhang, J.; Gao, G.; Liu, D.; Liu, R.; Fan, R.; Gan, S.; Wang, Y.; Wang, Y. 3D Metallic $Ti@Ni_{0.85}Se$ with Triple Hierarchy as High-Efficiency Electrocatalyst for Overall Water Splitting. *ChemSusChem* **2019**, *12*, 2271−2277.
(956) Fu, H.; Chen, Y.; Ren, C.; Jiang, H.; Tian, G. Nickel-Cobalt Diselenide Nanosheets Supported on Copper Nanowire Arrays for Synergistic Electrocatalytic Oxygen Evolution. *Adv. Mater. Interfaces* **2019**, *6*, 1802052.
(957) Yan, Q.; Yan, P.; Wei, T.; Wang, G.; Cheng, K.; Ye, K.; Zhu, K.; Yan, J.; Cao, D.; Li, Y. A Highly Efficient and Durable Water Splitting System: Platinum Sub-Nanocluster Functionalized Nickel-Iron Layered Double Hydroxide as the Cathode and Hierarchical Nickel-Iron Selenide as the Anode. *J. Mater. Chem. A* **2019**, *7*, 2831−2837.
(958) Wang, G.; Wang, H.; Chen, T.; Tan, Y. $Ni_{1-x}M_xSe_2$ (M = Fe, Co, Cu) Nanowires as Anodes for Ammonia-Borane Electrooxidation and the Derived $Ni_{1-x}M_xSe_{2-y}$-OOH Ultrathin Nanosheets as Efficient Electrocatalysts for Oxygen Evolution. *J. Mater. Chem. A* **2019**, *7*, 16372−16386.
(959) Tian, L.; Wang, K.; Wo, H.; Pang, X.; Zhai, X.; Zhuang, W.; Li, T.; Chen, Y. Bundle-Shaped Cobalt-Nickel Selenides as Advanced Electrocatalysts for Water Oxidation. *Int. J. Hydrog. EnergyInt. J. Hydrog. Energy* **2019**, *44*, 2868−2876.
(960) Sun, H.; Li, J.-G.; Lv, L.; Li, Z.; Ao, X.; Xu, C.; Xue, X.; Hong, G.; Wang, C. Engineering Hierarchical CoSe/NiFe Layered-Double-Hydroxide Nanoarrays as High Efficient Bifunctional Electrocatalyst for Overall Water Splitting. *J. Power Sources* **2019**, *425*, 138−146.
(961) Shi, W.; Lian, J. Facile Synthesis of Copper Selenide with Fluffy Intersected-Nanosheets Decorating Nanotubes Structure for Efficient Oxygen Evolution Reaction. *Int. J. Hydrog. EnergyInt. J. Hydrog. Energy* **2019**, *44*, 22983−22990.
(962) Shen, W.; Guo, X.; Sun, J.; Xu, S.; Xu, J. Prussian Blue Analogues Derived Binary Nickel-Cobalt Selenide for Enhanced Pseudocapacitance and Oxygen Evolution Reaction. *Vacuum* **2019**, *170*, 108965.
(963) Selvam, N. C. S.; Lee, J.; Choi, G. H.; Oh, M. J.; Xu, S.; Lim, B.; Yoo, P. J. MXene Supported Co_xA_y (A = OH, P, Se) Electrocatalysts for Overall Water Splitting: Unveiling the Role of Anions in Intrinsic Activity and Stability. *J. Mater. Chem. A* **2019**, *7*, 27383−27393.
(964) Jiao, C.; Bo, X.; Zhou, M. Electrocatalytic Water Splitting at Nitrogen-Doped Carbon Layers-Encapsulated Nickel Cobalt Selenide. *J. Energy Chem.* **2019**, *34*, 161−170.
(965) Karthick, K.; Jagadeesan, S. N.; Kumar, P.; Patchaiammal, S.; Kundu, S. Evaluating DNA Derived and Hydrothermally Aided Cobalt Selenide Catalysts for Electrocatalytic Water Oxidation. *Inorg. Chem.* **2019**, *58*, 6877−6884.
(966) Lin, L.; Chen, M.; Wu, L. Hierarchical Iron-Doped Nickel Diselenide Hollow Spheres for Efficient Oxygen Evolution Electrocatalysis. *ACS Appl. Energy Mater.* **2019**, *2*, 4737−4744.
(967) Qiu, B.; Cai, L.; Wang, Y.; Ma, S.; Tsang, Y. H.; Chai, Y. Accelerated Oxygen Evolution Kinetics on Nickel-Iron Diselenide Nanotubes by Modulating Electronic Structure. *Mater. Today Energy* **2019**, *11*, 89−96.
(968) Dai, J.; Zhao, D.; Sun, W.; Zhu, X.; Ma, L.-J.; Wu, Z.; Yang, C.; Cui, Z.; Li, L.; Chen, S. Cu(II) Ions Induced Structural Transformation of Cobalt Selenides for Remarkable Enhancement in Oxygen/Hydrogen Electrocatalysis. *ACS Catal.* **2019**, *9*, 10761−10772.
(969) Cao, J.; Wang, K.; Chen, J.; Lei, C.; Yang, B.; Li, Z.; Lei, L.; Hou, Y.; Ostrikov, K. Nitrogen-Doped Carbon-Encased Bimetallic

Selenide for High-Performance Water Electrolysis. *Nano-Micro Lett.* **2019**, *11*, 67.
(970) Li, J.; Fan, D.; Wang, M.; Wang, Z.; Liu, Z.; Zhao, K.; Zhou, L.; Mai, L. Hierarchical Bimetallic Selenide Nanosheet-Constructed Nanotubes for Efficient Electrocatalytic Water Oxidation. *ChemElectroChem* **2019**, *6*, 331−335.
(971) Zhou, L.; Zhang, X.; Zheng, D.; Xu, W.; Liu, J.; Lu, X. Ni_3S_2@PANI Core-Shell Nanosheets as a Durable and High-Energy Binder-Free Cathode for Aqueous Rechargeable Nickel-Zinc Batteries. *J. Mater. Chem. A* **2019**, *7*, 10629−10635.
(972) Nadeema, A.; Walko, P. S.; Devi, R. N.; Kurungot, S. Alkaline Water Electrolysis by NiZn-Double-Hydroxide-Derived Porous Nickel Selenide-Nitrogen-Doped Graphene Composite. *ACS Appl. Energy Mater.* **2018**, *1*, 5500−5510.
(973) Mei, G.; Liang, H.; Wei, B.; Shi, H.; Ming, F.; Xu, X.; Wang, Z. Bimetallic MnCo Selenide Yolk Shell Structures for Efficient Overall Water Splitting. *Electrochim. Acta* **2018**, *290*, 82−89.
(974) Zhao, Y.; Jin, B.; Zheng, Y.; Jin, H.; Jiao, Y.; Qiao, S.-Z. Charge State Manipulation of Cobalt Selenide Catalyst for Overall Seawater Electrolysis. *Adv. Energy Mater.* **2018**, *8*, 1801926.
(975) Xuan, C.; Xia, K.; Lei, W.; Xia, W.; Xiao, W.; Chen, L.; Xin, H. L.; Wang, D. Composition-Dependent Electrocatalytic Activities of NiFe-Based Selenides for the Oxygen Evolution Reaction. *Electrochim. Acta* **2018**, *291*, 64−72.
(976) Zheng, P.; Zhang, Y.; Dai, Z.; Zheng, Y.; Dinh, K. N.; Yang, J.; Dangol, R.; Liu, X.; Yan, Q. Constructing Multifunctional Heterostructure of Fe_2O_3@Ni_3Se_4 Nanotubes. *Small* **2018**, *14*, 1704065.
(977) Guo, K.; Zou, Z.; Du, J.; Zhao, Y.; Zhou, B.; Xu, C. Coupling $FeSe_2$ with CoSe: An Effective Strategy to Create Stable and Efficient Electrocatalysts for Water Oxidation. *Chem. Commun.* **2018**, *54*, 11140−11143.
(978) Zhao, X.; Li, X.; Yan, Y.; Xing, Y.; Lu, S.; Zhao, L.; Zhou, S.; Peng, Z.; Zeng, J. Electrical and Structural Engineering of Cobalt Selenide Nanosheets by Mn Modulation for Efficient Oxygen Evolution. *Appl. Catal. B: Environ.* **2018**, *236*, 569−575.
(979) Xu, B.; Chen, Z.; Yang, X.; Wang, X.; Huang, Y.; Li, C. Electronic Modulation of Carbon-Encapsulated NiSe Composites via Fe Doping for Synergistic Oxygen Evolution. *Chem. Commun.* **2018**, *54*, 9075−9078.
(980) Xiao, K.; Zhou, L.; Shao, M.; Wei, M. Fabrication of $(Ni,Co)_{0.85}Se$ Nanosheet Arrays Derived from Layered Double Hydroxides toward Largely Enhanced Overall Water Splitting. *J. Mater. Chem. A* **2018**, *6*, 7585−7591.
(981) Wu, Z.; Li, J.; Zou, Z.; Wang, X. Folded Nanosheet-like $Co_{0.85}Se$ Array for Overall Water Splitting. *J. Solid State Electrochem.* **2018**, *22*, 1785−1794.
(982) Du, J.; Zou, Z.; Liu, C.; Xu, C. Hierarchical Fe-Doped Ni_3Se_4 Ultrathin Nanosheets as an Efficient Electrocatalyst for Oxygen Evolution Reaction. *Nanoscale* **2018**, *10*, 5163−5170.
(983) Zhu, G.; Xie, X.; Li, X.; Liu, Y.; Shen, X.; Xu, K.; Chen, S. Nanocomposites Based on $CoSe_2$-Decorated $FeSe_2$ Nanoparticles Supported on Reduced Graphene Oxide as High-Performance Electrocatalysts toward Oxygen Evolution Reaction. *ACS Appl. Mater. Interfaces* **2018**, *10*, 19258−19270.
(984) Wang, M.; Dang, Z.; Prato, M.; Shinde, D. V.; De Trizio, L.; Manna, L. Ni-Co-S-Se Alloy Nanocrystals: Influence of the Composition on Their in Situ Transformation and Electrocatalytic Activity for the Oxygen Evolution Reaction. *ACS Appl. Nano Mater.* **2018**, *1*, 5753−5762.
(985) Li, J.; Wan, M.; Li, T.; Zhu, H.; Zhao, Z.; Wang, Z.; Wu, W.; Du, M. $NiCoSe_{2-x}$/N-Doped C Mushroom-like Core/Shell Nanorods on N-Doped Carbon Fiber for Efficiently Electrocatalyzed Overall Water Splitting. *Electrochim. Acta* **2018**, *272*, 161−168.
(986) Chen, Y.; Ren, Z.; Fu, H.; Zhang, X.; Tian, G.; Fu, H. NiSe-$Ni_{0.85}Se$ Heterostructure Nanoflake Arrays on Carbon Paper as Efficient Electrocatalysts for Overall Water Splitting. *Small* **2018**, *14*, 1800763.
(987) Du, J.; Yu, A.; Zou, Z.; Xu, C. One-Pot Synthesis of Iron-Nickel-Selenide Nanorods for Efficient and Durable Electrochemical Oxygen Evolution. *Inorg. Chem. Front.* **2018**, *5*, 814−818.
(988) Chen, T.; Li, S.; Wen, J.; Gui, P.; Guo, Y.; Guan, C.; Liu, J.; Fang, G. Rational Construction of Hollow Core-Branch $CoSe_2$ Nanoarrays for High-Performance Asymmetric Supercapacitor and Efficient Oxygen Evolution. *Small* **2018**, *14*, 1700979.
(989) Sun, Y.; Xu, K.; Wei, Z.; Li, H.; Zhang, T.; Li, X.; Cai, W.; Ma, J.; Fan, H. J.; Li, Y. Strong Electronic Interaction in Dual-Cation-Incorporated $NiSe_2$ Nanosheets with Lattice Distortion for Highly Efficient Overall Water Splitting. *Adv. Mater.* **2018**, *30*, 1802121.
(990) Lv, L.; Li, Z.; Xue, K.-H.; Ruan, Y.; Ao, X.; Wan, H.; Miao, X.; Zhang, B.; Jiang, J.; Wang, C.; Ostrikov, K. (Ken). Tailoring the Electrocatalytic Activity of Bimetallic Nickel-Iron Diselenide Hollow Nanochains for Water Oxidation. *Nano Energy* **2018**, *47*, 275−284.
(991) Wu, H.; Lu, X.; Zheng, G.; Ho, G. W. Topotactic Engineering of Ultrathin 2D Nonlayered Nickel Selenides for Full Water Electrolysis. *Adv. Energy Mater.* **2018**, *8*, 1702704.
(992) Yu, J.; Cheng, G.; Luo, W. 3D Mesoporous Rose-like Nickel-Iron Selenide Microspheres as Advanced Electrocatalysts for the Oxygen Evolution Reaction. *Nano Res.* **2018**, *11*, 2149−2158.
(993) Akbar, K.; Jeon, J. H.; Kim, M.; Jeong, J.; Yi, Y.; Chun, S.-H. Bifunctional Electrodeposited 3D $NiCoSe_2$/Nickle Foam Electrocatalysts for Its Applications in Enhanced Oxygen Evolution Reaction and for Hydrazine Oxidation. *ACS Sustainable Chem. Eng.* **2018**, *6*, 7735−7742.
(994) Chen, H.; Gao, Y.; Ye, L.; Yao, Y.; Chen, X.; Wei, Y.; Sun, L. A Cu_2Se-Cu_2O Film Electrodeposited on Titanium Foil as a Highly Active and Stable Electrocatalyst for the Oxygen Evolution Reaction. *Chem. Commun.* **2018**, *54*, 4979−4982.
(995) Chen, T.; Tan, Y. Hierarchical $CoNiSe_2$ Nano-Architecture as a High-Performance Electrocatalyst for Water Splitting. *Nano Res.* **2018**, *11*, 1331−1344.
(996) Li, H.; Chen, S.; Lin, H.; Xu, X.; Yang, H.; Song, L.; Wang, X. Nickel Diselenide Ultrathin Nanowires Decorated with Amorphous Nickel Oxide Nanoparticles for Enhanced Water Splitting Electrocatalysis. *Small* **2017**, *13*, 1701487.
(997) Du, Y.; Cheng, G.; Luo, W. $NiSe_2$/$FeSe_2$ Nanodendrites: A Highly Efficient Electrocatalyst for Oxygen Evolution Reaction. *Catal. Sci. Technol.* **2017**, *7*, 4604−4608.
(998) Zhang, J.-Y.; Lv, L.; Tian, Y.; Li, Z.; Ao, X.; Lan, Y.; Jiang, J.; Wang, C. Rational Design of Cobalt-Iron Selenides for Highly Efficient Electrochemical Water Oxidation. *ACS Appl. Mater. Interfaces* **2017**, *9*, 33833−33840.
(999) Dutta, S.; Indra, A.; Feng, Y.; Song, T.; Paik, U. Self-Supported Nickel Iron Layered Double Hydroxide-Nickel Selenide Electrocatalyst for Superior Water Splitting Activity. *ACS Appl. Mater. Interfaces* **2017**, *9*, 33766−33774.
(1000) Ming, F.; Liang, H.; Shi, H.; Mei, G.; Xu, X.; Wang, Z. Hierarchical $(Ni,Co)Se_2$/Carbon Hollow Rhombic Dodecahedra Derived from Metal-Organic Frameworks for Efficient Water-Splitting Electrocatalysis. *Electrochim. Acta* **2017**, *250*, 167−173.
(1001) Fang, Z.; Peng, L.; Lv, H.; Zhu, Y.; Yan, C.; Wang, S.; Kalyani, P.; Wu, X.; Yu, G. Metallic Transition Metal Selenide Holey Nanosheets for Efficient Oxygen Evolution Electrocatalysis. *ACS Nano* **2017**, *11*, 9550−9557.
(1002) Xu, X.; Liang, H.; Ming, F.; Qi, Z.; Xie, Y.; Wang, Z. Prussian Blue Analogues Derived Penroseite $(Ni,Co)Se_2$ Nanocages Anchored on 3D Graphene Aerogel for Efficient Water Splitting. *ACS Catal.* **2017**, *7*, 6394−6399.
(1003) Zhao, Q.; Zhong, D.; Liu, L.; Li, D.; Hao, G.; Li, J. Facile Fabrication of Robust 3D Fe-NiSe Nanowires Supported on Nickel Foam as a Highly Efficient, Durable Oxygen Evolution Catalyst. *J. Mater. Chem. A* **2017**, *5*, 14639−14645.
(1004) Du, Y.; Cheng, G.; Luo, W. Colloidal Synthesis of Urchin-like Fe Doped $NiSe_2$ for Efficient Oxygen Evolution. *Nanoscale* **2017**, *9*, 6821−6825.
(1005) Chi, J.-Q.; Shang, X.; Liang, F.; Dong, B.; Li, X.; Liu, Y.-R.; Yan, K.-L.; Gao, W.-K.; Chai, Y.-M.; Liu, C.-G. Facile Synthesis of

https://doi.org/10.1021/acs.chemrev.3c00005
Chem. Rev. 2023, 123, 12795−13208

Pyrite-Type Binary Nickel Iron Diselenides as Efficient Electrocatalyst for Oxygen Evolution Reaction. *Appl. Surf. Sci.* **2017**, *401*, 17−24.
(1006) Sivanantham, A.; Shanmugam, S. Nickel Selenide Supported on Nickel Foam as an Efficient and Durable Non-Precious Electrocatalyst for the Alkaline Water Electrolysis. *Appl. Catal. B: Environ.* **2017**, *203*, 485−493.
(1007) Anantharaj, S.; Kennedy, J.; Kundu, S. Microwave-Initiated Facile Formation of Ni_3Se_4 Nanoassemblies for Enhanced and Stable Water Splitting in Neutral and Alkaline Media. *ACS Appl. Mater. Interfaces* **2017**, *9*, 8714−8728.
(1008) Yu, J.; Li, Q.; Xu, C.-Y.; Chen, N.; Li, Y.; Liu, H.; Zhen, L.; Dravid, V. P.; Wu, J. $NiSe_2$ Pyramids Deposited on N-Doped Graphene Encapsulated Ni Foam for High-Performance Water Oxidation. *J. Mater. Chem. A* **2017**, *5*, 3981−3986.
(1009) Gao, Z.; Qi, J.; Chen, M.; Zhang, W.; Cao, R. An Electrodeposited NiSe for Electrocatalytic Hydrogen and Oxygen Evolution Reactions in Alkaline Solution. *Electrochim. Acta* **2017**, *224*, 412−418.
(1010) Xu, K.; Ding, H.; Lv, H.; Tao, S.; Chen, P.; Wu, X.; Chu, W.; Wu, C.; Xie, Y. Understanding Structure-Dependent Catalytic Performance of Nickel Selenides for Electrochemical Water Oxidation. *ACS Catal.* **2017**, *7*, 310−315.
(1011) Gao, R.; Zhang, H.; Yan, D. Iron Diselenide Nanoplatelets: Stable and Efficient Water-Electrolysis Catalysts. *Nano Energy* **2017**, *31*, 90−95.
(1012) Zhao, X.; Zhang, H.; Yan, Y.; Cao, J.; Li, X.; Zhou, S.; Peng, Z.; Zeng, J. Engineering the Electrical Conductivity of Lamellar Silver-Doped Cobalt(II) Selenide Nanobelts for Enhanced Oxygen Evolution. *Angew. Chem.* **2017**, *129*, 334−338.
(1013) Panda, C.; Menezes, P. W.; Walter, C.; Yao, S.; Miehlich, M. E.; Gutkin, V.; Meyer, K.; Driess, M. From a Molecular 2Fe-2Se Precursor to a Highly Efficient Iron Diselenide Electrocatalyst for Overall Water Splitting. *Angew. Chem. Int. Ed.* **2017**, *56*, 10506−10510.
(1014) Li, W.; Gao, X.; Xiong, D.; Wei, F.; Song, W.-G.; Xu, J.; Liu, L. Hydrothermal Synthesis of Monolithic Co_3Se_4 Nanowire Electrodes for Oxygen Evolution and Overall Water Splitting with High Efficiency and Extraordinary Catalytic Stability. *Adv. Energy Mater.* **2017**, *7*, 1602579.
(1015) Yang, Z.; Zhang, J.-Y.; Liu, Z.; Li, Z.; Lv, L.; Ao, X.; Tian, Y.; Zhang, Y.; Jiang, J.; Wang, C. Cuju"-Structured Iron Diselenide-Derived Oxide: A Highly Efficient Electrocatalyst for Water Oxidation. *ACS Appl. Mater. Interfaces* **2017**, *9*, 40351−40359.
(1016) Zhu, H.; Jiang, R.; Chen, X.; Chen, Y.; Wang, L. 3D Nickel-Cobalt Diselenide Nanonetwork for Highly Efficient Oxygen Evolution. *Sci. Bull.* **2017**, *62*, 1373−1379.
(1017) Swesi, A. T.; Masud, J.; Liyanage, W. P. R.; Umapathi, S.; Bohannan, E.; Medvedeva, J.; Nath, M. Textured $NiSe_2$ Film: Bifunctional Electrocatalyst for Full Water Splitting at Remarkably Low Overpotential with High Energy Efficiency. *Sci. Rep.* **2017**, *7*, 1−11.
(1018) Xu, Y.-Z.; Yuan, C.-Z.; Chen, X.-P. Co-Doped NiSe Nanowires on Nickel Foam via a Cation Exchange Approach as Efficient Electrocatalyst for Enhanced Oxygen Evolution Reaction. *RSC Adv.* **2016**, *6*, 106832−106836.
(1019) Ming, F.; Liang, H.; Shi, H.; Xu, X.; Mei, G.; Wang, Z. MOF-Derived Co-Doped Nickel Selenide/C Electrocatalysts Supported on Ni Foam for Overall Water Splitting. *J. Mater. Chem. A* **2016**, *4*, 15148−15155.
(1020) Li, X.; Zhang, L.; Huang, M.; Wang, S.; Li, X.; Zhu, H. Cobalt and Nickel Selenide Nanowalls Anchored on Graphene as Bifunctional Electrocatalysts for Overall Water Splitting. *J. Mater. Chem. A* **2016**, *4*, 14789−14795.
(1021) Swesi, A. T.; Masud, J.; Nath, M. Enhancing Electrocatalytic Activity of Bifunctional Ni_3Se_2 for Overall Water Splitting through Etching-Induced Surface Nanostructuring. *J. Mater. Res.* **2016**, *31*, 2888−2896.
(1022) Wang, Z.; Li, J.; Tian, X.; Wang, X.; Yu, Y.; Owusu, K. A.; He, L.; Mai, L. Porous Nickel-Iron Selenide Nanosheets as Highly Efficient Electrocatalysts for Oxygen Evolution Reaction. *ACS Appl. Mater. Interfaces* **2016**, *8*, 19386−19392.
(1023) Wu, X.; He, D.; Zhang, H.; Li, H.; Li, Z.; Yang, B.; Lin, Z.; Lei, L.; Zhang, X. $Ni_{0.85}Se$ as an Efficient Non-Noble Bifunctional Electrocatalyst for Full Water Splitting. *Int. J. Hydrog. Energy* **2016**, *41*, 10688−10694.
(1024) Xu, X.; Du, P.; Chen, Z.; Huang, M. An Electrodeposited Cobalt-Selenide-Based Film as an Efficient Bifunctional Electrocatalyst for Full Water Splitting. *J. Mater. Chem. A* **2016**, *4*, 10933−10939.
(1025) Xu, R.; Wu, R.; Shi, Y.; Zhang, J.; Zhang, B. Ni_3Se_2 Nanoforest/Ni Foam as a Hydrophilic, Metallic, and Self-Supported Bifunctional Electrocatalyst for Both H_2 and O_2 Generations. *Nano Energy* **2016**, *24*, 103−110.
(1026) Tang, C.; Asiri, A. M.; Sun, X. Highly-Active Oxygen Evolution Electrocatalyzed by a Fe-Doped NiSe Nanoflake Array Electrode. *Chem. Commun.* **2016**, *52*, 4529−4532.
(1027) Liao, M.; Zeng, G.; Luo, T.; Jin, Z.; Wang, Y.; Kou, X.; Xiao, D. Three-Dimensional Coral-like Cobalt Selenide as an Advanced Electrocatalyst for Highly Efficient Oxygen Evolution Reaction. *Electrochim. Acta* **2016**, *194*, 59−66.
(1028) Xu, K.; Ding, H.; Jia, K.; Lu, X.; Chen, P.; Zhou, T.; Cheng, H.; Liu, S.; Wu, C.; Xie, Y. Solution-Liquid-Solid Synthesis of Hexagonal Nickel Selenide Nanowire Arrays with a Nonmetal Catalyst. *Angew. Chem.* **2016**, *128*, 1742−1745.
(1029) Xia, C.; Jiang, Q.; Zhao, C.; Hedhili, M. N.; Alshareef, H. N. Selenide-Based Electrocatalysts and Scaffolds for Water Oxidation Applications. *Adv. Mater.* **2016**, *28*, 77−85.
(1030) Shi, J.; Hu, J.; Luo, Y.; Sun, X.; Asiri, A. M. Ni_3Se_2 Film as a Non-Precious Metal Bifunctional Electrocatalyst for Efficient Water Splitting. *Catal. Sci. Technol.* **2015**, *5*, 4954−4958.
(1031) Liu, T.; Liu, Q.; Asiri, A. M.; Luo, Y.; Sun, X. An Amorphous CoSe Film Behaves as an Active and Stable Full Water-Splitting Electrocatalyst under Strongly Alkaline Conditions. *Chem. Commun.* **2015**, *51*, 16683−16686.
(1032) Li, T.; Fu, H. C.; Chen, X. H.; Gu, F.; Li, N. B.; Luo, H. Q. Interface Engineering of Core-Shell $Ni_{0.85}Se$/NiTe Electrocatalyst for Enhanced Oxygen Evolution and Urea Oxidation Reactions. *J. Colloid. Interface Sci.* **2022**, *618*, 196−205.
(1033) He, J.; Qian, T.; Cai, C.; Xiang, X.; Li, S.; Zu, X. Nickel-Based Selenides with a Fractal Structure as an Excellent Bifunctional Electrocatalyst for Water Splitting. *Nanomaterials* **2022**, *12*, 281.
(1034) Huang, Y.; Jiang, L.-W.; Liu, X.-L.; Tan, T.; Liu, H.; Wang, J.-J. Precisely Engineering the Electronic Structure of Active Sites Boosts the Activity of Iron-Nickel Selenide on Nickel Foam for Highly Efficient and Stable Overall Water Splitting. *Appl. Catal. B: Environ.* **2021**, *299*, 120678.
(1035) Huang, Y.; Jiang, L.-W.; Shi, B.-Y.; Ryan, K. M.; Wang, J.-J. Highly Efficient Oxygen Evolution Reaction Enabled by Phosphorus Doping of the Fe Electronic Structure in Iron-Nickel Selenide Nanosheets. *Adv. Sci.* **2021**, *8*, 2101775.
(1036) Xu, F.; Qian, G.; Chen, W.; Luo, L.; Shen, F.; Yin, S. Copper-Iron Selenides Ultrafine Nanowires as Cost-Effective Catalysts for the Oxygen Evolution Reaction at Large-Current-Density. *J. Phys. Chem. C* **2020**, *124*, 19595−19602.
(1037) Esmailzadeh, S.; Shahrabi, T.; Barati Darband, Gh.; Yaghoubinezhad, Y. Pulse Electrodeposition of Nickel Selenide Nanostructure as a Binder-Free and High-Efficient Catalyst for Both Electrocatalytic Hydrogen and Oxygen Evolution Reactions in Alkaline Solution. *Electrochim. Acta* **2020**, *334*, 135549.
(1038) Fiaz, M.; Athar, M. Facile Room-Temperature In Situ Incorporation of Transition-Metal Selenide (TMSe) Nanoparticles into MOF-5 for Oxygen Evolution Reaction. *JOM* **2020**, *72*, 2219−2225.
(1039) Ding, J.; Wang, P.; Ji, S.; Wang, H.; Brett, D. J. L.; Wang, R. Mesoporous Nickel Selenide N-Doped Carbon as a Robust Electrocatalyst for Overall Water Splitting. *Electrochim. Acta* **2019**, *300*, 93−101.

https://doi.org/10.1021/acs.chemrev.3c00005
Chem. Rev. 2023, 123, 12795−13208

(1040) Fang, G.; Wang, Q.; Zhou, J.; Lei, Y.; Chen, Z.; Wang, Z.; Pan, A.; Liang, S. Metal Organic Framework-Templated Synthesis of Bimetallic Selenides with Rich Phase Boundaries for Sodium-Ion Storage and Oxygen Evolution Reaction. *ACS Nano* **2019**, *13*, 5635−5645.
(1041) Chandra Majhi, K.; Karfa, P.; Madhuri, R. Bimetallic Transition Metal Chalcogenide Nanowire Array: An Effective Catalyst for Overall Water Splitting. *Electrochim. Acta* **2019**, *318*, 901−912.
(1042) Cai, C.; Mi, Y.; Han, S.; Wang, Q.; Liu, W.; Wu, X.; Zheng, Z.; Xia, X.; Qiao, L.; Zhou, W.; et al. Engineering Ordered Dendrite-like Nickel Selenide as Electrocatalyst. *Electrochim. Acta* **2019**, *295*, 92−98.
(1043) Zhang, J.; Jiang, B.; Zhang, J.; Li, R.; Zhang, N.; Liu, R.; Li, J.; Zhang, D.; Zhang, R. Facile Synthesis of $NiSe_2$ Particles with Highly Efficient Electrocatalytic Oxygen Evolution Reaction. *Mater. Lett.* **2019**, *235*, 53−56.
(1044) Wei, C.; Zhong, D.; Li, D.; Hao, G.; Liu, G.; Li, J.; Zhao, Q. $Cu_{2-x}Se$@CuO Core-Shell Assembly Grew on Copper Foam for Efficient Oxygen Evolution. *Int. J. Hydrog. Energy* **2019**, *44*, 31979−31986.
(1045) Wang, S.; He, P.; Jia, L.; He, M.; Zhang, T.; Dong, F.; Liu, M.; Liu, H.; Zhang, Y.; Li, C.; et al. Nanocoral-like Composite of Nickel Selenide Nanoparticles Anchored on Two-Dimensional Multi-Layered Graphitic Carbon Nitride: A Highly Efficient Electrocatalyst for Oxygen Evolution Reaction. *Appl. Catal. B: Environ.* **2019**, *243*, 463−469.
(1046) Wan, J.; Ye, W.; Gao, R.; Fang, X.; Guo, Z.; Lu, Y.; Yan, D. Synthesis from a Layered Double Hydroxide Precursor for a Highly Efficient Oxygen Evolution Reaction. *Inorg. Chem. Front.* **2019**, *6*, 1793−1798.
(1047) Song, W.; Teng, X.; Liu, Y.; Wang, J.; Niu, Y.; He, X.; Zhang, C.; Chen, Z. Rational Construction of Self-Supported Triangle-like MOF-Derived Hollow $(Ni,Co)Se_2$ Arrays for Electrocatalysis and Supercapacitors. *Nanoscale* **2019**, *11*, 6401−6409.
(1048) Gui, L.; Huang, Z.; Ai, D.; He, B.; Zhou, W.; Sun, J.; Xu, J.; Wang, Q.; Zhao, L. Integrated Ultrafine $Co_{0.85}Se$ in Carbon Nanofibers: An Efficient and Robust Bifunctional Catalyst for Oxygen Electrocatalysis. *Chem.—Eur. J.* **2020**, *26*, 4063−4069.
(1049) Hosseini, H.; Shahrokhian, S. Self-Supported Nanoporous Zn-Ni-Co/Cu Selenides Microball Arrays for Hybrid Energy Storage and Electrocatalytic Water/Urea Splitting. *Chem. Eng. J.* **2019**, *375*, 122090.
(1050) Hu, X.; Zhou, Q.; Cheng, P.; Su, S.; Wang, X.; Gao, X.; Zhou, G.; Zhang, Z.; Liu, J. Nickel-Iron Selenide Polyhedral Nanocrystal with Optimized Surface Morphology as a High-Performance Bifunctional Electrocatalyst for Overall Water Splitting. *Appl. Surf. Sci.* **2019**, *488*, 326−334.
(1051) Li, J.-G.; Sun, H.; Lv, L.; Li, Z.; Ao, X.; Xu, C.; Li, Y.; Wang, C. Metal-Organic Framework-Derived Hierarchical $(Co,Ni)Se_2$@NiFe LDH Hollow Nanocages for Enhanced Oxygen Evolution. *ACS Appl. Mater. Interfaces* **2019**, *11*, 8106−8114.
(1052) Liu, S.; Jiang, Y.; Yang, M.; Zhang, M.; Guo, Q.; Shen, W.; He, R.; Li, M. Highly Conductive and Metallic Cobalt-Nickel Selenide Nanorods Supported on Ni Foam as an Efficient Electrocatalyst for Alkaline Water Splitting. *Nanoscale* **2019**, *11*, 7959−7966.
(1053) Lu, S.; Lian, J.; Zhang, F.; Jiang, W.; Hu, Q.; Li, D.; Zhang, B. $Fe_{40}Co_{40}Se_{20}$ Glassy Films Supported on Carbon Fiber Paper as Electrocatalysts in the Oxygen Evolution Reaction. *J. Electrochem. Soc.* **2019**, *166*, F620−F626.
(1054) Majhi, K. C.; Karfa, P.; De, S.; Madhuri, R. Hydrothermal Synthesis of Zinc Cobalt Telluride Nanorod towards Oxygen Evolution Reaction (OER). *IOP Conf. Ser.: Mater. Sci. Eng.* **2019**, *577*, 012076.
(1055) Pan, Q.-R.; Li, S.-J.; Tong, K.; Xie, C.; Peng, L.; Li, N.; Wang, D.-Y.; Su, H. Engineering Ni^{3+} inside Nickel Selenide as Efficient Bifunctional Oxygen Electrocatalysts for Zn-Air Batteries. *J. Mater. Sci.* **2019**, *54*, 9063−9074.
(1056) Premnath, K.; Arunachalam, P.; Amer, M. S.; Madhavan, J.; Al-Mayouf, A. M. Hydrothermally Synthesized Nickel Molybdenum Selenide Composites as Cost-Effective and Efficient Trifunctional Electrocatalysts for Water Splitting Reactions. *Int. J. Hydrog. Energy* **2019**, *44*, 22796−22805.
(1057) Zhong, Y.; Chang, B.; Shao, Y.; Xu, C.; Wu, Y.; Hao, X. Regulating Phase Conversion from Ni_3Se_2 into NiSe in a Bifunctional Electrocatalyst for Overall Water-Splitting Enhancement. *ChemSusChem* **2019**, *12*, 2008−2014.
(1058) Zheng, X.; Cao, Y.; Han, X.; Liu, H.; Wang, J.; Zhang, Z.; Wu, X.; Zhong, C.; Hu, W.; Deng, Y. Pt Embedded Ni_3Se_2@NiOOH Core-Shell Dendrite-like Nanoarrays on Nickel as Bifunctional Electrocatalysts for Overall Water Splitting. *Sci. China Mater.* **2019**, *62*, 1096−1104.
(1059) Zhang, W.; Zhang, H.; Luo, R.; Zhang, M.; Yan, X.; Sun, X.; Shen, J.; Han, W.; Wang, L.; Li, J. Prussian Blue Analogues-Derived Bimetallic Iron-Cobalt Selenides for Efficient Overall Water Splitting. *J. Colloid. Interface Sci.* **2019**, *548*, 48−55.
(1060) Ao, K.; Dong, J.; Fan, C.; Wang, D.; Cai, Y.; Li, D.; Huang, F.; Wei, Q. Formation of Yolk-Shelled Nickel-Cobalt Selenide Dodecahedral Nanocages from Metal-Organic Frameworks for Efficient Hydrogen and Oxygen Evolution. *ACS Sustainable Chem. Eng.* **2018**, *6*, 10952−10959.
(1061) Zhang, C.; Xin, B.; Duan, S.; Jiang, A.; Zhang, B.; Li, Z.; Hao, J. Controllable 1D and 2D Cobalt Oxide and Cobalt Selenide Nanostructures as Highly Efficient Electrocatalysts for the Oxygen Evolution Reaction. *Chem.—Asian J.* **2018**, *13*, 2700−2707.
(1062) Zhang, F.; Pei, Y.; Ge, Y.; Chu, H.; Craig, S.; Dong, P.; Cao, J.; Ajayan, P. M.; Ye, M.; Shen, J. Controlled Synthesis of Eutectic $NiSe/Ni_3Se_2$ Self-Supported on Ni Foam: An Excellent Bifunctional Electrocatalyst for Overall Water Splitting. *Adv. Mater. Interfaces* **2018**, *5*, 1701507.
(1063) Li, J.; Liu, G.; Liu, B.; Min, Z.; Qian, D.; Jiang, J.; Li, J. Fe-Doped $CoSe_2$ Nanoparticles Encapsulated in N-Doped Bamboo-like Carbon Nanotubes as an Efficient Electrocatalyst for Oxygen Evolution Reaction. *Electrochim. Acta* **2018**, *265*, 577−585.
(1064) Zhou, J.; Liu, Y.; Zhang, Z.; Huang, Z.; Chen, X.; Ren, X.; Ren, L.; Qi, X.; Zhong, J. Hierarchical $NiSe_2$ Sheet-like Nano-Architectures as an Efficient and Stable Bifunctional Electrocatalyst for Overall Water Splitting: Phase and Morphology Engineering. *Electrochim. Acta* **2018**, *279*, 195−203.
(1065) Wang, M.; Ge, H.; Jin, Z.; Wang, Y.; Zhang, M.; Zheng, G.; Wang, Z.-S. Hollow $NiCo_2Se_4$ Microspheres Composed of Nanoparticles as Multifunctional Electrocatalysts for Unassisted Artificial Photosynthesis. *Electrochim. Acta* **2018**, *283*, 628−637.
(1066) Zhang, J.-Y.; Tian, X.; He, T.; Zaman, S.; Miao, M.; Yan, Y.; Qi, K.; Dong, Z.; Liu, H.; Xia, B. Y. *In Situ* Formation of Ni_3Se_4 Nanorod Arrays as Versatile Electrocatalysts for Electrochemical Oxidation Reactions in Hybrid Water Electrolysis. *J. Mater. Chem. A* **2018**, *6*, 15653−15658.
(1067) Yu, J.; Tian, Y.; Zhou, F.; Zhang, M.; Chen, R.; Liu, Q.; Liu, J.; Xu, C.-Y.; Wang, J. Metallic and Superhydrophilic Nickel Cobalt Diselenide Nanosheets Electrodeposited on Carbon Cloth as a Bifunctional Electrocatalyst. *J. Mater. Chem. A* **2018**, *6*, 17353−17360.
(1068) Lv, L.; Li, Z.; Ruan, Y.; Chang, Y.; Ao, X.; Li, J.-G.; Yang, Z.; Wang, C. Nickel-Iron Diselenide Hollow Nanoparticles with Strongly Hydrophilic Surface for Enhanced Oxygen Evolution Reaction Activity. *Electrochim. Acta* **2018**, *286*, 172−178.
(1069) Zhu, J.; Ni, Y. Phase-Controlled Synthesis and the Phase-Dependent HER and OER Performances of Nickel Selenide Nanosheets Prepared by an Electrochemical Deposition Route. *CrystEngComm* **2018**, *20*, 3344−3352.
(1070) Ganesan, V.; Kim, J. Prussian Blue Analogue Metal Organic Framework-Derived $CoSe_2$ Nanoboxes for Highly Efficient Oxygen Evolution Reaction. *Mater. Lett.* **2018**, *223*, 49−52.
(1071) Zheng, X.; Wu, X.; Han, X.; Deng, Y.; Wang, J. Solution Process Synthesis of Morphology-Controllable $CoSe_2$ Nanocrystals with Efficient Bifunctional Catalytic Activity. *Ferroelectrics* **2018**, *523*, 126−133.
(1072) Wang, G.; Li, J.; Liu, M.; Du, L.; Liao, S. Three-Dimensional Biocarbon Framework Coupled with Uniformly Distributed FeSe

https://doi.org/10.1021/acs.chemrev.3c00005
Chem. Rev. 2023, 123, 12795−13208

Nanoparticles Derived from Pollen as Bifunctional Electrocatalysts for Oxygen Electrode Reactions. *ACS Appl. Mater. Interfaces* **2018**, *10*, 32133−32141.
(1073) Chen, S.; Mi, J.-L.; Zhang, P.; Feng, Y.-H.; Yong, Y.-C.; Shi, W.-D. Control Synthesis of Nickel Selenides and Their Multiwalled Carbon Nanotubes Composites as Electrocatalysts for Enhanced Water Oxidation. *J. Phys. Chem. C* **2018**, *122*, 26096−26104.
(1074) Chen, T.; Li, S.; Gui, P.; Wen, J.; Fu, X.; Fang, G. Bifunctional Bamboo-like $CoSe_2$ Arrays for High-Performance Asymmetric Supercapacitor and Electrocatalytic Oxygen Evolution. *Nanotechnology* **2018**, *29*, 205401.
(1075) Chi, J.-Q.; Shang, X.; Gao, W.-K.; Dong, B.; Yan, K.-L.; Li, X.; Liu, Y.-R.; Chai, Y.-M.; Liu, C.-G. Binary Metal $Fe_{0.5}Co_{0.5}Se_2$ Spheres Supported on Carbon Fiber Cloth for Efficient Oxygen Evolution Reaction. *Int. J. Hydrog. Energy* **2017**, *42*, 15189−15195.
(1076) Xu, Y.-Z.; Yuan, C.-Z.; Chen, X.-P. A Facile Strategy for the Synthesis of NiSe@CoOOH Core-Shell Nanowires on Nickel Foam with High Surface Area as Efficient Electrocatalyst for Oxygen Evolution Reaction. *Appl. Surf. Sci.* **2017**, *426*, 688−693.
(1077) Zhang, J.-J.; Su, H.; Wang, H.-H.; Xue, Z.-H.; Zhang, B.; Wei, X.; Li, X.-H.; Hirano, S.-I.; Chen, J.-S. Constructing Ohmic Contact in Cobalt Selenide/Ti Dyadic Electrode: The Third Aspect to Promote the Oxygen Evolution Reaction. *Nano Energy* **2017**, *39*, 321−327.
(1078) Wang, X.; Li, F.; Li, W.; Gao, W.; Tang, Y.; Li, R. Hollow Bimetallic Cobalt-Based Selenide Polyhedrons Derived from Metal-Organic Framework: An Efficient Bifunctional Electrocatalyst for Overall Water Splitting. *J. Mater. Chem. A* **2017**, *5*, 17982−17989.
(1079) Liu, X.; Liu, Y.; Fan, L.-Z. MOF-Derived $CoSe_2$ Microspheres with Hollow Interiors as High-Performance Electrocatalysts for the Enhanced Oxygen Evolution Reaction. *J. Mater. Chem. A* **2017**, *5*, 15310−15314.
(1080) Gao, J.; Liu, L.; Qiu, H.-J.; Wang, Y. Engineering Phase Transformation of Cobalt Selenide in Carbon Cages and the Phases' Bifunctional Electrocatalytic Activity for Water Splitting. *Nanotechnology* **2017**, *28*, 315401.
(1081) Meng, T.; Qin, J.; Wang, S.; Zhao, D.; Mao, B.; Cao, M. In Situ Coupling of $Co_{0.85}Se$ and N-Doped Carbon via One-Step Selenization of Metal-Organic Frameworks as a Trifunctional Catalyst for Overall Water Splitting and Zn-Air Batteries. *J. Mater. Chem. A* **2017**, *5*, 7001−7014.
(1082) Wang, X.; Zheng, Y.; Yuan, J.; Shen, J.; Hu, J.; Wang, A.; Wu, L.; Niu, L. Porous NiCo Diselenide Nanosheets Arrayed on Carbon Cloth as Promising Advanced Catalysts Used in Water Splitting. *Electrochim. Acta* **2017**, *225*, 503−513.
(1083) Li, S.; Peng, S.; Huang, L.; Cui, X.; Al-Enizi, A. M.; Zheng, G. Carbon-Coated Co^{3+}-Rich Cobalt Selenide Derived from ZIF-67 for Efficient Electrochemical Water Oxidation. *ACS Appl. Mater. Interfaces* **2016**, *8*, 20534−20539.
(1084) Zheng, Y.-R.; Gao, M.-R.; Gao, Q.; Li, H.-H.; Xu, J.; Wu, Z.-Y.; Yu, S.-H. An Efficient $CeO_2/CoSe_2$ Nanobelt Composite for Electrochemical Water Oxidation. *Small* **2015**, *11*, 182−188.
(1085) Sun, C.; Dong, Q.; Yang, J.; Dai, Z.; Lin, J.; Chen, P.; Huang, W.; Dong, X. Metal-Organic Framework Derived $CoSe_2$ Nanoparticles Anchored on Carbon Fibers as Bifunctional Electrocatalysts for Efficient Overall Water Splitting. *Nano Res.* **2016**, *9*, 2234−2243.
(1086) Li, X.; Han, G.-Q.; Liu, Y.-R.; Dong, B.; Shang, X.; Hu, W.-H.; Chai, Y.-M.; Liu, Y.-Q.; Liu, C.-G. In Situ Grown Pyramid Structures of Nickel Diselenides Dependent on Oxidized Nickel Foam as Efficient Electrocatalyst for Oxygen Evolution Reaction. *Electrochim. Acta* **2016**, *205*, 77−84.
(1087) Zhao, X.; Yang, Y.; Li, Y.; Cui, X.; Zhang, Y.; Xiao, P. NiCo-Selenide as a Novel Catalyst for Water Oxidation. *J. Mater. Sci.* **2016**, *51*, 3724−3734.
(1088) Hou, Y.; Lohe, M. R.; Zhang, J.; Liu, S.; Zhuang, X.; Feng, X. Vertically Oriented Cobalt Selenide/NiFe Layered-Double-Hydroxide Nanosheets Supported on Exfoliated Graphene Foil: An Efficient 3D Electrode for Overall Water Splitting. *Energy Environ. Sci.* **2016**, *9*, 478−483.
(1089) Poorahong, S.; Harding, D. J.; Keawmorakot, S.; Siaj, M. Free Standing Bimetallic Nickel Cobalt Selenide Nanosheets as Three-Dimensional Electrocatalyst for Water Splitting. *J. Electroanal. Chem.* **2021**, *897*, 115568.
(1090) Ganguli, S.; Ghosh, S.; Tudu, G.; Koppisetti, H. V. S. R. M.; Mahalingam, V. Design Principle of Monoclinic $NiCo_2Se_4$ and Co_3Se_4 Nanoparticles with Opposing Intrinsic and Geometric Electrocatalytic Activity toward the OER. *Inorg. Chem.* **2021**, *60*, 9542−9551.
(1091) He, D.; Cao, L.; Huang, J.; Feng, Y.; Li, G.; Yang, D.; Huang, Q.; Feng, L. Rational Design of Vanadium-Modulated Ni_3Se_2 Nanorod@Nanosheet Arrays as a Bifunctional Electrocatalyst for Overall Water Splitting. *ACS Sustainable Chem. Eng.* **2021**, *9*, 12005−12016.
(1092) Yang, M.; Yang, Y.; Wang, K.; Li, S.; Feng, F.; Lan, K.; Jiang, P.; Huang, X.; Yang, H.; Li, R. Facile Synthesis of CoSe Nanoparticles Encapsulated in N-Doped Carbon Nanotubes-Grafted N-Doped Carbon Nanosheets for Water Splitting. *Electrochim. Acta* **2020**, *337*, 135685.
(1093) Chen, M.; Xia, Z.; Liu, Q. Ethylenediamine-Assisted Hydrothermal Synthesis of $NaCaSiO_3OH$: Controlled Morphology, Mechanism, and Luminescence Properties by Doping Eu^{3+}/Tb^{3+}. *Inorg. Chem.* **2016**, *55*, 11316−11322.
(1094) Zhang, B.; Kang, F.; Tarascon, J.-M.; Kim, J.-K. Recent Advances in Electrospun Carbon Nanofibers and Their Application in Electrochemical Energy Storage. *Prog. Mater. Sci.* **2016**, *76*, 319−380.
(1095) Eftekhari, A. Molybdenum Diselenide ($MoSe_2$) for Energy Storage, Catalysis, and Optoelectronics. *Appl. Mater. Today* **2017**, *8*, 1−17.
(1096) Peng, X.; Yan, Y.; Jin, X.; Huang, C.; Jin, W.; Gao, B.; Chu, P. K. Recent Advance and Prospectives of Electrocatalysts Based on Transition Metal Selenides for Efficient Water Splitting. *Nano Energy* **2020**, *78*, 105234.
(1097) Konar, R.; Nessim, G. D. A Mini-Review Focusing on Ambient-Pressure Chemical Vapor Deposition (AP-CVD) Based Synthesis of Layered Transition Metal Selenides for Energy Storage Applications. *Mater. Adv.* **2022**, *3*, 4471−4488.
(1098) Song, X.; Bochmann, M. Synthesis of Phosphinochalcogenoic Amidato Complexes of Divalenttransition Metals and Their Thermolysis to Metal Selenide and Telluridephases. *J. Chem. Soc., Dalton Trans.* **1997**, No. 15, 2689−2692.
(1099) Panneerselvam, A.; Malik, M. A.; Afzaal, M.; O'Brien, P.; Helliwell, M. The Chemical Vapor Deposition of Nickel Phosphide or Selenide Thin Films from a Single Precursor. *J. Am. Chem. Soc.* **2008**, *130*, 2420−2421.
(1100) Zhao, W.; Zhang, C.; Geng, F.; Zhuo, S.; Zhang, B. Nanoporous Hollow Transition Metal Chalcogenide Nanosheets Synthesized via the Anion-Exchange Reaction of Metal Hydroxides with Chalcogenide Ions. *ACS Nano* **2014**, *8*, 10909−10919.
(1101) Moon, G. D.; Ko, S.; Min, Y.; Zeng, J.; Xia, Y.; Jeong, U. Chemical Transformations of Nanostructured Materials. *Nano Today* **2011**, *6*, 186−203.
(1102) Zhou, W.; Wu, X.-J.; Cao, X.; Huang, X.; Tan, C.; Tian, J.; Liu, H.; Wang, J.; Zhang, H. Ni_3S_2 Nanorods/Ni Foam Composite Electrode with Low Overpotential for Electrocatalytic Oxygen Evolution. *Energy Environ. Sci.* **2013**, *6*, 2921−2924.
(1103) Cao, S.; Chen, Y.; Kang, L.; Lin, Z.; Fu, W.-F. Enhanced Photocatalytic H_2-Evolution by Immobilizing CdS Nanocrystals on Ultrathin $Co_{0.85}Se$/RGO-PEI Nanosheets. *J. Mater. Chem. A* **2015**, *3*, 18711−18717.
(1104) Liu, Y.; Hua, X.; Xiao, C.; Zhou, T.; Huang, P.; Guo, Z.; Pan, B.; Xie, Y. Heterogeneous Spin States in Ultrathin Nanosheets Induce Subtle Lattice Distortion To Trigger Efficient Hydrogen Evolution. *J. Am. Chem. Soc.* **2016**, *138*, 5087−5092.
(1105) Hu, W.; Chen, R.; Xie, W.; Zou, L.; Qin, N.; Bao, D. $CoNi_2S_4$ Nanosheet Arrays Supported on Nickel Foams with Ultrahigh Capacitance for Aqueous Asymmetric Supercapacitor Applications. *ACS Appl. Mater. Interfaces* **2014**, *6*, 19318−19326.
(1106) Kobayashi, H.; Sugawara, Y.; Yamaguchi, T.; Honma, I. A Cobalt-Manganese Layered Oxide/Graphene Composite as an

https://doi.org/10.1021/acs.chemrev.3c00005
Chem. Rev. 2023, 123, 12795−13208

Outstanding Oxygen Evolution Reaction Electrocatalyst. *Chem. Commun.* **2021**, *57*, 9052−9055.
(1107) Liu, Z.; Yu, C.; Han, X.; Yang, J.; Zhao, C.; Huang, H.; Qiu, J. CoMn Layered Double Hydroxides/Carbon Nanotubes Architectures as High-Performance Electrocatalysts for the Oxygen Evolution Reaction. *ChemElectroChem* **2016**, *3*, 906−912.
(1108) Sun, Y.; Xu, K.; Wei, Z.; Li, H.; Zhang, T.; Li, X.; Cai, W.; Ma, J.; Fan, H. J.; Li, Y. Strong Electronic Interaction in Dual-Cation-Incorporated $NiSe_2$ Nanosheets with Lattice Distortion for Highly Efficient Overall Water Splitting. *Adv. Mater.* **2018**, *30*, 1802121.
(1109) Tang, Y.-J.; Wang, Y.; Zhou, K. In Situ Oxidation Transformation of Trimetallic Selenide to Amorphous FeCo-Oxyhydroxide by Self-Sacrificing $MoSe_2$ for Efficient Water Oxidation. *J. Mater. Chem. A* **2020**, *8*, 7925−7934.
(1110) Sun, Y.; Gao, S.; Lei, F.; Xie, Y. Atomically-Thin Two-Dimensional Sheets for Understanding Active Sites in Catalysis. *Chem. Soc. Rev.* **2015**, *44*, 623−636.
(1111) Zhang, C.; Huang, Y.; Yu, Y.; Zhang, J.; Zhuo, S.; Zhang, B. Sub-1.1 Nm Ultrathin Porous CoP Nanosheets with Dominant Reactive {200} Facets: A High Mass Activity and Efficient Electrocatalyst for the Hydrogen Evolution Reaction. *Chem. Sci.* **2017**, *8*, 2769−2775.
(1112) Zhang, Y.; Shi, Y.; Chen, R.; Tao, L.; Xie, C.; Liu, D.; Yan, D.; Wang, S. Enriched Nucleation Sites for Pt Deposition on Ultrathin WO_3 Nanosheets with Unique Interactions for Methanol Oxidation. *J. Mater. Chem. A* **2018**, *6*, 23028−23033.
(1113) Li, Y.; Li, F.-M.; Meng, X.-Y.; Li, S.-N.; Zeng, J.-H.; Chen, Y. Ultrathin Co_3O_4 Nanomeshes for the Oxygen Evolution Reaction. *ACS Catal.* **2018**, *8*, 1913−1920.
(1114) Xie, J.; Zhang, X.; Zhang, H.; Zhang, J.; Li, S.; Wang, R.; Pan, B.; Xie, Y. Intralayered Ostwald Ripening to Ultrathin Nanomesh Catalyst with Robust Oxygen-Evolving Performance. *Adv. Mater.* **2017**, *29*, 1604765.
(1115) Nørskov, J. K.; Bligaard, T.; Rossmeisl, J.; Christensen, C. H. Towards the Computational Design of Solid Catalysts. *Nat. Chem.* **2009**, *1*, 37−46.
(1116) Mohanty, B.; Jena, B. K.; Kandasamy, M.; Dalai, N.; Sahu, R. K.; Kadam, R. M.; Chakraborty, B.; Jena, B. The Role of Se Vacancies and Fe Doping of Nickel Selenide in the Water Oxidation Reaction. *Sustain. Energy Fuels* **2020**, *4*, 3058−3065.
(1117) Zheng, P.; Zhang, Y.; Dai, Z.; Zheng, Y.; Dinh, K. N.; Yang, J.; Dangol, R.; Liu, X.; Yan, Q. Constructing Multifunctional Heterostructure of Fe_2O_3@Ni_3Se_4 Nanotubes. *Small* **2018**, *14*, 1704065.
(1118) Taherinia, D.; Moravvej, S. H.; Moazzeni, M.; Akbarzadeh, E. Metal-Organic Framework Derived $NiSe_2/CeO_2$ Nanocomposite as a High-Performance Electrocatalyst for Oxygen Evolution Reaction (OER). *Sustain. Energy Fuels* **2021**, *5*, 2994−3000.
(1119) Li, J.; Wan, M.; Li, T.; Zhu, H.; Zhao, Z.; Wang, Z.; Wu, W.; Du, M. $NiCoSe_{2-x}$/N-Doped C Mushroom-like Core/Shell Nanorods on N-Doped Carbon Fiber for Efficiently Electrocatalyzed Overall Water Splitting. *Electrochim. Acta* **2018**, *272*, 161−168.
(1120) Ram Kumar, K.; Maiyalagan, T. Iron Nickel Sulphide Embedded on Multi-Walled Carbon Nanotubes as Efficient Electrocatalysts for Oxygen Evolution Reaction in Alkaline Medium. *Ceram. Int.* **2023**, *49*, 1195−1202.
(1121) Yeo, B. S.; Bell, A. T. In Situ Raman Study of Nickel Oxide and Gold-Supported Nickel Oxide Catalysts for the Electrochemical Evolution of Oxygen. *J. Phys. Chem. C* **2012**, *116*, 8394−8400.
(1122) Frydendal, R.; Busch, M.; Halck, N. B.; Paoli, E. A.; Krtil, P.; Chorkendorff, I.; Rossmeisl, J. Enhancing Activity for the Oxygen Evolution Reaction: The Beneficial Interaction of Gold with Manganese and Cobalt Oxides. *ChemCatChem* **2015**, *7*, 149−154.
(1123) Hassan, A.; Nisar, L.; Iqbal, R.; Sadaqat, M.; Hussain, F.; Ashiq, M. N.; Najam-ul-Haq, M.; Shah, A.; Joya, K. S. Copper Telluride Nanowires for High Performance Electrocatalytic Water Oxidation in Alkaline Media. *J. Power Sources* **2021**, *491*, 229628.
(1124) Nath, M.; De Silva, U.; Singh, H.; Perkins, M.; Liyanage, W. P. R.; Umapathi, S.; Chakravarty, S.; Masud, J. Cobalt Telluride: A Highly Efficient Trifunctional Electrocatalyst for Water Splitting and Oxygen Reduction. *ACS Appl. Energy Mater.* **2021**, *4*, 8158−8174.
(1125) Hu, L.; Zeng, X.; Wei, X.; Wang, H.; Wu, Y.; Gu, W.; Shi, L.; Zhu, C. Interface Engineering for Enhancing Electrocatalytic Oxygen Evolution of NiFe LDH/NiTe Heterostructures. *Appl. Catal. B: Environ.* **2020**, *273*, 119014.
(1126) Nisar, L.; Sadaqat, M.; Hassan, A.; Babar, N.-U.-A.; Shah, A.; Najam-Ul-Haq, M.; Ashiq, M. N.; Ehsan, M. F.; Joya, K. S. Ultrathin CoTe Nanoflakes Electrode Demonstrating Low Overpotential for Overall Water Splitting. *Fuel* **2020**, *280*, 118666.
(1127) Sadaqat, M.; Nisar, L.; Babar, N.-U.-A.; Hussain, F.; Naeem Ashiq, M.; Shah, A.; Fahad Ehsan, M.; Najam-Ul-Haq, M.; Saleem Joya, K. Zinc-Telluride Nanospheres as an Efficient Water Oxidation Electrocatalyst Displaying a Low Overpotential for Oxygen Evolution. *J. Mater. Chem. A* **2019**, *7*, 26410−26420.
(1128) Liu, M.; Lu, X.; Guo, C.; Wang, Z.; Li, Y.; Lin, Y.; Zhou, Y.; Wang, S.; Zhang, J. Architecting a Mesoporous N-Doped Graphitic Carbon Framework Encapsulating $CoTe_2$ as an Efficient Oxygen Evolution Electrocatalyst. *ACS Appl. Mater. Interfaces* **2017**, *9*, 36146−36153.
(1129) Gao, Q.; Huang, C.-Q.; Ju, Y.-M.; Gao, M.-R.; Liu, J.-W.; An, D.; Cui, C.-H.; Zheng, Y.-R.; Li, W.-X.; Yu, S.-H. Phase-Selective Syntheses of Cobalt Telluride Nanofleeces for Efficient Oxygen Evolution Catalysts. *Angew. Chem. Int. Ed.* **2017**, *56*, 7769−7773.
(1130) Qin, Q.; Zhang, G.; Chai, Z.; Zhang, J.; Cui, Y.; Li, T.; Zheng, W. Ionic Liquid-Assisted Synthesis of Cu_7Te_4 Ultrathin Nanosheets with Enhanced Electrocatalytic Activity for Water Oxidation. *Nano Energy* **2017**, *41*, 780−787.
(1131) Guo, P.; Cao, S.; Wang, Y.; Lu, X.; Zhang, Y.; Xin, X.; Chi, X.; Yu, X.; Tojiboyev, I.; Salari, H.; et al. Surface Self-Reconstruction of Telluride Induced by in-Situ Cathodic Electrochemical Activation for Enhanced Water Oxidation Performance. *Appl. Catal. B: Environ.* **2022**, *310*, 121355.
(1132) Lu, T.-H.; Chen, C.-J.; Lu, Y.-R.; Dong, C.-L.; Liu, R.-S. Synergistic-Effect-Controlled $CoTe_2$/Carbon Nanotube Hybrid Material for Efficient Water Oxidation. *J. Phys. Chem. C* **2016**, *120*, 28093−28099.
(1133) Tao, L.; Huang, M.; Guo, S.; Wang, Q.; Li, M.; Xiao, X.; Cao, G.; Shao, Y.; Shen, Y.; Fu, Y.; et al. Surface Modification of $NiCo_2Te_4$ Nanoclusters: A Highly Efficient Electrocatalyst for Overall Water-Splitting in Neutral Solution. *Appl. Catal. B: Environ.* **2019**, *254*, 424−431.
(1134) Qi, Y.; Yang, Z.; Peng, S.; Dong, Y.; Wang, M.; Bao, X.-Q.; Li, H.; Xiong, D. $CoTe_2$-$NiTe_2$ Heterojunction Directly Grown on CoNi Alloy Foam for Efficient Oxygen Evolution Reaction. *Inorg. Chem. Front.* **2022**, *9*, 332−342.
(1135) Yoo, R.; Min, K.; Kim, H.; Lim, D.; Baeck, S.-H. Prussian Blue Analog-Derived Co/CoTe Microcube as a Highly Efficient and Stable Electrocatalyst toward Oxygen Evolution Reaction. *Appl. Surf. Sci.* **2022**, *581*, 152405.
(1136) Qi, Y.; Yang, Z.; Dong, Y.; Bao, X.-Q.; Bai, J.; Li, H.; Wang, M.; Xiong, D. A CoNi Telluride Heterostructure Supported on Ni Foam as an Efficient Electrocatalyst for the Oxygen Evolution Reaction. *Inorg. Chem. Front.* **2022**, *9*, 5240−5251.
(1137) Wu, X.; Lu, L.; Liu, H.; Feng, L.; Li, W.; Sun, L. Metalloid Te-Doped Fe-Based Catalysts Applied for Electrochemical Water Oxidation. *ChemistrySelect* **2021**, *6*, 6154−6158.
(1138) Qi, Y.; Yang, Z.; Peng, S.; Wang, M.; Bai, J.; Li, H.; Xiong, D. Self-Supported Cobalt-Nickel Bimetallic Telluride as an Advanced Catalyst for the Oxygen Evolution Reaction. *Inorg. Chem. Front.* **2021**, *8*, 4247−4256.
(1139) Sadaqat, M.; Manzoor, S.; Nisar, L.; Hassan, A.; Tyagi, D.; Shah, J. H.; Ashiq, M. N.; Joya, K. S.; Alshahrani, T.; Najam-ul-Haq, M. Iron Doped Nickel Ditelluride Hierarchical Nanoflakes Arrays Directly Grown on Nickel Foam as Robust Electrodes for Oxygen Evolution Reaction. *Electrochim. Acta* **2021**, *371*, 137830.
(1140) Sun, H.; Yang, J.-M.; Li, J.-G.; Li, Z.; Ao, X.; Liu, Y.-Z.; Zhang, Y.; Li, Y.; Wang, C.; Tang, J. Synergistic Coupling of NiTe Nanoarrays with RuO_2 and NiFe-LDH Layers for High-Efficiency

https://doi.org/10.1021/acs.chemrev.3c00005
Chem. Rev. 2023, 123, 12795−13208

Electrochemical-/Photovoltage-Driven Overall Water Splitting. *Appl. Catal. B: Environ.* **2020**, *272*, 118988.
(1141) Xu, B.; Yang, X.; Liu, X.; Song, W.; Sun, Y.; Liu, Q.; Yang, H.; Li, C. Lattice Distortion in Hybrid $NiTe_2/Ni(OH)_2$ Nanosheets as Efficient Synergistic Electrocatalyst for Water and Urea Oxidation. *J. Power Sources* **2020**, *449*, 227585.
(1142) Qi, Y.; Wu, J.; Xu, J.; Gao, H.; Du, Z.; Liu, B.; Liu, L.; Xiong, D. One-Step Fabrication of a Self-Supported Co@$CoTe_2$ Electrocatalyst for Efficient and Durable Oxygen Evolution Reactions. *Inorg. Chem. Front.* **2020**, *7*, 2523−2532.
(1143) Yang, L.; Xu, H.; Liu, H.; Cheng, D.; Cao, D. Active Site Identification and Evaluation Criteria of In Situ Grown CoTe and NiTe Nanoarrays for Hydrogen Evolution and Oxygen Evolution Reactions. *Small Methods* **2019**, *3*, 1900113.
(1144) Zhong, L.; Bao, Y.; Feng, L. Fe-Doping Effect on CoTe Catalyst with Greatly Boosted Intrinsic Activity for Electrochemical Oxygen Evolution Reaction. *Electrochim. Acta* **2019**, *321*, 134656.
(1145) Xu, J.; Yin, Y.; Xiong, H.; Du, X.; Jiang, Y.; Guo, W.; Wang, Z.; Xie, Z.; Qu, D.; Tang, H.; et al. Improving Catalytic Activity of Metal Telluride by Hybridization: An Efficient Ni_3Te_2-CoTe Composite Electrocatalyst for Oxygen Evolution Reaction. *Appl. Surf. Sci.* **2019**, *490*, 516−521.
(1146) Yin, Y.; Xu, J.; Guo, W.; Wang, Z.; Du, X.; Chen, C.; Zheng, Z.; Liu, D.; Qu, D.; Xie, Z.; et al. A Single-Step Fabrication of $CoTe_2$ Nanofilm Electrode toward Efficient Overall Water Splitting. *Electrochim. Acta* **2019**, *307*, 451−458.
(1147) Ji, L.; Wang, Z.; Wang, H.; Shi, X.; Asiri, A. M.; Sun, X. Hierarchical $CoTe_2$ Nanowire Array: An Effective Oxygen Evolution Catalyst in Alkaline Media. *ACS Sustainable Chem. Eng.* **2018**, *6*, 4481−4485.
(1148) Wang, Z.; Zhang, L. In Situ Growth of NiTe Nanosheet Film on Nickel Foam as Electrocatalyst for Oxygen Evolution Reaction. *Electrochem. Commun.* **2018**, *88*, 29−33.
(1149) Wang, Z.; Zhang, L. Nickel Ditelluride Nanosheet Arrays: A Highly Efficient Electrocatalyst for the Oxygen Evolution Reaction. *ChemElectroChem* **2018**, *5*, 1153−1158.
(1150) McKendry, I. G.; Thenuwara, A. C.; Sun, J.; Peng, H.; Perdew, J. P.; Strongin, D. R.; Zdilla, M. J. Water Oxidation Catalyzed by Cobalt Oxide Supported on the Mattagamite Phase of $CoTe_2$. *ACS Catal.* **2016**, *6*, 7393−7397.
(1151) Zhang, T.; Li, J.; Bi, R.; Song, J.; Du, L.; Li, T.; Zhang, H.; Guo, Q.; Luo, J. One-Step Microwave Synthesis of in Situ Grown NiTe Nanosheets for Solid-State Asymmetric Supercapacitors and Oxygen Evolution Reaction. *J. Alloys Compd.* **2022**, *909*, 164786.
(1152) Tang, Y.-J.; Zou, Y.; Zhu, D. Efficient Water Oxidation Using an Fe-Doped Nickel Telluride-Nickel Phosphide Electrocatalyst by Partial Phosphating. *J. Mater. Chem. A* **2022**, *10*, 12438−12446.
(1153) Yang, L.; Qin, H.; Dong, Z.; Wang, T.; Wang, G.; Jiao, L. Metallic S-CoTe with Surface Reconstruction Activated by Electrochemical Oxidation for Oxygen Evolution Catalysis. *Small* **2021**, *17*, 2102027.
(1154) Li, W.; Chen, J.; Zhang, Y.; Gong, W.; Sun, M.; Wang, Y.; Wang, X.; Rao, H.; Ye, J.; Lu, Z. Hollow Fe/Ni-CoTe@NCFs Nanoarchitecture Derived from MOF@MOF as High-Efficiency Electrocatalysts for Boosting Oxygen Evolution Reaction. *Int. J. Hydrog. Energy* **2021**, *46*, 39912−39920.
(1155) Chen, Z.; Chen, M.; Yan, X.; Jia, H.; Fei, B.; Ha, Y.; Qing, H.; Yang, H.; Liu, M.; Wu, R. Vacancy Occupation-Driven Polymorphic Transformation in Cobalt Ditelluride for Boosted Oxygen Evolution Reaction. *ACS Nano* **2020**, *14*, 6968−6979.
(1156) Wang, Z.; Guo, P.; Liu, M.; Guo, C.; Liu, H.; Wei, S.; Zhang, J.; Lu, X. Rational Design of Metallic $NiTe_x$ (x = 1 or 2) as Bifunctional Electrocatalysts for Efficient Urea Conversion. *ACS Appl. Energy Mater.* **2019**, *2*, 3363−3372.
(1157) Wang, Q.; Zhu, J.; Wang, H.; Yu, S.; Wu, X. Anchoring NiTe Domains with Unusual Composition on $Pb_{0.95}Ni_{0.05}Te$ Nanorod as Superior Lithium-Ion Battery Anodes and Oxygen Evolution Catalysts. *Mater. Today Energy* **2019**, *11*, 199−210.
(1158) Wang, Z.; Ren, X.; Wang, L.; Cui, G.; Wang, H.; Sun, X. A Hierarchical $CoTe_2$-$MnTe_2$ Hybrid Nanowire Array Enables High Activity for Oxygen Evolution Reactions. *Chem. Commun.* **2018**, *54*, 10993−10996.
(1159) Wang, X.; Huang, X.; Gao, W.; Tang, Y.; Jiang, P.; Lan, K.; Yang, R.; Wang, B.; Li, R. Metal-Organic Framework Derived $CoTe_2$ Encapsulated in Nitrogen-Doped Carbon Nanotube Frameworks: A High-Efficiency Bifunctional Electrocatalyst for Overall Water Splitting. *J. Mater. Chem. A* **2018**, *6*, 3684−3691.
(1160) Kim, E.-K.; Bui, H. T.; Shrestha, N. K.; Shin, C. Y.; Patil, S. A.; Khadtare, S.; Bathula, C.; Noh, Y.-Y.; Han, S.-H. An Enhanced Electrochemical Energy Conversion Behavior of Thermally Treated Thin Film of 1-Dimensional CoTe Synthesized from Aqueous Solution at Room Temperature. *Electrochim. Acta* **2018**, *260*, 365−371.
(1161) Bhat, K. S.; Barshilia, H. C.; Nagaraja, H. S. Porous Nickel Telluride Nanostructures as Bifunctional Electrocatalyst towards Hydrogen and Oxygen Evolution Reaction. *Int. J. Hydrog. Energy* **2017**, *42*, 24645−24655.
(1162) Patil, S. A.; Kim, E.-K.; Shrestha, N. K.; Chang, J.; Lee, J. K.; Han, S.-H. Formation of Semimetallic Cobalt Telluride Nanotube Film via Anion Exchange Tellurization Strategy in Aqueous Solution for Electrocatalytic Applications. *ACS Appl. Mater. Interfaces* **2015**, *7*, 25914−25922.
(1163) Tian, J.; Liu, Q.; Cheng, N.; Asiri, A. M.; Sun, X. Self-Supported Cu_3P Nanowire Arrays as an Integrated High-Performance Three-Dimensional Cathode for Generating Hydrogen from Water. *Angew. Chem.* **2014**, *126*, 9731−9735.
(1164) Jiang, P.; Liu, Q.; Liang, Y.; Tian, J.; Asiri, A. M.; Sun, X. A Cost-Effective 3D Hydrogen Evolution Cathode with High Catalytic Activity: FeP Nanowire Array as the Active Phase. *Angew. Chem. Int. Ed.* **2014**, *53*, 12855−12859.
(1165) Shinde, D. V.; Ahn, D. Y.; Jadhav, V. V.; Lee, D. Y.; Shrestha, N. K.; Lee, J. K.; Lee, H. Y.; Mane, R. S.; Han, S.-H. A Coordination Chemistry Approach for Shape Controlled Synthesis of Indium Oxide Nanostructures and Their Photoelectrochemical Properties. *J. Mater. Chem. A* **2014**, *2*, 5490−5498.
(1166) Chen, C.; Yang, Q.-H.; Yang, Y.; Lv, W.; Wen, Y.; Hou, P.-X.; Wang, M.; Cheng, H.-M. Self-Assembled Free-Standing Graphite Oxide Membrane. *Adv. Mater.* **2009**, *21*, 3007−3011.
(1167) Bensch, W.; Heid, W.; Muhler, M.; Jobic, S.; Brec, R.; Rouxel, J. Anionic Polymeric Bonds in Nickel Ditelluride: Crystal Structure, and Experimental and Theoretical Band Structure. *J. Solid State Chem.* **1996**, *121*, 87−94.
(1168) Rotlevi, O.; Dobson, K. D.; Rose, D.; Hodes, G. Electroless Ni and $NiTe_2$ Ohmic Contacts for CdTe/CdS PV Cells. *Thin Solid Films* **2001**, *387*, 155−157.
(1169) Schenck, C. V.; Dillard, J. G.; Murray, J. W. Surface Analysis and the Adsorption of Co(II) on Goethite. *J. Colloid. Interface Sci.* **1983**, *95*, 398−409.
(1170) Dutton, W. A.; Cooper, W. C. The Oxides and Oxyacids of Tellurium. *Chem. Rev.* **1966**, *66*, 657−675.
(1171) Lee, J.-I.; Chae, H. R.; Ryu, J. H. Tellurium-Incorporated Nickel-Cobalt Layered Double Hydroxide and Its Oxygen Evolution Reaction. *Korean J. Met. Mater.* **2021**, *59*, 491−498.
(1172) Zuo, Y.; Rao, D.; Ma, S.; Li, T.; Tsang, Y. H.; Kment, S.; Chai, Y. Valence Engineering via Dual-Cation and Boron Doping in Pyrite Selenide for Highly Efficient Oxygen Evolution. *ACS Nano* **2019**, *13*, 11469−11476.
(1173) Zhang, Z.; Zhang, T.; Lee, J. Y. Electrochemical Performance of Borate-Doped Nickel Sulfide: Enhancement of the Bifunctional Activity for Total Water Splitting. *ChemElectroChem* **2019**, *6*, 1443−1449.
(1174) Masud, J.; Ioannou, P.-C.; Levesanos, N.; Kyritsis, P.; Nath, M. A Molecular Ni-Complex Containing Tetrahedral Nickel Selenide Core as Highly Efficient Electrocatalyst for Water Oxidation. *ChemSusChem* **2016**, *9*, 3128−3132.
(1175) He, C.; Zhang, D.; Cai, Y.; Hou, C.; Wu, X.; Ma, Z.; Huang, Y.; Wang, H.; Li, Q. Robust Oxygen Electrocatalysis Enabled by Bulk

Nitrogen-Doped Hierarchical Structure Cobalt Carbide. *J. Mater. Chem. A* **2022**, *10*, 20924−20933.
(1176) Wang, Q.; Zhang, Z.; Zhao, X.; Xiao, J.; Manoj, D.; Wei, F.; Xiao, F.; Wang, H.; Wang, S. MOF-Derived Copper Nitride/Phosphide Heterostructure Coated by Multi-Doped Carbon as Electrocatalyst for Efficient Water Splitting and Neutral-pH Hydrogen Evolution Reaction. *ChemElectroChem* **2020**, *7*, 289−298.
(1177) Wang, Y.; LIu, S.; Hao, X.; Luan, S.; You, H.; Zhou, J.; Song, D.; Wang, D.; Li, H.; Gao, F. Surface Reorganization Engineering of the N-Doped MoS_2 Heterostructures MoO_x@N-Doped MoS_{2-x} by in Situ Electrochemical Oxidation Activation for Efficient Oxygen Evolution Reaction. *J. Mater. Chem. A* **2019**, *7*, 10572−10580.
(1178) Hu, F.; Wang, H.; Zhang, Y.; Shen, X.; Zhang, G.; Pan, Y.; Miller, J. T.; Wang, K.; Zhu, S.; Yang, X.; et al. Designing Highly Efficient and Long-Term Durable Electrocatalyst for Oxygen Evolution by Coupling B and P into Amorphous Porous NiFe-Based Material. *Small* **2019**, *15*, 1901020.
(1179) He, B.; Kuang, P.; Li, X.; Chen, H.; Yu, J.; Fan, K. In Situ Transformation of Prussian-Blue Analogue-Derived Bimetallic Carbide Nanocubes by Water Oxidation: Applications for Energy Storage and Conversion. *Chem.—Eur. J.* **2020**, *26*, 4052−4062.
(1180) Mukherjee, D.; P, M. A.; Sampath, S. Few-Layer Iron Selenophosphate, $FePSe_3$: Efficient Electrocatalyst toward Water Splitting and Oxygen Reduction Reactions. *ACS Appl. Energy Mater.* **2018**, *1*, 220−231.
(1181) Zhang, Z.; Tang, S.; Lin, X.; Liu, C.; Hu, S.; Huang, Q. N, P-Doped Multiphase Transition Metal Sulfides Are Used for Efficient Electrocatalytic Oxygen Evolution Reaction. *Appl. Surf. Sci.* **2022**, *584*, 152546.
(1182) Fang, X.; Wang, Z.; Wang, Y.; Kang, S.; Jiang, Z.; Dong, M. Tuning Quaternary Hybride Co-Ni-S-Se Composition as a Bifunctional Electrocatalyst for Hydrogen and Oxygen Evolution Reactions. *Int. J. Hydrogen Energy* **2019**, *44*, 27685−27694.
(1183) Singh, A.; Yadav, R.; Kociok-Köhn, G.; Trivedi, M.; Azad, U. P.; Singh, A. K.; Kumar, A. Syntheses of Nickel Sulfides from 1,2-Bis(Diphenylphosphino)Ethane Nickel(II)Dithiolates and Their Application in the Oxygen Evolution Reaction. *Int. J. Hydrog. Energy* **2018**, *43*, 5985−5995.
(1184) Guo, Y.; Yuan, P.; Zhang, J.; Xia, H.; Cheng, F.; Zhou, M.; Li, J.; Qiao, Y.; Mu, S.; Xu, Q. Co_2P-CoN Double Active Centers Confined in N-Doped Carbon Nanotube: Heterostructural Engineering for Trifunctional Catalysis toward HER, ORR, OER, and Zn-Air Batteries Driven Water Splitting. *Adv. Funct. Mater.* **2018**, *28*, 1805641.
(1185) Levesanos, N.; Robertson, S. D.; Maganas, D.; Raptopoulou, C. P.; Terzis, A.; Kyritsis, P.; Chivers, T. $Ni[(EP^iPr_2)_2N]_2$ Complexes: Stereoisomers (E = Se) and Square-Planar Coordination (E = Te). *Inorg. Chem.* **2008**, *47*, 2949−2951.
(1186) Levesanos, N.; Liyanage, W. P. R.; Ferentinos, E.; Raptopoulos, G.; Paraskevopoulou, P.; Sanakis, Y.; Choudhury, A.; Stavropoulos, P.; Nath, M.; Kyritsis, P. Investigating the Structural, Spectroscopic, and Electrochemical Properties of $[Fe\{(EPiPr_2)_2N\}_2]$ (E = S, Se) and the Formation of Iron Selenides by Chemical Vapor Deposition. *Eur. J. Inorg. Chem.* **2016**, *2016*, 5332−5339.
(1187) Azam, A.; Kim, J.; Park, J.; Novak, T. G.; Tiwari, A. P.; Song, S. H.; Kim, B.; Jeon, S. Two-Dimensional WO_3 Nanosheets Chemically Converted from Layered WS_2 for High-Performance Electrochromic Devices. *Nano Lett.* **2018**, *18*, 5646−5651.
(1188) Jiang, H.; He, Q.; Zhang, Y.; Song, L. Structural Self-Reconstruction of Catalysts in Electrocatalysis. *Acc. Chem. Res.* **2018**, *51*, 2968−2977.
(1189) Zhu, Y.; Wang, J.; Chu, H.; Chu, Y.-C.; Chen, H. M. In Situ/Operando Studies for Designing Next-Generation Electrocatalysts. *ACS Energy Lett.* **2020**, *5*, 1281−1291.
(1190) Zhao, T.; Wang, Y.; Karuturi, S.; Catchpole, K.; Zhang, Q.; Zhao, C. Design and Operando/in Situ Characterization of Precious-Metal-Free Electrocatalysts for Alkaline Water Splitting. *Carbon Ener.* **2020**, *2*, 582−613.
(1191) Moysiadou, A.; Lee, S.; Hsu, C.-S.; Chen, H. M.; Hu, X. Mechanism of Oxygen Evolution Catalyzed by Cobalt Oxyhydroxide: Cobalt Superoxide Species as a Key Intermediate and Dioxygen Release as a Rate-Determining Step. *J. Am. Chem. Soc.* **2020**, *142*, 11901−11914.
(1192) Joya, K. S.; Sala, X. In Situ Raman and Surface-Enhanced Raman Spectroscopy on Working Electrodes: Spectroelectrochemical Characterization of Water Oxidation Electrocatalysts. *Phys. Chem. Chem. Phys.* **2015**, *17*, 21094−21103.
(1193) Wang, B.; Zhao, K.; Yu, Z.; Sun, C.; Wang, Z.; Feng, N.; Mai, L.; Wang, Y.; Xia, Y. In Situ Structural Evolution of the Multi-Site Alloy Electrocatalyst to Manipulate the Intermediate for Enhanced Water Oxidation Reaction. *Energy Environ. Sci.* **2020**, *13*, 2200−2208.
(1194) Zhai, L.; Benedict Lo, T. W.; Xu, Z.-L.; Potter, J.; Mo, J.; Guo, X.; Tang, C. C.; Edman Tsang, S. C.; Lau, S. P. In Situ Phase Transformation on Nickel-Based Selenides for Enhanced Hydrogen Evolution Reaction in Alkaline Medium. *ACS Energy Lett.* **2020**, *5*, 2483−2491.
(1195) Bau, J. A.; Haspel, H.; Ould-Chikh, S.; Aguilar-Tapia, A.; Hazemann, J.-L.; Idriss, H.; Takanabe, K. On the Reconstruction of NiMo Electrocatalysts by Operando Spectroscopy. *J. Mater. Chem. A* **2019**, *7*, 15031−15035.
(1196) Deng, Y.; Ting, L. R. L.; Neo, P. H. L.; Zhang, Y.-J.; Peterson, A. A.; Yeo, B. S. Operando Raman Spectroscopy of Amorphous Molybdenum Sulfide (MoS_x) during the Electrochemical Hydrogen Evolution Reaction: Identification of Sulfur Atoms as Catalytically Active Sites for H^+ Reduction. *ACS Catal.* **2016**, *6*, 7790−7798.
(1197) Xiao, Z.; Huang, Y.-C.; Dong, C.-L.; Xie, C.; Liu, Z.; Du, S.; Chen, W.; Yan, D.; Tao, L.; Shu, Z.; et al. Operando Identification of the Dynamic Behavior of Oxygen Vacancy-Rich Co_3O_4 for Oxygen Evolution Reaction. *J. Am. Chem. Soc.* **2020**, *142*, 12087−12095.
(1198) Cole, K. M.; Kirk, D. W.; Thorpe, S. J. In Situ Raman Study of Amorphous and Crystalline Ni-Co Alloys for the Alkaline Oxygen Evolution Reaction. *J. Electrochem. Soc.* **2018**, *165*, J3122−J3129.
(1199) Diaz-Morales, O.; Ferrus-Suspedra, D.; Koper, M. T. M. The Importance of Nickel Oxyhydroxide Deprotonation on Its Activity towards Electrochemical Water Oxidation. *Chem. Sci.* **2016**, *7*, 2639−2645.
(1200) Kostecki, R.; McLarnon, F. Electrochemical and In Situ Raman Spectroscopic Characterization of Nickel Hydroxide Electrodes I. Pure Nickel Hydroxide. *J. Electrochem. Soc.* **1997**, *144*, 485−493.
(1201) Landon, J.; Demeter, E.; İnoğlu, N.; Keturakis, C.; Wachs, I. E.; Vasić, R.; Frenkel, A. I.; Kitchin, J. R. Spectroscopic Characterization of Mixed Fe-Ni Oxide Electrocatalysts for the Oxygen Evolution Reaction in Alkaline Electrolytes. *ACS Catal.* **2012**, *2*, 1793−1801.
(1202) Lee, S.; Banjac, K.; Lingenfelder, M.; Hu, X. Oxygen Isotope Labeling Experiments Reveal Different Reaction Sites for the Oxygen Evolution Reaction on Nickel and Nickel Iron Oxides. *Angew. Chem. Int. Ed Engl* **2019**, *58*, 10295−10299.
(1203) Song, F.; Busch, M. M.; Lassalle-Kaiser, B.; Hsu, C.-S.; Petkucheva, E.; Bensimon, M.; Chen, H. M.; Corminboeuf, C.; Hu, X. An Unconventional Iron Nickel Catalyst for the Oxygen Evolution Reaction. *ACS Cent. Sci.* **2019**, *5*, 558−568.
(1204) Yeo, B. S.; Bell, A. T. Enhanced Activity of Gold-Supported Cobalt Oxide for the Electrochemical Evolution of Oxygen. *J. Am. Chem. Soc.* **2011**, *133*, 5587−5593.
(1205) Zhu, K.; Zhu, X.; Yang, W. Application of In Situ Techniques for the Characterization of NiFe-Based Oxygen Evolution Reaction (OER) Electrocatalysts. *Angew. Chem. Int. Ed.* **2019**, *58*, 1252−1265.
(1206) Shih, M.-C.; Jhang, R.-H.; Tsai, Y.-T.; Huang, C.-W.; Hung, Y.-J.; Liao, M.-Y.; Huang, J.; Chen, C.-H. Discontinuity-Enhanced Thin Film Electrocatalytic Oxygen Evolution. *Small* **2019**, *15*, 1903363.
(1207) Tan, S. M.; Ambrosi, A.; Sofer, Z.; Huber, S.; Sedmidubský, D.; Pumera, M. Pristine Basal- and Edge-Plane-Oriented Molybdenite MoS_2 Exhibiting Highly Anisotropic Properties. *Chem.—Eur. J.* **2015**, *21*, 7170−7178.

https://doi.org/10.1021/acs.chemrev.3c00005
Chem. Rev. 2023, 123, 12795−13208

(1208) Trotochaud, L.; Mills, T. J.; Boettcher, S. W. An Optocatalytic Model for Semiconductor-Catalyst Water-Splitting Photoelectrodes Based on In Situ Optical Measurements on Operational Catalysts. *J. Phys. Chem. Lett.* **2013**, *4*, 931−935.
(1209) Goldsmith, Z. K.; Harshan, A. K.; Gerken, J. B.; Vörös, M.; Galli, G.; Stahl, S. S.; Hammes-Schiffer, S. Characterization of NiFe Oxyhydroxide Electrocatalysts by Integrated Electronic Structure Calculations and Spectroelectrochemistry. *Proc. Natl. Acad. Sci. U.S.A.* **2017**, *114*, 3050−3055.
(1210) Wang, M.; Árnadóttir, L.; Xu, Z. J.; Feng, Z. In Situ X-Ray Absorption Spectroscopy Studies of Nanoscale Electrocatalysts. *Nano-Micro Lett.* **2019**, *11*, 47.
(1211) van Oversteeg, C. H. M.; Doan, H. Q.; de Groot, F. M. F.; Cuk, T. In Situ X-Ray Absorption Spectroscopy of Transition Metal Based Water Oxidation Catalysts. *Chem. Soc. Rev.* **2017**, *46*, 102−125.
(1212) Weng, Z.; Wu, Y.; Wang, M.; Jiang, J.; Yang, K.; Huo, S.; Wang, X.-F.; Ma, Q.; Brudvig, G. W.; Batista, V. S.; et al. Active Sites of Copper-Complex Catalytic Materials for Electrochemical Carbon Dioxide Reduction. *Nat. Commun.* **2018**, *9*, 415.
(1213) Zhang, Y.; Wu, C.; Jiang, H.; Lin, Y.; Liu, H.; He, Q.; Chen, S.; Duan, T.; Song, L. Atomic Iridium Incorporated in Cobalt Hydroxide for Efficient Oxygen Evolution Catalysis in Neutral Electrolyte. *Adv. Mater.* **2018**, *30*, 1707522.
(1214) Drevon, D.; Görlin, M.; Chernev, P.; Xi, L.; Dau, H.; Lange, K. M. Uncovering The Role of Oxygen in Ni-Fe(O_xH_y) Electrocatalysts Using In Situ Soft X-Ray Absorption Spectroscopy during the Oxygen Evolution Reaction. *Sci. Rep.* **2019**, *9*, 1532.
(1215) Song, S.; Zhou, J.; Su, X.; Wang, Y.; Li, J.; Zhang, L.; Xiao, G.; Guan, C.; Liu, R.; Chen, S.; et al. Operando X-Ray Spectroscopic Tracking of Self-Reconstruction for Anchored Nanoparticles as High-Performance Electrocatalysts towards Oxygen Evolution. *Energy Environ. Sci.* **2018**, *11*, 2945−2953.
(1216) Mueller, D. N.; Machala, M. L.; Bluhm, H.; Chueh, W. C. Redox Activity of Surface Oxygen Anions in Oxygen-Deficient Perovskite Oxides during Electrochemical Reactions. *Nat. Commun.* **2015**, *6*, 6097.
(1217) Zheng, X.; Zhang, B.; De Luna, P.; Liang, Y.; Comin, R.; Voznyy, O.; Han, L.; García de Arquer, F. P.; Liu, M.; Dinh, C. T.; et al. Theory-Driven Design of High-Valence Metal Sites for Water Oxidation Confirmed Using in Situ Soft X-Ray Absorption. *Nat. Chem.* **2018**, *10*, 149−154.
(1218) Hung, S.-F.; Chan, Y.-T.; Chang, C.-C.; Tsai, M.-K.; Liao, Y.-F.; Hiraoka, N.; Hsu, C.-S.; Chen, H. M. Identification of Stabilizing High-Valent Active Sites by Operando High-Energy Resolution Fluorescence-Detected X-Ray Absorption Spectroscopy for High-Efficiency Water Oxidation. *J. Am. Chem. Soc.* **2018**, *140*, 17263−17270.
(1219) Gu, H.; Shi, G.; Chen, H.-C.; Xie, S.; Li, Y.; Tong, H.; Yang, C.; Zhu, C.; Mefford, J. T.; Xia, H.; et al. Strong Catalyst-Support Interactions in Electrochemical Oxygen Evolution on Ni-Fe Layered Double Hydroxide. *ACS Energy Lett.* **2020**, *5*, 3185−3194.
(1220) Deng, X.; Sorescu, D. C.; Waluyo, I.; Hunt, A.; Kauffman, D. R. Bulk vs Intrinsic Activity of NiFeOx Electrocatalysts in the Oxygen Evolution Reaction: The Influence of Catalyst Loading, Morphology, and Support Material. *ACS Catal.* **2020**, *10*, 11768−11778.
(1221) Gorlin, Y.; Lassalle-Kaiser, B.; Benck, J. D.; Gul, S.; Webb, S. M.; Yachandra, V. K.; Yano, J.; Jaramillo, T. F. In-Situ X-Ray Absorption Spectroscopy (XAS) Investigation of a Bifunctional Manganese Oxide Catalyst with High Activity for Electrochemical Water Oxidation and Oxygen Reduction. *J. Am. Chem. Soc.* **2013**, *135*, 8525−8534.
(1222) Hu, C.; Ma, Q.; Hung, S.-F.; Chen, Z.-N.; Ou, D.; Ren, B.; Chen, H. M.; Fu, G.; Zheng, N. In Situ Electrochemical Production of Ultrathin Nickel Nanosheets for Hydrogen Evolution Electrocatalysis. *Chem.* **2017**, *3*, 122−133.
(1223) Tung, C.-W.; Hsu, Y.-Y.; Shen, Y.-P.; Zheng, Y.; Chan, T.-S.; Sheu, H.-S.; Cheng, Y.-C.; Chen, H. M. Reversible Adapting Layer Produces Robust Single-Crystal Electrocatalyst for Oxygen Evolution. *Nat. Commun.* **2015**, *6*, 8106.
(1224) Seh, Z. W.; Kibsgaard, J.; Dickens, C. F.; Chorkendorff, I.; Nørskov, J. K.; Jaramillo, T. F. Combining Theory and Experiment in Electrocatalysis: Insights into Materials Design. *Science* **2017**, *355*, No. eaad4998.
(1225) Hodnik, N.; Dehm, G.; Mayrhofer, K. J. J. Importance and Challenges of Electrochemical in Situ Liquid Cell Electron Microscopy for Energy Conversion Research. *Acc. Chem. Res.* **2016**, *49*, 2015−2022.
(1226) Wu, Y.; Liu, N. Visualizing Battery Reactions and Processes by Using In Situ and In Operando Microscopies. *Chem.* **2018**, *4*, 438−465.
(1227) Baldizzone, C.; Gan, L.; Hodnik, N.; Keeley, G. P.; Kostka, A.; Heggen, M.; Strasser, P.; Mayrhofer, K. J. J. Stability of Dealloyed Porous Pt/Ni Nanoparticles. *ACS Catal.* **2015**, *5*, 5000−5007.
(1228) Hodnik, N.; Jovanovič, P.; Pavlišič, A.; Jozinović, B.; Zorko, M.; Bele, M.; Šelih, V. S.; Šala, M.; Hočevar, S.; Gaberšček, M. New Insights into Corrosion of Ruthenium and Ruthenium Oxide Nanoparticles in Acidic Media. *J. Phys. Chem. C* **2015**, *119*, 10140−10147.
(1229) Roy, C.; Sebok, B.; Scott, S. B.; Fiordaliso, E. M.; Sørensen, J. E.; Bodin, A.; Trimarco, D. B.; Damsgaard, C. D.; Vesborg, P. C. K.; Hansen, O.; et al. Impact of Nanoparticle Size and Lattice Oxygen on Water Oxidation on $NiFeO_xH_y$. *Nat. Catal.* **2018**, *1*, 820−829.
(1230) Ortiz Peña, N.; Ihiawakrim, D.; Han, M.; Lassalle-Kaiser, B.; Carenco, S.; Sanchez, C.; Laberty-Robert, C.; Portehault, D.; Ersen, O. Morphological and Structural Evolution of Co_3O_4 Nanoparticles Revealed by in Situ Electrochemical Transmission Electron Microscopy during Electrocatalytic Water Oxidation. *ACS Nano* **2019**, *13*, 11372−11381.
(1231) Lichterman, M. F.; Hu, S.; Richter, M. H.; Crumlin, E. J.; Axnanda, S.; Favaro, M.; Drisdell, W.; Hussain, Z.; Mayer, T.; Brunschwig, B. S.; et al. Direct Observation of the Energetics at a Semiconductor/Liquid Junction by Operando X-Ray Photoelectron Spectroscopy. *Energy Environ. Sci.* **2015**, *8*, 2409−2416.
(1232) Ali-Löytty, H.; Louie, M. W.; Singh, M. R.; Li, L.; Sanchez Casalongue, H. G.; Ogasawara, H.; Crumlin, E. J.; Liu, Z.; Bell, A. T.; Nilsson, A.; et al. Ambient-Pressure XPS Study of a Ni-Fe Electrocatalyst for the Oxygen Evolution Reaction. *J. Phys. Chem. C* **2016**, *120*, 2247−2253.
(1233) Favaro, M.; Yang, J.; Nappini, S.; Magnano, E.; Toma, F. M.; Crumlin, E. J.; Yano, J.; Sharp, I. D. Understanding the Oxygen Evolution Reaction Mechanism on CoO_x Using Operando Ambient-Pressure X-Ray Photoelectron Spectroscopy. *J. Am. Chem. Soc.* **2017**, *139*, 8960−8970.
(1234) Li, L.; Yang, H.; Miao, J.; Zhang, L.; Wang, H.-Y.; Zeng, Z.; Huang, W.; Dong, X.; Liu, B. Unraveling Oxygen Evolution Reaction on Carbon-Based Electrocatalysts: Effect of Oxygen Doping on Adsorption of Oxygenated Intermediates. *ACS Energy Lett.* **2017**, *2*, 294−300.
(1235) Bentley, C. L.; Edmondson, J.; Meloni, G. N.; Perry, D.; Shkirskiy, V.; Unwin, P. R. Nanoscale Electrochemical Mapping. *Anal. Chem.* **2019**, *91*, 84−108.
(1236) Pfisterer, J. H. K.; Liang, Y.; Schneider, O.; Bandarenka, A. S. Direct Instrumental Identification of Catalytically Active Surface Sites. *Nature* **2017**, *549*, 74−77.
(1237) Jaramillo, T. F.; Jørgensen, K. P.; Bonde, J.; Nielsen, J. H.; Horch, S.; Chorkendorff, I. Identification of Active Edge Sites for Electrochemical H_2 Evolution from MoS_2 Nanocatalysts. *Science* **2007**, *317*, 100−102.
(1238) Nellist, M. R.; Laskowski, F. A. L.; Qiu, J.; Hajibabaei, H.; Sivula, K.; Hamann, T. W.; Boettcher, S. W. Potential-Sensing Electrochemical Atomic Force Microscopy for in Operando Analysis of Water-Splitting Catalysts and Interfaces. *Nat. Energy* **2018**, *3*, 46−52.
(1239) Mefford, J. T.; Akbashev, A. R.; Zhang, L.; Chueh, W. C. Electrochemical Reactivity of Faceted β-$Co(OH)_2$ Single Crystal Platelet Particles in Alkaline Electrolytes. *J. Phys. Chem. C* **2019**, *123*, 18783−18794.

https://doi.org/10.1021/acs.chemrev.3c00005
Chem. Rev. 2023, 123, 12795−13208

(1240) Deng, J.; Nellist, M. R.; Stevens, M. B.; Dette, C.; Wang, Y.; Boettcher, S. W. Morphology Dynamics of Single-Layered $Ni(OH)_2$/NiOOH Nanosheets and Subsequent Fe Incorporation Studied by in Situ Electrochemical Atomic Force Microscopy. *Nano Lett.* **2017**, *17*, 6922−6926.
(1241) Dette, C.; Hurst, M. R.; Deng, J.; Nellist, M. R.; Boettcher, S. W. Structural Evolution of Metal (Oxy)Hydroxide Nanosheets during the Oxygen Evolution Reaction. *ACS Appl. Mater. Interfaces* **2019**, *11*, 5590−5594.
(1242) Laskowski, F. A. L.; Oener, S. Z.; Nellist, M. R.; Gordon, A. M.; Bain, D. C.; Fehrs, J. L.; Boettcher, S. W. Nanoscale Semiconductor/Catalyst Interfaces in Photoelectrochemistry. *Nat. Mater.* **2020**, *19*, 69−76.
(1243) Bentley, C. L.; Kang, M.; Maddar, F. M.; Li, F.; Walker, M.; Zhang, J.; Unwin, P. R. Electrochemical Maps and Movies of the Hydrogen Evolution Reaction on Natural Crystals of Molybdenite (MoS_2): Basal vs. Edge Plane Activity. *Chem. Sci.* **2017**, *8*, 6583−6593.
(1244) Kim, J.; Renault, C.; Nioradze, N.; Arroyo-Currás, N.; Leonard, K. C.; Bard, A. J. Electrocatalytic Activity of Individual Pt Nanoparticles Studied by Nanoscale Scanning Electrochemical Microscopy. *J. Am. Chem. Soc.* **2016**, *138*, 8560−8568.
(1245) Sun, T.; Wang, D.; Mirkin, M. V.; Cheng, H.; Zheng, J.-C.; Richards, R. M.; Lin, F.; Xin, H. L. Direct High-Resolution Mapping of Electrocatalytic Activity of Semi-Two-Dimensional Catalysts with Single-Edge Sensitivity. *Proc. Natl. Acad. Sci. U.S.A.* **2019**, *116*, 11618−11623.
(1246) Jin, Z.; Bard, A. J. Surface Interrogation of Electrodeposited MnO_x and $CaMnO_3$ Perovskites by Scanning Electrochemical Microscopy: Probing Active Sites and Kinetics for the Oxygen Evolution Reaction. *Angew. Chem. Int. Ed.* **2021**, *133*, 807−812.
(1247) Ahn, H. S.; Bard, A. J. Surface Interrogation of CoPi Water Oxidation Catalyst by Scanning Electrochemical Microscopy. *J. Am. Chem. Soc.* **2015**, *137*, 612−615.
(1248) Ahn, H. S.; Bard, A. J. Surface Interrogation Scanning Electrochemical Microscopy of $Ni_{1-x}Fe_xOOH$ ($0 < x < 0.27$) Oxygen Evolving Catalyst: Kinetics of the "Fast" Iron Sites. *J. Am. Chem. Soc.* **2016**, *138*, 313−318.
(1249) Bentley, C. L.; Kang, M.; Unwin, P. R. Nanoscale Surface Structure-Activity in Electrochemistry and Electrocatalysis. *J. Am. Chem. Soc.* **2019**, *141*, 2179−2193.
(1250) Bentley, C. L.; Kang, M.; Unwin, P. R. Nanoscale Structure Dynamics within Electrocatalytic Materials. *J. Am. Chem. Soc.* **2017**, *139*, 16813−16821.
(1251) Kang, M.; Perry, D.; Bentley, C. L.; West, G.; Page, A.; Unwin, P. R. Simultaneous Topography and Reaction Flux Mapping at and around Electrocatalytic Nanoparticles. *ACS Nano* **2017**, *11*, 9525−9535.
(1252) Bentley, C. L.; Andronescu, C.; Smialkowski, M.; Kang, M.; Tarnev, T.; Marler, B.; Unwin, P. R.; Apfel, U.-P.; Schuhmann, W. Local Surface Structure and Composition Control the Hydrogen Evolution Reaction on Iron Nickel Sulfides. *Angew. Chem. Int. Ed.* **2018**, *57*, 4093−4097.
(1253) Yule, L. C.; Shkirskiy, V.; Aarons, J.; West, G.; Bentley, C. L.; Shollock, B. A.; Unwin, P. R. Nanoscale Active Sites for the Hydrogen Evolution Reaction on Low Carbon Steel. *J. Phys. Chem. C* **2019**, *123*, 24146−24155.
(1254) Tao, B.; Unwin, P. R.; Bentley, C. L. Nanoscale Variations in the Electrocatalytic Activity of Layered Transition-Metal Dichalcogenides. *J. Phys. Chem. C* **2020**, *124*, 789−798.
(1255) Ustarroz, J.; Ornelas, I. M.; Zhang, G.; Perry, D.; Kang, M.; Bentley, C. L.; Walker, M.; Unwin, P. R. Mobility and Poisoning of Mass-Selected Platinum Nanoclusters during the Oxygen Reduction Reaction. *ACS Catal.* **2018**, *8*, 6775−6790.
(1256) Yule, L. C.; Bentley, C. L.; West, G.; Shollock, B. A.; Unwin, P. R. Scanning Electrochemical Cell Microscopy: A Versatile Method for Highly Localised Corrosion Related Measurements on Metal Surfaces. *Electrochim. Acta* **2019**, *298*, 80−88.
(1257) Stevens, M. B.; Trang, C. D. M.; Enman, L. J.; Deng, J.; Boettcher, S. W. Reactive Fe-Sites in Ni/Fe (Oxy)Hydroxide Are Responsible for Exceptional Oxygen Electrocatalysis Activity. *J. Am. Chem. Soc.* **2017**, *139*, 11361−11364.
(1258) Cherevko, S.; Zeradjanin, A. R.; Topalov, A. A.; Kulyk, N.; Katsounaros, I.; Mayrhofer, K. J. J. Dissolution of Noble Metals during Oxygen Evolution in Acidic Media. *ChemCatChem* **2014**, *6*, 2219−2223.
(1259) Gatalo, M.; Jovanovič, P.; Polymeros, G.; Grote, J.-P.; Pavlišič, A.; Ruiz- Zepeda, F.; Šelih, V. S.; Šala, M.; Hočevar, S.; Bele, M.; et al. Positive Effect of Surface Doping with Au on the Stability of Pt-Based Electrocatalysts. *ACS Catal.* **2016**, *6*, 1630−1634.
(1260) Kasian, O.; Geiger, S.; Li, T.; Grote, J.-P.; Schweinar, K.; Zhang, S.; Scheu, C.; Raabe, D.; Cherevko, S.; Gault, B.; et al. Degradation of Iridium Oxides via Oxygen Evolution from the Lattice: Correlating Atomic Scale Structure with Reaction Mechanisms. *Energy Environ. Sci.* **2019**, *12*, 3548−3555.
(1261) Schalenbach, M.; Kasian, O.; Ledendecker, M.; Speck, F. D.; Mingers, A. M.; Mayrhofer, K. J. J.; Cherevko, S. The Electrochemical Dissolution of Noble Metals in Alkaline Media. *Electrocatalysis* **2018**, *9*, 153−161.
(1262) He, Q.; Wan, Y.; Jiang, H.; Pan, Z.; Wu, C.; Wang, M.; Wu, X.; Ye, B.; Ajayan, P. M.; Song, L. Nickel Vacancies Boost Reconstruction in Nickel Hydroxide Electrocatalyst. *ACS Energy Lett.* **2018**, *3*, 1373−1380.
(1263) De La Calle, I.; Cabaleiro, N.; Romero, V.; Lavilla, I.; Bendicho, C. Sample Pretreatment Strategies for Total Reflection X-Ray Fluorescence Analysis: A Tutorial Review. *Spectrochimica Acta Part B: Atomic Spectroscopy* **2013**, *90*, 23−54.
(1264) Wobrauschek, P. Total Reflection X-Ray Fluorescence Analysis—a Review. *X-Ray Spectrom.* **2007**, *36*, 289−300.
(1265) Hutton, L. A.; O'Neil, G. D.; Read, T. L.; Ayres, Z. J.; Newton, M. E.; Macpherson, J. V. Electrochemical X-Ray Fluorescence Spectroscopy for Trace Heavy Metal Analysis: Enhancing X-Ray Fluorescence Detection Capabilities by Four Orders of Magnitude. *Anal. Chem.* **2014**, *86*, 4566−4572.
(1266) Chourashiya, M.; Sharma, R.; Andersen, S. M. Accurate Determination of Catalyst Loading on Glassy Carbon Disk and Its Impact on Thin Film Rotating Disk Electrode for Oxygen Reduction Reaction. *Anal. Chem.* **2018**, *90*, 14181−14187.
(1267) Lin, Y.; Deng, C.; Wu, L.; Zhang, Y.; Chen, C.; Ma, W.; Zhao, J. Quantitative Isotope Measurements in Heterogeneous Photocatalysis and Electrocatalysis. *Energy Environ. Sci.* **2020**, *13*, 2602−2617.
(1268) Baltruschat, H. Differential Electrochemical Mass Spectrometry. *J. Am. Soc. Mass Spectrom.* **2004**, *15*, 1693−1706.
(1269) Abd-El-Latif, A. A.; Bondue, C. J.; Ernst, S.; Hegemann, M.; Kaul, J. K.; Khodayari, M.; Mostafa, E.; Stefanova, A.; Baltruschat, H. Insights into Electrochemical Reactions by Differential Electrochemical Mass Spectrometry. *TrAC Trends in Analytical Chemistry* **2015**, *70*, 4−13.
(1270) Hetterscheid, D. G. H. In Operando Studies on the Electrochemical Oxidation of Water Mediated by Molecular Catalysts. *Chem. Commun.* **2017**, *53*, 10622−10631.
(1271) Oberacher, H.; Pitterl, F.; Erb, R.; Plattner, S. Mass Spectrometric Methods for Monitoring Redox Processes in Electrochemical Cells. *Mass Spectrom. Rev.* **2015**, *34*, 64−92.
(1272) Jusys, Z.; Massong, H.; Baltruschat, H. A New Approach for Simultaneous DEMS and EQCM: Electro-oxidation of Adsorbed CO on Pt and Pt-Ru. *J. Electrochem. Soc.* **1999**, *146*, 1093.
(1273) Wonders, A. H.; Housmans, T. H. M.; Rosca, V.; Koper, M. T. M. On-Line Mass Spectrometry System for Measurements at Single-Crystal Electrodes in Hanging Meniscus Configuration. *J. Appl. Electrochem.* **2006**, *36*, 1215−1221.
(1274) Clark, E. L.; Singh, M. R.; Kwon, Y.; Bell, A. T. Differential Electrochemical Mass Spectrometer Cell Design for Online Quantification of Products Produced during Electrochemical Reduction of CO_2. *Anal. Chem.* **2015**, *87*, 8013−8020.

https://doi.org/10.1021/acs.chemrev.3c00005
Chem. Rev. 2023, 123, 12795−13208

(1275) Zwaschka, G.; Nahalka, I.; Marchioro, A.; Tong, Y.; Roke, S.; Campen, R. K. Imaging the Heterogeneity of the Oxygen Evolution Reaction on Gold Electrodes Operando: Activity Is Highly Local. *ACS Catal.* **2020**, *10*, 6084−6093.
(1276) Gaudette, A. F.; Burns, A. W.; Hayes, J. R.; Smith, M. C.; Bowker, R. H.; Seda, T.; Bussell, M. E. Mössbauer Spectroscopy Investigation and Hydrodesulfurization Properties of Iron-Nickel Phosphide Catalysts. *J. Catal.* **2010**, *272*, 18−27.
(1277) McAlpin, J. G.; Surendranath, Y.; Dincă, M.; Stich, T. A.; Stoian, S. A.; Casey, W. H.; Nocera, D. G.; Britt, R. D. EPR Evidence for Co(IV) Species Produced During Water Oxidation at Neutral pH. *J. Am. Chem. Soc.* **2010**, *132*, 6882−6883.
(1278) Gerken, J. B.; McAlpin, J. G.; Chen, J. Y. C.; Rigsby, M. L.; Casey, W. H.; Britt, R. D.; Stahl, S. S. Electrochemical Water Oxidation with Cobalt-Based Electrocatalysts from pH 0-14: The Thermodynamic Basis for Catalyst Structure, Stability, and Activity. *J. Am. Chem. Soc.* **2011**, *133*, 14431−14442.
(1279) Sayler, R. I.; Hunter, B. M.; Fu, W.; Gray, H. B.; Britt, R. D. EPR Spectroscopy of Iron- and Nickel-Doped [ZnAl]-Layered Double Hydroxides: Modeling Active Sites in Heterogeneous Water Oxidation Catalysts. *J. Am. Chem. Soc.* **2020**, *142*, 1838−1845.
(1280) Jiang, P.; Chen, J.-L.; Borondics, F.; Glans, P.-A.; West, M. W.; Chang, C.-L.; Salmeron, M.; Guo, J. In Situ Soft X-Ray Absorption Spectroscopy Investigation of Electrochemical Corrosion of Copper in Aqueous $NaHCO_3$ Solution. *Electrochem. Commun.* **2010**, *12*, 820−822.
(1281) Risch, M.; Stoerzinger, K. A.; Regier, T. Z.; Peak, D.; Sayed, S. Y.; Shao-Horn, Y. Reversibility of Ferri-/Ferrocyanide Redox during Operando Soft X-Ray Spectroscopy. *J. Phys. Chem. C* **2015**, *119*, 18903−18910.
(1282) Erickson, E. M.; Thorum, M. S.; Vasić, R.; Marinković, N. S.; Frenkel, A. I.; Gewirth, A. A.; Nuzzo, R. G. In Situ Electrochemical X-Ray Absorption Spectroscopy of Oxygen Reduction Electrocatalysis with High Oxygen Flux. *J. Am. Chem. Soc.* **2012**, *134*, 197−200.
(1283) Márquez-Montes, R. A.; Collins-Martínez, V. H.; Pérez-Reyes, I.; Chávez-Flores, D.; Graeve, O. A.; Ramos-Sánchez, V. H. Electrochemical Engineering Assessment of a Novel 3D-Printed Filter-Press Electrochemical Reactor for Multipurpose Laboratory Applications. *ACS Sustain. Chem. Eng.* **2020**, *8*, 3896−3905.
(1284) Stühmeier, B. M.; Pietsch, M. R.; Schwämmlein, J. N.; Gasteiger, H. A. Pressure and Temperature Dependence of the Hydrogen Oxidation and Evolution Reaction Kinetics on Pt Electrocatalysts via PEMFC-Based Hydrogen-Pump Measurements. *J. Electrochem. Soc.* **2021**, *168*, 064516.
(1285) Rao, C. N. R.; Subba Rao, G. V. Electrical Conduction in Metal Oxides. *Physica Status Solidi (a)* **1970**, *1*, 597−652.
(1286) Ehlers, J. C.; Feidenhans'l, A. A.; Therkildsen, K. T.; Larrazábal, G. O. Affordable Green Hydrogen from Alkaline Water Electrolysis: Key Research Needs from an Industrial Perspective. *ACS Energy Lett.* **2023**, *8*, 1502−1509.
(1287) Liu, L.; Chen, W.; Li, Y. An Overview of the Proton Conductivity of Nafion Membranes through a Statistical Analysis. *J. Membr. Sci.* **2016**, *504*, 1−9.
(1288) Duan, J.; Chen, S.; Zhao, C. Ultrathin Metal-Organic Framework Array for Efficient Electrocatalytic Water Splitting. *Nat. Commun.* **2017**, *8*, 15341.
(1289) Ji, J.; Hou, Y.; Zhou, S.; Qiu, T.; Zhang, L.; Ma, L.; Qian, C.; Zhou, S.; Liang, C.; Ling, M. Oxygen-Coordinated Low-Nucleus Cluster Catalysts for Enhanced Electrocatalytic Water Oxidation. *Carbon Energy* **2023**, *5*, No. e216.
(1290) Fritz, K. E.; Beaucage, P. A.; Matsuoka, F.; Wiesner, U.; Suntivich, J. Mesoporous Titanium and Niobium Nitrides as Conductive and Stable Electrocatalyst Supports in Acid Environments. *Chem. Commun.* **2017**, *53*, 7250−7253.
(1291) Guo, S.; Liang, S.; Zhang, B.; Fang, G.; Ma, D.; Zhou, J. Cathode Interfacial Layer Formation via in Situ Electrochemically Charging in Aqueous Zinc-Ion Battery. *ACS Nano* **2019**, *13*, 13456−13464.
(1292) Wildfeuer, L.; Gieler, P.; Karger, A. Combining the Distribution of Relaxation Times from EIS and Time-Domain Data for Parameterizing Equivalent Circuit Models of Lithium-Ion Batteries. *Batteries* **2021**, *7*, 52.
(1293) Huang, J.; Sullivan, N. P.; Zakutayev, A.; O'Hayre, R. How Reliable Is Distribution of Relaxation Times (DRT) Analysis? A Dual Regression-Classification Perspective on DRT Estimation, Interpretation, and Accuracy. *Electrochim. Acta* **2023**, *443*, 141879.
(1294) IRENA. *Green Hydrogen Cost Reduction: Scaling up Electrolysers to Meet the 1.5°C Climate Goal*; International Renewable Energy Agency: Abu Dhabi, 2020. https://www.irena.org/-/media/Files/IRENA/Agency/Publication/2020/Dec/IRENA_Green_hydrogen_cost_2020.pdf (accessed 2023-07-26).
(1295) Pivovar, B.; Rustagi, N.; Satyapal, S. Hydrogen at Scale (H_2@Scale): Key to a Clean, Economic, and Sustainable Energy System. *Electrochem. Soc. Interface* **2018**, *27*, 47.
(1296) Lohmann-Richters, F. P.; Renz, S.; Lehnert, W.; Müller, M.; Carmo, M. Review—Challenges and Opportunities for Increased Current Density in Alkaline Electrolysis by Increasing the Operating Temperature. *J. Electrochem. Soc.* **2021**, *168*, 114501.
(1297) Wan, L.; Xu, Z.; Xu, Q.; Pang, M.; Lin, D.; Liu, J.; Wang, B. Key Components and Design Strategy of the Membrane Electrode Assembly for Alkaline Water Electrolysis. *Energy Environ. Sci.* **2023**, *16*, 1384−1430.
(1298) Márquez, R. A.; Kawashima, K.; Son, Y. J.; Rose, R.; Smith, L. A.; Miller, N.; Carrasco Jaim, O. A.; Celio, H.; Mullins, C. B. Tailoring 3D-Printed Electrodes for Enhanced Water Splitting. *ACS Appl. Mater. Interfaces* **2022**, *14*, 42153−42170.
(1299) Glenn, J. R.; Lindquist, G. A.; Roberts, G. M.; Boettcher, S. W.; Ayers, K. E. Standard Operating Procedure for Post-Operation Component Disassembly and Observation of Benchtop Water Electrolyzer Testing. *Front. Energy Res.* **2022**, *10*, 908672.
(1300) Márquez, R. A.; Kawashima, K.; Son, Y. J.; Castelino, G.; Miller, N.; Smith, L. A.; Chukwuneke, C. E.; Mullins, C. B. Getting the Basics Right: Preparing Alkaline Electrolytes for Electrochemical Applications. *ACS Energy Lett.* **2023**, *8*, 1141−1146.
(1301) Lee, J.; Jung, H.; Park, Y. S.; Kwon, N.; Woo, S.; Selvam, N. C. S.; Han, G. S.; Jung, H. S.; Yoo, P. J.; Choi, S. M.; et al. Chemical Transformation Approach for High-Performance Ternary NiFeCo Metal Compound-Based Water Splitting Electrodes. *Appl. Catal. B: Environ.* **2021**, *294*, 120246.
(1302) Zhao, Y.; Sun, M.; Wen, Q.; Wang, S.; Han, S.; Huang, L.; Cheng, G.; Liu, Y.; Yu, L. Homologous NiCoP@NiFeP Heterojunction Array Achieving High-Current Hydrogen Evolution for Alkaline Anion Exchange Membrane Electrolyzers. *J. Mater. Chem. A* **2022**, *10*, 10209−10218.
(1303) Chanda, D.; Kannan, K.; Gautam, J.; Meshesha, M. M.; Jang, S. G.; Dinh, V. A.; Yang, B. L. Effect of the Interfacial Electronic Coupling of Nickel-Iron Sulfide Nanosheets with Layer Ti_3C_2 MXenes as Efficient Bifunctional Electrocatalysts for Anion-Exchange Membrane Water Electrolysis. *Appl. Catal. B: Environ.* **2023**, *321*, 122039.
(1304) Schalenbach, M.; Kasian, O.; Mayrhofer, K. J. J. An Alkaline Water Electrolyzer with Nickel Electrodes Enables Efficient High Current Density Operation. *Int. J. Hydrogen Energy* **2018**, *43*, 11932−11938.
(1305) King, L. A.; Hubert, M. A.; Capuano, C.; Manco, J.; Danilovic, N.; Valle, E.; Hellstern, T. R.; Ayers, K.; Jaramillo, T. F. A Non-Precious Metal Hydrogen Catalyst in a Commercial Polymer Electrolyte Membrane Electrolyser. *Nat. Nanotechnol.* **2019**, *14*, 1071−1074.
(1306) Chen, L.; Zhang, X.; Chen, A.; Yao, S.; Hu, X.; Zhou, Z. Targeted Design of Advanced Electrocatalysts by Machine Learning. *Chin. J. Catal.* **2022**, *43*, 11−32.
(1307) Mai, H.; Le, T. C.; Chen, D.; Winkler, D. A.; Caruso, R. A. Machine Learning for Electrocatalyst and Photocatalyst Design and Discovery. *Chem. Rev.* **2022**, *122*, 13478−13515.

https://doi.org/10.1021/acs.chemrev.3c00005
Chem. Rev. 2023, 123, 12795−13208

(1308) Steinmann, S. N.; Wang, Q.; Seh, Z. W. How Machine Learning Can Accelerate Electrocatalysis Discovery and Optimization. *Mater. Horiz.* **2023**, *10*, 393−406.
(1309) Zhang, X.; Tian, Y.; Chen, L.; Hu, X.; Zhou, Z. Machine Learning: A New Paradigm in Computational Electrocatalysis. *J. Phys. Chem. Lett.* **2022**, *13*, 7920−7930.
(1310) Liu, J.; Luo, W.; Wang, L.; Zhang, J.; Fu, X.-Z.; Luo, J.-L. Toward Excellence of Electrocatalyst Design by Emerging Descriptor-Oriented Machine Learning. *Adv. Funct. Mater.* **2022**, *32*, 2110748.
(1311) Wang, X.; Xiao, B.; Li, Y.; Tang, Y.; Liu, F.; Chen, J.; Liu, Y. First-Principles Based Machine Learning Study of Oxygen Evolution Reactions of Perovskite Oxides Using a Surface Center-Environment Feature Model. *Appl. Surf. Sci.* **2020**, *531*, 147323.
(1312) Ge, L.; Yuan, H.; Min, Y.; Li, L.; Chen, S.; Xu, L.; Goddard, W. A. I. Predicted Optimal Bifunctional Electrocatalysts for the Hydrogen Evolution Reaction and the Oxygen Evolution Reaction Using Chalcogenide Heterostructures Based on Machine Learning Analysis of in Silico Quantum Mechanics Based High Throughput Screening. *J. Phys. Chem. Lett.* **2020**, *11*, 869−876.
(1313) Ling, C. A Review of the Recent Progress in Battery Informatics. *npj Comput. Mater.* **2022**, *8*, 1−22.
(1314) Lombardo, T.; Duquesnoy, M.; El-Bouysidy, H.; Årén, F.; Gallo-Bueno, A.; Jørgensen, P. B.; Bhowmik, A.; Demortière, A.; Ayerbe, E.; Alcaide, F.; et al. Artificial Intelligence Applied to Battery Research: Hype or Reality? *Chem. Rev.* **2022**, *122*, 10899−10969.
(1315) Seifrid, M.; Pollice, R.; Aguilar-Granda, A.; Morgan Chan, Z.; Hotta, K.; Ser, C. T.; Vestfrid, J.; Wu, T. C.; Aspuru-Guzik, A. Autonomous Chemical Experiments: Challenges and Perspectives on Establishing a Self-Driving Lab. *Acc. Chem. Res.* **2022**, *55*, 2454−2466.
(1316) Abolhasani, M.; Kumacheva, E. The Rise of Self-Driving Labs in Chemical and Materials Sciences. *Nat. Synth.* **2023**, *2*, 483−492.
(1317) Anantharaj, S.; Noda, S.; Driess, M.; Menezes, P. W. The Pitfalls of Using Potentiodynamic Polarization Curves for Tafel Analysis in Electrocatalytic Water Splitting. *ACS Energy Lett.* **2021**, *6*, 1607−1611.
(1318) Morales, D. M.; Risch, M. Seven Steps to Reliable Cyclic Voltammetry Measurements for the Determination of Double Layer Capacitance. *J. Phys. Energy* **2021**, *3*, 034013.
(1319) Trunschke, A. Prospects and Challenges for Autonomous Catalyst Discovery Viewed from an Experimental Perspective. *Catal. Sci. Technol.* **2022**, *12*, 3650−3669.
(1320) Batchellor, A. S.; Boettcher, S. W. Pulse-Electrodeposited Ni-Fe (Oxy)Hydroxide Oxygen Evolution Electrocatalysts with High Geometric and Intrinsic Activities at Large Mass Loadings. *ACS Catal.* **2015**, *5*, 6680−6689.
(1321) Yoon, Y.; Yan, B.; Surendranath, Y. Suppressing Ion Transfer Enables Versatile Measurements of Electrochemical Surface Area for Intrinsic Activity Comparisons. *J. Am. Chem. Soc.* **2018**, *140*, 2397−2400.
(1322) Shinagawa, T.; Garcia-Esparza, A. T.; Takanabe, K. Insight on Tafel Slopes from a Microkinetic Analysis of Aqueous Electrocatalysis for Energy Conversion. *Sci. Rep.* **2015**, *5*, 13801.
(1323) Peugeot, A.; Creissen, C. E.; Karapinar, D.; Tran, H. N.; Schreiber, M.; Fontecave, M. Benchmarking of Oxygen Evolution Catalysts on Porous Nickel Supports. *Joule* **2021**, *5*, 1281−1300.
(1324) Son, Y. J.; Kawashima, K.; Márquez, R. A.; Smith, L. A.; Chukwuneke, C. E.; Mullins, C. B. Key Concepts for Understanding Alkaline Oxygen Evolution Reaction at the Atomic/Molecular Scale. *Curr. Opin. Electrochem.* **2023**, *39*, 101298.

NOTE ADDED AFTER ASAP PUBLICATION

This paper was published ASAP on November 15, 2023, with errors in Figure 2 and eqs 1−6. The corrected version was reposted on December 13, 2023.

https://doi.org/10.1021/acs.chemrev.3c00005
Chem. Rev. 2023, 123, 12795−13208